2009

Proceedings of the 2009 Monitoring Research Review:
Ground-Based Nuclear Explosion Monitoring Technologies

To view these Proceedings online, visit
https://na22.nnsa.doe.gov/mrr/2009

Vol. I

Proceedings of the 2009 Monitoring Research Review: Ground-Based Nuclear Explosion Monitoring Technologies

September 21–23, 2009

Tucson, Arizona

Volume I

Seismic Regional Characterizationand Wave Propagation
Seismic Event Detection and Location
Seismic Identification and Source Characterization

Approved for Public Release; further dissemination unlimited.

National Nuclear Security Administration

AIR FORCE RESEARCH LABORATORY

LA-UR-09-05276

ACKNOWLEDGEMENTS

The National Nuclear Security Administration (NNSA) and the Air Force Research Laboratory (AFRL) gratefully acknowledge the important contributions of the following people for their work to produce the ***Proceedings of the 2009 Monitoring Research Review: Ground-Based Nuclear Explosion Monitoring Technologies.***

Authors of papers for excellent research, technical documentation, and cooperation with electronic submission processes.

Dr. Anton M. Dainty, Mr. Robert J. Raistrick, Dr. Frederick R. Schult, AFRL/VSBYE, and ***Ms. Doris Richards***, ESC/PAM, for review and clearance of abstracts and papers related to AFRL contracts.

Dr. Stanley D. Ruppert, Lawrence Livermore National Laboratory (LLNL), for assistance in ensuring that the CDs could be read on a variety of platforms and for burning the CDs.

Mr. Marvin A. Wetovsky, Los Alamos National Laboratory (LANL), Managing Editor of the Proceedings.

Ms. Eileen F. Patterson, LANL, for technical editing of papers.

Dr. Marie D. Arrowsmith, LANL, for technical editing of papers, design of the CD label, composition of the hardcopy covers, and numerous technical consultations.

Ms. Leslie A. Casey, NNSA, for review and clearance of abstracts and papers related to NNSA contracts and for NNSA overall support of the Proceedings.

Ms. Mary L. Girven, Sandia National Laboratories (SNL), for making everyone's job easier with web-based technology for abstract and paper submission, on-line review and approval tools, and creation of the master files for the hardcopy, CD, and website versions of the Proceedings.

Ms. Guadalupe (Lupe) Massoth, SNL, for providing assistance to Mary Girven on website development and help in creating the master files.

Dr. William R. Wallter, LLNL; ***Dr. Stephen C. Myers***, LLNL; ***Dr. Dale N. Anderson***, LANL, ***Mr. Ward L. Hawkins***, LANL; ***Dr. Martin E. Keillor,*** Pacific Northwest National Laboratory (PNNL); ***Dr. Theodore W. Bowyer***, PNNL; ***Dr. Timothy S. McDonald***, SNL; and ***Dr. Christopher J. Young***, SNL, for a myriad of internal management and technical reviews of NNSA abstracts and papers.

PREVIOUS PROCEEDINGS

Year	Title of the Proceedings
2008	Proceedings of the 30th Monitoring Research Review: Ground-Based Nuclear Explosion Monitoring Technologies
2007	Proceedings of the 29th Monitoring Research Review: Ground-Based Nuclear Explosion Monitoring Technologies
2006	Proceedings of the 28th Seismic Research Review: Ground-Based Nuclear Explosion Monitoring Technologies
2005	Proceedings of the 27th Seismic Research Review: Ground-Based Nuclear Explosion Monitoring Technologies
2004	Proceedings of the 26th Seismic Research Review: Trends in Nuclear Explosion Monitoring
2003	Proceedings of the 25th Seismic Research Review: Nuclear Explosion Monitoring: Building the Knowledge Base
2002	Proceedings of the 24th Seismic Research Review: Nuclear Explosion Monitoring: Innovation and Integration
2001	Proceedings of the 23rd Seismic Research Review: Worldwide Monitoring of Nuclear Explosions
2000	Proceedings of the 22nd Annual DoD/DoE Seismic Research Symposium: Planning for Verification of and Compliance with the Comprehensive Nuclear-Test-Ban Treaty (CTBT)
1999	Proceedings of the 21st Seismic Research Symposium: Technologies for Monitoring the Comprehensive Nuclear-Test-Ban Treaty

Table of Contents - Volume I

1. Seismic Regional Characterization and Wave Propagation 1

1-01 **Ammon, C. and M. Maceira**
3D Modeling of Iran and Surrounding Areas from Simultaneous Inversion of Multiple Geophysical Datasets 3

1-02 **Baker, D., W. Kim, H. Patton, G. Randall, and P. Richards**
Improvements to a Major Digital Archive of Seismic Waveforms from Nuclear Explosions: the Borovoye Seismogram Archive 12

1-03 **Bergman, E., E. Engdahl, M. Ritzwoller, and S. Myers**
Crustal Structure from In-Country and Ground-Truth Data 22

1-04 **Bonner, J., D. Harkrider, J. Britton, and J. Orrey**
Modeling Regional Seismic Phases and Coda from Earthquakes and Explosions Using Generalized Fourier Methods in 2D/3D 32

1-05 **Ferris, A., D. Reiter, and K. Murphy**
Improved Phase Characterization of Far-Regional Body Wave Arrivals in Central Asia 42

1-06 **Fisk, M. and W. Phillips**
A Stepwise, Iterative Procedure to Constrain Stress Drop, Regional Attenuation Models, and Site Effects 52

1-07 **Gerstoft, P., J. Zhang, and S. Taylor**
Estimating Bodywave Arrivals and Attenuation from Seismic Noise 62

1-08 **Hauser, J., K. Dyer, M. Pasyanos, H. Bungum, J. Faleide, and S. Clark**
Development and Tuning of a 3-D Stochastic Inversion Methodology to the European Arctic 73

1-09 **Hipp, J., M. Chang, M. Gonzales, B. Lawry, A. Encarnacao, and G. Barker**
Global 3D Seismic Tomography Using Multi-Core Distributed Memory Parallel Computers 84

1-10 **Julia, J., A. Nyblade, S. Hansen, A. Rodgers, and E. Matzel**
Developing Regionalized Models of Lithospheric Thickness and Velocity Structure Across Eurasia and the Middle East from Jointly Inverting P-Wave and S-Wave Receiver Functions with Rayleigh Wave Group and Phase Velocities 93

1-11 **Lay, T., X. Xie, and X. Yang**
Development of Regional Phase Tomographic Attenuation Models for Eurasia 101

1-12 **Maceira, M., C. Rowe, H. Zhang, R. Modrak, M. Begnaud, L. Steck, G. Randall, and X. Yang**
Advanced Multivariate Inversion Techniques for High Resolution 3D Geophysical Modeling 111

1-13 **Mackey, K. and H. Hartse**
Analysis of Digitized Seismograms from Russian Geophysical Survey Stations of Soviet Peaceful Nuclear Explosions 121

1-14 **Mackey, K., K. Fujita, H. Hartse, M. Begnaud, and M. Pasyanos**
Seismic and Geophysical Characterization of Northern Asia 131

1-15 **Martin, R., L. Gulen, Y. Sun, and M. Toksoz**
Extension of the Caucasus Seismic Information Network Study Into Central Asia 140

1-16 **Mellors, R., R. Gok, M. Pasyanos, G. Skobeltsyn, E. Sandvol, U. Teoman, G. Yetirmishli, and T. Godoladze**
High-Resolution Seismic Velocity and Attenuation Models of the Caucasus-Caspian Region 150

1-17 **Nabelek, J., J. Braunmiller, and W. Phillips**
Source and Path Calibration in Regions of Poor Crustal Propagation Using Temporary, Large-Aperture, High-Resolution Seismic Arrays 158

1-18 **Nowack, R., W. Chen, and T. Tseng**
Frequency-Dependent Nature of Pn in Western China 166

1-19 **Pulliam, J., M. Sen, N. Simmons, and M. Pasyanos**
Seismic Velocity Estimation in the Middle East from Multiple Waveform Functionals: P & S Receiver Functions, Waveform Fitting, and Surface Wave Dispersion 176

1-20 **Reiter, D., W. Rodi, and S. Myers**
Estimating the Uncertainty and Predictive Capabilities of Three-Dimensional Earth Models 184

1-21 **Savage, B., D. Peter, B. Covellone, A. Rodgers, and J. Tromp**
Progress towards Next Generation, Waveform Based Three-Dimensional Models and Metrics to Improve Nuclear Explosion Monitoring in the Middle East 194

1-22 **Shen, Y., W. Zhang, Z. Zhang, L. Zhao, and X. Yang**
Unified Regional Tomography and Source Moment Tensor Inversions Based on Finite-Difference Strain Green Tensor Databases 201

1-23 **Simmons, N., S. Myers, and A. Ramirez**
Multi-Resolution Seismic Tomography Based on a Recursive Tessellation Hierarchy 211

1-24 **Song, X., Z. Xu, X. Sun, S. Zheng, Y. Yang, and M. Ritzwoller**
Surface Wave Dispersion Measurements and Tomography from Ambient Seismic Noise Correlation in China 221

1-25 **Stump, B., R. Burlacu, C. Hayward, T. Kim, S. Arrowsmith, R. Zhou, and K. Pankow**
Seismo-Acoustic Generation by Earthquakes and Explosions and Near-Regional Propagation 230

1-26 **Toksoz, M., R. Van der Hilst, Y. Sun, H. Zhang, X. Zeng, and S. Pei**
Seismic Tomography of the Arabian-Eurasian Collision Zone and Surrounding Areas 239

1-27 **Young, C., S. Ballard, J. Hipp, M. Chang, J. Lewis, C. Rowe, and M. Begnaud**
A Global 3D P-Velocity Model of the Earth's Crust and Mantle for Improved Event Location 249

1-28 **Zhang, H., K. Mackey, K. Fujita, C. Thurber, L. Steck, C. Rowe, S. Roecker, and M. Toksoz**
Regional-Scale Differential Time Tomography Methods: Development and Application to the Siberia Data Set 258

2. Seismic Event Detection and Location 269

2-01 **Abramovich, I. and T. Zhu**
Next Generation Robust Low-Noise Seismometer for Nuclear Monitoring 271

2-02 **Brogan, R., S. Nava, R. Read, Y. Jia, N. Brachet, and J. Coyne**
Seismo-Acoustic Analysis in the Zalesovo Region of Central Asia 287

2-03 **Carr, D., G. Bogart, S. Goodman, P. Baldwin, H. Milburn, and D. Robinson**
Development of a Laser Interferometric Miniature Seismometer 296

2-04 **Carr, D., M. Resor, C. Young, and M. Procopio**
Exploring the Limits of Waveform Correlation Event Detection as Applied to the 1994 Northridge Earthquake Aftershock Sequence 303

2-05 **Flanagan, M., S. van der Lee, S. Myers, S. Chang, and M. Pasyanos**
Regional Travel-Time and Location Uncertainty Assessment along the Tethyan Margin Using a New Three-Dimensional P-Velocity Model 313

2-06 **Fourguette, D., M. Otugen, L. Larocque, G. Ritter, T. Ioppolo, and D. Hart**
Optical MEMS-Based Seismometer 323

2-07 **Garcia, C., G. Onaran, B. Avenson, M. Ellis, and N. Hall**
Micro-Seismometers via Advanced Meso-Scale Fabrication 330

2-08 **Leugoud, R.**
Seismic Detection Utilizing a Mini Sensor 338

2-09 **Merchant, B. and M. Okandan**
An Interferometric MEMS Seismometer: Design and Testing 352

2-10 **Myers, S., M. Begnaud, S. Ballard, M. Pasyanos, W. Phillips, A. Ramirez, M. Antolik, K. Hutchenson, G. Wagner, J. Dwyer, and C. Rowe**
A Model and Methods for Regional Travel-Time Calculation 359

2-11 **Ringdal, F., D. Harris, D. Dodge, and S. Gibbons**
Adaptive Waveform Correlation Detectors for Arrays: Algorithms for Autonomous Calibration 369

2-12 **Ringdal, F., D. Harris, T. Kvaerna, and S. Gibbons**
Expanding Coherent Array Processing to Larger Apertures Using Empirical Matched Field Processing 379

2-13 **Ritzwoller, M., M. Barmin, A. Levshin, and Y. Yang**
Epicentral Location of Regional Seismic Events Based on Empirical Green's Functions from Ambient Noise 389

2-14 **Rodi, W., D. Reiter, S. Myers, and N. Simmons**
A Unified Approach to Joint Regional/Teleseismic Calibration and Event Location with a 3D Earth Model 399

2-15 **Rowe, C., S. Ballard, M. Begnaud, C. Young, L. Steck, and J. Hipp**
Validating 3D Geophysical Models for use in Global Travel-Time Calculation for Improved Event Locations 408

3. Seismic Identification and Source Characterization 417

3-01 **Abercrombie, R., K. Mayeda, W. Walter, G. Viegas, and R. Gok**
Seismic Source Scaling and Discrimination in Diverse Tectonic Environments 419

3-02 **Anderson, D.**
Sources of Error: Regional Amplitude and Teleseismic Magnitude Discriminants 430

3-03 **Arrowsmith, M., B. Stump, S. Arrowsmith, and M. Hedlin**
Mining Explosion Identification and Discriminant Assessment in Two Unique Regions 436

3-04 **Bonner, J., A. Stroujkova, R. Shumway, R. Herrmann, and D. Anderson**
Incorporating Love- and Rayleigh-Wave Magnitudes, Unequal Earthquake and Explosion Variance Assumptions, and Intrastation Complexity for Improved Event Screening 445

3-05 **Dreger, D., S. Ford, and W. Walter**
Identifying Isotropic Events Using a Regional Moment Tensor Inversion Technique 455

3-06 **Fisk, M., S. Taylor, W. Walter, and G. Randall**
Seismic Event Discrimination Using Two-Dimensional Grids of Regional P/S Spectral Ratios: Applications to Novaya Zemlya and the Korean Peninsula 465

3-07 **Ford, S., W. Walter, S. Ruppert, E. Matzel, T. Hauk, and R. Gok**
Towards an Empirically Based Parametric Explosion Spectral Model 475

3-08 **Julia, J., A. Nyblade, R. Gok, W. Walter, L. Linzer, and R. Durrheim**
Developing and Exploiting a Unique Dataset from South African Gold Mines for Source Characterization and Wave Propagation 482

3-09 **Leidig, M., R. Martin, P. Boyd, J. Bonner, and A. Stroujkova**
Quantification of Rock Damage from Small Explosions and its Effect on Shear-Wave Generation: Phase I—Homogenous Crystalline Rock 492

3-10 **Mayeda, K.**
Small Event Yield and Source Characterization Using Local P and S-wave Coda Source Spectra 502

3-11 **Murphy, J. and B. Barker**
An Analysis of the Seismic Source Characteristics of Explosions in Low-Coupling Dry Porous Media 506

3-12 **Pasyanos, M., W. Walter, E. Matzel, A. Rodgers, S. Ford, R. Gok, and J. Sweeney**
Improving Earthquake-Explosion Discrimination Using Attenuation Models of the Crust and Upper Mantle 516

3-13 **Patton, H.**
Explosion Source Model Development in Support of Seismic Monitoring Technologies: Applications of New Models for Shock-Induced Tensile Failure 525

3-14 **Phillips, W., X. Yang, G. Randall, H. Hartse, and R. Stead**
Regional Phase Attenuation Tomography for Central and Eastern Asia 536

3-15 **Rodgers, A., O. Vorobiev, A. Petersson, B. Sjogreen, and M. Avants**
Toward End-To-End Seismic Simulations for Nuclear Explosion Monitoring 547

3-16 **Sammis, C., H. Bhat, and A. Rosakis**
Numerical Modeling of S-Wave Generation by Fracture Damage in Underground Nuclear Explosions 557

3-17 **Srinivasan, C., Y. Willy, and P. Nawani**
Source Parameters of Seismic Events in the Mines of Kolar Gold Fields 566

3-18 **Stevens, J. and H. Xu**
Wave Propagation from Complex 3D Sources Using the Representation Theorem 574

3-19 **Stroujkova, A. and J. Bonner**
Improving Ms:mb Discrimination Using Maxmimum Likelihood Estimation: Application to Middle East Earthquake Data 582

3-20 **Stroujkova, A., J. Bonner, X. Yang, B. Stump, and W. Walter**
Source Mechanisms for Explosions in Barre Granite 592

Seismic Regional Characterization and Wave Propagation

3D MODELING OF IRAN AND SURROUNDING AREAS FROM SIMULTANEOUS INVERSION OF MULTIPLE GEOPHYSICAL DATASETS

Charles J. Ammon[1] and Monica Maceira[2]

Penn State[1] and Los Alamos National Laboratory[2]

Sponsored by the Air Force Research Laboratory and the National Nuclear Security Administration

Award Nos. FA8718-09C-0007[1] and LA09-BAA09-12-NDD03[2]
Proposal No. BAA09-12

ABSTRACT

The objective of this work is to help improve seismic monitoring technology through the development and application of advanced multivariate inversion techniques to generate realistic, comprehensive, and high-resolution 3D models of the seismic structure of the crust and upper mantle that satisfy independent geophysical datasets. Our focus is on the region surrounding Iran from the east coast of the Mediterranean in the west, to Pakistan in the east, an area of prime importance to nuclear explosion monitoring (NEM), and a region with adequate calibration events to validate our model and to quantify its accuracy. Specifically, we plan to integrate surface-wave dispersion, receiver function, and satellite and ground-based gravity observations to help constrain the shallow seismic structure in the Arabian-Eurasian collision zone. Building on our earlier work combining receiver functions and surface wave dispersion, and surface-wave dispersion and gravity, we plan to continue to integrate geophysical data sets to create more compatible earth models. We also intend to explore geologically based smoothness constraints to help resolve sharp features in the underlying shallow 3D structure.

OBJECTIVES

The National Nuclear Security Administration (NNSA) and Air Force Research Laboratory (AFRL) have decided to investigate 3D modeling as part of the effort to improve knowledge of Earth's compressional and shear velocity structure and to enable a reduction of uncertainty in our ability to accurately detect, locate, and identify small (mb < 4) seismic events, which will lead to improved capabilities for NEM. For seismically active areas, with good ground-truth event coverage, earth models with limited accuracy can be corrected by interpolating results from nearby 'ground-truth' events (using the kriging methodology) making it possible to detect, locate, and identify large events even with limited resolution of Earth's structure. However, such approaches may not be effective for smaller events, and remain a challenge for aseismic regions. To improve monitoring capability in such instances, we must develop better seismic models.

The objective of this work is to help improve seismic monitoring technology through the development and application of advanced multivariate inversion techniques to generate realistic, comprehensive, and high-resolution 3D models of the seismic structure of the crust and upper mantle that satisfy independent geophysical datasets. Our focus is on the region surrounding Iran (Figure 1) from the east coast of the Mediterranean in the west, to Pakistan in the east, an area of prime importance to NEM, and a region with adequate calibration events to validate our models and to quantify their accuracy.

Background

Estimating subsurface geologic variations is a challenge. Seismologists have worked on the problem for more than a century (e.g., Milne, 1899; Macelwane and Sohon, 1936; Dahlen and Tromp, 1999). As data quantity and quality and computational ability have improved, we have made important advances in our understanding of the subsurface. Our best knowledge applies to the shallowest regions as well as depths with the sharpest global interfaces (sediment-basement contacts, the base of the crust, base of the mantle, and transitions near 410 km and 660 km depths), where resolution is improved as a result of the strong interactions of body waves with sharp geologic transitions (e.g., Helmberger, 1968; Langston, 1979; Shearer, 1991; Lay t al., 2004). We have also done well modeling regions with smooth velocity changes such as the lower mantle, which allows us to exploit the information in teleseismic body-wave travel times to locate seismic sources reasonably well (e.g., Kennett and Engdahl, 1991). Still, many details within and just beneath the lithosphere elude us. We have been able to surmise that geologic variations here are substantial, and we know that they frustrate attempts to use robust observations such as regional seismic travel times to locate events in many parts of the Earth (e.g., Bondar et al., 2004).

Travel-time based tomography opened the doors to 3D imaging but the models remain blurry, often suffer from interpretational ambiguity, and are not easily used to predict other, independent seismic observations. From our own analyses (Maceira et al., 2005), we have seen how high-resolution surface-wave tomography fails to produce the extremes in seismic shear-wave speed that are evident from independent observations (we discuss more details below). In particular, achieving a model with low enough seismic wave speeds within the Tarim Basin to match seismograms from high-quality observations remains an issue. Waveform tomography methods improve the situation somewhat, including information from both the amplitude and phase of the signal, but restriction of these methods to lower frequency bands limits the resolution of the methods. More recent finite-frequency methods (e.g., Zhou et al., 2004; Dahlen and Zhou, 2006) and adjoint methods (e.g., Tarantola, 1984; Tromp et al., 2008) offer more complete approaches to modeling waveforms and computing sensitivity kernels. But even these approaches face limits imposed by data bandwidth. In any event, such fully 3D waveform methods could benefit greatly from accurate, if approximate, starting models derived from more piecewise interpretation of seismic observables combined with other observations.

RESEARCH ACCOMPLISHED

Our award was made late in the Spring of 2009, so much of this section is a review of earlier work upon which future work will be based – and much of that work was more thoroughly documented in earlier Seismic and Monitoring Research Review Proceedings. We direct the reader to those compilations for greater detail. We begin with a simple conceptual illustration of the challenges we face.

Including Geologic Information

Geologic boundaries can be sharp, and a sharp geologic transition can cause problems when we use smooth seismic models to predict observations for events or stations located near the sharp geologic transition (throughout this report sharp should be interpreted to mean sharp relative to typical seismic wavelengths). A smooth model can predict the travel times well if the source and the station are located in regions with smooth velocity structures that are well modeled in smooth earth models. Thus to be generally applicable, our models should contain sharp features where needed (ocean-continent transitions, across major geologic terrane boundaries, etc.). How can we reconstruct geologic images with sharp lateral boundaries? Or how can we use long-period observations to create models that we can use to estimate short-period wave travel times and amplitudes? Imaging sharp boundaries requires broadband observations. We are, however, usually limited in the short period bands because of their strong sensitivity to structure and substantial spatial aliasing; we are often limited at the long-period end by noise (i.e., long-period signals from many small events are smaller than background seismic ground motions). Even when they are available, long period signals average the heterogeneity over broad regions. Thus arises the conundrum of resolving geologic detail needed to explain short-period observations using long-period data, which leads to the problems associated with using models derived using long periods to account for or remove propagation effects from short-period signals.

To produce models that have realistic 'sharp' boundaries requires that we include independent information on the location of those boundaries. Such information is available (for the shallow part of the model) in independent data sets such as gravity, surface geologic maps, and even something as simple as topography. As part of this work, we plan to resolve sharp features by adapting our imaging algorithms to allow the inclusion of geologic information on the location and nature of the boundary into shear-velocity inversions that permit such features (implemented through custom geologic smoothness constraints that allow velocities to be de-correlated across major geologic transitions). Including a priori information into an inversion is obviously only as good as the information that is included. Thus the inclusion of this type of information into the reconstruction of shear-velocity models of the subsurface must proceed carefully and include documentation of the importance of the assumed a priori information on the resulting model. From a probabilistic approach, uncertainties on the a priori information need to be combined and included in the computations of the shear-wave speeds.

Combining Gravity And Rayleigh-Wave Dispersion Observations

Inversion of surface wave dispersion observations is a standard method for estimating 3D shear velocity structure of Earth's crust and upper mantle. Nevertheless, it is well known that traditional state-of-the-art inversion techniques suffer from poor resolution and nonuniqueness, especially when a single surface wave mode is used (Huang et al., 2003). This is particularly true at shallow depths where the shorter periods, which are primarily sensitive to upper crustal structures, are difficult to measure, especially in tectonically and geologically complex areas. On the other hand, gravity inversions have the greatest resolving power at shallow depths since gravity anomalies decrease in amplitude and increase in wavelength with increasing depth. Gravity measurements also supply constraints on rock density variations. Thus by combining surface-wave dispersion and gravity observations in a single inversion, we can obtain a self-consistent high-resolution 3D shear-velocity/density model with increased resolution of shallow geologic structures.

As an example, consider a small study of a joint surface-wave/gravity inversion performed for the Tarim Basin in western China, which shows the promise of this approach (Maceira and Ammon, 2009). We used gravity observations extracted from the global gravity model derived from the GRACE satellite mission (Tapley et al., 2005). Specifically, we combined Bouguer gravity anomalies with high-resolution surface-wave slowness tomographic maps (Maceira et al., 2005) that provide group velocity dispersion values in the period range between 8 and 100 s. Figure 2 shows the gravity (bottom left) and dispersion (top left) data for a typical cell in our gridded model together with the fits to these observations resulting from the inversion of only dispersion data (second column from the left), from the inversion of only gravity data (third column from the left), and from the joint inversion of both data (right column). The best fit to the gravity anomalies comes from inverting the gravity data alone, meanwhile that same model is not able to fit the dispersion observations. In the same way, the best fit to the observed dispersion values results from inverting dispersion observations alone, but this model does not predict the gravity observations adequately. The 3D velocity model obtained from the joint inversion fits both data simultaneously and reasonably well.

Figure 3 shows the 3D shear-wave speeds derived from the joint inversion at depths of 2, 6, 10, 14, 28, 46, 55, 75, and 100 km. In general, the model agrees well with the main features observed in previous studies (e.g., Villasenor

et al., 2001; Ritzwoller et al., 2002; Liang et al., 2004; Hearn et al., 2004; Sun et al., 2004; Sun and Toksoz, 2006; Huang and Zhao, 2006). At shallow depths, low velocities in the Tarim and Junggar basins dominate the images. This is a predictable result because of the clear presence of low velocities associated with the known major sedimentary basins in the tomographic images at short periods (e.g., Maceira et al., 2005). However, the seismic wave speeds in the model's basins is lower than those obtained without including the gravity in the inversion. We think that this is an improvement of our 3D model since seismic discrimination has proven the need of slower velocities at shorter periods (i.e., shallower layers) in those sedimentary basins (H. J. Patton, see Acknowledgements). Although improved, note that the inversion needs further refinement since the high wavenumber features at depths of 75 and 100 km must be artifacts – none of the data used in the inversion can constrain such features (long-period dispersion and gravity).

To quantify the improvement in the shallow parts of the velocity model, we tested the ability of the 3D model to predict surface-wave arrival times at short periods, which is necessary for performing surface-wave magnitude measurements, which can help reduce the detection threshold for seismic discrimination (Taylor and Patton, 2006). We applied the method described by Maceira (2006) to a set of waveforms from 26 nuclear explosions. The new 3D model is able to better predict the arrival of the surface waves at shorter periods. We found that in 73% of the cases, the 3D model from the joint inversion predicts the surface wave arrival times of short period Rayleigh waves when the dispersion-only inversion model does not. The combination of multiple and complementary geophysical data (surface wave dispersion observations and gravity measurements in this case) in a simultaneous inversion not only offers a simple and elegant compromise between fitting both data sets, but actually improves the geophysical model in a tangible way to more confidently and accurately detect, locate, and identify small seismic events, which can help improve NEM capabilities.

CONCLUSIONS

We have initiated a two-year project to map the subsurface geologic variations using seismic dispersion, gravity, and receiver-function observations. We face significant challenges in our efforts to include effective point constraints on structure (receiver functions) with the spatially continuous surface-wave tomography and gravity observations. Our work complements ongoing work at Los Alamos National Laboratory to integrate body-wave travel times into the same formalism. The basic philosophy is that models that explain more data are better. The ultimate utility of the derived earth models is to provide improved predictive capabilities for routine seismic analyses and to provide adequate starting models for 3D waveform inversion approaches.

ACKNOWLEDGEMENTS

We thank the scientists, engineers, and technicians that have created the seismic recording systems and networks that provide excellent broad-band seismic observations. In particular, we thank the USGS and the IRIS Consortia (NSF) who share information and data with the global community in an effective and efficient manner. We also thank the many international groups involved in collecting and sharing quality seismic observations. We also thank Wessel and Smith (1991), the developers of the Generic Mapping Tools software that we use to create many of the illustrations of our research. Finally, we would like to thank Howard J. Patton for information gleaned from personal communications.

REFERENCES

Bondar, I., S. C. Myers, R. E. Engdahl, and E. A. Bergman (2004). Epicentre accuracy based on seismic network criteria, *Geophys. J. Int.* 156: 483–496.

Dahlen, F. A. and J. Tromp (1999). *Theoretical Global Seismology*. Princeton University Press, Princeton, NJ, 1025 pp.

Dahlen, F.A. and Y. Zhou (2006). Surface-wave group-delay and attunuation kernels, *Geophys. J. Int*. 165: 545–554.

Hearn, T. M., S. Wang, J. F. Ni, Z. Xu, Y. Yu, and X. Zhang (2004). Uppermost mantle velocities beneath China and surrounding regions, *J. Geophys. Res*., 109, B11301, doi:10.1029/2003JB002874.

Helmberger, D. (1968). The crust-mantle transition in the Bering Sea, *Bull. Seism. Soc. Am*. 58: 179–214.

Huang, J. and D. Zhao (2006). High-resolution mantle tomography of China and surrounding regions, *J. Geophys. Res.* 111: doi:10.1029/2005JB004066.

Huang, Z., W. Su, Y. Peng, Y. Zheng, and H. Li (2003). Rayleigh wave tomography of China and adjacent regions, *J. Geophys. Res*. 108: doi:10.1029/2001JB001696.

Kennett, B. L. N., and E. R. Engdahl (1991). Traveltimes for Global Earthquake Location and Phase Identification, *Geophys. J. Int*. 105: 429–465.

Langston, C. A. (1979). Structure under Mount Rainier, Washington, inferred from teleseismic body waves, *J. Geophys. Res.* 84: 4749–4762.

Lay, T., E. J. Garnero, and S. Russell (2004). Lateral variation of the D'' Discontinuity beneath the Cocos Plate, *Geophys. Res. Lett*. 31: L15612, doi:10.1029/2004GL020300.

Liang, C., X. Song, and J. Huang (2004). Tomographic inversion of Pn travel times in China, *J. Geophys. Res*. 109: B11304, doi:10.1029/2003JB002789.

Maceira, M. and C. J. Ammon (2009). Joint Inversion of Surface Wave Velocity and Gravity Observations and its Application to Central Asian Basins Shear Velocity Structure, *J. Geophys. Res.* 114: B02314, doi:10.1029/2007JB005157.

Maceira, M. (2006). *Surface Waves, Earth Structure, and Seismic Discrimination*, Ph.D. thesis, The Pennsylvania State University, State College, PA.

Maceira, M, S. R. Taylor, C. J. Ammon, X. Yang (2005). High-resolution Rayleigh wave slowness tomography of central Asia, *J. Geophys. Res*. 110: doi:10.1029/2004JB003429.

Macelwane, J. B. and F. W. Sohon (1936). *Introduction to Theoretical Seismology, Part I, Geodynamics*. John Wiley and Sons, Inc., New York, 336 pp.

Milne, J. (1899). *Earthquakes and Other Earth Movements* (4th Edition). D. Appleton and Company, New York, 376 pp.

Ritzwoller, M. H., M. P. Barmin, A. Villaseñor, A. L. Levshin, and E. R. Engdahl (2002). Pn and Sn tomography across Eurasia to improve regional seismic event locations, *Tectonophys*. 358: 39–55.

Shearer, P. M. (1991). Constraints on upper mantle dscontinuities from observations of long-period reflected and converted phases, *J. Geophys. Res*. 96: 18147–18182.

Sun, Y. and M. N. Toksoz (2006). Crustal structure of China and surrounding regions from P wave traveltime tomography, *J. Geophys. Res*. 111: doi:10.1029/2005JB003962.

Sun, Y., X. Li, S. Kuleli, F. D. Morgan, and M. N. Toksoz (2004). Adaptive moving window method for 3D P-Velocity tomography and its application in China, *Bull. Seismo. Soc. Am.* 94: 740–746.

Tapley, B., J. Ries, S. Bettadpur, D. Chambers, M. Cheng, F. Condi, B. Gunter, Z. Kang, P. Nagel, R. Pastor, t. Pekker, S. Poole, and F. Wang (2005). GGM02 - An improved Earth gravity field model from GRACE, *J. Geodesy*, DOI 10.1007/s00190-005-0480-z.

Tarantola, A. (1984). Inversion of seismic reflection data in the acoustic approximation, *Geophysics* 49: 1259–1266.

Taylor, S. R. and H. J. Patton (2006). A probability of detection method for reducing short-period m_b - M_s false alarm rates, *Bull. Seism. Soc. Am*. 96: 1078–1090.

Tromp, J., D. Komatisch, and Q. Liu (2008). Spectral-element and adjoint methods in seismology, *Communications in Comp. Physics* 3: 1–32.

Villaseñor, A., M. H. Ritzwoller, A L. Levshin, M. P. Barmin, E. R. Engdahl, W. Spakman, and J. Trampert (2001). Shear velocity structure of central Eurasia from inversion of surface wave velocities, *Phys. Earth Planet. Inter*. 123: 169–184.

Wessel, P., and W. H. F. Smith (1991). Free software helps map and display data, *EOS, Trans. of Am. Geophys. Union,* 72: 441–445.

Zhou, Y. F. A. Dahlen, G. Nolet, and G. Laske (2004). Finite-frequency effects in global surface-wave tomography, *Geophys. J. Int*. 163: 1087–1111.

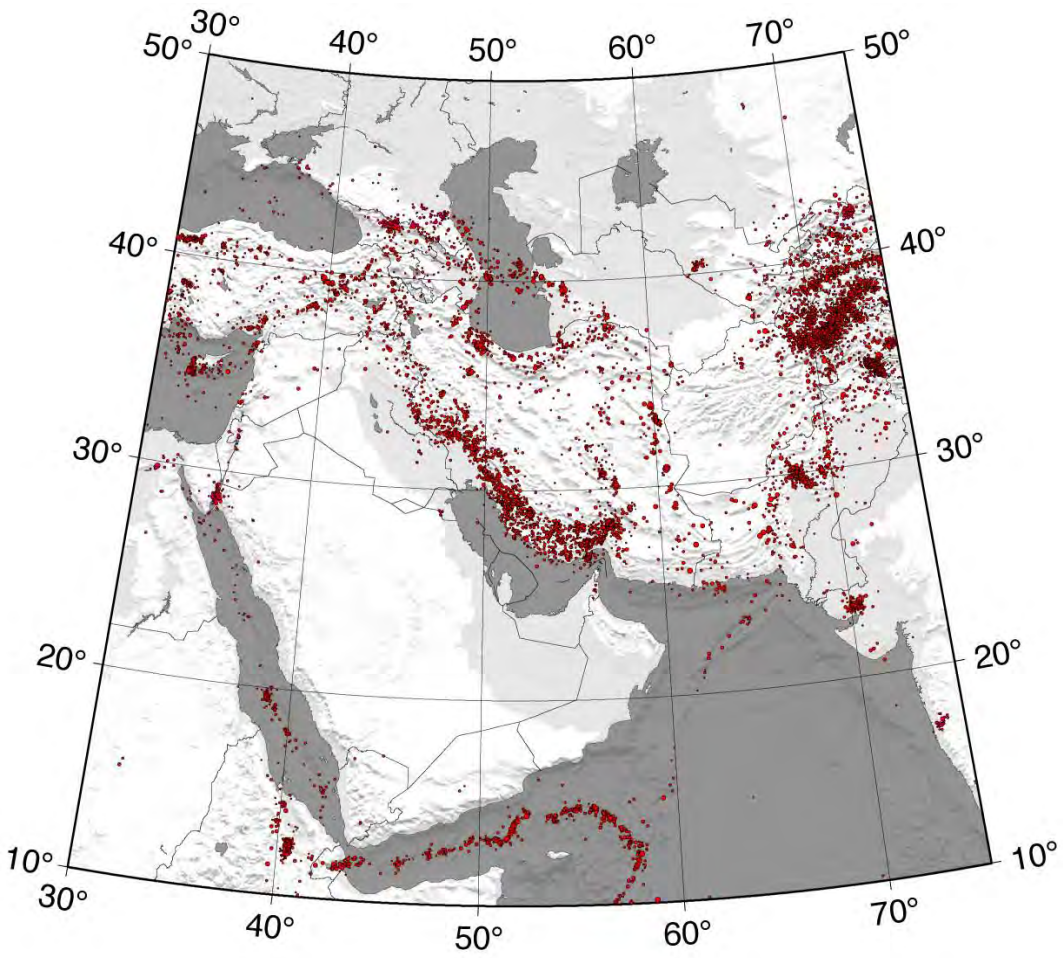

Figure 1. Map of focus region show with topographic and bathymetric shading and moderate to large earthquake locations (magnitudes ≥ 3.5 from 1990 to Spring, 2008). The region contains the Arabian plate and the middle segment of the Alpine to Himalyan collision zone, which is constructed primarily of Phanerozoic terranes amalgamated onto southern Eurasia during the closing of the Tethys Ocean.

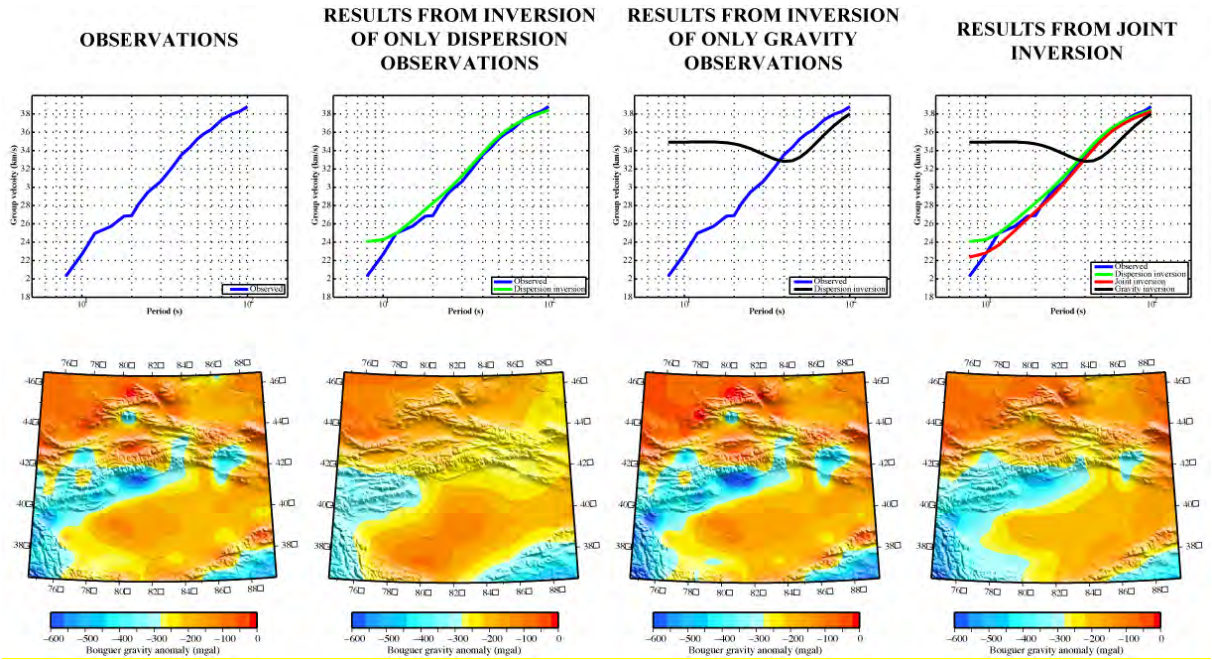

Figure 2. Comparison of data fits from the inversion of only surface wave dispersion observations, the inversion of only gravity observations, and the joint inversion of dispersion and gravity observations. Top panels from left to right: surface wave dispersion data for a typical cell in our gridded model (blue line); fit to the dispersion data from inverting only dispersion data (green line); fit to the dispersion data from inverting only gravity observations (black line); fit to the dispersion data from the joint inversion (red line). Bottom panels from left to right: simple Bouguer anomalies for the region under study; predicted Bouguer anomalies from the model resulting from inverting only dispersion observations; predicted Bouguer anomalies from the model resulting from inverting only gravity observations; predicted Bouguer anomalies from the model resulting from the joint inversion.

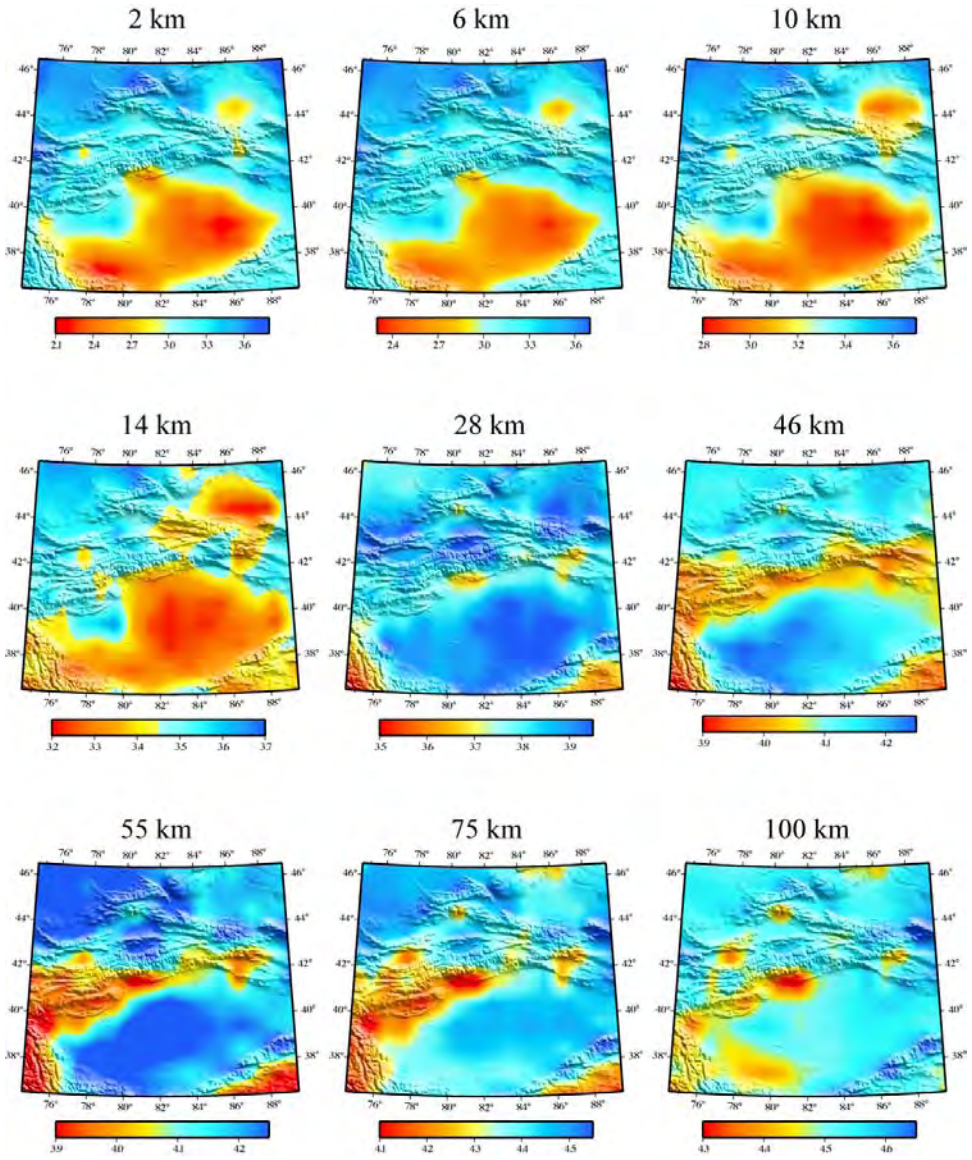

Figure 3. S-wave velocity model at constant depth slices. The depth of each image is shown at the top of each map. Velocity values are expressed in km/s. Note the color scheme is different for each image. The high wavenumber features at depth are clearly artifacts of the simple smoothing scheme used in the current inversion algorithm – none of the data (long-period surface wave dispersion or gravity) can constrain such sharp features at those depths.

IMPROVEMENTS TO A MAJOR DIGITAL ARCHIVE OF SEISMIC WAVEFORMS FROM NUCLEAR EXPLOSIONS: THE BOROVOYE SEISMOGRAM ARCHIVE

Diane Baker[1], Won-Young Kim[2], Howard Patton[1], George Randall[1], and Paul Richards[2]

Los Alamos National Laboratory[1] and Lamont-Doherty Earth Observatory of Columbia University[2]

Sponsored by the Air Force Research Laboratory

Award No. FA8718-07-C-0004

ABSTRACT

We are in the final year of a three-year project to generate in modern form an easily usable archive of digital seismograms derived from regional waveforms recorded at the Borovoye Observatory (BRV), northern Kazakhstan, over a thirty-year period going back to 1966 and forward to the time when state-of-the-art sensors and dataloggers were introduced at this site by several different western groups. The BRV seismograms, which include multi-channel regional signals from 350 underground nuclear test explosions carried out in Eurasia, were made generally available to western scientists in 2001, but only as copies of the bits in the original digital waveforms. Those copies contain large numbers of glitches and did not include instrument responses for approximately two-thirds of the events. Our project is a joint effort by scientists at Lamont-Doherty Earth Observatory of Columbia University (LDEO) and at Los Alamos National Laboratory (LANL). The work of deglitching all the Borovoye digital seismograms has now been completed (at LANL). The initial work of determining instrument responses for the many different channels of the three different digital systems used at Borovoye over the thirty-year period has also been completed (at LDEO).

Three different sets of Soviet-style instruments and recording systems were used at BRV from 1966 to 1996. LANL scientists had processed the BRV regional signals for 210 nuclear tests (1355 traces) before the present project started, mainly those for which instrument responses were available (the TSG system). In this project LANL processed the waveforms of the so-called SS system for 148 nuclear tests (1679 traces), some of which were also recorded on the TSG system, and these have now been processed too (281 traces). The remaining main block of events was recorded on the oldest, so-called KOD, system, which was used in operations beginning in 1966 and which operated continuously from 1967 to 1973. The KOD system, based on three component short-period seismometers, is important as one of the few digital systems anywhere in the world in the late 1960s and early 1970s. In this final batch of deglitched (KOD) waveforms from 101 nuclear explosions, there were 835 traces.

We present examples of the resulting de-glitched waveform data, in order to indicate to potential users the quality of these recordings, and their suitability for phase picking, and for studies of amplitude, coda, and spectra.

We note that waveform data from the Borovoye archive are being used to develop new source models for Balapan nuclear tests. In the 1970s and 1980s, long-period surface waves from these tests were noted for their anomalous behavior, including large Love-wave excitation, and Rayleigh waves with polarity reversals and significant time delays. Repeated attempts in previous studies to model such observations only by tectonic release were unsuccessful. New models that also include the effects of tensile failure represented by a compensated linear vector dipole, have yet to be tested. TSG DS recordings bridge the frequency gap between the long-period observations and higher mode surface waves making up the low frequency Lg spectrum. This additional bandwidth is needed for resolving source parameters to test new models. We have made two sets of measurements on DS recordings: 20-s Ms and a slope measurement on the Lg spectrum between 0.1 and 0.8 Hz. Lg displacement spectra are not flat as expected for frequencies below the corner frequency. Rather, the spectral amplitudes roll off toward low frequency by an amount that is correlated with mb-Ms differences. These observations suggest a link between higher-mode and long-period surface wave excitations, a feature that will be exploited for investigating new source models.

OBJECTIVES

Our goal is to generate in modern form an easily usable archive of digital seismograms derived from regional waveforms recorded at the Borovoye Observatory (BRV), northern Kazakstan, over a thirty-year period going back to 1966 and spanning the time when state-of-the-art sensors and dataloggers were introduced at this site in the summer of 1994. Specifically, we expect to process 1200 to 1400 digital waveforms from the Borovoye archive, for more than 200 underground nuclear explosions in Eurasia for which digital records are available but not yet in useful form due to problems with glitches and instrument calibration that have not yet been taken into account.

RESEARCH ACCOMPLISHED

The BRV digital archive of nuclear explosion waveforms from 711 underground nuclear explosions became generally available in April 2001 as an outcome of an International Science and Technology Center (ISTC) project conducted jointly from 1997 to 2000 by the Kazakhstan National Nuclear Centre, the Russian Academy of Sciences Institute of Dynamics of the Geosphere in Moscow, and the Lamont-Doherty Earth Observatory of Columbia University. That project was initiated by Lamont, and provided 180 man-years of funding to scientists and technicians in Kazakhstan and Russia for several different projects, of which the most time-consuming was saving the Borovoye waveform archive.

The archive of nuclear explosion signals was issued as a series of modern databases, described by Kim et al. (2001). The archive was derived from original Soviet-era magnetic tapes that in many cases were in very bad condition, and for which only a limited number of tape readers existed. The tapes were written in complicated formats that had not been used even in the USSR for decades. For example, many tapes were 35 mm wide, and had 24 channels of information written across 17 separate tracks. The first steps in salvaging the archive were reading all the bits one last time from the original tapes using one of the few available tape readers, and then writing them to a mid-1990s mass store hard drive. Later steps entailed extraction of timing information, de-multiplexing, and re-formatting.

Three different sets of Soviet-style instruments and recording systems were deployed at BRV from 1966 to 1996. They are known as the KOD, STsR-SS, and STsR-TSG systems (sometimes abbreviated to KO or KOD, SS, and TS or TSG). The first BRV digital seismic system, KOD, began recording in 1966 and operated continuously from 1967 to 1973. It is based on three-component, short-period seismometers, and is important as one of the few digital seismic systems anywhere in the world in the late 1960s and early 1970s. The other Soviet-era BRV digital systems began operation in February 1973. STsR-SS is intended mainly for low-gain recording. STsR-TSG includes six long-period and seven short-period Kirnos seismometers, most recorded at two gain levels, for a total (SS + TS) of 20 data channels. The highest sensitivity is 100,000 counts/micron based on a short-period Kirnos with a special magnet and a low-noise amplifier. This instrument was important at BRV for teleseismic monitoring of numerous French and U.S. UNEs, but for purposes of this proposal it is not so important today as the lower-gain channels, on which regional signals have been recorded from UNEs in and near Central Asia. Kim and Ekström (1996) have published details of the STsR-TSG instrument responses (many channels, extending across almost 3 decades in frequency). All of these main systems are approximately flat to ground displacement over a range of frequencies. With the different instruments and gain levels, the station as a whole had a dynamic range well over 120 dB during the Soviet era.

When the BRV archive was made generally available from Lamont in 2001, the decision was made that it be essentially in its original unprocessed form (though with the addition of basic header information), but converted to a modern and widely use format for digital seismic data (CSS3.0). The original Soviet-era recordings had some severe problems, most notoriously that the digitizer typically did not write a count value on seismic waveform channels at the time when the time channel was writing the marker for an integer second. The waveform data therefore ended up with numerous glitches. Also, the original recording system addressed the practical problem of input signal with wide dynamic range, by having several different channels set at different gain levels, each recording with a limited number of bits (often, only 11 bits), so that although each UNE was usually recorded on several channels, in practice these channels were often either clipped or had inadequate resolution.

The work of deglitching thousands of digital waveforms in this project has now been completed at LANL, with the delivery in early 2009 to LDEO of 835 deglitched traces derived from 101 underground nuclear explosions in Eurasia. These events were recorded on the KOD system—the oldest and most-difficult to work with, because of the low dynamic range, the condition of the recording tapes, and the unusual instrument response (which has a notch

intended to suppress microseisms). Earlier in this project, LANL had completed deglitching SS system records (1689 traces) and TSG system records (282 traces), to add to 1,335 TSG traces deglitched several years ago.

The work of deglitching has thus been completed, after nearly eighteen years since the existence of these data was first made known to western scientists (in 1991, when Richards and Göran Ekström made a two-week visit to Borovoye). Figure 1 shows examples drawn from the three systems used at the Borovoye Observatory.

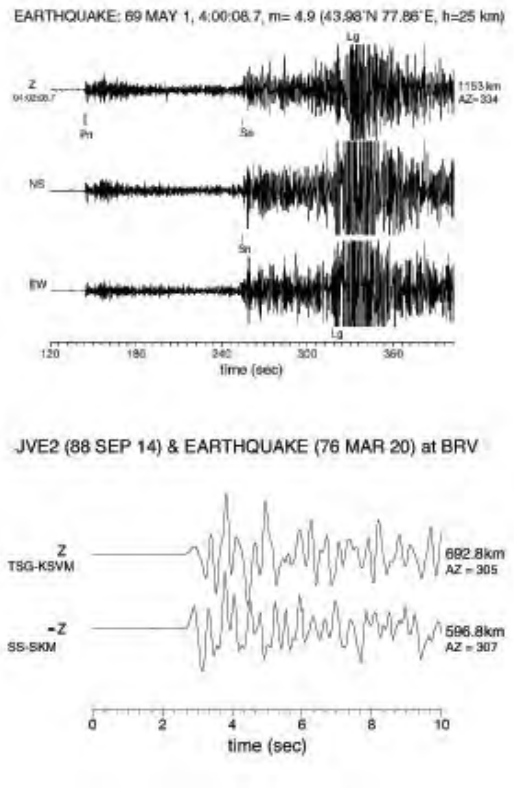

Figure 1. Shows examples from all three of the digitizing systems in use at the Borovoye Observatory (BRV), Kazakhstan, in the Soviet era. At the top, recorded on the KOD system (the oldest), is a three-component recording of the Kazakhstan earthquake of May 1, 1969. Though slightly clipped, this data is of remarkable quality and can be used for phase picking and quantitative studies of coda (albeit not for study of spectra of the strongest ground motion). At the bottom, is a comparison of the first arrivals at BRV of an explosion signal from a Shagan River explosion (JVE2, September 14, 1988, on the TSG system which was the third recording system in operation at BRV); and an earthquake signal on March 20, 1976 (recorded on a channel of the SS system, the second system in operation at BRV). Note the polarity reversal of the earthquake arrival compared to that of the explosion.

There are many possible uses of the dataset being generated in this project, as listed for example below, in the Conclusions and Recommendations section. In this paper, we next give a brief preliminary report on some of the surface-wave signals recorded at BRV, showing how they document effects of tectonics release, and perhaps spall and/or tensile failure, as well as the usual isotropic radiation expected from an explosion.

Analysis of Surface Waves Recorded at Borovoye, for their Indications of Non-Isotropic Source Effects

In the 1970s and 1980s, long-period excitation of surface waves in the Balapan sub-region of the Soviet Semipalatinsk test site in central Asia were noted for anomalous behavior, including the generation of large Love waves and Rayleigh waves with polarity reversals and significant time delays (Rygg, 1979; Cleary, 1981; Helle and Rygg, 1984; Herrin and Goforth, 1986). Repeated attempts to model the observations with tectonic release were not completely successful (Given and Mellman, 1986; Ekström and Richards, 1994), although tectonic release models of reverse faulting explained observations best (Patton, 1980; Harkrider, 1981; Day and Stevens, 1986; Day et al., 1987). New explosion source models for tensile failure represented by a compensated linear vector dipole (CLVD) (Patton and Taylor, 2008) have yet to be tested to see if they can explain the full suit of observations, including m_b–M_s scaling with respect to predictions of the Mueller-Murphy model (Mueller and Murphy, 1971; hereafter referred to as MM71). Due to broader frequency content and a fairly complete recording history of Semipalatinsk Test Site (STS) explosions, waveform data from the Borovoye archive offer the opportunity to re-evaluate old models and test new models of the explosion source.

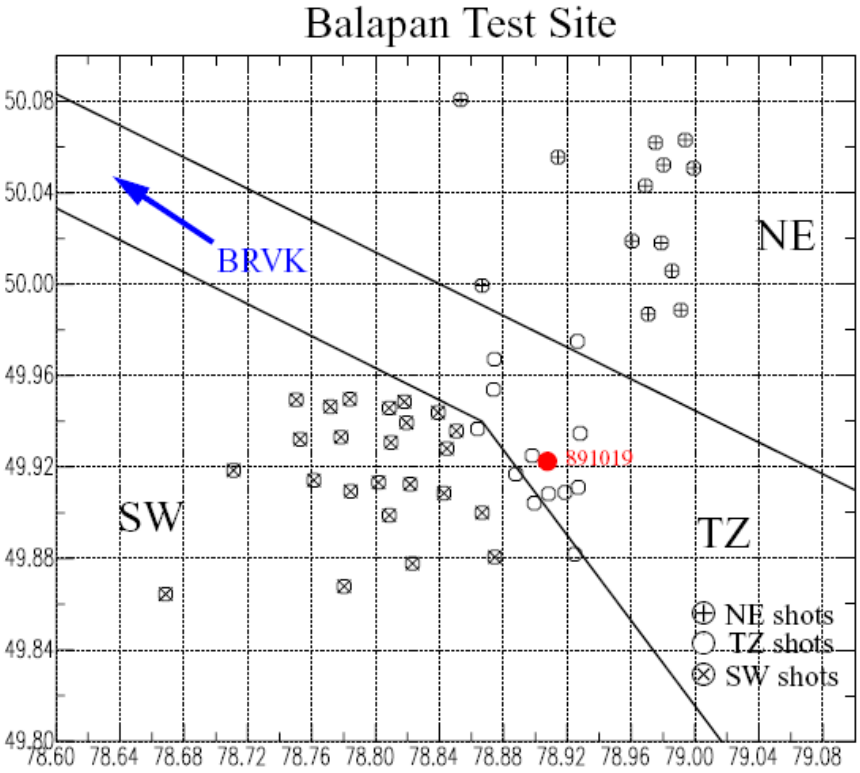

Figure 2. Map of the Balapan sub-region of the Semipalatinsk Test Site showing locations of 50 tests currently understudy and the boundaries of NE, TZ, and SW test areas introduced by Ringdal et al. (1992). The explosion on 891019 is used as the master for subsequent cross-correlation analysis.

Figure 2 shows locations from the report of Kim et al. (2001) for 50 Balapan explosions currently under study. Also shown are test areas called Northeast (NE), Transition Zone (TZ), and Southwest (SW) from the study of Ringdal et al. (1992). Filtered vertical-component displacement traces of the TSG DS instrument system for these 50 explosions are given in Figure 3 along with epicentral distances to Borovoye (BRV), teleseismic m_b calculated by Blacknest seismologists (Ringdal et al. 1992), and a reference to the study of Ekström and Richards (E&R94) for those events whose surface waves were analyzed for moment tensor descriptions. In Fig. 3 the traces are arranged in order of increasing distance from 679.7 to 696.1 km, a span of only 16.4 km. Red and blue boxes demarcate the arrivals of fundamental- and higher-mode Rayleigh waves.

A cross-correlation analysis was carried out on the fundamental-mode Rayleigh waves in order to detect polarity reversals and time delays. This analysis was applied to two filter bands, one between 0.04 and 0.1 Hz and the other at lower frequencies between 0.03 and 0.07 Hz. Before cross-correlation, the seismograms were distance-equalized by accounting for the slight differences in distance of the different explosions, using a phase velocity dispersion based upon an average Balapan velocity model (Bonner et al., 2001).

The explosion on 891019 was chosen as the master for cross-correlation (CC) analysis because of its excellent signal quality, low level of tectonic release (E&R94), and location on a back-azimuth near the population centroid. The polarity of 891019's signal was assumed to be normal. The CC analysis yields polarity and apparent time delay relative to 891019. A measure of confidence in the CC results based on the ratio of the 2nd maximum absolute value to the maximum absolute value of the c-c function is also computed and called R. There are more reversed polarities for the lower frequency pass-band than for the higher. Theory predicts that reversals occur first at low frequencies and progress to higher frequencies as the strength of the CLVD source increases. A threshold of 0.9 was arbitrarily selected to indicate results of lower confidence.

A summary plot of polarity reversals and time delays determined from cross-correlation analysis is shown in Figure 4. By definition, the delay for the master event, plotted as a blue dot, is 0.0. Different symbols are used to identify events according to polarity and confidence level (e.g., $R \geq 0.9$, shown with a × symbol). A solid dot indicates the polarity identified by E&R94. For 770629 and 831120, no dot is given because their surface waves were not analyzed by E&R94.

To tie results in Figure 4 with those determined from teleseismic studies, there must be events in common since the CC method used here and by Helle and Rygg, as well as the phase-matched filter method of Herrin and Goforth, is inherently relative to the chosen master event. The shot 791202 is in common with Helle and Rygg's data set. A small time advance of 0.4 s was found for Borovoye while Helle and Rygg measured a delay of 0.8 s. This suggests a correction of 1.2 s added to all measurements in Fig. 4 in order to compare with their results. After making this correction, the time delays for reversed NW shots range between 3 and 6 s in agreement with the delays determined by Helle and Rygg.

Low-frequency observations of Lg spectra and correlations with M_s.
Fisk (2006) presents *Pn/Lg* spectral ratio observations for STS explosions. For large explosions, SNR appears to be adequate for *Pn* and *Lg* waves recorded at WMQ and MAK for frequencies as low as ~0.2 Hz (see his Fig. 11). As such, the behavior of *Pn/Lg* spectral ratios is considered reliable at low frequencies for large explosion groupings in his Figs. 14 - 17. The observed up-turn in spectral ratios at low frequencies is qualitatively consistent with a roll-off in the spectra of *Lg* waves if the low-frequency spectrum of *Pn* waves is flat as predicted by the MM71 model.

Path-corrected *Lg* displacement spectra were obtained by Fourier transforming BRV signals recorded on the DS instrument system for a time window corresponding to average apparent velocities of 3.77 and 3.21 km/s. For an average distance of 688 km, the corresponding window length is 32 s. A multi-taper algorithm was applied involving 512-point transforms and 7 tapers. Amplitude corrections for instrumental response were performed in the frequency domain, and signal-to-noise checks were made to ensure at least a factor of two threshold for the frequency band of interest. Noise spectra were taken in a window just proceeding the signal window (e.g., ending with an apparent velocity of ~3.8 km/s). A correction for attenuation was made using a power-law Q model, $746 * f^{0.2}$ (W. S. Phillips and J. Xie, pers. comm.).

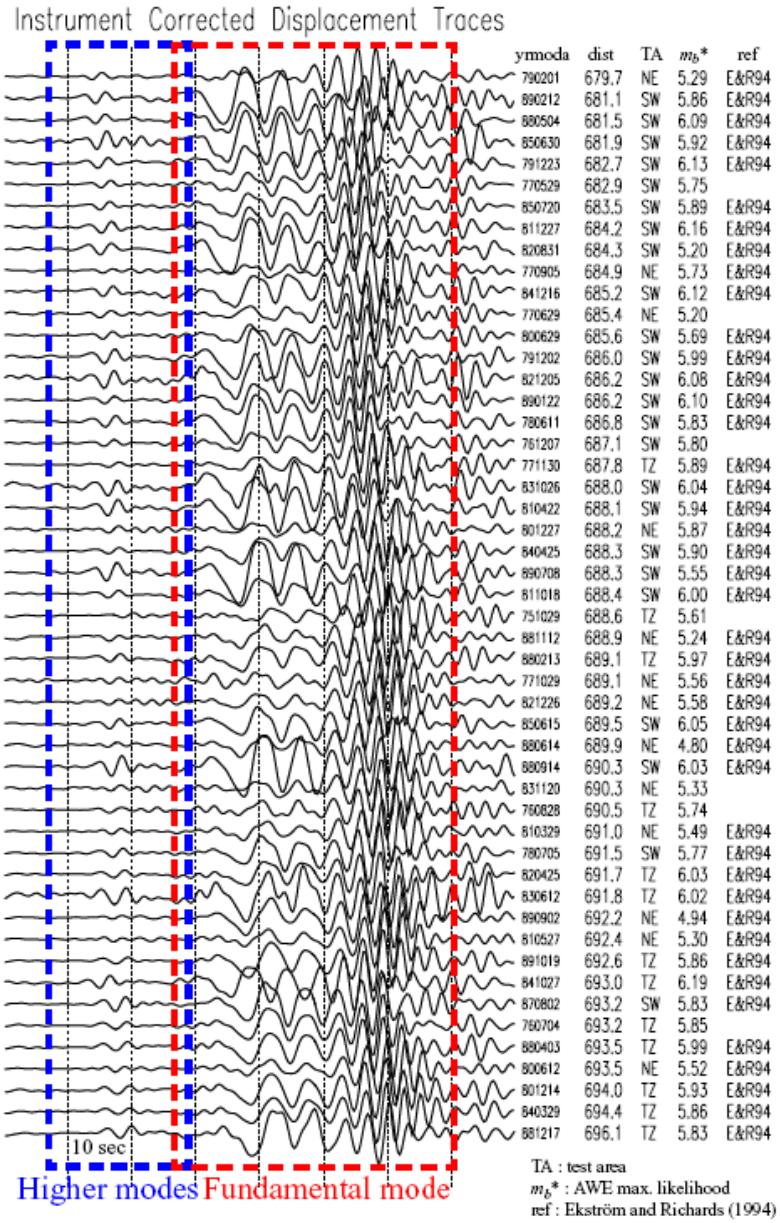

Figure 3. Profile of instrument-corrected, vertical-component displacement traces for the TSG DS system, ordered by increasing distance from the Borovoye station. Passband is 0.03 – 0.5 hz. Blue box demarcates higher-mode arrivals making up Lg waves at low frequencies. Red box demarcates arrivals of the fundamental-mode Rayleigh wave.

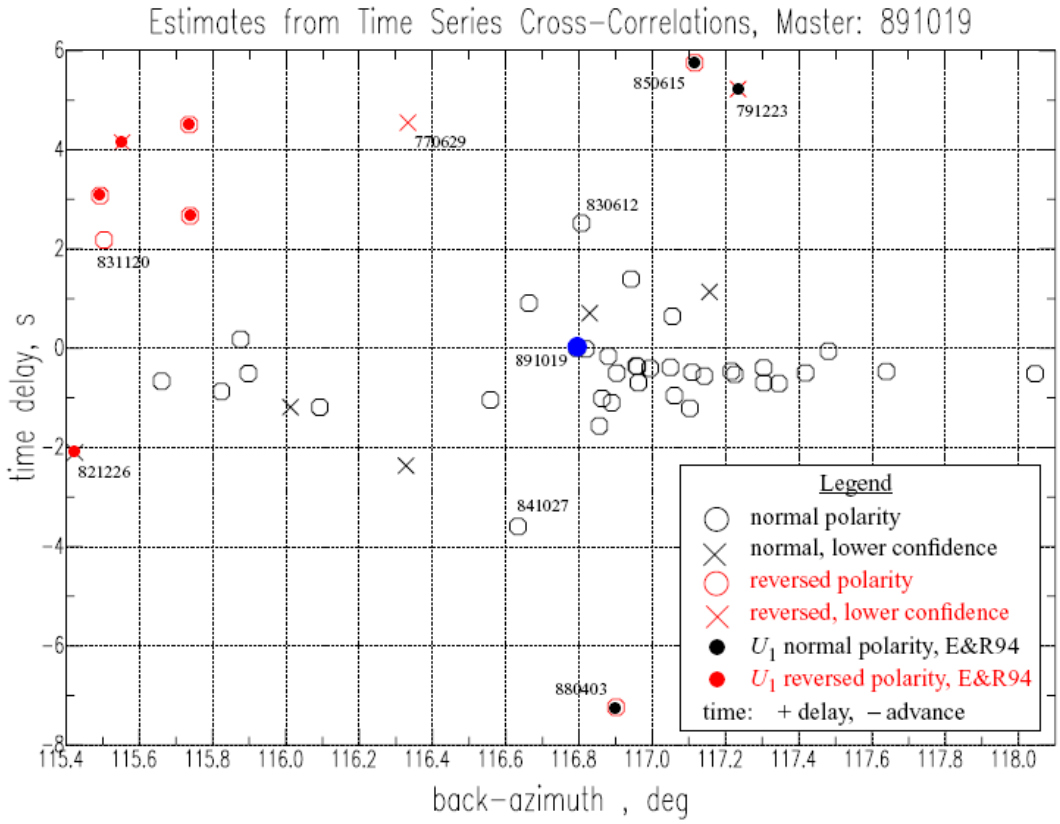

Figure 4. Summary of time delays as a function of back-azimuth across the array of explosion sources, showing events with reversed waveforms and significant time delays compared to normal waveforms.

Lg displacement spectra are not flat for frequencies below the corner frequency as expected based on the model of MM71. Rather, the spectral amplitudes are found to roll-off toward low frequency, consistent with the *Pn*/*Lg* observations of Fisk. Furthermore, the shots with the highest slopes also show reversed Rayleigh waves at BRV and in the E&R94 study. These observation suggest that the low-frequency slope of *Lg* spectra may be correlated with effects on Rayleigh waves as predicted by the monopole + CLVD source model and *Rg*-to-*S* scattering. This possibility is explored in Figure 5 where slope estimates are plotted against m_b–M_s differences.

Figure 5a shows a plot of slope for the *Lg* spectrum in the range 0.1 to 0.8 hz, against m_b–M_s where m_b is the Blacknest maximum-likelihood estimate reported in Ringdal et al and M_s is determined from DS recordings using the Marshall and Basham method (Marshall and Basham, 1972). All M_s determinations but one (831120) are based on Rayleigh wave amplitudes in the 17–23-s period pass-band. Figure 5b shows the same slope measurements but m_b–M_s has been adjusted for test site m_b bias as determined Ringdal et al. While the cause of systematic variations of m_b-m_{bLg} across Balapan is not well understood, conventional wisdom holds that the effect is in the m_b, not the m_{bLg}. As such, m_b has been adjusted on an event-by-event basis for those explosions with both m_b and NORSAR m_{bLg} measurements. When m_{bLg} is not available, the average bias for the test area given in equation (18) of Ringdal et al. is used.

Three explosions (881112, 880614, 810319 - ordered by decreasing slope estimate) show obvious reduced correlation since the slopes are among the highest values, yet their m_b–M_s estimates are near the mean of the population. 880614 does not have a NORSAR m_{bLg} measurement and is the smallest event in the dataset (4.8 m_b).

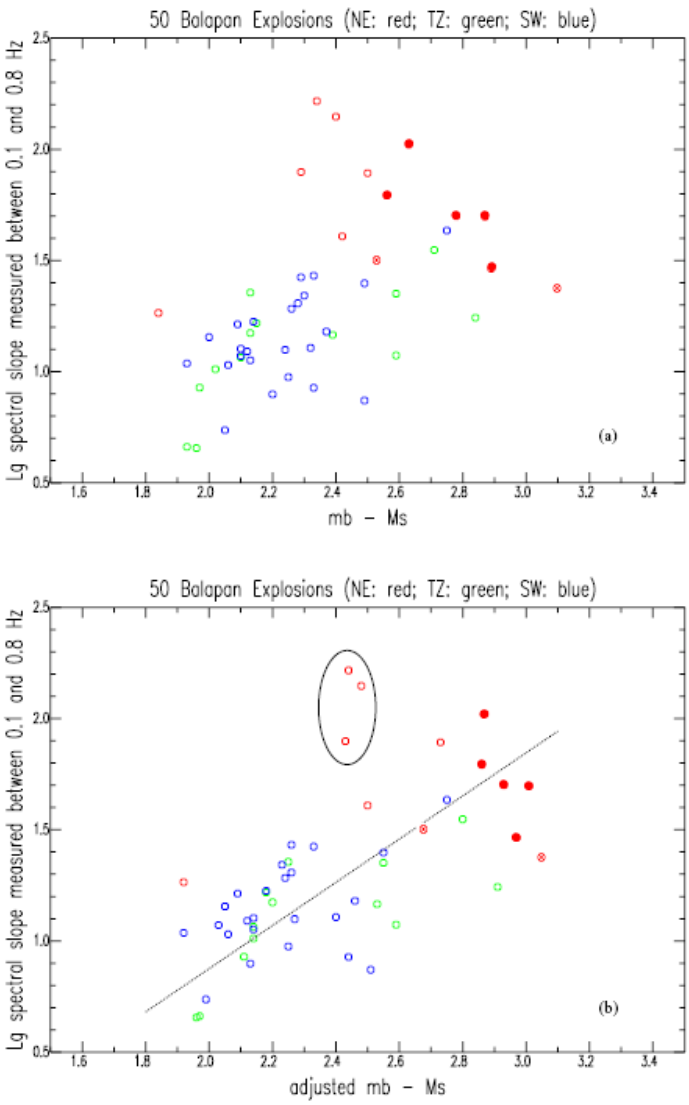

Figure 5. Plots of Lg spectral slope measured between 0.1 and 0.8 hz against m_b–M_s for all 50 Balapan explosions analyzed so far in this study. (a) shows the correlation for raw m_b–M_s values, while (b) shows the correlatian for adjusted m_b–M_s values where m_b has been corrected on an event-by-event basis for m_b–m_{bLg} residuals showing systematic variation around the test site. Solid red dots are those NE explosions with negative polarity from E&R94. Waveforms for two NE explosions are plotted with a red circle-and-cross symbol because waveform cross-correlation suggests they are reversed polarity with sizable time delays (770629, 831120). Three obvious data points with poor correlation are enclosed by an ellipse. The line plotted in Figure 5b has a slope that is identical Rg synthetics plotted in Figures 6a and 6c of Patton (2009, these Proceedings).

Summarizing these observations, a correlation does appear to exist between low-frequency *Lg* spectral slope and M_s corrected for source size using m_b. This finding is very interesting in the context of spectral ratio observations of Fisk (2006) where regional spectral ratios are seen to turn upward at low frequencies in contradiction to the Mueller-Murphy model. The correlations shown here suggest that the upturn is real, and is related to roll-off in *Lg* spectra at low frequencies. A correlation is predicted on the basis of fundamental- mode Rayleigh wave excitation due to a compound monopole + CLVD source.

CONCLUSIONS AND RECOMMENDATIONS

We have been able successfully to deglitch a major archive of digitally-recorded nuclear explosions conducted in Eurasia, all recordings coming from the same Observatory namely that at Borovoye, Kazakhstan, the oldest explosion having occurred in 1966. We plan to release this dataset at the conclusion of the present project. The dataset consists of multi-channel recordings of hundreds of underground nuclear explosions in Eurasia, most of them recorded on the three Soviet-era systems in use at Borovoye from 1966 to the early 1990s, and brought up-to-date with recordings of a few explosions after the installation of western sensors and data-loggers beginning in 1994.

Ongoing studies likely to benefit from an improved Borovoye digital waveform archive (and that can also help assure we have the correct gains and responses), include new source models as discussed above, and also:

- Yield estimation, using RMS Lg, Rg, and coda.
- Effects of source depth and shot-point geology, for example using PNEs from different regions.
- Discrimination using spectral ratios of seismic signals from earthquakes and UNEs, for example at the Semipalatinsk and Lop Nor test sites (in shafts and tunnels — which may impose their own slight differences on observed spectra).
- Discrimination between regional seismic signals of nuclear explosions and mining blasts of various types. (Note that mining blast signals are being routinely acquired today by the well-instrumented modem BRVK station.)

Because modern seismographic stations, now being installed in large numbers for many different purposes, lack archives of nuclear explosion signals, it is important to build up such archives for stations in a wide variety of sites. We recommend a program of acquiring and circulating electronic versions of hard copies of nuclear explosion signals from areas of interest, often recorded photographically or as ink on paper, and therefore requiring digitizing. If this work is not done soon, it may be too late to save the original recordings.

ACKNOWLEDGEMENTS

We thank staff at the Institute for Dynamics of Geosphere, Moscow, Russia led by Drs. Vitaly Adushkin and Vladimir Ovtchinnikov, who copied the BRV waveform archive from old 35-mm tapes onto modern media (tape cassettes) and performed extensive data reformatting work. We also thank staff at the Institute of Geophysical Research, National Nuclear Center, Republic of Kazakhstan led by Drs. Nadezhda Belyashova and Natalia Mihailova who provided us with ground truth data on shot hole locations of Semipalatinsk test site.

REFERENCES

Bonner, J. L., D. C. Pearson, W. S. Phillips, and S. R. Taylor (2001). Shallow velocity structure at the Shagan River test site in Kazakhstan, *Pure appl. Geophys*. 158: 2017–2039.

Cleary, J. R. (1981). Anomalous Rayleigh waves from presumed explosions in East Kazakh, in *Identification of Seismic Sources--Earthquake or Underground Explosion, NATO Advanced Study Institute Series,* E. S. Huseby and S. Mykkeltveit, Editors, D. Reidel Publishing Co., Dordrecht, 191–199.

Day, S. M. and J. L. Stevens (1986). An explanation for apparent time delays in phase-reversed Rayleigh waves from underground nuclear explosions, *Geophys. Res. Lett.* 13: 1423–1425.

Day, S. M., J. T. Cherry, N. Rimer, and J. L. Stevens (1987). Nonlinear model of tectonic release from underground explosions, *Bull. Seismol. Soc. Am*. 77: 996–1016.

Ekström, G. and P. G. Richards (1994). Empirical measurements of tectonic moment release in nuclear explosions from teleseismic surface waves and body waves, *Geophys. J. Int.* 117: 120–140.

Fisk, M. D. (2006). Source spectral modeling of regional *P/S* discriminants at nuclear test sites in China and the former Soviet Union, *Bull. Seismol. Soc. Am.* 96: 2348–2367.

Given, J. W. and G. R. Mellman (1986). Estimating explosion and tectonic release source parameters of underground nuclear explosions from Rayleigh and Love wave observations, Final report, Part I, AFGL-TR-86-0171(I), Air Force Geophysics Laboratory, Hanscom Air Force Base, MA, 70 pp.

Harkrider, D. G. (1981). Coupling near-source phenomena into surface wave generation, in *Identification of Seismic Sources--Earthquake or Underground Explosion, NATO Advanced Study Institute Series,* E. S. Huseby and S. Mykkeltveit, Editors, D. Reidel Publishing Co., Dordrecht, 277–326.

Helle, H. B. and E. Rygg (1986). Determination of tectonic release from surface waves generated by nuclear explosions in Eastern Kazakhstan, *Bull. Seismol. Soc. Am.* 74: 1883–1898.

Herrin, E. and T. Goforth (1986). Phase analysis of Rayleigh waves from the Shagan River test site in the USSR, *Bull. Seismol. Soc. Am.* 76: 1739–1754.

Kim, W.-Y. and G. Ekström (1996). Instrument responses of digital seismographs at Borovoye, Kazakhstan, by inversion of transient calibration pulses, *Bull. Seismol. Soc. Am.* 86: 191–203.

Kim, W.-Y., P. G. Richards, V. Adushkin, and V. Ovtchinnikov (2001). Borovoye digital archive for underground nuclear tests during 1966-1996, Data report on the web at http://www.ldeo.columbia.edu/Monitoring/Data/Brv_arch_ex/brv_text_table.pdf, Borovoye Archive for UNT.

Marshall, P. D. and P. W. Basham (1972). Discrimination between earthquakes and underground explosions employing an improved M_s scale, *Geophys. J. R. Astr. Soc.* 28: 431–458.

Mueller, R. A. and J. R. Murphy (1971). Seismic characteristics of underground nuclear detonations Part I. Seismic spectrum scaling, *Bull. Seismol. Soc. Am.* 61: 1675–1692.

Patton, H. J. (1980). Surface-wave generation by underground nuclear explosions releasing tectonic strain, Lawrence Livermore National Laboratory, University of California, Report No. UCRL-53062, 16 pp.

Patton, H. J. and S. R. Taylor (2008). Effects of shock-induced tensile failure on m_b-M_s discrimination: Contrasts between historic nuclear explosions and the North Korean test of 9 October 2006, *Geophys. Res. Lett.* 35: L14301.

Patton, H. J. (2009). Explosion source model development in support of seismic monitoring technologies: applications of new models for shock-induced tensile failure, these Proceedings.

Ringdal, F., P. D. Marshall, and R. W. Alewine (1992). Seismic yield determination of Soviet underground nuclear explosions at the Shagan River test site, *Geophys. J. Int*. 109: 65–77.

Rygg, E. (1979). Anomalous surface waves from underground explosions, *Bull. Seismol. Soc. Am.* 69: 1995–2002.

CRUSTAL STRUCTURE FROM IN-COUNTRY AND GROUND-TRUTH DATA

Eric A. Bergman[1], E. Robert Engdahl[1], Michael H. Ritzwoller[1], and Stephen C. Myers[2]

University of Colorado[1] and Lawrence Livermore National Laboratory[2]

Sponsored by the Air Force Research Laboratory and the by the National Nuclear Security Administration

Award Nos. FA8718-08-C-0020[1] and DE-AC52-07NA27344[2]
Proposal No. BAA08-69

ABSTRACT

We are investigating the crustal and upper mantle structure of the region in central Asia bounded approximately by longitude 41-67°E and latitude 20-44°N by using in-country datasets of seismic phase arrival times, supplemented by ground truth datasets developed from our previous research efforts. We present the results of *Pn* tomography using a dataset consisting entirely of GT5 events in the region. From 27 calibrated earthquake clusters we extract 832 events that qualify as ground truth (GT)5 at the 90% confidence level. The raypaths of *Pn* readings from these events provide good coverage of most of the region except for the Makran region in the southeast. To determine an appropriate reference model for the region we compared empirical travel times calculated from the GT5 dataset to those predicted by several models: the ak135 global model (Kennett et al., 1995), the CUB2.0 model (Ritzwoller et al., 2003), and the so-called "Unified" model a 3-D velocity model of the crust and upper mantle in Eurasia, constructed from models developed by researchers at Lawrence Livermore National Laboratory (LLNL) and Los Alamos National Laboratory (LANL) (Pasyanos et al, 2004; Begnaud et al., 2004; Steck et al., 2004; Flanagan et al., 2007). Although the CUB2.0 and Unified models do vary laterally, in the study region they vary quite slowly and capture little of the variability of observed travel times. All three models predict *Pn* travel times that are systematically too fast. These baseline errors range from 2-4 seconds. For this initial round of tomography we stretched the ak135 model to a crustal thickness of 45 km for the reference model.

Tomography is first performed in a "traditional" way, allowing for individual event corrections as well as station corrections. Through relative event relocation, however, these clusters of GT5 events have very strong constraints on relative location, depth, and origin time of the associated earthquakes. For each cluster, then, we can assign a single "cluster correction". This dramatically reduces the number of free parameters and stabilizes the inversion. This exercise helps reveal problems in the GT5 dataset that can in some cases (e.g., erroneous station coordinates) be corrected, enhancing the value of the GT5 dataset for validation of tomography based on larger, uncalibrated datasets. It also reveals patterns in *Pn* velocities in the study region which have much shorter wavelength than previous studies. We also investigated the possible contribution of crustal thickness variations to account for the observed variability of empirical travel times for *Pn*. The experiment is based on a simple model of a single-layer crust over a halfspace. A digital terrain map is filtered at 100 km and converted to Moho depth, under the asumption of full isostatic compensation, which is almost certainly an over-estimate. For reasonable density contrast the Moho depth variation is about 5 times the topography. For a set of raypaths based on the locations of the actual events in the GT dataset and actual stations we calculate the *Pn* travel time through the crust and along the crust-mantle boundary of the perturbed model and also through the unperturbed flat-layered model, and take the difference. The variance of these differences is about 4% of the variance of observed Pn travel times in the study region, suggesting that crustal thickness variations contribute only at a low level to the observed variability. Most of the variability in Pn travel times presumably arrises from lateral variations in bulk velocity, perturbations to the ray paths caused by those lateral variations, errors in cluster calibration, and phase identification errors.

OBJECTIVES

This research has the goal of developing in-country datasets that can be used to improve ground-based monitoring capabilities in the study region, by providing information needed to develop and test more accurate travel time models for seismic phases that propagate in the crust and upper mantle. The main dataset to be produced is a bulletin of earthquakes in the region at magnitudes of 2.5 and higher, associated with readings from seismograph stations operating in-country for the period 1995–2005. These events and readings will be integrated with the best available catalog of regional seismicity for that period that includes associated regional and teleseismic phase arrival times. All events will be relocated, carefully reviewed, and calibrated, where possible, with ground truth data. We will conduct preliminary modeling experiments with these data, using *Pn/Sn* tomography to image broad-scale features of the crust and upper mantle in the region. The tomographic experiments will also help reveal problems in the datasets of earthquake locations and phase identifications, and thus serve a quality control function. The resulting datasets and model results will provide a solid foundation for further research.

RESEARCH ACCOMPLISHED

In-Country Data

The main sources of in-country data are the seismic networks operated by the International Institute of Earthquake Engineering and Seismology (IIEES) and the University of Tehran Institute of Geophysics (UTIG). We have acquired all phase reading data from these networks through 2005, and integrated the data with other readings from regional and global networks. We have also acquired phase reading data from 2005 through 2008 for both networks but this data is still being processed.

We have also acquired independent datasets of phase readings from the Oman network (2004–2007) (Figure 1) and the Kuwait network (2000-2008) for earthquakes in the study region and these are being merged with other readings. The Oman data in particular is of great value for improving location accuracy in the southernmost part of the study region.

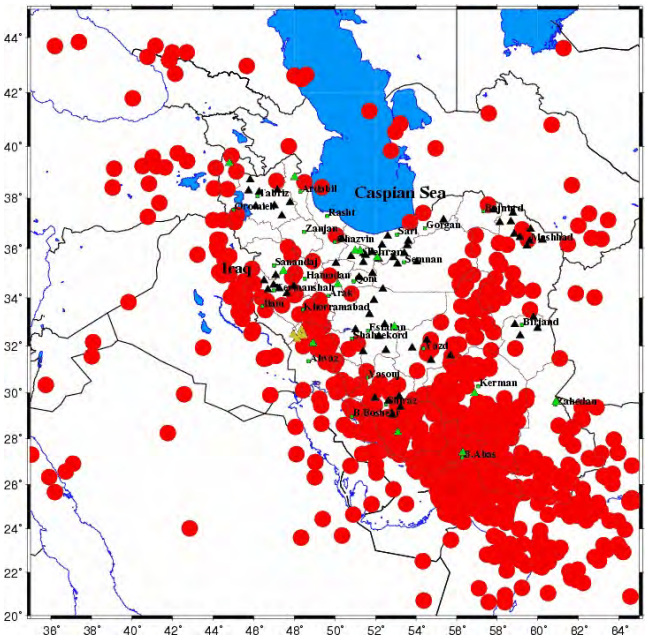

Figure 1. Locations of events determined by the Oman network during 2005-2007, for which phase readings have been acquired. These network locations are extremely poor and it is a difficult task to properly associate these readings with well-constrained events in our main catalog.

Our colleagues in the region have been conducting careful reanalysis of events in certain parts of the region, repicking all readings and relocating events. We have acquired these datasets for the Tehran, Zanjan, and Tabriz regions (Figures 2 and 3). These datasets have been very valuable for our location calibration studies in these regions.

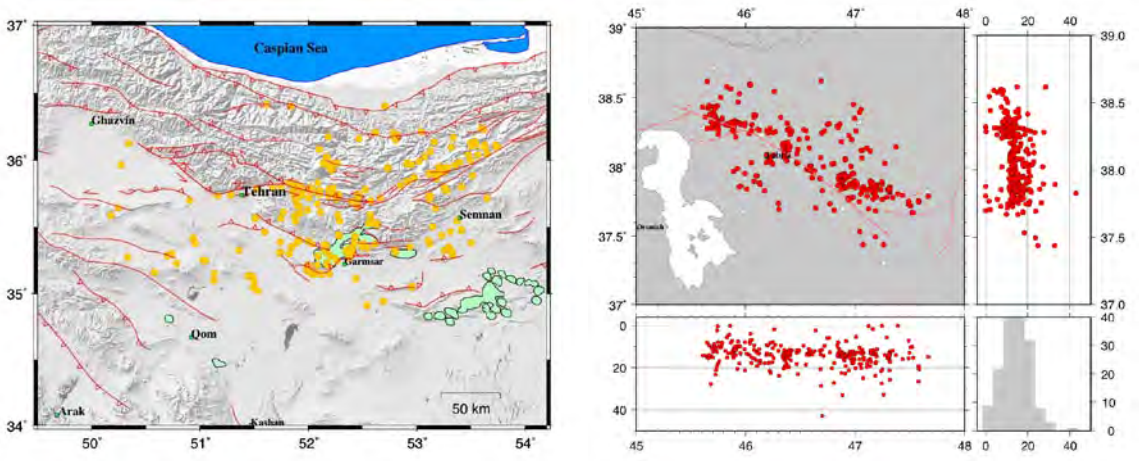

Figure 2. Seismicity in the Left) Tehran region and Right) Tabriz region, from a specialized study involving repicking all waveforms, combining all available in-country data, and relocating. This work is done by our colleagues in-country.

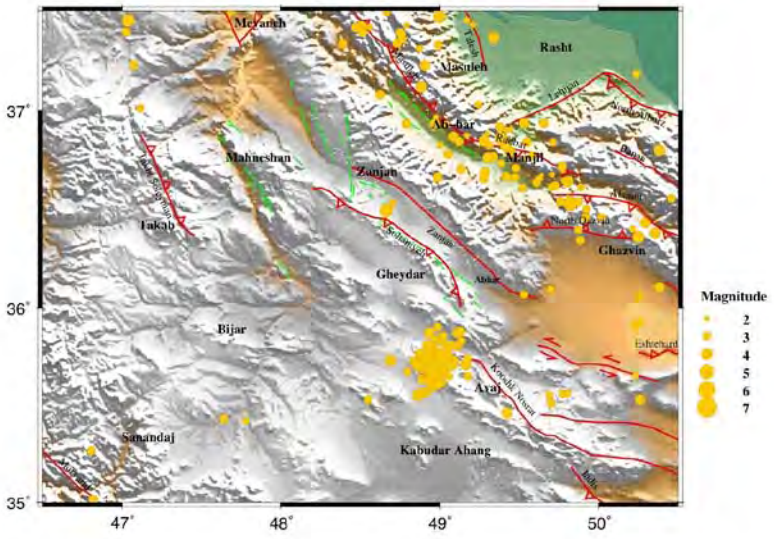

Figure 3. Seismicity in the Zanjan region from a specialized study involving repicking all waveforms, combining all available in-country data, and relocating. This study produced a large number of new events for the Avaj cluster. This work is done by our colleagues in-country.

Finally, we have acquired from colleagues several valuable datasets of phase readings from temporary deployments that are extremely valuable for our location calibration studies.

Catalog of Earthquakes

Our latest update to the catalog of seismicity in the region includes 26,973 events from 1923 through December 2008. Events with magnitude 2.5 or larger are retained. Some events with unknown magnitude are retained if they can be reliably located. For the major sources of data the current catalog's completeness is given below:

- International Seismological Centre (ISC): complete through 2006.
- U.S. Geological Survey Preliminary Determination of Epicenters (PDE): complete through 2008.
- UTIG: complete through 2005. We have the full catalog for 2006-2008 and it will be merged with the catalog.

- IIEES: complete through 2008 for data reported to the ISC, but not all readings are reported that way. We have the full IIEES catalog through 2008 and it will be merged with the catalog.

A subset of 7592 events from this catalog which satisfy the condition that secondary azimuth gap (largest azimuth filled by a single station) is less than 180° are shown in Figure 4.

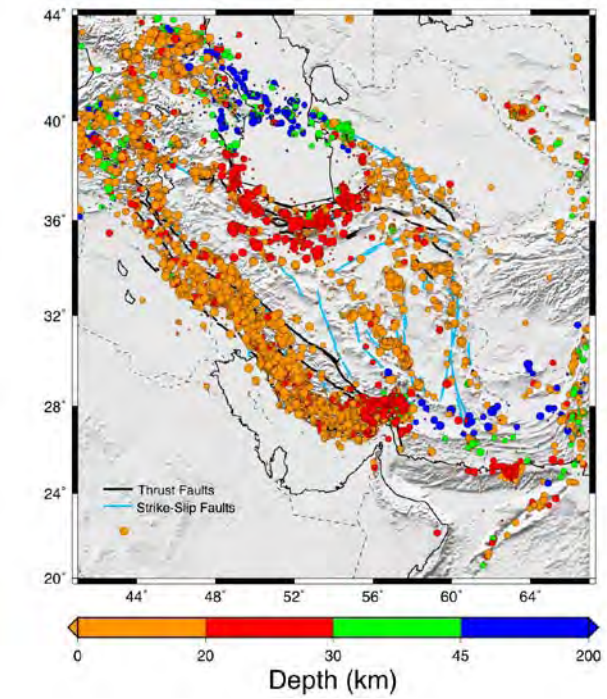

Figure 4. A subset of earthquakes from our earthquake catalog in the study region, showing the locations of 7592 events that satisfy the requirement that secondary azimuth gap is less than 180°. The epicenters of these events are therefore better constrained than other events in the catalog, even though the locations are not calibrated. Focal depths are color-coded.

Calibrated Locations

We have been building our dataset of calibrated earthquake clusters in the study region through several projects spanning about 10 years. We now have 28 earthquake clusters, containing 1,271 earthquakes, in the region that are calibrated in location and 27 of those are also calibrated in origin time (Figure 5). These 28 clusters contain 832 events that qualify as $GT5_{90}$ or better.

The latest clusters that we have calibrated are Tiab, Fin, Siah-Kuh, Qom, Aradan, and Ardebil. We have data with which several other clusters can be calibrated as well, and these are in process.

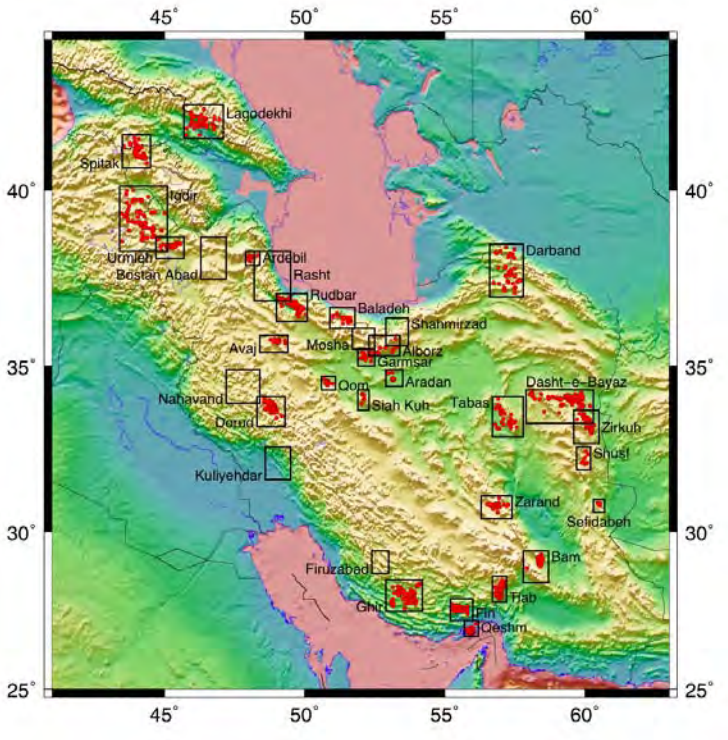

Figure 5. Locations of earthquake clusters with calibrated locations and, in most cases, origin times. Epicenters shown by red circles. Boxes without epicenters indicate clusters whose calibration analysis is in process.

Pn Tomography

Our goal in conducting tomographic experiments with our data is two-fold: 1) to obtain a better image of first-order variations in crustal and upper mantle structure in the region; and 2) to use the results of tomography to reveal outliers in our dataset that may indicate errors in our calibration work or in phase identification. The results we show here deal mainly with the first effort. Tomography is conducted with the method described by Ritzwoller et al. (2002). Only *Pn* tomography has been attempted so far.

A Baseline Model

For our initial tomographic studies, in which we are trying to obtain a reasonable base model for more detailed studies with the full dataset of arrival time readings, we use only *Pn* readings from events that are calibrated to $GT5_{90}$ or better. Before any tomography was performed, we simply compared the predicted travel times through several reference models to the empircally-determined travel times from our GT dataset (Figure 6). The comparisons shown here were done for a single source region (the Dorud cluster, Figure 5), sampling paths to existing seismic stations in the study region.

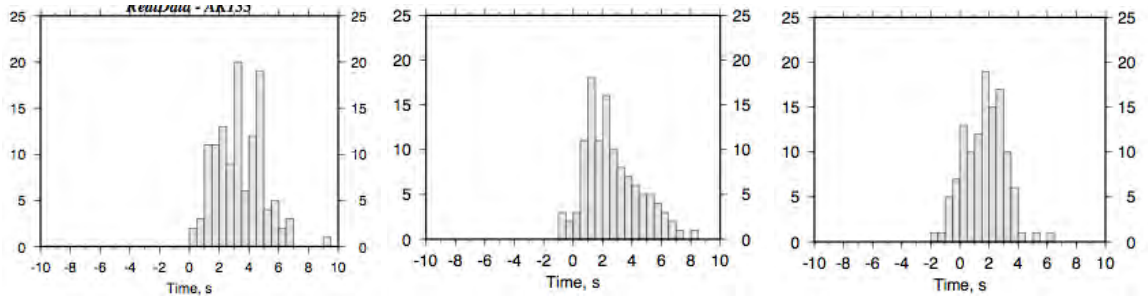

Figure 6. Histograms of the residuals against our GT dataset for the Dorud cluster of predicted travel times for Pn through Left) ak135, Center) CUB2.0, and Right) Unified model.

All three models are too fast by 2–4 seconds on average, compared to the GT dataset travel times. The three primary sources for these discrepancies are 1) average crustal thickness which is too small, 2) average crustal velocities that are too high, and 3) average upper mantle *Pn* velocities that are too high. *Pn* data alone provide only very weak resolving power between these factors, and so we try to use information from other sources to place some constraints on a baseline model.

One such constraint comes from numerous studies (e.g., Doloei and Roberts, 2003; Sodoudi et al., 2004; Mokhtari et al. 2004; Kaviani et al., 2007) that indicate Moho depth in the study region ranges over 40-55 km. Therefore it is likely that the residuals of the ak135 model (which has a 35-km thick crust) against the GT dataset are partly the result of a too-thin crust. A model in which the two crustal layers of ak135 are stretched proportionally to a total thickness of 45 km improves the fit to observed *Pn* travel times, but there is still a systematic positive residual. We next decreased the crustal velocities by 10%, which gives a good average fit to the observed *Pn* data (Figure 7)

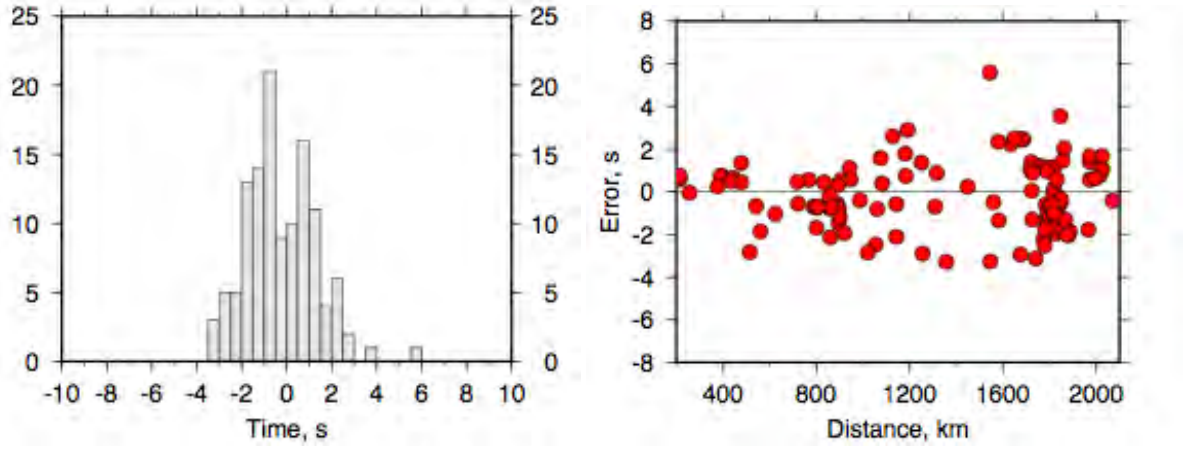

Figure 7. Left) Histogram of residuals against out GT dataset of predicted travel times for *Pn* with a model based on the ak135 model with crustal layers stretched proportionally to a total thickness of 45 km and crustal velocities reduced by 10%. Right) Same residuals plotted as a function of epicentral distance, showing that there is no trend with distance that would indicate the need for a different average *Pn* velocity in the model.

The fact that there is no evidence of distance-dependent trend in the residuals in Figure 7 indicates that the ak135 *Pn* velocity (8.045 km/s) is a reasonable average for this source region. This baseline model is derived for one source region in the study region. We will repeat the exercise with other source regions, and with the entire GT dataset, in order to better understand the variability of such models across the study region and to derive a full-region baseline model for *Pn* tomography with larger datasets. It is not yet clear if we will be able to use a single crustal thickness across the entire region, or whether we will adopt a baseline model which incorporates some degree of variability in Moho depth. The issue of Moho depth variations as it relates to *Pn* tomography is further considered below.

Event Corrections vs. Cluster Corrections

In standard *Pn* tomography studies, a source correction term is allowed for each earthquake source to absorb errors in assumed location, focal depth, and origin time, as well as near-source crustal velocity variations. This adds a large number of free parameters to the problem. In our case however, the multiple event relocation algorithm we use to develop clusters of calibrated earthquake locations provides very string constraints on the relative locations and origin times of the events in a given cluster. Therefore, we can reduce the number of free parameters dramatically by specifying a “cluster correction” which is common to all events in each cluster. The consequence of doing tomography with the two types of correction is shown in Figure 8.

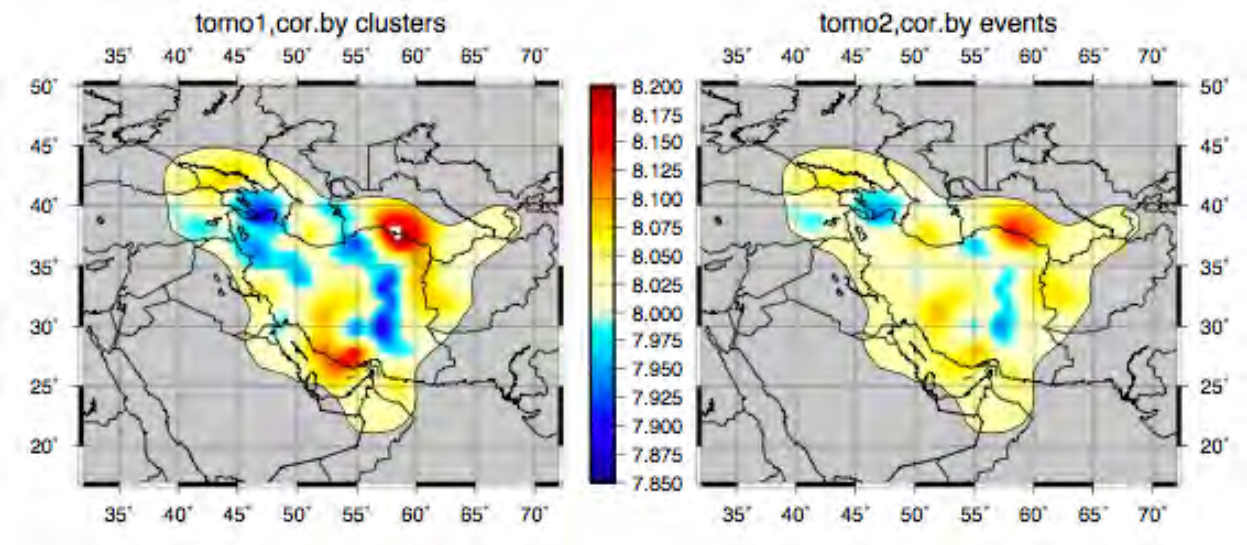

Figure 8. Comparison of *Pn* tomography done with Left) cluster corrections, and Right) event corrections, using 6,135 *Pn* raypaths from GT5 events to stations in the region. The clipping region, within which results are shown in color, is defined by a raypath density of at least 50 rays within a 2°x2° cell.

The use of event corrections clearly allows them to absorb some of the signal that would otherwise be reflected in greater variations in *Pn* velocity. The reduction in velocity variations when using event corrections is about 0.3%.

Relative Importance of Source and Station Corrections

We carried out several tomographic studies to determine the relative importance of source corrections (i.e., cluster corrections) and station corrections, which mainly account for departures of the crustal velocities from those of our model. The reference model is ak135, stretched to have a 45 km crustal thickness, retaining ak135 crustal velocities. The consequence of using no source or station corrections is shown in Figure 9.

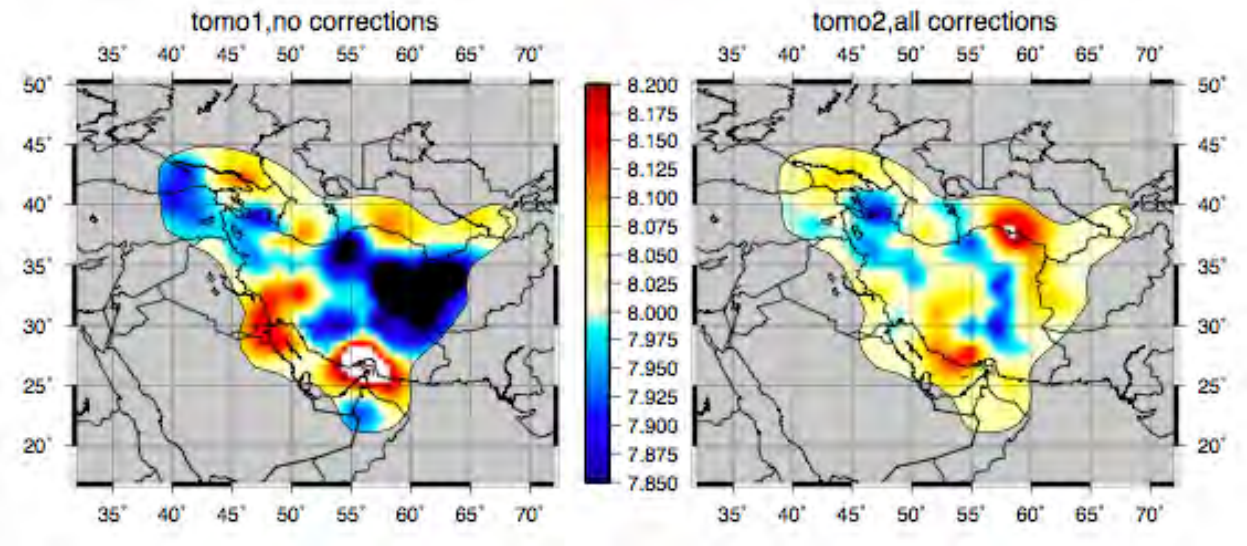

Figure 9. Left) Tomographic results when neither cluster nor station corrections are applied, compared to Right) tomographic results when both cluster and station corrections are applied. Same dataset as Figure 8.

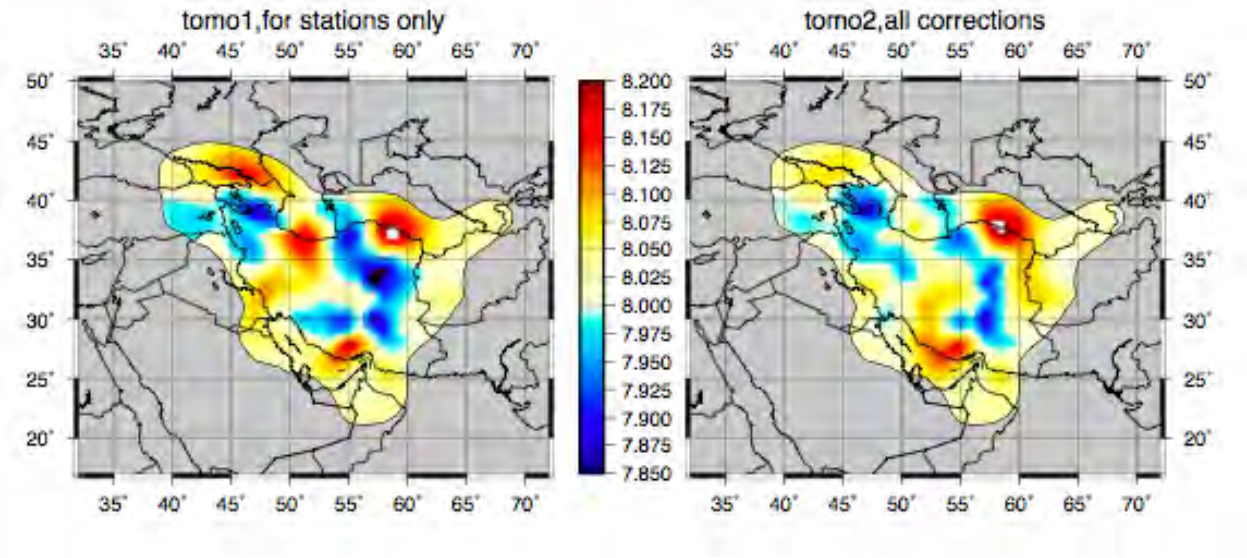

Figure 10. Left) Tomographic results when station corrections, but no cluster corrections, are applied, compared to Right) tomographic results when both cluster and station corrections are applied. Same dataset as Figure 8.

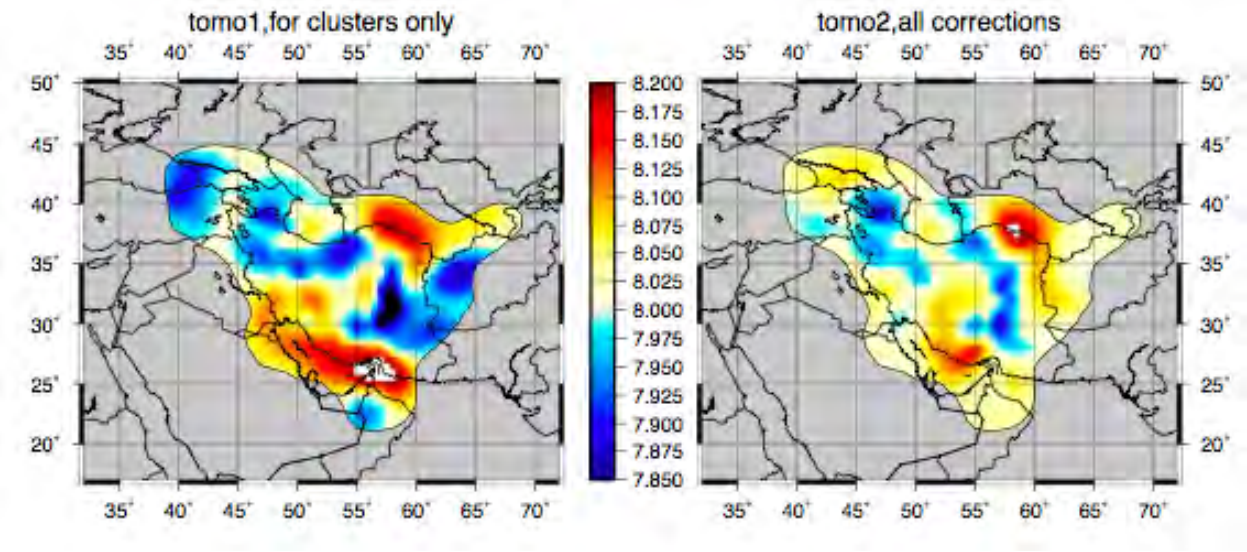

Figure 11. Left) Tomographic results when cluster corrections, but no station corrections, are applied, compared to Right) tomographic results when both cluster and station corrections are applied. Same dataset as Figure 8.

Qualitatively, tomography using station corrections but no source corrections appears rather similar to the result when using all corrections (Figure 10), while tomography using source (cluster) corrections without station corrections leads to an image of *Pn* velocity variations that differs significantly from the case of using both source and station corrections (Figure 11). The magnitude of the difference in *Pn* velocities in each pair of cases is about the same, however, and we suspect that the greater apparent importance of station corrections is an artifact of source and station distribution. It is clear that both source and station corrections are needed, and examination of these corrections is a good indicator of data quality problems, such as poor calibration of a cluster or erroneous station coordinates or timing problems.

Contribution of Moho depth variations

If *Pn* tomography is performed assuming a flat-layered Moho, any actual variations in Moho depth will cause variability in *Pn* arrival times that will be mapped into *Pn* velocity variations. To estimate the degree to which this

could occur in the study region we calculated travel times through a model with variable Moho depth based on observed topography, and compared their variability with that of the observed dataset of calibrated *Pn* travel times.

To generate a model of Moho depth variability we converted topography to Moho depth through the assumption of full isostatic compensation. With reasonable assumptions about density contrast, the surface topography (low pass filtered at a wavelength of 100 km) transforms into inverse Moho depth variations that are larger by a factor of 5.

The variability of observed *Pn* arrival times from our GT dataset is shown in Figure 12, and the variability of *Pn* travel times through the model with artificial Moho undulations based on observed topography and the assumption of full isostasy is shown in Figure 13. Note that the same horizontal scale is used for both plots. The raypaths through the model with undulating Moho were based on the actual source locations of events in the GT dataset and actual stations in the study region.

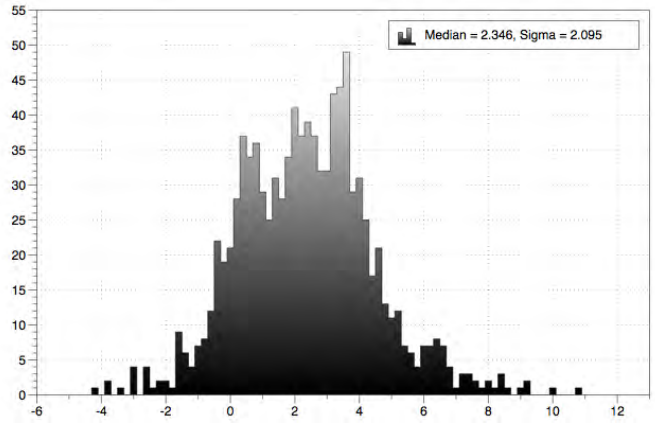

Figure 12. Histogram of residuals for *Pn* arrivals at less than 10° epicentral distance from the GT dataset.

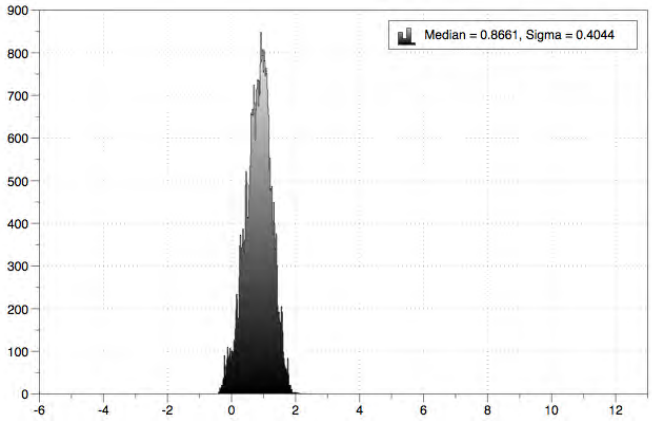

Figure 13. Histogram of residuals for synthetic *Pn* phases traced through the model with Moho undulations based on observed topography and the assumption of full isostatic compensation. Same horizontal scale as Figure 12.

The variance of *Pn* arrival times through the model with undulating Moho $\sigma^2 = 0.16$ is only about 4% of the variance of the observed dataset ($\sigma^2 = 4.38$). Therefore Moho variability is a minor component of the observed variability of *Pn* travel times in the study region. The major factors in the observed variability must be related velocity variations in the crust and upper mantle, departures of raypaths from the geometric assumption, errors in cluster calibration, and errors in phase identification.

CONCLUSIONS AND RECOMMENDATIONS

At this point of the project we have assembled a catalog of seismicity that incorporates a large amount of in-country phase readings. Most earthquakes were carefully relocated in a single event process. We continue to develop this catalog, but it is already a good dataset for use in general tomographic studies of the region. We have also developed

28 calibrated clusters of earthquakes, containing over 800 $GT5_{90}$ events, which are well enough distributed to permit useful tomography to be conducted using only events with calibrated locations and origin times, and datasets of phase readings that have been carefully reviewed and filtered for outliers in a multiple event location analysis. We continue to add new calibrated clusters. Our initial tomographic studies have been concerned with developing a suitable baseline model for tomography. Existing models are generally too fast (theoretical *Pn* arrivals are early by 2-4 seconds). A model similar to ak135 with 45 km thick crust and somewhat slower crustal velocities appears to be a good candidate for the baseline model but further testing is needed. When using our GT dataset for tomography, it is advantageous to parameterize source corrections as cluster corrections (applied to all events in the cluster) rather than individual event corrections. A synthetic experiment suggests that variability of Moho depth in the study region accounts for only a small fraction of the observed variability of *Pn* travel times. The major sources of the observed variability must be velocity varitaions in the crust and upper mantle, perturbations of the raypaths by lateral heterogeneity, and errors in location calibration and phase identification.

ACKNOWLEDGEMENTS

We have received invaluable assistance in this work from numerous colleagues in the study region who prefer to remain unnamed.

REFERENCES

Begnaud, M. L., C. A. Rowe, and L. K. Steck (2004). Validating three-dimensional velocity models in China and East-Asia for use in regional seismic event location, *Eos Trans. Am. Geophys. Union* 85: (47, Fall Meet. Suppl.), T11C-1277.

Doloei, J. and R. Roberts (2003). Crust and uppermost mantle structure of Tehran region from analysis of teleseismic P-waveform receiver functions, *Tectonophysics* 364: (3-4), 115–133.

Flanagan, M. P., S. C. Myers, and K. D. Koper (2007). Regional travel-time uncertainty and seismic location improvement using a three-dimensional *a priori* velocity model, *Bull. Seismol. Soc. Am.* 97: (3), 804–825.

Kaviani, A., A. Paul, E. Bourova, D. Hatzfeld, H. Pedersen, and M. Mokhtari (2007). A strong seismic velocity contrast in the shallow mantle across the Zagros collision zone (Iran), *Geophys. J. Int.* 17: (1), 399–410.

Kennett, B. L. N., E. R. Engdahl, and R. P. Buland (1995). Constraints on seismic velocities in the Earth from traveltimes, *Geophys. J. Int.* 122: (1), 108–124.

Mokhtari, M., A. M. Farahbod, C. Lindholm, M. Alahyarkhani, and H. Bungum (2004). An approach to a comprehensive Moho depth map and crust and upper mantle velocity model for Iran, *Iranian Int. J. Sci.* 5: (2), 223–244.

Pasyanos, M. E., W. R. Walter, M. P. Flanagan, P. Goldstein, and J. Bhattacharyya (2004). Building and testing an *a priori* geophysical model for Western Eurasia and North Africa, *Pageoph* 161: 235–281.

Ritzwoller, M. H., N. M. Shapiro, M. P. Barmin, and A. L. Levshin (2002). Global surface wave diffraction tomography, *J. Geophys. Res*. 107: (B12), 2335, doi:10.1029/2002JB001777.

Ritzwoller, M. H., N. M. Shapiro, A. L. Levshin, E. A. Bergman, and E. R. Engdahl (2003). Ability of a global three-dimensional model to locate regional events, *J. Geophys. Res.* 108: (B7), 2353, doi:10.1029/2002JB002167.

Sodoudi, F., R. Kind, N. Kamalian, and A. Sadidkhoy (2004). The crustal and upper mantle structure of the central Alborz (Iran) using teleseismic receiver functions, *Geophys Res Abs* 6: 01353.

Steck, L. K., C. A. Rowe, M. L. Begnaud, W. S. Phillips, V. L. Gee, and A. A. Velasco (2004). Advancing seismic event location through difference constraints and three-dimensional models, in *Proceedings of the 26th Seismic Research Review: Trends in Nuclear Explosion Monitoring*, LA-UR-04-5801, Vol. 1, pp. 346–355.

MODELING REGIONAL SEISMIC PHASES AND CODA FROM EARTHQUAKES AND EXPLOSIONS USING GENERALIZED FOURIER METHODS IN 2D/3D

Jessie L. Bonner[1], David G. Harkrider[1], James Britton[1], and Jeffrey L. Orrey[2]

Weston Geophysical Corp.[1] and GeoVisual Technologies, Inc. [2]

Sponsored by the National Nuclear Security Administration

Contract No. DE-AC52-05NA26610
Proposal No. BAA05-59

ABSTRACT

We continue to develop a numerical code for modeling regional seismic phases from earthquakes and explosions in 2D/3D media using Generalized Fourier Methods (GFM). During the past year, we have modified the GFM code by implementing efficient and accurate *Q* parameterization and variable gridding in order to simulate topography. The objective of our current modeling is to better understand *Lg* and *Lg* coda propagation using synthetics generated with both earthquake and explosion source models.

We have studied five velocity models as described in Yang (2002), including two Tibet models, a Chinese model, and a Tarim Basin model. We parameterized the models for 2D GFM with a grid spacing of 0.25 km, horizontal dimension of 962 km, and depth dimension of 110 km. We used a double couple source with and without attenuation to generate the synthetics. We estimated the geometrical spreading for *Lg* using the GFM synthetics without attenuation. We determined that *Lg* decays at a rate of $\Delta^{-0.52}$ and $\Delta^{-1.01}$ for spectral versus time domain measurements, which are similar to Yang's (2002) results for wavenumber-integration synthetics. We are currently examining the 3D effects on geometric spreading.

Next, we applied a Q_β=200 and Q_α=2.25*Q_β throughout the entire model and generated synthetics using the 2D GFM for source depths of 1, 5, 10, and 30 km. We then used the two-station technique (Xie et al., 2006) to estimate power-law Q_o and η from the synthetics. For all models and depths, the Q_os estimated from the synthetics were within 5% of the input Q_β. With the exception of the two Tibetan models at a source depth of 1 km (η>0.4), all frequency-dependence η results were ~0. The estimated Q_os are all reduced when stochastic variations are added to the model. For example, when we add perterbations with von Karman distributions, 10% amplitudes, and 1 km correlation lengths, the Q_o is decreased from the input *Q* by 6-25%. The amount of reduction caused by the heterogeneities is both model and depth dependent.

In the process of porting source-time functions with our synthetics, we reviewed the available explosion source theories. We have included the Haskell (1961) source theory. Haskell suggested that simple analytical functions could fit the calculated reduced displacement potentials from near-source measurements of nuclear tests detonated in different lithologies. He showed that displacement scaling is inversely proportional to the cube root of yield at high frequencies and proportional to yield at low frequencies. The theory is based on continuum mechanics, which allows for either realistic plastic or fractured emplacement media. Additionally, it allows for different pressure and gas porosity considerations both above and below the water table. The theory also allows for different cavity and vapor radii, which could be used to model decoupled explosions. These and additional features of the Haskell source theory result in accurate predictions of the observed characteristics (e.g., corner frequencies, ψ_∞, etc) of Nevada Test Site (NTS) explosions such as Cowboy and Rainier.

We modeled small chemical explosions and found that the Haskell-predicted M_ws are typically within 7% of the observed estimates based on moment tensor inversions. Haskell's source performed better at estimating the moment magnitudes than Denny and Johnson (1991), which was based on NTS data. Our next step is to convolve the Haskell source with the GFM synthetics to examine source effects on regional phase partitioning from explosions.

OBJECTIVES

We continue to develop a numerical code for modeling regional seismic phases from earthquakes and explosions in 2D/3D media using Generalized Fourier Methods (GFM). During the past year, we have modified the GFM code by implementing efficient and accurate *Q* parameterization and variable gridding in order to simulate topography. The objective of our current modeling is to better understand *Lg* and *Lg* coda propagation using synthetics generated with both earthquake and explosion source models.

RESEARCH ACCOMPLISHED

Code Improvements

Anelasticity. We have successfully implemented anelastic attenuation (*Q*) in the GFM with parallelization. The *Q* implementation makes use of a time-domain approximation of frequency-dependent attenuation through a superposition of relaxation mechanisms (Emmerich and Korn, 1987). In order to apply this technique in the parallel computation environment used with GFM, it was necessary to extend the Message Passing Interface (MPI) calls to the additional "memory variables" that make up the relaxation mechanism contributions to the stress tensor. Our *Q* implementation is completely general, in that it is possible to assign independent Q_p and Q_s values, for *P*-waves and *S*-waves, respectively, to each node in the 3D computational grid. This requires significant additional memory since the memory variables are stored for all nodes in 3D, but it affords the most detailed specification of *Q* models. In future efforts, we can consider reducing the number of independent *Q* values stored in the grid to less than the total number of computational nodes in the model, where a simplified *Q* structure will suffice and significant memory savings will allow us to run simulations to greater distances and/or to high frequencies.

There is some computational complexity added by the parallelization of the *Q* implementation, in that since each computational node has a (potentially) unique *Q* value and those values must be read into memory for each processor that is assigned the associated sub-region of the computational grid. We store the *Q* structure of the Earth model along with the other model parameters (i.e., *Vp*, *Vs* and density), and then we read all material values using the master processor, which in turn distributes the material values for each sub-region associated with each slave processor to begin time step iterations.

Non-uniform Grid for Topography. We have successfully implemented an irregularly-spaced grid into GFM in the vertical coordinate direction – a final step in demonstrating the generalized technique of applying a coordinate transformation to the computation grid to simulate non-regular physical spaces such as a topographic surface (Orrey, 1995). The practical application of an irregular vertical grid spacing is to improve the accuracy of the solutions for signals affected by the free surface (i.e., fundamental and higher mode surface waves – *Rg*, *Lg*, etc.). The improvement is realized by reducing the computational node spacing near the free surface so that signals near the surface are spatially sampled with relatively more nodes. The denser grid spacing (in the vertical direction) better supports the curvature of the wavefront near the surface and the interaction of the wavefront with the boundary.

The other practical advantage of using a non-uniform grid in the vertical direction is to save grid points (and therefore, memory). For most Earth models of interest, the relatively lower velocity values near the surface require higher spatial sampling for a maximum solution frequency of interest due to the relatively higher wavelengths in the low velocity zone. Therefore, using a smaller grid spacing in the low velocity zone only, versus throughout the entire grid, is a more efficient implementation.

In our final task to implement surface topography, we will extend the non-uniform grid formulation to the case where the vertical grid point distribution is also a function of the horizontal coordinates. Then the grid can be "stretched" and "compressed" in the vertical direction as needed to match the topography of the region of interest.

Examining the Effects of Crustal Heterogeneity on Regional Phases

In his paper examining the geometric spreading of *Lg*, Yang (2002) studied five velocity models, including a primary model (Levin et al., 1995), two Tibet models (Jih, 1998; Li and Mooney, 1998), a Chinese model (Jih, 1998), and a Tarim Basin model (Jih, 1998). The reader is referred to Yang's (2002) Figure 1 and Table 1 for the models. We parameterized the Yang (2002) models for the two-dimensional version of GFM (2D GFM) with a grid spacing of 0.25 km, horizontal dimension of 962 km, and depth dimension of 110 km. We used a double couple source with and without attenuation to generate the synthetics. For models with attenuation, we applied a Q_β=200 and Q_α=2.25*Q_β throughout the entire model and generated synthetics using 2D GFM for source depths of 1, 5, 10, and 30 km. We have also added stochastic variations to the media to examine the effects of crustal heterogeneity of regional phases. For this study, we added perterbations with von Karman distributions, 10% and 20% amplitudes, and 1 km horizontal and vertical correlation lengths.

Example of the synthetics from a 10 km deep double couple earthquake source propagated through homogenous and heterogeneous versions of the China model (Jih, 1998) at a distance of 500 km are shown in Figure 1. The phases are highlighted by group velocity windows, which for *Lg* (e.g., 3.72 and 3.12 km/sec) were taken from Yang (2002). Spectral ratios were formed between the homogenous model synthetic (top in Figure 1) in the numerator and the synthetics for the two heterogeneous models (Figure 2) in the denominator. The effect of the random perturbations is to decrease the amplitudes of the direct arrivals *Pn*, *Pg*, and *Lg* at frequencies above 0.5 Hz. The energy from these direct phases is scattered into the *P* coda (Figure 2) and *Lg* coda (not shown on Figure 2 but obvious from Figure 1). While this is expected, we did not expect to see that the amplitudes for the short-period surface waves (e.g., *Rg*) are increased by a factor of 2-3x for the models with the stochastic variations between 0.5 and 1.5 Hz. It is generally thought that *Rg* would be highly scattered into *S*-waves or coda.

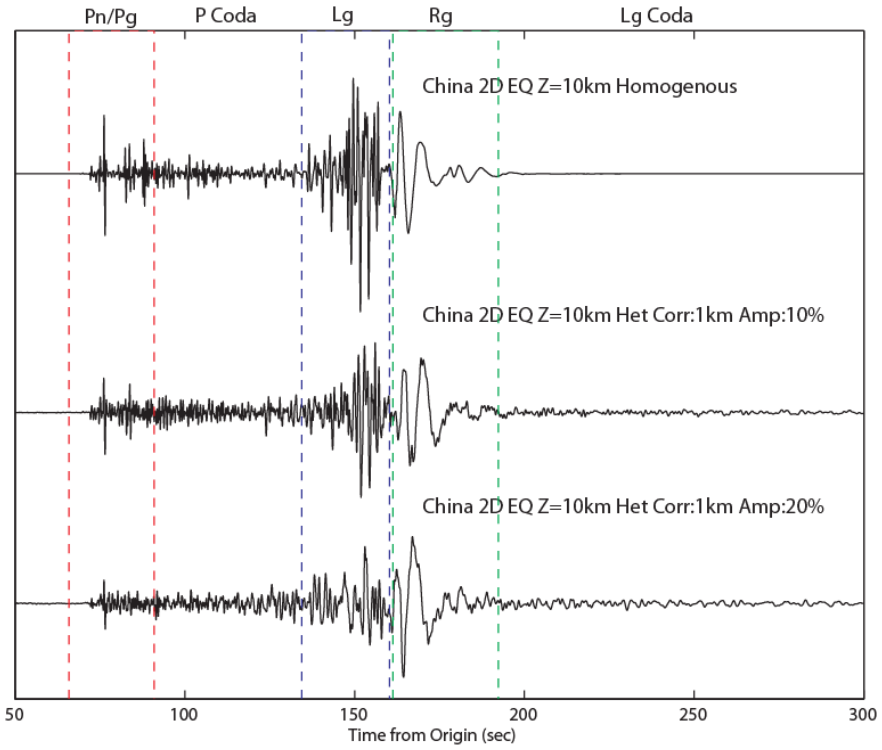

Figure 1. 2D GFM synthetics for a China model (Jih, 1998) at a distance of 500 km. The model for the upper trace had no stochastic variations, while the lower two traces were propagated through a model with stochastic variations with amplitudes of 10% (middle) and 20% (bottom). The regional phases are highlighted by dashed lines.

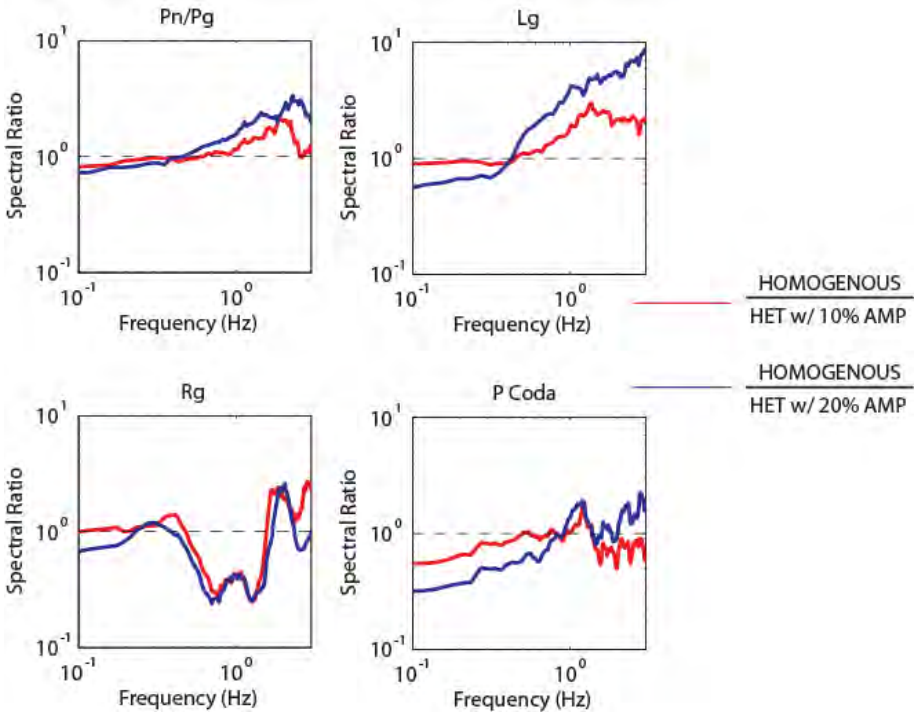

Figure 2. Spectral ratios for the regional phases shown in Figure 1. In each case, the signal in the numerator is from synthetics propagated through a homogenous model while the signal in the denominator is from the heterogeneous model. The red and blue lines represent 10% and 20% stochastic perturbations, respectively.

The next stage of modeling involved quantifying the effects of heterogeneity on *Lg Q*. The synthetic *Lg* were windowed using a group velocity window based on Yang (2002). Pre-event noise was similarly windowed, and Fourier spectra of synthetic noise and *Lg* were calculated. Assuming that *Lg Q* follow the power-law frequency dependence of $Q = Q_0 f^{\eta}$ (where Q_o is the *Lg Q* at 1 Hz and η is the frequency dependence), the interstation Q can be estimated using Xie et al. (2004, 2006):

$$\ln\left\{\frac{V_{Lg}}{\pi\Delta_{i,j}}\ln\left[\frac{\Delta_i^{1/2}}{\Delta_j^{1/2}}\times\frac{A_i(f)}{A_j(f)}\right]\right\} = (1-\eta)\ln f - \ln Q_o, \qquad (1)$$

where V_{Lg} is the typical *Lg* group velocity of 3.5 km/sec, Δ_i and Δ_j are the epicentral distances to the two aligned stations where the *Lg* spectra *Ai(f)* and *Aj(f)* were observed, and $\Delta_{i,j}$ is the interstation distance. In Equation 1, the left hand quantity is calculable from the observed spectral ratios and can be averaged over repeating two-station paths to provide stable estimates of Q_o and η by a linear regression.

We used Equation 1 to estimate *Lg* Q_o and η for all possible two-station combinations of the GFM synthetics with interstation separation greater than 200 km. We considered frequencies between 0.1 and 2 Hz due to the accuracy limitations of GFM and a 0.25 km grid spacing. Figure 3 shows the estimated *Lg Q* and η as a function of the interstation distance for the China model and a synthetic earthquake at 10 km depth. For this model, inclusion of the stochastic variations reduced the average estimated Q_o from 202 to 178 (10% perturbation of amplitudes) to 146 (20%). The error in the estimated values increases at shorter interstation distances, which was theorized in the Appendix of Xie et al. (2004). Also of interest is the change in the frequency dependence when increasing the amplitude of the stochastic variations. The mean η ranges from -0.1, which, when the error is considered could be assumed to be frequency independent, to 0.5 for the stochastic model with 20% amplitude perturbations. This later value is similar to what is often observed on real seismic data.

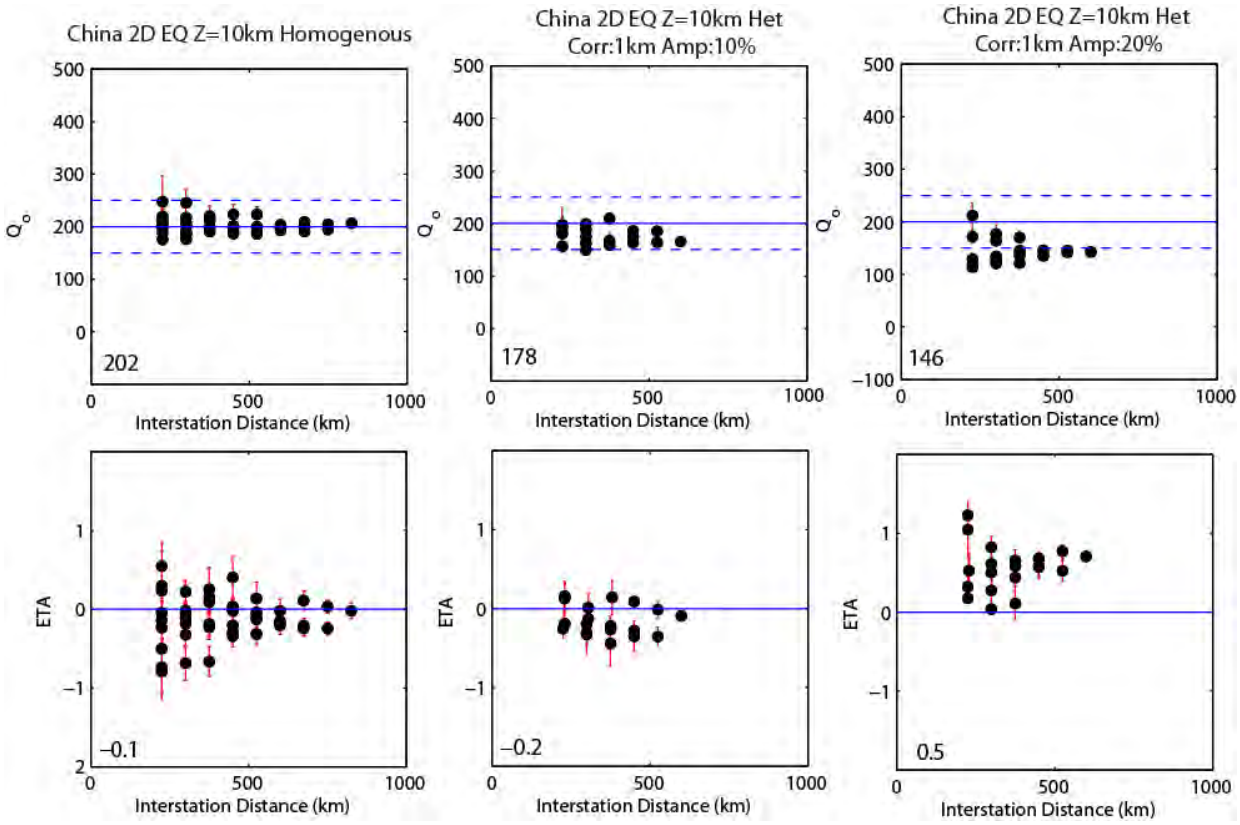

Figure 3. Two-station *Lg* Q_o and η (ETA) processing for a synthetic earthquake at 10 km depth and a China velocity model (Jih, 1998) without (left column) and with stochastic variations (middle and right columns). The initial shear-wave Q_β value of the crust was set to 200 (solid blue line in upper plots with ±20% shown as dashed lines), and we expected no frequency dependence in the results (e.g., ETA=0; blue line in lower plots). Each *Lg* Q_o and ETA value shows the error as a vertical red line. Mean values are listed in the left corner of each plot.

Figure 4 shows the results for all models except the Tarim Basin model. The very low velocities coupled with the low Q_β in this model resulted in instabilites in GFM, which are currently being investigated. The problem is asymptotic drift of the synthetics at simulation times greater than 100 seconds. For all other homogenous models and depths, the Q_os estimated from the synthetics were within 5% of the input Q_β. With the exception of the two Tibetan models at a source depth of 1 km (η>0.4), all frequency-dependence η results were ~0.

The estimated Q_os are reduced when stochastic variations are added to the model. For example, when we add perturbations with von Karman distributions, 10% perturbation amplitudes, and 1 km correlation lengths, the Q_o is decreased from the input Q_β by 10–25%. The amount of reduction caused by the heterogeneities is both model and depth dependent. For example, the "primary" model shows the largest decrease in the Q_o estimates for synethtic earthquakes at 1, 5, and 10 km depths; however the estimate for the 30 km deep source is anomalously above the input Q_β value. There is currently no explanation for this observation, as it does not appear to be measurement error.

Adding the stochastic variations with 10% perturbation amplitudes to the velocity models has little effect on the frequency dependence of the synthetic *Lg*. However, increasing the perturbation amplitude to 20% increases the frequency dependence from ~0 to positive values as large as 0.9 depending on source depth. The Q_o is decreased from the input Q_β by 10–40% for the models with the larger amplitude perturbations. These synthetic results have important implications as to how *Lg* Q_o and η estimates from observed seismic data should be interpreted.

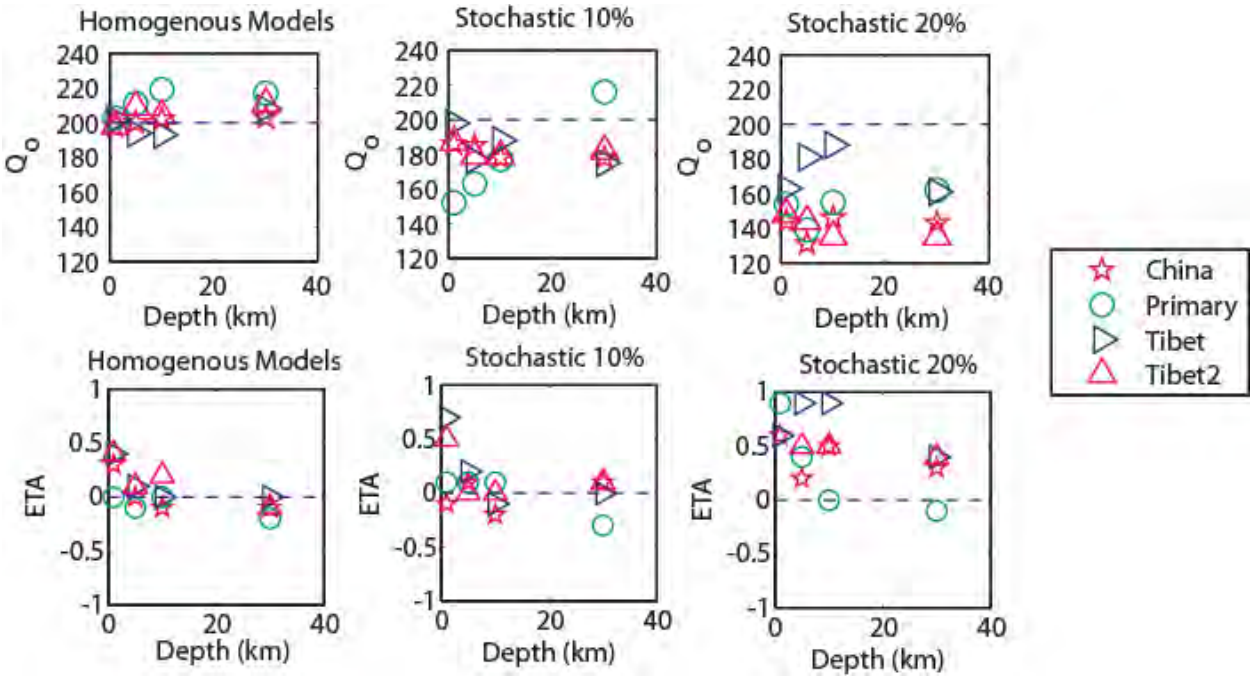

Figure 4. Two-station *Lg* Q_o and η (ETA) processing for a synthetic earthquakes at depths of 1, 5, 10, and 30 km for four different models without (left column) and with stochastic variations (middle and right columns). The initial shear-wave Q_β value of the crust was set to 200 (dashed blue line in upper plots). No frequency dependence (e.g., ETA~0) is shown as the dashed line in the lower subplots.

3D Simulations for the NTS

Bonner et al. (2008) examined earthquake and explosion synthetics for 2D GFM models for the NTS region. We are currently extending this modeling to 3D GFM. The background velocity structure for NTS is based on a regional model for the Basin and Range similar to the model developed by Benz et al. (1991). The velocities in the upper crust are based on borehole data, geologic and gravity data, refraction studies and seismic experiments. We have used various techniques to estimate stochastic parameters for the Basin and Range. This includes using previous well-located nuclear explosions to estimate correlation lengths for scattering of the *Lg* phase (Tibuleac et al., 2006). These results suggest that the horizontal correlation lengths for a von Karman stochastic model range between 0.5–2 km with smaller vertical correlation lengths. The Hurst numbers (H) are related to the fractal dimension of the medium and range between 0.3 and 0.6. Bonner et al. (2008) obtained their best 2D modeling results using the Patton and Taylor (1984) attenuation model, which is characterized by low Q_β (85–172) throughout the entire crust. We have used the Patton and Taylor (1984) *Q* model in the 3D synthetic runs.

Figures 5 and 6 present several different synthetic seismograms recorded at 200 km propagated through a 3D model with grid spacing of 0.5 km. For the stochastic model runs, we considered horizontal and vertical correlation lengths of 2 km, with smaller correlation length simulations planned. For reference, we plot wavenumber-intergration synthetics (Herrmann, 2002) for 1D homogenous versions of the 3D model. Finally, we show an NTS explosion recorded at Mina, Nevada (MNV) at a distance of 201 km.

While we await the results for smaller correlation lengths, it is clear that adding stochastic variations to the NTS model provides a better match to the observed NTS data. The large amplitude explosion-generated *Rg* predicted by the wavenumber-integration synthetics in Figure 5 is not visible in the Mast waveform at MNV. The phase has also been scattered in the GFM synthetics with stochastic variations. The GFM synthetics also predict the larger amplitude phase–possibly higher mode surface waves–at MNV just after the *Lg* window, although the observed arrival appears to be lower frequency than the synthetics.

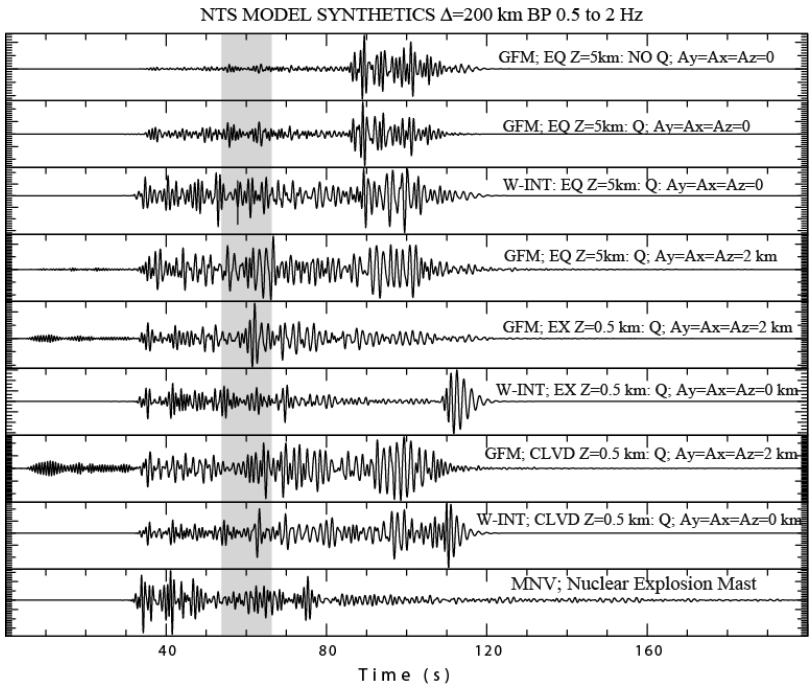

Figure 5. 3D GFM and 1D wavenumber-integration (W-INT) synthetics bandpass filtered between 0.5 and 2 Hz for an NTS model. The top four traces are for a synthetic earthquake at 5 km depth, and final synthetics are either for a monopole explosion or CLVD source. The first trace was propagated without *Q* while all other simulations had attenuation. The models were either homogenous (e.g., Ax=Ay=Az=0) or stochastic with 2 km correlation lengths. All GFM simulations were for 3D models while W-INT solutions were for a 1D homogenous slice of the NTS model. Also shown are the records for the nuclear explosion Mast at MNV. The *Lg* group velocity window is shown in gray.

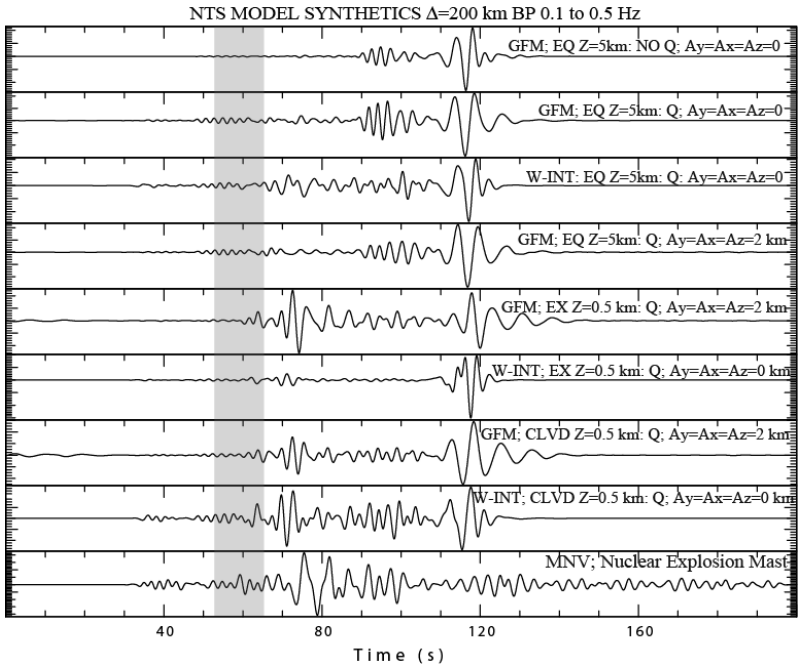

Figure 6. 3D GFM and 1D wavenumber-integration (W-INT) synthetics bandpass filtered between 0.1 and 0.5 Hz for an NTS model. See Figure 5 caption for further explanation.

Re-Evaluation of the Haskell Source with Application to Small Explosions

The theoretical derivation of explosion source time-functions begins with Sharpe (1942) among others. Today, the most popular explosion source theory is arguably the Mueller-Murphy (1971) model, which was based on the initial source theory of Sharpe and free-field observations from the NTS to develop an analytic approximation to the pressure field acting at the elastic radius. The Mueller-Murphy model has been shown to predict the source characteristics of nuclear explosions as well as smaller chemical and mining explosions.

In the process of porting the Harkrider (1964) synthetics programs into our synthetic calculations, we reviewed the available explosion source theories for inclusion in the new software package. We included the Haskell (1961) static source theory. Primarily interested in decoupling, Haskell assumed that the source region was composed of a vaporization region surrounded by the containment media, which behaved elastically beyond the elastic radius (r_2). Inside the elastic radius to the vapor radius (r_o), a region of stress greater than the plastic yield stress is governed by the Coulomb-Mohr yield criteria. During the explosion, the plastic state of the material is forced by the expanding gasses out to a radius, which is assumed to be the observed cavity radius (r_1). This formulation requires the explosive yield, the ratio of the vapor to the cavity radius, and a plastic parameter that is a simple function the Coulomb coefficient of friction and the tensile strength of the material, to obtain a unique solution. This solution, predicts the vapor, cavity and elastic radii as well as ψ_∞. This solution, predicts the vapor, cavity and elastic radii as well as the steady-state estimate of the reduced displacement potential (e.g., ψ_∞).

The equation used to determine ψ_∞, r_1, and r_2 as functions of r_o is:

$$\left(\frac{r_0}{r_1}\right)^3 = 1 - \frac{3k(\sigma_1 + P_0)}{\mu(3-k)}\left(\frac{r_2}{r_1}\right)^3 - \frac{3(\sigma_1 + P_0)}{(3\lambda + 2\mu)}\left[1 + \frac{4k}{3-k}\left(\frac{r_2}{r_1}\right)^3 - \frac{3(1+k)}{3-k}\left(\frac{r_2}{r_1}\right)^m\right], \qquad (2)$$

where σ_1 is a principal stress, k is internal friction, m = $4k/(1+k)$, λ and μ are Lame's constants, and P_o is the static or overburden pressure. The corresponding initial radius is then computed as:

$$r_0^3 = \frac{3(\gamma - 1)W}{4\pi P}\left(\frac{r_0}{r_1}\right)^{3\gamma}, \qquad (3)$$

where γ is the specific heat ratio of the gas, W is the explosion yield, and P is the final cavity pressure. ψ_∞ is estimated with the equation:

$$\psi_\infty = \frac{r_2^3 k(\sigma_1 + P_0)}{\mu(3-k)}. \qquad (4)$$

Haskell used his formulation for the Cowboy experiments and the contained Rainier event. Since then, seismic moment, cavity radius, and corner frequency for NTS events have been regressed by Denny and Johnson (1991) as a function of yield and elastic confinement media constants. The Haskell solution of the Rainier event, assuming the calculated or observed ratio of the vapor to cavity radii, agreed remarkably well with the regression values (Table 1). Since the relation between explosion moment and ψ_∞ had not been defined in 1961, we used the Haskell and elastic radius to calculate the moment and the corner frequency from the elastic radius and body velocity.

Table 1. Comparison of Haskell (1961) versus Denny and Johnson (1991) results for the NTS event Rainier

Parameter	Haskell (1961)	Denny and Johnson (1991)	%Difference
Cavity Radius (m)	18.6	17.9	3.9
Moment (N-m)	2.4E14	2.7E14	11.1
Corner Frequency (Hz)	1.9	2.1	9.5

The Haskell (1961) theory is most useful for predicting ψ_∞ and the corner-frequency and is basically a tool for surface wave and M_s calculations. Although, assuming that the pressure history on the cavity wall is a step function,

one can obtain a reduced displacement history for which ψ_∞ is the long time value for use in body wave m_b calculations.

We have modeled small chemical explosions in limestone and granite (Table 2) using the Haskell (1961) source. Haskell proposed that his method could be applied to chemical explosions and that r_o would be equal to the radius of the explosive charge. Since Denny and Johnson (1991) and Haskell (1961) agreed on the cavity radius for Rainier, we used Denny and Johnson (1991) to estimate r_c for the chemical explosions, which provided us with the r_o/r_c needed for the Haskell (1961) source.

Table 2. Parameters used to model chemical explosions using the Haskell (1961) explosion source.

Test Case 1	Arizona Coal Mine	Arizona Copper Mine
Medium	Limestone	Granodiorite
Chemical Explosion Yields	200 lbs – 13,807 lbs	1700 lbs – 13,600 lbs
Charge Radius (ro)	0.1 m	0.1 m
V_p:V_s	3.35 : 0.83 km/sec	5 km/sec
Emplacement Depths	13-35 meters	13-33 meters
Observed M_ws	Yang and Bonner (2009) moment tensor inversions	Zhou et al. (2005) moment tensor inversions

We predicted M_w within 5% of the observed M_w for fully-confined shots in limestone (Figure 7) when using the Haskell (1961) source theory to estimate ψ_∞ and Denny and Johnson (1991) to estimate cavity radius (r_1). It is interesting to note that the Denny and Johnson (1991) predicted $M_w s$, based on regression results from NTS, are off by 8–14% (smaller than observed). For the unconfined shots, which exhibited retarc (crater spelled backwards), the predicted $M_w s$ were 8–12% larger than observed. For the free face shots, the predicted $M_w s$ were 10–22% larger than observed.

We predicted M_w within 2–7% of the observed M_w for fully-confined shots in granodiorite (Figure 7). The Denny and Johnson (1991) predicted $M_w s$ varied from the observed by 8–11%. As expected, Haskell (1961) overpredicts the M_w for free face and unconfined shots, which produced blowout craters, by more than 12%.

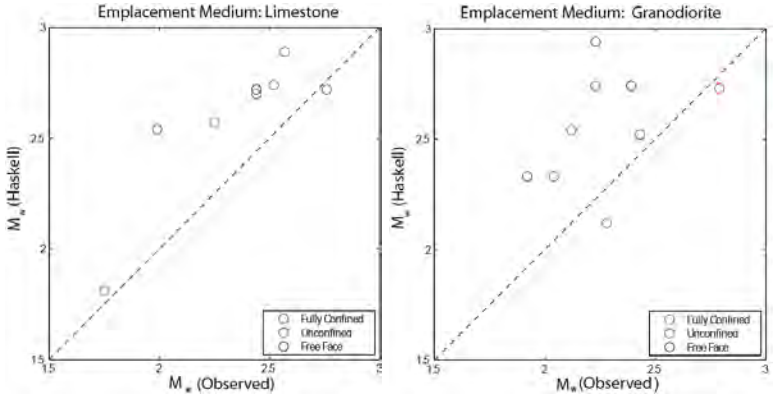

Figure 7. Predicted $M_w s$ using the Haskell (1961) static explosion source theory and explosion parameters in limestone (left) and granodiorite (right).

CONCLUSIONS AND RECOMMENDATIONS

In the remaining months of this project, we will finalize our 3D deterministic and stochastic simulations for the NTS model. We will then convolve the monopole and CLVD Green's functions with the reduced displacement potentials from either the Mueller and Murphy (1971) or Haskell (1961) sources. We will then compare the resulting synthetics to observed seismic data from NTS explosions. We also hope to be able to add topography to these models, which Myers (2007) has shown to be an important source of explosion-generated *S*-waves.

ACKNOWLEDGEMENTS

We wish to thank John Davies for assistance on the code development and Anastasia Stroujkova for help with model development.

REFERENCES

Benz, H. M., Unger, J. D., Leith, W. and V. Ryaboy (1991). The Norilsk DSS Profile in Northern Siberia: Interpretation of the velocity structure and comparison with Basin and Range and New England profiling results, Abstracts of the 13th Annual PL/DARPA Seismic Research Symposium: 85–100.

Bonner, J. L., A. Stroujkova, and K. Mayeda (2008). Predicting explosion-generated *Sn* and *Lg* coda using synthetic seismograms. in *Proceedings of the 30th Monitoring Research Review: Ground-Based Nuclear Explosion Monitoring Technologies*, LA-UR-08-05261, Vol. 1, pp. 10–19.

Denny, M.D. and L. R. Johnson (1991). The explosion seismic source function: model and scaling laws revisited, in H.J. Patton and P.G. Richards, Eds., Explosion Source Phenomenology, Geophysics Monograph 65, American Geophysical Union, Washington, 1–24.

Emmerich, H. and M. Korn (1987). Incorporation of attenuation and time-domain components of seismic wave fields, *Geophys.* 52: 1252–1264.

Harkrider, D.G. (1964). Surface waves in multilayered elastic media I. Rayleigh and Love waves from buried sources in a multilayered elastic half-space. *Bull. Seism. Soc. Am*. 54: 627–679.

Haskell, N. (1961). A static theory of the seismic coupling of a contained underground nuclear explosion, *J. Geophys. Res:* 3297.

Herrmann, R. H. (2002). An overview of synthetic seismogram computation. In *Computer Programs in Seismology, Version 3.30*.

Jih, R. S. (1998). Location calibration efforts in China, in *Proc. 20th Annual Seismic Research Symposium on Monitoring a Comprehensive Test Ban Treaty*, 21–23 September 1998: 44–55.

Levin, V., W.-Y. Kim, and W. Menke (1995). Seismic velocities in the shallow crust of western New England and northern New York, *Bull. Seism. Soc. Am.* 85: 207–219.

Li, S., and W. D. Mooney (1998). Crustal structure of China from deep seismic sounding profiles, *Tectonophysics* 288: 105–113.

Myers, S .C. (2007). Numerical ex periments i nvesigating t he s ource o f ex plosion S -waves. *Seism. Res. Letts.* 78: 240.

Mueller, R. A. and J. R. Murphy, (1971). Seismic characteristics of underground nulear detonations: Part I, Seismic scaling law of underground detonations, *Bull Seism. Soc. Am*. 61: 1675.

Orrey, J. L., (1995). A generalized Fourier pseudospectral method for elastodynamics . Ph. D. Thesis. University of Colorado, Boulder.

Patton, H.J. and S. R. Taylor, (1994). *Q* structure of the Basin and Range from surface waves, *J. Geophys. Res.* 89: 6929–6940

Sharpe, J. A., (1942). The production of elastic waves by explosion pressures: I, Theory and Empirical field observations*, Geophys*. 7: 144.

Tibuleac, I. M., A. Stroujkova, J. L. Bonner, K. Mayeda, and J. Britton (2006). Predicting explosion generated *Lg* and *Sn* using synthetic seismograms, in *28th Seismic Research Review: Ground-Based Nuclear Explosion Monitoring Technologies*: LA-UR-06-5471, Vol. 1, pp. 283–294.

Xie, J. R . Gok, J . N i a nd Y . A oki (2004), L ateral variations o f c rustal s eismic a ttenuation a long t he INDEPTH Profiles in Tibet from Lg *Q* inversion, *J. Geophys. Res*., *109*, B10308, doi:10.1029/2004JB002988.

Xie. J., Z. Wu, D. Schaff, Y. Liu, and J. Liang (2006). Tomographic regionalization of crustal *Lg Q* in eastern Eurasia. *Geophys. Res. Letts*, 33, L03315, doi. 1029/2005GL024410.

Yang, X. and J. L. Bonner (2009). Characteristics of chemical explosive sources from time-dependent moment tensors. *Bull. Seism. Soc. Am.* 99: 36–51.

Yang, X. (2002). A numerical investigation of *Lg* geometrical spreading. *Bull. Seism. Soc. Am*. 92: 3067–3079.

Zhou, R., B. W. Stump and X. Yang (2005). Moment tensor inversions of single-fired mining explosions at a copper mine in Arizona, *Eos Trans. AGU*, 86(52), Fall Meet. Suppl., Abstract S11B–0166.

IMPROVED PHASE CHARACTERIZATION OF FAR-REGIONAL BODY WAVE ARRIVALS IN CENTRAL ASIA

Aaron Ferris, Delaine Reiter, and Katherine Murphy

Weston Geophysical Corporation

Sponsored by the Air Force Research Laboratory

Award No. FA8718-06-C-0002

ABSTRACT

The early body-wave coda of far-regional events (14˚– 29˚ degrees) contains triplicated arrivals from upper-mantle discontinuities that, when properly identified, can improve seismic monitoring functions. However, far-regional seismograms are typically under-utilized because along-path heterogeneity and phase interactions make the arrival suite difficult to interpret accurately. We have developed a set of techniques for small aperture arrays that improve phase characterization and identification at these distances. We have focused our efforts on two arrays in Kazakhstan (MKAR and KKAR), which record far-regional events throughout South-Central Asia. Our techniques include improved array processing methods (e.g., phase-weight semblance stacking) to characterize arrival time, back-azimuth and slowness of individual phases within the *P*-coda arrival suite, and methods to more accurately identify the measured arrivals (e.g., tau-p transformation and clustering analysis to determine wavefield templates).

The most direct means of phase identification is through matching arrival time and slowness estimates to theoretical predictions. In complex tectonic regions such as South-Central Asia, global reference models perform poorly at far-regional distances, and more specific knowledge of the along-path and near-array earth structure is required for confident primary and secondary phase identification. To account for near-array effects on the array measurements, we use receiver functions to image below the arrays. Receiver functions allow a direct estimate of the structure below the array (e.g. Moho dip), independent of the array measurements and without bias to other along-path effects. We then use array measurements (slowness and arrival times) to empirically derive regionalized velocity-depth profiles that more accurately predict the far-regional phase succession. These are based on tau-p transformation of both array measurements and waveforms to form generalized representations of the along-path earth structure that is sensitive to far-regional propagation. To understand the far-regional phase behavior not predicted by tau-p ray methods, we use the velocity-depth profiles to synthesize suites of seismograms that are used as part of a waveform clustering algorithm. The clustering algorithm processes array beams to derive 'wavefield templates', i.e., grouped observations with similar phase characteristics. The wavefield templates are further analyzed in a non-linear fashion by comparing them with the synthetic seismograms, looking for quantitative explanations for the phase behaviors not predicted by tau-p ray methods. This work has resulted in a methodology that improves the usefulness of small-aperture array in the phase characterization of far-regional earthquakes. Our research has also yielded insight into body-wave phases that are regularly observed on the MKAR and KKAR arrays, including information on expected wave propagation behavior and the regional nature of the upper-mantle discontinuities.

OBJECTIVE

The objective of our research is to enhance the usefulness of regional, small-aperture arrays by developing array-based methods that can more accurately characterize far-regional (14˚-29˚) *P*-coda arrivals. At these distances seismograms are particularly interesting, due to multipathing through the lithosphere and upper-mantle. A suite of body-wave arrivals is often observed in a short time window (1-20 seconds) that bottom near the discontinuities at 220 km, 410 km, and 660 km depth, depending on epicentral distance and along-path structure. The arrivals can be closely spaced in time and exhibit amplitude anomalies related to triplication effects. When these arrivals can be properly identified they can be used to further enhance information regarding seismic source parameters, as well as earth structure. However, far-regional seismograms exhibit significant complexity due to regional heterogeneity and interference effects from depth-phase multiples and near-receiver scattered arrivals. It is the goal of this project to improve the characterization of the far-regional arrivals from South-Central Asian events by employing refined array processing techniques.

The regional seismic arrays that have been built in the last fifteen years should be a rich data source for the study of far-regional phase behavior. The arrays are composed of high-quality borehole seismometers that make high fidelity, low-noise recordings. However, beyond regional distances, the small apertures of these arrays (< 5km) limit their usefulness beyond first-arrival *P*- and S- onset picks. Standard array methods (e.g., slant stacking and frequency-wavenumber analysis) poorly resolve the azimuth and slownesses of primary and secondary arrivals, making confident arrival identification and classification quite difficult. We are overcoming this limitation by applying refined array processing techniques in conjunction with straightforward wavefield generalization methodologies. Our goal is to characterize the commonly observed early coda arrivals that propagate from the different seismic regions of South-Central Asia, utilizing recordings from the Makanchi (MKAR) and Karatau (KKAR) arrays in Kazakhstan (Fig. 1). This research improves the usefulness of small-aperture arrays by increasing their ability to classify small-magnitude events that may be poorly recorded regionally and teleseismically.

RESEARCH ACCOMPLISHED

We have developed array-based methodologies to characterize the *P* coda of far-regional events using small aperture arrays. Our methodology includes several components: 1) enhanced array calibration to account for near-array structure; 2) improved small-aperture array processing to effectively measure delay-times (τ) and slownesses (p) of primary and secondary arrivals; 3) construction of region-specific velocity-depth profiles derived from the τ-p measurements (i.e., τ-p transformations), as well as models derived from wavefield continuation methods; and 4) the derivation of 'wavefield templates' from clustering of array beams to capture the commonly observed arrival structure. These methods employ both theoretical and empirical techniques to reduce a large waveform dataset (~600 earthquakes; Fig. 1) into a smaller set of robustly observed wave phenomena. We then attempt to explain these phenomena using well-accepted, straightforward techniques. The separate components of our methodologies are discussed below.

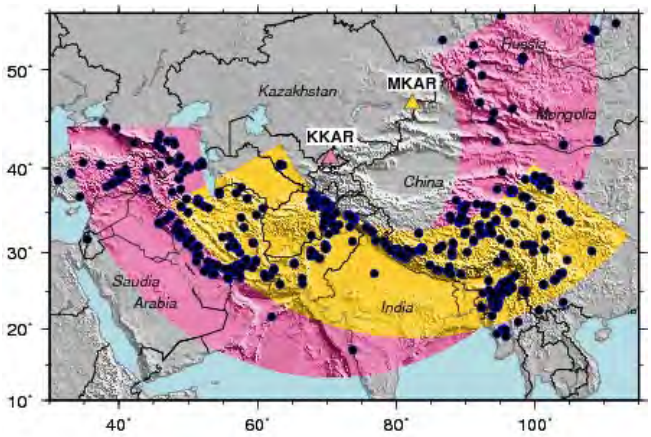

Figure 1. Map of South-Central Asia showing the location of the Makanchi (MKAR) and Karatau (KKAR) arrays in Kazakhstan, as well as earthquakes (circles) used in this study. Colored bands mark the 14˚-29˚ distance range from each array.

Near-Array Earth Structure from Receiver Functions

Array-based observations of slowness and back-azimuth typically deviate from 1D earth predictions because of structural heterogeneity along the ray path. These deviations need to be corrected in order to confidently identify particular arrivals. In many cases, heterogeneities directly below the array can account for most of the observed anomalies (e.g. Niazi, 1966; Havskov and Kansewich, 1978). Interactions with upper mantle structure, such as topographic relief on the discontinuities, can also produce anomalous observations. At the MKAR and KKAR arrays, we observe both back-azimuth and slowness anomalies, where azimuth residuals are ±20˚ in some instances. We think that near-array structure, as well as along-path effects, contribute to these observations.

A common method to account for near-array structure is to calibrate the array by correcting the array-based measurements to theoretical values of slowness and back-azimuth. For example, published earthquake epicenters are used to determine the expected great-circle azimuth angle, and a 1D earth model is used to compute expected ray parameters. In the case of a single non-lateral interface, (e.g., dipping Moho), the azimuth and slowness residuals, relative to the theoretical values, have a sinusoidal pattern with respect to back-azimuth. The amplitude and phase of these patterns can be used to solve for dip and strike of the interface, and thus a correction can be computed for each event based on its observed back-azimuth angle. This method works well only if near-array structure causes the anomalous residuals, the residuals are systematic with respect to back-azimuth, and there is good azimuth coverage of array measurements. However, for the MKAR and KKAR arrays these criteria are not well met, and we require a different approach.

To obtain a more accurate accounting of the near-array structure, and thus improve our array measurements, we are employing receiver function techniques to image the structure below the arrays. Our goal is to separate near-array effects on the azimuth and slowness measurements from the far-off path effects by accounting for the near-array structure independent of the array measurements. Determining structure from receiver functions has several benefits over array-based methods: 1) only the near-array structure is imaged and far-off path effects have no influence, 2) earth structure is not determined from the measurements you are trying to correct (the array measurements in our case), and 3) teleseismic events used for the receiver functions are more azimuthally distributed compared to the far-regional events.

For the MKAR and KKAR arrays, we compute receiver functions using data from the single 3-component instrument installed at each array using a time domain deconvolution method. The distribution of teleseismic events is shown in Figure 2, displayed as the Moho *P*-to-*S* conversion points around each array. Several hundred receiver functions are computed for each array. The distribution for the MKAR array is more azimuthally complete than the KKAR array, but we are attempting to acquire more events to fill the gaps. Receiver function images are shown in Figure 3 for MKAR and Figure 4 for KKAR.

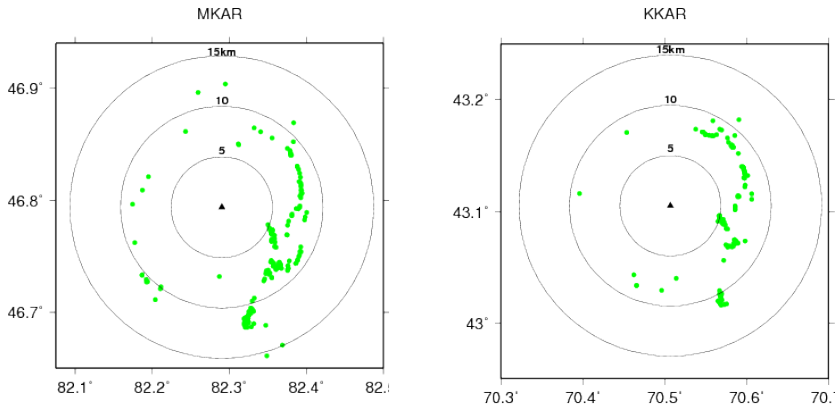

Figure 2. Azimuthal distribution of teleseismic events used in the receiver function calculations. The green dots mark the Moho conversion point for each of the receiver functions.

Using the radial and tangential receiver functions we form azimuthal record sections to image *P*-to-*S* converted phases below each array. The record sections (Figures 3 and 4) are constructed by stacking receiver functions at constant azimuth spacing. To account for variation in ray parameter of the teleseismic events and to minimize incoherent scattered energy, we use a 2D Gaussian weighting function where the weight is a function of nearness to the back-azimuth stacking point and ray parameter (Neal and Pavlis, 1999). In this manner, we are able to construct an evenly sampled (in back-azimuth), smoothed record sections that can be used in subsequent analysis.

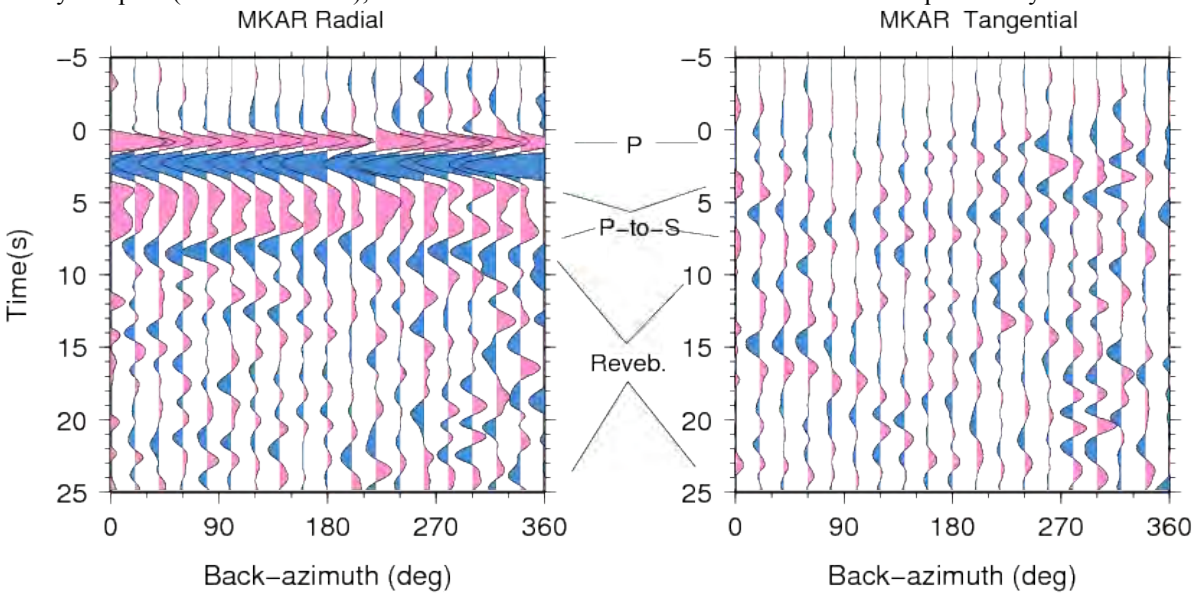

Figure 3. MKAR receiver functions record sections. The receiver functions are aligned on the minimum-phase time and have been filtered at 0.1 to 0.4 Hz.

Figures 3 and 4 show the MKAR and KKAR record sections. The main *P*-to-*S* signal at both MKAR and KKAR has a delay of ~6.0 seconds for the high-frequency band we are examining. It is most obvious in the radial component sections, and it shows some variation in arrival-time and amplitude for different back-azimuths. Preceding this phase is a large amplitude negative pulse, which may be related to a low-velocity zone near the surface. Later arriving reverberations are also apparent in both the MKAR and KKAR sections and show variations with back azimuth. Coherent energy is apparent on the tangential component sections, which is typically indicative of dipping structure or, in some cases, anisotropy. Coherent energy on the tangential components is clearest in KKAR record sections, where amplitude polarity changes are also seen. However, observed phases and the coherency of the record sections seem to have frequency dependence. At lower frequencies, the main *P*-to-*S* phase is less prominent and the tangential record sections are less coherent (not shown). This may be related to the nature of the velocity contrasts across the discontinuities below the arrays, and will likely be sorted out from our analysis

We are still in the process of analyzing and interpreting the receiver function images. The moveout of the radial component reverberations and the existence of coherent energy on the tangential components receiver functions seem to imply that the earth structure below the arrays is not laterally homogeneous, as we expected from the array measurements. In order to understand the earth structure we are taking a simple forward modeling approach. We start with a simple flat-layer velocity model determined from inverting a cumulative stack of the radial receiver functions. Using this model, we systematically vary the strike and dip of the Moho to compute a suite of synthetic receiver functions. The synthetic radial and tangential record sections are then quantitatively compared to the observed record sections. In this manner we are trying to solve for the strike and dip that minimizes the difference between the observed and computed record sections. Preliminary results from this exercise for the MKAR array show that much of the receiver function arrival structure can be explained by a prominent discontinuity at 48 km depth striking 210˚ N with a dip of 10˚.

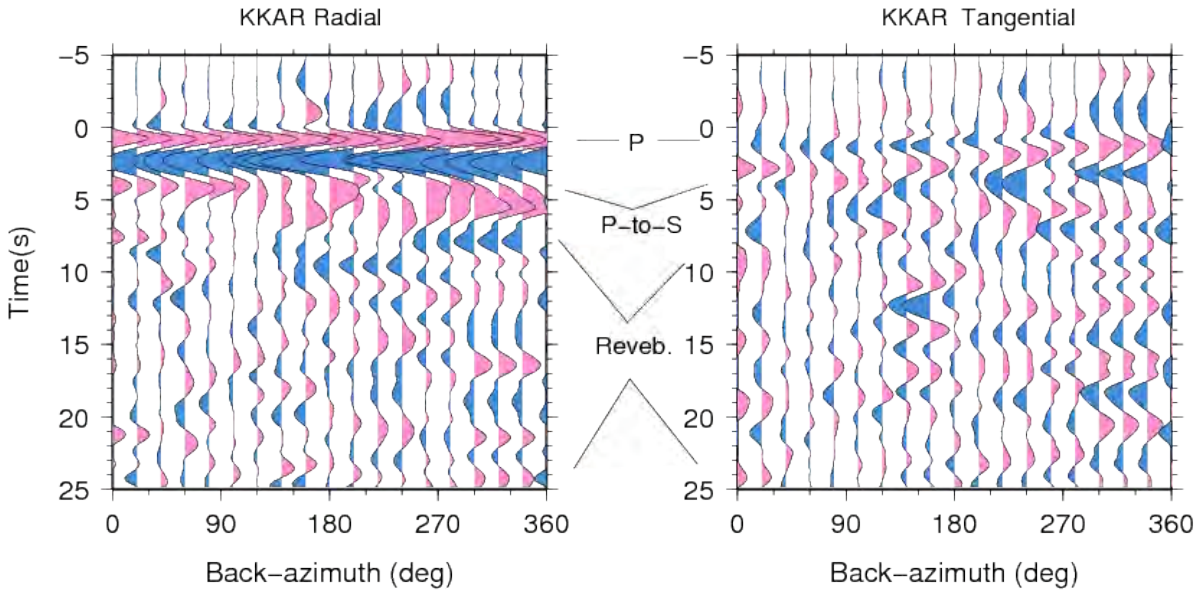

Figure 4. KKAR receiver function record sections. The receiver functions are aligned on the minimum-phase time and have been filtered at 0.1 to 0.4 Hz.

Improved Small-Aperture Array Processing

Our objective for the array processing is to compile a set a phase delay times (τ), back-azimuth and slowness measurements (*p*) and array beams for our waveform data set of ~600 earthquakes. The small aperture (< 5 km) of many of the newer arrays installed for nuclear monitoring purposes presents a serious challenge for typical array processing methods at far-regional distances. The restricted array aperture and limited number of array channels provides limited resolving power, particularly for slowness measurements. However, we have developed and applied a phase-weight semblance stacking method that improves the usage of small-aperture arrays at far-regional distances. The method combines an amplitude unbiased measure of coherency, the phase-weight stack (e.g. Schimmel and Paulssen, 1997), with semblance, an energy coherency measure. By combining the two coherency measures the signal-to-noise level is increased without detrimentally affecting small amplitude, emergent arrivals. The semblance stack also has the added benefit of being directly related to the F statistic, allowing confidence testing at particular signal-to-noise levels. Our results indicate that in many cases we can detect closely-spaced arrivals by their slowness values in a time window that includes the direct *P* arrival, depth phases and arrivals from upper-mantle discontinuities (Ferris and Reiter, 2007).

In Figure 5 we show two examples of applying the phase-weight semblance stacking to far-regional events recorded by the MKAR array. The first event was recorded at a distance of 25˚ where the main *P* arrivals bottom near the 660 km discontinuity and appear in the first few seconds of the seismograms. The other dominant phases are the *pP* and *sP* depth phase packets that follow a similar path, exhibiting similar slowness structure as the main P arrivals (as seen in the slowness vespagram) but increased signal amplitude. The second event was recorded at a distance 14.9˚. At this distance the first arrivals are *Pn* followed by arrivals bottoming near 220 km depth. Later arrivals include the *P*410 phase (~8 seconds later), followed by larger amplitude *P*410 depth phases.

The back azimuth vespagrams show variations in azimuth over the 20-second arrival window of the *P* phases. This is most evident for the event at 25˚ distance and reflects out of plane effects from along-path and near-array heterogeneity. While the slowness vespagrams are able to isolate the individual arrivals as a function of time, the phase weight semblance shows smearing in the slowness dimension. This is a related to wave-number aliasing and is a function of the array configuration. Further improvement to the slowness and azimuth vespagrams may only be realized by increasing the number of sensors at the arrays and modifying its geometry.

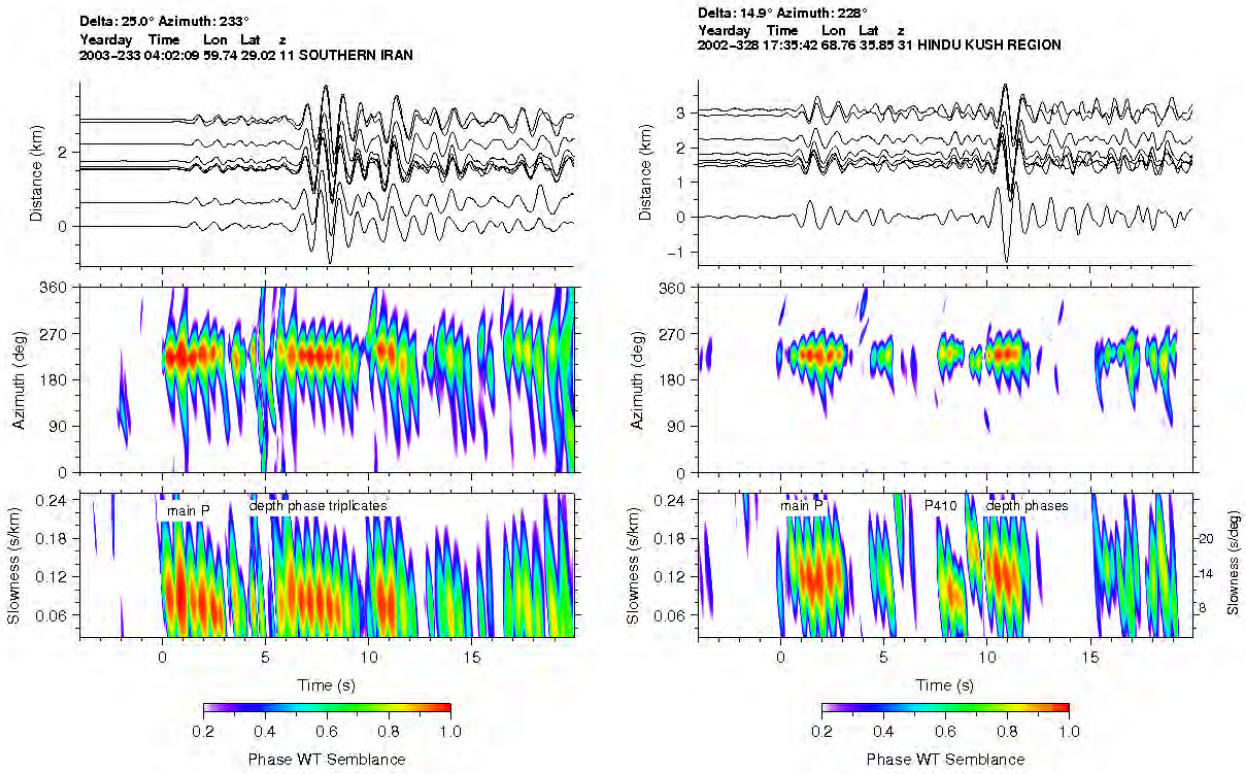

Figure 5. Example of phase-weight semblance processing for two separate earthquakes recorded by the MKAR array at a epicentral distance of 25˚ (left) and 14.9˚ (right). The top row shows the array gathers, the middle row shows the arrival back-azimuth vespagrams, and the bottom row shows the slowness vespagrams.

As part of the slowness and back-azimuth measurement exercise we compared our slowness estimates to those predicted by the AK135 reference model. This illuminated the need for more region-specific models in order to make accurate identifications. The next component of our improved phase characterization scheme uses the array measurement and subsequent array beams to derive models that can more accurately match the observations. Our methodologies to accomplish this and results are discussed in the following sections.

Regional Velocity Depth Profiles

To address the need for more applicable earth models and to generalize our array observations, we derived velocity-depth profiles for the specific regions monitored by the MKAR and KKAR arrays. We employed two methods based on *τ-p* (i.e. delay-time/slowness) techniques that decompose wavefields into their components parts. The first method involves applying wavefield continuation techniques (i.e., *τ-p* transformations) to the array-based delay-time and slowness measurements to solve for a velocity-depth function through a migration procedure. The second method applies the same techniques to full-waveform record sections, accomplishing the same goal (e.g., McMechan, 1984). While these methods are not new, they are not typically applied to small-aperture array data, but rather to data from long linear arrays of seismometers (e.g., Morozov et al., 2005). Since we apply these methods to multiple events records, a main challenge is accounting for the effects of differing source parameters (origin time, event depth, and focal mechanism), which may be unknown or poorly constrained. Our results show that we are able to extract reasonable models for specific regions in our study area that can more consistently match observed arrival parameters.

Figure 6 illustrates how we prepare array-based delay-time and slowness measurements for velocity-depth inversion. In this example we groom the outliers from data set of measurements made at MKAR, consisting of 110 earthquakes ranging from 14°-29° epicentral distance, which includes earthquakes extending from the Hindu Kush region of Pakistan/Afghanistan to the Makran coast and Zagros Mountains of Iran. The grooming removes everything outside

the 8.0 – 14.5 (sec/deg) slowness range, to help eliminate measurements from *P*-to-*S* scattered signals and coherent noise. We also discard measurements that exhibit significant slowness smearing (i.e., large measurement uncertainties) during the processing. Once the groomed measurements (Figure 6a) have been collected, we reduce them to a single τ-p curve by computing the error-weighted-mean τ value within evenly spaced slowness bins (Figure 6b), excluding bins with only a few measurements. Averaging the τ's within a common slowness bin acts to correct for errors in focal depth by accounting for the $\pm\tau$ offset between *P* and *pP*. While this is not a perfect correction due to missed phases in the array processing, the inclusion of *sP* arrivals, and measurement error, we have found it more effective and feasible than correcting τ on an event basis using catalog depths, which typically have large uncertainties. The averaged τ-p curves, while useful in their own right, are further processed in velocity-depth using wavefield continuation methods, which we describe below as applied to full-waveform record sections.

The wavefield continuation method consists of two linear transformations of the wavefield. These are illustrated in Figure 7. First, record sections are slant stacked, transforming them from the distance-time domain into the τ-p domain (Figure 7b). This is followed by a downward continuation, or depth migration, of the wavefield to transform the τ-p data to the slowness-depth plane. This second step is an iterative process, where the τ-p data are repeatedly migrated until the slowness-depth image converges to the input velocity model (Figure 7c). There are several ways to update the velocity model between iterations. We are currently using a scheme that picks the maximum amplitude at each depth from the slowness-depth image and then computing the weighted average between it in the input velocity model. This scheme performs adequately; however, noise in the initial τ-p transformation can cause artifacts in the final velocity-depth profile that needs to be corrected *a posteriori*.

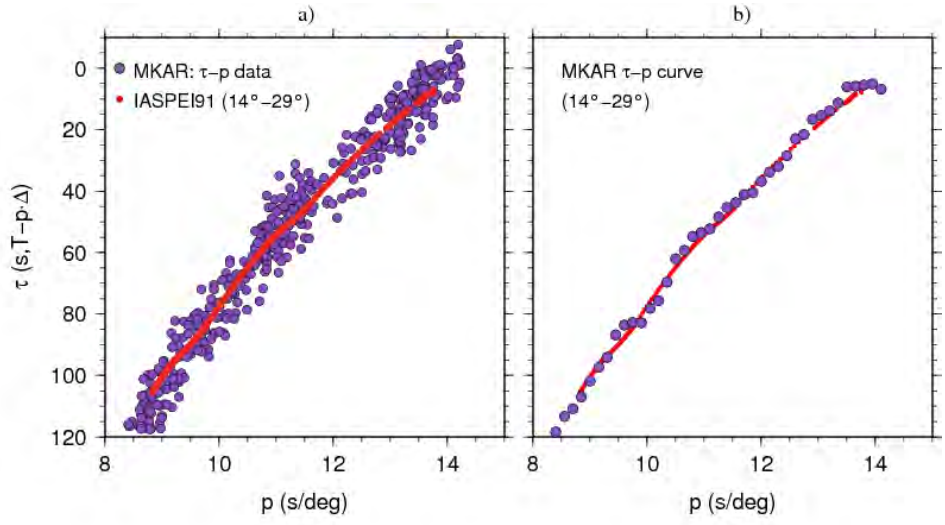

Figure 6. Sample τ-p data from the MKAR array. a) The groomed MKAR data (blue circles); red dots show the iasp91 τ-p curve for a surface-focus source. The range in τ for a particular slowness is caused by the difference in τ for earthquakes at different depths, rather than just measurement error. b) The averaged τ-p curve from the groomed data, evenly sampled in slowness at 0.15 sec/deg.

The resulting velocity-depth profiles show general agreement between the array-based measurement transforms and full-waveform transforms. The models more accurately match the far-regional arrival observations at MKAR and KKAR than reference models such as iasp91 and AK135. The main upper-mantle discontinuities are found at 250 km, 415 km and 670 km depth (Fig 7). In general, the wavefield continuation results exhibit moderately slower velocities than iasp91 below 250 km depth, and a gradient zone is observed near 410 km depth rather than a sharp discontinuity.

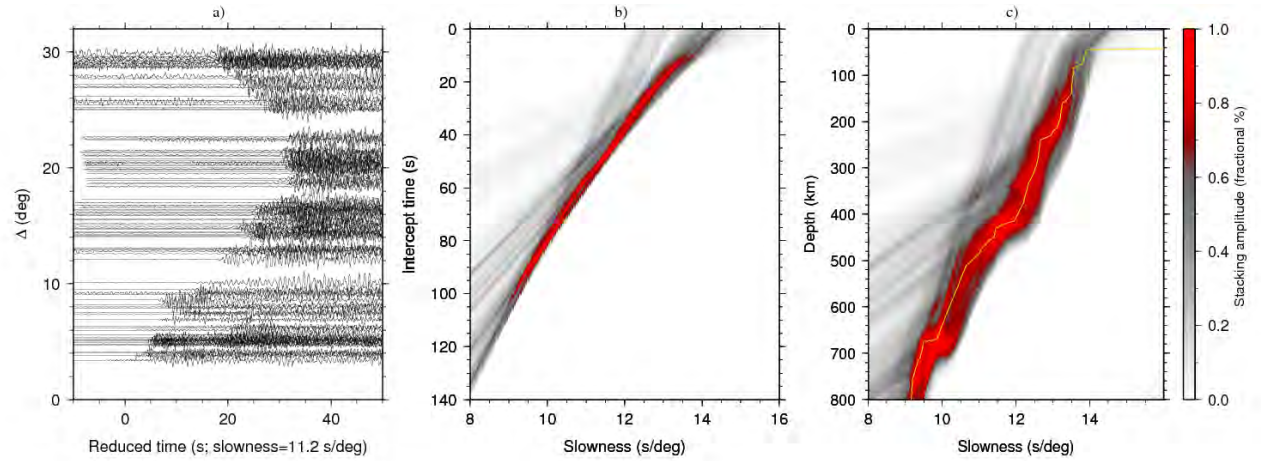

Figure 7. Example showing the transformation of a record section (a) to the *τ-p* domain (b) and the downward continuation to the slowness-depth domain (c). Array beams are from 104 earthquakes that extend from the Hindu Kush region of Pakistan/Afghanistan to the Makran coast and Zagros mountains of Iran.

Waveform Templating for Groups of Like Waveforms

Another component of our phase characterization methodology is the analysis of the array beams using clustering techniques. In addition to the arrival times and slowness of the coda phase arrivals, phase-weight semblance stacking analysis yields array beams, which are then input to a waveform clustering algorithm. The algorithm is based on 'fuzzy clustering' to form groups of beams that exhibit similar characteristics; it has been used widely in pattern recognition applications (Bezdek, 1981). Clusters are defined by assigning each beam a cluster membership value, which is a quantitative measure that incorporates a distance measure between each array beam and a representation of the cluster centers. We have experimented with distance measures involving *L1* and *L2* norms, as well as waveform semblance, with varying degrees of success that depend on data noise levels. From each cluster of similar beams, we derive a template waveform using a stacking process that weights each cluster member by its degree of membership to that particular cluster. The 'fuzziness' of the method allows a single beam to be a member of more than one cluster group. The objective behind the waveform clustering is to reduce the database of observations to a set of representative waveforms that exhibit consistent phase arrival behavior. Sometimes the clustering is geographic, but there are other wave phenomena that can also produce groupings of similar waveforms

Figure 8a shows the cluster group and its associated wavefield template that results from applying our waveform clustering algorithm to the set of 100 events shown in Figure 8b. These beams are derived from seismograms recorded by the MKAR array in the 14°-29° distance range that extends from northern Pakistan to the Makran coast in Iran. In this example the algorithm clusters the events into 5 groups, with 12-24 members per group. We applied an *L2*-norm distance measure and aligned the array beams prior to clustering using multi-channel cross correlation applied to the first four seconds of each beam signal. We have found the alignment of the beams to be beneficial to the clustering procedure. However, the length of the cross-correlation window is an important variable. For example, if the window is too long, the array beams align on the maximum amplitude signal in the record. For some beams the maximum amplitude arrival may occur early in the seismogram, while for others it occurs much later. This can result in some unusual clustering of events that seems counter-intuitive. For this reason, we find clustering methods based strictly on cross correlation, as used in other types of studies (e.g., Menke 1999) are not suitable for our particular needs.

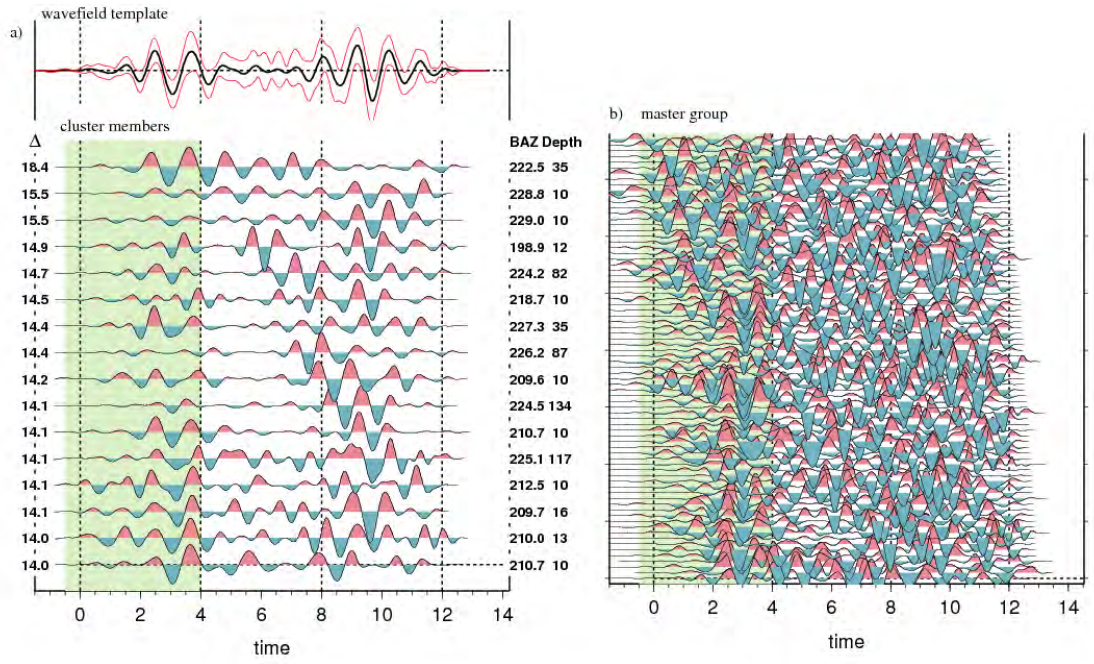

Figure 8. Example of wavefield clustering to generate a wavefield template. (a) The bottom panel shows the cluster members sorted by epicentral distance (shown on the left). The green band highlights the time band of cross correlation. The top panel shows the computed wavefield template (black) and 1-σ deviation (red). (b) A record section of all 100 earthquakes input to the clustering algorithm.

For the example shown in Figure 8, the resulting cluster members include earthquakes that are near the 14.3° distance range, but some more distant earthquakes are also included. The earthquake depth range is also variable, but may be due to poorly constrained catalog depths. In general, the cluster members show consistent waveform structure in the cross-correlated portion of the signal. Later arrivals show more variability between the cluster members, but still appear to align well at approximately 8 seconds and later. The most variability occurs between 4 and 8 seconds delay time, where some records show large amplitude arrivals while other show little signal. Some of this variability is likely due to differences in earthquake distance, triplicated arrivals, and the presence of depth phases. We continue to refine and improve the wavefield clustering algorithm.

Phase Characterization Analysis

A final component of our far-regional methodology is to characterize the observed phase arrivals. One way we have been attempting to do this is to quantitatively compare arrivals predicted from the derived velocity-depth profiles to those observed in the 'wavefield templates'. The purpose of this exercise is to determine how much of the arrival structure can be explained by simple and straightforward methods and models. Using these velocity-depth models we generate a suite of synthetic seismograms, which we then use to compute several different misfit measures between the synthetics and the observed wavefield templates. Since the synthetic waveforms are generated from models derived from the τ-p data, arrival times of the wavefield templates should be well matched. We note that to derive meaningful measurements we must account for frequency content and amplitude variations.

While this exercise in waveform modeling is relatively crude, we are finding general agreement between the synthetic waveforms and the 'wavefield' templates. This suggests to us that a significant portion of the observed far-regional arrival structure can be explained by regional-specific 1D models.

CONCLUSIONS AND RECOMMENDATIONS

Regional seismic arrays that have been recently installed for nuclear monitoring are under-utilized in the study of far-regional arrivals. The small aperture of many of these arrays (< 5km) restricts their usefulness at these distances

beyond first arrival onset picks of *P* and *S* waves. However, our research is overcoming this limitation by applying refined array processing techniques in conjunction with τ-*p* and wavefield templating analysis methods. Our methodology improves the characterization of primary and early coda phase arrivals observed at far-regional and near-teleseismic distances. Our approach is to distill the wide variety of seismicity we observe to subsets of commonly and robustly observed phase arrival phenomena. We are then using well-accepted modeling and inversion techniques to explain these phenomena. Our aim is to explain as much of the phenomena as we can with simple and straightforward techniques, leaving the anomalies for future research

We are developing and applying our techniques to South-Central Asian earthquakes recorded on the MKAR and KKAR arrays in Kazahkstan. Our results indicate that we can differentiate between the numerous arrivals of the early P-coda. However, global reference models cannot capture the phase succession and arrival-time behavior we observe from the complex tectonic regions of South-Central Asia. To address this, we have developed regional 1D models directly from the array measurements (delay-times, slowness, and beams). Since these models are derived from the data, they are able to explain the phase behavior we observe from specific regions. To test these models and further improve phase characterization, we have constructed 'wavefield templates' through cluster analysis to generalize the waveform structure from the difference seismic regions. The templates are then used in a waveform fitting analysis to gain a better understanding of the phase phenomenon observed from the complex seismic regions of central Asia.

While our methodology improves the usefulness of small-aperture arrays at analyzing far-regional P-coda arrivals, greater gains could be made by installing more elements and increasing the effective array aperture at both MKAR and KKAR. Modifying the array geometry would reduce the wave-number aliasing for arrivals with slowness values between 8-11 s/deg and increasing the aperture would improve both slowness and azimuth resolution. An addition of 2-6 new sensors in an outer-ring configuration would significantly improve far-regional array analysis.

REFERENCES

Bezdek, J. C. (1981). Pattern recognition with fuzzy objective function algorithms, Plenum Press, New York.

Carbonell, R., and S. B. Smithson, (1994). Inversion of reflected *PP*, *SS*, and converted *PS*/*PP* travel times for crustal structure, *Bull. Seism. Soc. Am.* 84: 1889–1902.

Ferris, A. and D. Reiter (2007). Using small-aperture arrays to identify far-regional P-wave arrivals, in *Proceedings of the 29th Monitoring Research Review: Ground-based Nuclear Explosion Monitoring Technologies*, LA-UR-07-5613, Vol. 1, pp. 14–23.

Havskov, J. and E. R. Kanasewich (1978). Determination of the dip and strike of the Moho from array analysis, *Bull. Seism. Soc. Am*. 68: 1415–1419.

McMechan, G. A. (1984). Inversion of a refraction wavefield by imaging in the p-x and v-z planes, *Geophys. J. R. Astr. Soc.* 78: 723–733.

Menke, W. (1999). Using waveform similarity to constrain earthquake location, *Bull. Seism. Soc. Am.* 89: 4, 1141–1146.

Morozov, I. B., E.A. Morozova, S. B. Smithson, P. G. Richards, V. I. Khalturin, and L. N. Solodilov (2005). 3D First-arrival regional calibration model of northern Eurasia, *Bull. Seism. Soc. Am.* 95: 951–964.

Neal, S. L. and G. L. Pavlis (1999). Imaging P-to-S conversions with multichannel receiver functions, *Geophys. Res. Lett.* 26: 2581–2584.

Niazi, M., (1966). Corrections to apparent azimuths and travel-time gradients for a dipping Mohorovocic discontinuity, *Bull. Seism. Soc. Am.* 56: 491–509.

Schimmel N. and H Paulssen, (1997). Noise reduction and detection of weak, coherent signals through phase weighted stacking, *Geophys. J. Int.* 130: 497–505.

A STEPWISE, ITERATIVE PROCEDURE TO CONSTRAIN STRESS DROP, REGIONAL ATTENUATION MODELS, AND SITE EFFECTS

Mark D. Fisk[1] and W. Scott Phillips[2]

Alliant Techsystems[1] and Los Alamos National Laboratory[2]

Sponsored by the Air Force Research Laboratory[1] and the National Nuclear Security Administration[2]

Contract Nos. FA8718-09-C-0005[1] and LA09-BAA09-01-NDD03[2]
Proposal No. BAA09-01

ABSTRACT

Accurate corrections for distance, source size, and site effects are needed for reliable use of regional seismic phases for discrimination and magnitude estimation. Procedures that simultaneously invert for attenuation, geometrical spreading, site, and source parameters have been shown to include many trade-offs and instabilities that have led to significantly inaccurate corrections for distance and source terms. Under previous work, we developed and applied an approach to constrain source parameters, including stress drop, for events throughout Eurasia, using Brune (1970) model fits to relative spectra of regional phases for event pairs with similar locations and mechanisms (assessed by waveform correlations), but different moments. We further fit the combined distance and site terms to the source-corrected spectra, showing that robust estimates of these combined effects are possible by first constraining source terms. Further work is needed to separately constrain the path and site effects. We have just started a three-year project to implement, apply, and evaluate a stepwise, iterative procedure to constrain all of the remaining trade-offs among these terms. Using spectra of regional seismic phases that are already corrected for source terms, we will estimate and apply corrections for frequency-independent geometrical spreading and site factors, based on distance, and then constrain separate estimates of frequency-dependent site parameters and Q. This is expected to provide accurate estimates of all source, distance, and site effects for regional phases in Eurasia for paths/stations with suitable data. We also plan to use coda measurements and methods to (1) augment our source terms computed from spectra of direct phases, (2) independently estimate site terms, and (3) compare and validate the results using direct phases or coda. We will use analysis of variance (ANOVA) and variogram methods to partition the uncertainties and their correlation lengths for use in Bayesian kriging to interpolate grids of stress drop, geometrical spreading, and Q estimates, and to merge our results with previous developments at Los Alamos National Laboratory (LANL). We will evaluate the corrections and uncertainties using two large data sets and cross-validation methods. We will document and deliver the techniques, estimates of physical parameters, and kriged grids of corrections and uncertainties, for incorporation in the Air Force Technical Applications Center Knowledge Base.

OBJECTIVES

We have just started a project to develop, apply, and evaluate methods to improve the accuracy of attenuation models, geometrical spreading, site terms, and their uncertainties for regional phases in Eurasia, by constraining trade-offs among the parameters at various stages of the analysis. The approach is to break up traditional grid-search inversions, which are known to have many trade-offs and instabilities, into manageable pieces, canceling out certain physical effects (e.g., distance and site) to allow reliable estimation of others (e.g., source), and then correcting for the latter to then estimate reliable parameters for the former. We plan to use complementary datasets based on direct phases and coda measurements to augment and compare source terms and independently estimate site terms. We also plan to use multiple methods to estimate the correction parameters and to validate the results at key stages. We will partition the uncertainties and their correlation lengths for use in Bayesian kriging to interpolate grids of stress drop, geometrical spreading, and Q estimates, and to merge our results with previous developments at LANL. We will evaluate the corrections and uncertainties using two large datasets and cross-validation methods.

RESEARCH ACCOMPLISHED

Procedures that simultaneously invert (i.e., grid search) for Q, geometrical spreading, site, and source parameters have been shown (e.g., Taylor and Hartse, 1998; Fisk and Taylor, 2006; Fisk et al., 2008) to have many trade-offs and instabilities that have led to significantly inaccurate corrections. This motivated our development of an approach to better constrain the parameters. Under previous work, we developed and applied a method to constrain source parameters, including stress drop, for events throughout Eurasia, using Brune (1970) model fits to relative spectra of regional phases for event pairs with similar locations and mechanisms (assessed by waveform correlations), but different moments. We then corrected the spectra for the source terms and fit the combined distance and site effects, showing that robust estimates of these combined terms are possible by first constraining source terms. Further work is planned to separately constrain path and site effects. Here we summarize relevant past work and plans for this project.

Constrained Inversion Approach

Following Sereno et al. (1988), Taylor and Hartse (1998), and Taylor et al. (2002), the amplitude spectrum for a given phase and station, for event i, may be modeled by

$$A_i(f) = S_i(f;f_c(\sigma_b^{(0)}, \psi))G(r_i;r_0, \eta)\exp\left(-\frac{\pi f^{1-\gamma}}{Q_0 \nu} r_i\right)P(f;a, b) \qquad \text{(EQ 1)}$$

where $S_i(f, f_c)$ is the source spectrum with corner frequency f_c, r_i is epicentral distance, $P(f)$ is the site term, ν is group velocity, $Q_0 f^{\gamma}$ treats attenuation, and $G(r, r_0)$ is frequency-independent geometrical spreading, inversely proportional to distance to a power η, beyond a reference distance r_0. Taylor et al. (2002) and many others have used the logarithm of Equation (1) in grid searches to simultaneously estimate all of the parameters. However, significant trade-offs among the parameter estimates are well known and difficult to constrain by such techniques and available data. The problem arises because the earth and the distribution of events and stations are not uniform.

Figure 1 illustrates the problem for two earthquakes at the Lop Nor test site (LNTS). It shows ratios of Pn, Sn, and Lg spectra for the larger event (M_W 5.7) relative to the smaller (M_W 4.4), computed at 18 stations and averaged. The events have similar hypocenters and mechanisms; thus path, site, and radiation pattern effects cancel in the relative spectra. Also shown are Brune (1970) model predictions using stress drop estimates from (1) an unconstrained grid search (Taylor et al., 2002) and (2) our fits of the relative spectra. The unconstrained result clearly does not match the observed relative spectra. Also, using our fits of the source terms, Figure 2 compares the source-corrected Lg spectra at MAKZ for the same earthquakes to Q model predictions from (1) unconstrained MDAC parameters and (2) our fit. The unconstrained result diverges by over an order of magnitude at higher frequencies. A trade-off of Q and stress

drop for the unconstrained grid search leads to very inaccurate corrections for both.

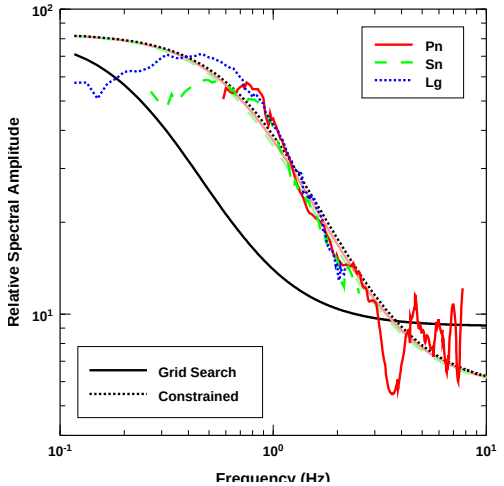

Figure 1. Station-averaged relative spectra of Pn, Sn, and Lg for a pair of earthquakes (M_W 5.7 and 4.4) at LNTS. Also shown are Brune model results using stress drop estimates from an unconstrained grid search (black) and our fits of the relative spectra.

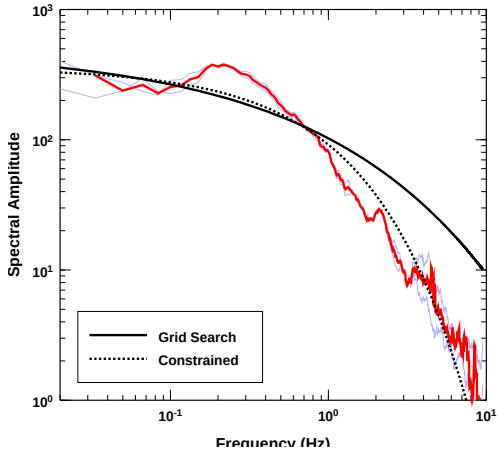

Figure 2. Source-corrected Lg spectra for the LNTS earthquakes at MAKZ, the result using Q from a grid search (solid), and our Q model fit (dotted).

This case not only illustrates the problem, but also a solution. Instead of performing a grid search for all parameters simultaneously, we use relative spectra for event pairs with similar locations and focal mechanisms (assessed by waveform cross-correlations), but different moments, to factor out path and site effects and obtain reliable estimates of the source terms. Once accurate source terms are estimated, we can then obtain reliable estimates of the distance and site terms. That is, for a pair of nearby earthquakes with similar radiation patterns, the relative spectra for a given phase type is modeled by

$$\frac{A_1(f)}{A_2(f)} = \frac{S_1(f)}{S_2(f)} = \frac{M_0^{(1)}[1+(f/f_c^{(2)})^2]}{M_0^{(2)}[1+(f/f_c^{(1)})^2]} \quad . \qquad \text{(EQ 2)}$$

The corner frequency may be parameterized in terms of moment M_0, stress drop $\sigma_b^{(0)}$, and a scaling parameter ψ. Using pairs of similar earthquakes, we fit $\sigma_b^{(0)}$ and ψ to relative spectra. Figure 3 shows network-averaged relative spectra and model fits for an earthquake pair in Kyrgyzstan during 1997. The relative spectra are similar for the various phases, although over different frequency ranges because of phase-dependent SNR effects. Hence, the corner frequencies are very similar, a common and important phenomenon for the earthquakes analyzed.

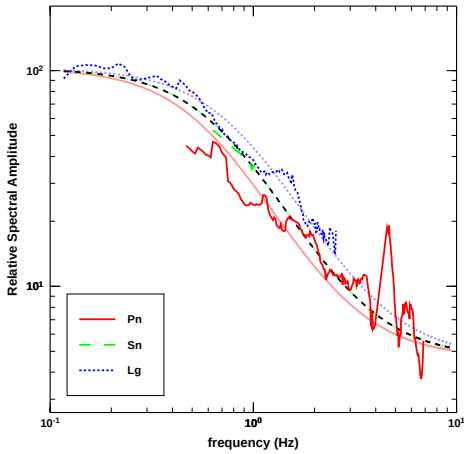

Figure 3. Example of relative spectra for a pair of M_W 6.0 and 4.7 earthquakes. Model fits are shown for each phase and using all phases (black dashed).

For this approach to be viable, many pairs are needed. Using waveform cross-correlations for 4,236 events in Eurasia prior to 2000 (Schaff and Richards, 2004) we found a subset of pairs in the LANL database, acquired data from IRIS, added/refined phase picks, computed and averaged relative spectra over stations, and fit the model for each phase and for all phases simultaneously. Figure 4 shows that Pn and Lg corner frequencies are similar for most of the earthquakes analyzed in Eurasia, comparable to findings by Walter and Taylor (2002) for western U.S. earthquakes. This allows more robust fitting of Brune source parameters, using a broader range of frequencies, by combining relative spectra of regional

P and S phases for earthquakes (e.g., black dashed curve in Figure 3). Figure 5 shows initial kriged grids of stress drop based on Lg and Pn data. The grids are very similar, indicating similar stress-drop estimates from Lg and Pn.

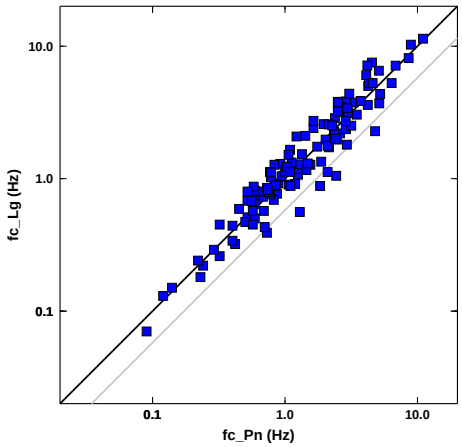

Figure 4. Estimated Lg versus Pn corner frequencies, indicating similar values for most of the earthquakes. Black and gray lines represent ratios of 1.0 and 1.73.

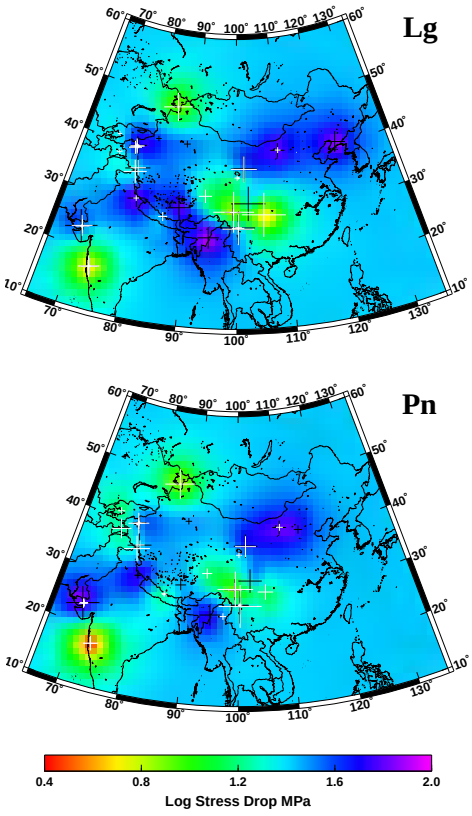

Figure 5. Initial kriged stress-drop grids estimated from Lg (top) and Pn (bottom) relative spectra.

We extended our analysis of relative spectra to event pairs in Eurasia from 2000 to 2006 (Figure 6). Using the Preliminary Determination of Epicenters (PDE) catalog, we formed a list of candidate pairs, based on proximity and relative mb or M_W values in the PDE, and acquired regional data for the events from IRIS. We computed waveform cross-correlations to find similar event pairs (*á la* Schaff and Richards, 2004). We computed and fit network-median relative spectra for almost 3600 pairs. We semi-automated these processing steps, although it is necessary to review and refine the results. In the fitting analysis, we fix M_0 of the larger event, assuming it is better recorded and, hence, has a more reliable moment estimate, and estimate M_0 of the smaller event.

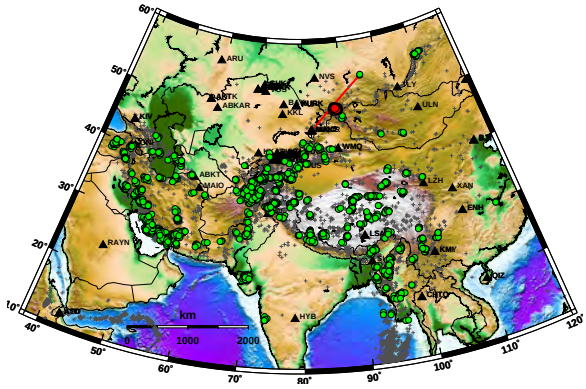

Figure 6. Events and stations used to process relative spectra and fit corner frequencies and estimate stress drop. The cluster highlighted in red and the path along two clusters to MAKZ are discussed below.

Figure 7 shows an example for a pair of the highlighted cluster in Figure 6. Figure 8 shows corner frequency estimates and their scaling relation for the entire cluster. Using the estimated source terms to correct the spectra, we fit the combined distance and site dependence. For example, Figure 9 shows source-corrected Lg spectra at BRVK for the cluster, illustrating several important aspects of our analysis. (Results were computed for 23 stations.) First, the light blue curves show the corrected Lg spectra for each event. They have similar shapes and offsets, indicating that the source corrections (moments and corner frequencies) are effective and consistent. Modest departures at low and high frequencies are due to noise effects. Second, the median (red curve) for the cluster is robust to outliers. For example, the lowest blue curve is due to a bad BRVK recording that slipped

through the automated QC criteria. The mean is much more sensitive to outliers. Third, the fit (black curve) of the median spectrum agrees very well over a wide range of frequencies. We generated comparable results for all of the stations and for other clusters/paths.

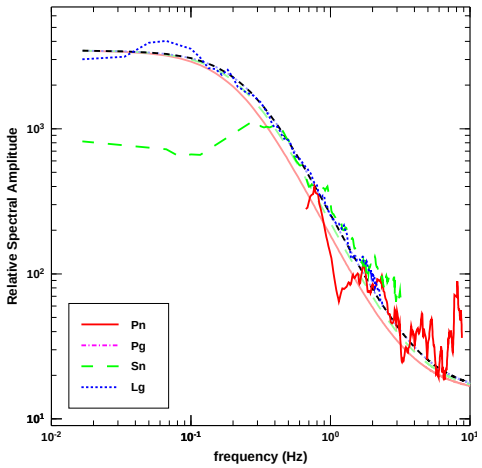

Figure 7. Network-median relative spectra of Pn, Sn, and Lg and model fits (smooth curves) for an event pair in the highlighted cluster in Figure 6.

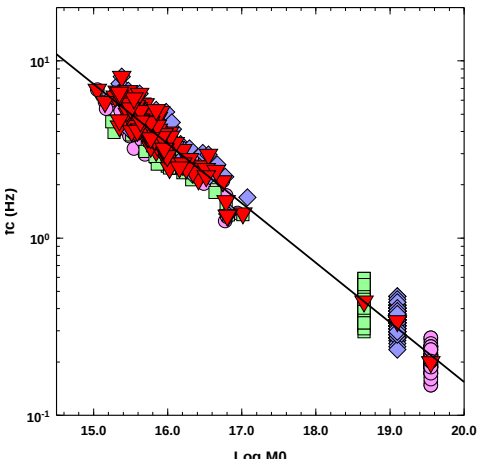

Figure 8. Corner frequencies versus log moment for the highlighted cluster in Figure 6, by jointly fitting the relative Pn, Sn, and Lg spectra. Estimates are shown for all pairwise combinations using 3 master events (circles, diamonds, squares), the median for each event (triangles), and the scaling relation (line).

The source parameters (Figures 7 and 8) and the dashed curve of Figure 9 provide excellent/complete calibration over a wide range of frequencies for all of the combined source distance, and site effects for this path/station. For an isolated cluster, the fits do not provide independent, reliable estimates of Q, spreading, and site parameters. New work focuses on constraining remaining trade-offs.

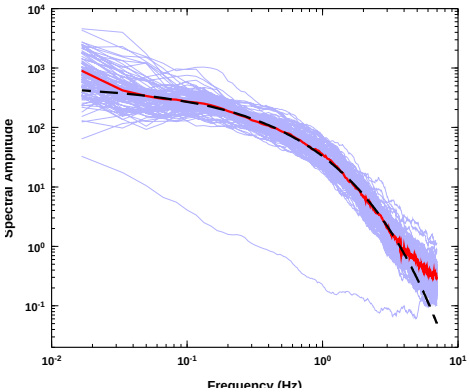

Figure 9. Lg spectra at BRVK, corrected for response and source terms, for all events in the cluster (blue), the median (red), and a model fit of the combined distance and site effects (black dashed).

Comparisons of Q Parameters

We compared our effective Q estimates to independent results. First, Dr. Jiakang Xie provided estimates of Q_0, computed as an integrated average of Q_0^{-1} along the same paths, using an Lg Q tomographic map generated by the two-station method (Xie et al., 2005, 2006). As a convenient way to compare the results, Figure 10 shows maps of Lg Q_0 estimates from our analysis and from Xie (2008, pers. comm.) for paths from the same cluster to 23 stations. The maps were generated by kriging and are only intended to aid visual comparisons. Compared to Xie's estimates, we obtain higher Q_0 estimates for paths to stations in northern Kazakhstan and, to a lesser extent, to stations in Kyrgyzstan, as well as a lower Q_0 estimate for the path to WMQ. The Q_0 estimates are comparable for the path to ULN. Further work is needed to evaluate and interpret these results, after separately estimating site effects. We do note that our estimates of Lg Q_0 for these stations seem to be more consistent with results by Taylor et al. (2003), specifically higher Q_0 for paths to northern Kazakhstan and lower Q_0 for paths to northwestern China.

For paths from LNTS to regional stations, we compared our Q_0 estimates for Pn, Sn, and Lg to those computed from averages of Q_0^{-1} along the paths using tomographic maps from Phillips (2005, pers. comm.). Our results

were generated using only one event pair at LNTS. Figure 11 shows source-corrected Lg spectra and model fits, giving estimates of effective Q parameters. Similar to Figure 10, Figure 12 compares kriged grids the Lg Q_0 estimates. As noted, these grids are merely a convenient graphical representation of the spatial Q_0 variations for comparison. The grids have some very similar patterns, e.g., our results agree very well with those from Phillips for stations in Kazakhstan and Kyrgyzstan. The average of our Lg Q_0 estimates is 442 versus 478 from Phillips for the paths/stations shown. The largest differences are that our Q_0 values are 18% to 32% lower than those from Phillips for TLY, NIL, LZH, ULN, and WMQ. We plan to include more data to improve and validate our results. However, it is interesting that we obtain qualitatively similar results using only a single pair of events with well-constrained source terms.

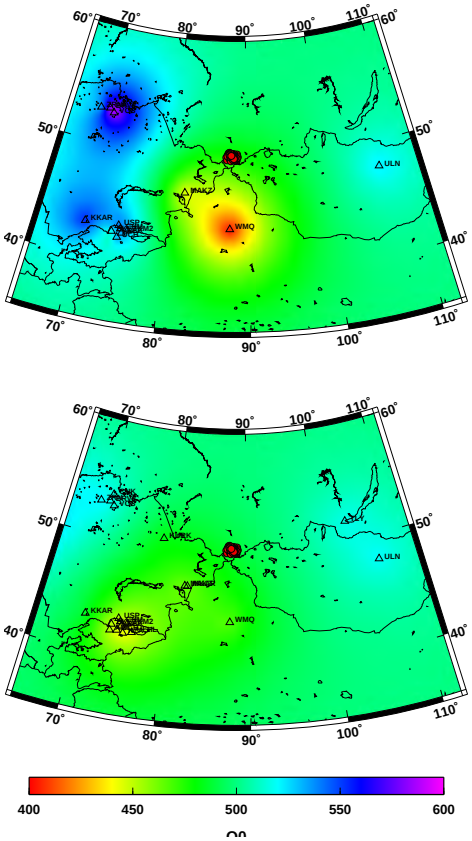

Figure 10. Interpolated grids of Lg Q_0 from our analysis (top) and from Xie (2008, pers. comm.) (bottom) for stations with recordings of the cluster shown in red. (These are not tomographic Q_0 maps. They represent the effective Q_0 along various paths.)

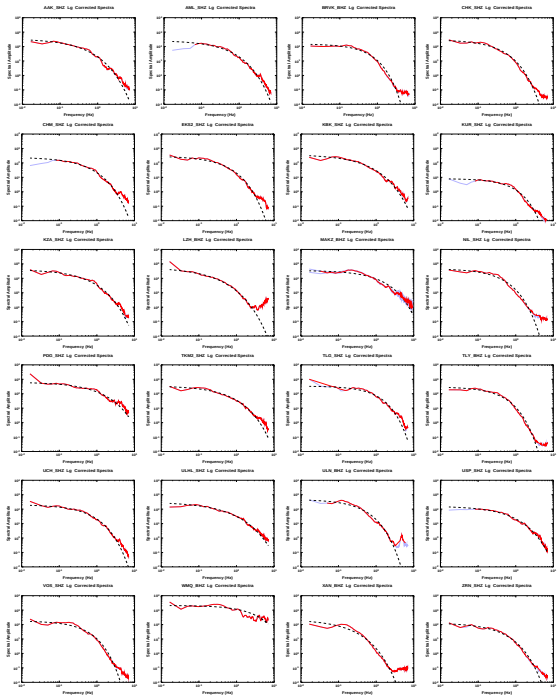

Figure 11. Source-corrected Lg spectra and Q model fits for LNTS earthquakes recorded by 24 stations.

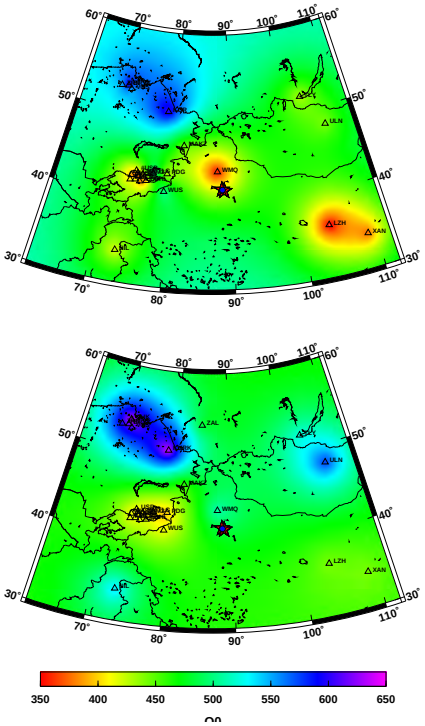

Figure 12. Interpolated grids of effective Lg Q_0 for paths from LNTS to regional stations from our analysis (top) and based on Q tomography (bottom).

New Work

The previous effort showed that, by first eliminating path and site effects, accurate source terms can be estimated and used to then reliably estimate combined distance and site dependence. This fully calibrates paths/stations with data. We are now extending the constrained approach to eliminate remaining trade-offs, to separate path and site effects. This will allow spatial interpolation and physical interpretation of estimated parameters, more meaningful comparisons to existing results, and to merge our results with existing models at LANL. Note, for example, that site corrections generally have frequency dependence, but the behavior varies by station and is not necessarily intuitive, as illustrated by different dependence for P and S waves for two stations (Figure 13). We need to assess whether this dependence real or due to a trade-off with Q. Inaccurate estimates of site effects will adversely impact Q estimates. As before, non-uniformity of the earth and the data complicate this matter. New work is planned to separately constrain site from distance terms.

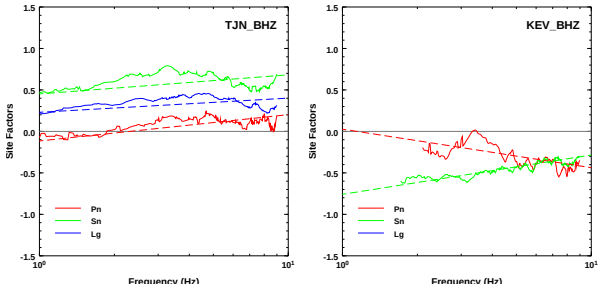

Figure 13. Site corrections for stations TJN in South Korea and KEV in Finland, computed as residuals of source- and distance-corrected spectra.

Figure 14 shows key processing steps of our approach, indicating several key aspects. First, for this project, we plan to greatly augment the dataset based on direct P and S phases from similar event pairs, by using Lg coda measurements. That is, in addition to the data depicted in Figure 6, we plan to use the coda measurements shown in Figure 15. Mayeda et al. (2007) have shown that coda measurements allow the criteria of similar events and locations to be relaxed, greatly increasing the number of observations. Phillips et al. (2008) used the Lg coda data of Figure 15 to invert for relative site and 2D path terms. We are using these complementary datasets, with coda providing greater density and direct phases providing information about P and S phases and allowing source term fits over broader frequencies, as shown above. We plan to (1) compare source terms estimated by different data and methods to validate them; (2) independently estimate site terms; and (3) to cross-validate and merge the final correction and uncertainty terms.

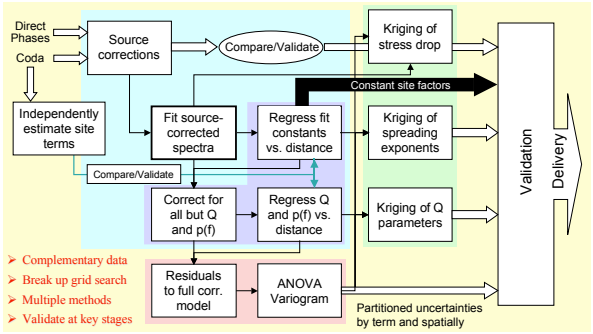

Figure 14. Schematic flow chart of planned analyses.

Second, we will further dissect the grid-search approach (represented by the large cyan box of Figure 15) into more manageable pieces. We have already accomplished part of the problem, giving source corrections for many events and fitting the source-corrected spectra. We will further break up the analysis of the three boxes (grouped in blue), as described further below. Third, we plan to use multiple methods within each of these boxes, to compare and validate the results at key stages. Other key aspects of the analyses are to partition the uncertainties, interpolate the physical parameters by kriging, and to merge our results with existing models.

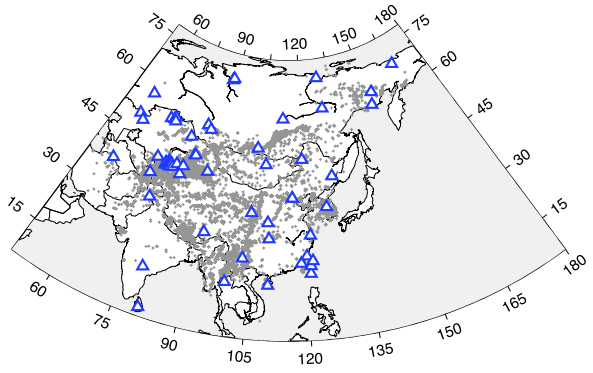

Figure 15. Stations (triangles) and events (crosses) used by LANL to calibrate Lg coda in east Asia.

To illustrate some details of the planned methods, note that the constant offsets of the model fits to the

source-corrected spectra (e.g., black dashed curves in Figures 9 and 11) depend on geometrical spreading and a constant site factor. Since the former depends on distance and the latter does not, we can regress the constants of the fits for all clusters/pairs of events recorded by a given station at different distances to separately constrain them. We plan to use larger datasets to perform this analysis.

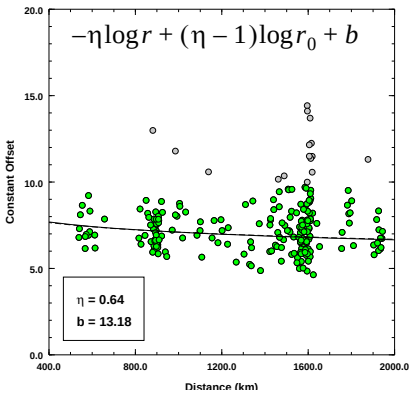

Figure 16. Constant terms of the model fits versus distance (circles) and regression versus log distance. Gray circles were excluded from the analysis. The legend lists the estimated values of the geometrical spreading exponent and the constant site factor.

Once we estimate these terms, the only parameters to be resolved are Q_0 , γ , and one that governs the frequency dependence of the site term. We have investigated various approaches for this final step. One is to insert the spectral amplitudes for all of the events in our datasets, now corrected for all but these terms, into a grid search for three parameters. This is a much smaller parameter space than the full space associated with Equation (1). As in separating the spreading and constant site terms, Q_0 and γ can be separated from the frequency-dependent site term by distance. A second approach, is to use constraints from coda measurements and methods to independently estimate (relative) site terms.

A third approach that imposes an additional constraint on these last three parameters, is to use relative spectra for clusters with similar paths, but at different distances from a station, to factor out the site term and obtain a robust estimate of Q for that path. This estimate of Q has no trade-off with source, site, or geometrical spreading effects. Figure 17 illustrates this approach. It shows the ratio of the median source-corrected spectra at MAKZ (Makanchi, Kazakhstan) for the two clusters along the path shown in Figure 6. This relative spectrum factors out the site term, and the spreading terms are different constants, i.e., independent of frequency. Assuming the effective Q is relatively constant over a path, the ratio of source-corrected median spectra for the two clusters is simply modeled by

$$\log(\tilde{A}_1 / \tilde{A}_2) = \frac{\pi f^{1-\gamma}}{Q_0 v} \Delta r \ , \qquad \text{(EQ 3)}$$

where Δr is the separation of the clusters. Fitting this expression to empirical spectral ratios (dashed curve in Figure 17) gives constrained estimates of Q_0 and γ (e.g., Lg $Q_0 = 546$ for the path depicted in Figure 6.

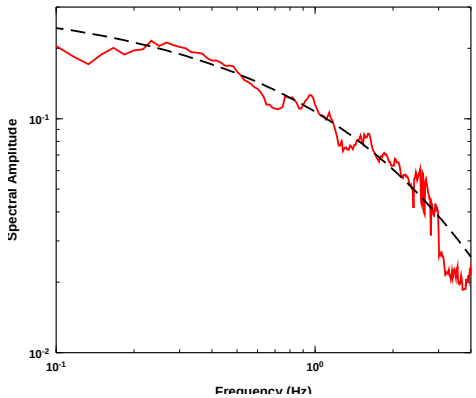

Figure 17. Ratio of source-corrected median spectra at MAKZ for two clusters along the great-circle path in Figure 6. The relative spectrum factors out the site term and allows a robust estimate of Q for this path.

Correcting the source-corrected spectra of these clusters now for Q, the remaining frequency dependence is due to site effects. Once this is done for at least one path, the frequency-dependent site term may be estimated and fixed, under the assumption of the standard model that $P(f)$ is independent of azimuth. We can then estimate Q for all paths with available data. The other assumption is that a suitable path exists for a given station along which Q is fairly constant. We need to investigate its validity for stations of interest, e.g., using existing tomographic maps as an *a priori* guideline. We refer to the overall approach as a stepwise, iterative procedure to constrain all of the parameters of the standard model, using our available datasets (Figures 6 and 15), source-corrected spectra, and model fits (e.g., Figure 9) as a starting point.

CONCLUSIONS AND RECOMMENDATIONS

This effort focuses on developing and testing methods to improve source, distance, and site correction parameters, and their uncertainties, for regional seismic phases. It has been well know for over a decade (e.g., Taylor and Hartse, 1998) that there are significant trade-offs among distance and source terms, using standard grid-search techniques to invert for all parameters simultaneously. We illustrated the problem for LNTS. Fisk and Taylor (2006) and Fisk et al. (2008) discuss additional cases by various researchers for which unconstrained inversion methods have led to large errors in both distance and source corrections. Such errors, and the potential impact on nuclear explosion monitoring using regional phases, motivated the development of our constrained approach to eliminate such trade-offs. Under a previous project, we developed and tested a method that first estimates source parameters using Brune model fits to relative spectra of regional phases for event pairs with similar mechanisms, but different moments. Using such relative spectra ensures that path and site effects cancel out, thereby allowing accurate estimation of the source terms. Once the spectra are corrected by reliable source terms, we can accurately estimate distance and site effects. We applied our constrained approach to two large datasets in Eurasia. We automated the various processing steps, including assessing event pairs from waveform cross-correlations, computing network-median of relative spectra (large over small events), and fitting the Brune model to estimate corner frequencies and stress drop. We used kriging to interpolate grids of stress drop for Eurasia. We compared these preliminary grids to existing ones at LANL. Further work is needed to interpret the stress-drop grids in terms of large-scale geophysical structure.

A key result of that research is that the relative spectra for a given earthquake pair are often quite similar for the various phases, although over different frequency ranges because of phase-dependent signal-to-noise limitations. Hence, the model fits and estimated corner frequencies for the various phases are very similar. This appears to be a fairly common and important phenomenon for the earthquakes analyzed. It allows a more robust approach of fitting Brune source parameters, using a broader range of frequencies, by combining relative spectra of regional P and S phases for earthquakes (e.g., the black dashed curve in Figure 3).

Correcting the spectra for the source terms, we then fit the combined distance and site effects for the various events and stations in our dataset, showing that good calibration of non-source-related physical effects (distance and site terms) may be obtained over a wide range of frequencies for paths with data. The estimates of the source terms from relative spectra and the fits to the median source-corrected spectra (viz. the black dashed curves in Figures 9 and 11) provide all information necessary to completely correct the spectra for all source, distance, and site effects. Thus, by first constraining the source terms, we are now able to fully calibrate paths/stations with suitable data. Of particular interest, we obtain very similar Lg Q_0 estimates for many paths from LNTS to regional stations, as well as some notable differences, using only a single pair of earthquakes with well-constrained source terms, as compared to estimates from a tomographic Q_0 map. Our results illustrate how even a small number of events with well constrained source terms provide comparable or improved estimates of Lg Q.

The focus of this new project, which has just started, is to extend the constrained inversion approach to eliminate remaining trade-offs among Q, geometrical spreading, and site terms that have different distance and frequency dependence. We refer to the approach as a stepwise, iterative procedure to constrain estimates of all of the correction parameters. Starting with our source-corrected spectra and the model fits, the procedure would separate the spreading and constant site factors, apply those corrections, and then resolve Q and frequency-dependent site terms. We illustrated some of the ideas for station MAKZ. This is expected to provide more accurate estimates of all of the physical parameters of Equation (1) than currently exist. We also plan to incorporate coda measurements and methods (1) to greatly augment the source terms estimated using spectra of direct phases, relaxing the restriction on event pairs with similar mechanisms; and (2) as a way to independently estimate site dependence. Other key aspects of this work are to quantify uncertainties, validate the results, merge our results with existing models, and deliver the results.

ACKNOWLEDGMENTS

We are grateful to Jiakang Xie for Lg Q_0 estimates and useful discussions. Seismic data from the IRIS DMC were used in this study.

REFERENCES

Brune, J. N. (1970). Tectonic stress and the spectra of seismic shear waves from earthquakes, *J. Geophys. Res.* 75: 4997–5009.

Fisk, M. D., G. D. McCartor, and S. R. Taylor (2008). Robust Magnitude, Distance, and Path-Specific Corrections for Regional Seismic Phases by Constrained Inversion and Enhanced Kriging Methods, ATK/NCR-0608-501, Final Technical Report.

Fisk, M. D. and S. R. Taylor (2006). Robust magnitude and path corrections for regional seismic phases in Eurasia by constrained inversion and enhanced kriging techniques, in *Proceedings of the 28th Seismic Research Review: Ground-Based Nuclear Explosion Monitoring Technologies,* LA-UR-06-5471, Vol. 1, pp. 15–24.

Mayeda, K. M., L. Malagnini, and W. R. Walter (2007). A new spectral ratio method using narrow band coda envelopes: evidence for non-self-similarity in the Hector Mine sequence, *Geophys. Res. Lett.* 34: L11303.

Phillips, W. S., R. J. Stead, G. E. Randall, H. E. Hartse, and K. Mayeda (2008). Source effects from broad area network calibration of regional distance coda waves, in Scattering of Short Period Waves in the Heterogeneous Earth, H. Sato and M.C. Fehler, Editors., D. P. and P. G. Richards (2004). Repeating seismic events in China, *Science* 303: 1176–1178.

Sereno T. J., S. R. Bratt, and T. C. Bache (1988). Simultaneous inversion of regional wave spectra for attenuation and seismic moment in Scandinavia, *J. Geophys. Res.* 93: 2019–2035.

Taylor, S. R., and H. E. Hartse (1998). A procedure for estimation of source and propagation amplitude corrections for regional seismic discriminants, *J. Geophys. Res.* 103: 2781–2789.

Taylor, S. R., A. A. Velasco, H. E. Hartse, W. S. Phillips, W. R. Walter, and A. J. Rodgers (2002). Amplitude corrections for regional seismic discriminants, *Pure and Appl. Geophys., Special Edition on Monitoring the Comprehensive Nuclear-Test-Ban Treaty: Seismic Event Discrimination and Identification*, 159: 623–650.

Walter, W. R. and S. R. Taylor (2002). A Revised Magnitude and Distance Amplitude Correction (MDAC2) Procedure for Regional Seismic Discriminants: Theory and Testing at NTS, *UCRL-ID-146882,* LA-UR-02-1008.

Xie, J., D. Schaff, and Y. Liu (2005). Tomographic mapping of Lg Q in eastern Asia, in *Proceedings of the 27th Seismic Research Review: Ground-Based Nuclear Explosion Monitoring Technologies*, LA-UR-05-6407, Vol. 1, pp. 242–248.

Xie, J., Z. Wu, R. Liu, D. Schaff, Y. Liu, and J. Liang (2006). Tomographic regionalization of crustal Lg Q in eastern Eurasia, *Geophys. Res. Lett.*, 33, L03315.

ESTIMATING BODYWAVE ARRIVALS AND ATTENUATION FROM SEISMIC NOISE

Peter Gerstoft[1], Jian Zhang[1], and Steven R Taylor[2]

University of California, San Diego[1] and Rocky Mountain Geophysics, LLC [2]

Sponsored by the Air Force Research Laboratory

Award No. FA8718-07-C-0005
Proposal No. BAA07-70

ABSTRACT

This paper investigates the utility of computing Time-Domain Green's Functions (TDGF) to be used for estimating velocity and attenuation structure for the purposes of nuclear explosion monitoring over local and near-regional distances. We have focused on two topics:

Earth's background vibrations at frequencies below about 0.5 Hz have been attributed to ocean-wave energy coupling into the ground and propagating as surface waves and *P* waves (compressional waves deep within the Earth). However, the origin and nature of seismic noise on land at frequencies around 1 Hz has not yet been well studied. Using array beamforming, we analyze the seismic noise fields at two remote sites (Parkfield and Mojave Deserts) in California, for durations of one and six months respectively. We find that (1) the seismic background noise at about 0.6–2 Hz consists of a significant amount of continuous *P* waves originating offshore, and (2) the power of the *P*-wave noise is highly correlated with the offshore wind speed, demonstrating that these high-frequency *P* waves are excited by distant ocean winds.

We present a methodology to obtain frequency-dependent relative site amplification factors using ambient seismic noise. We treat a seismic network or array as a forced damped harmonic oscillator system where each station responds to a forcing function obtained from frequency-wavenumber beams of the ambient noise field. Taken over long time periods, each station responds to the forcing function showing a frequency-dependent resonance peak whose amplitude and spectral width depends upon the elastic and anelastic properties of the underlying medium. Our results are encouraging in that hard rock sites generally show narrower resonance peaks with reduced amplitudes relative to soft rock sites in sedimentary basins. There is also a tendency for spectral peaks to shift to higher frequencies and become more asymmetric as the site amplification increases. This could be due to small-strain nonlinearity for stations having high site amplification.

One exciting aspect of this research is that noise analysis methods have the potential to be very useful in improving body-wave tomography for Earth's structure, just as noise cross-correlation methods have recently proven successful in surface-wave tomography. A preliminary test examining teleseismic *P* waves recorded in southern California shows that similar arrival-time anomalies can be obtained both from direct *P* waves from a natural earthquake and *P*-wave noise generated by a large storm. In this case, the noise can be processed using waveform cross-correlation among different station pairs and optimal P relative arrival-time estimates can be computed using the same approach traditionally used to analyze earthquake arrival times.

OBJECTIVES

Our objective is to apply and extend the methodology of deriving TDGF for propagation between two receivers by cross-correlation of seismic noise observed at the receivers. We propose to add the following improvements of the TDGF method: 1) modifications to better handle cases having non-isotropic noise; 2) implementing a system identification approach for obtaining reliable amplitude information for the TDGF, allowing for the estimation of attenuation along paths between receivers. We also seek turning body-wave noise into relative arrival times, and thus improvements of traditional body-wave tomography.

RESEARCH ACCOMPLISHED

Estimating Site Amplification Factors from Ambient Noise

This part is based on Taylor et al. (2009). Most studies of ambient noise have focused on the measurement of interstation group velocities using the time-domain Green's function derived from noise cross correlation (e.g., Gerstoft et al*.,* 2006a). Little work to date has addressed the issue of obtaining attenuation from ambient noise. Recent work of Snieder (2007), Matzel (2008), Prieto and Beroza (2008) and Prieto et al., (2009) have begun to address this problem. Snieder (2007) shows that, for acoustic waves in homogeneous anelastic media, correlation-type Green's functions can be correctly estimated, but attenuation is not. In practical applications, however, multiple scattering may aid in recovering attenuation, but the issue remains unresolved. Snieder (2007) also points out the necessity of dividing observed power spectrum by that of the excitation (forcing) power spectrum that we use in our approach. Ambient noise has been used previously for estimating site effects (e.g., Field and Jacob, 1995) by taking the horizontal to vertical spectral ratio to obtain the resonant frequency. The motivation for our work is related to nuclear explosion monitoring, but may have other applications as well, particularly for seismic hazard studies, calibration of regional arrays and site selection for planned station installations.

We have developed a simple methodology for estimation of site amplification factors (and possibly relative attenuation) using ambient noise. The approach is to estimate site *Q* using standing waves as opposed to taking a propagating wave, tomographic approach (e.g. Matzel, 2008) or the spatial coherency (SPAC) approach of Aki (1957; e.g. Prieto et al., 2009). The idea is to treat time-varying frequency-wavenumber (FK) beams of the ambient noise field as a forcing function beneath a network of stations. Each station responds differently to the forcing function depending on the site structure and attenuation. Differential equations representing different forced, damped harmonic oscillator systems (FDHMO) can be used to estimate *Q* and resonance frequencies beneath stations. Additionally, the method does not rely on any time-domain normalization such as 1-bit normalization (e.g., Benson et al., 2007) that presumably will have a deleterious effect on amplitude measurements necessary for attenuation estimation.

For our analysis, we collected data for the month of January 2008 from the Southern California Earthquake Data Center (SCEDC) for 72 stations shown in Figure 1a. Stations CHF and BRE are examples of a hard rock and soft rock site, respectively, that will be discussed in subsequent analyses. Data for each station was examined for glitches, dropouts or other irregularities that may make them unsuitable for analysis.

Imagine that stations in a network or array are driven by a forcing function derived from the ambient noise field. Each site will respond differently depending upon the elastic and anelastic properties of the underlying medium. As a simple illustration, we use the differential equation for a FDHMO to simulate the response of each station to the forcing function given by (e.g., Lay and Wallace, 1995)

$$\ddot{x} + \gamma\dot{x} + \omega_0^2 x = \frac{1}{M} F(t) \qquad (1)$$

where $F(t)$ is the forcing function, x is the sensor displacement response to the forcing function, γ is the viscous damping term and ω_0 is the natural frequency of the oscillator and M is the mass. For light damping, $\gamma << \omega_0$, the resonance peak is narrow and most of the energy is concentrated around $\omega \approx \omega_0$. Using the approximation $(\omega_0 + \omega)(\omega_0 - \omega) \approx 2\omega_0(\omega_0 - \omega)$ the power spectrum for a particular site relative to that of the forcing function is then given by

$$P_{xF}(\omega) = \frac{P_x(\omega)}{P_F(\omega)} = \frac{M}{\omega_0^2\left[4(\omega_0 - \omega)^2 + \left(\frac{\omega}{Q}\right)^2\right]} \quad (2)$$

where $\gamma = \omega_0/Q$. We leave the mass, M, in the formulation because it will subsequently be related through our observations to the density at each receiver site. Note that the resonant frequency is given by $\omega_0 = \sqrt{(k/M)}$ where k is the spring constant. For each station, it is then possible to grid search over a range of ω_0 and Q values to match the observed resonance peaks. Of course, the single oscillator FDHMO is a very simple system and, as will be seen below, observations suggest that a more complicated representation possibly involving slight nonlinearity may be required.

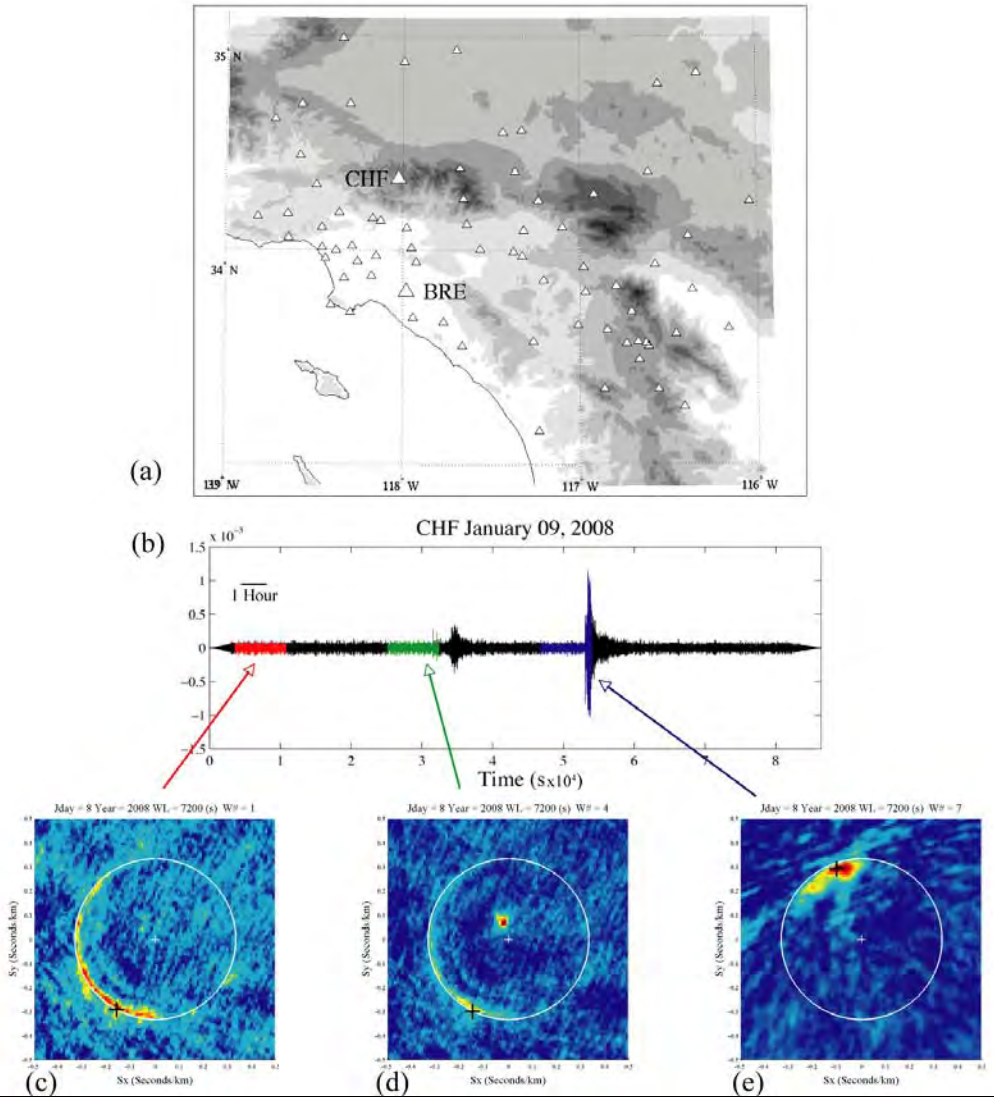

Figure 1. (a) Map showing seismic stations of the SCEDC used in this study. CHF and BRE are examples of hard rock and soft rock sites, respectively. (b) One day of BHZ channel data at station CHF for January 9, 2008. Bottom portion of figure shows FK beams for three 2-hour samples of noise each with a color-coded arrow indicating the portion of the signal used to compute the beam. White circle corresponds to a phase velocity of 3 km/s and black + symbol to the point at which beam is computed. Note that all available stations for this day shown in Figure 1a were used to compute the FK spectrum.

The power spectrum of the forcing function, $P_F(\omega)$ in Equation (2) is computed from the network or array beam directed towards the maximum power of the ambient noise field. A network or array beam is necessary for estimating the forcing function. This process is illustrated in Figure 1 where we compute the FK spectrum between 0.03 and 0.25 Hz. Figure 1b shows the record at station CHF for January 9, 2008, with three two-hour time windows indicated by red, green and blue. Note that all available stations for this day shown in Figure 1a were used to compute the FK spectrum. Three examples of FK spectra are shown color-coded to time windows on the seismogram in Figure 1b. We compute a beam at the point marked by a + symbol for the maximum power between phase velocities of 2.9 and 3.2 km/s.

The FK spectrum in Figure 1c is typical for a noise sample uncontaminated by signal transients. Figure 1d is contaminated by the arrival of a teleseismic *P* wave from the northwest at a high phase velocity although the noise arrivals at relatively lower power can still be seen arriving from the southwest. Restriction of the phase velocities to those between 2.9 and 3.2 km/s allows us to remove the power from the transient *P* wave. Figure 1e shows the FK spectrum for a time window that was excluded from our analysis. A large regional surface wave arrives from the northwest at phase velocities similar to ambient noise. It is a simple matter to identify this and eliminate this time window from the analysis. For the month of January, the noise field arrives predominantly from the southwest although a range of azimuths can be observed consistent with Gerstoft and Tanimoto (2007). In practice, a greater sampling of azimuths will help stabilize results and reduce potential directionally-dependent interference effects on the wavefield from multiple sources and lateral heterogenity. This can be achieved in two ways. The first is by obtaining noise samples over different times of the year. The second is by integrating the FK beam along a semi-circle of azimuth and phase velocity to capture a wider range of ambient noise energy.

Figure 2 shows the processing steps involved with obtaining a site amplification factor from ambient noise for January 9, 2008 shown in Figure 1. We divide the data into two-hour non-overlapping time windows. Figure 2a shows the CHF BHZ power spectrum for each of the noise samples shown in Figure 1b. The power spectrum is computed from each of the broadband FK beam points using the full array and is shown in Figure 2b. Treating the beam power in Figure 2b as the network forcing function and the individual channel power as the response (Figure 2a), we use the center portion of Equation (3) and estimate the site response by computing the power spectral ratio shown in Figure 2c. In our analysis below, we compute the median of the power spectra for each two-hour time segment over all samples passing QC for the month of January 2008 at each station. Note that in our figures the spectral smoothing is only for illustration purposes and not actually performed until the final processing step.

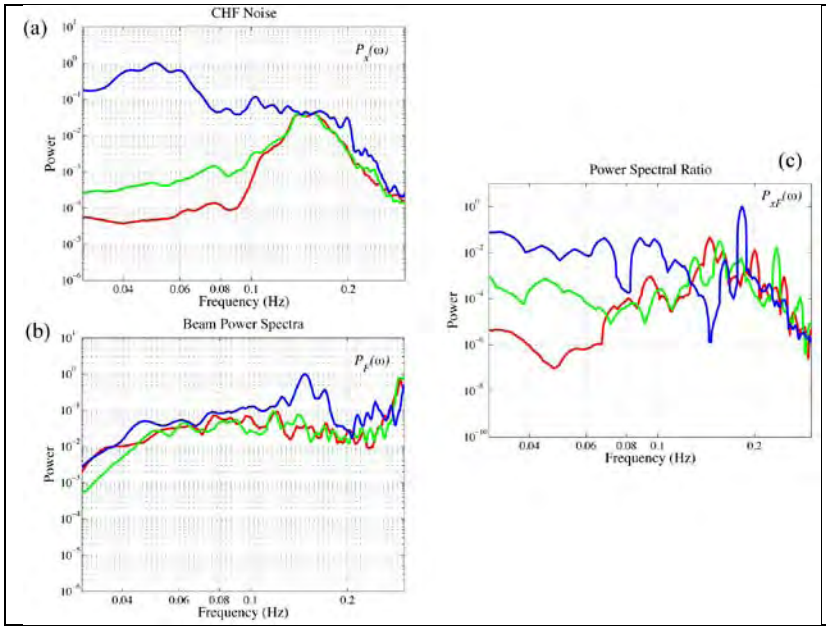

Figure 2. (a) CHF single-channel power spectra from noise taken from each of the three windows of Figure 1b using the same color-coding for station CHF as in Figure 1 for the January 9, 2008 noise sample. (b) Smoothed power spectrum for each of the FK beam points shown in Figure 1. (c) Ratio of CHF noise power (Figure 2a) relative to beam power (Figure 2b).

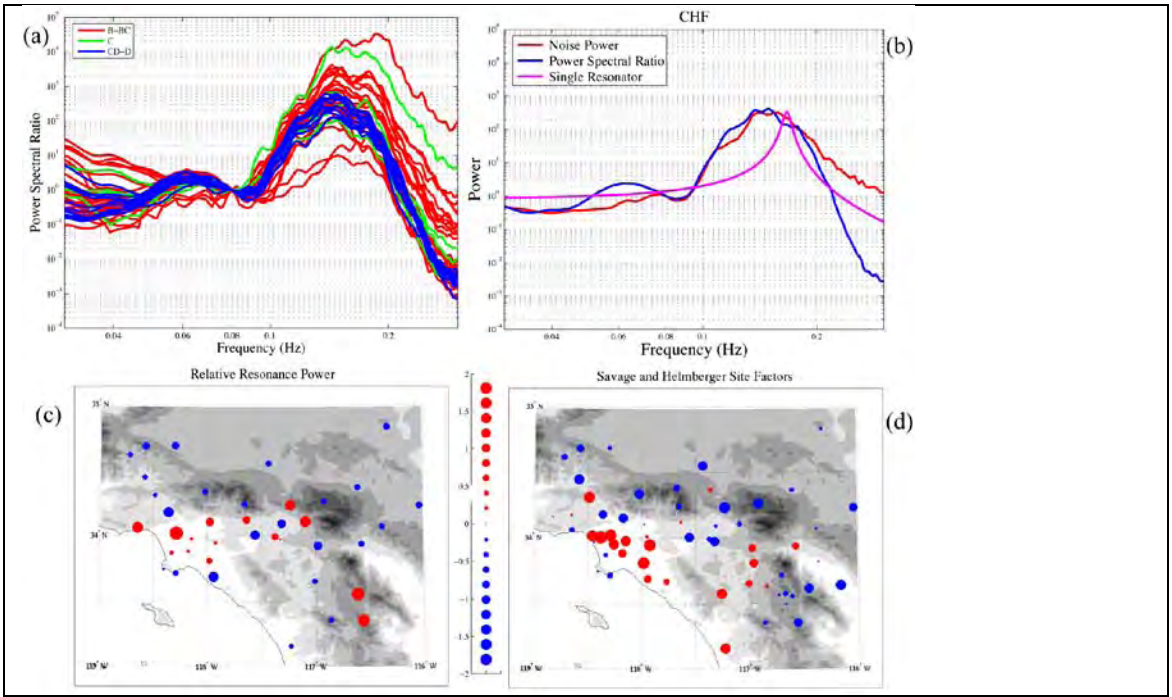

Figure 3. (a) Individual power spectral ratio median for all stations with NEHRP site classification factors in three groups all normalized at 0.08 Hz. (b) Station CHF smoothed noise power (red) for sample shown in Figure 2a, power spectral ratio median (blue) and single resonance peak (magenta). (c) Map showing standardized relative resonance power. (d) Standardized logarithm of site amplification terms from Savage and Helmberger (2004). In both (c) and (d) red indicates larger amplitudes and blue lower amplitudes. Size of symbol is proportional to absolute value of measurement. Frequency axis in (a) and (b) is between 0.03 and 0.3 Hz.

A number of features are observed in Figure 2. Most notably is the contamination of the third time window by the large regional event arriving from the northwest (as indicated by the FK plot in Figure 1e). The individual channel is strongly affected by this event as well as the power spectral ratio justifying the elimination of this window from subsequent analysis. In contrast, beamforming on the maximum noise power for the second time window effectively removes contamination of the small teleseismic event arriving from the northwest. The beam power shows a different spectral character than that of the individual channel noise. The individual channel noise spectra show a prominent spectral peak at approximately 0.167 Hz as expected for the microseismic noise peak. In contrast, the beam is flatter and has a subsidiary peak at about 0.3 Hz. A histogram of station spacing indicates that spatial aliasing effects for surface waves propagating at 3 km/s may start to occur at frequencies around 0.3 Hz. Thus, our subsequent analysis focuses on frequencies less than 0.3 Hz.

Figure 3a shows individual station power spectral ratio medians (all normalized at 0.08 Hz) grouped by National Earthquake Hazard Reduction Program (NEHRP) site classifications of Yong et al., (2008). Group B-BC represent soft rock sites, C intermediate, and CD-D hard rock sites. All stations show the same general character with a spectral peak between 0.14 and 0.16 Hz. The hard rock sites (blue) show similar power spectral ratios. In contrast, the soft rock sites show significant variability and there is a tendency for spectral medians to shift to higher frequencies and become broader as the amplitude increases. This could be due either lower density materials at higher amplification sites shifting the resonance frequency to larger values or to slight small-strain nonlinearity for stations having high site amplification (e.g. Assimaki et al., 2008). Figure 3b shows station CHF smoothed noise power (red) for the noise sample shown in Figure 2c, the power spectral ratio median for January 2008 (blue) and single resonance peak (magenta) computed using Equation (3) with a Q of 20 and resonance frequency of 0.167 Hz. The shape of the observed spectrum is similar to that of the microseismic noise except that it is narrower and shifted to slightly lower frequencies. This effect is observed for the other stations as well. This suggests that the power spectral peak is indeed a resonance peak driven by microseisms. Obviously, a single resonator model is not the

correct representation but has the general character of the observed resonance peak in that the lower frequency power level (where the forcing function and site response are in phase) is greater than that of the high frequency power level (where the forcing function and site response are phase shifted by 180°). More complicated attenuation representations (such as absorption band models) will be required to model the nature of the observed resonance peaks (e.g., Liu et al., 1976).

We compute relative resonance power is by taking the average of the logarithm of each station power spectral ratios shown in Figure 3a to that of the median for all stations between 0.08 and 0.3 Hz. Figure 3c shows a map of the standardized resonance power, $Z = (X - \mu_X)/\sigma_X$, (where X is the logarithm of the relative resonance power) and Figure 3d the standardized site amplification terms from Savage and Helmberger (2004) who used the *Pnl* ratio of vertical to radial energy. In general, there is a good comparison between the relative amplitudes of the observed resonance power and the Savage and Helmberger site factors with larger amplitudes in the basin regions and lower amplitudes in the mountainous terrain. Two stations showing large resonance power located at approximately 33.5º N and 116.5º W correspond to low velocities observed along the San Jacinto fault zone (Hong and Menke, 2006).

Local High-Frequency *P* Waves at the Parkfield Array

This part is based on Zhang et al (2009). We analyze vertical-component noise recorded at the Parkfield small-aperture array in California (Figure 4a, ~11 km aperture, mid-January to mid-February 2002) using similar beamforming as in the previous section. Slowness-azimuth spectra from 1-hour noise windows (Figure 9b) shows that most 0.6–2 Hz noise energy at Parkfield comes from the coastal direction at a horizontal slowness of ~0.2 s/km, i.e., a velocity of ~5 km/s. We calibrate the beamformer output using earthquakes with known locations in order to provide reference points for tracking the noise sources. The *P* wave of a coastal earthquake (July 13, 2002; M_L 1.8; 66 km SW of the Parkfield array) shows a slowness of ~0.2 s/km (Figure 9c), implying that the source of the *P*-wave noise is located at a similar distance from the array, i.e., offshore.

The power of the high-frequency *P*-wave noise (1–1.3 Hz) strongly correlates with the offshore wind speed (Figure 5), unlike microseisms that have been found correlating with significant wave heights. We calculated the cross-corrrelation of the beamformed *P*-wave noise power with the wind speed obtained at 8 Pacific sites and 4 land sites. The wind speeds at Pacific sites have indeed similar variations. However, Figure 5a shows that the correlation rises to its highest (CC=0.88) at an offshore site (red square) at azimuth 248º, in agreement with the direction of the noise observed from beamforming (225–270º). In contrast, the correlation is poor at all land sites. The time series of the *P*-wave noise power and the wind speed at the best-correlated site is shown in Figure 5b. Assuming a linear relation, the noise power varies with wind speed at a rate of ~1 dB per m/s.

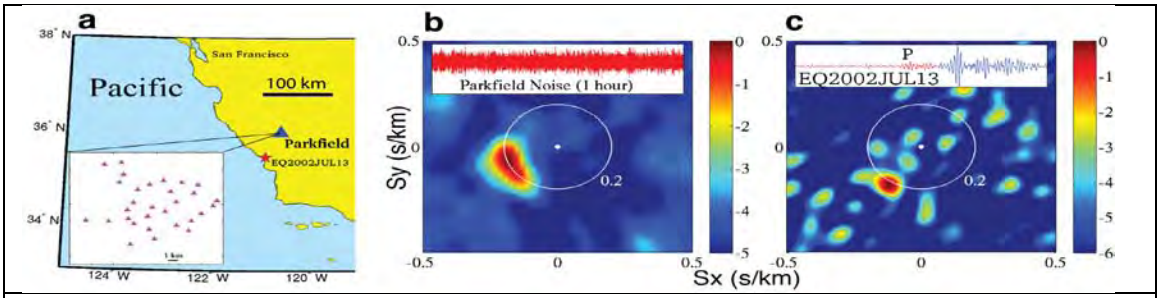

Figure 4. *P*-wave seismic noise observed from beamforming. (a), Map of the Parkfield and one earthquake (red star) for comparison with noise observations. Slowness-azimuth spectra (dB) at 0.7–1.6 Hz are shown for (b) noise and (c) *P*-wave part of a coastal earthquake (July 13, 2002). Waveforms of the noise and earthquakes are shown in the inserts.

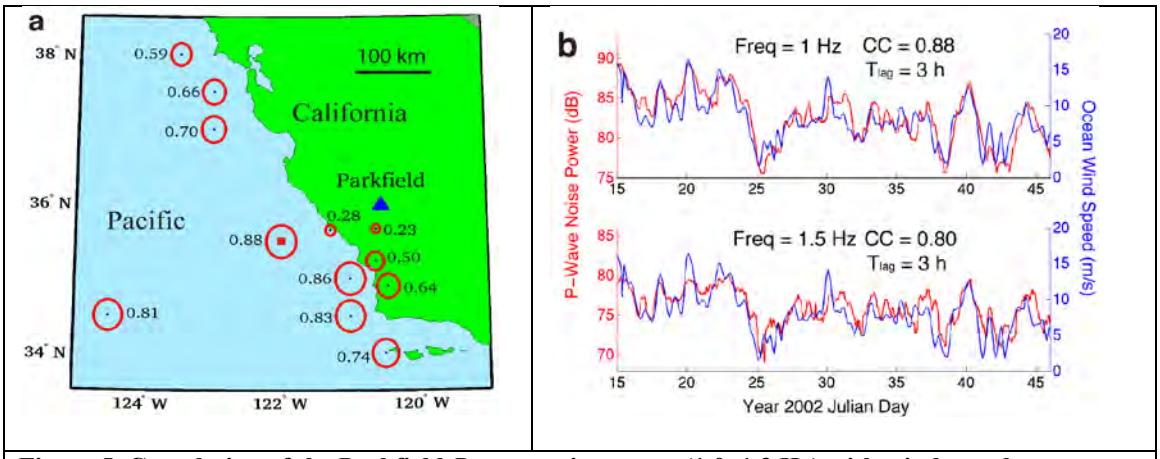

Figure 5. Correlation of the Parkfield *P*-wave noise power (1.0–1.3 Hz) with wind speeds at offshore and onshore sites. (a), Map view of the sites of the Parkfield array (blue triangle) and the wind stations (red circles). The circle size indicates the correlation-coefficient (CC) at each station as marked beside the circles. (b), Time series of noise power (red, at 1 Hz and 1.5 Hz respectively) and wind speed (blue) for the site (red square in a) with the strongest correlation. T_{lag} is the lag time of the peak correlation.

Relative *P*-Wave Arrival Times from Hurricane Katrina to Southern California

The *P* waves observed in Gerstoft et al. (2006b and 2008b) using the southern California seismic network (SCSN), as well as Zhang et al. (2009), can be used to measure relative *P*-wave arrival times across the array from distant noise sources. These relative times contain information about 3-D seismic velocity anomalies under the array. This suggests that it may be possible to perform tomography for crust and upper-mantle structure using a similar approach to that long used to analyze teleseismic *P* waves from earthquakes (e.g., Aki and Lee, 1976), but with the advantage of obtaining data from additional source regions, i.e., the areas of active storms discussed above. Following VanDecar and Crosson (1990), we have validated the basic approach by obtaining a pattern of *P*-wave arrival-time anomalies beneath southern California observed from Hurricane Katrina as a noise source, which is well correlated with that measured by using a nearby earthquake in the Gulf of Mexico (Figure 6).

Our approach includes cross-correlation measurements of relative delay times between station pairs by taking advantage of coherent *P* waves among microseisms, and optimization of relative arrival-time estimates through an over-determined system of timing residual equations in a least-squares sense, assuming that errors in cross-correlation derived delay times are primarily random in nature. For station pairs with a sufficient signal-to-noise ratio (SNR), we generate a system of equations given by $t_i - t_j = \Delta t_{ij}$, and we add the constraint equation $\sum t_i = 0$ to force the arbitrary mean of the relative arrival times to be zero. This system is expressed as $A \cdot t = \Delta t$, where A is a sparse coefficient matrix, for which the i^{th} and j^{th} columns in a row associated with Δt_{ij} are 1 and -1 respectively, while the other columns are zeros. If we weight the equations to reflect the quality of the observations, we have the linear system of the form $W \cdot A \cdot t = W \cdot \Delta t$, where W is a diagonal matrix to weight each equation based on residuals from previously determined unweighted estimate, $res_{ij} = \Delta t_{ij} - (t_i^{est} - t_j^{est})$. A standard approach to solving the equation system in a least-squares sense is the use of normal equations $t^{est} = (A^T \cdot W \cdot A)^{-1} \cdot A^T \cdot W \cdot \Delta t$ by using either the method of singular value decomposition (SVD) or the conjugate gradient algorithm LSQR of Paige and Saunders (1982).

Based on the beamforming output (Figure 7 a & b, [Gerstoft et al. 2006b]), *P*-wave microseisms from Katrina to southern California can be approximated as a plane wave arriving at the network with an apparent speed of 11.7 km/s. The *P* waves can also be clearly revealed by cross-correlating the vertical-component seismic noise recorded at pairs of stations (Figure 7c). The time lags between traces (Δt_{ij}) at any station pair are then obtained as the offset of the maximum of their cross-correlation functions (red dots in Figure 7c).

We have found that the equation residuals derived from the best-fitting solutions are nearly normally distributed (Figure 8a). To evaluate the reliability of the least-squares estimates of the relative *P* arrival times using seismic noise, we then perform a statistical resampling analysis ("bootstrap" method, Efron, 1982; Shearer, 1997; Waldhauser and Ellsworth, 2000). Figure 8b shows that a level of 0.1 s of timing errors can be reached, which may be sufficient for revealing large travel-time anomalies on the order of 1 s.

Figure 6. Map of the Southern California Seismic Network, Hurricane Katrina (schematic) on August 28, 2005, and an Mw 5.9 earthquake on September 10, 2006. The dashed line indicates the great circle path (27°) of the *P* waves from Katrina to Southern California.

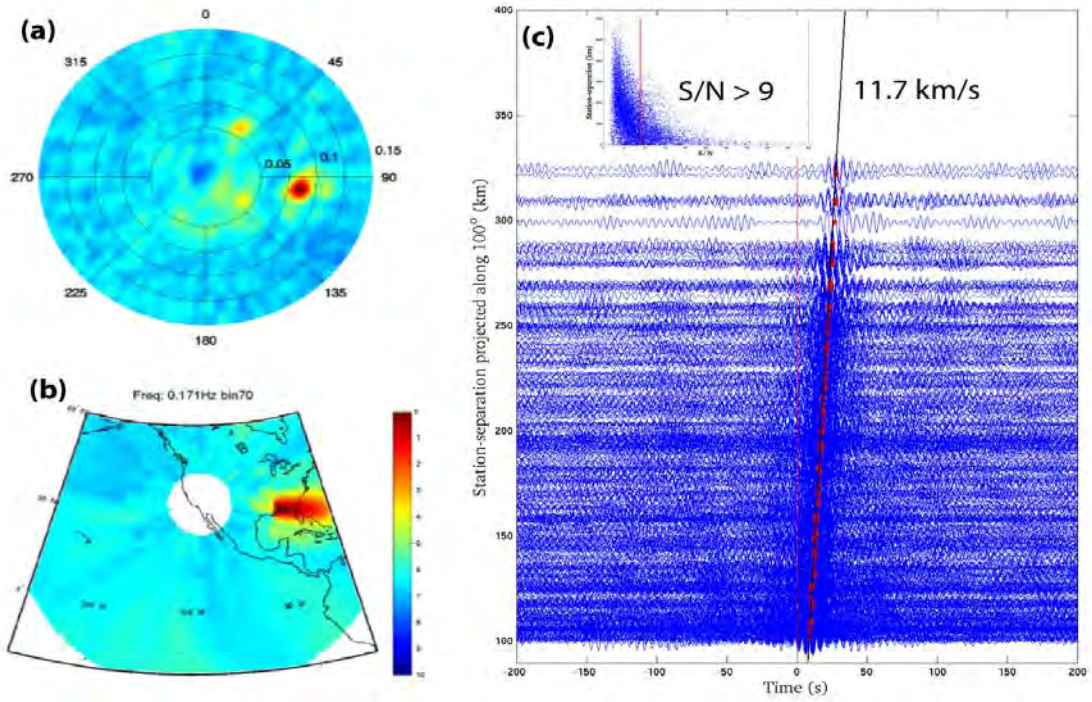

Figure 7. Katrina-generated *P* waves observed in southern California and relative *P* arrival times from cross-correlation. (a) Beamforming of 0.19-Hz vertical-component seismic noise recorded by the Southern California network, showing *P* waves (0.085 s/km, i.e., 11.7 km/s) coming from 100° during Katrina's landing; (b) Source region of *P* waves approximated by back-propagating the slowness-azimuth spectra from (a); (c) Range-time representation of the cross-correlation time series for 400 station pairs with SNR>9. Red dots mark the relative arrival-time measurements as the offset of the cross-correlation maximum. Black line indicates an 11.7 km/s plane wave. The insert shows SNR versus station separation (projected along 100°).

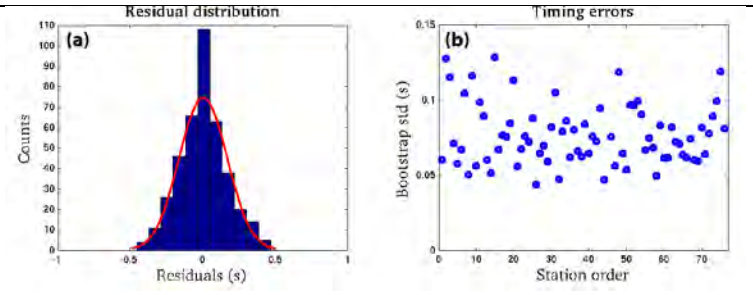

Figure 8. Least squares and uncertainty estimation. (a) Histogram of cross-correlation residuals derived arrival-time lags and least-squares solutions, showing a Gaussian-like distribution. (b) Bootstrap-resampling derived timing uncertainties of the *P* relative arrival times from Katrina noise.

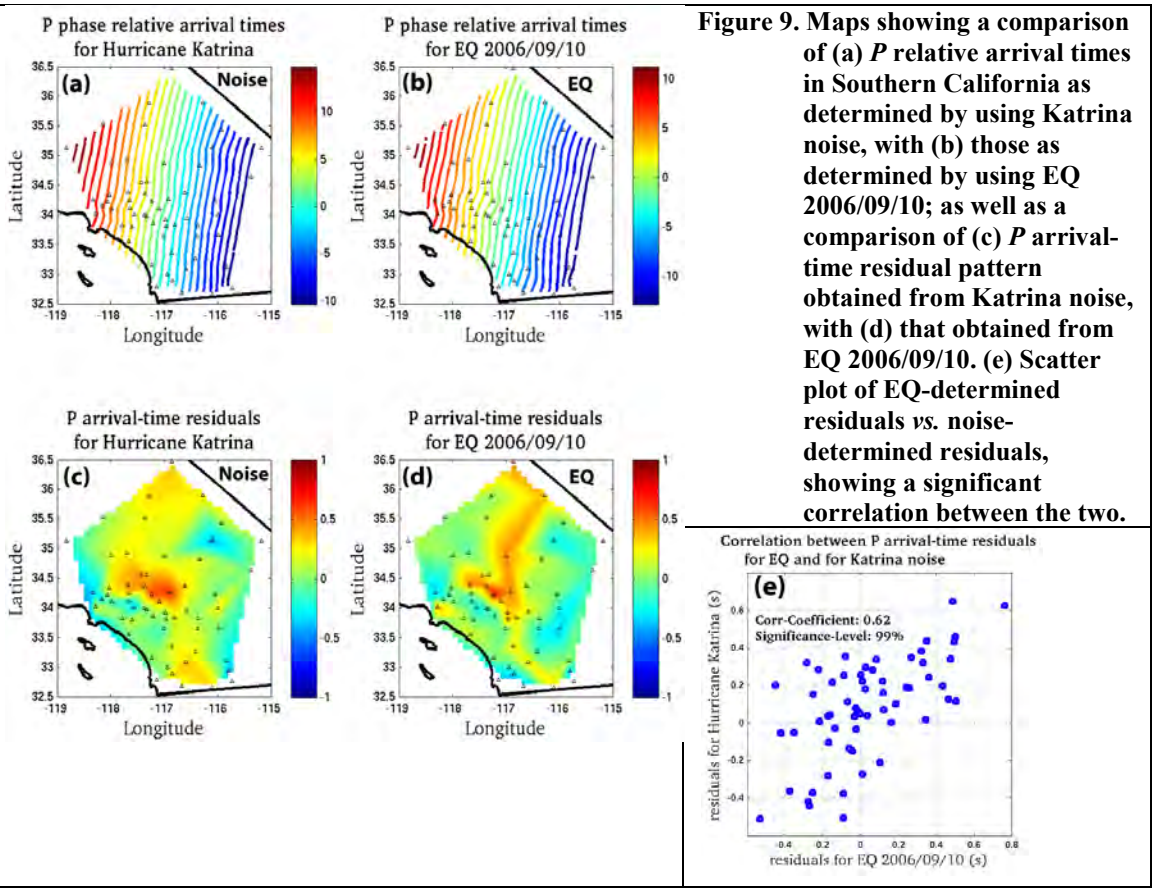

Figure 9. Maps showing a comparison of (a) *P* relative arrival times in Southern California as determined by using Katrina noise, with (b) those as determined by using EQ 2006/09/10; as well as a comparison of (c) *P* arrival-time residual pattern obtained from Katrina noise, with (d) that obtained from EQ 2006/09/10. (e) Scatter plot of EQ-determined residuals *vs.* noise-determined residuals, showing a significant correlation between the two.

To demonstrate this approach, we compare the relative *P* arrival-time estimates by using Katrina microseisms with those estimates through the same processing but by using an Mw 5.9 earthquake that occurred in the Gulf of Mexico on September 10, 2006. The relative *P* arrival times using the earthquake and, thus, their residuals relative to the ak135-predicted times are shown in Figure 9 a & c respectively. Similarly, the estimates using Katrina noise and their residuals relative to an 11.7 km/s plane wave are shown in Figure 9 b & d respectively. It can be seen that the relative arrival times and their anomalies resulting from using *P*-wave microseisms are reasonably well correlated with those resulting from using traditional sources, i.e., earthquakes. To quantify this, the correlation between the two residual patterns is 0.62 with a significance level over 99% (see Figure 9e).

CONCLUSIONS AND RECOMMENDATIONS

1. We have developed a standing-wave methodology that has the potential for estimating frequency-dependent site factors for a network or array of stations using ambient noise. The basic idea behind the method is to use the FK

beam of the ambient noise field to simulate the forcing function beneath the network. Each site will respond differently to the forcing function depending on the local velocity and attenuation structure. The frequency range of applicability is controlled by the spatial aperture and station spacing used to construct the FK beam. Results using a month of ambient noise data in southern California are encouraging in that the shape and amplitude of individual station resonance peaks appear to correlate with local geology and with site factors of Savage and Helmberger (2004). In general, hard rock sites are characterized by lower amplitude, narrower resonance peaks than those from soft rock sites. There is also a tendency for spectral peaks to shift to higher frequencies and become more asymmetric as the amplitude increases. This could be due to lower densities or to small-strain nonlinearity at stations having high site amplification (e.g., Assimaki et al., 2008).

2. A test examining teleseismic *P* waves recorded in southern California shows that similar arrival-time anomalies can be obtained both from direct *P* waves from a natural earthquake and *P*-wave noise generated by a large storm. This suggests using storms as additional sources for relative arrival time measurements.

REFERENCES

Aki, K. (1957). Space and time spectra of stationary stochastic waves, with special reference to microtremors, *Bull. Earthq. Res. Inst.* 35: 415–457.

Aki, K. and W. H. K. Lee (1976). Determination of three-dimensional velocity anomalies under a seismic array using first P arrival times from local earthquakes 1. A homogeneous initial model, *J. Geophys. Res*. 81: 4381–4399.

Assimaki, D., W. L. J. Steidl, and J. Schmedes (2008). Quantifying nonlinearity susceptibility via site-response modeling uncertainty at three sites in the Los Angeles Basin, *Bull. Seismol. Soc. Am*. 98: 2364–2390.

Bensen, G.D., M.H. Ritzwwoller, M.P. Barmin, A.L. Levshin, F. Lin, M.P. Moschetti, N.M. Shapiro and Y. Yang (2007). Processing seismic ambient noise data to obtain reliable broad-band surface wave dispersion measurements, *Geophys. J. Int*. 169: 1239–1260.

Efron, B. (1982). *The jackknife, the bootstrap, and other resampling plans*, SIAM, Stanford University, Philadelphia, 92 pp.

Field, E. H. and K. H. Jacob (1995), A comparison and test of various site-response estimation techniques including three that are not reference-site dependent*, Bull. Seismol. Soc. Am*. 85: 1127–1143.

Gerstoft, P., K. G. Sabra, P. Roux, W.A. Kuperman, and M.C. Fehler (2006a). Green's functions extraction and surface-wave tomography from microseisms in southern California, *Geophys*. 71: SI23–SI31.

Gerstoft, P., M.C. Fehler, and K. G. Sabra (2006b). When Katrina hit California, *Geophys. Res. Lett*. 33: L17308, doi:10.1029/2006GL027270.

Gerstoft, P. and T. Tanimoto (2007). A year of microseisms in southern California, *Geophys. Res. Lett*. 34: L20304, doi:10.1029/2007GL031091.

Gerstoft, P, P Shearer, N Harmon, and J Zhang (2008b). Global P, PP, and PKP wave microseisms observed from distant storms, *Geophys. Res. Lett*. 35: L23307, doi:10.1029/2008GL036111.

Hong, T.K. and W. Menke (2006). Tomographic investigation of the wear along the San Jacinto fault, southern California, Phys. Earth and Planet. Int., 155, 236-248.

Lay, T. and T. Wallace (1995). Modern Global Seismology, Academic Press, San Diego, CA.

Liu, H.P., D.L. Anderson and H. Kanamori (1976). Velocity dispersion due to anelasticity: Implications for seismology and mantle composition, Geophys. J.R. Astron. Soc., 47, 41-58.

Matzel, E.M. (2008). Attenuation tomography using ambient noise correlation, *Seism. Res. Lett*. 79: 358.

Paige, C. C., and M. A. Saunders (1982). LSQR: Sparse linear equations and least squares problems, ACM Transactions on Mathematical Software 8/2, 195–209.

Prieto, G.A. and G.C. Beroza (2008). Earthquake ground motion prediction using the ambient seismic field, *Geophys. Res. Lett*. 35: L14304, doi:10.1029/2008GL034428.

Prieto, G. A., J. F. Lawrence and G. C. Beroza (2009). Anelastic Earth structure from the coherence of the ambient seismic field, accepted by *J. Geophys. Res*.

Savage, B. and D. V. Helmberger (2004). Site response from incident Pnl waves, *Bull. Seismol. Soc. Am*. 94: 357–362.

Shearer, P. (1997). Improving local earthquake locations using the L1 norm and waveform cross correlation: application to the Whittier Narrows, California, after shock sequence, *J. Geophys. Res*. 102: 8269–8283.

Snieder, R. (2007). Extracting the Green's function of attenuating heterogeneous acoustic media from uncorrelated waves, *J. Acoust. Soc. Am*., doi: 10.1121/1.2713673.

Taylor, Steven R., P. Gerstoft, and M. C. Fehler (2009). Estimating site amplification factors from ambient noise, *Geophys. Res. Lett*. 36: L09303, doi:10.1029/2009GL037838.

VanDecar, J. C., and R. S. Crossen (1990). Determination of teleseismic relative phase arrival times using multi-channel cross-correlation and least squares. Bull Seismol Soc Am, 80: 150–169.

Waldhauser, F. and W. L. Ellsworth (2000). A double-difference earthquake location algorithm: method and application to the northern Hayward fault, California, *Bull. Seismol. Soc. Am*. 90: 1353–1368.

Zhang, J., P. Gerstoft, and P. M. Shearer (2009). High-Frequency seismic noise driven by ocean winds, *Geophys. Res. Lett*. 36: L39302, doi:10.1029/2009GL037761.

DEVELOPMENT AND TUNING OF A 3-D STOCHASTIC INVERSION METHODOLOGY TO THE EUROPEAN ARCTIC

Juerg Hauser[1], Kathleen M. Dyer[2], Michael E. Pasyanos[2], Hilmar Bungum[1], Jan Inge Faleide[3], and Stephen A. Clark[3]

NORSAR[1], Lawrence Livermore National Laboratory[2], and University of Oslo[3]

Sponsored by the National Nuclear Security Administration

Award Nos. DE-AC52-08NA28651[1,3] and LL08-BAA08-38-NDD03[2]
Proposal No. BAA08-38

ABSTRACT

The development of seismic models for the European Arctic, as for most regions, has traditionally been limited to proposing one model that provides the best possible fit to one or several datasets while observing some regularization constraints. This approach ignores a fundamental property of any inverse problem in geophysics, non-uniqueness, that is, if a model can be found to satisfy given datasets an infinite number of alternative models will exist that satisfy the datasets equally well. In this study we apply a Bayesian formulation to the problem of developing a geophysical model for the Barents Sea. The solution to the inverse problem presented here is no longer only the best-fitting model, but an ensemble of models that satisfy the data to the same degree: the posterior distribution. It is based on two sources of information: (1) the different datasets, notably surface-wave group velocities, regional body-wave travel times, gravity data, compiled 1D velocity models, and thickness relationships between sedimentary rocks and underlying crystalline rocks; and (2) prior information, which is independent from the data. In this work, the posterior distribution is generated using a Monte Carlo Markov Chain (MCMC) algorithm, which has successfully been applied to Yellow-Sea Korean Peninsula region. It samples models from the prior distribution, the set of plausible models based on a priori information, and tests them against the different datasets. While being computationally much more expensive, such a stochastic inversion provides a more complete picture of solution space. It gives an overview of the different structures that can explain the observed datasets while taking the uncertainties in the data into account. A notable improvement with respect to BARENTS3D and previous applications of the MCMC methodology is the model parameterization introduced in this work. We allow for linear changes of seismic parameters within the layers. This results in a parameterization that is superior to the concept of constant seismic parameters for each layer.

The European Arctic, encompassing oceanic crust, continental shelf regions, rift basins, and old cratonic crust, is a challenging setting for any imaging technique and therefore an ideal environment for demonstrating the practical advantages of an MCMC methodology. The MCMC technique under development in this study allowed us to develop a first stochastic model for the region, albeit at a low spatial resolution. The preliminary results show the posterior distribution to be in agreement with knowledge of the regional tectonic setting. We can for example resolve the changes in crustal thickness associated with the northern edge of the continental shelf. More important than absolute values for the crustal thickness are the uncertainties associated with them. The predicted uncertainties correlate well with the variation in the data coverage and data quality in the region. The uncertainties are significantly smaller in data rich regions (e.g., Northern Norway) than in regions with poor data coverage (e.g., Novaya Zemlya). This indicates that the technique behaves as expected; thus, we are properly tuning the methodology by allowing the Markov Chain adequate time to fully sample the model space. Plans for the next phase of the project include increasing the spatial resolution, optimizing the parameterization, and focusing on a more detailed analysis of the posterior distribution.

OBJECTIVES

The area of interest for this study is the European Arctic, in particular the Barents Sea and surrounding regions such as the Norwegian-Greenland Sea, the Southern Eurasian Basin, Novaya Zemlya, the Kara Sea, the East-European Lowlands, the Kola Peninsula and the Arctic plate boundary. The region is characterized by large variations in sediment thicknesses, crustal velocities, crustal thicknesses, and upper mantle velocities. The aim is to develop a stochastic geophysical model i.e., sample the posterior distribution, the ensemble of models that are all in agreement with our set of observations. The posterior distribution is generated from the prior distribution by probabilistically sampling the model space and preferentially accepting models that produce a good fit between the model predictions and the observed data. The observations used in this study are surface-wave group velocities, regional body-wave travel times, gravity data, compiled 1D velocity models, and thickness relationships between sedimentary rocks and underlying crystalline rocks. The MCMC methodology employed here is based on the technique used by Pasyanos et al. (2006) to derive a geophysical model for the Yellow Sea/Korean Peninsula region given surface-wave group velocities, body-wave travel times, receiver functions and gravity data.

Our initiative stands in contrast to recent approaches to modeling the crust and mantle lithosphere in the European Arctic, where the aim has been to find one best-fitting model and little to no attention was devoted to systematically analyzing the model uncertainties (e.g., Levshin et al., 2007; Ebbing et al., 2007; Ritzmann et al., 2007; Ritzmann and Faleide, 2008). A notable exception in this context is the global shear wave velocity model of the crust and upper mantle by Shapiro and Ritzwoller (2002). In the final stage of their inversion procedure, an MCMC technique is used to generate a posterior distribution and thereby estimate model uncertainties.

The stochastic model under development in this study is an ensemble of models that satisfy the datasets to similar degrees. Given a posterior distribution one can draw inferences about the true nature of the Earth and identify robust features in these models. We characterize the posterior distribution by computing the mean and standard deviation for each model parameter. It is however important to realize that these summary statistics do not provide the full picture of the posterior distribution. In the case of a multimodal posterior distribution computing a mean is a poor reflection of the ensemble. A more complete picture of the posterior could be obtained by cluster analysis. Vasco et al. (1993) uses this statistical technique to characterize the posterior and make inferences about properties that are shared by all the models forming the posterior. The importance of knowledge about the robustness of features in a geophysical model can not be over-emphasized, especially when interpreting such models in a geological context. Another important advantage of a stochastic model is that it allows estimating the uncertainties in model predictions due to uncertainties in the model parameters, e.g., uncertainties for travel times and travel-time corrections based on the uncertainties in the model parameters. Such information can be included in earthquake location procedures, thus resulting in much more realistic estimates of location uncertainties.

One of the aims of this project is to improve the MCMC methodology of Pasyanos et al. (2006) for application to a variety of regions of interest. What is an appropriate model parameterization in one region might not be capable of capturing the geological characteristics in another area. Constraining the structure at the nodes of a mesh based on a fixed degree interval between the nodes is an appropriate parameterization near the equator but not in the Barents Sea region. We therefore changed the parameterization to allow for an arbitrary distribution of nodes. Another important improvement is that seismic parameters can now vary linearly with depth in the layers used to describe the sediments, the crystalline crust, and the mantle. This is an enhancement over the constant velocity and density layers used in previous studies (e.g., Pasyanos et al., 2006; Ritzmann et al., 2007).

RESEARCH ACCOMPLISHED

A practical MCMC scheme needs to address four challenges: (1) Development of a mechanism to propose random perturbations to the state in model space that are in agreement with fundamental knowledge about the Earth's structure; (2) Limited computational resources, requiring efficient forward solvers and the smallest number of free parameters necessary to capture the structure; (3) Assignment of uncertainties to all observables; and (4) Application of statistical concepts to describe the posterior. In the first phase of the project we have made significant progress in overcoming these challenges for the European Arctic and have consequently developed a first stochastic model for the European Arctic, albeit at a low spatial resolution.

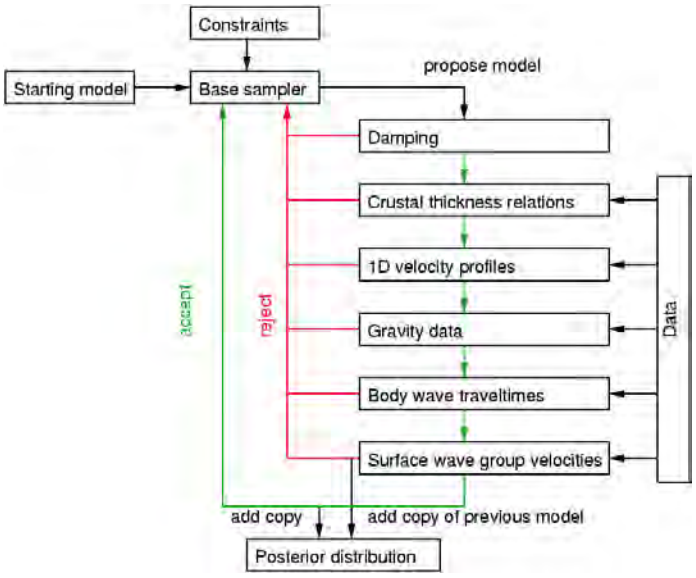

Figure 1. Cartoon showing the multistage MCMC inversion methodology used in this study.

We begin this paper with a short introduction of the MCMC methodology. After discussing the datasets and starting model, we will present our stochastic model and conclude with a discussion of areas of the methodology where we expect to make progress in the second half of the project.

Methodology and Approach

Different inversion algorithms can be classified by the tradeoff between exploration and exploitation (Sambridge and Mosegaard, 2002). Exploration means that one tries to improve the misfit between predictions and observations by choosing a new model entirely at random. Exploitation means that one tries to propose a better fitting model based on the information available from previous samples or sometimes just the current best-fit model. The steepest descent algorithm (Gill et al., 1981) is a good example of a method that only exploits information available from the current sample of model space, while a uniform search algorithm is an example of a method that tries to explore the model space completely. Exploitative algorithms will be more efficient, but are more likely to fall into a local minimum. Explorative algorithms on the other hand are less efficient at converging to a solution, but less likely to get trapped in a local minimum. MCMC and other Monte Carlo techniques try to be exploitative and explorative at the same time.

An MCMC algorithm recovers the posterior distribution using a cleverly constructed Markov Chain. In our work, a Markov Chain is a perturbative sequence of random changes to the starting model. Constructing the Markov Chain in such a way that it preferably contains models that satisfy data allows one to reconstruct the posterior, given sufficient time to move away from the starting model. Figure 1 illustrates the MCMC algorithm used in this study. The base sampler generates a proposed model m_j, a random perturbation of the current model m_i, also referred to as the current state in model space. The current model is the last model that has been added to the posterior or in the case of the first iteration of the algorithm the starting model. Given the model prediction $d_i(m)$ (i.e., the data predicted using the proposed model), the observed data d_i and the standard deviation (i.e., uncertainty) for each observation σ_i, one can determine the likelihood $L(m|d)$ for a model m using Equation 1.

$$L(m|d) = k \exp\left[\sum_i \left(\frac{\left|d_i(m) - d_{obs,i}\right|^n}{\sigma_i^{\,n}}\right)\right] \quad (1)$$

The normalization constant k will be discussed in more detail later. The value of n determines the weight assigned to outliers. For n=2 the L^2 norm of the misfit vector is used, resulting in a good tradeoff between minimizing misfit weights (i.e., being insensitive to outliers) and maximizing them (i.e., being overly sensitive to outliers).

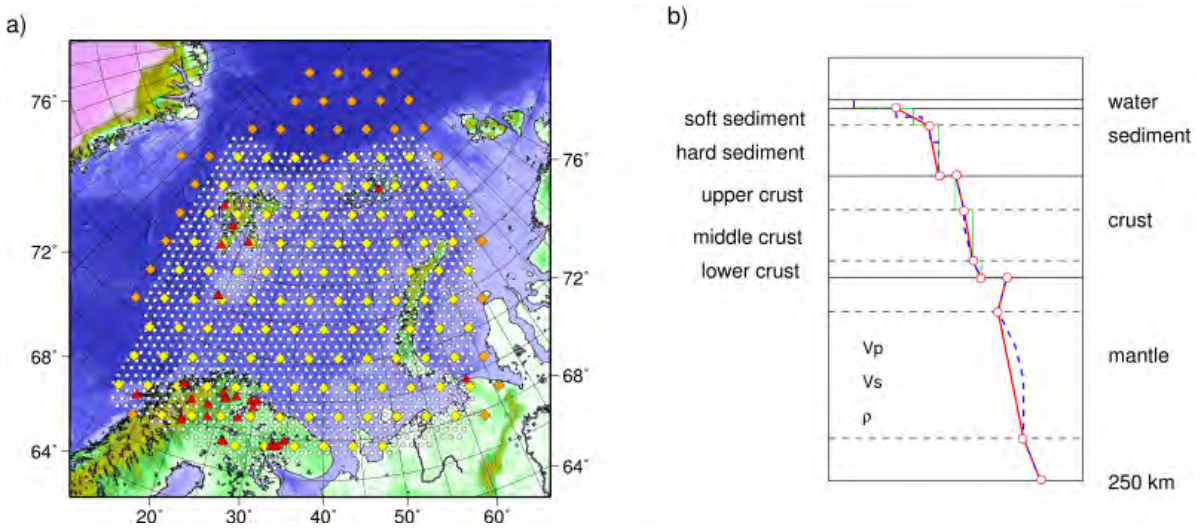

Figure 2. Model parameterization used in this study. a) Map of the region of interest. Locations of the 1D models in BARENTS50 are marked by white circles. The diamonds mark the positions of the 1D models to be constrained in this study. They are yellow if their initial value is based on BARENTS50 and BARMOD and orange if CRUST2.0 has been used to initialize them. b) 1D model parameterization. The dashed blue line represents a typical Vp versus depth curve for the region of interest. The red line is a piecewise interpolation of the red circles where the seismic parameters are defined in this study. The green line illustrates for the crust the limitations of a parameterization based on layers with constant seismic parameters, when trying to describe Vp as a function of depth.

Given the likelihood for a proposed model $L(m_j|d)$ and the current model $L(m_i|d)$, a decision has to be made whether or not the proposed model m_j should be accepted into the posterior distribution. If we would accept all models, we would simply recover the prior, the ensemble of models based on a priori information contained in the base sampler and starting model and not constraint by the data. For $L(m_j|d) \leq L(m_i|d)$ we accept the proposed model and add it to the posterior distribution. For $L(m_j|d) > L(m_i|d)$, the proposed model is accepted if the probability $L(m_j|d) / L(m_i|d)$ is larger than a random number drawn from a uniform distribution between 0 and 1. Otherwise, we reject the proposed model and add a copy of the current model to the posterior. The explorative component of the MCMC methodology, accepting models with worse fit to the data with a certain probability, allows one to move away from a local extremum. The resulting MCMC algorithm performs a guided search through model space. It tends to focus on regions in model space that better fit the prior information and the data, a process known as importance sampling.

In this work we develop a model that satisfies more than one dataset. Given a proposed model, a separate likelihood function is computed for each dataset (i.e., stage of the inversion) and a model is only added to the posterior if it has been accepted in all stages; otherwise, the previous model is added to the posterior (see Figure 1). The normalization constant k plays an important role in adjusting the influence the different datasets have on the posterior distribution. Ideally, when generating the posterior distribution, each stage should have the same influence, the acceptance rates in the individual stages should be comparable to each other, and no dataset should dominate the inversion result. This can be achieved by carefully tuning the normalization constant k.

Prior Information

Our starting model is based on BARENTS50 (Ritzmann et al., 2007), BARMOD (Levshin et al., 2007), and CRUST2.0 (Bassin et al., 2000). CRUST2.0 is used to initialize the model for nodes that fall outside the area covered by BARENTS50 and BARMOD (see Figure 2a). We parameterize the model as a set of 1D models, which define the main layers (water, sediments, crystalline crust, and mantle) that represent the geological structure. Figure 2b illustrates the parameters used to describe the structure at each node. This parameterization of structure associated with every 1D model represents a trade-off between trying to describe the structure as accurately as possible and limiting the number of parameters to avoid having to search a model space which is unnecessarily large. The parameterization results in 47 unknowns for each 1D model and a total of 6,721 unknowns. Note that

these unknowns are not completely independent of each other due to the constraints imposed on the prior distribution.

The success of an MCMC methodology relies partly on a mechanism for generating plausible models based on the prior information. In a Bayesian formulation this process is known as sampling the prior distribution. The prior distribution is given by the starting model and constraints for the individual parameters. The most basic constraints are the upper and lower limits and the standard deviation for the normal distribution from which we randomly draw new model parameters when perturbing the model. More sophisticated constraints employed in this study are ranges for acceptable Vp/Vs ratios, a positive velocity contrast imposed across the Moho and across the interface between the crystalline crust and sediments, and a limit on the maximum decrease of seismic parameters with increasing depth. Plausible ranges for seismic parameters in the area of interest and the relationship between them were derived from previous studies covering the region (e.g., Levshin et al., 2007; Ritzmann, et al., 2007; Breivik et al., 2002).

It is possible that the starting model represents a local minimum of the misfit function. The starting model is therefore jumbled before starting the inversion to ensure that the MCMC algorithm does not get trapped in a local minimum of the misfit function. This is commonly done by exchanging a subset (e.g., 10%) of the 1D models between randomly selected nodes. In this work, the 1D models have been randomly exchanged between all the nodes to begin the inversion very far away from the starting model and to thereby also demonstrate the explorative capabilities of our MCMC algorithm. Another important consideration is the step size in model space - the degree of perturbation applied to the model. If the current model exhibits a good fit to the data, we might be interested in taking smaller steps in model space. On the other hand, if the current model does not satisfy the data, we might be interested in taking larger steps in model space. When perturbing the model, we randomly choose a set of nodes where we will perturb the seismic parameters. We vary the degree of perturbation by randomly varying the size of the set of nodes. Any realistic geological structure is likely to exhibit a certain degree of spatial smoothness. The structure at an individual node should therefore not be completely independent from its neighbors. The base sampler takes this into account by applying spatial smoothing to each node that has been perturbed when proposing a new model. This is critical for proposing models which are more likely to be accepted in the different stages of the inversion.

Given the high quality of a priori knowledge about the structure in the target region already included in the starting model, one could decide to reject models which deviate too far from the starting model. We therefore added a stage to our inversion scheme whereby each proposed model can be compared with a reference model, e.g., the starting model (Figure 1). The same effect is achieved in iterative non-linear tomography through damping. It remains to be seen whether or not we need a damping stage to obtain a meaningful model for the target region. The low-resolution model presented in this paper was developed without using the damping stage. However, a damping stage might be necessary for obtaining meaningful results once the spatial resolution is increased.

Datasets

An important result of Ritzmann et al. (2007) is that the thickness relationships between sedimentary rocks and underlying crystalline rocks can be resolved to some degree within discrete geological provinces. Comparing layer thicknesses is computationally far less demanding than calculating group velocities. The first stage of our inversion is therefore the crustal thickness relations stage. Only when a model has passed this stage do we move to the computationally more expensive stages to determine whether or not it should be added to the posterior. Ordering the stages by the computation time helps to decrease the overall computation time.

Local crustal structure is explicitly constrained by seismic reflection and refraction lines. A velocity profile database, based on a subset of the sampled profiles used by Ritzmann et al. (2007), provides important constraints for the crustal part of the model. The 1D crustal velocity models are available as Vp as a function of depth for positions along the reflection and refraction lines. They were obtained by sampling velocity grids derived from seismic reflection or refraction lines. It would be beyond the scope of this work to revisit the methods used by Ritzmann et al. (2007) to derive the velocity profiles in detail. We parameterize the profile database in the same way our model is parameterized and compare each proposed model with the profiles in the database at predefined depth intervals. Uncertainties have been assigned to each profile based on the categories derived by Ritzmann et al. (2007). Figure 3b shows the coverage of the target region by the velocity profiles colored according to their uncertainty in Vp. Clearly the data quality in the Eastern Barents Sea (Figure 3c) is much lower than in the Western Barents Sea (Figure 3a). The crustal velocities shown in Figure 3c justify the relatively large uncertainty of 0.4 km/s

assigned to the whole seismic line. New deep seismic surveys have been collected and processed by the University of Oslo and should become available for this study in the coming months.

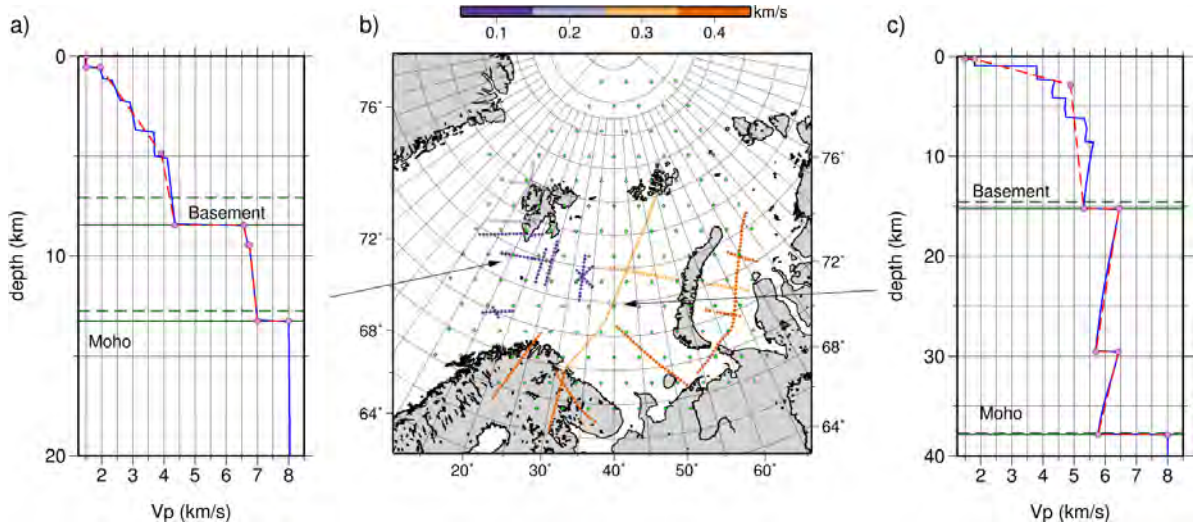

Figure 3. 1D velocity profile data. a) Example of a 1D velocity profile with a low uncertainty assigned to the data. The blue line shows the Vp derived by Ritzmann et al. (2007). The green dashed lines indicate the depths of the basement and Moho, interpolated from BARENTS50. The solid green lines mark the depth of the basement and Moho based on the sampled Vp. The violet points connected by the dashed red line are the control points for the best-fitting profile in the parameterization used in this study. b) Points where the seismic lines were sampled have been colored according to the uncertainty in Vp. The green diamonds mark the locations of the 1D models used to describe the structure in the region of interest. c) Example for a 1D velocity profile with a high assigned uncertainty.

Surface-wave group velocities (Levshin et al., 2007) and regional body-wave travel-time data provided by Lawrence Livermore National Laboratory are used to constrain the lithosphere and upper mantle. The Mid-Atlantic ridge and the Arctic plate boundary are the dominant sources for seismicity in the region. We only use events where the entire propagation path is within the boundaries of the model. Our region of interest therefore extends further north than BARENTS50. This means that we are now also imaging the changes in structure associated with the northern edge of the continental shelf. Figure 4 shows the path coverage of the target region by the different types of body and surface waves. Clearly events associated with the plate boundary to the north provide additional ray paths in the Barents Sea which provide valuable constraints. For the regional body-wave data and surface-wave group velocities, uncertainty information was available from previous studies using these data. All four datasets discussed so far provide much more constraints for the Western Barents Sea than for the eastern part, and do not constrain the density.

There are two sources of information that can be used to constrain density: (1) information about the relationship between Vs and density for different crustal lithologies (Breivik et al., 2002) and (2) a uniform coverage of the area with free air gravity data from the Arctic Gravity project (http://earth-info.nga.mil/GandG/wgs84/agp/). The surface wave tomography by Levshin et al. (2007) recovered a higher-velocity body in the upper mantle below the Eastern Barents Sea Basin, Novaya Zemlya, and the Kara Sea. Such a seismic velocity anomaly within the upper mantle is predominantly caused by temperature variations, rather than compositional effects (Goes et al. 2000), thus one would expect a density anomaly. However, gravity modeling (Ebbing et al., 2007; Ritzmann and Faleide, 2008) suggests a simple horizontally layered mantle density structure. This suggests, that the Eastern Barents Sea is underlain by a cold cratonic keel similar to the Siberian Craton (Ritzmann and Faleide, 2008), as density contrasts due to temperature variations below cratons are presumed to be entirely compensated by chemical depletion. This assumption has an important consequence for the base sampler: we do not impose any constraints on the relationship between Vs and density within the mantle.

Preliminary Results

One Markov chain consisting of 20,000 iterations of the engine was computed. The posterior distribution is given by the last 25% of the chain to ensure that the results have achieved the independent post burn in convergence. The number of iterations is significantly larger than in the previous study by Pasyanos et al. (2006). There are three factors contributing to the slower convergence in this work: (1) we have randomly swapped the profiles for all and not just 10% of the nodes in our model; (2) we take smaller steps in model space by only perturbing the model at randomly selected nodes and (3) we have two additional stages of model evaluation.

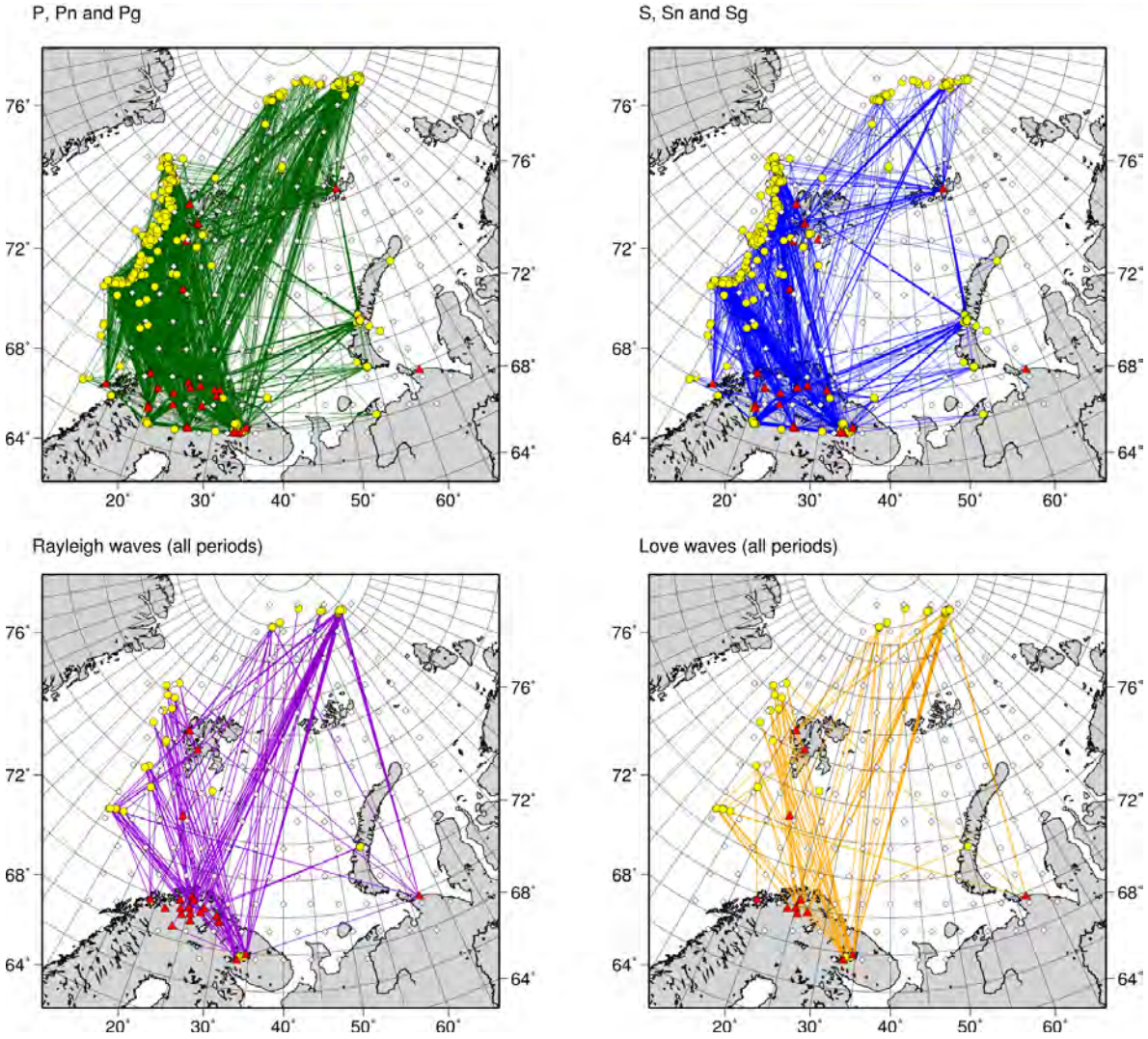

Figure 4. Path coverage of the target region for various seismic phases; white diamonds denote the location of the 1D models, earthquakes are shown as yellow circles and the stations are plotted as red triangles.

Figure 5 (a and b) shows the summary statistics for the thickness of crystalline crust. Clearly the method has recovered the dominant feature of crystalline crustal thickness in the region, the change in thickness associated with the continent-ocean transition. Figure 5a also illustrates the problem caused by the low spatial resolution of the model. Our preliminary model can only recover large scale features extending for more than 100km. The model developed by Ritzmann et al. (2007) proposes thicknesses for the crystalline crust under Novaya Zemlya of locally up to 50 km. We cannot recover such features at this stage because our 1D models are representative of an average structure in the vicinity of the node, not for local extrema of, for example, thickness of the crystalline crust.

More interesting than the mean value for the thickness of the crystalline crust is its standard deviation shown in Figure 5b. Overall the standard deviations (i.e., uncertainties) tend to be lower in Northern Norway when compared with the ones in the region around Novaya Zemlya. Nevertheless, they vary significantly between neighbouring nodes of the model. We recall that seismic reflection and refraction lines are the dominant constraints for the crustal structure. It therefore comes as no surprise that the amount of data available in the vicinity of a given node correlates to some degree with the standard deviation, in particular in the Western Barents Sea (see Figure 5b).

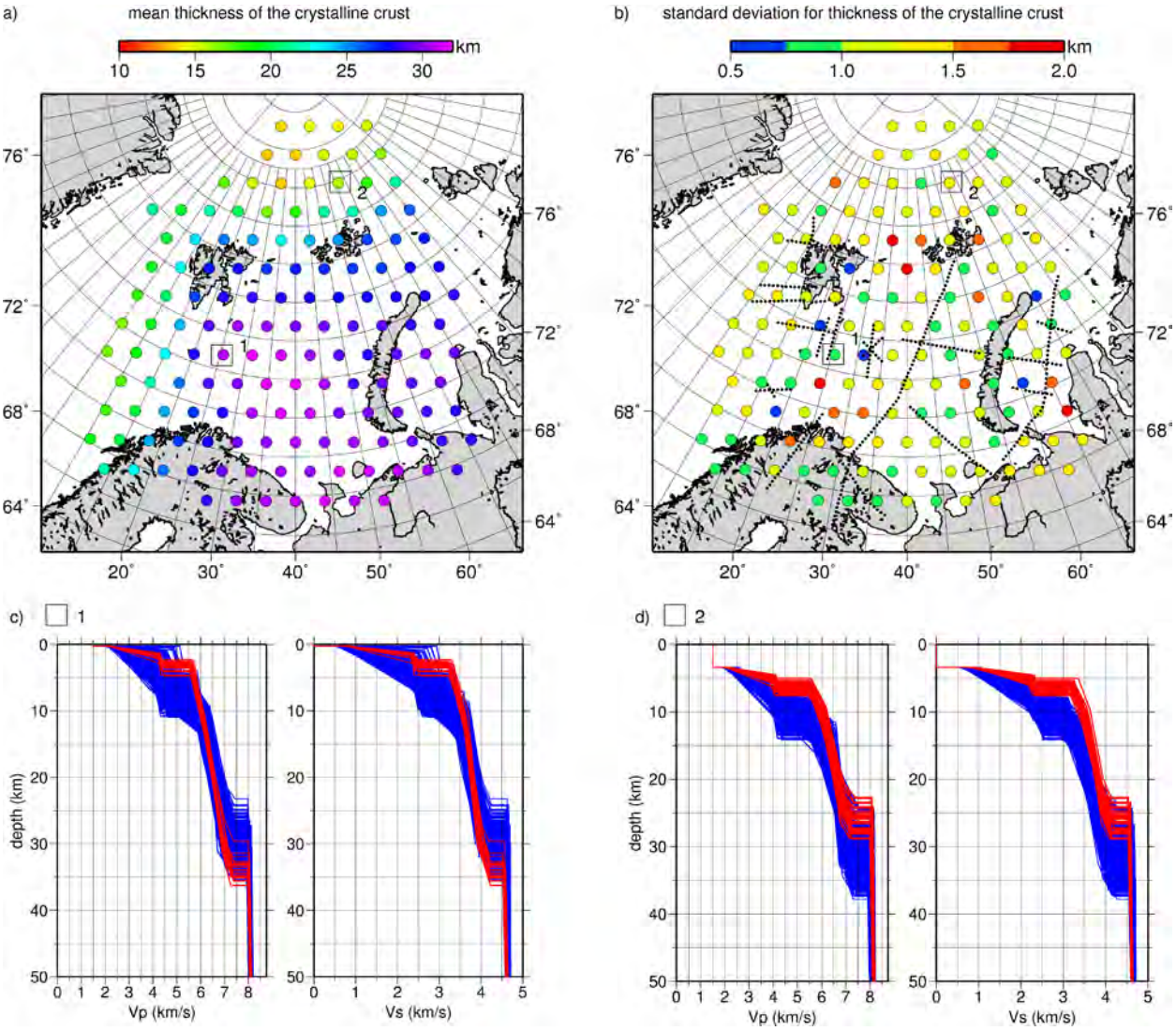

Figure 5. Stochastic model for the Barents Sea. Mean (a) and standard deviation (b) for thickness of the crystalline crust. The black dots in (b) show the locations of the 1D velocity profiles obtained from seismic reflection and refraction lines. For the two nodes labeled 1 and 2 the model profile distributions for Vp and Vs are shown (c and d). Blue lines show the prior distribution and red lines show the posterior distribution.

One way to see how the method is performing is to look at the prior and posterior distribution of individual nodes. Figure 5 (c and d) shows the prior and posterior distribution for two selected nodes, one located in a data-rich region (Figure 5c) and one in a data-poor region (Figure 5d). In both cases, the data have constrained the posterior distribution but, as we would expect, the variability of the models forming the posterior distribution is much higher for the node located in the data-poor region.

It is important to be aware of the fact that computing summary statistics for the posterior distribution can be deceptive. The posterior distribution might be multimodal especially in a joint inversion, where the constraints imposed on model parameters by the different datasets might not be in agreement with each other. Plotting the posterior distributions of profiles for individual nodes can help in determining whether or not the posterior distribution is multimodal. For the two nodes shown in Figure 5, computing the mean and standard deviation can clearly capture the main characteristics of the posterior distribution.

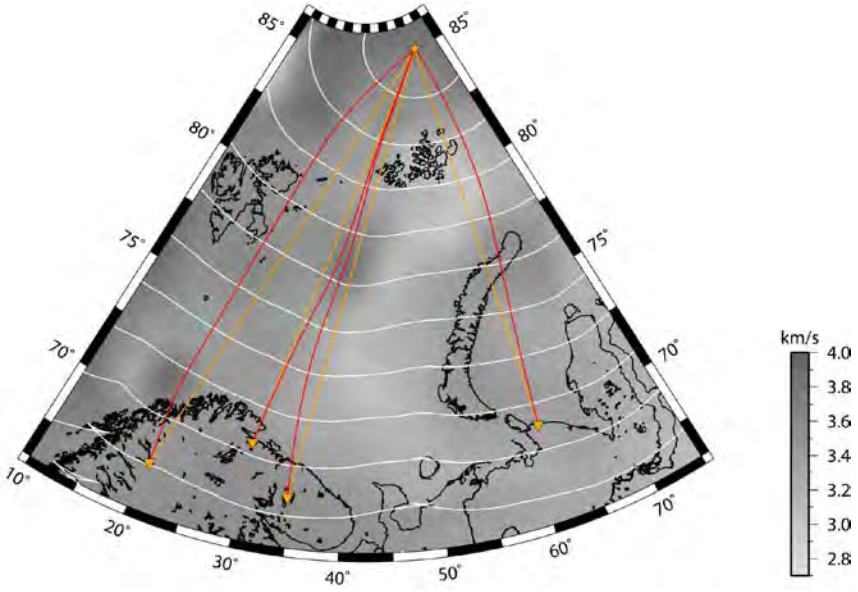

Figure 6. Phase velocity map for Rayleigh waves with a period of 16s based on the starting model. The orange star marks the source location and the orange triangles denote receivers. The great circle ray path is plotted as an orange line. Ray paths have been computed using ray theory and are plotted red. Note that the wave front plotted in white starts to triplicate due to the lateral changes in velocity.

CONCLUSIONS AND RECOMMENDATIONS

The preliminary results clearly show that an MCMC technique can be used to recover large-scale geological features in our region of interest. The main drawback of the stochastic model presented here is its low spatial resolution; the distance between the individual 1D models is about 180 km. The final model will need to have a spatial resolution comparable to the best-fitting models published for this region. We would prefer to use a variable spatial resolution higher in data rich regions and lower in data poor regions. Our implementation currently allows for an arbitrary distribution of the nodes. It is therefore possible to locally increase the spatial resolution by adding additional nodes.

Ideally, one would optimize the distribution of 1D models as part of the inversion process. The idea of a self-adapting parameterization is not new to seismic imaging and has for example been applied to cross-borehole tomography by Curtis and Snieder (1997). Part of optimizing the model parameterization is finding the optimum number of 1D models needed to constrain the structure. Trans-dimensional MCMC algorithms (e.g., Green, 1995; Geyer and Møller, 1994) can deal with cases where the number of model parameters is unknown. Whether or not these methods can be used in the construction of our model will depend to some degree on the influence they have on the computation time and convergence.

Computation time is an important consideration when using an MCMC technique. Predicting the different datasets for thousands of different models requires efficient forward solvers. In practice this means that one has to resort to using very simple forward solvers, such as 1D ray tracing for body waves using a path-average model. The dilemma between the need for an efficient forward solver and the need to be as accurate as possible can be illustrated using

the example of the surface-wave data. In a first approximation, surface waves follow the great circle paths. This allows us to compute group velocities by sampling the model along the great circle path. In the presence of lateral velocity variations, however, surface waves will no longer follow the great circle path. Rayleigh wave paths (at T = 16s), computed using ray theory, clearly deviate from the great circle path (Figure 6). The largest lateral variations in velocity are found in the upper crust. The shorter the period the more sensitive a surface wave is to structure near the surface and therefore the more the surface wave paths deviate from the great circle path. For longer periods (50s in the case of our starting model) the surface wave paths no longer deviate significantly from the great circle paths. The planned use of ray theory will be a significant improvement over the great circle approximation especially for the group velocity observations made for high frequencies. Nevertheless, one should keep in mind that ray theory is still an approximation; it neglects finite frequency effects which could be captured by solving the full wave equation. This is however currently not feasible given the computational requirements.

So far we only have computed summary statistics for the posterior distribution. This means we are not harvesting all the information contained in the posterior distribution. In the second half of the project, we will have to investigate new ways to analyze and visualize the posterior distribution. Cluster analysis which tries to group models based on their similarity appears to be a promising tool in this context.

ACKNOWLEDGEMENTS

We thank the Department of Geosciences at the University of Oslo for providing us with access to the Titan III high performance computing facilities.

REFERENCES

Bassin, C., G. Laske, and G. Masters (2000). The Current Limits of Resolution for Surface Wave Tomography in North America, *EOS Trans AGU* 81: F897.

Breivik, A. J., R. Mjelde, P. Grogan, H. Shimamura, Y. Murai, Y. Nishimura, and A Kuwano (2002). A possible Caledonide arm through the Barents Sea imaged by OBS data, *Tectonophysics* 355: 67–97.

Curtis, A., and Snieder, R. (1997). Reconditioning inverse problems using the genetic algorithm and revised parameterisation, *Geophysics* 62: 1524–1532.

Ebbing, J., C. Braitenberg, and S. Wienecke (2007). Insights into the lithospheric structure and the tectonic setting of the Barents Sea region by isostatic considerations, *Geophys. J. Int.* 171: 1390–1403, doi:10.1111/j.1365-246X.2007.03602.x.

Geyer G. and Møller J. (1994). Simulation procedures and likelihood inferences for spatial point processes, *Scandinavian Journal of Statistics* 21: (4), 369–373.

Gill, P. E., W. Murray, and Wright M. H. (1981). *Practical Optimization*, Academic San Diego, CA.

Goes, S., Govers, R. and Vacher, P. (2000). Shallow mantle temperature under Europe from P and S wave tomography, *J. Geophys. Res*. 105: (B5), 11153–11169.

Green, P. (1995). Reversible jump Markov chain Monte Carlo computation and Bayesian model determination, *Biometrika* 82: (4), 711–732; doi:10.1093/biomet/82.4.711.

Levshin, A., J. Schweitzer, C. Weidle, N. Shapiro, N. Maercklin, and M. Ritzwoller (2007). Surface wave tomography for the Barents Sea and Surrounding Regions, *Geophys. J. Int*. 170 : 441–459, doi:10.1111/j.1365-246X.2006.03285.x.

Pasyanos, M. E., G. A. Franz, and A. L. Ramirez, (2006). Reconciling a geophysical model to data using a Markov Chain Monte Carlo algorithm: An application to the Yellow Sea-Korean Peninsula region, *J. Geophys. Res.* 111: B03313, doi:10.1029/2005JB003851.

Ritzmann, O. and J. I. Faleide (2008). The crust and mantle lithosphere in the Barents Sea/Kara Sea region, *Tectonophysics*, TECTO 124236, doi: 10.1016/j.tecto.2008.06.018.

Ritzmann, O., N. Maercklin, J. I. Faleide, H. Bungum, W. D. Mooney, and S. T. Detweiler (2007). A 3D geophysical model for the crust in the greater Barents Sea region: Model construction and basement characterization, *Geophys. J. Int*. 170: 417–435, doi: 10.1111/j.1365-246X.2007.03337.x.

Sambridge, M. and K. Mosegaard (2002). Monte Carlo methods in geophysical inverse problems, *Rev. Geophys.,* 40: (3), 1009, doi:10.1029/2000RG000089.

Shapiro, N. M. and M. H. Ritzwoller (2002). Monte-Carlo inversion for a global shear-velocity model of the crust and upper mantle, *Geophys. J.Int*. 151: 88–105.

Vasco, D. W., L. R. Johnson, and E. L. Majer (1993). Ensemble inference in geophysical inverse problems, *Geophys. J. Int*. 115: (3), 711–728.

GLOBAL 3D SEISMIC TOMOGRAPHY USING MULTI-CORE DISTRUBUTED MEMORY PARALLEL COMPUTERS

James R. Hipp, Marcus C. Chang, Mark A. Gonzales, Benjamin J. Lawry,
Andre V. Encarnacao, and Glenn T. Barker

Sandia National Laboratories

Sponsored by the National Nuclear Security Administration

Award No. DE-AC04-94AL85000/SL09-3D-Earth-NDD02

ABSTRACT

The rapid growth of multi-core computing hardware has made it possible for scientific researchers to run complex, computationally intensive software on affordable, in-house commodity hardware. Multi-core CPU's (Central Processing Unit) and GPU's (Graphics Processing Unit) are now commonplace in desktops and servers. Researchers today have access to extremely powerful hardware that enables the execution of software that could previously only be run on expensive, massively-parallel systems. It is no longer cost-prohibitive for an institution to build a parallel computing cluster consisting of commodity multi-core servers. With each server offering 24 or more processing cores, researchers can easily have access to hundreds of parallel processing threads to facilitate complex calculations. One research area where a distributed multi-core computing system has proved to be critical is in the development of global 3D earth models. Traditionally, computational limitations have forced certain assumptions and shortcuts in the calculation of tomographic models; however, with the recent rapid growth in computational hardware including faster CPU's, increased RAM, and the development of multi-core computers, it is now possible to perform seismic tomography and location using distributed parallel algorithms running on commodity hardware, thereby eliminating the need for these shortcuts. In this paper we will describe the multi-core distributed computing system that we have designed to support our in-house geophysical algorithm research including, in particular, the task-based parallel framework used for calculational processing along with the resource management system developed for sharing computing resources among multiple simultaneous developers.

OBJECTIVE

The overall objective for this project is to improve the pace at which computationally intensive Ground-based Nuclear Explosion Monitoring Research & Development (GNEMRD) research can be performed by developing scalable software that will enable GNEMRD researchers to easily assemble a platform-portable, cost-effective, and practical distributed parallel system comprised of any number of modern commodity, multi-core computers. The availability of such a system to the Sandia National Laboratories (SNL) GNEMRD research group has dramatically accelerated the pace at which our computationally intensive 3D tomographic research is conducted, and we believe it can prove equally valuable to other GNEMRD researchers. Our design emphasis targets large scientific computing solutions, specifically geophysics problems, which commonly require a large amount of in-core memory as well as significant file and database resources. Additionally, we require an environment that supports many users / developers operating in a simultaneous fashion. Our initial testing of this system has been restricted to the SNL GNEMRD LAN, but our eventual goal is to develop a software package that can be easily deployed at other sites where GNEMRD research products are developed to improve U.S. monitoring capability.

RESEARCH ACCOMPLISHED

Background

Realistic and practical Earth structure tomography problems are generally solved using either iterative matrix solutions or with stochastic methods such as Monte Carlo (MC) or Markov Chain Monte Carlo (MCMC) techniques (Tarantola, 2005). Event location, while less strenuous, utilizes similar numerical frameworks (e.g., Levenberg-Marquardt). These types of solutions are inherently large and generally involve hundreds of thousands to many millions of ray prediction calculations when solving for realistic three dimensional Earth wave velocity structure and event positions. Additionally, they may involve many support calculations for determining optimum control parameter settings (e.g., damping, regularization), ray similarity, event clustering or for performing a statistical assessment of how well the resulting model approximates the data used to develop the model.

In the past, much of this type of research was executed on simple sequential processors using a single desktop workstation to perform the calculations. With this type of minimal processing power, typical tomography problems were by necessity defined with low spatial resolution or severely restricted in domain extent (Soldati, 2006). In the last 15 years or so some researchers have had access to small shared memory systems or clusters for performing this type of research, but these were generally expensive costing several hundred thousand dollars and not widely available to the typical researcher. These types of older cluster machines generally possessed 16 to 64 processors with an accompanying amount of memory that was usually less than 100 MB. The significant computational resources required for performing high-fidelity large seismic tomography investigations could only be found at major research institutions that could afford multi-million dollar massively parallel machines. For most researchers the only option was to simplify their approach if they wanted to produce models.

In the meantime microprocessor manufacturers have achieved higher performance rates by manipulating the processors' fidelity at handling Instruction Level Parallelism (ILP). Eventually, large power consumption and heat dissipation problems drove these manufactures to investigate Thread Level Parallelism (TLP) where performance is achieved using many different cores (CPU assemblies) contained on a single chip where clock rates are controlled to effectively manage power consumption and heat dissipation issues (Buttari, 2008). This latest direction of using multi-core processors has defined a new paradigm in affordable multi-processor parallel computation available to almost any researcher. Without exploiting this new multi-core paradigm, even the most advanced single-threaded software algorithms can only run on a single core, leaving the remaining cores idle, and thus wasting a significant amount of available processor resources. On the other hand, algorithms designed to run on multiple cores concurrently can theoretically approach an n-fold increase in performance given a multi-core processor offering n cores.

Today we are sitting on the threshold of harnessing computational resources in a manner not seen in the past. The multi-core CPU and, to a similar extent, the GPU turned numerical processor, are paving the way for a new paradigm in scientific computing. To fully realize this potential, researchers need methodologies and frameworks to integrate disparate platforms and systems into a single common computing environment.

In this report we examine such a system that we have assembled to support our in-house 3D geophysical algorithms research. In particular, we will describe a multi-core parallel processing framework that includes a processing task distribution system and a resource management system. The task distribution system handles computational work unit assignment for individual clients (applications) while the resource management system allocates physical processing nodes, memory, and IO capabilities to each application. These systems provide a crucial capability that enables many researchers and developers to simultaneously take advantage of parallel computation using an easily configurable set of disparate resources.

Before beginning with the overall framework discussion, however, we will first provide some basic background on the main types of modern multi-core hardware and the two primary types of processing parallelism (i.e., task- and data-parallelism). Understanding these terms and definitions is critical towards understanding how the entire system can provide the necessary set of capabilities to ensure that all types of numerically intensive solutions can be solved in an efficient manner.

Definition (Multi-core CPU versus Multi-core GPU)

Multi-core or "many-core" computing is a form of parallel processing that takes advantage of the presence of multiple processing cores within a single chip. For the purposes of our discussion, we will be focusing on two types of multi-core hardware: multi-core CPUs and multi-core GPUs. A single machine can contain multiple CPUs and GPUs, so the number of processing cores available in a given machine can be significant (number of processors * number of cores per processor).

The CPU is the traditional computer processor that is used in everything from laptops to desktops to servers. Today, it is nearly impossible to purchase a computer that does not include at least one multi-core processor. For desktops, quad-core (or higher) processors are becoming the norm. However, most applications do not take advantage of the presence of multiple CPU cores; instead, most off the shelf software today runs sequentially on a single core.

The GPU has traditionally been viewed as part of the video card, used by computers to render graphics. Historically, the drive for advanced GPUs came from the video gaming market, where realistic 3D visualizations have become the standard. This forced the development of GPU processors containing large numbers of pipelined cores for performing various graphical operations such as coordinate transformation, polygon rendering, texture mapping, and shading. Recently, however, the General Purpose GPU (GPGPU) concept has emerged where the massive floating point power provided by GPUs is being harnessed to perform scientific mathematical computations which can yield several orders of magnitude increase in performance over standard CPUs. In 2009, Nvidia offered a Tesla GPU with 240 cores per video card and up to four cards per machine at a cost of $1500 per card.

The determination of the best type of multi-core hardware to use will typically depend on the problem that is being solved. Some problems have a very small ratio of floating point operations per memory access, while others have large ratios. Problems spanning small to large ratios execute better on certain multi-core platforms. In the next section we will describe the two primary classes of parallelism and the types of multi-core platforms best suited for solving problems belonging to either of those categories.

Task-Parallelism and Data-Parallelism

Most problems can be grouped into one of two parallel classes distinquished by the frequency with which they access hardware memory resources. The first, task parallelism, is the simultaneous execution of a specific computation on many CPUs/GPUs using the same or different data. The work done in the computation is executed in a separate thread and in the simplest case there is no need for communication between threads. Task parallelism is also known as coarse-grained parallelism. Coarse-grained parallelism implies that each separate task requires very little communication with other tasks. It is known as "embarrassingly" parallel if the tasks require no communication with each other. We use task-parallelism to solve ray bending solutions through a 3D Earth model (Ballard et al., 2008; 2009). Each ray bending calculation is entirely independent from all other ray bending calculations. That is, you do not need any information from a ray to be able to solve for another ray.

We also use task-parallelism to solve many Least Squares QR (LSQR) solutions simultaneously in Earth model tomography. Here we are interested in determining an optimal regularization parameter to avoid over- or under-smoothing while calculating a new Earth model (Aster, 2005). Again each LSQR computation is independent and

does not require information from any other LSQR computation. We also utilize an out-of-core blocked Cholesky solver which can solve an Earth tomography problem setup as a rectangular matrix,

$$Gs = r \qquad (1)$$

where G is the tomography path length weight matrix and s is the incremental slowness perturbation for which we are solving. The travel time residual is the column vector r. Multiplying each side of the matrix by G^T forms a positive definite system that can be solved using the out-of-core blocked Cholesky solver. Each Cholesky block is updated with other blocks and scaled with its associated diagonal block on separated processors. Although some communication is required to avoid scaling a block before it is completely updated, it remains largely a task-parallel solution technique.

Other examples of our current research that use task-parallelism include determining ray-similarity and performing ray clustering from the similarity results (Young et al., 2009). Ray clustering is used to reduce the total number of rays, many of which are slight perturbations of other rays, for performing Earth tomography calculations. Having many essentially equal rays in a tomography calculation can overweight the solution in the neighborhood of the rays' path, often leading to very locally biased results. Reducing a family of nearly identical rays to a single representative helps to alleviate the biasing. Determining ray similarity is a comparison evaluation of one ray with all other rays in a dataset. Since each ray must be compared to all other rays, the total computation involves $N(N+1)/2$ comparisons where N is the number of rays in the dataset. In practice a significant number of pairs can be excluded by applying a few obvious constraints (e.g., only comparing rays to the same station), but the total number of pairs can still be very large. We can solve this problem in a parallel fashion by dividing up the rays into a number of groups such that each group is compared with other groups on a set of multi-core processors. Once the ray similarity has been determined, a clustering algorithm is used to form the ray representatives. Here again we can utilize multi-processors to form clusters from disjoint groups of rays that are only linked to a subset of other rays by way of the similarity measure. Each subset can be processed on an individual processor simultaneously thereby speeding up the entire calculation.

Residing at the other extreme of parallel problem classes are those that present what is known as data parallelism. Data-parallelism is the simultaneous execution of the same computation across the same data, and is often referred to as fine-grained parallelism. It is also known as loop-level parallelism as it focuses on the inherent parallelism in a program loop. The work done by a data-parallel application executes in separate threads and usually shares information between threads. An example of data parallelism is matrix inversion and matrix decomposition algorithms, where each processing thread is working on a subset of the matrix (performing the exact same operation on each piece of data). We have several data-parallel problems within our research umbrella that require solution in a parallel manner. These include individual LSQR calculations and Cholesky decompositions. In the case of the LSQR solution we are not talking about solving several independent LSQR calculations simultaneously, as we described above, but instead we mean solving a single large LSQR problem in parallel (Liu, 2006). In this mode the entire sparse matrix (G in the tomography problem above) is dispersed among many processors (typically GPUs) and the solution is performed on each piece of the matrix simultaneously.

The distinction between task- and data-parallelism is important as all geophysics problems, and scientific problems in general, will exhibit one or the other or some combination of both types of parallelism. Our design ensures that both types of parallelism are supported including support for task-parallel applications which utilize multi-core CPUs and data-parallel applications which use predominantly GPUs.

Java Parallel Processing Framework

Given the basic definitions of multi-core CPUs and GPUs and the application divisions between task-parallel and data-parallel algorithms, we now consider the primary components in our design. The first component is the task distribution and processing system. We have integrated a 3rd party application called the Java Parallel Processing Framework (JPPF) into our design to manage the requirements of this component (Cohen, 2009). The JPPF provides a flexible and innovative way to take advantage of modern multi-core hardware. This Java-based, platform-independent framework allows research applications to submit units of work, known as JPPF tasks, to be processed on a distributed network of computers. JPPF is made up of a JPPF *task driver* and a set of *processing nodes*. Applications use JPPF by creating JPPF *tasks* that are sent to the JPPF task driver for execution via a JPPF

client that resides in the primary client application's task interface. The JPPF task driver maintains a queue of JPPF tasks and sends JPPF tasks out to the various processing nodes as they become available (see Figure 1).

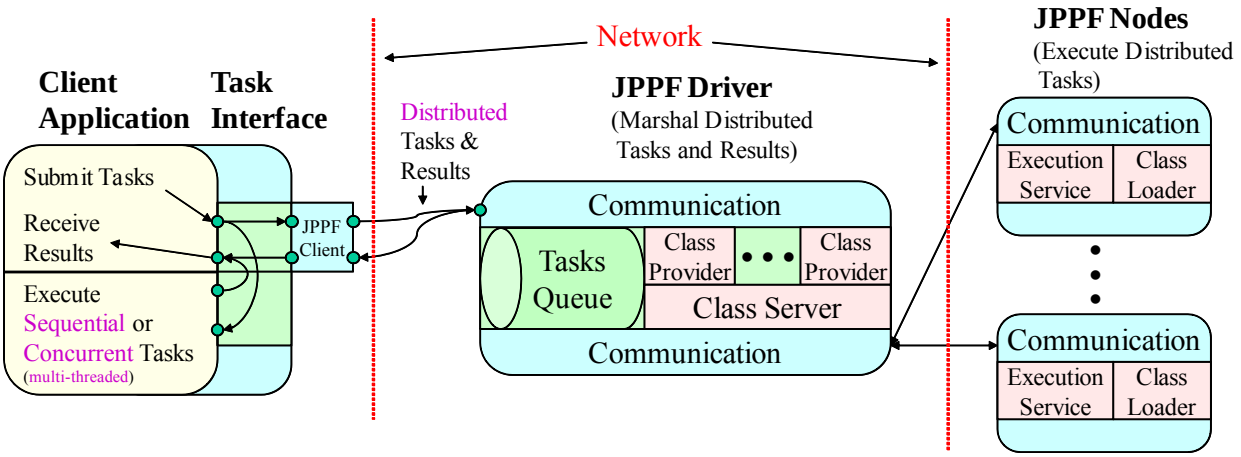

Figure 1 The JPPF computation framework and task distribution system.

We have amended the front end of the task-parallel process in the client application to include the ability to drive a solution in "sequential" mode on a single node or in "concurrent" mode (multi-threaded) using all multi-cores available on a single machine. This capability does not require JPPF but allows a user to configure their application to run on a single platform without the need of a system of distributed nodes, should they not be available. This convenience gives the user the ability to quickly switch computing modes to meet the current need, e.g., from debug mode where running on a single processor might be useful, to full "distributed" mode using all machine resources across the network when producing a real tomographic model.

All the processing nodes of the system (which can consist of servers, desktops, and even laptops as illustrated in Figure 2 below) execute the JPPF tasks in parallel, enabling algorithms to scale linearly with the number of processing nodes available. In general, one processing node is launched per CPU processor core; for example, a server with 16 cores would have 16 processing nodes. This distribution of JPPF tasks to CPU processing nodes via a JPPF driver is how JPPF achieves task-based parallelism.

In addition, the framework will also allow a processing node to be setup as a "data parallel node" to support data parallelism. In this case a data-parallel node is configured to solve a portion of the total problem by operating on a predefined subset of the data. Using data-parallelism with JPPF requires that each node be configured with its partial data allotment after which each node executes the process and sends the subsequent results back to the driver, and eventually, back to the client. The client ensures that all results are gathered and combined to finish the process.

Precise control over JPPF in a data-parallel mode requires that a client can dictate which processor executes with what data. In a task-parallel mode this type of control is not necessary as any processor can execute with any data. Marshalling tasks in JPPF with specific node execution control during the process allows JPPF to achieve data parallelism. Possessing the ability to operate with and without node control means JPPF supports both task- and data-parallelism in a hybrid manner.

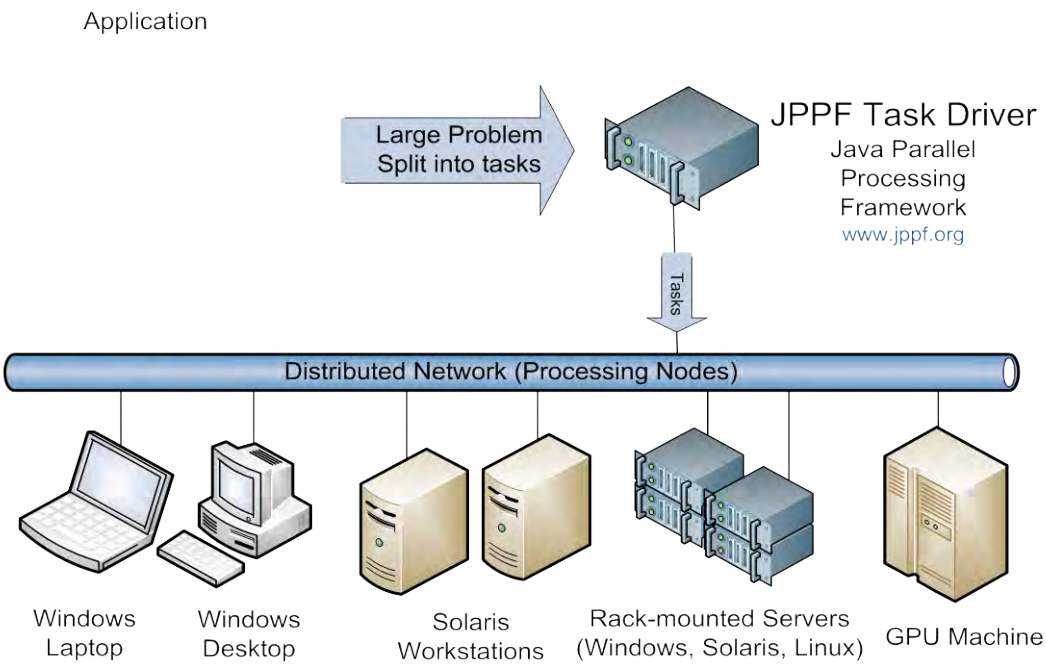

Figure 2 The Heterogeneous JPPF Distributed Network of Processing Nodes.

Node Resource Management (NRM) Framework

While the JPPF is charged with actually executing a set of tasks for one or more applications, it has no real ability to configure resources, start them, and make them available for use in the parallel environment. This is the job of the Node Resource Management (NRM) framework (see Figure 3). The NRM framework is an independent management system that works in tandem with JPPF and facilitates access to distributed computing environments. One of the main goals of the NRM framework is to make it easier to manage and share JPPF processing nodes in the distributed system.

The NRM system employs a client-server architecture and consists of three main software components: NRM server, NRM client, and NRM host. The NRM *server* is the primary component of the system and is responsible for providing applications access to the distributed computing environment and underlying JPPF processing nodes. NRM treats each system in the distributed computing environment as a resource and automatically shares these resources fairly amongst multiple applications simultaneously. The NRM *client* is responsible for connecting applications to the services and resources provided by the NRM Server. The NRM client provides an interface API to the client providing control and status information services. Lastly, the NRM *host* operates on machines that contribute JPPF nodes to NRM and is responsible for starting/stopping JPPF nodes on those machines, as governed by the NRM server.

NRM builds upon many of the benefits provided by JPPF. The primary benefits are its user friendliness, ability to effectively and fairly share resources, and robustness. Each of these benefits is discussed in more detail below.

NRM provides developers with an easy-to-use Application Programming Interface (API) that allows access to the distributed computing environment. All services are made available to the developer as part of the NRM client via singular function calls, minimizing the amount of knowledge required to use the system. Because NRM is based on a client-server architecture, any user/developer can utilize the system from any machine on the network. Additionally, the NRM client provides the user with an embeddable GUI frontend with many features. These include the ability to start/stop JPPF drivers and associated applications, request/release JPPF processing nodes, along with various monitoring capabilities.

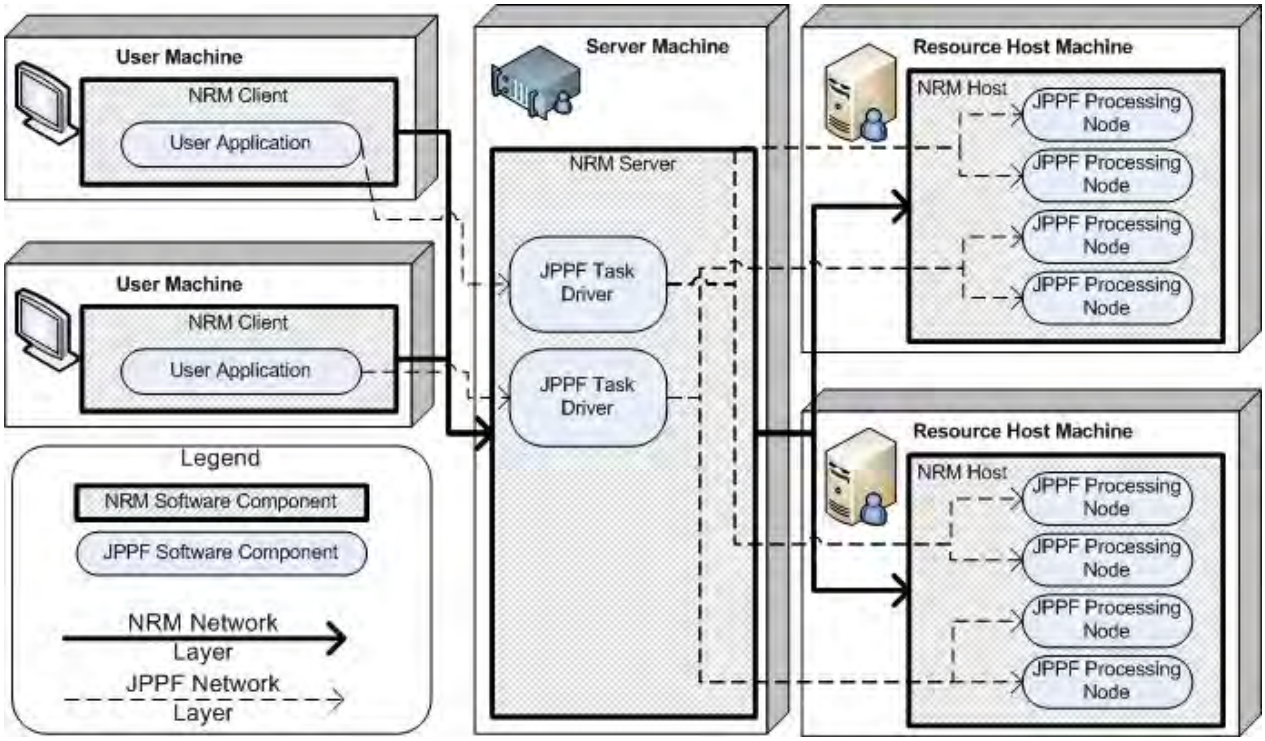

Figure 3 The Node Resource Management Framework Architecture Overview.

Most capabilities come in the form of automated periodic statistics updates. The NRM client automatically monitors every application running on the framework and displays information on CPU usage, number of nodes in use, total available resources, and more. The NRM client also tracks statistics for each running application, making it possible to determine the efficiency of distributed applications. For easier debugging, the NRM client is equipped with extensive logging capabilities and has functionality to display error notifications generated by the various JPPF components used in the system.

NRM is designed to simplify the overhead involved with setting up a distributed computing network as much as possible. Written in the latest release of Java (6.0), NRM is fully platform independent, allowing developers to run their applications simultaneously in mixed-environment networks including Windows, Linux, Unix, and Apple operating systems, without having to rewrite code for any specific platform. NRM is also architecture independent and supports computation on any combination of 32- and 64- bit architectures. In addition to the portability features mentioned above, NRM provides automated code distribution – whenever a developer wishes to run code on the system, the NRM framework automatically distributes compiled libraries to each machine on the network, simplifying the deployment process.

Besides user friendliness, NRM also has the ability to effectively and fairly share computing resources among multiple users and their applications in a transparent manner. More specifically, NRM implements a node balancing algorithm that provides all connected applications access to a shared pool of processing nodes. Given the nature of JPPF, each node can only be assigned to one application at a given time. For each application using the NRM, the node balancing algorithm maintains a weighted node count metric based on the application's priority and the processing power of the nodes that application is currently using. The basic idea behind the algorithm is to keep NRM 'balanced' by ensuring that these application-specific metrics remain roughly equal for all connected applications, at all times. Over the course of its operation, there are certain events that can place the algorithm in an un-balanced state, thus requiring nodes to be dynamically reassigned from one application to another in order to rebalance the system. The most common events are when a new application joins the system and wants to acquire its own processing nodes, or when a new host joins the system and additional processing nodes are available for use. In

these and other cases, node reassignments can occur. In order to minimize any disruptions to the applications, reassignments only take place after the completion of one or more JPPF tasks. This allows the node balancing algorithm to remain transparent to JPPF and ultimately the end-user of the application. Also, prior to making node reassignments (as well as initial assignments), the node balancing algorithm ensures that an application is only given nodes that meet certain memory and minimum processor performance constraints that it may have specified. This prevents processing nodes from being assigned to applications that are incapable of making use of it.

Resource management is handled directly by the NRM server. NRM hosts are added to a database that is read by the NRM to identify which hosts belong to the system. These NRM hosts connect with the server and specify the number of processors that will be made available for use. Furthermore, NRM facilitates the sharing of resources by giving end-users the ability to contribute their own computing resources to the NRM system. Using a policy-based and database-driven approach, users can specify the number of processors to contribute at different times of the day. For example, a user may wish to contribute only a subset of the processors on their desktop computer while present in their office and performing work, but all of their processors when away from the office. Additionally, users are allowed to override their policy at any time through the NRM client.

In addition to user friendliness and resource sharing NRM is also a robust framework. One of the major pitfalls of distributed computing is that as the system grows larger the likelihood that any one component of the system will fail increases. NRM has been designed with this problem in mind, making sure to remain in a stable state and minimize the effect on applications using the system. The most common scenarios are node and host machine failures. In the event that a single node fails, the NRM server automatically detects the failure and restarts the node. If the node cannot be restarted, or it is determined that a configuration issue caused the failure, a notification is sent to the user immediately. In the event that an entire host machine fails (during task execution), the NRM server again automatically detects the failure. If the failure causes an unfair imbalance in processing nodes between connected applications, node reassignments will occur to rebalance the system. In both failure cases, the directly affected applications will continue to function normally since the underlying JPPF components also detect these failures and are able to re-schedule unfinished tasks as necessary.

NRM also ensures that actions taken by one application do not affect other applications using the system. For example, when an application exits the system, either voluntarily after completing all of its processing tasks or as a result of a failure, other applications connected to the system are not negatively impacted. In fact, the NRM server detects such an event and ensures that the resources released by the terminated application are distributed fairly amongst the remaining applications. Similarly, when an additional application joins the system, the NRM server again performs node balancing to redistribute the computing resources in a fair manner.

CONCLUSIONS AND RECOMMENDATIONS

We have described a multi-core parallel processing framework that can be run on affordable commodity hardware to dramatically decrease the time needed to solve large complex geophysical problems, such as 3D seismic tomography. Our framework is comprised of two major sub-components: a processing task distribution system and a resource management system. The task distribution system, JPPF, handles computational work unit assignment for individual clients (applications) in both a task- and data-parallel manner. This dual hybrid system allows us to solve all types of geophysically defined problems with great efficiency.

The resource management system allocates physical processing nodes, memory, and IO capabilities to each application. It provides an easy to use API for control and abstracts the complexity of processing node configuration and assignment from the client. Additionally, it provides a fair and automatic system for assigning nodes to client applications that works seamlessly with the JPPF task processing system. These capabilities ensure that the client need only be concerned with the scientific problem of interest and not the particulars of hardware and software interaction required to perform a parallel solution. These abilities also imply that the system is made to order for everything from simple processing tasks to multi-pipelined operational systems. A system such as this can support multiple independent, but simultaneously functioning, research, development, and operational pipelines.

Our system is easily scalable from a single node with a single processor to many nodes executing multi-core and GPU processors over a widely distributed network. Using Java as the computing language guarantees platform portability and removes communication issues associated with disparate hardware platforms (Unix, Linux,

Windows, MacOS). The hardware used in our research consists of standard over-the-counter laptops, desktops, and servers. All of these points imply that the system is simply scalable and expandable and will compliment any research budget.

We have successfully deployed this system on the SNL GNEMRD LAN and demonstrated that it allows us to generate tomographic models 2 orders of magnitude faster than is possible with standard, single-processor serial processing. Our system is general and we believe it can be applied to aid research involving any other computationally intensive algorithm that is readily parallelizable. Recently we have started using it for waveform correlation event detection with similarly impressive performance improvements. We continue to work on improving the robustness and ease of use of the system toward the eventual goal of a package that can be easily installed and configured on the LANS of other GNEMRD researcher organizations to improve their computational capability and thereby accelerate the overall pace at which computationally intensive GNEMRD research can be conducted.

REFERENCES

Aster, Richard C., B. Borchers, and C. H. Thurber (2005). *Parameter Estimation and Inverse Problems*, Elsevier Academic Press, ISBN 0-12-065604-3.

Ballard, S., J. Hipp, and C. Young (2008). Robust, extensible representation of complex earth models for use in seismological software systems, in *Proceedings of the 30th Monitoring Research Review: Ground-Based Nuclear Explosion Monitoring Technologies*, LA-UR-08-05261, Vol. 1, pp. 347–355.

Ballard, S., J. Hipp, and C. J. Young (2009). Efficient and accurate calculation of ray theory seismic travel time through variable resolution 3D earth models, *Seism. Res. Lett*. (in press).

Buttari, A., J. Langou, J. Kurzak, and J. Dongarra (2008). A class of parallel tiled linear algebra algorithms for multicore architectures, arXiv:0709.1272v3 [cs.MS].

Cohen, L. (2009). Java Parallel Processing Framework, http://www.jppf.org/.

Liu, Jing-Song., Liu, Fu-Tian, Liu, Jun, Hao, Tian-Yao (2006). Parallel LSQR Algorithms Used In Seismic Tomography; *Chinese Journal of Geophysics* 49: N 2.

Soldati, G., L. Bochi, and A. Piersanti (2006). Global Seismic Tomography and Modern Parallel Computers, *Annals of Geophysics*, 49: N 4/5.

Tarantola, Albert (2005). Inverse problem theory and methods for model parameter estimation, SIAM, ISBN-13 978-0-898715-72-9.

Young, C., S. Ballard, J. Hipp, M. Chang, J. Lewis, C. Rowe, and M. Begnaud (2009). A global 3D *P*-velocity model of the Earth's crust and mantle for improved event location, these Proceedings.

DEVELOPING REGIONALIZED MODELS OF LITHOSPHERIC THICKNESS AND VELOCITY STRUCTURE ACROSS EURASIA AND THE MIDDLE EAST FROM JOINTLY INVERTING P-WAVE AND S-WAVE RECEIVER FUNCTIONS WITH RAYLEIGH WAVE GROUP AND PHASE VELOCITIES

Jordi Julià[1], Andrew A. Nyblade[1], Samantha E. Hansen[1], Arthur J. Rodgers[2], and Eric Matzel[2]

Penn State University[1] and Lawrence Livermore National Laboratory[2]

Sponsored by the National Nuclear Security Administration

Award Nos. DE-AC52-09NA29322[1] and DE-AC52-07NA27344[2]
Proposal No. BAA09-13

ABSTRACT

In this project, we are developing models of lithospheric structure for a wide variety of tectonic regions throughout Eurasia and the Middle East by regionalizing 1D velocity models obtained by jointly inverting *P*-wave and *S*-wave receiver functions with Rayleigh wave group and phase velocities. We expect the regionalized velocity models will improve our ability to predict travel-times for local and regional phases, such as Pg, Pn, Sn and Lg, as well as travel-times for body-waves at upper mantle triplication distances in both seismic and aseismic regions of Eurasia and the Middle East. We anticipate the models will help inform and strengthen ongoing and future efforts within the NNSA labs to develop 3D velocity models for Eurasia and the Middle East, and will assist in obtaining model-based predictions where no empirical data are available and for improving locations from sparse networks using kriging.

The codes needed to conduct the joint inversion of *P*-wave receiver functions (PRFs), *S*-wave receiver functions (SRFs), and dispersion velocities have already been assembled as part of ongoing research on lithospheric structure in Africa. The methodology has been tested with synthetic "data" and case studies have been investigated with data collected at an open broadband station in South Africa. PRFs constrain the size and *S*-*P* travel-time of seismic discontinuities in the crust and uppermost mantle, SRFs constrain the size and *P*-*S* travel-time of the lithosphere-sublithosphere boundary, and dispersion velocities constrain average *S*-wave velocity within frequency-dependent depth-ranges. Preliminary results show that the combination yields integrated 1D velocity models local to the recording station, where the discontinuities constrained by the receiver functions are superimposed to a background velocity model constrained by the dispersion velocities.

In our first year of this project we will (i) generate 1D velocity models for open broadband seismic stations in the western half of the study area (Eurasia and the Middle East) and (ii) identify well located seismic events with event-station paths isolated to individual tectonic provinces within the study area and collect broadband waveforms and source parameters for the selected events. The 1D models obtained from the joint inversion will then be combined with published geologic terrain maps to produce regionalized models for distinctive tectonic areas within the study area, and the models will be validated through full waveform modeling of well-located seismic events recorded at local and regional distances.

OBJECTIVES

Velocity models of lithospheric structure (crust and uppermost mantle) are critical for accurately predicting travel times and the propagation of local and regional seismic phases, such as Pg, Pn, Sn and Lg. The stability of wave propagation for these and other phases of relevance to improving our capability to locate and discriminate seismic events can be greatly affected by 2- and 3-D heterogeneity in both lithospheric and sublithospheric structure. In particular, velocity models of the lithosphere are key to accurately modeling travel times, in addition to surface wave dispersion and full waveforms at regional (2^o-15^o) and far-regional (15^o-25^o) distances.

Ongoing efforts within the National Nuclear Security Administration (NNSA) labs to develop 3-D velocity models for Eurasia and the Middle East are the Seismic Location Baseline Model (SLBM) and its follow-on, the Regional Seismic Travel Time project (RSTT). Starting models for SLBM inversions include the WENA model (Pasyanos et al., 2004) and the UNIFIED model (Pasyanos et al., 2003), which have been constructed from *a priori* information in the published literature. These models subdivide Eurasia and the Middle East into tectonically distinct regions, as shown in Figure 1, each of which is characterized by multiple sediment, crustal, and upper mantle layers with specified thicknesses, compressional and shear velocities, densities, and attenuation factors (Pasyanos et al., 2004). However, below the Moho, the models consist of a mantle half-space with a constant velocity gradient. As such, the SLBM inversions cannot accurately model rays penetrating below the lithosphere and cannot be used for waveform modeling or travel time predictions past about 12°.

The main objective of this project is to develop new velocity models of lithospheric thickness and velocity structure for Eurasia and the Middle East with predictive capabilities past 12^o. To develop such models, local velocity models will be first obtained by jointly inverting multiple datasets collected at open broadband stations, including *P*-wave receiver functions (PRFs), *S*-wave receiver functions (SRFs), fundamental-mode Rayleigh-wave phase velocities, and fundamental-mode Rayleigh-wave group velocities. The local 1D models will then be combined for stations within tectonic regions identified in the WENA and UNIFIED models to produce regionalized velocity models of the crust and upper mantle. These regionalized, 1-D models will characterize the average structure within the corresponding tectonic region, including lithospheric thickness, velocity structure of the lithospheric mantle, and structure of the low-velocity zone beneath the lithospheric lid, and have better resolution than other published

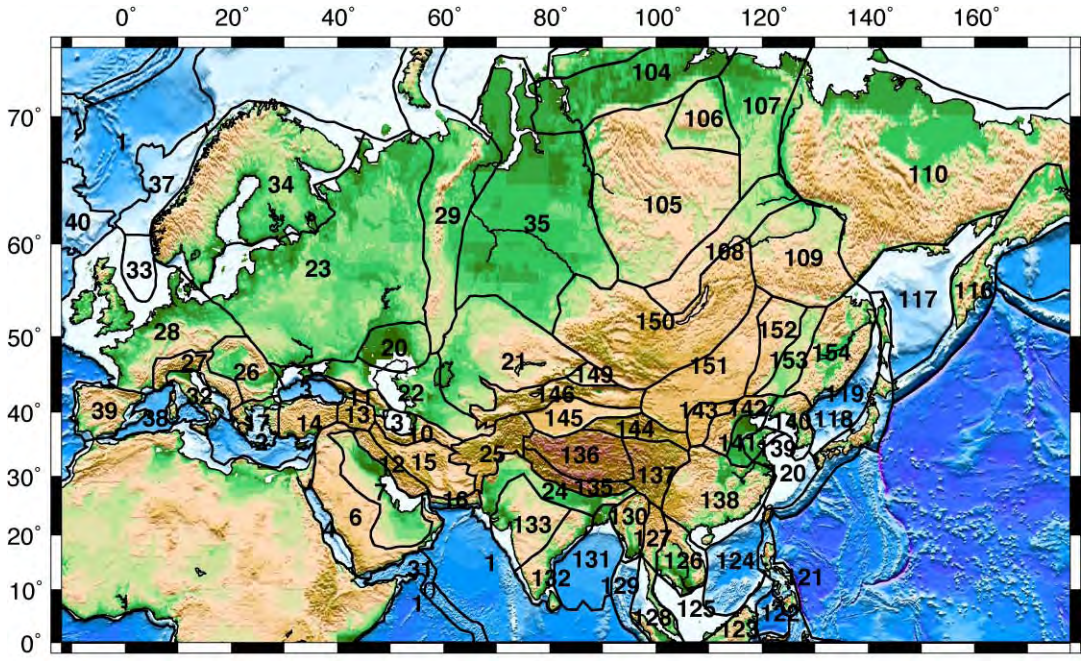

Figure 1. The UNIFIED model, with contributions from both LLNL and LANL. The numbered areas mark tectonically distinct regions defined by Pasyanos et al. (2003; 2004).

models for Eurasia and the Middle East as they will be fitting four independent seismic datasets. Moreover, a large number of seismic stations are openly available across Eurasia and the Middle East, which allows average 1-D models to be obtained for the majority of tectonic regions identified in the WENA and UNIFIED models.

The regionalized models will be evaluated with 1-D waveform modeling for events with well-determined source parameters (depth, seismic moment, and focal mechanism) and broadband recordings with ray-paths predominately in a single tectonic/geologic region. The model validation efforts will focus on regions where there is good event-station coverage (i.e., pure path propagation with a region) over a range of local and regional distances and will also include an investigation of the misfits between data and synthetics to understand how the regionalized models need to be perturbed to improve the fits in phase and amplitude.

The regionalized velocity models will improve our ability to predict Pg, Pn, Sn and Lg travel times in both seismic and aseismic regions of Eurasia and the Middle East and will help inform and strengthen ongoing and future efforts within the NNSA labs to develop 3-D velocity models for Eurasia and the Middle East. Importantly, our new velocity models will assist in obtaining model-based predictions where no empirical data are available (e.g., Flanagan et al., 2006), and in improving locations from sparse networks (e.g., Schultz et al., 1998; Myers and Schultz, 2000).

RESEARCH ACCOMPLISHED

The deliverables for the first year of application of this project include the development of joint inversion models for the western half of the study area. The development of the joint inversion codes needed to conduct the proposed research was already completed as part of an investigation of the lithospheric structure of southern Africa. We have now started gathering the data needed for the application of the joint inversion procedure.

Data Gathering

PRF and SRF waveforms for Eurasia and the Middle East will be obtained for all of the broadband stations belonging to the open networks available through the Incorporated Research Institutions for Seismology (IRIS) Data Management Center, both permanent and temporary. For the western half of the study area (Europe and the Middle East), the number of available stations totals 273 and have recording time windows ranging from a few years (e.g., station ROGR, belonging to the temporary RUSH deployment in Scotland) to almost two decades (e.g., station OBN, in Russia, which is part of the permanent GSN network).

Seismic sources ideally suited for the computation of PRFs commonly are at epicentral distances between 30^o and 90^o from the recording station and have magnitudes above 5.5. Following these criteria a total of 4,713 seismic sources have been selected from the Weekly Hypocenter Data File catalog, and the corresponding waveforms have already been downloaded for all the selected stations. The events have been recorded in the hundreds for the stations with the shorter recording time windows and in the thousands for the stations with the longer recording time windows. PRFs are presently being computed. The selection criteria for seismic sources commonly considered for the computation of SRFs are considerably more restrictive due to the interference of other teleseismic waves with the time window of interest, and include epicentral distances between 60^o and 85^o and magnitudes above 5.7 (see Wilson et al., 2006). The waveforms for the computation of SRFs at the selected stations are being downloaded.

Rayleigh wave group and phase velocities across Eurasia and the Middle East, on the other hand, will be obtained from a number of independent surface-wave tomography studies. Group velocity studies include Ritzwoller and Levshin (1998), who generated Rayleigh wave group velocity maps from 20 to 200 s with a resolution of about 5^o across most of Eurasia using about 9000 dispersion measurements, and Pasyanos (2005), who measured over 30,000 Rayleigh wave dispersion curves and used the conjugate gradient method with variable smoothness to invert for surface wave group velocity across Eurasia, the Middle East and surrounding areas. The Pasyanos (2005) model highlights lateral variations across the region for periods between 7 and 100 s with a resolution approaching 1^o. Phase velocities studies include those of Ekström et al. (1997), who used a method based on phase-matched filter theory to develop a global surface wave phase velocity model for periods between 35 and 150 s and, on a more regional scale, Curtis et al. (1998) who obtained phase velocity measurements along 4,020 Rayleigh wave paths across Eurasia and inverted this data for phase velocity maps at periods between 26 and 150 s. Overall, excellent coverage across Eurasia and the Middle East is provided by these studies, extending from periods of approximately

5 to 150 s, providing sensitivity within the crust as well as down into the lithospheric and sublithospheric mantle.

Code Development

The joint inversion of PRFs, SRFs, and surface-wave dispersion velocities is a straight-forward extension of the iterative, linearized scheme introduced by Julià et al. (2000; 2003) to jointly invert PRFs and dispersion velocities. The joint inversion scheme integrates the constraints conveyed by the individual datasets into velocity models that simultaneously explain all the data sets. PRFs constrain *S*-wave velocity contrasts across discontinuities and vertical *S*-*P* travel-times, but do not uniquely constrain the subsurface structure (Ammon et al., 1990); surface-wave dispersion velocities constrain absolute *S*-wave velocities within broad, frequency-dependent depth-ranges, but do not resolve rapid velocity variations with depth. Both data sets are thus sensitive to the same parameter, *S*-wave velocity, and the constraints complement each other, so that they bridge resolution gaps between the datasets. The combination produces *S*-wave velocity models where the high-resolution details constrained by the receiver functions are superimposed to a background velocity model constrained by the dispersion velocities (Julià et al., 2000). The joint inversion scheme has been applied to a variety of tectonic settings around the world, which include the Arabian shield (Julià et al., 2003), East Africa (Julià et al., 2005; Dugda et al., 2007; Keranen et al., 2009), the Paraná basin of Brazil (Julià et al., 2008), and the Indian shield (Julià et al., 2009).

The joint inversion scheme of Julià et al. (2000; 2003) is implemented through the following set of equations:

$$\begin{bmatrix} \sqrt{\frac{p}{w_s^2}}\,D_s \\ \sqrt{\frac{q}{w_b^2}}\,D_b \\ \sigma\Delta \\ A \end{bmatrix} \vec{m} = \begin{bmatrix} \sqrt{\frac{p}{w_s^2}}\,\vec{r}_s \\ \sqrt{\frac{q}{w_b^2}}\,\vec{r}_b \\ \vec{0} \\ A\,\vec{m}_a \end{bmatrix} + \begin{bmatrix} \sqrt{\frac{p}{w_s^2}}\,D_s \\ \sqrt{\frac{q}{w_b^2}}\,D_b \\ \vec{0} \\ \vec{0} \end{bmatrix} \vec{m}_0 \qquad (1)$$

where D_s and D_b are partial derivative matrices for the dispersion and the PRF estimates, respectively, $\mathbf{r}_s$ and $\mathbf{r}_b$ are the corresponding vectors of residuals, w_s^2 and w_b^2 are weights that equalize the data sets, the vector **m** contains the velocities of fixed thickness layers overlying a half-space, and $\mathbf{m}_0$ contains an initial estimate for the velocities. The matrix Δ constructs the second difference model and makes the resulting profiles vary smoothly, and the diagonal matrix W contains constraint weights to the *a priori* velocity values $\mathbf{m}_a$. The influence factor 'p' controls the trade-off between fitting the receiver functions and the dispersion curves, and the smoothness parameter σ controls the trade-off between fitting the data and model smoothness. The values of these parameters are determined empirically by performing suites of inversions. The parameter q=1-p, with $0 \le p \le 1$, so that p = 0 means inverting receiver function data only and p = 1 means inverting dispersion data only. The weights w_s^2 and w_b^2 are computed as $N\sigma^2$, where N is the number of data points and σ^2 is the variance of the observations.

SRFs have been incorporated into the joint inversion scheme by simply adding the partial derivatives and the vector of residuals into D_b and $\mathbf{r}_b$, respectively, in the system of equations (1). Similar to PRFs, SRFs constrain *S*-wave velocity contrasts across seismic discontinuities and vertical P-S travel-times, but do not uniquely constrain the subsurface structure. The main contribution is that SRFs provide better constraints on the depth and structure of the lithosphere-asthenosphere boundary than PRFs (e.g., Kumar et al., 2007; Hansen et al., 2007) and that they help reduce trade-offs within the upper mantle. The performance of the new methodology is illustrated through inversion of noise-free, "synthetic" data in Figure 2. The starting model is a simple half-space of ~4.0 km/s, parameterized as a stack of thin layers of constant velocity and thickness. After the first iteration the match between "observed" and predicted dispersion velocities improves dramatically, and this translates into an inverted model with average velocities close to that of the true model. The predicted receiver functions, however, do not match the peaks and troughs correctly, and the discontinuities are shifted in the inverted model with respect to the true model. After the second iteration the match between "observed" and predicted receiver functions improves, and the depths of the discontinuities are placed at the expected depths. Subsequent iterations keep tuning the inverted models until a perfect match to the true model is achieved.

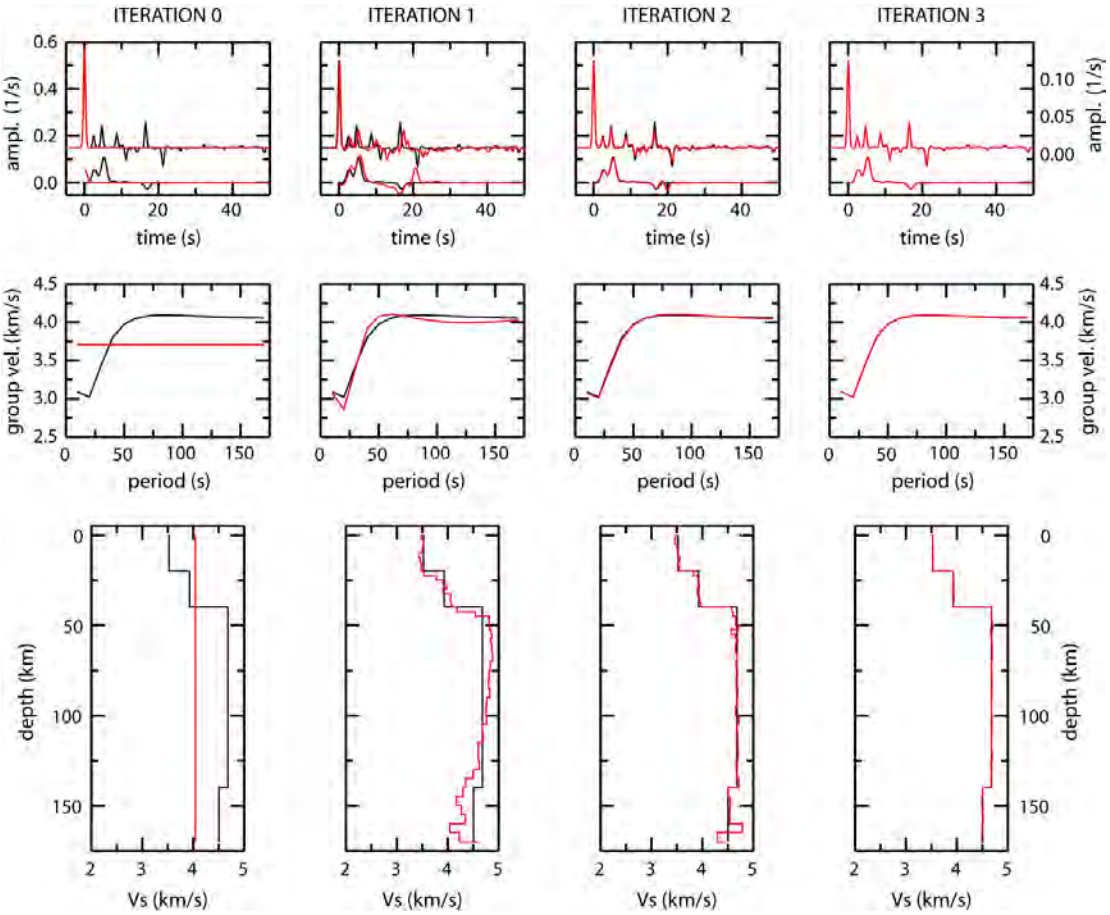

Figure 2. Joint inversion of synthetic PRFs, SRFs, and dispersion velocities. Each columns displays the joint inversion after each iteration (indicated on top). The top frames display "observed" (black) and predicted (red) PRF (upper trace) and SRF (lower trace) waveforms; the middle frames show the "observed" (black) and predicted (red) Rayleigh-wave group velocities; and the bottom frames show the inverted (red) and true (black) velocity models.

Figure 3 shows the results of jointly inverting PRFs, SRFs, and surface-wave dispersion velocities at station BOSA, which is located in the stable interior of the Kaapvaal craton in southern Africa. The figure shows 6 PRF averages (4 of them at two overlapping frequency bands) obtained by stacking the receiver functions for this station in tight ray parameter and back-azimuth ranges, 1 SRF average, and fundamental-mode Rayleigh wave dispersion velocities obtained from the tomographic inversion of Pasyanos (2005). The starting model was constructed as a 40-km thick gradational crust overlying PREM (Dziewonski and Anderson, 1981). Note that a single model can satisfactorily match all the PRF and SRF averages, implying that the structure under the station is laterally homogeneous, as well as the dispersion velocities. In the inverted model, the crust is ~35 km thick and is separated from the uppermost mantle by a sharp discontinuity, which is in excellent agreement with independent seismic studies (e.g., Niu and James, 2002). The upper mantle consists of a linear velocity increase down to ~160 km depth, a small LVZ between 160 and 180 km depth, and a velocity decrease at ~240 km depth. Figure 3 also overlays the velocity model resulting from the joint inversion of PRFs and dispersion velocities only. Little difference is observed down to ~150 km depth between the joint inversion models with and without the SRF. The main differences lie in the sublithospheric mantle where the small LVZ between 160 and 180 km depth and the velocity decrease at ~240 km depth are required to match the SRF waveforms. The overlay demonstrates that the upper mantle features are mainly constrained by the SRF waveforms, as the velocities are averaged through a linear velocity increase down to ~270 km in the joint inversion models with no SRF constraints.

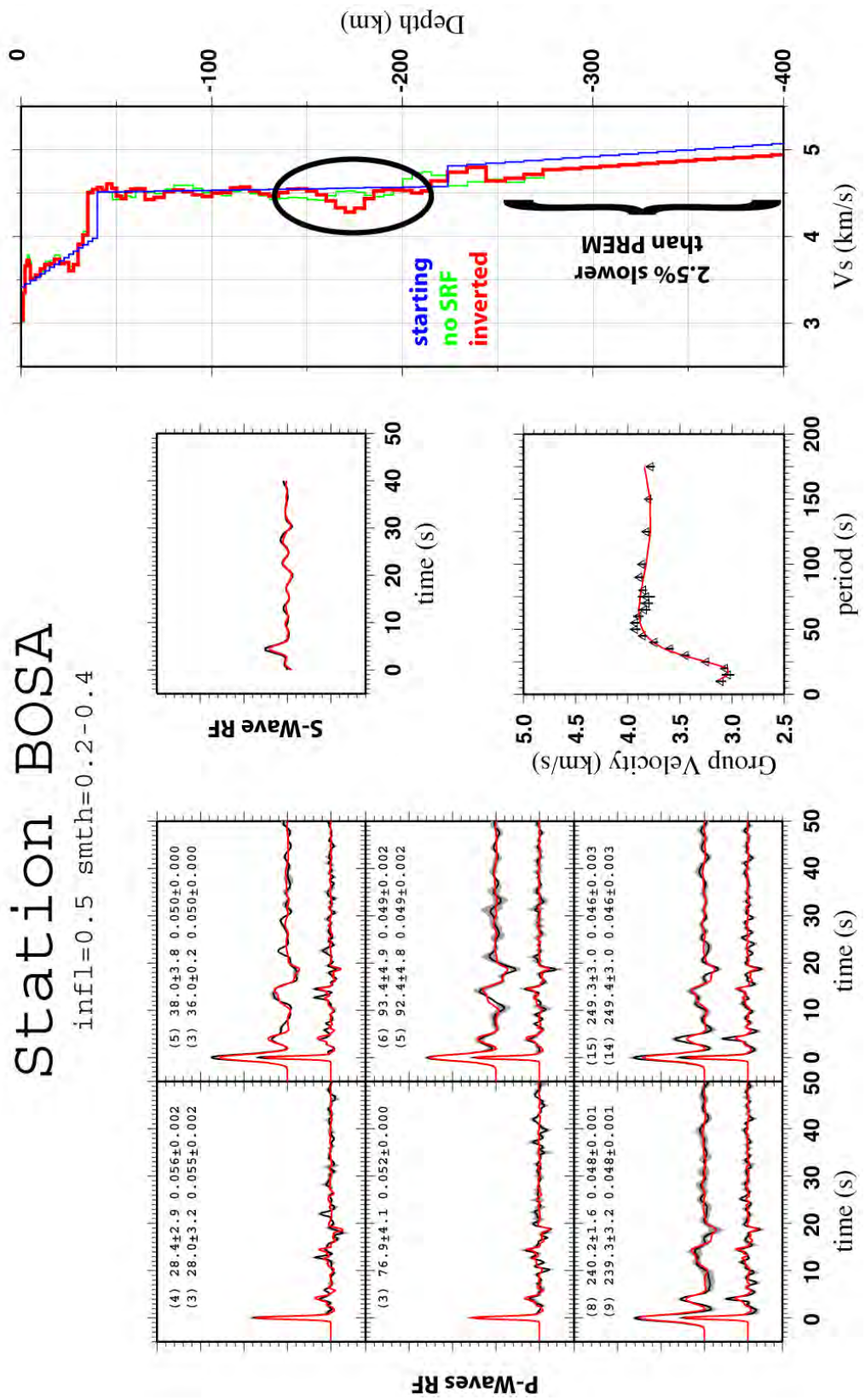

Figure 3. Joint inversion results at station BOSA in southern Africa. The left panels display the six PRF averages (black) and the corresponding predictions (red) from the joint inversion model. The middle panels show the SRF averages (black) and the corresponding prediction (red) in the top and the observed (triangles) and predicted (red line) dispersion velocities at the bottom. The right panel overlays the starting (blue), and inverted models with (red) and without (green) SRF constraints.

CONCLUSIONS AND RECOMMENDATIONS

We have started downloading broadband seismic waveforms needed for the computation of PRFs and SRFs from the seismic stations within western Eurasia and the Middle East that are openly available through the IRIS archive. The resulting dataset consists of tens of thousands of waveforms recorded in as many as 273 broadband stations. The codes needed to jointly invert the complementary seismic data sets have already been implemented and tested with broadband stations in southern Africa. The development of the joint inversion models for the targeted area will start as soon as the phase and group velocities are extracted from the corresponding tomographic studies and the computation of PRFs and SRFs is completed.

REFERENCES

Ammon, C., G. Randall, and G. Zandt (1990). On the nonuniqueness of receiver function inversions, *J. Geophys. Res.* 95: 15303–15318.

Curtis, A., J. Trampert, R. Snieder, and B. Dost (1998). Eurasian fundamental mode surface wave phase velocities and their relationship with tectonic structures, *J. Geophys. Res.* 103: 26919–26947.

Dugda, M., A. Nyblade, and J. Julià (2007). Thin lithosphere beneath the Ethiopian Plateau revealed by a joint inversion of Rayleigh wave group velocities and receiver functions*, J. Geophys. Res.* 112: doi: 10.1029/2006JB004918.

Dziewonski, A., and D. Anderson (1981). Preliminary reference earth model, *Phys. Earth Plant. Int.* 25: 297–356.

Ekström, G., J. Tromp, and E. Larson (1997). Measurements and global models of surface wave propagation, *J. Geophys. Res.* 102: 8137–8157.

Flanagan, M., S. Myers, and K. Koper (2006). Regional travel-time uncertainty and seismic location improvement using a three-dimensional a priori velocity model, *EOS Trans. AGU* 87: S31B-0194.

Hansen, S., A. Rodgers, S. Schwartz, and A. Al-Amri (2007). Imaging ruptured lithosphere beneath the Red Sea and Arabian Peninsula, *Earth Planet. Sci. Lett.* 259: 256–265.

Julià, J., C. Ammon, R. Herrmann, and A.M. Correig (2000). Joint inversion of receiver function and surface wave dispersion observations, *Geophys. J. Int.* 143: 99–112.

Julià, J., C. Ammon, and R. Herrmann (2003). Lithospheric structure of the Arabian Shield from the joint inversion of receiver functions and surface-wave group velocities, *Tectonophysics* 371:1–21.

Julià, J., C. Ammon, and A. Nyblade (2005). Evidence for mafic lower crust in Tanzania, East Africa, from joint inversion of receiver functions and Rayleigh wave dispersion velocities, *Geophys. J. Int*. 162: 555–569.

Julià, J., M. Assumpção, and M. Rocha (2008). Deep crustal structure of the Paraná Basin from receiver functions and Rayleigh-wave dispersion: Evidence for a fragmented cratonic root, *J. Geophys. Res.* 113: B08318, doi:10.1029/2007jb005374.

Julià, J., J. Jagadeesh, S.S. Rai, and T.J. Owens (2009). Deep crustal structure of the Indian shield from joint inversion of P-wave receiver functions and Rayleigh-wave group velocities: Implications for Precambrian crustal evolution, *J. Geophys. Res.* (in press).

Keranen, K. M., S. L. Klemperer, J. Julia, J. F. Lawrence, and A. A. Nyblade (2009). Low lower crustal velocity across Ethiopia: Is the Main Ethiopian Rift a narrow rift in a hot craton?, *Geochem. Geophys. Geosyst.* 10: Q0AB01, doi:10.1029/2008GC002293.

Kumar, P., X.H. Yuan, M.R. Kumar, R. Kind, X.Q. Li, and R.K. Chadha (2007). The rapid drift of the Indian tectonic plate, *Nature* 449: 894–897.

Myers, S., and C. Schultz (2000). Improving sparse network seismic location with Bayesian kriging and teleseismically constrained calibration events, *Bull. Seis. Soc. Am.* 90: 199–211.

Niu, F., and D. James (2002), Fine structure of the lowermost crust beneath the Kaapvaal craton and its implications for crustal formation and evolution, *Earth Planet. Sci. Lett.* 200: 121–130.

Pasyanos, M., W. Walter, and M. Flanagan (2003). Geophysical models for nuclear explosion monitoring, in *Proceedings of the 25th Seismic Research Review—Nuclear Explosion Monitoring: Building the Knowledge Base*, LA-UR-03-6029, Vol. 1, pp. 125–134.

Pasyanos, M., W. Walter, M. Flanagan, P. Goldstein, and J. Bhattacharyya (2004). Building and testing an a priori geophysical model for western Eurasia and North America, *Pure Appl. Geophys* 161: 235–281.

Pasyanos, M. (2005). A variable resolution surface wave dispersion study of Eurasia, North Africa, and surrounding regions, *J. Geophys. Res.* 110: doi: 10.1029/2005JB003749.

Ritzwoller, M. and A. Levshin (1998). Eurasian surface wave tomography: group velocities, *J. Geophys. Res.* 103: 4839–4878.

Schultz, C., S. Myers, J. Hipp, and C. Young (1998). Nonstationary Bayesian kriging; a predictive technique to genereate spatial corrections for seismic detection, location, and identification, *Bull. Seis. Soc. Am.* 88: 1275–1288.

Wilson, D. C., D. A. Angus, J. F. Ni, and S. P. Grand (2006). Constraints on the interpretation of S-to-P receiver functions, *Geophys. J. Int.* 165: 969–980.

DEVELOPMENT OF REGIONAL PHASE TOMOGRAPHIC ATTENUATION MODELS FOR EURASIA

Thorne Lay[1], Xiao-Bi Xie[1], and Xiaoning (David) Yang[2]

University of California, Santa Cruz[1] and Los Alamos National Laboratory[2]

Sponsored by National Nuclear Security Administration

Award Nos. DE-FC52-05NA26606[1]and DE-AC52-06NA25396[2]
Proposal No. BAA05-23

ABSTRACT

We are developing regional-phase (*Pn*, *Pg*, *Sn*, *Lg*) tomographic attenuation models for Eurasia. The models will be integrated into the National Nuclear Security Administration (NNSA) Knowledge Base and used in the Magnitude and Distance Amplitude Correction (MDAC) station calibration for the development of regional seismic discriminants. Our current focus is on *Pn*, an extremely important phase in seismic event identification.

Accurately accounting for regional-phase geometric spreading is critical for the development of useful attenuation models. It is particularly important for *Pn* and *Sn* waves because the propagation mode of these waves makes them more susceptible to upper mantle velocity structures and the Earth's sphericity, which in turn causes the geometric spreading of *Pn* (and *Sn*) to be dependent on frequency as well as on range in a complicated way. We conduct numerical simulations to quantify *Pn* and *Sn* geometric spreading in a spherical Earth model with constant mantle velocities. Based on our simulation results, we have presented new *Pn* and *Sn* geometric spreading models in the form $G(r,f) = [10^{n_3(f)}/r_0](r_0/r)^{n_1(f)\log(r_0/r)+n_2(f)}$ and $n_i(f) = n_{i1}\left[\log(f/f_0)\right]^2 + n_{i2}\log(f/f_0) + n_{i3}$, where i = 1, 2 or 3. r is epicentral distance; f is frequency; r_0 = 1 km and f_0 = 1 Hz. We derive values of coefficients n_{ij} by fitting the model to computed *Pn* and *Sn* amplitudes for a spherical Earth model having a 40-km-thick crust, generic values of *P* and *S* velocities and a constant-velocity uppermost mantle.

We applied the new spreading model to observed data in Eurasia to estimate average *Pn* attenuation, obtaining more reasonable results compared to using a standard power-law model. Our new *Pn* and *Sn* geometric-spreading models provide generally applicable reference behavior for spherical Earth models with constant uppermost-mantle velocities.

We have extended numerical modeling of Pn behavior in the presence of laterally varying structure in both the Moho discontinuity and fine-scale structure of the uppermost mantle lid. Observations of Pn show larger path variance than for other regional phases, and we find that even weak heterogeneities in the lid can produce large scatter in Pn amplitudes and significant deviations from the ideal geometric spreading relation given above. Similar scatter and deviation from the ideal geometric spreading result from statistical irregularities in the Moho discontinuity. We explore statistical influences of random heterogeneities for exponential and power law models of volumetric and boundary heterogeneity for many models, and provide an assessment of the efficacy of any simple parameterized model of *Pn* spreading. The presence of realistic volumetric heterogeneities and rough Moho boundary can produce behavior viably parameterized with a power law model, but as the heterogeneity decreases the data converge on the model above. This implies strong trade-offs between choice of spreading parameterization and frequency dependence of inferred attenuation. If the attenuation models are to be used for detailed analysis of thermal structure or other secondary inferences, caution must be used and the associated geometric spreading model either justified or its uncertainties folded into the attenuation estimates.

OBJECTIVES

The ultimate objective of this project is to develop 1-Hz, two-dimensional, regional-phase (*Pn, Pg, Sn* and *Lg*) tomographic attenuation models for Eurasia. The models will be used in MDAC for improved event identification. The major technical objective is to understand the geometric spreading needed for *Pn* and *Sn*.

RESEARCH ACCOMPLISHED

Pn geometric spreading

Accurately accounting for geometric spreading is critical for the development of meaningful regional-phase attenuation models. This is particularly true for *Pn* and *Sn* waves because the nature of their wave propagation renders them acutely sensitive to uppermost mantle velocity structure and the Earth's sphericity. Even simple one-dimensional (1D) velocity models can produce geometric spreading of *Pn* and *Sn* that is strongly dependent on frequency and range (e.g., Sereno and Given, 1990). If frequency dependence of the geometric spreading actually occurs and is neglected, the attenuation model will acquire incorrect frequency dependence. Similar arrival times of *Pg* and *Pn* phases and *Pn* and *P* phases at their respective crossover distances result in rapidly changing *P*-wave amplitudes, difficulty in phase isolation and identification, and uncertainty in appropriate specification of the propagation path and geometric spreading at these distances. Lateral variation of Moho topography and upper-mantle lid velocity and fine scale heterogeneity of the lower crust and/or mantle lid further introduce 2D and 3D complexities into *Pn* and *Sn* spreading.

In our previous modeling efforts, primarily based on the reflectivity method and earth flattening transform (EFT) of the spherical model under consideration, we generate complete synthetic seismograms within a specified slowness range for 1D, plane-layered velocity models. The EFT transformations of velocity v and depth z are (Chapman, 1973; Müller, 1977)

$$v_f = \frac{R}{R - z_r} v_r \quad \text{and} \quad z_f = R \ln\left(\frac{R}{R - z_r}\right), \tag{1}$$

where R is the radius of the Earth. Subscript r designates values in the spherical (radially symmetric) model and subscript f designates values in the plane (flat) model. The density ρ transformation is

$$\rho_f = \left(\frac{R}{R - z_r}\right)^m \rho_r, \tag{2}$$

which is not unique since m can take any value between -5 and 1. For regional body-waves, the choice of m is not critical (Müller, 1977). We choose m = -1 for *P/SV* simulations (Müller, 1977) and m = -5 for *SH* simulations (Chapman, 1973). We experimented with different values of m and the results were basically unchanged. Finally the transformation of amplitudes calculated from plane-model simulations back to corresponding amplitudes in the spherical model is

$$A_r = \left(\frac{\Delta}{\sin\Delta}\right)^{1/2} \left(\frac{R}{R - Z_r}\right)^{\frac{m+5}{2}} A_f, \tag{3}$$

where Z_r is the depth of the source in the spherical model and Δ is epicentral distance in radians.

We approximate the velocity gradient resulting from the EFT (Equations 1 and 2) with homogeneous layers in the plane Earth model, as is required by the reflectivity method. The thickness of these layers affects the accuracy of the approximation, with thinner layers yielding more accurate results. We set the thickness of these layers to be about 0.4 of the minimum wavelength of the waves to be modeled, which appears to be more than adequate. Further reducing the ratio (e.g., from 0.4 to 0.2 of the minimum wavelength) does not alter the results appreciably. The total thickness of the gradient zone is set to be more than 100 km larger than the maximum penetration depth of the direct wave in a homogeneous spherical model recorded at the longest epicentral distance considered. This thickness guarantees that no *Pn* or *Sn* waves observed within

the distance range of interest are affected by the lower boundary of the gradient zone. Below the gradient zone, the velocity is constant.

We use the same generic spherical Earth model considered by Sereno and Given (1990) as the Base Earth Model for our simulations and use the synthetics from the simulation to derive parameters of the *Pn* and *Sn* geometric-spreading models that we develop. The Base Earth Model consists of a 40-km-thick outer layer, representative of an average continental crust, with a constant-velocity mantle underneath (Figure 1). The model has no anelastic attenuation. The simplicity of this model allows us to isolate the effects of the sphericity on *Pn* and *Sn* geometric spreading. We use an isotropic point source for *Pn* simulations. The source for *Sn*(*SH*) simulations is a fundamental fault vertical strike-slip source and the source for *Sn*(*SV*) simulations is a dip-slip source. For all source types in our main calculations, a delta function is used as the source time function; source depth is 15 km and source strength is 10^{15} N m. Three-component synthetic ground displacements are computed at 33 locations distributed log-evenly along a linear profile from 200 km (1.8°) to 2500 km (22.5°). The Nyquist frequency of the seismograms is 20 Hz.

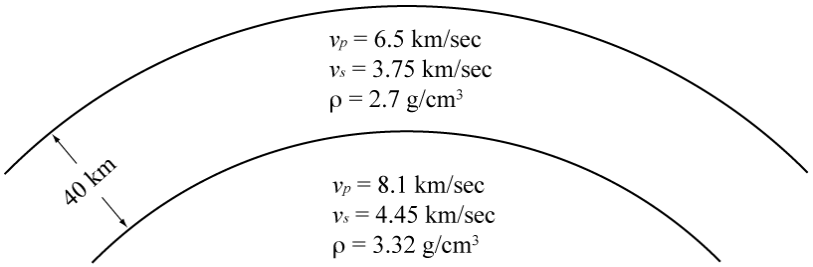

Figure 1. Base Earth model used for *Pn* and *Sn* simulations and the development of new *Pn* and *Sn* geometric-spreading models. Quality factor *Q* is infinite throughout the model.

We cut *Pn* and *Sn* portions of the synthetic seismograms using fixed-velocity windows. The velocities that we use to define the widths of *Pn* windows are 7.6 km/sec and 8.2 km/sec and those for *Sn* windows are 4.0 km/sec and 4.7 km/sec (Hartse, et al., 1997). The windows are centered at the peaks of the phases. We also tested a fixed-window-width method and the results remained essentially the same. We window *Pn* and *Sn*(*SV*) from vertical-component seismograms and *Sn*(*SH*) from transverse-component seismograms. After *Pn* and *Sn* seismograms are windowed, we taper the seismograms with small tapers (between 2% to 20% depending on the length of the signal relative to the window length) and Fourier transform the seismograms to obtain the amplitude spectra. We make spectral-amplitude measurements at 100 frequencies log-evenly distributed between 0.75 and 13 Hz. Amplitude at each frequency f_i is calculated by taking the average of the amplitudes between frequencies $f_i/\sqrt{2}$ and $\sqrt{2} f_i$.

Pn Modeling Results for the Base Earth Model

To visualize the *Pn* amplitude decay in a spherical Earth model, we plot 10-Hz *Pn* amplitudes for the base model in Figure 2. We extend the epicentral-distance range to between 135 km (1.2°) and 8000 km (71.9°) for this particular simulation in order to better depict the evolution of *Pn* waves. Amplitudes at distances beyond about 20° are measured from the direct wave that has been completely separated from the interference head waves. The amplitudes are corrected for the free-surface effect, which is only important at teleseismic distances. Also plotted in the figure are the amplitude decay of a conical head wave in a plane one-layer-over-half-space model (Aki and Richards, 2002; Eq. 6.26) and the amplitude decay of infinite-frequency direct wave in a spherical Earth model from ray tracing. At distances close to the critical distance, *Pn* geometric spreading behaves like that of a conical head wave. As distance increases, *Pn* spreading starts to deviate from that of the head wave and at about 5°, *Pn* amplitudes begin to increase. 10-Hz direct-wave energy separates from the rest of the interference head wave at about 10°. It is seen from the figure that this separation is manifested in a change in the smoothness of the *Pn* amplitude variation followed by a reduced rate of amplitude increase. In the range beyond the critical distance and before the direct-wave separation, *Pn* evolves from a wave similar to a conical head wave to the interference head wave, which is a superposition of multiple waves reflected from the Moho. As the epicentral distance approaches teleseismic distances, the direct-wave spreading approaches that of the infinite-frequency wave

from ray tracing results, as expected. The direct wave dominates the whole *Pn* wave packet at long distances. We do not see significant difference between spectral amplitudes obtained by windowing the whole *Pn* wave packet and those obtained by just windowing the direct wave after its separation from the packet. This is consistent with theoretical predictions (Červený and Ravindra, 1971).

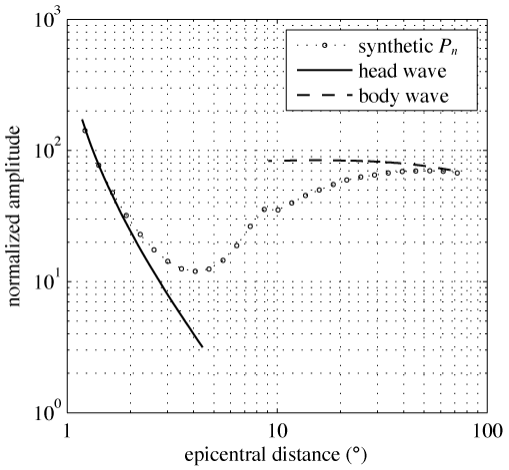

Figure 2. 10-Hz synthetic *Pn* amplitude decay in a spherical Earth model with constant mantle velocities. The solid line depicts the theoretical amplitude decay of a conical head wave in a plane one-layer-over-half-space Earth model. The dashed line is the amplitude decay of infinite-frequency direct wave in a spherical homogeneous Earth model from ray-tracing calculations.

Pn geometric spreading in a spherical Earth model is not only different from that of a head wave as is shown in Figure 2, but also frequency dependent. Figure 3 shows the *Pn* amplitude-variation surface as a function of distance and frequency for the base model. The strong frequency dependence of the amplitudes is apparent. Amplitudes at higher frequencies are affected more by the sphericity than are lower-frequency amplitudes.

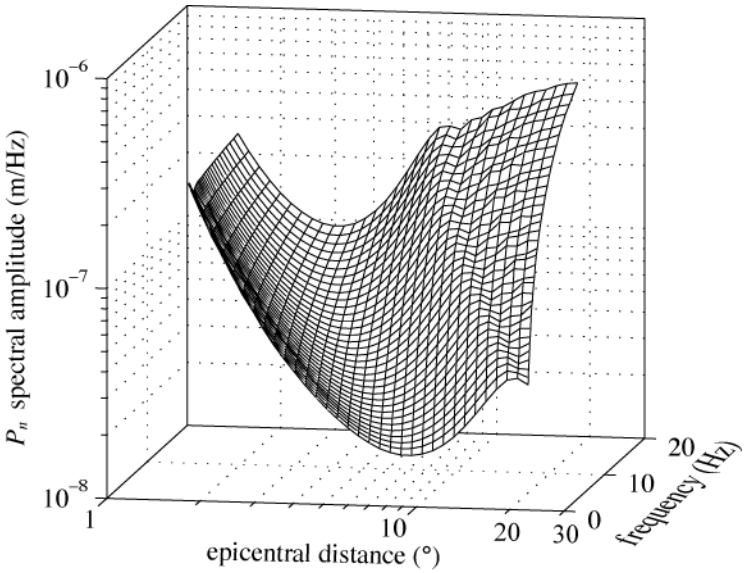

Figure 3. Synthetic *Pn* amplitudes as a function of epicentral distance and frequency.

In our first year's report, and as published in Yang et al. (2007) we presented a parameterized description of *Pn* geometric spreading for this simple reference model. The amplitude spectrum of *Pn* can be parameterized as

$$A(r,\theta,f) = K(f)M_0R(\theta)G(r,f)\exp\left(-\frac{\pi f}{Q(f)v}r\right)S(f) \tag{4}$$

with the new geometric-spreading model expressed as

$$G(r,f) = \frac{10^{n_3(f)}}{r_0}\left(\frac{r_0}{r}\right)^{n_1(f)\log\left(\frac{r_0}{r}\right)+n_2(f)} \qquad (r_0 = 1 \text{ km}) \tag{5}$$

and

$$n_i(f) = n_{i1}\left[\log\left(\frac{f}{f_0}\right)\right]^2 + n_{i2}\log\left(\frac{f}{f_0}\right) + n_{i3} \qquad (i = 1, 2, 3; f_0 = 1 \text{ Hz}). \tag{6}$$

In Equation 4, K is a frequency-dependent scaling factor; M_0 is source moment; R is source radiation pattern; Q is *Pn* quality factor; v is *Pn* velocity; S is receiver site response; r is epicentral distance; θ is azimuth angle and f is frequency. r_0 and f_0 are included in Equations 5 and 6 in order for the new model to have the same dimension as standard power-law models (e.g., Street et al., 1975; Sereno et al., 1988). The main differences between the new geometric-spreading model (Equations 5 and 6) and the standard frequency-independent power-law model are the addition of the first term in the exponent and the frequency dependence of parameters n_i. In the logarithm domain, the new model is a quadratic function of log-distance, whereas the power-law model is linear. The reason for choosing a log-quadratic function is to keep the parameterization as simple as possible while providing a good fit to the synthetics. The adoption of a quadratic functional form for n_i (Equation 6) is based on the behavior of n_i versus frequency obtained by fitting Equation 6 to synthetic *Pn* amplitudes at individual frequencies.

If we take common logarithm of Equation 5, substitute Equation 6 into the result and let r_0 and f_0 equal one, we obtain

$$\begin{aligned}\log\left[G(r,f)\right] = {} & n_{11}(\log f)^2(\log r)^2 + n_{12}\log f(\log r)^2 + n_{13}(\log r)^2 \\ & -n_{21}(\log f)^2\log r - n_{22}\log f\log r - n_{23}\log r \\ & +n_{31}(\log f)^2 + n_{32}\log f + n_{33}\end{aligned} \tag{7}$$

where r is in kilometers and f is in hertz. To derive coefficients n_{ij}, we fit Equation 7 to synthetic *Pn* amplitudes shown in Figure 3 in a least-squares sense. *Pn* amplitudes are corrected for M_0 used in the simulation (10^{15} N m) and K before the fitting. This yielded the coefficients in Table 1.

Table 1 Coefficients of the new *Pn* geometric-spreading model

n_{11}	n_{12}	n_{13}	n_{21}	n_{22}	n_{23}	n_{31}	n_{32}	n_{33}
-0.217	1.79	3.16	-1.94	8.43	18.6	-3.39	9.94	20.7

Similar processing provided an *Sn* geometric spreading model for the Base Earth Model structure.

Pn Spreading Sensitivity to Mantle Velocity Gradients

The velocity structure of the mantle lid is seldom well-constrained. The most direct constraint is provided by shape of the *Pn* travel time curve as a function of distance over a wide-enough distance range for reliable measurement, and even when there is apparent travel time branch curvature, it is difficult to distinguish between a smooth gradient with depth versus constant velocity layering with small step increases. Receiver function methods and surface wave dispersion inversions sometimes indicate gradients in the lid structure, but resolution tends to be poor, especially for *P*-velocity. As a result, reference velocity structures often assume constant or near-constant velocity in the mantle lid by default, so our Base Earth Model is not a bad starting point in many cases. However, there are regions where the lid velocity appears to increase or decrease with depth. The effects of positive *P*-velocity gradients in the mantle lid on the frequency-dependent spreading of *Pn* are illustrated in Figure 4. The basic shape of the spreading behavior

is preserved, but the distance-behavior shifts systematically to shorter distances, with overall higher *Pn* amplitudes as the gradient increases. It is possible to determine appropriate coefficients for a spreading representation like Equation (7) for any specific gradient, but this is only warranted if there are a priori constraints on the specific model in the region for which the spreading is to be utilized. Of course, use of an inappropriate spreading relationship will directly map into any inferred frequency-dependent attenuation structure, so it is clear that precise knowledge of the lid gradient is essential for robust attenuation estimation. This non-linear sensitivity of the spreading to the velocity model is a formidable issue for *Pn* and *Sn* attenuation determination that has not been widely appreciated.

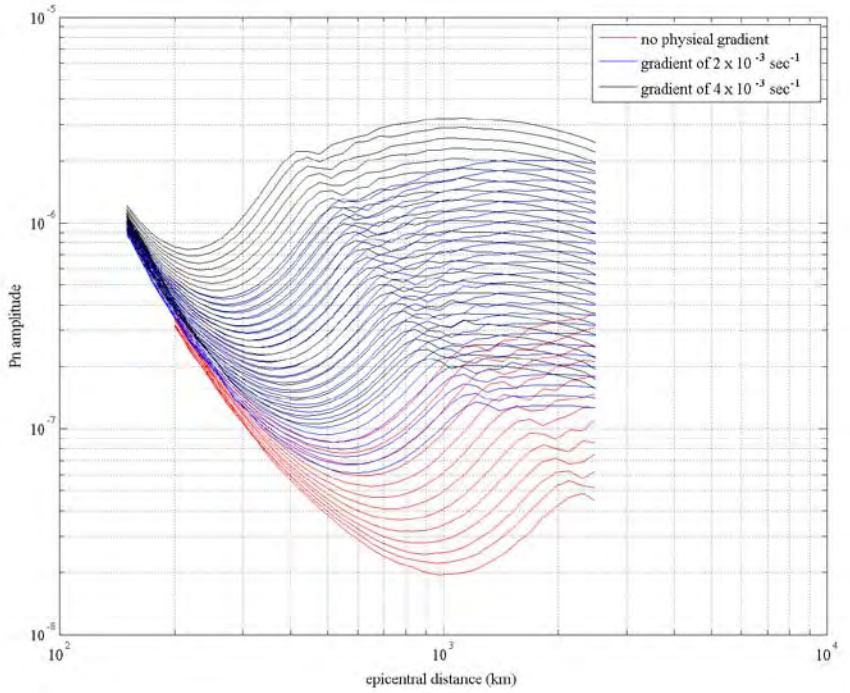

Figure 4. *Pn* amplitude versus distance curves similar to Figure 3, but for the Base Earth Model (red curves, for no physical gradient in the lid) and for two models with mild positive gradients in the mantle lid. The suite of curves for each case correspond to frequencies ranging from 0.75 Hz (lowest curve) to 12 Hz (highest curve).

Pn Spreading Sensitivity to Lateral Mantle Velocity Volumetric Heterogeneity

Given the disconcerting sensitivity of *Pn* spreading to a typically poorly-constrained attribute of the reference velocity model (the velocity gradient in the uppermost mantle lid), the prospect of robust attenuation determination for the uppermost mantle appears limited. Most standard seismological practices assume rather simple reference models, known to be gross approximations of the real structure, under the assumption that errors in the reference model produce only mild biases in other properties such as attenuation. This is simply not the case here, given the non-linear sensitivity of the *Pn* and *Sn* whispering gallery arrivals for 1D structures. But the non-linearity itself raises the question of how stable is the precise behavior in the presence of lateral heterogeneity? Clearly the actual mantle lid has multi-scale lateral heterogeneities; does their presence weaken the acute sensitivity of *Pn* spreading to the reference structure?

In last year's report, we explored the effects of lateral heterogeneity in the mantle lid velocity structure using a 2D finite-difference code (Xie and Lay, 1994) in which we impose random lateral velocity fluctuations characterized by root mean square (RMS) velocity fluctuations of a particular strength and horizontal and vertical averaging functions with different length scales. This allows us to consider 2D random heterogeneity models like that shown in Figure 5.

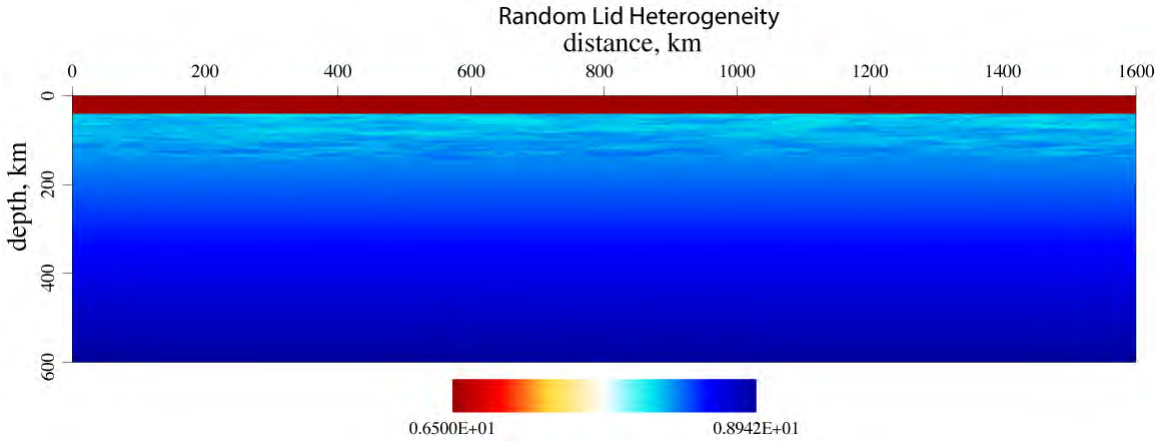

Figure 5. Visualization of 2D velocity model with 0.5% (RMS) *P*-velocity heterogeneity in the upper one hundred kilometers of the mantle lid. The background model is the EFT version of the Base Earth Model, so there is a slight positive velocity gradient across the crust and mantle.

The 2D finite-different modeling approach cannot achieve the very high frequencies of the 1D wave-number integration method, as the synthetics are limited to about 1 sec dominant period. Tests with simple 1D models indicate that the basic behavior of *Pn* spreading is accurately reproduced. Analysis of effects of random heterogeneity requires a statistical sampling of the effects associated with different realizations of the random velocity parameters. Many models have been run for various statistical properties of the mantle lid structure, with complete synthetic seismograms being computed.

Figure 6 shows the synthetic *Pn* amplitudes for 5 realizations of structures like that in Figure 5, along with an average of the ensemble, which can be directly compared to the result for the Base Earth Model.

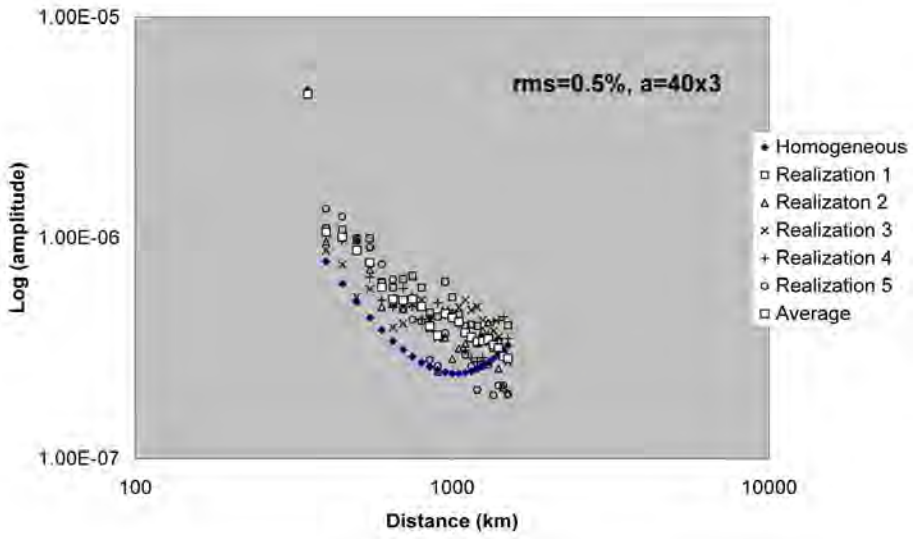

Figure 6. *Pn* amplitudes for 5 realizations of random velocity models with 0.5% velocity heterogeneity, 40 km horizontal averaging length and 3 km vertical averaging length. The average amplitude (white boxes) can be compared with results for the Base Earth Model.

An interesting behavior in Figure 6 is that the presence of velocity fluctuations affects the basic shape of the spreading, and can be represented adequately by a power-law type behavior at this frequency. This suggests that the 1D spreading behavior is rather delicate, with modest heterogeneity disrupting the specific

interference that gives rise to the complex shape. Similar ensembles of simulations for variable aspect ratios, from isotropic heterogeneities to horizontally elongated heterogeneities show that the change in spreading from the Base Earth Model to something closer to a power-law behavior increases with the degree of anisotropy (i.e., the minimum in the spreading curve is progressively eliminated as the heterogeneities become more pancake-like). For a specific heterogeneity aspect ratio (40 km x 3 km), the effect of variable RMS velocity level is shown in Figure 7. As the strength of the velocity functions increases, there is progressive reduction of curvature of the amplitude-distance trend, and the overall amplitude behavior is increasingly power-law like.

These results present something of a conundrum; the simple 1D velocity structures are very simple, but produce complex geometric spreading behavior that is non-linearly sensitive to the model parameters, while 2D models with geologically realistic lateral heterogeneities produce relatively simple geometric spreading behavior. It is likely that 3D effects will further enhance the tendencies manifested in the 2D calculations. In essence, prior efforts that have assumed simple power-law geometric spreading behavior, which is not a realistic form of spreading for any known 1D velocity model, may actually be reasonable results to the extent that the specific power law corresponds to a viable level of uppermost mantle velocity heterogeneity. Of course, the precise spectrum and statistical distribution of real mantle lid heterogeneities is not known for any specific path, just as the precise 'best' 1D lid velocity gradient is not known. Thus, propagating uncertainties in the geometric spreading model into uncertainties in attenuation model estimates remains very difficult. The effects of the heterogeneities on shorter period signals have not been assessed, and doing so present formidable computational challenges for long-range *Pn* and *Sn*: the overall frequency dependent behavior remains to be characterized. The effects of rough Moho structure and deep crustal heterogeneity also need to be evaluated before settling on a procedure for attenuation estimation.

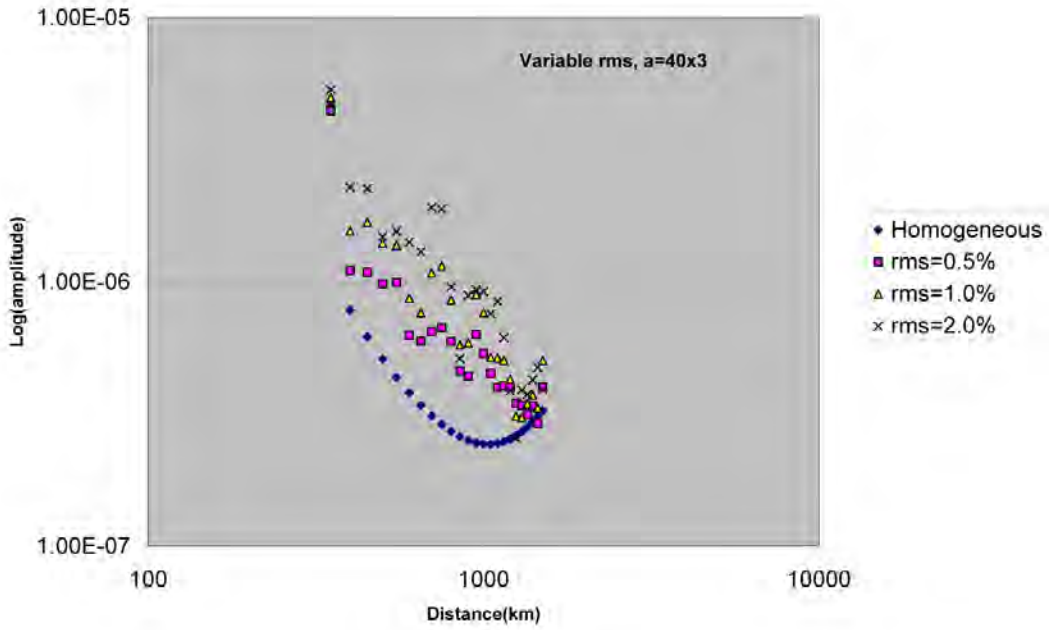

Figure 7. *Pn* amplitudes for averages of ensembles of 5 realizations for random velocity models with varying 0.5 to 2.0% RMS velocity heterogeneity, with 40 km horizontal averaging length and 3 km vertical averaging length.

Pn Spreading Sensitivity to Lateral Moho Topography

Just as volumetric heterogeneity is expected to result from geological processes during crustal formation and evolution, the same holds for Moho irregularities on multiple scales. *Pn* and *Sn* interactions with the

Moho near the source and receiver as well as throughout the propagation and whispering gallery development provide sensitivity to the Moho roughness. We have parameterized 2D exponential (Figure 8) and Gaussian statistical irregularities in the Moho depth to explore the effects of random structures, along with simple step-like structure in the Moho.

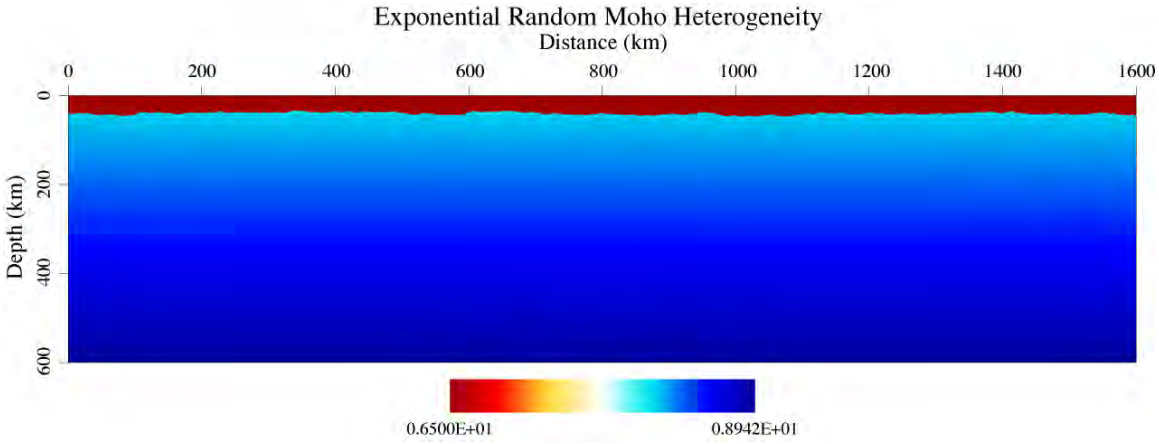

Figure 8. Visualization of 2D velocity model with exponential 3% (RMS) roughness of the Moho with 40 km scale horizontal averaging length. The background model is the EFT version of the Base Earth Model, so there is a slight positive velocity gradient across the crust and mantle.

The exponential model is much richer in small-scale structure and produces longer enduring coda than the smoother Gaussian model, but the overall behavior of the models is similar for the 1 sec dominant period (Figure 9). For an 80 km horizontal averaging function the amplitude decay effects become significant for 5% RMS heterogeneity in the depth of the Moho. There is only minor sensitivity to the choice of horizontal averaging function for values larger than 40 km for a given statistical model.

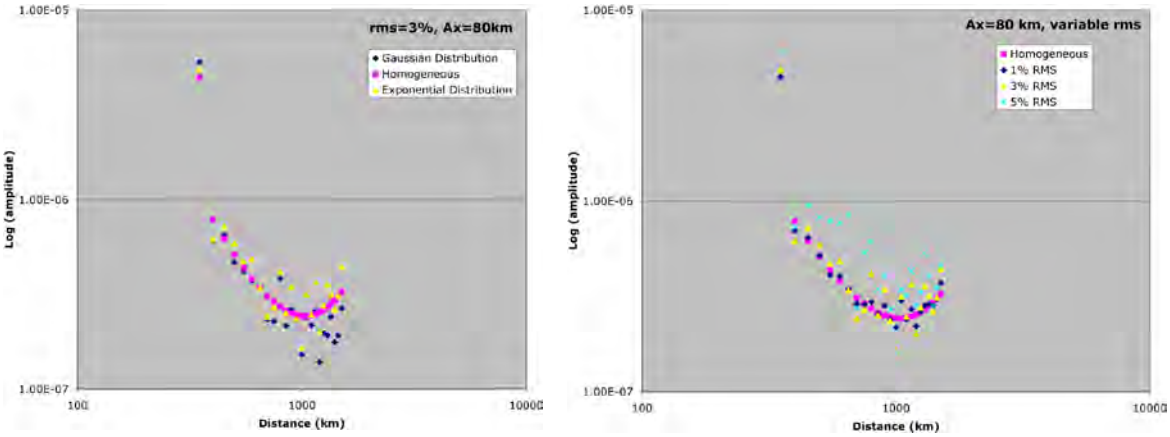

Figure 9. Pn amplitude decay versus distance for models with 80 km horizontal averaging functions and RMS roughness of 3% (of 40 km) for Gaussian and exponential distributions (left) and for variable RMS roughness for exponential heterogeneity (right).

CONCLUSIONS AND RECOMMENDATIONS

The behavior of geometric-spreading for *Pn* and *Sn* is surprisingly subtle and complex, even for simple 1D reference models (e.g., Menke and Richards, 1980; Sereno and Given, 1990). This project has shown that the effects of variable 1D mantle lid gradients preserve the basic function form of the frequency-dependent complexity of the constant-velocity mantle lid model, but the effects are so strong that new coefficients would need to be determined for the spreading model to be adequate. Indeed, the

sensitivity to gradient is non-linear, raising questions about the choice of spreading model given typical situations where there is little or no information on the local lid velocity gradients. Of course, if the data for a given region are sufficient to constrain the lid velocity gradient (this may be the case across the Russian platform, for example), specific spreading computations can clearly provide a reference behavior relative to which attenuation estimates can be performed. In detail even this is not going to be easy given the degenerate nature of layered versus gradient model fits to first arrival times.

Computations with lateral volumetric heterogeneities in the mantle lid and on the Moho add an additional, complexity to the problem of *Pn* and *Sn* geometric spreading. 2D finite-difference simulations indicate that the precise shape of the geometric spreading behavior for 1D models can be disrupted by even moderate levels of lateral heterogeneity, and the behavior for 1 sec period waves moves toward a power-law representation as the level of heterogeneity increases and as the horizontal/vertical aspect ratio of the heterogeneities increases. This behavior needs further quantification and exploration of its frequency dependence, but may provide a basis for using a conventional power law type geometric spreading with new recognition that the associated model for which it is approximating the amplitude decay is not a conventional 1D constant velocity mantle model or even a constant lid-gradient model, but is intrinsically a statistically heterogeneous model with some form of power-law heterogeneity, akin to those for very complex, multiple-arrival phases such as *Lg* (Yang, 2002). While specifying a preferred geometric spreading relation is still going to be difficult given the very limited knowledge of actual lid heterogeneity on any given path or in any given region, some understanding of trade-offs with attenuation model inferences may prove possible. Further modeling with rough Moho, crustal heterogeneity and broader band seismograms is required before final recommendations and attenuation models can be achieved.

REFERENCES

Aki, K. and P. G. Richards (2002). *Quantitative Seismology*, 2nd edition, University Science Books, Sausalito, California.

Červený, V. and R. Ravindra (1971). *Theory of Seismic Head Waves*, University of Toronto Press, Toronto.

Chapman, C. H. (1973). The Earth flattening transformation in body wave theory, *Geophys. J. R. Astr. Soc.* 35: 55–70.

Hartse, H. E., S. R. Taylor, W. S. Phillips, and G. E. Randall (1997). A preliminary study of regional seismic discrimination in central Asia with emphasis on western China, *Bull. Seism. Soc. Am.* 87: 551–568.

Menke, W. H. and P. G. Richards (1980). Crust-mantle whispering gallery phases: a deterministic model of teleseismic *Pn* wave propagation, *J. Geophys. Res.* 85: 5416–5422.

Müller, G. (1977). Earth-flattening approximation for body waves derived from geometric ray theory—improvements, corrections and range of applicability, *J. Geophys.* 42: 429–436.

Sereno, T. J. and J. W. Given (1990). *Pn* attenuation for a spherically symmetric Earth model, *Geophys. Res. Lett.* 17: 1141–1144.

Sereno, T. J., S. R. Bratt, and T. C. Bache (1988). Simultaneous inversion of regional wave spectra for attenuation and seismic moment in Scandinavia, *J. Geophys. Res.* 93: 2019–2035.

Street, R. L., R. B. Herrmann, and O. W. Nuttli (1975). Spectral characteristics of the *Lg* wave generated by central United States earthquakes, *Geophys. J. R. Astr. Soc.* 41**:** 51–63.

Xie, X.-B. and T. Lay (1994). The excitation of *Lg* waves by explosions: A finite-difference investigation, *Bull. Seism. Soc. Am.* 84: 324–342.

Yang, X. (2002). A numerical investigation of *Lg* geometric spreading, *Bull. Seism. Soc. Am.* 92: 3067–3079.

Yang, X., T. Lay, X.-B. Xie, and M. S. Thorne (2007). Geometric spreading of *Pn* and *Sn* in a spherical Earth model, *Bull. Seism. Soc. Am*. 97: 2053–2065, doi:10.1785/0120070031.

ADVANCED MULTIVARIATE INVERSION TECHNIQUES FOR HIGH RESOLUTION 3D GEOPHYSICAL MODELING

Monica Maceira[1], Charlotte A. Rowe[1], Haijiang Zhang[2], Ryan T. Modrak[1], Michael L. Begnaud[1], Lee K. Steck[1], George R. Randall[1], and Xiaoning (David) Yang[1]

Los Alamos National Laboratory[1] and Massachusetts Institute of Technology[2]

Sponsored by the National Nuclear Security Administration

Award No. DE-AC52-06NA25396/LA09-3D Inv-NDD02

ABSTRACT

To meet the United States Government (USG) nuclear explosion monitoring (NEM) requirements with high confidence, the Air Force Technical Applications Center (AFTAC) needs new and improved capabilities for analyzing regional seismic, teleseismic, and infrasound event data. Recently, the National Nuclear Security Administration (NNSA) has decided to move toward 3D modeling to improve knowledge of the compressional and shear velocity structure and enable us to reduce uncertainty and more accurately detect, locate, and identify small (body wave magnitude m_b<4) seismic events. For seismically active areas, with good ground truth event coverage, inaccurate models can be corrected by interpolating results from nearby archived events (using the kriging methodology) and, therefore, it is possible to detect, locate, and identify large events even with limited resolution models. This is not necessarily the case for smaller events, however, and it is even more of a challenge for aseismic regions. On the other hand, focus on near-regional to local monitoring, demands that we address the Earth's heterogeneities and 3D complexities.

Motivated by the shortcomings of existing single-parameter inversion methods in accurate prediction of both seismic waveforms and other geophysical parameters, this research focuses on the development and application of advanced multivariate inversion techniques to generate a realistic, comprehensive, and high-resolution 3D model of the seismic structure of the crust and upper mantle that satisfies multiple independent geophysical datasets. Building on previous efforts, we have added a fourth dataset to the simultaneous joint inversion methodology. We present a 3D seismic velocity model of the crust and upper mantle of northwest China resulting from the simultaneous joint inversion of surface wave dispersion observations, teleseismic P-wave receiver functions, gravity anomalies, and body wave (P and S phases) travel times. Surface wave dispersion measurements are primarily sensitive to seismic shear-wave velocities. But, at shallow depths, it is difficult to obtain high-resolution velocities and to constrain the structure. This is because the longer the period, the deeper the surface wave energy penetrates, so shorter periods are primarily sensitive to upper crustal structures. Short periods are difficult to measure especially in tectonically and geologically complex areas. On the other hand, gravity inversions have the greatest resolving power at shallow depths because gravity anomalies decrease in amplitude and increase in wavelength with increasing depth. Gravity measurements also provide constraints on rock density variations. In addition, surface wave dispersion measurements are primarily sensitive to vertical shear-wave velocity averages; while body wave receiver functions are sensitive to shear-wave velocity contrasts and vertical travel-times. The addition of the fourth dataset consisting of seismic body wave travel-time data helps to constrain the seismic wave velocities both vertically and horizontally in the model cells crossed by the ray paths. An iterative, conjugate gradient-based least squares inversion is used to jointly model the four different data sets.

At the same time, we are testing different relationships between seismic velocities and density in a region in east Africa where we have obtained on-land Bouguer gravity measurements. These sensitivity studies will ensure the validity of the relations used in our 3D seismic imaging efforts.

OBJECTIVES

The ultimate goal of this study is to improve our knowledge of the 3D compressional and shear velocity structure and enable us to reduce uncertainty and more accurately detect, locate, and identify small (body wave magnitude m_b<4) seismic events, and therefore improve our capabilities for NEM. This project specifically improves seismic monitoring technology through the development and application of advanced multivariate inversion techniques to generate a realistic, comprehensive, and high-resolution 3D model of the seismic structure of the crust and upper mantle that satisfies numerous independent geophysical datasets.

RESEARCH ACCOMPLISHED

The characterization of the 3D continental structure is of fundamental importance to understanding crustal generation and its geodynamic evolution. Researchers from a variety of institutions have been investigating the idea of 3D geophysical modeling for decades. Inversion methods for determining the 3D velocity structure of the crust and mantle have been used since the late 70's (e.g., Aki et al., 1977). The so-called "cooperative inversion" defined by Lines et al. (1988) refers to the inversion of various, potentially different sets of geophysical observations, and can be formulated as a simultaneous inversion or as a sequential inversion. Joint inversion incorporates all the data sets simultaneously and in one data vector. This approach was followed by Lees and VanDecar (1991) to model seismic travel times and gravity data. On the other hand, sequential inversion treats each data set separately on alternating steps so the results of one inversion are used as the initial constraint for the next step. This approach was preferred by Lines et al. (1988) and Parsons et al. (2001) among others. The different data sets used in these "cooperative inversions" varied from resistivity and magnetotelluric data (Jupp and Vozoff, 1975), to teleseismic or local travel times and gravity data (Oppenheimer and Herkenhoff, 1981; Onizawa et al., 2002), to receiver function and surface wave dispersion observations (Julià et al., 2000; 2003; 2005), or to surface wave group and phase velocities (Villaseñor et al., 2001).

Maceira and Ammon (2006) were pioneers in implementing a method to jointly invert surface wave group velocities and free-air gravity observations. Inversion of surface wave dispersion data is a standard method for determining 3D shear velocity structure of the crust and upper mantle of the Earth. Nevertheless, it is well known that traditional state-of-the-art inversion techniques suffer from poor resolution and nonuniqueness, especially when a single surface wave mode is used (Huang et al., 2003). This is particularly true at shallow depths where the shorter periods, which are primarily sensitive to upper crustal structures, are difficult to measure especially in tectonically and geologically complex areas such as China and surrounding regions. On the other hand, gravity inversions have the greatest resolving power at shallow depths because gravity anomalies decrease in amplitude and increase in wavelength with increasing depth. Moreover, gravity measurements also supply constraints on rock density variations. Maceira and Ammon (2009) successfully applied this methodology to investigate the 3D shear velocity structure beneath the Tarim and Junggar basins in central Asia. Since then, LANL has been in the forefront of the development of joint inversion methods for high-resolution 3D modeling. During 2007 LANL researchers extended the surface wave/gravity inversion methodology to include P-wave teleseismic receiver functions (Rowe et al., 2007).

Method

Building on the mentioned previous efforts, we have added a fourth dataset to the simultaneous joint inversion methodology. The new 3D seismic velocity model of the crust and upper mantle results from the simultaneous joint inversion of surface wave dispersion observations, teleseismic *P*-wave receiver functions, gravity anomalies, and body wave (*P* and *S* phases) travel times. Surface wave dispersion measurements are primarily sensitive to vertical shear-wave velocity averages; while body wave receiver functions are sensitive to shear-wave velocity contrasts and vertical travel-times. Addition of the fourth dataset consisting of seismic body wave travel-time data helps to constrain the seismic wave velocities both vertically and horizontally in the model cells crossed by the ray paths.

We have based the addition of the fourth data set to our joint inversion code on the regional version of the double-difference (DD) tomography program *tomoDD* (Zhang and Thurber, 2003, 2006). DD tomography is a generalization of DD location (Waldhauser and Ellsworth, 2000) and it simultaneously solves for the 3D velocity structure and seismic event locations. DD tomography uses a combination of absolute and more accurate differential arrival times and hierarchically determines the velocity structure from larger scale to smaller scale. The differential times can be calculated from cross-correlation techniques for similar waveforms and by directly subtracting catalog arrival times for pairs of events at common stations.

The body-wave arrival time T from an earthquake i to a seismic station k is expressed using ray theory as a path integral,

$$T_k^i = \tau^i + \int_i^k u ds \tag{1}$$

where τ^i is the origin time of event i, u is the slowness field, and ds is an element of path length. The source coordinates ($x1$, $x2$, $x3$), origin times, ray paths, and the slowness field are the unknowns. The relationship between the arrival time and the event location is highly nonlinear, so a truncated Taylor series expansion is generally used to linearize equation (1). This linearly relates the misfit between the observed and predicted arrival times r_k^i to the desired perturbations to the hypocenter and velocity structure parameters:

$$r_k^i = \sum_{l=1}^{3} \frac{\partial T_k^i}{\partial x_l^i} \Delta x_l^i + \Delta \tau^i + \int_i^k \delta u ds. \tag{2}$$

Subtracting a similar equation for event j observed at station k from equation (2), we have

$$r_k^i - r_k^j = \sum_{l=1}^{3} \frac{\partial T_k^i}{\partial x_l^i} \Delta x_l^i + \Delta \tau^i + \int_i^k \delta u ds - \sum_{l=1}^{3} \frac{\partial T_k^j}{\partial x_l^j} \Delta x_l^j - \Delta \tau^j - \int_j^k \delta u ds. \tag{3}$$

Assuming that these two events are near each other so that the paths from the events to a common station are almost identical (Figure 1) and the velocity structure is known, then equation (3) can be simplified as

$$dr_k^{ij} = r_k^i - r_k^j = \sum_{l=1}^{3} \frac{\partial T_k^i}{\partial x_l^i} \Delta x_l^i + \Delta \tau^i - \sum_{l=1}^{3} \frac{\partial T_k^j}{\partial x_l^j} \Delta x_l^j - \Delta \tau^j, \tag{4}$$

where dr_k^{ij} is the so called double-difference (Waldhauser and Ellsworth, 2000) and equation (4) is known as the DD earthquake location algorithm. This term is the difference between observed and calculated differential arrival times for the two events and can also be written as

$$dr_k^{ij} = r_k^i - r_k^j = (T_k^i - T_k^j)^{obs} - (T_k^i - T_k^j)^{cal}. \tag{5}$$

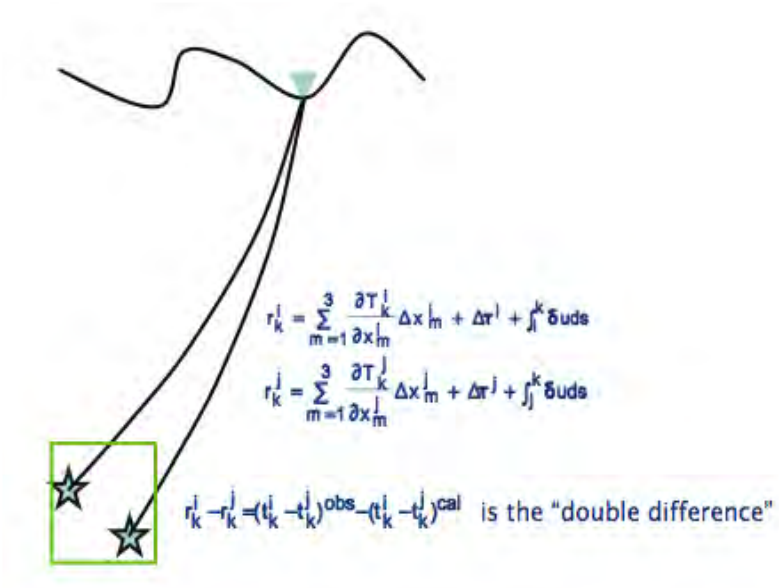

Figure 1. Sketch illustrating the DD concept for two close events (stars) recorded at the same station (triangle).

TomoDD is built upon the double-difference location code hypoDD written by Waldhauser (2001). In the original *tomoDD* algorithm, an approximate pseudo-bending (ART-PB) ray-tracing algorithm (Um and Thurber, 1987) is used to find the rays and calculate the travel times between events and stations. The model is represented by velocity values specified on a regular set of 3-D nodes and the velocity values are interpolated by using the linear B-spline interpolation method. The hypocentral partial derivatives are calculated from the direction of the ray and the local velocity at the source (Lee and Stewart, 1981). The ray path is divided into a set of segments and the model partial derivatives are evaluated by apportioning the derivative to its eight surrounding nodes according to their interpolation weights on the segment midpoint (Thurber, 1983).

TomoDD assumes a flat earth model and is appropriate for local scale problems (10's to 100's of kilometers). At the regional scale (100's to 1000's of kilometers), however, sphericity of the earth should be taken into account. Major velocity discontinuities such as Conrad, Moho, and subducting slab boundary should also be considered. The ART-PB approach assumes a continuous velocity model and cannot deal properly with velocity discontinuities. For this reason and considering that our focus region of study is continental scale, we use the regional DD seismic tomography method (*tomoFDD*) that deals effectively with discontinuous velocity structures without knowing them a priori. *TomoFDD* uses a finite-difference method for determining travel times and ray paths, and treats the spherical Earth by embedding it (in part or in whole) within a Cartesian ''box''. *TomoFDD* uses a regular inversion grid.

Data

We will first conduct the proposed research in the Asian continent (in particular, between 20° N to 60° N latitude and 65° E to 140° E longitude) to then extend it to the whole Eurasia. We have obtained all gravity data for the full region of interest. These gravity observations were extracted from the global gravity model derived from the Gravity Recovery and Climate Experiment (GRACE) satellite mission (Tapley et al., 2005). These observations represent free-air gravity anomalies. Free-air gravity anomalies contain information not only of the subsurface density but also of topography. While in flat areas this may not represent a problem, in this region of great relief the topographic effect should be removed (Figure 2). Therefore, free-air gravity anomalies were converted into simple Bouguer gravity anomalies considering the standard density of 2670 kg/m^3.

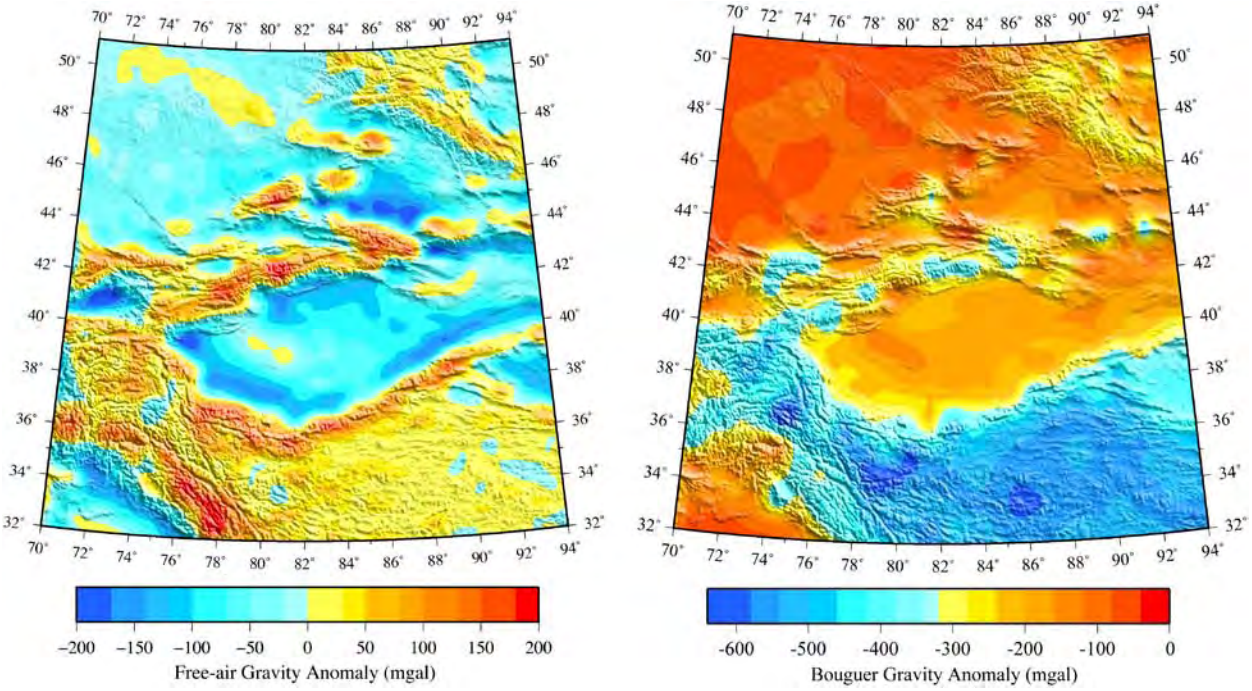

Figure 2. Gravity observations for the area surrounding the Tarim basin. (left) Free-air gravity anomalies extracted from the global gravity model derived from the GRACE satellite mission. Cold colors represent gravity lows meaning a mass deficit. Warm colors are gravity highs; (right) Bouguer gravity anomalies computed from the observations to the left.

We have obtained surface waves (Rayleigh and Love) dispersion observations for the Asian continent. These observations were generated considering the CUB (Colorado University at Boulder) surface wave tomographic models (Ritzwoller and Levshin, 1998; Levshin et al., 2001, 2002), and LANL Rayleigh wave slowness model (Maceira et al., 2005). In general, the tomographic patterns in these models (Figure 3) show a very good correlation with known geologic and tectonic features in the area.

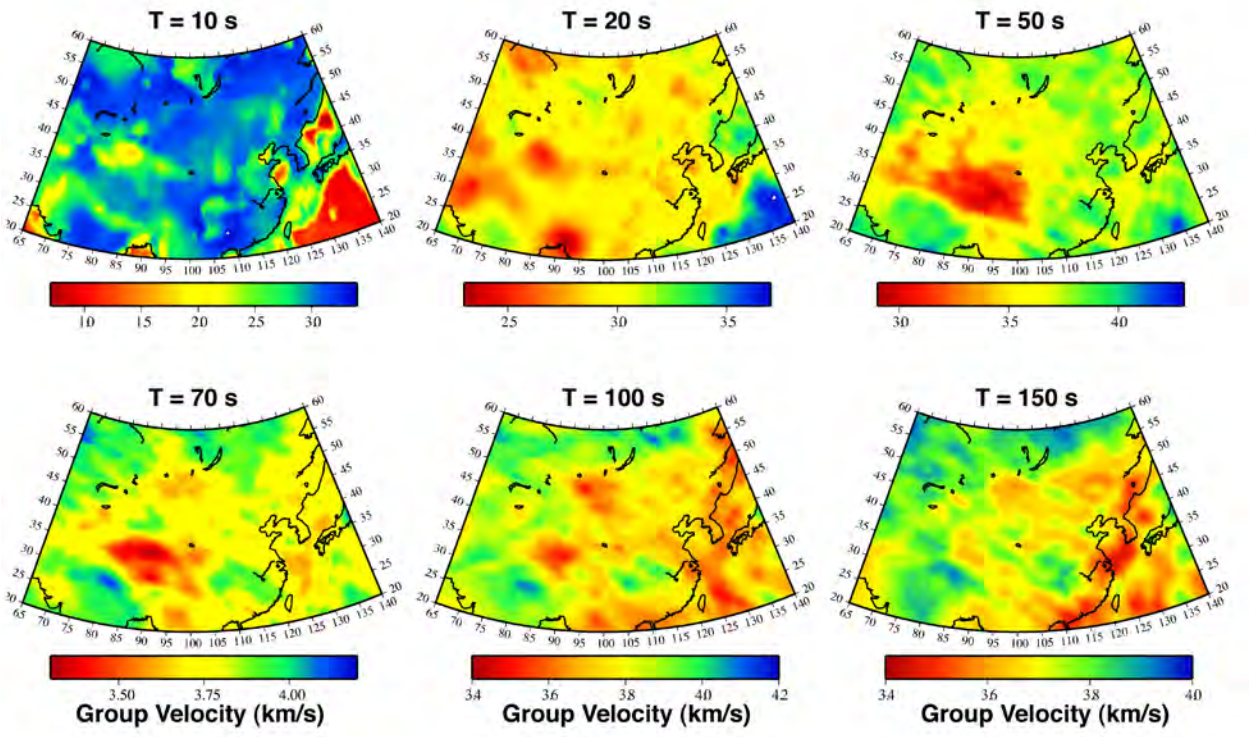

Figure 3. Fundamental mode Rayleigh wave group-velocity tomographic maps used to derive surface wave dispersion observations for each cell in our gridded model. Note that the color scale varies to preserve the details in each image.

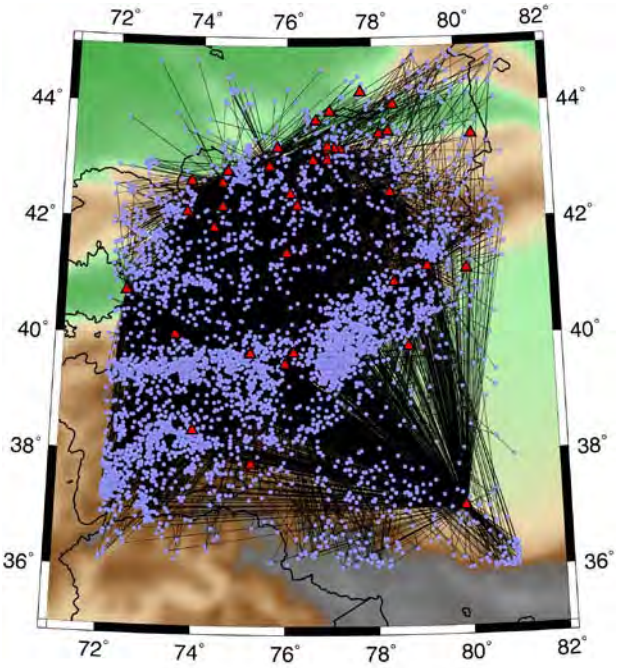

Figure 4. *S*-wave raypaths used for testing the joint inversion of 4 independent datasets. Red triangles are stations; blue dots are events.

The study area is seismically very active providing us with thousands of earthquakes recorded at regional and teleseismic distances. We have retrieved body wave travel time observations for 38 stations and 4,315 events in a small region in northwest China (Figure 4). These observations were retrieved from the LANL Knowledge Base. They represent a very small subset of all the available data and are being used to test the simultaneous joint inversion methodology of these 4 data sets.

We have obtained teleseismic *P*-wave receiver functions for 53 stations across the Asian continent. These observations were obtained via a joint Pennsylvania State University (PSU) and LANL effort (Ammon et al., 2004).

Preliminary results

We are testing the simultaneous joint inversion technique for the four datasets mentioned above in a small region that comprises the northwest corner of the Tarim basin. Figure 5 shows preliminary 3D shear wave velocity variations at constant depths of 5, 15, 27, and 52.5 km. Please note that the color scale is different for each depth slice.

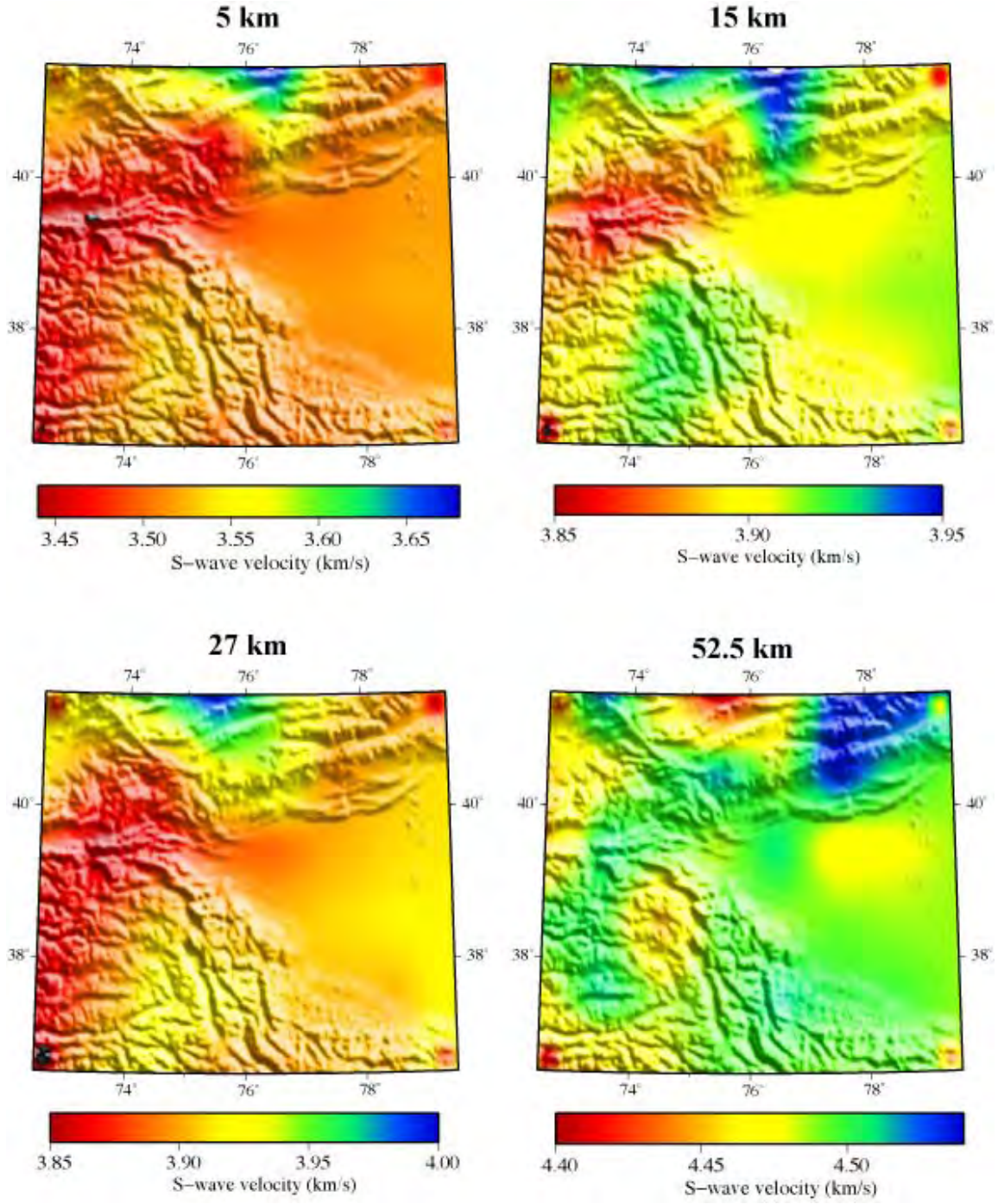

Figure 5. Preliminary *S*-wave velocity model at constant depth slices. The depth of each image is shown at the top of each map. Note the color scheme different for each image.

The results shown on Figure 5 are still preliminary and much work is still needed regarding the relative weighting of the four independent datasets as well as smoothing constrains and inclusion of *a priori* information into our inversion scheme.

Relations between seismic velocities and density

One of the difficulties with joint inversions is to determine a relationship between the independent data sets. In this case, we require constraints between seismic velocities and density. There is not a unique and universal relationship applicable to all types of lithologies at every single depth under all possible conditions of temperature and pressure. We are testing three different relationships between seismic velocities and density: (1) a combination of two existing empirical relationships; one more suitable for sedimentary rocks after Nafe and Drake (1963) and the well-known Birch's (1961) law more appropriate for basement rock; (2) Brocher's (2005); and (3) Harkrider's (see Acknowledgements). The testing area is a region in east Africa (Figure 5) where we have obtained on-land Bouguer gravity measurements (Ebinger et al., 1993; Tiberi et al., 2005) which we combine with LLNL surface wave tomographic models (Pasyanos and Nyblade, 2007). These sensitivity studies will ensure the validity of the relations used in our 3D seismic imaging efforts.

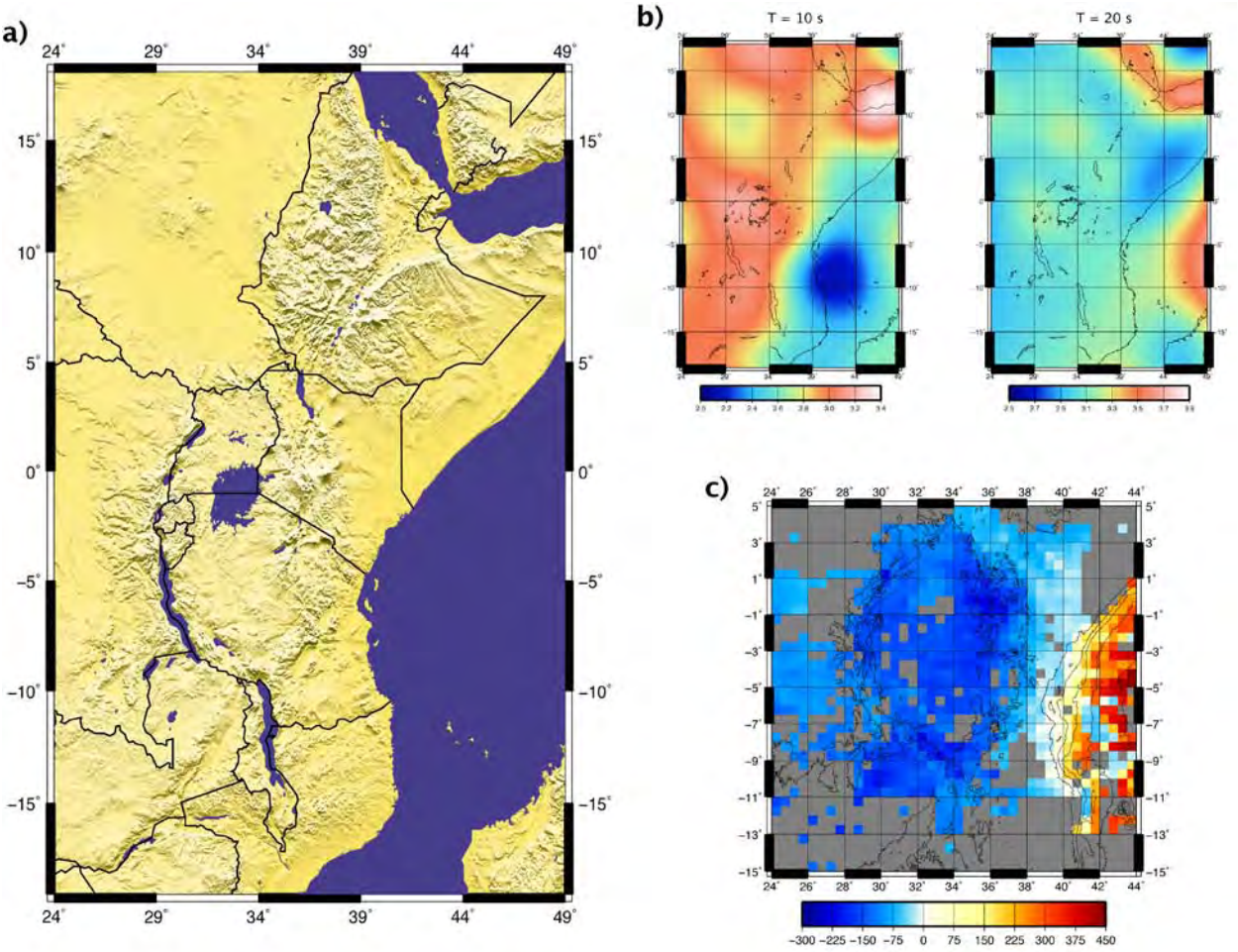

Figure 6. (a) Topographic map of East Africa; (b) Rayleigh wave group-velocity tomographic maps for the same area shown in (a) from Pasyanos and Nyblade (2007); (c) Bouguer gravity anomalies for the area under study from Ebinger et al. (1993).

CONCLUSIONS AND RECOMMENDATIONS

We have initiated a three-year project to map the three-dimensional (3D) seismic structure of the crust and upper mantle using seismic dispersion, gravity, receiver function, and travel time observations. 3D geophysical model development through the simultaneous inversion of complementary data sets to reduce uncertainty and bias is the future of 3D modeling. Geophysical models play an important role in Ground-based Nuclear Explosion Monitoring (GNEM). To more confidently and accurately detect, locate, and identify small seismic events, better high-resolution 3D structural models are needed. Therefore, the ongoing research directly addresses this challenge, and our results will also be of fundamental importance for understanding the geodynamic evolution and formation of continents, as well as the processes acting within and on the continental lithosphere.

We are first focusing on the Asian continent, an area of prime importance to NEM, and where we know there are adequate calibration events to validate our model and quantify its accuracy. We will then extend the modeling efforts to other regions including aseismic areas of interest to NEM.

Building on previous efforts, we have added body waves travel time observations to our simultaneous joint inversion technique. We now face the main challenge of relative weighting of the four independent datasets as well as smoothing constrains and inclusion of *a priori* information into our inversion scheme.

ACKNOWLEDGEMENTS

Special thanks to Cindy Ebinger for kindly providing us with her gravity measurements. We thank Anatoli Levshin, Michael Ritzwoller, and Mike Pasyanos for allowing us to use their tomographic maps for this research. Thanks also to Chuck Ammon for providing us with the receiver function observations. We thank the scientists, engineers, and technicians that have created the seismic recording systems and networks that provide excellent broad-band seismic observations. In particular, we thank the USGS and the IRIS Consortia (NSF) who share information and data with the global community in an effective and efficient manner. Thanks to Paul Wessel and Walter Smith for developing and maintaining their Generic Mapping Tool (GMT) that we use to create many of the illustrations used in our research. Many thanks to David Harkrider for valuable information gleaned from personal communication. Finally, our thanks to Jody Benson and Marv Wetovsky for editorial assistance.

REFERENCES

Aki, K., A. Christoffersson, and E. S. Husebye (1977). Determination of the three-dimensional seismic structure of the lithosphere, *J. Geophys. Res*. 82: 277–296.

Ammon, C. J., W. Sevilla, R. B. Herrmann, and G. E. Randall (2004). Systematic inversion of receiver functions and surface wave dispersion for crustal structure in central Asia, in *Proceedings of the 26th Seismic Research Review: Trends in Nuclear Explosion Monitoring*, LA-UR-04-5801, Vol.1, pp. 29–38.

Birch, F. (1961). The velocity of compressional waves in rocks to 10 kilobars, part 2, *J. Geophys. Res*. 66: 2199– 2224.

Brocher, T. M. (2005). Empirical relations between elastic wavespeeds and density in the Earth's crust, *Bull. Seismol. Soc. Am.* 95: 2081–2092.

Ebinger, C. J., A. L. Deino, A. L. Tesha, T. Becker, and U. Ring (1993). Tectonic controls on rift basin morphology: Evolution of the northern Malawi (Nyasa) rift, *J. Geophys. Res*. 98: 17821–17836.

Huang, Z., W. Su, Y. Peng, Y. Zheng, and H. Li (2003). Rayleigh wave tomography of China and adjacent regions, *J. Geophys. Res*. 108: doi:10.1029/2001JB001696.

Julià, J., C. J. Ammon, R. B. Herrmann, and A. M. Correig (2000). Joint inversion of receiver function and surface wave dispersion observations, *Geophys. J. Int*. 143: 99–112.

Julià, J., C. J. Ammon, and R. B. Herrmann (2003). Lithospheric structure of the Arabian shield from the joint inversion of receiver functions and surface wave dispersion, *Tectonophysics,* 371: 1–21.

Julià, J., C. J. Ammon, and A. A. Nyblade (2005). Evidence for mafic lower crust in Tanzania, East Africa, from joint inversion of receiver functions and Rayleigh wave dispersion velocities, *Geophys. J. Int.* 162: 555–569.

Jupp, D. L. B, and K. Vozoff (1975). Stable iterative methods for the inversion of geophysical data, *Geophys. J. R. Astr. Soc*. 42: 957–976.

Lee, W. H. K., and S. W. Stewart (1981). Principles and applications of microearthquake networks, *Adv. Geophys. Suppl.* 2, 293 pp.

Lees, J. M., and J. C. VanDecar (1991). Seismic tomography constrained by Bouguer gravity anomalies: Applications in western Washington, *Pure and Appl. Geophys*. 135: 31–52.

Levshin, A. L., M. H. Ritzwoller, M. P. Barmin, and J. L. Stevens (2001). Short period group velocity measurements and maps in central Asia, in *Proceedings of the 23rd Seismic Research Review: Worldwide Monitoring of Nuclear Explosions*, LA-UR-01-4454, Vol. 1, pp. 258–269.

Levshin, A. L., J. L. Stevens, M. H. Ritzwoller, and D. A. Adams (2002). Short-period (7-s to 15-s) group velocity measurements and maps in central Asia, in *Proceedings of the 24th Seismic Research Review—Nuclear Explosion Monitoring: Innovation and Integration,* LA-UR-02-5048, Vol. 1, pp. 97–106.

Lines, L. R., A. K. Schultz, and S. Treitel (1988). Cooperative inversion of geophysical data, *Geophysics* 53: 8–20.

Maceira, M. and C. J. Ammon (2009). Joint inversion of surface wave velocity and gravity observations and its application to Central Asian basins shear velocity structure, *J. Geophys. Res*. 114: B02314, doi:10.1029/2007JB005157.

Maceira, M. and C. J. Ammon (2006). Joint inversion of surface wave velocity and gravity observations and its application to Central Asian basins shear velocity structure, *Seismol. Res. Lett*. 77: 2, 297.

Maceira, M., S. R. Taylor, C. J. Ammon, X. Yang, and A.A. Velasco (2005). High Resolution Rayleigh Wave Slowness Tomography of Central Asia, *J. Geophys. Research*., 110: No. B6, B06304, doi:10.1029/2004JB003429.

Nafe, J. E., and C. L. Drake (1963). Physical properties of marine sediments, in *The Sea*, vol. 3, edited by M. N. Hill, pp. 794–815, Interscience, New York.

Onizawa, S., H. Mikada, H. Watanabe, and S. Sakashita (2002). A method for simultaneous velocity and density inversion and its application to exploration of subsurface structure beneath Izu-Oshima volcano, Japan, *Earth Planets Space* 54: 803–817.

Oppenheimer, D. H., and K. E. Herkenhoff (1981). Velocity-density properties of the lithosphere from three-dimensional modeling at the Geysers-Clear Lake region, California, *J. Geophys. Res*. 86: 6057–6065.

Parsons, T., R. J. Blakely, and T. M. Brocher (2001). A simple algorithm for sequentially incorporating gravity observations in seismic traveltime tomography, *International Geol. Rev*. 43: 1073–1086.

Pasyanos, M. E., and A. A. Nyblade (2007). A top to bottom lithospheric study of Africa and Arabia, *Tectonophys.* 444: 27–44.

Ritzwoller, M. H. and A. L. Levshin (1998). Eurasian surface wave tomography: group velocities, *J. Geophys. Res*. 103: 4839–4878.

Rowe, C. A., W. S. Phillips, M. Maceira, M. Begnaud, L. Steck, X. Yang, C. Lucero, H. Hartse, R. Stead, K. Mackey, K. Fujita, and C. Ammon (2007). Geophysical Imaging of Asia and Siberia: Tomograhy for Seismic Velocity, Upper Mantle Gradient, Lg Attenuation, and Joint Inversion of Surface Wave Dispersion, Receiver Functions and Satellite Gravity Data, in *Proceedings of the 29th Monitoring Research Review: Ground-Based Nuclear Explosion Monitoring Technologies*, LA-UR-07-5613, Vo. 1, pp. 256–265.

Tapley, B., et al. (2005). GGM02 - An improved Earth gravity field model from GRACE, *J. Geodesy*, DOI 10.1007/s00190-005-0480-z.

Tiberi, C., C. Ebinger, V. Ballu, G. Stuart, and B. Oluma (2005). Inverse models of gravity data from the Red Sea-Aden–East African rifts triple junction zone, *J. Geophys. Int*. 163: 775–787.

Thurber, C. H. (1983). Earthquake locations and three-dimensional crustal structure in the Coyote Lake area, central California, *J. Geophys. Res.* 88: 8226–8236.

Um, J., and C. H. Thurber (1987). A fast algorithm for two-point seismic ray tracing, Bull. Seism. Soc. Am. 77: 972–986.

Villaseñor, A., M. H. Ritzwoller, A L. Levshin, M. P. Barmin, E. R. Engdahl, W. Spakman, and J. Trampert (2001). Shear velocity structure of central Eurasia from inversion of surface wave velocities, *Phys. Earth Planet. Inter.* 123: 169–184.

Waldhauser, F. (2001). hypoDD: a computer program to compute double difference hypocenter locations, *U.S. Geol. Surv. Open File Rept. 01-113*, 25 pp.

Waldhauser, F., and W. L. Ellsworth (2000). A double-difference earthquake location algorithm: method and application to the northern Hayward Fault, California, *Bull. Seism. Soc. Am.* 90: 1353–1368.

Zhang, H., and C. Thurber (2006). Development and applications of double-difference tomography, *Pure and Applied Geophys.*, 163, 373-403, doi:10.1007/s00024-005-0021-y.

Zhang, H., and C. H. Thurber (2003). Double-Difference Tomography: The Method and Its Application to the Hayward Fault, California, *Bull. Seism. Soc. Am*. 93: 1875–1889.

ANALYSIS OF DIGITIZED SEISMOGRAMS FROM RUSSIAN GEOPHYSICAL SURVEY STATIONS OF SOVIET PEACEFUL NUCLEAR EXPLOSIONS

Kevin G. Mackey[1] and Hans E. Hartse[2]

Michigan State University[1] and Los Alamos National Laboratory[2]

Sponsored by the Air Force Research Laboratory

Award No. FA8718-08-C-0018

ABSTRACT

Throughout the 1970s and 1980s, the permanent seismic stations of the Soviet Union recorded over 100 peaceful nuclear explosions (PNEs) detonated within the Soviet Union. These records represent a large data set that has not been fully utilized. Digitization and analysis of the historic seismograms has allowed the extension of long-range PNE profile data into geographic regions not previously covered. Although the resolution of the profiles is limited by the distribution of permanent seismic stations operating at the time, the first long range profiles have been constructed through the Magadan and Chukotka regions. The Magadan region profile indicates velocities slower than those found from Kimberlite-4, the closest of the old PNE profiles. Western portions of the Magadan profile associated with the Siberian Platform and western Verkhoyansk Fold Belt are elevated relative to iasp91. Beyond the platform in the tectonically active areas, velocities are reduced and closer to iasp91. The Chukotka profile shows elevated velocities relative to iasp91, which decreases at station Zyryanka on the Kolyma-Omolon Superterrane. The delayed P arrival may be an effect of the large Indigirka-Zyryanka Basin in the vicinity of the station. Continuing east through Chukotka, velocities are much closer to iasp91. The digitized historic seismograms will be useful for explosion discrimination and other studies if the data are reliable and of sufficient quality. A direct comparison relating digitized short-period photopaper records to modern digital data was conducted to establish the range of useful frequency content and quality of data. For this study, digitized short period (Russian SKM seismometer) photopaper seismograms recorded at Yuzhno Sakhalinsk from September 2008 were compared to seismograms from the IRIS GSN station at Yuzhno Sakhalinsk (YSS). Seismograms show nearly identical waveforms and amplitude content in the 1-5 Hz range for all three components. Below 1 Hz, the amplitude response of the digitized records drops-off due to different instrument responses, but is probably correctable down to about 0.3 Hz. From 5-8 Hz, the general amplitude response is similar, though specific frequency spikes do not correlate well and there is deterioration in the correlation of waveforms. The digitized PNE data will result in useful seismic discriminants that utilize frequencies in the 1-5 Hz range for many different regions of Eurasia.

OBJECTIVES

This study seeks to obtain, scan, digitize, and analyze seismograms from Soviet permanent seismic station networks of Soviet PNEs. The analysis seeks to better resolve the crustal and velocity structure of Russia, particularly the Russian Far East where Deep Seismic Sounding (DSS) profiles using the PNEs were not conducted.

RESEARCH ACCOMPLISHED

Seismogram Acquisition and Digitization

We are working with the Institute for Petroleum Geology and Geophysics (IPGG) in Novosibirsk and several other institutes and seismic networks to assemble, digitize, and analyze PNE seismograms from seismic stations of the regional networks of Russia. Figure 1 shows the raypaths of seismograms already collected and scanned or digitized in this study. The original photopaper records are scanned at high resolution (usually 600 dpi) to preserve faint traces. The digitization process is manual, with as many points along the trace entered as needed to create an un-aliased waveform (Figure 2). The digitized seismogram is then re-sampled at 20 or 50 sps, depending on the frequency content of the seismic signal, regional trends in the data are removed, time corrections are applied, and amplitudes are converted to microns.

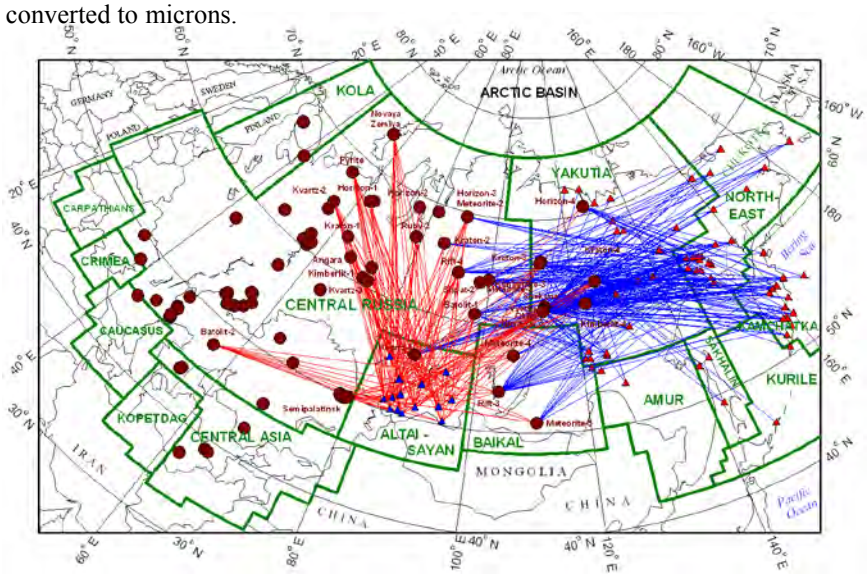

Figure 1. Raypath coverage of PNE seismograms acquired, scanned, and/or digitized for this study. Large dots indicate PNE locations and triangles indicate seismic stations. Blue paths indicate MSU holdings and red are IPGG holdings.

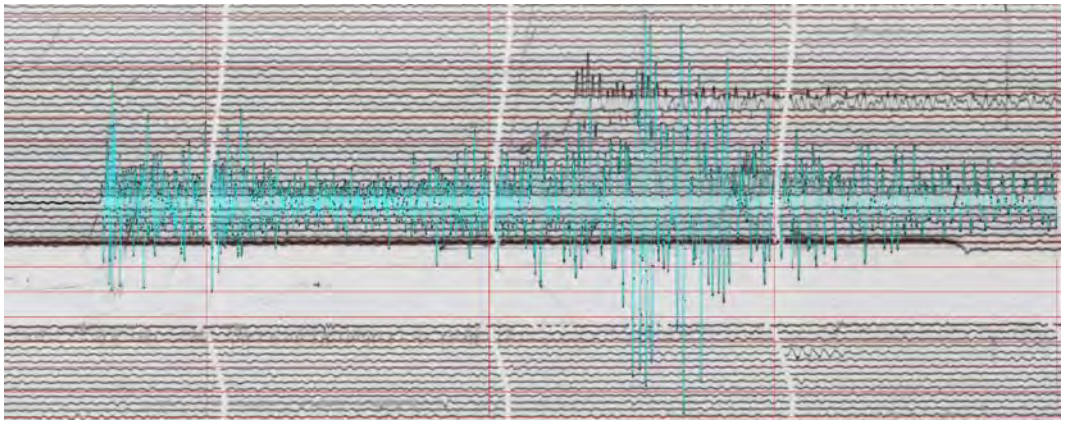

Figure 2. Sample record of the digitization process showing the vertical component of the Neva 2-2 PNE as recorded at Ust'Nyukzha (746 km distant).

Quality of Digitized Seismograms

To verify the quality of data from the digitized photo paper records, it is necessary to make a direct comparison with modern digital data. Many of the seismograms collected here are from sites currently operating as IRIS GSN digital stations, though conduction of the PNEs ceased prior to the opening of these Russian digital stations. Fortunately, as a part of their tsunami warning system, Yuzhno Sakhalinsk continues to operate an older style photo paper station co-located and in parallel with the IRIS GSN station at Yuzhno Sakhalinsk (YSS). The tsunami warning station is 3-component and records short period (0.3-0.83 second dominant period) SM-3 seismometers. Recording is on photo paper at 60 mm/min with an amplification of 22,230, and appears to use the older radio-clock timing system. In virtually all aspects, the YSS tsunami warning station and its seismograms are identical to those being digitized in this study.

Several Yuzhno Sakhalinsk tsunami warning station photo paper seismograms containing a variety of event sizes and hypocentral distances from September 2008 were acquired. The seismograms were scanned at 600 dpi and digitized in the same manner as the PNE records in this study. To preserve a truly independent analysis and quality test of the digitized waveforms, digital data from the co-located IRIS GSN station (YSS) was not viewed or referenced in any way during the selection or digitization of the photo paper records.

The waveforms, amplitudes, and frequency content of events digitized from the photo paper records and those recorded at the IRIS GSN station were compared. Generally, seismograms show nearly identical waveforms and amplitude content in the 1-5 Hz range for all three components. Below 1 Hz, the amplitude response of the digitized records drops-off due to different instrument responses, but is probably correctable down to about 0.3 Hz. From 5-8 Hz, the general amplitude response is similar, though specific frequency spikes do not correlate well and there is deterioration in the correlation of waveforms. The frequency responses and waveform correlation vary slightly from event to event.

Two specific test examples are shown. The first, depicted in Figure 3, is a small local event about 20 km from station YSS. Figure 3a plots the raw 3 component digitized data derived from the photo paper record. Figures 3b–d, left, compare the frequency-amplitude content of the GSN and digitized photo paper data of both the complete event waveform and a representative section of background noise. The Z and E-W components match very well in the 1–5-Hz range having nearly the same amplitudes and peaks in the response. From 5–7 Hz, the amplitude responses of the GSN data are higher on the Z component, and lower on the E-W component, but with peaks at the same frequencies. The N-S component responses match similar amplitudes from low frequencies through about 7 Hz, though there are discrepancies in the peak locations above 2 Hz. Figures 3b-d, right, depict waveform overlays by component of the GSN and digitized photo paper data bandpass filtered 1–5 Hz. For all three components, comparison of the overlaid components reveals several things. The overall character of the waveform is nearly identical. Virtually all the waveform peaks from the hand digitized data match those of the GSN data in terms of time, frequency, and shape. Inflections in both seismic traces also match quite well. One discrepancy that we note is a lower amplitude first motion on the GSN trace compared to the hand digitized data.

The second test example, shown in Figure 4, is a larger, deep event several hundred kilometers distant. Figure 4a plots the raw 3 component digitized data derived from the photo paper record. Figures 4b-d, left, compare the frequency-amplitude content of the GSN and digitized photo paper data of both the complete event waveform and a representative section of background noise. All components match very well in the 0.9–5-Hz range with nearly identical shapes in the response curve. From about 0.3–0.9 Hz, the response curves show the same peaks, but diverge with lower frequency. At frequencies above 5 Hz, the overall response is similar though individual peaks generally do not correlate. Figures 4b-d, right, depict waveform overlays by component of the GSN and digitized photo paper data bandpass filtered 1–5 Hz. As in Figure 3 above, the overall character of the waveform is nearly identical. Virtually all the waveform peaks from the hand digitized data match those of the GSN data in terms of time, frequency, and shape. Inflections in both seismic traces also match quite well.

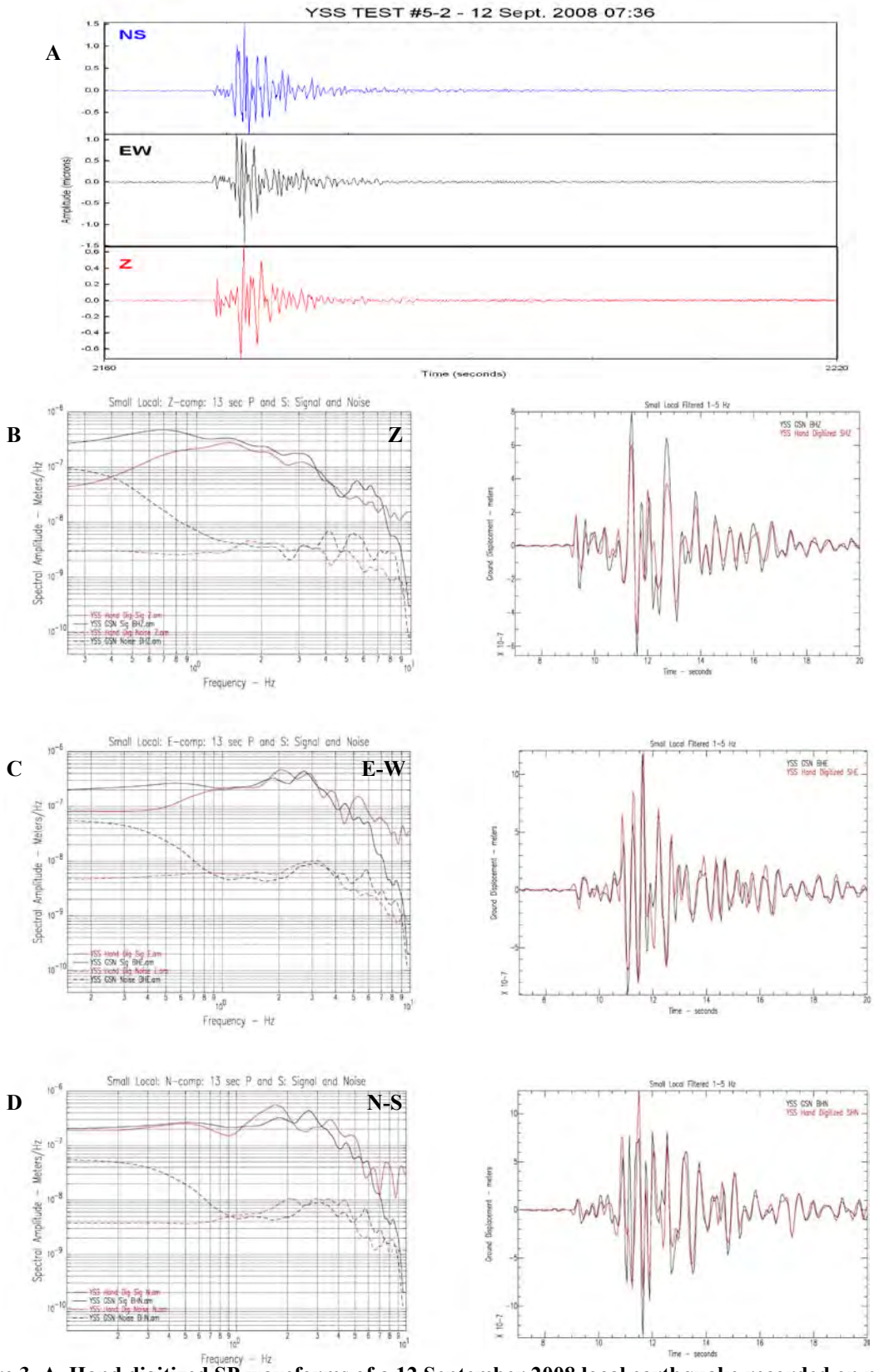

Figure 3. A. Hand digitized SP waveforms of a 12 September 2008 local earthquake recorded on photo paper at Yuzhno Sakhalinsk. B-D. Comparisons of frequency responses (left) and waveforms (right) of the digitized data to GSN data from the co-located IRIS station (YSS). Components are, top to bottom, Z, E-W, and N-S.

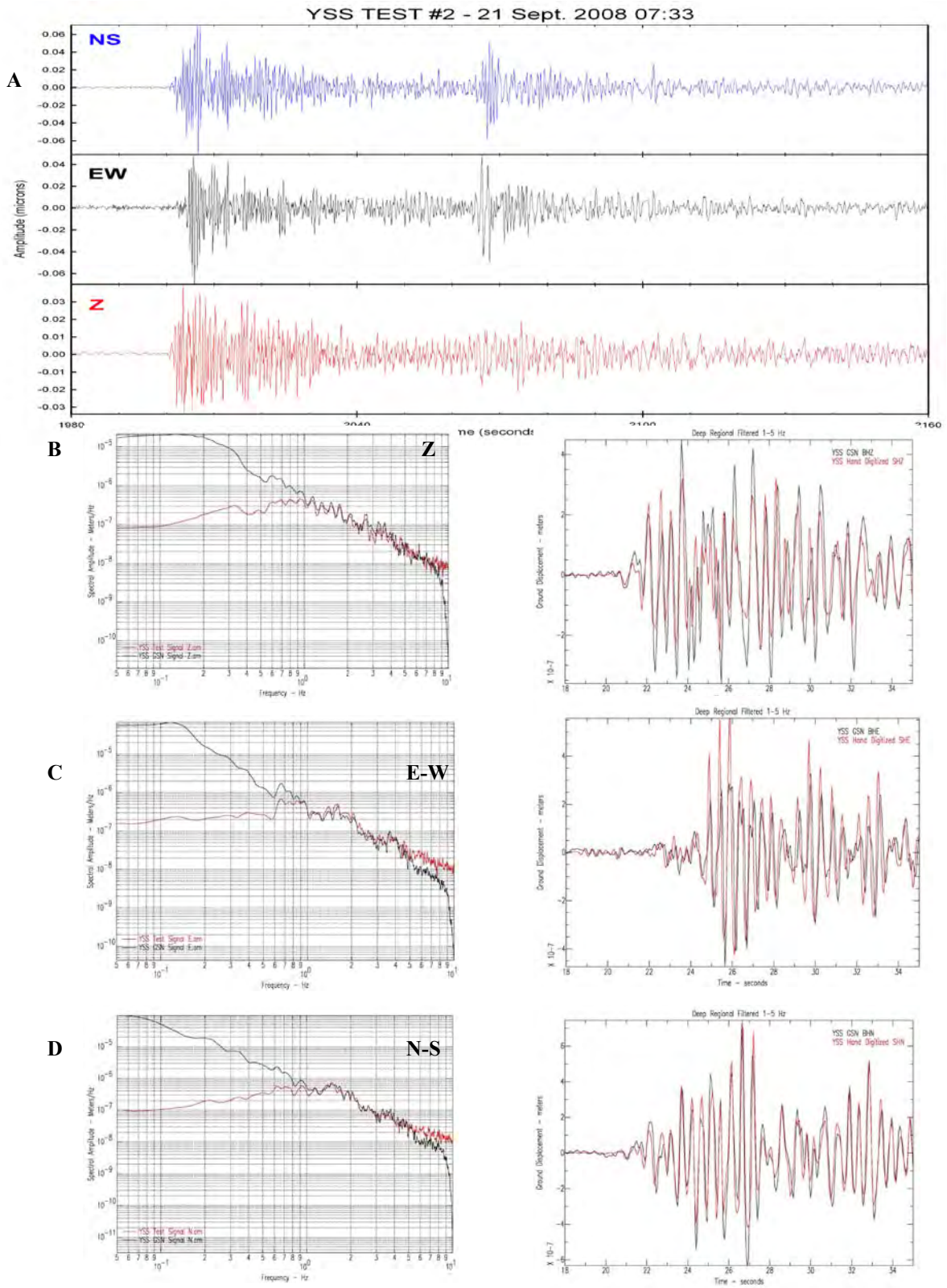

Figure 4. A. Hand digitized SP waveforms of a 21 Sept. 2008 regional earthquake recorded on photo paper at Yuzhno Sakhalinsk. B-D. Comparisons of frequency responses (left) and 1-5 Hz filtered waveforms (right) of the digitized data to GSN data from the co-located IRIS station (YSS). Components are, top to bottom, Z, E-W, and N-S.

Nuclear Explosion Discrimination

The digitized seismograms produced in this study allow the first possibility of using digital seismic data to develop seismic discriminants for many regions of the former Soviet Union as well as at specific stations. Many of the stations for which we are digitizing seismograms are now GSN or CTBTO sites, but did not become so until after cessation of most testing, thus there is no digital base of nuclear explosion records. Most of the GSN or CTBTO stations are situated at the longer-running, historic station sites that have the most extensive archives of PNEs.

A comparison of the 23 July 1987 Neva 2-2 PNE (15 kt; m_b 5.1) and a southern Yakutia earthquake (26 April 1994; m_b 5.3) as recorded at Yakutsk (Figure 5 inset). The PNE is digitized to 20 sps from the short period analog record, and the earthquake is from the digital GSN station (YAK). Seismograms are plotted both as raw data (Figure 5 top) and with a 4 Hz high pass filter (Figure 5 bottom). In both cases, relative Lg/P amplitude ratios are high for the earthquake (green) and low for the PNE (red).

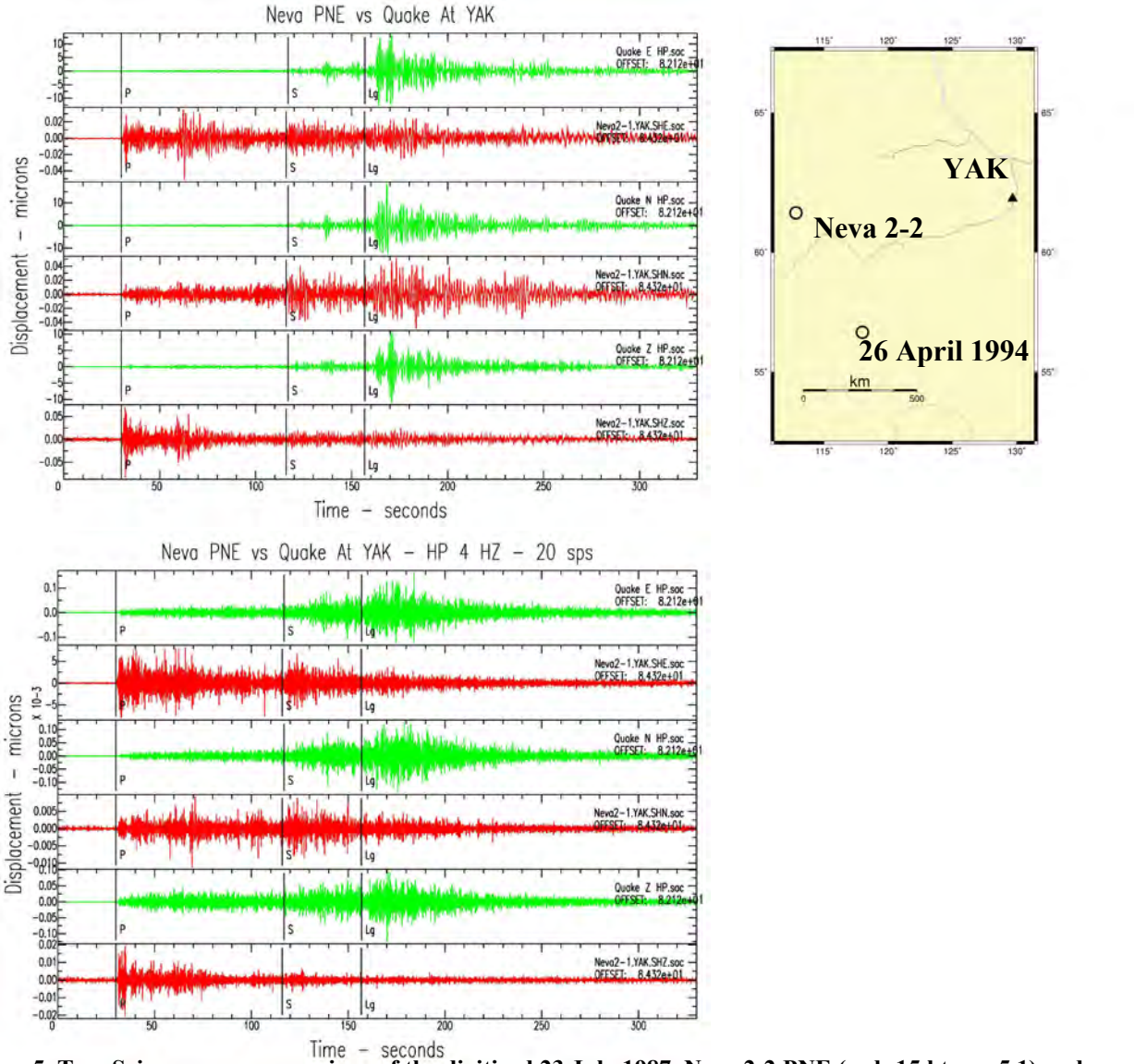

Figure 5. Top. Seismogram comparison of the digitized 23 July 1987, Neva 2-2 PNE (red; 15 kt; m_b 5.1) and a southern Yakutia earthquake (green; 26 April 1994; m_b 5.3) as recorded at Yakutsk. Bottom. The same seismograms with a 4-Hz high pass filter applied. In both cases, the differences in the Lg/P ratios can discriminate the events. Locations of the PNE, earthquake, and station Yakutsk (YAK) shown on map.

Seismic Record Sections

The distribution of seismic stations and PNEs allow seismic record sections to be produced, both as a multiple source composite as well as a single source profile. Using the Neva PNEs, we produce three specific profiles (Figure 6). The Magadan and Chukotka profiles extending eastward are the first extension of the PNE profiles through this area. The Magadan profile (Figure 7) indicates velocities essentially identical to those from the Kimberlite-4 profile in the Siberian Platform, which includes stations Yakutsk and Khandyga. The Siberian Platform portion of the Magadan profile intersects the Kimberlite-4 profile between the Neva site and station Yakutsk, thus our result is consistent. Velocities drop relative to Kimberlite-4 at station Nezhdaninsk located in the Verkhoyansk fold and thrust and the first profile station located off the Siberian Platform. Relative to iasp91 (I-91), velocities in the western portions of the Magadan profile associated with the Siberian Platform and western Verkhoyansk Fold Belt are elevated relative to I-91. Beyond the platform in the tectonically active areas, velocities are reduced and closer to I-91. The Chukotka profile (Figure 8) shows elevated velocities relative to I-91, which quickly decreases at station Zyryanka on the Kolyma-Omolon Super Terrane. The delayed *P* arrival may be an effect of the large Zyryanka Basin in the vicinity of the station. Continuing east through Chukotka, velocities are much closer to I-91. The Altai profile (Figure 9) shows velocities consistently elevated relative to I-91, which may be a result of paths contained almost entirely within the Siberian Platform. A sample composite record section from many PNEs as recorded by Altai-Sayan network stations is shown in Figure 10. The composite record section is representative of the Siberian Platform.

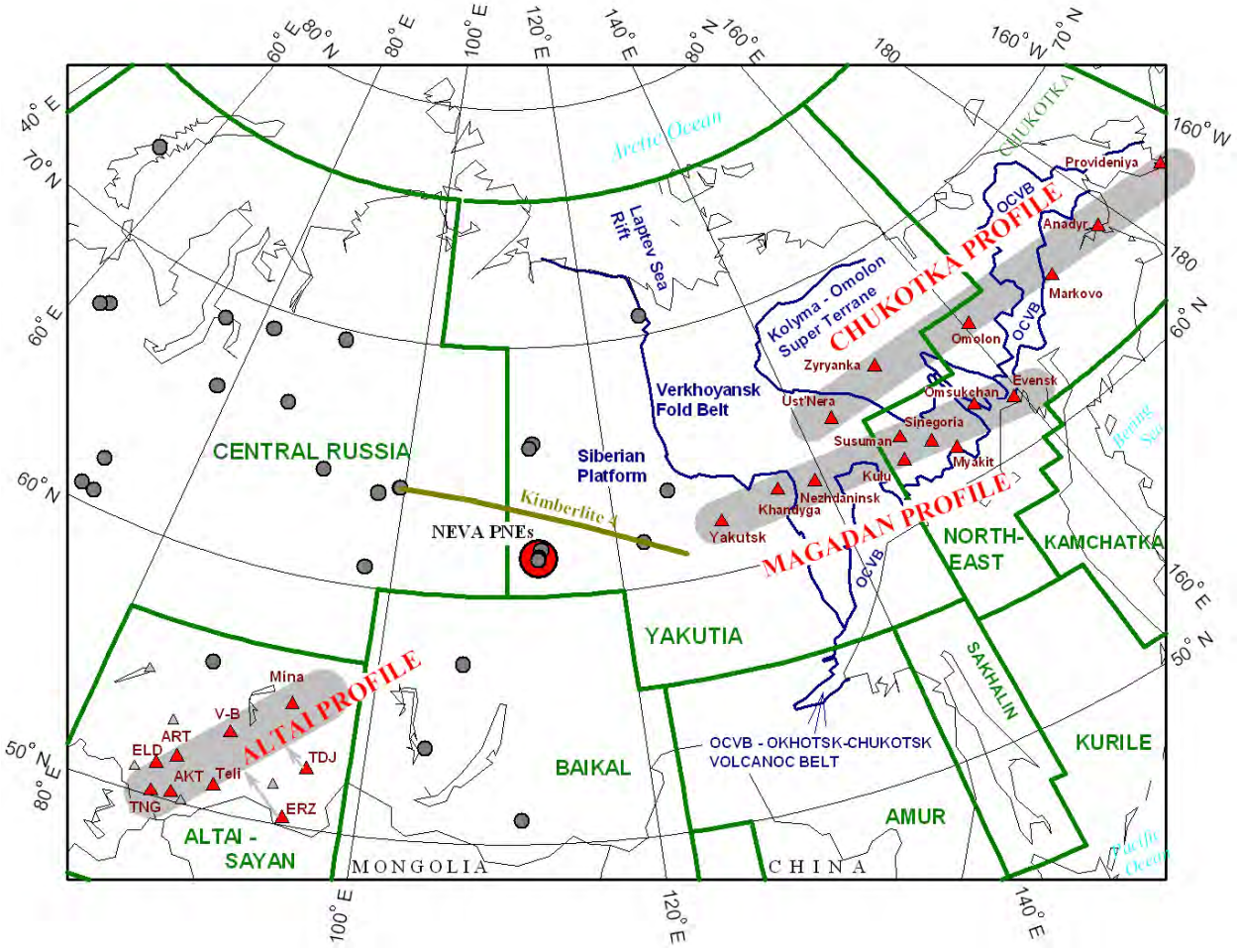

Figure 6. Index map of record sections displayed in Figures 7-10 class. The Magadan, Chukotka, and Altai profiles all use data from the Neva PNEs with stations used shown in red and labeled. The composite record section in Figure 10 used PNEs throughout Siberia (gray dots) and all stations of the Altai-Sayan seismic Network (all triangles in that region). Seismic networks shown and named in green and generalized tectonic provinces in the Russian Far-East shown in blue.

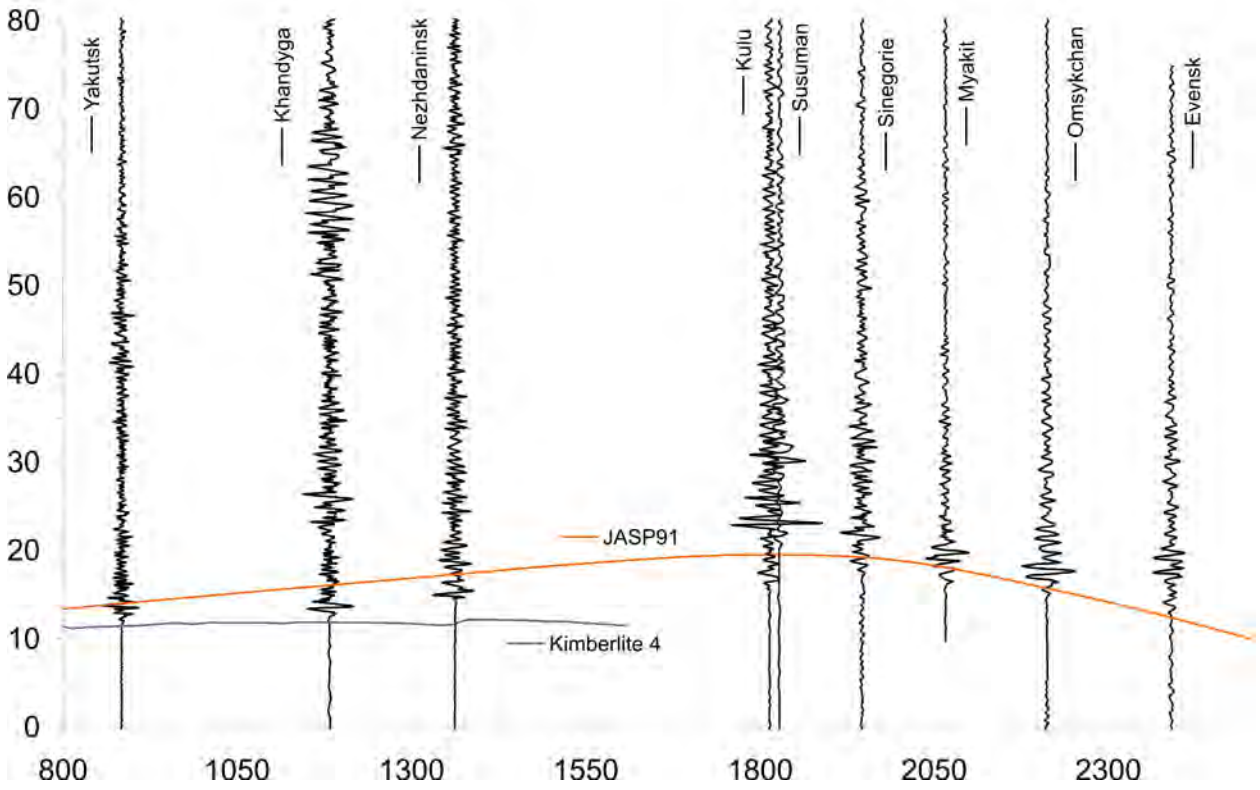

Figure 7. Record section crossing the Magadan region from the Neva PNEs. Reduction velocity is 9.0 km/sec.

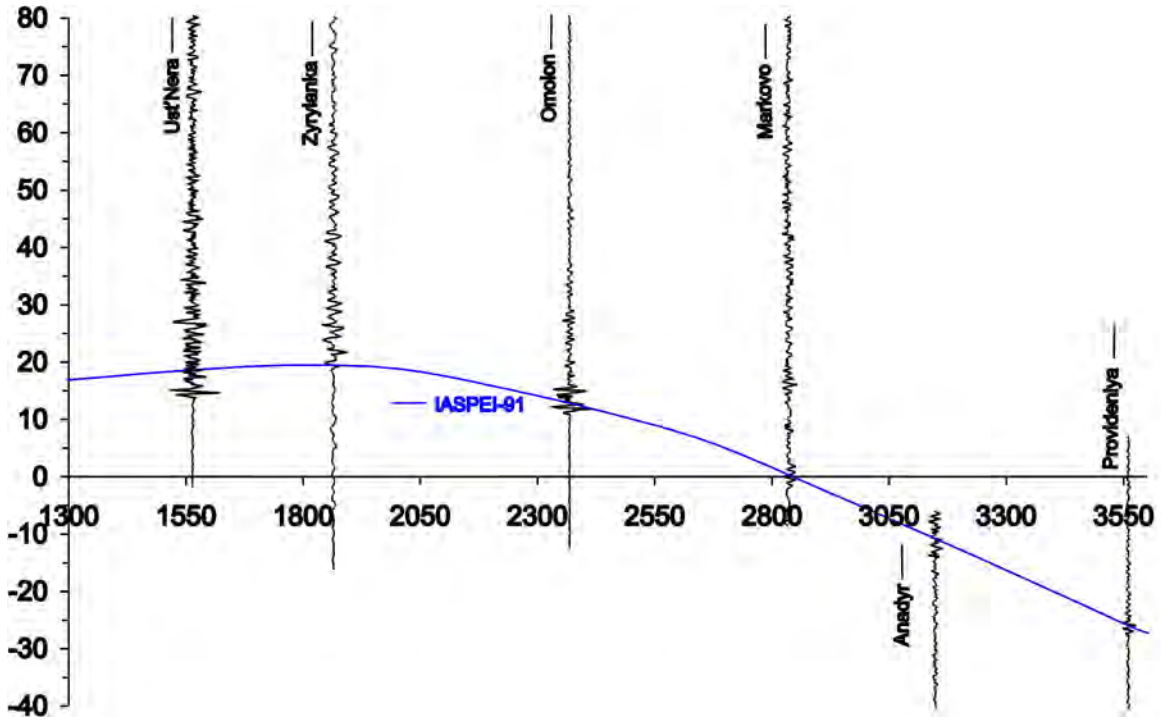

Figure 8. Record section crossing Chukotka from the Neva PNEs. Reduction velocity is 9.0 km/sec.

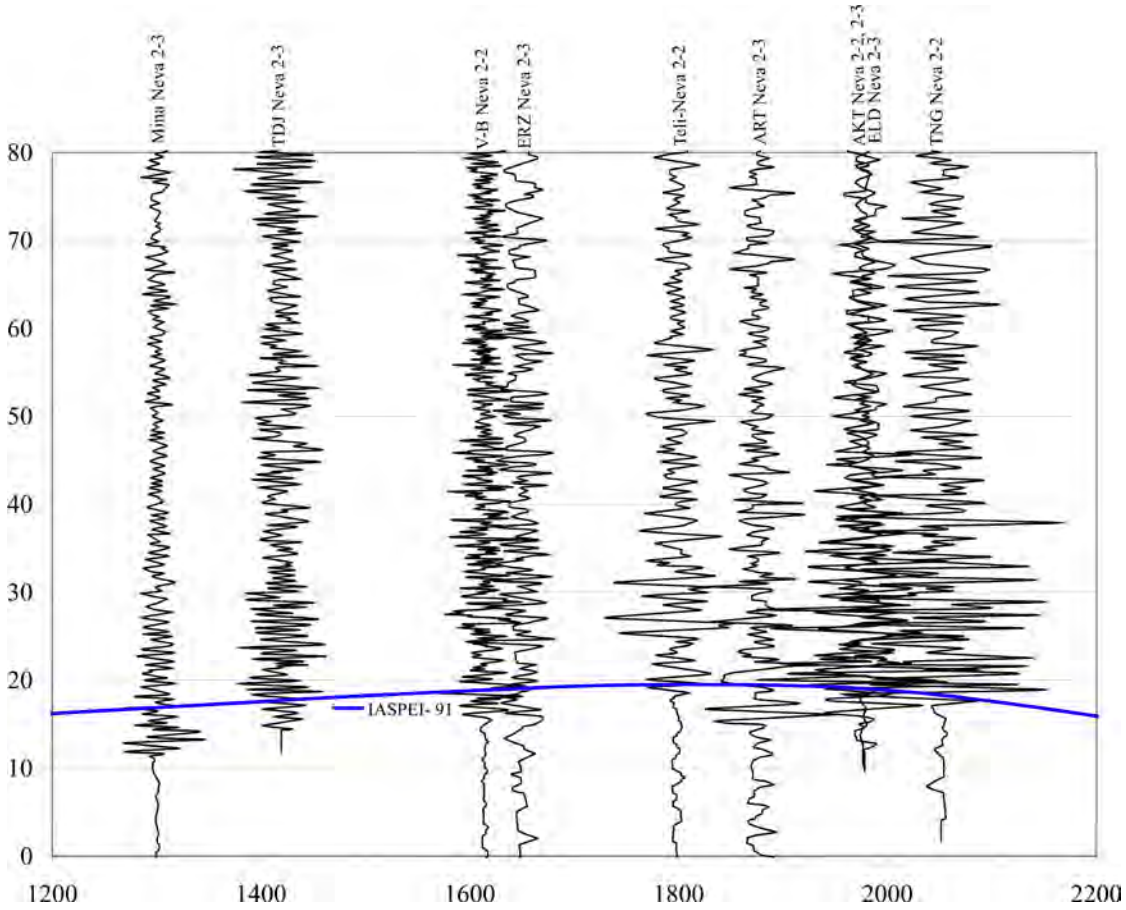

Figure 9. Record section crossing the Altai region from the Neva PNEs. Reduction velocity is 9.0 km/sec.

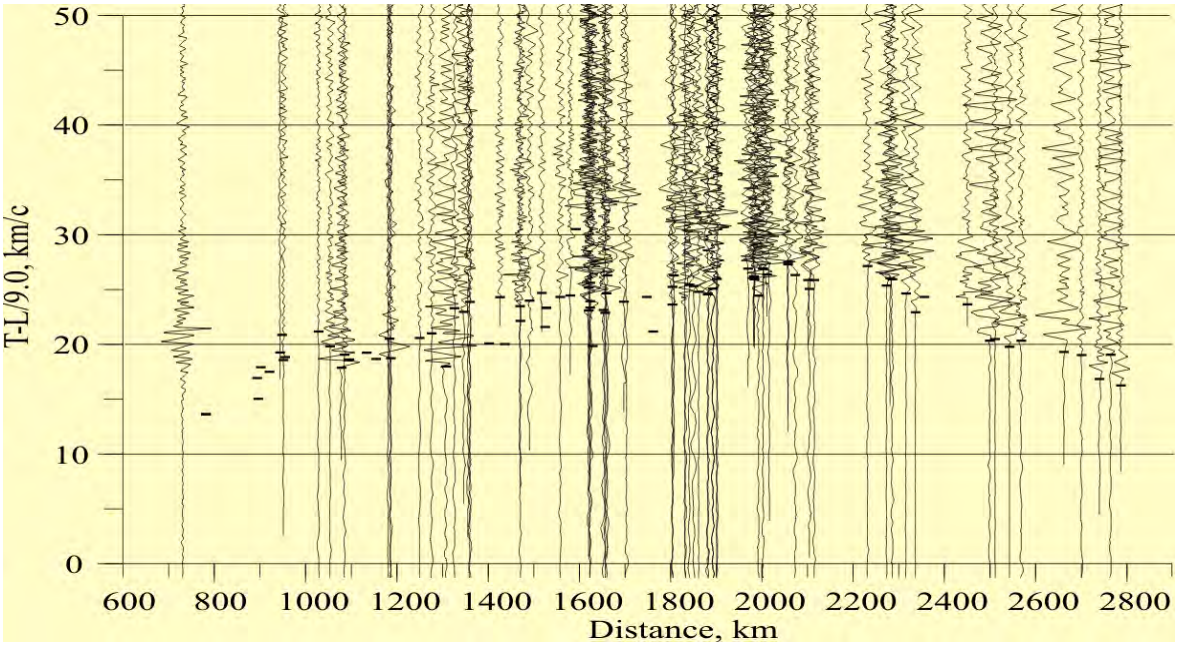

Figure 10. Composite record section using PNEs from throughout Siberia as recorded by the Altai Sayan seismic network. This section is representative of the Siberian Platform. Reduction velocity is 9.0 km/sec.

CONCLUSIONS AND RECOMMENDATIONS

The historic photo paper seismograms of PNEs conducted in the Soviet Union represent a large data set that remains to be fully exploited. These data can be useful for nuclear explosion discrimination, velocity studies, etc. at stations and in areas not previously researched. It is possible to digitize these seismograms to obtain digital seismograms compatible with more advanced computer based analysis. Digitization of the seismograms, most of which are short period, does a very good job of frequency/amplitude recovery in the 1–5-Hz range. Analysis of the deviation of observed travel time from the I-91 curve appears to correlate with tectonic settings and crustal structure.

ACKNOWLEDGEMENTS

Special thanks to Vladimir Suvorov of the Institute of Petroleum Geology and Geophysics, Novosibirsk, Russia, and Kazuya Fujita of Michigan State University

SEISMIC AND GEOPHYSICAL CHARACTERIZATION OF NORTHERN ASIA

Kevin G. Mackey[1], Kazuya Fujita[1], Hans H. Hartse[2], Michael L. Begnaud[2], and Michael E. Pasyanos[3]

Michigan State University[1], Los Alamos National Laboratory[2], and Lawrence Livermore National Laboratory[3]

Sponsored by the National Nuclear Security Administration

Award Nos. DE-AC52-09NA29323[1], DE-AC52-06NA25396[2], and DE-AC52-07NA27344[3]
Proposal No. BAA09-19

ABSTRACT

We are beginning a major research effort consisting of a combination of seismic field deployments, historical seismic data retrieval, and seismic data analysis to calibrate northern Asia for Nuclear Explosion Monitoring purposes. This project is a cooperative effort between Michigan State University (MSU), Los Alamos National Laboratory (LANL), Lawrence Livermore National Laboratory (LLNL), and several seismic networks in Russia, Mongolia, and Japan. The geographic scope of this project covers, Russia from the Urals to the Bering Strait and from the Arctic Ocean to the North Korean border. We are expanding our unique and previously unobtainable historical datasets on earthquakes and nuclear and industrial explosions. Combining these historic datasets with data from approximately 50 existing Russian and MSU/Russian and Japanese/Russian digital seismic stations, new deployments, and geologic information, we will dramatically increase ground-truth (GT) data and our understanding of the seismicity, velocity structure, explosion discrimination, and wave propagation characteristics in northern Asia. Our work will further improve location and detection and discrimination capabilities and data on crustal and upper mantle structure, wave propagation, and natural seismic source characteristics of northern Asia.

OBJECTIVES

Research is being undertaken to characterize seismicity and geophysical parameters of northern Asia. This project is a continuation of our long-running eastern Russia project with an expanded geographic area (Mackey, 2008; Mackey et al., 2007, 2006). This project is cooperative between Michigan State University, Los Alamos National Laboratory, Lawrence Livermore National Laboratory, and several institutes and organizations in Russia, Mongolia, and Japan.

RESEARCH DIRECTIONS

Seismic Networks, Digital Stations, and Deployments

We plan to continue our active field program, deploying and operating both broadband and short-period digital stations in eastern Russia. Our existing short-period network will continue operation in roughly the current configuration (Figure 1). Network changes will focus primarily on improvement of the broadband stations and their distribution in the Baikal and Yakutsk regions, as well as joint work with the main office of the Geophysical Survey, Russian Academy of Sciences in Obninsk (GSRAS) as discussed below. MSU has additional cooperative work with the seismic networks in Yuzhno Sakhalinsk, Yakutsk, and Petropavlovsk-Kamchatski in Russia, as well as with Ulaanbaatar, Mongolia. MSU also has a cooperative agreement with the University of Hokkaido (HKU), Japan, for research and data exchange, using their stations operating in eastern Russia.

Three MSU broadband stations are currently operating in the Baikal network (Figure 1). We plan to upgrade the seismic recorders for these stations because the initially purchased recorders are obsolete and are no longer possible to repair. We will purchase three Geotech Instruments SMART-24 recorders to pair with the existing Geotech Instruments KS-2000 seismometers already deployed.

We also plan to upgrade the short-period station at Vitim in the Yakutsk network to a broadband seismometer and recorder. Vitim is only a few kilometers from the non-operational Peledui station and array; lies within the Siberian Platform, which historically has been under-instrumented relative to seismically active areas; and is an important location for improving the ray path coverage in Eurasia. If political or logistical issues prevent a deployment at Vitim, an alternate site will be chosen (one possibility is Lensk).

We plan several options for temporary seismic deployments. MSU and the Magadan network (MAGN) maintain four portable digital stations in Magadan, operable by generator, solar panels, or batteries. We maintain these stations so that they can be deployed rapidly for earthquake aftershock studies to acquire GT data if the opportunity arises; equipment can also be transported to other networks if needed. Second, we will deploy temporary stations to record industrial explosions for discrimination, velocity profile, or GT studies, depending on opportunities or needs of the project. For temporary deployments, we are not restricted to the summer. MSU and MAGN maintain three snowmobiles, sleds, and associated equipment, and both MSU and MAGN are experienced at winter deployment operations in remote areas of eastern Russia.

MSU, jointly with GSRAS, and the Yakutsk Affiliate of the Geophysical Survey, RAS, are planning a 2010 or 2011 field expedition and temporary network deployment in the remote eastern Stanovoi Range of southern Yakutia (see Figure 1). Most of this highly seismically active region has never been instrumented, and no permanent stations operate within several hundred kilometers. In 2006, MSU deployed the first seismic stations in this area. In this current study, we plan to deploy to the east of the 2006 study and hope to acquire GT events, with some events also recorded by regional stations. Together with field observations, this may help delineate unknown active faults in the region. Second, this deployment will be cooperative with, and partially supported by, GSRAS, with whom MSU recently ratified an agreement.

MSU and Japanese researchers from HKU have also recently signed a cooperative agreement for mutual program support and data exchange. HKU, in conjunction with GSRAS, operates eight broadband stations in eastern Russia, primarily in the Amur region (Figure 1), which are of great interest to this project. Some of the MSU-supported stations are located in areas of interest to HKU (deep mantle structure around the Sea of Okhotsk). As there is no scientific conflict between the respective HKU and MSU studies, each can benefit from data exchange. Waveforms obtained will be analyzed in conjunction with other northern Asia broadband stations included in this project.

Database Improvements

First, we will expand our historic database to include the Altai-Sayan network. MSU has in hard copy (in *Materiali po Seismichnosti Sibiri*) the full seismic catalog of the Altai-Sayan network for 1970–1993, with the hypocenteral parameters of tens of thousands of events and the complete bulletin (all analyzed phases, their time picks, 3-component amplitudes, station magnitudes, and first motions) for the same time period for earthquakes larger than magnitude ~3.0 (tens of thousands of arrival times). It is necessary to hand enter data into a computer-readable format by student workers at MSU as character recognition software is not sufficient. It will also be necessary to develop a table of all seismic station parameters for the Altai-Sayan Network. Experience shows that this can be a a difficult task as stations were often moved and changes not documented; parameters for temporary stations were often not recorded.

As MSU acquires data from northern Asia, LANL's primary objective will be to ensure that the information (both historic and new) is parsed, merged, organized, and quality controlled for inclusion in the MSU/LANL database so it will be useful for model derivation and other geophysical characterizations of this region.

In collaborating with MSU, LANL has developed codes that improve our ability to manage incoming data. As LANL receives bulletins, we will evaluate the incoming formats and apply the appropriate parser to create flat file database tables. We will then load newly parsed flat files into temporary database space to conduct quality-control processes. Quality control efforts rely heavily on automated processes developed and described by Stead et al. (2006). After quality control, we will merge new tables with existing tables. As a result of the long-standing cooperation between LANL and MSU, this work will be performed more efficiently than during prior collaborations. However, we must emphasize that this effort is far more complicated than is routine parsing and loading of standard global bulletins, such as the ISC or EDR. The northern Asia data originate from disparate regional seismic networks with limited funding and computing capability. Often, formats change abruptly, stations are renamed (or moved) without warning, channel naming conventions vary between networks, and many other unanticipated situations occur.

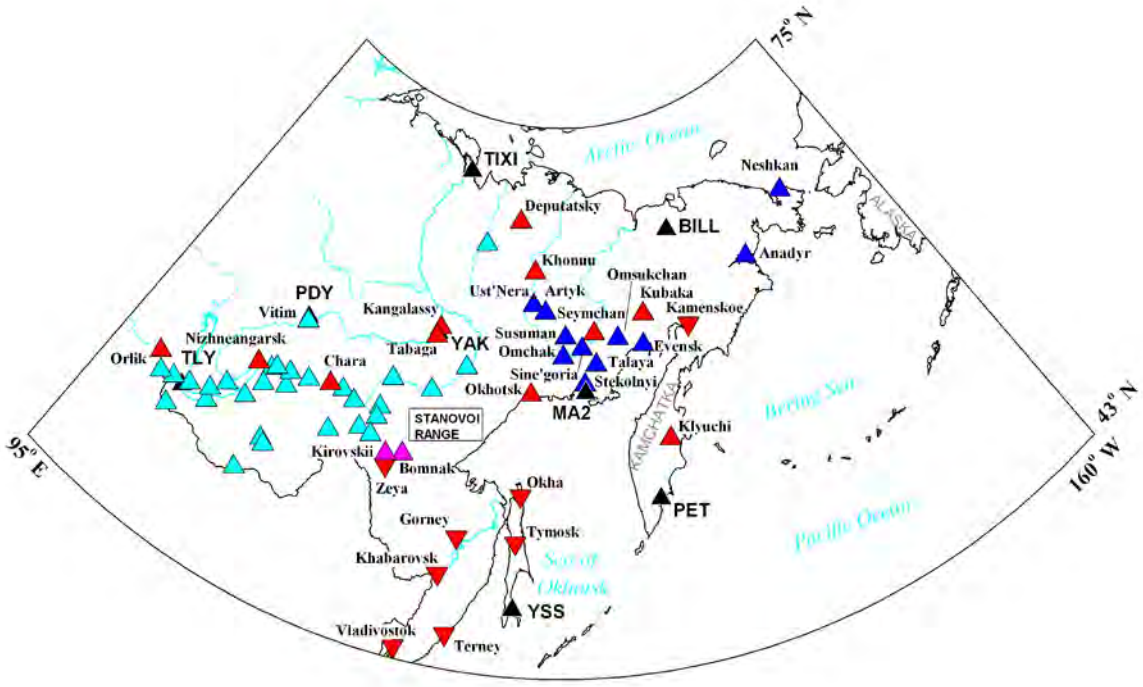

Figure 1. Digital seismic stations currently operating in eastern Russia that are part of this proposed research. Upward triangles—Red, MSU broadband stations; Dark Blue, MSU short-period stations; Light Blue, Russian short-period stations available to MSU; Pink, 2008 broadband deployments. Black triangles are IRIS stations or other digital stations for which data are available internationally. Downward triangles are Japanese broadband stations.

Waveform Collection

LANL will continue to collect digital waveforms from northern Asia as MSU provides them. As with bulletin information, these waves originate within several networks, each with somewhat different recording practices. From experience, we know the waves can have header problems, such as incorrect time stamps and/or sample rates. LANL has codes in place that check for such situations, and we will use reported pick times within the database to confirm that final wfdisc lines hold correct start time information.

Ground Truth Studies—Extension and Improvement of GT Criteria

To further improve the database, LANL will evaluate events for both location and event GT. Event type GT (explosion or earthquake) will allow for expanded discrimination studies in northern Asia, and calibration efforts that rely on earthquake populations, such as coda-magnitude efforts, will avoid explosion contamination of datasets. This work will be supplemented by source association and characterization studies conducted by MSU (below).

For newly acquired northeastern Asia bulletin data, we will scan the data for events near known mining sites for GT2–3 events. The GT levels for mines can usually be set based on the size of mine. We then scan for events that have the specific station distribution and phases to already pass the Bondár criteria. Using the distance ranges outlined, we will relocate the new events with subsets of the arrivals, matching locations to the GT criteria.

Eastern Russia bulletin data do not typically lend themselves to the Bondár criteria, given their use of S phases and the distance distribution of the defining phases that typically cross the 2.5 deg boundary from local GT into the near-regional range. If arrivals are limited to P phases within 2.5 deg, few events have the azimuthal coverage necessary to define GT5. Figure 2 shows the distance distribution of P phases in our current bulletin. Sufficient distance coverage is attained at distances under about 8 deg, with most arrivals within about 4 deg and crossing into the local distance range of 2.5 deg. In addition, there are high-quality Pg phases available beyond the Pg/Pn crossover that are not accepted in the Bondár criteria.

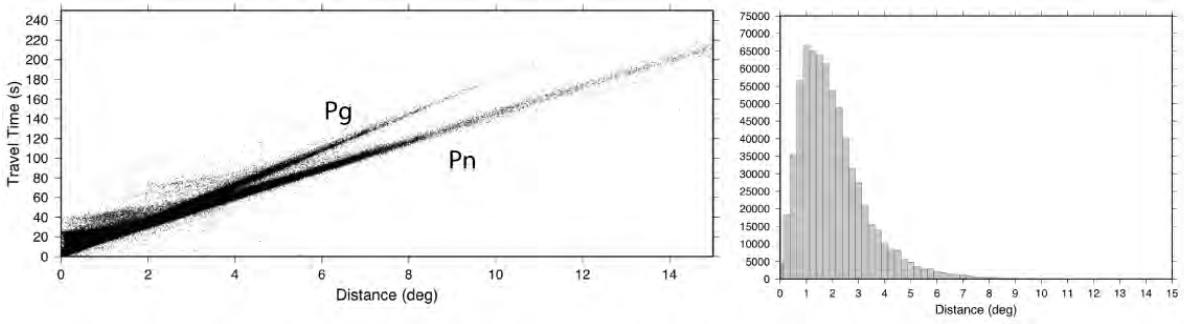

Figure 2. Travel times for P phases from previous Siberia/northern Asia catalogs. Note the preponderance of arrivals at less than 8 deg and the density of arrivals crossing into the local (0–2.5 deg) distance range.

We plan additional analysis to extend the current GT criteria to better address the distinct arrival distribution of the northern Asia catalog. This will involve phase distance distribution, azimuthal distribution at various ranges, travel-time residuals, and comparison to mining events. We will also assess whether the dominantly reported Sg phase can be included in any new criteria we develop.

Event Ground Truth Studies—Mining Event Identification

For both existing and newly obtained northern Asia bulletin information, we propose to evaluate event type GT through an analysis of event size, event time of day, and event magnitude, following MacCarthy et al. (2008).

Using the northern Asia database, we will evaluate reported event times relative to local daytime hours and location, similar to analysis by Mackey et al. (2003). Mackey et al. (2003) confirmed contamination of the region's seismicity catalogs using a grid analysis of event origin times in specific regions or cells. Many cells showed dominantly daytime and winter origin times, consistent with mining practices in the region.

Guided by our initial explosion contamination study, we will select waveforms from nearby stations, cross correlate the waves, and cluster events based on correlation coefficient size. Figure 3 shows the types of information that can be obtained by combining location and magnitude with cross-correlation information. This example shows the locations of over 100 events, with magnitude 2.25–3.25 and origin times during hour 7 or hour 13 GMT (1 pm and 7 pm local time). Even though the locations are scattered (mostly based on a single array), we know these events are from a particular mine because of waveform similarity.

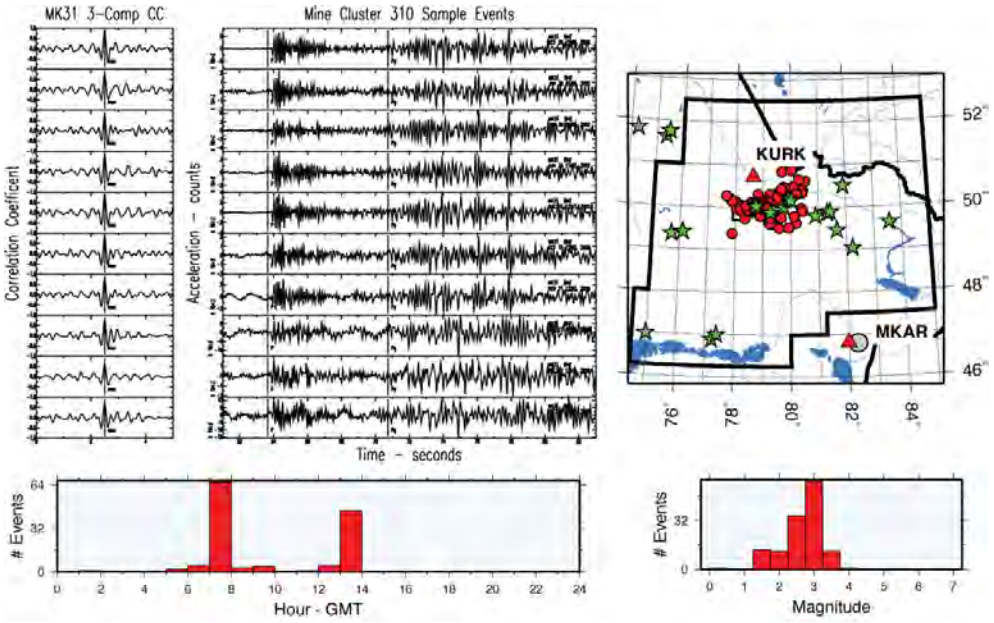

Figure 3. Sample waveform correlation and time-of-day analysis from Kazakhstan, showing waves from a single mine where nearly all origin times are near hour 7 or hour 13 GMT and magnitudes are between 2.25 and 3.25. Red circles are the event locations, and green stars are reported approximate mine locations. Origin time and other parameters were reported by the Kazakh National Data Centre. We propose a similar study of small events for northern and eastern Asia.

For our proposed cross correlation efforts, we will use waveforms from waveform data archived at MSU, new data from Russian/MSU stations, and GSN stations obtained via the IRIS DMC. From experience in Kazakhstan, mining events must be within 300 to 400 km of a station to obtain signals above background noise. We will use available imagery to assign explosions to particular mines whenever possible.

Association of Seismicity to Active Faulting

In regions where mines and their associated explosions are not readily identifiable or available, GT criteria estimates can be tested by associating events with specific faults. Previous studies have shown that relocated teleseismic events can be closely associated with specific faults in the Magadan district (McLean et al., 2000). We propose to continue our previous studies, identifying active faults through a combination of remote sensing and field observations.

Most eastern Russian studies have focused on identifying faults that are presently or recently active by identifying seismically generated features (fault scarps, large landslides, etc.; e.g., Vazhenin, 1992, Imaev et al., 2000) with little attention paid to river offsets, geomorphology, and active seismicity. Most of the work has been conducted in the Magadan district and adjacent parts of the Sakha Republic (Yakutia). The northeastern Sakha Republic (Yakutia) and far northeastern Russia remain entirely unstudied.

The availability of such tools as Google Earth make topographic reconnaissance easy and allow for the identification of drainage offsets, realignment of river networks, areas of active uplift, and other geomorphological indicators. This, combined with the MSU eastern Russia seismic database, allow for the first time, the possibility of detailed

correlations between earthquakes epicenters and focal mechanisms and lineaments and geologic offsets observable in satellite imagery. As a result, active segments of faults can be identified.

To support GT studies, we plan to make a detailed study of satellite imagery to identify possible GT events by associating earthquakes with specific faults and to identify which faults are active in the present day. This study will incorporate both the Magadan district, where epicentral location accuracy and the level of geologic mapping is relatively high, as well as the northwest Chersky and Verkhoyansk Ranges, where both location accuracy and geologic mapping are poor but little information is available except immediately south of Tiksi; however, the region is seismically and tectonically active (Fujita et al., in press; Imaev et al., 2000). A by-product of this study will be the identification and location of mines which may be sources for explosions. Attention will also be paid to the southeast extension of the Ulakhan fault from the Seimchan basin to Kamchatka.

For events with aftershock sequences, relative event relocations may help identify the approximate strike of the fault rupture. The elongation of isoseismals in the strike of the fault plane has also been noted in the region.

Source Characterization

We propose to continue studies of focal mechanisms of the larger earthquakes in northeastern Russia to determine the nature, tectonics, and orientation of faults. This will help event GT studies by determining the nature of natural seismic sources as well as discriminating natural from mining sources by identifying aftershock sequences, strikes of active faults, and (in some cases) focal depth. Our compilations of focal mechanisms have indicated that there are many inconsistent and poorly constrained mechanisms. In collaboration with our colleagues in Yakutia, we plan to re-examine many of the larger pre-moment tensor events in Yakutia and the Magadan district as well as determine new mechanisms using regional first motions and waveform modeling. We have a substantial collection of World-Wide Standardized Seismographic Network (WWSSN) microform records as well as access to the WWSSN seismogram collection at Northwestern University. Depending on the quality of the available data, additional methods may be applied.

We also plan to expand our compilations of previously-determined focal mechanisms to include Sakhalin and the Laptev Sea, and to upgrade our compilations for the Amur region.

Digitization of PNE Records

Long-range refraction profiles were conducted in the Soviet Union from 1971 to 1988 to conduct deep seismic sounding (DSS), using peaceful nuclear explosions (PNEs) as sources (e.g., Benz et al., 1992). These profiles have been extensively analyzed, using the original profile data both in Russia (e.g., Belousov et al., 1991), and more recently reprocessed in the west (e.g., Morozov et al., 2005). These PNEs were recorded using instruments deployed along the profiles at distances of 100–200 km spacing. These PNE profiles have been used to study a wide range of seismological phenomena, including attenuation, lithospheric and upper mantle structure, and scattering (e.g., Egorkin et al., 1987). Given that most of the PNEs were detonated in stable, cratonic areas, while the regional networks were located in the seismically active periphery, study of the PNEs recorded at the regional network stations will add a great number of previously unutilized ray paths through the seismically more complex fold belts and accretionary zones, in particular, in eastern Russia and along the Russian border with China.

These PNEs were recorded at analog seismic stations operated by the regional networks, resulting in over 7,800 of seismograms (GSRAS, 2001) from the permanent Russian seismic stations. Only one systematic study has been conducted with these records, basically consisting of P- and S-phase time picks for calibrating Russian geophysical stations for Comprehensive Nuclear-Test-Ban Treaty (CTBT) monitoring. Although broad in scope, the study did not conduct any waveform analysis (GSRAS, 2001). Many seismograms were digitally scanned but are of poor quality and low resolution and thus of little use beyond picking some basic arrival times. The study did not address stations in the now former-Soviet republics besides Russia.

We are working with the seismology group at the Institute of Petroleum Geology and Geophysics (IPGG) in Nobosibirsk to begin assembling, digitizing, and analyzing records from the regional networks of Russia. The current state this project is summarized in Mackey and Hartse (2009, these Proceedings). We will expand this study by collecting, digitizing, and analyzing additional seismograms from the various archives in Russia, focusing

initially in the Far East and along the border with Mongolia and northeast China, followed by other former-Soviet republics and Mongolia, as time allows.

Surface Wave Studies

We plan on using data from the Siberian deployments to make surface wave dispersion measurements of this region. Figure 4 shows an existing path map for 15-sec Rayleigh waves (Pasyanos, 2005). Coverage of the region south of 60°N is dense, but due to the lack of seismic sources and limited number of seismic stations, the area north of this latitude is sparsely covered. As a result, when we tomographically invert the region for group velocities (Figure 5), the velocities at this period correspond well with sediment thickness maps (Laske and Masters, 1997) south of 60°N (Figure 5); both the Song Liao Basin in China and the Sea of Okhotsk are well imaged as slow velocities. However, the slow velocities from large sediment deposits along the Lena River are not isolated but smeared out in the northern portion of the map. Also, slow velocities from the sediments in the Laptev Sea and East Siberian Sea (north of the Eurasian landmass) are smeared south.

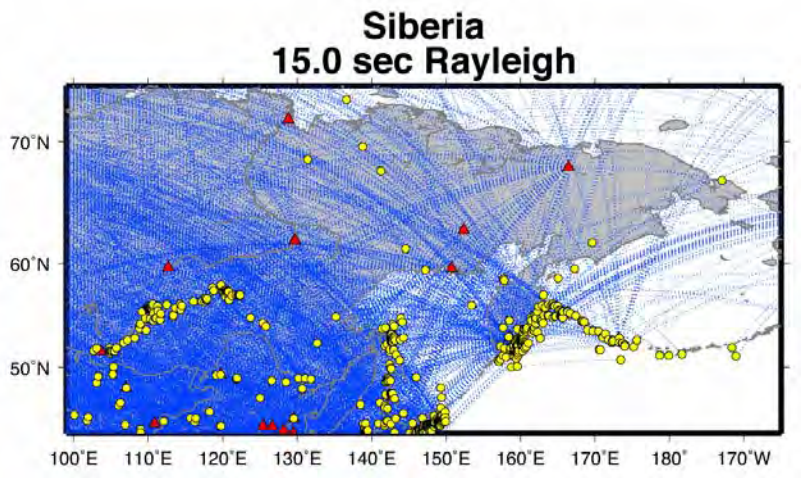

Figure 4. Ray path coverage currently available for 15-sec surface wave studies. Very few events and stations are available north of 60° and in the Russian Far East. The existing MSU broadband stations and their waveforms from regional and near-teleseismic events over the past several years and through the course of this project will improve the ray path coverage in these sparse areas.

Use of broadband stations throughout northern Asia (Figure 1) should improve coverage of this area considerably, particularly at short periods, allowing us to better image shallow structures like sedimentary basins. Similar improvements in coverage and resolution at intermediate and long periods will allow us to make advances in crustal thickness, upper-mantle velocity, and lithospheric thickness in this region.

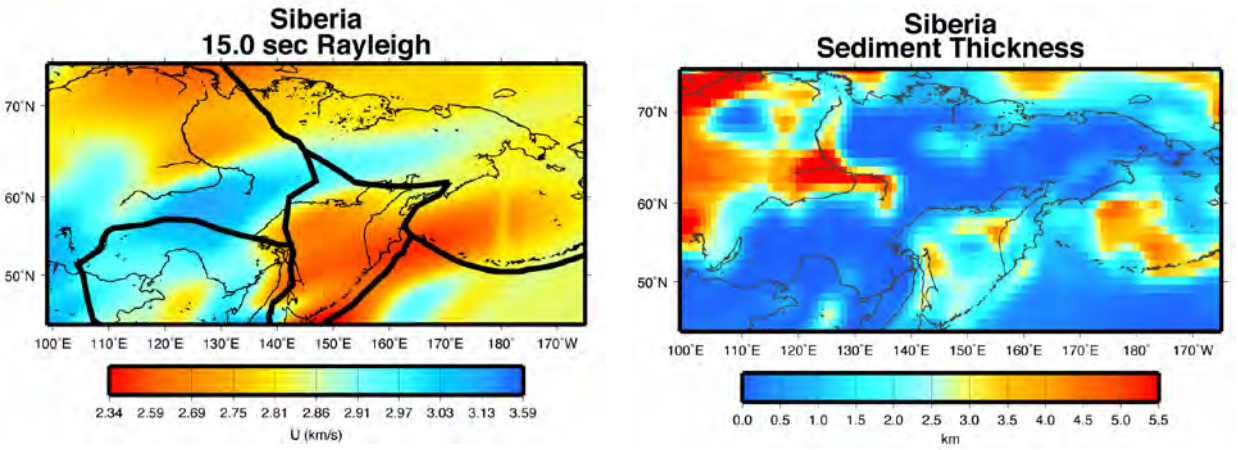

Figure 5. Left, 15-sec Rayleigh wave group velocities resulting from tomographic inversion of available ray paths, as depicted in Figure 4. Right, comparison to the sediment thickness map (Laske and Masters, 1997) shows that virtually all anomalies north of 60° are smeared or unresolved. Most anomalies present are not currently resolvable using surface-wave studies due to insufficient ray path coverage at short periods

REFERENCES

Beloussov, V. V., N. I. Pavlenkova, and G. N. Kvyatkovskaya (1991). *Deep Structure of the USSR*. Moscow: Nauka (in Russian)

Benz, H. M., J. D. Unger, W. S. Leith, W. D. Mooney, L. Solodilov, A. V. Egorkin, and V. Z. Ryaboy (1992). Deep seismic sounding in northern Eurasia, *Eos Trans. Am. Geophys. Union* 73: 297–300.

Egorkin, A. V., S. K. Zuganov, N. A. Pavlenkova, and N. M. Chernyshev (1987). Results of lithospheric studies from long-range profiles in Siberia, *Tectonophys.* 140: 29–47.

Fujita, K., B. M. Koz'min, K. G. Mackey, S. A. Riegel, M. S. McLean, and V. S. Imaev (2009). Seismotectonics of the Chersky seismic belt, northeastern Sakha Republic (Yakutia) and Magadan District, Russia. *Northeastern Russia, Geology, Geophysics and Tectonics: A tribute to Leonid Parfeno*v, D. B. Stone, D. B. Ed., Stephan Mueller series, EGU (in press).

GSRAS (2001). C alibration o f the s eismic s tations o f t he R ussian Academy o f S ciences for C TBT s eismic Monitoring Purposes. Annual technical report SAIC-02/3029.

Imaev, V. S., L. P. Imaeva, and B. M. Koz'min (2000). *Seismotectonics of Yakutia*. Moscow: Geos (in Russian)

Laske, G. and G. Masters (1997). A global digital map of sediment thickness, *Eos Trans. Am. Geophys. Union*, 78: F483.

MacCarthy, J. K., H. E. Hartse, M. Greene, and C. Rowe (2008). Using waveform cross-correlation and satellite imagery to identify repeating mine blasts in eastern Kazakhstan, *Seismol. Res. Lett.* 79: 393–399.

Mackey, K. G., K. Fujita, L. Gounbina, B. Koz'min, V. Imaev, L. Imaeva, and B. Sedov (2003). Explosion contamination of the northeast Siberian seismicity catalog: Implications for natural earthquake distributions and the location of the Tanlu fault in Russia, *Bull. Seismol. Soc. Am.* 93: 737–46.

Mackey, K. G., H. Hartse, K. Fujita, L. Linkimer, L. Steck, R. Stead, and C. Rowe (2006). Seismic characterization of Northeast Asia, in *Proceedings of the 28th Seismic Research Review: Ground-Based Nuclear Explosion Monitoring Technologies,* LA-UR-06-5471, Vol. 1, pp. 93–102.

Mackey, K. G., H. Hartse, L. Steck, R. Stead, C. Rowe, K. Fujita, and L. Gutirrez (2007). Seismic characterization of Northeast Asia, in *Proceedings of the 29th Monitoring Research Review: Ground-Based Nuclear Explosion Monitoring Technologies,* LA-UR-07-5613, Vol. 1, pp. 123–132.

Mackey, K. G., (2008). Analysis of digitizied seismograms from Russian Geophysical Survey stations of Soviet peaceful nuclear Explosions, in *Proceedings of the 30th Monitoring Research Review: Ground-Based Nuclear Explosion Monitoring Technologies,* LA-UR-08-05261, Vol. 1, pp. 118–121.

Mackey, K. G. and H. E. Hartse (2009). Analysis of digitized seismograms from Russian Geophysical Survey stations of Soviet peaceful nuclear explosions, these Proceedings.

McLean, M. S., K. Fujita, and K. G. Mackey (2000). Neotectonics of the central Chersky seismic belt, northeastern Russia, *Eos Trans. Am. Geophy. Union*, 81: Suppl. S414.

Morozov, I. B., E. A. Morozova, S. B. Smithson, P. G. Richards, V. I. Khalturin, and L. N. Solodilov (2005). 3D first arrival regional calibration model of northern Eurasia, *Bull. Seismol. Soc. Am.*, 95: 951–964.

Pasyanos, M. E. (2005). A variable-resolution surface wave dispersion study of Eurasia, North Africa and surrounding regions, *J. Geophys. Res.*110: B12301, doi:10.1029/2005JB003749.

Stead, R., M. Begnaud, and J. Aguilar-Chang (2006). Advances in data integration and quality control in support of the NNSA Knowledge Base, in *Proceedings of the 28th Seismic Research Review: Ground-Based Nuclear Explkosion Monitoring Technologies*, LA-UR-06-5471, Vol. 2, pp. 1028–1038

Vazhenin, B. P. (1992). Paleo-seismodislocations in the Chersky seismic belt, *Seismologic and Petrophysical Investigations in Northeast Russia*, T. I. Lin'kova Ed. SVKNII DVO RAS, Magadan (in Russian)

EXTENSION OF THE CAUCASUS SEISMIC INFORMATION NETWORK STUDY INTO CENTRAL ASIA

Randolph J. Martin[1], Levent Gülen[2], Youshun Sun[2], M. Nafi Toksöz[2]

New England Research[1] and Massachusetts Institute of Technology[2]

Sponsored by the National Nuclear Security Administration

Award No. DE-AC52-08NA28751

ABSTRACT

The active tectonics of Central Asia is the result of ongoing, active continental collision between the Indian and the Eurasian plates. This geologically and tectonically complex area is also one of the most seismically active regions in the world. Due to many different reasons, access to the local seismic data in this area was very limited. Previous studies in this region mostly depended on teleseismic data as well as local and regional data from the stations located in western and southern China. In this study we used the local travel time data from Kazakhstan, Kyrgyzstan, Tajikistan, and Uzbekistan to study the crustal structure in this region. We selected the events and stations between 32°N-65°E and 45°N-85°E and focused on the areas of Pamir and western Tien Shan. In this dataset, there are more than 3000 *P* and *S* arrivals recorded at 68 stations from about 220 events. Double difference tomography is applied to relocate events and to invert for seismic structures simultaneously. Our results provide accurate locations of earthquakes and high resolution crustal structure in this region. We use local and regional travel times to invert the 3D crustal velocity structure in this region. More than 2200 *P*-wave phase picks were used in the inversion. The average grid spacing is 100 km and the inverted grids lay on six layers. Then we use the double difference tomography method developed by Zhang and Thurber (2003, 2006) to invert for the 3D *P*-wave velocity structure.

Our tomographic results show strong heterogeneities in the crust and upper mantle of the Central Asia. The crustal low velocity zones are found near Tien Shan, the northern Pamir, and the Tajik depression, while high velocity anomalies are found beneath the Kazakh shield, the southern Pamir, and the Tarim basin. The Moho discontinuity can be illustrated as a velocity contour line. If an average *Pn* velocity of 8.0 km/s is chosen for the Moho, then most Moho depths are greater than 70 km.

OBJECTIVES

The main goal of this project is to develop a database consisting of: new waveform data, seismic event catalogs, and information on the geology and active tectonics in the Central Asian region. Over the past years, we have collected geologic, geophysical, seismic event catalog and phase arrival data from local networks in the Caucasus region; this project extends the work into the CASRI (Central Asia Seismic Research Initiative) region (Kazakhstan, Kyrgyzstan, Uzbekistan, and Tajikistan). The new database is crucial in generating a detailed crust and mantle structure model and characterizing seismic wave propagation and attenuation in Central Asia. The local seismic networks, calibration events, improved crust and mantle structure models and better location algorithms (e.g., multiple-event grid search, double-difference methods) will improve the event locations. This new database will form the basis for mitigating earthquake hazard in Central Asia, and it will aid in the monitoring of these regions of strategic interest to U.S. national security.

RESEARCH ACCOMPLISHED

The Central Asian Tectonic Setting

The active tectonics of Asia is predominantly the result of the continental collision and the continuing continental convergence between the Indian and the Eurasian Plates. As a result, large scale structures such as the Himalayas, Tibet, Hindu Kush-Pamir, and the Tien Shan have been produced by the collision and the post-collisional convergence. The overall continental deformation of Asia was explained by the lateral escape of rigid lithospheric blocks bounded by major strike-slip faults due to the continental collision of the Indian and Eurasian Plates based on the analysis of geological and seismological data (Molnar and Tapponnier, 1975).

The India-Eurasia collision is also accommodated by major thrusting and crustal shortening as evidenced by the high elevation and compressional structures such as the Himalayas, Hindu Kush-Pamir, and the Tien Shan regions (Figure 1). An alternative model suggesting that the mode of continental deformation can be explained by continuum mechanics was proposed to explain the continental deformation of Asia (England and Houseman, 1986; Houseman and England, 1993). This alternative model assumes that the collision and convergence of the Indian and Eurasian Plates are mainly accommodated by lithospheric thickening, and the resultant increased gravitational body forces drive the active tectonics of Asia. The Global Positioning System (GPS) measurements and crustal rheology modeling in Asia provide evidence that the deformation in the shallow brittle crust occurs on a distributed network of faults, and some regions such as the Tarim Basin, the Ordos and South China behave as rigid blocks; however, deformation of a continuous medium at depth is the best description of the present day tectonics of Asia (Royden et al., 1997; Wang et al., 2001; Calais et al., 2003; Zhang and Gan, 2008).

The countries that are within the interest area of the CASRI project are primarily affected by the tectonic deformations and associated seismic activity of the Tien Shan and the Pamir-Hindu Kush regions. Since we have covered the Neotectonic analysis of the Tien Shan region previously, we will briefly summarize the active tectonics of the Pamir-Hindu Kush region in this paper.

The Pamir-Hindu Kush Region

The Pamir-Hindu Kush region is located at the western syntaxis of the Himalayan belt and it has an elevation of 4000–5000 m. This orojenic syntaxis consists of several terranes that were accreted to the southern margin of Asia during the Paleozoic-Mesozoic closure of the Tethys Ocean (Tapponnier et al., 1981; Burtman and Molnar, 1993; Yin and Harrison, 2000; Schwab et al., 2004; Robinson et al., 2007). Before the India-Asia continental collision took place about 45–50 my ago, the Pamir region was an Andean-style plate margin. The post-collisional indentation of the Indian Plate into the Eurasian Plate caused intense deformation and crustal shortening and created major thrusts and strike-slip faults bounding the region (Figure 1). The Main Pamir Thrust forms the northern boundary separating the Pamirs from the Tien Shan. The left-lateral strike-slip Darvaz-Karakul Fault Zone marks the boundary in the west between the Tadjik Depression and the Pamirs. The right-lateral strike-slip Karakorum fault zone forms the eastern boundary that separates the Pamirs from the western Kunlun and the Tarim Basin (Molnar and Tapponnier, 1978). The Main Pamir Thrust has been interpreted to have accommodated about 300 km of crustal shortening, and

additionally at least 300 km of shortening was also accommodated internally by thrusting and faulting within the Pamirs during the Cenozoic (Burtman and Molnar, 1993).

The Pamir-Hindu Kush region has high seismic activity and many large earthquakes have occurred in the region. The focal mechanism solutions for the earthquakes in this region indicate predominantly thrust events, as would be expected, and some strike-slip events along major shear zones that form the boundaries of the region (Figure 2).

The most interesting aspect of the Pamir-Hindu Kush seismicity is that this region is one of the most active regions of intermediate depth seismicity. Many studies have been carried out to evaluate the seismicity of the Pamir-Hindu Kush region (Chatelain et al., 1980; Roecker 1982; Fan and Ni, 1989; Burtman and Molnar, 1993; Fan et al., 1994; Pegler and Das, 1998). More recently, seismic tomographic studies of the mantle structure beneath the Pamir-Hindu Kush region have revealed that the intermediate depth seismicity is the result of the existence of two opposing sense subduction zones (Freiderich, 2003; Kumar et al., 2005; Koulakov and Sobolev, 2006; Negredo et al., 2007). The Indian lithosphere subducts steeply northward beneath the Hindu Kush, and the Asian lithosphere subducts southward beneath the Pamirs; the interface of the two converging lithospheres, at mantle depths beneath the Pamir-Hindu Kush region, forms the zone of intermediate depth seismicity.

Travel-Time Data

An important task under this project is to collect arrival time data from seismic stations situated in the Central Asia. A significant number of these stations are in networks whose data are not available from global data centers such as IRIS (Incorporated Research Institutions for Seismology) or ISC (International Seismological Centre). Figure 3 shows seismic stations in the region from which we have obtained data either through data centers or by bilateral arrangements. In the previous studies of this region, teleseismic data and surface wave data were the main data sources. Although teleseismic data provide us with much information about the mantle, shallow structure is still unclear. The horizontal resolution is also limited by available periods of surface waves. Therefore, we use the local and regional travel times to invert for the 3D crustal velocity structure in this region. We selected the stations and events between 32°N-65°E and 45°N-85°E where there are 68 stations and 220 events (Figure 3). More than 2200 *P*-wave phase picks are employed in the inversion. The average grid spacing is 100 km and the inverted grids lay on six layers. The source-station ray paths are also shown in Figure 3 and the ray density is dense enough to obtain good tomographic resolution.

***P*- and *S*-Wave Travel-Time Tomography of the Crust and Upper Mantle**

A high-resolution tomographic model for the heterogeneous crust is constructed by iterative, non-linear tomography. To generate adequate starting models for the nonlinear inversion, we combine pertinent information from global (Mooney et al., 1998; Stevens et al., 2001; Ritzwoller et al., 2002), regional, and local crust and uppermost mantle models. Next, we use the adaptive moving window (AMW) approach (Sun et al., 2004, 2008) to obtain crustal velocities and *Pn* and *Sn* models from a 1D Monte Carlo inversion of local ($\leq 20°$) arrival time data in the whole region, building these into the next model (Model #2). The third step is a tomographic inversion of the local and regional arrival time data for 3D variations in the *P*- and *S*-wave speed, using Model #2 as the initial input model.

For this purpose we use a modified version of Zhao's tomographic method (Zhao et al., 1992, 1994; Zhao, 2001; Sun and Toksöz, 2006), which allows for 3D velocity variations everywhere in the model and can accommodate velocity discontinuities. The velocity structure is discretized using a 3D grid. The velocity perturbation at each point is calculated by linear interpolation of the velocity perturbations at surrounding (adjacent) grid nodes. The velocity perturbations at grid nodes are the unknown parameters for the inversion procedure. To calculate travel-times and ray paths accurately and rapidly, the pseudo-bending technique (Um and Thurber, 1987) is used iteratively. We correct for station elevations by including station correction terms in the inversion. The nonlinear tomographic problem is solved by repeated linear inversions. At each iteration, perturbations to hypocentral parameters and velocity structure are determined simultaneously.

Starting from the *P* and *S* models obtained from the above strategy, we apply an adaptive-mesh double-difference tomography method to the newly assembled data set to further improve event locations and velocity models (Zhang and Thurber, 2003; 2006). In this approach, the configuration of model cells is adjusted to sampling density to stabilize the inversion and (locally) optimize spatial resolution. Figure 4 shows the *P* and *S* travel-time, distance graphs, and *P*-wave

travel-time residual distribution before and after the 3D inversion. The standard deviation improved from 2.1 seconds to 0.9 seconds as a result of the 3D inversion.

The Moho depth is set to 50 km in the relocation of events, but no Moho discontinuity is used in our starting model. Figures 5 and 6 show the tomographic results obtained for the central Asian crustal structure. Since most phase arrivals are *Pn*, the layers around the Moho (50 km and 70 km) are imaged with the best resolution. In addition, the shallower structure can also be recovered along the China boundary. Figure 7 shows the upper mantle velocity structure at the depths of 100, 200, 400 and 700 km obtained by the double difference tomography method.

CONCLUSIONS AND RECOMMENDATIONS

Our results show strong crustal and mantle heterogeneities in Central Asia. The low velocity zones are found near the Tien Shan, northern Pamirs, and Tajik depression, whereas high velocity anomalies exist beneath the southern Pamir, Kazakh shield, and the Tarim basin.

The Moho discontinuity can be illustrated as a velocity contour line. If an average Pn velocity of 8.0 km/s is chosen for the Moho, then most Moho depths are greater than 70 km.

We will coordinate the installation of three broadband seismic stations in Tajikistan, in cooperation with the Seismic Monitoring Center in Georgia, to improve the quality of regional seismic networks, and to obtain near real-time access to data throughout the Central Asia region.

The extension of the velocity models into the mantle transition zone will be accomplished by adding the teleseismic data from the 1964–2007 ISC/EHB database, which contains over 10 million *P*-wave travel-times, and from datasets obtained by the various national data centers.

REFERENCES

Burtman, V. S. and P. Molnar (1993). Geological and geophysical evidence for deep subduction of continental crust beneath the Pamir, *Geol. Soc. Am. Spec. Paper 281*, 76 p.

Calais, E., M. Vergnolle, V. San'kov, A. Lukhnev, A. Miroshnitchenko, S. Amarjargal, and J. Déverchère (2003). GPS measurements of crustal deformation in the Baikal-Mongolia area (1994-2002): Implications for current kinematics of Asia, *J. Geophys. Res.* 108: doi:10.1029/2002JB002373.

Chatelain, J. L., S. W. Roecker, D. Hatzfeld, and P. Molnar (1980). Microearthquake seismicity and fault plane solutions in the Hindu Kush region and their tectonic implications, *J. Geophys. Res.* 85: 1365–1387.

England, P. and G. Houseman (1986). Finite strain calculations of continental deformation: 2. Comparison with the India-Eurasia collision zone, *J. Geophys. Res.* 91: 3664–3676.

Fan, G. and J. F. Ni (1989). Source parameters of the 13 February Karakoram earthquake, *Bull. Seism. Soc. Am.* 79: 945–954.

Fan, G., J. F. Ni, and T. C. Wallace (1994). Active tectonics of the Pamirs and Karakorum, *J. Geophys. Res.* 99: 7131–7160.

Friederich, W. (2003). The S-velocity structure of the east Asian mantle from inversion of shear and surface waveforms, *Geophys. J. Int*. 153: 88–102.

Houseman, G. and P. England (1993). Crustal thickening versus lateral expulsion in the India-Asia continental collision, *J. Geophys. Res.* 98: 12,233–12,249.

Koulakov, I. S. and V. Sobolev (2006). A tomographic image of Indian lithosphere break-off beneath the Pamir-Hindukush region, *Geophys. J. Int*. 164: 425–440.

Kumar, P., X. Yuan, R. Kind, G. L. Kosarev (2005). The lithosphere-asthenosphere boundary in the Tien Shan-Karakoram region from S receiver functions: Evidence for continental subduction, *Geophys. Res. Lett.* 32: doi: 10.1029/2004GL022291.

Molnar, P. and P. Tapponnier (1975) Cenozoic tectonics of Asia, *Science* 189: 419–426.

Molnar, P. and P. Tapponnier (1978) Active tectonics of Tibet, *J. Geophys. Res*. 83: 5361–5375.

Mooney, W.D., G. Laske, and G. Masters (1998). CRUST 5.1: A global crustal model at 5°× 5°, *J. Geophys. Res.* 103: 727–747.

Negredo, A. M., A. Replumaz, A. Villasenor, and S. Guillot (2007). Modeling the evolution of continental subduction process in the Pamir-Hindu Kush region, *Earth Planet. Sci. Lett.* 259: 212-225.

Pegler, G. and S. Das (1998). An enhanced image of the Pamir-Hindu Kush seismic zone from relocated earthquake hypocenters, *Geophys. J. Int*. 134: 573–595.

Ritzwoller, M.H., M. P. Barmin, A. Villasenor, A. L. Levshin, and E. R. Engdahl (2002). Pn and Sn tomography across Eurasia to improve regional seismic event locations, *Tectonophysics* 358: 39-55.

Robinson, A. C., A. Yin, C. E. Manning, T. M. Harrison, S. H. Zhang, and X. F. Wang (2007). Cenozoic evolution of the eastern Pamir: Implications for strain-accommodation mechanisms at the western end of the Himalayan-Tibetan orogen, *Geol. Soc. Am. Bull.* 119: doi: 10.1130/B25981.1

Roecker, S. W. (1982). Velocity structure of the Pamir-Hindu Kush region: possible evidence of subducted crust, *J. Geophys. Res.* 87: 945–959.

Royden, L.H., B.C. Burchfiel, R.W. King, E. Wang, Z. Chen, F. Shen, and L. Yuping (1997). Surface deformation and lower crustal flow in eastern Tibet, *Science* 276: 788–790.

Schwab, M., L. Ratschbacher, W. Siebel, M. McWilliams, V. Minaev, V. Lutkov, F. Chen, K. Stanek, B. Nelson, W. Frisch, and J. L. Wooden (2004). Assembly of the Pamirs: Age and origin of magmatic belts from the southern Tien Shan to the southern Pamirs and their relation to Tibet, *Tectonics* 23: doi:1029/2003TC001583.

Stevens, J. L., D. A. Adams, and G. E. Baker (2001). Improved surface wave detection and measurement using phase-matched filtering with a global one-degree dispersion model, in *Proceedings of the 23rd Seismic Research Review: Worldwide Monitoring of Nuclear Explosions*, LA-UR-01-4454, Vol. 1, pp. 420–430,

Sun, Y., L. Xu, S. Kuleli, F. D. Morgan, and M. N. Toksöz (2004). Adaptive moving window method for 3-D P-velocity tomography and its application in China, *Bull. Seism. Soc. Am*. 94: 740–746.

Sun, Y. and M. N. Toksöz (2006). Crustal structure of China and surrounding regions from P wave traveltime tomography, *J. Geophys. Res*. 111: doi:10.1029/2005JB003962.

Sun, Y., M. N. Toksöz, S. Pei, D. Zhao, F. D. Morgan, and A. Rosca (2008). S-wave tomography of the crust and uppermost mantle in China, *J. Geophys. Res*. 113: doi:10.1029/2008JB005836.

Tapponnier, P., M. Mattauer, F. Proust, and C. Cassaigneau (1981). Mesozoic ophiolites, sutures, and large scale tectonic movements in Afghanistan, *Earth Planet. Sci. Lett*. 52: 355–371.

Um, J. and C. Thurber (1987). A fast algorithm for two-point seismic ray tracing, *Bull. Seism. Soc. Am*. 77: 972–986.

Wang, Q. P. Zhang, J. T. Freymueller, R. Bilham, K. M. Larson, X. Lai, X. You, Z. Niu, J. Wu, Y. Li, J. Liu, Z. Yang, and Q. Chen (2001). Present-day crustal deformation in China constrained by Global Positioning System measurements, *Science* 294: 574–577.

Yin, A. and T. M. Harrison (2000). Geologic evolution of the Himalayan-Tibetan Orogen, *Annu. Rev. Earth Planet. Sci.* 28: 211–280.

Zhang, H. and C. Thurber (2003). Double-Difference Tomography: The Method and Its Application to the Hayward Fault, California, *Bull. Seism. Soc. Am*. 93: doi: 10.1785/0120020190.

Zhang, H. and C. Thurber (2006). Development and applications of double-difference tomography, *Pure and Applied Geophys.* 163: doi:10.1007/s00024-005-0021-y.

Zhang, P.-Zh. and W. Gan (2008). Combined model of rigid-block motion with continuous deformation: Patterns of present-day deformation in continental China, *in* Burchfiel, B.C., and Wang, E., Eds., Investigations into the Tectonics of the Tibetan Plateau, *Geological Society of America Special Paper* 444, 59–71, doi:10.1130/2008.2444.

Zhao, D. (2001). Seismic structure and origin of hotspots and mantle plumes, *Earth Planet. Sci. Lett*. 192: 251–265.

Zhao, D., A. Hasewaga, and S. Horiuchi (1992). Tomographic imaging of P and S wave velocity structure beneath northeastern Japan, *J. Geophys. Res*. 97: 19909–19928.

Zhao, D., A. Hasegawa, and H. Kanamori (1994). Deep structure of Japan subduction zone as derived from local, regional and teleseismic events, *J. Geophys. Res.* 99: 22313–22329.

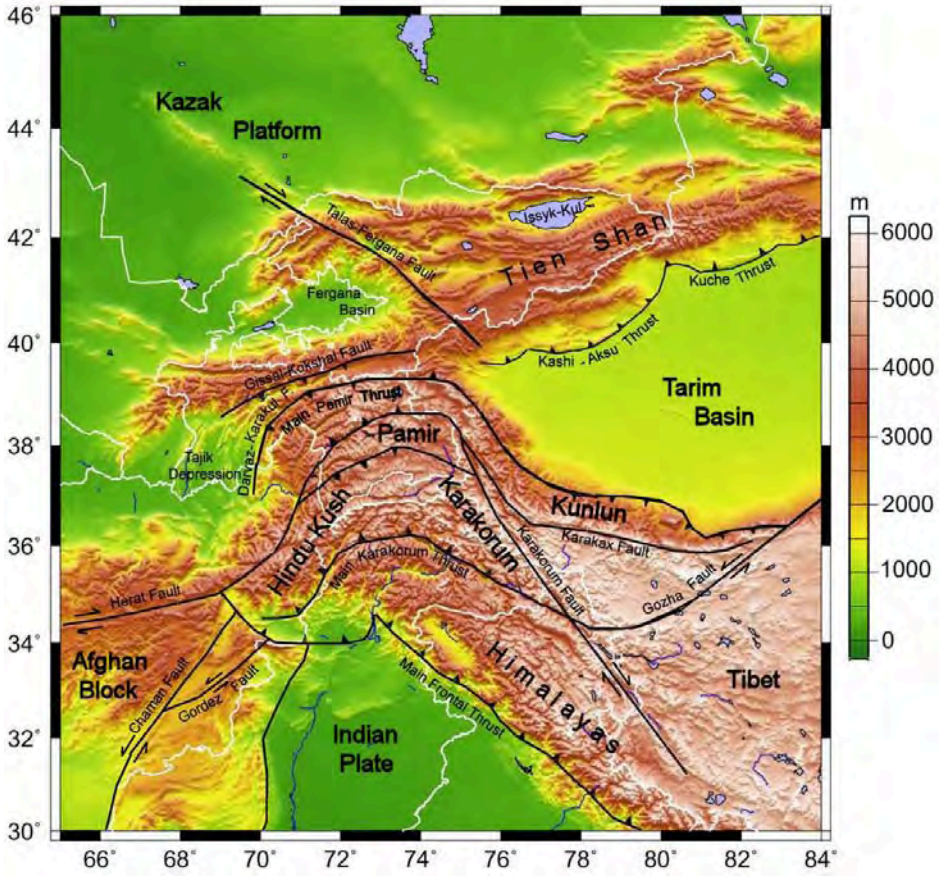

Figure 1. Map of the Pamir-Hindu Kush and surrounding areas showing major tectonic features.

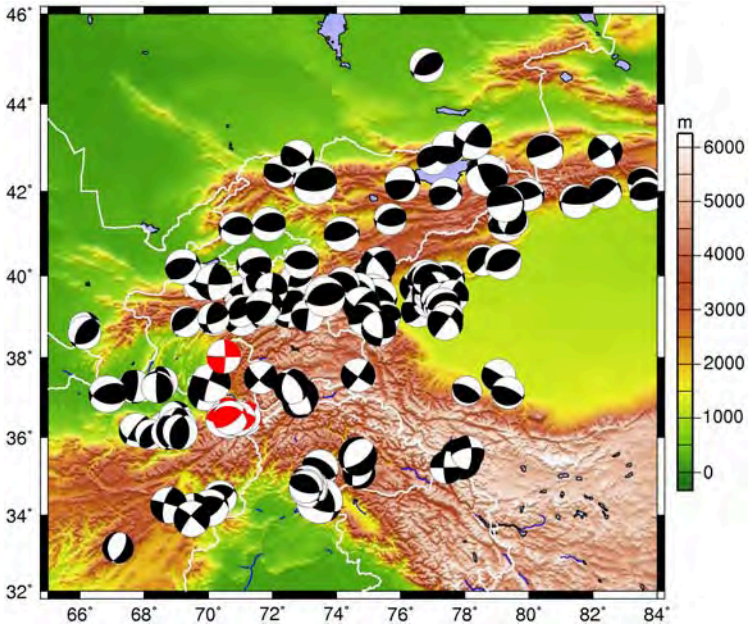

Figure 2. Digital topographic image of the Pamir-Hindu Kush and the Tien Shan regions showing the focal mechanism solutions from the Global Centroid Moment Tensor (CMT) catalog for the events with M>5.0 (1976-2009 period, compressional quadrants are black for the events with <70 km depth, and red for the events with >70 km depth).

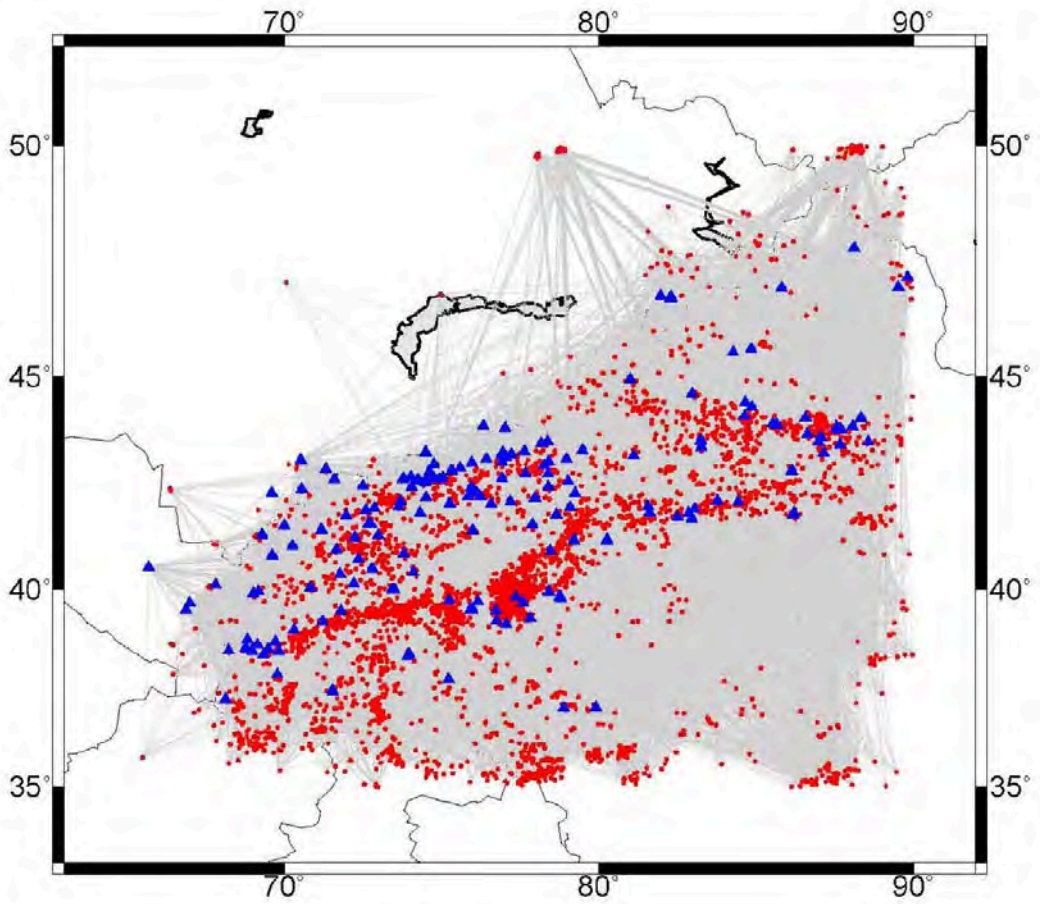

Figure 3. Ray path distribution in Central Asia. The stations are shown with blue triangles and the events are shown with red dots.

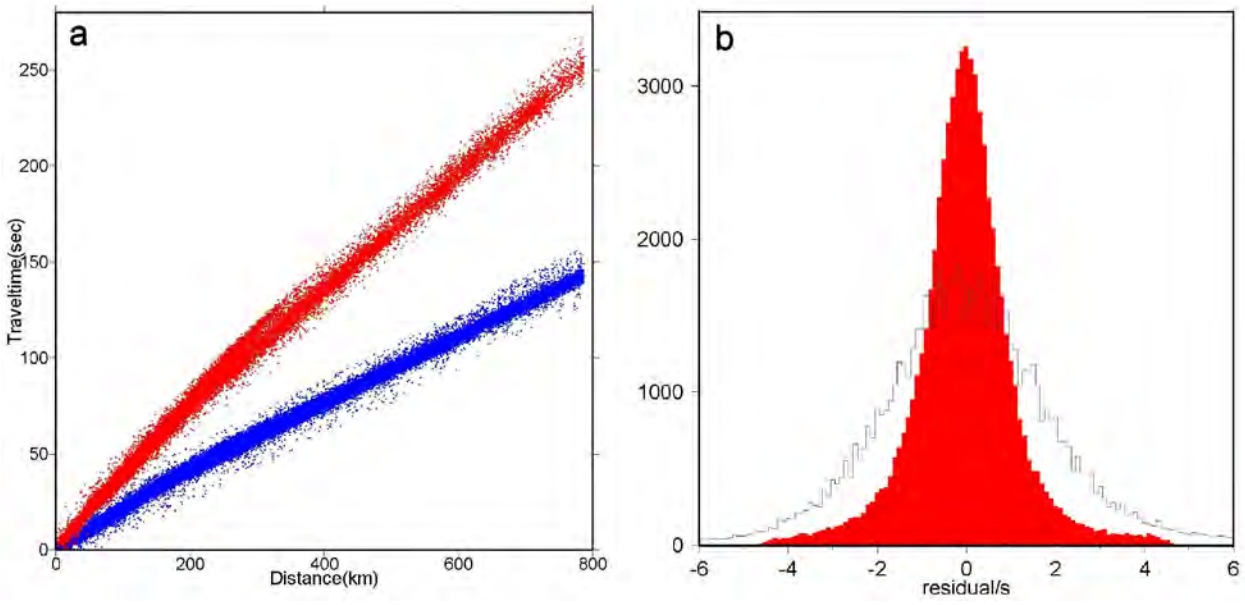

Figure 4. (a) *P* and *S* travel time distribution in the study area. (b) *P*-wave travel time residual distribution before and after (red) 3-D inversion. The standard deviation decreased from 2.1 seconds to 0.9 seconds.

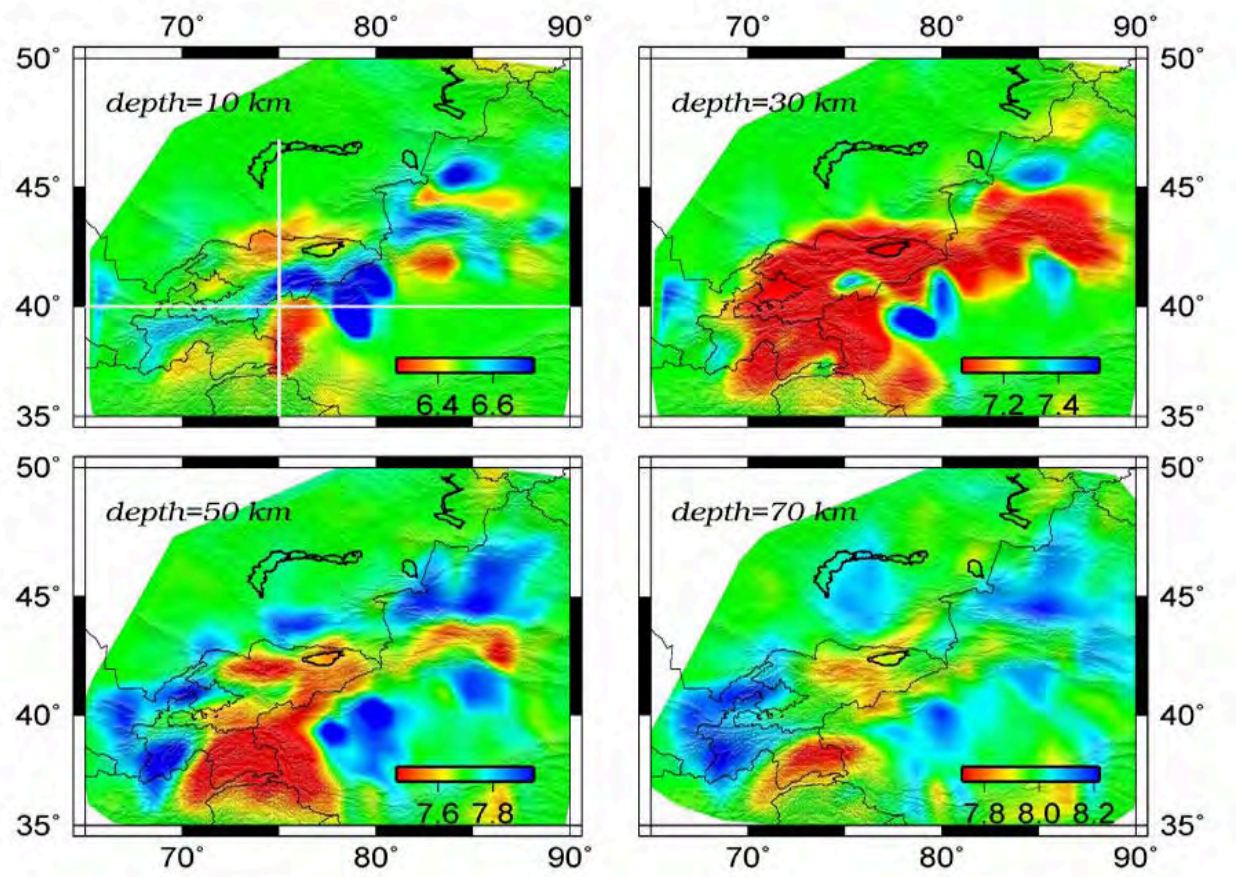

Figure 5. 3-D *P*-wave velocity structure for different depths in Central Asia. These maps were generated by assuming different *P*-wave reference velocities for each depth.

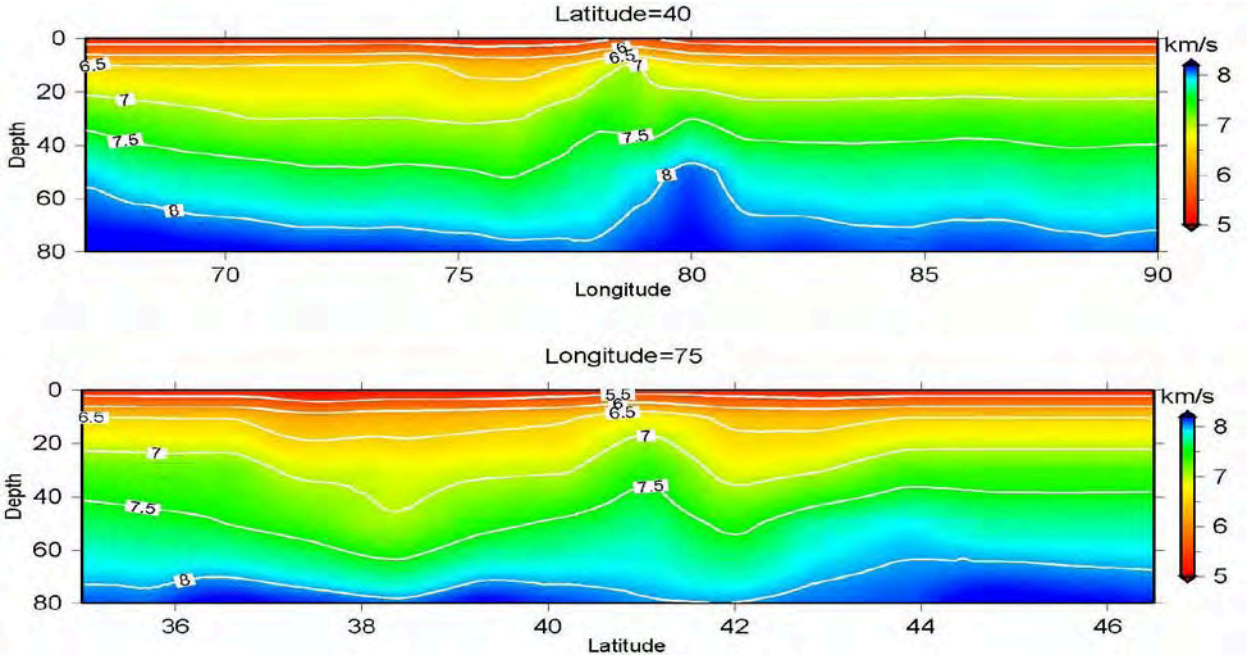

Figure 6. Vertical velocity profiles (the locations are shown in Figure 5).

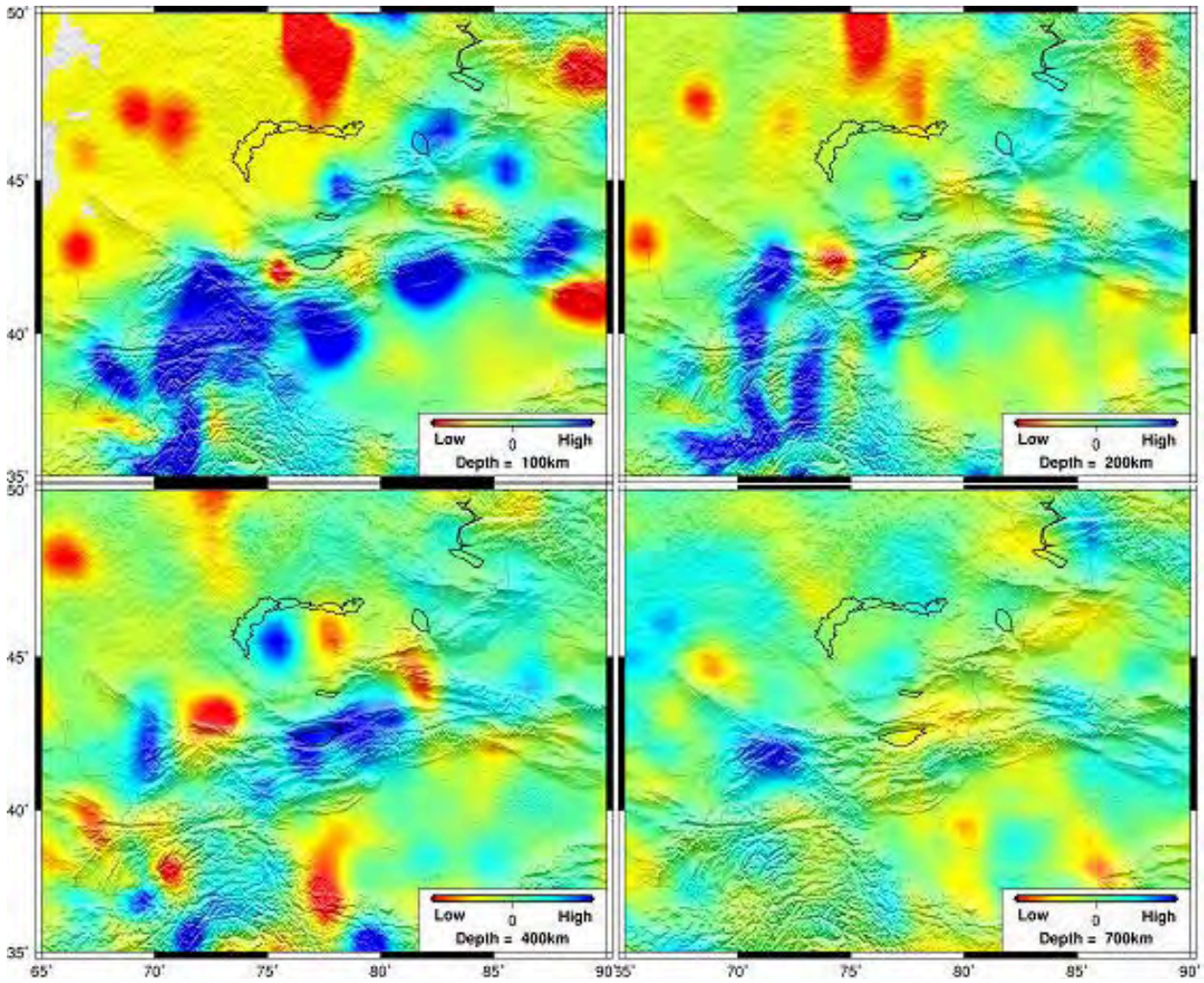

Figure 7. Upper mantle velocity structure at the depths of 100, 200, 400, and 700 km obtained by the double difference tomography method.

HIGH-RESOLUTION SEISMIC VELOCITY AND ATTENUATION MODELS OF THE CAUCASUS-CASPIAN REGION

Robert J.Mellors[1], Rengin Gök[2], Michael E. Pasyanos[2], Gleb Skobeltsyn[3], Eric Sandvol[3], Ugur Teoman[4], Gurban Yetirmishli[5], and Tea Godoladze[6]

San Diego State University[1], Lawrence Livermore National Laboratory[2], University of Missouri-Columbia[3], Kandilli Observatory and Earthquake Research Institute, Turkey[4], Azerbaijan Republic Seismic Survey[5], and Seismic Monitoring Center, Georgia[6]

Sponsored by the Air Force Research Laboratory

Award No. FA8718-07-C-0007
Proposal No. BAA07-18

ABSTRACT

The Caucasus-Caspian region is part of the Alpine-Himalayan collision belt and is an area of complex structure accompanied by large variations in seismic wave velocities. Using data from 29 new broadband seismic stations in the region as well as data from a temporary (1999-2001) deployment in eastern Turkey, a unified velocity structure is developed using teleseismic receiver functions and surface waves. Joint inversion of surface wave group dispersion curves generated from ambient noise with receiver functions show that crustal thickness varies from 34 to 52 km in the region. The thickest crust is in Lesser Caucasus and the thinnest is in the Arabian Plate. Thin crust is also observed near the Caspian. The lithospheric mantle in the Greater Caucasus and the Kura depression is faster than the Anatolian Plateau and Lesser Caucasus. This possibly indicates the presence of cold lithosphere. The lower crust is slowest in the northeastern part of the Anatolian Plateau where Holocene volcanoes are located. Fundamental mode Rayleigh wave phase velocities are determined at periods between 20 and 145 seconds. We observe a relatively high-velocity zone located in the upper mantle under the Kura basin and the western part of Caspian Sea that is continuous to the Moho. The images show very low velocities beneath the eastern Anatolian plateau implying the existence of a partially molten asthenospheric material underlying a very thin lithosphere. Using a two-station method, both *Lg* and *Pg* attenuation is measured and tomograpically inverted to yield attenuation maps. Efficient *Lg* propagation is observed throughout much of the Arabian plate. Moderate *Lg* Q is observed in the Lesser Caucasus and Kura Basin while low *Lg* Q is observed in the East Anatolian plateau. *Pg* shows highly variable propagation throughout the region.

OBJECTIVES

The objective of the research is to develop 3D seismic velocity structure and regional phase attenuation models for the Caucasus-Caspian region (Figure 1). Specifically, the purpose of this work was to:

- Create upper mantle/crustal velocity models using data from new stations in the region.
- Construct detailed maps of regional phase attenuation.
- Compare and validate results and models using the various algorithms as well as independent datasets

The work consisted of four main tasks: data collection, regional phase analysis, crustal and upper mantle velocity determination, and model validation.

RESEARCH ACCOMPLISHED

Data collection. Waveform data was collected from 33 stations (Figure 1) in the region as part of collaborative effort with the individual seismic surveys. The primary focus was collecting continuous data from 2006-2008, although waveform data from other years was collected as available. All data has been provided to the Knowledge Base at Lawrence Livermore National Laboratory.

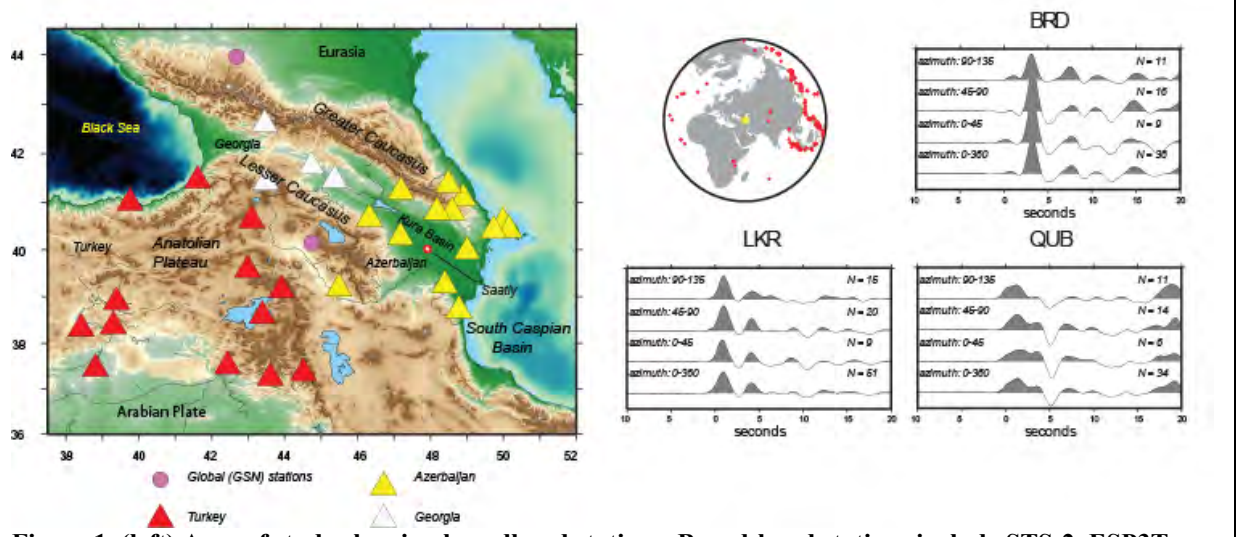

Figure 1. (left) Area of study showing broadband stations. Broad-band stations include STS-2, ESP3T, ESP3ESD and CMG40T type instruments.(right) Example receiver functions stacked by back-azimuth for selected Azerbaijan stations. Global map shows recorded events (red dots) and location of stations (yellow star). Small red circle shows position of Saatly 8 km deep well used for model validation.

Surface wave group velocity and receiver function joint inversion. To develop a comprehensive model of crustal and upper mantle velocities, joint inversion of receiver functions and surface waves was applied. Crustal receiver functions are sensitive to velocity discontinuities while surface wave dispersion is controlled by average S-wave velocity structure (e.g. Julia et al., 2000). Therefore, combining the two methods yields a robust estimate of crustal and upper mantle velocities. Receiver functions using events at distances between 30 and 90 degrees were calculated for all stations using iterative deconvolution at Gaussian widths of 1.0, 1.5, and 2.5 seconds. Each receiver function (Figure 1) was examined for consistency and signals with excessive amplitudes on the tangential component or grossly different from the stacked average for each station was discarded. Coverage was best for back-azimuths to the east and sparse to the west. Initially, the receiver functions were modeled independently to investigate quality. The slant stacking of Zhu and Kanamori (2000) was also used to estimate Moho depths. In general, the stations near the Caspian show poor quality receiver functions with indications of considerable crustal scattering and reverberations due to the thick sediments. These were difficult to model. Some indications of 3D structure were observed for stations in the Greater Caucasus as the receiver functions showed clear variations with back azimuth.

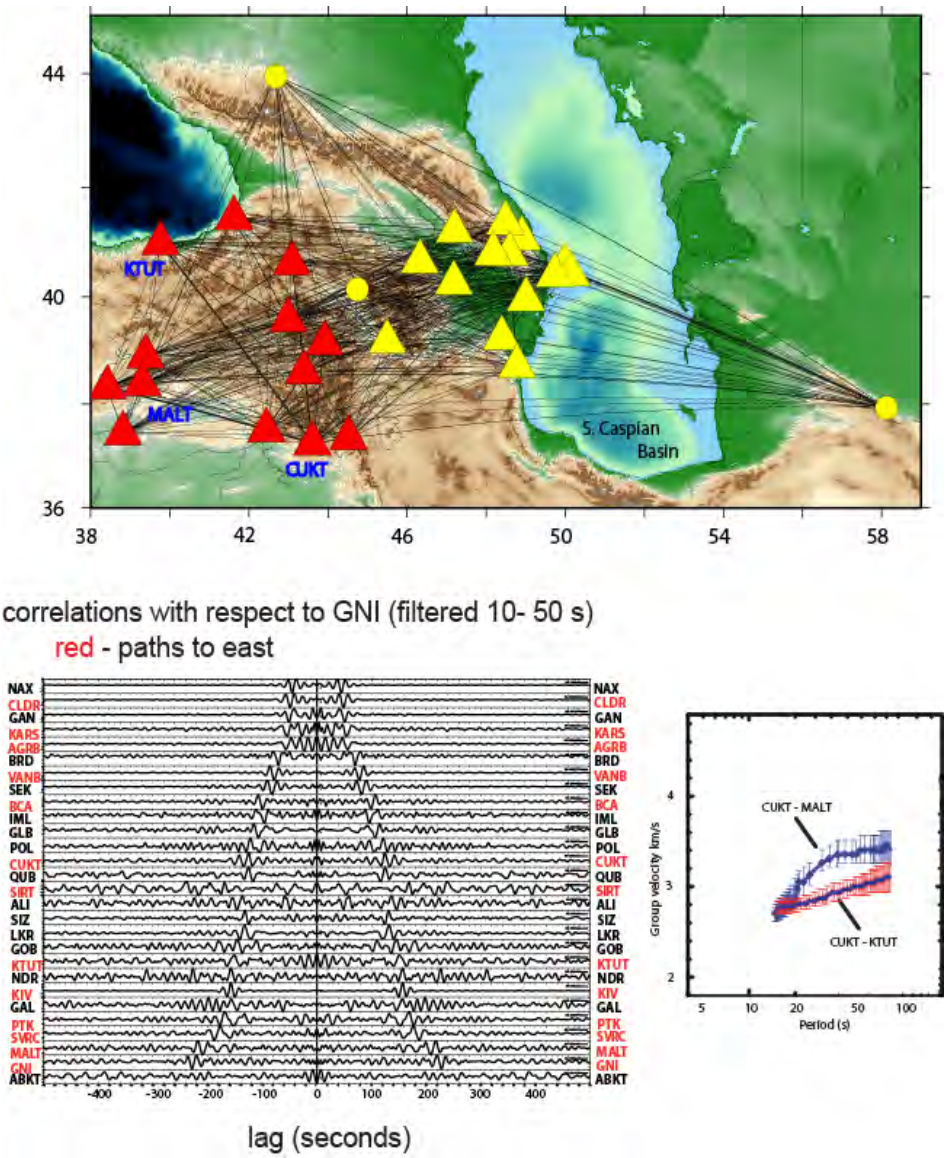

Figure 2. (top) Ray paths used in ambient noise surface wave correlation. (bottom, left) Correlations of stations with respect to station GNI. Stations marked in red show ray paths from west and stations in yellow are east of GNI. (bottom, right) Dispersion curves for stations pairs located in the Anatolia plateau and across the South Caspian.

Surface wave group velocity dispersion measurements were made using both event-based and ambient noise correlation methods. Love and Rayleigh wave group velocity dispersion curves were estimated for over 1,500 waveforms at periods of 7–100 sec. Ambient noise correlation was applied to all possible station pairs (~400) to obtain Rayleigh wave group velocities. All dispersion curves were picked manually and then included in the global/regional tomographic inversion of Pasyanos et al. (2005). We then extracted the dispersion curves from the tomography maps of surface waves and combined them with stacked receiver functions.

Horizontal depth slices of 11, 35 and 87 km are shown in Figure 3 as well as an estimated Moho thickness map. The thick sediments of Kura Basin are evident in upper crust with low velocities averaging Vs=2.8 km/s. The eastern part of the Greater Caucasus shows similar low velocities in the upper crust. The slowest lower crustal velocities are observed in the northeastern Anatolian plateau and Lesser Caucasus region where considerable Neogene/Quaternary, Holocene volcanic activity has occurred. Faster lower crustal velocities occur at the edge of

the Caspian and in the Arabian plate. The upper mantle appears distinctly slow under the Anatolian plateau and to the southeast. Indications of faster upper mantle velocities occur under the Greater Caucasus. It was noted that inversion for Love and Rayleigh waves provided slightly different results, possibly due to anisotropy.

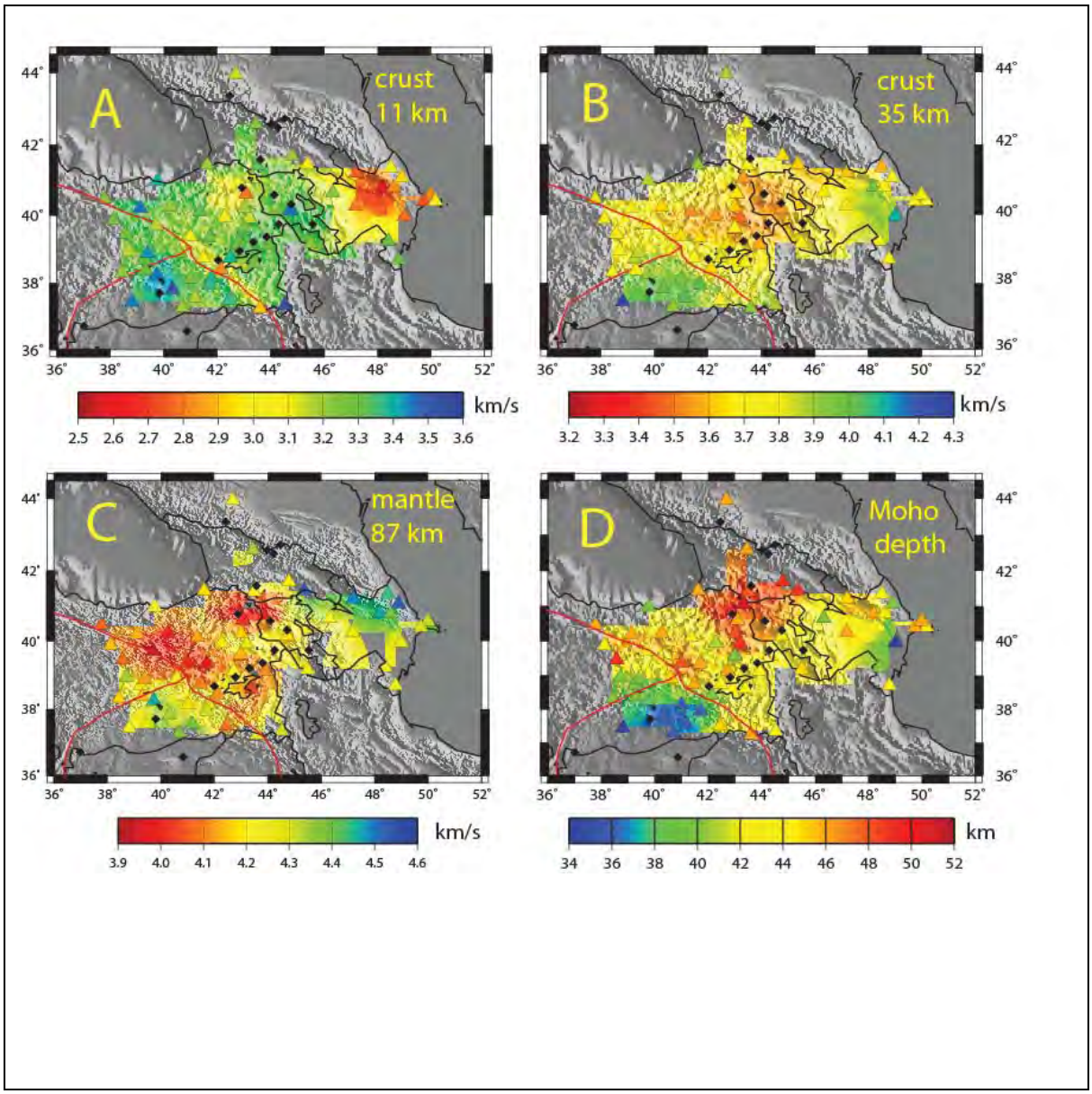

Figure 3. A, B) Crustal S velocities estimated from joint inversion at depths of 11 (left) and 35.5 km (right). C) Upper mantle S velocities at a depth of 87 km. D) Moho depth inferred from velocity profiles based from joint inversion. Black lines mark international borders and coastlines; red lines show major faults and suture zones. Black dots are Holocene volcanics.

Surface wave phase velocity inversion. To investigate variations in upper mantle velocities, surface wave phase velocities measured from earthquakes were also inverted. Data from an earlier temporary deployment of 29 stations was used as well as the newer data. Teleseismic earthquakes with a magnitude greater than 5.8 were selected and the waveforms were evaluated for high signal to noise at the longer periods (50 and 125 seconds). Unfortunately, many of the Azerbaijan stations showed high noise levels at the longer periods even on the vertical component, possibly due to barometric variations. This restricted the data set to 20 events. The data for each event were filtered to create 13 frequency bands with corresponding centered periods ranging from 20 to 145 seconds and dispersion curves were

estimated from these results. Initially, the Rayleigh wave phase dispersion was inverted to estimate 1D velocities. The results were topographically inverted for 2D structure on a 50 km grid using two methods: Forsyth et al. (1998) and Yang and Forsyth (2006). The two methods are similar but the Yang and Forsyth technique attempts to compensate for scattering caused by local heterogeneities and therefore should improve spatial resolution (Figure 4). The results at shorter wavelengths were more robust than for the longer wavelengths especially for the area covered by the Azeri stations, possibly due to excessive noise at longer wavelengths. Higher upper mantle velocities were observed under Anatolia and lower velocities under the Caucasus/Caspian.

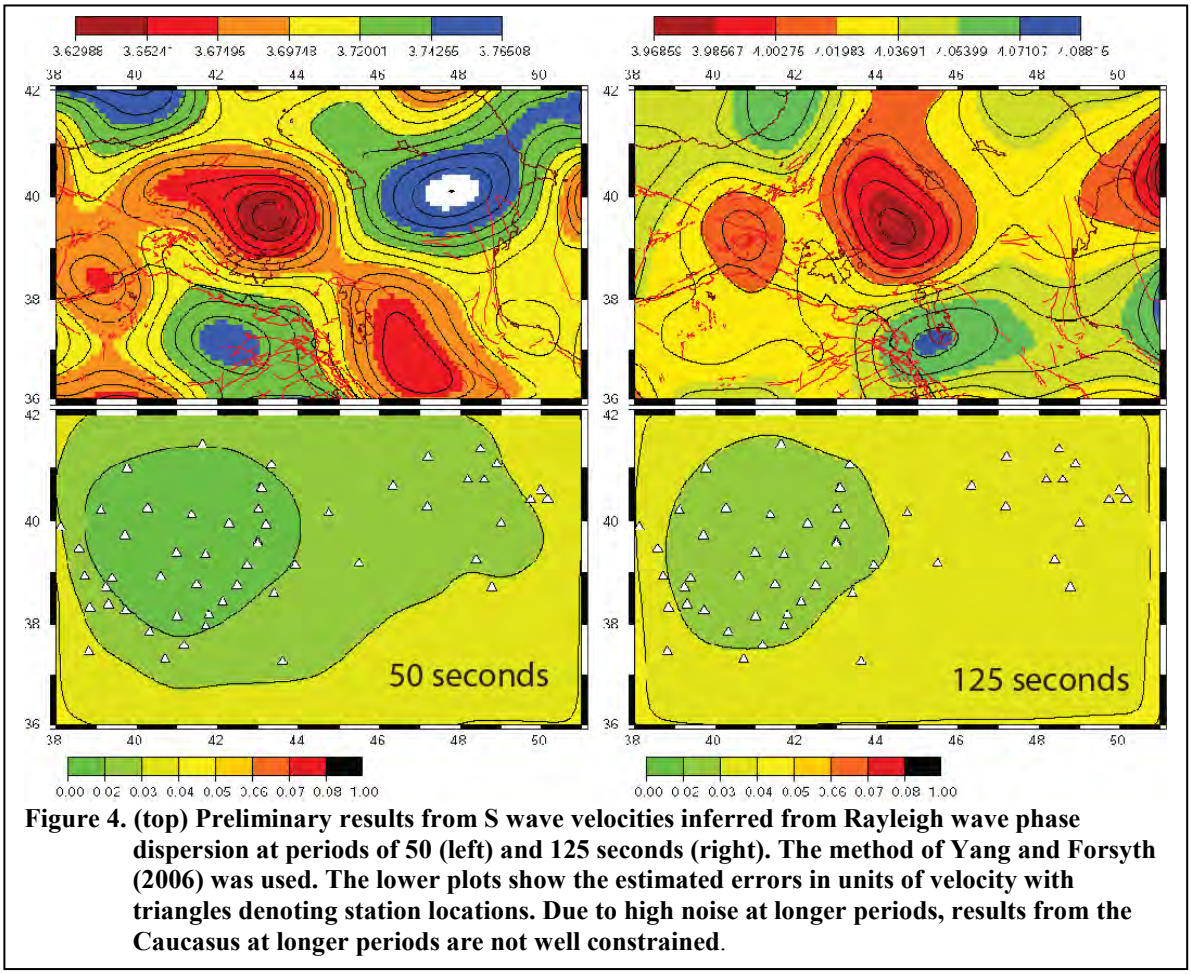

Figure 4. (top) Preliminary results from S wave velocities inferred from Rayleigh wave phase dispersion at periods of 50 (left) and 125 seconds (right). The method of Yang and Forsyth (2006) was used. The lower plots show the estimated errors in units of velocity with triangles denoting station locations. Due to high noise at longer periods, results from the Caucasus at longer periods are not well constrained.

Regional phase analysis. The purpose of the regional phase analysis was to extend regional phase attenuation maps (e.g., Al-Lazki et al., 2003; Gok et al., 2003) throughout Anatolia and the Caucasus (Figure 5). The mapping was performed by first measuring attenuation between stations and then inverting to solve for the average Q in discrete spatial cells. The direct two-station method was used (e.g., Zor et al., 2007; Xie et al., 2004) to estimate attenuation for each path. This method relies on spectral ratios between pairs of station aligned with the ray paths from each event. Phases were identified manually to avoid problems caused by variations in crustal velocities. Spectra for each phase were estimated after windowing. Station pairs for each event were selected using a criteria based on inter-station distance and alignment with event (±15°). The spectral ratio between two stations was calculated for appropriate station pairs after correction for distance (Xie et al., 2004) and geometrical spreading. Q and η (frequency dependence) were then estimated from the spectral ratios using linear regression. This Q and η represents the attenuation along a line between the two stations. These attenuation measurements were added to an existing Middle East dataset which was inverted to create a regional map (Figure 5). The dataset includes approximately 3000 station pairs. Separate inversions were conducted for both *Lg* and *Pg*. Checkerboard tests were performed to evaluate resolution and both ART and LSQR inversion algorithms were tested to evaluate the effect of possible numerical artifacts. Results were similar for both algorithms. Raypath coverage is good in eastern Anatolia but is sparser towards the Caucasus and Caspian.

The 1 Hz *Lg* results show a broad zone of high attenuation (low Q) extending roughly east-west north of the Arabian plate from Anatolia to the Caspian (Figure 5). Considerable spatial variation exists which likely reflects the complicated tectonics. *Lg* appears to propagate well in the Arabian plate but is dramatically attenuated in the Lesser Caucasus. This may be due to the volcanism and the possibility of partial melt in the crust. The Kura basin and the extreme eastern Caucasus show moderate to low attenuation, which may reflect the influence of the Eurasia plate. It is clear from these results that the Kura basin is underlain by continental crust and is distinct from the South Caspian. The variations in *Lg* attenuation appear to result from a combination of both crustal heterogeneity and changes in crustal thickness. While Moho depth increases by 5 to 10 km at the northern edge of the Arabian Plate the variation in depth from Anatolia to the Lesser Caucasus is fairly small and yet relatively low *Lg* Q is observed. Volcanic regions are often observed to possess low Lg Q possibly due to high attenuation of shear waves by partial melt in the crust. *Pg* reveals a distinctly different pattern. The transition between the Arabian plate and Anatolian plateau is defined by an abrupt change in *Pg* Q east of about 38 E longitude but a clear zone of high Q exists in the Lesser Caucasus. The zone of low Q along the Caspian and Kura basin may be caused by the abrupt thickening in sediments and dipping Moho, which decreases the efficiency of the crustal *P* waveguide.

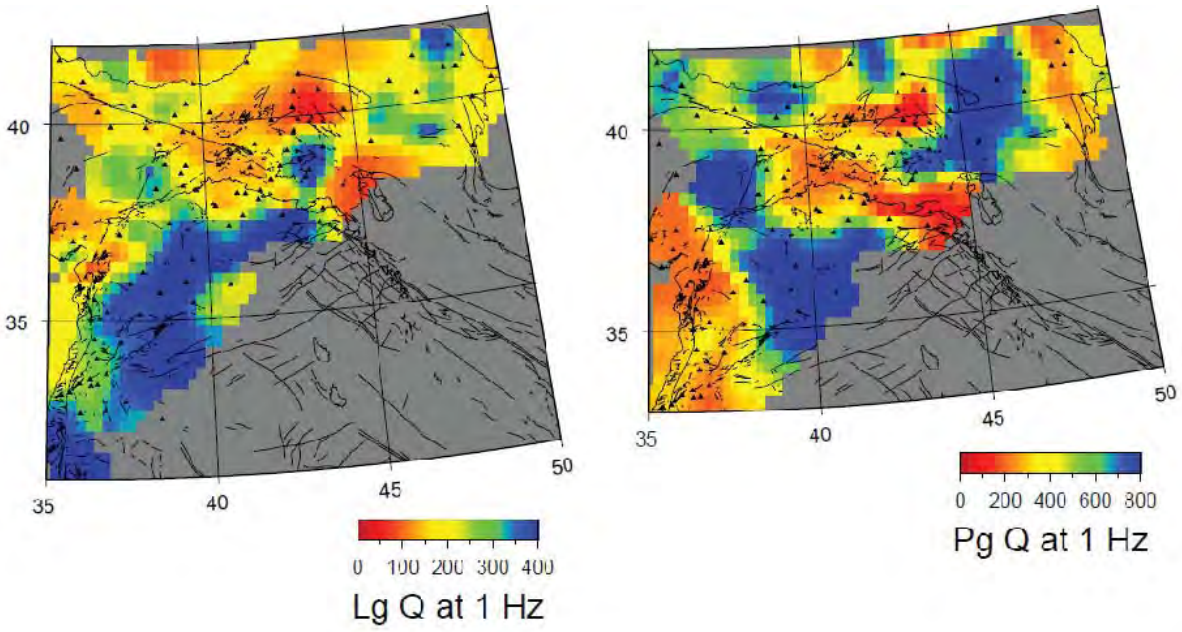

Figure 5. Attenuation maps for *Lg* (left) and *Pg* (right).

Model validation. The model was tested in several ways: comparison with alternate datasets such as reflection seismic and gravity, earthquake hypocenters comparison, and with waveform modeling. Seismic reflection refraction data shows clearly the deep sedimentary layers in the South Caspian and coastline (Knapp et al., 2004; Mangino and Priestley, 1998). Gravity data also suggests deep basement, which closely matches the low velocities for the area observed by the joint inversion. The Moho depths inferred by refraction data are also similar. 2D modeling of gravity data through the center of the Kura basin shows a clear gravity high that runs roughly north-south and parallel to the Caspian coast and delineates the Kura from the South Caspian. The existence of this basement high is confirmed by the Saatly deep well, which penetrated to a depth of 9 km through a succession of sediment and then volcanoclastic layers. To first order, alternate datasets are consistent with our results, both for crustal and mantle velocities and with phase propagation.

A second set of tests was conducted with earthquake locations. This effort was focused in the Azerbaijan region. The 3D model was averaged to produce an average 1d model. Hypocenter locations were calculated using this model and compared with global PDE (Preliminary Determination of Epicenters) locations. Significant differences in location were observed (up to 30 km) (Figure 6). A major factor is the exceptionally thick sedimentary package in Kura Basin and nearby South Caspian Basin. Waveforms for events with known focal mechanisms were also calculated using this model.

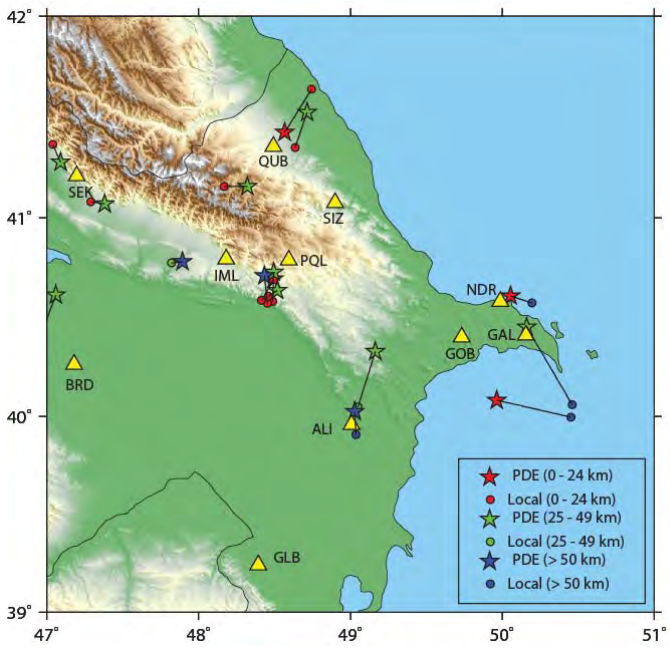

Figure 6. Comparison of global earthquake locations (stars, PDE) with locations determined using the local network (circles) with the new velocity model. Red is shallower than 25 km, green between 25 and 50, and blue is deeper than 50 km. Lines connect different locations of the same event.

CONCLUSIONS AND RECOMMENDATIONS

An improved crustal and upper mantle velocity and attenuation model has been developed for the Caucasus/Caspian region and Anatolian plateau. The Caspian and Kura basins show pronounced low velocities in the upper crust but slightly elevated lower crustal velocities. Crustal thickness varies from about 50 km in the Lesser Caucasus to 35 km in the Arabian plate. The upper mantles display strong heterogeneities in the region. It is slow under the Anatolian plateau and slightly fast under the Greater Caucasus. These are likely related to slab remnants and ongoing volcanism.

Striking variations in regional phase propagation and velocities are mapped. *Lg* is highly attenuated not only in the South Caspian and Black Sea basins but also in the Anatolian plateau, possibly due to a combination of crustal properties under the volcanic areas and varying crustal thickness. A clear change in *Lg* attenuation occurs at the northern edge of the Arabian plate. A narrow band of moderate *Lg* attenuation exists in the Kura basin and along the Caspian. *Pg* also shows variations in attenuation.

Due to the strong spatial variations in both crustal and mantle properties, regional seismic waves should be expected to vary significantly both in travel-time and amplitude in this region. More seismic stations are scheduled to be installed in the region by the various surveys and this data would be useful in increasing the resolution of these results.

ACKNOWLEDGEMENTS

We thank all members of the Kandilli, Georgian, and Azerbaijan seismic surveys for their assistance in gathering data. R. Herrman, C. Ammon, J. Xie, Y. Yang, and J. Julia provided software used in the analysis of this data.

REFERENCES

Al-Lazki, A.I., D. Seber, E. Sandvol, E.,N. Turkelli, R. Mohamad, and M. Barazangi (2003). Tomographic Pn velocity and anisotropy structure beneath the Anatolian plateau (eastern Turkey) and the surrounding regions, *Geophys. Res. Lett*. 30: (24).

Forsyth, D. W., S. C. Webb, L. M. Dorman, and Y. (1998). Phase velocities of Rayleigh waves in the MELT experiment on the East Pacific Rise, *Science* 280: 1235–1238.

Gök R., E. Sandvol, N. Türkelli, D. Seber, and M. Barazangi (2003). *Sn* attenuation in the Anatolian and Iranian plateau and surrounding regions, *Geophys. Res. Lett*. 30: 24, 8042.

Julia, J., C. Ammon, R. Herrman, and A. Correig (2000). Joint inversion of receiver function and surface wave dispersion observations, *Geophys. J. Int*. 143: 1, 99–112.

Knapp, C., J. Knapp, and J. A. Connor (2004). Crust-scale structure of the South Caspian Basin revealed by deep seismic reflection profiling, *Marine and Petro. Geol.* 21: 1073–1081.

Mangino, S and K. Priestley (1998). The crustal structure of the southern Caspian region, *Geophys. J. Inter*. 133: (3), 630–648.

Pasyanos, M. E. (2005). A variable resolution surface wave dispersion study of Eurasia, North Africa, and surrounding regions, *J. Geophys. Res*. 110: B12301, doi: 10.1029/2005JB003749.

Yang, Y. and D. W. Forsyth (2006). Regional tomographic inversion of the amplitude and phase of Rayleigh waves with 2-D sensitivity kernels, *Geophys. J. Int* 166: 1148–1160.

Xie, J., R. Gok, J. Ni, and Y. Aoki (2004). Lateral variations of crustal seismic attenuation along the INDEPTH profiles in Tibet from Lg Q inversion, *J. Geophys. Res*. 109: B10308, doi 10.1029/2004JB002988.

Zhu, L., and H. Kanamori, (2000). Moho depth variation in Southern California from teleseismic receiver functions, *J. Geophys. Res*. 105: (2), 2969–2980.

Zor, E., E. Sandvol, J. Xie, N. Tu¨rkelli, B. Mitchell, A. H. Gasanov, and G. Yetirmishli (2007). Crustal attenuation within the Turkish Plateau and surrounding regions, *Bull. Seismo. Soc. Am*. 97: 1B, 151–161.

SOURCE AND PATH CALIBRATION IN REGIONS OF POOR CRUSTAL PROPAGATION USING TEMPORARY, LARGE-APERTURE, HIGH-RESOLUTION SEISMIC ARRAYS

John L. Nabelek[1], Jochen Braunmiller[1], and W. Scott Phillips[2]

Oregon State University[1] and Los Alamos National Laboratory[2]

Sponsored by the Air Force Research Laboratory

Sponsored by the National Nuclear Security Administration

Award No. FA8718-09-C-004[1] and DE-AC52-06NA25396[2]
Proposal No. BAA09-28

ABSTRACT

Broadband seismic data acquired during the Hi-CLIMB field experiment are used to study seismic events and path propagation in the Nepal Himalaya and south-central Tibetan Plateau. Similarities in regional propagation between Tibet and Iran motivate this new study. The 2002–2005 Hi-CLIMB experiment consisted of 233 stations distributed along a dense 800 km linear north-south array extending from the Himalayan foreland into the central Tibetan Plateau. The main array was flanked by a 350 km x 350 km sub-array in southern Tibet and central and eastern Nepal. Our dataset provides an opportunity to obtain seismic event locations for ground truth (GT) evaluation, with emphasis on depth, to determine source parameters, and to study distance evolution of seismic coda for yield estimation in low Q regions. Event detection and preliminary automatic location analysis show tens of thousands, otherwise undetected, local seismic events. We will obtain high-quality event locations from manual *P*- and *S*-wave picks by joint inversion for location and 2D and 3D velocity structure. We will also perform relative locations to resolve spatial relations of several highly active event clusters. Besides GT-compatibility, high-quality locations are essential for the source parameter and coda evolution portions of the study. We will perform moment tensor inversions in a wide magnitude range ($1.5 \le M_w \le 6$), paying particular attention to event depth and size. Full waveform moment-tensor depth is important for validating traveltime-derived depth; seismic moment calibrates spectral coda levels and local and regional magnitudes. The dense station spacing of the Hi-CLIMB array is unique for any highly attenuating crustal path region, permitting fine-scale analysis of decay properties for multiple coda types, which is a globally important, unresolved issue in monitoring research. The GT-level locations and moment tensor depths will contribute to Seismic Location Baseline Model (SLBM) tomographic efforts, allow evaluation of depth mislocation for crustal models, and enhance model accuracy throughout central and southern Asia.

OBJECTIVES

The broadband dataset from the 2002–2005 Hi-CLIMB seismic array in the Himalayan-Tibetan collision zone is unique in its large aperture and dense station spacing. The purpose of our research is to improve source and path calibration in regions of poor crustal propagation to enhance the monitoring community's capabilities to estimate magnitude and yield of future nuclear tests in low Q and highly scattering environments. We have three closely linked objectives. The first is to obtain high-precision ground-truth seismic event hypocenters. The second is to provide seismic moment and independent depth estimates from waveform modeling of local and regional earthquakes. And the third is to determine the distance evolution of seismic coda, utilizing the quasi-continuous control offered by the dense, laterally large network (paying emphasis on mantle coda), important for low Q areas.

RESEARCH ACCOMPLISHED

Data

The Hi-CLIMB broadband seismic experiment (Nabelek et al., 2005; 2009) consisted of 233 sites in Nepal and the south-central Tibetan Plateau (Figure 1). The network operated from 2002 through 2005 and each site was occupied for 12 to 20 months. The network consisted of an 800-km long north-south array covering the India-Eurasia collision zone from the Ganges foreland across the Higher Himalayas into the Tibetan Plateau. Station spacing was 3-4 km in the south and about 8 km north of the Yarlung-Tsangpo suture. Complementary lateral deployments, with 30 to 40 km station spacing, in central and eastern Nepal and southern Tibet improve earthquake location capabilities and provide wave propagation control for the transition from the foreland into the plateau. All data were recorded continuously at 50 sps. The Hi-CLIMB data provide an opportunity to determine locations, source parameters and coda distance evolution of small sized seismic events at unprecedented accuracy in central Asia.

Additional broadband data are available from the earlier HIMNT experiment in eastern Nepal and southern Tibet (e.g., Sheehan et al., 2004; Monsalve et al., 2005; de la Torre et al., 2006) and from the five-station Program for the Array Seismic Studies of the Continental Lithosphere (PASSCAL) Bhutan pilot experiment (Velasco et al., 2003). HIMNT occupied a similar area as our eastern-Nepal/southern-Tibet subnet (Figure 1), but with fewer stations and shorter operation times from late 2001 into 2002.

Figure 1 shows the large spatial extent and high station density of the Hi-CLIMB project. Coupled with long recording durations, this results in a much-improved coverage of this large, complicated tectonic region. We observe a very high seismicity rate with about 1000 events per week (Figure 2) compared to fewer than 1700 events for an 18-month period during HIMNT (e.g., de la Torre et al., 2006) that were mainly located in Nepal. As an example, Figure 3 shows preliminary locations from central and southern Tibet, largely in areas not covered by any previous experiments or permanent networks.

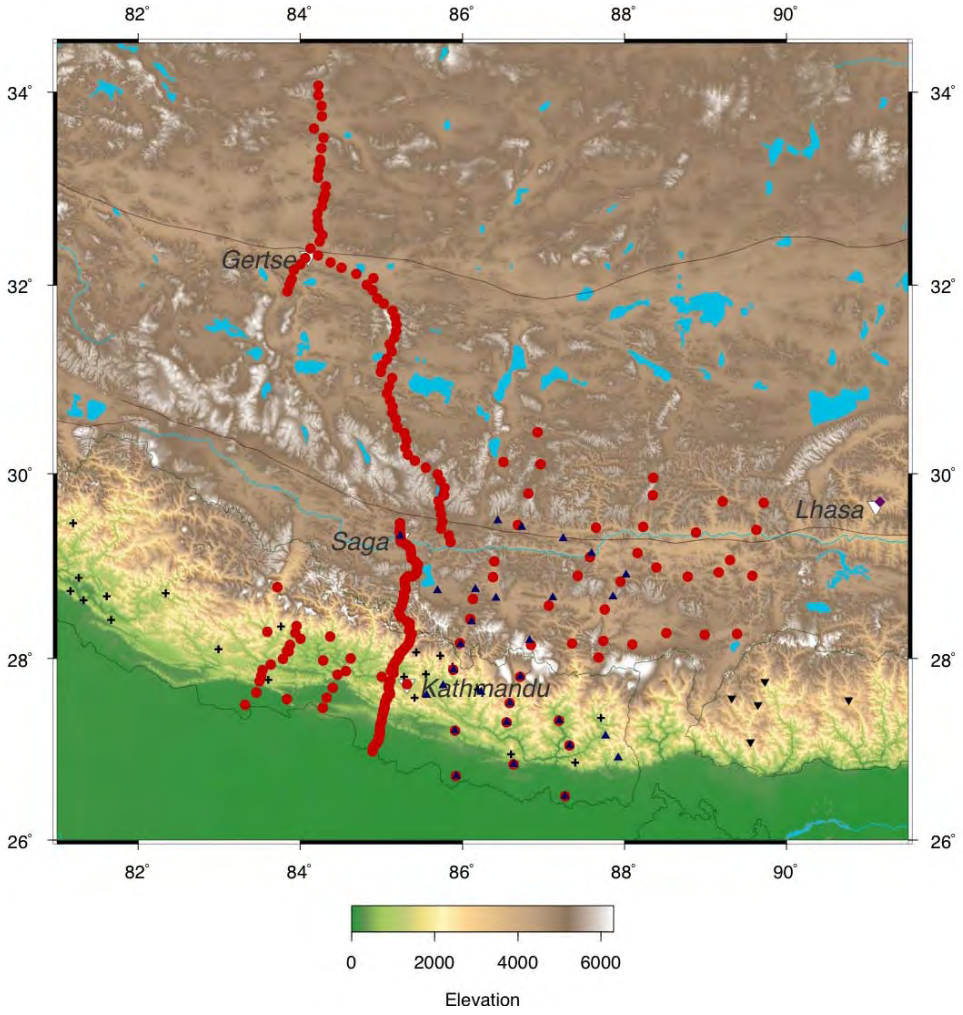

Figure 1. Hi-CLIMB (red circles), HIMNT (blue upright triangles), and Bhutan (black inverted triangles) broadband temporary stations and Nepalese National Seismic Network (crosses). During the first 20 months of Hi-CLIMB (Nepal and South Tibet), 75 broadband instruments were available while during the second 15 months (South and Central Tibet), 111 instruments were available. Altogether, 233 sites were occupied.

Event Detection and Preliminary Location

The entire Hi-CLIMB waveform database (1.4 TB) has been organized using the Antelope software developed by Boulder Real Time Technologies (BRTT). The package includes modules for automatic detection and arrival time picking, event-arrival association and event location. Preliminary analysis of event detections reveals about a thousand legitimate event detections per week (Figure 2). For the second half of the experiment, we located over 60,000 events of magnitude greater than 0. This is more than 300 times the number of events listed in the United States Geological Survey (USGS) Preliminary Determination of Epicenters (PDE) catalog for the same region and period. For some events, the PDE locations also show a mismatch of up to 50 km.

We developed several modules to weed out spurious detections as well as erroneous phase and event associations to automate data management. Figure 3 shows the resulting fully automatic preliminary event locations for a 15-month time period for events with at least 15 *P* and *S* arrivals corresponding roughly to M≥2, which is a relevant cut-off for monitoring purposes. Most shallow seismicity north of the Yarlung-Tsangpo suture (north of 29.5°N) is in an area

not investigated by most other experiments. These locations, although fully automatic, utilize many S-arrivals and correlate with geologic structures seen in satellite imagery suggesting they are already quite accurate.

We will locate as many events as possible, but will focus on locating selected events at the GT20 level and better with careful consideration of depth and absolute location uncertainties as required. We plan to arrive at accurate locations through a succession of location steps eliminating events that do not pass more strict requirements and resulting in a subset of refined locations. An important part of this work will include improving crustal structure models.

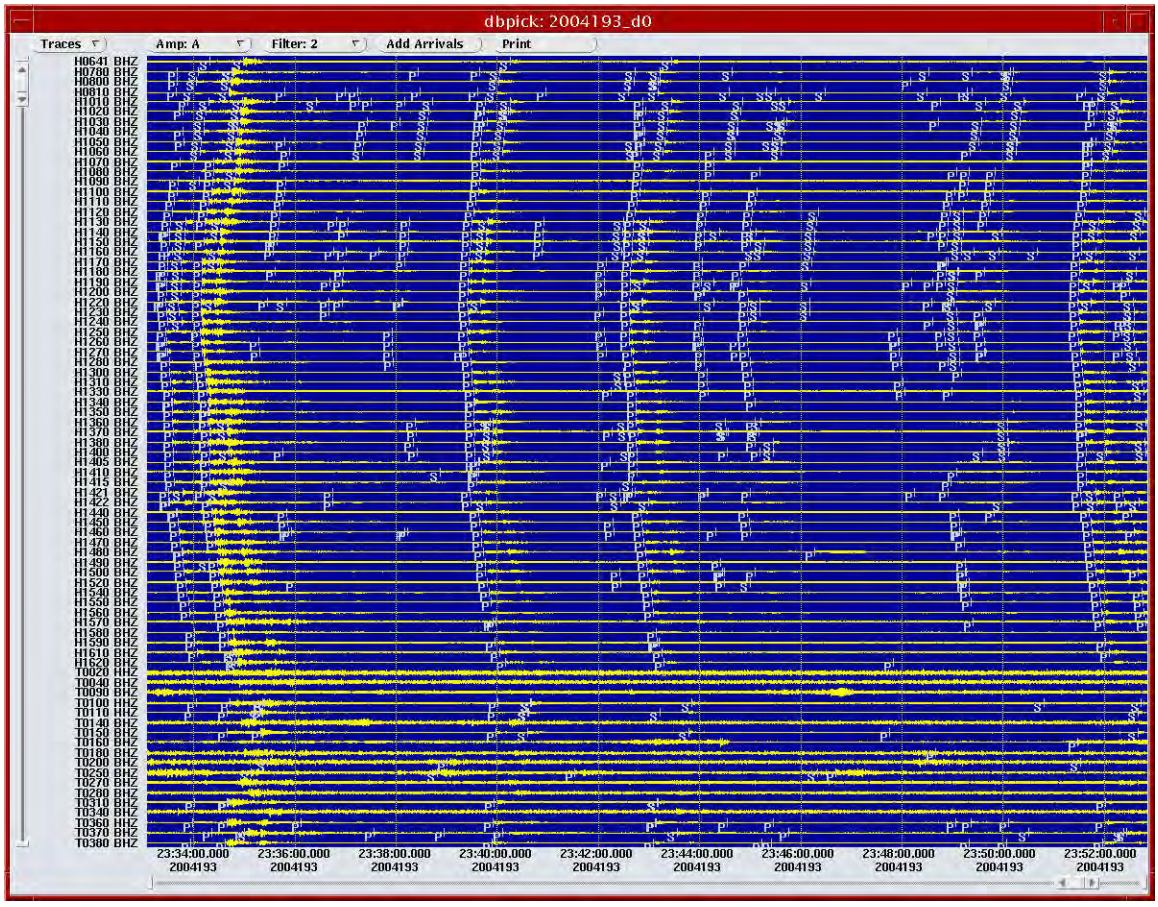

Figure 2. Event detection for a 20-minute Hi-CLIMB data window (Julian day 193, 2004, start 23:33 UTC). *P*- and *S*-phase association has been performed and four stronger local events were recorded across the array and many smaller events at specific station groups only.

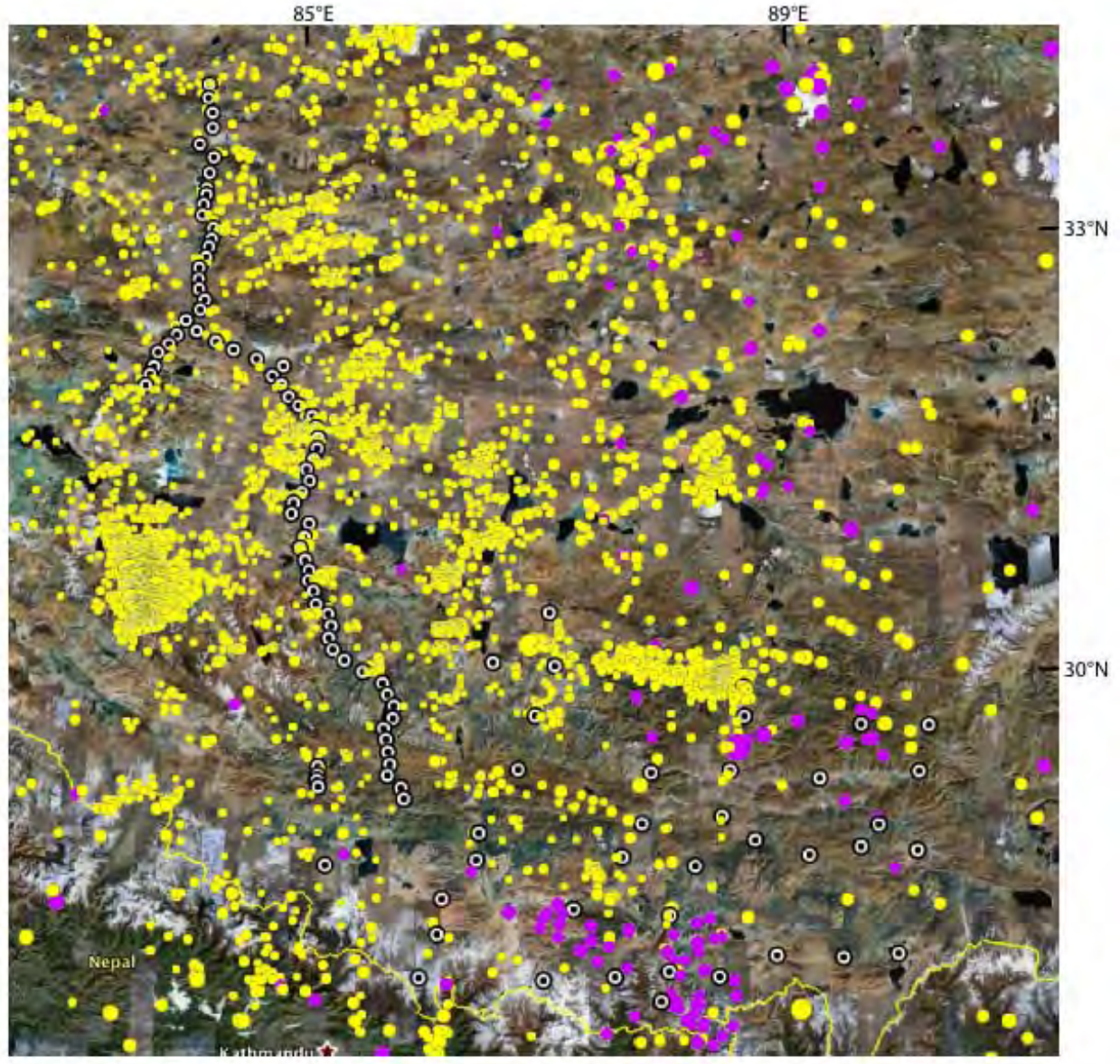

Figure 3. Preliminary epicenter map (colored circles) for 15-month period covering the second half of the Hi-CLIMB experiment (recording stations black circles). Over 60,000 events have been located. We plot 11,000 events with at least 15 *P* and *S* arrivals. Yellow: depth ≤ 60 km (crustal events) and purple: depth > 60 km (potential upper mantle events). The numerous shallow events north of the Yarlung-Tsangpo suture (>29°N) have not been covered by previous experiments.

Source Parameters from Regional Moment Tensor Inversion

Regional moment tensor studies in the Himalayan-Tibetan region have been performed (Burtin, 2005; Burtin et al., 2005; Baur, 2007) for selected larger earthquakes using the full waveform inversion code developed by Nabelek and Xia (1995). Results obtained thus far are summarized in Figure 4. Burtin (2005) tested analysis feasibility with permanent far-regional stations. Deriving station specific velocity models, he analyzed 29 M_w>4.5 events that occurred from 1988 to 2000 within 1000 km of closest station LSA (Lhasa, Figure 1) along the southern boundary of the Tibetan Plateau. Long paths require analysis at long periods (T≥33 s), which limits parameter resolution and sets a high analysis threshold. The Hi-CLIMB data allow analysis of much smaller M_w≈3.5 events with near-regional seismograms at periods of T≥15–20 s (Baur, 2007); so far, we have obtained more than 100 moment

tensors (Figure 4). The high data quality and redundancy allow parameter resolution tests for size, depth, and moment tensor. Preliminary analysis suggests a depth resolution for shallow crustal events on the order of ±5 km and an estimated M_w uncertainty of ±0.1–0.2 units with currently used velocity models and event locations.

Quality event locations and improved structural models that are being developed as part of the GT effort will be important to increase accuracy and resolution of the source parameters. The improved models will also be used to analyze smaller events near M=3 at near-regional distances and to model larger-event waveforms reliably for distances up to 1000 km at short periods near T=10 s. Selected smaller events near the dense array will be analyzed in conjunction with the GT location effort (e.g., to obtain independent depth estimates) and requirements of the coda wave modeling (e.g., to provide seismic moment over a range of event sizes for calibration of absolute spectral levels from coda to bands approaching those used for yield estimation).

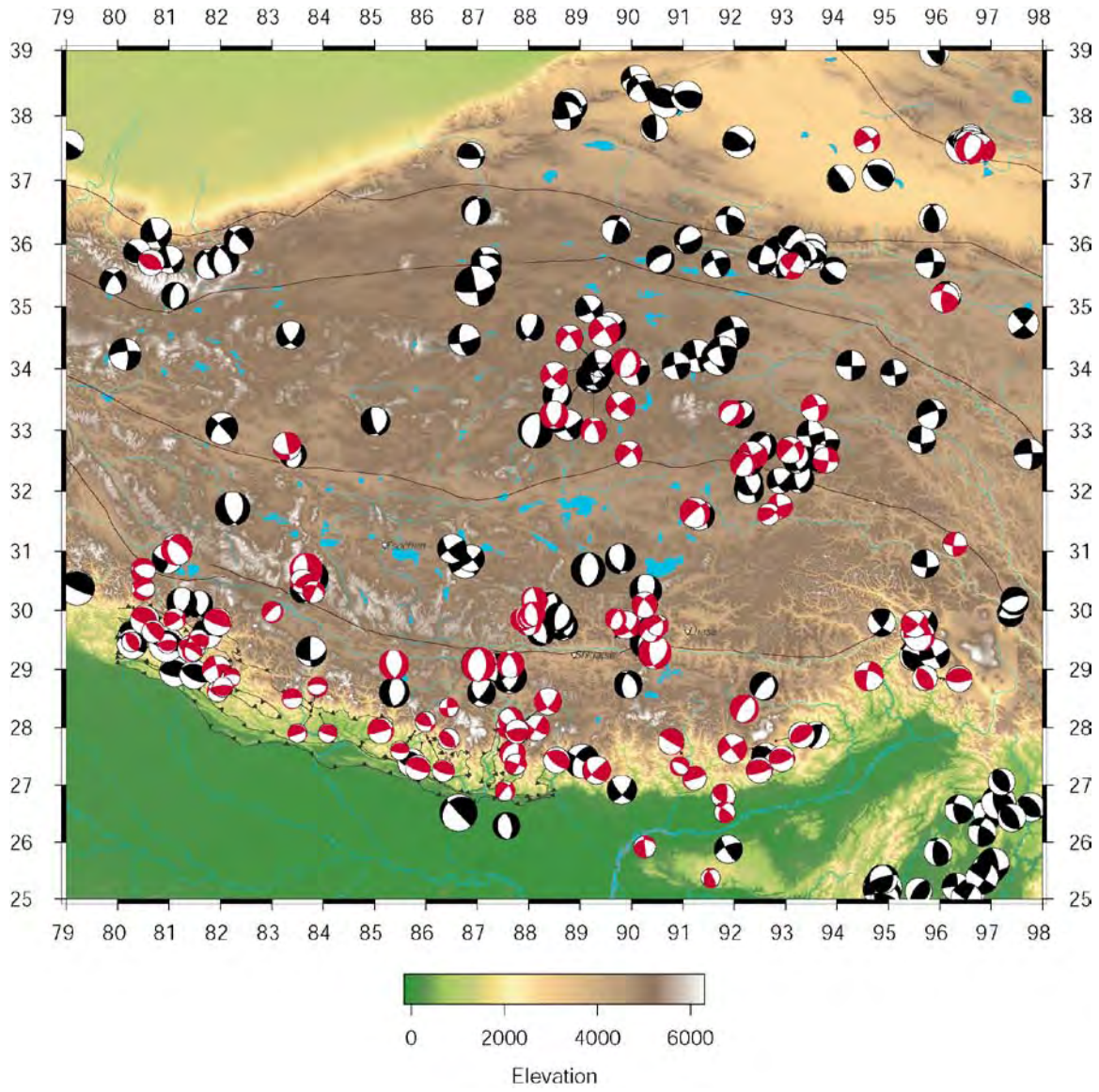

Figure 4. Regional moment tensors (red: Burtin, 2005: Baur, 2007) and Global Harvard centroid moment tensors (CMTs) (black). We completed analysis of 150+ largest events in the Tibet region using all high-quality waveforms. The Hi-CLIMB set of 130+ solutions contains events as small as M_w=3.5. 166 CMT solutions, mainly M_w>5.0, exist for 1976–2005. In southern Tibet and Nepal our efforts substantially expand the moment-tensor catalog.

Propagation Models for Multiple Coda Types

Analysis of coda waves provides stable, high precision amplitude measurements for magnitude and yield estimation. The averaging nature of the scattered waves that form the coda reduces the effects of source mechanism and path, allowing measurement stability from one station that would only be obtainable from a dense array for direct waves.

Coda measurements incorporate corrections to account for distance dependent amplitude decay under the usual assumption that one phase (surface waves, *Lg*, *Sn*, or *P*) dominates the coda. However regions of extremely low crustal Q or *Lg* phase blockage support diverse types of coda even within one frequency band as a result of *Lg* phase stripping exposing mantle coda associated with *Sn* and/or *P*n. Mantle coda are not as well excited as *Lg* coda, but higher Q at depth supports their longer duration such that low crustal Q allows observation of mantle coda at shorter distances. Figure 5 shows coda evolving from *Lg* to *Sn* over regional distances for station LSA in Tibet.

The length and station density of the Hi-CLIMB array offers a unique opportunity to study the evolution of multiple coda types and develop new models and parameters to enable their use. Specifically, we are interested in: 1) precise determination of short distance path parameters for *Lg* coda from amplitude differences, a technique requiring high station density, which is unavailable across most of Asia, 2) development of path models and relative transfer functions for multiple coda types (e.g., Phillips et al., 2008); and 3) development of strategies for integrating measurements for different coda types to obtain absolute source spectra for M_w and yield estimation. In regions of extremely low crustal Q, like Tibet and Iran, identification of dominant coda type at a given distance and its decay are crucial for accurate size estimation.

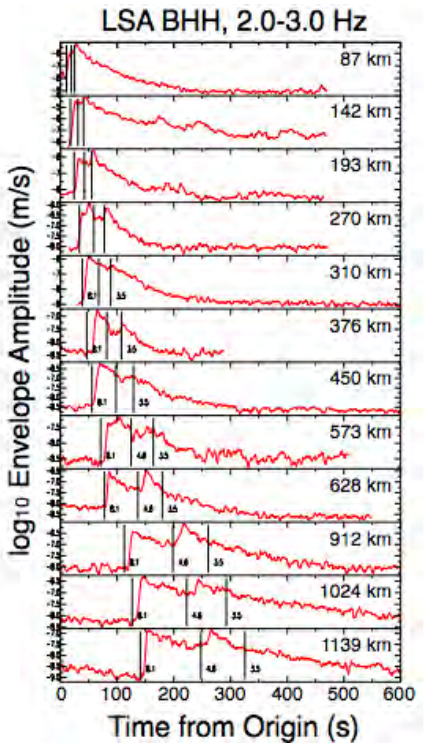

Figure 5. Evolution of 2-3 Hz coda from *Lg* to *Sn* in Tibet for events recorded at LSA. Distances are noted to the right of each envelope. Group velocities of 8.1, 4.6 and 3.5 km/s, representing *Pn*, *Sn*, and *Lg*, respectively, are marked.

CONCLUSIONS AND RECOMMENDATIONS

The Hi-CLIMB broadband seismic dataset provides the opportunity for ground truth location and source parameter determination and the study of distance evolution of seismic coda in central Asia. The dataset reveals an abundance of seismic events that are not included in any other catalog. Initial waveform modeling efforts resulted in a 150+ event moment tensor database. The GT level locations and moment tensor depths will contribute to SLBM tomographic efforts, allow evaluation of depth for crustal models, and enhance model accuracy throughout central and southern Asia and, in general, will contribute to the National Nuclear Security Administration (NNSA) Knowledge Base. The high station density of the network allows a detailed study of seismic coda to gain understanding of its distance evolution in a region of low crustal Q; results will probably not transport directly from Tibet to other regions of low crustal Q, like Iran, but will lead to development of strategies for coda analysis that are globally useful.

REFERENCES

Baur, J. (2007). Seismotectonic analysis of the Himalayan-Tibetan collision zone from regional seismic moment tensor analysis with Hi-CLIMB data, *M.Sc. thesis, Oregon State University, Corvallis, Oregon*, 276 pp.

Burtin, A. (2005). Seismotectonics of the Himalayan arc from regional seismogram moment tensor inversion, *Internship Report, Oregon State University, Corvallis, Oregon*, 42 pp.

Burtin, A., J. Nabelek, J. Baur, and J. Vergne (2005). Evidence for the decoupling of stress above and beneath the Main Himalayan Thrust, *Eos Trans. Am. Geophys. Union* 86(52): Fall Meet. Suppl., Abstract T43A–1379.

de La Torre, T., G. Monsalve-Mejia, A. F. Sheehan, C. Rowe, and M. Begnaud (2006). Ground truth hypocenters and 3D crustal velocity structure in central Asia from in-country networks, in *Proceedings of the 28th Seismic Research Review: Ground-Based Nuclear Explosion Monitoring Technologies*, LA-UR-06-5471, Vol. 1, pp. 377–386.

Monsalve, G., A. F. Sheehan, T. de la Torre, C. Rowe, and M. Begnaud (2005). Ground truth in central Asia from in-country networks, in *Proceedings of the 27th Seismic Research Review: Ground-Based Nuclear Explosion Monitoring Technologies*, LA-UR-05-6407, Vol. 1, pp. 372–382.

Nabelek, J., and G. Xia (1995). Moment-tensor analysis using regional data: application to the 25 March, 1994, Scotts Mills, Oregon earthquake, *Geophys. Res. Lett.* 22: 13–16.

Nabelek, J., J. Vergne, G. Hetenyi, and the Hi-CLIMB Team (2005). Project Hi-CLIMB: a synoptic view of the Himalayan collision zone and southern Tibet, *Eos Trans. Am. Geophys. Union* 86(52): Fall Meet. Suppl., Abstract T52A-02.

Nabelek, J., G. Hetényi, J. Vergne, S. Sapkota, B. Kafle, M. Jiang, H. Su, J. Chen, B.-S. Huang, and the Hi-CLIMB Team (2009). Underplating in the Himalaya-Tibet collision zone revealed by the Hi-CLIMB experiment, *Science*, in press.

Phillips, W. S., R. J. Stead, G. E. Randall, H. E. Hartse and K. Mayeda (2008). Source effects from broad area network calibration of regional distance coda waves, in *Scattering of Short Period Waves in the Heterogeneous Earth*, H. Sato and M. C. Fehler, Eds., in press.

Sheehan, A. F., G. Monsalve, C. Rowe, and M. Begnaud (2004). Ground truth in central Asia from in-country networks, in *Proceedings of the 26th Seismic Research Review: Trends in Nuclear Explosion Monitoring*, LA-UR-04-5801, Vol. 1, pp. 338–345.

Velasco, A. A., K. C. Miller, and L. S. Hollister (2003). Results from a temporary seismic network in Bhutan, *Eos Trans. Am. Geophys. Union* 84(46): Fall Meet. Suppl., Abstract S21F–0398.

FREQUENCY-DEPENDENT NATURE OF *Pn* IN WESTERN CHINA

Robert L. Nowack[1], Wang-Ping Chen[2], and Tai-Lin Tseng[2]

Purdue University[1] and University of Illinois[2]

Sponsored by the Air Force Research Laboratory

Award No. FA8718-08-C-0025
Proposal No. BAA08-42

ABSTRACT

We are investigating *Pn* propagation in Western China based on regional events recorded by the Hi-CLIMB (An Integrated Study of the Himalayan-Tibetan Continental Lithosphere during Mountain Building) array in the region. Seismic attributes, including arrival times, Hilbert envelope amplitudes and instantaneous and spectral frequencies, are being used to investigate how the crustal and upper mantle velocity and attenuation structure affects the propagation of *Pn* arrivals in Tibet. We have constructed more than 30 high-quality regional seismic profiles, and of these, 14 events have been selected with excellent crustal and *Pn* arrivals for further analysis. Regional travel-times recorded by the Hi-CLIMB array are used to constrain the larger scale velocity structure in the region, with four events near the array used to constrain the crustal structure. We are also independently constraining the variation of upper mantle velocity and depth of the Moho by modeling *SV*-coupled shear waves at teleseismic distances. The amplitude of the *SsPmP* phase is particularly sensitive to upper mantle velocities when it is near critical. The initial modeling of the *SsPmP* phase indicates that the Moho beneath southern Lhasa is over 75 km deep with *Pn* velocities greater than 8 km/s. In contrast, the data sampling the Qiangtang terrane north of the Bangong-Nujiang suture shows thinner crust with *Pn* velocities less than 8 km/s. This is generally consistent with the results from the *Pn* travel-times for regional events recorded on the Hi-CLIMB array. Nonetheless, there is additional variability of the regional travel-time data, suggesting further 3D complexities. Seismic amplitude and frequency attributes are being extracted from the crustal and *Pn* wave-trains, and these data are being compared with numerical and analytical results for models with upper mantle velocity gradients, which can strongly affect *Pn* amplitudes and frequencies. The numerical modeling is performed using approximate ray and beam methods and the more complete spectral element method (SEM). The results from the SEM method are in good agreement with analytical and reflectivity results for different models with upper mantle velocity gradients. Using the SEM method, we are testing the effects of random crustal and Moho depth heterogeneities to see how this variability impacts the range of *Pn* attributes observed. Ultimately the approach we are following is a mostly data-driven analysis of *Pn* seismic attributes in order to investigate the trade-offs of large scale lithospheric structure, small scale heterogeneities and attenuation in Tibet.

OBJECTIVES

We are analyzing the propagation of regional *Pn* waves recorded by Hi-CLIMB in Tibet. Considering the station-spacing (3 to 8 km) and large aperture (800 km) of the Hi-CLIMB seismic experiment, our objective is to use these densely recorded data to construct a self-consistent model of *Pn* propagation over a large region in western China. In turn, a better understanding of the effects of propagation from analysis of the data will improve frequency dependent attenuation models of regional *Pn* phases, leading to a clearer separation of elastic and anelastic effects in a laterally varying crust and upper mantle, eventually eliminating the assumption of a simplified, frequency-independent geometric spreading component.

To account for the intricate nature of *Pn* propagation, we are applying fast ray and beam methods (Nowack and Stacy, 2002), as well as SEM (Komatitsch and Vilotte, 1998; Komatitsch et al., 2005). In contrast, alternatives such as the reflectivity method, are restricted to 1D media. SEM can be applied in 2D or 3D and implemented in parallel using MPI on large cluster computing. Ray and beam methods are faster and can provide asymptotic results appropriate when a large number of forward calculations are required, such as in large-scale inversions. However, for small-scale scattering, complete numerical methods, such as SEM, may be more appropriate. As a practical measure, essential features of *Pn* waveforms are being distilled into seismic attributes including arrival times, envelopes of wave amplitudes, and pulse frequencies for modeling and inversion.

RESEARCH ACCOMPLISHED

We have constructed more than 30 high-quality seismic profiles recorded on the Tibet Hi-CLIMB array and from these 14, have been selected for further analysis. Similarities in the seismic profiles for events in clusters are outstanding. About two thirds of the larger earthquakes have fault plane solutions available in the global Harvard Centroid Moment Tensor (CMT) catalog (Dziewonski et al., 1981) and the report by Baur (2007). For those without fault plane solutions, we have identified the ones that can potentially be resolved using regional waveforms recorded by Hi-CLIMB stations for their appropriate azimuthal coverage, or by using teleseismic waveforms (Figure 1). The analysis of moment tensor inversion is in progress. The fault plane solutions that cannot be obtained through this method may be roughly estimated based on geologic structures or historic solutions.

As a complimentary approach to the analysis of regional seismograms, we are independently constraining the variation of upper mantle velocity and the depth of Moho by modeling shear waveforms at teleseismic distances shorter than 50 degrees. In essence, the amplitude of the *SV*-coupled *P* phase *SsPmp* is very sensitive to the upper mantle velocities when the rays hit the Moho near the critical angle. Our results indicate that the significant decrease in amplitude of *SsPmp* near northern Hi-CLIMB stations can be explained by slow velocity anomalies in the uppermost mantle beneath northern central Tibet.

Regional events recorded by the Tibet Hi-CLIMB array with locations approximately in-line with the array have been chosen for initial analysis. However, other events in specific terranes have also been selected for later processing. Four of the in-line events have epicenters less than 200 km from the Hi-CLIMB array; these events were relocated with data from the Hi-CLIMB array using the earthquake location program HYPOINVERSE-2000 (Klein, 2002). The locations of selected in-line events are shown in Figure 2, using the EHB (Engdahl et al., 1998) or the Preliminary Determination of Epicenters (PDE) catalogs for all events except for the four nearby events (L2a, L2d, L3a and L3b), which were relocated using Hi-CLIMB data. These relocations improved the fit to the travel-times, but moved the epicenters by less than 5 km. For more distant events in Tibet, a focal depth normalization procedure was used since events on Tibetan plateau are dominantly less than 15 km in focal depth (e.g., Molnar and Chen, 1983; Chen and Molnar, 1983; Langin et al., 2003).

The observed arrival times for the four nearby events were then used to refine the crustal velocity model beneath the array with the 3D ray tracing code CRT (ver. 6.0) using the approach described by Cerveny et al. (1988). The calculated travel-times were compared with the observed arrival times in order to iteratively refine the crustal velocity model. The initial velocity model was based on seismic refraction analysis of controlled shots for the INDEPTH III experiment by Meissner et al. (2004). It was found that the relocated nearby events combined with the refined crustal velocity model provide a reasonable fit to the observed crustal travel-times. An example of the observed and calculated travel-times for nearby event L3a is shown in Figure 3.

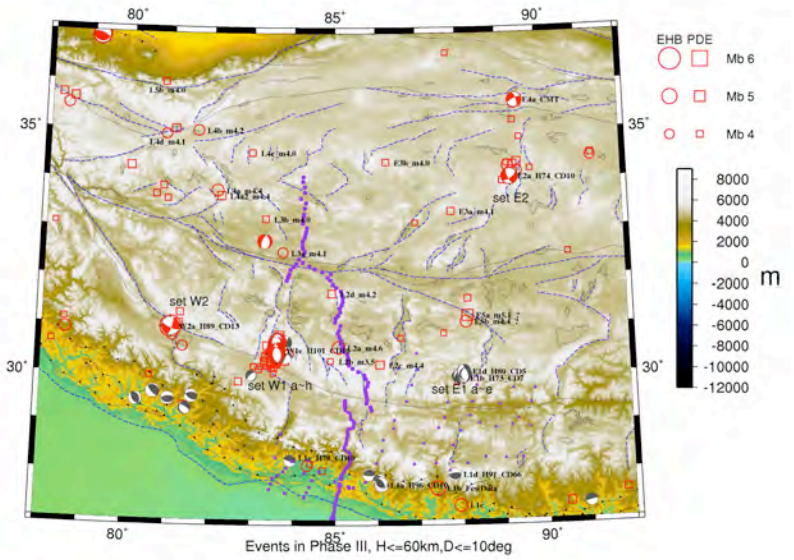

Figure 1. Map of the Hi-CLIMB array with selected labeled events for which seismic profiles have been constructed. The red focal mechanisms were obtained from the global CMT catalog and the gray ones from Baur (2007).

In order to model the *Pn* phase arrival times, work is currently being performed to pick the *Pn* branches and refine the Moho depths. An example of the ray tracing for the *Pn* diving ray for the southern event L1a is shown in Figure 4. For events such as L1a, located along the Himalayan front, the *Pn* arrival times are complicated. There exist rapid variations of Moho depth with a shallowing of the Moho along the Himalayan front and south to the Indian shield. The Lhasa terrane in the central Tibetan plateau has a much greater Moho depth, and north of the Bangong-Nuijiang suture in the Qiangtang terrane of Tibet, the Moho moderately shallows. After modeling all the *Pn* arrival times, the other seismic attributes will be modeled, including seismic amplitudes and pulse frequencies

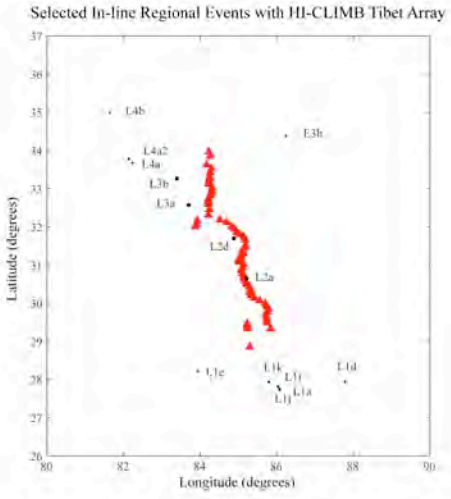

Figure 2. Selected regional events approximately in-line with the Hi-CLIMB Tibet seismic array.

For examples of shot profiles with longer *Pn* branches, we have modeled the travel-times for event L1e to the south and event E3b to the north of the Hi-CLIMB array. The left plot of Figure 5 shows the travel-times for event

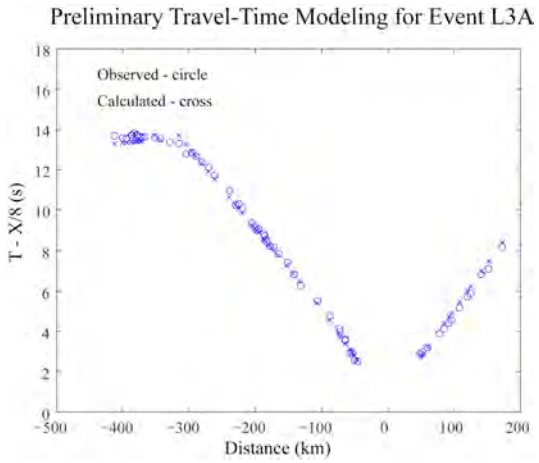

Figure 3. Initial travel-time modeling of Event L3a to constrain crustal structure beneath the Hi-CLIMB array in Tibet.

L1e, where the circles are the observed times and the crosses are calculated times using the 3D ray tracer CRT for the preliminary model shown in the right plot. Similar to the modeling of travel-times for the nearby events to the array, the crustal phases for distances <260 km for event L1e are relatively slow down to the Moho. The modeling of the *Pn* branch shows a deepening of the Moho from the Himalayan front down to 75 km for the Lhasa terrane in central Tibet with *Pn* speeds between 8.2 and 8.3 km/s. Then, to the north of the Bangong-Nujiang suture (BNS) in the Qiantang terrane, the Moho shallows by about 10 km to 63–65 km with slower *Pn* speeds of about 7.8 km/s. In the left plot of Figure 5, the *Pn* branch is first, resulting from the deepening Moho, and then becomes earlier resulting from the thinning of the crust to the north. The upper mantle gradient inferred from the modeling is about 0.003 to 0.004 km/s per km consistent with the work of Philips et al. (2007) for the region.

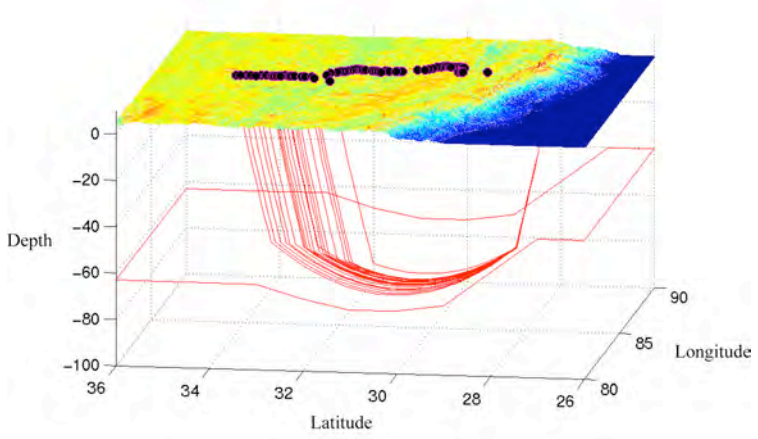

Figure 4. An example of 3D ray tracing of the diving Pn phase for event L1a using a Tibet model with a highly variable Moho topography

The second event-gather to be modeled is from Event E3b located to the north of the Hi-CLIMB array (shown in Figure 2). The travel-times are shown in the left plot of Figure 6 where the circles are the observed times and the crosses are the calculated times using the 3D ray tracer CRT and the preliminary model is shown in the right plot. Again the crust is relatively slow down to the Moho with no indication of a higher velocity lower crust. The *Pn* branch then arrives initially early, indicating the shallower Moho to the north and then is delayed, resulting from the deeper Moho in the Lhasa terrane in central Tibet. However, to match the complete travel-time curve, a slower *Pn* speed is required to the north with the *Pn* speed increasing to the south as the Moho deepens. The modeling of this event located north of the array is consistent with the modeling of event L1e to the south of the array. For the

modeling of both event-gathers, upper mantle gradients of between 0.003 and 0.004 km/s per km are consistent with the data and similar to the results found by Philips et al. (2007) for the region.

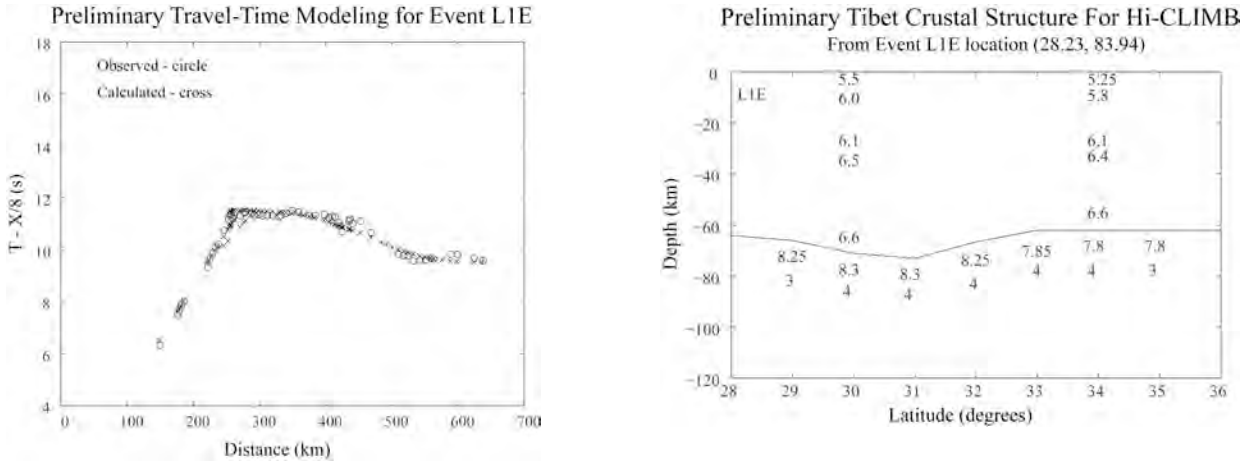

Figure 5. Initial travel-time modeling of Event L1e to constrain upper mantle structure near the Hi-CLIMB array in Tibet. The left plot shows the observed (circles) and calculated (crosses) travel-times. The right figure shows the initial crustal and upper mantle model in the vicinity of the Hi-CLIMB array from travel-time modeling for event L1e. Velocities are shown in km/s and single digits show upper mantle velocity gradients in units of 0.001 (km/s per km).

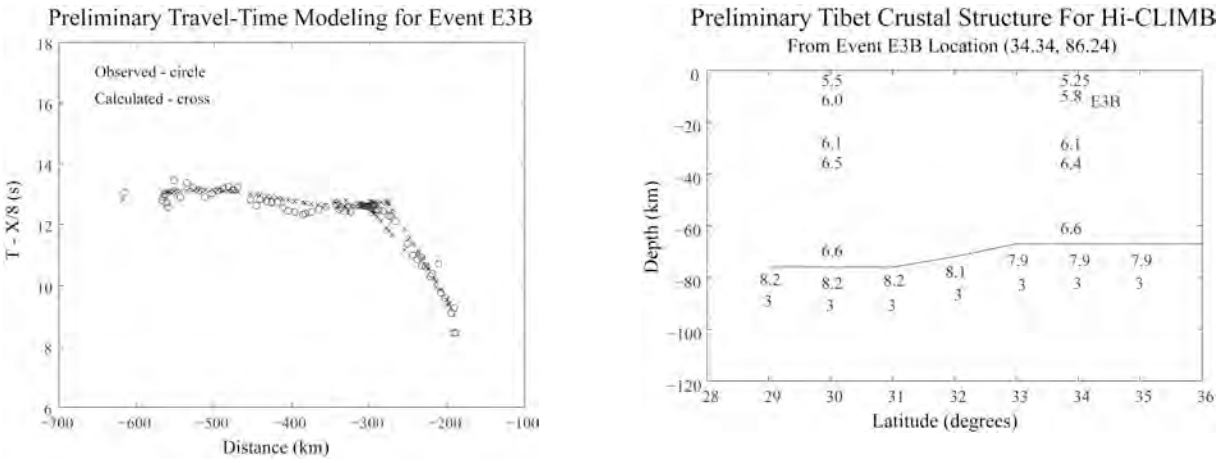

Figure 6. Initial travel-time modeling of Event E3b to constrain upper mantle structure near the Hi-CLIMB array in Tibet. The left plot shows the observed (circles) and calculated (crosses) travel-times. The right figure shows the initial crustal and upper mantle model in the vicinity of the Hi-CLIMB array from travel-time modeling for event L1e. Velocities are shown in km/s and single digits show upper mantle velocity gradients in units of 0.001 (km/s per km in km/s and single digits show upper mantle velocity gradients in units of .001 (km/s per km).

As a preliminary example of seismic amplitudes, Figure 7 shows the Hilbert envelope amplitudes for Event L1e. The dots in the figure are envelope amplitudes obtained from a two second window after the arrival times.The lines are curves proportional to 1/R and $1/(R^2)$ set to be equal at 200 km. Between distances of about 260–340 km, the *Pn* amplitudes are lower and then increase to between 340 to 425 km. After 425 km and north of the BNS in the Qiantang terrane, the *Pn* amplitudes decrease relative to the two decay curves. Since the Moho decreases in depth by about 10 km across the BNS, the amplitudes for event L1e suggest that large scale structural features are influencing the amplitude attributes. Nonetheless, the Moho structure beneath the Himalayas and Tibet is complicated and more analysis is needed to interpret the observed seismic attributes on the different seismic profiles. We are still analyzing

the results for pulse frequency attributes, as well as the decay of amplitudes with distance. However, we are applying a data driven approach to interpret the trade-offs between structural effects of the medium as opposed to other attenuation effects, and not driven by an assumed model for the analysis of the observed seismic attributes. In any case, large-scale structural features need to be taken into account for the modeling of seismic attributes, such as amplitudes and pulse frequencies, in addition to the modeling of scattering from small scale features and intrinsic attenuation.

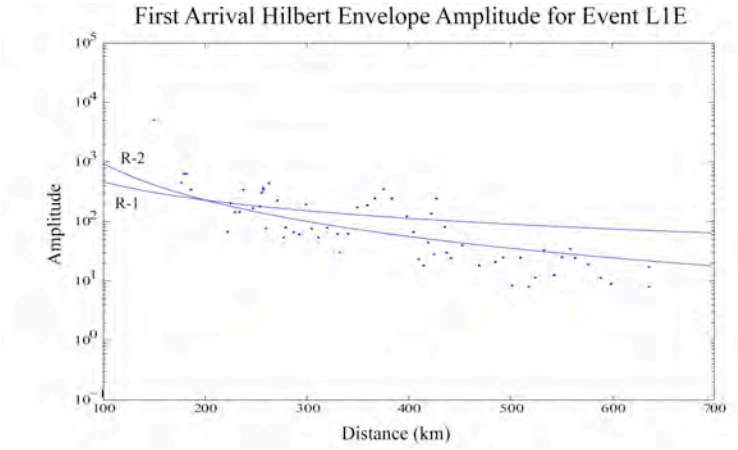

Figure 7. Hilbert envelope amplitudes of first arrivals for Event L1E. The two lines illustrate R-1 and R-2 decay curves shown to coincide with the data at 200 km. Note that after 250 km the amplitudes first decay and then get larger from 350 to 430 km. For distances greater than 450 km, the amplitudes are lower again, possibly correlated with the Bangong-Nujiang Suture in Tibet.

We are currently performing numerical simulations of elastic wave solutions for later comparison with the observed data. We have implemented SEM using the parallel code Specfem2d for the simulation of 2D viscoelastic and anisotropic media (Komatitsch and Vilotte, 1998; Komatitsch et al., 2005). This code allows us to use the cluster computing facilities available at Purdue University and the University of Illinois. These SEM calculations let us compare with asymptotic ray and beam calculations and gain insight into the parameters that affect the *Pn* arrivals, including crustal and upper mantle velocities and gradients, lateral variability in the Moho depth, and small scale scattering and intrinsic attenuation in the crust and upper mantle.

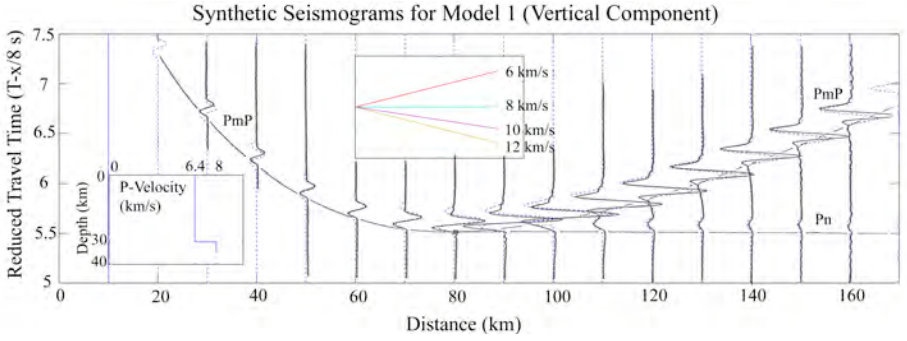

Figure 8a. Comparison between the results from SEM (dotted) and the reflectivity results (solid) of Braile and Smith (1975) for a constant velocity 30 km crust over a constant velocity mantle. The amplitudes of the reflectivity results are multiplied by distance and the SEM results are multiplied by the square-root of distance.

Figure 8a shows an example synthetic record section for a model with a 6.4 km/s crust, a sharp discontinuity at the Moho and a constant 8.0 km/s mantle. The times are reduced by 8.0 km/s. The *PmP* reflected waves and *Pn* head waves are designated on the record section. The solid lines are the seismograms computed using the reflectivity method by Braile and Smith (1975) and the dotted lines are our calculations using SEM modeling, where the

amplitudes are scaled by distance for the reflectivity calculation and by the square root of the distance for the 2D SEM synthetics. The comparison between them is very good, and suggests that we are implementing the SEM code correctly. Note the small amplitude of the pure head wave phase on the synthetics in this ideal case.

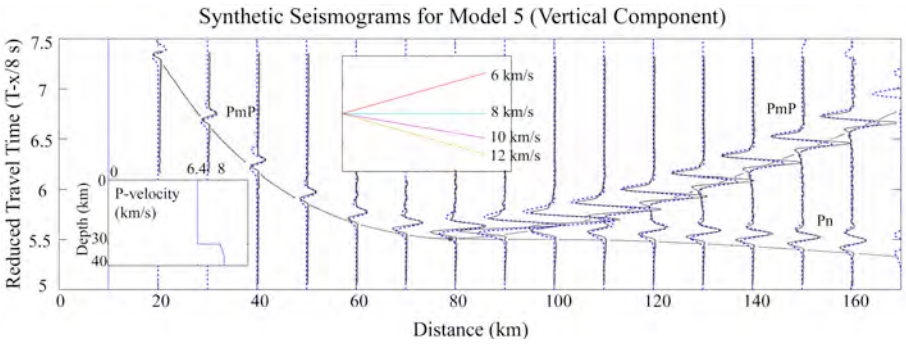

Figure 8b. This shows a comparison between the results from our spectral element calculation (dotted) and the reflectivity results (solid) of Braile and Smith (1975) for a constant velocity 30 km crust over a mantle with a velocity gradient in the top 5 km. The amplitudes of the reflectivity results are multiplied by distance and the SEM results are multiplied by the square-root of distance.

Figure 8b shows an example of synthetic seismograms for a velocity model with an upper mantle gradient in the first 5 km below the Moho. This model is referred to as Moho-5 in Braile and Smith (1975). The solid seismograms are from the reflectivity calculations of Braile and Smith (1975) and the dotted seismograms are from our calculations using the SEM modeling. The reflectivity amplitudes are multiplied by distance and the SEM results are multiplied by the square root of distance. Again, the comparison between the two results is very good, suggesting that we are implementing the SEM modeling correctly. Note the large *Pn* amplitudes resulting from the upper mantle gradient in contrast to the ideal head wave case in Figure 8a. Even in the 1970s, it was recognized that there was a trade-off between large-scale structural features, such as upper mantle velocity gradients and other forms of seismic attenuation.

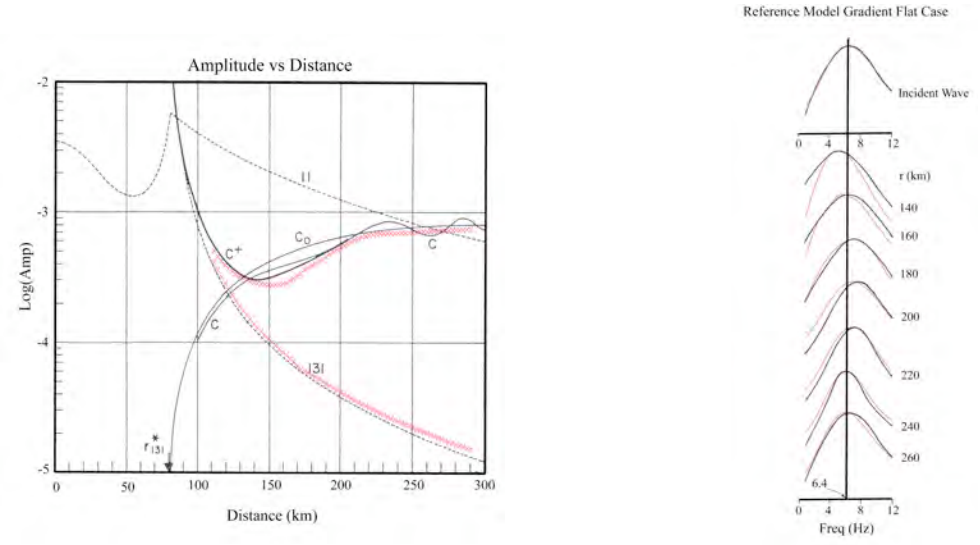

Figure 9. The left plot shows a comparison of the spectral element results (red crosses) with the asymptotic results of Cerveny and Ravindra (1971) for a layer over a halfspace (131 curve) and for a C+ interference head wave for a layer over a velocity gradient. The background curves are from Cerveny and Ravindra (1971). The right plot shows the amplitude spectra, where the black curves are from Cerveny and Ravindra (1971) and the red curves are from the SEM results. Pulse distances for the spectra are shown to the right.

The left plot of Figure 9 shows a comparison between the log-amplitudes from the SEM calculations and the asymptotic results are from Cerveny and Ravindra (1971) for a layer over a half space and a layer over a velocity gradient. The Moho is at a depth of 30 km with a contrast of 6.4 km/s over 8 km/s. For the velocity gradient case, the gradient is 0.02264 km/s per km. This is larger than typically observed mantle gradient values (0.001 and .005 km/s per km) but decreases the distance range for different frequency and amplitude effects to occur, making it more efficient for numerical calculations. Note that the flattening of a spherical earth will result in an effective velocity gradient of about 0.001 km/s per km in the flattened Earth (Yang et al., 2007). The background figure is from Cerveny and Ravindra (1971) where the C+ wave is the interference head wave, the Co wave is the pure diving wave and the 131 wave is the pure head wave case. The red crosses are from the SEM calculations for the interference and pure head wave cases. For the asymptotic results of Cerveny and Ravindra (1971), the amplitude blows up at the critical distance near 80 km and the comparisons are shown only for distances greater than 110 km. For the C+ interference head wave, the amplitude initially decreases after the critical distance and then recovers as the diving wave becomes the dominant wide-angle wave. There are some undulations in the asymptotic results of Cerveny and Ravindra (1971) for distances greater than 220 km for the C+ wave that are not seen in the SEM calculations, but otherwise the results of the SEM calculations are reasonably consistent.

The right plot of Figure 9 shows the amplitude spectra as a function of distance for the interference head wave. The black curves are from Cerveny and Ravindra (1971), and the red curves are from the SEM calculations for the same layer over a velocity gradient model. Both results show that the dominant frequency initially decreases at 140 km with the maximum of the amplitude spectrum less than that of the incident wave because of the frequency decrease of the pure head wave. As the diving wave begins to emerge, the dominant frequency increases. However, because of tuning effects between the different interference waves, the dominant frequency overshoots that of the incident wave to higher frequencies. This was also found by Nowack and Stacy (2002) using both Gaussian beams and reflectivity calculations.

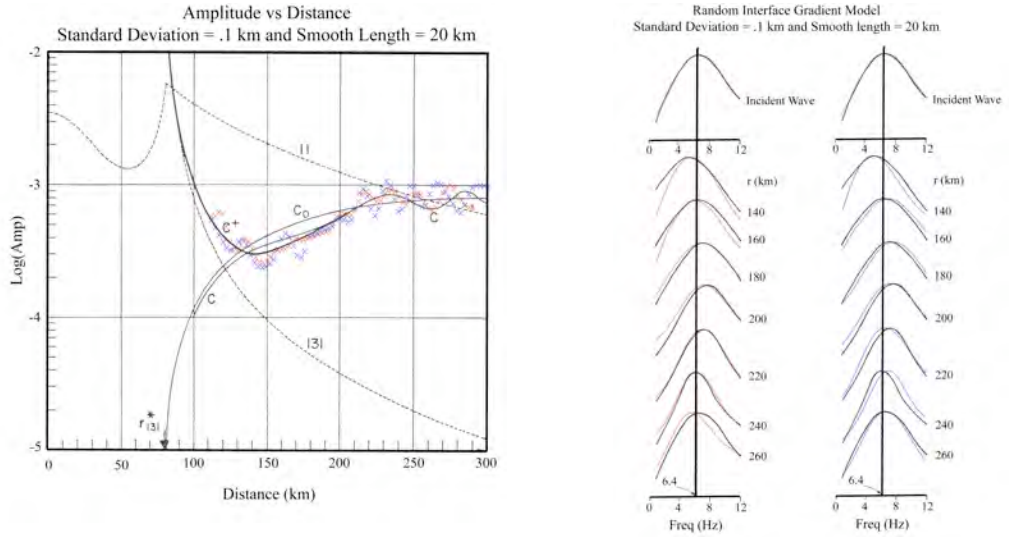

Figure 10. The left figure shows a comparison of the SEM results (red crosses) with the asymptotic results of Cerveny and Ravindra (1971) for a layer over a velocity gradient. The red and the blue crosses are for the random perturbations on the Moho shown in Fig. 11. The background curves are from Cerveny and Ravindra (1971). The right figure shows the amplitude spectra for the two perturbed Moho interfaces for a layer over a velocity gradient. The black curves are from Cerveny and Ravindra (1971) and the red and blue curves are from the SEM results. Pulse distances for the spectra are shown to the right.

The left plot of Figure 10 shows the amplitude comparison between SEM calculations for two random Moho interfaces with a standard deviation of 0.1 km and a smoothing length of 20 km with the unperturbed, asymptotic

results of Cerveny and Ravindra (1971) for a layer over a velocity gradient. Normal random numbers are first generated in Matlab and then are smoothed using three passes of a boxcar smoothing of length 6.5, 6.5 and 7 km in order to smooth out the higher wavenumbers. The right plot of Figure 10 shows the effect of two random perturbations of the Moho depth on the pulse spectra at different distances. The results show that the main features of the C+ interference wave are preserved for small perturbations of the Moho depth. Numerical results for longer smoothing lengths for the perturbation, but the same average vertical deviation, show similar results but with longer average wavenumbers for the amplitude perturbation. Numerical examples with a standard deviation of 0.25 km in vertical depth perturbation of the Moho shows larger perturbations of the interference head wave amplitude but still vary about the main feature trend of the reference case. Nonetheless, preliminary calculations with larger scale structure features have more significant effects on the amplitude and frequency characteristics of the *Pn* wave and will be investigated in the future.

CONCLUSIONS AND RECOMMENDATIONS

We have assembled a number of record sections from regional events recorded by the Hi-CLIMB array. For several events nearby the Hi-CLIMB array, we have relocated the events using Hi-CLIMB data. For more distant events in Tibet, a focal depth normalization procedure has been used since events on theTibetan plateau are dominantly less than 15 km in focal depth (e.g., Molnar and Chen, 1983). From these record sections, seismic attributes of the *Pn* phase are being extracted from the data, including arrival times, envelope amplitudes and instantaneous and spectral pulse frequencies. Several nearby events to the Hi-CLIMB array have been used to constrain crustal velocities from crustal branches. For the *Pn* phase, the travel-times are being modeled using 3D ray tracing in order to constrain large scale structural features including Moho depths, upper mantle velocities and velocity gradients. The modeling of travel-times for all the selected event gathers will result in an integrated 3D model for the region. Also, teleseismic analysis of the *SsPmp* phase is being performed to further constrain the crustal and upper mantle structure.

Numerical modeling is performed using the spectral element method (SEM) in order to compare the effects of large-scale crustal structure on seismic attributes. For the layer over a velocity gradient case, the SEM results compare favorably with the asymptotic results of Cerveny and Ravindra (1971) and the reflectivity calculations of Braile and Smith (1975). Seismic amplitude and pulse frequency results using SEM are stable for small interface perturbations. Lay et al. (2008) reported more drastic variations obtained from finite difference modeling for upper mantle velocity perturbations. Presumably these results occur since the mantle velocity perturbations change the upper mantle gradients, which control the primary properties of the interference head wave. Nonetheless, larger variations of Moho depth have more pronounced focusing and defocusing effects on *Pn* amplitudes than shown here. We are starting to perform SEM tests for large scale structural models that occur in Tibet and these are anticipated to have strong effects on the properties of the *Pn* wave.

REFERENCES

Baur, J. R. (2007). Seismotectonics of the Himalayas and the Tibetan Plateau: moment tensor analysis of regional seismograms, M.S. thesis, Oregon State University.

Braile, L. W. and R. B. Smith (1975). Guide to the interpretation of crustal refraction profiles, *Geophys. J.R. Astr. Soc.* 40: 145–176.

Cerveny, V., L. Klimes, and I. Psencik (1988). Complete Seismic-Ray Tracing in Three-Dimensional Structures. In *Seismological Alogorithms*, London: Academic Press: 89–168

Cerveny, V. and R. Ravindra (1971). *Theory of Seismic Head Waves*, Univ. of Toronto Press.

Chen, W.-P., and P. Molnar (1983). Focal depths of intracontinental and intraplate earthquakes and their implications for the thermal and mechanical properties of the lithosphere, *J. Geophys. Res.* 88: 4183–4214.

Dziewonski, A. M., T.-A. Chou and J. H. Woodhouse (1981). Determination of earthquake source parameters from waveform data for studies of global and regional seismicity, *J. Geophys. Res.* 86: 2825–2852.

Engdahl, E. R., R. D. van der Hilst, and R.P. Buland (1998). Global teleseismic earthquake relocation with improved travel times and procedures for depth determination, *Bull. Seism. Soc. Am.* 88: 722–743.

Klein, F. (2002). HYPOINVERSE-2000 (4/2002 vers.) [Computer Software]. Menlo Park, CA: U.S. Geological Survey.

Komatitsch, D. and J. P. Vilotte (1998). The spectral element method: an efficient tool to simulate the seismic response of 2D and 3D geological structures, *Bull. Seismol. Soc. Am.* 88: 368–392.

Komatitsch, D., S. Tsuboi and J. Tromp (2005). The spectral-element method in seismology, in *Seismic Earth: Array Analysis of Broadband Seismograms,* (Eds. A. Levander and G. Nolet), Geophysical Monograph Series, Vol. 157, American Geophysical Union, Washington D.C.: 205–227.

Langin, W. R., L. D. Brown, and E. A. Sandvol (2003). Seismicity of central Tibet from Project INDEPTH III seismic recordings, *Bull. Seism. Soc. Am.* 93: 2146–2159.

Lay, T., X. B. Xie and X. Yang (2008). Development of regional phase tomographic attenuation models for Eurasia, in *Proceedings of the 30th Monitoring Research Review: Ground-Based Nuclear Explosion Monitoring Technologies,* LA-UR-08-05261, Vol. 1, pp. 98–107.

Meissner, R., F. Tilmann, and S. Haines (2004). About the lithospheric structure of central Tibet, based on seismic data from the INDEPTH III profile, *Tectonophysics* 380: 1–25.

Molnar, P. and W.-P. Chen (1983). Depths and fault plane solutions of earthquakes under the Tibetan plateau, *J. Geophys. Res.* 88: 1180–1196.

Nowack, R. L. and S. M. Stacy (2002). Synthetic seismograms and wide-angle seismic attributes from the Gaussian beam and reflectivity methods for models with interfaces and velocity gradients, *Pure Appl. Geophys.* 159: 1447–1464.

Phillips, W. S., M. L. Begnaud, C. A. Rowe, L. K. Steck, S. C. Myers, M. E. Pasyanos, and S. Ballard (2007). Accounting for lateral variations of the upper mantle gradient in Pn tomography studies, *Geophys. Res. Lett.* 34: doi:10.1029/2007GL029338.

Yang, X., T. Lay, X. B. Xie, and M. S. Thorne (2007). Geometric spreading of Pn and Sn in a spherical earth model, *Bull. Seism. Soc. Am.* 97: 2053–2065.

SEISMIC VELOCITY ESTIMATION IN THE MIDDLE EAST FROM MULTIPLE WAVEFORM FUNCTIONALS: *P & S* RECEIVER FUNCTIONS, WAVEFORM FITTING, AND SURFACE WAVE DISPERSION

Jay Pulliam[1,2], Mrinal K. Sen[2], Nathan Simmons[3], and Michael Pasyanos[3]

Baylor University[1], The University of Texas at Austin[2], and
Lawrence Livermore National Laboratory[3]

Sponsored by the National Nuclear Security Administration

Award Nos. DE-AC52-09NA29327[1,2] and DE-AC52-07NA27344[3]
Proposal No. BAA09-58

ABSTRACT

A novel velocity estimation algorithm that will be developed and applied that incorporates the constraints of three seismic functionals: Receiver functions, waveform modeling, and surface wave dispersion measurements. These functionals have distinct but complementary sensitivities to Earth structure and have all been employed in modeling studies previously, yet each fails to resolve ambiguities between realistic models when used alone. By incorporating constraints from all three functionals we can minimize the part of the model space for which data constraints fail to distinguish between models. While several recent studies attempt to model two of these functionals jointly, none explores or assesses adequately the improvements in model reliability that are gained by incorporating additional constraints.

The general search techniques and assessment tools we will employ allow us to describe the size and characteristics of the acceptable model space, proscribe the set of unacceptable models, and identify characteristics that are *required* by the data, rather than those that are simply *consistent* with the data. As a result, the method will quantitatively evaluate the strengths of the constraints imposed by each data functional on each model parameter. The Bayesian formulation we propose provides a formal mechanism for incorporating the results of one inversion (as a "prior") into the inversion of a second type, to produce a multi-step "joint" (as opposed to "simultaneous") modeling procedure. The final results will be models that are accompanied by detailed, quantitative assessments of model reliability. In addition, these tools will guide us toward the types and characteristics of additional data that should be sought in order to improve model constraints and, therefore, model reliability.

Another benefit of the proposed modeling method is that it will allow seismologists to produce models for relatively aseismic regions of the world, where station density is sparse, and where, for example, one particular data functional is rarely observed. It will therefore result in a method that is more broadly applicable than methods that rely upon one data functional alone.

Lastly, numerous areas have been studied with "campaign"-style temporary deployments, which often produce a relatively small dataset compared to permanent stations. Broadening the range of data types employed in modeling will generally produce more reliable models for sparsely sampled regions. We will ultimately apply our modeling to stations in the Middle East. Besides being an area of monitoring interest, the Middle East is tectonically complex. As such, it is a region where fitting multiple datasets can choose among various non-unique models, as well as reconcile seemingly inconsistent data.

This award begins September 1, 2009, so in this paper we describe our approach and goals for this project.

OBJECTIVES

Knowledge of crust and upper mantle velocity structure is essential to locating seismic events and, specifically, for constraining event focal depths. Seismic locations, discriminants, and yield estimates are all affected negatively by errors in seismic velocity models. Accurately assessing and quantitatively describing model errors is a critical component of estimating velocity and attenuation structure and such assessment is especially difficult in nonlinear modeling. Here we propose a multi-step modeling procedure for the estimation of crust and upper mantle velocity models using distinct types of regional and teleseismic waveform data.

One goal of the BAA to which this proposal responds is to develop optimal procedures for the use of multiple datasets. Due to the inherent variability, inconsistency, and peculiarities of disparate datasets and the well-known nonlinearity and non-uniqueness associated with geophysical modeling, such procedures must include methods for evaluating the performance and contribution of each dataset to the final results.

Our approach makes use of quantitative assessment tools and a well-developed Bayesian approach to explore and evaluate each step of the modeling process, rather than to simply toss all constraints into a simultaneous fitting procedure to find the single solution that satisfies particular criteria. The procedure we propose, best characterized as velocity analysis via optimization, is analogous to velocity analysis in exploration seismology, rather than "inversion". It will provide quantitative error measures of structural parameter estimates that can then be translated to earthquake location errors, and thus guide seismologists toward the most effective and efficient ways to improve model reliability.

RESEARCH ACCOMPLISHED

We have already made substantial progress on several aspects of the proposed research: waveform modeling, receiver functions, and one proposed variant of simulated annealing. During the last several years we developed, tested, and applied the method for waveform modeling via global optimization described above (Gangopadhyay et al., 2007; Pulliam and Sen, 2005; Pulliam et al., 2006). Earlier we developed, with Lian-She Zhao and Cliff Frohlich, a VFSA-based inversion algorithm for *P*-wave receiver functions (Zhao and Frohlich, 1996; Zhao et al., 1996). Additional tools developed at UTIG include fast, parallelized reflectivity code that incorporates anisotropic model parameters, additional global optimization methods based upon genetic algorithms, and numerous imaging algorithms.

Specifically with regard to waveform modeling: We developed a code that computes synthetic seismograms with a parallelized reflectivity method and fits the observed waveforms by global optimization. Assuming a one-dimensional, isotropic, layered Earth, our code computes the synthetic seismograms independently for all layers, frequencies, and ray parameters. The code implements a global optimization algorithm using Very Fast Simulated Annealing (VFSA) that allows for searching within a broad spectrum of models in order to find the global minimum, and hence minimizes dependency on the starting model. Our method also computes the Posterior Probability Density (PPD) function and correlation matrix, to evaluate the uniqueness of the resulting models, and the trade-offs between individual model parameters therein. We applied the code to determine the crust and upper mantle structure beneath permanent broadband seismic stations in Africa using teleseismic earthquakes (M 5.5–7.0 and 200-800 km focal depth) recorded at these stations. We modeled the *S*, *SP*, *SsPmP*, and shear-coupled *PL* waves from these earthquakes and our *P*- and *S*-wave velocity models compare well with, and in some cases improve upon the models obtained from other existing methods. We obtained *P*- and *S*-wave velocities simultaneously and our use of the shear-coupled PL phase wherever available improved constraints on the models of the lower crust and upper mantle(Gangopadhyay et al., 2007). Preliminary results of applications to data from permanent broadband seismic stations in China and Canada are summarized below.

In China, based on our selection criteria, the number of earthquakes recorded at each station range between 3 and 31. The stations encompass tectonic provinces such as the north and south China blocks, Tibetan plateau, and Tien Shan Mountains. Results from the application of our technique are consistent with regional tectonics and models obtained from earlier studies using receiver functions and seismic tomography. The crustal thicknesses beneath stations in the north China block range between ~35–42 km with the crust in the central part of the block near station BJT being thicker. However, within the north China block towards its western edge, the crust appears anomalously thick (~55 km) beneath station LZH. This region also coincides with the border of the north China block and Tibetan plateau. The south China block consists of widely varying crustal thicknesses: ~37 km beneath station ENH in the northern part of the block and ~52 km beneath station KMI in the southern part, for example. The southern part of the south China block near station KMI also coincides with its border with the Tibetan plateau, where the

Moho significantly deeper than elsewhere in China, implying a deep crustal root. Station LSA, in Lhasa, Tibet, has a crustal thickness of ~53 km. In the Tien Shan Mountains in northwestern China, the crust is thicker than average (~42 km) but not as thick as that beneath the Tibetan plateau.

The seismic stations in Canada each recorded between 3 and 26 earthquakes suitable for analysis. The chosen stations span major tectonic provinces within the Canadian landmass such as the Cordilleran orogen, western plains and Slave province in western Canada, Grenville province and Appalachian orogen in eastern Canada, and the Canadian Arctic. Initial results from the application of our technique are consistent with earlier studies and regional tectonics. Crustal thicknesses beneath stations in the northern Cordilleran orogen, western plains, and Slave province range between 35-37 km. The Moho appears to be slightly shallower (31-35 km) beneath stations in the southern Cordilleran orogen. In eastern Canada, the crust beneath stations of the Grenville province and Appalachian orogen is generally thick (~44 km) with the exception of that beneath station DRLN, in the northeast, where it is ~33 km. Moho depths beneath stations in the Canadian Arctic range between ~35-42 km. We also observe low-velocity zones in the crust and uppermost mantle at some stations, however the constraints on them are not strong. Taken together, the results provide a comprehensive snapshot of the velocity structure beneath Canada.

These results demonstrate that the waveform modeling method is tractable and effective when the data are available. Unfortunately we discovered during our global search that SPL waves, in particular, are relatively uncommon. It makes sense, therefore, to include additional data functionals for joint modeling, in order to broaden the applicability of the enhanced method to more regions of the world and to increase sensitivities to Earth structure, and therefore model reliability.

Estimation of Uncertainties

Geophysical inverse problems are often non-unique. That is, their error functions either have broad minima or are multi-valued, indicating that models that are slightly different from the best-fitting model satisfy the data nearly as well, in the first case, or that one or more very different models also satisfy the data, in the second case. It is therefore necessary to explore the model space and thus identify the range of models that fit the data, and perhaps to identify characteristics of the models that are required by the data, rather than which simply are allowed by the data. VFSA conducts such a search efficiently, and the products of multiple such searches enable us to evaluate the uncertainty in a single, best-fitting solution. This evaluation is particularly necessary in seismic waveform modeling because more than one model can often explain the observed data equally well and trade-offs between different model parameters are common (Pulliam and Sen, 2005). The waveform inversion method we use in this study incorporates important statistical tools that allow the user to evaluate the uniqueness, and physical feasibility of the resulting model. The most useful of these tools in evaluating the results' reliability are the PPD function, and the parameter correlation matrix. To estimate these statistical parameters we cast the inverse problem in a Bayesian framework (Sen and Stoffa, 1995; Tarantola, 1994), and employ "importance sampling" based on a Gibbs' sampler (GS) (Pulliam and Sen, 2005; Sen and Stoffa, 1996).

The goal of "importance sampling" is to concentrate sample points in the regions that are the most "significant", in some sense (perhaps, for example, where the error function is rapidly varying, or many acceptable solutions lie). Because this concentration is achieved using a Gibbs' probability distribution, it has been named the "Gibbs' sampler" (Sen and Stoffa, 1996). The PPD function $[\sigma(\mathbf{m}|\mathbf{d}_{obs})]$ is defined as a product of a likelihood function $[e^{-E(\mathbf{m})}]$, and prior probability density function, $p(\mathbf{m})$. The prior probability density function $p(\mathbf{m})$, describes the available information on the model without the knowledge of the data and defines the probability of the model **m** independent of the data. In our application here, we use a uniform prior within a minimum and maximum bound for each model parameter. The likelihood function defines the data misfit and its choice depends on the distribution of error in the data (Sen and Stoffa, 1996). Sen and Stoffa (1996) examined several different approaches to sampling models from the PPD and concluded that a multiple-VFSA based approach, though theoretically approximate, is the most efficient. In a multiple-VFSA approach we make several VFSA runs with different random starting models and use all the models sampled along to characterize uncertainty in the model. We use all these sampled models to compute approximate marginal PPD and posterior correlation matrices to characterize uncertainties in the derived results. The posterior correlation matrix measures the relative trade-off between individual model parameters and is computed by normalizing the covariance between two model parameters . Computationally, the correlation between i^{th} and j^{th} model parameters is given by their covariances divided by the square root of the product of the covariances of each parameter with itself. Next we discuss an application of the technique to seismological data recorded in Africa, including descriptions and interpretations of the resulting computations of the PPD and correlation matrix.

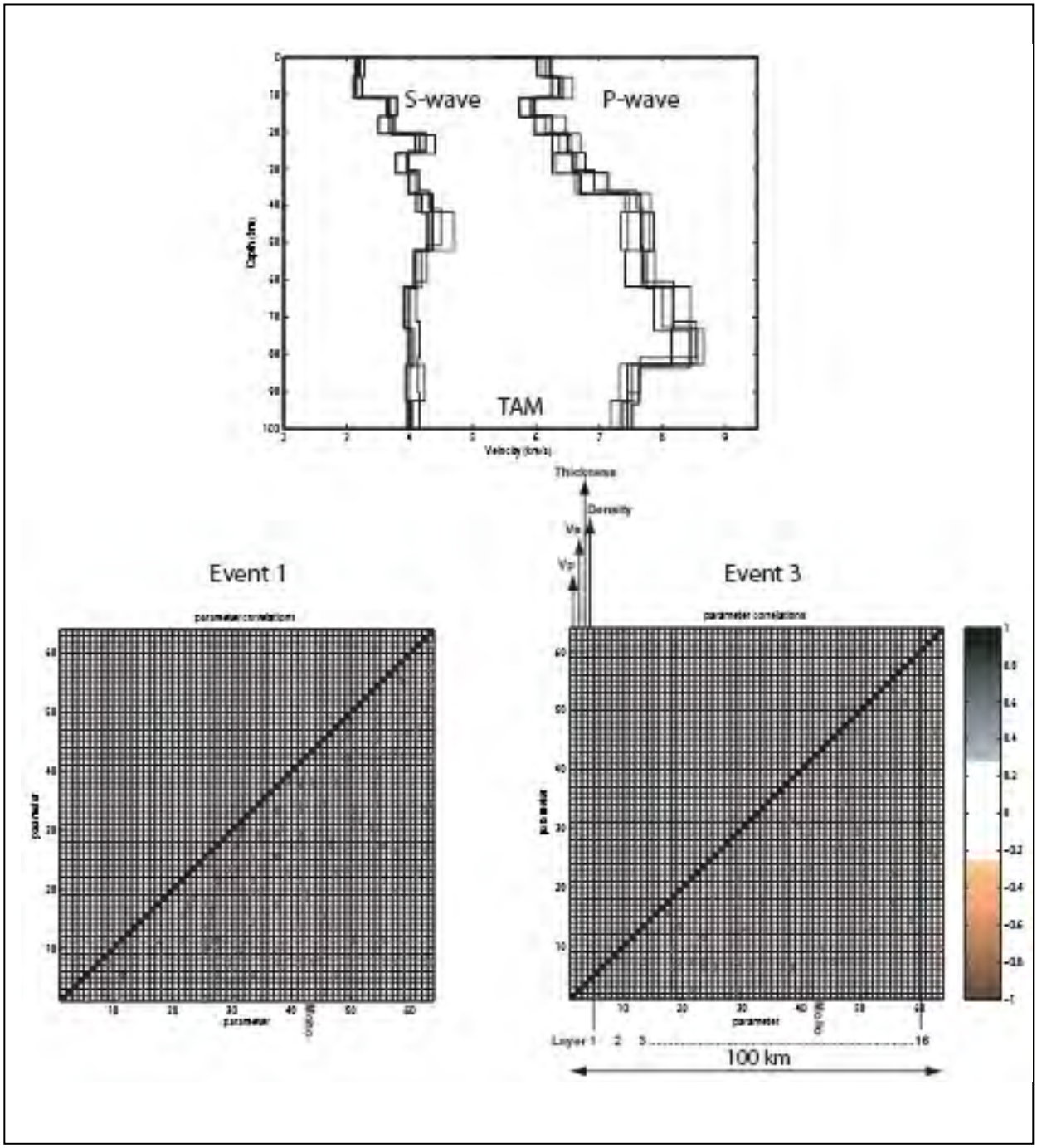

Figure 1. (Top panel) *P*- and *S*-wave velocity models up to 100 km for station TAM from the inversion results for individual events recorded at TAM. (Lower panels) Model parameter correlation matrices for events 1 (left panel), in which SPL was not observed, and 3 (right panel), for which SPL was observed, recorded at TAM. Each small square represents a model parameter (Vp, Vs, Thickness of layer, and Density) on both the horizontal and vertical axes. The correlations range between -1 and 1. Sparse colored squares off-diagonal in the lower crust - upper mantle in event 3 (right panel) compared to that in event 1 (left panel) indicate better resolution and confidence (less trade-off) in this region.

In a paper published in Geophysical Journal International (Gangopadhyay et al., 2007) we generated *P*- and *S*-wave velocity models up to a depth of 100 km for the broadband station TAM, in North Africa (Figure 1). We observed some variability in the models, and hence computed the uncertainties for each model using the statistical tools described earlier to choose the "best" model. In Figure 1 we show examples of parameter correlation matrices computed from the modeling results of two events (we call them events 1 and 3). Each small square along an axis of the parameter correlation matrix, either horizontally or vertically, represents a model parameter. Since every model layer consists of four independent model parameters (V_p, V_s, thickness, and density), four small squares combined together represent a model layer on both axes. Correlation values range between -1 and 1 and are symmetric about the diagonal of the matrix, hence, for clarity, we show only values below the diagonal. Values along the diagonal are ones, simply indicating that each parameter is perfectly correlated with itself. Off-diagonal colored squares indicate significant cross-correlation (trade-offs) between corresponding model parameters. In the parameter correlation matrices for both events, layers comprising the upper crust have greater independence, as indicated by the sparse distribution of off-diagonal cross-correlations whose absolute values are greater than ±0.5 (colored squares). Also, for both events, the level of tradeoffs among model parameters in these shallow layers is similar. For event 1, however, the layers comprising the lower crust and upper mantle have larger off-diagonal cross-correlations, indicating significant tradeoffs (Figure 1, lower left). On the contrary, for event 3, even the lower crustal and upper mantle layers appear better constrained (Figure 1, lower right). The main difference between the two events is that an SPL phase is also observed in the seismogram of event 3 but not in that of event 1. This observation attests to the fact that if SPL is present in the seismogram and is well modeled, we are able to better constrain the structure of the lower crust and upper mantle. This result confirms our expectation that, due to the sensitivity of SPL to those parts of the model, adding SPL to the modeling, when present, improves constraints on parameters at and just below the Moho.

CONCLUSIONS AND RECOMMENDATIONS

Joint Modeling of Multiple Datasets

There are several advantages to jointly modeling multiple datasets. First, each data functional has unique sensitivities to Earth structure. For example, receiver functions are primarily sensitive to shear wave velocity contrasts and vertical traveltimes while surface wave dispersion measurements are sensitive to vertical shear wave velocity averages (Julia et al., 2000). Full waveform modeling of *S*, *Sp*, *SsPmP* phases, in contrast, are more sensitive compressional wave velocity contrasts and vertical traveltimes; adding *SPL* to the modeling improves senstivity to the uppermost mantle shear wave structure and to velocity contrasts across the Moho (Gangopadhyay et al., 2007). Mutually satisfying constraints imposed by the three datasets may constrain a larger subset of model parameters than a single set alone, resulting in a single model that better represents the true structure beneath a station.

Second, the amplitudes and signal-to-noise characteristics of waves that produce these data functionals depend on several factors, including epicentral distance, event focal depth, fault mechanism and radiation patterns, source time function, properties of the intervening Earth structure (including attenuation, low velocity zones, velocities, heterogeneity, and anisotropy), and characteristics of the recording seismometer. Since regions of high seismicity are highly restricted, many stations are not well situated to record a large number of ideal events. Or a station may be deployed only temporarily, resulting in inadequate sampling to produce some functionals. An algorithm that incorporates more than one type of data will most likely be more widely applicable than one that relies solely on a single type.

However, with these advantages come some disadvantages. For example, combining disparate data types requires great care in their treatment and assessment (Roy et al., 2005). Benefits of additional data may be null if the method used to model them preferentially fits one type. Or, worse, minimizing an inappropriate criterion in conjunction with incompatible data may "split the difference" between them to choose a model that is wholly inaccurate and inappropriate for its intended purpose. In geophysical modeling, one does not often have the luxury of choosing a model based solely upon its numerical characteristics. If the model is to be used for regional or local earthquake locations, for example, it would be a mistake to rely on the best fit to surface wave dispersion. The judgment and experience of seismologists who keep a clear eye on their goal is critical, and this experience must be combined with rigor in the computational modeling. This experience and judgment can be incorporated after the fact, as is sometimes the case with, for example, the smoothing applied to 3D tomographic models but it is usually better to

acknowledge the "prior" explicitly at the outset. This is one advantage of the Bayesian approach that we propose here. While such priors are sometimes referred to pejoratively as "bias", the explicit statement of a prior during the formulation of the modeling algorithm forestalls serious criticism and enables a clear discussion of the "bias" that was imposed on the modeling.

Next, as a general rule of thumb, a greater number of data functionals incorporated into modeling will result in a broader range of model parameter sensitivities, and it will be less likely that a linear inversion approach will be adequate. This is unfortunate because linear approaches are much more tractable and straightforward than nonlinear methods. But only a broad search of the model space will demonstrate whether a linear approach is valid. Non-linear global optimization algorithms require no change in the algorithm to include multi-part objective function with different norms. A variety of methods for nonlinear inversion are now available and the only real cost for conducting a thorough search and finding the single best-fitting model is in computational effort and complexity. The downside is that theoretically exact methods for assessing model uncertainties and model reliability are not generally tractable, and approximate methods result in significantly greater cost and complexity than is required to find the best-fitting model alone. Nevertheless, our previous work has demonstrated that useful methods are indeed tractable, and the method we propose will add only marginal increases in computation time. Fortunately, with two of the world's largest parallel computers at our disposal at UT, we have the tools we need to undertake these tasks.

While surface wave dispersion and receiver functions have been modeled jointly (Ammon et al., 2005; Ammon et al., 2004; Cakir and Erduran, 2004; Chang et al., 2004; Dugda and Nyblade, 2006; Herrmann et al., 2001; Julia et al., 2000; Julia et al., 2005; Lawrence and Wiens, 2004; Ozalaybey et al., 1997; Tkalcic et al., 2006), no study has, to our knowledge, incorporated waveform constraints such as *S*, *Sp, SsPmP*, and Shear-coupled PL. Further, none has conducted a thorough, nonlinear assessment of the constraints provided by each functional.

Application: Modeling the crust and uppermost mantle beneath the Middle East

The Middle East has a complex tectonic history. This history has given rise to a complicated earth structure, with highly non-uniform spatial distributions of fundamental crustal properties, such as depth-to-basement and crustal thickness. Similarly large variations in upper-mantle velocity occur. These factors strongly affect the group velocities of surface waves propagating across the region, as well as discontinuities that convert *P* and *S* body wave energy.

Table 1. Sensitivities of the three seismic functionals under discussion. While this table summarizes what is known about sensitivities from previous studies, the degree to which tradeoffs between model parameters will be reduced by the joint modeling we propose is unknown. The degree of tradeoff and resolution will be quantitatively assessed during the course of this study.

Region Constrained	Parameter Constrained	Receiver Functions	Surface Wave Dispersion	Waveform Modeling of *S, Sp, SsPmP, SPL*
Vertical velocity average	Absolute Vs	High	Moderate	Moderate
	Absolute Vp	Low	Low	High
Internal boundaries in the crust	Vp Contrast	Low	Low	Moderate
	Vs Contrast	High	Low	Moderate
Moho	Vp Contrast	Moderate	Low	High
	Vs Contrast	Moderate	Low-to-Moderate	High
Crust	Absolute Vp	Low	Low	Moderate
	Absolute Vs	Moderate	Low-to-Moderate (depending on frequencies used)	Moderate
Uppermost Mantle	Absolute Vp	Low	Low	Low
	Absolute Vs	Moderate	High	High
Vertical Resolution	Absolute Vs	High	Low	Moderate
Lateral Resolution	Absolute Vs	Low	High	Moderate

Due to its complex tectonics, the Middle East is an appropriate location in which to apply methods that (a) reduce non-uniqueness by fitting multiple datasets and (b) assess the relative constraints placed on model parameters by each data type. These tools can help reconcile seemingly inconsistent datasets, such as the surface wave dispersion data (and models) proposed for the Zagros Mountains region (Pasyanos and Nyblade, 2007) and receiver function results for the same region (Ammon et al., 2005; Paul et al., 2006), although produced with data from different stations. What we need now are better constraints on *P* velocities and an algorithm that incorporates priors and data functionals in a step-wise manner, with assessment tools to evaluate the results. Lastly, the Middle East has the densest coverage and highest resolution in the surface wave model and is an area of interest for explosion monitoring.

REFERENCES

Ammon, C. J., M. Kosarian, R. Herrmann, M. Pasyanos, W. Walter, W. Sevillas, and G. Randall (2005). Simultaneous Inversion of Receiver Functions and Surface-Wave Dispersion Measurements for Lithospheric Structure Beneath Asia and North Africa, in *Proceedings of the 27th Seismic Research Review: Ground-Based Nuclear Explosion Monitoring Technologies*, LA-UR-05-6407, Vol. 1, pp. 3–12.

Ammon, C. J., M. Kosarian, R. Herrmann, M. Pasyanos, W. Walter, and H Tkalcic (2004). Simultaneous Inversion of Receiver Functions, Multi-mode Dispersion, and Travel-time Tomography for Lithospheric Structure Beneath the Middle East and North Africa, in Proceedings of the 26th Seismic Research Review - Trends in Nuclear Explosion Monitoring, LA-UR-04-5801, Vol. 1, pp. 17–28.

Cakir, O. and M. Erduran, (2004). Constraining crustal and uppermost mantle structure beneath station TBZ (Trabzon, Turkey) by receiver function and dispersion analyses. *Geophys. J. Int*. 158: (3), 955–971.

Chang, S.-J., Baag, C.-E. and C. Langston, (2004). Joint analysis of teleseismic receiver functions and surface wave dispersion using the genetic algorithm. *Bull. Seismol. Soc. Am*. 94: (2), 691–704.

Dugda, M. and A. A. Nyblade, (2006). New constraints on crustal structure in eastern Afar from the analysis of receiver functions and surface wave dispersion in Djibouti. Geological Society of London Special Publications, 259: 239–251.

Gangopadhyay, A., Pulliam, J. and M. K. Sen (2007). Waveform modeling of yeleseismic S, SP, SsPmP, and shear-coupled *PL* waves for crust and upper mantle velocity structure beneath Africa. *Geophys. J. Int*. 170: 1210–1226.

Herrmann, R. B., C. J. Ammon, and J. Julia (2001). Application of joint receiver-function surface-wave dispersion for local structure in Eurasia, in *Proceedings of the 23rd Seismic Research Review: Worldwide Monitoring of Nuclear Explosions*, LA-UR-01-4454, Vol. 1, pp. 46–54.

Julia, J., C. J. Ammon, R. B. Herrmann, and A. M. Correig, (2000). Joint inversion of receiver function and surface wave dispersion observations. *Geophys. J. Int*. 143: (1): 99–112.

Julia, J., C. J. Ammon, and A. A. Nyblade (2005). Evidence for mafic lower crust in Tanzania, East Africa, from joint inversion of receiver functions and Rayleigh wave dispersion velocities, *Geophys. J. Int*., Blackwell Science for the Royal Astronomical Society, the Deutsche Geophysikalische Gesellschaft and the European Geophysical Society, International, pp. 555.

Lawrence, J.F. and D. A. Wiens (2004). Combined receiver-function and surface wave phase-velocity inversion using a Niching genetic algorithm: application to Patagonia, *Bull. Seismol. Soc. Am*. 94: (3): 977–987.

Ozalaybey, S., M. K. Savage, A. F. Sheehan, J. N. Louie, and J. N. Brune (1997). Shear-wave velocity structure in the northern Basin and Range province from the combined analysis of receiver functions and surface waves. *Bull. Seismol. Soc. Am*. 87: (1) 183–199.

Pasyanos, M. and A. A. Nyblade (2007). A top to bottom lithospheric study of Africa and Arabia. *Tectonophysics*, 444: 27–44.

Paul, A., A. Kaviani, D. Hatzfeld, J. Vergne, and M. Mokhtari (2006). Seismological evidence for crustal-scale thrusting in the Zagros mountain belt (Iran). *Geophys. J. Int*. 166: 227–237.

Pulliam, J. and Sen, M.K., 2005. Assessing Uncertainties in Waveform Modeling of the Crust and Upper Mantle, Proceedings of the 27th Seismic Research Review: Ground-Based Nuclear Explosion Monitoring Technologies, Palm Springs, CA, pp. 152 – 160.

Pulliam, J., Sen, M.K. and Gangopadhyay, A., 2006. Determination of Crust and Upper Mantle Structure Beneath Africa Using a Global Optimization-Based Waveform Modeling Technique, Proceedings of the 28th Seismic Research Review: Ground-Based Nuclear Explosion Monitoring Technologies, Orlando, FL, pp. 196-208.

Roy, L., Sen, M.K., Stoffa, P.L., McIntosh, K. and Nakamura, Y., 2005. Joint inversion of first arrival travel time and gravity data. J. of Geophysics and Engineering, 2: 277-289.

Sen, M.K. and Stoffa, P.L., 1995. Bayesian inversion in geophysics, Union of Geodesy and Geophysics; XXI General Assembly, Boulder, CO, pp. 9.

Sen, M.K. and Stoffa, P.L., 1996. Bayesian inference, Gibbs' sampler and uncertainty estimation in geophysical inversion. Geophysical Prospecting, 44: 313-350.

Tarantola, A., 1994. Inverse Problem Theory: Methods for Data Fitting and Model Parameter Estimation. Elsevier, Amsterdam, The Netherlands, 600 pp.

Tkalcic, H. et al., 2006. A multistep approach for joint modeling of surface wave dispersion and teleseismic receiver functions: Implications for lithospheric structure of the Arabian Peninsula. J. Geophys. Res., 111(B11311): 10.1029/2005JB004130.

Zhao, L.-S. and Frohlich, C., 1996. Teleseismic body waveforms and receiver structures beneath seismic stations. Geophys. J. Int., 124: 525-540.

Zhao, L.-S., Sen, M.K., Stoffa, P. and Frohlich, C., 1996. Application of very fast simulated annealing to the determination of the crustal structure beneath Tibet. Geophys. J. Int., 125: 355-370.

ESTIMATING THE UNCERTAINTY AND PREDICTIVE CAPABILITIES OF THREE-DIMENSIONAL EARTH MODELS

Delaine T. Reiter[1], William L. Rodi[2], and Stephen C. Myers[3]

Weston Geophysical Corporation[1], Massachusetts Institute of Technology[2], and
Lawrence Livermore National Laboratory[3]

Sponsored by the Air Force Research Laboratory and the National Nuclear Security Administration

Award Nos. FA8718-09-C-0013[1,2] and DE-AC52-07NA27344[3]
Proposal No. BAA09-73

ABSTRACT

Many three-dimensional models of seismic velocity structure in Eurasia have been developed in recent years by the seismic nuclear monitoring community. Most of these models are not accompanied by quantitative estimates of uncertainty, either in the model velocities themselves or in geophysical observables predicted by the models (e.g., body-wave travel times). Moreover, the various 3D models produced by these studies have not been compared to one another for their predictive capabilities in any meaningful way. We have recently begun a new effort to address these issues, which will culminate in a comprehensive evaluation of the current generation of 3D seismic velocity models.

In this paper we show the results of applying two familiar validation techniques, or model evaluation metrics, to three seismic velocity models. The evaluation metrics are regional travel-time prediction and event relocation, each using a ground-truth (GT) dataset that includes events with epicenters known to 7 km or better and regional *P* and *S* arrivals within the footprint of the model region. The models include the Joint Weston/MIT (**JWM**) crust and upper-mantle velocity model for south-central Asia, which was derived by jointly inverting a large set of body-wave travel times and surface-wave group velocities in a coupled nonlinear procedure. We also derived models from the body-wave and surface-wave datasets separately, using the same initial model, inversion grids, constraints and regularization employed in the joint inversion. To make comparisons with the **JWM** model possible, we applied the Poisson's ratio of the initial model to convert the *P* velocity model constructed with travel times to an *S* velocity model (and vice versa). The results of these exercises reveal many factors that complicate the straightforward evaluation of the models.

OBJECTIVES

The main objective of our research project is to develop and apply meaningful measures of the predictive capabilities of 3D Earth models. We will specifically focus on seismic velocity models, although our general approach should be applicable to models of other geophysical parameters such as attenuation and density.

Our project will consist of two major elements. First, we will perform a comprehensive and methodical evaluation of a set of regional 3D velocity models for Asia based on data misfit and event mislocation metrics which we and other investigators have used in previous work. These metrics are already generally accepted as informative, if not complete, measures of the prediction capability of Earth models. The models will include our joint inversion model **JWM**, which will serve as the main test bed for the project. Metrics will be evaluated for each model based on a common ground-truth dataset comprising GT5 events and their arrival picks. A large part of this effort will be to establish rigorous validation tests employing standardized methods for model parameterization, forward modeling (e.g., ray tracing), and event relocation. The tools we need for these tests are available to us in-house from our previous tomography and location projects.

The second major element of our project will be the investigation of a new approach for estimating the predictive capability of 3D velocity models. Our approach will convert the uncertainty in the parameters of a 3D velocity model, as a function of position in the Earth, into the uncertainty in travel-time or other geophysical predictions. To do this requires covariance modeling capabilities we have developed for travel times in an earlier project (Rodi and Myers, 2007) and which can be extended to other observables given appropriate model sensitivities.

In this paper we show the results of applying two familiar validation techniques, or model evaluation metrics, to three seismic velocity models. The evaluation metrics are regional travel-time prediction and event relocation, each using a GT dataset that includes events with epicenters known to 7 km or better and regional *P* and *S* arrivals within the footprint of the model region. The results show that there are many factors that complicate the straightforward evaluation of the models.

RESEARCH ACCOMPLISHED

In previously funded work we applied a nonlinear joint inversion of body-wave travel times and surface-wave group velocities to data from a broad region in south-central Asia (Reiter and Rodi, 2009). The forward modeling incorporated in our inversion utilizes fully 3D ray tracing for the body-wave travel times, and a two-step procedure for the surface-wave dispersion data that includes 1D dispersion modeling at a geographic point followed by 2D ray tracing in the phase velocity maps. We numerically solved the inverse problem using a set of iterated inversion steps. Consistency between the *P* and *S* velocities was achieved by imposing bounds on Poisson's ratio and by invoking a regularization constraint that correlates variations in *P* and *S* velocity from an initial, or prior, model. We constructed the prior model as a composite of the CRUST2.0 model (Bassin et al., 2000) in the crust and the 1D AK135 reference model (Kennett et al., 1995) in the mantle. The resulting inversion model, dubbed **JWM** (for **J**oint **W**eston/**M**IT), shows good agreement with the persistent features seen in previous seismic velocity models produced from separate body- or surface-wave datasets, as well as some intriguing differences between the compressional and shear-wave structure.

Our primary goal in developing the new inversion approach and the **JWM** model was to improve regional seismic event location capability in a strongly heterogeneous crust and upper mantle. In our new work we will develop and apply a robust set of location metrics to compare the behavior of seismic velocity models. For this paper we have applied two standard metrics to our **JWM** model and two additional 'in-house' seismic velocity models: the direct comparison of predicted *Pn* and *Sn* travel times to the ground-truth observations; and relocation of the ground-truth events using regional arrivals. In the next sections we discuss the velocity models and ground-truth data used in our evaluation, as well as the results of applying the two metrics.

3D Seismic Velocity Models

JWM was derived by applying our joint inversion procedure to the combined *P*-wave travel-time and Rayleigh-wave group-velocity datasets. In contrast, the other two 3D models considered in this paper were derived from inverting each dataset separately, using the same initial model, grid parameters, constraints and regularization

employed in the joint inversion. To make comparisons with the **JWM** model, we used a simple scaling relationship to convert the final *P*-velocity model constructed with travel times to an *S*-velocity model. Conversely, the *S*-velocity model constructed from group velocities was converted to a *P*-velocity model. The scaled velocities were computed using the prior model's velocity ratio. For the separate surface-wave inversion the scaling relationship was employed at each iteration of our nonlinear inversion procedure, since group velocities depend on both *P* and *S* velocity. We also note that the crustal thickness was held to the values in the CRUST2.0 model in the body-wave only inversion, but was allowed to vary in the surface-wave only inversion.

Each inversion for the joint (**JWM**), body-wave only (**BWo**), and surface-wave only (**SWo**) models comprised ten iterations. The first five of these iterations were completely nonlinear, including the calculation of updated raypaths in the current *P* velocity model and group-velocity dispersion maps. Raypaths were held constant for the last five iterations, although the nonlinear dependence of the group-velocity maps on *S* velocity and crustal thickness was still accounted for. We chose the fifth iteration to stop calculating new ray-path sensitivities based on the insignificant changes that occurred in the ray paths between the 4^{th} and 5^{th} iterations.

We summarize the fit to the inversion datasets for the three models in Table 1, which shows the root-mean-square (RMS) residual from the observed the travel times and group delays achieved by each model. For comparison purposes we also included the fits to the initial and AK135 models. Table 1 shows that the **JWM** inversion model lowers the variance for both datasets with respect to the initial and AK135 models, which both illustrates the success of the inversion method and reveals how well we constructed our initial model.

With respect to the other 3D models, **JWM** fits the travel times nearly identically to the **BWo** model and significantly better than the SWo model. The fit to the group delays presents a more complicated story. The **JWM** model fits the group delays better than the **BWo** model, but not as well as the SWo model. In the joint inversion the influence of the *P* model (derived with travel times) has an effect on the predicted group-velocity curves that are inverted for shear velocities, even though the sensitivity of the group velocities is predominantly to the shear velocity. The SWo inversion used simple scaling to produce a *P* model at each inversion step, which resulted in the best fit to the group-velocity data, but a very poor fit to the *P* travel times (worse than the AK135 and initial models).

Table 1. RMS error of the datasets with respect to the AK135, initial and final inversion models; various subsets of the data are also shown.

Data Set		*RMS Error (s)*				
		AK135	*Initial Model*	*JWM*	*BW Only Model*	*SW Only Model*
P Travel Times	all distances	2.50	2.87	2.02	2.03	2.91
	Δ = 0 - 12°	2.27	2.43	1.86	1.87	2.75
	Δ = 12 - ~18.6°	2.81	3.42	2.24	2.26	3.13
Group Delays	all periods (T)	60.0	35.2	30.2	33.8	24.9
	T = 10 - 20 s	46.9	37.5	28.2	33.2	27.3
	T = 25 - 45 s	82.2	37.6	36.2	37.0	24.9
	T = 50 - 80 s	45.7	28.8	24.1	31.1	20.4
	T = 90 - 150 s	28.3	27.8	24.7	28.9	24.3

We applied our evaluation metrics to these three 3D inversion models to determine the merits of each model in relation to both the AK135 reference model as well as to one another. This represents an ideal comparison case in many ways, since the models were derived using identical datasets and methodologies.

Validation Data: Ground-Truth Explosions and Earthquakes

To show that 3D models improve regional travel-time prediction and event locations, we require a high-quality set of GT events whose locations, including depth and origin time, are known precisely. We used a subset of the reference events developed by the Group-2 Location Calibration Consortium (Bondár et al., 2004a). This valuable database includes nearly 2000 explosions and shallow earthquakes across the Middle East, North Africa, Europe, and Western Eurasia whose epicentral location accuracy is 10 km or less. The Group-2 Reference Event List (REL)

was used effectively by Yang et al. (2004) to demonstrate the validity of a set of regional and teleseismic travel-time models. We filtered the Group-2 REL to include events with epicentral ground-truth accuracies between 0 (GT0) and 7 (GT7) km in our study region (10-50° N, 40-110° E). We supplemented this list with some additional GT events from the EHB event bulletin (Engdahl et al., 1998) and a small list developed for an IASPEI location workshop (Engdahl, 2006). Within the boundaries of our study region there were 404 GT0–GT7 earthquakes and explosions, 319 of which fall into named event clusters. We note that we segregated the GT event database from the data used to develop the inversion models, so that we could use the events and arrivals in independent validation testing. This did not significantly impact the inversion dataset because the EHB bulletin provided a large amount of travel-time data from other well-located events. Figure 1 shows the distribution of the GT events, and Table 2 provides some details about the numbered events or clusters shown in the figure, including the numbers of events and phase arrivals that were used in our model evaluation tests.

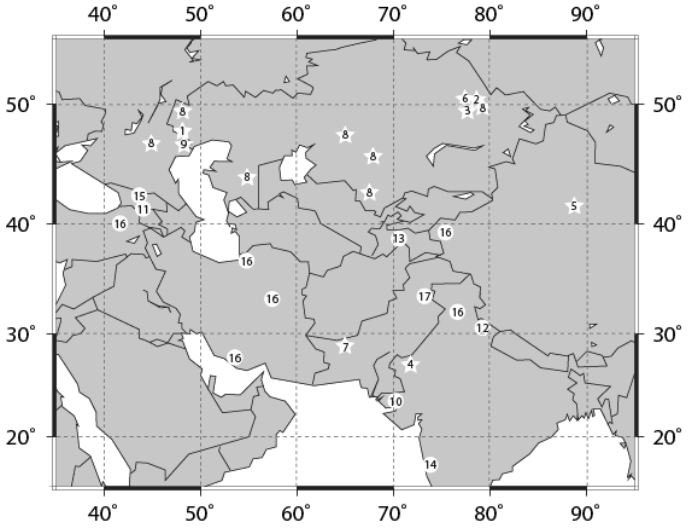

Figure 1. Locations of ground-truth epicenters (GT0-GT7) in the study region. Stars refer to explosions and circles to earthquakes; numbers are referenced to specific events or event clusters listed in Table 1.

Table 2. Details of the ground-truth database used in the model evaluation exercises.

Map Number	Event Type	N_{total} †	$N_{relocate}$ †	$N_{relocate\ S>10\%}$ †	GT Level (km)	P_{ndef}	S_{ndef}
	Nuclear Explosions						
1	PNE: Azgir	8	5	0	1	75	0
2	Balapan (Semipalatinsk)	56	7	7	1	342	81
3	Degelen (Semipalatinsk)	68	3	2	0-1	235	9
4	India	2	2	1	0-1	43	6
5	Lop Nor, China	19	15	7	1-5	395	52
6	Murzik (Semipalatinsk)	7	0	0	0-5	20	0
7	Pakistan	1	1	1	5	27	3
8	PNE: Miscellaneous	7	2	0	0-1	45	2
9	PNE: Vega	13	0	0	1	56	1
	Sum =	181	35	18		1238	154
	Earthquakes						
10	Bhuj, India	76	72	70	5-7	2370	812
11	Caucasus	6	4	4	5	160	83
12	Chamoli, India	58	51	42	5-7	1775	480
13	Garm, Tajikistan	27	27	27	5-7	843	288
14	Koyna, India	14	13	13	5	271	100
15	Racha, Georgia	35	33	28	5-7	891	243
16	Engdahl, 2006	6	6	5	5	239	60
17	Valentine's Day 1977, Pakistan	1	1	1	5	32	10
	Sum =	223	207	190		6581	2076

† N_{total} = total number of events in each geographic area; $N_{relocate}$ = events used in relocation exercise; $N_{relocate\ S>10\%}$ = events with S arrivals making up > 10% of their arrival set

The Group-2 REL does not contain a large number of regional readings, so we cross-referenced our event list to the EHB bulletin to retrieve a larger set of defining regional *P* and *S* observations. We include the *S* arrivals in the validation database because we would like to know whether the new 3D models can predict these observations because of the potentially high value *S* arrivals have for locating small events with sparse networks. However, it is important to bear in mind that *S* travel times are more likely to suffer from picking errors, and we excluded *S* travel times from the inversions.

We groomed the resulting set of arrivals by eliminating observations with residuals relative to AK135 greater than ±8.0 seconds or with clearly misidentified phase arrivals in crossover distances between various travel-time branches. With these criteria we derived a validation dataset of 7,819 regional *P*-wave arrivals and 2,230 regional *S*-wave arrivals observed at stations within a latitude-longitude box defined by (0-60° N, 30-120° E). The great-circle raypath coverage for these *P* and *S* GT observations is shown in Figure 2. The region of the inversion model that is sampled by the GT data raypaths is limited, which illustrates the difficulty of validating a model with travel times alone. However, the Group-2 REL database is currently the best available resource we have to definitively demonstrate the validity of an inversion model.

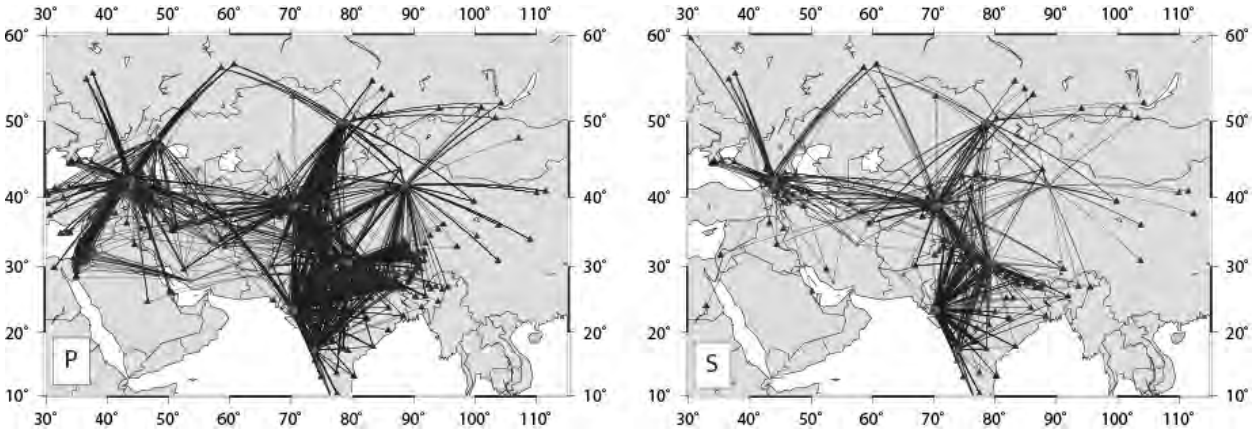

Figure 2. Great-circle raypath coverage for the *P* (left) and *S* (right) regional observations in the ground-truth database used to evaluate the inversion models. Stations are represented by black triangles and events by gray circles.

Model Evaluation Metric 1: Fits to Regional Travel Times

We follow other researchers in assessing our model for improvement in regional travel-time prediction and event location accuracy (c.f. Ritzwoller et al., 2003, Flanagan et al., 2007). The first assessment of the 3D models involves measuring their ability to accurately model the regional travel-time data. As noted by other authors, improved travel-time prediction is the most direct way to estimate the quality of a 3D model, because it eliminates the effects of network geometry and variable pick quality.

One of the more difficult questions we will address in our new project is how to present the model fits in a coherent and meaningful fashion. There are many ways to examine residuals; for example, on a station-by-station or event cluster basis (e.g. Flanagan et al., 2007), or through spatial patterns as a function of distance and station (e.g., Murphy et al. 2005), or by the fits to empirical phase path anomalies (e.g., Ritzwoller et al., 2003). Figure 3 represents a rudimentary attempt at presenting travel-time fits to the regional *P* data in the GT database relative to the AK135 and 3D inversion models. For this figure we binned the data as a function of event-to-station distance and the absolute value of the residual. By defining a visually distinct color scale and the bin sizes (here set to 0.25° in distance and 0.5 seconds in residual size), we can examine a distance-based measure of the fit; however, we remove any sense of the spatial/geographic variation or dependence of the model fits. Nevertheless, we can make some general observations about the models from these plots. The *P* residuals with respect to the AK135 model (Figure 3a) show a distinct pattern that is due to the tectonics of the study region. As noted in Ritzwoller et al. (2003), the increase in spread at the longer regional distances is likely due to some ray paths bottoming well below the bottom of the crust and encountering low velocity zones. The **JWM** and **BWo** models produce nearly identical

plots (Figure 3b,c), although detailed analysis of the differences between the two plots shows that **JWM** performs slightly better than **BWo** at most distances. The **SWo** model does as well as the other 3D inversion models at the shorter distances, but fits less well at distances greater than approximately 8°.

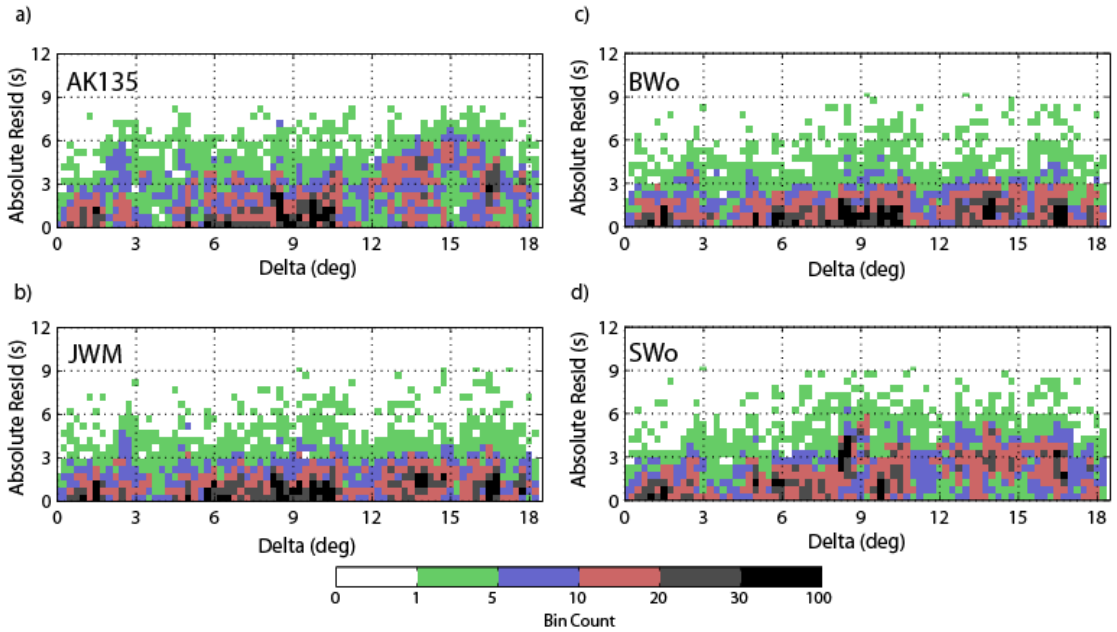

Figure 3. Ground-truth residuals for the *P* arrivals in our GT database, binned according to station-to-event distance and residual (intervals of 0.25° in distance and 0.5 seconds in residual size). The bin hit counts are plotted with the nonlinear color scale at the bottom of the plot. The residuals are calculated as the absolute value of the observations minus a) the AK135 model; b) the JWM model; c) the BWo model; and d) the SWo model.

As mentioned earlier, we are also interested in the performance of the 3D models with respect to regional *S* arrivals. *S* arrival data represent a crucial source of information in the regional recordings of a moderate-sized event, and we believe that increasing the attention paid to them for location purposes is worthwhile. Figure 4 shows the same information as Figure 3, but summarizes the travel-time prediction results from the significantly smaller and noisier GT *S* database. In this case we used nearly the same color scale, and the bin sizes were enlarged to 0.5° in distance and 1.0 seconds in residual size to eliminate poorly populated bins. It is clear from Figure 4 that the *S* GT observations exhibit much higher scatter and have no distinctive pattern in their variation compared to the *P* observations. There are significantly fewer *S* observations in the GT bulletin, particularly for the explosion events, which makes statistical conclusions more difficult. However, there are several features worth noting.

All of the models fit the data fairly well at distances less than about 5°, mainly because the paths are too short to generate large travel-time differences, no matter which velocity model is involved. It is also clear that picking error still dominates the *S* travel-time residuals, especially at the crossover distances. The residuals with respect to the AK135 model have an artificial cutoff of 8 seconds imposed on them (Figure 4a) that is not respected with the other models. In our study region, where crossover distances vary considerably, misidentified *S* phases that belong on later travel-time branches appear regularly, depending on the locations of low-velocity zones in the upper mantle of each respective *S* model. However, in spite of all these difficulties, the **JWM** model produces a slightly better fit to the *S* travel-time residuals, judging by the high bin counts at lower residuals across the entire distance range. Detailed analysis (not shown here) shows that **JWM** has a slight edge over **BWo** and does even better in comparison to **SWo**, in terms of having more hits at lower residual values.

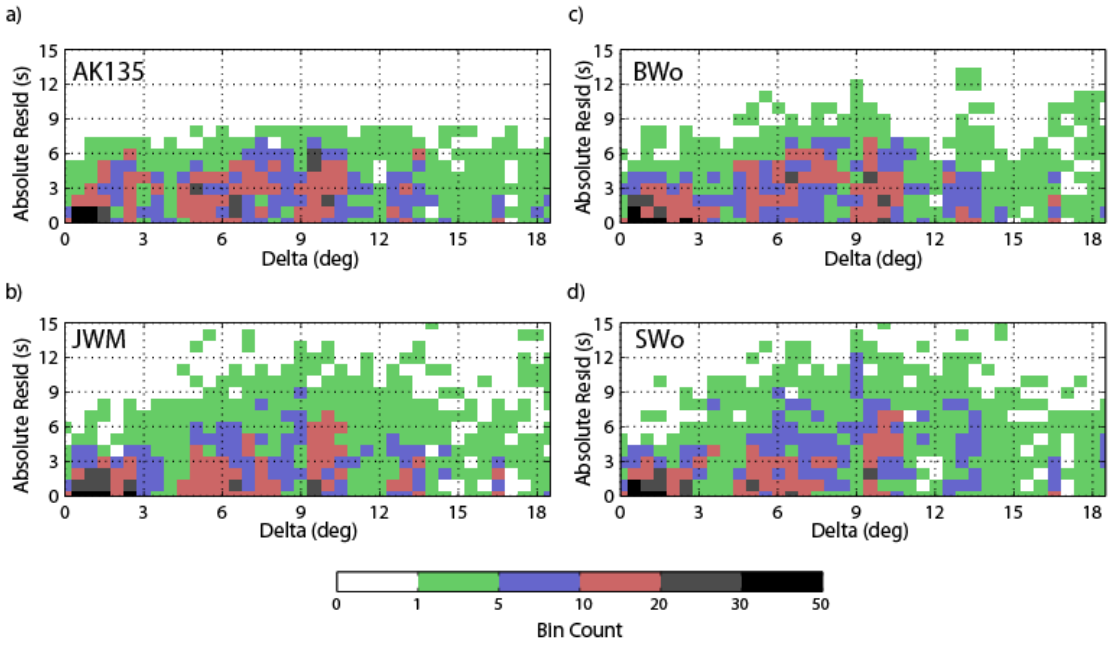

Figure 4. Ground-truth residuals for the *S* arrivals in our GT database, binned according to station-to-event distance and residual (intervals of 0.5° in distance and 1.0 seconds in residual size). The bin hit counts are plotted using the nonlinear color scale at the bottom of the plot. The residuals are calculated as the absolute value of the observations minus a) the AK135 model; b) the JWM model; c) the BWo model; and d) the SWo model.

Model Evaluation Metric 2: Locations Using Regional Travel Times

In the second assessment of the 3D inversion models we used a grid-search location method to estimate the epicenters of a subset of the events in the GT database using the arrivals at stations within the footprint of our models. In this exercise we fix the depth to the value in the GT database, because it trades off with origin time and has little effect on the epicenter. We filtered the GT data to include only those events whose regional station distribution within our model has a secondary azimuthal gap less than 270°; we included events with high secondary azimuth gaps to look at the abilities of the models when the network geometry is very poor. We also removed stations that were within 2.5° of the event and retained events with greater than 5 regional *P* arrivals. Table 2 shows the numbers of events that were relocated in each geographic location in the column labeled $N_{relocate}$.

This filtering reduced the testing dataset to a list of 35 explosions and 207 earthquakes within our region, with 7,041 regional *P*-wave arrivals and 1,826 regional *S*-wave arrivals. We used the Grid-search Multiple-Event Location (GMEL) algorithm (Rodi, 2006) to relocate the events in single-event mode, setting the arrival-time errors to 1.0 s for *P* and 2.0 s for *S* observations.

Figure 5 compares the mislocations for the AK135, **BWo** and **SWo** models versus **JWM** for the case when we locate using regional *P* arrivals. Events to the left of the unity line in these subplots are located better by the **JWM** model; we included overall **JWM** win percentages for explosions (red stars) and earthquakes (blue squares) in the bottom right of the plots. The results in Figure 5 indicate that **JWM** produces smaller mislocations than AK135 and the **SWo** model, which is no surprise; however, **JWM** also produces slightly better locations than the **BWo** model, even though the **BWo** model was generated from *P* travel times. One reason for this is that the **JWM** model locates the Bhuj cluster (No. 10 in Table 2) and the Lop Nor explosions (No. 5 in Table 2) better than the **BWo** model; these clusters account for a large component of the earthquake and explosion events in the exercise.

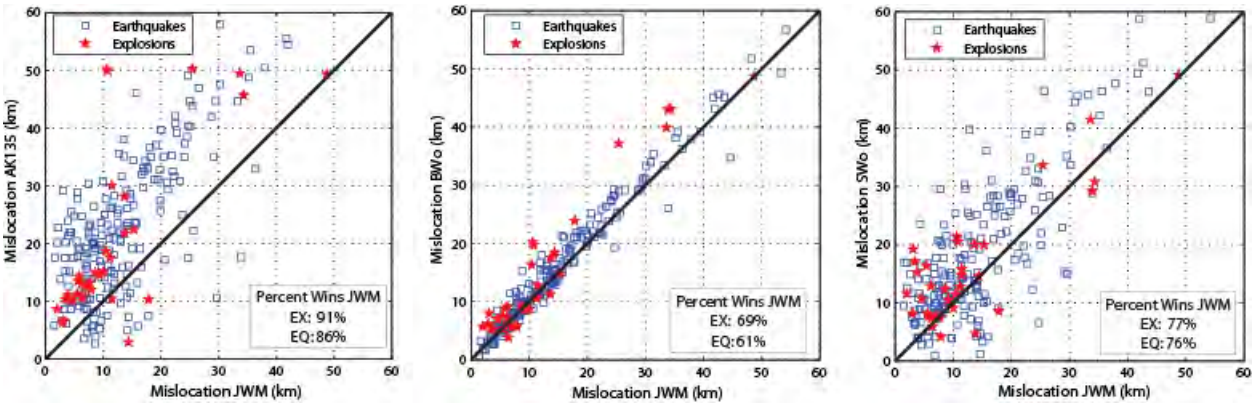

Figure 5. Epicenter mislocation comparisons for the JWM model versus the AK135 model (left), the BWo model (middle) and the SWo model (right). The locations were calculated using only *P* arrivals for the GT events in column $N_{relocate}$ in Table 2. Events to the left of the unity line indicate that JWM located the event better than the other model.

Figure 6 shows the results from locating with the *P* predictions from the 3D inversion models in a different manner, by displaying the difference in epicenter mislocation between **JWM** and the other models as a function of the secondary azimuth gap. All events in the gray-shaded areas below the zero line indicate smaller mislocations when **JWM** predictions were used. These plots demonstrate that as the network geometry degrades, **JWM** performs better than the other models. We note that this does not mean that the absolute mislocation is small for **JWM**, just that it is smaller than the mislocation produced by the **BWo** and **SWo** models.

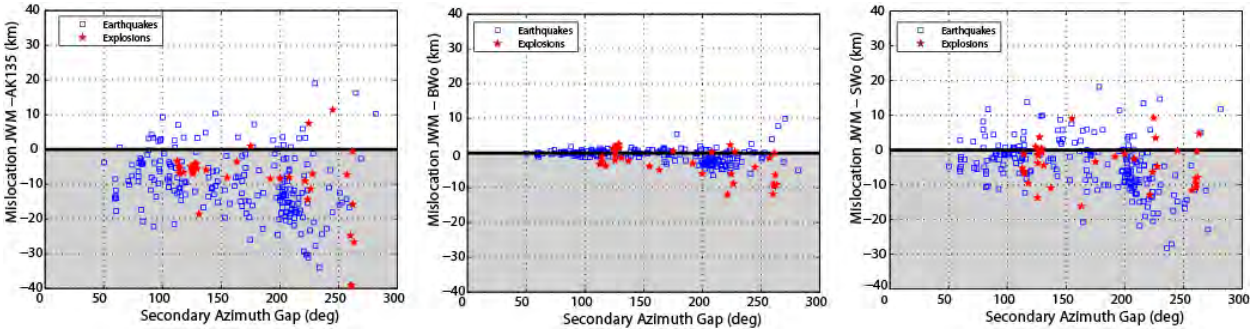

Figure 6. The differences between epicenter mislocations found with the JWM model and AK135 (left), BWo (middle) and SWo (right), as a function of secondary azimuth gap. Events in the gray-shaded regions below the zero line indicate that JWM located the event better than the other model. As the azimuth gap increases, JWM decreases event mislocations with respect to the other models.

We performed another relocation exercise to examine the influence of the *S* data and predictions from the 3D inversion models. In this case we further filtered those events designated $N_{relocate}$ to extract those for which the total regional bulletin had at least 10% *S* arrivals. This extra criterion significantly decreased the number of explosions, since nuclear tests typically do not have many *S* arrivals in the bulletin. This relocation exercise comprised 18 explosions and 190 earthquakes, listed as the column labeled $N_{relocate\ S>10\%}$ in Table 2**,** with 5,225 regional *P*-wave arrivals and 1,573 regional *S*-wave arrivals.

Figure 7 shows the results of relocating the $N_{relocate\ S>10\%}$ events, displaying them as the percentage improvement found when both *P* and *S* arrivals are included in the relocation compared to using the *P* arrivals alone, as a function of secondary azimuth gap. Events that are in the gray-shaded region below the zero line are the events for which the combined *P* and *S* arrivals resulted in an improved location. The total wins for the combined *P* and *S* relocation cases are shown plot insets. The results for **JWM** are shown on the left, **BWo** in the middle, and **SWo** on the right. The results show that the **JWM** model predicts the *S* data well enough to benefit the *P* and *S* locations over the

P-only locations. Adding the **BWo** *S* predictions to the locations produces better locations for the explosions but not for the earthquakes. Conversely, the **SWo** model predicts the *S* data well for the earthquakes, but not as well for the explosions. There is no strong correlation in percent improvement with secondary azimuth gap. However, for the cases in which the *P* and *S* combined bulletins produce smaller mislocations, **JWM** does a significantly better job of improving the results over **BWo** and **SWo**. In other words, when using both *P* and *S*, **JWM** has a stronger beneficial effect compared to the other two inversion models.

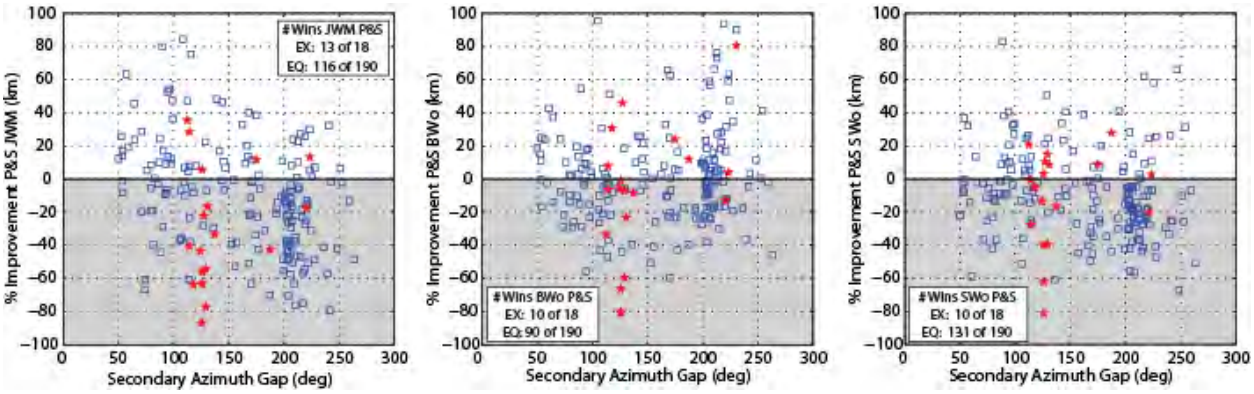

Figure 7. Epicenter mislocation comparisons when all *P* & *S* arrivals are included in the locations versus those with *P* arrivals only; JWM (left), BWo (middle) and SWo (right). The relocated events are listed in column $N_{relocate\ S>10\%}$ in Table 2. Results plotted as a function of secondary azimuth gap; inset boxes show the number of wins with *P* & *S* arrivals for explosions and earthquakes.

CONCLUSIONS AND RECOMMENDATIONS

The main objective of our new research project is to develop and apply meaningful measures of the predictive capabilities of 3D Earth models. As part of this work, we will perform a comprehensive and methodical evaluation of a set of regional velocity models for Asia based on data misfit and event mislocation metrics. These metrics are already generally accepted as informative, if not complete, measures of the prediction capability of Earth models. In this paper we applied two of these metrics to three inversion models that we derived from a 3D nonlinear inversion approach and a large database of *P*-wave travel times and Rayleigh-wave group velocities.

The primary motivation for computing the three different models, even though we plan to publish only **JWM**, was to explore the effects of a joint inversion approach under highly controlled conditions. When we hold out either the body-wave or surface-wave data from the inversion and use simple scaling relations to convert *P* to *S*, or *S* to *P*, the models that result differ in significant ways. It is clear from our analysis that using a simple scaling method will not yield the most successful model with respect to predicting travel times. This is especially true when converting an *S* model constructed with surface-wave data to a *P* model. Using our chosen constraints and velocity bounds, the group velocities produced an *S* model (and consequently a *P* model) that is too slow in the upper mantle.

A second motivation behind this work was to examine the regional *S* data available in the Group2 REL and EHB bulletin. We found that the scatter in the *S* data is significantly stronger than in the *P* data, which is disappointing but not unexpected. We also found that the GT *S* residuals with respect to the 3D models often reveal what seem to be phase identification errors. This phenomenon could be used to help identify incorrect associations and outliers along particular paths, if there are enough high-quality observations available. A subsequent benefit would be reduced picking errors in the *S* data, and further, their more successful incorporation into the location of small, regionally observed events.

REFERENCES

Bassin, C., G. Laske, and G. Masters (2000). The current limits of resolution for surface wave tomography in North America, *EOS Trans AGU* 81: F897.

Bondár, I., E. R. Engdahl, X. Yang, H. A. A. Ghalib, A. Hofstetter, V. Kirichenko, et al. (2004a). Collection of a reference event set for regional and teleseismic location calibration, *Bull. Seismol. Soc. Am.* 94: 1528–1545.

Engdahl, E. R., R. van der Hilst and R. Buland (1998). Global teleseismic earthquake relocation with improved travel times and procedures for depth determination, *Bull. Seismol. Soc. Am.* 88: 722–743.

Engdahl, E. R., 2006. Application of an improved algorithm to high precision relocation of ISC test events, *Phys. Earth. Planet In.* 158: 14–18.

Flanagan, M. P., S. C. Myers, and K. D. Koper (2007). Regional travel-time uncertainty and seismic location improvement using a three-dimensional a priori velocity model, *Bull. Seismol. Soc. Am*. 97: 804–825.

Kennett, B. L .N., E. R. Engdahl, and R. Buland (1995). Constraints on seismic velocities in the Earth from travel times, *Geophys. J. Int.* 122: 108–124.

Murphy, J.R., W. Rodi, M. Johnson, D. D. Sultanov, T. J. Bennett, M. N. Toksöz, et al. (2005). Calibration of International Monitoring System (IMS) stations in Central and Eastern Asia for improved seismic event location, *Bull. Seismol. Soc. Am*. 95: 1535–1560.

Ritzwoller, M. H., N. M. Shapiro, A. L. Levshin, E. A. Bergman, and E. R. Engdahl (2003). Ability of a global three-dimensional model to locate regional events, *J. Geophys. Res*. 108: 2353, doi:10.1029/2002JB002167.

Rodi, W. (2006). Grid-search event location with non-Gaussian error models, *Phys. Earth. Planet. Int.* 158: 55–66.

Rodi, W., and S. C. Myers (2007). Modeling travel-time correlations based on sensitivity kernels and correlated velocity anomalies, in *Proceedings of the 29th Monitoring Research Review*: *Ground-Based Nuclear Explosion Monitoring Technologies*, LA-UR-07-5613, Vol. 1, pp. 463–471.

Reiter, D. T., and W. L. Rodi (2009). Validated 3D velocity models in Asia from joint regional body- and surface-wave tomography, *Weston Geophysical Corporation*, Final Report, AFRL-RV-HA-TR-2009-1009.

Yang, X., I. Bondár, J. Bhattacharyya, M. Ritzwoller, N. Shapiro, M. Antolik, et al. (2004). Validation of regional and teleseismic travel-time models by relocating ground-truth events, *Bull. Seismol. Soc. Amer.* 94: 897– 919.

PROGRESS TOWARDS NEXT GENERATION, WAVEFORM BASED THREE-DIMENSIONAL MODELS AND METRICS TO IMPROVE NUCLEAR EXPLOSION MONITORING IN THE MIDDLE EAST

Brian Savage[1], Daniel Peter[2], Brian M. Covellone[1], Arthur J. Rodgers[3], and Jeroen Tromp[2]

University of Rhode Island[1], Princeton University[2], and Lawrence Livermore National Laboratory[3]

Sponsored by the Air Force Research Laboratory and the National Nuclear Security Administration

Contract No. FA8718-08-C-0009
Proposal No. BAA08-79

ABSTRACT

Efforts to update current wave speed models of the Middle East require a thoroughly tested database of sources and recordings. Recordings of seismic waves traversing the region from Tibet to the Red Sea will be the principal metric in guiding improvements to the current wave speed model. Precise characterizations of the earthquakes, specifically depths and faulting mechanisms, are essential to avoid mapping source errors into the refined wave speed model. Errors associated with the source are manifested in amplitude and phase changes. Source depths and paths near nodal planes are particularly error prone as small changes may severely affect the resulting wavefield. Once sources are quantified, regions requiring refinement will be highlighted using adjoint tomography methods based on spectral element simulations (Komatitsch and Tromp, 1999).

An initial database of 250 regional Middle Eastern events from 1990–2007, was inverted for depth and focal mechanism using teleseismic arrivals (Kikuchi and Kanamori, 1982) and regional surface and body waves (Zhao and Helmberger, 1994). From this initial database, we reinterpreted a large, well-recorded subset of 201 events through a direct comparison between data and synthetics based upon a centroid moment tensor inversion (Liu et al., 2004). Evaluation was done using both a 1D reference model (Dziewonski and Anderson, 1981) at periods greater than 80 seconds and a 3D model (Kustowski et al., 2008) at periods of 25 seconds and longer. The final source reinterpretations will be within the 3D model, as this is the initial starting point for the adjoint tomography. Transitioning from a 1D to 3D wave speed model shows dramatic improvements when comparisons are done at shorter periods, e.g., 25 s. Synthetics from the 1D model were created through mode summations while those from the 3D simulations were created using the spectral element method.

To further assess errors in source depth and focal mechanism, comparisons between the three methods were made. These comparisons help to identify problematic stations and sources which may bias the final solution. Estimates of standard errors were generated for each event's source depth and focal mechanism to identify poorly constrained events. A final, well-characterized set of sources and stations will be used to iteratively improve the wave speed model of the Middle East. After a few iterations during the adjoint inversion process, the sources will be reexamined and relocated to further reduce mapping of source errors into structural features.

Finally, efforts continue in developing the infrastructure required to "quickly" generate event kernels at the n^{th} iteration and invert for a new, $(n+1)^{th}$, wave speed model of the Middle East. While development of the infrastructure proceeds, initial tests using a limited number of events demonstrate that the 3D model, while showing vast improvement compared to the 1D model, still requires substantial modifications. Employing our new, full source set and iterating the adjoint inversions at successively shorter periods will lead to significant changes and refined wave speed structures of the Middle East.

OBJECTIVES

Improved models of 3D wave speeds within the greater Middle East, from the Turkish Plateau to the eastern edge of Tibet (Figure 1), will increase our ability to discriminate between natural and man-made events, locate these events, identify source depths, and determine magnitudes. Current wave speed models of the Middle East will be improved through an adjoint tomography method to iteratively update the models in three dimensions. The initial step towards any well-constrained tomography model involves the compilation of a database of relocated and characterized set of sources and waveforms. Events have been re-inverted in 1D and 3D and agree fairly well with currently available solutions. The adjoint tomography method (Tromp et al., 2005) uses full seismic waveforms as a measure of misfit of the current model iteration. Using the differences between data and synthetics, adjoint sources are constructed and used to generate kernels required to update the current iteration model. In future years, an improved wave speed model of the Middle East will be presented and distributed, built on the foundation of the seismic waveform data set.

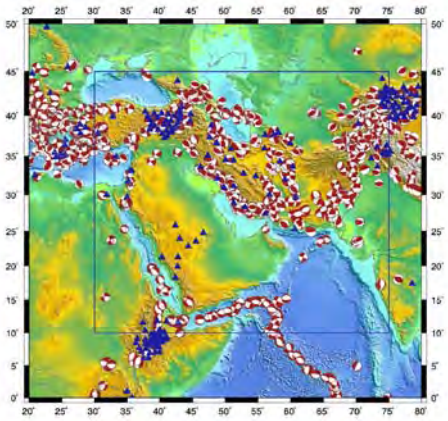

Figure 1. Map of the available sources and stations in the Middle East for the adjoint tomographic inversion.

RESEARCH ACCOMPLISHED

Tomographic updates will use starting model S2.9EA (Kustowski et al., 2008), but to avoid mapping source errors into the wave speed model, sources need to be re-evaluated within this model. Re-evaluation includes an assessment of the faulting parameters and locations using full waveforms. Multiple evaluations were conducted using synthetic and real waveform data to identify and eliminate possible problems and sources of error.

Synthetic Event Characterization

Using a synthetic waveform data set, the capabilities of the centroid moment tensor (CMT) inversion (Liu et al., 2004) were assessed. Figure 2 displays results from different parameterized inversions in an attempt to recover the solution in red at the top. Synthetics for the optimal solution and subsequent inversions were computed in model S2.9EA (Kustowski et al., 2008). Synthetics for the initial starting point were different in hypocenter and moment tensor elements to force the CMT inversion to recover the optimal solution. A simple CMT inversion, 6 parameters (black, top row), that does not solve for location or depth does a reasonable job in solution recovery. As more parameters are added, including depth, 7 parameters (black, middle row), and epicenter, 9 parameters (black, bottom row), the variance is further reduced as the original moment tensor and depth are well represented. The left and right columns of Figure 2 show inversions for only double couple (DC) or zero-trace (ZT) solutions. Zero-trace solutions perform better at representing the source as indicated by the smaller variance across the range of parameters used, 6–9. The new database of events will be built using the zero-trace (ZT) solutions.

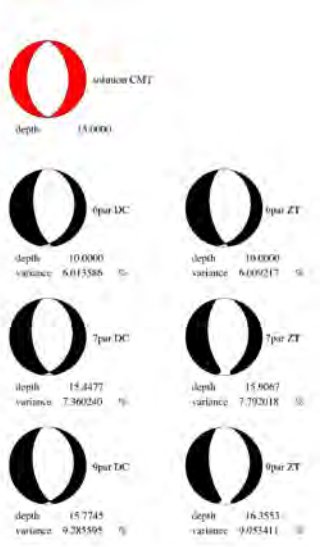

Figure 2. Performance of the CMT inversion to recover faulting parameters and source depth from a synthetic event (red) using several different parameterizations (black). Variance reductions and optimal depth for each parameterization are displayed beneath each moment tensor. See text for further explanation.

1D Event Characterization

Using the CMT inversion methodology of Liu et al. (2004), ~200 events in the Middle East were re-characterized using the 1D PREM model (Dziewonski and Anderson, 1981) at periods of 80 seconds and longer to accomplish two goals. First, the procedure of processing large amounts of data, comparing these to synthetics, and reevaluating

the source parameters and locations needed to be assessed and streamlined. This procedure needs to be straightforward and able to avoid problematic areas, as it will be used in the initial 3D event re-evaluation as well as two to three more times during the adjoint inversions. Second, problematic events and stations needed to be identified and removed before building the final waveform data set. Problematic stations and waveforms with dropouts and poorly characterized amplitude responses can negatively influence a CMT inversion. These stations were removed before any 3D CMT inversions were performed. Solutions from the long period 1D solutions are shown in Figure 3 (left). Faulting parameters and depths agree reasonably well with those from The Global CMT Project. Depths from the 1D model trend towards shallower depths, which is most likely due to the 3D model corrections used at The Global CMT Project.

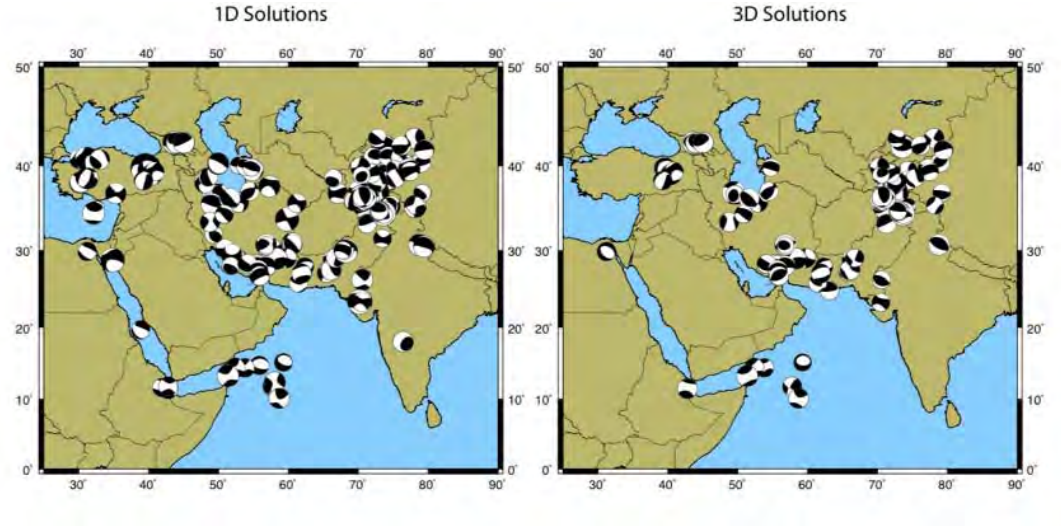

Figure 3. Comparison of new solutions using a 1D model, left, and 3D model, right. Fault plane solutions do not change appreciably when using either model, but the depths do change, especially when the events are deep. Catalog using the 1D model includes ~200 events, and the 3D model catalog currently has ~100 events (50% finished).

3D Event Characterization

The same events were also re-evaluated within the S2.9EA model (Kustowski et al., 2008) at a much shorter period of 25 seconds. Figure 3 (right) shows the current set of solutions, ~100 events (50% complete), inverted within the 3D wave speed model. Faulting solutions match well with the published solutions, and in contrast to the 1D solutions, the depths agree fairly well with published depths. While the solutions and depths match reasonably well when using either 1D or 3D wave speed models, the 3D wave speed synthetics use a much smaller minimum period, 25 seconds, that incorporates complicated body wave arrivals and more pronounced surface wave arrivals and dispersion.

Figure 4 displays vertical component data, black, and synthetics, red, for a single event on 2005/03/13 in the southern Zagros Mountains recorded by two stations to the north. Synthetics from the 1D PREM model at long and short periods are displayed in the first two columns. At long periods, the data and synthetics are relatively simple, with identifiable, small amplitude body wave arrivals and much larger amplitude, fundamental mode, surface wave arrivals. Synthetics match the absolute arrivals times rather well, but the amplitudes are misfit for each station at the longest period, 80 seconds. As shorter periods are included, middle column at 25 seconds, the synthetics remain simple arrivals as the data starts to shows dispersion due to traversing the continent, see 800 to 1100 seconds for station KURK.II.LHZ and 1000 to 1400 seconds for station KIEV.IU.LHZ. Body wave arrivals also show more complex propagation as compared to the 1D synthetics, including larger amplitudes, longer duration coda, 600 to 700 seconds for KURK.II.LHZ and 700 to 900 for KIEV.IU.LHZ in Figure 4 middle column. Simulations using the S2.9EA model (Kustowski et al., 2008) model reproduce the recorded data more closely than the 1D model at 25 seconds, Figure 4 right column. Use of the 3D wave speed model provides a more robust, shorter period estimation

of the faulting parameters without losing the essential, long period estimate of the moment/magnitude. The more complex propagation paths, represented by the waveform coda in the data and now the synthetics, do not influence the estimates of source epicenter, faulting parameters, and more importantly, source depth.

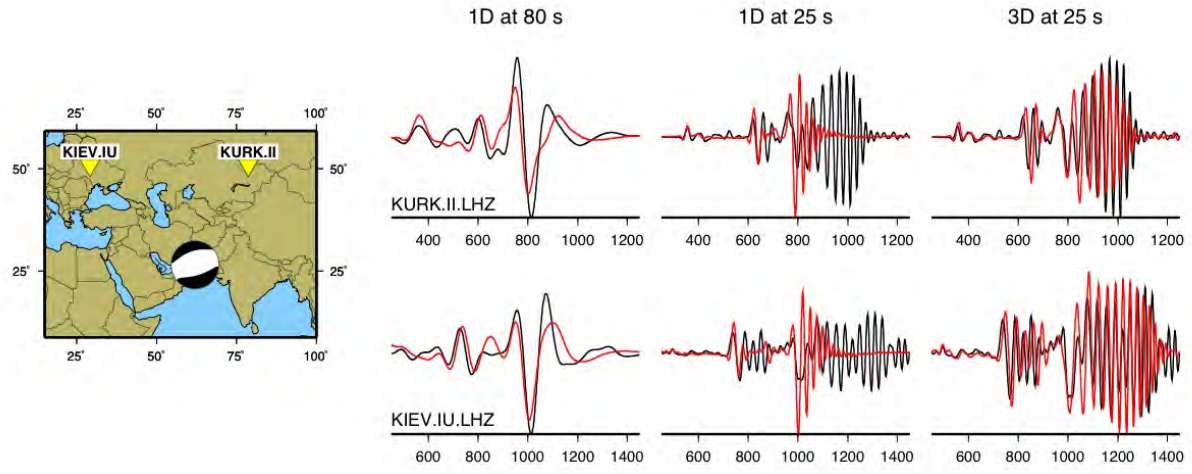

Figure 4. Comparison of vertical data and synthetics at long periods, 80 seconds, and short periods, 25 seconds, using 1D and 3D wave speed models. From the event shown in the map on the left, the data from two stations are compared to the different models. Inclusion of the 3D wave speed model improves the match between the data and synthetics, especially for the surface wave dispersion and the complex body wave arrivals.

Wave Speed Model Performance

As displayed in Figure 4, right column, the complexity of the waveforms is well represented by the 3D wave speed model, including the complex body wave arrivals and continental generated dispersion of the surface waves. While the general character of the wavefield is reproduced by the synthetics, the small variations in travel time and amplitude will be used to update the current iteration wave speed model within the adjoint tomography. Minor mismatches between data and synthetics are visible in a comparison for a single event on 2005/02/22 recorded at stations around the Middle East (Figure 5). Data from the tangential component, black, is compared with 3D synthetics, red, and plotted against azimuth to highlight different propagation paths. Paths towards the north show large amplitude, dispersive Love waves that are reasonably matched by the simulations, specifically the dispersion but not the amplitude. Recordings to the south show smaller, less dispersive Love waves as some paths include oceanic lithosphere and mantle (see waveforms at 180 degrees). Most of the surface wave energy is contained within the first pulse and the amplitude quickly diminishes with successive oscillations. Compared to the waveforms at 180 degrees, those at 350 degrees show an almost continuous surface wave amplitude of 300 to 400 seconds duration. These features are matched to first order by the current wave speed model, but improvements, primarily in amplitude, should be achievable through the adjoint, waveform methods.

Initial Adjoint Inversions

Using the mismatch between the observations and synthetic seismograms (e.g., Figure 5), an event kernel can be constructed using the adjoint method (Tromp et al., 2005) to guide updates of the current iteration, wave speed model. First, measurements between the data and synthetics are made automatically using the Flexwin tool (Maggi et al., 2009), which creates isolated data windows and generates metrics for each window, that are then used in the creation of the adjoint source. Windows, and thus the adjoint sources, are independent of any specific seismic phase and use only well matched data/synthetic pairs. Second, adjoint sources along with the full synthetic wavefield, are propagated in reverse time through the current iteration wave speed model. Third, the interactions

between the adjoint sources and the time-reversed wavefield, integrated over time, generate kernels specific to the measurement made, e.g., a simple difference between the data and synthetics.

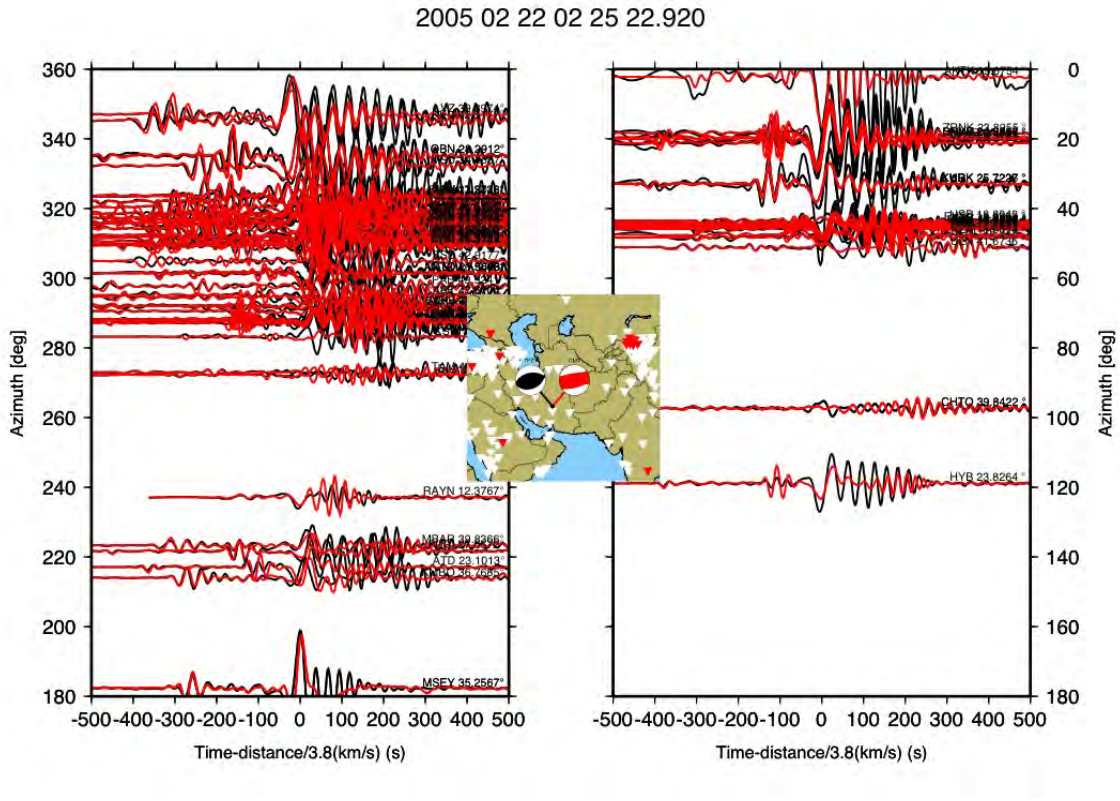

Figure 4. Comparison between tangential data and 3D synthetics for an event in the southern Zagros Mountains, map at center. Seismograms are plotted against azimuth to indicate the station coverage, wave field coherency, and to more readily identify where the wave speed model is deficient. Revised solution is in black and the globalcmt.org solution is in red.

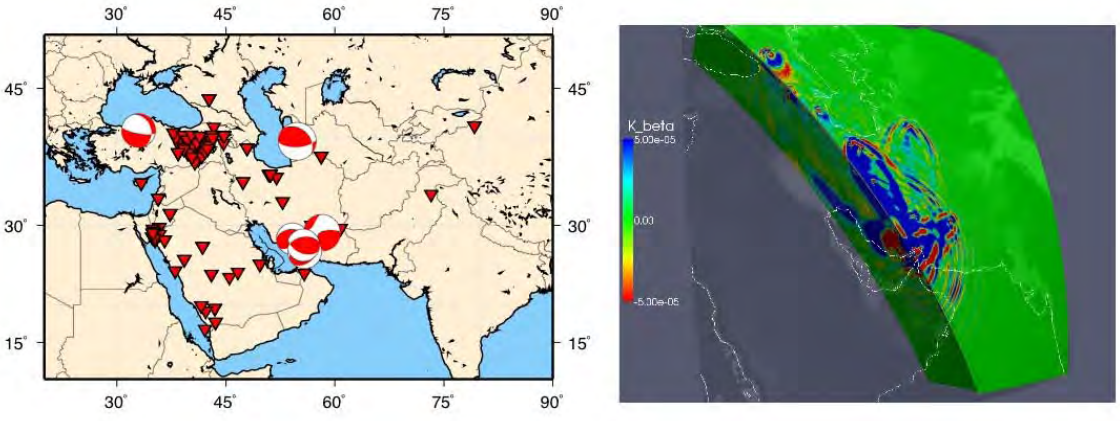

Figure 5. Example of a multiple-event kernel generated using the events and stations, left, for the Middle East. Colors for the shear kernel on the right indicate where the model requires adjustment. A north trending slice near the Persian Gulf demonstrates the kernel's volumetric nature.

Computation of a single-station, single-event kernel, or a multiple-station, single-event kernel, requires only one forward and one reverse simulation. Once all of the single-event kernels are created, multiple-event kernels for compressional modulus, shear modulus or density are produced by summing the individual event kernels together. Finally, it is these multiple-event kernels that are used to update the wave speed model. An example multiple-event kernel for a test set of 5 events is displayed in Figure 6. The map in Figure 6, left, shows the event and station locations used to construct the single-event kernels, and the multiple-event kernel for the shear modulus is shown on the right. A north trending slice through the multiple-event kernel near the Persian Gulf demonstrates the depth and volumetric nature of the kernel. Anticipated banana-doughnut shapes within the multiple-event kernel in Figure 6 are modified by a few important factors: 1) the simultaneous display of many source-to-station kernels, 2) kernels were computed in a 3D wave speed model generating more variable wave fields and many off great circle path arrivals, and 3) kernels presented here highlight regions where a mismatch is found between the forward and adjoint fields, i.e. where the model requires updating.

Initial tests, as displayed in Figure 6, demonstrate our ability to generate kernels from a set of events that are then required to update the current iteration wave speed model. Once all of the source re-evaluations are complete, the first in a series of model updates will commence. After a number of iterations, the sources will be reevaluated within the updated wave speed model to avoid mapping source errors into structural features. Iterations will continue until the misfit between the observations and synthetics has been sufficiently reduced.

CONCLUSIONS AND RECOMMENDATIONS

A seismic waveform database including source reinterpretations of the Middle East has been created. Work to characterize events within and around the Middle East has produced a large ~200 event database constrained by teleseismic and regional waveform CMT inversions. All inversion methods, the CMT inversion and previously used regional distance cut and paste (CAP) (Zhao and Helmberger, 1994) and teleseismic (Kikuchi and Kanamori, 1982) methods, provide robust estimates of source depth and faulting parameters. When used jointly, all offer an important verification of one another's result. Event characterization results from all inversions agree well with previously reported, routine determinations. Our initial tests using the 3D model S2.9EA have shown its ability to accurately simulate recorded seismic data within the Middle East at a minimum period of 25 seconds and a dramatic improvement over a simple 1D wave speed model at the same periods. Further, adjoint tomographic infrastructure for iteratively updating the current 3D wave speed model of the Middle East is in place and test inversions have already identified regions that will benefit from the adjoint methodology. We recommend, for the best possible 3D wave speed model result within the greater Middle East, that data from a wide range of sources be collected, quality checked, and added to this new waveform database, particularly seismic data from remote and/or sparsely instrumented areas.

REFERENCES

Dziewonski, A. M. and D. L. Anderson (1981). Preliminary reference Earth model, *Phys. Earth Planet Int.* 25: 297–356.

Kikuchi, M. and H. Kanamori (1982). Inversion of complex body waves, *Bull. Seism. Soc. Am*. 72: 491–506.

Komatitsch, D. and J. Tromp (1999). Introduction to the spectral-element method for 3-D seismic wave propagation, *Geophys. Jour. Int.* 139: 806–822.

Kustowski, B., G. Ekstrom, G., and A. M. Dziiwwonski (2008). The shear-wave velocity structure in the upper mantle beneath Eurasia, *Geophys. J. Int.* 174: 978–992.

Liu, Q., J. Polet, D. Komatitsch, and J. Tromp (2004). Spectral-Element Moment Tensor Inversions for Earthquakes in Southern California, *Bull. Seism. Soc. Am.* 94: 1748–1761.

Maggi, A., C. Tape, M. Chen, D. Chao, and J. Tromp (2009). An Automated time-window selection algorithm for seismic tomography, *Geophys. J. Int.* 178: 257–281.

Tromp, J., C. Tape, and Q. Liu (2005). Seismic tomography, adjoint methods, time reversal and banana-doughnut kernels, *Geophys. J. Int.* 160: 195–216.

Zhao, L. S. and D. V. Helmberger (1994). Source estimation from broadband regional seismograms, *Bull. Seism. Soc. Am.* 84: 91–104.

UNIFIED REGIONAL TOMOGRAPHY AND SOURCE MOMENT TENSOR INVERSIONS BASED ON FINITE-DIFFERENCE STRAIN GREEN TENSOR DATABASES

Yang Shen[1], Wei Zhang[1], Zhigang Zhang[1], Li Zhao[2], and Xiaoping Yang[3]

University of Rhode Island[1], Institute of Earth Sciences, Academia Sinica, Taiwan[2], and Science Applications International Corporation[3],

Sponsored by the Air Force Research Laboratory

Award No. FA8718-06-C-0014
Proposal No. BAA06-60

ABSTRACT

Seismic monitoring requires accurate source characterization in real time. Accurate 3D earth models are essential for accurate predictions of seismic observables and source characterization. While recovering the true earth structure has always been the goal of tomographic inversions, methods based on full wavefields in 3D reference models have several distinct advantages. Made possible by advances in high-performance computation, this full-wave approach accounts for complex wave propagation in 3D heterogeneous earth, enables fuller utilization of seismic records, and allows us to linearize the inverse problem by iteratively updating the 3D reference model. An important benefit of physically realistic and accurate modeling of wavefields in 3D models is the consistency of the system of equations in inversion. This is particularly important for the integration of different types of observations (*P*, *S*, and surface waves including empirical Green's functions derived from ambient noise) in inversion.

Two methods have been developed in this field to carry out full-wave tomography iteratively with 3D reference models. One is the adjoint-wavefield (AW) method, which back-propagates the data from the receivers to image the structure. The other is the scattering-integral (SI) method, which constructs the strain Green tensor (SGT) databases and calculates sensitivity kernels for each data functional. Both methods are based on the full-wave theory, and the main differences are in the computational approaches. In general, the adjoint method is CPU intensive, while the SGT-database approach requires a large disk space and fast network. To date, the AW and SI methods use two different approaches in calculating synthetic waveforms, i.e. the spectral-element method and finite-difference (FD) method, respectively. One notable advantage of the SI method is that the SGT databases make it possible to use 3D synthetics in real time seismic monitoring.

We have systematically developed a unified source mechanism and tomographic inversion method based on 3D finite-difference SGT (FDSGT) databases. The main developments include:

- a finite-difference code in the spherical coordinate system for regional and global wave propagation;
- a new and efficient implementation of the Perfectly Matched Layer that provides a better performance for waves incident at a near-grazing angle, low frequency waves or evanescent waves;
- accurate representation of *Pn*/*Sn* finite-frequency sensitivity kernels;
- a fuller utilization of an arrival on all three components of seismic records;
- the dependence of *P* waveforms on *S*-wave speed anomalies and Rayleigh waveforms on *P*-wave speed anomalies;
- moment tensor inversion using SGT databases; and
- joint *P* and *S* velocity tomography using an integrated body and surface wave dataset.

We have applied this method to Iran and the southeast Tibetan plateau and demonstrated our SGT-based, unified tomography and moment tensor inversion. The FDSGT moment tensor solutions agree well with the global centroid moment tensors (GCMT). Because of local/regional stations, 3D models, and shorter-period waves than in GCMT, FDSGT moment tensor solutions provide better locations, particularly in constraining depth. The joint *P* and *S* velocity model of the southeast Tibetan plateau from tomography of ~10,000 finite-frequency body and surface wave measurements shows an unprecedented resolution compared to previous models and tomography of similar scales.

OBJECTIVES

The objectives of this work are to obtain Finite-Frequency Seismic Tomography (FFST) velocity models for Eurasia and to refine crustal and shallow upper mantle velocity and attenuation models for focused areas of interest.

RESEARCH ACCOMPLISHED

Accurate 3D earth models are essential for accurate predictions of seismic observables and source characterization. While recovering the true form and magnitude of earth structures has always been the goal of tomographic inversions, recent studies show that methods based on full wavefields in 3D reference models have several distinct advantages in relating seismic observations to highly heterogeneous Earth structures. Made possible by advances in high-performance computation, this full-wavefield approach accounts for complex wave propagation in 3D heterogeneous Earth (Zhao et al., 2005; Tromp et al., 2005; Liu and Tromp, 2006; Zhang et al., 2007), enables fuller utilization of an arrival on all three components of seismic records (Shen et al., 2008a), and allows us to linearize the inverse problem by iteratively updating the 3D reference model. An important benefit of physically realistic and accurate modeling of full wavefields in 3D models is the consistency of the system of equations in inversion. This is particularly important for the integration of different types of observations (*P*, *S*, surface waves including empirical Green's functions derived from ambient noise) in inversion, which is an essential step to obtain a coherent and self-consistent model of the crust and mantle. Seismic tomography based on path- or structure-averaging (rays) and 1D or 2D reference models does not accurately place the 3D sensitivities of seismic observations in a complex 3D model. The mismatch in sensitivities due to approximations in theory becomes problematic when the target resolutions are at scales smaller than the Fresnel zone. For scale, a 1–Hz *Pn* wave recorded by a receiver ~1000 km from the source has a Fresnel zone width of ~200 km in the middle of the wave path (Zhang et al., 2007). van der Lee and Frederiksen (2005) recognize that a more consistent and linear system of equations offered by the full-wavefield approach would fit the combined datasets better under comparable regularization biases.

Two methods have been developed to carry out full-wave tomography iteratively with 3D reference models. One is the AW method, which back-propagates the data from the receivers to image structure (Tromp et al., 2005; Liu and Tromp, 2006). The other is the SGT-based, SI method, which calculates and stores the sensitivity kernels for each data functional (Zhao et al., 2005; Zhang et al., 2007). Both methods are based on the full wave theory. The main differences are in the computational approaches. In general, the adjoint method is CPU intensive, while the SGT database approach requires a large disk space and a fast network. A notable advantage of the SI method is that it provides both the Hessian and gradient of the misfit function in the tomographic inversion and requires a fewer number of simulations per model iteration to achieve the same level of data variance reduction (Chen et al., 2007). The SGT databases can also be used in source moment tensor inversions, making it possible to use 3D synthetics in real time seismic monitoring. To date, the AW and SI methods use two different approaches to calculate synthetic waveforms: the spectral-element method (SEM) (Komatitsch et al., 2002) and finite-difference method (Olsen, 1994; Zhang et al., 2008; Zhang and Shen, 2009; Zhang et al., 2009), respectively.

Unified tomography and source inversions based on finite-difference SGT database

In the SGT-based approach, the displacement can be expressed as (Zhao et al., 2006):

$$\begin{aligned} u_n(\mathbf{r};\mathbf{r}_s) &= \partial_i^s G_{nj}(\mathbf{r};\mathbf{r}_s) M_{ji} \\ &= \frac{1}{2}[\partial_i^s G_{jn}(\mathbf{r}_s;\mathbf{r}) + \partial_j^s G_{in}(\mathbf{r}_s;\mathbf{r})] M_{ji} \\ &= H_{ijn}(\mathbf{r}_s;\mathbf{r}) M_{ji} \end{aligned} \quad (1)$$

where $\mathbf{r}$ is the location vector, $\mathbf{r}_s$ is the source location, M_{ji} the moment tensor component (*i*,*j*=1-3), $G(\mathbf{r};\mathbf{r}_s)$ and $G(\mathbf{r}_s;\mathbf{r})$ the Green tensors for a unit impulsive force at the source and $\mathbf{r}$, respectively, and $H_{ijn}(\mathbf{r}_s;\mathbf{r})$ the strain Green tensor composed of the spatial gradient of the Green tensors. The subscript *n* denotes the component of the displacement. The source-receiver reciprocity and the symmetry of the moment tensor have been applied in Equation (1). Notice the SGT can be at any location in the medium and thus can also be at the receiver location $\mathbf{r}_R$. Equation (1) is the basis upon which the FDSGT moment tensor inversions are developed (Zhao et al., 2006; Shen et al., 2009).

The waveform change at $\mathbf{r}_R$ due to a local model perturbation at an arbitrary position $\mathbf{r}$, can be expressed as (Zhao et al., 2006):

$$\delta u_n(\mathbf{r}_R;\mathbf{r}_s) = H_{ijn}(\mathbf{r};\mathbf{r}_R)\delta C_{ijkl}(\mathbf{r})\varepsilon_{lk}(\mathbf{r};\mathbf{r}_s) \quad (2)$$

where $\delta C_{ijkl}(\mathbf{r})$ is the perturbation of the elasticity tensor and $\varepsilon_{lk}(\mathbf{r};\mathbf{r}_s)$ is spatial gradient elements of the displacement vector, which requires one forward wave simulation from the source. The total waveform change due to the model perturbation in the entire volume can be found by volume integration of Equation (2) in the model. The above waveform perturbation equation is the essential ingredient in the SGT-based tomographic method. The Fréchet kernels relating elastic and anelastic properties to any seismic data, such as frequency-dependent traveltime and amplitude anomalies, can be obtained from it (Zhao et al., 2005; Zhang et al., 2007).

Figure 1 is a schematic illustration of the unified tomography and source moment tensor inversion based on 3D FDSGT databases. Station SGT databases are constructed from 3D reference models by finite-difference simulation of the responses to orthogonal unit impulsive point forces acting at the stations. The SGTs in a small volume surrounding the source reference location extracted from the databases make it possible to invert for source moment tensors and location in a global optimization scheme. Forward wave propagation simulation from the source in the 3D reference model provides synthetic waveforms at the station and within the entire model. Travel time, amplitude, or waveform anomalies are measured from the observed and synthetic waveforms at stations. The forward wave field (from the source) and the station SGTs are used to calculate the finite-frequency sensitivities to perturbations in V_p, V_s (or bulk and shear moduli), density, and attenuation. Together with the sensitivities to source parameters, the measurements and structural sensitivity kernels are used to invert for the earth structure. The inversion results are added to the 3D reference model. This process can be repeated to progressively improve the resolution.

Source characterization and construction of hierarchical FDSGT databases

Most earthquake source studies to date utilize 1D earth models in the calculation of synthetic waveforms or Green's functions. To accommodate 3D structural heterogeneities, segments of body and surface waves are time-shifted before waveform fitting (e.g., Zhao and Helmberger, 1994; Zhu and Helmberger, 1996). In places with highly heterogeneous structure, this "cut-and-paste" of waveform segments may not fully account for the complexity of wave phenomena caused by 3D structures (e.g., wave focusing/defocusing). One of the major sources of errors in moment tensor inversion is phase skipping between the observed and synthetic waveforms. When traveltime delays due to 3D velocity heterogeneities are comparable to the wave period, phase skipping becomes a challenging problem.

Advance in computation has made the use of 3D Green's functions in earthquake source inversion an increasingly attractive option in routine operation. Liu et al. (2004) determined the source mechanisms of small to moderate earthquakes in southern California using synthetic waveforms calculated with the spectral-element method. Because the derivatives of the source parameters are determined numerically by differentiating synthetics with respect to the source parameters, up to 10 forward simulations are needed for each earthquake (six moment tensor components, latitude, longitude, depth, and the reference location). When the reference location is far from the true location, the derivatives of the location parameters may not adequately reflect the non-linear variation of waveforms as a function of location. Taking advantage of the source-receiver reciprocity, Zhao et al. (2006) introduced the use of strain Green's tensor in source inversion based on 3D reference models. We have extended the SGT-database approach to regional and teleseismic scales (Shen et al., 2009), so we are able to use any combination of local and teleseismic waveforms in source inversion. We fit filtered and time-shifted waveforms directly. For a given source location, the waveforms are linear functions of the moment tensor elements, which can be solved as a linear inverse problem. To account for perturbations in earthquake source location, we carry out a grid search in the vicinity of the reference location.

Figure 2 shows the selected earthquakes in the southeast Tibetan plateau and the stations used in moment tensor inversion (Shen et al., 2009). We calculate synthetic waveforms using a non-staggered grid finite-difference code in a polar-spherical coordinate system (Zhang et al., 2009). Wave simulations are carried out on three geographical scales: local/near regional, far regional, and teleseismic. An updated crust and upper mantle model (CUB 2.0, Shapiro and Ritzwoller, 2002) is used as the 3D reference model. The FDSGT moment tensors agree well with the global centroid moment tensor (GCMT) solutions (Figure 3), with one notable exception at the eastern Himalayan syntaxis (event 03.230 in Figure 3). The GCMT solution shows a strike-slip event at 33 km depth, while our FDSGT solution is a shallow (2±16 km) thrust event.

Figure 4 shows an example of the fit between the observed waveforms and the synthetics calculated from the FDSGT databases. An inspection of the waveforms in detail (Shen et al., 2009) shows that the regional stations, the 3D model, and shorter-period body waves than those used in the GCMT solutions tend to provide tighter constraints on the source location, particularly the depth.

Full-wave tomography and finite-frequency kernels based on 3D reference models

To date the inversions of *P*- and *S*-wave speeds have been carried out separately under the assumption that *P* traveltimes are affected only by the *P*-wave speed of the elastic media and *S* traveltimes by the *S*-wave speed. The practice stems from ray theory, in which *P* and *S* waves are completely decoupled except for conversions at discontinuities following the Snell's law. Based upon numerical and analytical solutions, we have shown that for finite-frequency waves, *S*-speed perturbation may have significant effects on *P* waveforms (Zhang and Shen, 2008). At places near the source or receiver, the cross-dependence of *P* waveforms on *S*-speed perturbation is substantial. For example, the integrated absolute *P*-traveltime sensitivity to *S*-speed perturbation is 31% of that to *P*-speed perturbation when the source-receiver distance is seven times the wavelength ($L/\lambda=7$, where λ is the wavelength and *L* the distance to the receiver). At a source-receiver distance of 100 wavelengths, the ratio is about 5%. This finite-frequency effect has important implications for seismic tomography, particularly at regional and local scales, where target structures are often located within several tens of wavelengths from receivers or from both sources and receivers. Even for regions far from sources and receivers, neglecting this cross-dependence means that the estimates of the *P* speed near the source and receiver are likely biased and such errors may propagate into the rest of the model in tomographic inversion.

Figure 5 shows the phase sensitivities of a regional Rayleigh wave to *S*- and *P*-wave speeds. Similar to the results for southern California in Liu and Tromp (2006), there are large 3D variations in the finite-frequency kernels due to wave-speed variations. Although commonly neglected in surface wave tomography, *P*-wave speed (and density) affects Rayleigh waves (also see Zhou et al. (2004) and Liu and Tromp (2006)). The maximum sensitivity to *P*-wave speed is on the surface and at a level comparable to the Vs kernel. It decreases to ~10% of the maximum at depth of $\sim\lambda/4$. Since the peak of the Vs sensitivity is at the depth of $\sim\lambda/3$ and heterogeneities in the mantle are generally much weaker than in the crust, it may be necessary to include the sensitivities to *P*-speed and density for long-period (~50+ s) Rayleigh waves in a high-resolution inversion. When integrated with *Pn*, *Sn*, and Love waves, Rayleigh waves may provide additional constraints on the *P*-wave structure in the crust. At the very least, incorporating the effects of *P*-speed on Rayleigh waves may minimize a likely cause contributing to the apparent Love-Rayleigh discrepancy and radial anisotropy.

Figure 6a and 6b show the *P* and *S* wave velocities, respectively, of the shallow crust of the southeast Tibetan plateau. The model is derived from a joint inversion of ~10,000 measurements of phase anomalies of *P*/*Pn*, *S*/*Sn* and Rayleigh/Love waves in three frequency bands ranging from 0.008–0.1 Hz (Shen et al., 2008b). After two iterations, the combined velocity anomalies relative to the initial reference model (CUB 2.0, Shapiro and Ritzwoller, 2002) show that the observations require P velocity increases just north of the Indus Yalu suture (IYS), near the Bangong-Nujiang suture (BNS), and west of the Xianshuhe Fault system (XSHF). These high-velocity anomalies correlate well with areas of granitic and/or more metamorphosed Proterozoic and Paleozoic rocks among the regional Mesozoic background (Geological map of the Tibetan plateau, China Academy of Geological Sciences, Chengdu). The P-wave resolution at such a shallow depth is attributed in part to the sensitivity of Rayleigh waves to *P*-wave speed perturbations (Figure 5). The updated *S*-velocity model (Figure 6b) shows a sharp velocity contrast that follows the boundary of the Tibetan plateau as outlined by the 1000 m elevation contour.

CONCLUSIONS AND RECOMMENDATIONS

We have developed a unified tomography and earthquake moment-tensor inversion based on 3D reference models. The new approach accounts for complex wave propagation, enables fuller utilization of an arrival on all three components of seismic records, and linearizes the inverse problem by iteratively updating the 3D reference model. We calculate synthetic waveforms using a non-staggered grid finite-difference code in a polar-spherical coordinate system. The new moment tensor solutions accommodate the 3D velocity heterogeneities and are an integral part of the unified tomography and source inversion. Body and surface wave traveltimes are inverted jointly for *P* and *S* wave speed perturbations. The results show a much-improved resolution compared to the reference model and regional models of similar scale.

ACKNOWLEDGEMENTS

Dr. Eric Engdahl provided data used to construct portions of Figure 4.

REFERENCES

Chen, P., T. H. Jordan, and L. Zhao (2007). Full three-dimensional tomography: a comparison between the scattering-integral and adjoint-wavefield methods, *Geophys. J. Int.* 170: 175–181.

Komastitsch, D., J. Ritsema, and J. Tromp (2002). The spectral-element method, Beowulf computing, and global seismology, *Science* 298: 1737–1742.

Liu, Q., J. Polet, D. Komatitsch, and J. Tromp (2004). Spectral-element moment tensor inversions for earthquakes in southern California, *Bull. Seism. Soc. Am.* 94: 1748–1761.

Liu, Q., and J. Tromp (2006). Finite-frequency kernels based on adjoint methods, *Bull. Seismol. Soc. Am.* 96: 2383–2397.

Olsen, K. B. (1994). Simulation of three-dimensional wave propagation in the Salt Lake Basin, Ph.D. Thesis, University of Utah, Salt Lake City, Utah, 157 p.

Shapiro, N. M. and M. H. Ritzwoller (2002). Monte-Carlo inversion for a global shear velocity model of the crust and upper mantle, *Geophys. J. Int.* 151: 88–105.

Shen, Y., Z. Zhang, and W. Zhang (2009). Moment inversions of earthquakes in the southeast Tibetan plateau using finite-difference strain Green tensor database, submitted to *Geophys. J. Int.*

Shen, Y., Z. Zhang, and L. Zhao (2008a). Component-dependent Fréchet sensitivity kernels and utility of three-component seismic records, *Bull. Seism. Soc. Am.* 98: doi:10.1785/0120070283.

Tromp, J., C. Tape, and Q. Liu (2005). Seismic tomography, adjoint methods, time reversal and banana-doughnut kernels, *Geophys. J. Int.* 160: 195–216.

van der Lee, S. and A. Frederiksen (2005). Surface wave tomography applied to the north American upper mantle, in Seismic Earth: Array Analysis of Broadband Seismograms, Geophys. Monograph Ser. 157, AGU, 67–80.

Zhang, W. and Y. Shen (2009). Unsplit Complex Frequency Shifted PML Implementation Using Auxiliary Differential Equation for Seismic Wave Modeling, submitted to *Geophysics*.

Zhang, W., Y. Shen, and X. Chen (2008). Numerical simulation of strong ground motion for the Ms8.0 Wenchuan earthquake of 12 May 2008, *Sci. China Ser. D-Earth Sci.* 51: 1673–1682

Zhang, W., Y. Shen, and L. Zhao (2009). 3D seismic wave modeling in spherical coordinate by a non-staggered finite difference method, manuscript in preparation.

Zhang, Z. and Y. Shen (2008). Cross-dependence of finite-frequency compressional waveforms to shear seismic wave-speeds, *Geophys. J. Int.* 174: doi:10.1111/j.1365-246X.2008.03840.x.

Zhang, Z., Y. Shen, and L. Zhao (2007). Finite-frequency sensitivity kernels for head waves, *Geophys. J. Int.* 171: 847–856.

Zhao, L., P. Chen, and T. H. Jordan (2006). Strain Green tensor, reciprocity, and their applications to seismic source and structure studies, *Bull. Seism. Soc. Am.* 96: doi:10.1785/0120050253.

Zhao, L., T. H. Jordan, K. B. Olsen, and P. Chen (2005). Fréchet kernels for imaging regional earth structure based on three-dimensional reference models, *Bull. Seism. Soc. Am.* 95: 2066–2080.

Zhao, L. and D. V. Helmberger (1994). Source estimation from broadband regional seismograms, *Bull. Seism. Soc. Am.* 84: 91–104.

Zhou, Y., F. A. Dahlen, and G. Nolet (2004). 3-D sensitivity kernels for surface-wave observables, *Geophys. J. Int.* 158: 142–168.

Zhu, L. and D. V. Helmberger (1996). Advancement in source estimation techniques using broadband regional seismograms, *Bull. Seism. Soc. Am.* 86: 1634–1641.

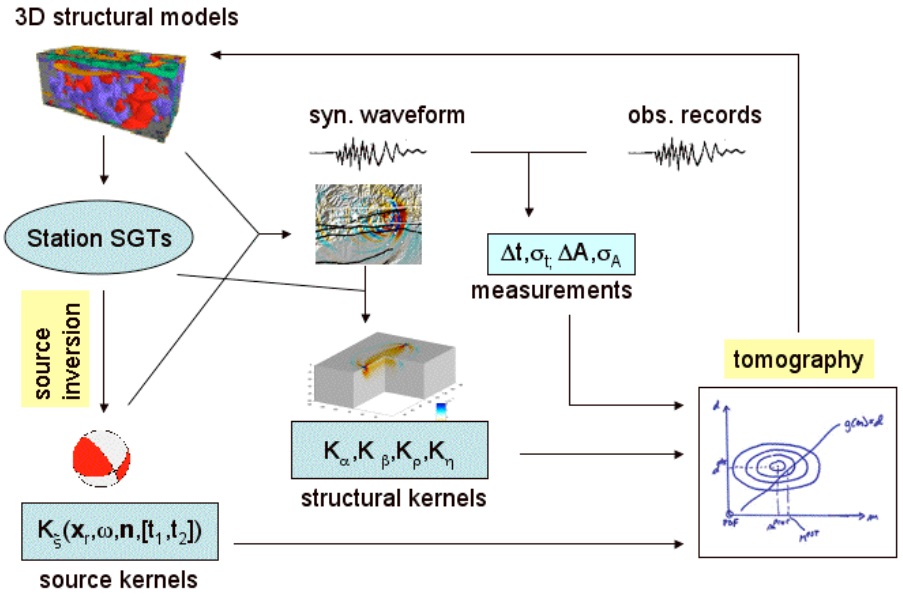

Figure 1. Schematic illustration of the unified tomography and moment tensor inversions based on 3D FDSGT databases.

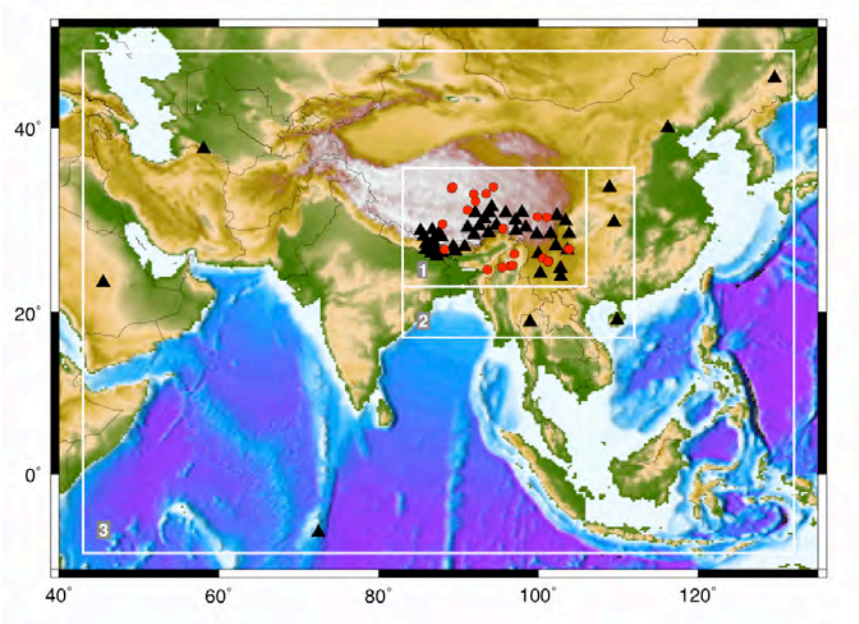

Figure 2. Selected earthquakes (red circles) in the southeast Tibetan plateau during 2001–2004 and the stations (black triangles) used in moment tensor inversions. White rectangles outline the three geographic scales of the finite-difference wave simulation: (1) local/near regional, (2) far-regional, and (3) teleseismic.

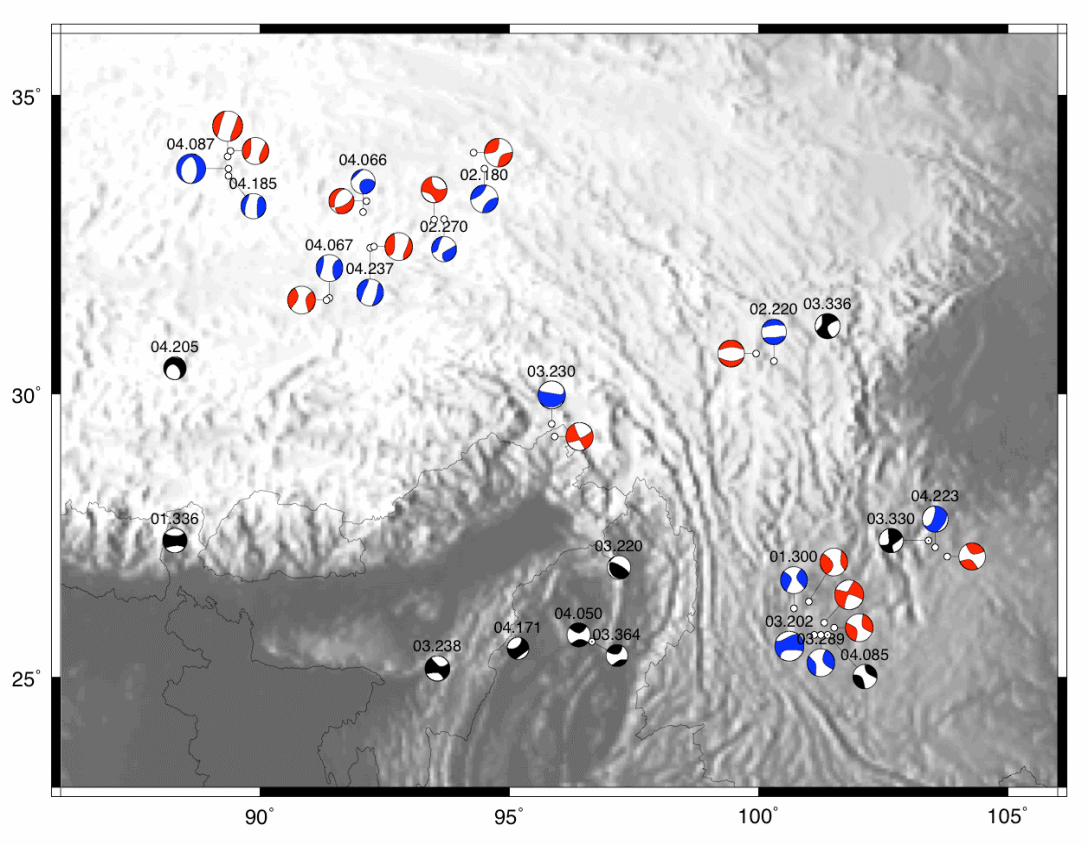

Figure 3. Comparison of the FDSGT (white-and-blue symbols) and GCMT (white-and-red symbols) solutions for 13 earthquakes during 2001–2004 in the southeast Tibetan plateau. The numbers above the FDSGT solution denote the year and Julian day of the earthquake. Also plotted are the source mechanisms of 10 additional earthquakes without GCMT solutions (black-and-white symbols).

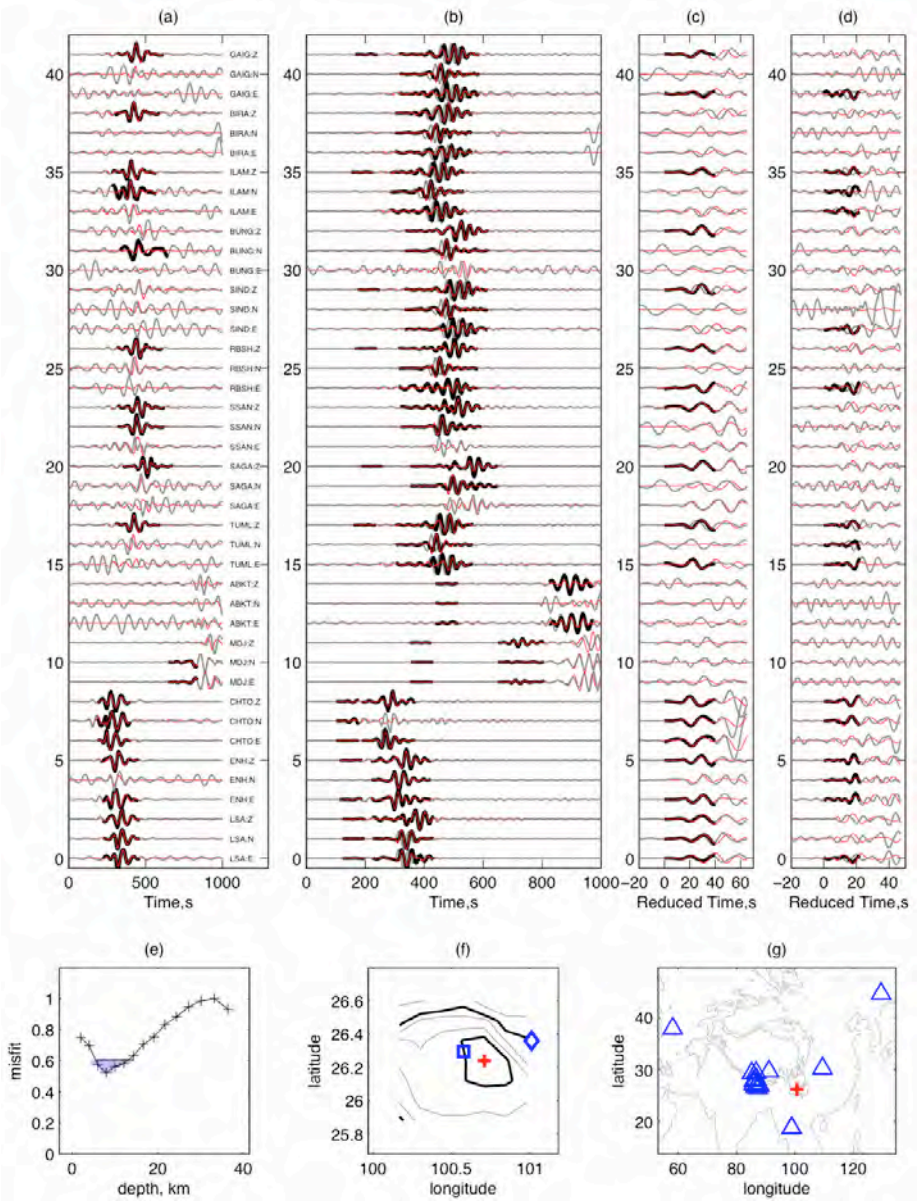

Figure 4. (a–d) Observed waveforms (thick gray lines) are compared with the synthetics for the best source moment tensor solution (red lines). The frequency bands are, from left to right, 0.00833–0.0167, 0.0167–0.0333, 0.0333–0.0667, and 0.0667–0.167 Hz. Dark thick lines are time-shifted observed waveforms used in the final inversion. For the first arrivals (in c and d), the time is reduced to align the arrivals within the time window. The amplitude is normalized by individual trace. (e) Normalized waveform misfit as a function of depth. Crosses mark the grid-search depths. The shaded region indicates the 1σ confidence limit. (f) Contours of various confidence limits at the depth of the global best solution (8 km for this event). The cross marks the FDSGT location; the square is the EHB location (Engdahl, see acknowledgements); and the diamond is the global centroid moment tensor location. From the innermost contour surrounding the FDSGT solution, the contours are the 68% (dark line), 80%, 90%, 95% (dark line), and 99% confidence limits. (g) Triangles and cross mark the stations used in the source inversion and the event, respectively. Gray contours follow 0, 2000 and 4000 m elevation.

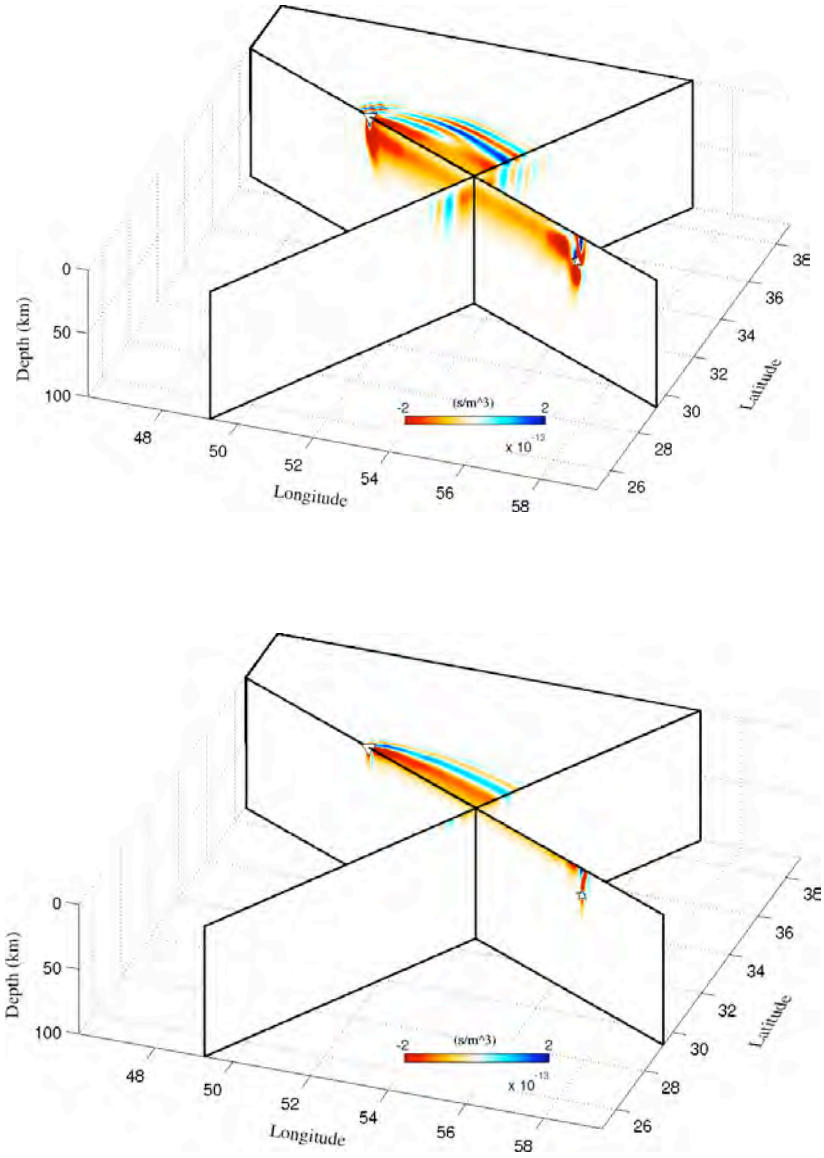

Figure 5. Phase sensitivity kernels of a regional Rayleigh wave to *S* wave-speed (top) and *P* wave-speed (bottom) perturbations relative to a 3D reference model. The period of the wave is 10–20 s. The two vertical cross-sections cut the model along the great circle path between the earthquake source (in the southeast corner of the model) and receiver (in the northwest corner of the model) and perpendicular to the great circle. Also shown is a quadrant of a horizontal section on the surface. The scale is ±2x10^{-13} s/m^3.

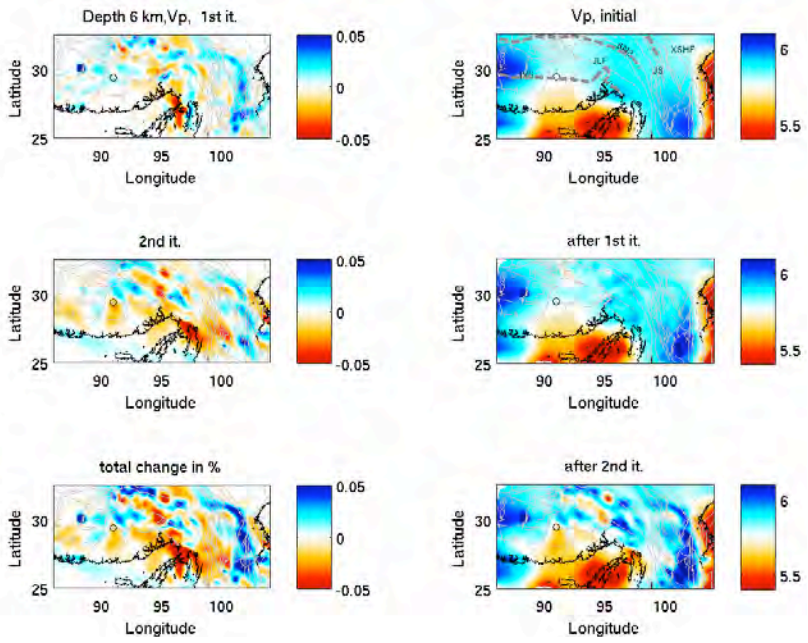

Figure 6a. ***P*-wave velocity variations at 6 km depth in the southeast Tibetan plateau. The initial 3D reference model (top right) is converted from CUB 2.0 by a V_p/V_s ratio of 1.74 in the crust and the V_p/V_s of AK135 in the mantle. The unit of the color bar is km/s. The left panels show the velocity perturbations after the 1st and 2nd iteration and the total velocity change in percent. The middle-right and bottom-right panels show the updated models after the 1st and 2nd iterations. The main tectonic features, the Indus-Yalu suture (IYS), Bangong-Nujiang suture (BNS), and the Xianshuihei Fault system (XSHF), are marked in the upper right panel. The 1000 m elevation contour outlines the southern margin of the Tibetan plateau and the boundary of the Sichuan basin.**

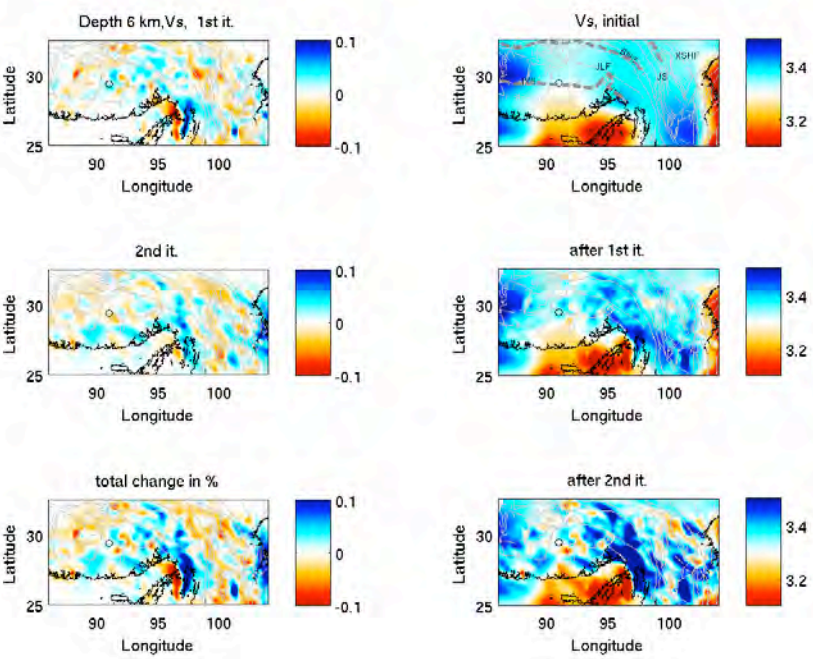

Figure 6b. Same as Figure 6a, except showing *S* velocity.

MULTI-RESOLUTION SEISMIC TOMOGRAPHY BASED ON A RECURSIVE TESSELLATION HIERARCHY

Nathan A. Simmons, Stephen C. Myers, and Abelardo Ramirez

Lawrence Livermore National Laboratory

Sponsored by the National Nuclear Security Administration

Award No. DE-AC52-07NA27344/LL09-3Dseismic-NDD02

ABSTRACT

A 3-D global tomographic model that reconstructs velocity structure at multiple scales and incorporates laterally variable seismic discontinuities is currently being developed. The model parameterization is node based, with nodes being placed along vertices defined by triangular tessellations of a spheroidal surface. The triangular tessellation framework is hierarchical. Starting with a tetrahexahedron representing the whole globe (1st level of the hierarchy, 24 faces), we divide each triangle of the tessellation into daughter triangles. The collection of all daughter triangles composes the 2nd level of the tessellation hierarchy, and further recursion produces an arbitrary number of tessellation levels and arbitrarily fine node spacing. We have developed an inversion procedure that takes advantage of the recursive properties of the tessellation hierarchies by progressively solving for shorter wavelength heterogeneities. In this procedure, we first perform the tomographic inversion, using a tessellation level with coarse node spacing. We find that a coarse node spacing of approximately 8° is adequate to capture bulk regional properties. We then conduct the tomographic inversion on a 4° tessellation level using the residuals and inversion results from the 8° run. In practice we find that the progressive tomography approach is robust, providing an intrinsic regularization for inversion stability, and avoids the issue of predefining resolution levels. Further, determining average regional properties with coarser tessellation levels enables long-wavelength heterogeneities to account for sparsely sampled regions (or regions of the mantle where longer wavelength patterns of heterogeneity suffice) while allowing shorter length-scale heterogeneities to emerge where necessary.

We demonstrate the inversion approach with a set of synthetic test cases that mimic the complex nature of data arrangements (mixed-determined inversion) common to most tomographic problems. We also apply the progressive inversion approach with *Pn* waves traveling within the Middle East region and compare the results to simple tomographic inversions. As expected from synthetic testing, the progressive approach results in detailed structure where there is high data density and broader regional anomalies where seismic information is sparse. The ultimate goal is to use these methods to produce a seamless, multi-resolution global tomographic model with local model resolution determined by the constraints afforded by available data. We envisage this new technique as the general approach to be employed for future multi-resolution model development with complex arrangements of regional and teleseismic information.

OBJECTIVES

The objective of this 3-year project is to create a seamless, 3-D tomographic model that reconstructs seismic heterogeneities at regional and global scales to enhance seismic event location capabilities through more-accurate travel time predictions. To achieve this overall objective, multiple sub-objectives must be achieved, including the following:

1. The development of a modeling framework that efficiently allows variations in continuous media, as well as discontinuities at geologic boundaries;
2. Fully 3-D ray tracing algorithms that communicate with such a framework to predict accurate travel times and define path sensitivities to the 3-D model space; and
3. A stable tomographic inversion technique that is suited to solve for structures at fine and broad scales simultaneously given the available seismic information and the variations of heterogeneity wavelengths often observed in Earth's crust and mantle.

Because variants of Objectives 1–2 have been outlined in previous MRR reports, the primary focus of the current report regards the development of a tomographic inversion technique (Objective 3) tailored to reconstruct 3-D seismic heterogeneity on multiple resolution scales. The technique takes advantage of the recursive nature of a tessellation-based model framework and eliminates the requirement of traditional regularization operators and/or pre-defining variable model parameter densities.

RESEARCH ACCOMPLISHED

As part of the Ground-based Nuclear Explosion Monitoring (GNEM) R&D program, we are developing a singular, global 3-D seismic model for the primary purpose of enhancing seismic event location capabilities. Our goal is to produce a model within a framework suitable for accurate and efficient computation of travel times without the strict requirement for station-phase-specific lookup tables and/or empirical corrections. We have made significant advances towards achieving this goal by focusing on the development of advanced tomographic inversion techniques required to generate accurate representations of Earth structure with complex arrangements of seismic information.

Model Framework and Starting Model Design

Our model representation is based upon a triangular tessellation procedure whereby the triangular facets of an initial object (in our case, a tetrahexahedron) are recursively broken down into smaller sub-triangles and projected onto a unit sphere (Figure 1). This general procedure has been adapted by multiple scientific disciplines including the representation of seismic models of the Earth (e.g. Wang & Dahlen 1995; Ishii & Dziewonski 2002; Ballard et al. 2008a; Myers et al. 2009). Each subdivision of a triangular facet ("parent") produces 4 triangular facets ("daughters"), thereby increasing the number of points and the resolution upon each recursion step. We refer to all sequentially produced objects as "Levels," starting with the initial object (Level 1; Figure 1a) up to Level *N*. In our case, model nodes are placed at any arbitrary distance (radii) along the vertices of the triangles, allowing for the representation of a spheroidal Earth with undulating layers (Figure 2b). For instance, Moho depth is independently defined along each geocentric vector, and continuous Moho depth within each tessellation triangle is determined by interpolating the set of nodes or "nodesets" that define each triangle.

The major benefit of the tessellation-based model design is the efficiency of referencing a complex model at any arbitrary location through a process called hierarchical triangulation (Figure 1). The 1st-level triangle containing the point of interest is found first, using basis vector arithmetic. Then only daughters of that 1st-level triangle are searched until the 2nd-level triangle containing the point is found. This hierarchical search is repeated to the desired tessellation level. Indexing parent-daughter triangle relationships from one tessellation level to the next allows for rapid identification of the vertices surrounding the point of interest at each successive tessellation involving testing a maximum of 24+4(N-1) triangles, where N represents the final level. For example, if we were interested in finding the triangle that encompasses a point at Level 7 (98,304 triangles; ~1° vertex spacing), we would need only to search a maximum of 24+4(7-1)=48 triangles.

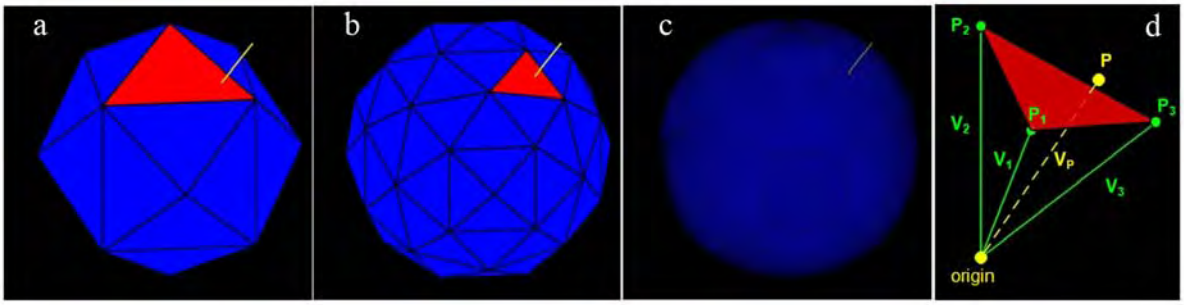

Figure 1. Tessellation-based model representation. The 24 triangular facets of a tetrahexahedron (a, Level 1) are recursively subdivided into 4 small triangular facets to produce a total of 96 faces (b, Level 2). The process is repeated to generate 24,576 faces with 12,290 vertices (c, Level 6). By defining a vector (yellow line) from the origin to a point *P* in space, the point can be quickly associated with a particular triangular facet at any tessellation level (red triangles) defined by vectors (V_1, V_2, V_3) through a process called hierarchical triangulation.

After identifying the triangle, we then compute barycentric (or areal) coordinates for each of the three points defining the triangle. These coordinate values are equivalent to weights placed at each node needed to physically balance the triangle at the arbitrary point *P* (Figure 2a). These coordinates serve as lateral interpolation weights for any model properties, including seismic velocities, velocity gradients, and nodeset radii. The laterally interpolated values for each bounding nodeset are then linearly interpolated in the radial direction along the point-of-interest vector (POI, Figure 2b), and simple linear interpolation determines the model property at the POI.

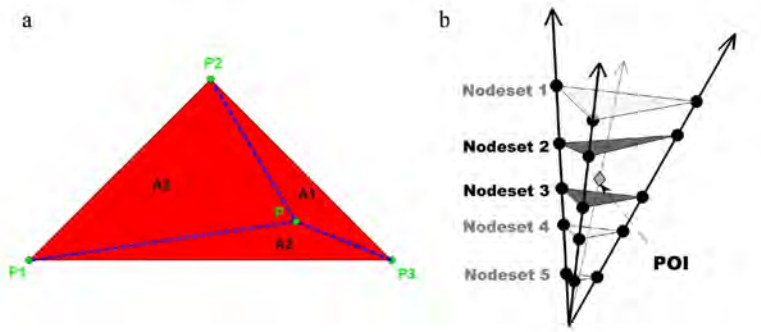

Figure 2. Schematic representation of the interpolation procedure to attain model properties at any arbitrary point. (a) Barycentric (or areal) coordinates serve as interpolation weights. Physically, these values are the masses required at each point defining the triangle to balance it about point *P*. Geometrically, these values are equivalent to the ratio of the opposite areas (*A1*, *A2*, *A3*) of the triangle normalized by the total area. For example, the barycentric weight at *P3* is *A3*/(*A1*+*A2*+*A3*). (b) The nodesets surrounding the POI are identified, and the model properties are computed at the intersection of the POI vector with the nodeset plane. Simple linear interpolation in the radial direction is then used to compute the model property at the POI.

We chose to build a starting global 3-D model within this framework suitable for reasonable 1st-order estimation of seismic ray paths, travel times, and testing purposes. The model integrates the components of the regional travel time model RSTT from Myers et al. (2009) and the global 3-D P-wave velocity model MIT-P08 from Li et al. (2008). The properties/components of the designed model include the following:

1) Spheroid (based on the GRS80 ellipsoid)
2) Tetrahexahedron build at Level 7 (~1° node spacing) down to 310 km below the spheroid
3) Tetrahexahedron build at Level 6 (~2° node spacing) below 310 km

4) Water, ice, sediment, and crustal layers from the RSTT model (7 discontinuous layers)
5) *Pn* and shallow upper-mantle velocities computed from the RSTT model (down to 120 km)
6) Averaged P-wave velocities from the RSTT and MIT-P08 models at 120 km
7) Discontinuous upper-mantle transition zone layers
8) P-wave velocity from 120 km below the spheroid to the core-mantle boundary from MIT-P08.

This designed model has served as a testing ground for 3-D ray tracing algorithm design and a starting solution for the real test case described within the remainder of this report.

3-D Ray Tracing and Sensitivity Kernel Definitions

In order to accurately predict travel times and model space sensitivities in complex 3-D media, we have adapted a 3-D ray tracing procedure specifically tailored to communicate with the aforementioned model design. The general approach we have taken is based on the techniques originally conceived by Zhao et al. (1992) to model direct arrivals within a subduction zone and extended to teleseismic phases by Zhao and Lei (2004). The technique uses pseudo-bending in continuous media developed by Um and Thurber (1987) while simultaneously satisfying Snell's Law at discontinuous interfaces through an iterative process. One major shortcoming of this approach is the inability to find global minimum travel times and paths for complex regional phases such as *Pn*. We have therefore adapted the procedure to find such global minima (Figure 3).

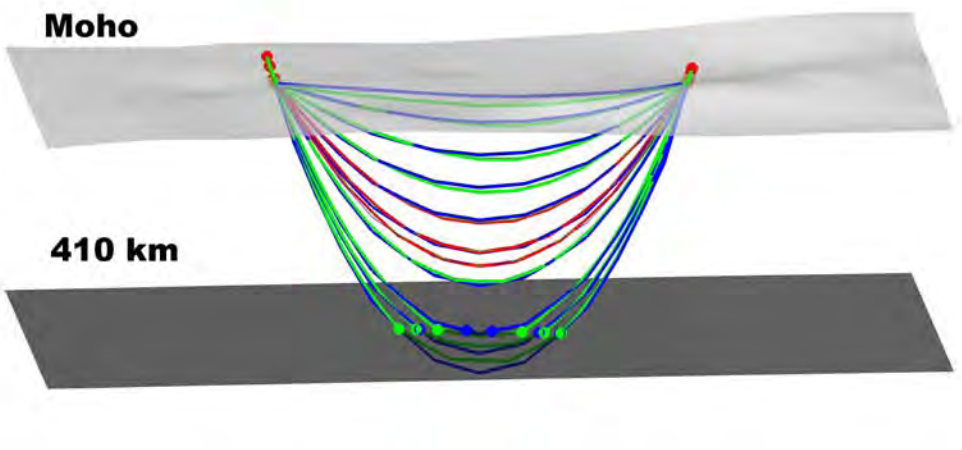

Figure 3. Example of a pseudo-bending/interface 3-D ray tracing approach for an 18° path. Initial path estimates (blue) are based on perturbations of the expected path for a 1-D Earth and a logical set of rules that define the possible paths for a given event-station pair. Two pseudo-bending iterations combined with enforced interface boundary conditions (Zhao et al. 1992) are performed to yield refined paths (green). All refined paths yielding a travel time within some tolerance of the minimum travel time provided by the set are further refined. Those paths yielding a travel time very near the minimum are kept (red) and form the basis of the sensitivity kernels used in the inversions. Note: the circles represent interface piercing points at all discontinuous boundaries along the paths. Only two such boundaries are shown (Moho and 410 km discontinuity).

In our approach, we initially create several crude ray path estimates based upon the 1-D ray path expectation. Each of the possible paths is iteratively perturbed within the 3-D media according to the pseudo-bending/interface technique (Zhao et al. 1992). Paths that are within some tolerance (we chose 1 second) of the minimum time are perturbed until convergence. The final possible paths are then defined as paths that generate the minimum time within a smaller time tolerance (we chose 0.2 seconds). These paths (Figure 3; red) form the basis for the sensitive kernel for a specific event/station pair and our inverse system of equations. A similar adaptation has recently been developed by Ballard et al. (2008b), in which the computational process was designed within a distributed parallel environment. Ballard et al. (2008b) demonstrated the ability to dramatically improve the efficiency of the technique,

thus providing support for the implementation of the approach for routine seismic event location. Moreover, our comparison of travel times computed through a finite difference technique has shown significant travel time disagreements with the more accurate 3-D ray tracing procedure that accounts for detailed undulations of discontinuous boundaries.

Inversion Technique and Synthetic Example

Traditional tomographic inversion approaches involve predefining a model space with a single set of parameters (nodes or constant-property blocks) that represent some part of the Earth. For a given set of seismic ray paths, sensitivity kernels are designed to represent travel time sensitivity to a number of these predefined model parameters. These sensitivities are collected into a matrix (**A**), and the residual travel times relative to some starting velocity model represent the data (***b***). Together, they form a forward system of equations **Ax=b**. In this linear system of equations, **x** is an unknown vector of slowness perturbations to be determined through an inversion routine. The inversion procedure is often unstable due to the mixed-determined nature of typical tomographic datasets. This requires some form of regularization such as damping (**D**) and/or smoothing (**S**) operators to stabilize the solution:

$$\begin{bmatrix} \mathbf{A} \\ w_d\mathbf{D} \\ w_s\mathbf{S} \end{bmatrix} \mathbf{x} = \begin{bmatrix} \mathbf{b} \\ \mathbf{0} \\ \mathbf{0} \end{bmatrix}$$

where w_d and w_s are damping and smoothing weights, respectively. For very ill-posed problems, determining the optimum weights is difficult and sometimes speculative. Mixing teleseismic and dense clusters of regional seismic information presents one such ill-posed problem in which we have an abundance of information in certain regions and a lack of information in other regions. Moreover, the standard tomographic technique requires the predefinition of a set of static model parameters, thereby defining the resolution level of the outcome model *a priori*.

The "progressive" inversion technique circumvents the need for predefining resolution scale and significantly reduces the need for regularization. The basic idea behind the approach is to solve for structure initially at lower resolutions before proceeding to finer detail. In doing so, long-wavelength regional trends are resolved first, which may be accomplished in regions with dense or sparse data coverage. Upon each step up in resolution, finer detail structures emerge from the regional trends only where it is necessary to explain the given set of observations. Therefore, data drive the resulting variable resolution scales rather than a predefinition of variable node densities and regularization operators. The technique is best described by the algorithm

$$\begin{aligned} &\mathbf{x}_1 = \mathbf{A}_1^{-1}\mathbf{b}_1 \\ &for\ i = 2 \ldots n \\ &\qquad \mathbf{b}_i = \mathbf{b}_{i-1} - \mathbf{A}_{i-1}\mathbf{x}_{i-1} \\ &\qquad \mathbf{x}_i = \mathbf{x}_{i-1} + \mathbf{A}_i^{-1}\mathbf{b}_i \\ &end \end{aligned}$$

In this algorithm, the subscripts denote the recursion level (or resolution level). The superscript "-1" refers to matrix inversion and the variables **A**, **x**, and **b** are the sensitivity kernels, slowness perturbation models, and residual data vectors, respectively. After each iteration, the travel time signals produced by the previous lower-resolution model is removed and the previous model is effectively used as the starting solution in the next stage. In the case of a tessellation-based model, $\mathbf{A}_1$ would correspond to sensitivity kernels defined on the starting object (i.e., the 1st-level

tessellation; in our case a tetrahexahedron), and $\mathbf{A}_2$ would correspond to sensitivities built upon the nodes defined by the 2nd-level tessellation (see Figure 1).

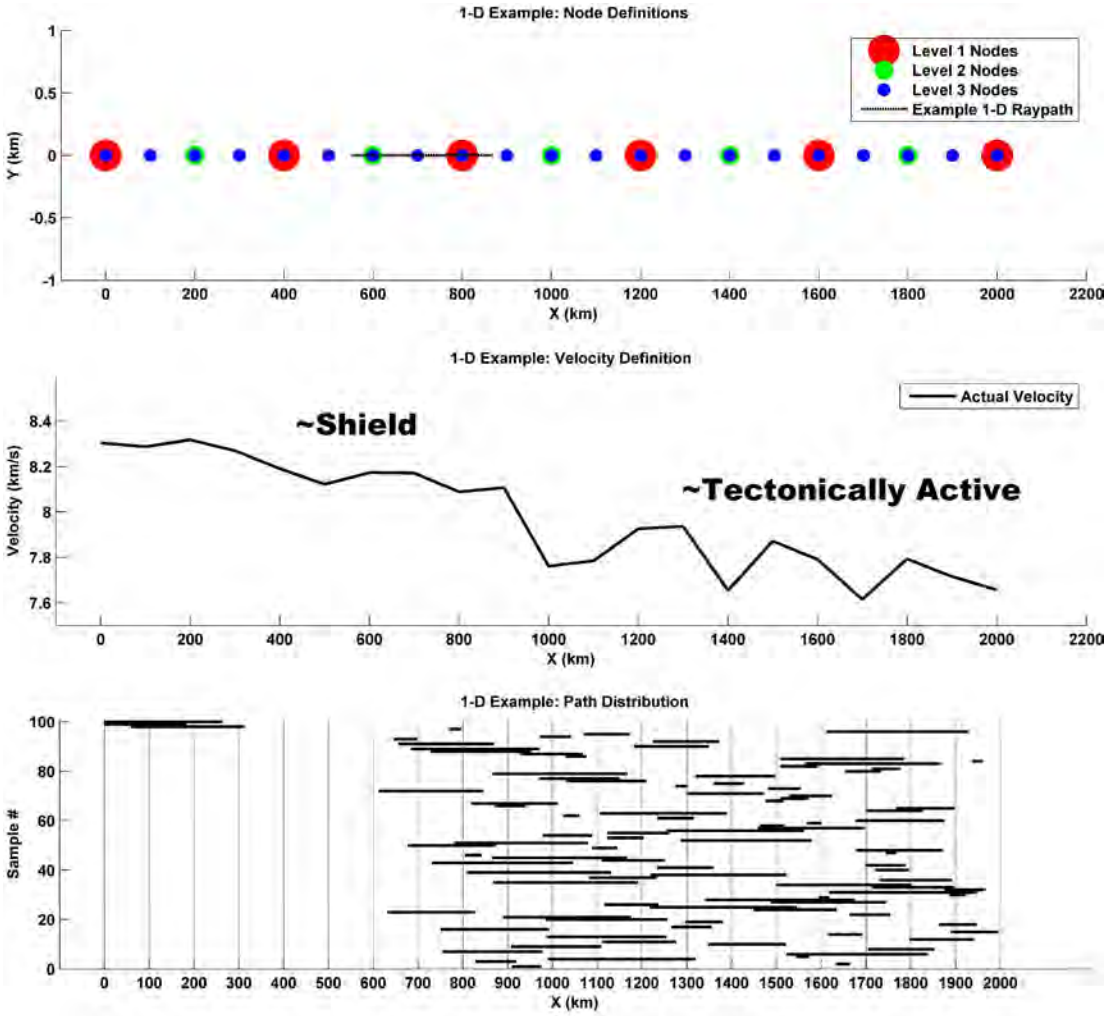

Figure 4. Synthetic inversion test case along a line with varying velocity. (Top) Node definitions at 3 recursion levels. (Middle) Node velocity definitions that are meant to simulate a high-velocity shield that is relatively homogeneous, and a lower-velocity tectonic region that is inhomogeneous. (Bottom) An example 1-D ray path distribution yielding a mixed determined set of linear equations. This arrangement of data is not uncommon to real tomographic cases in which few data may be available in an aseismic shield region and an abundance of data in a tectonic region.

To evaluate the behavior of this inversion technique, we devised a simple 1-D synthetic test case that mimics an ill-posed, mixed determined tomographic problem (Figure 4). For this synthetic test, we placed 6 equally spaced nodes along a line to represent the 1st recursion level (Figure 4, top). Points were then placed at the midpoints between the 1st level points. These points, along with the 1st level points, comprise of the 2nd recursion level. This recursion was repeated once again to give a total of 21 node points. For a single test, we then randomly generated 100 ray paths along the line of points while forcing a much larger number of paths to be to one end of the line to mimic a mixed-determined problem. Travel times were calculated on the basis of a known starting model, and a substantial amount of random noise (standard deviation of 0.5 seconds) was added to complete the setup of an ill-posed inversion problem. We randomly generated ray paths (and data) 100 times while regulating the system with a range of simple damping weights. For each realization of paths and noise, we inverted the resulting system of

equations using a simple inversion approach (directly inverted at the highest level) and the progressive inversion approach. It is concluded from these tests that the progressive inversion method is most capable of reproducing the known velocity model (Figure 5). In particular, the approach simultaneously resolves the long-wavelength regional trend, where the system is underdetermined, and the shorter-wavelength structures where there is sufficient data. With this synthetic test case design, it is difficult to accurately reproduce the known model with a simple inversion given the mixed determined nature of the problem and the realistic noise characteristics.

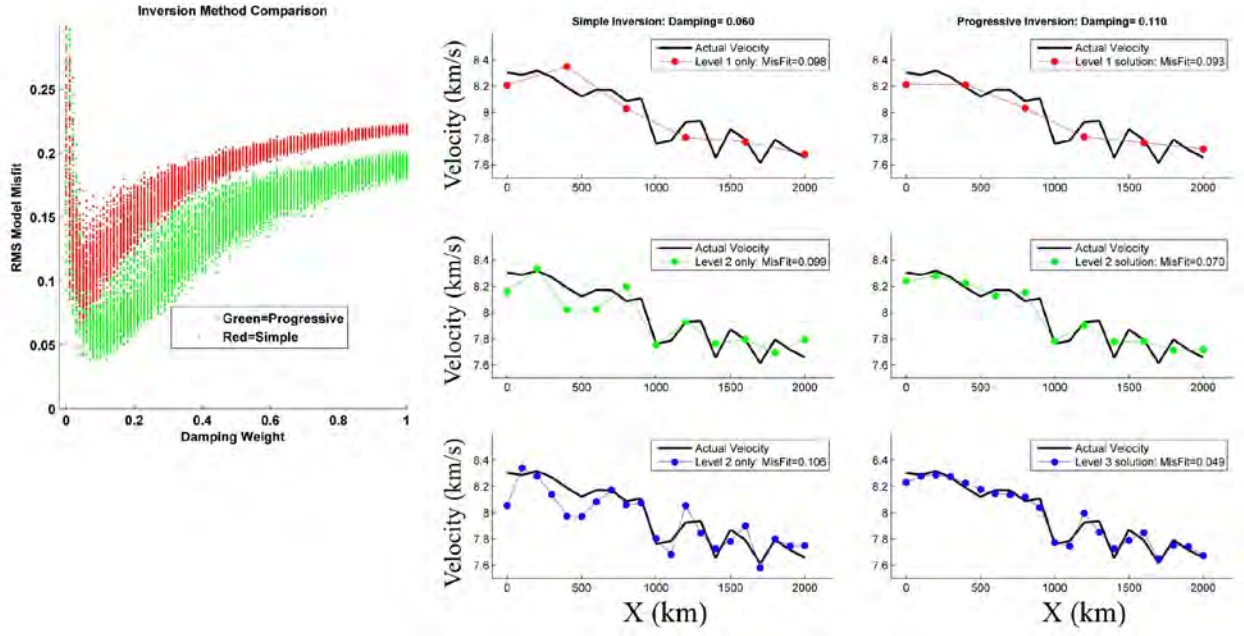

Figure 5. Comparison of simple and progressive inversion methods. (Left) RMS misfit to the known model for 10,100 data realizations and each inversion technique. The progressive inversion approach most often yields models most closely resembling the known solution. (Middle) A simple inversion solution for an arbitrary data realization with the optimum damping for that case. (Right) Progressive inversion solution for the same realization as the simple inversion case.

Application to Middle East *Pn* Data

The next phase in the evaluation of the progressive inversion technique is application to real data in a fully 3-D model space. We compiled *Pn* summary travel times from the Lawrence Livermore National Laboratory (LLNL) database for events occurring in the Middle East region and seismic stations located within 15° of the initial event locations (Figure 6). Event locations were revised through the probabilistic multiple event locater (BayesLoc) described in Myers et al. (2007, 2009), and the data were reduced to ~19,000 summary arrivals. Ray paths were computed using our 3-D ray tracing algorithms on the basis of the global 3-D model design discussed above. Because small variations in velocity can dramatically change the ray path, all 3-D ray paths that generated travel times within 0.2 seconds of the minimum path time for each event-station pair were used to construct the tomographic sensitivity kernel. This approach allows the whole tomographic dataset to help in the determination of the minimum-time ray. Sensitivity kernels were developed for nodes defined at tessellation Level 4 (~8° node spacing), Level 5 (~4° node spacing), Level 6 (~2° node spacing), and Level 7 (~1° node spacing).

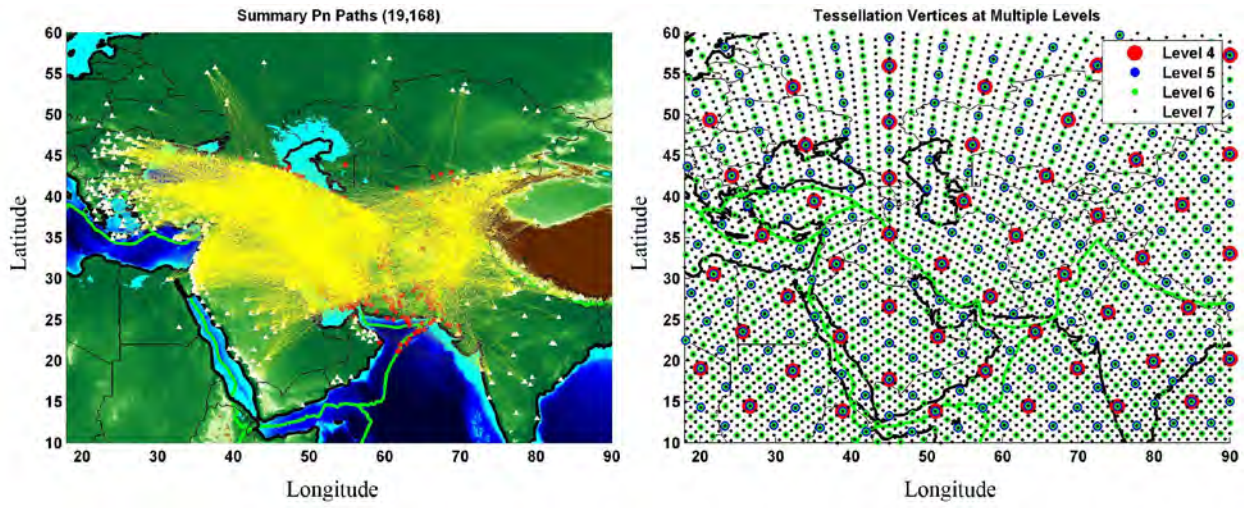

Figure 6. *Pn* paths and tessellation vertices in the Middle East region.

Tomographic inversions using the simple (direct inversion at the highest tessellation level) and progressive techniques were performed to image the shallow upper mantle beneath the Middle East and surrounding regions. Similar to the synthetic case, we performed the inversions with the iterative LSQR routine of Paige and Saunders (1982) considering a range of damping weights. It should be noted that smoothing constraints were not incorporated. Although the complex 3-D starting model was employed as the basis for computing the 3-D ray paths and sensitivity kernels, we chose to use an average model as the starting solution in order to best demonstrate the inversion procedure. Thus, we selected the average values within nodesets (such as the nodeset defining the *Pn* layer, etc.) as the values to perturb in 3-D.

The resulting *Pn* velocity structures and effects of damping weight are illustrated in Figure 7. At any given damping weight, the progressive inversion approach yields models that are more consistent with the data than is a simple inversion. There are multiple causes for this result, including the fact that the total number of LSQR iterations performed varies amongst the inversion techniques. More specifically, we performed 64 LSQR iterations at each progression. Therefore, the total number of iterations is 64*4 for the progressive approach, while 64*1 iterations were executed for the simple inversion. This evaluation is not entirely even; however, we find that increasing the number of total iterations for the simple inversion results in unreasonably rough models and marginal improvement to data fit.

The models selected for comparison (Figure 7) are very similar where there is an abundance of data (i.e., along the Zagros mountain chain). One of the major differences between the two solutions is the streaky behavior exhibited with the simple inversion where data are sparse and crossing ray paths are nonexistent (see Figure 6). On the other hand, the progressive approach produces long-wavelength structures in these regions and a smooth transition from these poorly sampled zones to the more detailed structures along the Zagros chain. This effect is consistent with our results from the synthetic 1-D case outlined in this report. Consequently, the progressive approach produces models that are multi-resolution without *a priori* declaration of node density variations. The approach also circumvents the requirement for smoothing constraints that would likely necessitate decisions regarding optimum smoothing levels and regional variations of smoothing kernels to achieve a similar result. In effect, the procedure allows the data rather than the modeler to drive the resolution level.

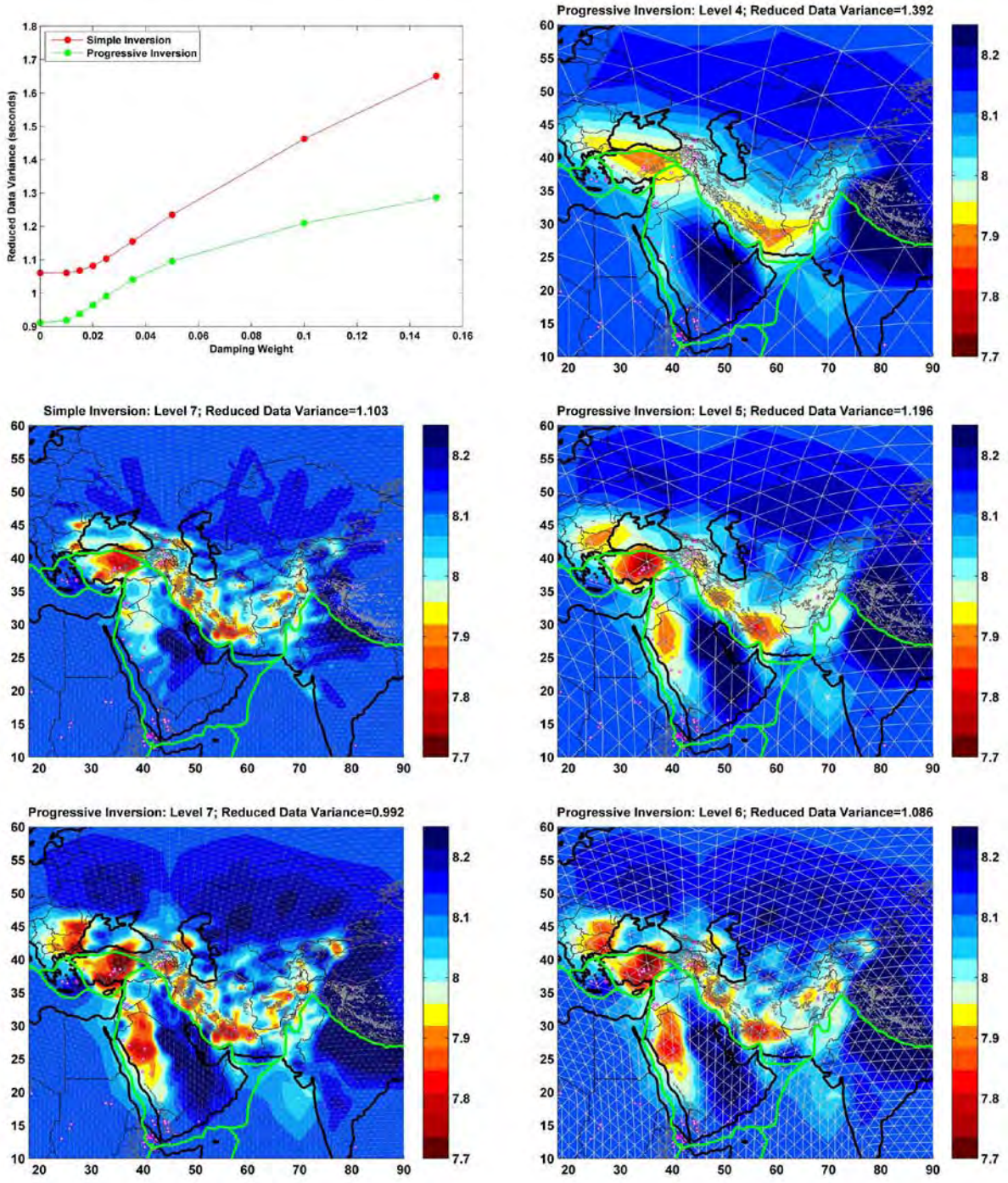

Figure 7. ***Pn*** **velocity structure in the Middle East and surrounding regions determined through a simple inversion and the progressive approach. (Left Column) Data misfit as a function of damping weight and solutions for each case with a damping weight of 0.025. The simple inversion exhibits streaks and spikes where data are limited, whereas the progressive inversion generates long-wavelength regional trends smoothly transitioning into zones with more-detailed information. (Right Column) The progressive inversion results at each stage of the progression.**

CONCLUSIONS AND RECOMMENDATIONS

The development of a self-consistent regional/global-scale 3-D model for the enhancement of event location capabilities requires advanced inversion techniques to adequately capture structure at multiple scales with complex configurations of seismic information. We developed an inversion approach based on the recursive nature of a tessellation model design that allows such models to be produced without pre-defining node densities or optimizing smoothing conditions. This approach is a viable technique for further development of global, multi-resolution 3-D seismic models.

REFERENCES

Ballard, S., J. Hipp, and C. Young (2008a). Robust, extensible representation of complex Earth models for use in seismological software systems, in *Proceedings of the 30th Monitoring Research Review: Ground-Based Nuclear Explosion Monitoring Technologies*, LA-UR-08-05261, Vol. 1, pp. 347–355.

Ballard, S., J. Hipp, C. Young, G. T. Barker, M. Chang (2008b). Implementation of a pseudo-bending seismic travel time calculator in a distributed parallel computing environment, in *Proceedings of the 30th Monitoring Research Review: Ground-Based Nuclear Explosion Monitoring Technologies*, LA-UR-08-05261, Vol. 1, pp. 338–346.

Ishii, M. and A. M. Dziewonski (2002). The innermost inner core of the Earth: Evidence for a change in anisotropic behavior at the radius of about 300 km, *PNAS* 99: 14026–14030.

Li, C., R. D. van der Hilst, E. R. Engdahl, and S. Burdick (2008). A new global model for P wave speed variations in Earth's mantle, *Geochem. Geophys. Geosystems* 9: 1–21.

Myers, S. C., G. Johannesson, and W. Hanley (2009). Incorporation of probabilistic seismic phase labels into a Bayesian multiple-event locator, *Geophys. J. Int*. 177: 193–204.

Myers, S. C., G. Johannesson, and W. Hanley, A Bayesian hierarchical method for multiple-event seismic location, *Geophys. J. Int*. 171: 1049–1063.

Paige, C. C. and M. A. Saunders (1982). LSQR: An algorithm for sparse linear equations and sparse least squares, *ACM Trans. Math. Soft*. 8: 43–71.

Um, J. and C. Thurber (1987). A fast algorithm for two-point seismic ray tracing, *Bull. Seis. Soc. America*, 77: 972–986.

Wang, Z. and F. A. Dahlen (1995). Spherical-spline paramterization of three-dimensional Earth, *Geophys. Res. Lett*. 22: 3099–3102.

Zhao, D., A. Hasegawa, and S. Horiuchi (1992). Tomographic imaging of P and S wave velocity structure beneath northeastern Japan, *J. Geophys. Res.* 97: B13, 19909–19928.

Zhao, D. and J. Lei (2004). Seismic ray path variations in a 3D global velocity model, *Phys. Earth. Planet. Int.* 141: 153–166.

SURFACE WAVE DISPERSION MEASUREMENTS AND TOMOGRAPHY FROM AMBIENT SEISMIC NOISE CORRELATION IN CHINA

Xiaodong Song[1], Zhen Xu[1], Xinlei Sun[1], Sihua Zheng[2], Yingjie Yang[3], and Michael H. Ritzwoller[3]

The University of Illinois at Urbana-Champaign[1], the Institute of Earthquake Science, China Earthquake Administration[2], and the University of Colorado at Boulder[3]

Sponsored by the Air Force Research Laboratory

Contract No. FA8718-07-C-0006
Proposal No. BAA07-24

ABSTRACT

We perform ambient noise tomography of China using the data from the China National Seismic Network and surrounding global and PASSCAL stations. The results so far are summarized below. (1) Dispersion measurements and tomography. For most of the station pairs, we retrieve good Rayleigh waveforms from ambient noise correlations using 18-months of continuous data at all distance ranges across the entire region (over 5000 km) and for periods from 70 s down to about 8 s. We obtain Rayleigh wave group and phase velocity dispersion measurements using a frequency-time analysis method and invert for Rayleigh dispersion maps for periods from 8 to 60 s. The dispersion maps correlate nicely with surface geology. (2) Error estimates using bootstrap analysis. A major feature of the ambient noise method is that the whole process is completely repeatable with different time segments, which make it possible to evaluate the uncertainties. We adopt a bootstrap method to quantify the errors in the Rayleigh wave group velocity dispersion measurements and the tomographic maps. Most of the pairs show similar dispersion curves between different runs and small standard deviations, indicating good data quality and convergence of the Green function. Group velocity at long period end generally has a larger error, which is consistent with the notion that the long period needs longer time to converge. The best retrieved periods are from 10 to 30 s with the optimal period of around 15 to 20 s.

Pairs with large errors do not depend on the orientations of the paths or the locations of the stations. Rather, they are associated with a few stations with large average standard errors. The likely causes are missing data and poor instrumentation (or site conditions). Where ray coverage is good, there is only subtle difference in tomography maps between different runs, suggesting that our solution is very stable. (3) 3D structure. We invert the Rayleigh group and phase dispersion maps for 3D shear-wave velocity structure. The 3D model shows some remarkable features, including slow sedimentary layers of all the major basins in China at the shallow depth, Moho depth variation, fast (strong) mid-lower crust and mantle lithosphere in major basins surrounding the Tibetan Plateau (TP) (Tarim, Ordos, and Sichuan). These strong blocks thus seem to play an important role in confining the deformation of the TP to be a triangular shape. The Moho change from plateau to the marginal basins (Tarim and Sichuan) is rapid, corresponding to the rapid change of the surface topography. In northwest TP, slow anomalies extend from shallow crust to mantle lithosphere (at least 100 km). Widespread, prominent low-velocity zone is observed in mid-crust in much of the TP, but not in the margin areas, consistent with the crustal channel flow model.

OBJECTIVES

The overall objective of this project is to obtain surface wave dispersion measurements from ambient seismic noise correlations of the Chinese backbone stations (CNSN) and use these measurements to produce surface wave dispersion maps of China. More specifically, the objectives are: (1) to obtain dispersion measurements between CNSN stations; (2) to obtain dispersion measurements between CNSN and FDSN, regional networks, and temporary stations; (3) to obtain dispersion maps from these dispersion measurements.

RESEARCH ACCOMPLISHED

We reported the basic metholodgy, data sets, and initial results in the last year's review (Song et al., 2008), part of which has also been published in Zheng et al. (2008). Below is an update to that report. In this report, we nearly double the amount of the data and the number of stations used, and as a result, we provide new dispersion measurements, dispersion maps, and 3D velocity model. We have also conducted resolution tests of our 3D inversion.

Method and Data

Theoretical and laboratory studies have shown that the Green functions of a structure can be obtained from the cross-correlation of diffuse wavefields (e.g., Lobkis and Weaver, 2001; Campillo, 2006). The basic idea is that linear waves preserve, regardless of scattering, a residual coherence that can be stacked and amplified to extract coherent information between receivers. The idea has found rapid applications in seismology. In particular, surface waves have been found to be most easily retrievable from the cross-correlations of seismic coda (Campillo and Paul, 2003) or ambient noise (Shapiro et al., 2005; Sabra et al., 2005) between two stations. Both Rayleigh waves and Love waves can be retrieved. The new type of data has rapidly been used for tomographic mapping at regional or local scales and on continental scales. Most studies have focused on Rayleigh wave group velocity tomography from ambient noise. However, the method is applicable to Love waves and phase velocity measurements.

Ambient noise tomography (ANT) overcomes several important limitations of conventional methods based on earthquakes; i.e., uneven distribution of earthquake sources, uncertainty in earthquake location, and attenuation of short-period surface waves. Thus, the method is particularly useful for surface-wave path calibration and for tomographic mapping in aseismic regions especially at short periods (below 30 s). In addition, the method can be applied any time without the need to wait for earthquakes and is completely repeatable, allowing the quantification of errors.

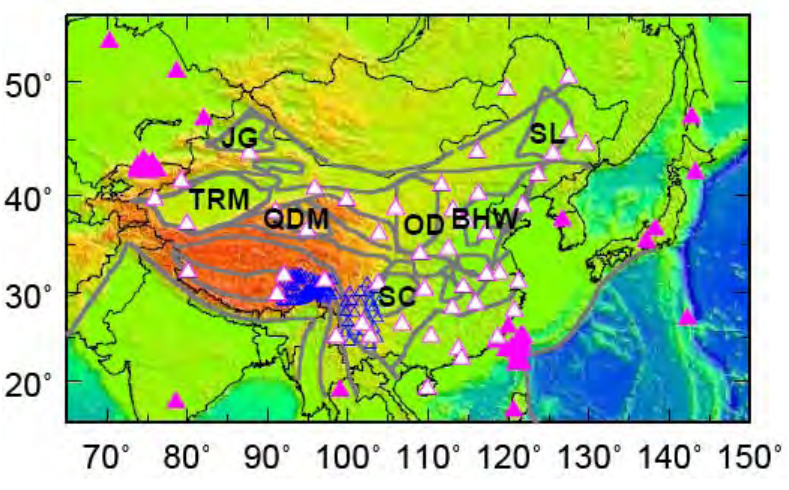

Figure 1. Distribution of seismic stations used in this study, including China National Seismic Network (CNSN) stations (solid white triangles), global and regional stations in the surrounding regions (solid pink triangles), and PASSCAL stations (open blue triangle). We have also used some 175 temporary stations in western Tibet from HiClimb not included in this map. Plotted also are major tectonic boundaries and major basins. The basins (labeled) include: Tarim (TRM), Junggar (JG), Qaidam (QD), Sichuan (SC), Ordos (OD), Bohai Wan (BHW), and Songliao (SL) Basins.

Our main stations are from the China National Seismic Network (CNSN) (Figure 1). The CNSN is the national backbone network, established around 2000, with a relatively uniform distribution across the continental China. To increase data coverage, we also include permanent and temporary stations in the region. We use 12 or more months of continuous data from 47 CNSN stations and 39 stations in surrounding regions and some 270 PASSCAL stations in the TP. All stations are broadband. The bandwidths of the CNSN stations are from 20 Hz to at least 120 s. We use the data processing and imaging techniques described in great detail by Bensen et al. (2007). Below is a brief outline of our data procedure. First, we obtain the empirical Green function (EGF) from ambient noise cross-correlation. Continuous data are pre-processed before correlation and stacking, which includes clock synchronization, removal of instrument response, time-domain filtering, temporal normalization and spectral whitening. The purpose is to reduce the influence of earthquake signals and instrument irregularities and to enhance the strength and bandwidth of the ambient noise correlations. Second, if the signal-to-noise ratio (SNR) is sufficiently large, Rayleigh wave group speeds are measured using a frequency-time analysis (Ritzwoller and Levshin, 1998). Finally, the inter-station dispersion measurements are used to invert for the Rayleigh wave group velocity maps, in exactly the same way as earthquake-based measurements.

Dispersion Measurements and Tomography

For most of the station pairs, we are able to retrieve good Rayleigh wave signals from the ambient noise correlations (Zheng et al., 2008). Figure 2 shows typical examples of EGFs and group velocity measurements of Rayleigh waves retrieved from ambient noise correlations. Our cross-correlations show clear arrivals at different settings (near the coast or well into the continental interior) and at both relatively low frequencies (20-50 s) and high frequencies (5-20 s). The EGFs can be retrieved over the entire region (at distances of over 5000 km) (Figure 2a).

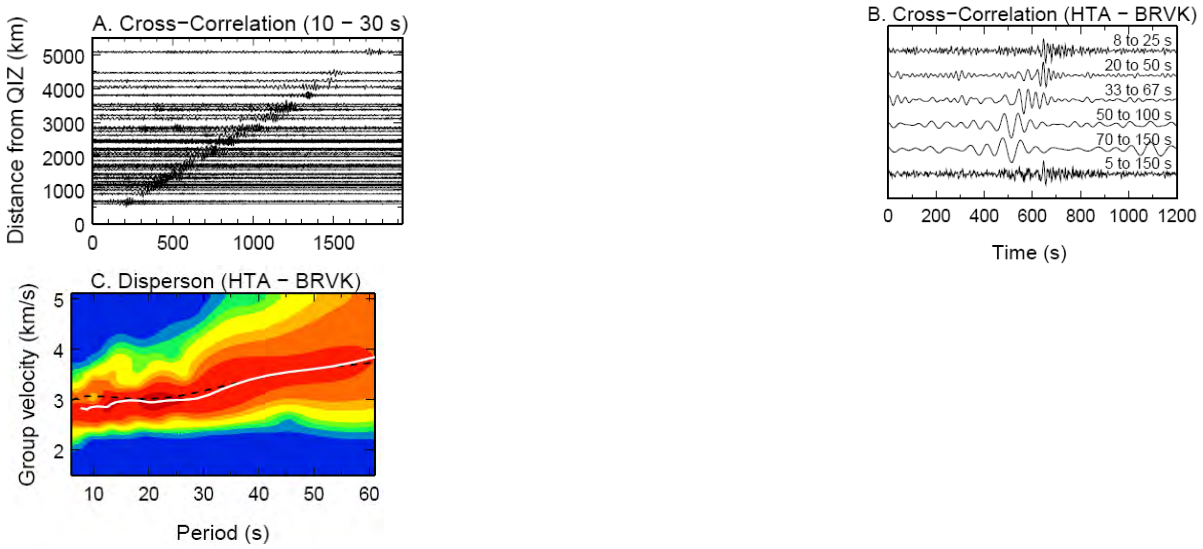

Figure 2. **Example of Rayleigh wave EGFs and dispersion measurements obtained from ambient noise correlations. (a) Symmetric component of the correlations between station QIZ (in Hainan Province, China) and other stations. The traces are band-pass filtered at relatively short periods (10-30 s). (b) EGFs filtered in different frequency bands. Long-period surface waves are clearly faster than short-period ones. The path is between HTA (bordering Tarim in the south) and BRVK (Borovoye, Kazakhstan). (c) Frequency-time analysis (Ritzwoller and Levshin, 1998) used to retrieve Rayleigh wave group velocity dispersion curve (white) for the HTA-BRVK path. The black dashed curve is the prediction from the 3D global shear velocity model of Shapiro and Ritzwoller (2002), which is used for phase-matched filtering in the data analysis and for comparison with measurements**.

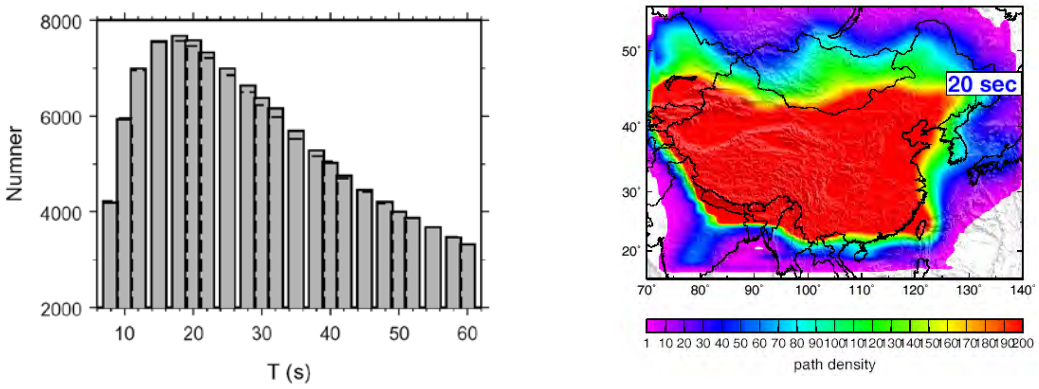

Figure 3. **Distribution of Rayleigh group (solid) and phase (dashed) dispersion measurements for different periods (left) and ray density map for Rayleigh group dispersion measurements at the period of 20 s (right). The ray density is the number of rays inside 1 degree by 1 degree cell. The rays are station pairs for which dispersion measurements have been obtained. The ray coverage is best for periods 10 to 30 s. Coverages for shorter or longer periods deteriorate, but the spatial coverage patterns remain similar.**

We measured group velocity dispersion curves (Figure 2c) for station pairs with Rayleigh wave SNR>10. The SNR is defined as the ratio of the peak amplitude of the Rayleigh wave to the root-mean-square value of the background. The measurement is very stable. Clear dispersion can be commonly observed directly from the EGFs (**Figure 2b**). We found that the group velocity measurements can extend to periods of 10 s or shorter even for station pairs that are separated over thousands of kilometers. The group velocities of the HTA-BRVK path (**Figure 2b,c**), which samples the Tarim Basin, agree with a global 3D earthquake-based model (Shapiro and Ritzwoller, 2002) at longer periods but differ significantly at short periods (below 30 s). The slow group velocities at short periods are caused by the thick sediments of the Tarim Basin (see discussion below).

We have obtained dispersion measurements with SNR>10 for periods 8 s to 70 s (Figure 3, left). The best observed frequency band is 10 to 30 s with a retrieval rate of 50 to 80% of all the possible pairs. The ray paths provide good coverage of almost the entire Chinese continent except at the margins (Figure 3, right).

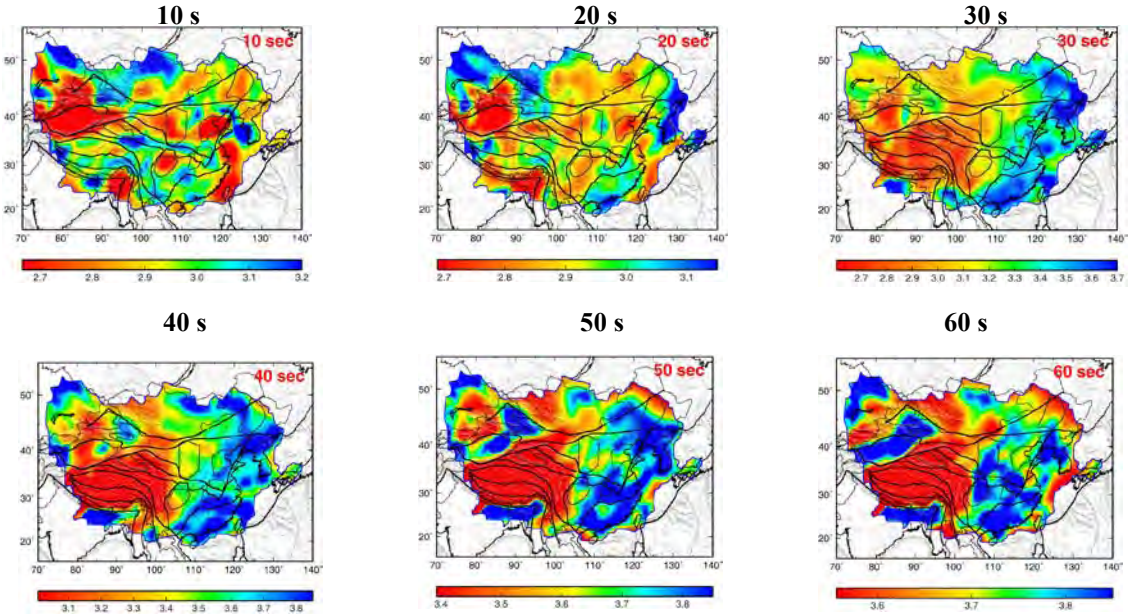

Figure 4. **Rayleigh wave group velocities obtained in this study. Shown are the maps at periods 10 to 60 s, respectively. Plotted in the background are major block boundaries and basin outlines (Figure 1).**

The ray coverage of our dispersion measurements is sufficient for us to invert for Rayleigh wave group velocity maps at periods from 8 s to 60 s (Figure 4). The results show remarkable features that correlate with large-scale geological structures of China (discussed in more details in Zheng et al., 2008). Major basins are well delineated with low velocities at short periods (8 to 20 s), including Bohai-Wan Basin (North China Basin), Sichuan Basin, Qaidam Basin, and Tarim Basin. The stable Yangtz Craton also shows up well with high velocities. At longer periods (25-50 s), the group velocity maps display striking bimodal distribution with high velocity in the east and low velocity in the west, which corresponds very well with the thinner crust in the east and much thicker crust in the west (e.g. Liang et al., 2004) as in global reference model CRUST 2.0 (http://mahi.ucsd.edu/Gabi/rem.html). The NNE-SSW trending boundary between fast and slow velocities (around longitude 108^{o}E) coincides with the sharp topographic change and with the well-known Gravity Lineation.

3D shear-wave Structure

We use the Rayleigh wave group and phase velocity maps (8-60 s) obtained from the ANT to invert for 3D S structure. The inversion is done using programs by Bob Herrmann of St. Louis U. Resolution tests suggest that a 4x4 degree pattern can be resolved in most region of China (Figure 5). The inversion results show some remarkable features for continental China and in particular the Tibetan Plateau (TP) (Figure 6), including slow sedimentary layers of all the major basins at the shallow depth, striking east-west contrasts in Moho depth variation and lithosphere thickness, fast (strong) mid-lower crust and mantle lithosphere in major basins surrounding the TP (Tarim, Ordos, and Sichuan) (in contrast, Qaidam Basin does not have such a "deep root"). These strong blocks thus seem to play an important role in confining the deformation of the TP to be a triangular shape. The Moho change from plateau to the marginal basins (Tarim and Sichuan) is rapid, corresponding to the rapid change of the surface topography. . In northwest TP, slow anomalies extend from shallow crust to mantle lithosphere (at least 100 km).

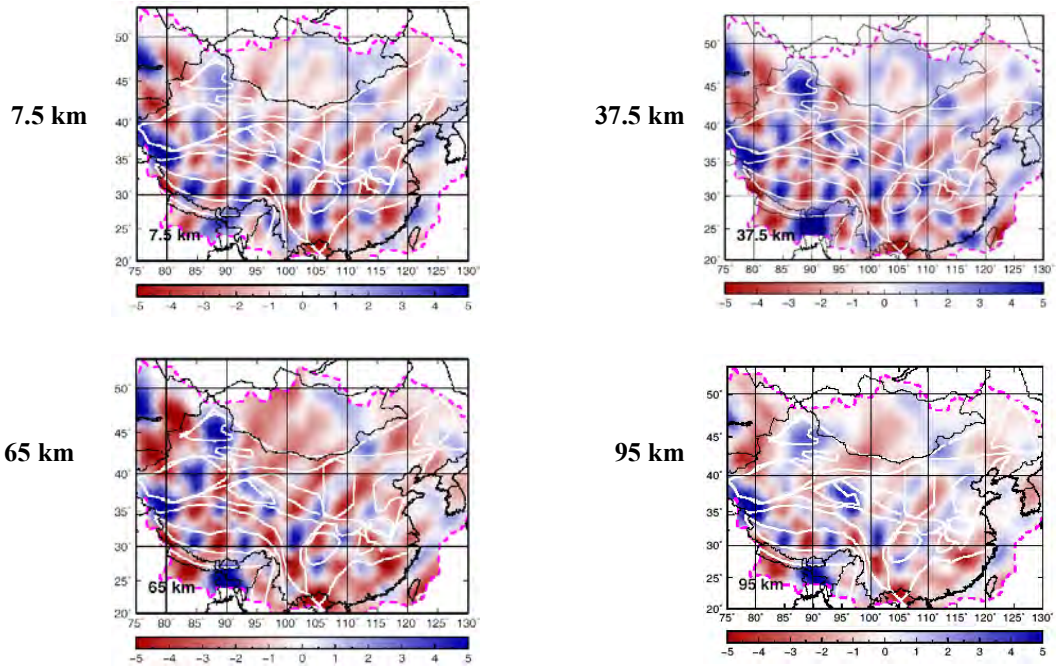

Figure 5. Results of a checker-board test. The input is alternating pattern of 4x4 degrees with S velocity perturbations of 5%.

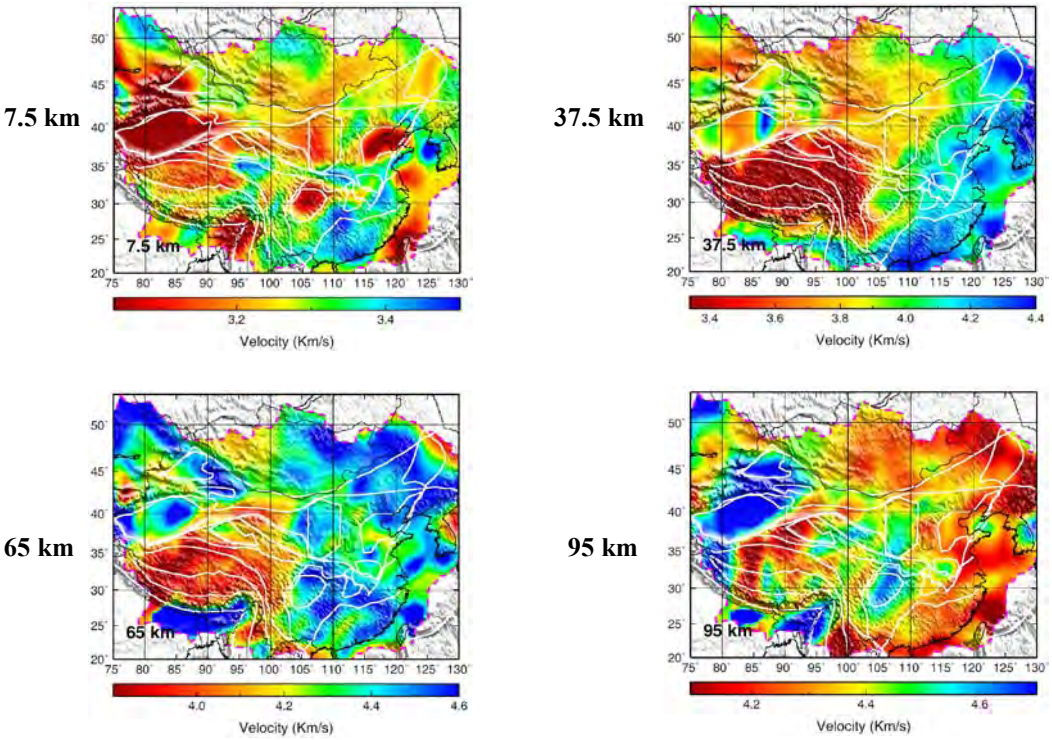

Figure 6. **Inversion results of S velocity at 7.5, 37.5, 65, and 95 km.**

Extremely slow *S* velocities mark the mid-crust in much of the central, eastern, and southeastern TP. These slow velocities are widespread and often (but not always) connected in a laminar form. They seem to reach to the surface at certain localities in western, southern, northern, and southeastern margins. The mid/lower crust low velocity zone provides support for the channel flow model that has been proposed for the outward growth and uplift of the TP (e.g. Clark and Royden, 2000) and for the extrusion of crustal materials to the surface (Beaumont et al., 2001).

We are exploring the S velocity model we have derived on its characters and tectonic implications. Because of the apparent correlation of the S velocities and crustal thickness, one useful exercise is to derive a crustal thickness model based on the Vs model. If we obtain the Vs that corresponds to the depth of the Moho as defined by the reference model CRUST 2.0, we find that the average of the S velocities is nearly constant (Figure 7). We thus use the linear trend as a calibration of using the *S* velocity to find the true Moho (The linear trend has nearly the same Vs value with only a small positive slope). Thus to find the true Moho for any given point, we follow the steps: (1) Find the reference Moho depth from CRUST 2.0, (2) find the reference Vs from the linear trend, and (3) find the depth that corresponds to the reference Vs (and close to the CRUST 2.0 depth). The procedure ensures that the newly derived Moho map (Figure 8, left) is similar to the CRUST 2.0 (Figure 8, right) overall, but the new map shows detailed variations that correspond to variation in *S* velocities.

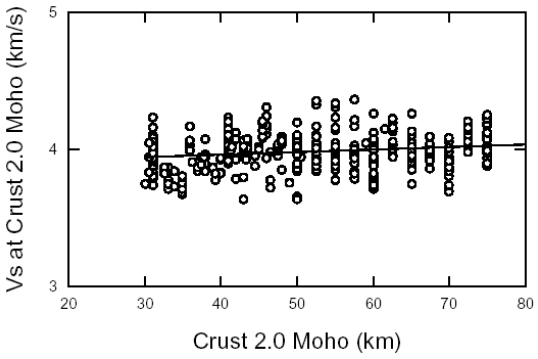

Figure 7. *S* velocities at the depth of CRUST 2.0 Moho that are retrieved from our *S* model.

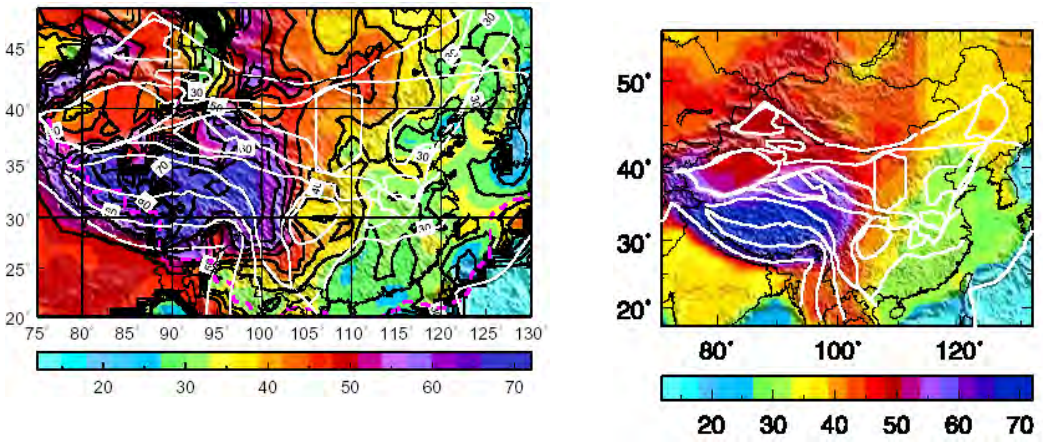

Figure 8. Crustal thickness map derived from the *S* velocity model (left), in comparison to reference CRUST 2.0 model (right). Note the map scales are different.

Validation and Error Analyses of Dispersion Measurements and Tomography

We have examined the errors of our dispersion measurements and tomography in a variety of ways (see a summary by Zheng et al., 2008). The methods include the following. (1) Validation with surface observables. Comparison of the tomographic maps with the geological features discussed above provides an important initial validation of the ambient noise tomography (ANT) methodology; i.e., the method provides models of group wave speeds that are consistent with well-known geological features and other geophysical observations. (2) Direct validation with surface wave generated by an earthquake along the same path (e.g., Shapiro et al., 2005; Bensen et al., 2007). (3) Comparing EGFs obtained from ambient noise and that from seismic coda (Yao et al., 2006). (4) Temporal stability: Comparing the EGFs from the data observed at different time periods (e.g., different months) (Shapiro et al., 2005; Yao et al., 2006; Bensen et al., 2007). Furthermore, because the principal ambient noise sources are believed to come from the oceans, which are seasonal, the consistency of the correlations from different seasons gives a measure of the stability and error of the EGFs. (5) Spatial consistency: Comparing station-pairs along similar paths (Bensen et al., 2007). The EGFs between a far-away station to two or more stations that are close to one another should be similar as the paths sample similar structure. We have examined temporal and spatial consistency of our dispersion measurements and found that they are very consistent whenever the SNRs of the EGFs are high (see examples in Zheng et al., 2008). (6) Model-based validation: comparing predictions with earthquake-based measurements (Figure 9). (7) Bootstrap analyses (Xu et al., 2008) (see below).

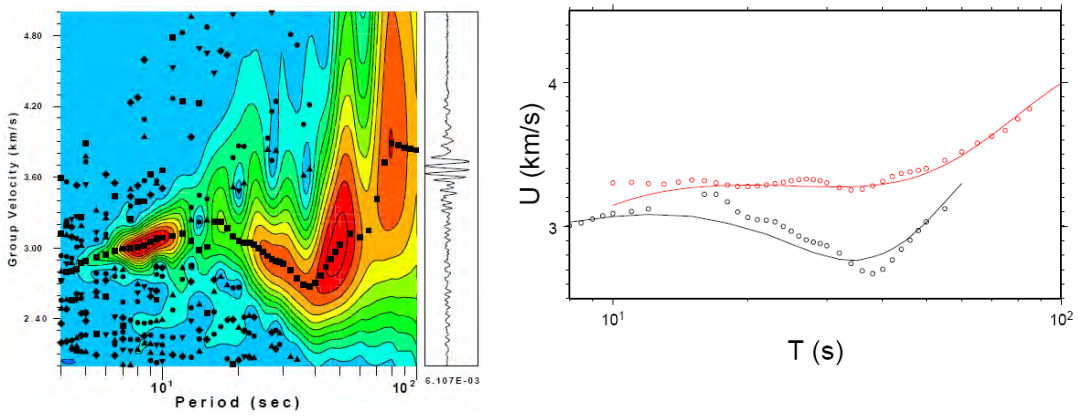

Figure 9. (Left) Retrieval of Rayleigh wave group velocity of a 2008 Wenchuan aftershock at Lhasa station. (Right) Comparison of observed (dots) and predicted group velocities of Rayleigh (black) and Love (red) waves along the path. Lines are predictions for the ambient noise tomographic model. The retrieval of the surface wave EGF relies on the stacking of cross correlation of continuous data for long enough time series. The total length of data required for the Green function to converge is empirical and highly frequency

dependent: generally the longer the period the longer the time is needed. Furthermore, the ambient noise source and station site conditions (including instrumentation stability) are uncertain. We have recently proposed a bootstrap method to quantify the errors in Rayleigh group velocity dispersion measurements and group velocity tomographic maps, based on the complete repeatability of the ambient noise correlation and tomography process (Xu et al., 2008).

Our bootstrap analysis follows the following steps. 1) We obtain the EGF using one month of data for each of the 18 months. 2) We select 18 random months among the months that we have data. The selection process is a random sampling with replacement as in any boostrap methods. We then obtain the statck EGF using the EGFs of these months for each and every station pair. Using these stacked GFs, we measure dispersion curves for all station pairs and construct tomographic maps as usual. 3) We repeat the step 2 for 50 times. 4) We obtain the mean and the standard deviation of the dispersion curve for each station pair from the 50 dispersion curves obtained in step 3. We regard the mean and the standard deviation as the group velocity estimate and the associated error. 5) Similarly, we obtain the standard errors of our tomographic models using the models obtained from the 50 iterations described in steps 2 and 3.

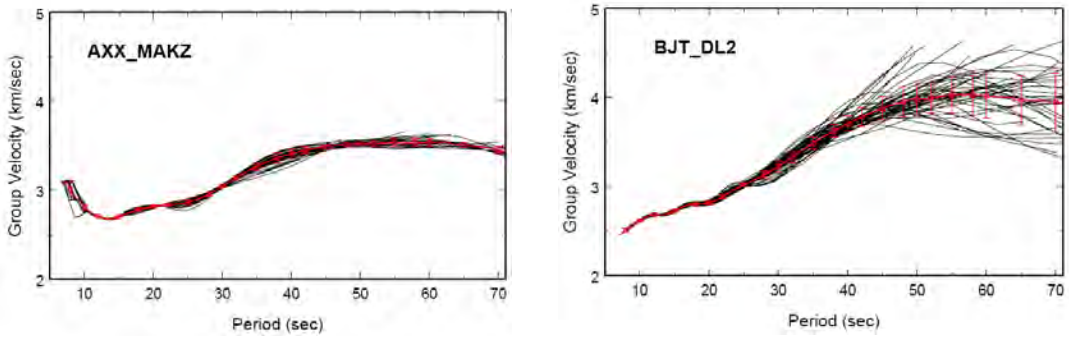

Figure 10. Examples of error estimates of dispersion curves from bootstrap with a good pair (left) and a bad pair (right). Black curves are dispersion measurements for all the 50 runs. Red curves are the mean values. Error bars at different periods indicate the standard deviations. For the good pair (AXX-MAKZ), dispersion curves for different runs are very close to each other. The standard deviations are small throughout the whole periods. For the bad pair (BJT-DL2), dispersion curves spread out at long periods. The large standard deviations at long periods indicate large errors in the measurements.

Figure 10 shows two examples of error estimates of the dispersion curves using the boostrap method. Most pairs show similar dispersion curves between different runs and small standard deviation (generally less than 0.1 km/s), indicating good data quality and convergence of the Green function. Group velocity at a long period generally has a larger error, which is consistent with the notion that the long period needs longer time to converge. There is only subtle difference in tomography maps between different runs, suggesting that our solution is very stable. Standard deviation in the region with good ray coverage is small (generally less than 0.1 km/s), indicating a stable and reliable solution in well-sampled regions. The Rayleigh waves are best retrieved from 10 to 30 s with the best periods around 15 to 20 s. A pitfall of the model error estimates is that the standard deviations in the regions with poor ray coverage (at the margins) are also small, due to regularization in the tomographic inversion process. Our tomographic inversion includes regularization using a prior model. Thus the inversions for the poorly sampled regions from different runs all converge to the prior model, giving an artifact of small errors.

We found that the pairs with large variations do not have a preferred orientation or a particular geographical location. Rather, these pairs are generally associated with a few stations with large standard deviations. We derive average standard deviation of the surface wave velocity for each station at each period by averaging over all the pairs associated with that station. The exercises provide a way to identify and sort out good and poor stations efficiently.

CONCLUSIONS AND RECOMMENDATIONS

We have obtained Rayleigh dispersion curves for some 30,000 station pairs at periods of 8 to 70 s from ambient noise correlation using 12 or more months of continuous data from CNSN, global and regional permanent, and PASSCAL temporary stations. The best observed frequency band is 10 to 30 s with a retrieval rate of 50 to 80% of the station-pairs. We constructed new tomographic maps of China for periods from 8 to 60 s, which correlate with surface geology. Temporal and spatial analyses suggest that the dispersion measurements and tompography are robust. We proposed a bootstrap method, which allowed us to quantify the errors of each of our dispersion curves and the errors of the dispersion maps. For best periods (10–30 s) and most regions, the Rayleigh waves have standard errors of less than 0.1 km/s. We have inverted the dispersion maps for 3D S model (down to about 100 km). The models show remarkable details of the crust and uppermost mantle, including major blocks, rapid changes in Moho, mid/lower crust low velocities in TP, and variations in lithosphere velocities. The resolution is about 4x4 degrees.

REFERENCES

Beaumont, C., R. A. Jamieson, M. H. Nguyen, and B. Lee (2001). Himalayan tectonics explained by extrusion of a low-viscosity crustal channel coupled to focused surface denudation, *Nature* 414: 738–742.

Benson, G., M. Ritzwoller, M. Barmin, A. L. Levshin, F. Lin, M. P. Moschetti, N. M. Shapiro, and Y. Yang (2007). Processing seismic ambient noise data to obtain reliable broad-band surface wave dispersion measurements, *Geophys. J. Int.* 169: (3), 1239–1260.

Campillo, M. (2006). Phase and correlation in random seismic fields and the reconstruction of the Green function, *Pure Appl. Geophys.* 163: 475–502.

Campillo M. and A. Paul (2003). Long-range correlations in the diffuse seismic coda, *Science* 299: 547–549.

Clark, M. K., and L. H. Royden (2000). Topographic ooze: Building the eastern margin of Tibet by lower crustal flow, *Geology* 28: 703–706.

Liang C., X. D. Song, and J. L. Huang (2004). Tomographic Inversion of Pn Travel-Times in China, *J. Geophys. Res*. 109: B11304, doi. 10.1029/2003JB002789.

Lobkis, O. I., and R. L. Weaver (2001). On the emergence of the Greens function in the correlations of a diffuse field, *J. Acoust. Soc. Am.* 110: 3011–3017.

Ritzwoller, M.H. and A. L. Levshin (1998). Eurasian surface wave tomography: Group velocities, *J. Geophys. Res.* 103: 4839–4878 .

Sabra, K.G., P. Gerstoft, P. Roux, W. A. Kuperman, and M. C. Fehler (2005). Surface wave tomography from microseisms in Southern California, *Geophys. Res. Lett.* 32: doi:10.1029/2005GL023155.

Shapiro, N. M., M. Campillo, L. Stehly, and M. H. Ritzwoller (2005). High resolution surface wave tomography from ambient seismic noise, *Science* 307: (5715), 1615–1618.

Shapiro, N. M. and M. H. Ritzwoller (2002). Monte-Carlo inversion for a global shear velocity model of the crust and upper mantle, *Geophys. J. Int.* 151: 88–105.

Song, X. D., X. L. Sun, S. H. Zheng, Z. J. Xu, M. Ritzwoller, and Y. J. Yang (2008). Surface Wave Dispersion Measurements and Tomography from Ambient Seismic Noise in China, in *Proceedings of the 30th Monitoring Research Review: Ground-Based Nuclear Explosion Monitoring Technologies*, LA-UR-08-05261, Vol. 1, pp. 268–278.

Xu, Z., X. D. Song, S. H. Zheng, M. H. Ritzwoller (2008). Bootstrap analysis on surface wave dispersion and tomography derived from ambient noise cross-correlation, *IRIS Workshop*, Skamania Lodge, Stevenson, WA.Zheng, S. H., X. L. Sun, X. D. Song, Y. J. Yang, and M. H. Ritzwoller (2008). Surface wave tomography of China from ambient seismic noise correlation, *Geochem. Geophys. Geosyst.* 9: Q05020, doi:10.1029/2008GC001981.

SEISMO-ACOUSTIC GENERATION BY EARTHQUAKES AND EXPLOSIONS AND NEAR-REGIONAL PROPAGATION

Brian W. Stump[1], Relu Burlacu[2], Christopher T. Hayward[1], Tae-Sung Kim[1, 3], Stephen J. Arrowsmith[4], Rongmao Zhou[4] and Kristine Pankow[2]

Southern Methodist University[1], University of Utah Seismograph Stations[2], Korea Institute of Geoscience and Mineral Resources[3], and Los Alamos National Laboratory[4]

Sponsored by the Air Force Research Laboratory

Award No. FA8718-05-C-00020
Proposal No. BAA08-65

ABSTRACT

Seismo-acoustic measurements provide an opportunity to quantify natural and man-made sources that are at or near the Earth's surface. We have operated three acoustic arrays collocated with seismometers from the University of Utah Seismograph Stations (BGU, EPU, NOQ). We report on progress in three separate areas of research related to these seismo-acoustic databases. The first topic investigates seismo-acoustic signals from the Wells, Nevada earthquake that occurred on February 21, 2008 at 14:16:02 UTC (M_W 6.0). The detailed research and interpretation of this event has been conducted under a separate effort (Arrowsmith et al., 2009c, these Proceedings). The focus in this work is on the data acquisition and highlighting the sources of seismo-acoustic signals that can be observed on regional seismo-acoustic arrays. This event was well recorded by many seismic stations, including the EarthScope Transportable Array (TA) stations, and was also recorded by three infrasonic arrays in Utah (BGU, EPU, NOQ), one in Nevada (NVIAR), and one in Wyoming (PDIAR). The waveforms recorded from the Wells sequence (main event and aftershocks) at the five infrasonic arrays are characterized by complex signals that correspond to: (1) *P* and *S* arrivals, a result of the coupling-to-air of the seismic waves that traveled to the vicinity of the infrasonic stations (local infrasound); (2) a secondary source of infrasound between the source and receiver; and (3) epicentral infrasound (acoustic energy that was generated by the ground motion at the epicenter and traveled through the atmosphere to the arrays at air sound speed). The second area of work focuses on characterizing acoustic to seismic coupling. In August 2007, infrasound microphones were added at Earthscope stations P13A, M13A, M14A, and N12A as part of an experiment to record 40,000 lb explosions at the Utah Test and Training Range on Hill Air Force Base (AFB). These multiple observations provide insight into the infrasound-to-seismic transfer functions during this time. Thirteen seismic/infrasound stations in the University of Utah Regional Seismic Network provide additional observations on infrasound-to-seismic coupling. Strong infrasound-to-seismic coupling is observed at most stations and in most cases can be described with a few term pole-zero empirical transfer function. At some stations, additional infrasound-to-seismic converted signals were observed at significant distances from the site. These converted signals seem to be site dependent but may also be source dependent. Understanding of where the coupling occurs is useful for characterizing infrasound propagation and should provide information about the very shallow velocity structure in the region. Finally, additional work has been completed in assessing infrasound wave propagation inside of the "zone of silence" (McKenna, 2005). Data from the August 2007 experiment have been further analyzed including the use of atmospheric data from rawinsondes. Based on the data analysis, the infrasonic arrivals were classified into two groups: the arrivals at the distance less than 100 km (local arrivals) and those between 150 and 210 km (regional arrivals). Group velocities at local distances are near the speed of sound at the surface, indicative of guided phases along this boundary, while those at regional distances are greater, indicative of turning rays from the stratosphere or thermosphere. Parabolic equation (PE) modeling based on atmospheric models from the rawinsondes is used to explore the trapped infrasonic wave propagation. The spatial and temporal variability of these models is quantified. The seismic stations deployed in NE China as part of this contract were removed in 2008. Analysis of these seismic data continues. Shear wave velocities beneath the Yanqing-Huailai Basin were estimated from the joint inversion of surface wave phase velocities and teleseismic receiver functions. The resulting models suggest low-velocity basin sediments to 2 km followed by a positive velocity gradient to 15 km, with shear wave velocity increasing from 2.0 to 3.55 km/sec. The total crustal thickness is 38 to 42 km with a smooth Moho transition to an upper mantle shear velocity of 4.3 km/sec. We are continuing the joint inversion study for crustal shear velocity structure in the second focus area, Haicheng, NE China.

OBJECTIVES

The primary goal of the collaborative study between Southern Methodist University and the Institute of Geophysics, China Earthquake Administration (formerly the Institute of Geology, China Seismological Bureau) is to develop a database of seismic events in NE China; to refine crust and upper mantle structure in Yanqing-Huailai Basin and Haicheng area; to understand source characterization of natural and human-induced events; and to separate source and propagation path effects at regional distance.

A second objective of this project is the instrumental quantification of seismic and infrasound signals observed at regional distances. The focus in this case is on man-made and natural sources that generate both infrasound and seismic waves. Initially, plans called for infrasound gauges to be collocated with the seismometers deployed in NE China. After acquisition of the infrasound gauges, the deployment was made in the US, collocating infrasound gauges with seismometers operated by University of Utah Seismograph Stations (UUSS). These data are being used to assess atmospheric propagation path effects from known explosion sources.

RESEARCH ACCOMPLISHED

Infrasound Observations of the Wells Earthquake

Most studies documenting earthquake-generated infrasound are based on the analysis of very large earthquakes (Le Pichon et al., 2002; Kim et al., 2004; Le Pichon et al., 2006). The February 2008 Wells, Nevada earthquake is an interesting case because it is a moderate-strong earthquake (M_W 6.0) that was recorded regionally by multiple infrasound arrays, as well as seismic stations including the EarthScope TA. This well-recorded event provides a good opportunity to advance our understanding of the mechanism by which earthquakes generate infrasound. Three infrasonic arrays in Utah (BGU, EPU, and NOQ), one in Nevada (NVIAR), and one in Wyoming (PDIAR) recorded the main event and some of the aftershocks. The waveforms recorded from the Wells sequence at the five infrasonic arrays are characterized by complex signals that correspond to: (1) *P* and *S* arrivals that are the result of coupling-to-air of the seismic waves that traveled to the vicinity of the infrasonic stations (local infrasound); (2) epicentral infrasound (acoustic energy that was generated by the ground motion at the epicenter and traveled through the atmosphere to the arrays at air sound speed; and (3) a secondary source of infrasound between the source and receiver.

To understand the infrasound signal character, we used the software package InfraMonitor (Arrowsmith et al., 2008). InfraMonitor uses a coherent detector with an adaptive noise hypothesis to account for variations in ambient noise (Arrowsmith et al., 2009b). Using the bulletin data generated by the coherent detector, the InfraMonitor software package searches a geographic region (using a grid-search algorithm) to locate the source based on estimated backazimuths and inter-array delay times. Figures 1 and 2 present a summary of the infrasonic observations of the Wells mainshock and the location polygon generated by the InfraMonitor software.

An interesting observation is related to high-amplitude signals recorded at the array BGU, arriving between the seismic arrivals and epicentral infrasound labeled ‘Ground-air coupled infrasound’ (Figure 1), that are not associated with corresponding signals at the other arrays. An in-depth analysis of these signals is presented in Arrowsmith et al. (2009a) and is discussed in more detail in Arrowsmith et al. (2009c, these Proceedings).

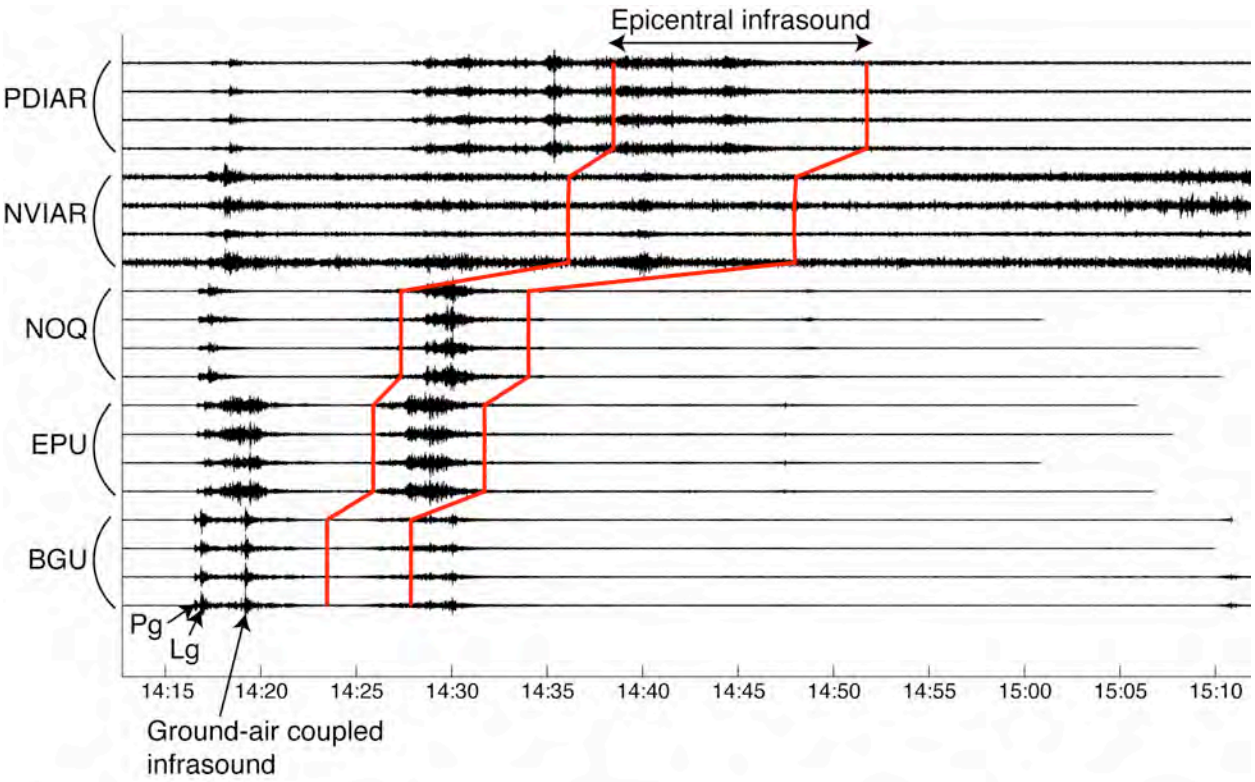

Figure 1. Summary of all infrasonic observations of the Wells, Nevada earthquake mainshock. Epicentral infrasound, observed at all five arrays (within the red lines), is located using the technique outlined in Arrowsmith et al., 2008.

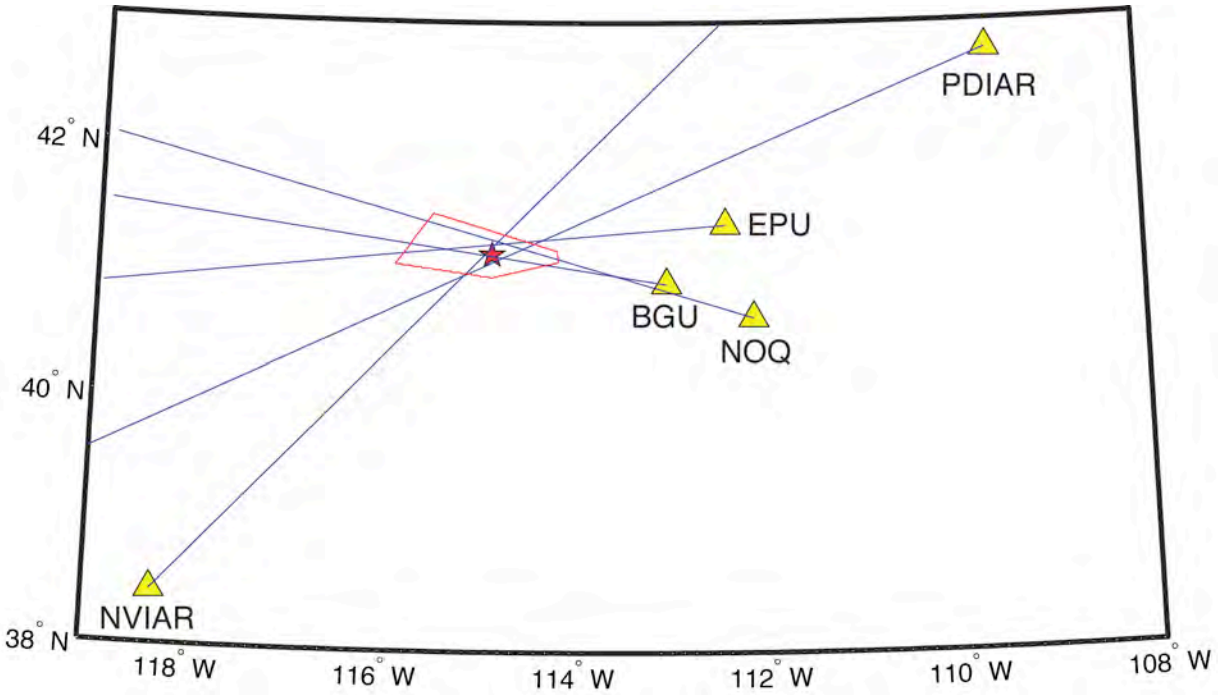

Figure 2. The location polygon obtained using InfraMonitor for the epicentral infrasound (red polygon), with the corresponding seismic location (red star) shown for reference.

Observations of Acoustic to Seismic Coupling

The three permanent infrasound arrays deployed in Utah as a result of this effort motivated the installation of additional infrasound gauges at both UUSS and EarthScope stations for a short time period in August of 2007. As reported previously (Stump et al., 2007a, 2007b), these deployments were designed to characterize infrasound wave propagation in the 1 to 210 km distance range from large surface explosions. Figure 3 documents the effective seismic-to-acoustic coupling observed. In this case, twenty explosions from the Utah Test and Training Range (UTTR) are recorded at the EarthScope site N15A. The seismic waveforms are quite consistent from blast to blast, primarily reflecting the differences in explosive yield. The acoustic-to-seismic coupled energy is robust, documenting differences in propagation path in the atmosphere for the individual days of the explosions.

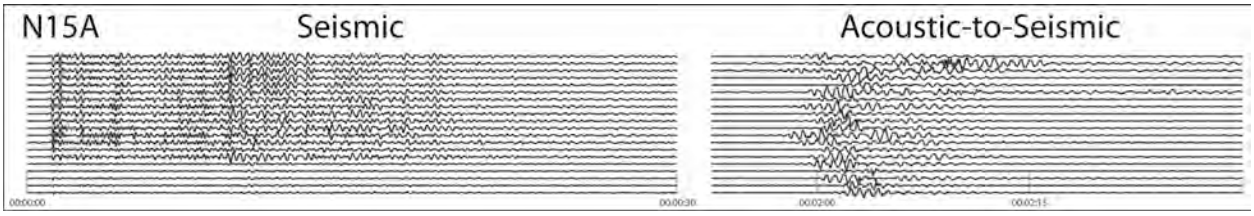

Figure 3. Seismic records from twenty explosions at UTTR as observed at the EarthScope site N15A. The left panel displays the seismic waves and the right panel the acoustic-to-seismic coupling at the site.

Observations like those displayed in Figure 3 illustrate the utility of using seismic stations to quantify infrasonic arrivals as result of acoustic to seismic coupling at seismic receivers. These observations have motivated two parallel lines of investigation. First, seismic stations can be used to produce robust record sections of infrasonic arrivals for purposes of characterizing wave propagation in the atmosphere and second, acoustic-to-seismic transfer functions can be calculated to understand the physical parameters that control coupling. Seismic and infrasound record sections for UTTR were constructed using seismometers and are displayed in Figure 4.

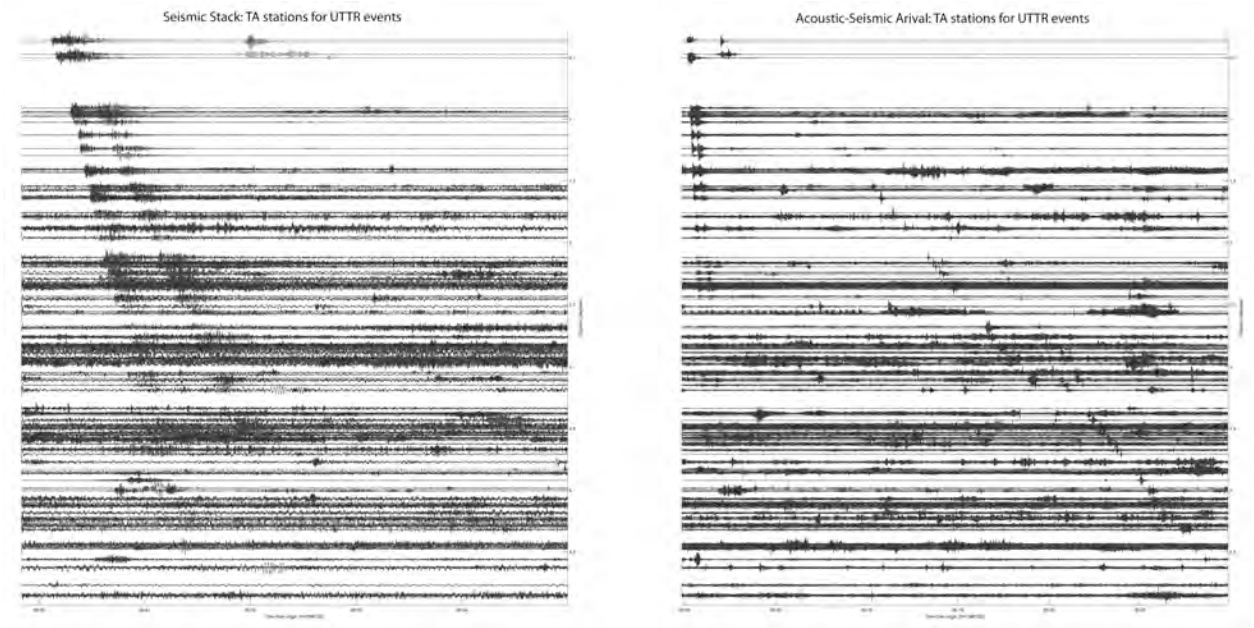

Figure 4. Record sections from the vertical (BHZ) component EarthScope stations. The left panel was produced by stacking four of the UTTR explosions while the right panel is the recording of a single UTTR blast windowed to emphasize the infrasound arrivals.

The data displayed in Figure 4 demonstrate the capability of seismic stations and EarthScope sites in general to document infrasound wave propagation at regional distances. The data demonstrate that for these near-surface explosions the infrasound signals are observed at greater distances than the accompanying seismic signals from the same event. Preliminary results from the transfer function analysis suggest that the transfer functions are highly variable from site to site and that further empirical studies are needed the quantify the variability.

Spatial and Temporal Variation in the Atmosphere and Impact on Infrasound Propagation

Interpretation of the near-regional infrasonic data has continued. We continue the analysis of observations in the 1 to 210 km distance range recorded from the UTTR explosions. Previous results identified the possible importance of shallow waveguides to the observations in this distance range. The new work has focused on the spatial and temporal variability of these waveguides. Two approaches were undertaken to explore this variability. The first is a quantification of the spatial and temporal variation in shallow atmospheric sampling based upon data from rawinsondes. The second approach involves the utilization of atmospheric models based upon the empirical data in developing PE models for the distances and azimuths for which there are infrasonic observations.

Balloon launches were made before and at the time of each of the detonations. Launches were made at the explosion site as well as at a distance of 50 km from the source. Acquisition of meteorological data contributes to the modeling of propagation path effects for the infrasound data. Spatial and temporal variations of atmospheric temperature and wind conditions are assessed from atmospheric sampling at the time of the four detonations at the UTTR source site and at a range of 50 km as depicted in Figure 5. Variation of temperature is relatively small compared to large variations in the near-surface winds. This result illustrates the importance of three-dimensional effects at these distance ranges.

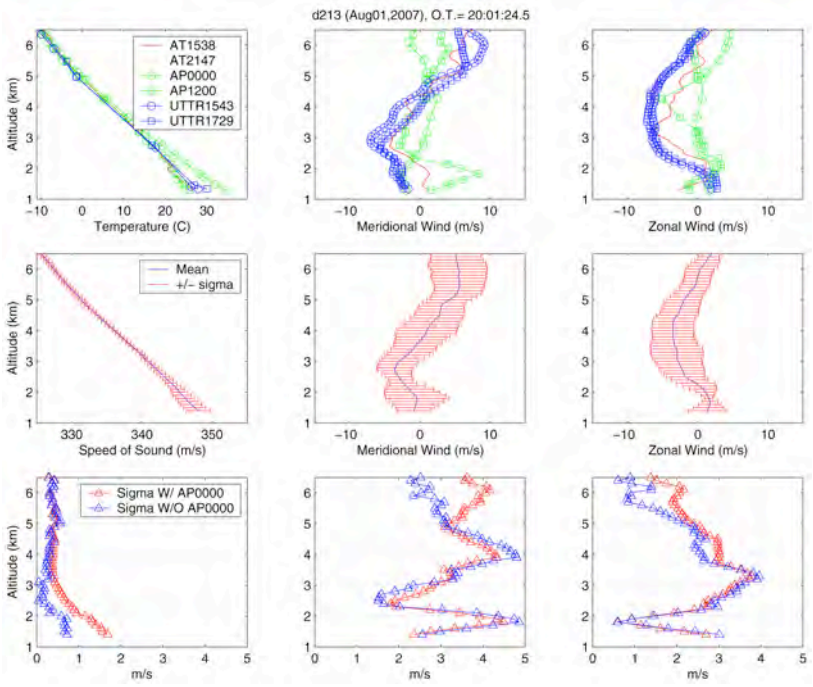

Figure 5. Atmospheric profiling was taken at three sites in the region where the UTTR explosions were undertaken 1 August 2007. The first location is at the detonation site (UTTR), the second site is 50 km to the SE of the shot at Antelope Island (AP) and the final location at the Salt Lake City airport (AP). The four digit numbers that accompany each site document the time of the atmospheric monitoring. The first row of figures represents the actual temperature, meridional and zonal winds at the three sites. The second row uses these data to create mean and variance estimates of atmospheric velocity.

The temporal variation of these wind patterns is documented by comparing the results from 1 August 2007 (Figure 5) with similar data from 6 August 2007 (Figure 6). These data also support the consistency of temperature data across the three sampling sites and the large variation in winds over the first 6 km. The absolute wind values and their directions are quite different between the two days illustrating the importance of such sampling in order to quantify the wave propagation path effects.

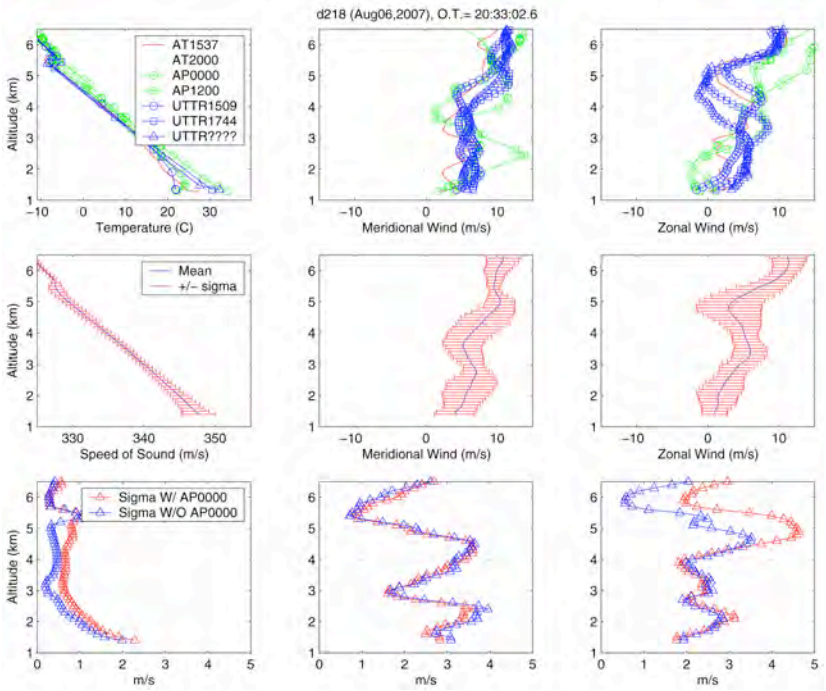

Figure 6. Atmospheric profiling was taken at three sites in the region where the UTTR explosions were undertaken 6 August 2007. Figure format is the same as in Figure 5.

PE modeling was conducted using these observations in order to quantify the effects of time and space on the predicted travel times and amplitudes. The effects are large in terms of predicted amplitudes from 1 to 210 km and suggest that temporal and spatial effects in the shallow atmosphere will be critical to the interpretation of the data.

Seismic Studies in NE China

The seismic stations deployed in NE China as part of this contract were removed in 2008. Analysis of these seismic data continues. Shear wave velocities beneath the Yanqing-Huailai Basin were estimated from the joint inversion of surface wave phase velocities and teleseismic receiver functions.

An average velocity model for the region was determined by inverting all receiver functions from the seven stations with the phase velocities from the teleseismic events (Zhou et al., 2009). Figure 7 plots the station specific velocity models (red) against the averaged model for the region (blue). The individual velocity models at depth exhibit little or no difference across the network as expected based on the common surface wave dispersion data. The models have a positive velocity gradient from the surface to approximately 15 km with shear wave velocity increasing from 2.0 km/sec to 3.55 km/sec. A slight negative gradient in velocity starts at about 15 km resulting in an extended low velocity layer to approximately 25 km with velocity near 3.3 km/sec. There is evidence of a low velocity layer in the mid-crust at all stations. There is no sharp Moho interface with the Moho represented as a transition in velocity from 38 to 42 km, consistent with other studies in the region (Zhang et al., 1996; Zhao et al., 2005).

Predicted first arrival times (red) from the inverted model are compared with results from a nearby refraction/wide angle reflection profiles (blue) as well as the AK135F model (green) in Figure 8, the difference reflects the slower velocities in the very shallow crust in our models.

We are continuing the joint inversion study for crustal shear velocity structure in the second focus area, Haicheng, NE China. The radial component receiver functions for 81 and 64 events that occurred from September 2004 to May 2008 at FFANG and LJIA are plotted as a function of source azimuth in Figure 9.

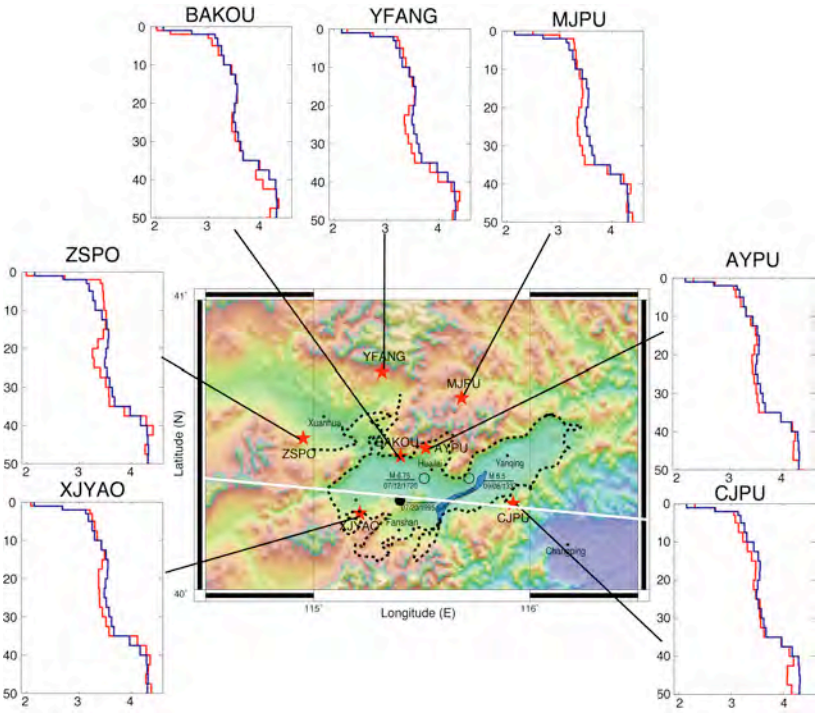

Figure 7. Map of stations and shear-wave velocity models from joint inversions at each of the seven stations (red) compared to the averaged model inverted using all seven stations (blue) simultaneously.

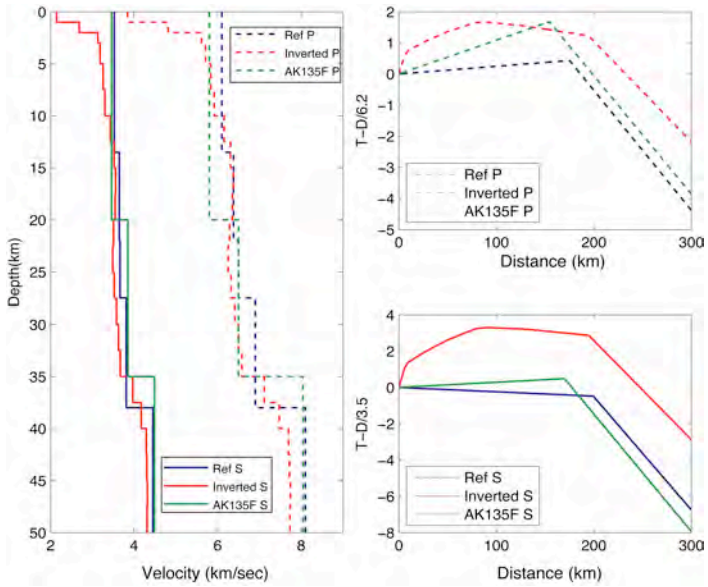

Figure 8. Comparison between the model resulting from the joint inversion (receiver functions and phase velocities) using all station data (red) and the model from a refraction/wide-angle reflection survey (blue), and AK135F model (green). Right: Predicted first arrival times of *P* (upper) and *S* (lower) from the three different models.

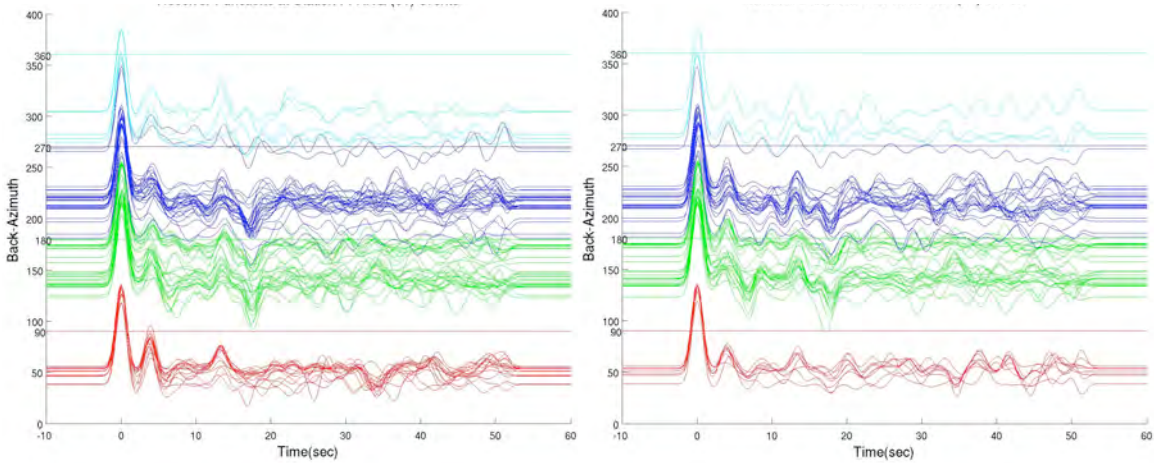

Figure 9. Plot of receiver functions (Gaussian window parameter α = 1.0) versus back-azimuth for events recorded at station FFANG (left, 81 events) and LJIA (right, 64 events).

CONCLUSIONS AND RECOMMENDATIONS

Infrasound Observations of the Wells Earthquake – A number of infrasound observations obtained from the Wells earthquake were recovered from stations deployed as part of this contract. These observations have been used to locate the event using infrasound arrivals, as well as identify infrasound generated not only in the epicentral region but also along the path from the event to receiver. A more detailed account of this analysis can be found in the companion paper in Arrowsmith et al. (2009c, these Proceedings).

Observations of Acoustic to Seismic Coupling – Strong acoustic-to-seismic coupling is observed at EarthScope stations out to nearly five degrees from the UTTR explosions. These observations illustrate that seismic observations can be used to interpret infrasonic wave propagation in the absence of acoustic gauges. The details of the acoustic to seismic coupling are station dependent and need further study. Infrasonic observations of UTTR explosions extend to a greater range than the seismic observations.

Spatial and Temporal Variation in the Atmosphere and Impact on Infrasound Propagation – Atmospheric temperature and wind profiles based on rawinsondes illustrate significant temporal and regional spatial scale variation. Utilization of these models illustrates that they can have a significant effect on infrasonic wave propagation in the 1 to 210 km distance range. Preliminary results suggest that 3D effects may play an important role in the explaining observations.

Seismic Studies in NE China – The seismic deployments in NE China are complete. A velocity model for the Yanqing-Huailai Basin region near Beijing has now been developed and published using receiver functions and surface wave analysis. These methods are being extended to Haicheng area where the stations were deployed at the end of the experiment.

ACKNOWLEDGEMENTS

The IRIS PASSCAL instrumentation Center provided the STS-2 seismometers, Quanterra Q-330 and Baler systems deployed in China. Professors Yun-tai Chen and Zhi-Xian Yang at the Institute of Geophysics, China Earthquake Administration supported the China component of the work.

REFERENCES

Arrowsmith, S. J., R. Burlacu, R. Whitaker, and G. Randall (2009a). A repeating secondary source of infrasound from the Wells, Nevada, earthquake sequence, *Geophys. Res. Lett. 36:* doi:10.1029/2009GL038363.

Arrowsmith, S. J., R. Whitaker, C. Katz, and C. Hayward (2009b). The F-detector Revisited: An Improved Strategy for Signal Detection at Seismic and Infrasound Arrays, *Bull. Seism. Soc. Am.* 99: 449–453.

Arrowsmith, S. J., R. Whitaker, S. R. Taylor, R. Burlacu, B. Stump, M. Hedlin, G. Randall, C. Hayward, and D. ReVelle (2008). Regional monitoring of infrasound events using multiple arrays: application to Utah and Washington State, *Geophys. J. Int.* doi: 10.1111/j.1365-246X.2008.03912.x.

Arrowsmith, S. J., H. E. Hartse, G. E. Randall and S. R. Taylor (2009c). Infrasound as a depth discriminat: Construction of a unique dataset and preliminary analysis, these Proceedings.

Kim, T. S., C. Hayward, and B. Stump (2004). Local infrasound signals from the Tokachi-Oki earthquake, *Geophys. Res. Lett.* doi:10.1029/2004GL021178.

Le Pichon, A., J. Guilbert, A. Vega, M. Garces, and N. Brachet (2002). Ground-coupled air waves and diffracted infrasound from the Arequipa earthquake of June 23, 2001, *Geophys. Res. Lett*. doi:10.1029/2002GL015052.

Le Pichon, A., P. Mialle, J. Guilbert and J. Vergoz (2006). Multistation infrasonic observations of the Chilean earthquake of 2005 June 13, *Geophys. J. Int.* doi:10.1111/j.1365-246X.2006.03190.x.

McKenna, S. M. H. (2005). Infrasound Wave Propagation at Near-Regional and Tele-Infrasonic Distances, *Ph.D. Thesis,* Southern Methodist University.

Stump, B., R. Burlacu, C. Hayward, J. Bonner, K. Pankow, A. Fisher, and S. Nava (2007a). Seismic and Infrasound Energy Generation and Propagation at Local and Regional Distances: Phase I – Divine Strake Experiment, in *Proceedings of the 29th Monitoring Research Review: Ground-Based Nuclear Explosion Monitoring Technologies*, LA-UR-07-5613, Vol 1, pp. 674–683.

Stump, B., R. Burlacu, C. Hayward, K. Pankow, S. Nava, J. Bonner, S. Hock, D. Whiteman, A. Fisher, T.S. Kim, R. Kubacki, M. Leidig, J. Britton, D. Drobeck, P. O'Neill, K. Jensen, K. Whipp, G. Johnson, P. Roberson, R. Read, R. Brogan and S. Masters (2007b) Seismic and Infrasonic Energy Generation and Propagation at Local and Regional Distances: Phase I – Divine Strake Experiment, Air Force Research Laboratory, AFRL-RV-HA-TR-2007-1188.

Zhang, X.-K., C.-Y. Wang, G.-D. Liu, J.-L. Song, L.-L. Luo, T. Wu and J.-C. Wu (1996). Fine crustal structure in Yanqing-Huailai region by deep seismic reflection profiling, *Chinese J. Geophys.* 39: 356–364.

Zhao, J.-R., X.-K. Zhang, C.-K. Zhang, J.-S. Zhang, B.-F. Liu, Q.-F. Ren, S.-Z. Pan and Y. Hai (2005). The heterogeneous characteristics of crust-mantle structures and the seismic activities in the northwest Beijing region, *ACTA Seismologica Sinica* 18: 125–134.

Zhou, R.-M., B. W. Stump, R. B. Herrmann, Z.-X. Yang and Y.-T. Chen (2009). Teleseismic receiver function and surface-wave study of velocity structure beneath the Yanqing-Huailai basin northeast of Beijing, *Bull. Seism. Soc. Am.* 99: 1937–1952.

SEISMIC TOMOGRAPHY OF THE ARABIAN-EURASIAN COLLISION ZONE AND SURROUNDING AREAS

M. Nafi Toksöz, Robert D. Van der Hilst, Youshun Sun, Haijiang Zhang,
Xiangfang Zeng, and Shunping Pei

Massachusetts Institute of Technology

Sponsored by the Air Force Research Laboratory

Award No. FA8718-07-C-0001
Proposal No. BAA07-09

ABSTRACT

The objectives of this study are to determine *P*- and *S*-wave velocity structures in the crust and upper mantle, and to characterize seismic wave propagation in the Arabian-Eurasian collision zone and surrounding areas, including Iran, Arabia, Eastern Turkey, and the Caucasus. The Arabian-Eurasian plate boundary is a complex tectonic zone shaped by continent-continent collision processes. In recent years the number of seismic stations has increased greatly in the region because of expanded seismic networks in Azerbaijan, Turkey, Iran and the Gulf countries. We have been collecting the data through cooperation with individual network operators and the countries. Considerable effort has been directed to collecting *P* and S seismic arrival time data recorded by the new networks in Iran. Using arrival time data we obtained *Pn* and *Sn* images of the uppermost mantle beneath Arabian-Eurasian Collision Zone including Iran, the Caucasus, and the Arabian Peninsula by tomographic inversion. With the newly obtained data from Central Asia incorporated into our database, we improved the ray coverage in our study region.

Our current plan is to utilize the new data from Iran to improve the velocity models. This effort will include tomographic inversions for velocity structure in the crust and upper mantle, relocation of all events, and the validation of models using synthetic seismograms to fit available broad-band waveforms.

OBJECTIVES

The objectives of this study are to determine *P*- and *S*-wave velocity structures in the crust and upper mantle, and to characterize seismic wave propagation in the Arabian-Eurasian collision zone and surrounding areas, including Iran, Arabia, Eastern Turkey, and the Caucasus. The area of the study, shown in Figure 1, extends east-west from the Mediterranean to Central Asia, and north-south from the Caspian to the Gulf of Aden and the Arabian Sea. The area covers all of the Arabian plate, the collision zone, and the areas in the Eurasian plate whose structure and tectonics are affected by the collision. The project will include data from countries whose seismic networks have expanded significantly in recent years, such as Turkey, Azerbaijan, Iran, Kuwait, United Arab Emirates (UAE), Oman, and Saudi Arabia. These locations provide data for high-resolution P and S wave travel-time tomography. Recent observations show that wave propagation and attenuation vary significantly even with small changes across the suture zone, indicating rapid spatial changes in the crust and mantle properties.

A number of unanswered questions remain about the structure and processes in the upper mantle beneath the collision zone. The fate of the Neotethys plate subducted prior to the continental collision remains largely unknown. There are no intermediate and deep earthquakes under the Zagros-Bitlis suture zone, yet the subduction is too recent for the slab to reach thermal equilibrium and be assimilated. Some studies have suggested that the slab has recently broken off beneath the suture zone (Bird, 1978; Molinaro et al., 2005). In the Makran subduction zone in the south, seismicity and structure have been studied with the deployment of dense seismic networks (Yamini-Fard and Hatzfeld, 2006), confirming the Makran subduction, yet the nature of the transition from the subduction zone to the Zagros suture zone has not been fully resolved. High-resolution travel-time tomography would be a major step towards defining the present-day crustal and mantle structure of the Middle East region.

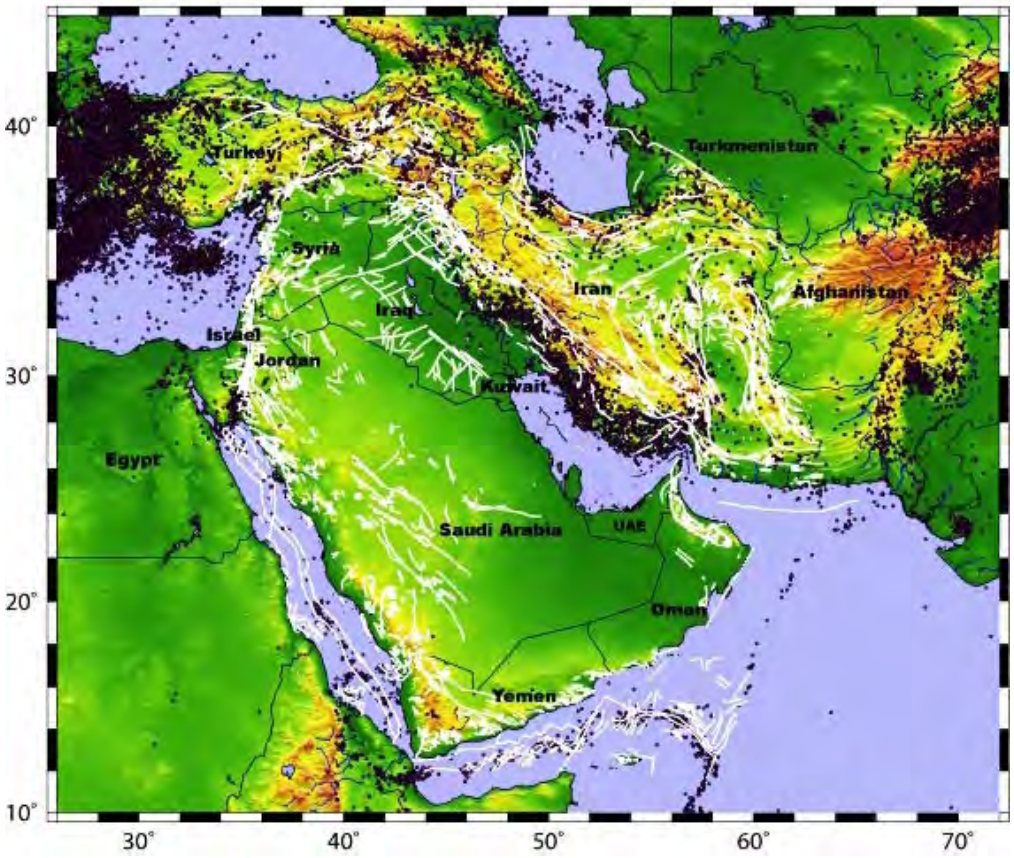

Figure 1. Topographic map of the Middle East and surrounding regions. White lines denote the location of known faults, while the black dots represent the epicenter locations of earthquakes in the region.

RESEARCH ACCOMPLISHED

Tectonic Setting

The Arabian-Eurasian plate boundary is extremely complex, and it is an ideal region to study a young (geologically) continent-continent collision belt. The current tectonics of the region are controlled by the collision and continuing convergence of the Arabian and Eurasian plates. The Arabian and Eurasian plates collided in the early Miocene, after the Neotethys Sea was subducted beneath Eurasia (Bird, 1978; Şengör and Yılmaz, 1981; Jackson and McKenzie, 1984; Dewey et al., 1986). Pre-, syn-, and post-collision tectonics produced very complex structures in the region. Over the last decade, a number of seismic studies have examined the crust and upper mantle structure beneath the Middle East to constrain the nature of the Arabian-Eurasian collision zone. Large-scale surface-wave tomography studies have shown variable crustal thickness and upper mantle velocities (Ritzwoller and Levshin, 1998; Pasyanos et al., 2001; Villasenor et al., 2001; Pasyanos and Walter, 2002; Shapiro and Ritzwoller, 2002; Alinaghi et al., 2007; Reiter and Rodi, 2006). Regional-scale surface wave tomographic studies further highlight the complexity of the collision zone (Mindevalli and Mitchell, 1989; Rodgers et al., 1999; Mokhtar et al., 2001; Maggi and Priestley, 2005) showing a thickened crust under the Caucasus and Zagros, and low shear velocity beneath the Turkish and Iranian plateaus.

Hearn and Ni (1994), Ritzwoller et al. (1998), Al-Lazki et al. (2003; 2004), and Phillips et al. (2007) found slow *Pn* velocities ($\leq$ 8 km/s) beneath the Anatolian plateau, northwestern Iran, the Greater Caucasus, and southwestern Arabia. The Pn velocities beneath northern Arabia and the Caspian region are faster than average (Al Lazki et al., 2004; Ritzwoller et al., 2002). This high degree of variability suggests that the Earth structure may be extremely complicated in the region.

Studies of the propagation and attenuation characteristics of regional waves (e.g., Pn, Sn, and Lg) provide additional evidence for strong heterogeneities. Surface wave studies show high shear wave attenuation beneath Iran, Anatolia and the western part of the Arabian plate, and relatively low attenuation in central and eastern Arabia (Seber and Mitchell, 1992; Sandvol et al., 2001; Jamberie and Mitchell, 2004; Molinaro et al., 2005; Bergman et al., 2008; Priestley et al., 2008; Pasyanos et al., 2009). Sn and Lg waves are attenuated through much of the collision zone between the Arabian and Eurasian plates (Kadinsky-Cade et al., 1981; Rodgers et al., 1987; Mitchell et al., 1997; Cong and Mitchell, 1998; Gök et al., 2000; Sandvol et al., 2001; Al-Damegh et al., 2004; Zor et al., 2007). An Lg blockage exists across the Bitlis suture zone and across the Zagros fold and thrust belt. The studies mentioned above present consistent results for the crust and uppermost mantle seismic properties on a regional scale. Significant variation in waveforms, observed particularly in short-period seismograms, over propagation paths that are close to each other, suggests structural variations over short distances at regional boundaries. Delineating these features requires seismic data from dense local and regional seismic networks. During this year we were able to increase the phase (arrival time) data significantly by adding readings from Iran and other regional networks.

Travel-Time Data and *Pn* and *Sn* Tomography

An important task under this project is to collect arrival time data from seismic stations situated in more than 20 countries in the region. A significant number of these stations are in networks that are relatively new and whose data are not available from global data centers such as IRIS or ISC. Figure 2 shows seismic stations in the region from which data may be obtained either through data centers or by bilateral arrangements. In the past year, Iran started to make available phase data from its networks. In Iran there are seven regional networks, deployed around major cities, with a total of 73 stations. Recently, Tehran University was designated as the central location that would collect and integrate data from the regional networks into a central database. The use of data from stations in Iran required deciphering of nomenclature and resolution of some apparent discrepancies between data from individual networks and the central database. We were able to obtain 100,000 *P* and 70,000 *S* arrival time recordings from local earthquakes in the time period between January 2006 and March 2008. Our database for the *Pn* tomography in the whole study region includes 160,000 arrival times from 850 stations and 18,000 earthquakes. The source-station ray paths are shown in Figure 3A. For *Sn*, the data are fewer, with 75,000 total phase reading. The ray paths are shown in Figure 3B.

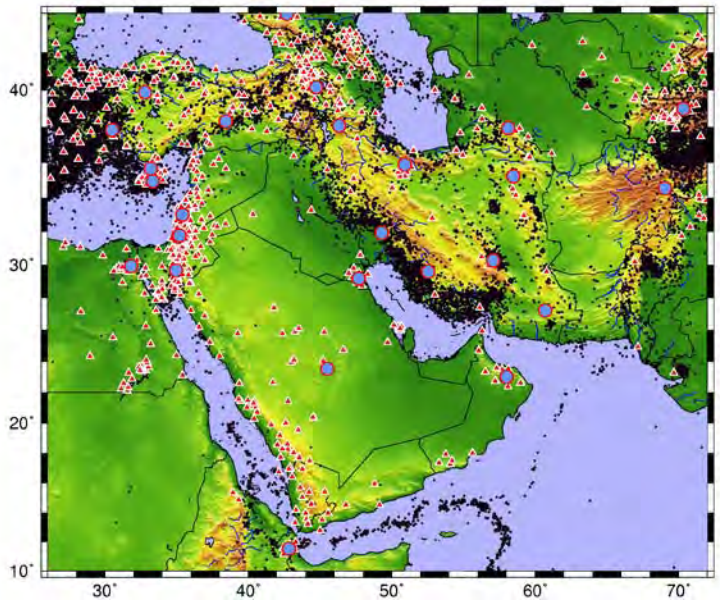

Figure 2. Seismic stations (triangles) and events (black dots) in the region. Circles show broadband stations.

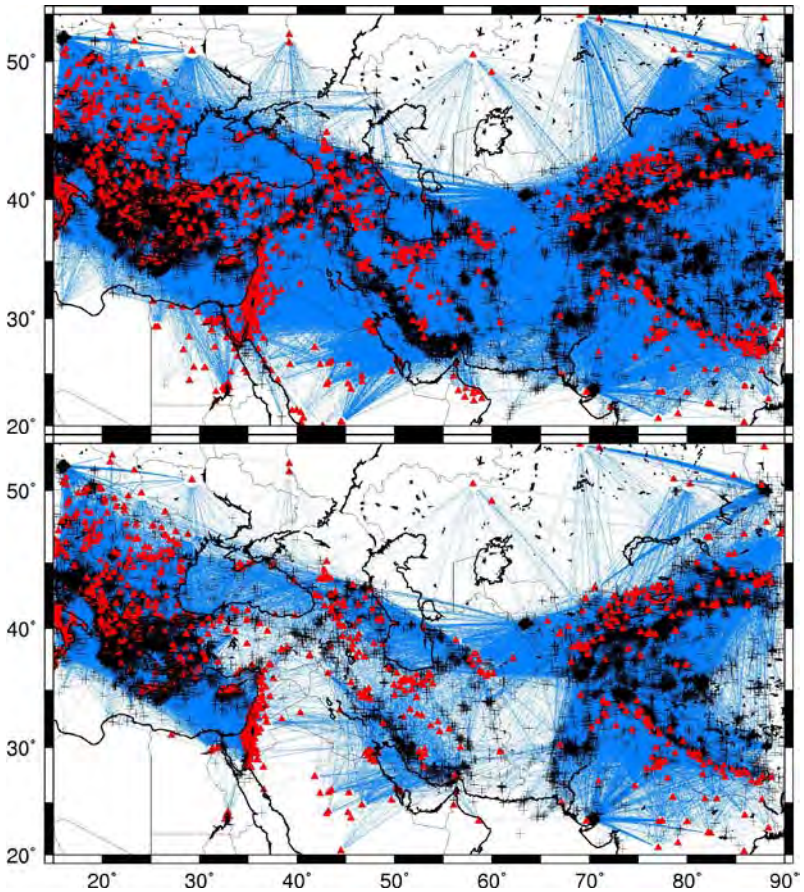

Figure 3. (A) Top: Ray paths for Pn travel times. From 18,000 events recorded by 850 stations (red triangles), 160,000 Pn rays were obtained (black crosses). (B) Bottom: Ray paths for 75,000 Sn travel times.

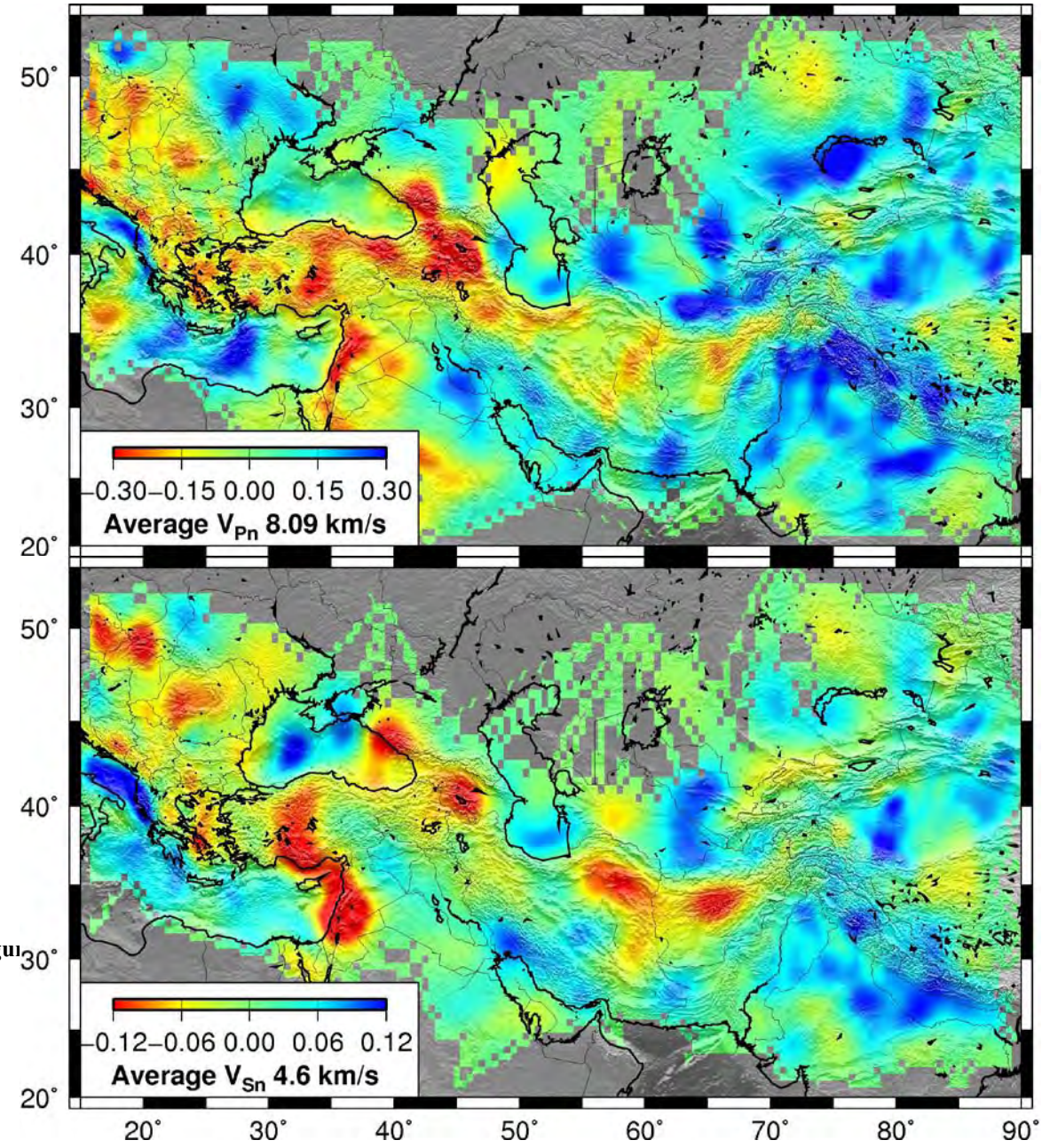

Figure 4. (A) Top: Pn velocity lateral variations. Average Pn velocity is 8.09 km/s. (B) Bottom: Sn velocity lateral variations. Average Sn velocity is 4.6 km/s.

The *Pn* and *Sn* travel times (residuals) are inverted for lateral velocity variations using Hearn's approach (Hearn, 1996; Hearn et al., 2004), modified by Pei et al. (2007). Figures 4A and 4B show *Pn* and *Sn* velocities, respectively. The general features of *Pn* velocities are similar to those of Philips et al. (2007) except that Figure 4A has finer spatial resolution. *Pn* velocities are low under eastern Anatolia, NW Iran, and the Southern Caucasus. Isolated low-velocity anomalies exist along the Levant Fracture (Dead Sea Fault) Zone. A prominent low-velocity feature is observed just to the south of the Caspian Sea. The Iranian plateau is characterized by lower than average *Pn* velocity. *Pn* velocities are high under the Arabian platform, the Persian Gulf, and under the Zagros fold belt. Most likely these are the velocities associated with the top of the Neotethys lithosphere. In the north, the higher velocities are under the Black Sea, the Rioni and Kara Basins between the Greater and Lesser Caucasus, under the southern

Caspian, and the Kyzyl and Kara Kum Basins of Turkmenistan. These are most likely the remnants of the Paleotethys (Gülen, 1989). *Sn* velocities shown in Figure 4B are similar to *Pn*. In general, the regional features correlate quite well. Some isolated anomalies (e.g., the Levant Fracture Zone) are very similar between the *Pn* and *Sn*.

Data from Iran

Most important new data for this study come from two seismic networks in Iran: Iranian Seismic Telemetry Network (ISTN) and Iran National Seismic Network (INSN) (Figure 5). The ISTN was founded in 1995. In total 73 stations are grouped into ten sub-networks distributed in most parts of Iran. There are 67 three-component short period stations and six analogue stations. The International Institute of Earthquake Engineering and Seismology operates the other nation wide seismic network: INSN. All 30 INSN stations use broadband seismographs. Figure 5 shows the station distributions in both networks.

The Institute of Geophysics at Tehran University serves as the central processing facility for ISTN. Under their management, the data quality has improved significantly in the past few years. They make available through their website travel time, amplitude, and, for selected events, waveform data. Figure 6 shows examples of travel time data from both ISTN and INSN networks. We collected phase arrivals and maximum amplitudes reported by both networks from July, 2004 to May, 2009. This dataset provides abundant local and regional phase arrivals, which are useful in extracting crustal seismic structure. The ISTN catalogue includes 25,471 earthquakes between Feb, 2006 and Apr, 2009. More than 240,000 arrivals were reported. There are about 160,000 *P* arrivals and 80,000 *S* arrivals. The INSN reported 3,342 events before 2008 and used 15,112 *P*-wave arrivals, 4,927 *S*-wave arrivals to locate events.

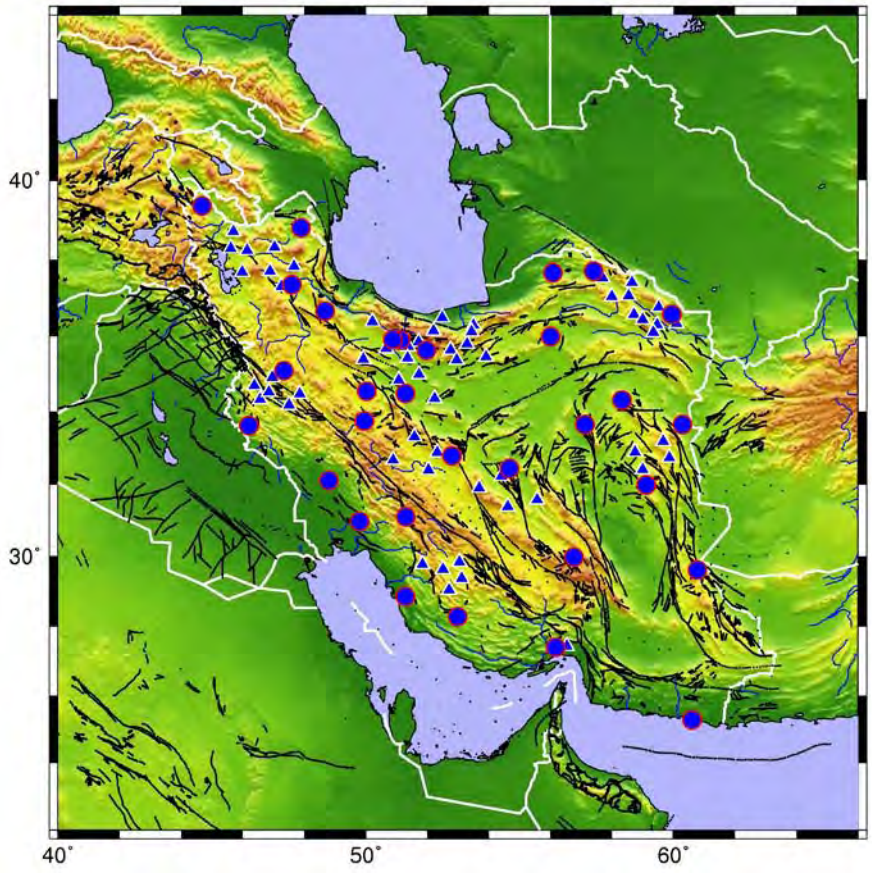

Figure 5. Seismic stations in Iran. INSN stations are in circles and ISTN stations are in triangles.

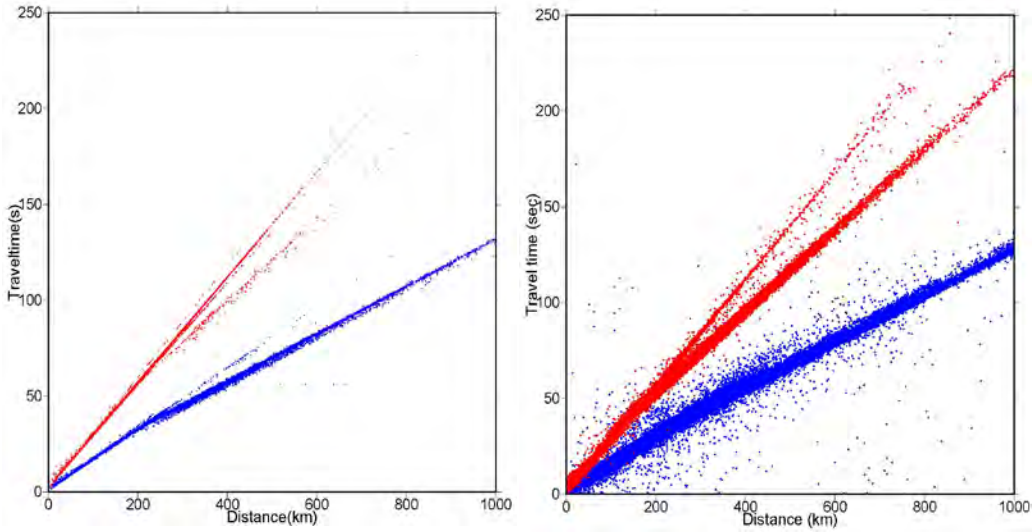

Figure 6. Available *P* and *S* travel times from INSN (left) and ISTN (right) networks.

Relocation of Earthquakes in Iran

The local and regional networks (shown in Figure 5) provide good data coverage (Figure 6) to relocate earthquakes using high-quality *P*- and *S*-wave travel-times. We apply an adaptive-mesh, double-difference tomography method to the Iranian data set to improve event locations and to obtain preliminary velocity models (Zhang and Thurber, 2003; 2005). Figure 7 shows the comparison of travel-time residuals using 1-D and 3-D models for event relocation. The 1-D *P* and *S* models used for relocation were adopted from Crust 2.0 and the 3-D models were obtained while simultaneously locating events. The overall residuals are reduced from 1.2 s to 0.9 s. Figure 8 shows the relocation of a group of events in the year of 2006 and an example of event relocation using 1-D and 3-D models. The average difference between the original locations and the 3-D relocations is 10 km.

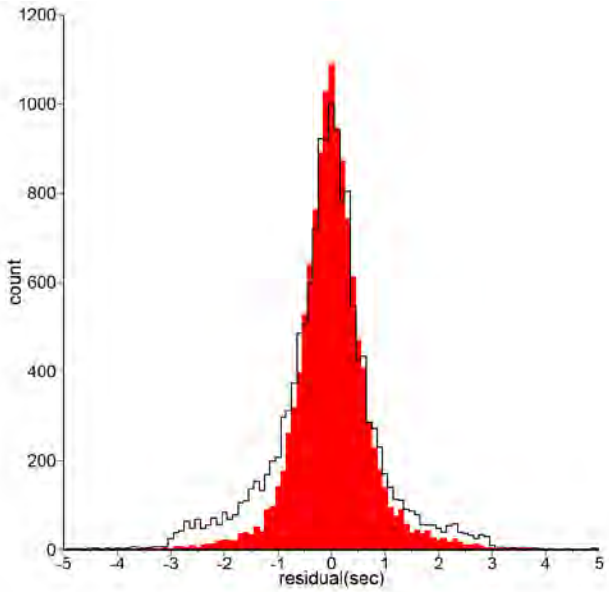

Figure 7. Comparison of residuals using 1-D model (solid line) and 3-D model (red).

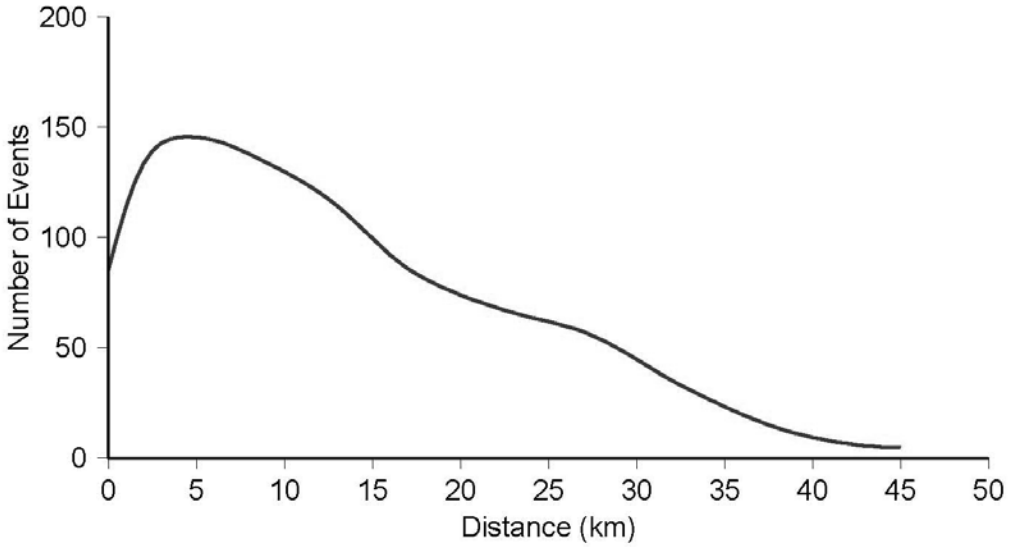

Figure 8. Epicentral differences between the relocations and original locations of earthquakes in Iran.

CONCLUSIONS AND RECOMMENDATIONS

Primary activities were dedicated to collecting P and S wave local/regional arrival time data from more than 750 stations in the study area. For the first time we were able to obtain arrival-time data from 103 stations in Iran. Altogether 200,000 *P* arrivals and 100,000 *S* arrivals from Iran were added to the database to do a seamless tomography of the crust and upper mantle. The tomographic results reveal a significant low velocity zone to the south of the Caspian Sea. Along the Zagros belt, a large low-velocity zone is clearly observed. Other prominent low *Pn* and *Sn* anomalies are visible in the Northwestern Iran, the Caucasus Anatolian Plateau and the Easternmost Mediterranean. We are in the process of testing these models using well-located ground-truth events and synthetic seismograms to fit available broad-band waveforms.

REFERENCES

Al-Damegh, K., E. Sandvol, A. Al-Lazki, and M. Barazangi (2004). Regional seismic wave propagation (Lg and Sn) and Pn attenuation in the Arabian Plate and surrounding regions, *Geophys. J. Int*. 157: 775–795.

Alinaghi, A., I. Koulakov, and H. Thybo (2007). Seismic tomographic imaging of P- and S-waves velocity perturbations in the upper mantle beneath Iran, *Geophys. J. Inter.* 169: 3, 1089–1102.

Al-Lazki, A., E. Sandvol, D. Seber, M. Barazangi, and N. Turkelli (2003). Pn tomographic imaging of mantle lid velocity and anisotropy at the junction of the Arabian, Eurasian, and African plates, *Geophys. Res. Lett.* 30: doi:10.1029/2003GL017391.

Al-Lazki, A. I., E. Sandvol, D. Seber, M. Barazangi, N. Turkelli, and R. Mohamad (2004). Pn tomographic imaging of mantle lid velocity and anisotropy at the junction of the Arabian, Eurasian and African plates, *Geophys. J. Int*. 158*:* 1024–1040.

Bergman, E.A., E.R. Engdahl, M.H. Ritzwoller, and S.C. Myers (2008). Crustal structure of the Iran region from in-country and ground-truth data, in *Proceedings of the 30th Monitoring Research Review: Ground-Based Nuclear Explosion Monitoring Technologies*, LA-UR-08-05261, Vol. 1, pp. 3–9.

Bird, P. (1978). Finite-element modeling of lithosphere deformation: The Zagros collision orogeny, *Tectonophysics* 50: 307–336.

Cong, L. and B. J. Mitchell (1998). Seismic velocity and Q structure of the Middle Eastern crust and upper mantle from surface wave dispersion and attenuation, *Pure Appl. Geophys.* 153: 503–538.

Dewey, J. F., M. R. Hempton, W. S. F. Kidd, F. Saroglu, and A. M. C. Şengör (1986). Shortening of continental lithosphere: The neotectonics of eastern Anatolia—A young collision zone, in *Collision Tectonics*, M. P. Coward and A. C. Ries (eds.) London: Geol. Soc. London, pp. 3–36.

Gök, R., N. Turkelli, E. Sandvol, D. Seber, and M. Barazangi (2000). Regional wave propagation in Turkey and surrounding regions, *Geophys. Res. Lett.* 27: 429–432.

Gülen L. (1989). From plate tectonics to global domain tectonics, in *Crust/Mantle Recycling at Convergence Zones*, S. R. Hart and L. Gülen (eds.), NATO ASI Series, C258. Boston: Kluwer Academic Publishers, 173–179.

Hearn, T. M., S. Wang, J. Ni, Z. Xu, Y. Yu, and X. Zhang (2004). Uppermost mantle velocities beneath China and surrounding regions, *J. Geophys. Res*. 109: doi:10.1029/2003JB002874.

Hearn, T. M. and J. Ni (1994). Pn velocities beneath continental collision zones: The Turkish-Iranian plateau, *Geophys. J. Int*. 117: 273–283.

Hearn, T. M. (1996). Anisotropic Pn tomography in the western United States, *J. Geophys. Res*. 101: 8403–8414.

Jackson, J. and D. McKenzie (1984). The active tectonics of the Alpine-Himalayan belt between western Turkey and Pakistan, *Geophys. J. R. Astron. Soc*. 77: 185–265.

Jamberie, A. L. and B. J. Mitchell (2004). Shear wave Q structure and its lateral variation in the crust of China and surrounding regions, *Geophys. J. Int*. 157: 363–380.

Kadinsky-Cade, J., M. Barazangi, J. Oliver, and V. Isacks (1981). Lateral variation in high-frequency seismic wave propagation at regional distances across the Turkish and Iranian plateaus, *J. Geophys. Res*. 86: 9377–9396.

Maggi, A. and K. Priestley (2005). Surface waveform tomography of the Turkish-Iranian plateau, *Geophys. J. Int.* 160: 1068–1080.

Mindevalli, O. Y. and B. J. Mitchell (1989). Crustal structure and possible anisotropy in Turkey from seismic surface wave dispersion, *Geophys. J. R. Astron. Soc*. 98: 93–106.

Mitchell, B. J., Y. Pan, J. Xie, and L. Cong (1997). Lg code Q variation across Eurasia and its relation to crustal evolution, *J. Geophys. Res*. 102: 22,767–22,779.

Mokhtar, T. H., C. A. Ammon, R. B. Herrmann, and A. A. Ghalib (2001). Surface wave velocity across Arabia, *Pure Appl. Geophys.* 158: 144–1425.

Molinaro, M., H. Zeyen, and X. Laurencin (2005). Lithospheric structure beneath the southeastern Zagros Mountains, Iran: Recent slab break-off? *Terra Nova*, doi: 10.1111/j.1365-3121.2004.00575.

Pasyanos, M. E., E. M. Matzel, W. R. Walter, and A. J. Rodgers (2009). Broad-band Lg attenuation modelling in the Middle East, *Geophys. J. Int.* 177: 1166–1176.

Pasyanos, M. E., W. R. Walter, and S. E. Hazler (2001). A surface wave dispersion study of the Middle East and North Africa for monitoring the Comprehensive Nuclear-Test-Ban Treaty, *Pure Appl. Geophys*. 158: 1445–1474.

Pasyanos, M. E. and W. R. Walter (2002). Crust and upper mantle structure of North Africa, Europe, and the Middle East from inversion of surface waves, *J. Geophys. Int*. 149: 463–481.

Pei, S., J. Zhao, Y. Sun, Z. Xu, S. Wang, H. Liu, C. A. Rowe, M. N. Toksoz, and X. Gao (2007). Upper mantle seismic velocities and anisotropy in China determined through Pn and Sn tomography. *J. Geophys. Res.*, 112, B05312, doi:10.1029/2006JB004409.

Phillips, W. S., M. L. Begnaud, C. A. Rowe, L. K. Steck, S. C. Myers, M. E. Pasyanos, and S. Ballard (2007). Accounting for lateral variations of the upper mantle gradient in Pn tomography studies, *Geophys. Res. Lett.* 34: L14312, doi:10.1029/2007GL029338.

Priestley, K, D. McKenzie, E. Debayle, J. Jackson, M. Tatar, (2008). Thick lithospheric root beneath the Zagros Mountains of Iran, *Eos Trans. AGU* 89: 53, Fall Meeting Supplement, Abstract T23D-07.

Reiter, D. and W. Rodi (2006). Crustal and upper-mantle P- and S-velocity structure in central and southern Asia from joint body-and surface-wave inversion, in *Proceedings* of *the 28th Seismic Research Review: Ground-Based Nuclear Explosion Monitoring Technologies*, LA-UR-06-5471, Vol. 1, pp. 209–218.

Ritzwoller, M. and A. Levshin (1998). Eurasian surface wave tomography: Group velocities, *J. Geophys. Res*. 103: 4839–4878.

Ritzwoller, M., A. Levshin, L. Ratnikova, and A. Egorkin (1998). Intermediate-period group-velocity maps across Central Asia, western China, and parts of the Middle East, *Geophys. J. Int*. 134: 315–328.

Ritzwoller, M. H., M. P. Barmin, A. Villasenor, A. L. Levshin, and E. R. Engdahl (2002). Pn and Sn tomography across Eurasia to improve regional seismic event locations, *Tectonophysics* 358: 39–55.

Rodgers, A. J., J. F. Ni, and T. N. Hearn (1987). Propagation characteristics of short-period Sn and Lg in the Middle East, *Bull. Seism. Soc. Am*. 87: 396–413.

Rodgers, A. J., W. R. Walter, R. J. Mellors, A. M. S. Al-Amri, and Y-S. Zhang (1999). Lithospheric structure of the Arabian Shield and Platform from complete regional waveform modeling and surface wave group velocities, *Geophys. J. Int*. 138: 871–878.

Sandvol, E., K. Al-Damegh, A. Calvert, D. Seber, M. Barazangi, R. Mohamad, R. Gok, N. Turkelli, and C. Gurbuz (2001). Tomographic imaging of Lg and Sn propagation in the Middle East, *Pure and Appl.Geophys*. 158: 1121–1163.

Seber, D. and B. Mitchell (1992). Attenuation of surface waves across the Arabian Peninsula, *Tectonophysics* 204: 137–170.

Şengör, A. M. C. and Y. Yılmaz (1981). Tethyan evolution of Turkey: A plate tectonic approach, *Tectonophysics* 75: 181–241.

Shapiro, N. M. and M. H. Ritzwoller (2002). Monte-Carlo inversion for a global shear velocity model of the crust and upper mantle, *Geophys. J. Int*. 152: 88–105.

Villasenor, A., M. H. Ritzwoller, A. L. Levshin, M. P. Barmin, E. R. Engdahl, W. Spakman, and J. Trampert (2001). Shear velocity structure of central Eurasia from inversion of surface wave velocities, *Physics of the Earth and Planetary Interiors* 123: 169–184.

Yamini-Fard, F. and D. Hatzfeld (2006). Microseismicity and crustal structure of the Zagros-Makran Transition Zone (Iran): Evidence for a progressive transition from continental collision to oceanic subduction, in *Proceedings of the 2006 Gulf Seismic Forum*.

Zhang, H., and C. H. Thurber (2003). Double-Difference Tomography: The method and its application to the Hayward Fault, California, *Bull. Seismol. Soc. Am.* 93: 1875–1889.

Zhang, H., and C. Thurber (2005). Adaptive-mesh seismic tomography based on tetrahedral and Voronoi diagrams: Application to Parkfield, California, *J. Geophys. Res.* 110: B04303, doi:10.1029/2004JB003186.

Zhang, H., and C. Thurber (2006). Development and applications of double-difference tomography, *Pure and Applied Geophys.* 163: 373–403, doi:10.1007/s00024-005-0021-y.

Zor E., Sandvol E., J. Xie, N. Türkelli, B. Mitchell, A. H. Gasanov, and G. Yetirmishli (2007). Crustal Attenuation within the Turkish Plateau and Surrounding Regions. *Bull. Seismol. Soc. Am.* 97: 151–161.

A GLOBAL 3D *P*-VELOCITY MODEL OF THE EARTH'S CRUST AND MANTLE FOR IMPROVED EVENT LOCATION

Christopher J. Young[1], Sanford Ballard[1], James R. Hipp[1], Marcus C. Chang[1], Jennifer E. Lewis[1], Charlotte A. Rowe[2], and Michael A. Begnaud[2]

Sandia National Laboratories[1] and Los Alamos National Laboratory[2]

Sponsored by the National Nuclear Security Administration

Award Nos. DE-AC04-94AL85000/SL09-3D_Earth-NDD02[1] and DE-AC52-06NA25396/LA09-IRP-NDD02[2]

ABSTRACT

Effectively monitoring for nuclear tests with yields less than 1 kT using seismic data requires utilizing regional phases whose characteristics vary greatly between different geographic areas. Current approaches typically use separate models developed independently for each area or separate models for regional vs. teleseismic, causing problems when transitioning from one area to another, or from regional to teleseismic distances. Ultimately, what is needed is a single global seamless 3D model derived from a simultaneous inversion of a global data set encompassing regional and teleseismic data from a variety of areas. Several such models have been developed, but generally with the intent of providing insight into the structure of the inner Earth, not of improving treaty-monitoring capability. In this paper, we present our preliminary global *P*-velocity model developed specifically to improve event location using both teleseismic and regional distance phases.

Our base data set is the global EHB catalog, consisting of 130,000 events spanning some 46 years, which was compiled using a specialized algorithm to improve routine event hypocenter locations of global catalogs (e.g., the International Seismiological Centre's Preliminary Determination of Epicenters). We augment this with the more regionally selective Ground Truth (GT) catalog created by researchers at Los Alamos National Laboratory (LANL). The LANL catalog is less geographically-balanced than EHB (1998), but has both more and lower GT-level events for several areas of monitoring interest. Our total number of events is over 200,000, with more than 15 million *P*, *Pn*, and *Pg* ray paths. Because 3D tomography is a strongly non-linear problem, it is important to start with a high-quality initial model. We choose to use a simplified two-layer version of the Crust 2.0 model with a global mantle model recently published by Li et al (2008). To reduce the computational burden of the inversion, and to prevent overweighting due to ray path redundancy, we use representative rays for clusters of rays based on geometric similarity of the entire ray paths traced through our starting model. Using this method, we are able to reduce the number of ray paths by more than 50%. Our model is constructed using the variable resolution tessellation developed by Ballard et al (2009). For the travel time calculations, we use the robust and efficient ray bending algorithm developed by Ballard et al (2009). Sufficient damping is applied to keep the iterative velocity adjustments small enough to be stable, as the updated ray paths change for each iterative model. To produce a model with variable lateral resolution matching ray path coverage and velocity gradients, we use progressive tomographic scale refinement. Both event and site corrections are solved for, but they are introduced only after converging on an intermediate velocity model to force as much of the residual fit into the velocity model as possible. Our inversion was run using the distributed parallel computing framework developed by Sandia National Laboratories (SNL), providing us with over 150 processors, which has been shown to achieve an efficiency of better than 90% for the costly ray-tracing calculations, resulting in more than a 135x speedup over sequential algorithms.

OBJECTIVE

The overall objective of our research is to develop a single, global 3D *P*-velocity model specifically to improve seismic event location from local to teleseismic distances. Though complex to develop, the availability of such a model would considerably simplify the calculation of locations of events of monitoring interest, as well as improve the quality of the locations and the associated uncertainty estimates. Our objective for this first year of our project has been to create and evaluate a prototype model, in the process solving several of the important technical challenges that must be overcome to produce an operationally useful model.

INTRODUCTION

One of the most important characteristics to establish in evaluating a possible nuclear explosion is the location. Location is dependent both on the quality of the data available, which can generally not be controlled, and on the Earth model used, which can be. For large events that are well-recorded at teleseismic distances, an accurate location can be determined using a high-quality global radially-symmetric (1D) reference model such as AK135 (Kennet et al., 1995) because the source to receiver paths are predominantly through the deeper, more laterally homogeneous portions of the Earth and errors in predicted travel time tend to cancel out when azimuthal gap is small. For smaller events, however, some or even all of the signals will only be recorded at regional distances where the source to receiver paths traverse the crust and upper mantle, portions of the Earth that are much less laterally homogeneous. Also, azimuthal gap may be large. To get accurate travel time predictions for regional phases it is necessary to use models that include lateral heterogeneity. There are various possible approaches to doing this. Perhaps the most simple is to use different radially symmetric models for each station. Such models can often be readily obtained from local or regional network operators who use them to produce their catalogs. Any modifications to the event location software required to make use of these station-specific 1D models are generally trivial. However, applying this approach on a global scale introduces non-physical seams between the different 1D regional models and between each regional model and the background teleseismic model. The end result can be very complex and ensuring robust locator behavior across the various seams is not a trivial challenge.

A more practical approach is to model regional phases using a laterally heterogeneous model, such as has been done in the recent development of the Regional Seismic Travel Time (RSTT) model by the Ground-based Nuclear Explosion Monitoring Research & Development program (Myers et al., 2009). This approach is sometimes referred to as geometrically "2.5D" because the model varies fully in the lateral direction, but the mantle is modeled with a single (though laterally varying) gradient. This method produces significantly better travel time predictions and event locations compared to using a standard global 1D reference model, and it is more robust than the amalgamation of regional 1D models discussed above. However, because the regional representation of the Earth is not appropriate for teleseismic phases, it is still necessary to introduce a non-physical seam between the regional model and a background teleseismic model, and this seam must be properly conditioned to ensure proper locator behavior. Further, in producing the tomographic RSTT regional model, it is first necessary to "re-baseline" the known origin times of ground truth data using teleseismic data so that the resultant model will properly locate events with combined regional and teleseismic data.

Thus, while progress has been made towards a model that can produce better locations at regional and teleseismic distances and is simpler to maintain, there is still considerable room for improvement. What is ultimately needed is a model that can produce high quality locations for any data combination, regardless of distance, while possessing no problematic non-physical seams. In short, our ultimate goal is a true 3D model of the Earth, where any seams represent actual physical transitions between different materials within the body of the Earth rather than artifacts introduced by approximations in the modeling approach. Producing such a model is a difficult goal given the tomographer's usual problems of using noisy data that provides incomplete sampling for much of the Earth and oversamples in the limited seismically active regions. In spite of this, several global models have already been produced, providing valuable insight into the overall structure of the inner Earth (e.g., Li et al., 2009). For nuclear explosion monitoring purposes, however, it is not clear that any of the currently available global 3D models provides improved locations, a topic examined in a companion paper (Rowe et al., 2009). This is not necessarily an indication of questionable quality in these models but rather the original purpose in developing them: most tomographic models have been developed to image the Earth's interior, not to improve locations (RSTT being an exception). Our goal in this paper is to take the first step towards production of a global 3D tomographic model whose foremost purpose it to improve event locations from data recorded at distances from local to teleseismic. The model presented

is the first in a series that we hope will eventually lead to an operationally-capable model, and producing it has forced us to address some of important technical challenges, which we document here.

DATA

To provide good overall coverage, we choose as our base dataset the global EHB catalog (Engdahl et al., 1998), which was compiled using a specialized algorithm to improve routine event hypocenter locations of various global catalogs (e.g., ISC, PDE). We used the recently updated version of EHB consisting of 131,000 events spanning 46 years (http://www.isc.ac.uk/EHB/index.html). Sources and receivers for the EHB catalog are shown in Figure 1. For the purposes of this study, we use only *P*, *Pn*, and *Pg* data, resulting in about 14 million ray paths. Because we are interested in developing a model with the best possible location capability in focused areas of monitoring interest, we augment EHB with the more regionally selective GT catalog created by researchers at LANL. The 77,000-event LANL catalog is less geographically-balanced than EHB, but has both more and lower GT-level events for several areas of monitoring interest. The total number of *P*, *Pn*, and *Pg* ray paths for the LANL catalog is more than 8 million.

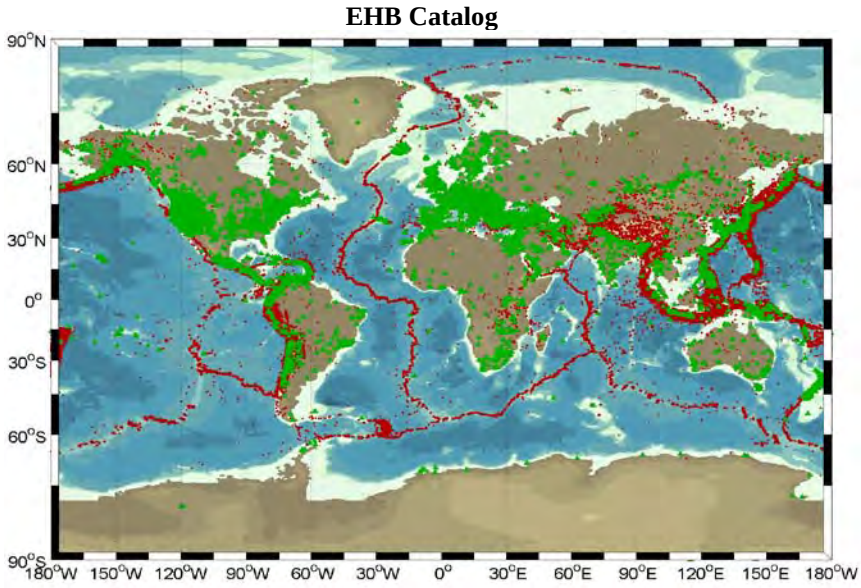

Figure 1. Origins (red circles) and stations (green triangle) for the EHB catalog.

Figure 2 shows histograms of travel time residuals relative to AK135 for the EHB catalog for both *P* and *Pn*. Because AK135 is global average model and this is a global data set, there is very little overall bias for either phase, as would be expected (0.103 s for *Pn* and 0.005 s for *P*). However, the standard deviations, especially for *Pn* (2.204 s), indicate that there is considerable misfit between the data and the model.

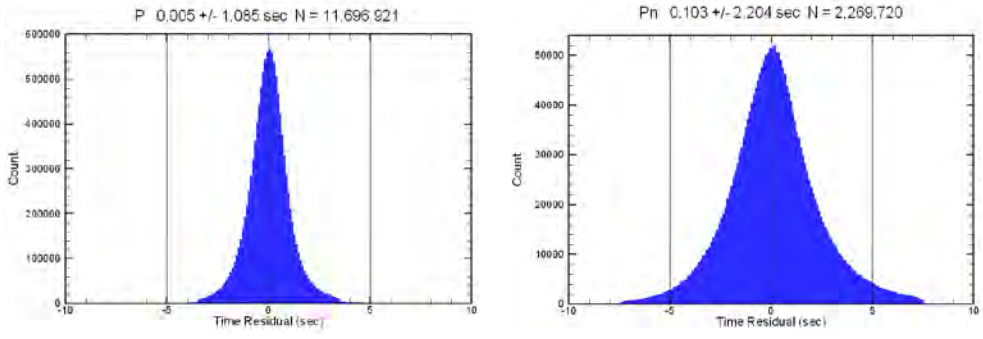

Figure 2. AK135 travel time residual histograms for (left) *P* and (right) *Pn* for all ray paths for the LANL GT catalog.

To establish whether this variance is due to inadequacy in the AK135 model or can be attributed entirely to random error in phase picks and/or in the source locations, we made maps of source-plotted residuals for individual stations. Many of these show coherent regionally varying trends in the residuals, suggesting that a large portion of the variance in the histograms is due to laterally varying velocity structure that is not modeled with the radial AK135 model. As a particularly compelling example, we show the map for station OBN in Russia in Figure 3. The most striking feature is a sharp transition from strongly negative residuals in the eastern Mediterranean and Middle East to positive residuals in the south central Asia. This pattern of residuals argues strongly for laterally varying Earth structure. Clearly there is no radially symmetric model that can fit these residuals.

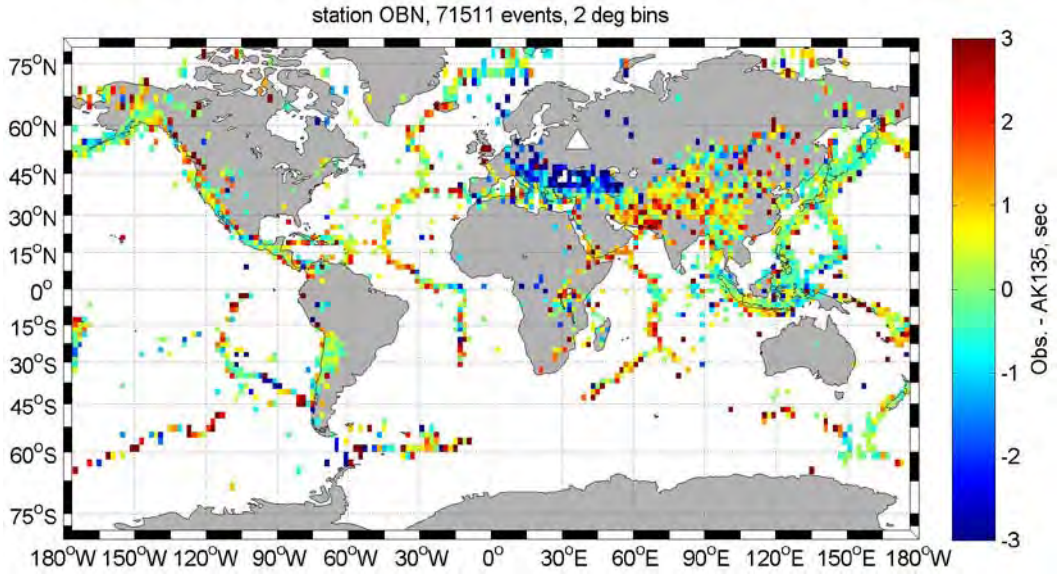

Figure 3. AK135 residuals for the EHB catalog plotted at source locations for station OBN (triangle).

MODEL REPRESENTATION AND INTERPOLATION

Our tomographic model is represented as a set of velocity/slowness nodes using the 3D grid approach described by Ballard et al. (2009). The model consists of different 1D layered radial profiles from the surface of the Earth to the core with all major velocity discontinuities represented, and each of these profiles is tied to one of a set of different geographic (latitude, longitude) nodes that are connected with an ordered set of nested tessellations. Progressively finer tessellation levels are generated by successive subdivision of the triangles of the first level tessellation, which is an icosahedron. Each subsequent level is assigned to progressively shallower discontinuities in the Earth, thereby achieving variable resolution in the radial dimension (Figure 4). An underlying assumption of this approach is that greater resolution is needed at shallower depths, which is in agreement with the conventional understanding of Earth structure. An important feature of this approach is the subdivision of triangles only occurs where the model needs additional resolution as defined both by ray hit count and by lateral variability in the velocity structure emerging during tomography, thus providing a variable scale model that is needed to reflect the uneven data sampling and the well-established laterally varying structure of the Earth. As described below (in the Tomographic Inversion section), we exploit this feature of the model representation to make the inversion process efficient and robust.

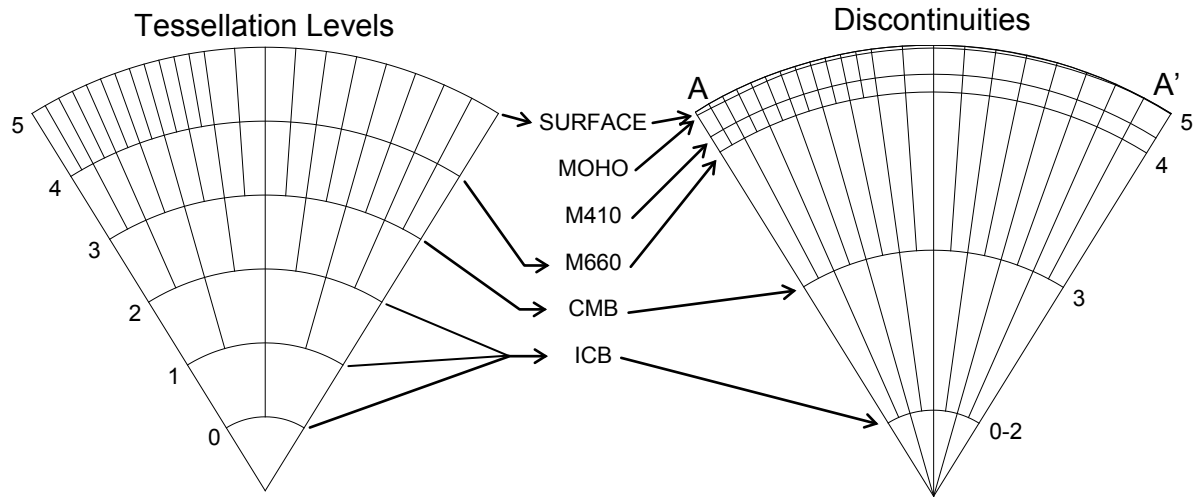

Figure 4. Progressive subdivision of icosahedron tessellation to level 6 and relationships to major velocity discontinuities.

Constructing ray paths and calculating travel times through the model requires obtaining velocity/slowness estimates at arbitrary positions in the mode. This is done through a two-stage interpolation process. First, using a walking triangle search (Lawson, 1977) we find the containing triangle in the surface tessellation for the latitude, longitude position of the point to be interpolated. This search starts at the coarsest tessellation level and proceeds to whatever finer tessellation levels are available for the position in question (i.e., we proceed to the next level if the containing triangle at the current level has been subdivided). The interpolation coefficients of the triangle nodes (the barycentric coordinates) are calculated as part of the triangle search and so they are already available when the containing triangle is found. Interpolation using these weights will produce a continuous result from one triangle to the next.

The second step is to find the layer within which the point of interest resides within the radial profiles corresponding to each of the nodes of the containing triangle. Once this is done, interpolation at the appropriate depth is completed for each of these profiles, and then these three interpolated values are combined using the containing triangle coefficients from the triangle search. In this manner, velocity at any point within our model can be quickly and accurately calculated. The process is described in much greater detail in Ballard et al. (2009).

RAY PATH AND TRAVEL TIME CALCULATIONS

Ray paths and corresponding travel times are calculated using our own version of the Um and Thurber (1987) ray pseudo-bender (Ballard et al., 2009). Our implementation includes a modified version of the Zhao and Lie (2004) method of handling discontinuities by implementing a 2D minimization algorithm that searches for the point on the velocity discontinuity surface where Snell's Law is satisfied. We reduce the likelihood that the pseudo-bending algorithm will return a local minimum by starting the ray calculation from several different starting rays. Specifically, interfaces are defined that include first order discontinuities plus additional interfaces at levels of the model where local minima are anticipated. Rays are computed that are constrained to bottom in each layer between these interfaces. The computed rays might be reflected off the top of the layer, turn within the layer, or diffract along the interfaces at the top and/or bottom of the layer. The computed ray that is seismologically valid and that has the shortest travel time is retained.

Once a ray path has been defined as a set of nodes via the pseudo-bender, including one node on each velocity discontinuity as part of the calculation to honor Snell's Law, we can calculate travel time by multiplying the inter-node segment lengths by the average slowness for the bounding nodes on each end of the segments and integrating over the entire path. Comparison with analytic tau-P calculations for a 3D version of the AK135 model demonstrate that our calculation is accurate to within a few hundredths of a second for distances from regional to teleseismic.

Though our pseudo-bender has been made as efficient as possible, calculating millions of 3D ray paths for each iteration of the tomography is time-consuming and could constrain the amount of model exploration that can be

done. We overcome this problem by calculating the rays utilizing a distributed parallel computing system that we have developed based on the Java Parallel Processing Framework (JPPF), providing us with 150 processors, which have been shown to achieve an efficiency of better than 90% for the costly ray-tracing calculations, resulting in more than a 135x speedup over sequential algorithms. Utilizing this framework allows us to produce a model in less than a day that would otherwise have taken weeks, hence making it possible for us to investigate a much richer range of the total model space.

TOMOGRAPHIC INVERSION

The tomographic inversion is a standard iterative least squares solution to the linearized relation between travel time residual for each path and slowness adjustments to each node:

$$\Delta t_j = \sum_{i=1}^{N} w_i \Delta s_i \tag{1}$$

Where Δt_j is the travel time residual for the j^{th} path, Δs_i is the slowness adjustment for the ith node (of N), and w_i is the weight for the ith node. Though not immediately obvious, this travel time calculation is in fact path length multiplied by delta slowness, but the path lengths have been incorporated into the node weights.

To account for differing quality of data, for each ray path both the residual and ray path summation are inversely weighted by the estimated measurement error for each observation. Damping is applied due to the fact that the many parts of the model are under-constrained by the data, and also to control the size of the slowness/velocity adjustments to the model between iterations, which is essential for true non-linear 3D tomography where path geometries are updated after each iteration. Our previous research has demonstrated that allowing large velocity changes between iterations can lead to correspondingly large changes in ray paths which in turn lead to instability in the overall tomographic process. Increasing the damping is a simple and effective way to control this. We also invert for both receiver and source static corrections, but only introduce these parameters after a stable tomographic model has been achieved (we restart the inversion with the stable model as the starting model) to control the amount of signal that is mapped into the corrections.

Because 3D tomography is a strongly non-linear problem with many local minima, it is important to start with as good an initial model as possible. We use the mantle model of the recent 3D global tomographic model by Li et al. (2009) overlain by a simplified two-layer crustal model derived from Crust 2.0 (Bassin et al., 2000).

To achieve variable resolution in our model, we use a progressive tomographic refinement approach (Simmons et al., 2009). In our implementation, the tomography is accomplished with two major iterative loops. The outer loop is over a fixed locally adapted model that can change for each new outer iteration. The inner iteration is a standard tomography calculation that uses the current outer iteration model and its set of "active nodes" to calculate the total change in slowness. By active nodes we mean the set of nodes defined within the current outer iteration model whose velocity is modifiable. The set of active nodes may include previously adapted nodes (added in an earlier outer iteration) and new nodes that were locally added specifically for the current iteration. One of the goals of our research is to define how previously adapted nodes are included in the current outer iteration. They may be entirely excluded, or included with some amount of damping. Active nodes added several iterations before may be entirely excluded with those closer to the current generation incurring less and less damping the nearer their generation is to the current iteration.

The inner iteration is a standard tomography calculation using the active node set from the current outer iteration model. Inner iteration convergence is declared when slowness is no longer appreciably changing. What is different from standard tomography is how active nodes are included in tomography. In the new adaptive inner iteration only nodes that are still included from previous iterations (based on damping considerations described in the previous paragraph) and those new ones in the current iteration are allowed to participate in the tomography calculation. Additionally, only nodes from this set that have a non-zero ray hit count are allowed to be modified. Nodes with zero hit count are excluded, which is equivalent to processing with infinite damping. This ensures that nodes that cannot contribute to the solution are not inadvertently refined because of movement caused by insufficient damping. It also reduces the total column count in the sparse matrix ensuring faster solution times.

Once an inner iteration tomography run converges, the change in slowness is examined on each node to see which nodes exceed some predefined input tolerance. Those nodes that exceed the tolerance are provided to a model constructor, along with the current model, to build the new refined model for the next outer iteration. Only nodes that surpassed the input slowness change criteria are refined, or split, into a new set of nodes within the new model. The new model is then used for the next outer iteration.

The entire process converges when no slowness change on any active node exceeds the input tolerance or if a predefined input refinement level is reached. This avoids refining to extremely small grid spacing.

RAY REDUCTION

Because of the repeating nature of earthquakes, there is tremendous redundancy in some of the ray paths through the Earth in our data sets. Prior to inverting the data for our tomographic model we choose to remove this redundancy for two reasons. First, unless properly accounted for, redundant ray paths through the Earth will result in a higher weight in the tomographic inversion, with the significance of these rays being effectively multiplied by the number of redundant observations. For our purposes, a single path from a low GT event in area of monitoring interest is at least important (if not more) than multiple repeated paths from deep earthquakes in a subduction zone, so this is an important consideration. Second, each observation requires an additional ray bender calculation through the 3D model, a computationally expensive operation that we would prefer to make no more often than necessary. Thus, by eliminating redundancy we can correct the weighting problem as well as speed up the inversion.

We remove redundant rays by hierarchical agglomerative clustering (dendrograms) based on similarity of the ray paths. We base our similarity on the node weights calculated in Equation 1. These weights completely and uniquely characterize the ray path geometry. The distance in node space between rays *j* and *k* is:

$$\Delta_{j,k} = \sqrt{\sum_{i=1}^{N} (w_{i,j} - w_{i,k})^2} \tag{2}$$

where *N* is the number of nodes in the model, and most weights are zero for a given ray path. To convert this into a similarity that scales between 0 and 1 we normalize and subtract from 1:

$$S_{j,k} = 1 - \frac{\Delta_{j,k}}{\sqrt{\sum_{j=1}^{N} w_j^2 + \sum_{k=1}^{N} w_k^2}} \tag{3}$$

Calculating similarities between every pair of rays in such a large data set is impractical, but fortunately also unnecessary. We can make a few simplifying assumptions. First, because we expect the ray reduction to be primarily due to nearby sources, we only calculate similarities for rays to the same station. Second, we do not want to combine rays from different GT quality levels. Third, we know that if the distances between the sources are large enough, then the rays are not similar. We conservatively chose our threshold to be 3 degrees. Thus, for each station, for each GT level, we calculated similarities for all rays with sources less than 3 degrees apart.

Based on these similarities we then perform a separate agglomerative hierarchical clustering for each station/GT level set to indentify similar rays that can be replaced with single representative rays. Based on trial and error, we established that a threshold similarity of 0.7 will result in ray clusters whose source span has a radius no bigger than 0.5 degree, which we felt was appropriate given the target resolution of our model. The position of the source for the representative ray for each cluster is the mean position of the individual sources. To compute a travel time for the representative ray, we first calculate residuals for each original ray relative to AK135, then find the inverse variance (σ^2) weighted average of the M individual residual times (t_i) to come up with a representative ray residual time (σ^2):

$$t_{rr} = \frac{\sum_{i=1}^{M} \frac{t_i}{\sigma_i^2}}{\sum_{i=1}^{M} \frac{1}{\sigma_i^2}} \tag{4}$$

which is then added back to the calculated AK135 time for the representative ray to get travel time. For the uncertainty associated with the representative time, we perform a similar inverse variance weighted average of the individual variances:

$$\sigma_{rr}^2 = \frac{\sum_{i=1}^{M} \frac{\sigma_i^2}{\sigma_i^2}}{\sum_{i=1}^{M} \frac{1}{\sigma_i^2}} = \frac{M}{\sum_{i=1}^{M} \frac{1}{\sigma_i^2}} \tag{5}$$

Our overall reduction in ray paths is greater than 50%, providing a significant improvement in computational efficiency for generating the tomographic model.

CONCLUSIONS AND RECOMMENDATIONS

We have developed and implemented an approach to constructing a single, seamless, mutli-scale global 3D *P* velocity model that we will apply to our large data set from the combined EHB and LANL GT catalogs. We hope that the resultant model will be the first step towards an operationally capable 3D global model. In our poster presentation we will show the model itself and evaluate its effectiveness in reducing geographic variations in travel time residuals and in improving event locations.

ACKNOWLEDGEMENTS

We are grateful to Bob Engdahl, Rob van der Hilst, and Ray Buland for creating and making available the EHB catalog, which has greatly aided this and many other research efforts. We are also indebted to the staff at the ISC for providing ready access to the most recent version of the EHB catalog through their web site.

REFERENCES

Ballard, S., J.R. Hipp, and C.J. Young (2009). Efficient and accurate calculation of ray theory seismic travel time through variable resolution 3D earth models, *Seismol. Res. Lett*. (in press).

Bassin, C., G. Laske, G. and Masters (2000). The current limits of resolution for surface wave tomography in North America (abstract), *EOS Trans AGU* 81: F897.

Engdahl, E.R., R. van der Hilst, and R. Buland (1998). Global teleseismic earthquake relocation with improved travel times and procedures for depth determination, *Bull. Seismol. Soc. Am*. 88: 722–743.

Kennett, B.L.N., E.R. Engdahl, R. Buland (1995). Constraints on seismic velocities in the Earth from taveltimes, *Geophys. J. Int*. 122: 108–124.

Lawson, C. L., 1977. *Software for C1 surface interpolation, in Mathematical Software III*, ed. J. Rice, Academic Press, New York.

Li, C., R. D. van der Hilst, E. R. Engdahl, S. Burdick (2008). A new global model for *P* wave speed variations in Earth's mantle, *Geochem. Geophys. & Geosystems* 9: 5, 21 pp.

Myers, S.C., S. Ballard, C. Rowe, G. Wagner, M. Antolik, W. S. Phillips, A. Ramirez, M. Begnaud, M. E. Pasyanos, D. Dodge, M. P. Flanagan, J. Dwyer, K. Hutchenson, D. Russell (2009). Gloal crust and upper mantle tomography for improved seismic location (abstract), presented at 2009 Seismol. Soc. Am. Annual Meeting.

Simmons, N.A., S.C. Myers, and A.L. Ramirez (2009). Multi-resolution seismic tomography of regional and mantle scale structures using tessellation-based node definitions (abstract), presented at 2009 SSA Annual Meeting.

Um, J. and C. H. Thurber (1987). A fast algorithm for two-point seismic ray tracing, *Bull. Seismol. Soc. Am*. 77: 972–986.

Zhao, D. and J. Lei (2004), Seismic ray path variations in a 3D global velocity model, *Phys. Earth Planet. In*. 141: 153–166.

REGIONAL-SCALE DIFFERENTIAL TIME TOMOGRAPHY METHODS: DEVELOPMENT AND APPLICATION TO THE SIBERIA DATA SET

Haijiang Zhang[1, 2], Kevin G. Mackey[3], Kazuya Fujita[3], Clifford H. Thurber[1], Lee K. Steck[4], Charlotte A. Rowe[4], Steven Roecker[5], and M. Nafi Toksoz[2]

University of Wisconsin-Madison[1], Massachusetts Institute of Technology[2], Michigan State University[3], Los Alamos National Laboratory[4], and Rensselaer Polytechnic Institute[5]

Sponsored by the National Nuclear Security Administration

Award No. DE-FC52-06NA27325
Proposal No. BAA06-77

ABSTRACT

This is the final year of a collaborative project by the University of Wisconsin-Madison (UW-Madison), Massachusetts Institute of Technology (MIT), Michigan State University (MSU), and Los Alamos National Laboratory (LANL). There are four main tasks in this project: (1) an extension of our development of double-difference (DD) seismic tomography to the use of station-pair residual differences, including incorporation of a new method for resolution matrix calculation; (2) testing, refinement, and adaptation of a method for spherical-earth finite-difference (SEFD) travel time calculations for use in DD tomography; (3) an extension of our Cartesian adaptive-grid DD tomography algorithm to spherical coordinates; and (4) collaborative work among the UW-Madison, MIT, MSU, and LANL groups to apply these analysis tools to the Siberia data set.

As reported in previous Monitoring Research Review proceedings, we have successfully incorporated station-pair differential times into the extended DD tomography code. A new resolution matrix calculation method based on the PROPACK package is also incorporated and tested, which is able to efficiently and accurately estimate singular values and vectors for large matrices based on the Lanczos bidiagonalization with partial reorthogonalization. In our tomography algorithm, we use a spherical-Earth finite-difference (SEFD) travel time method to calculate travel times and trace rays. The basic concept is the extension of a standard Cartesian FD travel time algorithm to the spherical case through development of a mesh in radius, co-latitude, and longitude, expression of the finite difference (FD) derivatives in a form appropriate to the spherical mesh, and the construction of "stencils" to calculate extrapolated travel times. We benchmarked the SEFD method against the "sphere-in-a-box" Cartesian FD travel time algorithm (Flanagan et al., 2007). We have applied the extended DD tomography algorithm separately to the southern (Baikal and Amur regions) and northern (Magadan and eastern Yakutsk regions) parts of the eastern Siberia. The velocity models in both parts show strong heterogeneities at shallow depths, as expected for the variable and complicated nature of the crust.

For this last year, we focus our effort on extending the spherical regular-grid DD tomography code to the adaptive version, in which the inversion grid nodes are adapted according to the data distribution. In addition to the data we already collected for the Baikal, Amur, Magadan and Yakutsk regions, we also collect the data for the Kamchatka region. We first apply the spherical regular-grid DD tomography method to the whole data set to obtain a seamless velocity model for eastern Siberia. The adaptive-grid DD tomography method will also be applied to the whole data set. The model will be tested using the peaceful nuclear explosions (PNEs) that occurred and were recorded in the region.

OBJECTIVES

The objectives of this project are to investigate and develop new and improved methodologies for regional-scale three-dimensional (3D) seismic tomography using a combination of event- and station-pair arrival time differences, and to apply the new methods to the MSU and LANL Siberia database. The tomographic work proposed here will provide a more reliable velocity model for both the crust and upper mantle of eastern Siberia. There are four main tasks in this project: (1) an extension of our development of double-difference (DD) seismic tomography to the use of station-pair residual differences, including the incorporation of a new method for resolution matrix calculation; (2) testing, refinement, and adaptation of a method for SEFD travel time calculations for use in DD tomography; (3) an extension of our Cartesian adaptive-grid DD tomography algorithm to spherical coordinates; and (4) collaborative work among the UW-Madison, LANL, and MSU groups to apply these analysis tools to the Siberia data set. In the last year of this project, our focus is to assemble a data set for the whole eastern Siberia region and determine both the 3D *P*- and *S*-wave velocity models.

RESEARCH ACCOMPLISHED

Tectonic Setting

Eastern Russia is composed of a series of allochthonous terranes that have accreted to the Precambrian Siberian (North Asian) craton (Figure 1). In the southern part (Baikal and Amur regions), terranes form a suture zone between the Siberian and North China cratons. The terranes vary in age, but a large majority of them accreted in the Mesozoic and Cenozoic. Superimposed on the Meso-Cenozoic accretionary complex is the present-day plate boundary system between the Eurasian, North American, and Pacific plates (Figure 2). The complexities of intracontinental deformation have resulted in the development of several microplates (or blocks) and broad zones of deformation. In addition to compressional features that dominate continental northeast Asia, there are extensive areas of Late Cenozoic coastal sediments and, in parts of the Russian Northeast and in Baikal, active and Cenozoic rift systems (Fujita et al., 1997).

The present-day plate boundaries are a result of the interaction of the North American, Eurasian, and Pacific plates. In northeastern Russia, the Arctic Mid-Ocean rift (Figure 2) propagates into the Asian continent in the Laptev Sea. Active rifting has been documented through focal mechanism studies (e.g., Fujita et al., 1990) and seismic reflection profiling (Drachev et al., 1998) through the Laptev Sea, up to the southern end of Bour Khaya Gulf. This tectonic evolution has created a very heterogenous crust, ranging from old Precambrian shields to young areas of active rifting. This heterogeneity should be reflected in both the crustal and upper mantle structure of the region, which can be identified through tomographic modeling

Data Collection and Quality Control

We have assembled a data set for the eastern Siberia region in the area of 40^o to 75^o latitude and 100^o to 175^o longitude for the period of 1977 to 2007 from the MSU and LANL Siberia database. There are ~228,000 *P* (*Pg*+*Pn*) and ~231,000 S (*Sg*+*Sn*) phases corresponding to ~28000 events and ~290 stations. For each event, there are at least 5 observations. Figure 3 shows composite travel curves for *Pg* and *Sg* and first *P* and *S* arrivals, respectively. From the travel time curves shown in Figure 3, we note there are some outliers in the catalog picks. We cleaned up the *P* and *S* times by removing outliers falling outside the major trend of the travel time curves (indicated by green bands for *Pg*+*Sg* and red bands for first *P*+*S* arrivals). As a result, we obtained ~190,000 first *P* and ~160,000 first *S* arrivals. In comparison, there are ~46,000 Pg and ~81,000 Sg times. In this paper, we only report on the seismic tomography study using the first *P* and *S* arrivals.

Model Resolution Analysis

For a linear inverse problem with *m* observations and *n* model parameters, the singular value decomposition (SVD) of the *m* by *n* sensitivity matrix **A** is

$$\mathbf{A} = \mathbf{U}\mathbf{S}\mathbf{V}^{\mathrm{T}} = \sum_{i=1}^{n} s_i \mathbf{u}_i \mathbf{v}_i^{\mathrm{T}} , \quad (1)$$

where the matrices $\mathbf{U} \in \mathrm{R}^{m \times m}$ and $\mathbf{V} \in \mathrm{R}^{n \times n}$ are orthogonal and **S** is an *m* by *n* diagonal matrix with nonnegative diagonal elements called singular values. The singular values are generally arranged in decreasing size (Aster et al., 2005).

If only the first *p* nonzero singular values are chosen, the truncated SVD of **A** is

$$\mathbf{A} = \mathbf{U}_p \mathbf{S}_p \mathbf{V}_p^T = \sum_{i=1}^{p} s_i \mathbf{u}_i \mathbf{v}_i^T \cdot \tag{2}$$

The pseudoinverse of **A** is then given by

$$\mathbf{A}^{-1} = \mathbf{V}_p \mathbf{S}_p^{-1} \mathbf{U}_p^T . \tag{3}$$

The resolution matrix **R** is represented as

$$\mathbf{R} = \mathbf{A}^{-1}\mathbf{A} = (\mathbf{A}^T\mathbf{A})^{-1}\mathbf{A}^T\mathbf{A} = \mathbf{V}_p\mathbf{V}_p^T , \tag{4}$$

which acts as a filter between the true and inverted model parameters.

Because of the noise in the data and ill-conditioning of the system, it is typically necessary to use some regularization methods to stabilize the inverse system. Suppose the regularization operator is **L**, then the regularized inverse of **A** is

$$\mathbf{A}^{-} = (\mathbf{A}^T\mathbf{A} + \alpha^2\mathbf{L}^T\mathbf{L})^{-1}\mathbf{A}^T . \tag{5}$$

The most common regularization tool is damping, or zeroth-order Tikhonov regularization (Aster et al., 2005). Assuming the damping factor is λ, the pseudoinverse of **A** in this case is defined as

$$\mathbf{A}^{-} = \mathbf{V}\mathbf{S}^{-1}\mathbf{D}\mathbf{U}^T , \tag{6}$$

where **D** is a diagonal matrix defined as

$$\mathbf{D} = \frac{\mathbf{S}^2}{\mathbf{S}^2 + \lambda^2\mathbf{I}} . \tag{7}$$

In the case of using other non-diagonal regularization methods such as first-order or second-order smoothing constraints, there is no simple way equivalent to Equation (6) to represent the pseudo-inverse of the matrix **A**, although the generalized SVD can be used to develop a similar representation (Aster et al., 2005).

Suppose the SVD of the augmented matrix $\mathbf{B} = \begin{bmatrix} \mathbf{A} \\ \alpha\mathbf{L} \end{bmatrix}$ is defined as $\mathbf{B}=\mathbf{Q}\mathbf{P}\mathbf{\Lambda}^T$. The resolution matrix **R** in this case is equal to

$$\mathbf{R} = \mathbf{Q}\mathbf{\Sigma}\mathbf{Q}^T , \tag{8}$$

where $\mathbf{\Sigma}$ is given by $\mathbf{\Sigma} = \mathbf{I} - \mathbf{\Lambda}^{-1}(\mathbf{P}_2)^T(\mathbf{P}_2)\mathbf{\Lambda}$ and $\mathbf{P}_2$ is the submatrix of **P** corresponding to the *Nr* rows of the smoothing constraints (Vasco et al., 2003). In many cases, one also includes damping in addition to the smoothing constraints. In this case $\mathbf{\Sigma}$ is given by

$$\mathbf{\Sigma} = \mathbf{D}\mathbf{\Lambda}^{-1}\left(\mathbf{I} - (\mathbf{P}_2)^T(\mathbf{P}_2)\right)\mathbf{\Lambda} \tag{9}$$

Recently, a package called PROPACK that can accurately estimate the singular values and vectors for sparse matrices was developed by Larsen (1998). The PROPACK package is based on the Lanczos bidiagonalization process but it is able to estimate the larger singular values and vectors more accurately. We integrate the PROPACK package into the spherical-earth double-difference seismic tomography code *tomoSPDD* to estimate model resolution and covariance matrices for various problem sizes, similar to what was done with *tomoDD* (Zhang and Thurber, 2007). This method is shown to be very efficient for estimating the full model resolution matrix for inverse problems having hundreds of thousands of observations and tens of thousands of model parameters. Using this method, estimating the full model resolution matrix is no longer a significant challenge for large inverse problems.

Determining the Velocity Model for the Eastern Siberia

We noticed that in the selected data base of first arrivals, many events actually lie in the Kamchatka region. We decimated events in the Kamchatka region by selecting those having the maximum number of phases in a 3D grid of 0.05° in latitude by 0.2° in longitude and by 1 km in depth. As a result, the number of events decreases from 19250 to 9513. In total, there are 109000 P and 87800 S phases selected on 257 stations (Figure 4). The inversion grid intervals are 1° in latitude and 2° in longitude. In depth, the grid nodes are positioned at 0, 15, 30, 35, 45, 75, and 115 km. Because of the large grid intervals, we only used the absolute arrivals in the spherical double-difference tomography code *tomoSPDD*, in which a spherical pseudo-bending ray tracing algorithm is adopted. We started the inversion from a 1D Vp velocity model with a constant Vp/Vs ratio of 1.732. Both smoothing and damping regularization methods are used to make the tomograhic system stable. The optimal smoothing weight and damping parameters are selected through a trade-off analysis of model variance and data variance. The initial travel time residuals show a skewed distribution centered around 2 s (Figure 5). After 5 simultaneous inversions, the travel time residuals have a Gaussian-like distribution (Figure 5), indicating the systematic errors in seismic event locations and velocity model are corrected. The unweighted root-mean-square (RMS) residual reduces from 2.927 s to 0.607 s. The model resolution is assessed using the diagonal values of the resolution matrix, calculated using PROPACK (Figure 6). Considering the smoothing, regions with resolution values greater than 0.2 are expected to be relatively well resolved.

The crustal Vp and Vs models (Z = 0 and 15 km of Figures 7 and 8) generally reflect many Cenozoic tectonic features and are in general agreement with previous studies. There are low velocities below the presently active Kamchatka volcanic arc. Sakhalin has low crustal velocities (Vp ~ 5.8-6.0 km/sec, Vs ~ 3.3-3.4 km/sec) as also determined by Mackey et al. (2003) and Steck et al. (2009). The shallow region under the Baikal rift has slightly elevated Vp and Vs, as noted by Mackey et al. (2003) and in Soviet long-range refraction profiles (e.g., Pavlenkova et al., 2002). Unfortunately, our results do not extend into the Siberian platform or outside the Chersky Seismic Belt (CSB) at shallow depths, thus we are unable to determine whether the CSB has a lower velocity than adjacent areas. Like other studies, there is insufficient resolution to determine if the crustal seismic velocities determined here reflect the accretionary history of the region in detail (Figures 1, 7, and 8).

The upper mantle slices (Z = 35-115 km of Figures 7 and 8), show lower velocities under the Baikal rift zone and extending under the basins to the northeast (e.g., Gao et al., 1994) and, possibly, eastwards towards Sakhalin as well. In Kamchatka, the low velocities appear to persist to a depth of about 100 km, presumably reflecting the mantle wedge and partial melting above the subducting lithosphere.

Lower velocities also appear to exist at both shallow and deeper depths in various parts of the CSB and near the coast of the Arctic Ocean. The former may reflect rifting in the presumed post-Pliocene Moma rift episode (e.g., Fujita et al., 1990) or widespread plume-like activity as suggested by Grachev (2003). In the 15 km depth slice of the Vp model (Figure 7), low velocities near 63°N, 135-140°E are close to a region of thin crust (Mackey et al., 1998) with elevated heat flow (Parfenov et al., 1988). The latter correlates with the southernmost extent of extension associated with the Arctic (Gakkel) mid-ocean ridge.

CONCLUSIONS AND RECOMMENDATIONS

We assembled a dataset for eastern Siberia comprising *Pn*+*Pg* and *Sn*+*Sg* picks. A spherical regular-grid double-difference tomography code *tomoSPDD* is applied to the assembled first *P* and *S* arrivals to obtain both Vp and Vs models of eastern Siberia. The PROPACK package is incorporated into the code to estimate the model resolution matrix based on the Lanczos bidiagonalization with partial reorthogonalization. The velocity model shows good correlation with the local geological settings and other studies. We plan to use the adaptive inversion mesh based on tetrahedral diagrams according to the data coverage to further refine the velocity model. We will also test it using the PNEs that occurred and were recorded in the region.

REFERENCES

Aster, R.C., B. Borchers, and C. H. Thurber (2005). *Parameter estimation and inverse problems*, Elsevier Academic Press, Burlington, MA, 301 pp.

Drachev, S. S., L. A. Savostin, V. G. Groshev, and I. E. Bruni (1998). Structure and geology of the continental shelf of the Laptev Sea, eastern Russian Arctic, *Tectonophysics* 298: 357–393.

Fujita, K., F. W. Cambray, and M. A. Velbel (1990). Tectonics of the Laptev Sea and Moma rift systems, northeastern USSR, *Mar. Geol.* 93: 95-118.

Fujita, K., D. B. Stone, P. W. Layer, L. M. Parfenov, and B. M. Koz'min (1997). Cooperative program helps decipher tectonics of northeastern Russia: *Transactions of the American Geophysical Union (Eos)* 78: 245, 252–253.

Flanagan, M. P., S. C. Myers, and K. D. Koper (2007). Regional travel-time uncertainty and seismic location improvement using a three-dimensional *a priori* velocity model, *Bull. Seism. Soc. Am.* 97: 804–825.

Grachev, A. F. (2003). The Arctic rift system and the boundary between the Eurasian and North American lithospheric plates: New insight to plate tectonic theory, *Russ. J. Earth Sc.* 5: 307–345.

Gao , S., P. M. Davis, H. Liu, P. D. Slack, Y. A. Zorin, N. A. Logatchev, M. Kogan, P. D. Burkholder, and R. P. Meyer (1994). Asymmetric upwarp of the asthenosphere beneath the Baikal rift zone, Siberia, *J. Geophys. Res.* 99: 15319–15330.

Larsen, R. M. (1998). Lanczos bidiagonalization with partial reorthogonalization, Department of Computer Science, Aarhus University, Technical Report, DAIMI PB-357, September 1998. The PROPACK package realizing this algorithm is available at http://soi.stanford.edu/~rmunk/PROPACK/.

Mackey, K. G., K. Fujita, and L. J. Ruff (1998). The crustal thickness of northeast Russia, *Tectonophysics* 284: 283–297.

Mackey, K. G., K. Fujita, L. K. Steck, and H. E. Hartse (2003). Seismic Regionalization in Eastern Russia, in *Proceedings of the 25th Seismic Research Review—Nuclear Explosion Monitoring: Building the Knowledge Base,* LA-UR-03-6029, Vol. 1, pp. 73–82.

Parfenov, L. M., B. M. Koz'min, O. V. Grinenko, V. S. Imaev, and L. P. Imaeva (1988). Geodynamics of the Chersky seismic belt, *J. Geodyn.* 9: 15–37.

Pavlenkova, G. A., K. Priestley, and J. Cipar (2002). 2D model of the crust and uppermost mantle along RIFT profile, Siberian craton, *Tectonophysics* 355: 171–186.

Steck, L. K., W. S. Philips, K. Mackey, M. L. Begnaud, R. J. Stead, and C. A. Rowe (2009). Seismic tomography of crustal *P* and *S* across Eurasia, *Geophys J. Int.* 177: 81–92.

Vasco, D.W., L. R. Johnson, and O. Marques (2003). Resolution, uncertainty, and whole Earth tomography, *J. Geophys. Res.* 108: (B1), 2022.

Zhang, H. and C. H. Thurber (2007). Estimating the model resolution matrix for large-seismic tomography problems based on Lanczos bidiagonalization with partial reorthogonalization, *Geophys. J. Int.* 170: 337–345.

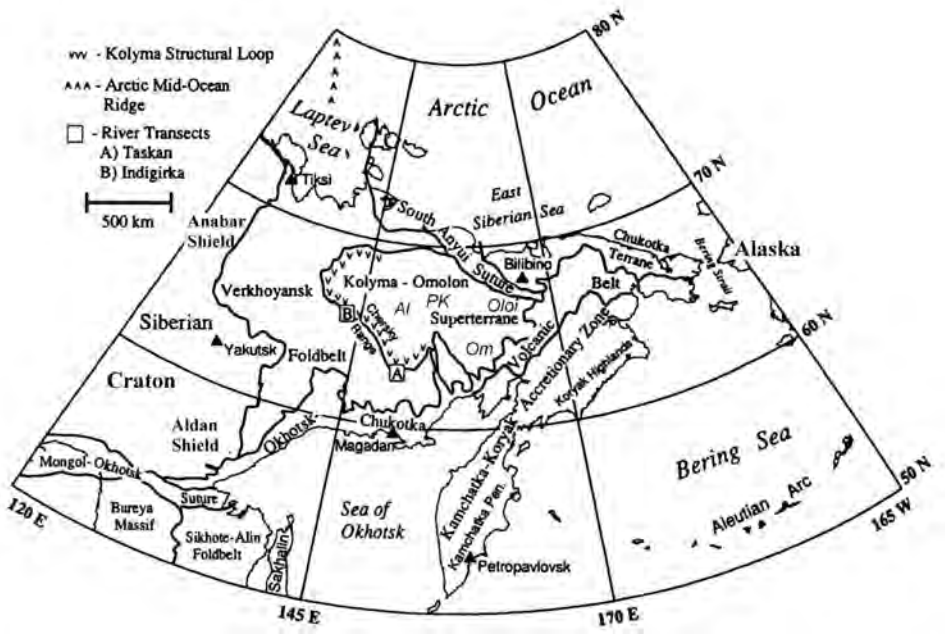

Figure 1. Geologic index map of northeastern Russia showing major tectonic provinces. The Arctic Mid-Ocean Ridge is shown by inverted v's, the Kolyma structural loop of Zonenshain *et al.* (1990) is shown by v's. Global seismic network stations are shown by triangles. River transects conducted by the University of Alaska (transect B also in conjunction with Michigan State University) are shown by lettered boxes. Abbreviations: Al – Alazeya arc, PK – Prikolyma terrane, Om – Omolon terrane, Oloi – Oloi arc. Figure adapted from Fujita *et al.* (1997).

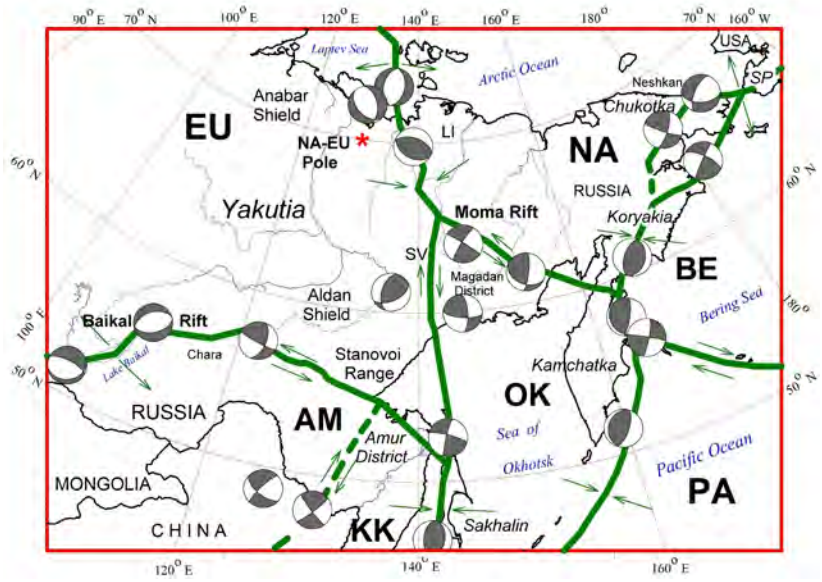

Figure 2. Present-day tectonic map of eastern Russia showing major plate and block boundaries, representative focal mechanisms, and localities and features discussed in the text. Arrows show directions of relative movement. Plate boundaries shown in green (dashed where speculative or uncertain). The red asterisk shows the approximate location of the North America – Eurasia (NA-EU) Euler pole of rotation. Plate and block abbreviations: EU – Eurasia, NA – North America, PA – Pacific, AM – Amur, OK – Okhotsk, BE – Bering, and KK – Korea-Khabarovsk. Other abbreviations: LI – Lower Indigirka rift zone, SV – South Verkhoyansk district, SP – Seward Peninsula.

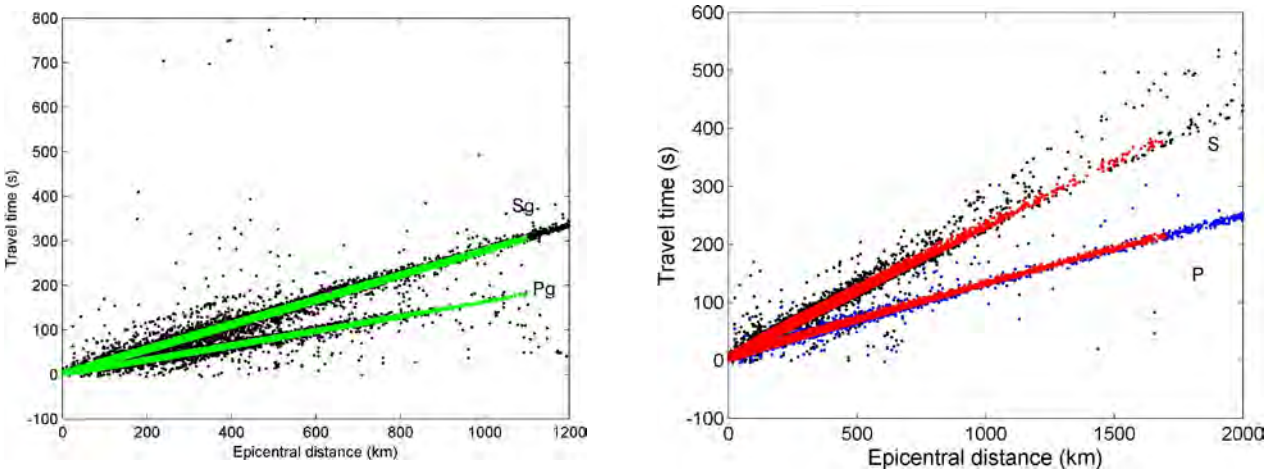

Figure 3. Travel time curves for (left) Pg and Sg phases and (right) first P and S phases. Green lines represent selected Pg and Sg phases and red lines indicate selected first P and S arrivals.

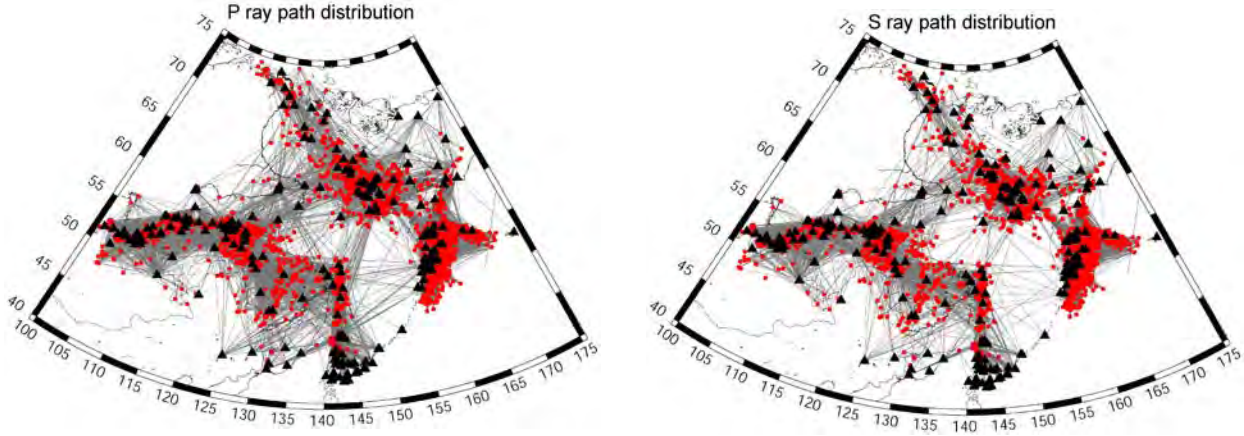

Figure 4. *P* and *S* ray path distributions for selected P and S first arrivals. Earthquakes are red dots and black triangles are stations.

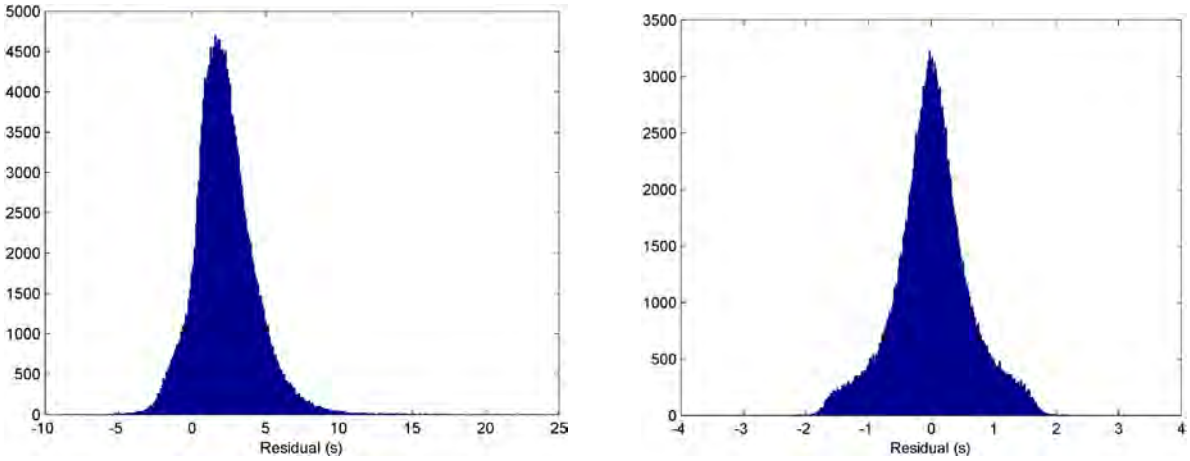

Figure 5. Comparison of histograms of travel time residuals (left) before and (right) after seismic tomography.

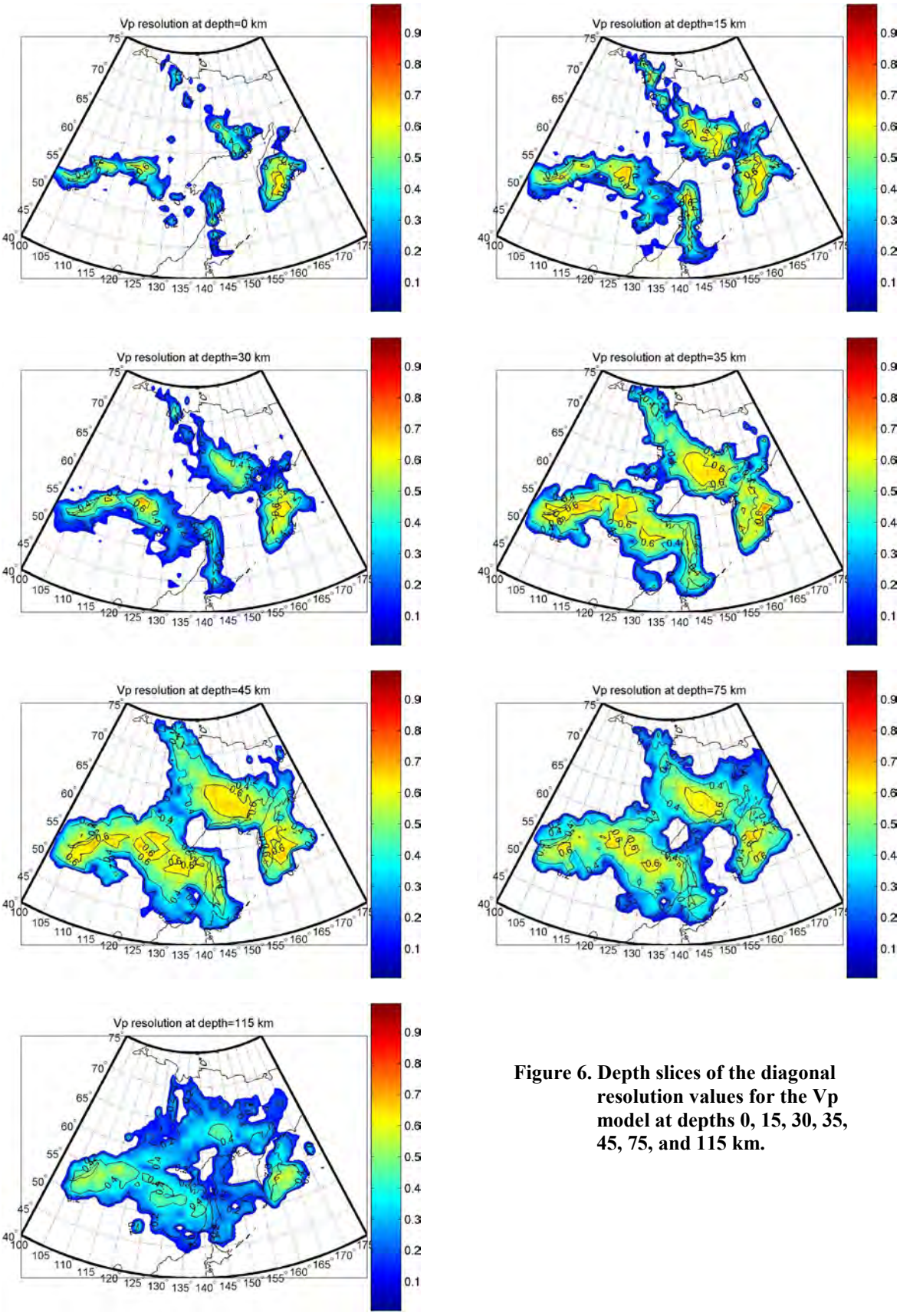

Figure 6. Depth slices of the diagonal resolution values for the Vp model at depths 0, 15, 30, 35, 45, 75, and 115 km.

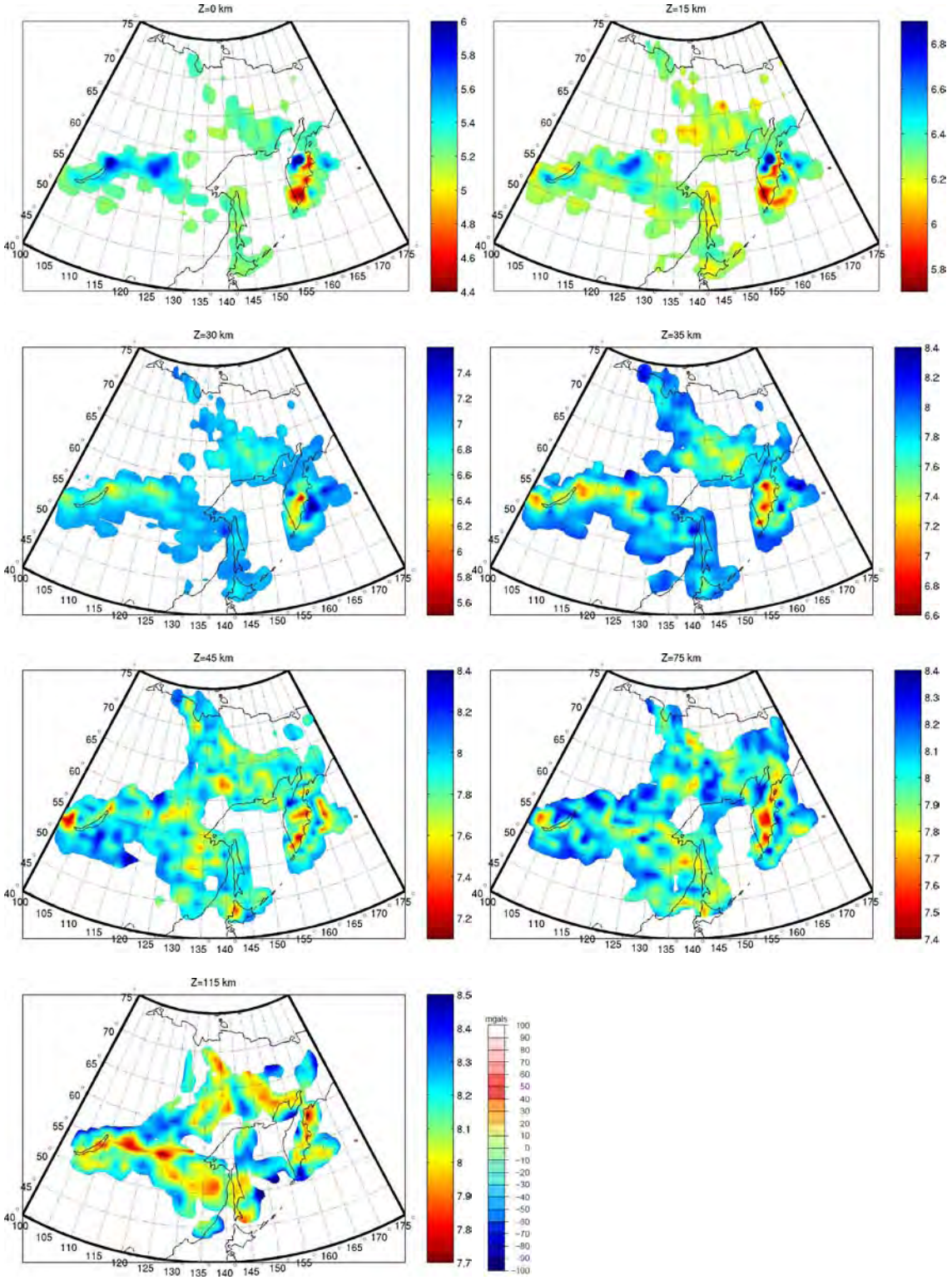

Figure 7. Depth slices of the Vp model at depths 0, 15, 30, 35, 45, 75, and 115 km.

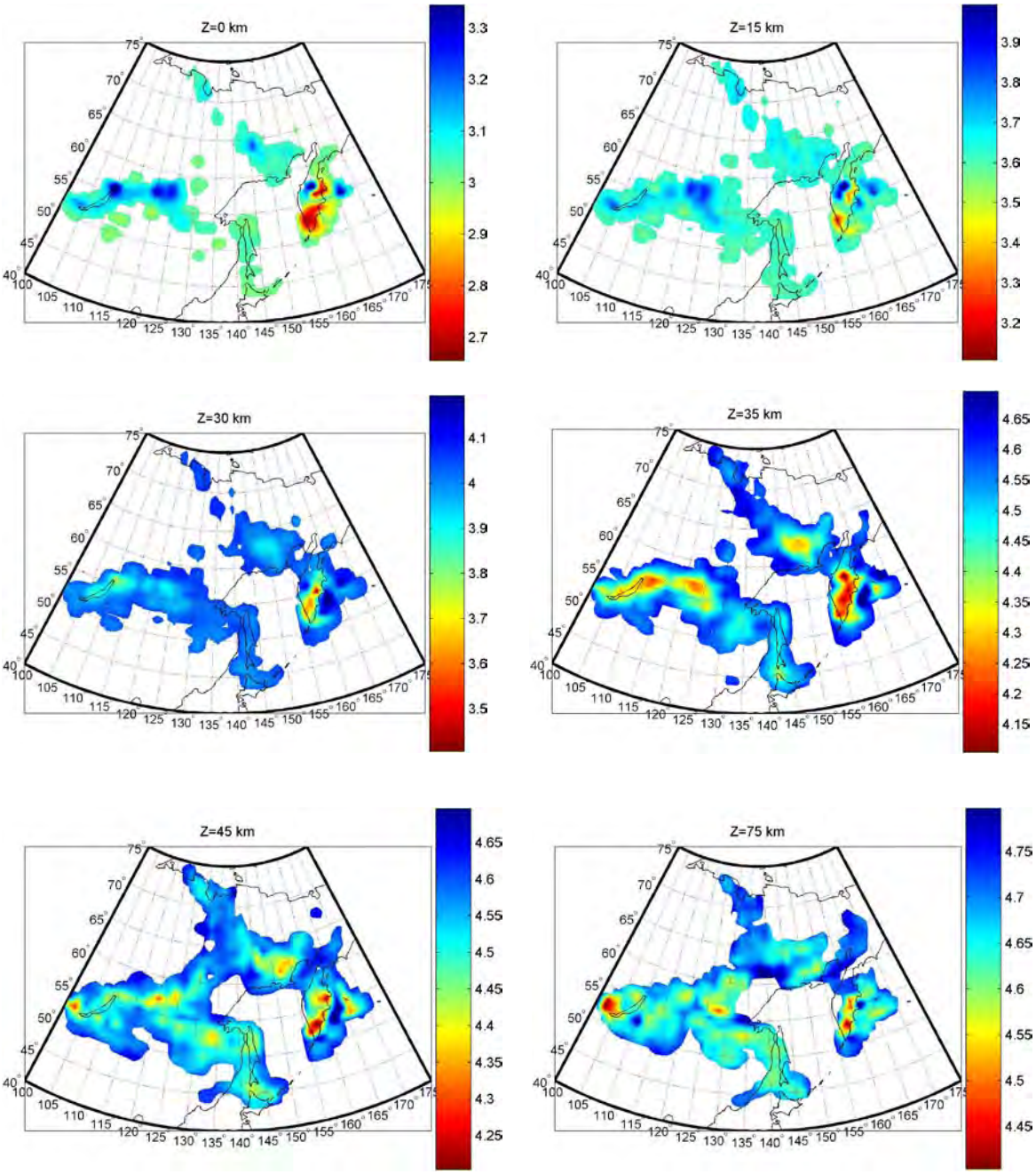

Figure 8. Depth slices of the Vs model at depths 0, 15, 30, 35, 45 and 75 km.

Seismic Event Detection and Location

NEXT GENERATION ROBUST LOW-NOISE SEISMOMETER FOR NUCLEAR MONITORING

Igor A. Abramovich and Tao Zhu

PMD Scientific, Inc.

Sponsored by the National Nuclear Security Administration

Award No. DE-FG02-07ER84738

ABSTRACT

Effective global monitoring of nuclear explosions calls for a worldwide network of seismic stations equipped with the next generation high quality digital seismometers for nuclear monitoring recording data in the 0.02–16Hz band. This project addresses these requirements: it is aimed at the implementation of the next generation, very low noise, broadband, wide dynamic range, robust force-balanced digital seismometer for seismic monitoring of nuclear explosions. Successful completion of Phases II of this project will serve vital national interests in greatly facilitating global compliance with nuclear non-proliferation and detection of possible violations of the Comprehensive Nuclear-Test-Ban Treaty by rogue states.

The new seismometers should also be competitive in various niches of the worldwide seismic market due to their valuable combination of high performance, especially the low noise over broad passband, and ruggedness.
The new generation seismometer will use improved electrochemical transducers built into three similar orthogonally mounted sensors, the latter based on conceptually new design ideas that, when implemented, will result in a drastic increase in signal to noise ratio. The principles of operation and detailed noise analysis of electrochemical motion sensors are presented along with the explanation of how such major noise reduction can be achieved. The new concept has already shown to be promising based on test results of the experimental sensor prototypes.
The new instruments will be deployable in field and stationary vault environments; they will be highly reliable and offer low cost of ownership since they require no maintenance: no mass locks; no mass position monitoring and/or mass centering over the full temperature range of -12 to +60C. No break-out boxes are needed. The rugged design will greatly reduce probability of damaging such instruments during transportation and handling. The seismometer will incorporate a high-resolution, low noise, very low power versatile 24-bit digitizer that will provide digital outputs with velocity-flat and optional acceleration flat and combined velocity/acceleration-flat response. The noise level of the proposed seismometers should be at least 10dB below the USGS New Low Earth Noise Model with the dynamic range of no less than 136dB over the 0.02 to 16Hz frequency band. Maintaining the wide dynamic range, the uniform frequency response over the passband, and the considerably reduced noise will be facilitated by the use of the efficient force-balancing electrodynamic feedback. At major developmental milestones the prototype instruments will be vault-tested side-by-side with STS2 seismometers. The complete digital seismometer is expected to consume less than 750mW.

OBJECTIVES

An advanced digital seismometer with the following features that are in full compliance with the goals set forth in the Phase I proposal and also, where possible, with the CTBTO "Minimum Requirements" (CTBT/PC/II/I/Add. 2) and AFTAC additional recommendations will be built:

- **Ruggedness**: the instrument will be able to survive and remain fully operational after a shock of ≥50g for 10ms. No mass locking mechanism will be used.
- **No Maintenance Operation:** no mass position monitoring and no mass centering will be required over the full operating temperature range.
- **Passband:** 0.02 – 16Hz.
  The passband will be defined by the -3 dB corner frequencies with the ripple in gain of no more than +/- 1 dB from the mean gain values as measured from one octave above the lower corner frequency to one octave below the upper corner frequency
- **Sensor Response:** Two sets of analog and/or digital outputs will be provided concurrently: velocity-flat and acceleration-flat over the passband. A 'hybrid' response utilizing the combination of both will also be available.
- **Seismometer Noise:** These objectives were set forth in Phase I Proposal:

Passband	Target Noise Level
0.02-0.1Hz	-185 -190dB – *below NLNM*
0.1 – 6Hz	-185 -190dB – *below NLNM*
6 – 16Hz	(-185 -190) –180dB – *below NLNM*

- **Calibration:** Within 5% in amplitude and 5º in phase over the passband referenced to the theoretical transfer function model.
- **Limited Leveling:** the sensor will stay fully operational at installation tilts of at least ±8°.
- **Application Types:** Field, vault, borehole.
- **Environmental:**
  - **Operating Temperature Range:** -12 to +65C.
  - **Fully Hermetical, Pressurized:** the land-based seismometer will remain fully operational when submerged to the depth of at least 2m or up to 20m when equipped with an underwater type connector. The borehole version will be designed to be fully operational in the flooded boreholes down to 100m (>10kg/cm^2)
- **Robust borehole seismometer**: A robust ≤6" diameter borehole seismometer with all of the above characteristics.

The following specifications relate to the digitizer that will be integrated into the proposed seismometer. This digitizer will be a significantly upgraded version of the present PMD Scientific Series SD6503.

- **Digitizer Sampling Rate**: programmable up to at least 100sps while complying with the noise specifications below.
- **Digitizer Resolution:** 12dB below the seismometer noise.
- **Digitizer Noise Referenced to its Input:** 10dB below the seismometer noise.
- **System Dynamic Range:** ≥ 135dB
- **Absolute Timing Accuracy**: better than ±0.5ms relative to the external GPS receiver
- **System Total Power Consumption:** <0.7W
- **Optional**: digital data storage, SATA SSD flash disk up to 32GB
- **Optional**: LAN connection

A. Sensor description

A typical electrochemical sensor (Figure 1) has a plastic housing filled with strong electrolytic solution: potassium iodide, *KI*, with a small addition of iodine, I_2. Electrolyte is contained between a pair of elastic membranes that significantly contribute to the sensor's transfer function. The transducer consists of four fine platinum mesh

electrodes, two anodes, and two cathodes, separated by thin polymer mesh or laser-perforated mica spacers. The stack is tightly held together between two flanges. The motion of the fluid caused by an external acceleration is converted into an electrical signal via convective diffusion of the ions in the electrolyte. When a small dc offset is applied between the anodes and cathodes, the flow of ions of each type can be described by the following expression (Newman, 1973; Koryta, 1993):

$$\mathbf{j}_a = -D \cdot \nabla c_a + q_a \cdot c_a \cdot \mu \cdot \mathbf{E} \qquad (1)$$

Where D = diffusion coefficient; μ = mobility and c_a = concentration of active ions; **E** = the electrical field vector. Since the strong electrolyte is an excellent conductor, the electric potential drops rapidly in the vicinity of the electrodes, and there is no electric field in the bulk of the fluid. Thus the second term in Equation 1 can therefore be ignored. Therefore, the application of a bias voltage results *only* in a concentration gradient. An acceleration, **a,** along the channel creates a pressure differential, **ΔP,** across the transducer, which forces the liquid to move with a velocity, **v**. This flow of electrolyte entrains ions and causes an additional charge transfer between the electrodes:

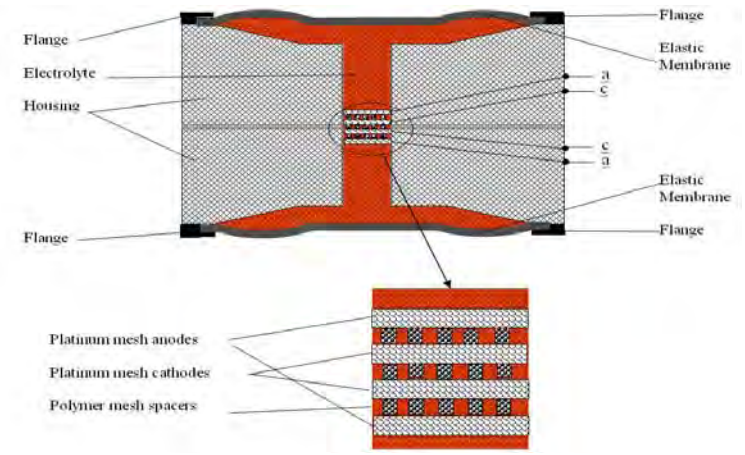

Figure 1. A Basic Electrochemical Seismic Sensor.

$$\mathbf{j}'_a = \mathbf{v} \cdot c_a \qquad (2)$$

The total current from active ions, in the presence of acceleration, can be expressed as:

$$\mathbf{j}_a = -D \cdot \nabla c_a + \mathbf{v} \cdot c_a \qquad (3)$$

Thus the transducer generates an electrical signal in response to acceleration.

A general expression describing noise in units of external acceleration (derived in by PMD consultant Dr. K. Sakharov [1992]):

$$\left\langle a^2 \right\rangle_\omega = \frac{2R_h kT}{(\rho L)^2} \qquad (4)$$

Where: ρ = electrolyte density; L = electrolyte effective length in the direction of the acceleration; k = Boltzmann constant; T = absolute temperature; R_h = hydraulic impedance. The nominator in Equation 4 represents hydrodynamic thermal noise, similar to the Nyquist noise in electric circuits with the R_h standing for the electric resistance R (Van der Ziel, 1970). The total noise of a sensor agrees with Equation 4 only in the mid-frequency region. The elevated noise spectral density at both ends of the passband is due to at least two addition sources. The additional noise is unavoidable even when the two halves of the transducer are exactly symmetrical and thus their noise components add up to zero at the transducer differential output. These two sources are: fluctuation noise of the current flowing in the transducer; noise of the electronic amplifiers

The spectral density of fluctuation noise is described by the general equation:

$$\left\langle I^2 \right\rangle_\omega = 2qI \qquad (5)$$

Where I = quiescent current of the transducer cell(Abramovich, 1992–94):

$$I = \frac{Dc_0 eS}{l}\left(1 - \exp(-\frac{qU_0}{kT})\right) \qquad (6)$$

q = elementary charge in the cell. As two electrons participate in each elementary charge exchange reaction at the electrodes, $q = 2e$; D = diffusion coefficient; c_0 = charge carriers equilibrium volumetric concentration; U_0—voltage between and S = effective area of the electrodes; l = distance between the electrodes. Since each transducer consists of two independently working identical cells that are together characterized by the transfer function W, the following equation describes sensor fluctuation noise in units of acceleration:

$$\left\langle a^2 \right\rangle_\omega = 8eI \Big/ (W/\omega)^2 \qquad (7)$$

The practical method of increasing the signal-to-noise ratio is an addition of an inertial mass. For example, vertical and horizontal sensors of the PMD BB603 broadband seismometer are equipped with ~650g masses which results in noise below NLNM in the 0.06–8Hz. To account for the additional mass Equation 4 is modified:

$$\left\langle a^2 \right\rangle_\omega = \frac{2R_h kT}{\left(\rho L + M/S_s\right)^2} \qquad (8)$$

Where M = external mass and S_s = effective area of the sensor membrane. This is a simple, proven approach; it is easy to change/adjust M; the additional mass ("frame") is mounted in such a way that the membranes are not deformed. The frame carries a voice coil that transmits the feedback force to the membrane. Both qualitative and quantitative validity of Equation 8 have been confirmed experimentally. Evidently, further increase of the inertial mass would be impractical.

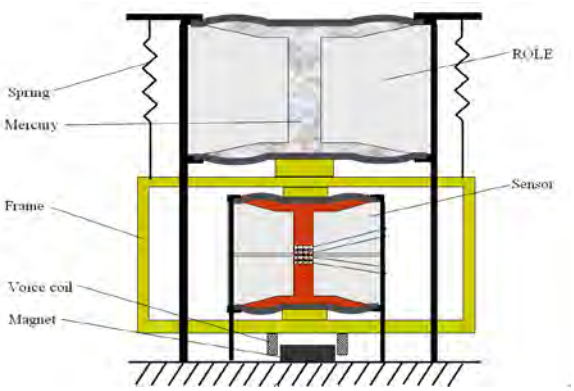

Figure 2: HEX design concept

To achieve the required noise levels a radically new approach was necessary. While there is no known electrolyte with much higher density, a well known exceptionally heavy liquid exists: ***mercury*** (13.6 g/cm^3). The conceptual design of a sensor that we called HEX ('**H**ybrid **E**lectro-**C**hemical **S**ensor') is shown in Figure 2. A smaller electrochemical sensor has a flame with a voice coil moving around a magnet working in the force-balancing loop. The frame's top is firmly tied to the lower membrane of a larger sensor-like structure filled with mercury. The frame in such structure performs several functions: it carries the voice coil and thus transfers the balancing force to the sensor; it transfers pressure from the upper to the lower device; finally, it is attached to the suspension springs that balance the weight of the total oscillatory mass consisting of the frame itself, mercury and electrolyte. An external acceleration along the sensitive axis is transformed into pressure differential, ΔP_i, between membranes in each of the two pairs: the large upper and the small lower. The following equation describes HEX noise:

$$\left\langle a^2 \right\rangle_\omega = \frac{2R_h kT}{\left(\rho_m h_m \dfrac{S_m}{S_s}\right)^2} \qquad (9)$$

Where ρ_m and h_m are respectively density and column height of mercury and S_m = area of the ROLE membrane (we called the mercury-filled device 'ROLE' – short for '**ρ**-**L**-**E**nhancer': see ρ, L terms in Equation 1). For a more detailed description of this sensor's principle of operation along with the derivation of the above equation see work plan section below.

Comparison of Equations 4 and 9 shows that the new concept not only capitalizes on the very high density of mercury, but achieves more than that: since the noise is inversely proportional to the ratio of the diameters of the two membranes it is possible to achieve an even larger increase in signal-to-noise ratio.

B. HEX Sensor Operating Principle

An external acceleration component acting along the device sensitive axis is transformed into pressure differential, $\boldsymbol{\Delta P_i}$, between membranes in each of the two pairs: the large (upper) and the small (lower) ones. For each pair, $\Delta P_i = \rho_i \cdot \vec{x} \cdot h_i$ where ρ_i = liquid's density; $\vec{x}$ = acceleration; and h_i = height. Force with which the lower membrane of the top structure acts on the frame, $F = \Delta P_m \cdot S_m$. The frame applies this force to the smaller sensor membrane and thus generates an additional pressure differential $\boldsymbol{\Delta P_{add}}$:

$$\Delta P_{add} = \frac{F + m_f \cdot \ddot{x}}{S_s} = \left(\rho_m \cdot h_m \frac{S_m}{S_s} + m_f \right) \cdot \ddot{x} \qquad (10)$$

Where $m_{f=}$ mass of the frame; S_m and S_s = areas of the larger and smaller membranes respectively; ***Hg*** specific gravity $\rho_m = 13600 kg/m^3$; h_m= height of the column of ***Hg***. It is important to notice that the *mass* of mercury does not enter into Equation 20, only the *height of its column*. Signal developed in the electrochemical transducer is proportional to the volumetric velocity, *q*, of the electrolyte that obeys the Darcy's Law:

$$q = -\Delta P / R_h \qquad (11)$$

As follows directly from Equation10, the signal will increase proportionally to

$$N = \frac{\Delta P_{add} + \Delta P_s}{\Delta P_s} \qquad (12)$$

The HEX noise expressed in acceleration units can now be written as:

$$\left\langle a^2 \right\rangle_\omega = \frac{2R_h kT}{\left(\rho_e h_e + \frac{m_f}{S_s} + \rho_m h_m \frac{S_m}{S_s} \right)^2} \approx \frac{2R_h kT}{\left(\rho_m h_m \frac{S_m}{S_s} \right)^2} \qquad (13)$$

Where ρ_e, h_e = density and column height of the electrolyte. Evidently the bigger the difference between the diameters of the larger and smaller membranes the more compact is HEX for a given noise level. The first term in the denominator is at least an order of magnitude smaller than the third and thus can be omitted. Finally, it is also evident that no practically feasible increase of the mass of the frame will contribute noticeably to the noise reduction; therefore the second term can also be deleted which results in the simplified Equation 6 above.

RESEARCH ACCOMPLISHED

A. Practical Implementation of the Noise Reduction Concept

The goal is to achieve the maximum possible noise reduction effect without sacrificing seismometer manufacturability and portability. Evidently, the following three parameters in the Equation 9 can be played with: the height of the ROLE, h_m and areas of the two membranes, S_m and S_s. The height cannot be made too large without significant increase in the overall dimensions of the instrument. Based on practical considerations, h_m should be selected equal to about 40mm. There are two factors limiting the value of S_m: the overall size and weight of the instrument and a possible pear-shaped sagging of these larger membranes in horizontal and their gravitational deformation in vertical sensors. At the same time, it is important to keep in mind that in order to achieve proper long period response the membranes cannot be made too rigid to alleviate these effects. Based on our experience, the maximum practical diameter of the larger membrane is ≤100mm. The sensor's membrane, on the other hand, should be made as small as possible. However, the smaller this membrane the more difficult it is to maintain its softness. This situation, however, changed dramatically when after many years of fruitless search we found the new membrane material, Santoprene, an elastomer alloy of EPDM rubber and polypropylene. Now it appears possible to design membranes with optimized rigidity and diameter at least as small as but most probably smaller than that of the membranes in the present smaller sensors (34mm). Indeed we hoped to construct a membrane with diameter as small as 25mm and did so in the Phase I effort. Unfortunately our first attempt to make such a membrane ended in failure: in our desire to make it much softer we went too far. The bell-shaped channel ("goffer") turned out to be too deep and the membrane was mechanically unstable. Please refer to the "Mini-Membranes" section below. If we use our standard 50mm membranes in ROLE device a 2:1 diameter ratio of the ROLE and sensor membranes becomes achievable. This choice of the geometries of both devices, as we hoped, should result in the most limited rise of the noise curve on the both ends of the passband at the same time yielding the desired noise reduction. Also, in doing so, the overall instrument dimensions should remain manageable. Based on multiple experiments, the noise of a

standard transducer in a 35mm high sensor was determined to be about -155dB. Then according to Equation 9 the proposed device noise in the flat part of the passband will be:

$$\left\langle a^2 \right\rangle_\omega = -155 + 20\log\frac{\rho_e h_e}{\left(\rho_m h_m \frac{S_m}{S_s}\right)} \approx -155 + 20\log\frac{1.25\cdot 0.035}{\left(13.6\cdot 0.04\cdot 2^2\right)} \approx -190dB$$

This number should be looked at with cautious optimism: on one hand, when decreasing the sensor's noise so drastically we are entering into *terra incognita*, where one should anticipate unexpected noise sources to reveal themselves, some of which are discussed in the next section. On the other hand, we can conceivably increase diameter of the ROLE membrane by a factor of, say, 1.5. This would yield an additional 6dB in noise reduction. Results of the tests performed at ASL showed exceptionally accurate estimate of noise level at long periods (due to the above mentioned instability of the 25mm Santoprene membranes, a standard sensor with 34mm membranes was used):

$$-155 + 20\log\left[1.25\cdot 0.035/\left(13.6\cdot 0.04\cdot\left(0.05/0.035\right)^2\right)\right] = \text{ -183dB}$$

At the same time, noise very sharply went up starting at approximately 1Hz toward the higher frequencies, on one hand, and less steeply toward the long periods, on the other. This phenomenon has been and continues to be thoroughly investigated. Though poor suspension quite certainly played a negative role, an identical suspension was employed in the electrodynamic test sensor with noticeably better results (of course in the higher frequency range only). On the other hand, the latter should by definition generate ever stronger signal with increasing frequency, and it is possible that the lower noise was due to higher signal-to-noise ratio as compared with the HEX sensor.

B. Mini-membranes

The main conclusion drawn from both the Phase I project and the first year of the Phase II effort is that the general HEX concept is valid though several problems have been encountered. Because of this conclusion we attempted to build the next generation prototype using electrochemical sensor with significantly smaller membranes. The initial attempt though was unsuccessful due to the design flaw in smaller membranes: in trying to make the membrane as soft as possible we made central isle of the membrane way too small to allow for a stable mechanical connection between ROLE and the sensor. Therefore we asked the manufacturer (Aero Rubber Co., Tinly Park, IL) to modify the mold. Original and modified mini-membranes along with the bigger one used on all previously tested sensors are shown in Figure 3:

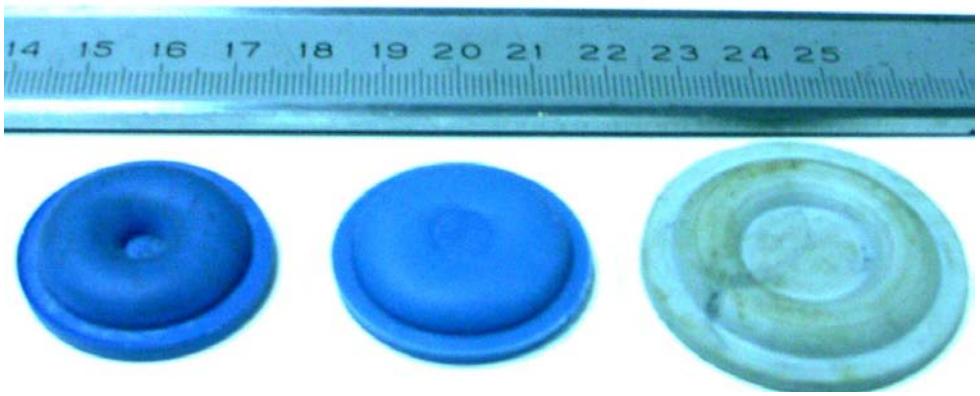

Figure 3. Left to right: original mini-membrane; modified mini-membrane; standard small membrane used in the first test sensor at the ASL.

The only difference between the two mini-membranes is that in the second one the center isle is twice as thick and therefore has a larger surface area. This modification took a very long time (over 2.5 months) but gave us a chance to do a very productive in-depth analysis of the initial prototypes design and behavior and also analyze and test a couple of modified sensor configurations. As a result, building of the next generation prototype with mini-membrane equipped sensors was delayed. Finally, we received several modified membranes (in the middle of Figure 3).

C. In-Depth Analysis of Prototype HEX Sensors

The limited time of Phase I project did not allow for a more thorough investigation of the HEX sensor properties; indeed we had concentrated totally on achieving the lowest possible noise levels without properly analyzing (and thus understanding) why, for example, we failed in getting the desired noise in the higher frequency region and, to our disappointment also at the lowest frequency when using the 25mm membranes. Designing a very complex device as HEX sensor turned out to be exceptionally time consuming and every finished prototype would be quickly calibrated and subjected to comparative noise testing. This is why in the Phase II effort we decided to first achieve a complete understanding of the device operation before undertaking any radical re-designs no matter how enticing one or another concept may seem.

Our standard quick calibration procedure yields values of R-C frequency correction components to substitute the selected standard initial values. As a rule, the second round of calibration results in the desired transfer functions. Data from intermediate calculation stages are not displayed. This time we used the unabridged procedure that allowed us to see results at every step. We were immediately puzzled by the shape of the sensor frequency response (sensor per se – without electronics) that contained two pronounced resonance peaks with a valley between them. The valley occupied just the region from a few Hertz up – right from the lowest noise valley to where HEX sensors demonstrated sharply increased noise. Thus the elevated noise was revealed but not yet understood.

Standard electrochemical sensors show bell-shaped frequency responses. We have known however that there are always two overlapping resonances: mechanical and electrochemical. The mechanical characteristic is described by a well known equation:

$$m \cdot \ddot{x} + D \cdot \dot{x} + K \cdot x = m \cdot \ddot{w} \qquad (14)$$

Where m = inertial mass; D – damping coefficient; and K=suspension rate. In our case the hydraulic impedance of the sensor provides the damping while the membranes account for about 80% of the suspension rate (the remaining 20% are provided by the spring(s)).

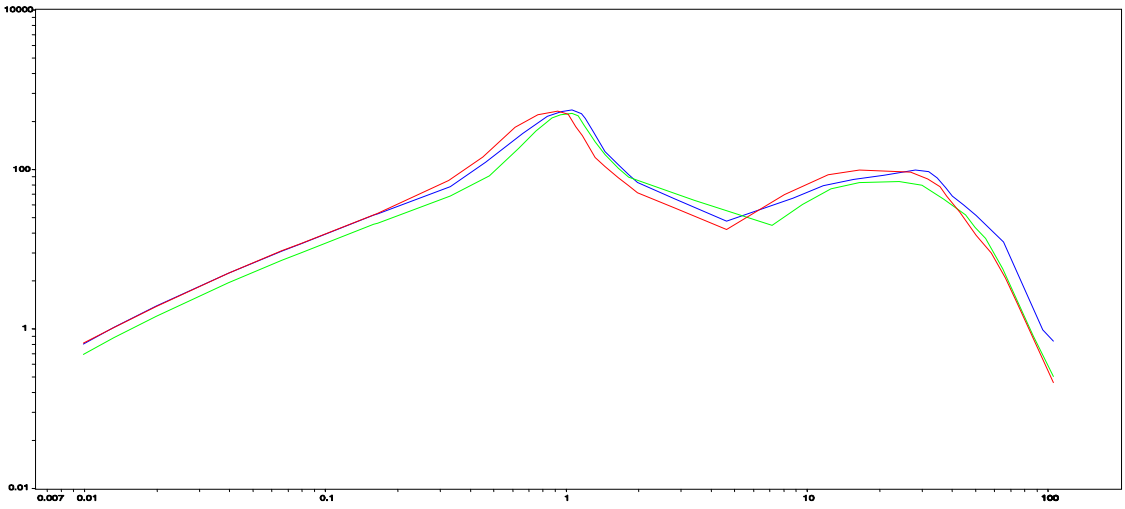

Figure 4. Sensors Frequency Responses.

The electrochemical transfer function, $W(q,\omega) = I(\omega,q)/q$, describes dependence of the transducer cell output current, I, on the external harmonic flow, q, and assumes different forms at limiting values of low and high frequency. When the system is exposed to weak low frequency flows, there is sufficient time for the formation of the diffusion layer and the current is proportional to the amount of electrolyte that flows through the electrodes. The characteristic parameter of such system is the time required for the formation of the diffusion

layer: $\tau_0 \sim (2d)^2 / D$, where *d*=½ of the distance between electrodes; *D*=diffusion coefficient. The transfer function, $W(q)$, will be increasing at frequencies $\omega < \omega_0 \sim 1/\tau_0$ and decreasing at $\omega > \omega_0 \sim 1/\tau_0$. At sufficiently high frequencies, when the distribution of concentration is determined by the rate of change of the signal, there is not enough time for the diffusion layer to form and because of that the output current is proportional to both the amount of electrolyte flown through the cell and the ratio of the signal change time to that of the diffusion layer formation. As a result, in this frequency region the transfer function decreases reversely proportionally to ω.

The two resonance peaks were almost indistinguishably close to each other. With the introduction of the ROLE device the relationship between the two resonances changes drastically and now we see two hills and a valley. While the feedback and electronic correction smooth and flatten this response, the valley is positioned right where it does the damage in terms of the high frequency noise.

While analyzing the HEX sensor behavior we also tested a few modifications of the original prototypes. In Figure 4 three plots are shown representing frequency responses of various modifications. The blue curve shows the response of the initial Phase 2 prototype. The green curve belongs to the HEX assembly where channel diameter in the ROLE device was increased by 35%. Finally, the red plot shows the response of the HEX similar to the previous one but with much softer ROLE membranes. Neither modification resulted in a radical improvement though the last one shows some shift of the whole response toward the lower frequencies thus promising some reduction of the noise at low and, quite unexpectedly, also at higher frequencies. Both increases though still do not lead to the target noise levels.

We also attempted to further flatten the response by employing an additional damping: a low impedance coil and a magnet (see magnetic system – 'Damping/EM Sensor' – at the bottom, below the electrochemical sensor in Figure 5; a similar but modified magnetic system was used in later experiments with additional electrodynamic sensor). Such damping did not result in any noticeable response changes. Evidently, the hydrodynamic damping effect of the sensor was at least an order of magnitude, and probably more than that, stronger than any electromagnetic damping we could implement within the design constrains of the existing prototype.

Presently practically all hydraulic impedance of the HEX system, essentially the very parameter that is responsible for the steepness of the main resonance peak, is concentrated inside the electrochemical sensor. It appears that a more beneficial result will be achieved is we decrease the sensor's impedance and increase that of the ROLE device. We can reduce diameter of the channel in the ROLE as much as it is practically possible and, in turn, double the diameter of the transducer cell thus decreasing its impedance by the factor of 16. Now at about the same noise level the membranes will not be deforming and the pressure will be transferred more uniformly from ROLE to the sensor in the passband of interest. Actually this approach is prompted at least in part by the plots in Figure 4. In combination with the use of smaller membranes in the sensor and thus overall increase in the signal-to-noise ratio this may conceivably bring us close – or directly to the target noise levels. Such modified sensor is presently being tested. The main difficulty should be anticipated in preventing the parasitic lateral electrolyte motion (lateral convection) across the electrodes. Such convection leads to a noticeable noise increase. On the other hand, we have some experience in building experimental low R_h transducers; a couple of them were tested successfully at Berkeley several years ago.

Another test prototype has been build using the smaller membranes (25mm). This time the result was more predictable since we have accumulated significant understanding of various factors impacting the HEX sensor behavior. The signal at the main resonance frequency was stronger in full compliance with the Equation 9. On the other hand, the resonance peak was much sharper. As a result, we achieved a very low noise at around the main resonance peak and even stronger noise at either end of the passband. This problem is being addressed presently and several measures are being considered; in particular changing the transducer design by using laser-perforated mica spacers instead of the polymer mesh ones. This should result in more compact transducer (due to the fact that mica is thin and exceptionally flat while the mesh has quite uneven microstructure). Then the possibility of the parasitic convection will be conceivably nil and the long period noise should go down significantly. Since these transducers are being tested right now, we cannot yet report experimental results.

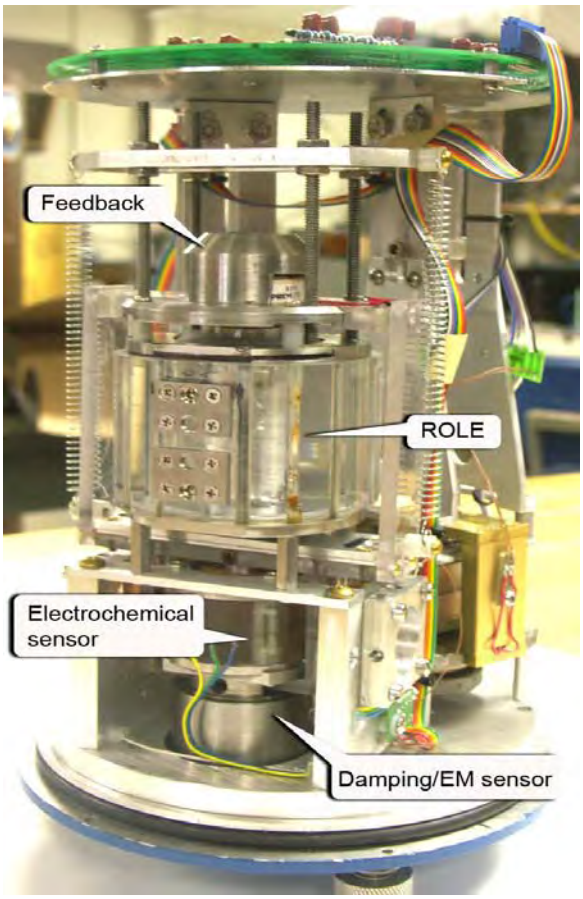

Figure 5. The latest prototype HEX sensor. A standard electrochemical sensor with large inertial mass is seen behind the HEX. Placing both sensors on a common base and in the same housing allows for very accurate correlation calculations.

Another test prototype has been build using the smaller membranes (25mm). This time the result was more predictable since we have accumulated significant understanding of various factors impacting the HEX sensor behavior. The signal at the main resonance frequency was stronger in full compliance with the Equation 9. On the other hand, the resonance peak was much sharper. As a result, we achieved a very low noise at around the main resonance peak and even stronger noise at either end of the passband. This problem is being addressed presently and several measures are being considered; in particular changing the transducer design by using laser-perforated mica spacers instead of the polymer mesh ones. This should result in more compact transducer (due to the fact that mica is thin and exceptionally flat while the mesh has quite uneven microstructure). Then the possibility of the parasitic convection will be conceivably nil and the long period noise should go down significantly. Since these transducers are being tested right now, we cannot yet report experimental results.

D. The EC/EM Combination Sensor

If the above approach turns out to be insufficient in terms of achieving the target noise levels at higher frequencies, we can turn to using the combination sensor. We tested a HEX equipped with an additional electro-dynamic transducer. The inscription in Figure 5: (“Damping/EM Sensor”) emphasizes that the magnetic system shown may contain either a damper or an electromagnetic sensor. The simpler combination we tested was an open-loop system and no special efforts were spent to achieve a flat response. However, as one can clearly see from the plots below in Figure 6, the resulting response is more manageable as compared to those shown in Figure 4 and may be readily flattened in a closed loop configuration.

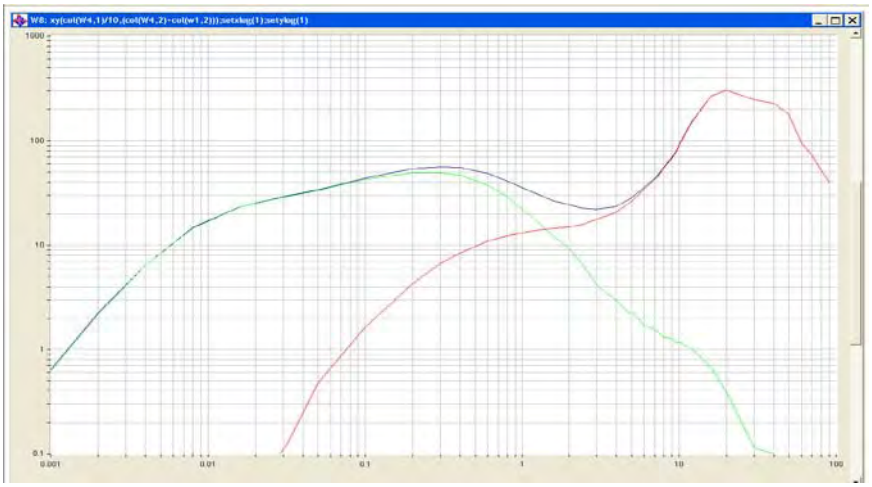

Figure 6. The Electrochemical/electrodynamic combination sensor response: green – electrochemical; red – electrodynamic; blue – combined response.

E. The Electrochemical "Gyro" sensor

This is the most exotic but quite realistic device despite its seeming complexity. We have been working on this design for a several years unrelated to any government-sponsored projects. We think it is unlikely that we will have time to incorporate this "gyro" sensor into the HEX device within the remaining year but we determined to do it rather sooner than later.

1. Concept

This unusual sensor configuration was conceived during the development of our rotational seismometer with magneto-hydrodynamic (MHD) feedback presently manufactured commercially.

In order to test the concept (see sketch in Figure 7) we modified our standard rotational sensor by adding a transverse tube. The ring contains a conventional electrochemical transducer and an MHD cell (that works as force-balancing feedback in rotational sensor). This cell consists of a pair of platinum electrodes inside the channel and a pair of strong Neodymium magnets. When a *dc* voltage is applied to the electrodes, the cell moves the strongly conductive electrolyte along the ring (solid arrow). A ground motion component along the sensitivity axis causes electrolyte to flow in/out of the main ring (dashed lines). This, in turn, effectively modulates the steady motion of the electrolyte through the transducer cell and results in a signal proportional to the ground motion velocity. Our experiments demonstrate that such sensor yields at least twice as strong signal at low and four times stronger at high frequencies than a standard electrochemical sensor. Moreover, even the open-loop system shown has close to the same linearity as our standard force-balanced instruments. The signal-to-noise ratio of this sensor can be increased even further by adding a second MHD cell and still further – the second transducer cell. Finally, due to the strong high frequency signal yield such sensor would be paired response-wise more readily and smoothly with an electro-dynamic sensor, if necessary.

Figure 8 shows the way a Gyro sensor can be built into a standard one with membranes and thus be equipped with a feedback and an inertial mass or ROLE, if desired.

While the configuration in Figure 8 may seem too complicated to make, it is actually a combination, with some additions, of our standard translational and rotational seismometers and as such it will not require any above usual design efforts be they mechanical or electronic. As for the size of the Gyro sensor, it would be actually much smaller that it may seem from observing the sketches where various dimensions were intentionally stretched in order to explain the principles of operation more clearly.

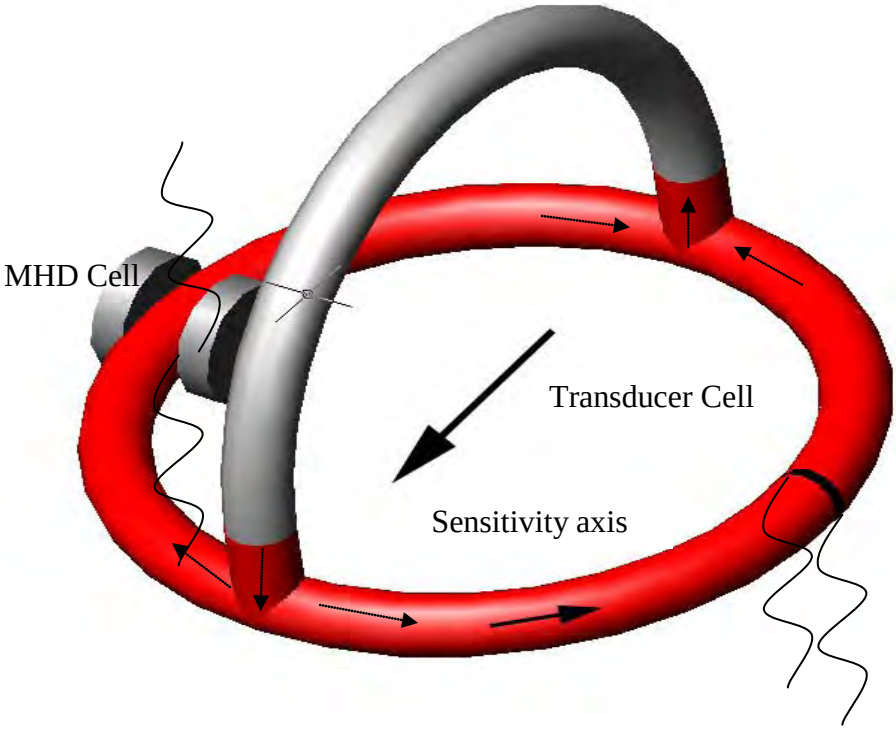

Figure 7. The Gyro type electrochemical sensor

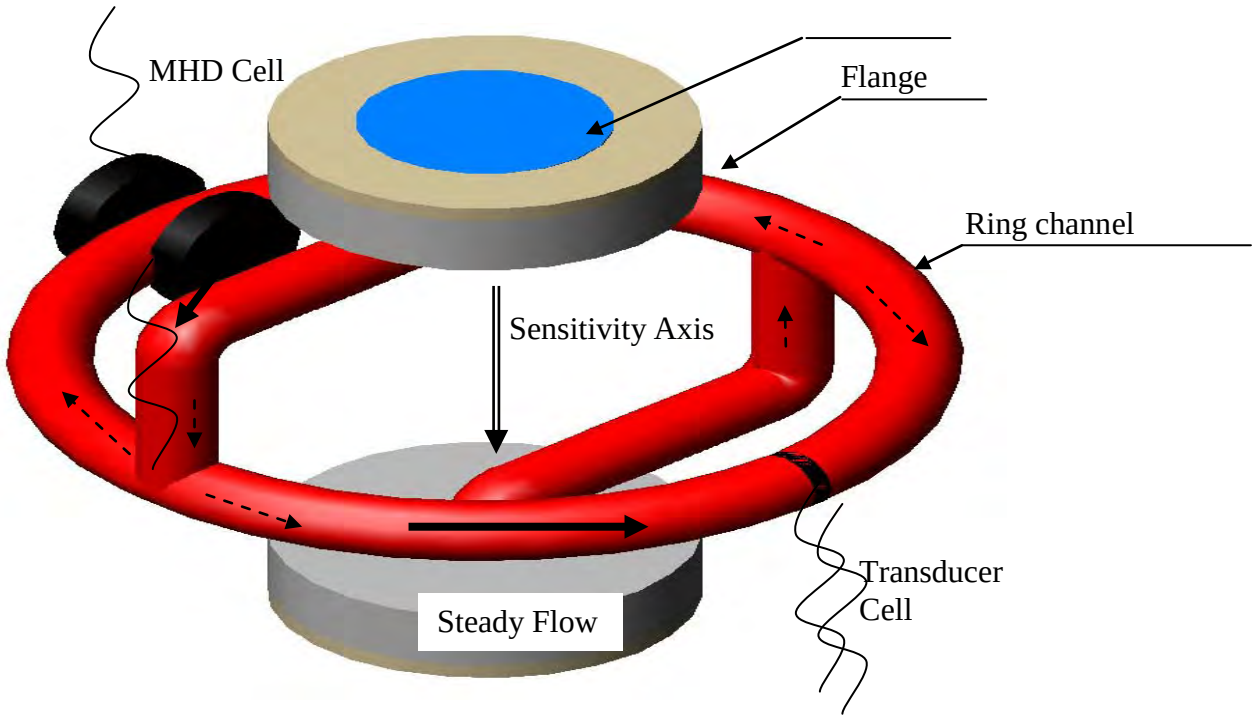

Figure 8. Sketch of a Gyro sensor ready for the addition of feedback and ROLE device.

2. *Theory of Operation*

The subject of the discussion below is an electrochemical transducer with flat mesh electrodes through with electrolyte flows with velocity

$$V = V_C + V_0 \exp(i\omega t) \tag{15}$$

where $V_C = const.$

Operation of an electrochemical transducer is described the convective diffusion equation; for this sensor configuration it can be considered single-dimensional:

$$\frac{\partial n}{\partial t} - D\frac{\partial^2 n}{\partial x^2} = -V\frac{\partial n}{\partial x} \tag{16}$$

With two boundary conditions:

1) Nernst relationship:

$$\frac{n_{-d}}{n_d} = \exp(\frac{eU}{kT}) \tag{17}$$

2) Preservation of equilibrium concentration at the anode:

$$n_{-d} = n_0 \tag{18}$$

Where n_0=concentration far away from the electrodes; U=voltage between the electrodes; n_{-d} and n_d= concentrations at the anode and cathode respectively. Solution of the equation results in the following expression[1] for the current flowing through the cathode:

$$I = -esD\frac{\partial n}{\partial x}\Big| - esD\frac{\partial n}{\partial x}\Big|_{x=d} = -esD\frac{\partial n_c}{\partial x}\Big|_{x=d} - esD\frac{\partial c}{\partial x}\Big|_{x=d} = I_C + I_W \tag{19}$$

Where:

$$I_C = \frac{eSn_0V_C}{2sh(2R_C)}\left(\exp\left(-\frac{eU}{kT}\right)-1\right)\exp(2R_C) \tag{20}$$

And

$$I_W = -\frac{eSn_0V_C}{2sh(2R_C)}\left(\exp\left(-\frac{eU}{kT}\right)-1\right)\frac{V_0\exp(i\omega t)}{i\omega d}\left((R_C - R_W)\exp(2R_C)\right) + R_W\frac{1-\exp(2(R_C-R_W))}{sh(2R_W)} \tag{21}$$

Finally

$$R_C = d\frac{V_C}{2D} \text{ and } R_W = d\sqrt{\left(\frac{V_C}{2D}\right)^2 + \frac{i\omega}{D}} \tag{22, 23}$$

In the above expressions D=diffusion coefficient; d,h,s= geometrical parameters of the transducer. Theoretical calculations of values of the transfer function $W(\omega,V_C) = I_W(\omega,V_C)/V_0(\omega)$ of the transducer at different levels of the constant electrolyte flow are plotted in Figure 9.

[1] Originally the general solution of this equation was obtained by the former PMD employee, Dr. Alex Panferov.

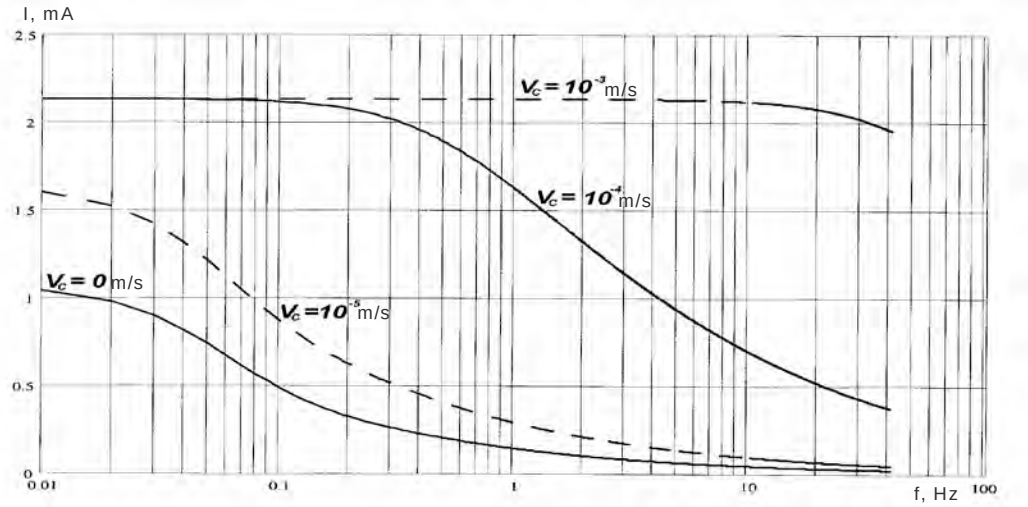

Figure 9. Transducer transfer function at different values of the permanent flow.

The plots clearly demonstrate that in the presence of a stationary flow of electrolyte the transfer coefficient of the electrochemical transducer increases while its passband extends farther toward the higher frequencies.

3. Experimental Data

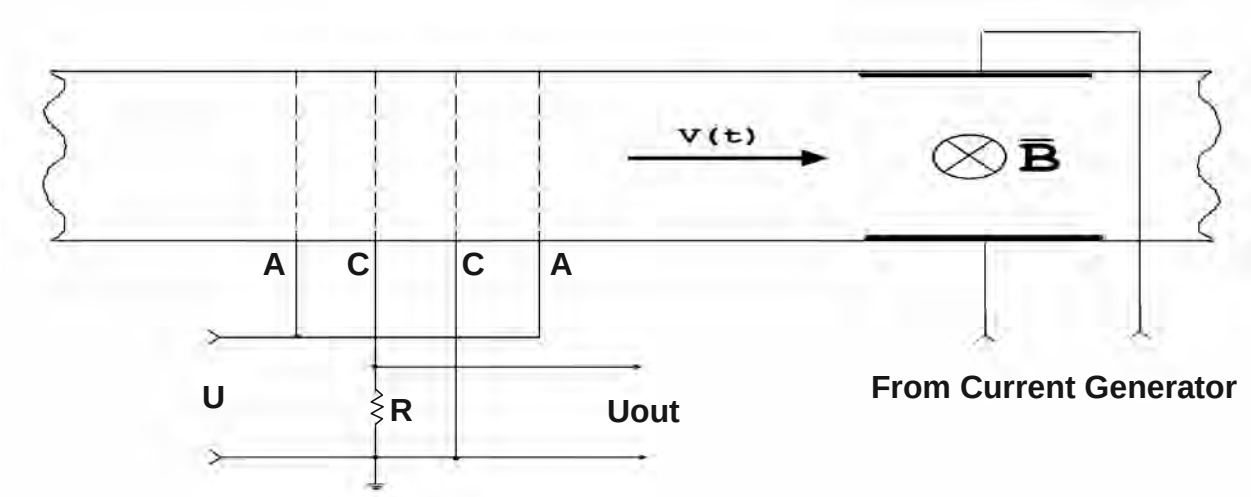

Figure 10: Experimental setup

A rotational sensor that is used in the current RSB20m rotational seismometer model was used in the experiments. The sensor consists of a polycarbonate toroidal channel filled with electrolyte. Built in the channel are a standard 4-electrode electrochemical transducer and an MHD cell. A constant voltage differential *U* was maintained between the cathodes and anodes. Transducer's output current generates voltage drop on the resistor R. This voltage war recorded into computer via a 22-bit ADC.

Both constant and modulating currents are injected into MHD electrodes. As a result, a force that is proportional to the cross product of the current density and magnetic induction is applied to the electrolyte. The pressure differential in the system generated by the moving liquid:

$$\Delta P = \frac{(\mathrm{B} \times \mathrm{I})L}{S} \qquad (24)$$

Where *L*=distance between electrodes and *S*=channel cross-section. Input signal of the transducer is the volumetric velocity, *q*, of the electrolyte that is related with the pressure differential in accordance with the Darcy law:

$$q = -\frac{\Delta P}{R_h} \qquad (25)$$

Where R_h=hydraulic impedance of the toroid.

In the first set of experiments we measured dependence between the transducer's output current and the velocity of the stationary flow of the electrolyte. The theoretical curve is plotted on Figure 11; the crosses show experimentally measured values.

In the second set we measured transfer coefficient of the transducer versus the stationary flow velocity. These results are presented on Figure 12. The ordinates here are the ratios of the transducer transfer functions in the presence and absence of the electrolyte flow: $W(V_C)/W(0)$. The test data prove rather convincingly that when the stationary flow velocity is higher than 10^{-5} m/s the upper cutoff frequency becomes noticeably higher and that the overall transfer coefficient grows several times over. It is important to emphasize that these experimental results agree very well with the above presented theory in a very broad frequency range: from 0.01 to several tens of Hz.

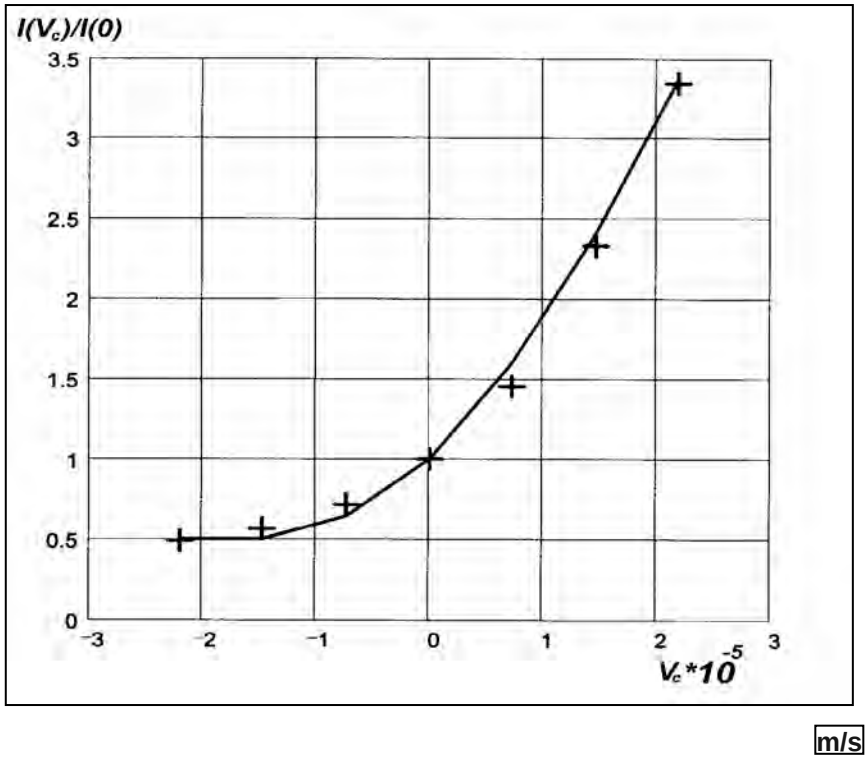

Figure 11. Transducer output current vs. the stationary flow velocity.

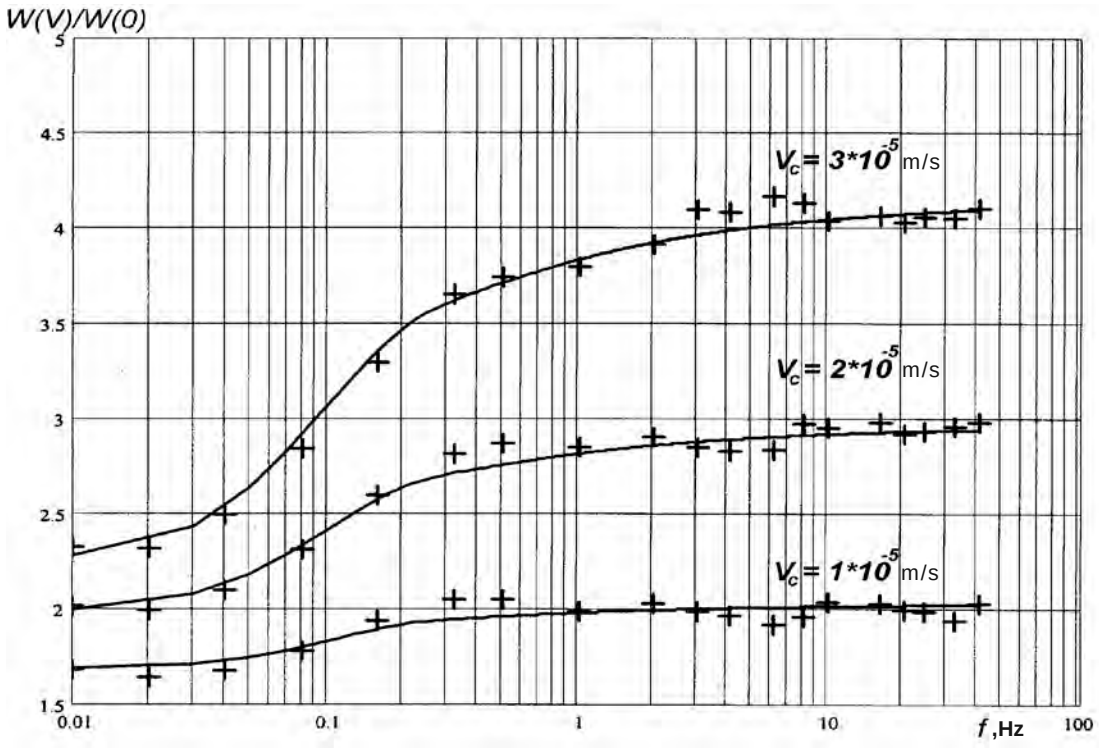

Figure 12. Transducer transfer coefficient vs. the stationary flow velocity.

F. Digitizer

This part of the project has been progressing rather smoothly and steadily. The block-diagram of the digitizer that is under development is shown below in Figure 13.

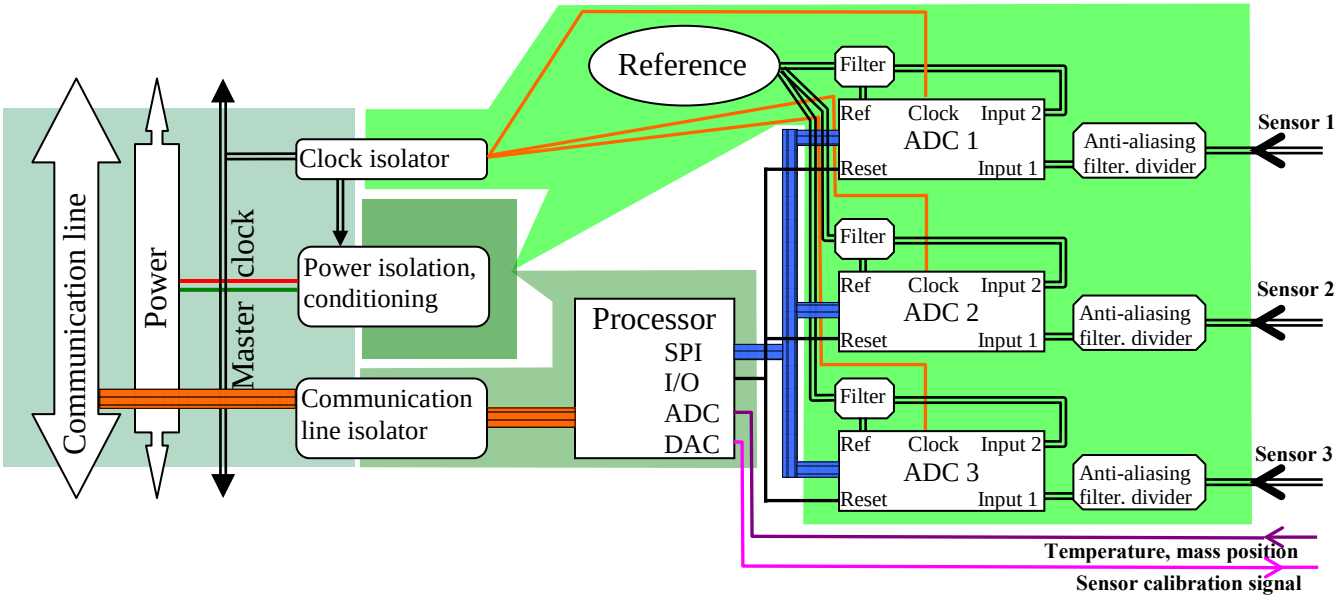

Figure 13. Digitizer Block Diagram

In order to make possible using the digitizer as a stand-alone device and/or work with other sensors the 'Mass Position' input (and 'Mass Centering' output not shown here) have been added. Also to allow for a multi-channel configuration the 'Master Clock' bus can be connected to similar digitizers in a common assembly.

An evaluation board for the Texas Instruments ADS1281/1282 has been purchased and used for the preliminary tests. A prototype board using TMS320VC5416 DSP and 3 ADS1282 converters was built and tested. The resulting noise was measured at ~1/3 bit higher than specified by TI.

An early decision had been made to have a dedicated microprocessor or a digital signal processor chip placed on the same board with the 3 channel converters. After an exhaustive search two possible processors have been selected for the final consideration: an MSP430 Ultra-low power microcontroller and a TMS320C55* low power DSP both manufactured by TI. While MSP430 offers several advantages, in particular, it had on-board ADC and DAC that can directly be used for state-of-health data recording, mass position readout, mass centering, etc. On the other hand, it seem unlikely that a microcontroller such as this one will be able to cope with extremely heavy computational load that is antialiasing filtering of three streams of data flowing with a maximum rate of up to 48 Kbaud. Therefore, at the moment we are inclined to use the above mentioned DSP even though additional 12-16 bit ADC/DAC chips will have to be deployed. Presently under development are the power regulators and clock circuits. Upon their completion the first three-channel prototype board will be built and tested.

CONCLUSIONS AND RECOMMENDATIONS

The first year of the Phase II project turned out to be more productive than anticipated. By the term "productive," we do not necessarily mean only positive results. It is well known that some negative results going against the anticipated ones may turn out to be very useful. In our case such "failures" prompted us to perform a more thorough theoretical analysis and come up with more practical designs. Several sensor configurations were thoroughly analyzed; most of them have been built and tested. Most importantly, the experimental results in general showed close agreement with the theoretically predicted data albeit in a rather narrow passband. At the moment our first priority will be an exhaustive testing of the HEX prototype with a mini-membrane sensor. In the next step two prototypes will be built: one with the current distribution of the hydraulic impedance and another – with the low R_h sensor. If we are sufficiently satisfied with the laboratory test results to the point where we consider it worthwhile taking the prototype for the field tests at ASL it will be done. If we still feel that the further noise reduction is necessary we will start building and testing step be step other weapons from our arsenal, i.e., those described above combination sensor or/and the gyro device.

ACKNOWLEDGEMENTS

The authors are deeply grateful to Dr. Bob Hutt for his exceptional hospitality and highly qualified help during our trip to the ASL. Personal contacts with Drs. Mark Woods, Rick Schult, Preston Herrington, Yuri Starovoit and Prof. Erhard Wielandt greatly helped in formulating the requirements to and specifications of the new sensor.
Dr. Alexander Shilov of PMD Scientific played a leading role in data processing and analysis and in the development of the new digitizer.

REFERENCES

Abramovich I. and S. Daragan (1992). New family of inexpensive broad band seismometers, NSF SBIR Grant No. III-9360412, 1992-94

Koryta L. and K. Dvorak K. (1993). *Principles of Electrochemistry*, J. Wiley, New York.

Newman J. (1973). *Electrochemical Systems*, Prentice-Hall, Englewood Cliffs, New Jersey.

Sakharov K., (1992). Analysis of self-noise of molecular electronic seismic sensors, in *Proceedings MIPT*, vol.26, No.3, 1992 (in Russian)

Van der Ziel A. (1970). Noise; sources, characterization, measurement, Prentice Hall, 1970

SEISMO-ACOUSTIC ANALYSIS IN THE ZALESOVO REGION OF CENTRAL ASIA

Ronald A. Brogan[1], Susan Nava[1], Raymond J. Read[1], Yan Jia[2], Nicolas Brachet[2], and John Coyne[2]

ENSCO, Inc.[1] and the Comprehensive Nuclear-Test-Ban Treaty Organization[2]

Sponsored by the Comprehensive Nuclear-Test-Ban Treaty Organization

Award Nos. 2006-1164[1] and 2008-0550[2]

ABSTRACT

Interactive seismo-acoustic data analysis was conducted on a one-month dataset to describe the station characteristics of the International Monitoring System (IMS) seismic station ZALV (Zalesovo, Russian Federation) located in central Asia. Specific study objectives included: the location of all local and regional seismic events observed by the station, including single station events; identification of seismic sources routinely observed at the station; background noise characterization; and identification of any biases in station azimuth, time, and slowness, etc. Additionally, these data provided a baseline for a separate study for evaluation, tuning, and enhancement of automatic and interactive processing functions at the International Data Centre (IDC). The compiled seismic catalog was used to identify infrasound detections on the co-sited IMS infrasound station I46RU that theoretically could be associated with these seismic events. For seismic events with proposed associated infrasound detections, the events were first relocated using both seismic and infrasound detections. Active mine sites located in the area of the seismic events were identified using Google Earth. Each event in the integrated seismo-acoustic catalog was relocated with epicenters fixed at the nearest mine source location and results evaluated.

Thirty days (16 February–15 March 2008) of continuous IMS waveform data from the co-sited seismic array ZALV and from the infrasound array I46RU were analyzed in this study. Approximately 800 seismic events at an epicentral distance less than 20° from station ZALV were human-analyst reviewed, including phase identification and event location. Twelve clusters of seismicity were identified. Infrasound detections were associated with approximately 200 of the events and appear to originate from roughly 50 mining complexes, the majority of which are located within 500 kilometers of Zalesovo. A small subset of the infrasound signals were observed on the seismic waveforms. No prominent noise sources on seismic station ZALV were observed in this data set. For regional events, ZALV shows good response across the full-frequency spectrum. Trends in observed biases were catalogued for each station based on azimuthal distribution. The biases for each cluster were determined by averaging residuals for each measurement (time, azimuth, velocity) and comparing them to the iasp91 travel time tables routinely used during production of the Reviewed Event Bulletin (REB). *Rg* phases at ZALV can often have large (late) time residuals, but are usually very clear on the waveform records.

OBJECTIVES

The objective of this study was to interactively review one month of data to describe station characteristics of the IMS seismic station ZALV and its co-located IMS infrasound station I46RU. Here, we focused on: (1) the location of all local and regional seismic events observed on ZALV, including events located using only a single station; (2) identification of routinely observed seismic sources; (3) background noise characterization; and (4) identification of waveform characteristics including any biases in station azimuth, time, and slowness, etc. Additionally, during this project, notes were kept on the thresholds necessary at ZALV for a given event to be recorded at other stations, trends in azimuth and velocity (slowness), optimal filter bands for analysis, and any timing errors. The compiled seismic catalog was then used to identify infrasound detections on the co-sited IMS infrasound station I46RU that could be associated with these seismic events. Mine sites located in the area of the seismic events were identified using Google Earth satellite imagery.

RESEARCH ACCOMPLISHED

Identification of Sources of Observed Seismic Activity

The first objective was to locate all seismic events (including single station events) observable on station ZALV. A total of thirty days of data were reviewed (February 16, 2008 thru March 15, 2008). Routine IDC analysis processing software, related configuration parameters, and database tables, including automated seismic detections and events, were provided by the IDC for this study. IDC's version of the Analyst Review Station (ARS) software package was the primary tool used for waveform review, phase identification, and location purposes. For routine frequency-wavenumber (F-K) processing, XfkDisplay and the multi-band F-K module from the program Geotool were used. Seismic data analysis for this study was performed by displaying the waveforms in a five minute window and manually scrolling page-by-page. In most cases, waveform filtering was performed on a nearly constant basis. A 1–5 Hz bandpass, causal, Butterworth filter was the primary filter used during analysis. This filter preserves, in most cases, the predominant frequencies of many teleseismic arrivals, while providing enough frequency content of regional arrivals to lead the analyst to further investigation. Extremely high frequency events are not very common at ZALV, although a few were observed, located mainly west of the station. The surface solution from the location program was used when only one station observed the events.

An intermittent, recurring noise burst was observed on the study dataset on seismic station ZALV. The noise bursts have an emergent onset and are incoherent; determination of the noise source was not possible. An example of noise bursts is shown in Figure 1. Two to three of these bursts per day were observed on average in this particular data set and the impact on analysis was minimal.

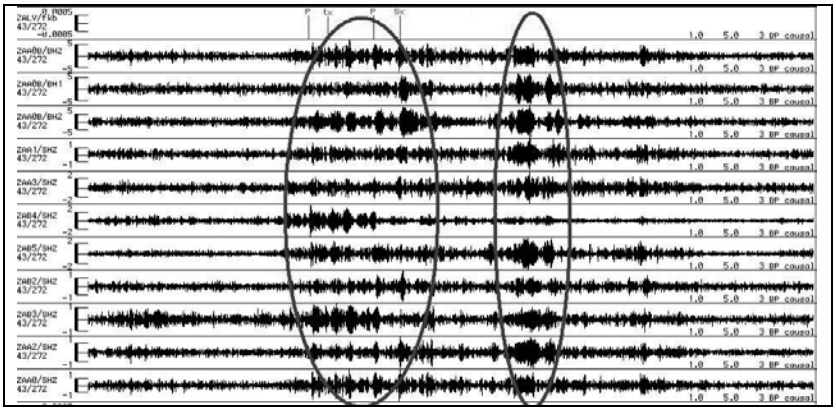

Figure 1. ARS screenshot showing an example of noise bursts observed periodically on station ZALV (prominent noise shown in ellipses).

Identification of regional phases was difficult for this station. Most events occurred near the *Pn*/*Pg* and *Sn*/*Lg* crossover distance. Thus, discerning whether a *P*-type phase was a *Pn* or *Pg*, or if the *S*-type phase was an *Sn* or *Lg* was problematic. Oftentimes the energy from phases in this distance range is mixed, resulting in less than optimal F-

K calculations. The shape of the envelope was often a determining factor since F-K values were generally mixed. The degree of confidence in the locations is still high however, since the phases have nearly identical travel-times in this distance range. When events were at located distances offering good separation of the phases, the determination was far less difficult. The key seismic phase used to identify events during this study was the ZALV *Lg* arrival as the *P*-type phases were particularly difficult to identify. For *Rg* phases, it was difficult to achieve F-K results that are consistent with theoretical velocities.

Routine analysis at the IDC included data from the Zalesovo array beginning on January 15, 2007. From the station start in IDC operations (January 15, 2007) through December 31, 2007, ZALV initial *P*-type arrivals were associated to 11,143 of the 27,506 (40.5%) of the events in the REB (Figure 2). ZALV records many different types of seismic phases, including regional and teleseismic signals, originating from all areas of the globe. Small clusters of local seismic events are commonly observed on the ZALV waveforms, many of which are presumed to be mining-related explosions.

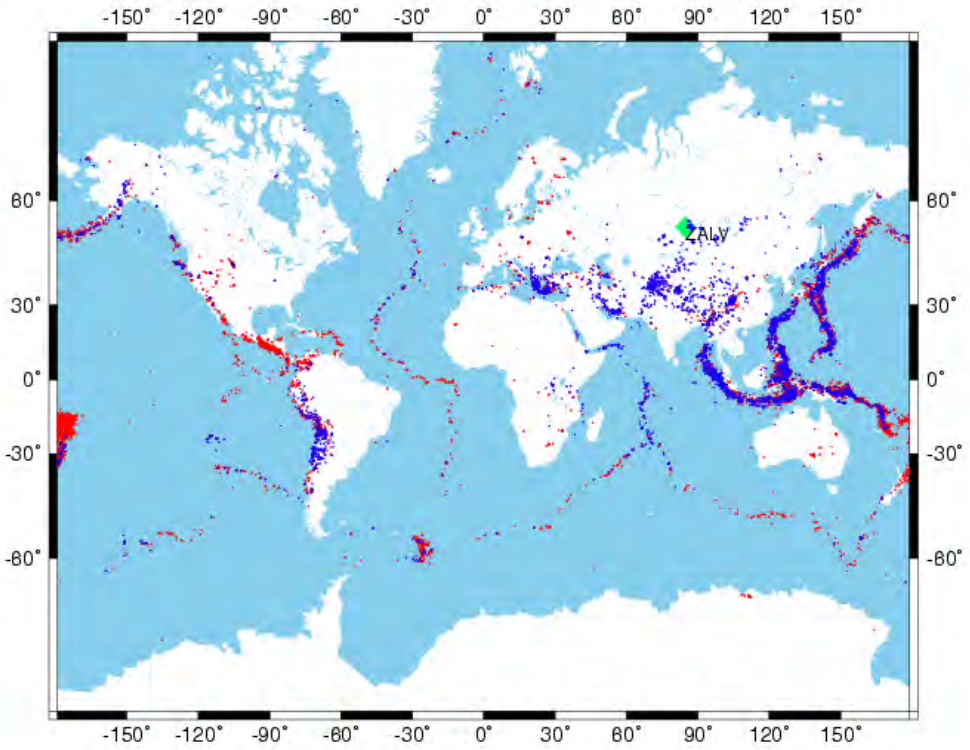

Figure 2. Map showing station ZALV *P*-type phase contributions to the 2008 REB. Events with an associated ZALV *P*-phase arrival are plotted in blue and events without a ZALV *P*-phase are plotted in red.

For the thirty-day dataset reviewed, approximately 800 seismic events occurring within an epicentral distance of less than twenty degrees from the ZALV seismic array were located during this study. Each of the events was human analyst reviewed, including phase identification and event location. Twelve clusters of seismic events (Figure 3) were identified, based on geographic and temporal distribution, during the seismic phase of this study, and later refined when detailed infrasound analysis was incorporated. The majority of the seismic events in these clusters are presumed to be mining-related explosions. Attributes used to characterize clusters at this stage were temporal distribution, Google Earth imagery, and waveform characteristics. Time-of-day and day-of-week pattern histograms were prepared for each cluster; however, space limitations prevent showing these intermediate results here.

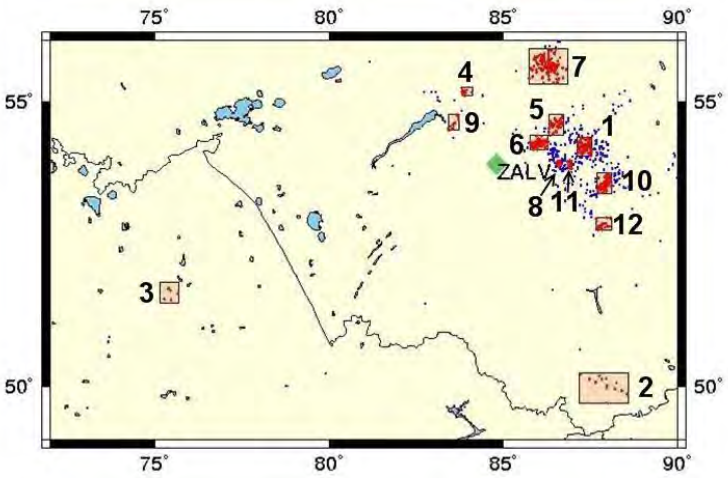

Figure 3. Map of events located in the vicinity of IMS station ZALV. Peach boxes with red dots denote cluster events; other events are shown as blue dots.

Table 1. Identified Seismic Clusters

Cluster Number	Event Count
1	51
2	14
3	5
4	10
5	35
6	61
7	115
8	15
9	9
10	67
11	18
12	17

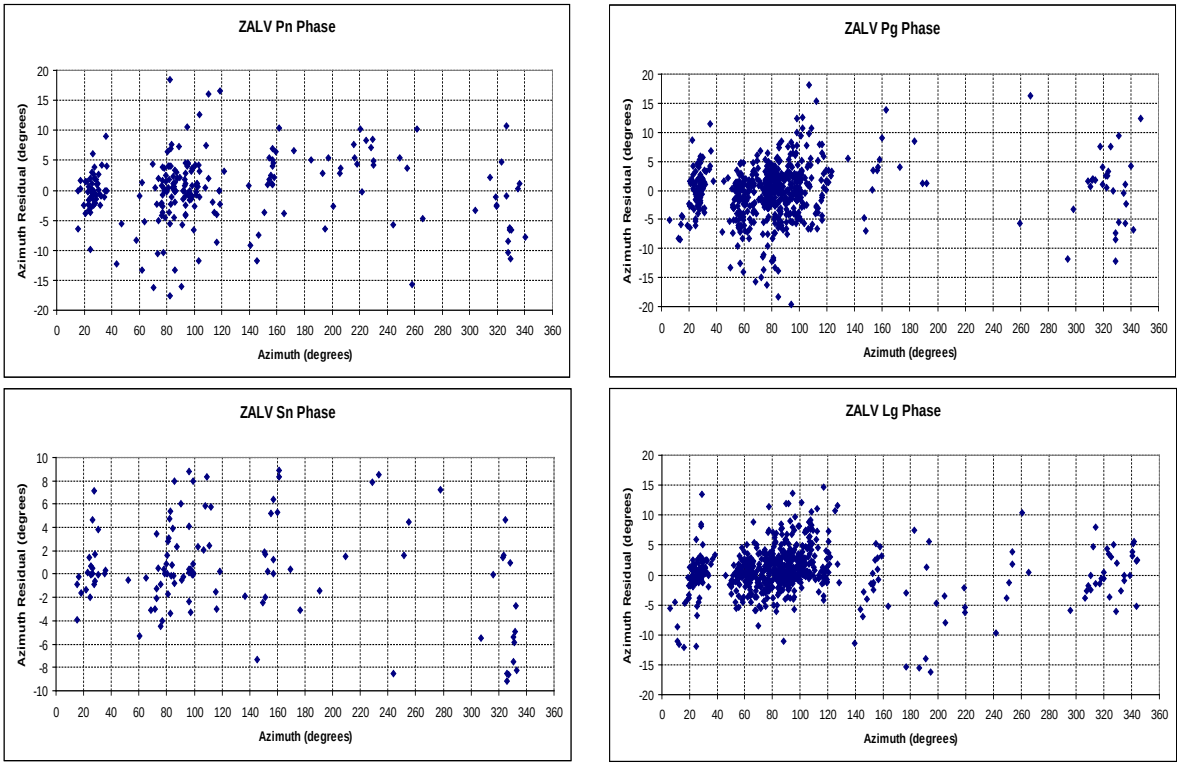

Figure 4. Azimuth residuals versus azimuth for ZALV regional seismic phases for study dataset.

Figure 4 shows the azimuth residuals of regional phases observed at ZALV during analysis of the study data. Figure 5 shows the velocity residuals versus azimuth of regional phases observed at ZALV during analysis of the study data.

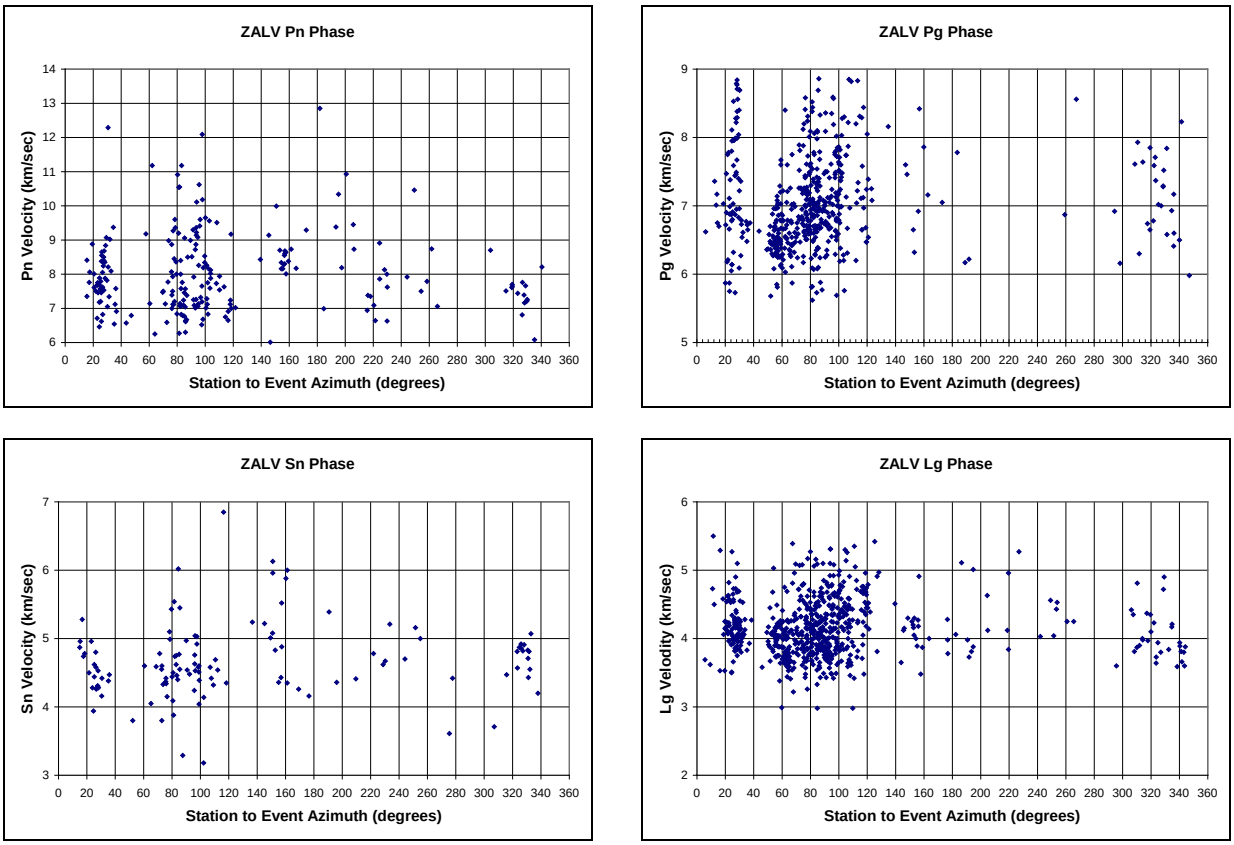

Figure 5. Velocity residuals versus azimuth for ZALV regional phases for study dataset.

Figure 6 shows the travel time of regional phases recorded at ZALV during the course of this study. The iasp91 travel-time tables were used to compute origin times in this study.

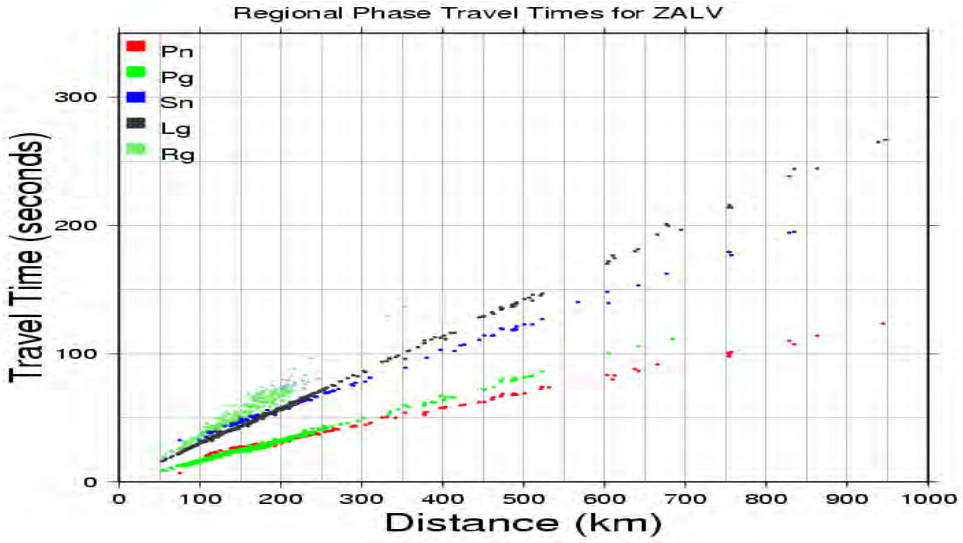

Figure 6. Plot of regional phase travel times for regional phases at ZALV.

There were several dozen observations of infrasound signals recorded on the seismometers at ZALV. The arrival time and azimuth of the acoustic signal on the co-sited infrasound station (I46RU) match the observations on the

seismic channels. Sample waveforms showing the acoustic signal recorded on the seismic sensors from two representative events are shown in Figure 7. Identification and study of acoustic signals observed on seismic waveforms was not an objective of this study, thus the number of observations is likely low. The presumed associated source mine locations are well distributed in azimuth from ZALV and originate from many different mines. However, not all mines identified in this study had acoustic signals observed on the seismic channels.

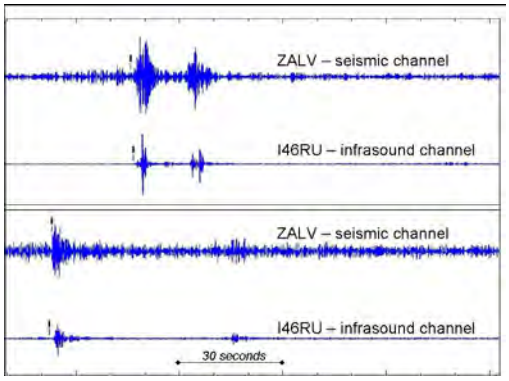

Figure 7. Two examples of infrasound signals observed on the seismic sensors at station ZALV. All waveforms are bandpass filtered between 2–5 Hz. Waveforms are not time aligned.

Association of Infrasound Detections with Seismic Event Catalog

Using the compiled seismic catalog, we identified all signals in the IDC-provided infrasound detection database from the co-sited IMS infrasound station I46RU that theoretically could be associated with these seismic events. For seismic events with proposed associated infrasound detections, the events were first relocated using both seismic and infrasound detections. The event epicenters were plotted using Google Earth; we then searched the imagery for possible mining sources. The nearest town name was used to identify the mines. Events believed to be associated with a mining source were relocated, with the event location fixed to the center of the mining activity. Celerity was checked at this stage and iterative adjustments made to event associations, or mine locations. There were several cases of mines located close to one another. Infrasound detections were determined to be associated with approximately 200 of the seismic catalog events (~25%) and appear to originate from roughly 50 mining complexes (Figure 8 and Table 2). About 80% of the events moved less than 20 km when relocated using both seismic and acoustic data and associated to a mine site. The majority of the identified mine complexes are located within 500 kilometers of Zalesovo. Figure 9 is a detailed map of the mine sites located within several hundred kilometers of the IMS arrays I46RU/ZALV.

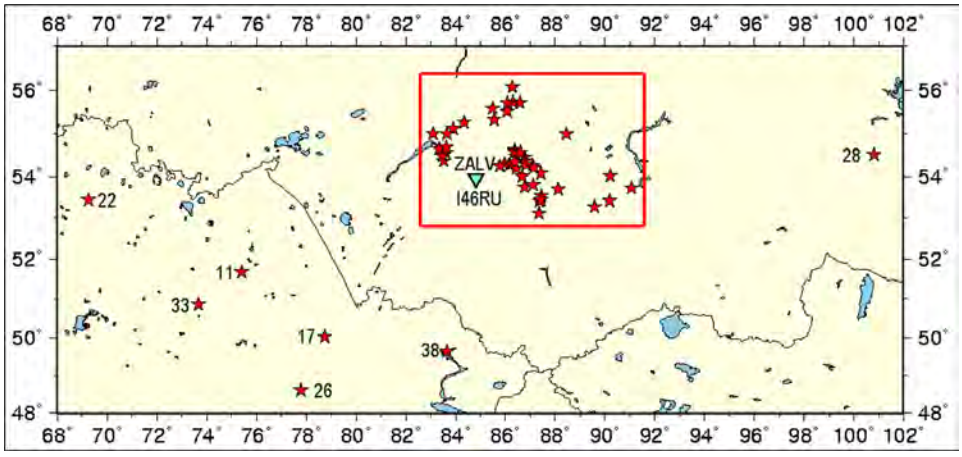

Figure 8. Map showing the source locations (mine complexes) identified using combined seismic and infrasound event locations within the one month dataset (red stars). Inverted triangle shows IMS station locations. The red box is the detail area shown in Figure 9. The labels are keyed to Table 2.

Table 2. Mine complex locations

ID	Nearest Town	Count	ID	Nearest Town	Count	ID	Nearest Town	Count
1	Bachatkiy	9	**18**	Karakan	10	**35**	Nov. Put	4
2	Barzas	4	**19**	Kedrovka	5	**36**	Novokuznetsk	2
3	Belogorsk	1	**20**	Khakassia	1	**37**	Novosibirisk	2
4	Belova	2	**21**	Kiselevsk	14	**38**	Oktjabrskij	1
5	Berezovskiy	8	**22**	Kokchetav	1	**39**	Rudnichnyy	3
6	Bol Kedrovka	1	**23**	Krasnobrodskiy	12	**40**	Salair	3
7	Bol'sheyamnoye	1	**24**	Krasnoyarka	1	**41**	Sartaki	4
8	Chernogorsk	6	**25**	Kyrgay	2	**42**	Simanovo	5
9	Chernyy Kaltan	1	**26**	KZ221	1	**43**	Sorsk	2
10	Dunaevka	2	**27**	Lekarstvennoye	1	**44**	Sukharinka	1
11	Ekibastuz	1	**28**	Listvyakana	1	**45**	Svet	10
12	Gornyy	9	**29**	Mayskiy	2	**46**	Toguchin	1
13	Gramoteino	2	**30**	Medvedskoye	1	**47**	Urgun	1
14	Gur'evsk	2	**31**	Mezhdurechensk	31	**48**	Uspenka	1
15	Iskitim	2	**32**	Mokhovo	1	**49**	Ust Chem	3
16	Kaltan	2	**33**	Molodezhnoye	2	**50**	Vershina Tei	2
17	Kara Zhyra	1	**34**	Nov. Gorodok	1	**51**	Yerunakova	9
						52	Zhernovo	11

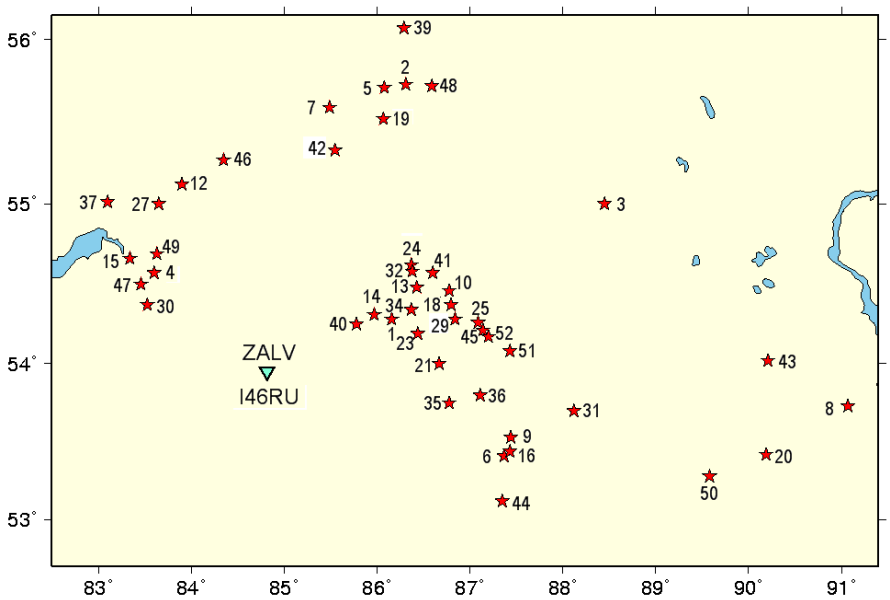

Figure 9. Detailed map (red box in Figure 8) showing mine sites (red stars) identified during study located near IMS stations ZALV/I46RU (inverted triangle). The labels are keyed to Table 2.

For those mine complexes with ten or more events associated, we provide time-of-day (GMT) and day-of-week histograms (Figure 10). Although not conclusive, these histograms support a mining-related source for the seismic events. All events shown here occurred during daytime hours at these mine sources and no events occurred on Sundays.

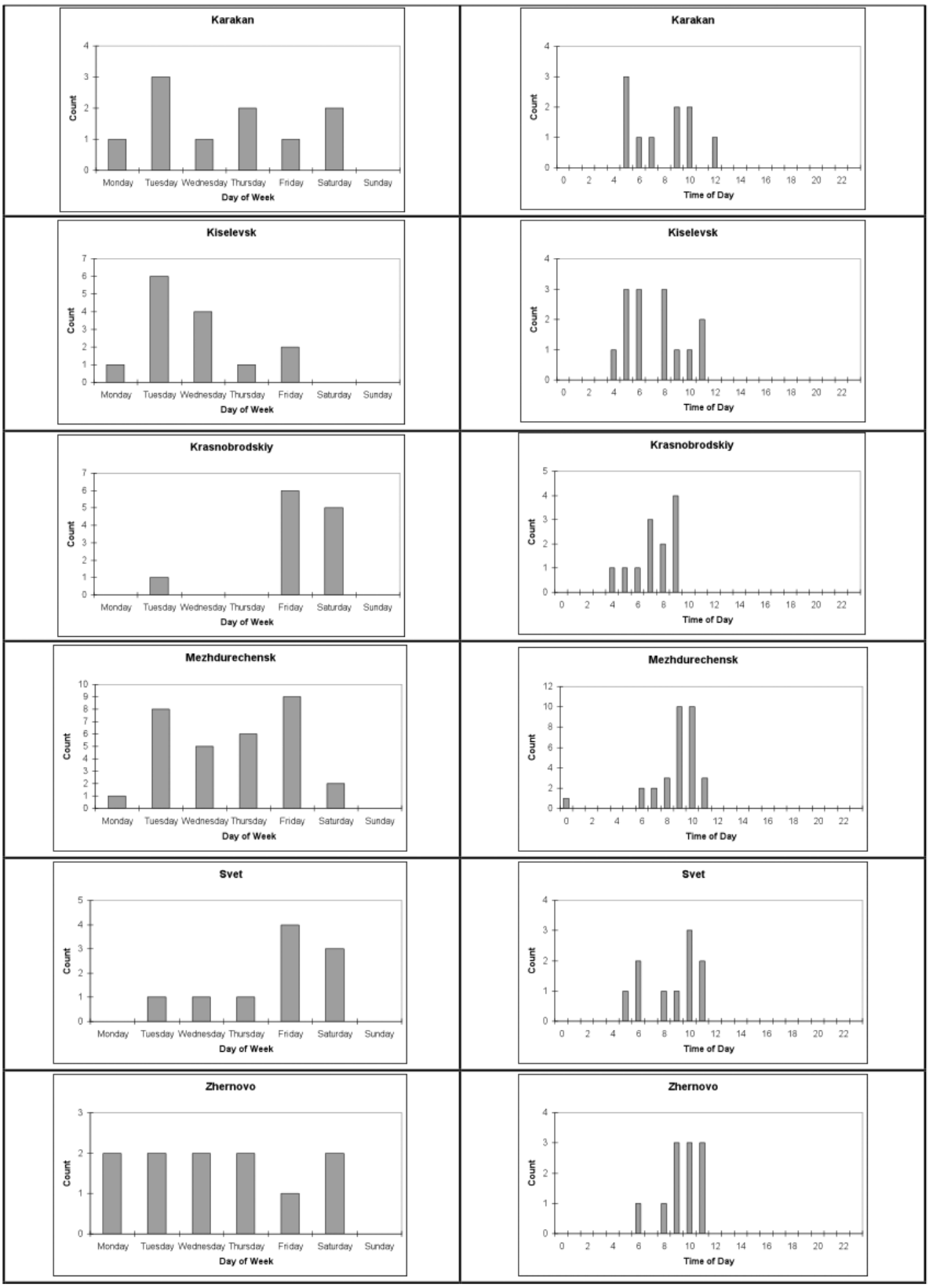

Figure 10. Temporal histograms of selected mine complexes.

CONCLUSIONS AND RECOMMENDATIONS

The ZALV array is a vast improvement for CTBT monitoring purposes over the previously operational three-component IMS station ZAL. The ability to calculate reliable azimuth and slowness estimates from the array improves regional and global monitoring capability. Most teleseismic signals recorded on station ZALV appear to have lower frequency content than on neighboring station MKAR, although for many teleseismic events the path is quite similar. For regional events, ZALV shows good response across the full-frequency spectrum. *Rg* phases at ZALV can often have large (late) time residuals (based on the iasp91 velocity model), but are usually very clear on the waveforms. The reviewed dataset will be used as a benchmark baseline for tuning automated processing software.

A high-quality human-analyzed 800-event seismic catalog was used as a starting point to identify infrasound detections observed on the IMS infrasound station I46RU. Events were reprocessed and located using both infrasound detections (azimuth defining only; not time defining in locations) and seismic detections (time and azimuth defining as appropriate). Each epicenter was reviewed using Google Earth to attempt to identify nearby mines as potential sources of these signals. When a mine complex was identified near the epicenter, the event was reprocessed with its location fixed at the center of the mine complex. Over 200 events from the master catalog had infrasound detections associated, leading to identification of over 50 source mines. While not a substitute for field validation of ground truth events, the compiled dataset could potentially be used in explosion discrimination studies.

As data from the IMS infrasound network are integrated into routine processing, the IDC inevitably must deal with review of a growing number of events detected at one or more infrasound stations. A portion of this study focused on association of infrasound signals with seismic events occurring in a very active mining region surrounding the IMS infrasound array, I46RU. The reference database of characteristic signals from the identified sources can be used for tuning and validating algorithms in automatic station and network processing, and by IDC analysts during the interactive review process.

ACKNOWLEDGEMENTS

The authors would like to thank Mr. Ivan Henson for contributing stand-alone versions of integral Geotool functions, that without, this work would still be in progress. A great deal of thanks to Ms. Elena Tomuta, CTBTO, whose assistance in configuring a very capable LINUX version of the software was invaluable.

Maps in this document were produced using the program Generic Mapping Tools (Wessel and Smith, 1998).

The views expressed herein are those of the authors and do not necessarily reflect the views of the CTBTO Preparatory Commission.

REFERENCES

Wessel, P. and W. Smith (1998). New, improved version of Generic Mapping Tools released, *EOS Trans. Amer. Geophys. U*. 79: 579.

DEVELOPMENT OF A LASER INTERFEROMETRIC MINIATURE SEISMOMETER

Dustin W. Carr, Gregory R. Bogart, Seth Goodman, Patrick Baldwin, Howard Milburn, and David Robinson

Symphony Acoustics, Inc.

Sponsored by the National Nuclear Security Administration

Award No. DE-FG02-08ER85108

ABSTRACT

Miniature seismic sensors that maintain very low noise performance are a critical need for nuclear test monitoring. Ground-based monitoring systems have proven to be very capable in identifying nuclear tests and can provide somewhat precise information on the location and yield of the explosive device. Making these measurements, however, currently requires very expensive and bulky seismometers that are difficult to deploy in places where they are most needed. A high-performance, compact device can enable rapid deployment of large-scale arrays, which can in turn be used to provide high-quality data.

During our Phase I SBIR research, we designed and built a seismic sensor prototype that is 40 times smaller than existing state-of-the-art sensors. This acceleration sensor integrates optoelectronics, passive optics, and micromechanical structures in a compact assembly that is robust and extensible to manufacturing. The use of an optical interference transducer provides very high gain in the displacement measurement, which in turn leads to mechanical design parameters that are optimal for miniaturization without performance being sacrificed.

During this phase of the project, our goal was to gain a better understanding of the capabilities and limitations of such a sensor, especially with regard to low-frequency noise sources. We employed techniques for the reduction of these noise sources and tested the optoelectronics and control circuits in a laboratory test stand. We showed that we could reduce the dominant source of low-frequency noise in lasers 40 dB by using a simple wavelength control system. This was then implemented in an acceleration sensor that was initially designed to achieve an equivalent acceleration noise of –145 dB/Hz relative to 1 (m^2/s^4). Initial characterization showed that we achieved –139 dB/Hz down to 1 Hz. The sensor capsule was 15 mm in diameter by 15 mm high.

Our next step is to transfer this to a mechanical system that is capable of achieving –168 dB/Hz, which would be lower than the new low-noise model down to 0.1 Hz. This design is currently under development and will be the subject of our Phase II research.

OBJECTIVES

A smaller, simpler-to-deploy seismic sensor is highly desirable for a number of applications, including the monitoring of nuclear testing. A significant fraction of the cost of a sensor station is related to the environmental requirements of the sensors and to the cost of putting large sensors deep underground in borehole installations. Reducing the sensor size and mass can greatly simplify these deployments. There are, however, fundamental limits associated with the extent to which existing sensors can be size reduced. In our previous paper at this conference (Carr, 2008), we described our planned research and development on a sensor that uses a new type of optical interference transducer. The performance of this transduction mechanism does not depend on the size, enabling an optimal mechanical design for the sensor.

We had four objectives for this SBIR Phase I project that guided our work.

1. Development of a robust mechanical design that will result in a sufficient range of motion and a thermal noise limit that is below the low-noise model (LNM) target, combined with an optical design that will result in the required motion sensitivity.
2. Characterization of optical sources and identification of methods to mitigate the effects of wavelength noise.
3. Development of an electronics design that will not contribute to the noise floor defined by the photodiode shot noise and the mechanical thermal noise and that maintains an overall power consumption below 30 mW per axis.
4. Assembly and testing of a compact single-axis sensor capsule that will demonstrate the feasibility of this approach.

RESEARCH ACCOMPLISHED

For our transducer, we are using a simple Fabry-Perot transducer that is composed of two dielectric mirrors that are bound in an optical cavity, as shown in Figure 1. In our original proposal, we described the fundamental noise floor for such a system as being the sum of the shot noise in the detection photodiodes and the thermally driven mechanical noise of the spring-mass system. The latter noise source is common to all approaches and does not depend on the transduction technology used.

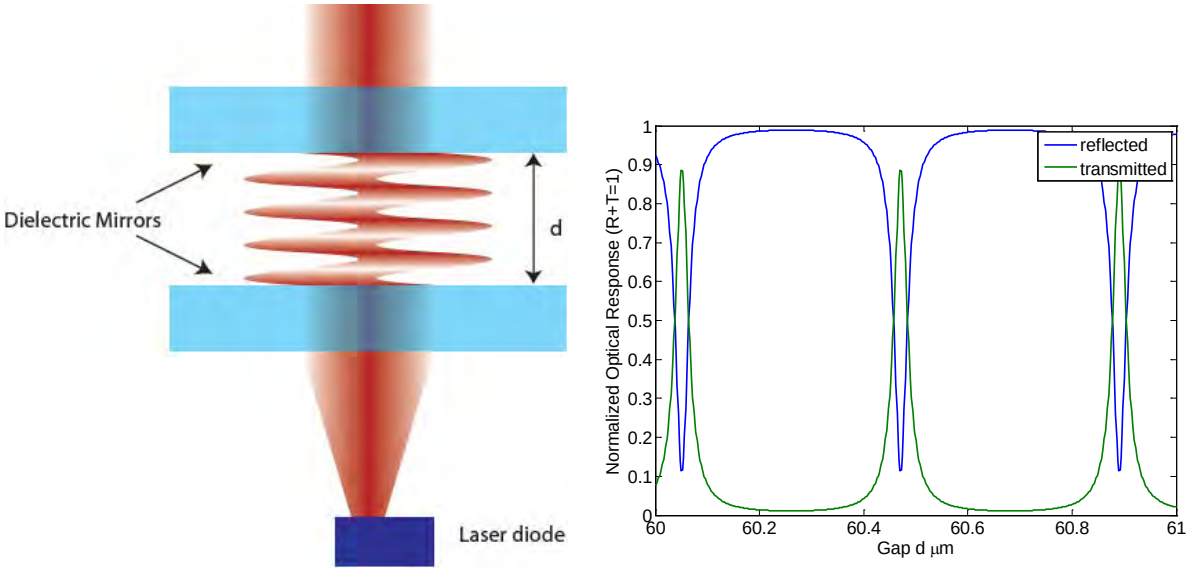

Figure 1. A simplified diagram of an optical interference transducer.

A plot of the combined noise floor is shown in Figure 3, with assumed values for the laser intensity, cavity finesse factor, and the quality factor of the proof mass fundamental resonance.

Our approach is to make a relatively high resonant frequency device, above 100 Hz, that is highly underdamped. The amount of damping determines the mechanical thermal noise force amplitude. While an underdamped system may have a problematic response function, this will be at a frequency that is well above the intended operating bandwidth of these seismic devices. The packaging can also be designed to reduce the transfer of high-frequency vibration to the device and thus eliminate large amplitudes at the resonance that could result in intermodulation distortion.

The green shaded region in the plot (Figure 2) indicates where the device is limited by mechanical thermal noise. Operation at a higher frequency also means that the proof mass must be increased to about 1 gram. Such masses cannot be achieved in a compact form factor unless materials of high density, compared with silicon, are used.

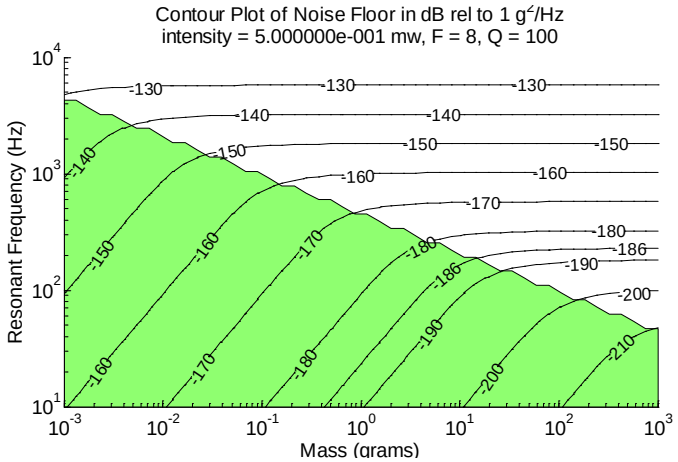

Figure 2. Contours of the white noise spectral density. Within the shaded area, the noise floor is dominated by thermal noise in the spring and mass. In the unshaded region, the photodiode shot noise is the dominant factor.

Evaluation of Optoelectronic Noise Sources

Low-frequency 1/f noise has also been a major area of focus during this study. The primary sources of 1/f noise are the optoelectronic components, including the lasers and photodiodes. For the lasers, there are two types of 1/f noise to consider: intensity noise and wavelength noise. Intensity noise can be eliminated very effectively in a balanced receiver, wherein all of the light that is reflected or transmitted from our sensor cavity is collected, and the balanced differential is our output signal. Wavelength noise is more problematic, as it is indistinguishable from a change in cavity length and can thus not be separated from the desired sensor output signal.

We have built a few laboratory test stands that have enabled us to explore these noise sources and develop solutions for eliminating them from the system. An optical ray-trace of the initial test stand design is shown in Figure 4, along with an image of the implementation on our optical table. This system has an extremely quiet current source, along with a detector circuit that is shot-noise limited. We use this to probe a fixed etalon that consists of a 120-µm-thick fused silica die that is coated on both sides with an 85% reflecting mirror.

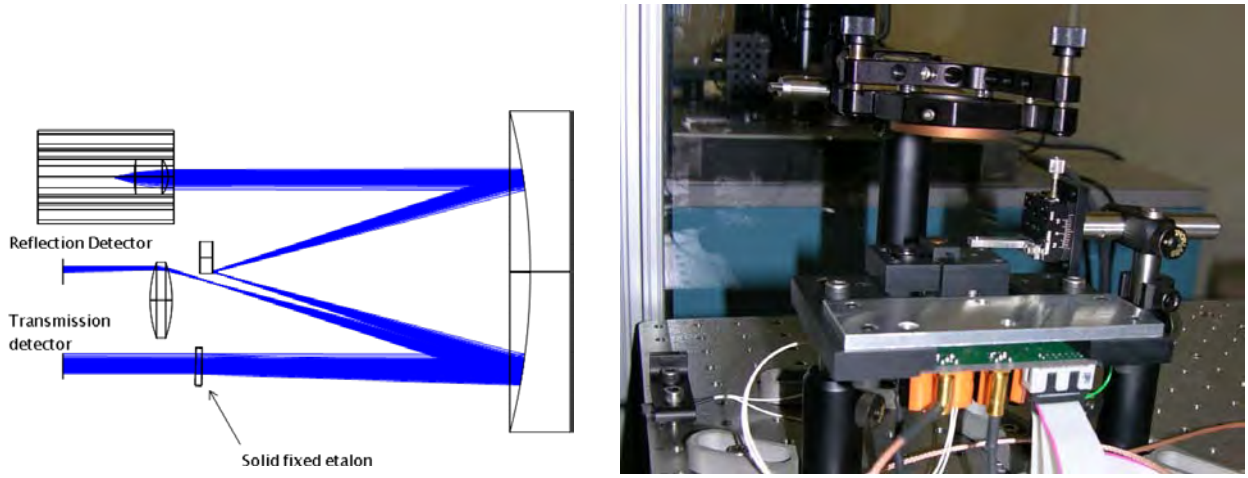

Figure 3. Test stand system design and implementation. The purpose of this system was to provide a way to characterize noise sources in diode lasers and optical sources. Collimated light is directed to a solid. fixed etalon, which could be tilted to position the optical response at the point of maximum sensitivity to wavelength variation.

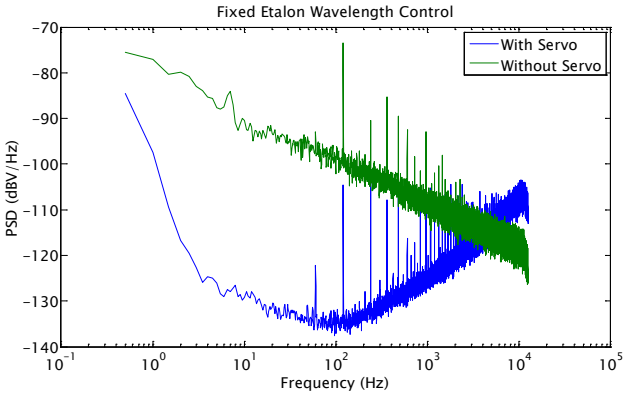

Figure 4. This is the observed noise spectrum at the differential output of our system. The 60-Hz peaks are present due to the ambient light in our laboratory. The 1/f spectrum shown is entirely due to wavelength noise. When we employed a servo to the laser current, we could suppress this noise by 40 dB within the bandwidth of the servo controller.

This fixed etalon is about 30 dB more sensitive to variations in wavelength than our typical sensor design would be. As such, it allows us to magnify the effect of wavelength noise in the hope that we may better understand and control it at the source.

Because the laser output wavelength varies with laser current, we made modifications to the test stand wherein we created a closed-loop current controller to stabilize the laser wavelength. We used the fixed etalon to convert laser wavelength changes to intensity changes detected at the photodiodes. The resulting detected signal then becomes the input to our control loop. Our first attempt used a controller that had a limited frequency range, as this was implemented in a piggyback board that interfaced with the original test stand. With that approach we achieved a reduction in wavelength noise by 40 dB (Figure 4) over the range of 10–100 Hz. As mentioned above, this fixed etalon had a wavelength sensitivity that was intentionally 30 dB higher than that of a typical sensor etalon. This type of wavelength control has since been implemented in our sensor capsules, enabling the suppression of this noise source to frequencies below 0.1 Hz.

Laboratory Prototype Sensors

Our first prototype sensor capsules integrated the optics, mechanics, and sensor electronics into a compact 15-mm-diameter package, as shown in Figure 6. The initial mechanical design for these devices was designed as a significant step towards a LNM device. We intentionally aimed for an intermediate point because the complexities involved in this design demanded that we first and foremost build a sensor that shed light on the dominant remaining issues to be addressed in the next phase. The mechanical resonant frequency of this device was 380 Hz, with a quality factor of around 100.

This device plugs into a signal conditioning and control circuit board. For these initial tests, the board was 50×50 mm^2. This is not indicative, however, of the size required for these electronics, as we have since reduced this to a 22-mm-diameter printed circuit board (PCB) design. We placed the capsule and the board in a housing as shown in Figure 5 for our initial testing.

We acquired the output acceleration from these capsules simultaneously with the output from a Sercel L4C geophone co-located in our facility. In the bandwidth of interest, the L4C certainly has a lower noise floor than that of the Symphony Acoustics prototype, and so by compensating the L4C output so that its response is expressed in terms of acceleration, we were able to determine the approximate noise floor of our device. A power spectral density (PSD) plot is shown below, expressed in dB relative to 1 m^2/s^4/Hz. While we are still well above our target performance, this is still a major step forward and rivals the performance of any known miniature acceleration sensors reported in the literature over this range of frequencies (Krishnamoorthy, 2008). During our acquisition, we also acquired a low-frequency seismic event, which helped to demonstrate our coherence down to very low frequencies.

The noise sources that dominate at low frequencies are related to our digital control implementations, as well as our sensitivity to thermal fluctuations. We have a clear path to further reducing this noise floor by at least 25 dB with mechanical and electronic design enhancements during the next phase of this project.

Figure 5. On the left is an image of our sensor capsule. On the right is the laboratory prototype sensor, including signal conditioning and control electronics that were integrated in a "debug" form factor for this phase. The L4C sensor used for device characterization is also shown.

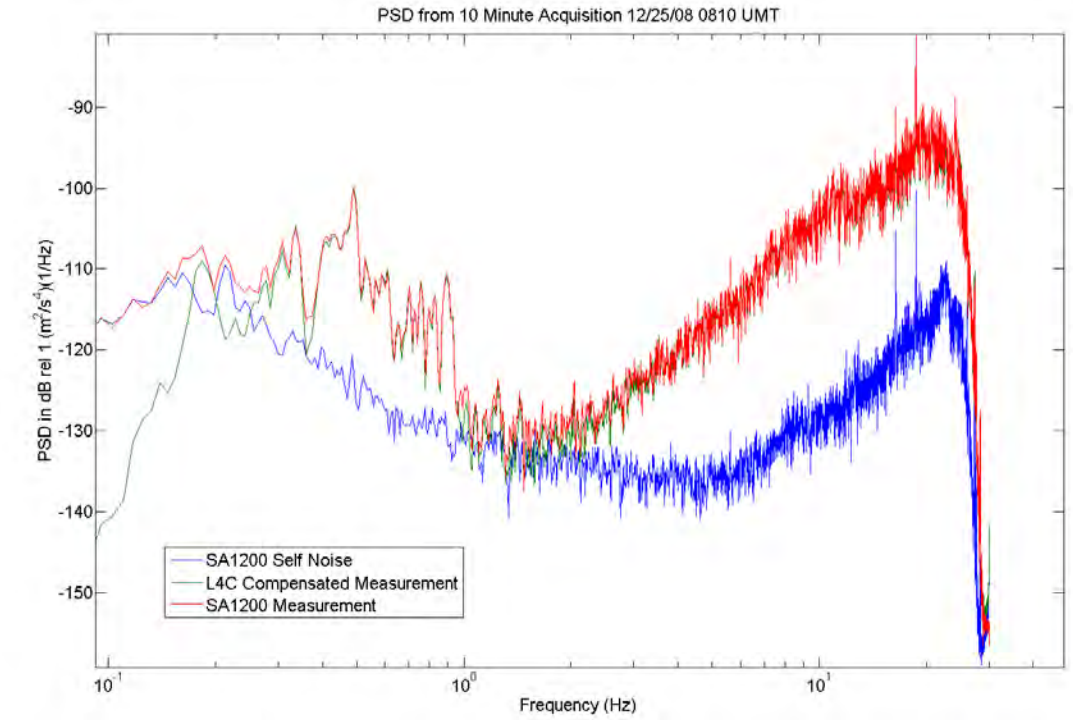

Figure 6. A power spectral density of our device (red) along with that of a Sercel L4C 1 Hz geophone sensor, compensated to provide an acceleration output. The difference signal from these two is representative of our noise floor, at frequencies below 4 Hz. At higher frequencies, we still see a common mode signal in the PSD due to imperfect coherence, which could easily be caused by a slight angular misalignment.

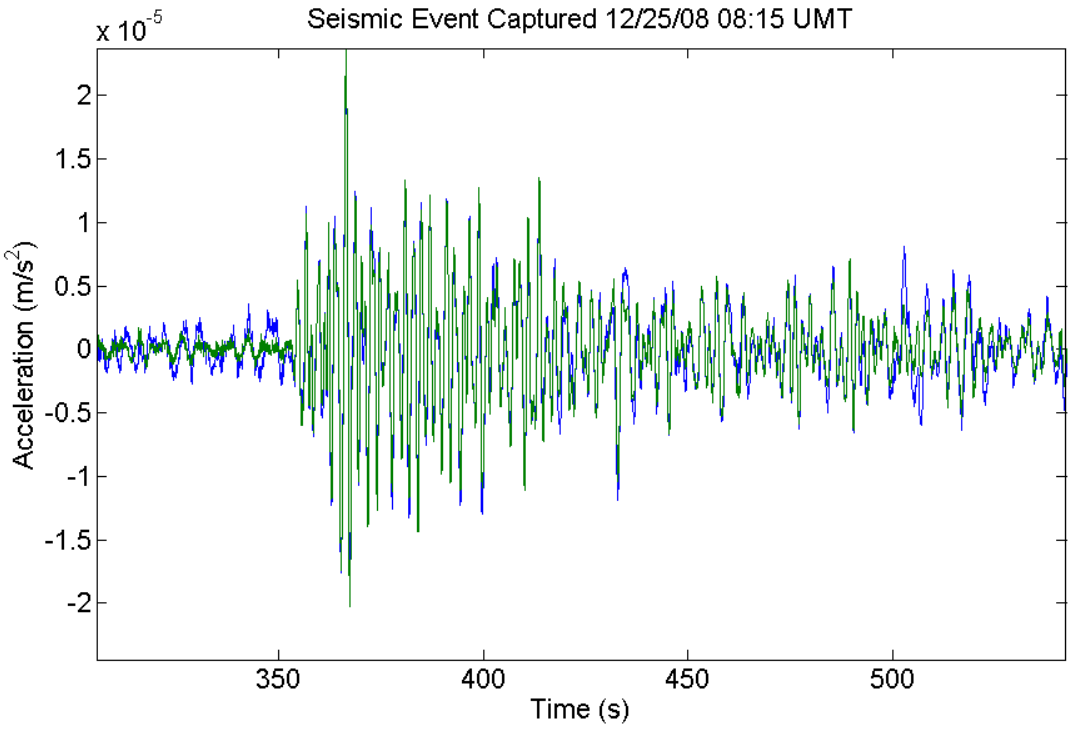

Figure 7. Time series data of a low-frequency seismic event captured by the two sensors.

CONCLUSIONS AND RECOMMENDATIONS

We adhered well to our original proposed plan and made considerable strides towards the realization of a miniature seismic sensor that is capable of LNM limited operation. There is still much more work to be done in Phases II and III, and we are committed to pursuing this effort. We have not yet achieved the ultimate acceleration noise floor required, but that is primarily because we aimed for an intermediate point that would allow us to better understand the remaining issues. Time constraints also prevented us from pursuing a complete testing plan with a qualified external facility.

The technical objectives of our Phase II research are as follows:

1. Refine our sensor designs from Phase I so that they may extend to new LNM limited performance, along with the commensurate testing and verification procedures necessary to prove this performance.
2. Establish robustness and reliability testing for this new technology to enhance the opportunity for rapid acceptance in the marketplace.
3. Execute field tests using arrays of devices (10 to 100) in collaboration with systems integration companies and/or government test facilities.
4. Establish collaborations with chip manufacturers and system integrators to create a digital output sensor that can be rapidly deployed in arrays.
5. Package a compact 3-axis digital sensor prototype that can be operated in any orientation and that meets the specifications as spelled out by the Department of Energy.

ACKNOWLEDGEMENTS

We acknowledge the management and technical staff at Science Horizons, Inc., who provided the digitizing equipment and geophone used for the characterization of these devices.

REFERENCE

Krishnamoorthy, U., D. W. Carr, G. R. Bogart, M. S. Baker, P. J. Clews, T. P. Swiler, and Olsson, R. H. (2008). In-plane MEMS-based nano-G accelerometer with sub-wavelength optical resonant sensor, *Sens. Act. A.* 145: 283–290.

EXPLORING THE LIMITS OF WAVEFORM CORRELATION EVENT DETECTION AS APPLIED TO THE 1994 NORTHRIDGE EARTHQUAKE AFTERSHOCK SEQUENCE

Dorthe B. Carr, Megan E. Resor, Christopher J. Young, and Michael J. Procopio

Sandia National Laboratories

Sponsored by the National Nuclear Security Administration

Award No. DE-AC04-94AL85000/SL09-WFCorr-NDD02

ABSTRACT

Swarms of earthquakes and/or aftershock sequences can dramatically increase the level of seismicity in a region for a period of time lasting from days to months, depending on the swarm or sequence. Such occurrences can provide a large amount of useful information to seismologists. For those who monitor seismic events for possible nuclear explosions, however, these swarms/sequences are a nuisance. In an explosion monitoring system, each event must be treated as a possible nuclear test until it can be proven, to a high degree of confidence, not to be.

Correlation provides a measure of similarity between two waveforms, scaled from 0 (no similarity) to 1 (identical). Seismic events recorded by the same station which correlate well almost certainly have a similar location and source type, so clusters of events within a swarm can quickly be identified as earthquakes. We have developed a number of tools that can be used to exploit the high degree of waveform similarity expected to be associated with swarms/sequences: Dendro Tool (Merchant, 2007), the Waveform Correlation Detector (Resor et al., 2008) and the Self Scanner (Resor et al., 2009). Dendro Tool measures correlations between known events that have been detected by other means. The Waveform Correlation Detector creates its own event library of families that have correlated signals. The Self Scanner is used to establish the overall amount of correlation within a data steam and does not require an event library. All three techniques together provide an opportunity to study the similarities of events in an aftershock sequence in different ways.

We chose the well-studied aftershock sequence from the 1994 Northridge earthquake and used the three different methods to comprehensively characterize the waveform similarity available in a major aftershock sequence. Two different catalogs – the Earthquake Data Report (EDR) and the Southern California Earthquake Center (SCEC) catalog—provide ground truth for event locations and magnitudes. Station PAS from the Terrascope seismic network was the closest station to the Northridge data at a distance of approximately 33 kilometers from the main shock. We clustered events on PAS using all three methods—Dendro Tool, Waveform Correlation Detector and the Self Scanner. Most known events clustered in a similar manner, but with both the Waveform Correlation Detector and Self Scanner, we found significant numbers of new events that were not in either the EDR or SCEC catalog.

Because this sequence occurred in Southern California, there were many recordings of the aftershocks at a variety of azimuths and distances. Using Dendro Tool, we clustered known events occurring in the first 5 hours of the aftershock sequence on 13 stations from the Northern California Seismic Network (NCSN), along a transect of nearly constant azimuth from the Northridge events (338–347 degrees). Distances ranged from 238 to 960 kilometers away. Due to attenuation of the signal, the number of clusters with correlation values over 0.70 decreased from 7 clusters at the station 238 km away to only 1 cluster at the three stations over 850 kilometers away. In addition, the correlation values for the clusters decreased with distance as well. The Waveform Correlation Detector detected events that were not in either the EDR or SCEC bulletins and grouped them into families with known events. For non-catalog events, we estimate magnitudes based on scaling with events in the family. We found that we were getting good correlations for events where the amplitudes were 1000 times lower than the master event. This suggests that the Waveform Correlation Detector can be used to create a more complete catalog, and establish detailed clusters that can help better characterize the total seismicity in aftershock sequences.

OBJECTIVES

Previous work has established, to a high degree of certainty, that events with high correlation values are from the same location (Israelsson, 1990). The Northridge Earthquake of 1994 provides a wealth of data with which to study the effectiveness of correlation-based detection and classification schemes. We compared the results obtained from three correlation-based analysis and detection methods developed by Sandia National Laboratories. In addition, we studied how the output of correlation-based algorithms changed with regards to the distance between earthquake and station.

RESEARCH ACCOMPLISHED

Analysis was performed using three analysis tools developed and implemented by Sandia: Dendro Tool, Waveform Correlation Detector, and Self Scanner. All three tools implement correlation based algorithms to find similar events. They differ primarily in whether they are used on cataloged origins or raw data and in their post processing techniques. The three methods are summarized below (Table 1); detailed descriptions follow.

Table 1. Summary of the features of the three correlation tools used in the study.

	Dendro Tool	Waveform Correlation Detector	Self Scanner
Type of event/data	Cataloged origins	Compares cataloged origins with raw data	Raw data
Function	Measures similarity of cataloged origins	Finds all signals similar to the cataloged origins	Finds all similar signals in raw data
Clustering Actions	Several cluster options; shows dendrogram of clustering	No true clustering; creates families of events related to cataloged origins	Clusters results into families of similar signals
Output plots	Graphical interface shows connectedness of all origins	Plots show catalog origins and all matched signals found in raw data	Plots show all signals in an event family
Speed	Fastest – nearly instantaneous	Faster - ~1 week of data processed overnight	Fast - ~3 days of data processed overnight

Dendro Tool

The Dendro Tool (Merchant, 2007) allows analysts to quickly and easily determine the similarity between seismic origins by computing the cross-correlation values of the origin waveforms. Origins can then be categorized into clusters of similar events. This analysis technique can be used to characterize historical archives of seismic events in order to determine many of the unique sources that are present. In addition, the source of any new events can be quickly identified simply by comparing the new origin to the historical set.

The primary interface of the tool is the dendrogram window which plots the correlation relationship between all the origins. Selecting a correlation threshold value separates the waveforms into clusters. A detailed discussion of the clustering process can be found in Merchant (2007).

Waveform Correlation Detector

The Waveform Correlation Detector (Resor et al., 2008) was developed to simulate a real-time system where incoming raw data is compared to cataloged origins to try to screen out similar events. Catalog origins can include historical data and events from earlier in an aftershock/swarm sequence. The Waveform Correlation Detector is

intended for use during an aftershock/swarm sequence to aid analysts by allowing them to prioritize signals with new locations and/or source types (possible explosions) over signals with a high degree of similarity to a cataloged origin known to be an earthquake, and therefore almost certainly an aftershock. Motivation for the tool was to provide the following benefits during a swarm/sequence scenario:

- Better use of analyst resources
- Faster processing
- Reduction of detection threshold
- More accurate phase picks.

A flow chart of the algorithm and how it compares with the traditional pipeline is shown in Figure 1.

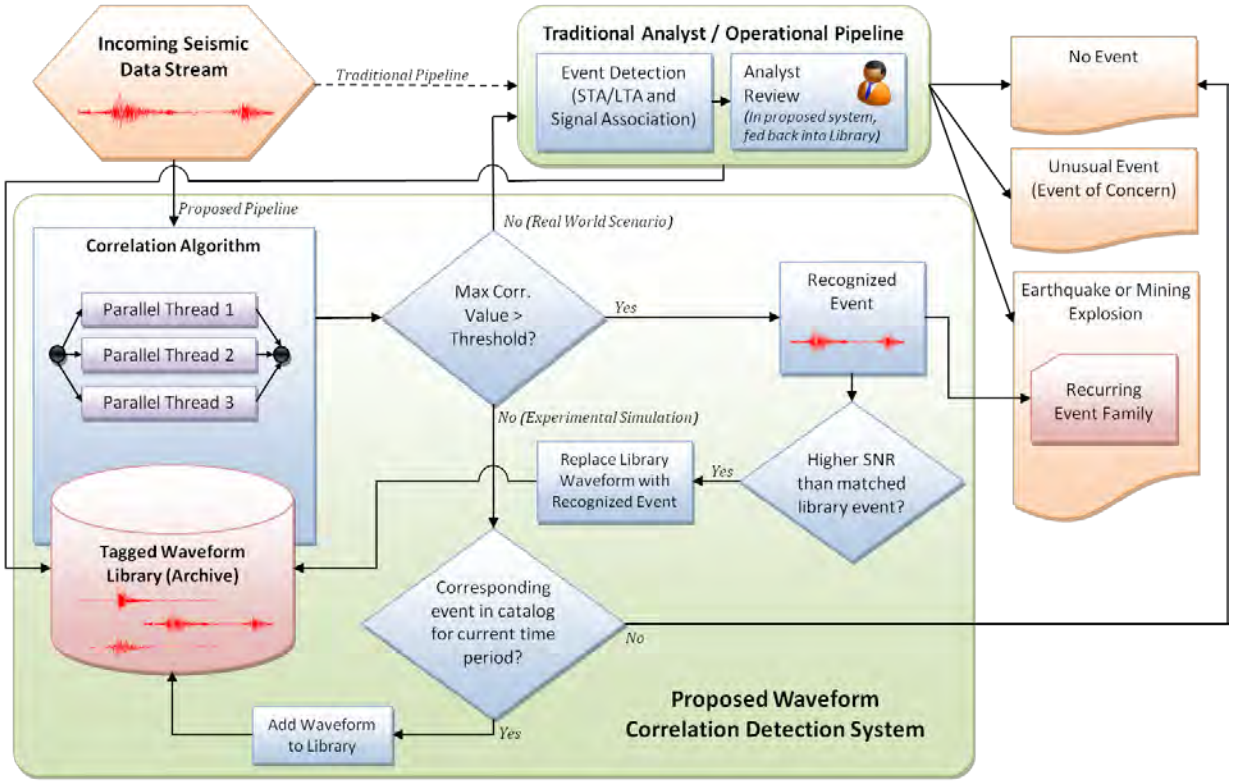

Figure 1. Waveform Correlation Detector algorithm flow chart.

In a traditional monitoring pipeline, an incoming data stream is passed through an event detector, followed by analyst review to categorize the event. The Waveform Correlation Detector is designed to be inserted before the traditional pipeline, reducing the analyst workload by screening out events similar to those which have been seen and previously categorized.

Our system compares the incoming data stream to previously identified origins held in a "library" or archive of tagged events. If the data stream and a particular library entry have a correlation value above a threshold, then we declare a recognized similar event. During a swarm, the library will grow as previously unseen waveforms, detected using traditional detection methods and verified by an analyst, are added to the library. In our experiments, the library is initially empty, though in practice the library could be pre-populated with historical data. The Waveform Correlation Detector outputs all the signals in the raw data found to correlate well with each cataloged origin (library master origin).

Self Scanner

The Self Scanner was developed to find all similar signals within a raw data stream (Resor et al., 2009). Each segment of data is correlated with every other segment. The correlation values are then run through a clustering algorithm which outputs families of similar waveforms. Figure 2 shows the self scanning correlation algorithm in pseudo-code. In this manner, every segment of raw data is correlated with every other segment.

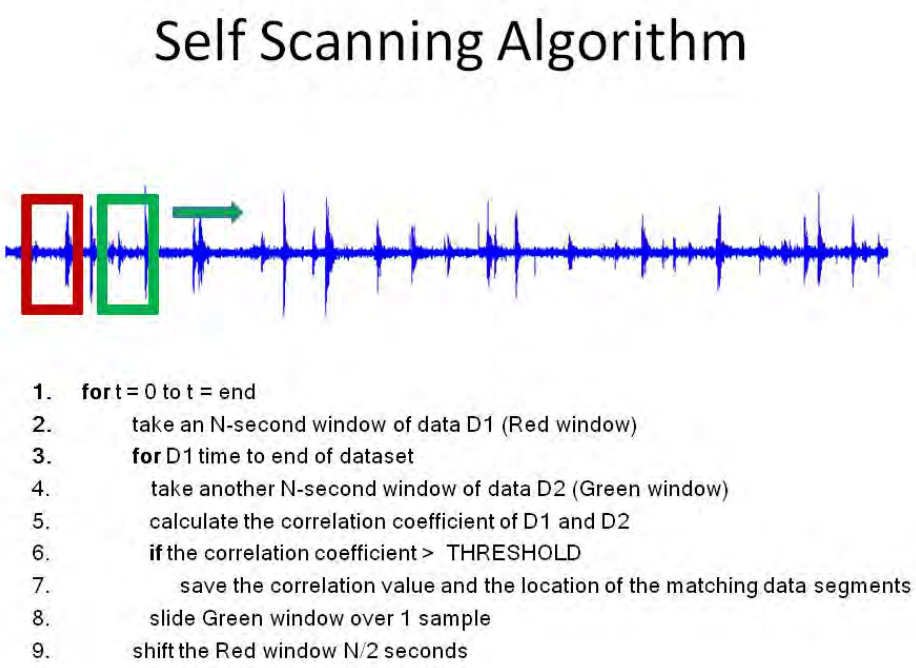

Figure 2.Self Scanning Algorithm.

The clustering routine is run after performing the self scanning algorithm. The algorithm links events with high correlation values to create families of similar signals.

Data

The Northridge Earthquake occurred at local time 4:30 am on January 17, 1994 and had a moment magnitude (Mw) of 6.7. This earthquake produced the strongest ground motions ever instrumentally recorded in an urban setting in North America at that time. The location of the earthquake was 34.213°N, 118.547°W and at a depth of 18.4 km according to the EDR catalog from the United States Geological Survey (USGS). There were numerous aftershocks from this major earthquake. In a period of 7 days, January 17-23, 1994, the EDR recorded 457 origins with m_b magnitudes between 2.9 and 6.4 in the lat-lon box of 33.9°-34.6°N and 118.8°-118.2°W (Figure 3). In that same time period and lat-lon box, the SCEC catalog recorded 2395 origins. Local magnitudes from the SCEC catalog ranged from 1.5 to 5.9.

We collected waveforms from the Incorporated Research Institutions for Seismology (IRIS) on station PAS for the time period January 17-23. Station PAS is only 35 km from the main shock, and has good signal to noise. Because the Northridge Earthquake occurred in Southern California, it provides a good opportunity to get waveform data from a large number of stations in the area to determine how correlation is affected by the distance from the station to the aftershock swarm. We collected waveforms from the Northern California Earthquake Data Center (NCEDC) and Northern California Seismic Network of the USGS for 13 stations that were at various distances from the main shock, but all along a transect of nearly constant azimuth of 338 to 347 degrees. Figure 3 shows a map of where the stations are located with relation to the Northridge Earthquake aftershocks.

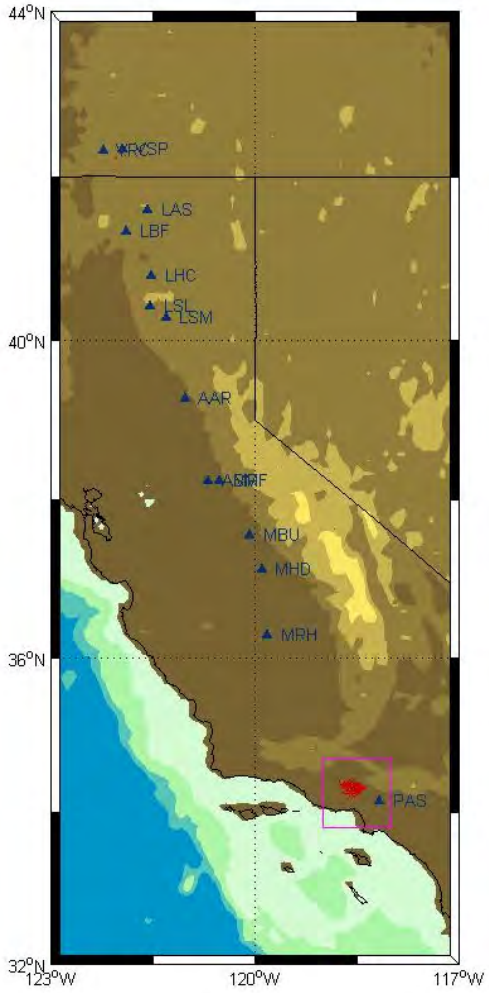

Figure 3. The Northridge Earthquake aftershock sequences (pink box) and stations used in the study.

Comparison of Waveform Correlation Tools

We began with Dendro Tool to cluster the 412 origins found in the EDR catalog in the chosen time period and lat-lon box. Filter and window parameters are given in Table 2. One hundred eighty of the 412 origins (44%) were categorized into 50 clusters of similar signals using a correlation threshold of 0.7. The largest cluster had 19 origins and there were 33 clusters that had only 2 origins. Figure 4a shows part of the dendrogram that was created using Dendro Tool on this data and Figure 4b is a map showing the locations of the 7 clusters with more than 5 origins. The color of the origins on the map correlates to the color of the cluster on the dendrogram. The seven clusters separate fairly well, but there are some origins that may not have an accurate location.

Next we applied the Waveform Correlation Detector using origins from the EDR catalog as master origins and the parameters given in Table 2. There are 326 master origins and signals in the data stream are matched using a correlation value of 0.7. The signals that are matched are either known origins from the EDR catalog or unknown signals. The biggest event family had 16 signals that matched the master origin (17 signals total) and there were 183 master origins (56%) that matched no other signals in the data. Figure 5 shows events from one of the event families created by running the Waveform Correlation Detector on the Northridge data. The master origin for event family #20 is orid 81501. Signals that match this waveform are orids 81538, 81540 and 81544, plus a new signal that occurred at 1994017 15:46:23 that was not in the EDR origin table. In a pipeline scenario, an analyst would not have had to look at the signals that matched orid 81501. These signals would have been considered as matches to an

Table 2. Input parameters for the correlation tools.

	Dendro Tool	Waveform Correlation Detector	Self Scanner
Time	1994017 12:30 to 1994021 14:35	1994017 12:30 to 1994021 14:35	1994017 12:30 to 1994021 14:35
Latitude Span	33.9°N to 34.6°N	33.9°N to 34.6°N	Not needed
Longitude Span	118.8°W to 118.2°W	118.8°W to 118.2°W	Not needed
Catalog	Earthquake Data Report	Earthquake Data Report	Not needed
Station/Channel	PAS, BHZ	PAS, BHZ	PAS, BHZ
Window length	55 seconds, starting 5 seconds before P	40 seconds starting 5 seconds before P	36 seconds
Correlation Threshold Value	0.7	0.7	0.7
Filter	0.8-3.5 Butterworth, order 3, filter before windowing	0.8-3.5 Butterworth, order 6	0.8-3.5 Butterworth, order 3, forward and backwards

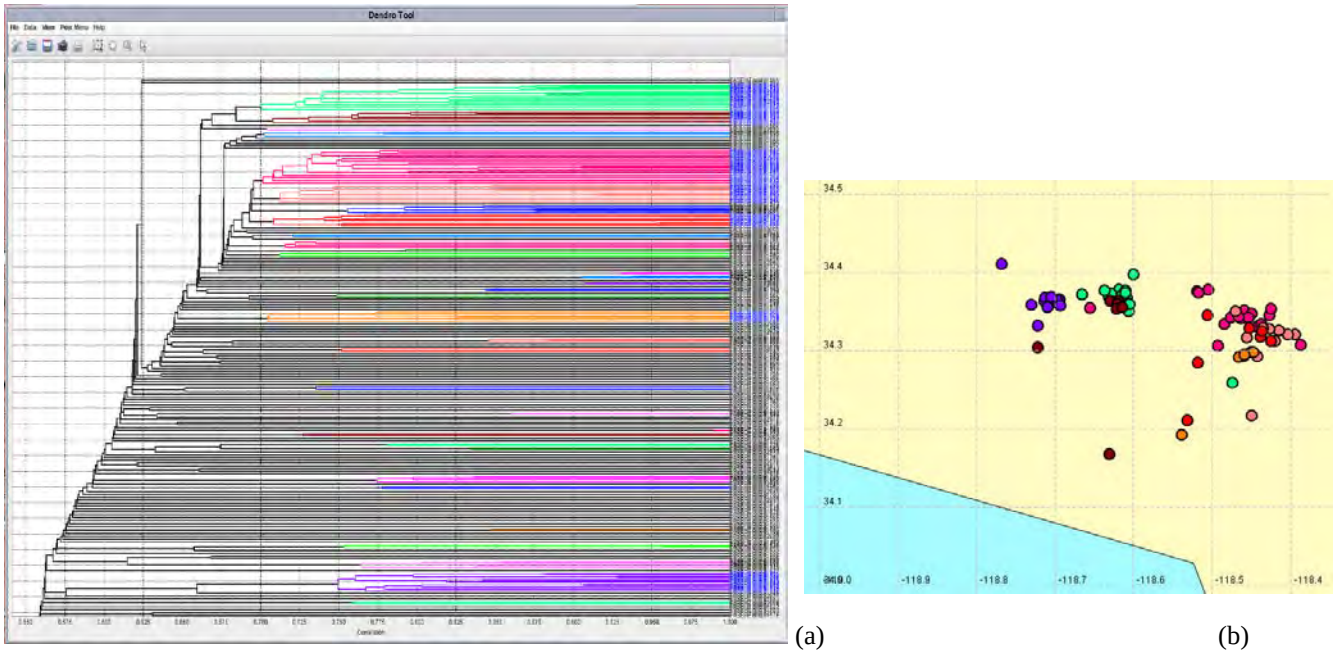

(a) (b)

Figure 4 (a)Dendrogram showing the some of the clusters formed on the Northridge data from station PAS and (b) Locations of the seven dendrogram clusters that had more than 5 origins. The color of the origins matches the colors of the clusters in 4(a).

already analyzed event. The signal found that didn't match a known origin indicates that using the Waveform Correlation Detector can find additional aftershock data without increasing analyst burden.

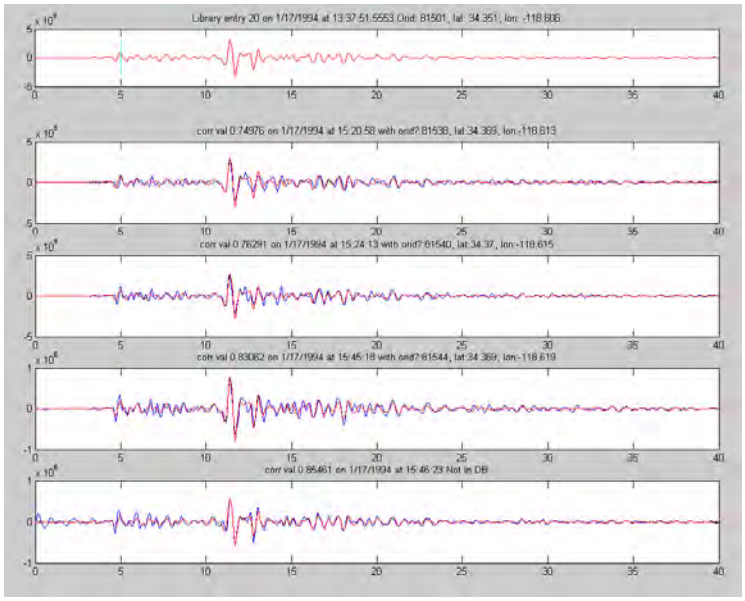

Figure 5. Waveform Correlation Detector output plot for event family #20 (5 of the 17 signals in library).

The Self Scanner did not use any origin information. Correlations were made with signals that were found as the self scanner went through the data and clustered signals based on correlation values over 0.7. Over 950 families were created with the Self Scanner. Most of the families had only 2 signals, but the top 10 families had between 63 and 202 signals. Figure 6 shows the first few signals in a family that was composed of 92 signals, designated Family 4. The signals from Family 4 are the same signals that were in the Waveform Correlation Detector event Family 20 (Figure 5). The signals at times 13:37:46, 15:20:48, 15:24:03 and 15:45:10 are the signals from orids 81501, 81538, 81540 and 81544 respectively. Additionally, the signal at time 15:46:17 matches up to the signal timed at 15:46:23

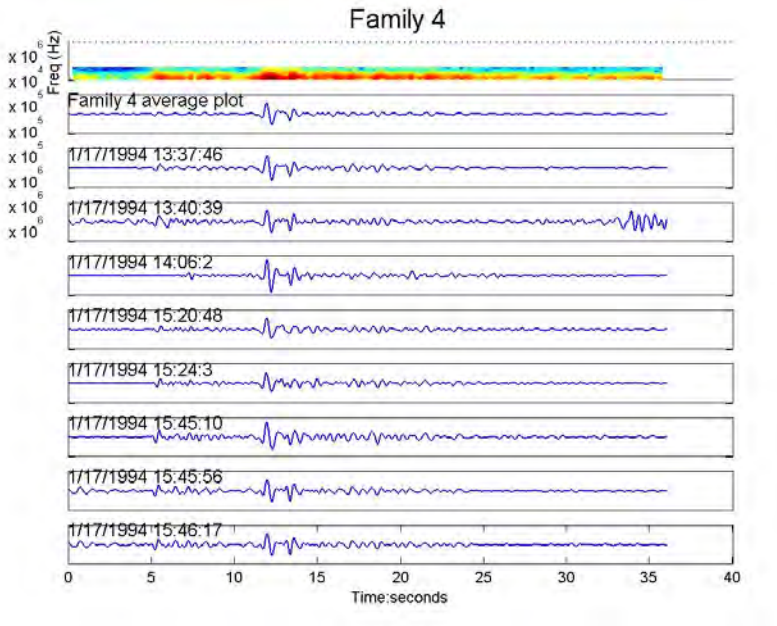

Figure 6. Self Scanner output plot for Family #4 (8 of the 92 signals).

in Figure 5. The Self Scanner found some additional signals as well (13:40:39 and 14:06:02). These signals are small and have low correlation values (0.71, 0.73) with the first signal at 13:37:46. The Self Scanner also extends the known families found with Dendro Tool, finding smaller events that make the family more complete.

To get the best idea of the differences seen with the three different correlation tools, we looked at the results seen in Figures 5 and 6 from the Waveform Correlation Detector and Self Scanner to see how those tools correlated the events in the Dendro cluster (cluster 1, green cluster on Figure 4). Cluster 1 consisted of 16 origins that spanned the time from 1994017 13:37 through 1994021 11:31. These events are listed in Table 3. Fifteen of the 16 origins had locations that fit into the lat-lon box of 34.35-34.40°N latitude 118.66-118.60°W latitude. One origin, orid 81543 was outside this box at a location of 34.26°N, 118.47°W. We looked at the output from the Waveform Correlation Detector and Self Scanner to see how the origins in Dendro Cluster #1 were matched/clustered with these tools (Table 3). The origins fell into four different event families with the Waveform Correlation Detector, Families 20, 91, 94, and 279. Eleven of the 16 origins in the Dendro Cluster were found in the Self Scanner Family 4. The other origins did not have correlation values with the other signals in Family 4 that were greater than 0.7. Two of the origins, orid 81598 and 81601, correlated well with each other (correlation value = 0.83), but not with any other of the 16 origins in Dendro Cluster 1. The Waveform Correlation Detector and Self Scanner subdivided the Dendro Cluster in an identical manner. The fact that Dendro put all the events in one cluster is due to slight differences in the algorithms handling of lower correlated waveforms.

To compare the correlation algorithms in the three different tools, we compared the correlation value between the same origins with each tool where it was possible. The correlation value between origins 81501 and 81548 can be found looking at all three methods. The value is 0.891 for Dendro Tool, 0.893 for the Waveform Correlation Detector, and 0.89 for the Self Scanner. Additionally, the origins 81598 and 81601 both have correlation values of

Table 3. Results from the three tools using Dendro Cluster #1.

Cluster origins	Lat (°N)	Long (°W)	Waveform Correlation Detector Family	Self Scanner Family
81501	34.351	118.606	20 – master orid	4
81538	34.369	118.613	20	4
81540	34.37	118.615	20	4
81543	34.259	118.474	-	-
81544	34.369	118.619	20	4
81548	34.374	118.622	20	4
81554	34.398	118.6	20	4
81598	34.373	118.629	91 – master orid	103
81601	34.37	118.632	94 – master orid	103
81812	34.36	118.605	20	4
81930	34.378	118.618	20	4
81944	34.377	118.61	20	4
81950	34.372	118.666	279 – master orid	-
81965	34.374	118.61	-	4
82102	34.377	118.637	-	4
82106	34.367	118.608	-	-

0.83 in Dendro Tool and the Self Scanner; although they were found not to match with the Waveform Correlation Detector since they are in different families.

In addition to the known origins, the Waveform Correlation Detector and Self Scanner also matched signals that were not known origins in the EDR catalog. There were 13 new signals that matched the origins in the 4 Waveform Correlation Detector families. Six of those signals matched up to origins in the SCEC catalog. The locations of the SCEC origins all fit within the lat-lon box of 34.35-34.40°N and 118.66-118.60°W, except for SCEC orid 3143149 which had a location or 34.304°N, 118.447°W. Seven of the new signals that were in the Waveform Correlation Detector families were also found with the Self Scanner and clustered into Family #4.

Waveform Correlation and Magnitude

Changes in the size of events imply changes in the source mechanism (e.g., corner frequency) which might affect correlation between nearby events. To investigate this, we examined the range in magnitude within the clusters/families of origins found by our processing. Unfortunately, the EDR does not always provide magnitude estimates for their origins. The SCEC catalog provides magnitudes, but they are one of three types – local, coda or hand determined, so it is difficult to do direct comparisons. For the known SCEC origins that were grouped into the four Waveform Correlation Detection families 20, 91, 94, and 279, the origins with local magnitudes range from 2.43 to 5.07, a difference of 2.7 magnitude units.

Because some of the signals that were matched with the Waveform Correlation Detector were not origins in the SCEC catalog, we calculated our own magnitude range within families based on log of amplitude of the Lg phase and found ranges of up to 3.5. We believe that the Waveform Correlation Detector can find and match signals that are more than 2 magnitude units apart in size.

Waveform Correlation and Distance

Both attenuation of the signal and the signal-to-noise ratio for a signal can have impacts on the correlation values. To study the relationship between correlation/clustering and distance, we correlated 5 hours of data, starting at 1994017 12:00, on 13 different stations that were between 238 to 961 km from the Northridge swarm (Figure 3, Table 4). We used Dendro Tool to do the correlation, since we chose to base our analysis on catalog origins only. For each station we counted the number of clusters and determined how many orids were in each cluster. Table 4 shows how many clusters were created with Dendro Tool at each station, and the number of origins in the cluster with the most events.

Table 4. Station information for stations used in the distance study.

Station	MRH	MHD	MBU	MRF	ASM	AAR	LSM	LSL	LHC	LBF	LAS	VSP	VRC
Distance (km)	238	348	399	484	549	607	720	743	780	849	866	954	961
Azimuth (°)	347	339	340	338	340	339	341	340	341	340	343	342	342
# of clusters	8	5	5	2	4	3	2	2	2	3	2	2	2
Max # of origins	4	4	3	2	3	2	2	2	2	2	2	2	2

As expected, the number of clusters formed at a station decreased with distance. Origins that are seen well and without filtering at stations within 400 km of the aftershock sequence cannot be seen, even with filtering, at the stations over 800 km away from the aftershock sequence. One cluster was seen at all the stations except for the station closest to the source, MRH. The two origins in this cluster are 81481 and 81488 which have local magnitudes of 4.89 and 4.62 respectively, two of the largest events in the swarm. According to the SCEC catalog, there are 3 other events that occur within two minutes of origin 81481 and there is an overlap of all the different signals for

these 4 events in the time window being used to do the correlation of orid 81481 on station MRH. Therefore, this signal does not correlate well to orid 81488. Since the other stations are farther away, the overlap of signals does not impact the correlation as much, although the correlation values for these two orids at stations MHD and MRF are lower than the correlation values at the stations between 450 and 900 km.

Our results suggest that attenuation of the signals does play a role in how well a station can correlate signals seen from an aftershock sequence. In order to match and correlate signals from smaller events, the station used to do the correlation must be within 200–400 km from the signals.

CONCLUSIONS AND RECOMMENDATIONS

The three different methods we have developed for doing waveform correlation work similarly and provide good information about how similar events from an aftershock sequence or swarm are related. The Dendro Tool can be used for historical archive data where good origin information exists. The Waveform Correlation Detector can be used in a real-time system, detecting and matching signals to known events in the library. The Self Scanner works on "raw" data where there is either sketchy or no origin information. A combination of all three tools can be valuable when doing in-depth studies of aftershocks or swarms. Smaller signals that may or may not have origin information can be found and matched/correlated to known origins, even those that are several magnitude units greater.

REFERENCES

Israelsson, H. (1990). Correlation of waveforms from closely-spaced regional events, *Bull. Seism. Soc. Am*. 80: pp 2177–2193

Merchant, B. J. (2007). The GNEMRE Dendro Tool, SAND Report #2007-6439. Sandia National Laboratories, Albuquerque, NM, October 2007 (Unclassified).

Resor, M. E, D. B. Carr, M. J. Procopio, C. J. Young, and C. Rowe (2009). Self Scanning Event Detection in Volcanic Swarms [abstract], *Seismological Research Letters*, 80: 340.

Resor, M. E., M. J. Procopio, C. J. Young and D. B. Carr (2008). Processing Aftershock Sequences Using Waveform Correlation [abstract], *AGU Fall Meeting Abstracts*, 1802.

REGIONAL TRAVEL-TIME AND LOCATION UNCERTAINTY ASSESSMENT ALONG THE TETHYAN MARGIN USING A NEW THREE-DIMENSIONAL *P*-VELOCITY MODEL

Megan P. Flanagan [1], Suzan van der Lee[2], Steven C. Myers [1], Sung-Joon Chang [2], and Michael E. Pasyanos[1]

Lawrence Livermore National Laboratory[1] and Northwestern University[2]

Sponsored by the National Nuclear Security Administration

Award Nos. DE-AC52-07NA27344[1] and DE-FC52-04NA25541[2]
Proposal No. BAA04-40

ABSTRACT

We have completed a new, comprehensive three-dimensional model of *S*-velocity in a broad region extending from the western Mediterranean Sea to the Hindu Kush and encompassing Northern Africa, the Arabian Peninsula, and the Middle East. Our joint inversion is an integration of regional waveform constraints, surface-wave group velocity measurements, teleseismic *P* and *S* arrival times, and receiver functions. The data offer complementary sensitivity to crust and mantle structures and are jointly inverted to image the complexity of this tectonically diverse area.

The *S*-wave model is now converted to a *P*-wave model such that we can compute finite difference travel-times through the new model to evaluate *P*-wave arrival times from 'ground-truth' events. The travel times are well predicted by the Joint model at several stations, and the Joint model outperforms the WENA1.0 model, as measured by a higher variance reduction at stations AJM, CFTV, ELL, FRU, KHO, MFP, NIL, RYD, and SVE. The Joint model seems to predict the *P*-wave times particularly well in the eastern part of the model and over portions of northern Africa.

We now use *P*-wave travel-time correction surfaces with our location algorithm to account for three-dimensional *P*-velocity structure and to improve the location estimates of several GT5 and better events that have been regionally recorded throughout the Middle East and North Africa.

OBJECTIVES

Our primary objective is developing new 3-D *S*- and *P*-velocity models for the Middle East and Mediterranean region, including North Africa, southern Europe, and Arabia that

1) are resolved in aseismic regions,
2) are resolved throughout the upper mantle (to 660 km),
3) resolve laterally varying crustal thickness,
4) contain laterally varying vertical velocity gradients,
5) are simultaneously compatible with multiple data sets,
6) utilize several recent, unique waveform data sets, and
7) include uncertainties of the model parameters.

These features would increase the model's ability to predict and calibrate regional travel times and waveforms, thereby providing improved event locations, focal mechanisms, and other event discriminants.

After completing the *S*-wave model we now convert it to a 3-D *P*-velocity model, using teleseismic *P*-arrival times. We test the *P*-wave model's ability to predict regional *P* travel times and to improve location estimates of small regionally recorded events.

RESEARCH ACCOMPLISHED

The study region is centered around the Africa-Arabia-Eurasia triple junction and extends west to the Africa-Eurasia-North America junction at the Azores, and east to the Arabia-Eurasia-Indian Plate junction. The interaction of these five major tectonic plates with each other and with several microplates within an area of one quarter of the Earth's circumference yields this region rich with tectonic complexity. We plan to capture various renditions of this structurally complicated part of the world in one *S*-velocity model through the joint inversion of several different types of seismic data simultaneously; the new model will refine our understanding of the structure and tectonics in this region of the Earth. The data types we combine are constraints from independent studies on the depth to the Moho, fundamental-mode Rayleigh-wave group velocity measurements, waveform fits of regional *S* and Rayleigh waves, and arrival times of teleseismic *S* and *SKS* waves. We convert the resulting *S*-velocity model to a *P*-velocity model with over 2.9 million teleseismic *P* arrival times. Then, we validate our model by performing travel-time prediction with a dataset of ground truth events.

Regional Waveform Fits

We fit over 5,600 available waveforms from the Lawrence Livermore National Laboratory (LLNL) database and MIDSEA dataset (Marone et al., 2004) which sample the Mediterranean region, North Africa, the Middle East, Pakistan, and Afghanistan using the non-linear inversion procedure employed by partitioned waveform inversion. We utilize events with magnitude larger than 4.0 and seismograms with epicentral distance from 5º to 50º. The great-circle wave paths for these seismograms are shown in Figure 1(a). We have estimated path-averaged *S*-velocity structures for these paths using the same starting *S*-velocity model but a different crustal thickness (in 5-km increments) for each path, based on *a priori* reported estimates (Marone et al., 2004).

Teleseismic *S* and *SKS* Arrival Times

We obtained *S* and *SKS* phase arrival time data from two different sources. Both arrival times are adjusted for topography and Earth's ellipticity before inversion. First, we used high-quality relative arrival times of teleseismic *S* and *SKS* waves (Benoit et al., 2006; Park et al., 2007; Schmid et al., 2004) that are measured on broadband seismograms with use of multi-channel cross-correlation (MCCC; VanDecar and Crosson, 1990). Benoit et al. (2006), Park et al. (2007), and Schmid et al. (2004) used seismograms recorded in the Mediterranean, Ethiopia, and Saudi Arabia, respectively. Moreover, we measured additional relative delay times at Turkey and central Asia. The number of *S* phase relative arrival times is over 5900 with epicentral distance of 30º – 90º and the number of *SKS* phase is over 1400 with distance of 87º – 140º; over 7300 in total. Second, we obtained over 223,000 *S* phase arrival time data from the reprocessed ISC database (Engdahl et al., 1998) from 1964 to 2007. We illustrate location of stations and events for each of the two types of arrival-time data in Figure 1(b).

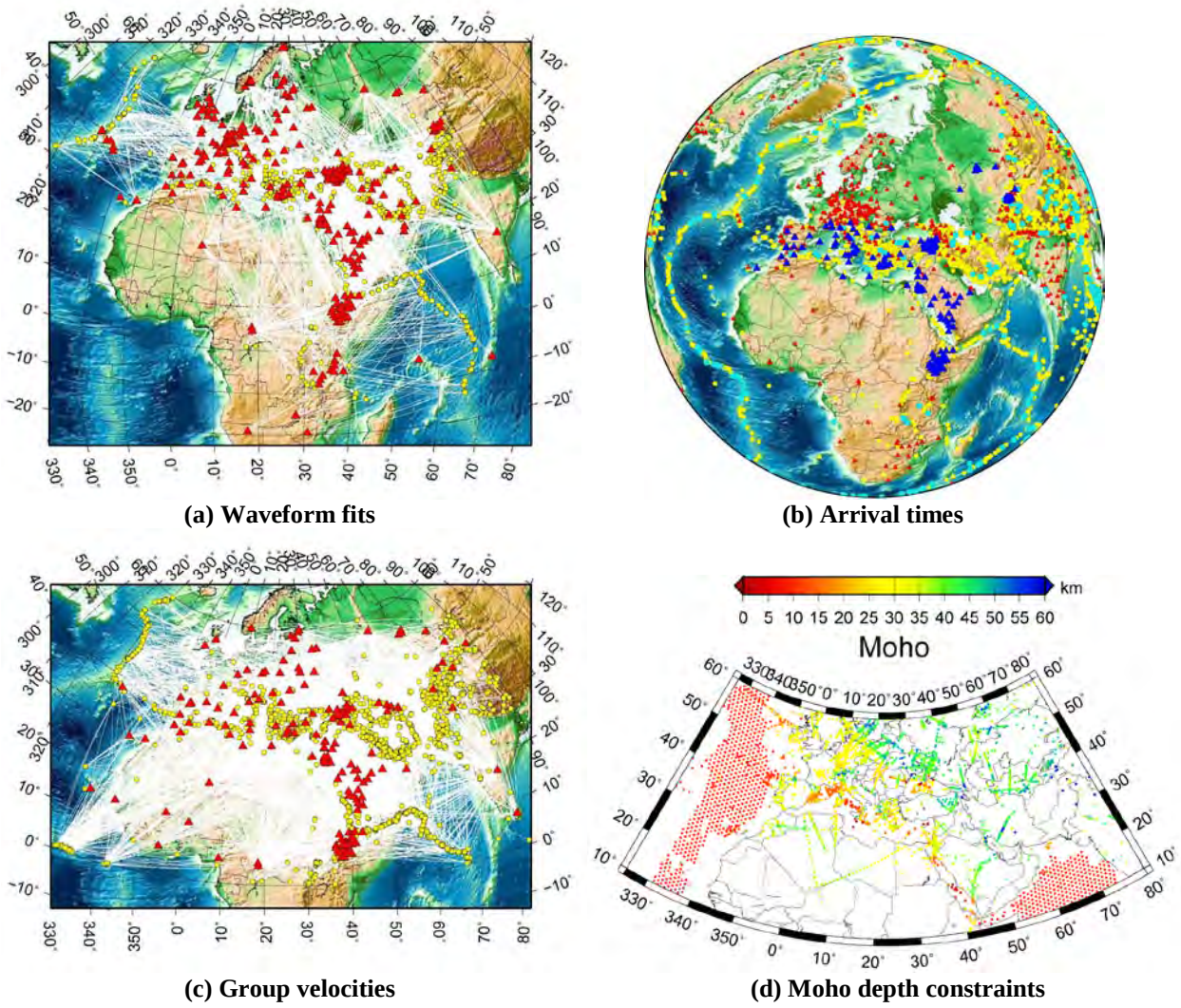

(a) Waveform fits **(b) Arrival times**

(c) Group velocities **(d) Moho depth constraints**

Figure 1. Datasets used for the joint inversion. (a) Ray path coverage for regional waveform fits. Stations are illustrated as red triangles, and events as yellow circles. (b) Events and stations used for teleseismic *S* and *SKS* arrival time estimation. Cyan circles and blue triangles represent events and stations used for relative delay time estimation with MCCC, respectively. Yellow circles and red triangles are events and stations from the reprocessed ISC catalogue. (c) Great-circle wave paths for 45 s period Rayleigh waves. Stations are illustrated as red triangles, and events as yellow circles. (d) Map of the Moho depth distribution acquired from literatures. Artificial point constraints of 10 km depth are placed to the Atlantic and Indian Oceans where measurements are absent.

Surface Wave Group Velocities

We measure over 105,000 group velocities of fundamental-mode Rayleigh waves recorded at MIDSEA and other stations in the region and used them to update previous group velocity maps (Pasyanos, 2005). Figure 1(c) shows the great-circle wave paths for which we included fundamental-mode Rayleigh wave group velocities in our joint inversion. Compared to other data types we include, lateral coverage is best for this group velocity data set, though vertical coverage is provided mainly by the teleseismic arrival times and regional *S* and Rayleigh waveforms. The period for group velocities ranges from 7 to 100 sec.

Crustal Thickness Constraints

While the fundamental-mode Rayleigh-wave group velocities and regional *S* and Rayleigh waveforms have significant sensitivity to Moho depth, they cannot uniquely resolve it. We therefore include independent estimates of crustal thickness as point constraints in the joint inversion and thus compile such measurements from a large number of published studies. A partial list of these studies is provided in Marone et al. (2003) and part of these points stem from the database used for CRUST5.1 (Mooney et al., 2001). We have added new estimates of Moho depth from more recent studies and interactively resolved or removed conflicting data and outliers from the data set. Over 4,700 Moho depth constraints are mapped in Figure 1(d). For the oceans we use a constraint of 10 km for Moho depth, but only for points also covered by data from our other data sets.

Inversion Results

The joint inversion of constraints from regional waveform fits, crustal estimates, group velocities, and teleseismic arrival times produces a new S-wave velocity model shown in Figure 2. The resolving power of the combined data is superior to that of each of the data sets alone. The joint inversion reduces the variance in the data sets by 38% for the teleseismic delay times, 55% for the Rayleigh-wave group velocities, 90% for the Moho point constraints, and 88% for the regional waveform fits. The Moho map, Figure 2a, shows a good resemblance with the point constraints in Figure 1(d), but is much smoother due to the regional waveforms and group velocity data, as well as regularization constraints in the inversion. The map is also broadly consistent with CRUST2.0, except in northern Africa, where the crust from our joint inversion is about 5 km thinner.

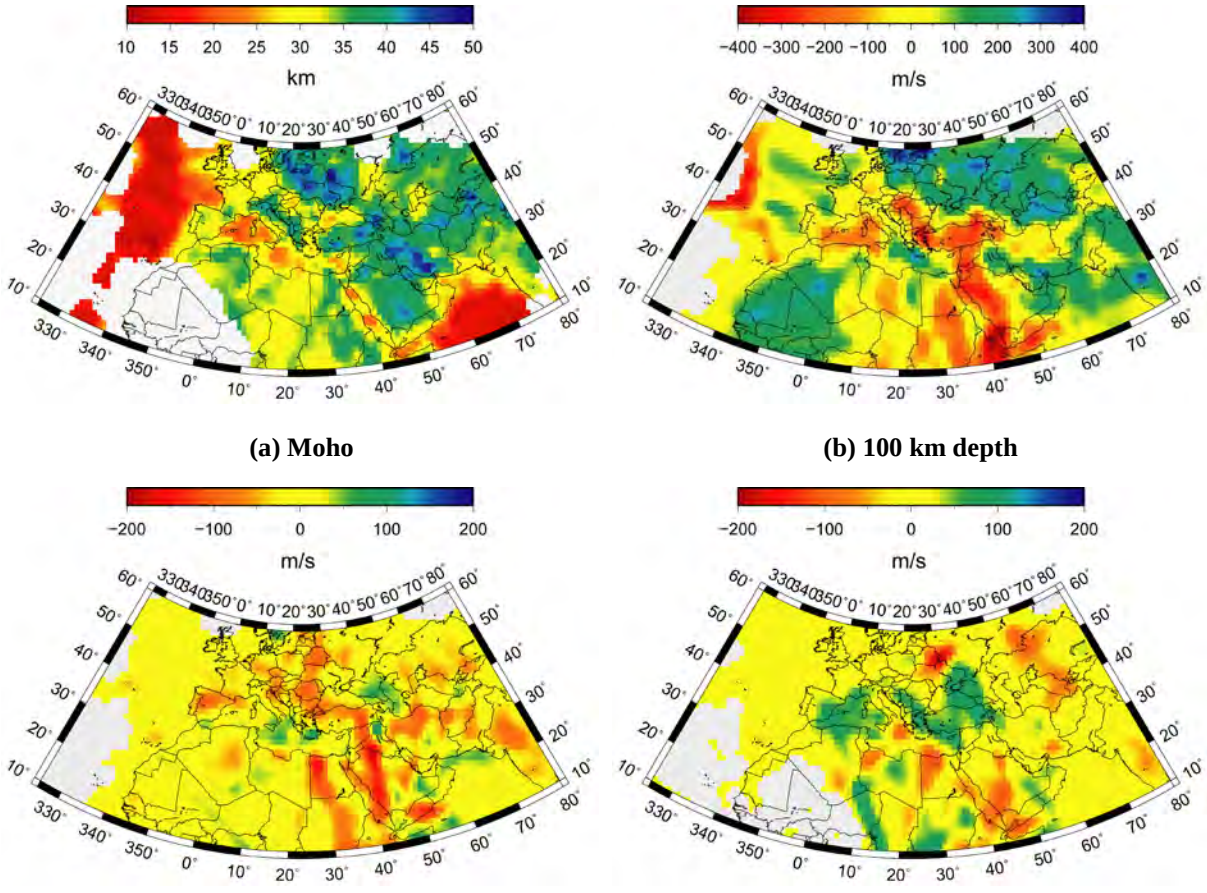

(a) Moho **(b) 100 km depth**

(c) 300 km depth **(d) 500 km depth**

Figure 2. Moho and *S*-wave velocity perturbations resulting from our joint inversion. Moho map (a) and velocity perturbations at 100 km (b), 300 km (c), and 500 km depth (d) are illustrated.

Fast-velocity anomalies are found beneath the West African Craton, the Hellenic trench, the Apennines, the East European Platform, and the Arabian Platform at 75-150 km depth, whereas low-velocity anomalies are located along the plate boundaries such as the mid-Atlantic ridge, Afar, the Anatolian Plateau, Iran, Afghanistan, western Mediterranean Sea, and the Red Sea.

Conversion of *S*-Velocity Model to *P*-Velocity Model

We obtain a *P*-velocity model by performing a *P*-wave arrival time inversion using the equation: $\mathbf{G}_\alpha \mathbf{m}_\alpha = \mathbf{d}_\alpha$, where $\mathbf{G}_\alpha$ is the sensitivity kernel matrix for *P*-wave arrival times, $\mathbf{m}_\alpha$ is the 3-D *P*-velocity model vector, and $\mathbf{d}_\alpha$ is the teleseismic *P*-wave delay vector which is obtained by subtracting predicted arrival times through a reference model from observed arrival times. We use the *S*-velocity model as a preliminary model, because the *S*-velocity model has good resolution for both shallow and deep stucture. We assume that *P*-wave velocity are very close to the *S*-wave velocity anomalies if temperature is the dominant cause of the velocity perturbations based on results in Schmid et al. (2004) in which similarity between *P*- and *S*-velocity anomalies is drawn with use of delay time ratio (see Figure 3a). By multiplication of the *S*-velocity model and *P*-wave sensitivity kernels, we can get predicted *P*-wave delays $\mathbf{d}_{\beta\to\alpha}$ by $\mathbf{m}_\beta$ as in $\mathbf{G}_\alpha \mathbf{m}_\beta = \mathbf{d}_{\beta\to\alpha}$, where $\mathbf{m}_\beta$ is the 3-D *S*-velocity model in m/s scale, and $\mathbf{d}_{\beta\to\alpha}$ is predicted *P* delays by $\mathbf{m}_\beta$. Then, teleseismic *P*-wave delays $\mathbf{d}_\alpha$ can be divided as $\mathbf{d}_\alpha = \mathbf{d}_{\beta\to\alpha} + \mathbf{d}_{res}$, where $\mathbf{d}_{res}$ is the residual *P* delay vector ($\mathbf{d}_\alpha$ and $\mathbf{d}_{\beta\to\alpha}$). Therefore, we have $\mathbf{G}_\alpha(\mathbf{m}_\beta + \mathbf{m}_{new}) = \mathbf{d}_{\beta\to\alpha} + \mathbf{d}_{res}$, which is a linear equation, so we perform the *P*-wave arrival time inversion for $\mathbf{m}_{new}$ using $\mathbf{G}_\alpha \mathbf{m}_{new} = \mathbf{d}_{res}$. A *P*-velocity model is finally obtained by adding $\mathbf{m}_{new}$ to the *S*-velocity model, $\mathbf{m}_\alpha = \mathbf{m}_\beta + \mathbf{m}_{new}$.

The resulting *P*-velocity model with teleseismic *P* arrival time data in Figure 3(b) is shown at various depths in Figure 4. The results are similar to *S*-velocity perturbation results in Figure 2, which means *P*-velocity variations from the *S*-velocity model are small. But higher-velocity anomalies are found in Alps, Hellenides, Turkey, and Hindu Kush than in *S*-velocity model.

Model Evaluation

Distributions of the travel-time residuals with respect to *iasp91* and our joint inversion model (Joint Model) are shown in histogram form in Figure 4 for stations AJM, FRU, KHO, NIL, QUE, PTO, TAM, and TIO. We report both the *L2* norm (variance reduction, VR) and *L1* norm statistics (scaled median absolute deviation reduction, SMADR). The SMAD provides an estimate of the spread of values which is less sensitive to outliers and so is often more appropriate in the presence of non-Gaussian errors.

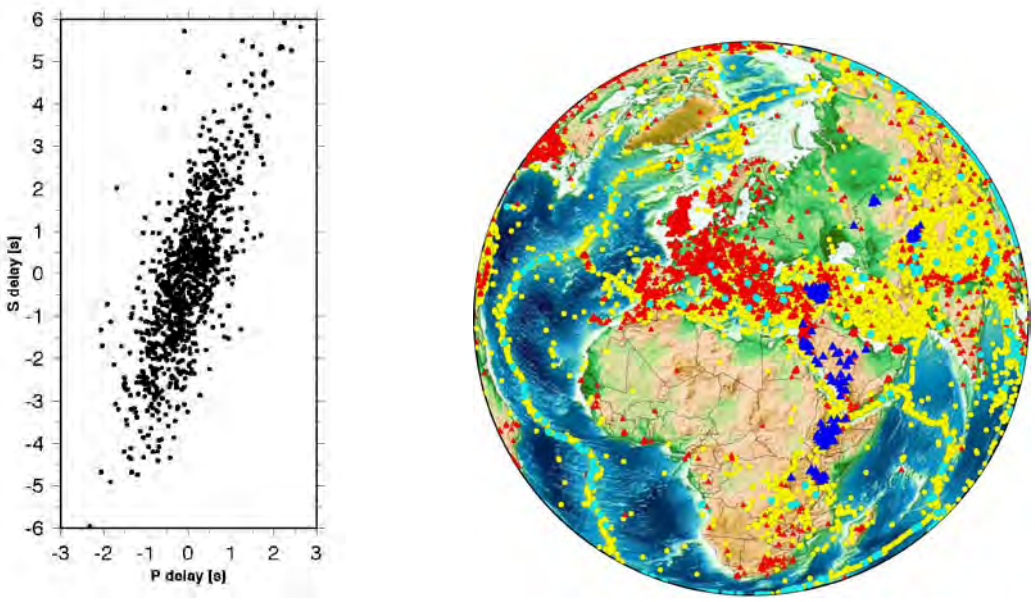

(a) **(b)**

Figure 3. (a) *S* delays versus *P* delays (Schmid et al., 2004). (b) Events and stations used for teleseismic *P* arrival time estimation. Cyan circles and blue triangles represent events and stations used for relative delay time estimation with MCCC, respectively. Yellow circles and red triangles mean events and stations from the reprocessed ISC catalogue.

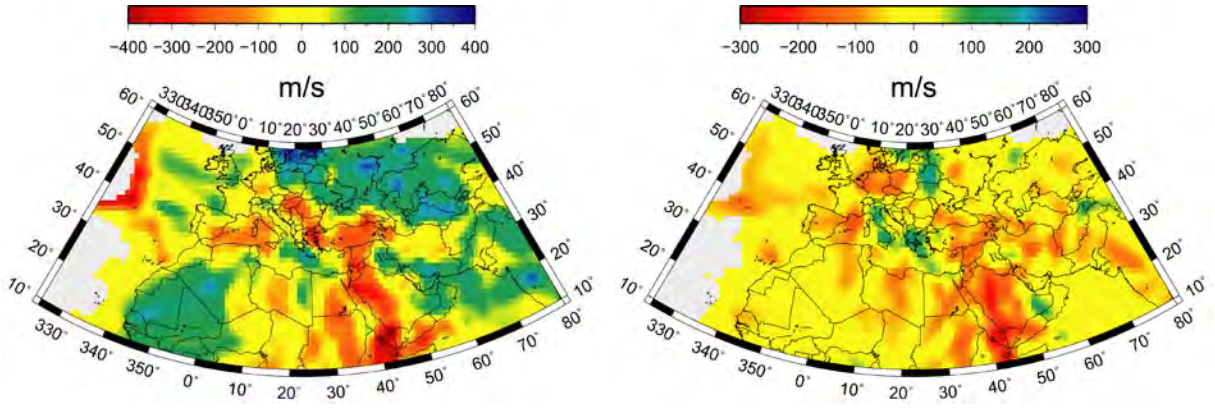

(a) 100 km depth **(b) 200 km depth**

Figure 4. *P*-velocity perturbations at (a) 100 and (b) 200 km depth.

Visually we can evaluate how well the joint inversion model (Joint Model) predicts the data geographically by computing 3D travel-time correction surfaces for some stations. To compute such model-based correction surfaces we subtract the *iasp91*-predicted time from the Joint Model-predicted time using 3D finite-difference algorithm. Example surfaces are shown in Figure 5 for the stations for a source depth of 10 km. Color-coded residuals (data-*iasp91*) from events of focal depth 0 to 20 km are also plotted on top of the surfaces in Figure 5.

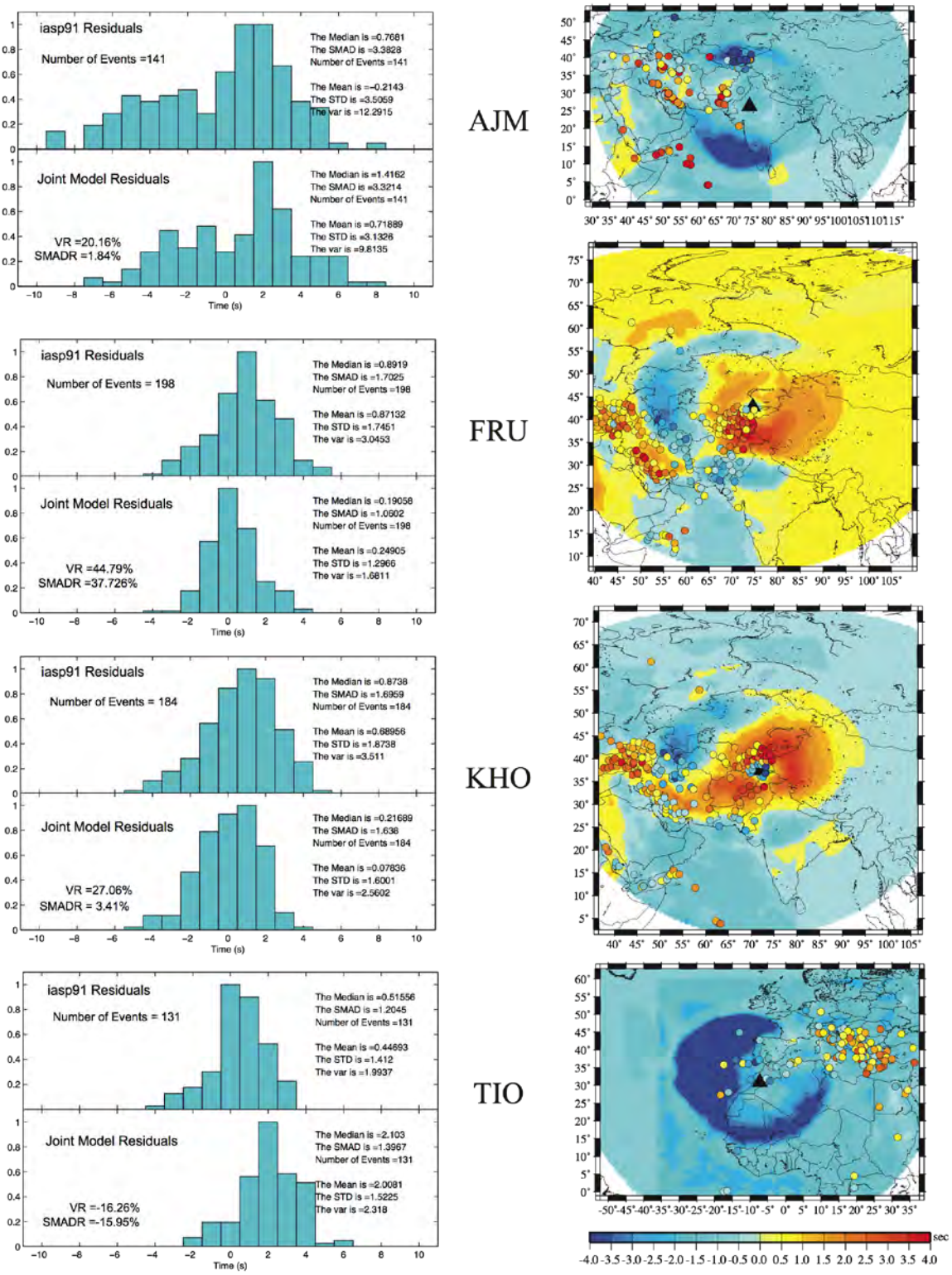
iasp91 Residuals
Number of Events =141
The Median is =0.7681
The SMAD is =3.3828
Number of Events =141
The Mean is =-0.2143
The STD is =3.5059
The var is =12.2915
Joint Model Residuals
VR =20.16%
SMADR =1.84%
The Median is =1.4162
The SMAD is =3.3214
Number of Events =141
The Mean is =0.71889
The STD is =3.1328
The var is =9.8135
Time (s)
AJM
iasp91 Residuals
Number of Events = 198
The Median is =0.8919
The SMAD is =1.7025
Number of Events =198
The Mean is =0.87132
The STD is =1.7451
The var is =3.0453
Joint Model Residuals
VR =44.79%
SMADR =37.726%
The Median is =0.19058
The SMAD is =1.0602
Number of Events =198
The Mean is =0.24905
The STD is =1.2966
The var is =1.6811
Time (s)
FRU
iasp91 Residuals
Number of Events = 184
The Median is =0.8738
The SMAD is =1.6959
Number of Events =184
The Mean is =0.68956
The STD is =1.8738
The var is =3.511
Joint Model Residuals
VR =27.06%
SMADR = 3.41%
The Median is =0.21689
The SMAD is =1.636
Number of Events =184
The Mean is =0.07836
The STD is =1.6001
The var is =2.5602
Time (s)
KHO
iasp91 Residuals
Number of Events = 131
The Median is =0.51556
The SMAD is =1.2045
Number of Events =131
The Mean is =0.44693
The STD is =1.412
The var is =1.9937
Joint Model Residuals
VR =-16.26%
SMADR =-15.95%
The Median is =2.103
The SMAD is =1.3967
Number of Events =131
The Mean is =2.0081
The STD is =1.5225
The var is =2.318
Time (s)
TIO
sec

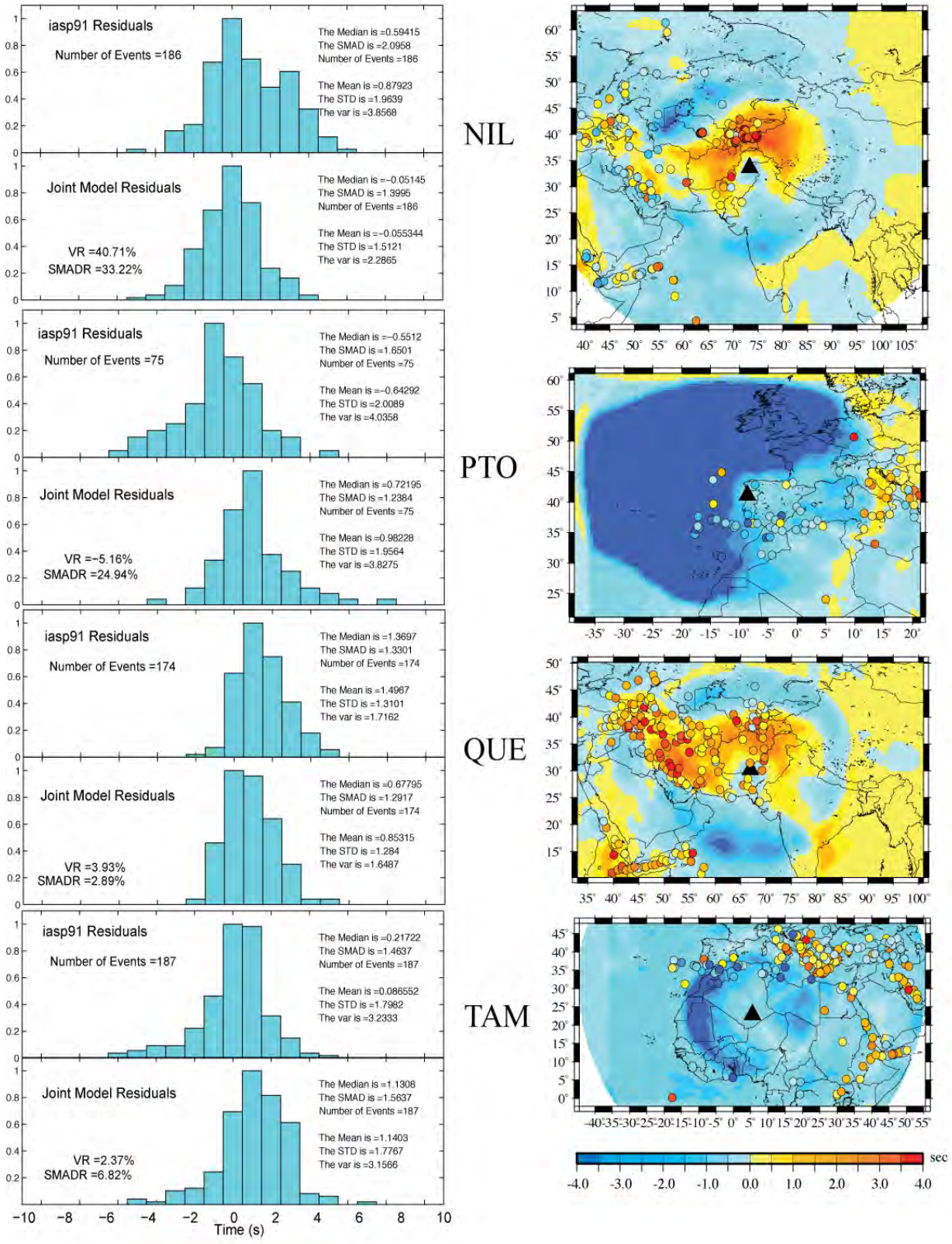

Figure 5. Histograms of *P*-wave travel-time residuals at stations AJM, FRU, KHO, TIO, NIL, PTO, QUE, and TAM along with the travel-time residual surfaces (Joint Model-*iasp91*).

Table 1. Statistics for P wave travel-time fits at each station compared to the WENA1.0 model.

Station	*Ndata*	WENA1.0 *VR*	Joint *VR*	WENA1.0 *smadR*	Joint *smadR*
AJM	141	12.060	20.161	-1.034	1.814
ARO	132	44.909	7.957	35.678	24.158
BGCA	37	-4.77	-7.890	-0.287	32.045
BKR	292	25.314	13.153	14.870	3.468
BRVK	68	32.742	21.539	25.082	12.634
CFTV	10	54.799	66.145	14.631	43.797
DHJN	72	19.160	13.720	-3.590	-20.255
ELL	260	22.270	26.112	6.594	-2.508
FRU	198	9.016	44.797	21.078	37.728
KAD	87	21.216	5.952	15.479	-7.744
KDS	44	51.832	50.409	18.916	17.138
KHO	184	17.485	27.080	4.973	3.419
KUK	35	-5.254	17.443	-14.575	-3.201
LKO	57	27.264	30.827	-11.342	3.912
MAIO	173	33.772	29.848	29.128	26.809
MBO	25	47.220	42.180	37.314	29.343
MFP	9	12.719	29.002	85.685	29.311
MLR	263	-0.201	-10.132	1.164	-16.051
NIL	186	26.998	40.715	19.843	33.224
OBN	341	36.251	18.148	30.332	22.922
PGD	123	-1.178	-7.303	-1.466	-16.850
PTO	75	25.279	5.160	33.897	24.948
QUE	174	-18.418	3.937	-6.033	2.890
RYD	97	1.833	14.488	-0.277	3.557
SHI	180	17.443	31.148	16.935	23.122
SVE	174	21.867	32.319	3.984	4.641
TAB	290	10.398	8.862	5.025	7.714
TAM	187	15.267	2.375	-3.510	-6.829
TCF	246	8.377	-70.257	-18.107	1.473
TIC	100	11.788	9.011	2.813	4.972
TIO	131	10.808	-16.266	-11.024	-15.959
UZH	319	19.898	6.267	-1.958	-0.250
ZGN	104	13.230	9.470	-1.753	-19.406
All data	4814	22.399	22.833	6.205	7.354
GT5 only	146	24.819	26.007	-0.534	6.170

Travel times are well predicted by the Joint model at several stations, and the Joint model outperforms the WENA1.0 model, as measured by a higher *VR*, at many stations. The new Joint model seems to predict the *P* times particularly well in eastern part of the model and over portions of northern Africa.

CONCLUSIONS AND RECOMMENDATIONS

Through a joint inversion of teleseismic *S*-wave arrival time delays, waveform fits of regional *S*- and Rayleigh waves, group velocity measurements of fundamental-mode Rayleigh waves, and independent constraints on Moho depth, we have achieved considerable variance reduction in each data set simultaneously. The new 3-D *S*-velocity model is converted to a *P*-velocity model with teleseismic *P* arrival times and the *P*-velocity model is used for travel-time prediction. Our model generally produces better prediction than *iasp91* 1D model. Our next task is to use travel time correction surfaces with our location algorithm to account for 3D P-velocity structure and improve the location estimates of several GT5 and better events that have been regionally recorded throughout the model area following the techniques of Flanagan et al., 2007.

REFERENCES

Benoit, M. H., A. A. Nyblade, and J. C. VanDecar (2006). Upper mantle *P*-wave speed variations beneath Ethiopia and the origin of the Afar hotspot, *Geology* 34: 329–332.

Engdahl, E.R., R. van der Hilst, and R. Buland (1998). Global teleseismic earthquake relocation with improved travel times and procedures for depth determination, *Bull. Seis. Soc. Am*. 88: 722–743.

Flanagan, M. P., S. C. Myers, and K. D. Koper (2007). Regional travel-time uncertainty and seismic location improvement using 3-dimensional *a priori* velocity models, *Bull Seismol. Soc. Am*. 97: 3, 804–825, *UCRL-JRNL-220179.*

Marone, F. S. Van der Lee, and D. Giardini (2003). Joint inversion of local, regional, and teleseismic data for crustal thickness in the Eurasia-Africa plate boundary region, *Geophys. J. Int*. 154: 499–514.

Marone, F., S. Van der Lee, and D. Giardini (2004). 3-D upper mantle *S*-velocity model for the Eurasia-Africa plate boundary region, *Geophys. J. Int*. 158: 109–130.

Mooney, W., G. Laske, and G. Masters (2001). http://igppweb.ucsd.edu/~gabi/crust.html.

Park, Y., A. A. Nyblade, A. J. Rodgers, and A. Al-Amri (2007). Upper mantle structure beneath the Arabian Peninsula and northern Red Sea from teleseismic body wave tomography: Implication for the origin of Cenozoic uplift and volcanism in the Arabian Shield, *Geochem. Geophys. Geosyst*. 8: Q06021, doi:10.1029/2006GC001566.

Pasyanos, M. E. (2005). A varible-resolution surface wave dispersion study of Eurasia, North Africa, and surrounding regions, *J. Geophys. Res*. 110: B12301, doi:10.1029/2005JB003749.

Schmid, C., S. van der Lee, and D. Giardini (2004). Delay times and shear wave splitting in the Mediterranean region, *Geophys. J. Int*. 159: 275–290.

VanDecar, J.C. and R.S. Crosson (1990). Determination of teleseismic relative phase arrival times using multi-channel cross-correlation and least-squares, *Bull. Seism. Soc. Am*. 80: 150–169.

OPTICAL MEMS-BASED SEISMOMETER

Dominique Fourguette[1], M. Volkan Ötügen[2], Liane M. Larocque[1], Greg A. Ritter[1],
Tindaro Ioppolo[2], and Darren Hart[3]

Michigan Aerospace Corporation[1], Southern Methodist University[2], and Sandia National Laboratories[3]

Sponsored by the National Nuclear Security Administration

Award No. DE-FG02-08ER85099

ABSTRACT

Low-yield man-made seismic activity is difficult to detect and most often occurs in remote areas where seismic detection is weak. The Whispering Gallery Seismometer (WhiGS)is an optical Micro-Electro-Mechanical System-based (MEMS) instrument. The seismometer is a three-axis instrument, is compact, has low power consumption and is capable of unattended operation.

WhiGS exploits morphology-dependent optical resonance shifts in small dielectric spheres (<1 mm in diameter). These optical resonances, called whispering gallery modes (WGM), are extremely narrow, making the transducer highly sensitive to force (< 10^{-9} Newtons). The MEMS sensing element in this seismometer has demonstrated an optical Q-factor of 10^7. As a result, the instrument will be capable of measuring accelerations as low as 10 nano-g.

The design and demonstration of the sensing element performance were completed in Phase I. Hollow dielectric microspheres, core of the sensing element, were capable of detecting nano-Newton forces. As a result, the proof mass weighs less than 10g per axis and the volume of the instrument is less than 5 cubic inches (< 80 cm^3). The on-board processor and electronics dissipate less than 160 mW per channel. This Phase II effort entails the final design, fabrication and testing of the deployable 3-axis seismometer.

OBJECTIVES

Michigan Aerospace Corporation, in collaboration with Southern Methodist University, is developing a compact Whispering Gallery Seismometer (WhiGS). The sensing principle of the seismometer exploits the morphology-dependent optical resonance shifts of dielectric spheres to detect ground motion. These optical resonances are extremely narrow, making the transducer highly sensitive to ground motion. The small dielectric spheres are easily packaged into a small instrument capable of measuring accelerations as low as 10 nano-g.

The Phase I objectives included the characterization of whispering gallery mode shifts in microspheres as force sensor, preliminary tests, and instrument design.

The optical MEMS sensing element, typically a microsphere (with diameters in the range 200 to 1000 μm), is weakly coupled to an optical fiber, as shown in Figure 1a. The optical fiber, which carries light from a tunable laser, serves as an input/output port for the microsphere. When the microsphere comes into contact with an exposed section of the fiber core, light is coupled into the outer layer of the sphere, (Figure 1b). Its resonances are observed as sharp dips in the transmission spectrum as depicted in Figure 1d. When the sphere is compressed (as shown in Figure 1c), the wavelength of the resonances shifts.

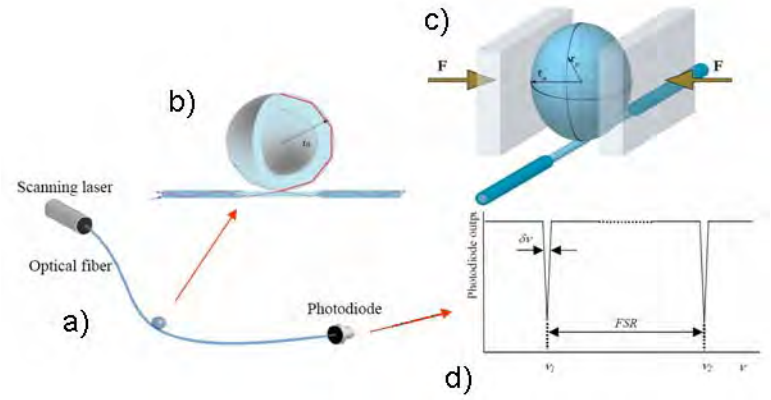

Figure 1: Principle of the WGM pressure-induced wavelength shift $\delta\nu$.

These optical resonances, also known as the "whispering gallery modes" (WGM), are extremely narrow and hence are highly sensitive to any morphological change in the microsphere. Other micro-resonator geometries, such as micro-discs, can be used as sensing elements in place of the microspheres.

The first objective of the Phase I effort was a computational and analytical analysis to determine the range of force/acceleration sensitivities and ranges for the sphere sizes and materials to be used in our sensor. For this, the analytical approach and finite element analysis (FEA) tools developed in our previous study will be used. These FEA tools are described in Nguyen et al. (2009). This objective entails the quantification of the precise effect of force and microsphere physical deformation on electromagnetic wave propagation in microspheres with the selected sizes and sphere material.

The second objective of this effort was the experimental investigation of WGM characteristics of different-sized spheres (ranging from ~ 200 μm and 1 mm). The candidate material to be used for the spheres is PDMS (commercially known as Sylgard 184). Different percentage of additives (cure agent) will be used to obtain different elastic modulus values and optical characteristics in order to determine the force sensitivity ranges that can be achieved and their suitability for the seismometer to be developed. Polymer base-to-cure agent ratios of up to 60:1 were used in this investigation.

The third objective of the Phase I effort was the design of a seismometer prototype. That included the design of the transducers and the mechanical design of the instrument. The design of the instrument entailed the following considerations:

- Determination of the inertial mass and shape
- Sensitivity
- Resonant frequency
- Ability to measure 3 axes
- Damping mechanism to prevent long-term oscillations
- Electronics circuitry and noise

RESEARCH ACCOMPLISHED

Force Measurements Using WGMs in Spheres

The transducer uses morphology-dependent optical resonances described by Benner and Hill (1988), whispering gallery modes (WGMs) in this case, investigated by Guan et al. (2006), to measure minute shape variations in dielectric spheres squeezed between the mass and the instrument base. Force resolution of $1x10^{-4}$ N was achieved using polymer spheres, and to $1x10^{-6}$ using hollow polymethyl methacrylate (PMMA) spheres, shown by Kozhevnikov et al. (2006) and Ioppolo et al. (2007). Current studies by the same team using 0.7 mm spheres of another polymer, polydimethylsiloxane (PDMS), indicate that a force resolution of 10^{-8} N is possibly exploiting the same sensing principle.

The dependence of the wavelength on the force is expressed as:

$$\delta F = \frac{\lambda}{Q}\left(\frac{d\lambda}{dF}\right)^{-1} \qquad (1)$$

where Q is the quality factor. The table below shows change of wavelength with force applied ($d\lambda/dF$) and the force resolution for several different sphere materials and dimensions.

Table 1: Comparison of force sensitivity and resolution for spheres of various materials with comparable diameter (910±50 mm). The sensitivity of PDMS spheres depends on the volumetric ratio of polymer to hardening material. In the present case, the ratio is 60:1.

Material	$d\lambda/dF$, pm/μN	Resolution, N
Hollow PDMS (60:1)	50,000	2×10^{-12}
Solid PDMS (60:1)	181.2	$7x10^{-10}$
Solid PDMS (20:1)	3.2	$4x10^{-8}$
Solid PnHMA	$86x10^{-3}$	$1.5x10^{-6}$
Hollow PMMA	$76x10^{-4}$	$1.7x10^{-5}$
Solid PMMA	$1.8x10^{-4}$	$7x10^{-4}$
Solid Silica	7.5×10^{-6}	$1.7x10^{-2}$

The model developed as part of this effort was compared to experimental results using PDMS spheres (Ioppolo et al. 2009), as shown in Figure 2. Good agreement is shown between the experimental and analytical data.

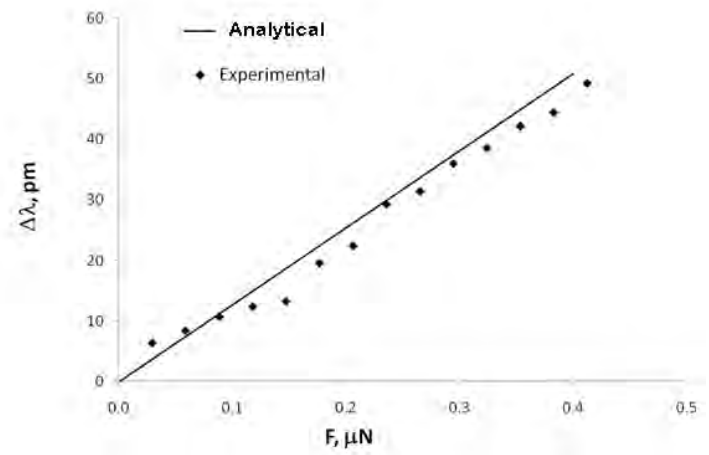

Figure 2 Analytical and experimental sensitivity results of a solid PDMS (50:1) sphere (D=910 mm)

Seismometer Design

The overall design of the seismometer is shown in Figure 3. The acceleration sensing elements are contained in the sealed canisters (3-Axis Sensing). The electronics and battery pack are compact and low dissipation. The overall package occupies less than 80 cm^3.

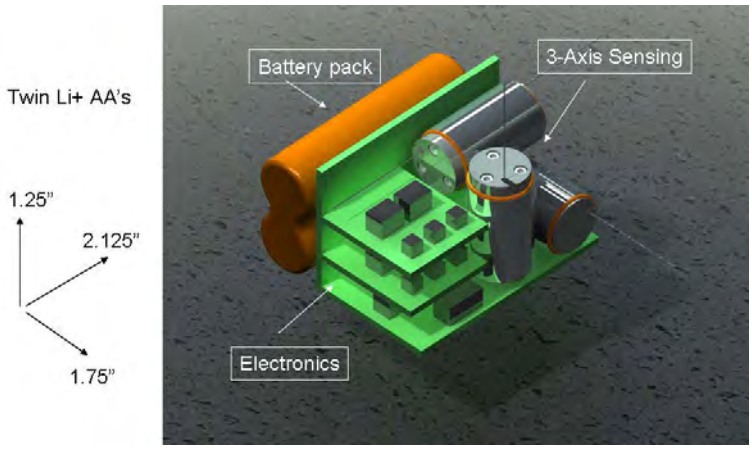

Figure 3: Seismometer design. The sensing apparatus is contained in the sealed cylinders

A model of the seismometer was developed to determine the characteristics of the principal components (mass, spring and sensing element). Table 2 lists the optimal characteristics for damping and sensitivity and Table 3 lists the electrical requirements of the seismometer.

Table 2: Parameters for the mechanical design

Parameters	
Mass (kg)	0.01
Stiffness (N/m)	631
Resistance Constant (kg/s)	0.5
Sphere: PDMS	181 pm/μN
Q Factor (Mechanical)	5
Decay Modulus (s)	0.04

Figure 4 and Figure 5 both show the SolidWorks™ model of one of the two horizontal axes of the seismometer. The proof mass is mounted off-axis on a jewel bearing. The microsphere is mounted closer to the axis, using the cantilever ratio to amplify the force transmitted to the microsphere, as shown in Figure 5 and Figure 6. The spring is mounted onto the axis.

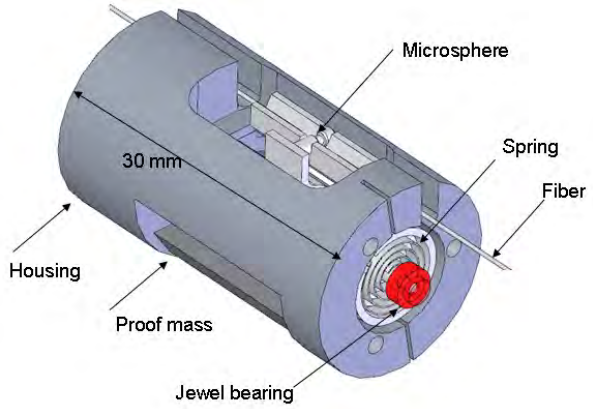

Figure 4: SolidWorks design of the instrument

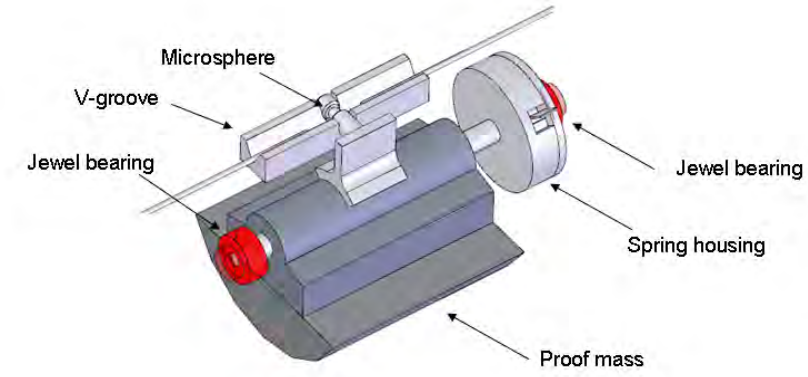

Figure 5 View of the seismometer without the housing

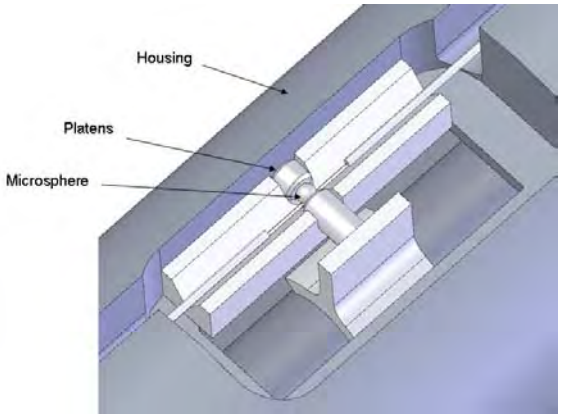

Figure 6: Microsphere positioning

The role of the processing electronics consists of identifying an optical resonance in the microsphere and tracking the wavelength shift of that resonance caused by the microsphere deformation, as shown in Figure 7. The processor

instructs the driver controller to scan the current of the laser, and therefore the wavelength. The processor selects a resonance (dip in the detector output), and then instructs the driver controller to scan around the resonance. Once the processor is "locked" around a resonance, the current is dithered around that value.

Space conservation is paramount in the design of this small seismometer. The easiest way to conserve space is to reduce the number of pins and traces required for the circuit. All the components have been selected based on pin count and power dissipation. An analog-to-digital converter will be sampling the waveform detected from the photodiode. Parts are readily available with our constraints which dissipate roughly 3-5mW of power. The analog-to-digital converter would ideally be a serially-operated device to conserve the number of pins required for it to operate. Examples of such devices would be the AD7694 or the AD7685. A Field Programmable Gate Array (FPGA) was selected for this application (ACTEL Igloo Series). Assuming a 1-MHz internal clock rate and complexity similar to some of our other designs, the Igloo FPGA is expected to consume no more than 5mW of power. If for some reason the clock rate had to be increased to 5 MHz, the estimated power consumption would increase to about 15 mW.

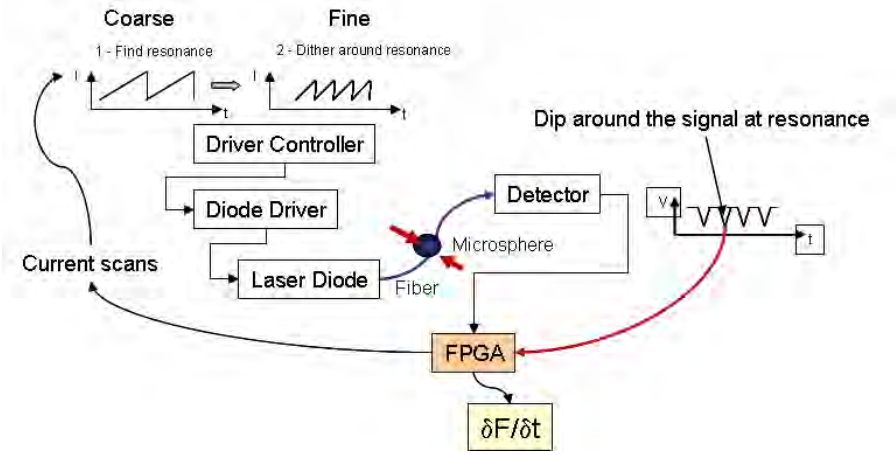

Figure 7: Functional diagram for the sensing element

Table 3: Electrical characteristics of the seismometer

Component	Dissipation (mW)
Laser Diode Controller	45
TEC Controller	100
Processor	15
Total	160

CONCLUSIONS AND RECOMMENDATION

The sensitivity of the sensing element was demonstrated and the design of the seismometer was completed in Phase I. The design will serve as a baseline for the Phase II effort. During the Phase II, a seismometer prototype will be fabricated and tested. Specific attention will be given to the critical components such as the mounting of the microspheres and the mechanical assembly.

ACKNOWLEDGEMENTS

The authors would like to thank Professor Brian Stump of Southern Methodist University for his expertise and insightful comments at the 2008 Monitoring Research Review.

REFERENCES

Benner, R.E.and S. C Hill (1988). Morphology-dependent Resonances, in *Optical effects Associated with Small Particles*, P.W. Barber and R.K. Chang, Eds., *Advanced Series in Applied Physics*, World Scientific.

Guan, G., S. Arnold and M.V. Ötügen, (2006). Temperature Measurements Using a Micro-Optical Sensor Based on Whispering Gallery Modes, *AIAA Journal* 44: 10, 2385–2389.

Ioppolo, T., M. Kozhevnikov, M.V. Ötügen, and V. Sheverev (2007). Performance of a whispering gallery mode resonator-based micro-optical force sensor, Paper 2007-1262, 45th AIAA Aerospace Sciences Meeting and Exhibit, Reno, NV.

Ioppolo, T., U. K. Ayaz, U.K., and M.V. Ötügen (2009). High-resolution whispering gallery mode force micro-sensor based on polymeric spheres, Paper 2009-1450, 47th AIAA Aerospace Sciences Meeting and Exhibit, Orlando, FL.

Kozhevnikov, M., T. Ioppolo, V. Stepaniuk, V. Sheverev, and V. Ötügen (2006). Optical force sensor based on whispering gallery mode resonators, Paper 2006-649, 44th AIAA Aerospace Sciences Meeting and Exhibit, Reno, NV.

Nguyen N., N. Gupta, T. Ioppolo, and V. Ötügen (2009). Whispering Gallery Mode-Based Micro-Optical Sensors for Structural Health Monitoring of Composite Materials, *J. Mat. Sci* 44: 1560–1571.

MICRO-SEISMOMETERS VIA ADVANCED MESO-SCALE FABRICATION

Caesar T. Garcia, Guclu Onaran, Brad Avenson, Matthew Ellis, and Neal A. Hall

Silicon Audio, LLC

Sponsored by the National Nuclear Security Administration

Contract No DE-FG02-08ER85106

ABSTRACT

The Department of Energy (DOE) and the National Nuclear Security Administration (NNSA) seek revolutionary innovations with respect to miniature seismic sensors for the monitoring of nuclear detonations. Specifically, the performance specifications are to be consistent with those obtainable by only an elite few products available today, but with orders of magnitude reduction in size, weight, power, and cost. The proposed commercial innovation calls upon several advanced fabrication methods and read-out technologies being pioneered by Silicon Audio, including the combination of silicon microfabrication, advanced meso-scale fabrication and assembly, and the use of advanced photonics-based displacement / motion detection methods. In Phase 1, the development team demonstrated the feasibility of the proposed innovation with a “macro” prototype. Specifically, two major goals were met: 1) proof mass elements capable of achieving sub 1ng noise were demonstrated, and 2) the high-fidelity, ultra-miniature motion detection principle used to monitor proof mass vibrations was successfully demonstrated. The upcoming Phase II development will focus on innovations aimed at complete sensor implementation. These include addressing low frequency noise challenges, low power consumption, ultra-miniature size, and low cross axis sensitivity. Successful implementation will result in a demonstration unit roughly the size of a 9-volt battery and with the ability to address advanced national security needs of the DOE/NNSA. Additional applications envisioned include military/ defense, scientific instrumentation, oil and gas exploration, inertial navigation, and civil infrastructure monitoring.

OBJECTIVES

The DOE/NNSA seeks revolutionary innovations with respect to miniature seismic sensors for the monitoring of nuclear detonations. Specifically, the performance specifications are to be consistent with those obtainable only by a few elite products available today, but with orders of magnitude reduction in size, weight, power, and cost. The specific sensor specifications solicited are as follows:

- Size – less than 1 in^3
- Power – less than 100 mW
- Sensor self noise – below USGS NLNM, or approximately 0.5 ng/√Hz
- Dynamic range at least 120 dB over a frequency band of 0.2 to 40 Hz.

In a prior review (Hall, 2008), we summarized basic design considerations for any proposed technology aiming to meet the aforementioned specifications. In particular, it was shown that meeting the noise requirement demands both a) ultra-low thermal mechanical noise from the seismometer proof mass, and b) high resolution displacement measuring capability of the proof mass motion. As an example, a design with a 2 gram proof mass and 50 Hz open loop resonant frequency may be considered. In this case, achieving the required 0.5 ng/√Hz acceleration noise requires a resonance quality factor *Q* of 100 and an ultra-low displacement resolving capability of 50 fm/√Hz (Hall, 2008). The high resonance *Q*, in-turn, requires the use of closed-loop feedback altered dynamics to realize the desired flat frequency response of the sensor. This discussion provides the motivation for Silicon Audio's proposed design innovation, which calls upon advanced meso-scale fabrication of mechanical proof-mass elements, photonics-based displacement / motion detection, micro-scale optoelectronic integration, and the integration of closed-loop sensing modalities for high stability and high dynamic range. In subsequent sections, Phase I results are presented which demonstrate the feasibility of the proposed approach. The figure below summarizes Phase I measurement results and Phase II projections plotted against the earth's background noise and the current best micro-electromechanical system (MEMS) demonstrations.

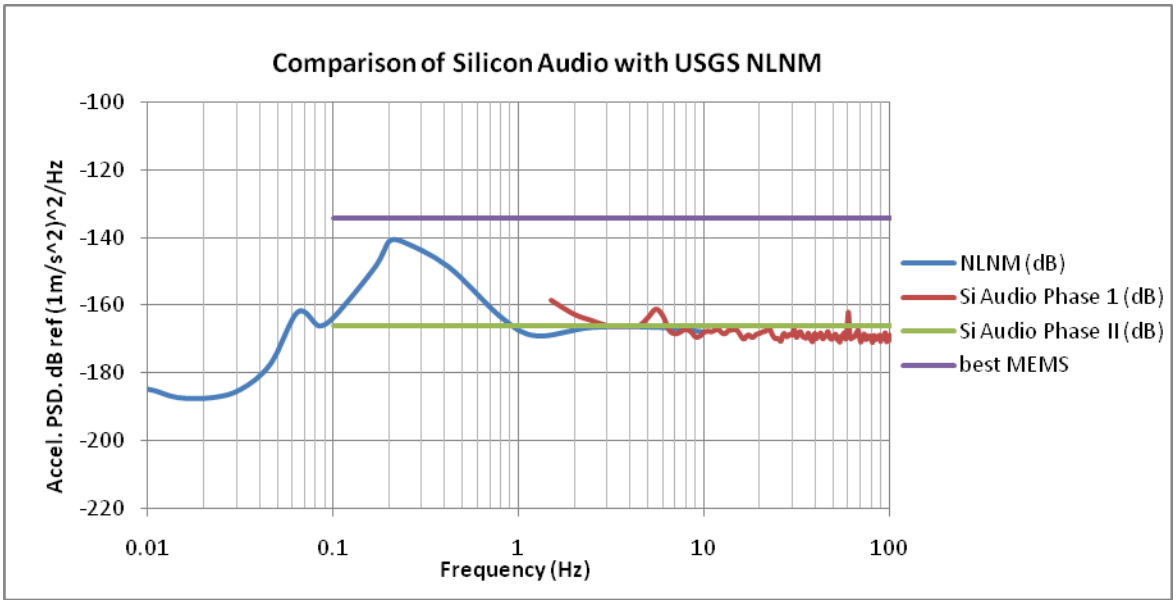

Figure 1. Acceleration noise power spectral density of the earth's background noise (NLNM), current best MEMS demonstrations, and Silicon Audio's Phase I and projected Phase II results.

Proposed Sensor Innovation

The sensor innovation must incorporate a proof mass displacement detection method capable of resolving 50 fm/√Hz. A major component of this innovation is the integration of an advanced photonics-based readout

architecture with meso-scale (i.e., larger than MEMS) mechanical proof mass structures. The focus of this review article is on one of the motion detection principles being investigated, which is illustrated in the following figure.

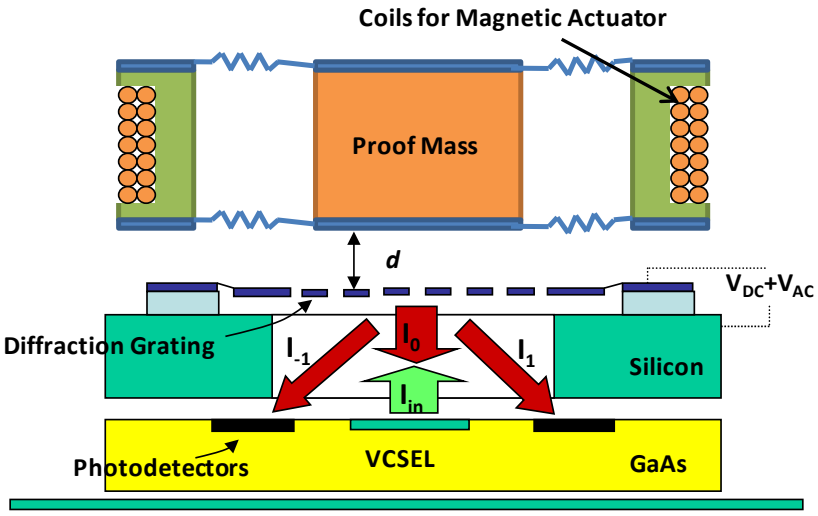

Figure 2. Schematic of a photonics based motion detection principle being developed by Silicon Audio. Light from a semiconductor laser such as a vertical cavity surface emitting laser (VCSEL) illuminates a diffraction grating fabricated on silicon. A portion of the incident light reflects directly off of the grating fingers, while the remaining light travels in between the grating fingers and to the proof mass and back to accrue additional phase. A diffracted field results consisting of a zero and higher orders whose angles remain fixed, but whose intensities are modulated by the relative distance between the proof mass and grating with the sensitivity of a Michelson type interferometer.

A sensing method very similar to that summarized in the caption of Figure 2 has been demonstrated and described in detail in prior developments (Lee et al., 2004; Hall et al., 2007; Hall, et al., 2008). The diffraction grating in this system serves the function of an optical beamsplitter, directly reflecting half of the incident light while passing the remaining half to travel to the proof-mass and back to accrue additional phase. Being an optical interference based approach, the displacement resolving capability of the method is of very high fidelity – on the order of 20 fm/√Hz when using small 500μW semiconductor lasers. The intrinsic open loop dynamic range of this approach (i.e., clip level) is limited to approximately λ/4, where λ is the optical wavelength. This corresponds to the peak-to-trough range of an interference cycle (i.e. fringe cycle) and is approximately 212 nm for an 850 nm wavelength semiconductor laser. Considering that 20 fm displacement can be resolved over a 1 Hz bandwidth, the intrinsic dynamic range is then 140 dB. Over the 40 Hz measurement bandwidth of interest, the open-loop dynamic range is 124 dB.

It should be emphasized that the schematic in Figure 2 is not drawn to scale. The total dimensions occupied by the silicon and GaAs chips is approximately $1 mm^3$, whereas the meso-fabricated proof mass is approximately 1 cm x 1 cm x 0.5 cm. To emphasize this, a micrograph of a packaged VCSEL and 2-element discrete photodiode array is provided in Figure 3 along with a separate micrograph of a fabricated grating structure.

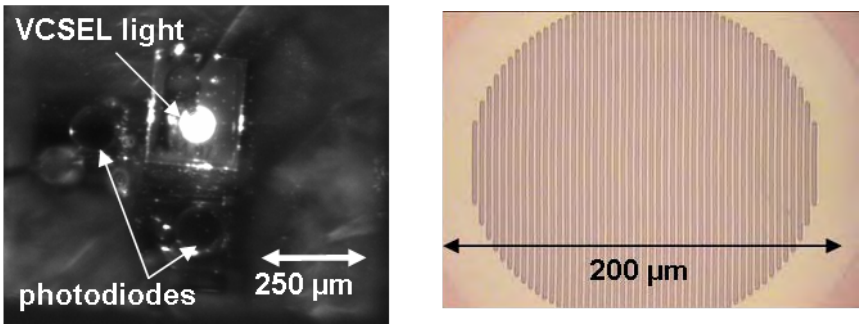

Figure 3. Left – micrograph of a packaged VCSEL (shown lasing) and centered amongst 2 photodiode elements. Right – micrograph of a fabricated grating structure. This structure has been etched into a 0.8µm thick silicon nitride layer.

The nominal distance "*d*" between the proof mass and grating structure as labeled in Figure 2 is relatively insignificant. It is important, however, that the interferometer be operated at a point of quadrature (i.e., a point of maximum slope and linearity on the interference curve). Figure 4 helps to clarify this by summarizing the theoretically predicted relationship between light intensity of the diffracted beams labeled in Figure 2 vs. the gap distance "d" also labeled in Figure 2. The center beam modulation is complementary to the sum of the exterior beams. Therefore, one can use the difference signal (in practice this is done by simple photocurrent subtraction), as the seismometer output signal. The linear operating region is highlighted in the figure. The slope of this curve is the displacement sensitivity of the detection method (after amplification through a photocurrent-to-voltage amplifier, the unit of the y axis is volts, and the sensitivity is therefore expressed in V/m).

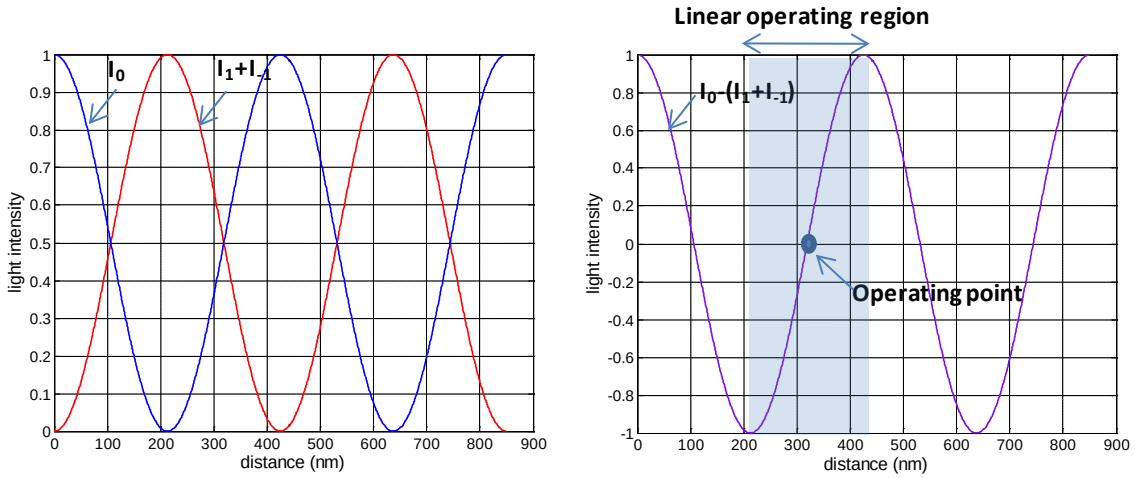

Figure 4. (left) Theoretically predicted relationship between the diffracted beams labeled in Figure 2 vs. gap distance "d" labeled in Figure 2. (right) The seismometer uses the difference signal to detect the proof mass motion within a single interference fringe.

Operation about a point of quadrature (i.e., the operating point labeled in Figure 4) can always be maintained by electrostatic actuation of the grating element as highlighted in Figure 2 with the applied electrostatic signals and/or by direct actuation of the proof mass using magnetic actuation. In addition, dynamic actuation of the proof mass also enables closed-loop measurement modalities. Closed loop operation is critical in high performance accelerometers, as the high *Q* of the open loop system required for low thermal noise must be electronically compensated for via feedback-altered-dynamics to achieve the desired flat frequency response (Liu and Kenny, 2001).

RESEARCH ACCOMPLISHED

The phase I feasibility study encompassed three primary goals:

1) Design, build, and experimentally demonstrate a meso-scale proof mass with a thermal mechanical noise level lower than 0.5ng/√Hz.
2) Demonstrate closed loop operation of the grating based motion detection system (summarized in Figure 2) and in particular the ability to use feedback to compensate for the high open loop resonance *Q* of the system, thereby demonstrating the desired flat frequency response.
3) Experimentally demonstrate the grating based motion detection system's ability to resolve the required 50fm/√Hz displacement.

The remainder of this review article will summarize accomplishments related to items 2 and 3.

Experimental Demonstration of Optical Interference

As a first experiment, the optical interference principle underlying the device operation was verified. This was accomplished by magnetically actuating the proof mass across a distance "d" relative the grating while measuring and recording the photodiode signals. The goal of this experiment is therefore to experimentally produce the theoretical curves presented in Figure 4. Figure 5 presents the result of this experiment, where the behavior predicted in Figure 4 is clearly verified. Note that the subtracted signal is the signal to be derived as the seismometer output. In operation, the proof mass is positioned to a point of maximum sensitivity (for example, d=2400nm in Figure 5), and small signal vibrations of the proof mass about this operating point are recorded.

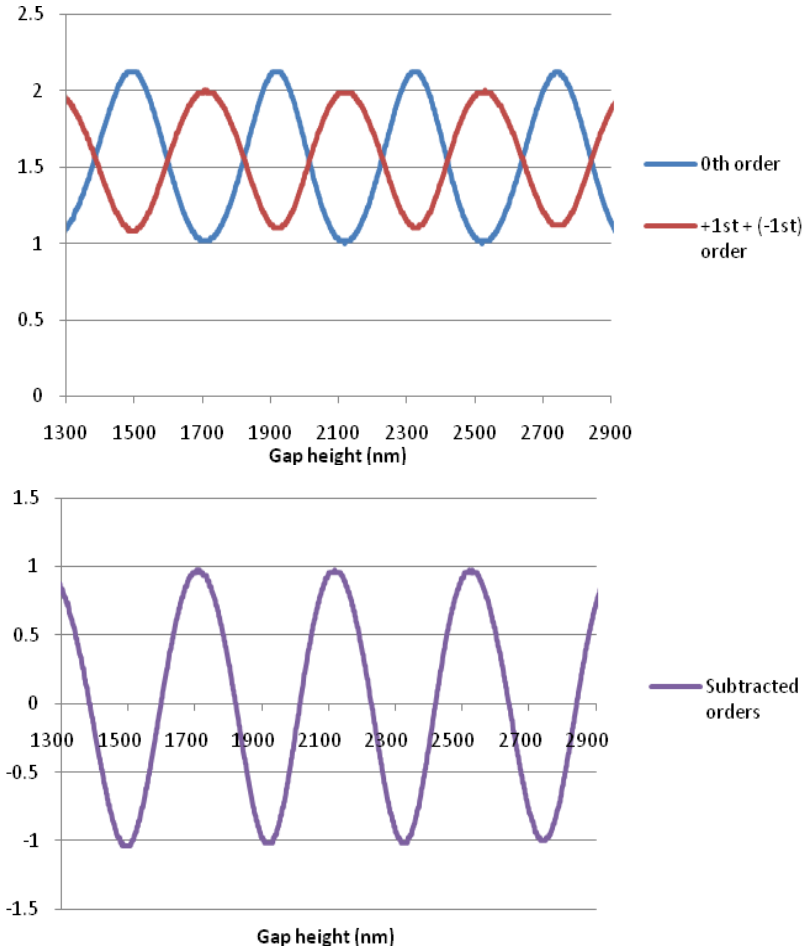

Figure 5. Experimental demonstration of the theoretical behavior predicted in Figure 4.

Experimental Demonstration of Closed Loop System Dynamics

A closed loop system schematic implemented in Phase I is depicted in Figure 6. Starting with an external inertial force input, the first block (i.e., the proof mass) converts this force into a displacement. The transfer function shown in this block is that of the well-known 2nd order system. The displacement is then converted into a voltage signal. The sensitivity noted in this block K_{tia} is simply the slope of the curve in Figure 4 (right) evaluated about the operating point. This measured displacement is the sensor output, V_{out}. The closed loop control block then applies magnetic forces to the proof mass in order to produce the desired flat frequency response. This technique has been used in other high fidelity measurement systems (Liu and Kenny, 2001).

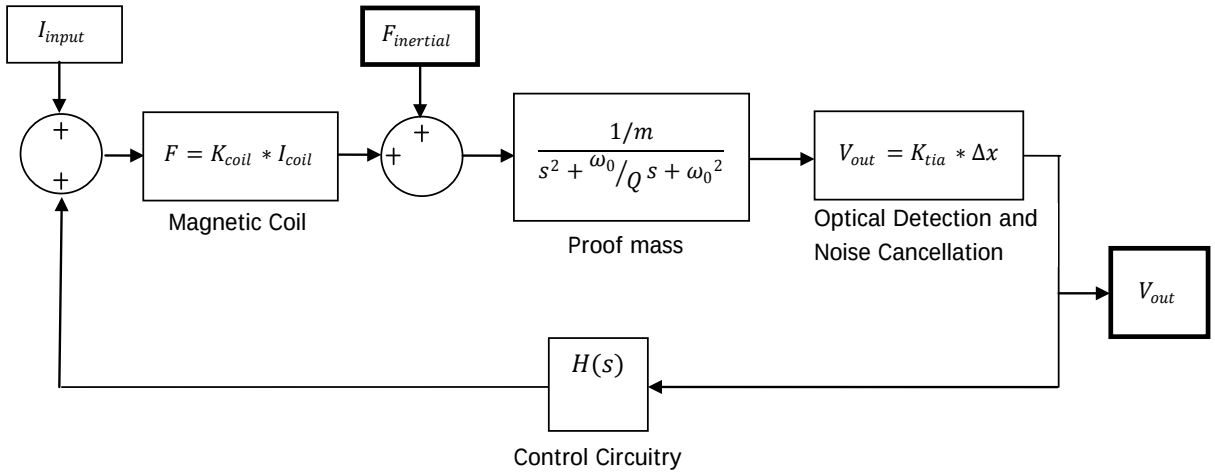

K_{coil} : Magnetic Coil force constant , units N/A
I_{coil} : Coil Current
I_{input} : Excitation current for response characterization
M, ω0 , Q : Open loop proof mass parameters
K_{tia} = TIA sensitivity V/m .
Δx = displacement relative to equilibrium position

Figure 6. Feedback control system schematic

A model for the closed loop system was developed in Matlab and utilized to design the control block. The additional coil current input shown in Figure 6 is used for self-test or dynamic characterization purposes. This port enables the generation of well controlled force inputs. The dynamics of the closed loop system were measured with a dynamic signal analyzer (model SRS 785) by applying a broadband swept sine input to this port while measuring the output signal. This experiment was repeated for several control settings to illustrate closed loop operation.

The results of this experiment are shown in Figure 7. The system can be modified with feedback forces to achieve the desired flat frequency response as shown by the "Measured response 3" case labeled in the figure. The frequency response below 1 Hz was filtered for convenience in these experiments, as the focus was on the resonance *Q*. The mechanical response of the proof mass below 1Hz is expected to be flat. Both stable operation and closed loop operation are successfully demonstrated with the sensor innovation summarized in Figure 2.

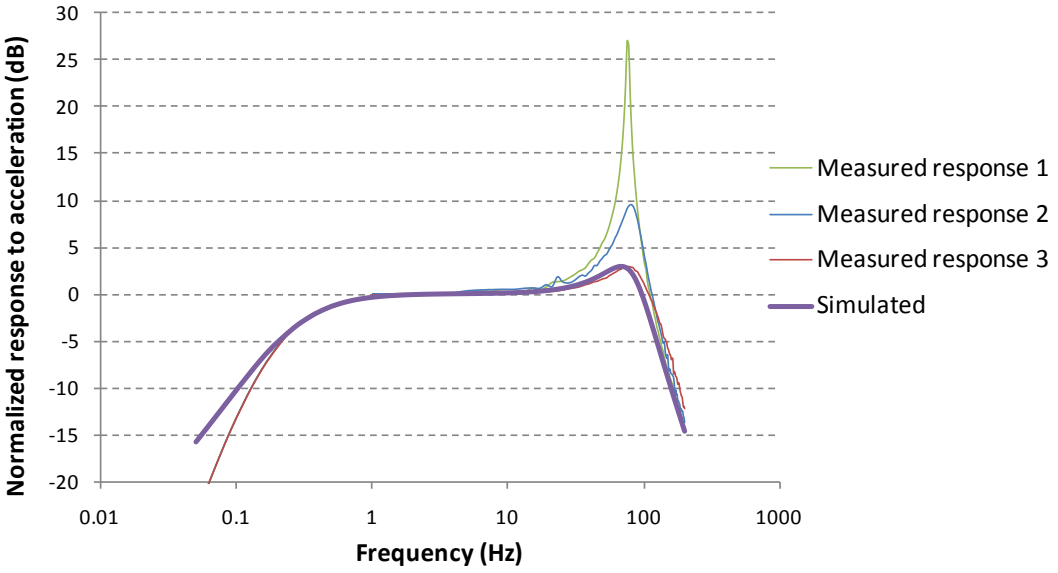

Figure 7. Measured closed loop system dynamics of the Phase I prototype. The low frequency roll-off is a design parameter and can easily be set to 100 mHz for the Phase II embodiment.

Displacement Noise Measurements

The third and final Phase I goal is demonstration of high fidelity displacement detection. For this experiment, the voltage noise spectrum at the sensor output is measured using the SRS 785 dynamic signal analyzer and referred to displacement units using K_{tia} (the displacement detection sensitivity in V/m). Since the goal of this particular experiment is to characterize specifically the displacement resolving characteristics of the approach, the system's sensitivity to ambient vibrations was removed by removing the proof mass from the system and replacing it with a rigid mirror. This removes external vibration noise from the measurement and allows the two dominant optical noise sources to be studied,

- Shot noise – the theoretical quantum noise limit which occurs at the photodiodes, and
- Laser intensity noise – small, broadband fluctuations in laser intensity

Since laser intensity noise occurs in both the zero and first diffracted orders, and since the signals are complementary, the common mode laser intensity noise can be cancelled without cancelling signal. This can be accomplished using a number of different approaches (Hobbs, 1997). An approach being investigated and developed by Silicon Audio was used to collect the data presented in Figure 8. With laser intensity noise cancellation, the displacement referred output noise is limited by shot noise, representing a displacement noise level of approximately 10fm/√Hz. This is lower than the resolution required for resolving the thermal mechanical noise of the proof mass and is a significant accomplishment of the Phase I study.

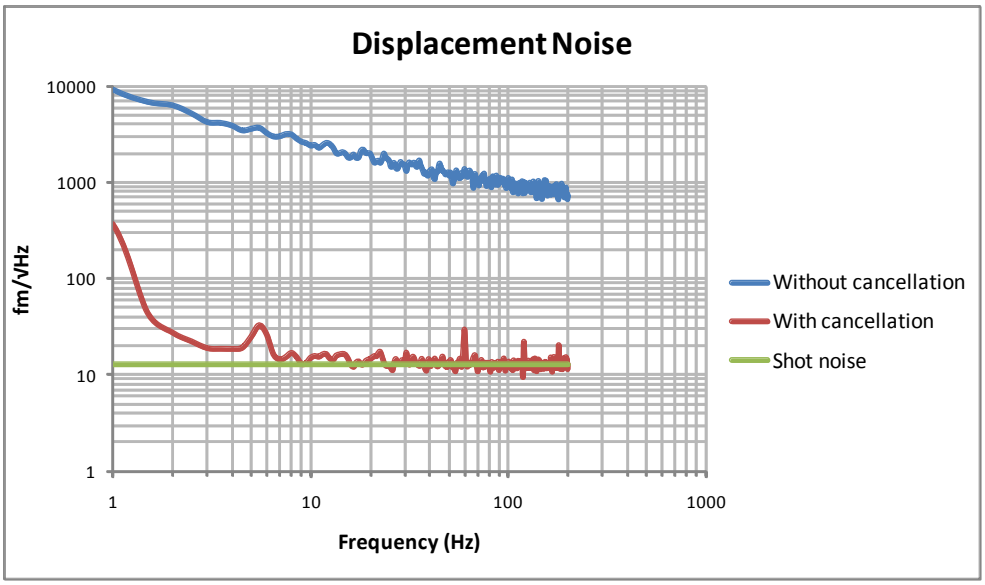

Figure 8. Measured displacement noise spectra of the Phase I prototype.

CONCLUSIONS AND RECOMMENDATIONS

Silicon Audio is addressing the NNSA's rigorous seismometer specifications using an approach that combines silicon micromachined optical elements, integrated semiconductor lasers, photodetection electronics, and meso-scale proof mass structures. This review article focused on a grating based implementation, and two significant Phase I accomplishments were discussed; high fidelity displacement detection and integration of feedback altered dynamics. Future development will focus on device design and noise mitigation for a 100-mHz–1-Hz frequency range, design for low cross axis sensitivity, and design for high thermal stability.

The timeliness of this innovative approach is worth noting. Low-cost, semiconductor lasers such as VCSELS are now fully commercialized and have been developed to the point where high quality, mode-stable, and polarization stable products are readily available. The movable grating actuator is readily fabricated with modern silicon microfabrication techniques. The vision for the Phase II development is a small, completely integrated, 3-axis sensor package roughly the size of a 9-volt battery.

ACKNOWLEDGEMENTS

The authors graciously thank the NNSA and the DOE SBIR program for support. We also thank the University of Texas, Institute of Geophysics for assistance with Phase I field test demonstrations.

REFERENCES

Hall, N. A. (2008). Micro-seismometers via advanced mesoscale fabrication, in *Proceedings of the Monitoring Research Review: Ground-Based Nuclear Explosion Monitoring Technologies*, LA-UR-08-05261, Vol. 1, pp. 610–614.

Hall, N. A., M. Okandan, R. Littrell, B. Bicen, and F. L. Degertekin (2007). Micromachined optical microphones with low thermal-mechanical noise levels, *J. Acous. Soc. Am*. 122 (4): 2031–2037.

Hall, N. A., M. Okandan, R. Littrell, D. K. Serkland, G. A. Keeler, and K. Peterson (2008). Micromachined accelerometers with optical interferometric read-out and integrated electrostatic actuation, *J. Microelectromech. Syst*. 17 :(1), 37–44.

Hobbs, P. C. D. (1997). Ultrasensitive laser measurements without tears, *Applied Optics* 36: (4): 903–920.

Lee, W., N. A. Hall, et al. (2004). Fabrication and characterization of a micromachined acoustic sensor with integrated optical readout. IEEE Journal on Selected Topics in Quantum Electronics 10: (3), 643–651.

Liu, C. H. and T. W. Kenny (2001). A high-precision, wide-bandwidth micromachined tunneling accelerometer, *J. Microelectromech. Syst*. 10: (3) 425–433.

SEISMIC DETECTION UTILIZING A MINI SENSOR

Robert J. Leugoud

eentec

Award No. DE-FG02-08ER85090

ABSTRACT

There is a need for a low cost, miniature, low power short-period sensor with the flexibility of packaging, not only for detection systems for nuclear treaty monitoring, but especially for the demanding requirements of free standing ocean-bottom (OBS) applications like offshore seismic monitoring and oil exploration. In this case, the very tight dimensions of the glass sphere or cylinder restrict the total assembly size, including seismometer, data acquisition systems, acoustic release, and batteries. Ideally, total sensor size should be less than the commonly used geophone size (several cubic inches) and power consumption should be very low, below 500 mW for a triaxial sensor and the digital recorder, while sensor self-noise should be close to or below the USGS Low Earth Noise Model, with dynamic range at least 120 dB to provide meaningful data. Such a sensor could provide valuable information by accurately recording signals far beyond the dynamic range of ordinary geophones.

The proposed sensors would also find applications in the area of earthquake engineering. The availability of miniature, very low-power, easily-installed, ruggedized, high-quality instruments costing *significantly less* than seismometers currently on the market would make the general instrumentation of structures in earthquake-prone areas affordable. Data from structures, which are susceptible to collapse, or significant damage, would enable engineers to better understand their nonlinear behavior and failure modes of structures. This would lead in turn to improved designs and building codes. In the interim, such data would identify those structures, which need to be reinforced. These sensors would also facilitate the instrumentation of historical structures in these earthquake-prone areas. Local networks of seismic or vibration detectors could prove an extremely cost-effective means of improving the safety of existing nuclear and other facilities. These applications require that the instruments be both reliable and inexpensive, so that they could be deployed even in today's environment of reduced utility budgets.

This technology would also lend itself to the extension of nano-g sensitivity. Nano-g sensors are of great interest to the space program. For example, their deployment on satellites offers the only practical means of monitoring satellite drag.

OBJECTIVES

This project, if successful, would lead to the implementation of miniature, affordable, rugged, reliable, easily installed high-quality instruments, well suited for mass production and use in all of the above areas.

Based on our investigation, we summarize below to meet the following requirements to such a seismometer as detailed in the original research specifications:

- miniature size – about 1 cubic inch
- power consumption should be below 100 mW for a basic analog sensor
- dynamic range - at least 120 dB
- high resolution in the required passband of 0.2 to 40Hz: below the USGS Low Earth Noise Model (e.g., approximately 0.5 ng/sqrt(Hz))
- the sensor must be capable of operation at any selected orientation of its axis of sensitivity.

RESEARCH ACCOMPLISHED

The last several decades have witnessed revolutionary changes in seismology and seismic-related applications like earthquake engineering, oil exploration, and nuclear plant monitoring. These changes caused by tremendous progress in the capabilities of advanced geophysical instrumentation coupled with the ever-growing power and accessibility of computers, networks and multi-channel compact low-power data acquisition systems. These new tools have provided large volumes of invaluable information on near-field and remote earthquakes or man made events such as explosions, the dynamic processes in the mantle, and the behavior of structures subjected to seismic activity. Their usefulness to seismic-related applications has been amplified by the use of large networks of low-noise seismic sensors. The use of these sensors, both in networks and in a wide variety of standalone applications, has been limited by the high cost of such instruments, especially given the reality of current budgetary restrictions. All commercially available high-performance seismometers are large in size, heavy and have a high power consumption. The user must often face a difficult choice: use instruments with significantly lower performance characteristics (geophones), or reduce the size of the network.

Using its proprietary technology, eentec was the first manufacturer to offer a low-cost medium-period seismometer. Prior seismometer models available jumped from short-period (1Hz and above) to broadband instruments. This medium period seismometer (eentec was the first to "coin" the medium period seismometer term in the market) instrument generated a steadily growing flow of requests and orders from all over the world. The sensor was originally intended as a low-cost replacement for the old-style short period passive instruments. Continuing internal research efforts have led to significant improvements in performance with only slight increases in cost. With continued development of its technology eentec has introduced the first low-cost field rotational seismometer (R-1). This new instrument has opened up many new avenues of scientific research.

Seismometer Characteristics

Seismometers designed for the above applications must satisfy a number of stringent requirements: miniature size, low cost, long term and environment-dependent parameter stability, ruggedness, ease of installation, very low power consumption, wide frequency band, high sensitivity, and wide dynamic range. We demonstrate below that no instruments based on current technology on the market satisfy all these requirements. The primary goal continued research and development of this technology will be the design of a conceptual prototype ***miniature low-cost medium-period low noise seismic sensor based on new technology derived from eentec's current proprietary technology and suitable for all of the above mentioned applications.***

Rotational seismometers

It has often been assumed that the movement of a small section of the ground surface is only translational. While this is approximately correct in the case of teleseismometry, the ground motion near the seismic source contains well-pronounced rotational components. Numerous observers have confirmed this. Our new technology will also allow development of the first direct readout miniature rotational seismometer, with a rather limited additional effort beyond that for the proposed linear seismometer.

Rotational motion for detection systems for nuclear treaty monitoring may be very useful by using measured rotations that can be used for better identification and separation of Love from Rayleigh waves. In addition enable better and more unique interpretation and identification of P versus SV versus SH wave components.

For structural monitoring of nuclear facilities, rotational motion could be very valuable by analysis of recorded rotations in and near foundations of structures can provide for the first time means to separate the effects of soil-structure interaction from the total recorded (translational) response. Simultaneous recording of 6-degrees of freedom (DOF) of accelerations will enable computations of permanent displacement in the structures, of soils and in the near field of shallow earthquake faults were the facility might be located. Recording of permanent rotations in structures and in soils will open new possibilities for accurate interpretation of non-linear deformations in the field and for verification of analysis that simulate those deformations. The boundaries of many structures coincide with their supports. At these boundaries the displacements are either small or zero, and so the measured translational data (accelerometers) brings little or no experimentally defined constraints to check theoretical or empirical models. Rotations on the other hand are often largest near supports (e.g., consider a simple beam) and therefore measuring rotations will provide excellent and the most direct data to compare against theory.

Proof of Concept in Phase I

Other competing technologies that were awarded Phase I funding for this topic.

We believe that the other technologies, although creative, would basically fail to provide both sensitivity (low noise) and a rugged instrument suitable for field deployment.

Technologies that use a small mass would have a high natural frequency of over 100Hz. Our technology of Proto 1 had a natural frequency of 8Hz. When evaluating the 1/f noise of the electronics, a high natural frequency would have major limitations on the low frequency performance.

It is also desirable to have each axis independent of the others. Hence, true measurement in the X, Y, and Z motions. Using interdependent axis to resolve the X, Y, and Z motions can lead to problems and complete failure of the instrument if one axis fails.

We not only proved our concept as described in the Phase I objectives but have built the first stage prototypes that the latest ones are currently undergoing testing. After we conclude our internal testing, we will be sending the unit to UCLA for further testing and comments with the more sophisticated test equipment available to them. To achieve this point of development we had to overcome a few challenging problems with new creative solutions.

There are more challenges that lie ahead in the research to finally meet the end objectives. With our experience in our technology and the creativity we demonstrated in the past, we are confident that we will solve these new problems when encountered.

The Proto 1 Instrument

Today's top of the line electromechanical seismometers effectively utilizes the best of modern mechanical and electrical engineering technology. Bandpass of the sensor is directly influenced by the size and weight of the mass. It would be unreasonable, therefore, to expect that even significant modifications could result in noticeable price reduction or changes in their specifications. To fill the need for miniature seismic sensors which offer low-noise, wide dynamic range, broad frequency band, very low power consumption, very wide operating temperature range, and, suitability for use in seismology and earthquake engineering, it is necessary to develop new a technology based on physical principles different from those used in the traditional devices. For the last several years, we have been investigating and developing ***electrochemical transducers*** currently used in our seismometers**,** a technology which has shown great promise for the future implementation of the kind of instruments specified in this research. We proposed a research and development program aimed at proving the feasibility of the implementation of miniature seismometers using ***liquid inertial masses*** and ***electrochemical transducers.*** The main feature of these instruments is that they would have ***neither moving mechanical parts nor precisely machined components, while their noise performance is already in nano-g range***. In Phase I of the research program addressed some of the limitations observed in the very early stage prototypes of these sensors and the optimization of their conceptual design.

For those readers who are not familiar with the technology used in the research the following is a brief description of our innovative electrochemical sensor technology.

Seismometers with Electrochemical Transducers

The first seismometer using a very simple electrochemical converter (“solion”) was built and tested in the late 60’s. Despite significant funding and multi-national research efforts, which lasted for almost three decades, the results turned out to be too modest to lead the development of a commercially viable product.

In the core of such seismometer is an electrochemical transducer, which is shown in Figure 1. The transducer is generally contained in a channel, (1), filled with a specially prepared electrolytic solution. It consists of fine platinum mesh electrodes – two anodes, (2), and two cathodes, (3), separated by thin, microporous polymer spacers (4). This stack is tightly held together by housing (5). The motion of the fluid caused by an external acceleration must be converted into an electrical signal. One way of achieving this is by using the convective diffusion of the ions in the electrolyte.

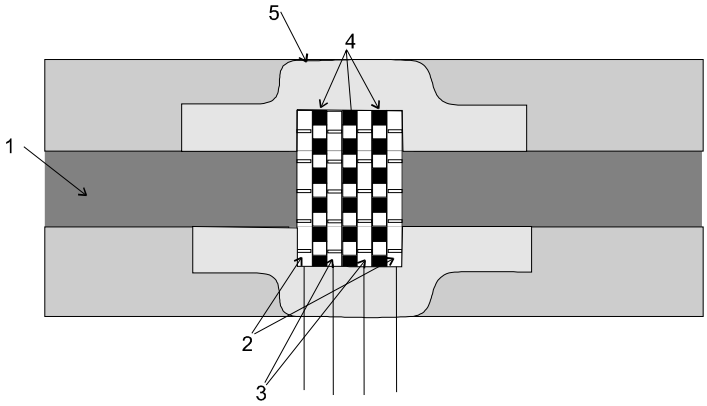

1 - Electrolyte channel
2 - Platinum mesh anodes
3 - Platinum mesh cathodes
4 - Microporous spacers
5 - Housing

Figure 1: Electrochemical Transducer

When a small dc offset is applied between the anodes and cathodes, the flow of ions of each type is given by the following expression:

$$\mathbf{j}_a = -D \cdot \nabla c_a + q_a \cdot c_a \cdot \mu \cdot \mathbf{E} \qquad (1)$$

where D = diffusion coefficient, μ = mobility, q_a = elementary charge, transferred in electrochemical reaction, c_a = concentration of active ions, E = the electrical field vector. Since the strong electrolyte is an excellent conductor, the electric potential drops rapidly in the vicinity of the electrodes, and there is no electric field, E, in the bulk of the fluid. The second term in Equation 1 can therefore be ignored. Thus, the application of a bias voltage results *only* in a concentration gradient. This is in contrast both to conductors, in which the current is driven by the external electric field, and to semiconductors, in which both the field and the concentration gradient determine the currents.

An external acceleration, **a,** along the channel creates a pressure differential, **ΔP,** across the transducer, which forces the liquid in motion with a velocity, **v**. This flow of electrolyte entrains ions and causes an additional charge transfer between the electrodes:

$$\mathbf{j}'_\mathbf{a} = \mathbf{v} \cdot c_a \qquad (2)$$

The total current from active ions, in the presence of acceleration, will thus be:

$$\mathbf{j}_\mathbf{a} = -D \cdot \nabla c_a + \mathbf{v} \cdot c_a \qquad (3)$$

The transducer thus generates an electrical signal in response to an input motion. The symmetric geometry of the transducer cell ensures its linear behavior over a wide range of input signals.

With a highly concentrated electrolyte, the electric field is non-zero only in a narrow boundary layer adjacent to the electrodes. In this case, the electric current is fully determined by the diffusion. If such a transducer cell is incorporated into a motion sensor, the latter can be used, for example, to respond to linear motion (or to angular motion in a different sensor design). Electrochemical transducers are characterized by a very high conversion coefficient of mechanical motion into electrical signal. That is why the electronics noise plays a noticeably smaller

role in the total signal-to-noise ratio than in the traditional electromechanical seismic motion sensors. In addition, this results in low power consumption, typically several times smaller than in any other active seismometers.

In practical the sensor design transducer is placed in a mechanical oscillating system that consists of two elastic membranes, which close the ends of electrolyte channel in Figure 1. Since electrodes and their assembly are relatively small in size (less than ¼ inch) there is no restriction to reduce the size of such a sensor to 1 cubic inch or even less.

Therefore, an electrochemical sensor may comply with the requirements set forth for the miniaturized seismometer. On the other hand, such commercially available seismometers manufactured by eentec, do not qualify in several other areas. In particular, like traditional high performance seismometers they employ additional solid inertial masses and springs to support them; their size, which is critical to the sensor operation, is noticeably larger than specified. A significant research and development effort is required to achieve the required high resolution in a device with much smaller cross-section.

In Phase I of the program, we enhanced and refined our model of the transducer; investigated several possible implementations of the noise reduction and selected the most promising; investigated and selected the best miniaturization technique; and, built a Phase I intermediate prototype instrument. This same prototype are expected to be made suitable for field-testing, which will be conducted in Phase II. Then the further miniaturization and increase of operating specifications will be researched. From this Phase II research and the testing of the proto 1 created in Phase I we will create a few Phase II prototypes until the complete specifications as originally outlined in this program's announcement are achieved or exceeded.

Below we present data that we have obtained so far. Final modifications and further test data will be submitted in our future reports.

Phase I Work Description

Main tasks of our SBIR Phase I project have been completed successfully. A new, miniature electrochemical seismic prototype sensor element has been developed which is shown on the photo in Figure 2.

Figure 2. Picture of Proto 1 sensor element

This sensor element is only about 1/3 cubic inch in size. Significantly smaller dimensions of this sensor forced us to develop a transducer cell with a significantly different geometry as compared to that of the standard device. As it will be discussed below, theory of operation of an electrochemical transducer cell is very complex. In many ways we were fortunate to have come up with an apparently viable design after only a few attempts, although more then a decade of working and improving similar transducers has provided a solid practical foundation and large amounts of data for this success. Implementing a well behaving sensor was the key to the overall success of the proof of concept

and prototypes for the project. Still another difficult problem, which under the stringent limitations imposed by the timing and budget had to be solved by relying mostly on approximate calculations, was the design of the membranes (Figure 3). There are two major mutually contradicting difficulties to be overcome: the membranes must be soft enough in order not to introduce strong premature attenuation of the lower signal frequencies, and still sufficiently strong to support external inertial mass without additional expensive suspension. However, we also were reasonably successful in both respects, which saved time and money.

Prototype sensors have been initially calibrated on our precision shake-table. Typical frequency response is shown on Figure 4 (red curve). Other tasks involved mechanical design of the external inertial mass and spring that would further increase the sensitivity (blue curve on figure 4) and thus reducing the noise of the sensor to the levels below USGS new low-noise model (NLNM). Inertial mass placed inside a spring to reduce the total size of the assembly to about 1 cubic inch (Figure 5).

We also developed a design for rotational and horizontal sensors, which does not require membranes, masses, springs and other moving mechanical parts, while being close to 1 cubic inch. This prototype is shown on Figure 5.

Figure 3. Standard membrane and two designs of a shrunken membrane.

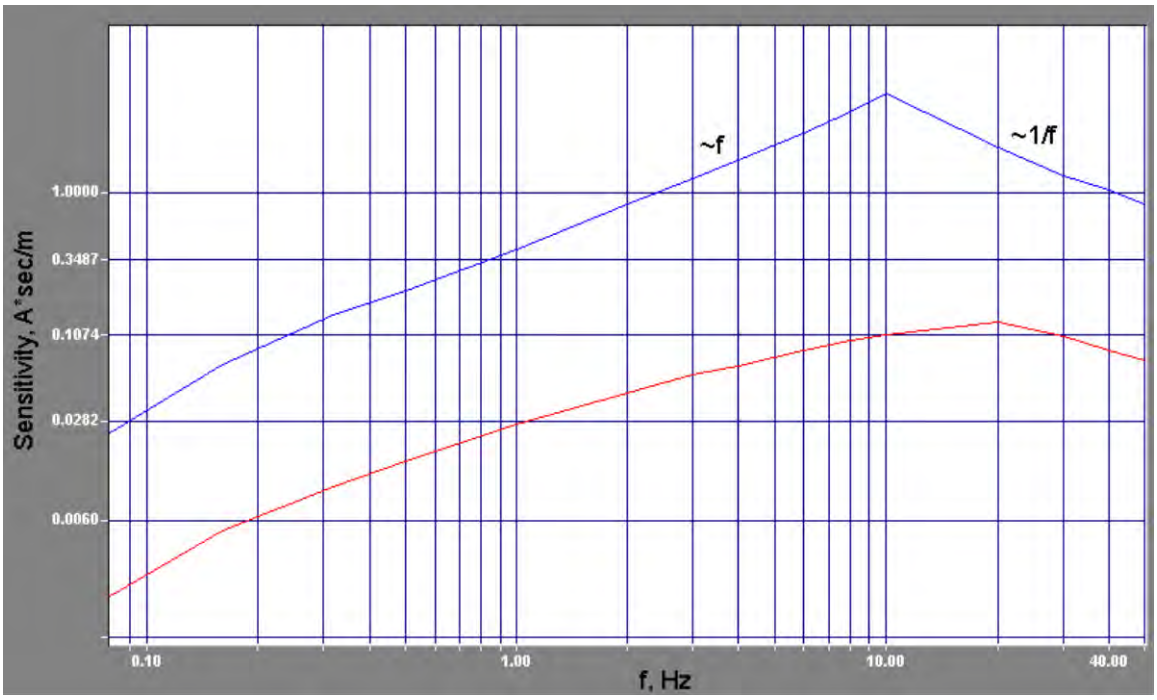

Figure 4. Effect of the additional inertial mass (blue) on a Proto 1 (red) sensitivity and form of the frequency response.

Figure 5. Vertical and horizontal/rotational prototype sensor assemblies.

The remaining tasks still require tedious and, at times, ingenious work; however, they were relatively routine and, at least partly, not as challenging. One of the most demanding was the design of the electronic circuit that should provide proper frequency correction to the new sensors. The electronic design was not as trivial a task as it may seem to those who are not familiar with rather complex transfer functions of electrochemical seismic sensors. Finally, with great difficulties, we squeezed the new electronic circuitry in a quad operational amplifier with few external components (see Figure 6). These efforts resulted in reduced power consumption to about 32 mW, which is 3 times lower than was proposed, and there is a potential of its further reduction since the sensor element itself consumes about 0.3mW.

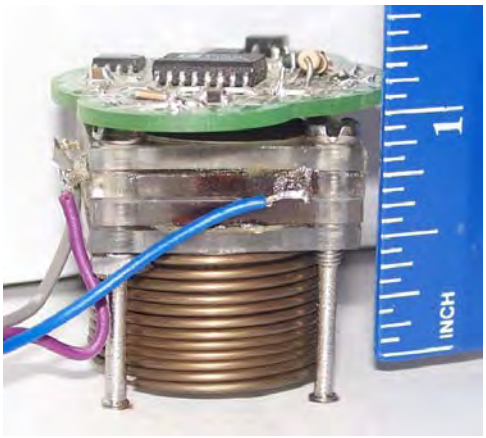

Figure 6. Prototype sensor with electronics.

Testing the Prototype Sensors

All six produced sensor elements were initially calibrated on the shaketable and tested to evaluate their noise characteristics. All of them demonstrated reasonably similar transfer functions and noise levels; therefore, one of them was selected at random and used to build the prototype. The latter was tested rigorously after the assembly against standard eentec SP-400 seismometer, which was used as a reference for in-house testing. All major characteristics proved to be very close to those targeted in the Phase I proposal (see Figure 7). Signal spectra recorded at eentec's facility shows a good correlation between the prototype sensor and the reference seismometer. Noise level of the prototype sensor is measured by fixing its inertial mass to minimize influence of background seismic signals. However we discovered some things that have to be improved. First of all, sensor noise level, while being below USGS NLNM or very close to it on most frequencies, has to be reduced by several dB in the middle of the passband. Most probably this should be attributed to getting much stronger membranes or the 1/f noise in the electronics, although at the moment, until more complicated and detailed computer tests and analysis are performed during future research, some of the "blame" may be placed onto the transducer cell itself. Also, frequency response of the prototype sensor is not perfectly flat over velocity, being within +/-3 dB from the reference sensor. These small deviations will be easily corrected later, mostly in electronics or in sensor design, if required.

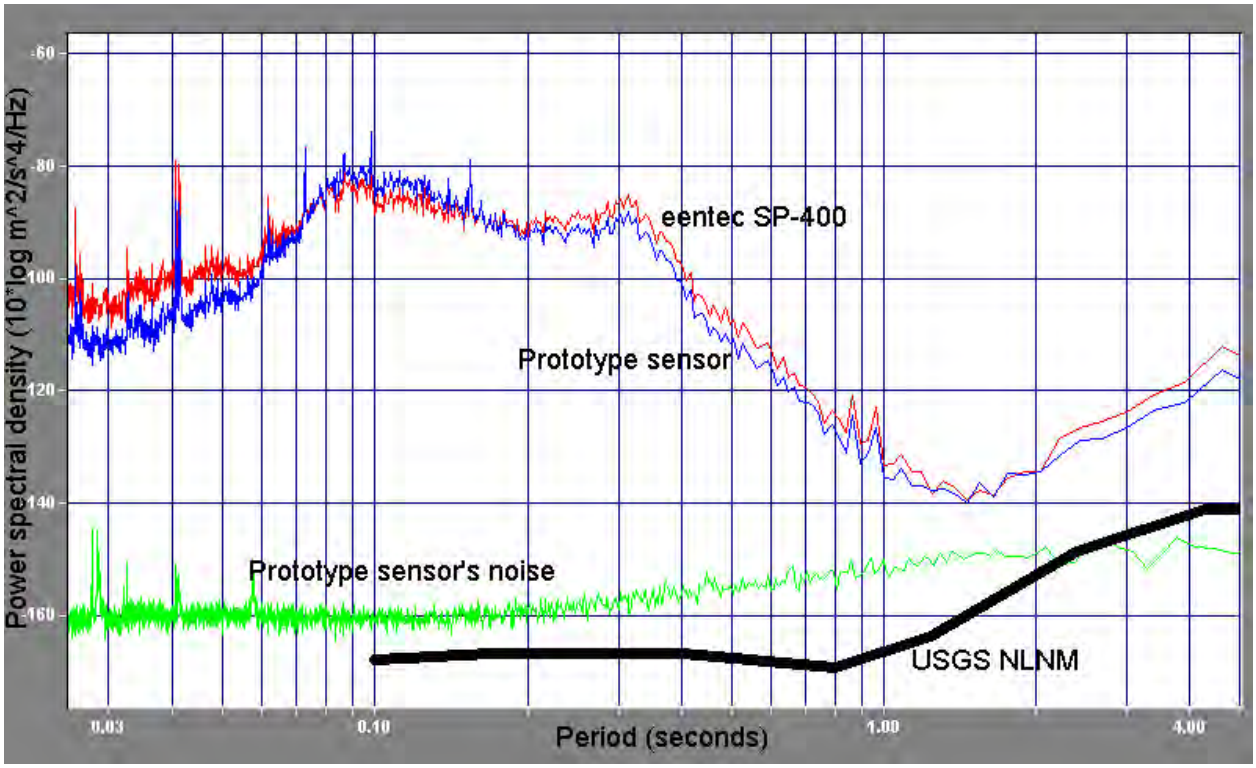

Figure 7. Signal and noise spectra of a prototype sensor.

Phase II Project

Technical Objectives

The goal of the Phase II effort is to prove that the technology developed in Phase I research can provide a sound foundation for practical implementation of miniaturized, inexpensive, high performance short-period seismic sensors. In order to achieve this goal, the following technical objectives will be met during the Phase II research:

1. Fabricate and test in the laboratory conceptual prototype 2 of miniaturized electrochemical sensor with the following parameters;
2. Miniature size – about 1 cubic inch;
3. Dynamic range of ≥132 dB;
4. Passband of 0.07Hz to 50Hz;
5. Self-noise in the required passband: below 0.5 ng/sqrt(Hz);
6. The sensor will be capable of operation at any selected orientation of its axis of sensitivity;
7. Demonstrate that the cost of such sensor will be significantly less than that of traditional mechanical instruments;
8. Develop and test a miniature prototype rotational accelerometer with translational sensitivity <0.5% and a frequency band of 0.07Hz to 50 Hz.; and
9. Identify commercialization and manufacturing plans to be performed in Phase III of this project.

Future Research

Evaluation of Phase I Test Results

We will initiate Phase II research with the analysis of data that has been collected in tests of our Proto 1 unit along with UCLA data and comments. During experiments in Phase I, large volumes of data were collected, but less than half of these data were analyzed in the limited time available. The Phase II program will therefore begin with a detailed analysis of all of these data, whose objective is aiding development of a more accurate mathematical model. Based on the results of the analysis of these experimental data, we expect to refine and carry out the tasks required for successful completion of a working unit, thereby meeting all the required objectives.

Further Refinement of Electrolytic Liquid for the Transducer

While there exists a possibility of noise reduction of a translational sensor by increasing attached solid inertial mass, this approach is not applicable to rotational sensor, where toroidal sensor element is completely filled with the electrolyte solution. For such a sensor increasing electrolyte density is the direct solution to the increase of signal-to-noise ratio. We investigated several heavy liquids in Phase I and found only one suitable electrolyte to replace the currently used one. Such replacements, along with the increased concentration, may result in up to 6 dB noise reduction. However this new electrolyte should be thoroughly tested for stability. *We consider this stability as one of our most important tasks, since the unstable electrolyte contributed significantly to the demise of the earlier solion experiments*. During the two years of Phase II work we will perform our accelerated aging experiments on the electrolyte stability.

Further Optimization of the Membrane Design

Background: Optimization of the membranes for the miniaturized sensor presents a formidable task. Description of dynamic properties of even simple flat membranes calls for the use of complex mathematics; smallest irregularities in such a membrane complicate such description much further. In our application where the membranes should work at very low frequencies they have to be as soft as possible. Therefore traditionally goffered configuration is technologically most preferable and when designed properly would possess the required frequency response. However, such proper design is very difficult to achieve. Sophisticated and very expensive programs exist which could be used to analyze various configurations. However, our long experience shows that the results may still not be sufficiently accurate and the true membrane performance can be evaluated only experimentally. Therefore, the more economical approach, both in term of time and money will be the gradual modification of the already developed membranes.

Phase I effort resulted in the two designs of membranes, 24mm and 16mm in diameter (Figure 3). The first design is implemented in a Proto 1 sensor, and as the tests have proven, would be marginally acceptable for further use, although its relatively large effective area requires heavy inertial mass to achieve noise levels below NLNM. Second smaller design proved to be not as soft as expected while it is most promising for the desired noise level. Initial calibration data and field test results of the sensors with these membranes indicated that the frequency cut-off of the sensor is not adequate for the target application and even less so for use in high performance broad-band seismometers. Therefore, one of the key tasks of the Phase II will be such modification of the membranes that would allow for stretching the sensor low cut-off frequency to 0.07Hz.

Based on our previous analyses the transfer function of an electrochemical sensor can be described within an approximately 3% accuracy by the following empirical expression:

$$W = \frac{en_0(\rho L + \frac{m}{S})}{R_h} \frac{1}{\sqrt{1+\frac{\omega_d^2}{\omega^2}}\sqrt{1+\frac{\omega_l^2}{\omega^2}}\sqrt{1+\frac{\omega^2}{\omega_h^2}}} \qquad (4)$$

Where: e = elementary change; n_0 = concentration of charge carriers in equilibrium; ρ = electrolyte density; L = height of the electrolyte column in the sensor; m - additionally attached mass, S - effective area of the membrane, R_h = hydraulic impedance of the transducer cell; ω_d =diffusion frequency, ω_h and ω_l = high- and low-frequency cut-offs of the mechanical system correspondingly.

The low cut-off frequency of the sensor depends on the volumetric rigidity, μ, of the membrane:

$$\omega_l \propto \frac{Eh^2}{R_h S^3\left(1-\mu^2\right)} \tag{5}$$

Where E = Young's modulus; h = thickness of the membrane and S = membrane effective area.

Membrane diameter cannot be increased without increasing the diameter of the sensor itself; the elasticity is more or less the same for the short list of the elastomers compatible with the highly volatile and chemically active electrolytes filling the sensor. Effective area can be manipulated slightly by changing configuration of the membrane. But a truly noticeable reduction of the rigidity can be achieved by decreasing h that is presently 0.5mm. While technologically the thickness can be reduced significantly, one has to be careful in doing so because if the membrane becomes too thin, the electrolyte may slowly escape over time even through membranes that are made out of elastomers with extremely poor permeability. We are less familiar with the volatility of other possible electrolytes that will have to be investigated for each particular compound of interest.

Development of the Force-balanced Feedback

Force-balanced feedback is implemented in all modern low-noise seismometers including sensors presently manufactured by eentec. It provides extension of the dynamic range; flat to velocity transfer function and long-term stability of all parameters. Development of the closed-loop sensor is the necessary task in Phase II to achieve at least 132dB of dynamic range.

The transfer function of the closed loop sensor can be described as:

$$S_S(\omega) = S_{sen}(\omega)\cdot S_{ff}(\omega)\cdot \frac{1}{1+S_{sen}(\omega)\cdot S_{ff}(\omega)\cdot S_{fb}(\omega)\cdot K_F} \tag{6}$$

where $S_{sen}(\omega)$ = the transfer function of the electrochemical cell; S_{ff} , S_{fb} represent transfer function of the feed-forward and feedback electronic paths respectively; and K_F = the transfer coefficient of the current-to-force converter, like MHD or coil-magnet systems.

As had been expected and was confirmed in the Phase I research, this transfer function is essentially independent of frequency. When the second term of the denominator is sufficiently large, *i.e.*, when:

$$S_{sen}(\omega)\cdot S_{ff}(\omega)\cdot S_{fb}(\omega)\cdot K_F >> 1 \tag{7}$$

The frequency response of the system will be completely determined by the transfer function of the feedback path:

$$S_s(\omega) \approx 1 / [S_{fb}(\omega)\cdot K_F]. \tag{8}$$

In order for Equation 8 to be true, the feed-forward circuit must be such that Equation 7 is always satisfied within the instrument passband and the operating temperature range.

We have necessary practical experience in development of force-balanced feedback for translational and rotational electrochemical sensors. Their principles of operation are very common. We are going to use the same approaches to miniaturized sensors in Phase II of this project.

Further Improvement and Miniaturization of the Electronics

Implementation of the force-balanced feedback will result in significant modifications in the electronic circuit. One approach to the implementation of the feed-forward circuit would be to simplify it to a bare minimum, limiting its functions only to the coupling with the transducer and generating input to the feedback network. In this case, the feedback circuit would have to meet two criteria: provide the necessary frequency response, and guarantee that Equation 7 is satisfied no matter how low the $S_{sen}(\omega) \cdot S_{ff}(\omega)$ product becomes. Such an approach does not seem optimal, with respect to either the complexity of the feedback circuit or the overall system noise level. The other extreme approach would involve the introduction of a comprehensive frequency and temperature correction network in the feed-forward path. In this case, while we still could maintain the condition of Equation 7, the feedback will play no useful role, other than possibly provide the expansion of the dynamic range. Clearly, an intermediate approach is preferable. This involves inserting some simple frequency and temperature correction into the feed-forward path, thereby facilitating the operation of the feedback circuit. The optimal balance between the two paths will be thoroughly investigated and determine the final design of the electronics.

Regardless of the above considerations, each design will be subjected to a thorough stability analysis using standard methods of feedback system theory.

The electrochemical sensor transfer function contains temperature-dependent terms such as viscosity. Any sensor therefore requires temperature compensation circuits in the electronic amplifiers. We are going to run a set of tests in a temperature chamber for final prototype sensors. The newly designed temperature compensation networks have to be tested and proved to be quite accurate within the specified temperature range.

Since electrochemical transducers have well-defined transfer function, only a few components are changed during calibration. This allows us to make single custom ASIC for the electronic circuitry to reduce its size and the overall dimensions of the instrument.

Assembly and Testing of Prototype Sensors

Intermediate Prototype Sensors

In Phase I we proved our concept on vertical sensor design, since it is most difficult in implementation. In Phase II, we will continue the optimization of various features and components of the proposed seismometer. In parallel, we will gradually begin to incorporate them into more and more advanced prototype vertical, horizontal and rotational electrochemical sensors.

At the very outset of this program, we will design vertical and horizontal sensors containing coil-magnet feedback. Then we will create rotational sensor with feedback.

Each generation of prototypes will undergo exhaustive experimental evaluation including:

- ◊ Calibration on the shake table over a wide frequency and amplitude range of harmonic input motion.
- ◊ Comparative field tests *via* cross-correlation and against STS-2 seismometers. We have generally run such tests at the USGS ASL in Albuquerque, NM.
- ◊ Temperature testing over the full operating range described above.
- ◊

Pilot Prototype Seismometers

Two to three generations of intermediate prototype sensors are expected to be built and tested. Each such single axis experimental sensor will be placed into the housing of a production three-component seismometer. This approach provides us with a very flexible, inexpensive and quick way to deploy the prototypes.

By the end of the sixth quarter of Phase II, we expect to be in a position to develop the layout, design and build pilot prototype seismometers incorporating all the key features. This will be a difficult task, especially with the frequency band extended to 0.07 Hertz. In this design, we will rely upon our long experience in the development of broadband seismometers and the advice of our colleagues and customers. We will pay special attention to the minimization of environmental effects and to the avoidance of internal temperature gradients (although the inherent low power consumption should reduce this potential problem). Even this prototype design will eliminate a number of items necessary to almost every traditional seismometer, such as mass centering and arresting mechanisms, because it is as small and rugged as a geophone.

CONCLUSION AND RECOMMENDATIONS

All major objectives of the Phase I research project have been met. The technical feasibility of our approach to the implementation of miniature, highly sensitive and very low power seismometer has been clearly proven with the manufacturing of an actual prototype.

AN INTERFEROMETRIC MEMS SEISMOMETER: DESIGN AND TESTING

B. John Merchant and Murat Okandan

Sandia National Laboratories

Sponsored by the National Nuclear Security Administration

Award No. DE-AC04-94AL85000/SL09-MEMS-NDD02

ABSTRACT

Current nuclear explosion monitoring efforts focus on processing signals collected at teleseismic (>2000 km) and, increasingly, regional (200 to 2000 km) distances from relatively large source events. The transition from teleseismic to regional monitoring has required great efforts in signal processing techniques (because of the increased complexity of the regional signals) and monitoring station design (because of the expanded frequency range and increased sensitivity desired). Local seismic monitoring (0 to 200 km from the source event) is desired to push detection, location, and identification to significantly lower limits.

Effective local seismic and vibration monitoring will require small, easily deployed sensors that operate reliably, autonomously, and robustly, given deployment conditions. Placing sensors in the best locations to receive signals of interest may be very problematic. Local terrain, land use, and restricted access to the site may severely limit options for deployment. These factors drive size, power, and communications specifications for the sensor package, limiting choices among existing sensors to less sensitive devices. Miniaturization through micro-electromechanical system (MEMS) techniques is essential to build sensors of the size and capability needed.

The objective of this project is to develop technology needed to build a new seismic sensor that is very sensitive but extremely small. A prototype sensor will be developed through integration of a MEMS optical grating transducer with an optoelectronic source, photo detector, and associated electronics. In the near term, this sensor will be capable of motion detection on the order of 10 ng/√Hz over a frequency band of 0.1 to 50 Hz with a large dynamic range, while offering a factor of 10 reduction in size over existing technologies. The mid-term goal for this proposal is to reduce the noise floor down to 1 ng/√Hz. The longer-term goal is a noise floor of < 1 ng/√Hz (near the low-noise model), reduced lower bandwidth limit of 0.01 Hz, and further optimizations in size and power consumption. This will substantially increase sensitivity in very small, low power accelerometers.

OBJECTIVES

The objective of this project is to develop technology needed to build a new seismic sensor that is very sensitive but extremely small. A prototype sensor will be developed through integration of a MEMS optical grating transducer with an optoelectronic source, photo detector, and associated electronics. In the near term, this sensor will be capable of motion detection on the order of 10 ng/√Hz over a frequency band of 0.1 to 50 Hz with a large dynamic range, while offering a factor of 10 reduction in size over existing technologies. The mid-term goal for this proposal is to reduce the noise floor down to 1 ng/√Hz. The longer-term goal is a noise floor of < 1 ng/√Hz (near the low-noise model), reduced lower bandwidth limit of 0.01 Hz, and further optimizations in size and power consumption. This will substantially push the state of the art for sensitivity in very small, low power accelerometers.

The monitoring community needs for high-frequency sensors, with an emphasis on small sensors needed for local monitoring, were explored at the Air Force Research Laboratory (AFRL) Seismic Sensor Workshop in September 2004 (AFRL, 2004). The following sensor capability needs were identified at the workshop (Figure 1):

- Self Noise Below New Low Noise Model (NLNM)
- Dynamic range > 120dB
- Linear response > 60dB
- Frequency range at least 0.2 -40 Hz
- Power consumption < 100 mW
- Installation flexibility
- Low weight
- Small size
- Robustness
- Stability of response

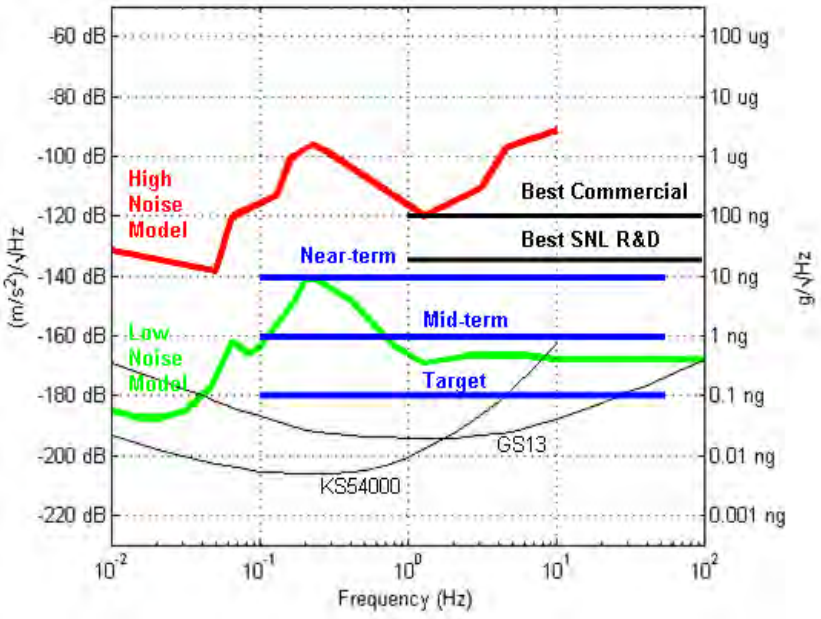

Figure 1. Comparison of projected MEMS accelerometer noise levels with the Low and High Noise Models. Current sensors are shown for reference.

Existing devices meet some combination of these requirements very well. Traditional short period seismometers easily meet the noise, dynamic range, linearity, and bandwidth requirements, but are larger and heavier than desired. Current small sensors (e.g., geophones, piezoelectric, or MEMS sensors) may meet the needs for emplacement flexibility, robustness, weight, size, and power, but do not deliver the sensitivity needed. Simultaneously addressing all of these specifications poses an extreme engineering challenge.

RESEARCH ACCOMPLISHED

Design Overview

The basis of the proposed inertial sensor system (Figure 2) is a motion detection transducer employing a fixed (or actuated) optical interferometer grating. The grating is made up of parallel lines of silicon. The individual grating lines are 1 μm wide and spaced 1 μm apart. A laser diode shines through this optical grating at a reflective surface on the proof mass frame.

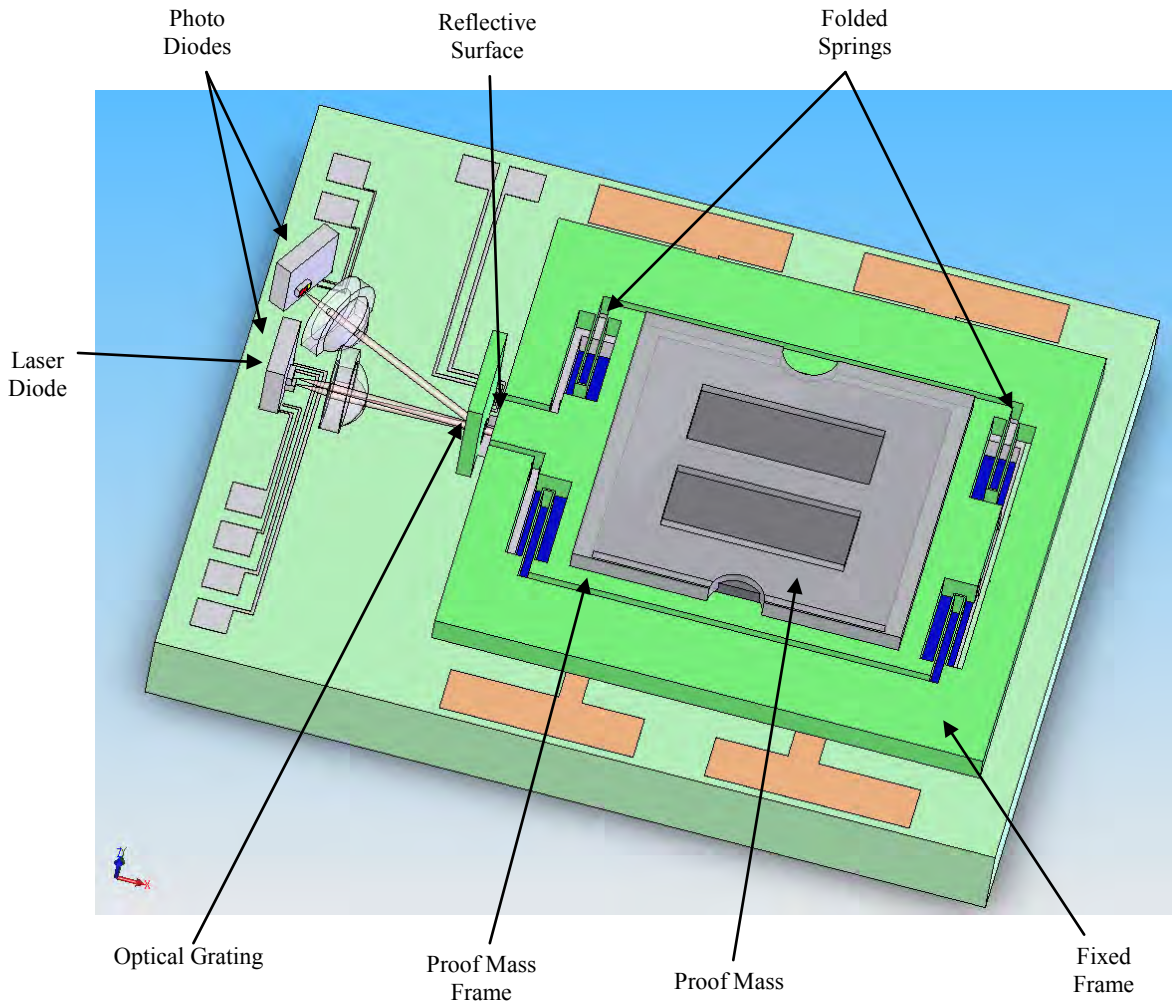

Figure 2. Proposed sensor design.

The proof mass frame on the opposite side of the grating is mounted to a fixed frame by folded springs. The proof mass frame is free to move in the direction of travel with the laser. Because of the optical detection method, the sensor will be insensitive to any cross axis or out-of-plane motion. A large mesoscale tungsten proof mass is positioned within the proof mass frame. Separating the assembly of the proof mass and the frame allows for the use of a significantly larger proof mass than would otherwise be possible using MEMS fabrication techniques.

Optical Detection

The reflective surface on the proof mass can be between 100 and 500 μm away from the optical grating. Depending upon the distance between the optical grating and the mass, some portion of the light from the laser will be reflected on-axis or diffracted off-axis from the direction of the incoming laser. For small changes in the spacing between the optical grating and the proof mass, a large change in the optical reflection is observed.

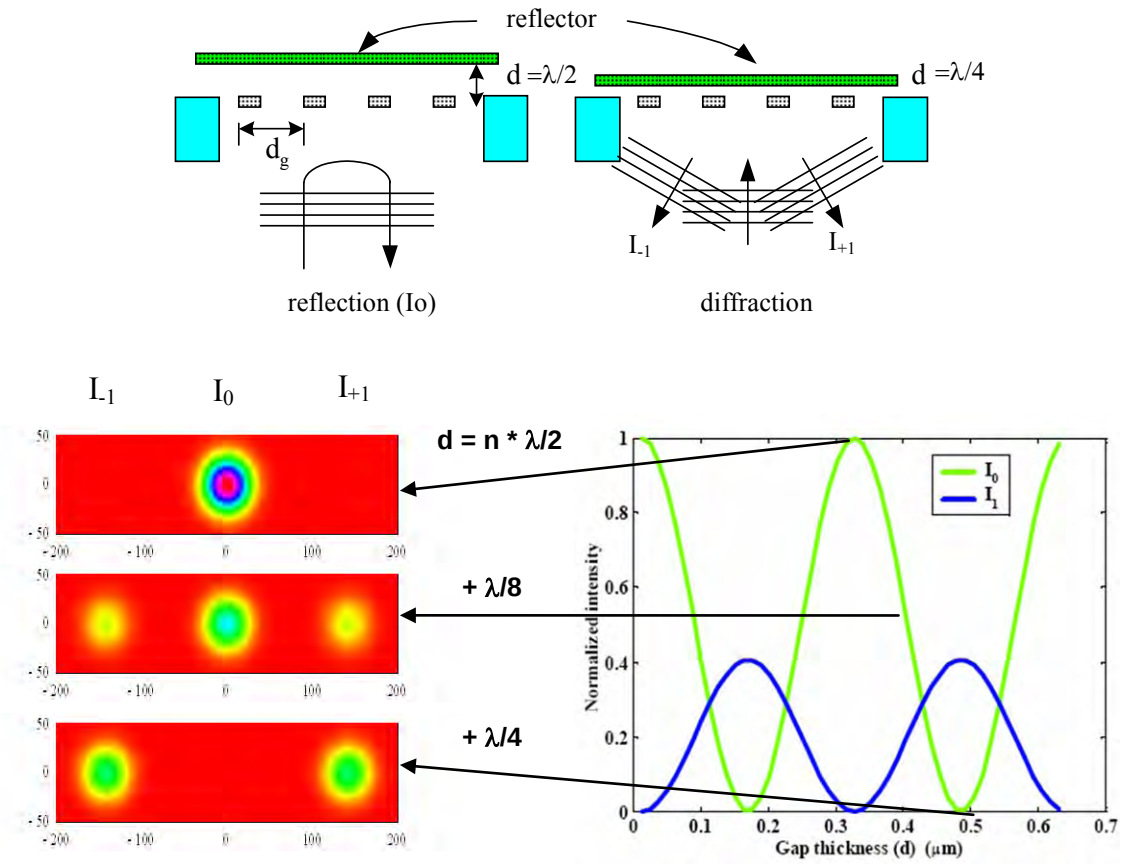

Figure 3. Images in the lower section show the variations in intensity of reflected and diffracted orders with the gap between the grating and reflector.

The most sensitive mode in which the optical displacement detection system can operate is in the +λ/8 position for the gap thickness. This corresponds to the point on the light intensity curve (Figure 3) at which the slope is the highest. Therefore, it is desirable for the sensor to operate at a gap size that is (n * λ/2) + λ/8 so as to maximize the optical sensitivity. The gap size can be controlled using feedback control.

There are several options for feedback control of the sensor. First, the optical grating can be actuated using electro-static force feedback. Second, the position of the proof mass can be controlled using magnetic force feedback. These feedback capabilities will make it possible to explore several different options for performing noise reduction, signal processing, and increasing dynamic range.

Two photo diodes will be positioned in the reflected (on-axis) and diffracted (off-axis) positions to measure the amount of reflected light (Figure 4). Typically, a small laser such as the one proposed, would be inherently noisy. In order to make them quieter, the laser would have to be significantly larger and precisely temperature controlled. However, by differencing both the reflected and diffracted light intensities, the common mode noise in the output of the laser diode can be minimized. The two photo diodes will still introduce some noise that is not common between their outputs; however, that noise is significantly less than the noise from the laser.

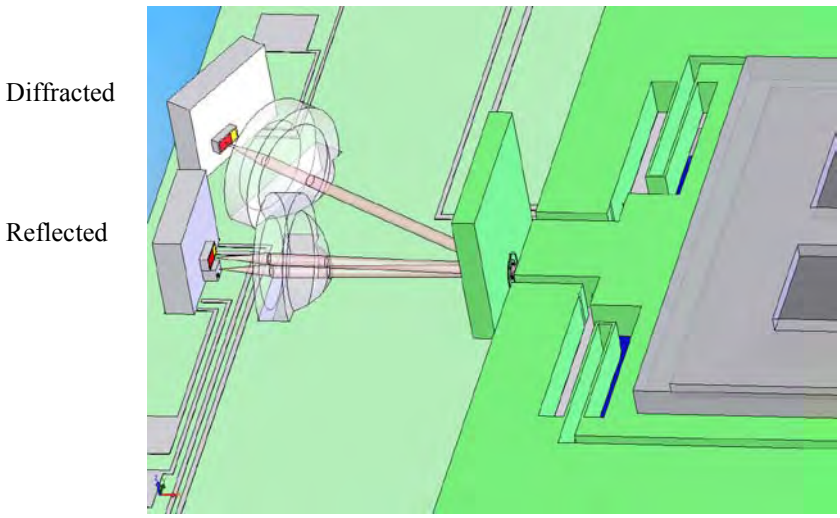

Figure 4. Laser and two photo diodes.

Self Noise

The theoretical self noise of this design is primarily driven by two physical limitations: thermal noise and optical-electronic noise. The thermal noise is due to the effects of atmosphere on the proof mass. As illustrated, the dominant source of noise (and resonant frequency of the system) is the thermal (Brownian) motion of the proof mass in a dissipative medium, which is a white noise source whose power spectral density is given by the relation shown in Equation 1:

Boltzman's Constant	k_B=1.38x10^{-23} J/K
Temperature	T = 300 K
Resonant Frequency	ω_o=314.16 rad/s (50Hz)
Quality Factor	Q = 1000
Proof Mass	m = 1 gram (10^{-3} kg)

$$a_n = \sqrt{\frac{4k_b T\omega_0}{Q \cdot m}} \frac{1}{\sqrt{Hz}} \qquad \approx 2.3\times10^{-9}\, m/s^2\sqrt{Hz} \;\; 0.2\; ng/\sqrt{Hz}$$

Equation 1. Thermal Noise

The optical-electronic noise is due to noise in the sensing mechanism for detecting the displacement of the proof mass relative to the optical grating shown in Equation 2:

Measured Displacement Noise	$x_n \approx 10^{-14}\, m/\sqrt{Hz}$
Spring Constant	k = 98.7 N/m
Proof Mass	m = 1 gram (10^{-3} kg)

$$k * x_n = m * a_n$$

Acceleration Noise: $a_n \approx 9.8\times10^{-10}\, m/s^2\sqrt{Hz}$ $\;\; 0.01\; ng/\sqrt{Hz}$

Equation 2. Optical Electronic Noise

These estimates of the thermal and optical-electronic noise are illustrative of the desired performance levels. Parameters have been selected that are consistent with proven fabrication technologies and that match the desired set of requirements.

Fabrication Accomplished

In the first phase of fabrication, some of the individual components have been fabricated separately: a silicon frame, tungsten proof-mass insert, and the optical grating structure. In addition, a ceramic frame was designed and constructed to hold the components in place during testing. Subsequent fabrication phases will focus on further refinements to the components as well as integration of the components, laser diodes, and photo diodes onto a single die (Figure 5).

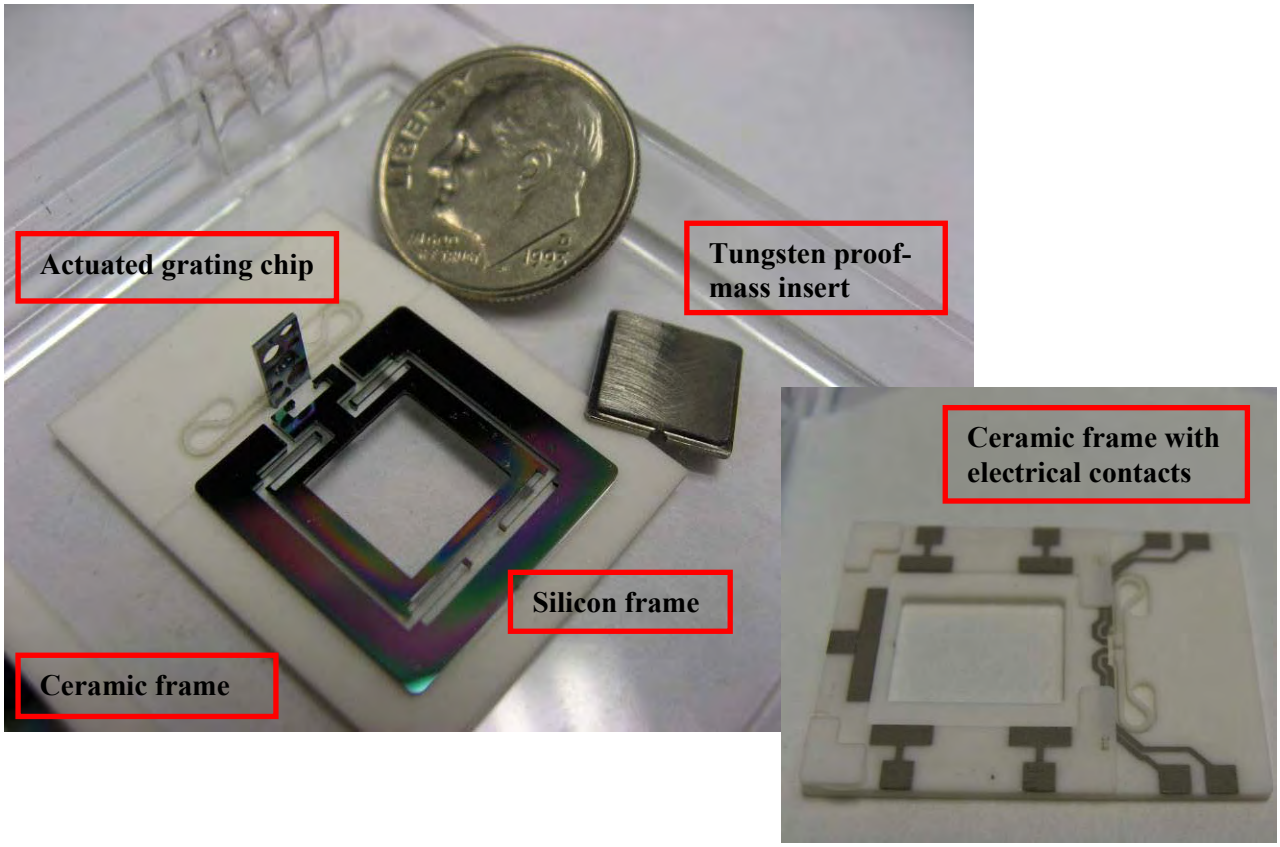

Figure 5. MEMS seismometer components.

Testing

We are in the early stages of assembling the test setup for the microseismometer. The first stage of functionality experiments is going to be performed in a laboratory environment and will focus on measuring the self-noise and response of the fabricated components. An external laser and photo detectors will be used to take measurements using the optical grating, reflective surface, and silicon frame. In addition, some amount of actuation of the grating chip will be possible as part of the testing.

The challenge in testing components such as these is that their targeted sensitivities are significantly below the ambient noise levels observed in a quiet laboratory environment. There are two approaches planned for resolving the sensor noise levels. First, multiple sensors can be co-located in the laboratory and coherence analysis used to attempt to identify their respective noises (Sleeman, 2006). This approach may have limited success given the high levels of noise expected in populated work areas and the ability to adequately co-locate sensors to ensure that they are all

sampling a common signal. Second, we are planning on moving a breadboard version of the test setup into a quieter environment such as at the Sandia National Laboratories FACT site and/or the United States Geological Survey ASL tunnel. At either of these quieter locations, a broadband seismic reference sensor would be deployed to verify the response and sensitivity

CONCLUSIONS AND RECOMMENDATIONS

Work thus far has focused primarily on the design and development of the silicon frame. Processing of the silicon frame and other components has been carried out for the first design iterations. Further development and testing of the process and designs for the complete system are ongoing.

The current design has an expected shock tolerance on the order of 1000 g's. This level of shock tolerance is acceptable while the MEMS seismometer is operating at a fixed location. However, during handling, the components may be exposed to considerably larger shocks. To attempt to address this problem, we are also planning on incorporating an electrically actuated bistable locking mechanism into the device to enable increased mobility of the overall system. When engaged, this lock will prevent mechanical damage from large accelerations that can be encountered during handling.

The feedback control mechanism utilizing both the grating structure (electro-static) and the proof-mass (magnetic) will also be ready for testing in the next version of the device. Employing a feedback control system will result in a significantly larger linear dynamic range (> 120 dB) that will be needed for the target applications.

REFERENCES

AFRL (2004). AFRL Seismic Sensor Workshop Summary.

Sleeman, R., A. van Wettum, and J. Trampert (2006). Three-channel correlation analysis: A new technique to measure instrumental noise of digitizers and seismic sensors, *Bull. Seism. Soc Am.* 96: 258–271.

A MODEL AND METHODS FOR REGIONAL TRAVEL-TIME CALCULATION

Stephen C. Myers[1], Michael L. Begnaud[2], Sanford Ballard[3], Michael E. Pasyanos[1], W. Scott Phillips[2], Abelardo L. Ramirez[1], Michael S. Antolik[5], Kevin D. Hutchenson[5], Gregory S. Wagner[5], John J. Dwyer[4], and Charlotte A. Rowe[2]

Lawrence Livermore National Laboratory[1], Los Alamos National Laboratory[2], Sandia National Laboratories[3], Air Force Technical Applications Center[4], and Quantum Technology Sciences, Inc.[5]

Sponsored by the National Nuclear Security Administration

Award Nos. DE-AC52-07NA27344[1], DE-AC52-06NA253963[2], DE-AC04-94AL8500[3], and FA8620-05-C-4301[5]

ABSTRACT

This project develops a model and methods for routine computation of regional seismic travel times (RSTT) for crustal events anywhere on the globe. To improve on existing methods, the travel-time calculations must capture the effect of the 3-dimensional earth, yet the computation must be exceedingly efficient. We achieve global coverage by defining a seamless global tessellation of nodes with spacing of approximately 1°. Three-dimensional crustal structure is captured by interpolating *P*- and *S*-velocity depth profiles at each node. Mantle structure is approximated by a linear velocity gradient (as a function of depth) at each node. The linear gradient parameterization in the mantle enables an analytical approximation for the diving *Pn*/Sn ray that allows computation of travel-times in approximately 1 millisecond. Regional *Pg* and Lg propagation are approximated with a ray traveling horizontally along a mid-crustal layer. At local distance, *P* and *S* travel times are computed using the layered velocity structure under the station.

In the last year we have refined the model using a tomographic formulation that adjusts mantle velocity at the Moho, mantle velocity gradient, and a bulk crustal velocity. We used summary rays derived from ~500,000 *Pn* arrivals throughout Eurasia and North Africa in the inversion. Ten percent of the tomography data were randomly selected and set aside for testing purposes. Across Eurasia and North Africa travel time residual variance for the validation data is reduced by 32%. Based on a geographically distributed set of validation events with epicenter accuracy of 5 km or better, epicenter error using 16 *Pn* arrivals is reduced by 46% from 17.3 km (*ak135* model) to 9.3 km after tomography. Epicenter uncertainty ellipses are validated and found to contain the expected number of ground-truth epicenters within expected variations. Relative to the *ak135* model, median uncertainty ellipse area is reduced by 68% from 3070 km^2 to 994 km^2, and the number of ellipses with area less than 1000 km^2, which is the area allowed for onsite inspection under the Comprehensive Nuclear-Test-Ban Treaty (CTBT), is increased from 0% to 51%. We are currently extending the tomographic formulation and data set to include *Pg*, *Sn*, and *Lg* phases.

OBJECTIVES

This project produces a laterally variable velocity model of the crust and upper mantle that is specifically designed to compute travel times for use in routine seismic location. Because the model is limited to the crust and upper mantle, the model and methods are applicable at regional distances and we refer to the project as the RSTT model/method. The RSTT method must return the following:

1. An accurate travel-time prediction.
2. An uncertainty estimate of the travel-time prediction error.

Because the RSTT is meant for use in routine location algorithms where networks can be dynamic and precomputation of travel times for all available data may not be possible, the RSTT must also do the following:

3. Compute the travel time on-the-fly, given regional- or local-distance station/event coordinates.
4. Return the travel time in milliseconds, thus enabling the estimation of a location in a few seconds.

We have compiled an *a priori* model of the crust and upper mantle, and we improve this model using a ground-truth dataset and a tomographic technique that is tailored to optimize model parameters that are important for accurate travel time prediction. Last, we use rigorous statistical tests to measure the improvement in both travel time prediction and epicenter accuracy.

RESEARCH ACCOMPLISHED

We meet the objectives outlined above by constructing one earth model that is used in the computation of all four regional phases. Further, we adapt several approaches for regional travel-time calculation into one software package that provides a convenient travel-time calculation utility for use in seismic location and other applications that require a fast and accurate calculation for crustal seismic events. In this paper, we report on *Pn* tomography results and validation testing. We also report on preliminary *Sn* tomography results, where the starting model is derived from the *Pn* tomography result.

Model Parameterization

The RSTT model parameterization is described in previous Monitoring Research Review papers (Myers et al., 2007, 2008), and we give a brief description here. We combine the laterally variable layer approach of Pasyanos et al. (2004) with the linear mantle gradient of Zhao and Xie (1993). Velocity vs. depth profiles are defined at nodes, and the profiles at the nodes are interpolated using an efficient code developed at Sandia National Laboratories (SNL) to determine velocity at any arbitrary location (lat,lon,depth). SNL has also developed a tessellation node structure on a spheroid with node spacing of approximately 1° (Figure 1). At present, the model development domain is Eurasia and North Africa, and nodes inside that domain capture the effects of 3D structure on travel times. Outside of the development domain nodes are set to a default velocity profile based on iasp91 (Kennett and Engdahl, 1991). We also have a version of the model that is CRUST2.0 (Bassin et al., 2000) with iasp91 in the mantle and core for the region outside of Eurasia and North Africa. This parameterization provides a seamless and extensible model. Expansion beyond Eurasia and North Africa does not require a change in the model parameterization itself, only modification of the velocity structure at previously defined nodes. Further, SNL has incorporated the GRS80 ellipsoid into the model, eliminating the need for the conventional ellipticity correction to travel time predictions.

Travel-Time Calculation, *Pn* and *Sn*

Travel time computation is described in detail in previous Monitoring Research Review papers (Myers et al., 2007, 2008). The travel-time calculation is based on the method described in Zhao (1993) and Zhao and Xie (1993). This calculation is similar to the widely used approach of Hearn (1984), with an additional term (γ) introduced to account for diving rays that may occur due to a positive velocity gradient with depth and Earth sphericity.

The travel-time calculation is

$$TT = \sum_{i=1}^{N} d_i s_i + \alpha + \beta + \gamma \quad (1)$$

where d and s are the distance and slowness (taken as 1/velocity in the upper mantle) in each of the i segments comprising the great-circle path between Moho pierce points near the event and station, α and β are the crustal travel times at the source and receiver, and γ is a term that accounts for the effect of both mantle velocity gradient and earth sphericity. We define α as the travel time for a crustal ray at the event. Similarly, β is the travel time along a ray from the Moho to the recording station (see Myers et al., 2007, 2008 for details).

Per Zhao and Xie (1993),

$$\gamma = -\frac{c^2 Xm^3}{24 V_0} \quad (2)$$

where X_m is the horizontal distance traveled in the mantle, c is a velocity gradient in the mantle that is normalized by the velocity at the crust mantle boundary plus an additional term to account for Earth sphericity (Helmberger, 1973), and V_0 is a regional average of *Pn* velocity over the entire study area.

We introduce spatially varying *c* into the model (Phillips et al., 2007), and we calculate γ by averaging c along each ray. V_0 remains an average *Pn* velocity over the whole model, which allows us to take advantage of linear tomographic inversion methods. Tests suggest that the approximation to V_0 introduces negligible travel time error given *Pn* velocities ranging from 7.5 km/s to 8.3 km/s.

Dataset

We combine bulletin data from the International Seismological Centre, U.S Geological Survey National Earthquake Information Center, and numerous regional networks across Eurasia into a reconciled database (Flanagan et al, 2009 and references therein). To this database we have added tens of thousands of arrival-time measurements made at Lawrence Livermore and Los Alamos National Laboratories, as well as numerous detailed studies of event location. Epicenter accuracy for each event in the reconciled bulletin has been assessed using the network coverage criteria of Bondar et al. (2004). We further add non-seismic constraints based on known explosion locations, ground displacement from interferometric synthetic aperture radar (InSAR), as well as satellite imagery of man-made seismic sources. In order to diminish the possibility of introducing travel times for phases that interact with velocity discontinuities at ~410 km and ~660 km, the maximum event-station distance range is set to 15°. The minimum event-station distance range is determined by the post-critical refraction for a wave interacting with the Moho. In practice, the minimum distance varies from tens of km in the ocean (thin crust) to over 200 km in the Himalayas (thick crust).

Because the goal of this work is to produce a model for *Pn* travel time-prediction for real-time monitoring, it is important that *Pn* prediction error is unbiased relative to teleseismic *P*-wave prediction error. Previous efforts have achieved unbiased *Pn* error by using an *ad hoc* travel time correction (Yang et al., 2004). To achieve unbiased *Pn* error, we recomputed each event origin time in the tomography data using at least 10 *P*-wave arrivals. The hypocenter is then fixed during the tomographic procedure, which forces *Pn* prediction error to be unbiased relative to teleseismic *P*-wave error.

All picks are evaluated against an uncertainty budget that accounts for event mislocation, a global average of *ak135* prediction uncertainty, and arrival-time measurement uncertainty. We map the epicenter accuracy estimates to travel time uncertainty using the formulation of Myers (2001).

$$\sigma_{\text{tepi}} = \frac{\partial t}{\partial \Delta} \frac{\sigma_{\text{epi}}}{2} \quad [3]$$

where σ_{tepi} (seconds) is the standard deviation of travel time uncertainty attributable to epicenter uncertainty, σ_{epi} (km) is the 1-σ confidence in the epicenter accuracy and $\partial t/\partial \Delta$ is the phase slowness (s/km). The factor of 2 accounts for a mislocation with vector magnitude distributed Gaussian and random vector direction. The total uncertainty for a given arrival time datum is the sum of uncertainty variance for event location, model-based travel time uncertainty (e.g., Flanagan et al., 2007) and arrival-time measurement uncertainty (σ^2_{meas}). Observations outside of the 99% confidence bounds for total uncertainty ($3\sigma_{datum}$) were removed.

$$\sigma_{\text{datum}} = \sqrt{\sigma^2_{\text{tepi}} + \sigma^2_{\text{model}} + \sigma^2_{\text{meas}}} \qquad [4]$$

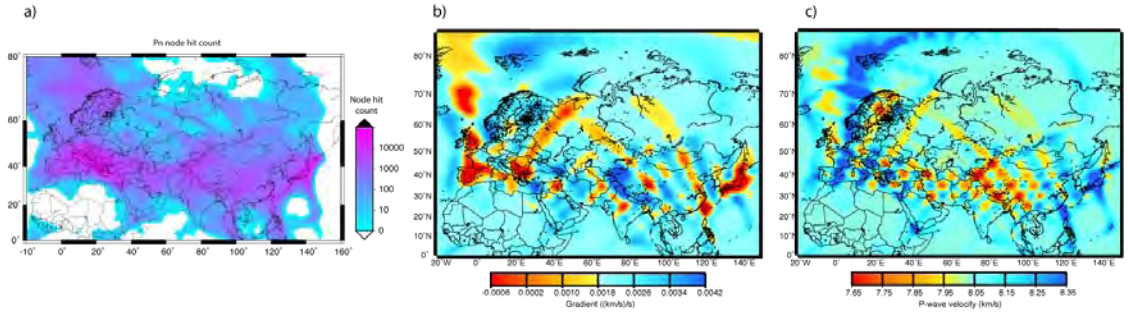

Figure 1. a) Node hit count for *Pn* rays. Nodes hit count exceeds 10,000 throughout the Tethys convergence zone and Scandinavia. Hit count varies across northern Eurasia from 10's of hits down to a few. North Africa and some ocean areas are devoid of data. b) Tomographic checkerboard test for the mantle velocity gradient (~1000 km squares). c) Tomographic checkerboard test for the mantle velocity at the Moho (~500 km squares).

In addition to data culling based on the datum-specific uncertainty budget, we also cull data based on a comparison of neighboring observations. This "local" outlier removal uses a kriging algorithm similar to the method outlined in Schultz et al. (1998). We gather all *Pn* residuals for a station and compute a geographic residual surface. The advantage of using the kriging method for interpolation is that we can also compute the point-specific uncertainty of the residual surface. Each residual is examined in the context of the station-specific residual and uncertainty surfaces and only data in the 95% confidence bounds are retained. We find that local outlier removal better identifies residuals that are due to measurement uncertainty than outlier removal based on the distribution of all residuals.

Following local outlier removal we produce summary rays for each station. Arrival time observations are again grouped by station and then evaluated at the epicenter of the associated event. For each event, we count the number of neighboring events within 0.5° (the nominal bin size), and we order events by the aforementioned count. Starting with the event having the highest count, we average residuals for all events within 0.5°, to produce a summary-ray travel time and an uncertainty estimate. Events comprising the summary ray are then discarded from the event list and the process is repeated on the event with next highest count. This process is repeated until all events for that station are exhausted. The data are reduced from ~600,000 to ~162,000 arrivals. The dramatic reduction reflects paths that are repeatedly sampled in areas with high seismicity. Reduction of the data set by summary rays not only reduces the number of data (and therefore reduces the computational expense of the tomography) by approximately 70%, but the average datum uncertainty is reduced from 1.73 seconds to 1.28 seconds. The use of summary rays also reduces sampling bias, which if left unaccounted, skews tomographic model adjustments to paths that are repeatedly sampled.

Tomography

The tomographic formulation is presented in Myers et al. (2007, 2008). In summary, we solve for the mantle velocity at the Moho, the mantle velocity gradient, and a scalar adjustment to crustal slowness at each model node. Solving for laterally variable mantle gradient is similar to the approach presented in

Phillips et al. (2007). A significant difference between the formulation presented here and more-typical *Pn*-tomography formulations is the introduction of a scalar adjustment to the slowness of the crustal stack, as opposed to a static time term to account for errors in crustal travel time. Our goal is to produce a model that improves prediction of travel time along the whole ray path, and adjusting crustal slowness better meets our goal.

Pn tomography results are presented in Figure 2. The general tectonic features that are present in the starting model are also seen in the tomographic model for mantle velocity (Figure 2a). Low-velocity anomalies in the Mediterranean region, Red Sea Rift, and Iranian Plateau remain in the RSTT model but the velocities are even lower. Mantle velocity gradient tends to be highest in convergence zones. The tomography map of mantle gradient (Figure 2b) shows a strong gradient along the Tethys convergence zone. Similarly, the mantle velocity gradient is high under the Pacific subduction zones, where the slow velocities of the wedge transition to the fast slab (See Myers et al., 2009 for further discussion).

Improvement in Travel-Time Prediction.

We leave out 10% of the tomographic data (validation data) so that non-circular tests may be performed. The validation data provides sampling across Eurasia, so residual summary statistics are a good measure of expected model performance. Recalling that origin times are determined by minimizing teleseismic *P*-wave arrival times to *ak135* predictions, it is perhaps surprising that the *Pn* error for the *ak135* model have a median value of 0.31 seconds. Median *Pn* error for the starting model is also 0.31 seconds. For the RSTT model, median *Pn* error is reduced to 0.16 seconds, a 48% reduction in median error from the *ak135* model. The Pn residual standard deviations (mean removed) relative to the *ak135*, starting model, and RSTT model are 1.99, 1.99, and 1.58 sec., respectively.

We use an interquartile measurement to compute a robust estimate of standard error for *Pn* prediction (Figure 3). Figure 3 includes the *ak135* error vs. distance curve, as well as the curve for the starting and RSTT models. The uncertainty vs. distance curve for the starting model and *ak135* are similar at near-regional distance. *ak135* uncertainty increases more rapidly with distance than the starting model in uncertainty, and the starting model uncertainty is ~0.2 seconds lower than *ak135* at far-regional distance. The RSTT model is significantly improved over both *ak135* and the starting model, with a relatively consistent error vs. distance of approximately 1.25 seconds. The RSTT model reduces error by 0.5 to 1.0 seconds compared to *ak135*. We note that a nominal 1-second measurement (pick) error variance was subtracted from the measured variance before plotting (Flanagan et al., 2007). For instance, the plotted value of 1.25 seconds (variance of 1.56 s^2) was an observed error of 1.6 seconds.

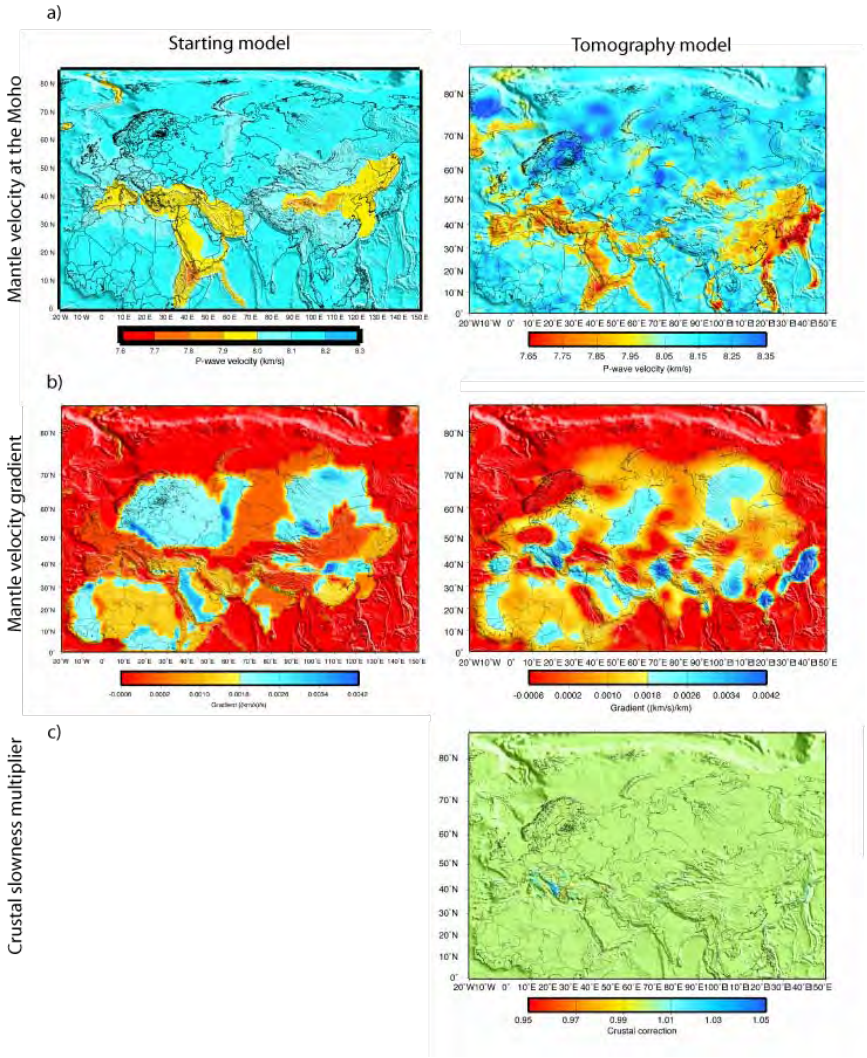

Figure 2. Comparison of starting and RSTTs. a) Velocity below the Moho. b) Mantle gradient (km/s/km). c) Scalar modification to crustal slowness.

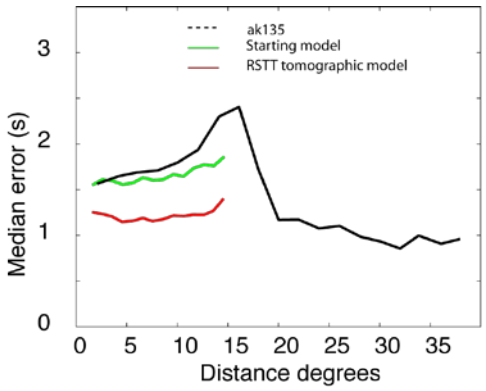

Figure 3. Travel-time error as a function of distance. The median residual in 1° distance bins is plotted for each model.

Location Tests

Figure 4 is a map of the events used in relocation tests. None of these events were used in the tomography and each of these events is either an explosion with an accurate location, or an earthquake that is surrounded by a local network (i.e., GT5 criteria of Bondar et al., 2004). These events are well distributed geographically, providing a representative sampling of location performance across the modeling region. Each event is located using *Pn* arrival times only. We use the LocOO code (Ballard, 2002), which is based on the single-event location method outlined in Jordan and Sverdrup (1981). Uncertainty ellipses were computed using the method of Evernden (1969), where "coverage" ellipse axes are scaled by *a priori* (input) model and pick uncertainties. For travel-time prediction uncertainties we use the distance-dependant curves in Figure 3, and either an analyst estimate of pick uncertainty or a nominal 1-second uncertainty. Because event depth is poorly constrained with a *Pn* data set, event depths are fixed. These events were selected partially because a large number of *Pn* arrival times are available for each event. We relocated the events using 4, 8, 16, and 32 *Pn* arrivals. Data selection was random and we created 10 realizations for each case (number of *Pn* arrivals). Results presented below are an average of the 10 realizations (See Myers et al, 2009 for details).

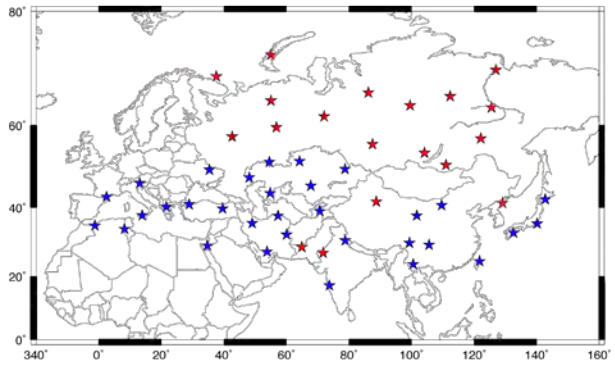

Figure 4. Validation data set used for location. The blue stars are GT5 epicenters, and the red stars are explosions with accurate epicenters.

Figure 5 summarizes epicenter error when the *ak135*, starting, and RSTT models are used for travel-time prediction in the location algorithm. Figure 5a shows that median epicenter error for the RSTT model is significantly lower than for *ak135* and the starting model, regardless of the number of *Pn* arrivals. Further, the RSTT model reaches a relatively constant level of epicenter error at ~9 km with only 8 *Pn* arrivals, whereas for *ak135* and the starting model a stable level of epicenter error at ~17 km is reached after 16 *Pn* arrivals are used.

Figure 5c summarizes ellipse area for *ak135*, the starting model, and the RSTT model, when 4, 8, 16, and 32 *Pn* arrivals are used. The primary difference between the results for the *ak135* and starting models is that there are fewer outliers that have an enormous ellipse area for the starting model than for *ak135* (i.e., the "tail" of the distribution is shorter). Ellipses for the RSTT model are consistently smaller than for the other two models. The 1000 km^2 metric (Figure 5b,c) is taken from the CTBT, which allows for an on-site inspection search area of 1000 km^2. The results show that with 4 to 8 *Pn* arrivals, none of the uncertainty ellipses are expected to be less than 1000 km^2, when either the *ak135* model or the starting model are used. Even using 32 *Pn* arrivals results in only ~23% of uncertainty ellipses with area less than 1000 km^2, when *ak135* or the starting model are used. Using the RSTT model, it is possible to achieve the 1000 km^2 goal with only 4 *Pn* arrivals, although the network configuration must be ideal. With 16 *Pn* arrivals approximately one-half of the events meet the 1000 km^2 goal, and with 32 *Pn* arrivals ~88% of ellipses meet the 1000 km^2 goal.

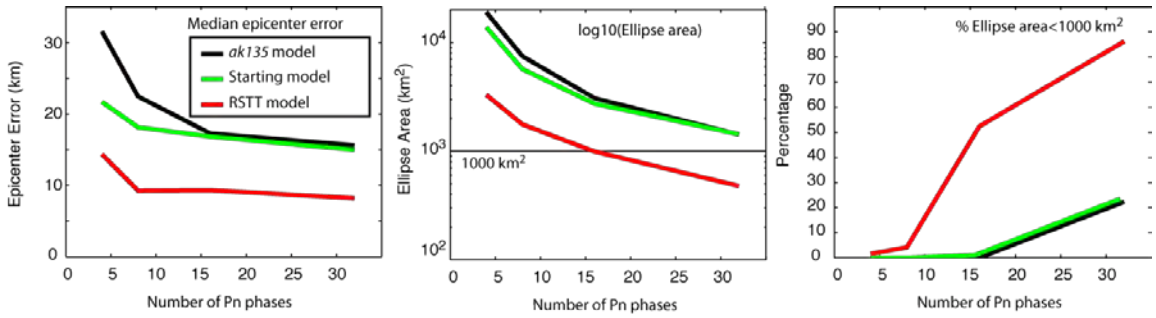

Figure 5. (a) Epicenter error, (b) semilog plot of median ellipse area, and (c) percentage of coverage ellipses with area < 1000 km^2. In (a), (b), and (c) parameters are plotted vs. number of *Pn* data used in the location. Starting model and ak135 overlap in (c).

Preliminary Results for Sn tomography.

For *Sn* tomography we first convert the *P*-wave model determined in the *Pn* tomography to an *S*-wave model. The conversion was based on the node and layer-specific *P*-wave/*S*-wave ratio (Vp/Vs) of the starting model (see above). Figure 6a shows the *S*-wave model that is derived from the *Pn* tomography model. The starting *S*-wave model is similar to the *P*-wave model presented in Figure 2, suggesting that Vp/Vs does not vary dramatically in the starting model. Figure 6b shows *Sn* coverage is good throughout Eurasia. While the *Sn* coverage is good, there is not as much *Sn* data redundancy as there is for the *Pn* data set (Figure 1). Last, Figure 6c shows the *Sn* tomography model. Changes from the starting model are modest, suggesting that the overall anomaly pattern is similar for *P* and *S* waves. The amplitudes of the anomalies are greater for the *S*-wave model, as expected.

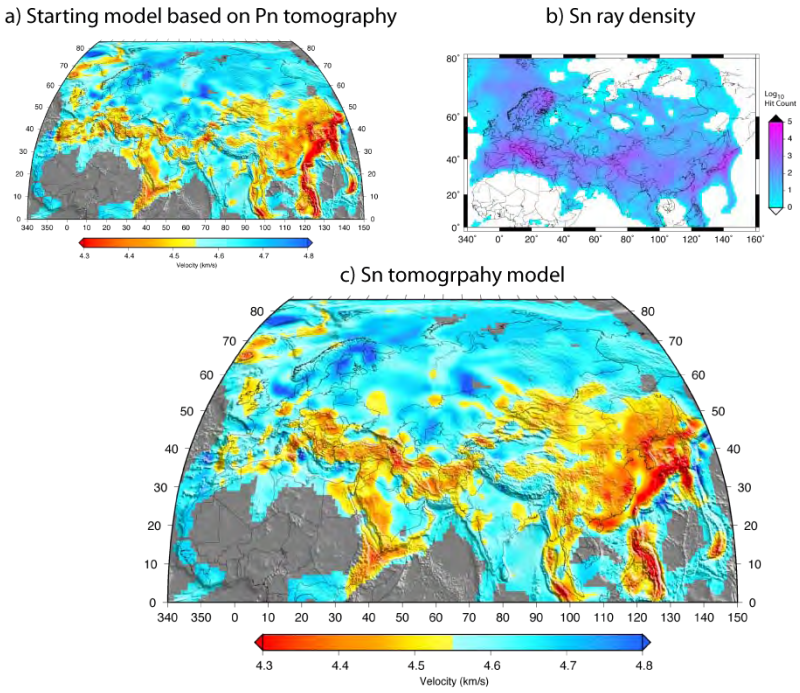

Figure 6. a) Starting *S*-wave model is derived from *Pn* tomography (see text). Upper mantle *S*-wave velocity is shown. b) *Sn* ray density. c) Preliminary upper mantle *S*-wave velocity from *Sn* tomography (see text for discussion)

CONCLUSIONS AND RECOMMENDATIONS

We describe the progress of the RSTT project to date. This project is distinct because it tailors the travel-time prediction algorithm and tomography results for use in routine seismic location algorithms. Emphasis is placed on travel-time prediction accuracy and computational efficiency of regional phases.

The tessellation model parameterization provides seamless global coverage. The use of a tessellation approach also allows fast interpolation of model parameters to extract the great-circle cross section of velocity structure that is needed to compute regional travel times. The current focus of the RSTT effort is Eurasia and North Africa, and model nodes outside of that area are set to a default velocity structure consisting of CRUST 2.0 (Bassin et al., 2000) with iasp91 for the mantle (Kennett and Engdahl, 1991). We note that the model is extensible, and a global calibration effort would entail updating node-centered velocity profiles (by whatever means), which does not require updates to the model tessellation or travel-time codes.

We make use of several approximations that result in a relatively simple algebraic form for travel-time calculations, Eq. (1). The algebraic form lends itself to a linear tomographic formulation, Eq. (8). LLNL and LANL have merged ground-truth databases to form a tomography dataset for this project. *Pn* ray coverage across Eurasia and North Africa is excellent (Figure 4). *Pn* tomographic results (Figure 5) are in general agreement with studies of the Eurasian subregions.

Across Eurasia and North Africa, travel time residual variance for the validation data is reduced by 32%. Based on a geographically distributed set of validation events with epicenter accuracy of 5 km or better, epicenter error using 16 *Pn* arrivals is reduced by 46% from 17.3 km (*ak135* model) to 9.3 km after tomography. Epicenter uncertainty ellipses are validated and found to contain the expected number of ground-truth epicenters within expected variations. Relative to the *ak135* model, median uncertainty ellipse area is reduced by 68% from 3070 km^2 to 994 km^2, and the number of ellipses with area less than 1000 km^2, which is the area allowed for onsite inspection under the Comprehensive Nuclear Test Ban Treaty, is increased from 0% to 51%.

Preliminary results for *Sn* tomography are also presented. The *S*-wave starting model is based on the *P*-wave model determined from *Pn* tomography. Conversion to *S*-waves is based on the Vp/Vs ratio of starting model at each node/layer. *Sn* and *Pn* data coverage are similar, but data redundancy is far greater for *Pn*. The *Sn* tomography model exhibits similar anomaly patterns as the *Pn* tomography model, and *Sn* anomalies are stronger when measured as a percentage of absolute velocity. The next steps in this project are to continue evaluation of S-wave inversions and to conduct validation tests on the *S*-wave model.

ACKNOWLEDGEMENTS

This project would not be possible without the full support of Leslie Casey in the Department of Energy/ NNSA Office of Nuclear Detonation Detection.

REFERENCES

Ballard, S. (2002). Seismic event location using Levenberg-Marquardt least squares inversion, Sandia National Laboratories Report, SAND2002-3083.

Bassin, C., G. Laske, and G. Masters (2000). The current limits of resolution for surface wave tomography in North America, *EOS Tran.s AGU* 81: F897.

Bondar, I., S. Myers, E. R. Engdahl, and E. Bergman, (2004). Epicenter accuracy based on seismic network criteria, *Geophys. J. Int.* 156: 483–496.

Evernden, J. F. (1969). Precision of epicenters obtained by small numbers of world wide stations, *Bull. Seismol. Soc. Am*. 59: 1365–1398.

Flanagan, M.P., S.C. Myers, and K.D. Koper (2007). Regional travel-time uncertainty and seismic location improvement using a three-dimensional a priori velocity model, *Bull. Seismol. Soc. Am*. 97: 804–825.

Hearn, T. M. (1984). *Pn* travel times in Southern California, *J. Geophys. Res*. 89: 1843–1855.

Helmberger, D. V. (1973). Numerical seismograms of long-period body waves from seventeen to forty degrees, *Bull. Seismol. Soc. Am*. 63: 633–646.

Jordan, T.H. and K.A. Sverdrup (1981). Teleseismic location techniques and their application to earthquake clusters in the south-central Pacific, *Bull. Seismol. Soc. Am*. 71: 1105–1130.

Kennett, B. L. N. and E. R. Engdahl, (1991). Traveltimes for global earthquake reference location and phase identification, *Geophys. J. Int.* 105: 429–465.

Myers, S. C. (2001). Methods of travel-time residual declustering for the Knowledge Base Calibration and Integration Tool (KBCIT), *Lawrence Livermore National Laboratory Report*, 14 pp., UCRL-ID-142521**.**

Myers, S. C., S. Ballard, C. Rowe, G. Wagner, M. Antolik, S. Phillips, A. Ramirez, M. Begnaud, M. Pasyanos, D. Dodge, M. Flanagan, K. Hutchenson, G. Barker, J. Dwyer, and D. Russell (2007). Tomography and methods of travel-time calculation for regional seismic location, in *Proceedings of the 29th Seismic Research Review: Ground-Based Nuclear Explosion Monitoring Technologies*, LA-UR-07-5613, Vol. 1, pp. 414–423.

Myers, S. C., S. Ballard, C. Rowe, G. Wagner, M. Antolik, S. Phillips, A. Ramirez, M. Begnaud, M. Pasyanos, D. Dodge, M. Flanagan, K. Hutchenson, G. Barker, J. Dwyer, and D. Russell (2008). A model and methods for regional travel-time calculation, in *Proceedings of the 29th Seismic Research Review: Ground-Based Nuclear Explosion Monitoring Technologies*, LA-UR-08-05261, Vol. 1, pp. 425–434.

Myers, S. C., S. Ballard, C. Rowe, G. Wagner, M. Antolik, S. Phillips, A. Ramirez, M. Begnaud, M. Pasyanos, D. Dodge, M. Flanagan, K. Hutchenson, G. Barker, J. Dwyer, and D. Russell (2009). Tomography and methods of travel-time calculation for regional seismic location, *Bull. Seismol. Soc. Am.*, in preparation.

Pasyanos, M. E., W. R. Walter, M. P. Flanagan, P. Goldstein, and J. Bhattacharyya (2004). Building and testing an a priori geophysical model for western Eurasia and North Africa, *Pure App. Geophys*. 161: 235–281.

Phillips, W. S., M. L. Begaud, C. A. Rowe, L. K. Steck, S. C. Myers, M. E. Pasyanos, and S. Ballard (2007). Accounting for lateral variations of the upper mantle gradient in *Pn* tomography studies, *Geophys. Res. Lett*. 34: doi:10.1029/2007GL029338.

Schultz , C.A., S. C. Myers, J. Hipp, and C. Young (1998). Nonstationary Bayesian kriging: a predictive technique to generate corrections for detection, location, and discrimination, *Bull. Seismol. Soc. Am.* 88: 1275–1288.

Yang, X., I. Bondar, J. Bhattacharyya, M. Ritzwoller, N. Shapiro, M. Antolik, G. Ekstro¨m, H. Israelsson, and K. McLaughlin (2004). Validation of regional and teleseismic travel-time models by relocating ground-truth events, *Bull. Seismol. Soc. Am*. 94; 897–919.

Zhao, L.-S. (1993). Lateral variations and azimuthal isotropy of *Pn* velocities beneath Basin and Range province, *J. Geophys. Res*. 98:109–122.

Zhao and Xie (1993). Lateral variations in compressional velocities beneath the Tibetan Plateau from *Pn* traveltime tomography, *Geophys. J. Int*. 115: 1070–1084.

ADAPTIVE WAVEFORM CORRELATION DETECTORS FOR ARRAYS: ALGORITHMS FOR AUTONOMOUS CALIBRATION

Frode Ringdal[1], David B. Harris[2,3], Doug Dodge[2], Steven J. Gibbons[1]

[1]NORSAR, [2]Lawrence Livermore National Laboratory, and [3]Deschutes Signal Processing, LLC

Sponsored by the National Nuclear Security Administration
Award Nos. DE-FC52-05NA26604[1] and DE-AC52-07NA27344[2,3]
Proposal No. BAA05-16

ABSTRACT

Waveform correlation detectors compare a signal template with successive windows of a continuous data stream and report a detection when the correlation coefficient, or some comparable detection statistic, exceeds a specified threshold. Since correlation detectors exploit the fine structure of the full waveform, they are exquisitely sensitive when compared to power (STA/LTA) detectors. The drawback of correlation detectors is that they require complete knowledge of the signal to be detected, which limits such methods to instances of seismicity in which a very similar signal has already been observed by every station used. Such instances include earthquake swarms, aftershock sequences, repeating industrial seismicity, and many other forms of controlled explosions. The reduction in the detection threshold is even greater when the techniques are applied to arrays since stacking can be performed on the individual channel correlation traces to achieve significant array gain.

In previous years we have characterized the decrease in detection threshold afforded by correlation detection across an array or network when observations of a previous event provide an adequate template for signals from subsequent events located near the calibration event. Last year we examined two related issues: (1) the size of the source region calibration footprint afforded by a master event, and (2) the use of temporally incoherent detectors designed to detect the gross envelope structure of the signal to extend the footprint. In Case 1, results from the PETROBAR-1 marine refraction profile indicated that array correlation gain was usable at inter-source separations out to one or two wavelengths. In Case 2, we found that incoherent detectors developed from a magnitude 6 event near Svalbard were successful at detecting aftershocks where correlation detectors derived from individual aftershocks were not. Incoherent detectors might provide “seed” events for correlation detectors that then could extend detection to lower magnitudes.

This year we addressed a problem long known to limit the acceptance of correlation detectors in practice: the labor intensive development of templates. For example, existing design methods cannot keep pace with rapidly unfolding aftershock sequences. We successfully built and tested an object-oriented framework (as described in our 2005 proposal) for autonomous calibration of waveform correlation detectors for an array. The framework contains a dynamic list of detectors of several types operating on a continuous array data stream. The list has permanent detectors: beamforming power (STA/LTA) detectors which serve the purpose of detecting signals not yet characterized with a waveform template. The framework also contains an arbitrary number of subspace detectors which are launched automatically using the waveforms from validated power detections as templates. The implementation is very efficient such that the computational cost of adding subspace detectors was low. The framework contains a supervisor that oversees the validation of power detections, and periodically halts the processing to revise the portfolio of detectors. The process of revision consists of collecting the waveforms from all detections, performing cross-correlations pairwise among all waveforms, clustering the detections using correlations as a distance measure, then creating a new subspace detector from each cluster. The collection of new subspace detectors replaces the
existing portfolio and processing of the data stream resumes. This elaborate scheme was implemented to prevent proliferation of closely-related subspace detectors.

The method performed very well on several simple sequences: 2005 “drumbeat” events observed locally at Mt. St. Helens, and the 2003 Orinda, CA aftershock sequence. Our principal test entailed detection of the aftershocks of the San Simeon earthquake using the NVAR array; in this case, the system automatically detected and categorized approximately 2/3 of the events above magnitude 2.8.

OBJECTIVE

Correlation detection is becoming a mainstream option for network operations due to its advantages in sensitivity and event screening. Correlation detectors wrap detection, location and event identification functions into a single operation, which potentially makes them effective at reducing the burden of analysts in network monitoring operations. Since such detectors both detect and categorize, they support a strategy of reviewing repeating events from
particular sources as aggregated groups rather than one at a time. This feature may lead to significant efficiencies during aftershock sequences and swarms and in regions with large amounts of mining activity.

However, the development of correlation detectors is labor intensive as currently practiced. Typically, large numbers of events must be assembled from catalogs or by running power detectors over continuous data streams. Cross-correlations among the event waveforms are computed and events are grouped by a clustering algorithm, which brings together events with significant waveform similarity. Waveforms from the clustered events then are selected to define a correlation template, which can be applied as a matched filter to the data in a continuous stream. Subspace
detectors, which are higher-dimensional extensions of correlation detectors require careful alignment of waveforms from multiple events in a cluster, construction of an orthonormal basis for the event waveforms and selection of an optimum basis dimension for signal representation. In return, they provide greater scope for signal representation.

As these detector design activities currently are manual or only semi-automated, it is not possible to keep up with the occurrence of swarm events or aftershock sequences. However, one of the most attractive potential applications of correlation detectors is as a real-time screen for the very large number of similar events that can overwhelm network operations.

It also is the case that a large number of sources surround many stations, requiring distinct, dedicated detectors. The number of detectors required is compounded by the fact that the detailed structure of signals may change over time for many of these sources, requiring detector updates.

Our solution to these problems is to automate correlation detector development to the extent possible, eventually under analyst review. The objective in seeking automation is not to replace analysts, but rather to assist them by organizing detected events into categories prior to review. We anticipate that even a partial organization of events can substantially reduce the burden of event formation and review by analysts.

RESEARCH ACCOMPLISHED

Our principal accomplishment this year was the construction and testing of a detection framework for autonomous calibration of correlation and subspace detectors (Figure 1). The heart of the system is a list of detectors that operate on a continuous stream of array data. The list contains a set of fixed STA/LTA (power) detectors implemented on a collection of beams (to allow beam recipes to be implemented for an array) that serve to obtain waveforms of new event types to spawn into correlation detectors. Correlation and subspace detectors are added dynamically to the list as described below. The system acquires a block of array data from the continuous stream, preprocesses (filters and decimates) it, then directs each detector in the list to calculate a detection statistic from the block of data. The system examines the statistic for excursions above a predetermined threshold, at which point a trigger is declared. When two or more detectors produce simultaneous triggers, the triggers are compared, and only one is promoted as a detection subject to the following rules:

(1) Triggers from the same type of detector (array power, or correlation /subspace) are promoted or eliminated based on which has the largest detection statistic value.

(2) Triggers from correlators and subspace detectors always are promoted over those from power detectors. All detections are archived to a database with information about the detector that originated them, the trigger time and the value of the detection statistic.

Detections from power detectors are assumed to be signals not yet seen: the system passes such detected waveforms through a series of screens (e.g., duration, bandwidth) in an attempt to eliminate spikes and other unwanted signal types. Waveforms that pass these tests are used to create correlation detectors which are added it to the detector list. The system then continues on to the next block of data.

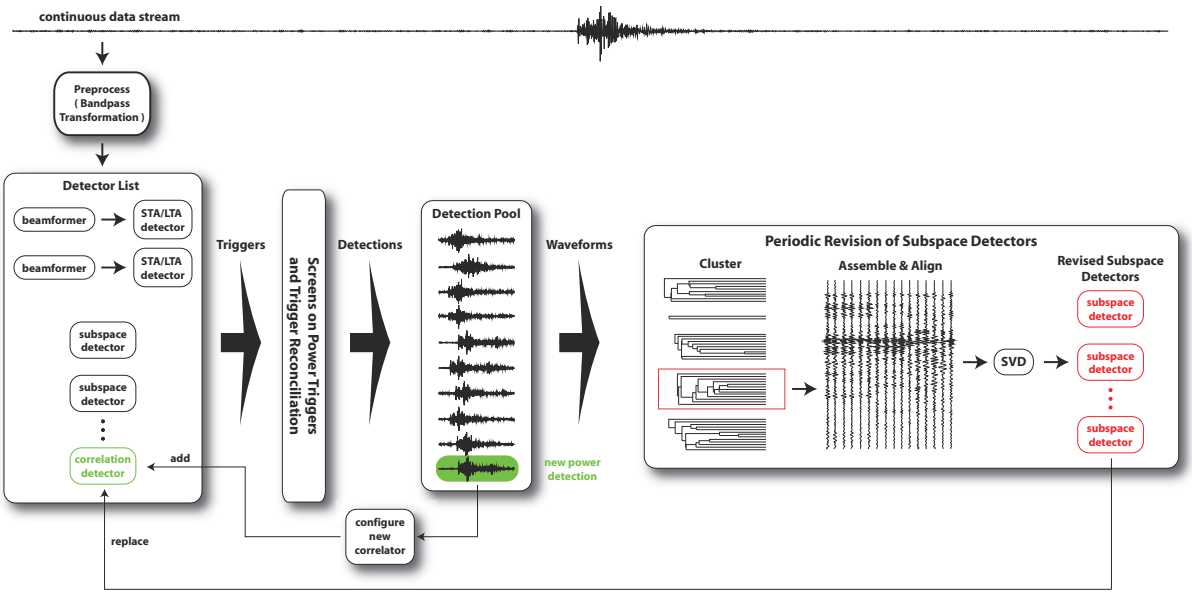

Figure 1. Diagram of the autonomous framework built to test the concept of automated construction of correlation detectors.

Periodically the system halts (after reaching a threshold in numbers of new detections) to recalibrate the correlation detectors. The purpose of this operation is to provide some check on the (otherwise unrestricted) growth in the number of correlation detectors. During recalibration, the new detections and some older detections are grouped to define new templates. Corresponding waveforms are extracted from the archive (detection pool in Figure 1). Correlations are calculated between the waveforms for all pairs of these events. The correlation values are used to cluster the events and the correlation lags are used to align event waveforms from individual clusters. A subspace detector template is constructed from the aligned waveforms from each cluster, and the collection of subspace detectors so created replaces the correlation detectors in the detector list. At this point the system continues from the point where it left off in the stream.

2003 San Simeon Earthquake

For a suitable test of this system, we sought an event that generated large numbers of aftershocks in a short period of time, endowed good ground truth information, and observed by an array at regional distance with many high-SNR observations suitable for generating correlation templates. We settled on the 2003 San Simeon earthquake (Figure 2). This was a moderately large event (mb 6.5) with thousands of aftershocks recorded by local networks in California. We acquired ten days of data (2003:356 - 2003:365) from the NVAR array for the test. NVAR is situated 390 kilometers from the main shock location. For ground truth information, we relied upon the Advanced National Seismic System (ANSS) composite catalog (NCEDC, 2009) which reported 1,433 events in a 1x1 degree square around the main shock during the last ten days of 2003.

Our objective in performing this test was not to reduce the detection threshold (as is a common objective with correlation detectors), but rather automatically to group detected events as an aid to analyst review. By this measure, a system is successful if it automatically classifies a large fraction of events as they occur or with periodic bulk processing during a sequence, without introducing large numbers of unwanted detections that are difficult to review. The system we implemented was able to process the 10 days of NVAR data (9 channels @ 40 samples/second) in 15

to 20 minutes on a modern laptop computer. For ease in catalog reconciliation, and to increase the number of detections, we added a second processing step in which the 98 subspace detectors created during the first pass were held fixed and used to reprocess the entire ten days of data. This reprocessing step took an additional ten minutes. Since the system is so fast, periodic reprocessing of weeks of data is possible in real-time monitoring operations.

We assume that, with such a system, analysts could review events in groups automatically determined to be related on the basis of waveform correlation. Our results suggest that this approach is possible, and could form the basis of an improvement to current practice in network operations. We imagine a scenario where, immediately following the occurrence of a large event, an analyst directs the system to deploy a beam to the slowness of the main shock, anticipating aftershocks. The system then attempts to detect and cluster aftershocks for subsequent review. By reviewing events in groups, time and effort could be minimized, as only one or a few of the largest events in the cluster would require intensive interpretation, and the remainder could be treated as local related events of similar origin.

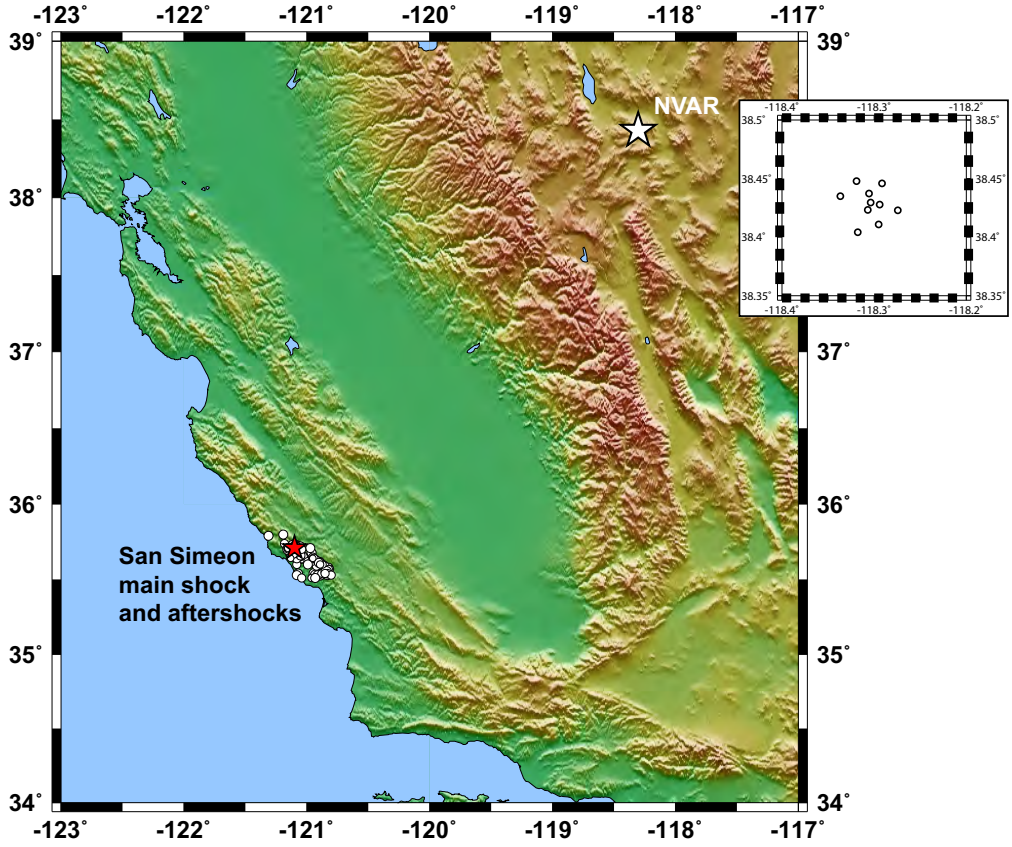

Figure 2. The main sequence of study consists of the magnitude 6.5 San Simeon earthquake and its aftershocks during the 10 day period Dec 22, 2003 - Dec 31, 2003. We acquired 10 days of data from the NVAR array to use in the test.

In our implementation, we used a standard beamformer with 9 elements of the NVAR array (2 of the 11 elements had very significant problems with dropouts). We used the great circle path backazimuth of 220 degrees and a velocity of 8 km/sec as the beamforming parameters. An STA/LTA detector was used on the beam to make power detections. The STA duration was 5 seconds, the LTA duration was 50 seconds and we inserted a 5 second gap between the STA and LTA windows. The detection threshold was set at 5 (in amplitude, 25 in power) in order to obtain high-quality signals for correlation templates.

We set the system to halt and recalibrate every time 200 new detections were made. We made distinctions between two classes of waveform correlation detectors: first generation and second generation. The first generation detectors were those created directly from STA/LTA detections (i.e., the correlators). Second generation detectors were those

created from a recalibration episode and could be subspace detectors of higher rank. A database of detections was maintained with each detection “linked” to its originating detector. During a reclustering interlude all new detections of any type and all detections from first generation detectors not previously reclustered were assembled into a secondary pool. The pool events then were correlated pairwise and reclustered using a single link algorithm with a correlation clustering threshold of 0.5. Subspace detectors were developed for each identified cluster, using an energy capture metric to define the dimension of the subspace (Harris, 2006). Events used to construct the new second- generation detectors were reassigned in the database to these new detectors. Detectors left with no detections following reassignment were removed from the system. Second generation detectors were assumed to be mature: their detections were not subject to reclustering.

This rather complex system was designed to control the number of detectors operating in the system. The number would tend to grow without bound without some process to identify and retire old detectors, replacing them with merged detectors created as new events reveal linkages among event groups. Our hypothesis was that natural groupings among the aftershocks of the San Simeon sequence and other events observed by the array would be revealed only as events accumulate over time. In our view, the system needed to be flexible to allow detectors generated early in the process to be replaced as more events allowed better correlation and subspace templates to be developed.

Over the course of processing the 10 days of data, the STA/LTA algorithm spawned 124 correlation detectors directly. The system halted and reclustered three times, ultimately reducing the number of correlation/subspace detectors to 98 (plus the beamformer). As mentioned earlier, we reprocessed the data completely a second time (starting over from the beginning) using the detectors in existence at the end of the first pass. The system was cleared of all detection records and entirely new detections were declared during the second pass. This operation had the effect of putting detections from a single detector on a common relative timing basis, which greatly simplified reconciliation against the ANSS catalog. It also increased the number of correlation and subspace detections, since templates developed from high-SNR events occurring late in the 10-day period matched smaller events occurring earlier in the sequence that were overlooked in the first pass.

Overall, the second reprocessing step produced 702 detections, of which 360 could be reconciled against the ANSS catalog. The locations of the detected events are indicated as red symbols in Figure 3 against the background of grey symbols representing the ANSS catalog. Note that most of the larger events were captured by the system and that the detected events were distributed over most of the aftershock region.

Figure 4 compares histograms of ANSS catalog events and our detections against event magnitude. These plots indicate that the system captured the majority of events above magnitude 2.8. We believe that we missed a number of the higher magnitude events due to the large duration of our long-term average in the beamforming detector. Many of these events occurred early in the sequence when large numbers of events packed together, loading the LTA and reducing the STA/LTA ratio below the detection threshold. By missing the additional templates provided by these high magnitude events, we also lost many lower magnitude events that might otherwise been detected.

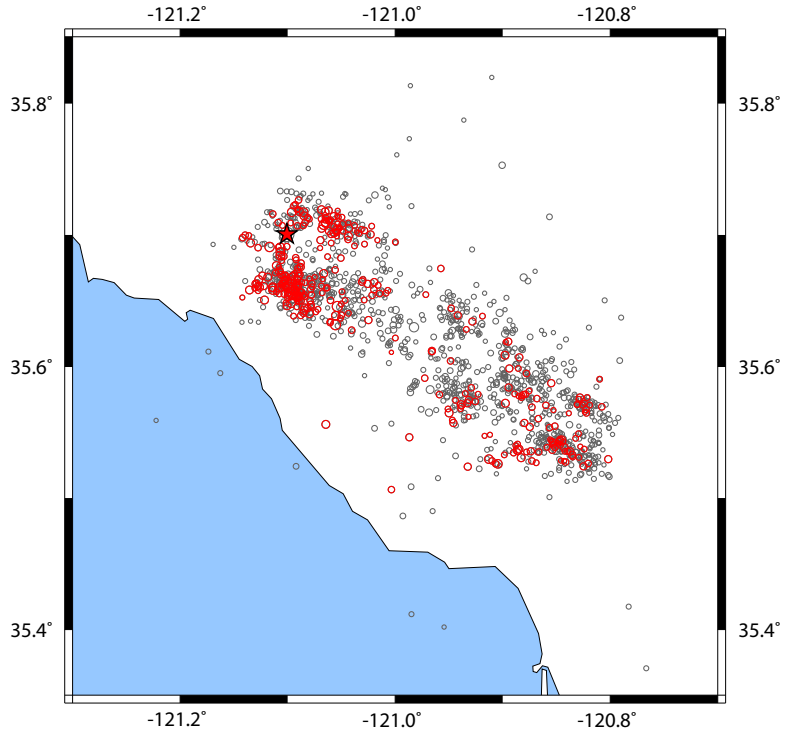

Figure 3. A map of the ANSS catalog events in the vicinity of the San Simeon main shock (grey) and the events automatically detected by our detection framework (red).

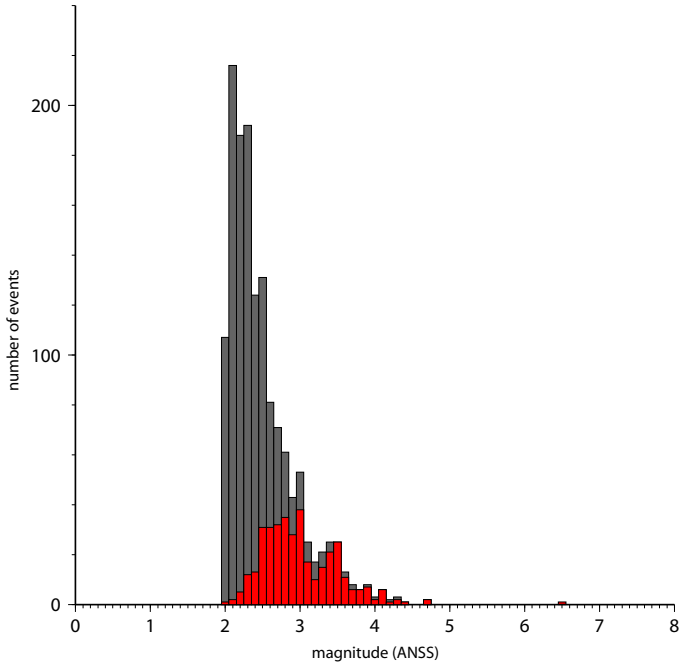

Figure 4. Histograms of the ANSS catalog events against magnitude (grey) and the events detected by our system (red). The system captured the majority of events above magnitude 2.8.

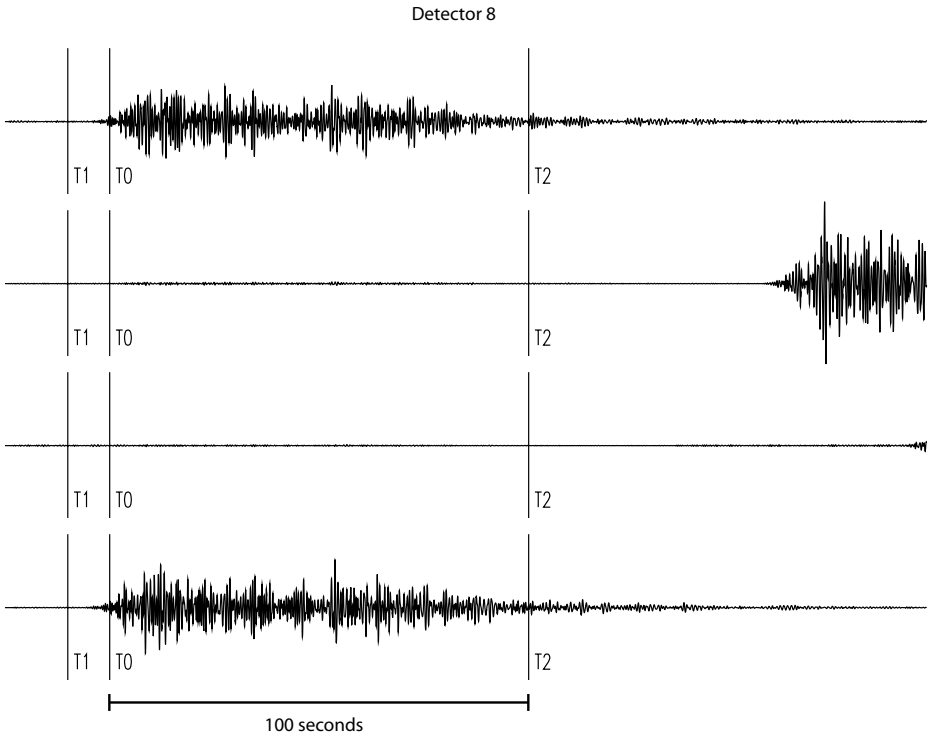

Figure 5. Example waveforms of detections associated with one detector (#8). The window used to create detectors is 110 seconds long and delimited by markers labeled T1 and T2. T0 is the nominal detection point (actually the point of detection by the STA/LTA algorithm). Common scaling of the traces causes the middle two events, which were smaller, to be invisible. The similarity of the traces allows multiple events to be interpreted simultaneously.

The key issue is whether the events are clustered in some fashion that supports a reduction in analyst effort. Figure 5 shows four detections from one detector, and demonstrates that the waveforms can be aligned automatically for comparison based on waveform correlation measurements. Several of the clusters have a large number of events (Figure 6) which should aid rapid interpretation of the sequence.

An issue of major concern is whether automatically spawned detectors introduce a large number of spurious detections, which could overwhelm any advantage gained by organizing aftershocks into compact groups for interpretation. We note that the San Simeon aftershocks occurred in 75 clusters containing 360 detections. The other 342 detections were split among 23 clusters. These detections were predominantly legitimate seismic detections from sources other than the San Simeon sequence. The largest two clusters of these detections are shown in Figure 7. These events (in fact most of the other detections) appear to be very local signals that may have entered the system through a sidelobe of the array processor. They are relatively easy to distinguish and occur in large groups that would simplify their interpretation and dismissal.

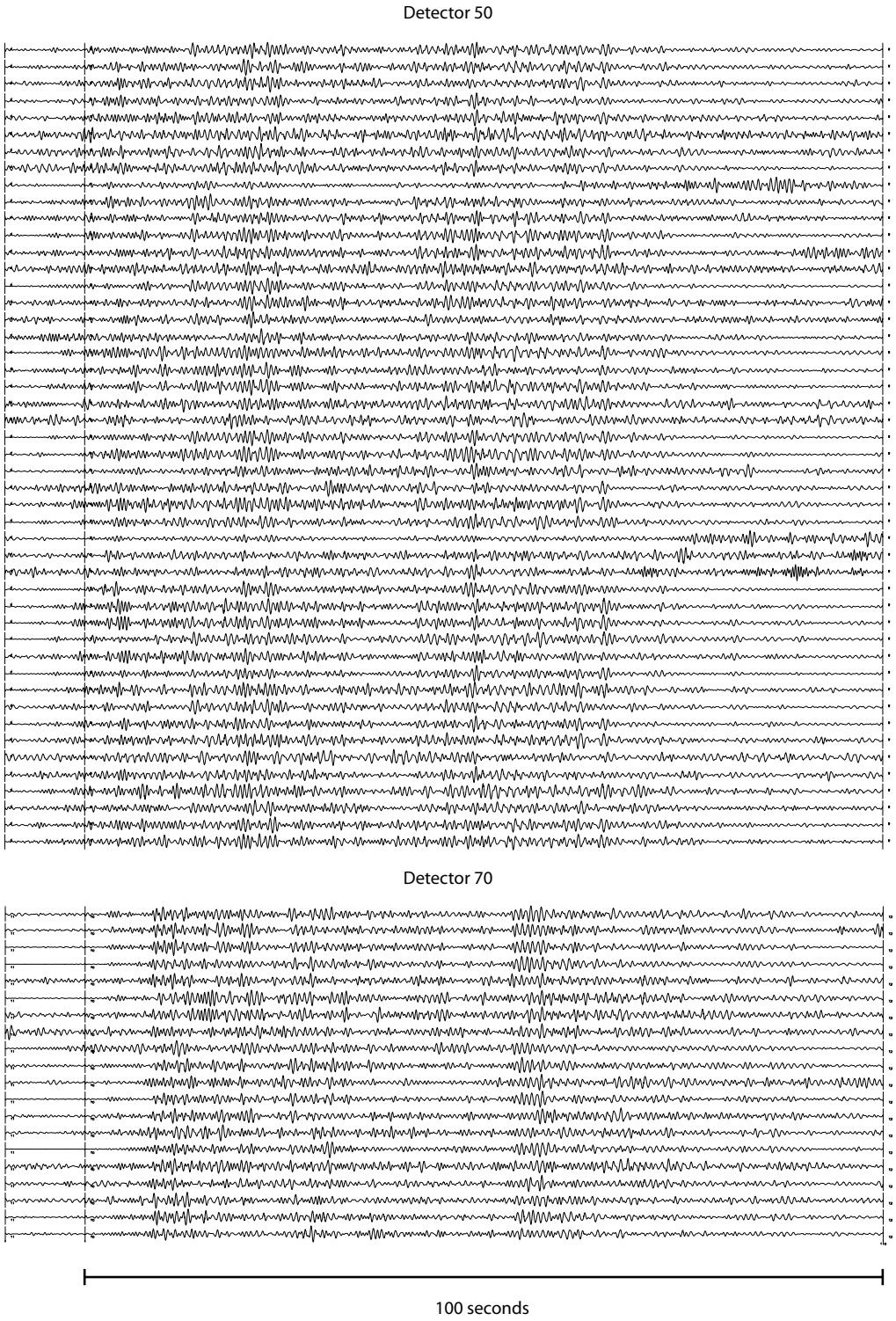

Figure 6. Two of the largest clusters of San Simeon aftershocks, automatically assembled and aligned, support our contention that efficient review by analysts would be enabled by future implementations of systems like this one.

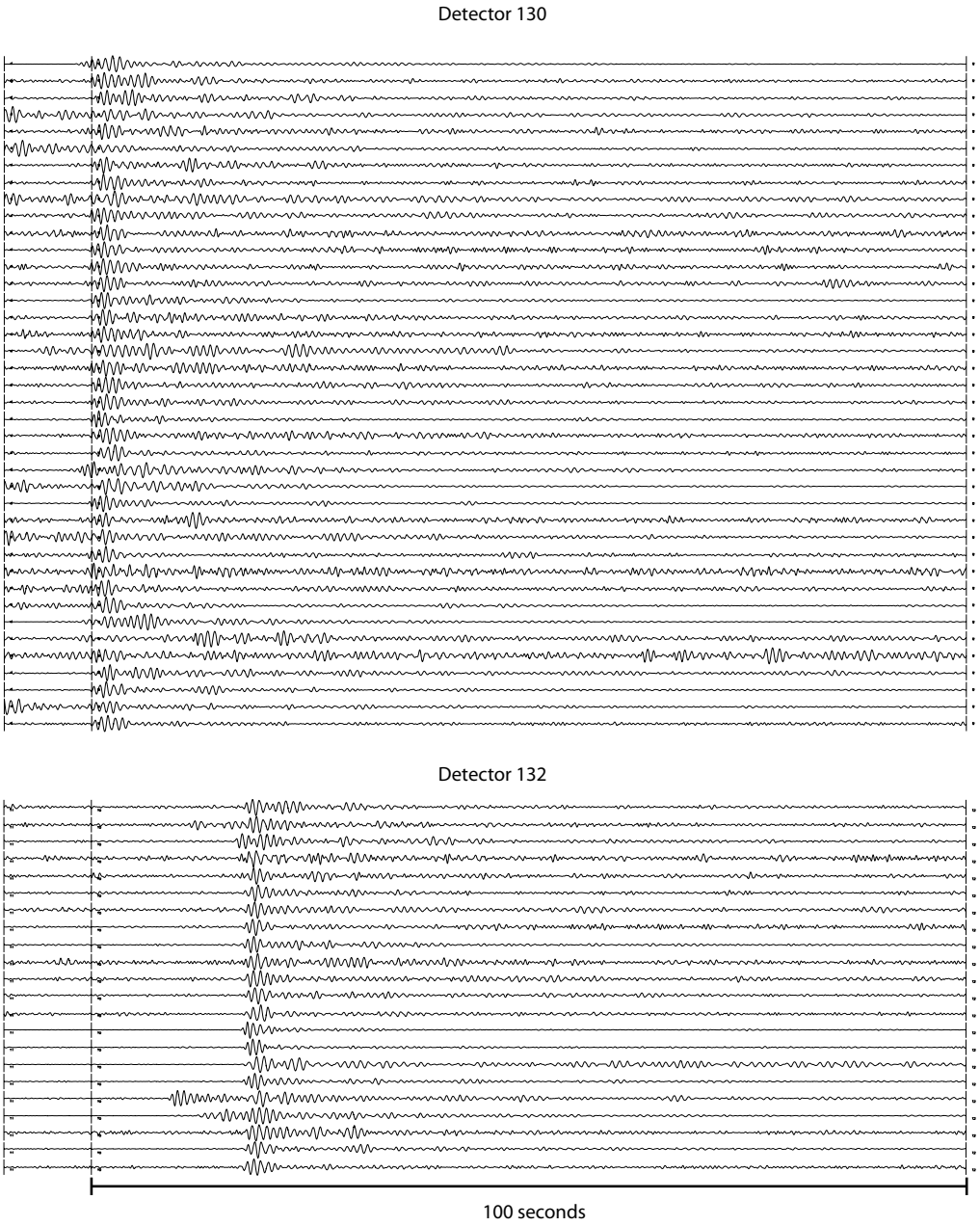

Figure 7. Two of the larger clusters of detections unrelated to the San Simeon sequence suggest that, while the system detects other local events generally not of interest, the majority of these are easily dismissed in automatically constructed groups.

CONCLUSIONS AND RECOMMENDATIONS

Overall we believe this work demonstrates that self-calibrating, autonomous correlation detection frameworks are feasible. The system we describe is a pilot; it is clear that many improvements are possible. In particular, significantly more attention should be paid to the power detector used to originate waveform correlation templates. Our system missed a significant number of the higher magnitude events, in part due to inter-event interference early in the sequence. The loss of templates from the larger events has a cascading effect, potentially eliminating large numbers of lower magnitude detections. Window selection is another area of potential improvement. We used a particularly simple algorithm, defining the template window to start and end with fixed offsets from the STA/LTA detection point. This choice of window propagates thereafter into all generations of correlation detectors. A better approach might examine windows about the detection point for temporal coherence among events within a cluster to optimize window selection. The availability of many snapshots of the same signature could be used to advantage in defining the template window. Finally, though our system did not create large numbers of spurious detections which were difficult to dismiss, potential for mischief in automatic detector creation remains. One way to suppress this problem is to extend the construction of correlation detectors to networks of stations or arrays. A network-wide correlator may have the effect of suppressing interfering signal sources local to individual stations.

REFERENCES

Harris, D. B. (2006). “Subspace Detectors: Theory”, Lawrence Livermore National Laboratory, internal report UCRL-TR-222758, 46 pp.

Harris, D. B. and Paik, T. (2006). “Subspace Detectors: Efficient Implementation”, Lawrence Livermore National Laboratory, internal report UCRL-TR-223177, 38 pp.

NCEDC (2009), ANSS catalog website, www.ncedc.org/anss/

EXPANDING COHERENT ARRAY PROCESSING TO LARGER APERTURES USING EMPIRICAL MATCHED FIELD PROCESSING

Frode Ringdal[1], David B. Harris[2,3], Tormod Kværna[1], Steven J. Gibbons[1]

NORSAR[1], Lawrence Livermore National Laboratory[2], and Deschutes Signal Processing LLC[3]

Sponsored by the Air Force Research Laboratory and the National Nuclear Security Administration
Contract Nos. FA8718-08-C-0007[1] and DE-AC52-07NA27344[2,3]
Proposal No. BAA08-39

ABSTRACT

We have adapted matched field processing—a method developed in underwater acoustics to detect and locate targets— to classify transient seismic signals arising from mining explosions. Matched field processing, as we apply it, is an empirical technique, using observations of historic events to calibrate the amplitude and phase structure of wavefields incident upon an array aperture for particular repeating sources. The objective of this project is to determine how broadly applicable the method is and to understand the phenomena that control its performance.

We obtained our original results in distinguishing events from ten mines in the Khibiny and Olenegorsk mining districts of the Kola Peninsula, for which we had exceptional ground truth information. In a cross-validation test, some 98.2% of 549 explosions were correctly classified by originating mine using just the Pn observations (2.5-12.5 Hz) on the ARCES array at ranges from 350 – 410 kilometers. These results were achieved despite the fact that the mines are as closely spaced as 3 kilometers. Such classification performance is significantly better than predicted by the Rayleigh limit. Scattering phenomena account for the increased resolution, as we make clear in an analysis of the information carrying capacity of Pn under two alternative propagation scenarios: free-space propagation and propagation with realistic (actually measured) spatial covariance structure. The increase in information capacity over a wide band is captured by the matched field calibrations and used to separate explosions from very closely-spaced sources. In part, the improvement occurs because the calibrations enable coherent processing at frequencies above those normally considered coherent.

We are investigating whether similar results can be expected in different regions, with apertures of increasing scale and for diffuse seismicity. We verified similar performance with the closely-spaced Zapolyarni mines, though discovered that it may be necessary to divide event populations from a single mine into identifiable subpopulations. For this purpose, we perform cluster analysis using matched field statistics calculated on pairs of individual events as a distance metric. In our initial work, calibrations were derived from ensembles of events ranging in number to more than 100. We are considering the performance now of matched field calibrations derived with many fewer events (even, as mentioned, individual events). Since these are high-variance estimates, we are testing the use of cross-channel, multitaper, spectral estimation methods to reduce the variance of calibrations and detection statistics derived from single-event observations.

To test the applicability of the technique in a different tectonic region, we have obtained four years of continuous data from 4 Kazakh arrays and are extracting large numbers of event segments. Our initial results using 132 mining explosions recorded by the Makanchi array are similar to those obtained in the European Arctic. Matched field processing clearly separates the explosions from three closely-spaced mines located approximately 400 kilometers from the array, again using waveforms in a band (6-10 Hz) normally considered incoherent for this array. Having reproduced ARCES-type performance with another small aperture array, we have two additional objectives for matched field processing. We will attempt to extend matched field processing to larger apertures: a 200 km aperture (the KNET) and, if data permit, to an aperture comprised of several Kazakh arrays. We also will investigate the potential of developing matched field processing to roughly locate and classify natural seismicity, which is more diffuse than the concentrated sources of mining explosions that we have investigated to date.

OBJECTIVE

The objectives of this project are

- To investigate the limits of empirical matched field processing and other coherent array detection and parameter estimation methods as receiver aperture size increases from a few kilometers to many hundreds of kilometers.
- To investigate techniques for extending the geographical source-region footprint over which empirical matched field processing and other coherent calibrated methods apply.

We will begin by reanalyzing data from the European Arctic in order to reconfirm the potential of empirical matched field processing that has been indicated by our work under a previous contract. We then will proceed to study the central Asia region to assure programmatic relevance and to exploit the large belts of natural and man-made seismicity to test the applicability of the technique to diffuse seismicity.

RESEARCH ACCOMPLISHED

The effort was focused initially on examining the degree to which empirical matched field processing (EMPF) can classify signals recorded on the ARCES array in northern Norway from closely spaced mining explosions. There were many good reasons for testing the new algorithms on this data set. Through close collaboration with scientists at the Kola Regional Seismological Center in Apatity, and with the operators of numerous mines on the Kola Peninsula, a superb database of Ground Truth information has been accumulated (Harris et al., 2003), consisting of many hundreds of events from a period of several years. In addition, the parameter estimation capabilities of the ARCES array for such signals have been explored in depth. The ability of the array to resolve source location using the classical array-processing paradigm is relatively well understood, providing an excellent basis for comparison with the new technology. The panel to the left of Figure 1 shows the location of the sources with respect to ARCES.

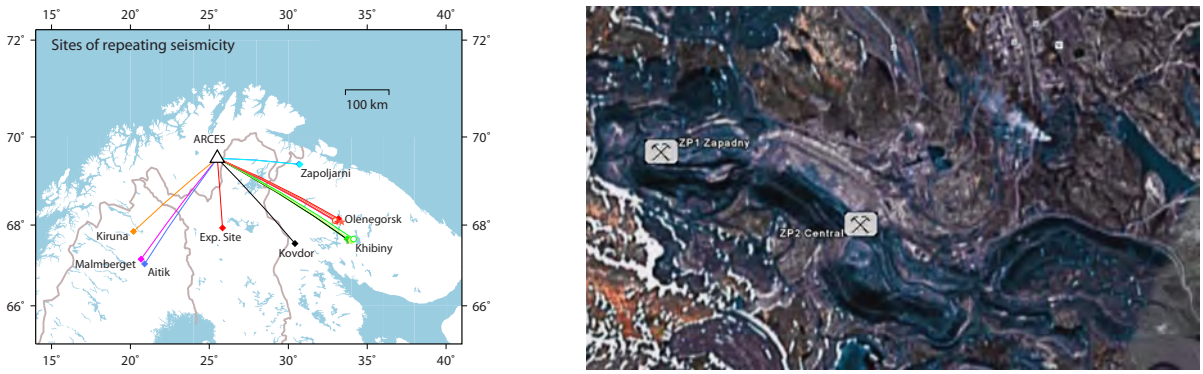

Figure 1. Locations of sites of industrial and repeating seismicity in relation to the ARCES array (left) and Google Earth image of the Zapoljarni open cast mining region with the ZP1 (Zapadny) and ZP2 (Central) mines labelled. The mines are separated by approximately 2.5 km and are approximately 200 km from ARCES.

The new data from Kazakhstan and Kyrgyzstan has allowed the application of the same techniques to a different tectonic setting, of programmatic relevance, with high levels of natural and artificial seismicity. Three different apertures of sensor configuration, with which the ability to expand Coherent Array Processing to greater sensor separations can be examined, are present. At the smallest scale, the four single arrays in Kazakhstan can be processed in the same way as ARCES. These arrays are however somewhat larger and far more sparse than ARCES which will have consequences for waveform semblance, in particular at the higher frequencies. At an intermediate scale, the stations of KNET constitute a network with an aperture of the order 200 km and a relatively broad spectrum of sensor separations. The largest aperture to be considered is that formed by the four Kazakh arrays as a single network.

Ground Truth of the kind which we have exploited in our examination of industrial seismicity on the Kola Peninsula is not yet available for Kazakhstan. This will complicate the evaluation of the event classification attempted under the current contract. We have however, been assisted greatly by access to classification results obtained by MacCarthy et

al. (2008) and Hartse et al. (2008). These studies are aimed at event screening and source identification using, in particular, waveform similarity techniques and satellite imagery. Their original source of information is the bulletin of the Kazakh National Data Center (KNDC).

Detected seismic phases are usually characterized by the parameters v_{app} (apparent velocity) and Θ (backazimuth) for the purpose of phase identification and association, and subsequent event location. In the estimation process, these parameters are coded in the slowness vector, $\boldsymbol{s}$, defined by

$$\boldsymbol{s} = (s_x, s_y) \quad \text{where} \quad s_x = s\sin(\Theta)\ , \quad s_y = s\cos(\Theta) \quad \text{and} \quad s = 1/v_{\mathrm{app}}\ . \tag{1}$$

If $\boldsymbol{x}_j$ denotes the coordinates of sensor *j*, relative to the array reference site, then we denote the time-series recorded at this site by $r(t, \boldsymbol{x}_j)$.

For a given frequency ω, the steering vector $\boldsymbol{\varepsilon}(\omega, \boldsymbol{s}) = \left[e^{-i\omega \boldsymbol{s}.\boldsymbol{x}_1} \quad \ldots \quad e^{-i\omega \boldsymbol{s}.\boldsymbol{x}_N}\right]^T$ allows a measurement of the energy incident on the array consistent with the plane wavefront hypothesis, $\boldsymbol{s}$, using (e.g. Capon, 1969)

$$P(\omega, \boldsymbol{s}) = \left| \int \sum_{j=1}^{N} r(t, \boldsymbol{x}_j) e^{i\omega(t - \boldsymbol{s}.\boldsymbol{x}_j)} \right|^2 = \boldsymbol{\varepsilon}(\omega, \boldsymbol{s})^H \boldsymbol{R}(\omega) \boldsymbol{\varepsilon}(\omega, \boldsymbol{s}) \tag{2}$$

where *N* denotes the number of sensors in the array, *H* denotes the Hermitian transpose, and the elements of the spatial covariance matrix, $\boldsymbol{R}(\omega)$, are given by

$$R_{mn}(\omega) = \left(\int r(t, \boldsymbol{x}_m) e^{-i\omega t} dt \right) \left(\int r(t, \boldsymbol{x}_n) e^{i\omega t} dt \right). \tag{3}$$

When estimating the slowness vector, $\boldsymbol{s}$, which best fits the incoming wavefront, it is typical to evaluate a normalized relative beam-power function of the form

$$\hat{P}(\boldsymbol{s}) = \frac{\sum_j \boldsymbol{\varepsilon}(\omega_j, \boldsymbol{s})^H \boldsymbol{R}(\omega_j) \boldsymbol{\varepsilon}(\omega_j, \boldsymbol{s})}{\sum_j tr\left\{\boldsymbol{R}(\omega_j)\right\}} \tag{4}$$

over a grid of slowness space and summed (incoherently) over a wide range of frequencies *j*.

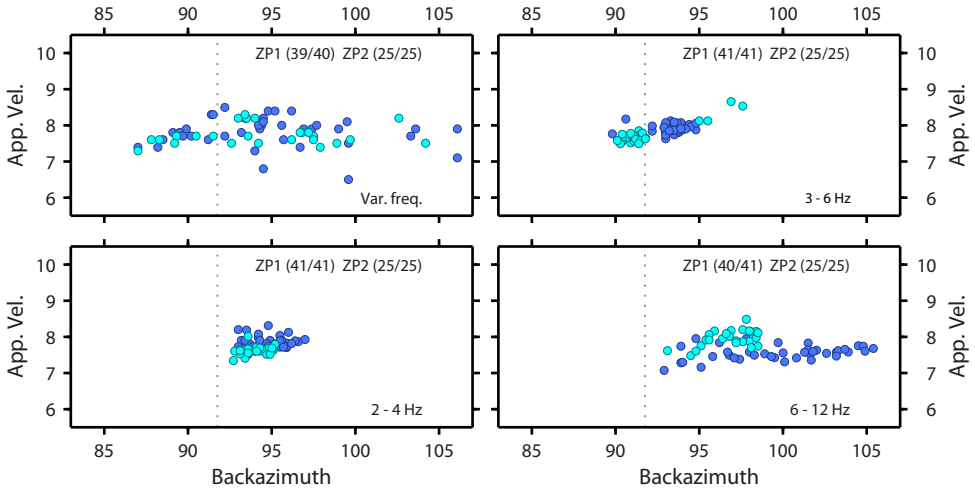

Figure 2. Slowness estimates at ARCES using broadband f-k analysis for first regional P-phases from the ZP1 (dark blue) and ZP2 (light blue) mines. The true backazimuth is approximately 91.8 degrees for both mines as indicated by the vertical dashed lines. The top left panel displays estimates taken from the fully automatic ARCES detection lists and the remaining panels are reprocessed in the fixed frequency bands as indicated. The 41 events from the ZP1 mine and the 25 events from the ZP2 mine all took place between October 2001 and September 2002.

The right panel of Figure 1 shows a satellite image of two mines, denoted ZP1 and ZP2, which are separated by less than 3 km. Figure 2 shows four panels of slowness estimates for initial P-arrivals from these two mines over a 12 month period from October 2001 to September 2002.

The top left panel (in which measurements are taken from the fully automatic detection lists) shows a very high spread in the measured backazimuth and no separation between the two populations. (Under standard array processing considerations, we would not anticipate being able to resolve these two nearby sources with a single seismic array at this distance.) The frequency band selected in the automatic detection lists is determined by an automatic algorithm on a case-by-case basis to try to optimize the signal-to-noise ratio (SNR). The high variability of the slowness estimates has significant consequences for the accuracy of fully-automatic event bulletins (e.g., Ringdal and Kværna, 1989) and all undertakings which can result in more stable parameter estimates should be investigated.

The three remaining panels are interesting as they demonstrate (a) that the stability is very much improved by selecting a fixed frequency band, (b) that the bias and spread of the slowness estimates are very different for the different frequency bands, and (c) that there is a significant separation in parameter space for the two different mines. Whilst this separation is evident visually, it would be very difficult to identify the source confidently just given the parameter estimates for the different frequency bands. It is the intention that, in bypassing the plane-wavefront parametrization, that Empirical Matched Field Processing will be able to exploit the characteristic source and path effects responsible for the patterns shown in order to identify a likely source.

If we calculate spatial covariance matrices, $\boldsymbol{R}(\omega)$, for seismic arrivals known to have originated from a given source, we can form an ensemble covariance matrix $\boldsymbol{R}_\alpha(\omega)$ from a specified population α of events. If we replace the theoretical plane wavefront steering vectors $\boldsymbol{\varepsilon}(\omega, \boldsymbol{s})$ in Equation 4 with the principal eigenvectors of $\boldsymbol{R}_\alpha(\omega)$, we can obtain an equivalent normalized measure of the energy incident on the array for the "α" hypothesis:

$$\hat{P}(\alpha) = \frac{\sum_j \boldsymbol{\varepsilon}(\omega_j, \alpha)^H \boldsymbol{R}(\omega_j) \boldsymbol{\varepsilon}(\omega_j, \alpha)}{\sum_j tr\,\{\boldsymbol{R}(\omega_j)\}} \qquad (5)$$

Ensemble spatial covariance matrices $\boldsymbol{R}_\alpha(\omega)$ were calculated for the two populations of events displayed in Figure 2 and the "matched field statistic" specified in Equation 5 was evaluated for both these empirical steering vectors for each event known to have taken place from the same two mines during the period 2003-2004 (see Figure 3).

Whilst the separation of the ZP1 and ZP2 populations against the calibrated empirical steering vectors is reasonable, many symbols lie in a zone of high uncertainty (shaded grey) where the match of the measured wavefield is quite similar for both of the source hypotheses. Two events from the ZP1 mine have been misclassified as belonging to the ZP2 cluster (with a marginal difference in detection statistics), although we do not rule out errors in the Ground Truth collection.
An ideal classification would see all of the dark blue symbols in the lower right corner and all the pale blue symbols in the upper left corner.

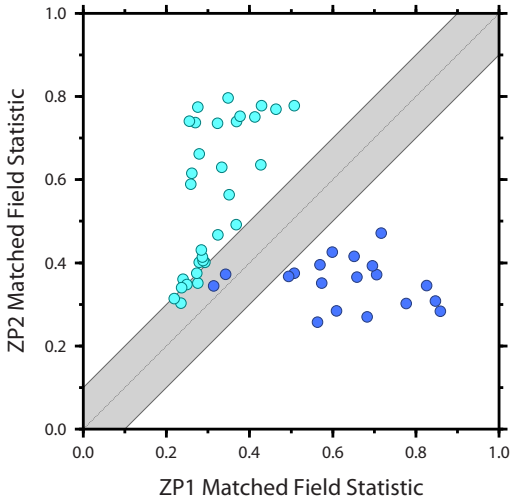

Figure 3. Matched field statistics as defined in Equation 5 for empirical steering vectors calibrated from the 2001-2002 populations for the ZP1 and ZP2 mines on the x and y axes respectively. Dark and light blue symbols indicate that the spatial covariance matrices were calculated from signals from ZP1 and ZP2 events respectively during the period 2003-2004. Frequency band used: 2.5 - 12.5 Hz.

There is a clear need to understand why the classification performance is as shown in Figure 3 and investigate which, if any, improvements are possible. The ability to attribute candidate signals to one or other of the sources will depend upon how well the principal eigenvector of the ensemble spatial covariance matrix for each cluster represents the spatial covariance observed for individual events associated with that source, and the degree to which the empirical steering vectors from the different sources differ from each other. To this end, we perform cluster analysis upon empirical steering vectors calculated from individual events. Specifically, we calculate a similarity measurement as defined in Equation 6 between the principal eigenvectors of the spatial covariance matrices between any two distinct data segments. Note that the measure is an average value taken over a wide range of frequency bands. Figures 4 and 5 show cross-matrices and corresponding single-linkage dendrograms for the ZP1 and ZP2 event sets for 2001-2002.

$$d_{\alpha\beta} = \frac{1}{N_{\mathrm{B}}} \sum_{j=1}^{N_{\mathrm{B}}} \left| \boldsymbol{\varepsilon}(\omega_j, \alpha)^H \boldsymbol{\varepsilon}(\omega_j, \beta) \right| \tag{6}$$

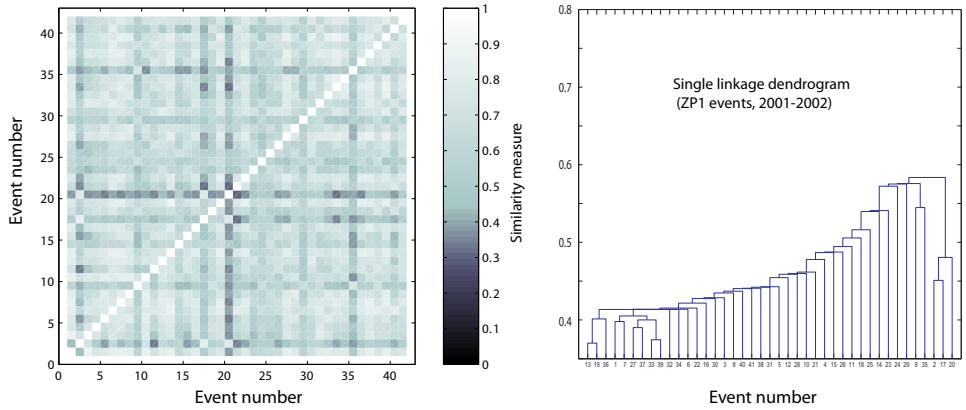

Figure 4. Similarity matrix and corresponding single-linkage dendrogram for events from the ZP1 mine 2001-2002.

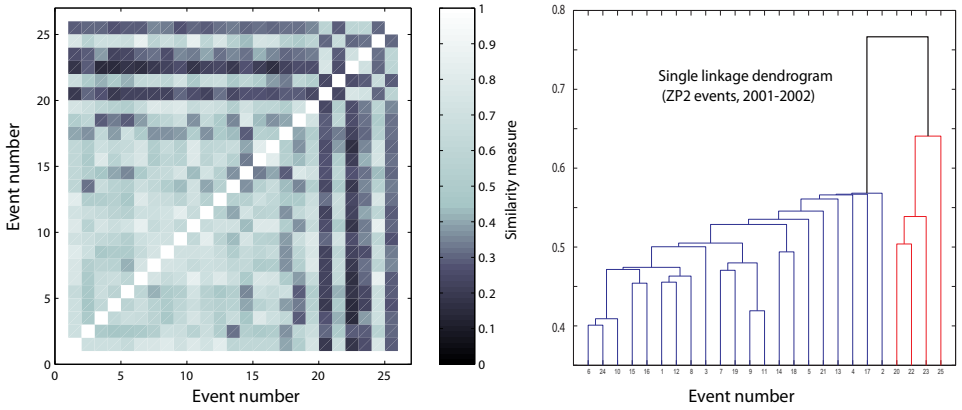

Figure 5. Similarity matrix and corresponding single-linkage dendrogram for events from the ZP2 mine 2001-2002.

It is clear from Figure 5 that the ensemble of events selected to represent the ZP2 mine consists of two distinct clusters according to the similarity metric defined in Equation 6. We then repeat the classification exercise displayed in Figure 3 but replacing the ZP2 matched field statistic with the maximum of two different statistics, calculated from the ensemble covariance matrices from each of the two clusters evident in Figure 5. It is clear in the right hand panel of Figure 6 that the classification is far better than that displayed in Figure 3 where only a single empirical steering vector was available to represent the whole ZP2 source region. Almost no events appear in the grey shaded region when the two steering vector representation was used for the ZP2 site. The same two events in the ZP1 population remain misclassified, and there is evidence in Figure 4 for (at least) two events which appear to match quite poorly.

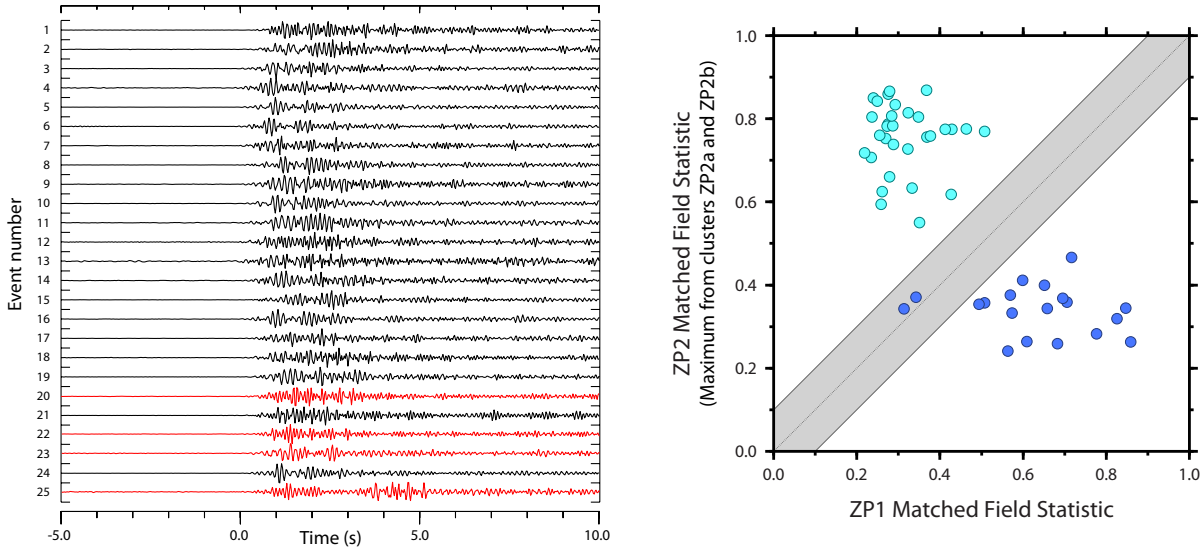

Figure 6. Waveforms from the ZP2 events (left) with traces colored according to the classification displayed in Figure 5, and Matched Field Statistics (right) with ZP2 events represented by two different empirical steering vectors. The empirical steering vectors for both mine clusters are calculated from the 2001-2002 event pools and the dark and light symbols represent ZP1 and ZP2 events respectively from 2003-2004. Frequency band used: 2.5 - 12.5 Hz.

We conclude that cluster analysis is necessary as a prerequisite to the calculation of ensemble covariance matrices in order that the validity of the selected cluster can be determined. If a cluster clearly separates into two populations, it is likely that matched field statistics calculated using an ensemble spatial covariance matrix generated from the full population are not going to provide a good classification. Events which are spurious and which clearly do not belong to the cluster will be identified using the procedure described here.

The scattering effects which are so problematic for coherent array processing of high frequency phases on ARCES are even more so for the arrays in Kazakhstan due to the sparse geometries (see Figure 7). Whilst the problem of low SNR at low frequencies is less acute than at ARCES, the SNR still improves greatly at higher frequencies (see Figure 8). Estimating the slowness using broadband f-k analysis is a trade-off between SNR and signal coherence.

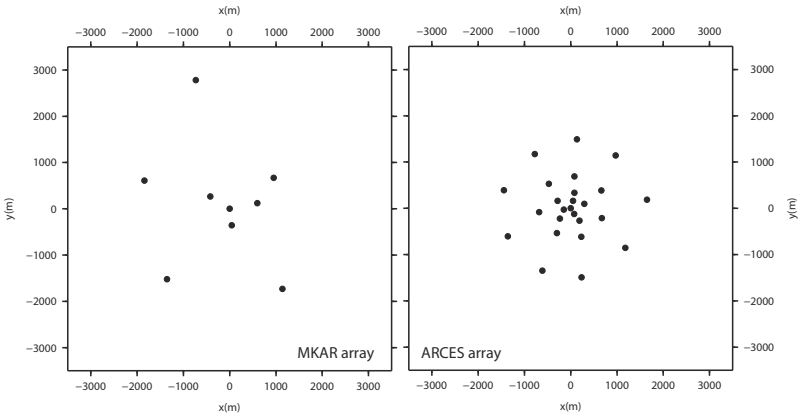

Figure 7. Comparison of the configurations of the MKAR and ARCES arrays. Whilst both arrays have the same fundamental design (of concentric rings with increasing numbers of sensors), the sparsity of the MKAR array makes processing of regional phases very difficult. The inner-most sensors of ARCES which are so crucial to the detection and estimation of high frequency phases are missing from MKAR.

The data segment in Figure 8 is the result of a mining explosion on June 30, 2007, at a distance of approximately 400 km from the MKAR array. This event belongs to the cluster labelled 344 by Hartse et al. (2008).
The SNR for the Pn arrival is high, but only for frequencies above 4 Hz. This is unfortunate from the point of view of phase estimation using traditional array processing since (see Figure 9) almost all slowness estimates above 4 Hz are qualitatively incorrect due to scattering and incoherence together with sidelobes in the array response function for these frequencies. Many of the estimates below 4 Hz are qualitatively misleading due to a low SNR.

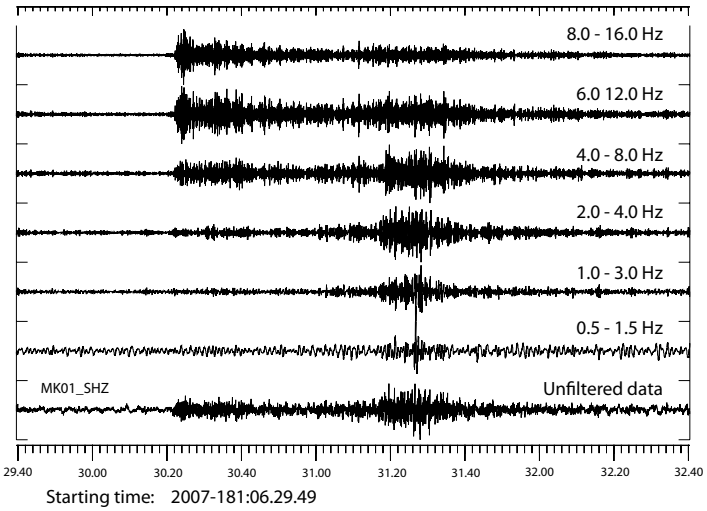

Figure 8. A three-minute long data segment on the single channel MK01_SHZ filtered in various frequency bands as indicated. See above text for details.

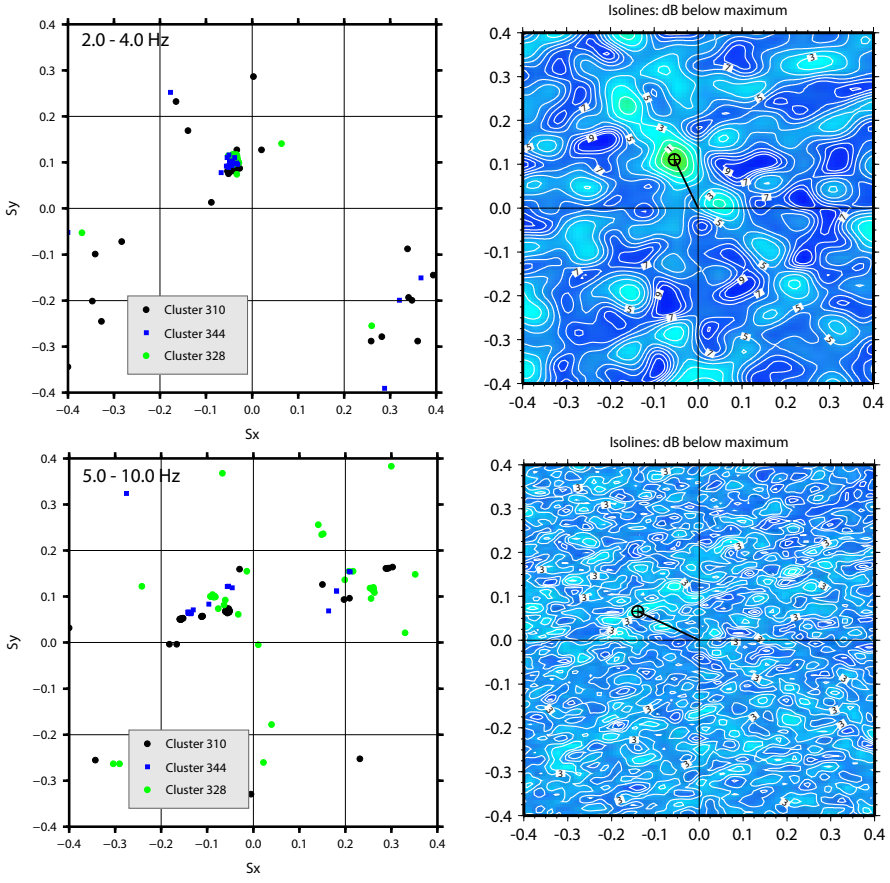

Figure 9. The left hand panels show scatter-plots of slowness estimates in the frequency bands indicated for initial Pn arrivals at MKAR for events in clusters 310, 328, and 344 in Hartse et al. (2008). The anticipated backazimuth for all events is close to 340^{O} and the apparent velocity should be close to 8 kms^{-1}. The f-k grids to the right display the relative beam-power as a function of slowness for the arrival at MKAR at a time 2007-181:06.30.31.425 (see Figure 8).

Figure 9 indicates at a glance that an attempt at source classification based upon direction estimates from traditional plane wavefront array processing are not likely to succeed given the abysmal coherence on the MKAR array for high frequency regional phases. We attempt a classification using empirical matched field processing; given that the clusters were derived by Hartse et al. (2008) and MacCarthy et al. (2007) using waveform correlation methods, some degree of success is anticipated. Cluster analysis was performed on the empirical steering vectors for each of the individual events prior to an attempt at classification using ensemble covariance matrices. The results are displayed in Figure 10. From this plot, it is clear that multiple empirical steering vectors are necessary to characterize the wavefields recorded by the range of events from each of these clusters.

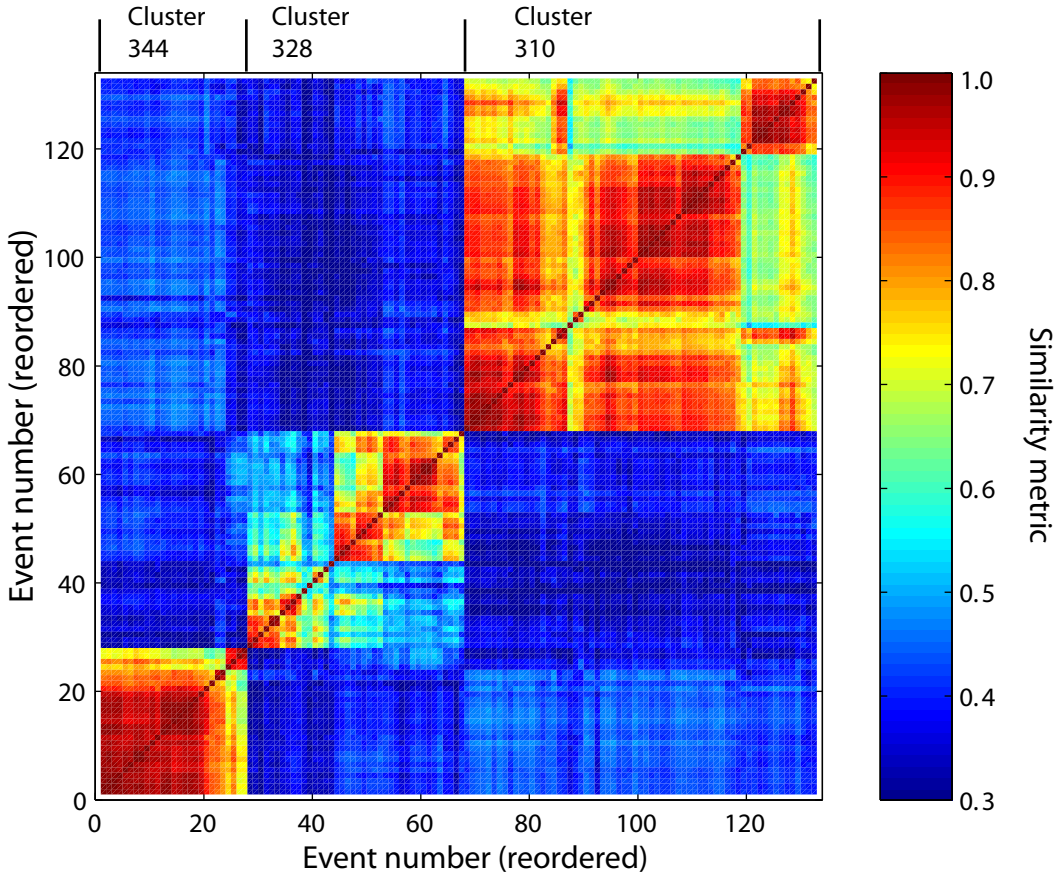

Figure 10. Matched field similarity matrix compiled over three distinct clusters (310, 328, and 344) from the study of Hartse et al. (2008). A number of distinct subpopulations are revealed from the cluster analysis of the empirical steering vectors for the Pn arrival at the MKAR array (especially for cluster 328) and these need to be taken into consideration prior to matched field classification using ensemble spatial covariance matrices.

Figure 11 shows that the matched field classification has attributed each of the individual events to the correct source. We have therefore demonstrated that the spatial covariance matrices provide a coherent array-processing technique which works at high frequencies over an aperture for which simply delay-and-stack beamforming and broadband f-k analysis fail.

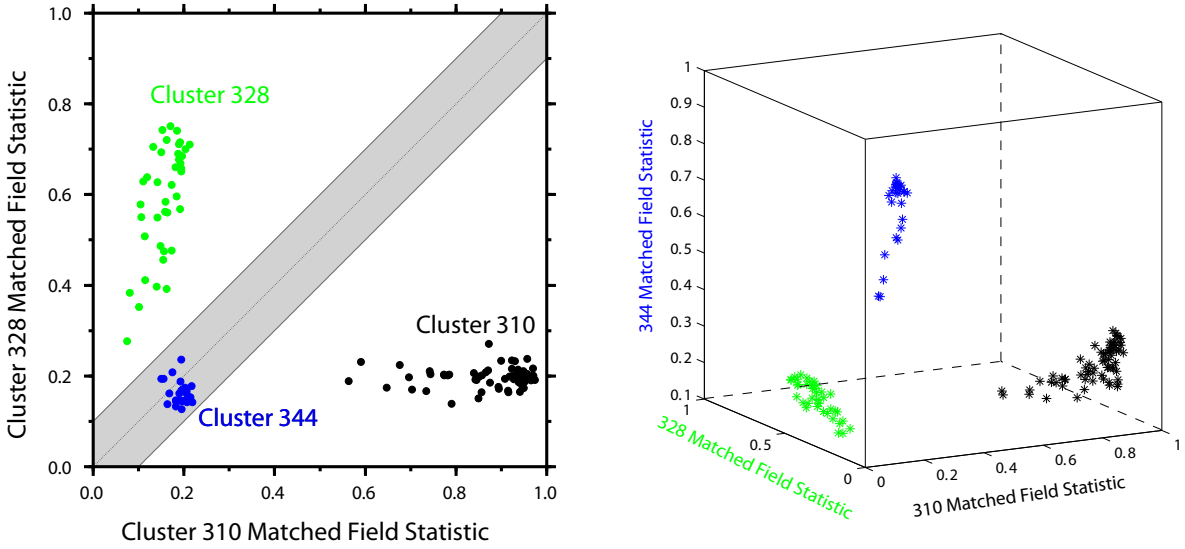

Figure 11. Classification results for clusters 310, 328, and 344, using multiple ensemble covariance matrices for each of the subpopulations displayed in Figure 11.

CONCLUSIONS AND RECOMMENDATIONS

We have demonstrated that empirical matched field processing is able to classify, with a high degree of confidence, events from sources of repeating seismicity even for cases where classical waveform correlation methods become problematic due to differences in the source time function. This has also been demonstrated for an array with an aperture over which incoherence defeats traditional methods of array processing.

One of the most important aspects of the procedure that has come to light during this reporting period is the necessity of performing cluster analysis on the empirical steering vectors prior to the building of ensemble covariance matrices. If an attempt is made to use an ensemble covariance matrix constructed from significantly differing subpopulations, this will result in empirical steering vectors which represent the entire population relatively poorly.

It is of great interest as to how many events are required to characterize a specified source region adequately; there are clearly circumstances where one would hope to achieve a reasonable performance with only a single observation. Part of the motivation for the construction of the ensemble covariance matrices is to reduce the variance in the narrow-band spatial covariance matrices (Equation 3). Multitaper methods (Thomson, 1982) produce spectral estimates with low variance and the recently published codes of Prieto et al. (2009) include routines for robust and stable multitaper coherence estimation. We have implemented these routines into our codes and are currently investigating the variability of the estimates of the spatial covariance matrices.

ACKNOWLEDGEMENTS

We are grateful to the National Data Center in Kazakhstan for permission to use the data from the Kazakh seismic arrays. We thank Hans Hartse of Los Alamos National Laboratory for kindly providing the results of waveform cross-correlation and cluster analysis for mining events in Kazakhstan. We are grateful to Prof. Germán Prieto of Universidad de los Andes, Bogotá, for making available the source code and documentation for the Multitaper Spectral Analysis code. We thank the IRIS DMC and the KN network for making continuous data from the KNET stations available. All maps produced using GMT software (Wessel and Smith, 1995).

REFERENCES

Capon, J. (1969), High-resolution frequency-wavenumber spectrum analysis, in *Proc. IEEE* 57:1408–1418.

Harris, D. B., F. Ringdal, E. O. Kremenetskaya, S. Mykkeltveit, J. Schweitzer, T. F. Hauk, V. E. Asming, D. W. Rock, and J. P. Lewis (2003). Ground-truth collection for mining explosions in Northern Fennoscandia and Russia, in *Proceedings of the 25th Seismic Research Review - Nuclear Explosion Monitoring: Building the Knowledge Base*, LA-UR-03-6029, Vol. 1, pp. 54–62.

Hartse, H. E., G. E. Randall, and S. J. Arrowsmith (2008). Regional event identification research in Asia, in *Proceedings of the 30th Monitoring Research Review, Ground-Based Nuclear Explosion Monitoring Technologies*, LA-UR-08-05261, Vol.1, pp. 615–624.

MacCarthy, J. K., H. Hartse, M. Greene, and C. Rowe (2008). Using waveform cross-correlation and satellite imagery to identify repeating mine blasts in Eastern Kazakhstan, in *Seism. Res. Lett.*, 79:393–399.

Prieto, G. A., R. L. Parker, and F. L. Vernon (2009). A Fortran 90 library for multitaper spectrum analysis, in *Computers and Geosciences (in press: corrected proof online).*

Ringdal, F. and T. Kværna (1989). A multi-channel processing approach to real time network detection, phase association, and threshold monitoring, in *Bull. Seism. Soc. Am.* 79:1927–1940.

Thomson, D. J. (1982). Spectrum estimation and harmonic analysis, in *Proc. IEEE* 70:1055–1096.

Wessel, P. and Smith, W. H. F. (1995), New version of the generic mapping tools, *EOS Trans., Am. geophys. Un.* 76: 329.

EPICENTRAL LOCATION OF REGIONAL SEISMIC EVENTS BASED ON EMPIRICAL GREEN'S FUNCTIONS FROM AMBIENT NOISE

Michael H. Ritzwoller, Mikhail P. Barmin, Anatoli L. Levshin, and Yingjie Yang

University of Colorado at Boulder

Sponsored by the National Nuclear Security Administration

Award No. DE-AC52-09NA29326
Proposal No. BAA09-50

ABSTRACT

The purpose of this research is to develop and test a novel method of regional seismic event location based on exploiting Empirical Green's Functions (EGF) that are produced using ambient noise methods. Elastic EGFs between pairs of seismic stations are determined by cross-correlating long ambient noise time-series recorded at the two stations. The EGFs principally contain Rayleigh and Love wave energy and focus is placed on utilizing these signals between 5- and 15-sec periods. We have begun the fundamental R&D needed to develop and test methods to produce a geographic grid of vertical and horizontal component EGFs, which can then be used to detect and locate events accurately using waveform correlation. Because the EGFs contain the full 3-D structural response of the Earth for surface waves, the method is tantamount to using an exceptionally accurate 3-D model for detection and location. Because the method is empirical, however, location error is expected to be unbiased by 3D structure. Furthermore, ambient noise is generated at the Earth's surface, so the EGFs are tuned for surface-focus events and are, therefore, ideal for detecting and locating human-made events.

Proof-of-concept applications of a preliminary version of the algorithm are presented to estimate epicentral locations in the western U.S. using EarthScope USArray data. These include the determination of station locations (GT0) by reciprocity, thirteen previously well located events (GT1) in California, and the Crandall Mine (GT0.5) collapse. Research is ongoing to extend and generalize the method to include hypocentral location and moment tensor determination.

OBJECTIVES

The purpose of this research is to improve seismic event location accuracy and event characterization by exploiting Empirical Green's Functions (EGFs) that emerge by cross-correlating long time sequences of ambient noise observed at pairs of seismic stations. Because ambient noise EGFs are dominated by surface waves, the method uses surface wave energy for location purposes. Present efforts apply Rayleigh wave EGFs from 5 to 15 sec period to the epicentral location problem. The method of epicentral location is described here as well as proof-of-concept applications for a series of seismic events in the western US. Future work will continue to refine the method, generalize its application to Love waves, introduce phase information, and explore the ability to constrain depth and the moment tensor using ambient noise.

RESEARCH ACCOMPLISHED

Non-Technical Description of the Method

We assume first that there is a temporary dense local array, termed the **base stations**, deployed in the `"region of interest" where seismic events may occur. Second, there is a more distant permanent (but potentially sparse) regional network of stations termed the **remote stations**. Using what are now well established methods (e.g., Bensen et al., 2007), the EGFs from every base to every remote station are computed. At this stage of the project, we use only vertical-to-vertical components of EGFs here, which are dominated by Rayleigh waves. The set of these EGFs can be used to calculate an EGF at any geographical point covered by the base station deployment by transforming and adding (stacking) the individual EGFs for a given remote station. Such EGFs are called Composite EGFs (CEGFs). These CEGFs then can be used to locate events within the region of interest using waveform correlation with event records at remote stations. The location technique applied here involves specific transformations of the input EGFs before stacking, which we do not describe in detail here. These transformations improve the signal/noise ratio and minimize the effect of waveform differences between event records and CEGFs.

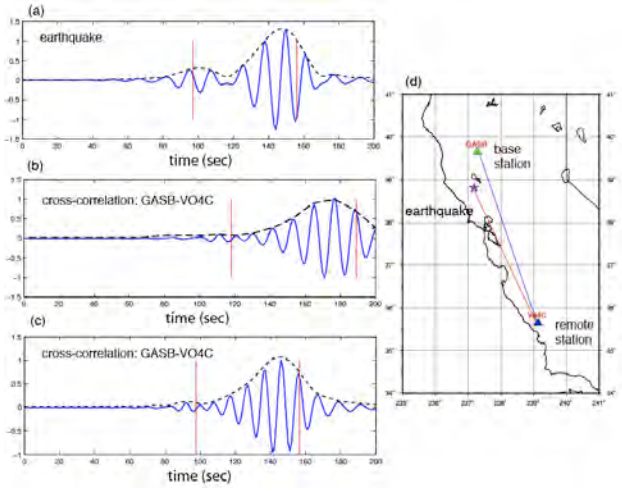

Figure 1. Comparison of an earthquake record with an EGF. (a) Earthquake record at station V04C in southern CA band-passed between 7 and 15 sec period. (Evt. #12 from Table 1.) (b) EGF between stations GASB (north of the earthquake) and V04C with the same pass-band. (c) The EGF has been shifted and deformed to correspond to the earthquake location. (d) Earthquake and station locations.

As an example that illustrates the idea of the method of epicentral location, consider the mb=4.5 earthquake that occurred north of the San Francisco Bay area on May 12, 2006, Figure 1d. This is Event #12 from Table 1. The vertical component of the earthquake record and the vertical-vertical EGF from a station near the epicenter are shown in Figures 1a, and 1b. The earthquake record is from station V04C, and the inter-station EGF is for stations GASB (about 100 km from the epicenter) and V04C. Both time-series are band-pass filtered between the 7- and 15-sec period and are dominated by the Rayleigh wave. The earthquake and EGF Rayleigh waveforms are similar, but are offset in time because the epicentral distance for V04C is smaller than the inter-station distance V04C-GASB. The EGF can be shifted in time and deformed to match the epicentral distance, Figure 1c. The technical details of this transformation are not presented here. The phase content of the two records differ appreciably, because earthquakes impart an initial phase that depends on hypocentral depth and source mechanism as well as epicentral distance. For this reason, at this early stage of research, we ignore phase information and summarize both the EGFs and the earthquake records with their envelope functions, seen in Figure 1 as dashed lines.

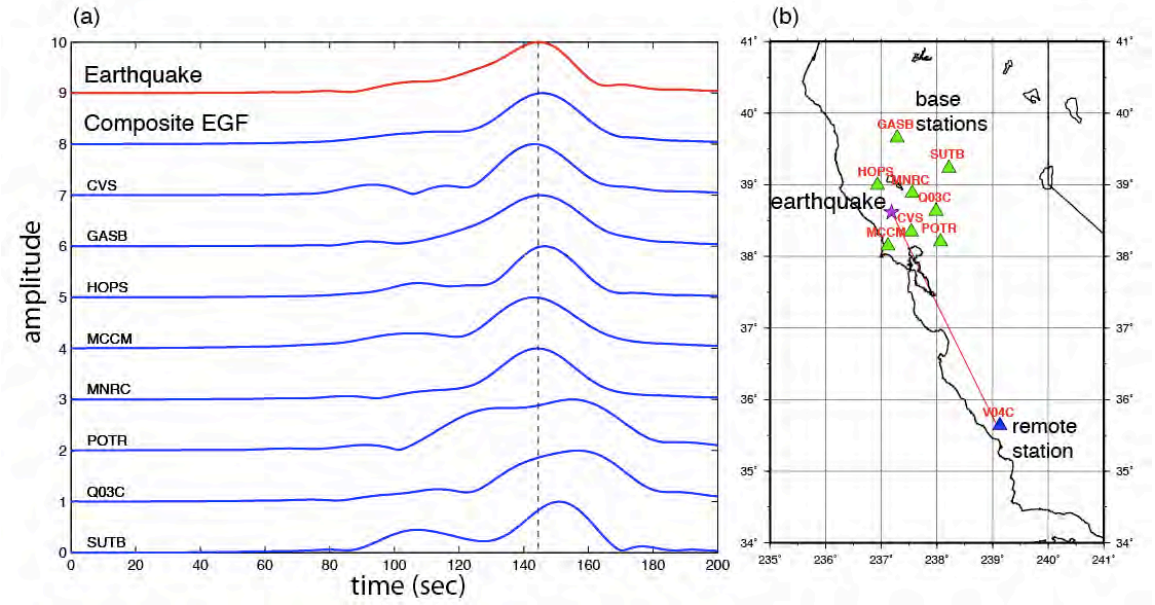

Figure 2. Comparison of EGFs for the set of base stations to a single remote station. Similar to Figure 1, but only the envelopes of the EGFs are shown for the eight base stations in (a). The envelope of the earthquake record is shown in red at top and the envelope of the Composite EGF (CEGF, sum of the individual EGFs) is on the second line. Individual EGFs and the CEGF are transformed to the epicentral location of the earthquake.

The EGFs for each of the base stations relative to the remote station can be similarly transformed to the earthquake location and stacked to produce a CEGF for a particular source location and remote station, as illustrated in Figure 2. Typically, the Composite EGF agrees with the earthquake record better than the individual EGFs from individual base stations. The Composite EGFs for a candidate event location can be produced for all remote stations, as the record section shown in Figure 3 illustrates. Inspection of fit between the Composite EGFs and the earthquake envelope functions reveals that 3-D structure similarly affects the EGFs and the earthquake records. For example, consider the arrivals at stations HUMO, Q08A, and PHL, which are within several kilometers in epicentral distance from each other. The Rayleigh wave arrives much earlier at Q08A than at the other stations because of fast propagation through the Sierra Nevada. In fact, the fast arrivals on the record section all propagate in part through the Sierra Nevada. In addition, some of the envelope functions are significantly broader than others. Stations ELFS and T06C present examples for wave propagation across and oblique to the Great Valley sediments of central California.

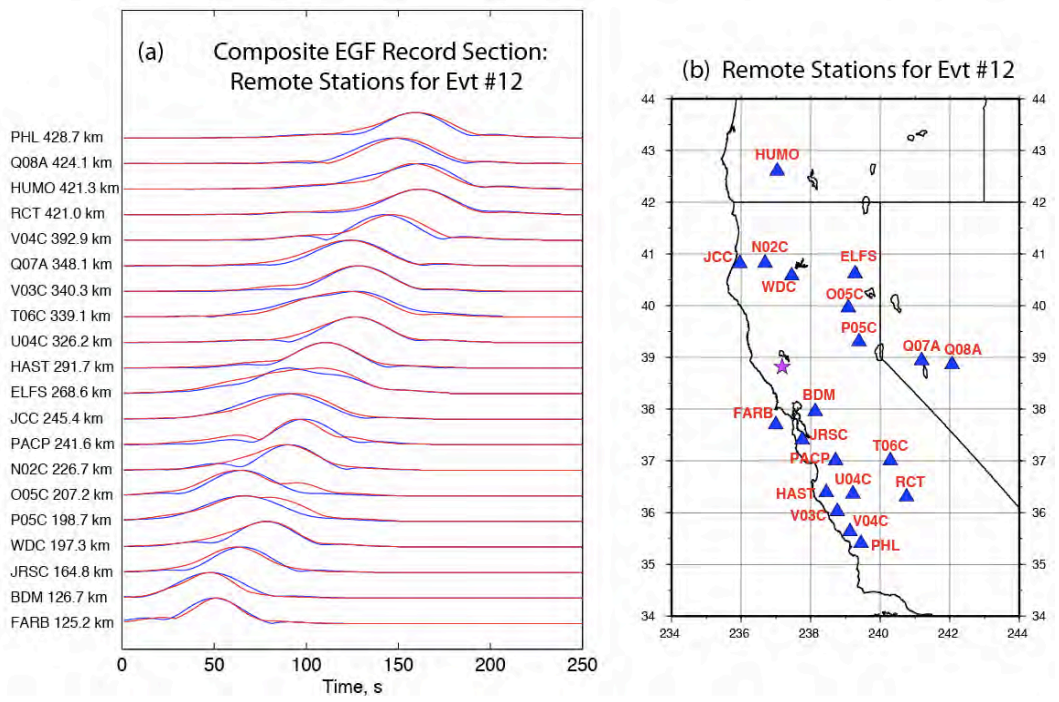

Figure 3. Record section of the CEGFs compared with the earthquake records at 20 remote stations for California Event #12. (a) Envelope functions of the earthquake observed at the remote stations (red lines) are compared with envelopes of the CEGFs (blue lines). Band-pass: 7- to 15-sec period. Epicentral distances and station names are indicated at left. (b) Locations of the remote stations (blue triangles) and earthquake (red star). The locations of the eight base stations are shown in Figure 1.

Our location procedure minimizes the misfit between the envelopes of the CEGFs and the earthquake records by waveform cross-correlation. The minimization is performed by a straightforward grid search, as illustrated in Figure 4. This is the same earthquake as in Figures 1-3, Event #12 of Table 1.To locate this event, we used eight base stations and 55 remote stations from the Northern California Network and EarthScope's Transportable Array (Figure 4a). The grid spacing for location was about 500 m. The reference location is indicated with a red star and our location is given by a yellow star in Figure 4b. Error ellipses are estimated with a method that is based on work of Flinn (1965) and Jordan and Sverdrup (1981). The estimated error ellipse is shown with a yellow curve. The difference in locations in this example is one grid spacing, which is approximately encompassed by the estimated error ellipse.

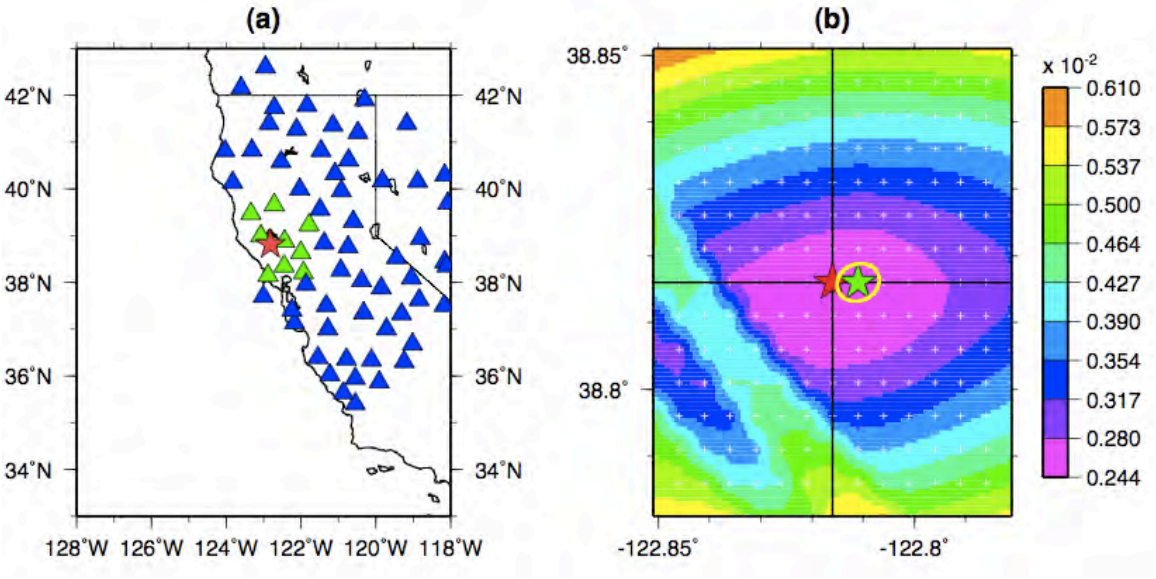

Figure 4. Example of the grid-search location of California Reference Event #12. (a) Stations used to locate this earthquake (red star): base stations (green triangles), remote stations (blue triangles). (b) Map of residuals, which is the basis for the location and error estimate: our event location (green star), reference location (red star), our 90% confidence ellipsoid (yellow line). Grid points are separated by about 500 m and are marked by white crosses.

Proof-of-Concept Applications

We present here several examples to assess the capabilities of the epicentral location method. At present, the method's development remains in preliminary stages and we consider the results presented here to be in the proof-of-concept category.

Locating stations by reciprocity (GT0). In computing EGFs from inter-station cross-correlations, either of the pair of stations can be considered to be a virtual source by reciprocity. Thus, the EGFs from a particular station to the set of other stations can be used to locate the common station. In this way we have used our epicentral location method to locate the EarthScope Transportable Array stations as well as some other local stations in the western US. The advantage of this test is that the station locations are known exactly (i.e., they are like genuine GT0 events) and, unlike earthquakes, the EGFs possess no unknown initial phase caused by event depth and mechanism or other complicated source characteristics. Thus, imperfect knowledge of real seismic events does not complicate the interpretation of the method's intrinsic accuracy. However, the method's ability in practice to locate real seismic events in all of their complexity still needs to be tested.

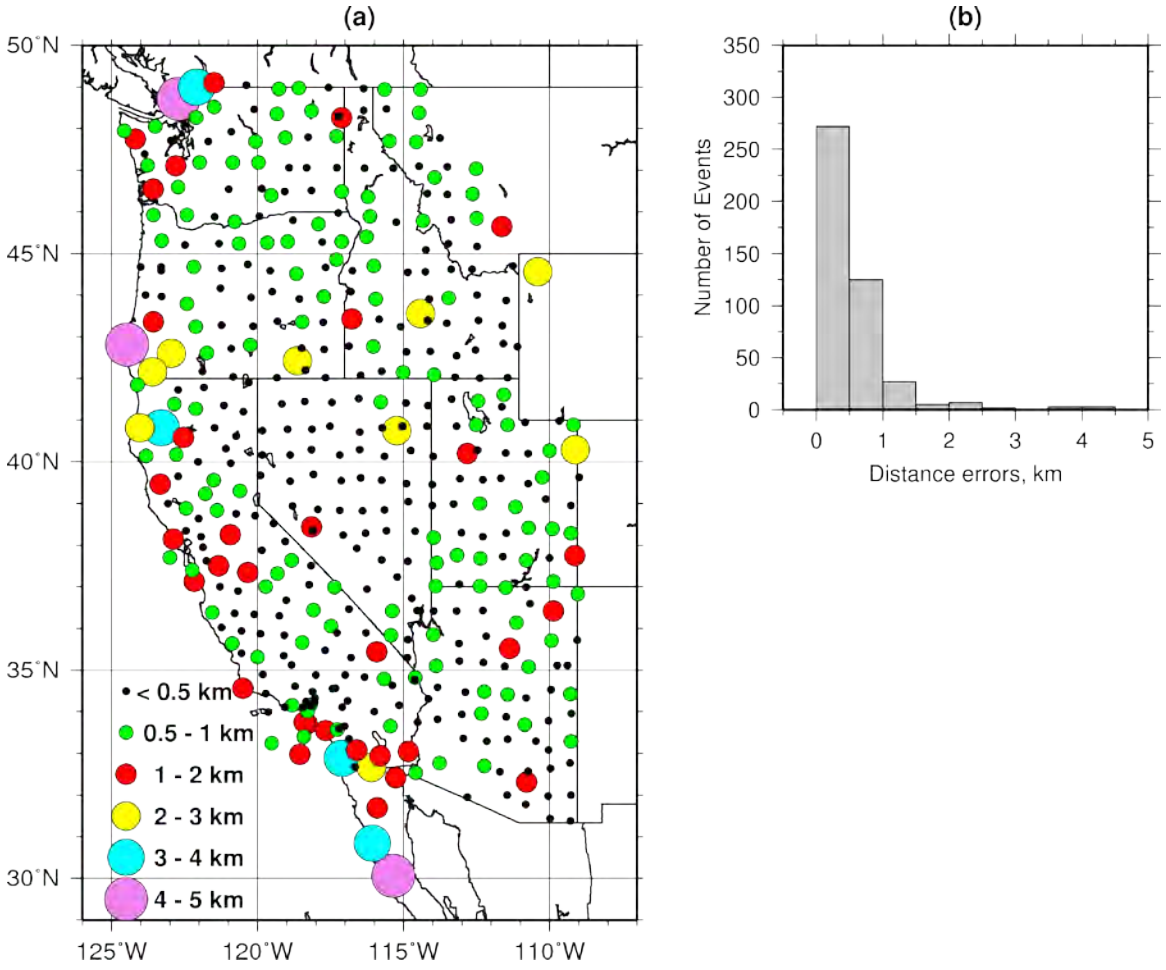

Figure 5: Location errors for 445 stations deployed in California and surrounding states located with the method described here from EGFs by reciprocity. (a) Map of location errors for existing stations. The distance between the station and the estimated location, in km, for each station position is shown with colored circles. (b) Histogram of location errors (in km).

The results of this exercise are shown in Figure 5. Test parameters include a location grid spacing of 0.5 km, base stations are located within 100 km of each station to be located, and remote stations are situated between 100 km and 400 km from the station. About 61% of the stations are located within 0.5 km of their real location, 28% between 0.5 km and 1.0 km, and only 7 of the 445 stations are located worse than 3 km. The bad locations are mostly near the coast where azimuthal coverage is less than 180 degrees and where structural gradients are profound. The worst locations are in southern California where azimuthal coverage is particularly incomplete and near the Mendocino Transform where numerous offshore earthquakes exist and tend to vitiate the EGFs. We need to continue to tune the method to make it less sensitive to these variables. Nevertheless, at present we estimate the intrinsic accuracy of the method in this nearly ideal observational setting to be better than 0.5 km.

The station-location test will be particularly useful to test the characteristics of the location method as the base stations or remote stations decrease in number and as the EGFs decrease in quality (as they may for short station deployments or in poor signal-to-noise environments). Knowledge of the performance of the location method as station coverage degrades is important to understand its reliability in realistic monitoring situations.

Locating the Crandall Canyon mine collapse (GT0.5). The next location test moves beyond the idealization of locating stations, to the location of a shallow mine collapse in central Utah. This seismic event of magnitude 3.9 occurred on Monday August 6, 2007, at about 08:48:40 UTC, caused by the collapse of the coal mine at a depth of about 1 km that permanently trapped several miners underground. The outline of the mine is shown in Figure 6 with a yellow line. The location of the collapse and the focus of the drilling efforts is shown by a yellow push-pin to be in

the far western part of the mine several km from the mine's entrance, beneath steeply sloping surface topography. The USGS location (actually performed by the University of Utah using local seismometers as well as recently installed stations from the EarthScope Transportable Array) is shown to lie about 1.2 km from the believed location of the trapped miners, in a valley west of the contours of the mine. To locate the event, we used seven base stations and 66 remote stations (instead of 33 used by USGS) affiliated with different networks: USGS, University of Utah, and EarthScope's Transportable Array (Figure 7a). The grid spacing for location was 100 m. The location results are: 39.465N (USGS 39.465N), 111.224W (USGS 111.237W), an origin time shift is equal to -0.26 sec relative to the USGS time, and confidence ellipse parameters (Flinn, 1965; Jordan and Sverdrup, 1981) of a=0.52 km (semi-major axis), and b=0.43 km (semi-minor axis). This location is within the contours of the mine and less than 0.5 km from the best estimate of the mine collapse, which is within the error ellipse of this event.

Figure 6. Schema of the Crandall Canyon mine, outlined with the yellow line. The location of the mine collapse and trapped miners and the USGS seismic location are shown with yellow push-pins. Our location is identified by a green star and error-ellipse.

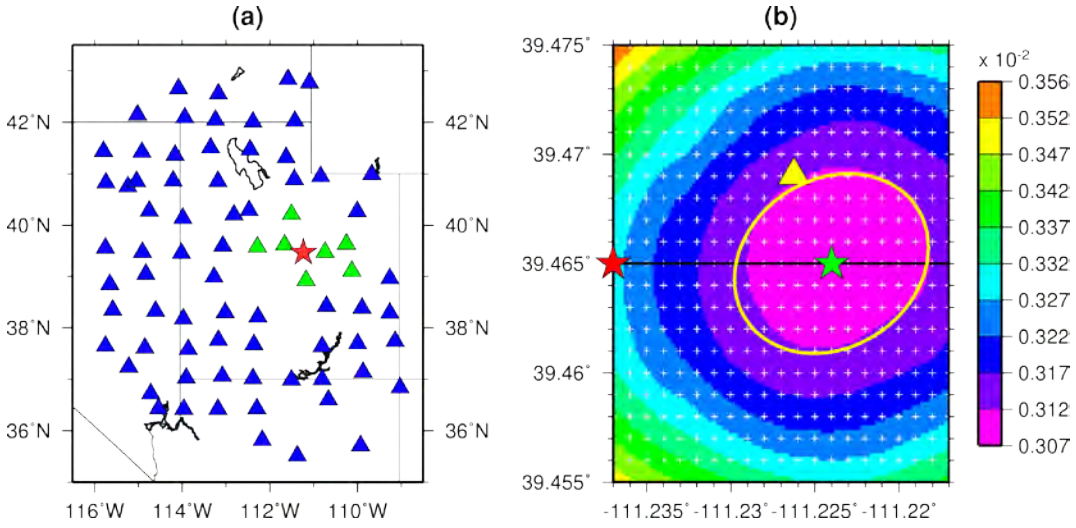

Figure 7. (a) Stations used to locate the Crandall Canyon mine collapse (red star): base stations (green triangles), remote stations (blue triangles). (b) Map of residuals, which is the basis for the location and error estimate: our event location (green star), USGS location (red star), our 90% confidence ellipsoid (yellow line), and best estimate for the location of trapped miners (yellow triangle). Grid points are separated by 100 m and are marked by white crosses.

Because this is a shallow seismic event, it provides a good test of the location method accuracy for human-made explosions. An accuracy of ~0.5 km within the context of a nearly ideal observational setting is a reasonable expectation. Tests of other mine collapses or historical nuclear explosions will help to calibrate these expectations. Further accuracy tests as a function of decreasing the number of observing stations are also needed.

Locating crustal earthquakes in California (GT1). Crustal events deeper than the Crandall Canyon mine collapse impart frequency dependent initial phase and group time shifts (Levshin et al., 1999) that are not known a priori. These shifts will degrade the epicentral location estimated with our method unless they are explicitly estimated or taken into account during the location process. At present, they are not modeled in our location procedure. To assess their effects, the next exercise extends the tests beyond shallow events to a set of well-located (~GT1) earthquakes within the California crust. Table 1 presents the locations of these reference earthquakes, which occurred in 2005 and 2006 and have mb values ranging between 4.5 and 5.1. The accuracy of these reference locations is believed to be better than 1 km in most cases. The uncertainty in the reference locations should be kept in mind in evaluating the locations from our method.

An example of the location procedure for Event #1 is shown in Figure 8. This is a southern California event where the reference locations are determined by CalTech. For events in northern California, such as those shown in Figures 1–4, the reference locations were determined by the Northern California Earthquake Center in Menlo Park. Both organizations use a combination of broad-band and short period instruments and apply 1-D models calibrated for each region. CalTech used both *P* and *S* phases, whereas only *P* phases were used in northern California. The location grid for a northern California earthquake (Event #12) is shown in Figure 4.

Table 1. Reference (GT1) events in California and location "errors".

event #	date (y/m/d)	time (h:m:s)	source†	lat	lon	m_b	Error (km)	Error (sec)
1	2005/04/16	19:18:13.00	P	35.027	-119.178	4.9	0.72	-0.16
2	2005/05/16	07:24:37.50	NC	35.929	-120.477	4.3	0.90	0.02
3	2005/06/12	15:41:46.54	P	33.529	-116.572	5.1	1.08	-0.15
4	2005/06/16	20:53:26.02	P	34.058	-117.010	4.8	0.72	-0.21
5	2005/06/26	18:45:57.82	NC	39.305	-120.093	4.6	1.02	-0.03
6	2005/08/31	22:47:45.64	P	33.165	-115.635	4.5	2.18	0.20
7	2005/08/31	22:50:24.03	P	33.172	-115.610	4.9	1.78	0.07
8	2005/08/31	23:32:11.04	P	33.190	-115.602	4.5	2.86	0.02
9	2005/09/02	01:27:19.81	P	33.160	-115.637	4.9	2.17	-0.04
10	2005/09/22	20:24:48.62	P	35.043	-119.013	4.8	1.07	0.00
11	2005/10/02	13:48:09.45	NC	35.651	-121.087	4.5	0.45	-0.08
12	2006/05/12	10:37:29.31	NC	38.816	-122.816	4.5	0.43	-0.09
13	2006/06/15	12:24:51.11	NC	37.102	-121.492	4.5	0.71	0.00
14	2006/08/03	03:08:12.86	NC	38.364	-122.589	4.6	0.71	-0.14

†: P – Pasadena, NC – Northern California.

We located the events listed in Table 1 and the differences in the epicentral locations and origin times between our method and the reference events are summarized in the last two columns of this table. The average difference in location (called "error" in Table 1) for these events is 1.2 km, and the average "error" in origin time is 0.04 s. When the uncertainties in the reference locations are accounted for, the 90% confidence level for our locations is about 1 km. These locations, however, are degraded relative to those for the stations or the Crandall mine collapse in our earlier tests, which we estimated to be better than 0.5 km. We conclude, therefore, that un-modeled earthquake depth is contributing a bias to our locations. For our method to yield epicentral locations better than the GT1 level for shallow crustal events such as those in California the effect of earthquake depth must be incorporated in the technique. This is a direction for on-going research.

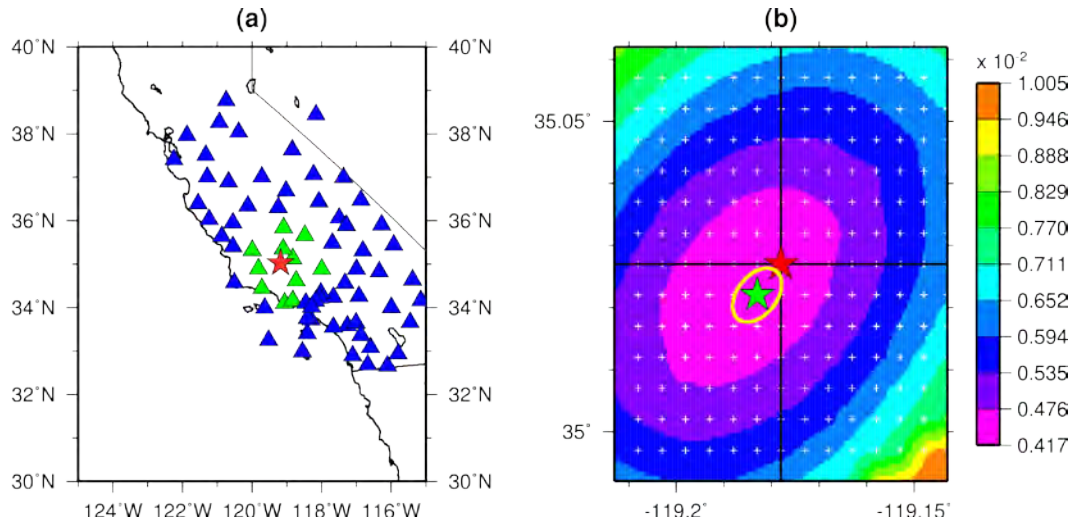

Figure 8. Epicentral location test for California Event #1. (a) Location of the stations used: base stations (green triangles), remote stations (blue triangles). Reference event location is marked with a red star. (b) Map of the grid of residuals which our location is based on: our event location (green star), reference location (red star), and the 90%confidence ellipsoid (yellow line). The ~0.5 km grid points are marked with white crosses.

CONCLUSIONS AND RECOMMENDATIONS

The work presented here has been performed at the very early stages of the contract, and remains preliminary in nature. Nevertheless, work to date demonstrates that absolute locations based on the use of ambient noise empirical Green's functions can, for stations (located by reciprocity) or shallow seismic events, yield epicentral locations with an intrinsic error of about 500 m, on average. Crustal earthquakes, however, impart phase and group time shifts that can bias the location, and we show how earthquakes in California are located with our method with an accuracy of about 1 km. In addition, the results presented here are for a nearly optimal observational setting, in which there are more than five base stations within 100 km of each event and dozens of high-quality remote stations within 400 km. Future work will generalize the method to use more information from the Empirical Green's function (e.g., Love waves, phase information, frequency dependence of misfit), explicitly estimate or correct for the biasing effect of non-surface event depth, and quantitatively assess how the reduction in base and remote stations degrades the method.

ACKNOWLEDGMENTS

The data used in this research were obtained from the IRIS Data Management Center and originate predominantly from the Transportable Array component of EarthScope/USArray. We would like to thank Egill Hauksson, James Dewey, and Bob Engdahl for valuable information gleaned from personal communications.

REFERENCES

Bensen, G. D., M.H. Ritzwoller, M. P. Barmin, A. L. Levshin, F. Lin, M. P. Moschetti, N. M. Shapiro, and Y. Yang (2007). Processing seismic ambient noise data to obtain reliable broad-band surface wave dispersion measurements, *Geophys. J. Int*. 169: 1239–1260.

Flinn, E.A. (1965). Confidence regions and error determinations for seismic event locations, *Rev. Geophys* 3: 157–185.

Jordan, T.H., Swerdrup K.A. (1981). Teleseismic location techniques and their application to earthquake clusters in the South-Central Pacific, *Bull. Seismol. Soc. Amer.* 71: 4, 1105–1130.

Levshin, A.L., Ritzwoller, M.H., Joe S. Resovsky (1999). Source effects on surface wave group travel times and group velocity maps, *Phys. Earth Planet. Inter.* 115: 293–312.

A UNIFIED APPROACH TO JOINT REGIONAL/TELESEISMIC CALIBRATION AND EVENT LOCATION WITH A 3D EARTH MODEL

William L. Rodi[1], Delaine T. Reiter[2], Stephen C. Myers[3], and Nathan A. Simmons[3]

Massachusetts Institute of Technology[1], Weston Geophysical Corporation[2], and
Lawrence Livermore National Laboratory[3]

Sponsored by the National Nuclear Security Administration

Award Nos. DE-AC52-08NA28539[1,2] and DE-AC52-07NA27344[3]
Proposal No. BAA08-19

ABSTRACT

This project addresses the problem of locating seismic events from combined data sets of regional and teleseismic arrival times. While the use of both types of data theoretically yields better location accuracy than can be achieved with either type alone, experience has shown that the realization of such improvement depends on the ability to predict regional and teleseismic travel times accurately and consistently. Inconsistencies between regional and teleseismic predictions arise from discrepancies between regional and global velocity models used for travel-time calculation, as well as from disparities in the techniques used for travel-time calibration with ground-truth data; e.g. tomographic vs. empirical calibration. Additionally, improper weighting of teleseismic vs. regional data in the event location process can degrade location accuracy.

To address these problems, this project is investigating a framework for seismic event location based on the use of a single 3D Earth model for calculating travel times for all seismic phases. A number of research problems ensue from this framework. One is how tomographic calibration of the Earth model can be most accurately and efficiently performed; for example, whether the velocities in the crust and upper mantle of different geographic regions and in the deeper mantle can be determined in separate analyses or must be done in a single, grand calibration. A second issue is whether and how one can use tomographic uncertainty analysis to provide an optimal weighting of different teleseismic and regional phases used in locating an event. In addition, we are addressing the practical difficulties involved in efficiently calculating travel times with a 3D Earth model as part of an event location procedure. In particular, the project is investigating which approximate methods – such as linearization around a 1D reference model or a hybrid technique that matches 3D and tau-p calculations done in different depth ranges – might be adequate for the purpose of event location.

This paper describes our progress to date in acquiring and developing the tools needed for the project, and shows the results of some preliminary tests with joint regional/teleseismic travel-time calibration in southern Asia.

OBJECTIVE

The development of three-dimensional models of Earth structure continues to be an active field of seismology advancing along several fronts. A small sampling of these efforts include global travel-time tomography (e.g. van der Hilst et al., 1997; Antolik et al., 2003), global surface-wave tomography (e.g., Ritzwoller et al., 2002), and regional models for Asia (Murphy et al., 2005; Li et al., 2006) and the Middle East (Pasyanos et al., 2004). An important question for nuclear monitoring is whether these, or improved, 3D Earth models can produce routine event locations with significantly reduced errors compared to 1D models when data at all event-station distances are used together.

Many previous studies have demonstrated improvement in regional event locations based on 3D crust/upper mantle models, using either *a priori* models (Ryaboy et al., 2001; Pasyanos et al., 2004) or tomographic models (e.g., Murphy et al., 2005; Reiter et al., 2005). However, relatively little work has been done on joint regional/teleseismic location with 3D models. In one of the few published studies, Yang et al. (2004) found that event locations obtained by combining regional and teleseismic data were only more accurate than locations found from the separate data sets *if* they corrected for a bias between the teleseismic and regional travel-time predictions, each made from a different 3D model (CUB1.0 for regional, J362 for teleseismic). The correction they inferred is small (0.79 s), which is consistent with the fact that 3D crust/upper mantle effects on teleseismic travel times are relatively small (<2 s). But even small, systematic shifts in teleseismic travel times can induce large location errors owing to the high apparent velocity of teleseismic arrivals.

We are investigating a methodology for seismic event location based on the principle that travel times for all seismic phases should be predicted consistently from a single 3D Earth model. This unified modeling approach would be applied as the forward model used in locating events from combined sets of regional and teleseismic data. Moreover, the 3D model would be calibrated with regional and teleseismic ground-truth data in a joint tomographic analysis. A unified approach to location and location calibration is not a new concept and, in fact, has been the approach taken with 1D Earth modeling for many decades. Applying the approach to 3D Earth models, however, presents many strategic and computational challenges, which this project is attempting to address. The techniques we develop will be tested on a variety of available 3D Earth models, including the JWM model of south-central Asia (Reiter and Rodi, 2009), the WENA1.0 model (Pasyanos et al., 2004), and global mantle models such as J362D28 (Antolik et al., 2003) and MITP07 (Li et al., 2008).

RESEARCH ACCOMPLISHED

The implementation of an event location and travel-time calibration methodology with 3D Earth models involves three main components:

1. Raytracing algorithms for computing travel times of arbitrary regional or teleseismic phases in a 3D model, and the sensitivity of the travel times to the model velocities.
2. An event location algorithm that accommodates arrival-time data from multiple phases, with forward modeling based on the raytracing algorithms of Item 1 applied to a unified 3D model.
3. A tomography algorithm that fits a 3D model of *P*- and *S*-wave velocity in the crust and mantle to ground-truth observations of regional and teleseismic arrival times. This algorithm is also based on the modeling techniques of Item 1.

Our project is developing these components primarily as modifications and enhancements to algorithms previously developed by MIT, Weston Geophysical, and LLNL in past or concurrent projects on location and tomography. The goal of this project is not to develop a complete and operations-ready 3D capability but rather to demonstrate the value and practicality of the unified approach. The following sections describe the techniques we are developing in more detail and our progress to date.

3D Raytracing

The choice of a raytracing algorithm involves somewhat different issues in location and tomography. An event locator requires travel-time predictions for arbitrary hypocenters as it searches for a best-fitting event location, while tomography is usually performed with event locations held fixed. In addition, tomography needs the sensitivity of each calculated travel time to the model velocity parameters, as derived from the ray trajectory connecting the source and receiver.

For travel-time calculation in a 1D model (e.g., AK135, Kennett et al., 1995) the choice of a raytracing algorithm is straightforward since analytical solutions for travel times and rays, for any seismic phase (direct, reflected, diffracted or converted) are available and easily implemented in fast algorithms. This project is developing a general 1D raytracer based on the tau-p method (Buland and Chapman, 1983) that generates travel-time tables and travel-time sensitivities to 3D velocity parameters that are compatible with 3D event location and tomography software that is being used in this project (discussed more below).

Travel-time calculation in 3D models is much more problematic. For the calculation of travel times of regional direct *P* arrivals, Reiter et al. (2005) used the finite-difference raytracing method of Podvin and Lecomte (1991), as implemented by Lomax et al. (2000), in their nonlinear inversion of *Pn* arrival times. Since the P-L algorithm is written for finely gridded, flat-Earth models in Cartesian coordinates, they developed appropriate transformations from more coarsely gridded, spherical Earth models, incorporating an earth-flattening transformation (Müller, 1971). Reiter et al. (2005) further augmented the Podvin-Lecomte (P-L) algorithm with a back-chaining algorithm to generate sensitivities of travel times with respect to velocity parameters of the Cartesian model, and the translation of these sensitivities to the spherical Earth parameterization. These same regional raytracing capabilities were used by Reiter and Rodi (2009) in the generation of model JWM.

The finite-difference method can also be applied to teleseismic paths, but the computation time and storage requirements grow with epicentral distance. Furthermore, the earth-flattening transformation, which is only exact for 1D models, becomes less accurate with distance. Another problem with using a finite-difference method as a general raytracer is that the method is designed for first-arrival *P* or *S* waves. This is especially a problem for teleseismic arrivals, which are often well identified secondary phases such as pP.

Global travel-time tomography has generally been performed with a linear approximation to the travel-time function. In this approximation, the travel time *T* through a 3D model of interest is obtained by integrating the model's slowness function along the Fermat raypath computed in a different, reference model velocity model:

$$T \approx \int d\mathbf{x}\, a(\mathbf{x}; v_{ref})\, v^{-1}(\mathbf{x}) \qquad (1)$$

where $\mathbf{x}$ is the position vector; $v(\mathbf{x})$ is the 3D velocity function of interest; and $a(\mathbf{x}; v_{ref})$ is a sensitivity distribution concentrated on the Fermat raypath evaluated in a reference velocity function, $v_{ref}(\mathbf{x})$. When $v_{ref} = v$, the travel time *T* is exact. Linearization of travel times offers great computational advantages in both computation time and storage if v_{ref} is 1D. It also greatly simplifies the computation of times for secondary arrivals.

Accuracy Test for Linearization

Our preliminary examination of the linearization technique indicates that it is not accurate for regional phases but it may be adequate for teleseismic phases, in application to earthquake location as well as tomography. We base this tentative conclusion on numerical tests performed with the JWM model of Reiter and Rodi (2009). JWM is a 3D model of crust and upper mantle *P* and *S* velocity in southern Asia derived from the joint inversion of *Pn* travel times from the EHB database (Engdahl et al., 1998) and Rayleigh-wave group delays in the period range 10–150 seconds. A vertical slice through the model is shown in Figure 1. First, we compared travel times calculated through JWM using the Podvin-Lecomte algorithm to the travel times calculated through AK135. The times were calculated between station JYP (33.1° N, 74.85° E) and a line of fictitious surface-focus events extending to near-teleseismic distances along a great circle at azimuth N30°W. (The model slice in Figure 1 also follows this great circle.) To calculate teleseismic times in JWM with Podvin-Lecomte, JWM was extended below 410 km depth with the AK135 velocity profile. The left panel of Figure 2 shows the difference between JWM and AK135 travel times as a function of distance. At regional distances the difference is large (up to 4 s), reflecting the

complex crust and upper mantle structure along this path. At teleseismic distances (>18°) the difference between the models is less than 1 s, due in part to our 1D extrapolation of JWM.

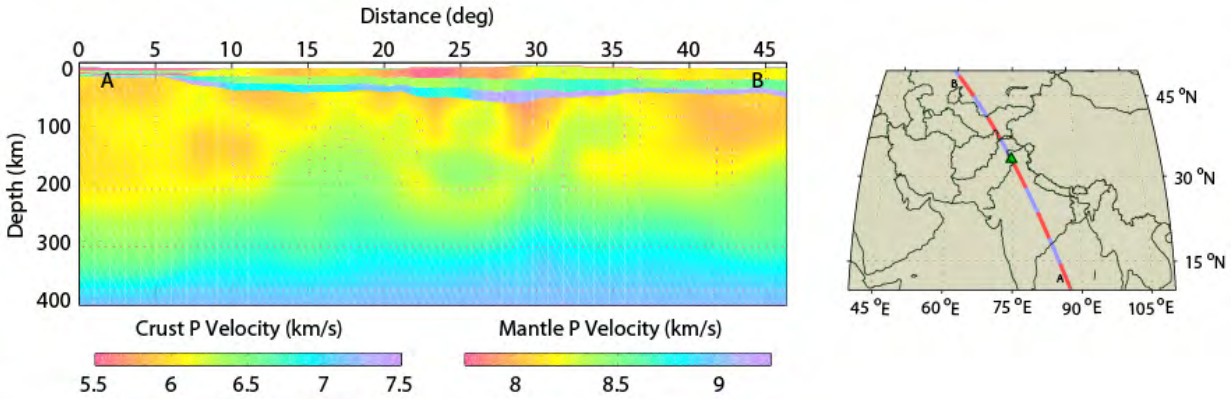

Figure 1. A vertical section through JWM, the Weston/MIT tomographic model of southern Asia (Reiter and Rodi, 2009). The section line (A-B) and station JYP (green triangle) are displayed on the accompanying map. Only the JWM *P*-wave velocity is shown. Note that a separate color scale is used for the crust and mantle.

The second part of the exercise tested whether travel times through JWM can be approximated with linearization around AK135, using Equation (1) with v taken as the JWM velocity and v_{ref} taken as the AK135 velocity. The right panel of Figure 2 shows the difference between the P-L calculated times ("Nonlin.") and the AK135 linearized approximation ("Linear"). We see that the errors in the linearized times at regional distances are as high as 25 s. Much of this difference owes to the thick crust over much of the traverse. Therefore, large pieces of the AK135 Pn raypaths are incorrectly located within the JWM crust. While it might be possible to correct for this effect, or optimize the 1D model used to obtain the reference raypaths, the fact is that integrating a 3D velocity model along reference rays from a 1D model cannot accurately model *Pn* travel times through a complex, 3D Earth model. However, we also see that the linearized travel times are much more accurate for the longest *Pn* paths (beyond 14°), corresponding to rays bottoming between 210 and 410 km in the AK135 model, which are much less affected by crustal thickness variations. Figure 2 also shows that the linearized approximation at teleseismic distances is quite accurate. While some of the accuracy may owe to the use of AK135 to extend JWM to below the upper mantle, the result still bodes well for linearization as a fast and accurate method for computing travel times at larger epicentral distances. We plan to conduct many more such tests with JWM and other 3D Earth models, and with secondary arrivals in addition to first arrivals as just shown.

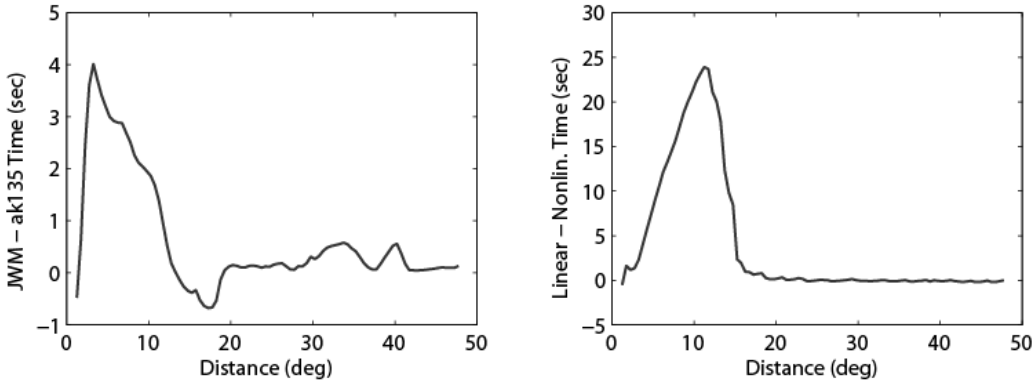

Figure 2. Experiments with regional and teleseismic travel-time calculation performed with model JWM. *Left*: Difference between calculated travel times for JWM and AK135. The JWM times were calculated with the Podvin-Lecomte (P-L) finite-difference algorithm. *Right*: Difference between calculated travel times from JWM, obtained two ways: "nonlinear" times obtained by the P-L method, and "linearized" times obtained by integrating the JWM slowness over AK135 raypaths. In both panels, times are plotted as a function of distance from JYP at an azimuth of N30°W.

Ray Bending Benchmark

Since the P-L method itself involves approximations and deals poorly with secondary arrivals, we have adapted a 3D raytracing procedure from Zhao et al. (1992) and Zhao and Lei (2004) as an alternative way to check the accuracy of travel-time calculations. This technique combines the pseudo-bending method for continuous media developed by Um and Thurber (1987) and refraction (Snell's law) at velocity discontinuities. The specific approach is outlined in Simmons et al. (these Proceedings). We find that the ray-bending approach is robust, always returning a travel time between two points in the Earth. There is no guarantee, however, that the bending method will converge to the minimum-time ray. We address this issue by testing a set of starting rays that span reasonable ray configurations. Using this approach, we have found that the ray bending method agrees with tauP calculations to within 0.01 s in spherically symmetric models and is in good agreement with finite-difference calculations in 3D models. Efficiency-wise, the ray bending is slow, taking approximately one second to compute a single travel time. This makes it impractical for routine use in an event locator run on commonly available computer platforms. However, the method is well suited as a benchmark for evaluating faster but less accurate methods.

Event Location with a 3D Model

The primary event locator we are using on this project is GMEL (Grid-search Multiple-Event Location), developed at MIT under previous projects and extended to 3D models in a previous joint project with Weston Geophysical (Reiter et al., 2001). GMEL uses travel-time predictions for either 1D reference velocity models or 3D reference models, using interpolation of pre-calculated tables in each case. A description of the numerical techniques used in GMEL is available in Rodi (2006). We are investigating the feasibility of replacing 3D table interpolation with "on-the-fly" linearized travel-time calculations for teleseismic phases, using Equation (1) with a 1D reference model. This entails incorporating into GMEL what we have built as stand-alone software for performing the linearization technique. This change to GMEL would avoid the need for pre-calculating and storing (on disk and in run-time memory) large 3D travel-time tables, each of which must contain travel times on a 3D hypocenter grid for a particular station and phase. Instead, only a single 3D Earth model, appropriate for all stations and phases, would be stored. A travel time calculation for a particular path and teleseismic phase would involve an on-demand tau-p calculation with the 1D reference model, followed by numerical integration to evaluate Equation (1). This will take more CPU time than a table interpolation but much less than the time needed for on-demand 3D raytracing. Furthermore, with much smaller memory requirements, the number of teleseismic phases GMEL can handle will increase. Whether this new version of GMEL will be sufficiently fast for routine use on a garden-variety computer remains to be seen since grid search typically tests 1000 or more hypocenter locations to find a solution.

Joint Regional/Teleseismic Tomography

The stand-alone 1D raytracer we have developed converts rays to travel-time sensitivities (partial derivatives) with respect to the same 3D velocity model parameterization we use in our regional tomography algorithm. The parameterization is described by Reiter and Rodi (2009). Moreover, the sensitivities are output in the same format as the regional travel-time sensitivities we generate with our extended Podvin-Lecomte algorithm. This provides an initial capability to perform joint regional/teleseismic travel-time calibration, a major goal of the project. The term "initial" alludes to several important enhancements that await our future efforts, as discussed later.

To test our initial joint calibration capability, we experimented with the updating of JWM through linearized tomography of combined data sets of regional and teleseismic *P*-wave travel times. The regional data set was identical to that used by Reiter and Rodi (2009) to construct JWM. Two teleseismic data sets were considered, both extracted from the EHB database, and both including arrivals only in the epicentral distance range 35° – 65°. In the first teleseismic data set (termed TelE), the stations were restricted to be located in or near the JWM study region, i.e. in the box 0°– 60° N, 30°– 120° E. The event locations were unrestricted (except for the distance criterion) and fell primarily outside this box. The second data set (TelS) restricted the events to be within the study box and accepted all stations obeying the distance criterion. The regional and both teleseismic data sets included only events which have EHB focal depths less than 200 km and which are deemed well-located in accordance with criteria described by Reiter and Rodi (2009). To reduce the size and redundancy of the data sets, individual events were lumped into summary events in the same manner as done for JWM. Each summary event is a node on a 0.5° geographic grid and variable depth grid. For a given station, the observed travel-time residual (relative to AK135) for a summary event is obtained by averaging the residuals for the individual events near the summary event. In

round numbers, teleseismic data set TelE contained 322,000 arrivals for 14,000 summary events and 800 stations, while TelS contained 278,000 arrivals for 3,700 summary events and 2500 stations. The regional data set contained 104,000 arrivals from 3700 summary events and 600 stations. More than 99% of the regional arrivals are the *Pn* phase, the rest being *Pg* or *Pb*. We point out that these data-set sizes approach the capacity of our current tomography software, which is why we considered teleseismic events and stations separately, and why we capped epicentral distances at 65°. Normally, linearized tomography is performed with a common reference model (v_{ref} in Equation (1)) for all data. Our tomography experiments used a different reference model for regional and teleseismic data: JWM for regional and AK135 for teleseismic. This is consistent with the necessity of doing 3D raytracing for regional travel-time calculation, and our proposed approximate modeling of teleseismic travel times with 1D reference rays.

Figure 3 shows a vertical slice through each of two joint regional/teleseismic tomography models, corresponding to the two versions of the teleseismic data set that were combined with the common regional data set. The model obtained with TelE as the teleseismic data set is labeled JWM_TelE, and the other is labeled JWM_TelS. We see that the models are quite similar to each other, and are not starkly different from JWM, for which the same slice was shown in Figure 1. The largest differences from JWM occur at depths below 200 km, where the *P* velocity is significantly slower. This is more easily seen in Figure 4, which displays the velocity deviation of the two regional/teleseismic inversion models relative to JWM.

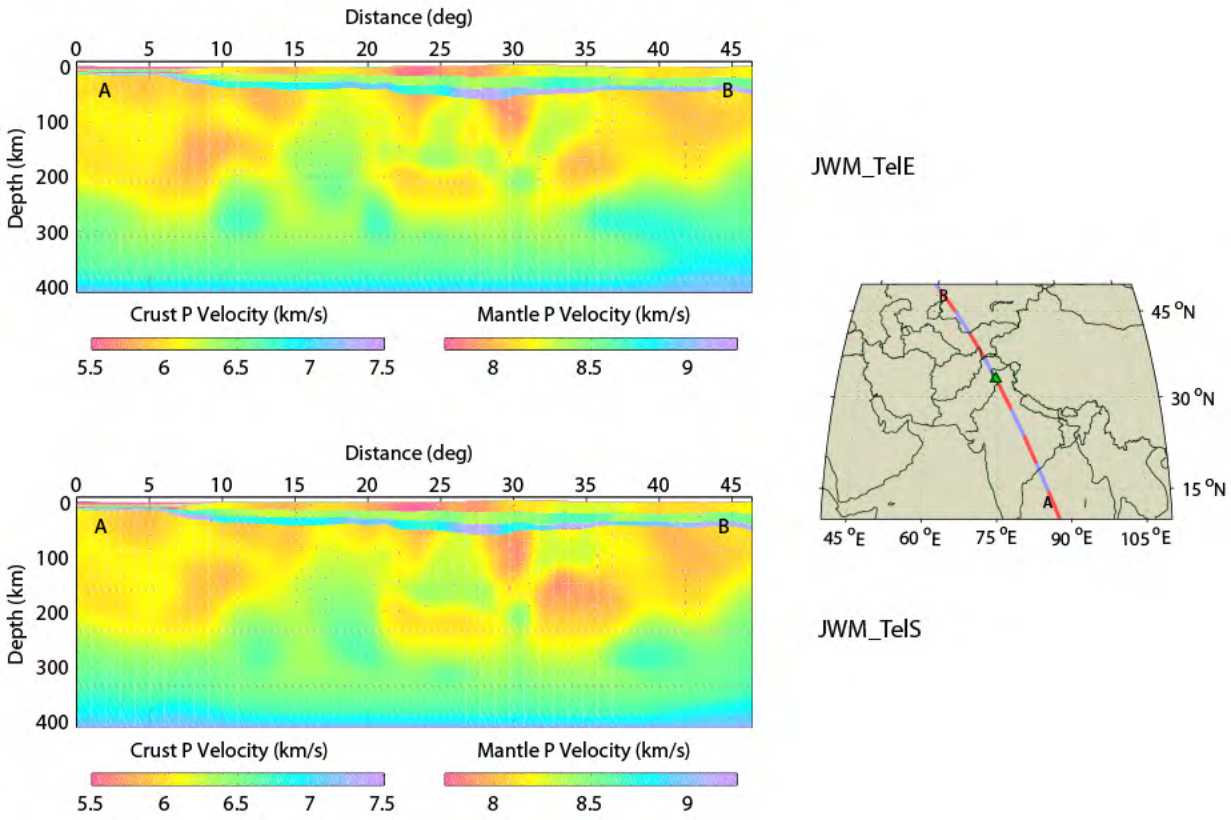

Figure 3. A vertical section through two 3D *P* velocity models obtained by joint inversion of regional and teleseismic *P*-wave travel times. The model shown at the top (JWM_TelE) used teleseismic data from local stations and teleseismic events, while the model shown at the bottom (JWM_TelS) used teleseismic data from local events and teleseismic stations. The regional data were the same in both cases and are from stations and events inside the model region.

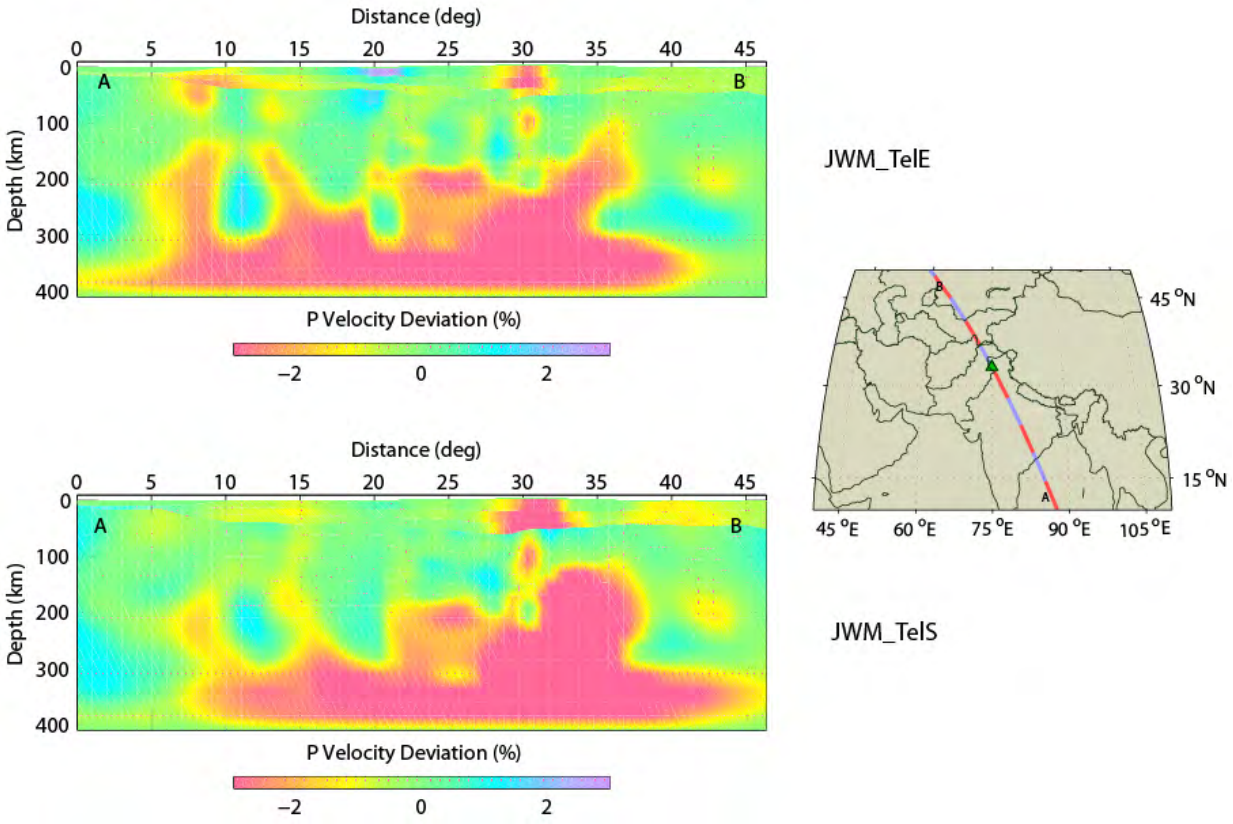

Figure 4. The inversion models shown in Figure 3 are displayed as velocity deviations from model JWM.

The reason for the lower mantle velocities in the joint regional/teleseismic models is clear if we compare their travel-time residuals to those of JWM. The comparison is quite similar for the two joint models, so we show it only for JWM_TelE. Figure 5 displays separate histograms of regional (left) and teleseismic (right) residuals, for each of the models JWM (blue lines) and JWM_TelE (red lines). We see that JWM yields regional residuals with a mean near zero but teleseismic residuals with a mean of about 1.5 s. JWM_TelE maintains the unbiased fit to the regional data and yields zero-mean teleseismic residuals as well. Apparently, the joint regional tomography removed the teleseismic travel-time bias of JWM by lowering the *P* velocity below 200 km depth, in a way that preserved the fit to the *Pn* data. Figure 6 displays the residual statistics for both models as a function of epicentral distance.

CONCLUSIONS AND RECOMMENDATIONS

In our first year we have begun acquiring and developing the tools needed to perform event location with regional and teleseismic data using a unified 3D Earth model, calibrated with both types of data, as the basis for travel-time prediction. We also began testing the effectiveness of joint regional/teleseismic tomography as a method for travel-time calibration. These initial tests involved the incorporation of teleseismic constraints to update a model of southern Asia, JWM, which had been constructed from regional *P*-wave times and surface-wave dispersion data. The tests yielded promising results in that the joint tomography preserved the fit to the regional travel-time data while removing JWM's teleseismic bias. However, these initial tests ignored several important issues that our future work will address. Among them are the effects of Earth structure below 410 km and outside our study region, which we ignored by restricting the model parameterization to that used to develop JWM. Further, we did not address the effects of event mislocations and the possible need to relocate events as part of the calibration analysis. We have also not properly validated the approximate teleseismic modeling used to obtain these results (linearization with respect to AK135 rays). Finally, our tests were limited by the unfinished status of our tomography algorithms, which are aimed toward nonlinear inversion of regional data (iteratively updating of *Pn* rays) and the incorporation of secondary teleseismic phases, among other features. Our second year's effort will

pursue these improvements in concert with the enhancement of our 3D event location capabilities, and continued testing and evaluation of 3D raytracing algorithms.

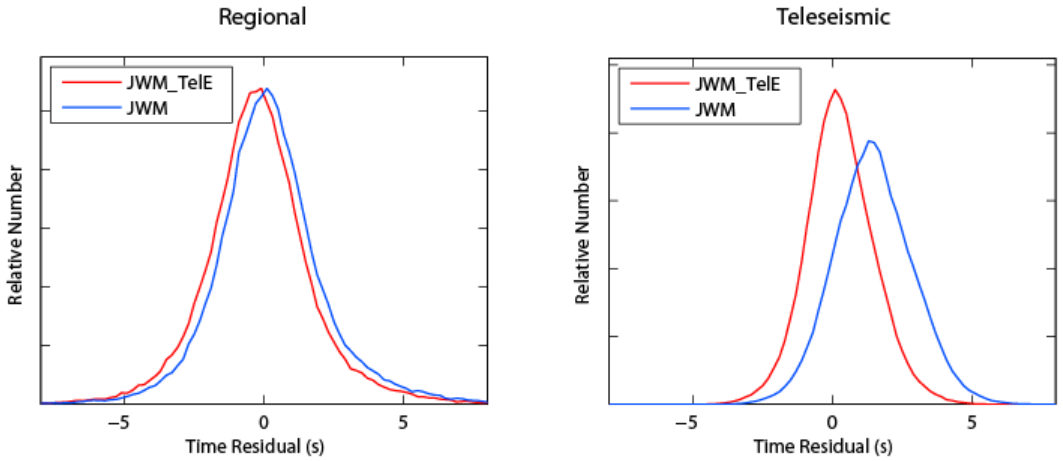

Figure 5. Distributions of regional (left) and teleseismic (right) travel-time residuals for model JWM (blue lines) and model JWM_TelE (red lines). For model JWM, the RMS residual is 2.0 s for both the regional and teleseismic data. For JWM_TelE, the RMS is 2.0 s for regional data and 1.3 s for teleseismic data.

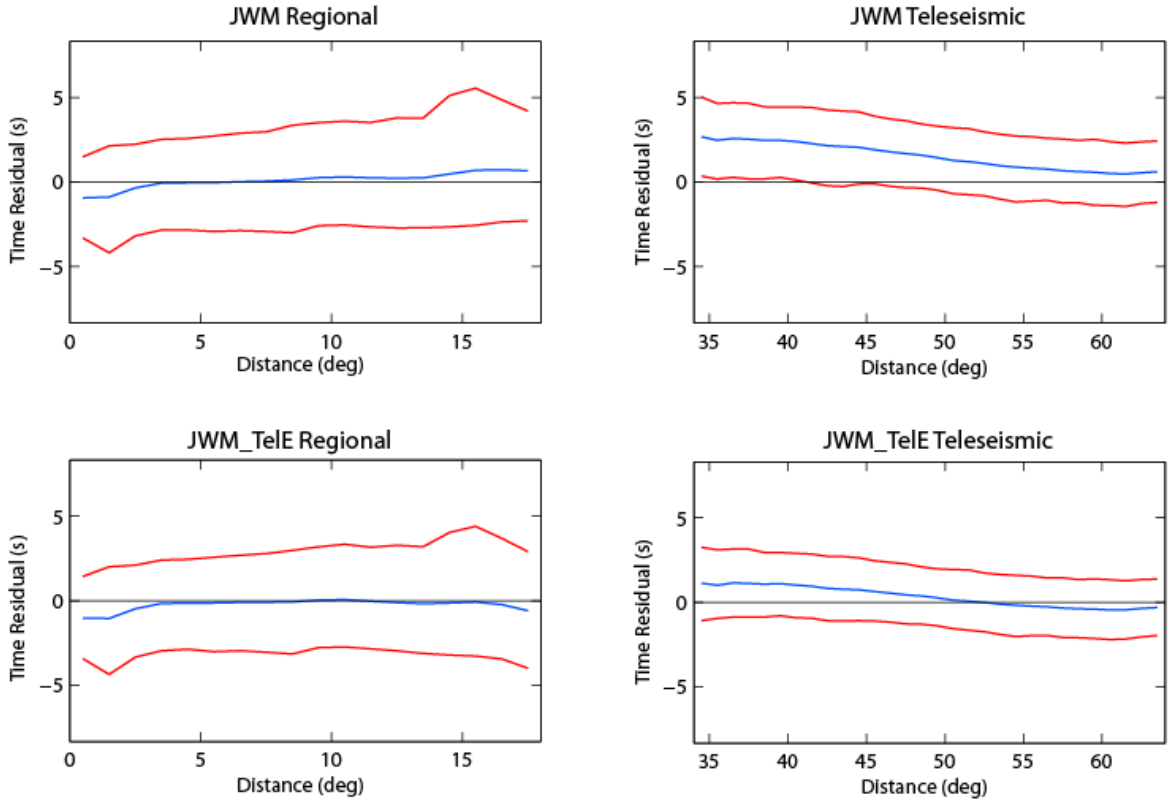

Figure 6. Travel-time residual statistics for models JWM and JWM_TelE, plotted as a function of 1° epicentral distance bins. The blue lines trace the mean residual in each bin; red lines show the 0.05 and 0.95 points (central 90%) of the residual distribution in each bin.

REFERENCES

Antolik, M., Y. J. Gu, G. Ekström, and A. M. Dziewonski (2003). J362D28: a new joint model of compressional and shear velocity in the Earth's mantle, *Geophys. J. Int.* 153: 2, 443–466.

Buland, R., and C. H. Chapman (1983). The computation of seismic travel times, *Bull. Seismol. Soc. Am*. 73: 1271–1302.

Engdahl E. R., R. van der Hilst, and R. Buland (1998). Global teleseismic earthquake relocation with improved travel times and procedures for depth determination, *Bull. Seismol. Soc. Am*. 88: 722–743.

Kennett, B. L. N., E. R. Engdahl and R. Buland (1995). Constraints on the velocity structure in the Earth from travel times, *Geophys. J. Int.* 122: 108–124.

Li, C., R. D. van der Hilst, and M. N. Toksöz (2006). Constraining *P*-wave velocity variations in the upper mantle beneath Southeast Asia, *Phys. Earth Planet. Int.* 154: 180–195.

Li, C., R. D. van der Hilst, E. R. Engdahl, and S. Burdick (2008). A new global model for *P*-wavespeed variations in Earth's mantle, *Geochemistry, Geophysics, Geosystems* 9: Q05018, doi:10.1029/2007GC001806.

Lomax, A., J. Virieux, P. Volant, and C. Berge (2000). Probabilistic earthquake location in 3D and layered models: Introduction of a Metropolis-Gibbs method and comparison with linear locations, in *Advances in Seismic Event Location*, Thurber, C.H., and N. Rabinowitz (eds.), Kluwer, Amsterdam, 101–134.

Müller, G. (1971). Exact ray theory and its application to the reflection of elastic waves from vertically inhomogeneous media, *Geophys. J. R. Astr. Soc.* 21: 261–283.

Murphy, J. R., W. Rodi, M. Johnson, D. D. Sultanov, T. J. Bennett, M. N. Toksöz, V. Ovtchinnikov, B. W. Barker, D. T. Reiter, A. C. Rosca, and Y. Shchukin (2005). Calibration of International Monitoring System (IMS) stations in central and eastern Asia for improved seismic event location, *Bull. Seismol. Soc. Am*. 95: 1535–1560.

Pasyanos. M. E., W. R. Walter and M. P. Flanagan (2004). Building and testing an a priori geophysical model for Western Eurasia and North Africa, *Pure Appl. Geophys.* 161: 235–281.

Podvin, P. and I. Lecomte (1991). Finite difference computation of traveltimes in very contrasted velocity models: a massively parallel approach and its associated tools, *Geophys. J. Int.* 105: 271–284.

Reiter, D. T. and W. L. Rodi (2009). Validated 3D velocity models in Asia from joint regional body- and surface-wave tomography. Final Report, *Weston Geophysical Corporation*, AFRL-RV-HA-TR-2009-1009.

Reiter, D., W. Rodi and M. Johnson (2005). Development of a tomographic upper mantle velocity model beneath Pakistan and northern India for improved regional seismic event location, *Bull. Seismol. Soc. Am*. 95: 926–940.

Reiter, D., C. Vincent, M. Johnson, A. Rosca and W. Rodi (2001). Methods of improving regional seismic event locations, in *Proceedings of the 23rd Seismic Research Review*: *Worldwide Monitoring of Nuclear Explosions,* LA-UR-01-4454, Vol. 1, pp. 298–304.

Ritzwoller, M. H., N. M. Shapiro, M. P. Barmin and A. L. Levshin (2002). Global surface wave diffraction tomography, *J. Geophys. Res*. 107: doi: 10.1029/2002JB001777.

Rodi, W. (2006). Grid-search event location with non-Gaussian error models, *Phys. Earth. Planet. Int.* 158: 55–66.

Ryaboy, V., D. R. Baumgardt, P. Firbas, and A. M. Dainty (2001). Application of 3-D crustal and upper mantle velocity model of North America for location of regional seismic events, *Pure and Appl. Geophys*. 158: 79–103.

Simmons, N. A., S. C. Myers and A. Ramirez (2009). Multi-resolution seismic tomography based on recursive tessellation hierarchy, these Proceedings.

Um, J. and C. H. Thurber (1987). A fast algorithm for two-point seismic ray tracing, *Bull. Seismol. Soc. Am*. 77: 972–986.

van der Hilst, R. D., S. Widyantoro and E. R. Engdahl (1997). Evidence for deep mantle circulation from global tomography, *Nature* 386: 578–584.

Yang, X. P., I. Bondar, J. Bhattacharyya, M. Ritzwoller, N. Shapiro, M. Antolik, G. Ekström, H. Israelsson, and K. McLaughlin (2004). Validation of regional and teleseismic travel-time models by relocating ground-truth events, *Bull. Seismol. Soc. Am.* 94: 897–919.

Zhao, D., A. Hasegawa and S. Horiuchi (1992). Tomographic imaging of *P* and *S* wave velocity structure beneath Northeastern Japan, *J. Geophys. Res*. 97: B13, 19,909–19,928.

Zhao, D. and J. Lei (2004). Seismic ray path variations in a 3D global velocity model, *Phys. Earth Planet. Int*. 141: 153–166.

VALIDATING 3D GEOPHYSICAL MODELS FOR USE IN GLOBAL TRAVEL-TIME CALCULATION FOR IMPROVED EVENT LOCATIONS

Charlotte A. Rowe[1], Sanford Ballard[2], Michael L. Begnaud[1], Christopher J. Young[2], Lee K. Steck[1], and James R. Hipp[2]

Los Alamos National Laboratory[1] and Sandia National Laboratories[2]

Sponsored by the National Nuclear Security Administration

Award Nos. DE-AC52-06NA25396/LA09-IRP-NDD02[1] and DE-AC04-94AL8500/SL09-3D-Earth-NDD02[2]

ABSTRACT

Towards developing a fully global, seamless travel-time calculation and event location capability, we evaluate existing 3D velocity models to test their ability to correctly predict travel times for ground-truth (GT) data. We have identified 513 GT5 or better events within the Los Alamos National Laboratory (LANL) seismic database, which provide us with 58,970 arrivals for our study.

We first verify that calculated travel times through our global, 3D ellipsoidal parameterization of the AK135 model are within our tolerance of 0.2 s to Tau-P predictions. Subsequently, we compare observed teleseismic P-wave travel times for our GT dataset to those predicted by dynamic ray tracing through a variety of crustal models superimposed on an AK135 mantle. These models were developed either through ad hoc combination of regional models, or through fitting of straight-ray propagation through a Cartesian system with smoothing over 1 to 3 degree grids. We examine the improvement to travel-time predictions for these models compared to the AK135 alone.

We next examine a recently published 3D, global mantle model (MITP08). This model was developed by inverting travel-time residuals along fixed rays for an AK135 model, with a Crust2.0 correction. When we adhere to the AK135 ray paths to calculate our GT event residuals, we find that the MITP08 model provides significant improvement to travel-time prediction compared to other models tested to date. Not surprisingly, when we calculate the travel times using dynamic rays, the performance is poorer.

GT travel times are best predicted through any given model when the calculation is performed using a method close to that used in generation of the model, as expected. Such considerations as Earth ellipticity correction, fixed ray vs. dynamic ray tracing, crustal corrections (for mantle models) and mantle values (for crustal models) need to be applied appropriately for a fair evaluation. Conversely, any model made available to the community is of little practical use unless the method of its derivation is also provided, or clearly explained so that it may be replicated for travel-time calculation and location procedures. Due to the existing heterogeneity in models and their methods of derivation, we conclude that towards our development of a seamless, global model and locator, existing models may best serve as starting models for a global inversion using a single, consistent ray tracing and travel-time calculation approach.

OBJECTIVES

The nuclear monitoring community strives to continually improve its ability to estimate seismic event locations and associated uncertainties through a variety of means. Nonlinear location algorithms, relative event relocation, waveform matching, and a plethora of seismic velocity models have all been applied to the problem over many years. The fundamental goal critical to obtaining better locations is the ability to better predict seismic phase travel times through the earth. Thus the creation of improved seismic velocity models is of paramount importance to solving the problem, yet the models themselves are of little use to the monitoring community if their derivation and method of travel-time fitting are not also available.

For many practical reasons, individual research groups often focus only on a particular region when producing their models, and these models are often not tested in a fully global paradigm due either to the incompatibility of their methods (small regions modeled in Cartesian systems, fixed great-circle paths assuming horizontal propagation, and so forth). It is our assertion that for truly robust and comprehensive location capability, the monitoring community must move towards fully integrated, global 3D models capable of fitting all types of observables (phases) that may be recorded and reported for seismic events. The model will be seamless, and no *ad hoc* switching among models (local to regional to teleseismic) should be employed within the location algorithm.

In concert with the global ray bending development of Sandia National Laboratories (Ballard et al., 2009), we begin testing the travel-time prediction capabilities of various models delivered to the monitoring community and we explore the adjustments required to incorporate these models into the fully elliptical whole-earth structure.

RESEARCH ACCOMPLISHED

Validation Dataset

To explore the travel-time prediction capabilities of test models, we have compiled a catalog of travel times for 513 events in the LANL Ground-Based Nuclear Explosion Monitoring database (Begnaud et al., 2004; Begnaud, 2005), which comply with a Ground Truth (GT) level (Bondár et al., 2004) of less than 5 km. Sources at this GT level are largely man-made, and are comprised of both chemical and nuclear explosions, including the Peaceful Nuclear Explosions (PNE's) recorded during the U.S.S.R. Deep Seismic Sounding (DSS) campaigns (Morosov et al., 2005). Sixty-seven very well-located earthquakes are also included. We report on preliminary tests using this dataset, whose initial examination is applied to teleseismic *P* arrivals. Figure 1 shows the ray coverage for Eurasia for the 58,970 source-receiver *P*-arrival pairs that we include in our study.

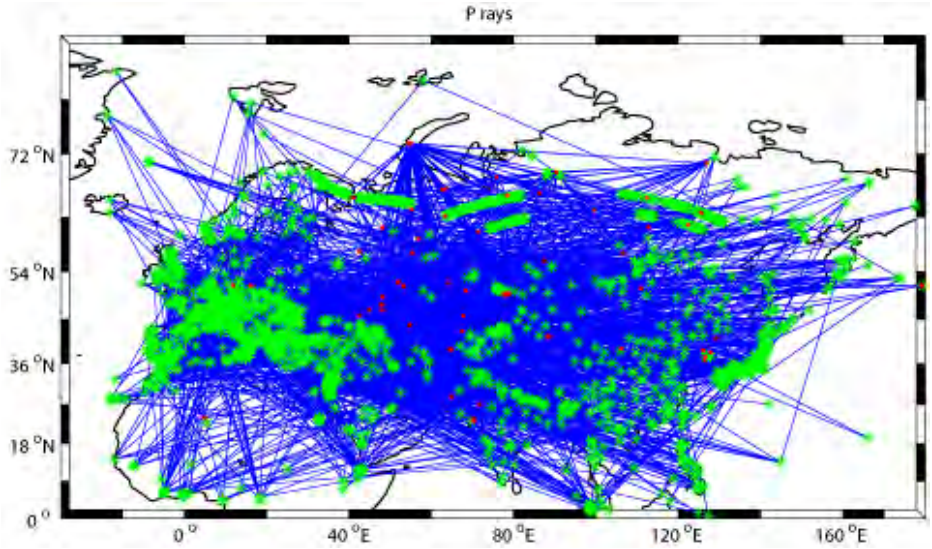

Figure 1. 58,970 *P*-wave paths in our validation dataset of 513 events of GT5 and less (Begnaud et al., 2004; Begnaud, 2005). Sources are shown as green asterisks; receivers as small red dots.

Test Models

We first explore the application of the ray bender to an elliptical representation of the standard AK135 (Kennett et al., 1995) model in our global, tessellated parameterization. We compare the calculated travel times through this model with those derived using TauP (Buland and Chapman, 1983; Crotwell et al., 1999). We then demonstrate the variations in these residuals from a global AK135 model that has had its crustal layers replaced by Crust2.0 (Bassin et al., 2000), a global crustal model generated at two-degree grid spacing using a variety of available sources: seismic tomography results, analyses from refraction profiles, and some assumptions derived from other topographic, geological and geophysical parameters. We then will examine the MITP08 model, which is a three-dimensional, global mantle model recently published by Li et al. (2008).

AK135

We begin with a simple test to validate the ray bender results in an AK135 model that has been parameterized in our global tessellation method, with ellipticity included in the model geometry (an oblate spheroid). The travel-time residuals we calculate in this model are compared against residuals calculated using the standard TauP Toolkit (Kennett and Gudmundsson, 1996) for source and receiver pairs, to ascertain how closely our travel-time calculations match the standard 1D approach currently in use. The TauP Toolkit results are corrected for ellipticity using the standard ellipticity corrections (Dziewonski and Gilbert, 1976; Kennett and Gudmundsson, 1996).

For teleseismic *P*-wave arrivals, the median difference between the 3D ray bender and TauP estimations (Figure 2) is 0.135 s, with a standard deviation of 0.0505 s. These differences are within our tolerances of 0.2 s, which gives us confidence in the bender results for *P* arrivals. Some minor differences are inevitable due to the parameterization of the model tessellation and geometry of the ray bending.

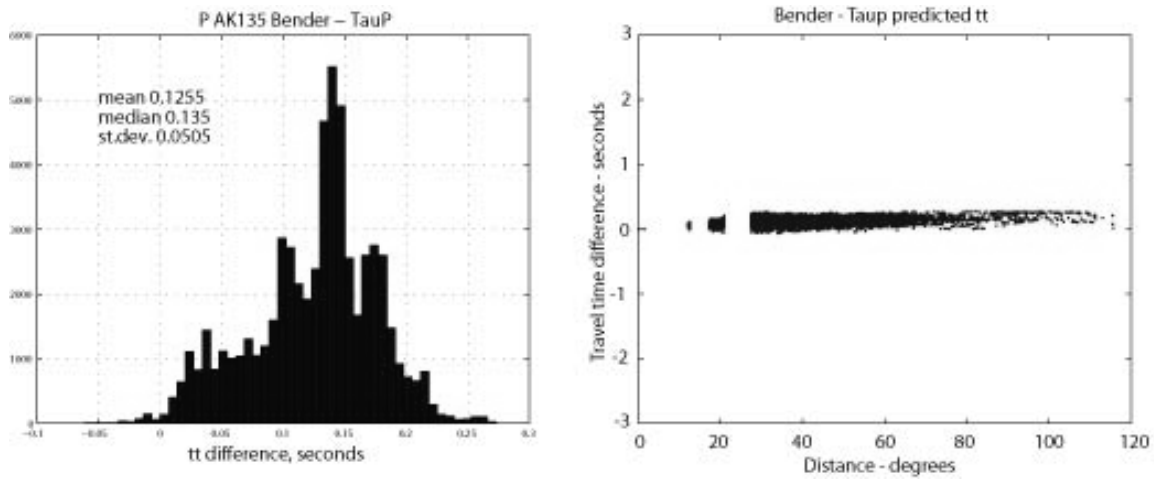

Figure 2. Ray bender calculated travel times for the GT dataset minus TauP calculated travel times for *P* (teleseismic) arrivals. Calculations performed using the AK135 earth model. Left: histogram of travel-time differences, with statistics. Right: travel-time differences as a function of distance.

Crustal 3D models over AK135

A preliminary examination of available regional crustal models superimposed on an AK135 core and mantle are compared to the globally averaged AK135 to explore the improvements to teleseismic *P* travel times that can be realized with some accommodation for the known variability in the crust. We recognize that any effect will be most pronounced in dealing with *Pn* and *Pg* phases, as teleseismic arrivals will have spent most of their time in the mantle. Our preliminary analysis is shown in Figure 3, in which we present the difference between predicted and observed travel times for our 58,970 arrivals in the GT dataset when we substitute crustal velocities of the AK135 with the Crust 2.0 model of Laske and Masters (1997), with the crustal *P*-velocity model of Sun et al. (2004) and the

crustal *P*-wave values found in the DoE Unified model (Begnaud et al., 2004; Flanagan et al., 2007; Pasyanos et al., 2004). The figure presents histograms of the travel time differences for each case, along with the mean, median and standard deviations. It is immediately clear that the poorest performance is found with the simple AK135 model. Much of the problem may lie in mantle variation that is unaccounted for in this 1D radially symmetric model; however, some of the travel-time residuals are no doubt the result of its failure to account for crustal variations.

For our GT dataset, the mean *P*-arrival residual for an AK135 model is 0.3796 s, with a median of 0.478 and a standard deviation of 1.6824 (Figure 3a). Figure 3b presents the results for an AK135 model whose outermost layers and Moho depths have been replaced by the Crust 2.0 values. We see an improvement over AK135 of better than 50%, with a mean residual of 0.1437 s, a median of 0.219 and standard deviation slightly improved at 1.6786, suggesting slightly fewer outliers. The Sun et al. (2004) China crustal model (Figure 3c) embedded in a Crust 2.0 outer layer over AK135 reduces the AK135 values somewhat from a mean of 0.3796 to 0.3384, a median from 0.478 to 0.402 and standard deviation of 1.6824 to 1.6721. We note that some of our rays may not be representative of the Sun et al. model's influence alone, as it is only valid for China, whereas our data cover Eurasia; thus, a more accurate analysis will require a study restricting data to that region.

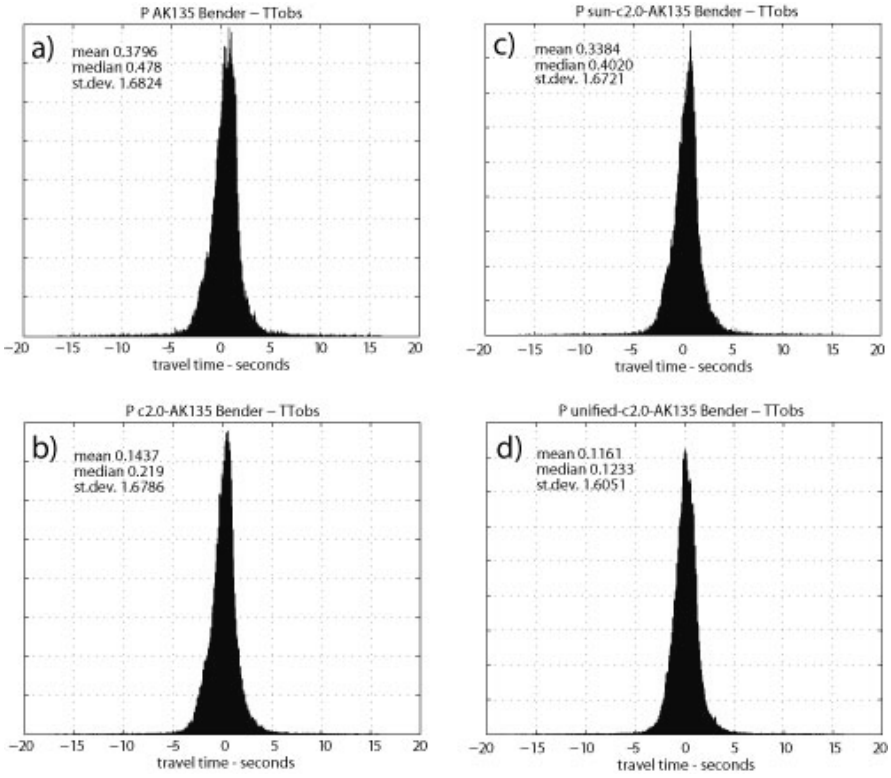

Figure 3. Predicted minus observed travel times for *P* waves using four models: a) AK135; b) Crust 2.0 overlying AK135; c) Sun et al. (2004) embedded in Crust 2.0 over AK135; and d) DOE Unified model embedded in Crust 2.0 over AK135.

Finally, modeling the *P* rays through an AK135 mantle and core overlain by Crust 2.0 with the DoE Unified Model gives rise to a reduction from AK135 for travel-time residuals as follows (Figure 3d): mean from 0.3796 to 0.1161, median from 0.478 to 0.1233 and standard deviation from 1.6824 to 1.6051. Among these models it appears that the Unified Model exhibits the sharpest reduction in residual for our GT dataset for *P* waves.

Mantle Model

We explore the improvements possible in our travel-time calculations by employing a fully three-dimensional, global P-wave model for the Earth's mantle, whose known variability is not addressed in the AK135 earth model. Li et al. (2008) have devised such a mantle model, which we test against the GT dataset travel times in our 3D tessellated parameterization. This seismic velocity model was developed to image in as much detail as possible the

tectonic variations in the Earth's mantle as a whole. The model has succeeded in revealing a number of interesting yet not unexpected mantle features, including subduction zones.

Figure 4 illustrates the details of mantle structure obtained in this model, in a series of cross-sections through Western Pacific subduction zones. We are keenly interested in adopting such a model in our global 3D location algorithm to replace the AK135 or iasp91 (Kennett and Engdahl, 1991) default models used in routine location practice, for seismic phases that pass through mantle depths between source and receiver. Appropriate use of the model is needed, however.

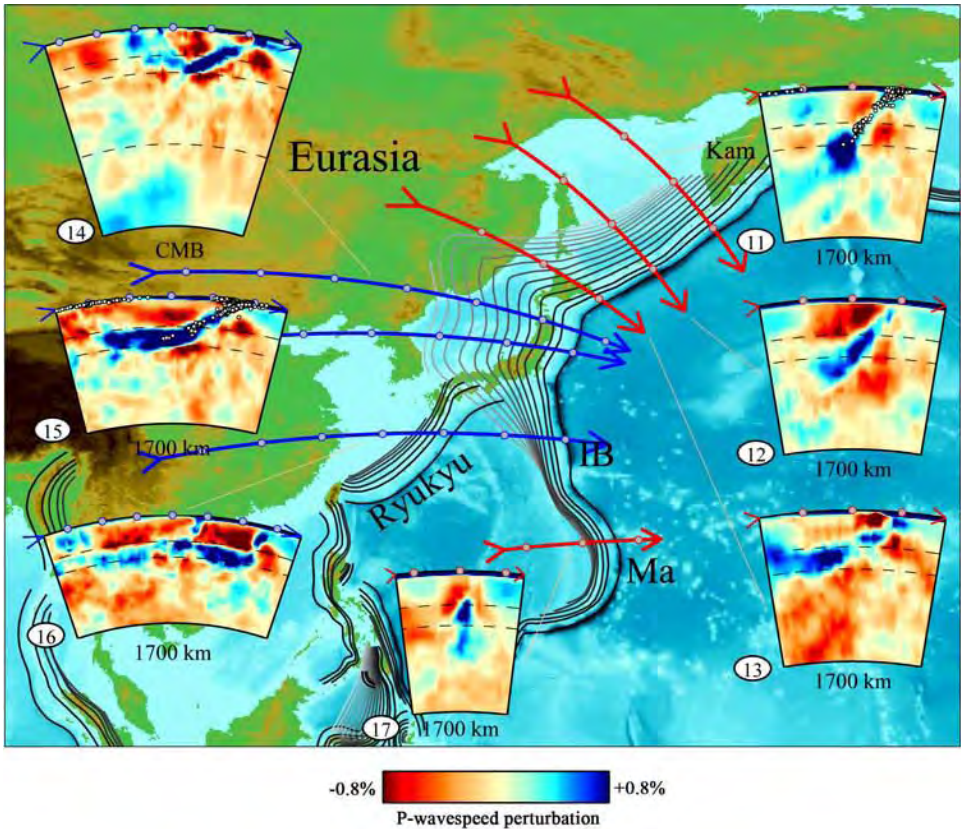

Figure 4. Selected cross-sections of mantle *P*-wave velocity variation across Western Pacific subduction zones (from Li et al., 2008).

Through discussions with the authors we have determined that the following considerations must be accommodated:

- The model was derived by calculating rays for source-receiver pairs through an AK135 earth model then inverting for mantle slowness variations by integrating along these fixed rays.
- Crustal variations were removed by assuming that Crust2.0 (Laske et al., 2001) perturbations account for travel-time variations for the rays passing through the crust.
- Ellipticity corrections were applied to the assumed rays after tracing.

The ray tracing algorithm we are using (Ballard et al., 2009) employs dynamic rays by default, so we needed to modify the code so that a requirement for fixed AK135 rays could be applied to testing of the MITP08 model. We built a 3D global model consisting of AK135 for inner and outer core, MITP08 mantle and fixed crustal corrections at all geographic points based on assumed travel-time through Crust2.0. We applied the ray bending algorithm to calculate travel times along the fixed AK135 rays integrated through our tessellated parameterization of the MITP08

model, and we examine the residuals between these predicted travel times and observed travel times for our test dataset.

In Figure 5, we show differences between observed and predicted *P*-wave arrivals for our GT dataset, to compare the performance of the MITP08 global mantle model for two different calculation methods: dynamic rays (left panel) and fixed AK135 rays (right panel). Both mean and median travel-time predictions are approximately five times better when using the fixed rays, as applied in the tomographic inversion by Li et al. (2008) when developing the model. Travel-time standard deviations are roughly equal in both applications.

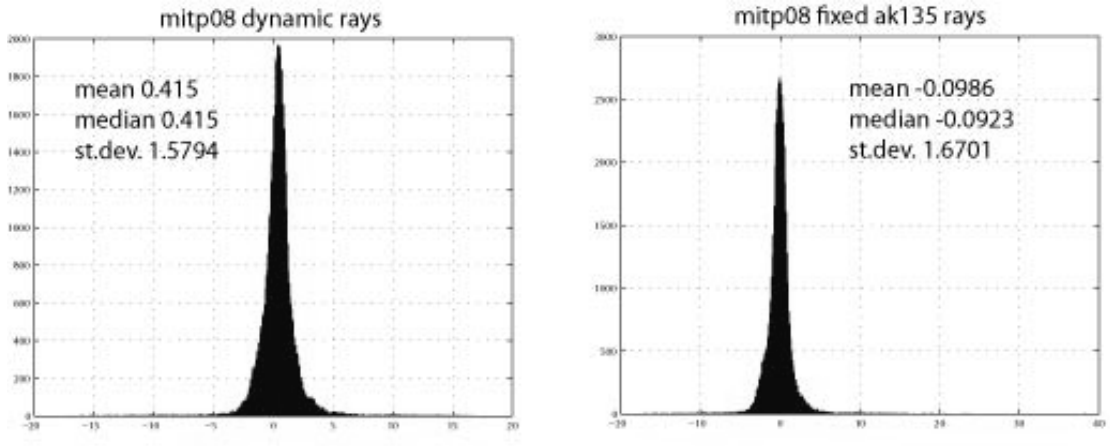

Figure 5. Comparison of performance of MITP08 global mantle model for *P* waves using the ray bender. Left panel: predicted travel times using dynamic ray bending. Right panel: predicted travel times using fixed AK135 rays.

Discussion

For teleseismic *P* waves we see that the use of a three-dimensional, variable crustal model over the standard AK135 model reduces the travel-time residuals compared to those computed through only AK135. This result is not unexpected and has been traditionally corrected for using station-centered correction surfaces that accommodate not only path residuals from the crust but also from mantle variations. Through our exploration of three crustal models available to us, we note sometimes significant reduction in residual. We note here that in all three cases, the crustal models are being used in a manner inconsistent with their derivation, so optimal performance is not expected. In the case of the Crust 2.0 and Unified models, velocities were estimated based on information from a variety of sources and these models cannot be said to have been data-driven. For example, the Unified model arose from literature searches, local tomography results, refraction profile, and was pieced together as a patchwork of broad, terrain-based, one-dimensional models which were smoothed at the terrain boundaries. The Sun et al. model was generated in a Cartesian system with no corrections for sphericity or ellipticity. Velocities were determined at each grid point over a 1 degree grid by a Monte Carlo search within prescribed velocity ranges for raypaths contained within one to three degrees of each grid point, providing implicit smoothing. Although the ranges over which seismic travel times were averaged are small enough to argue that earth curvature corrections were unnecessary, we have parameterized it in an ellipsoidal, triangular tessellation and we apply dynamic raytracing through it, which is inconsistent with its derivation; thus optimal results are not expected. The improvement demonstrated in the *P*-wave travel times for all our crustal examples are thus in some ways inevitable simply because the models must necessarily come closer to the true velocities compared to the globally averaged AK135 values, but in none of these cases can we be certain that the models are optimal for direct application to our location problem with our travel-time calculation method.

Examining mantle models, we have compared the residuals for predicted minus observed travel times both when using a model blindly and also using it appropriately for the manner in which it was derived. The MITP08 model was parameterized in our global, 3D tessellation. We then calculated travel times for teleseismic *P* waves using our default: dynamic ray bending. Clearly, based on Figure 5a, use of the model in this fashion does not provide good

results. In fact, AK135 alone does nearly as well (see Figure 4a) and the Crust2.0 over AK135 performs noticeably better (Figure 4b). Use of the dynamic ray tracing, however, is inappropriate for calculating travel times through this MITP08 model, given that the velocity perturbations in the model were obtained with respect to fixed rays through an AK135 model. We therefore apply the travel-time calculation to our GT dataset through the MITP08 model using fixed rays and obtain a mean residual of -0.0986 seconds, with a median of -0.0923. This is approximately 20% improvement over the Unified model results.

CONCLUSIONS AND RECOMMENDATIONS

In our preliminary tests of the ray bender in the 3D global tessellated application, we have validated the predicted travel times compared to standard, 1D TauP travel-time predictions for our GT dataset. We have explored the influence on teleseismic *P* waves of 3D crustal models, and we find that they provide added value to the reliability of travel-time predictions, although their improvements vary and their methods of development are not necessarily consistent with the manner in which we will be using them. We find that for models such as the MITP08, it is crucial for operational travel-time prediction that we apply this model using methods appropriate to the manner in which it was developed. Inappropriate use of the model, however, results in poorer performance. Because researchers use a variety of methods in developing their models to image mantle and lithospheric structure, we cannot expect uniform performance of models obtained as deliverables on DOE/AFRL contracts, using a single travel-time calculation method.

This raises questions regarding the usefulness of models developed for the monitoring community. Routine event location will ultimately be performed with a single, global 3D model, but the model must be appropriate for the method in which the seismic travel times will be calculated for location. We conclude that the many models being provided by the community can best be tested and validated only if their methods of derivation are provided with the models; even in cases where all the information is available, the best of these models may not be optimal as-is for implementation in routine travel-time calculation. We propose that the best global, 3D model for routine event location will be one that is derived using identical travel-time estimation to that in the location algorithm, using the best of the models from the monitoring community as starting models for this inversion.

ACKNOWLEDGEMENTS

We thank R. Van der Hilst at Massachusetts Institute of Technology for helpful discussions.

REFERENCES

Ballard, S., J.R. Hipp and C.J. Young (2009). Efficient and accurate calculation of ray theory seismic travel time through variable-resolution, 3D Earth models. *Seismol. Res. Lett.*, in press.

Bassin, C., G. Laske, and G. Masters (2000). The current limits of resolution for surface wave tomography in North America, *Eos, Trans. AGU* 81, F897.

Begnaud, M. L., C. A. Rowe, and L. K. Steck (2004). Validating three-dimensional velocity models in China and East-Asia for use in regional seismic event location, *Eos Trans. AGU* 85, 47, Fall Meet. Suppl., T11C-1277.

Begnaud, M. L. (2005). Using a dedicated location database to enhance the gathering of ground truth information, *Los Alamos National Laboratory* LA-UR-04-5992, 22 pp.

Bondár, I., S. C. Myers, E. R. Engdahl, and E. A. Bergman (2004). Epicentre accuracy based on seismic network criteria, *Geophys. J. Int.* 156: 483–496.

Buland, R., and C. H. Chapman (1983). The computation of seismic travel times, *Bull. Seismol. Soc. Am.* 73: 1271–1302.

Crotwell, H.P., T.J. Owens, and J. Ritsema (1999). The TauP toolkit: flexible seismic travel-time and ray-path utilities, *Seismol. Res. Lett*. 70: 154–160.

Dziewonski, A. M., and F. Gilbert (1976). The effect of small, aspherical perturbations on travel times and a re-examination of corrections for ellipticity. *Geophys. J. R. Astro. Soc*. 44: 7–17.

Flanagan, M. P., S. C. Myers, and K. D. Koper (2007). Regional travel-time uncertainty and seismic location improvement using a three-dimensional a priori velocity model, *Bull. Seismol. Soc. Am.* 97: 804–825.

Kennett, B. L. N., and E. R. Engdahl (1991). Travel times for global earthquake location and phase identification, *Geophys. J. Int.* 105**:** 429–465.

Kennett, B. L. N., E. R. Engdahl, and R. Buland (1995). Constraints on seismic velocities in the Earth from travel times, *Geophys. J. Int.* 122: 108–124.

Kennett, B. L. N. and O. Gudmundsson (1996). Ellipticity corrections for seismic phases, *Geophys. J. Int*. 127 40–48.

Laske, G. and T.G. Masters (1997). A global digital map of sediment thickness, *EOS Trans. AGU* 78; F483.

Laske, G., G. Masters and C. Reif (2001). CRUST 2.0: A New Global Crustal Model at 2x2 Degrees, http://igppweb.ucsd.edu/~gabi/rem.dir/crust/crust2.html

Li, C., R. D. van der Hilst, E. R. Engdahl, and S. Burdick (2008). A new global model for *P*-wave speed variations in Earth's mantle, *Geochemistry, Geophysics, Geosystems* 9: Q05018, doi:10.1029/2007GC001806.

Morosov, I.B., E.A. Morozova, S. B. Smithson and I. N. Kadurin (2005). Nuclear explosion profiles for seismic calibration of northern Eurasia, in *Proceedings of the 27th Seismic Research Review: Ground-Based Nuclear Explosion Monitoring Technologies*, LA-UR-05-6407, Vo1. 1, pp. 98–103.

Pasyanos, M. E., W. Walter, R., M. P. Flanagan, P. Goldstein, and J. Bhattacharyya (2004). Building and testing an a priori geophysical model for western Eurasia and North Africa, *PAGEOPH* 161, 235–281.

Sun, Y., L. Xu, S. Kuleli, F.D. Morgan and M.N. Toksoz (2004). Adaptive moving window method for 3D P-velocity tomography and its application to China. *Bull. Seismol. Soc. Am*. 94: 740–746.

Seismic Identification and Source Characterization

SEISMIC SOURCE SCALING AND DISCRIMINATION IN DIVERSE TECTONIC ENVIRONMENTS

Rachel E. Abercrombie[1], Kevin M. Mayeda[2], William R. Walter[3], Gisela M. Viegas[1], and Rengin Gök[3]

Boston University[1], Weston Geophysical Corporation[2], and Lawrence Livermore National Laboratories[3]

Sponsored by the Air Force Research Laboratory

Award No. FA8718-06-C-0024.
Proposal No. BAA06-70

ABSTRACT

The objectives of this study are to improve low-magnitude (concentrating on M2.5-5) regional seismic discrimination by performing a thorough investigation of earthquake source scaling using diverse, high-quality datasets from varied tectonic regions. Local-to-regional high-frequency discrimination requires an estimate of how earthquakes scale with size. Walter and Taylor (2001) developed the Magnitude and Distance Amplitude Corrections (MDAC) method to empirically account for these effects through regional calibration. The accuracy of these corrections has a direct impact on our ability to identify clandestine explosions in the broad regional areas characterized by low seismicity. Unfortunately our knowledge at small magnitudes (i.e., $m_b < \sim 4.0$) is poorly resolved, and source scaling remains a subject of on-going debate in the earthquake seismology community. Recently there have been a number of empirical studies suggesting scaling of micro-earthquakes is non-self-similar, yet there are an equal number of compelling studies that would suggest otherwise. It is not clear whether different studies obtain different results because they analyse different earthquakes, or because they use different methods. We investigate earthquake sources and scaling from different tectonic settings, comparing direct and coda wave analysis methods that both make use of Empirical Green's Function (EGF) earthquakes to remove path effects. We develop improved versions of the two methods, and then apply them to a range of data sets.

Our direct wave analysis uses local recordings of closely-located, well-correlated earthquakes, and a multi-taper method to obtain time-domain source-time-functions by frequency division. We only accept an earthquake and EGF pair if they are able to produce a clear, time-domain source pulse. Our improved, and simplified coda wave analysis method uses spectral ratios (as for the direct waves) but relies on the averaging nature of the coda waves to use EGF events that do not meet the strict criteria of similarity required for the direct wave analysis. Both coda and direct-wave methods are limited by the frequency bandwidth with good signal-to-noise, and recording limitations such as record length, clipping and sample rate. For both direct and coda waves, we fit the spectral ratios and perform a grid-search about the preferred parameters to ensure the fits are well constrained. We then model the spectral (amplitude) ratio to determine source parameters from both direct P and S waves. We investigate the effects of using different fitting approaches, and source-model variations on the results.

We analyze three clusters of aftershocks from the well-recorded sequence following the M5 Au Sable Forks, NY, earthquake to obtain some of the first accurate source parameters for small earthquakes in eastern North America. Each cluster contains a M~ 2, and two contain M~3, as well as smaller aftershocks. Using direct waves, we find that the corner frequencies and stress drops are high (averaging 100 MPa) confirming previous work suggesting that intraplate continental earthquakes have higher stress drops than events at plate boundaries. We also demonstrate that a scaling breakdown suggested by earlier work is simply an artifact of their more band-limited data. We also find that the ratio of Energy to Moment is high, around 10^{-4}. We estimate source parameters for the M5 mainshock using similar methods. The stress drop and energy/moment ratio for the mainshock are slightly higher than for the aftershocks. We then apply the coda method to the same sequence to investigate consistency, and uncertainties.

The large ($M \geq 4$) aftershocks of the 1994 Northridge, CA, earthquake are our second choice of sequence for comparison of the methods. These earthquakes already have source parameters determined using time-domain methods (Mori et al., 2003) and so by applying our spectral coda and direct wave methods, we can compare most approaches in common use.

We also apply one or both methods to a number of other earthquake sequences including those of recent moderate-sized earthquakes in Italy, and the Wells, Nevada, earthquake.

OBJECTIVES

The objectives of this study are to improve low-magnitude regional seismic discrimination by performing a thorough investigation of earthquake source scaling using diverse, high-quality datasets from varied tectonic regions. Local-to-regional high-frequency discrimination requires an estimate of how earthquakes scale with size. Walter and Taylor (2001) developed the MDAC method to empirically account for these effects through regional calibration. The accuracy of these corrections has a direct impact on our ability to identify clandestine explosions in the broad regional areas characterized by low seismicity. Unfortunately our knowledge at small magnitudes (i.e., $m_b < \sim 4.0$) is poorly resolved, and source scaling remains a subject of on-going debate in the earthquake seismology community. Recently there have been a number of empirical studies suggesting scaling of micro-earthquakes is non-self-similar (e.g., Kanamori et al., 1993; Abercrombie, 1995; Mayeda and Walter, 1996; Mori et al., 2003; Stork and Ito, 2004; and Izutani and Kanamori, 2001), yet there are an equal number of compelling studies that would suggest otherwise (e.g., McGarr, 1999; Ide and Beroza, 2001; Imanishi et al., 2004; and Prieto et al., 2004). It is not clear whether different studies reach different conclusions because they use different datasets and scaling varies with location, or because they use different methods. Sonley and Abercrombie (2006) show that small variations in the commonly used methods can lead to significant differences in results. Even in regions that are well studied, such as test sites or areas of high seismicity, we still rely on empirical scaling relations derived from studies taken from half-way around the world at inter-plate regions.

In summary, we address the following problems:

1. Do different studies obtain different results because they use different methods, or because they analyse different data sets? We will investigate whether coda and direct wave methods applied to the same datasets provide the same scaling.
2. Is scaling dependent upon the tectonic setting? We will investigate earthquakes from different tectonic settings and depth ranges, using the same coda and direct wave methods.
3. There have been few studies in intra-plate areas where seismicity is low and/or in regions where a clandestine test might occur. The MDAC method currently assumes earthquake source scaling that was derived exclusively from the western United States. Can we extrapolate or transport results from one region to others, or must we calibrate to each specific region? We will analyse earthquakes from both interplate (e.g. California) and intraplate (e.g. Eastern North America) regions to specifically address this question.

RESEARCH ACCOMPLISHED

Our approach to obtaining improved source parameters for small earthquakes focuses on the direct and coda wave methods: to improve and investigate them both, and then to apply them to diverse data sets.

Locally recorded, direct waves from events have been least affected by travel through the earth, and so are thought to be the best candidate for obtaining accurate source parameters. But there are only a limited number of earthquakes that are recorded locally, by sufficient stations to give good azimuthal coverage. Even fewer of these have an equivalently well recorded, very closely located smaller earthquake that meets the stringent criteria required to be a good EGF to remove path effects. This EGF method is the preferred one for isolating the source, but concern about the quality of the EGFs is a major source of uncertainty in studies that use these methods. In contrast, coda waves average radiation from all directions so single-station records should be adequate and previous work suggests that the requirements for the EGF event are much less stringent. It is thus ideal in regions with sparse stations and events so that most events are only well-recorded by a single station. Our approach is to:

1. Develop an easy to apply coda wave spectral ratio method to obtain source parameters for large groups of earthquakes
2. Identify the mainshock – EGF earthquake pairs that meet stringent criteria for selecting the EGF, and obtain source parameters from the direct waves for this subset of events.
3. Use the direct wave results to confirm, and if necessary correct, the coda wave results
4. Apply these methods to data sets from a range of tectonic environments.
5. Determine the implications of the determined source scaling results for both coda calibration and regional discrimination using MDAC and other similar means of source and path-corrected discriminants.

So far we have developed improved coda wave and direct wave methods that we will apply consistently to all the data sets. The new spectral-ratio method developed in this study makes the coda method much easier and simpler to apply, greatly extending the number of earthquakes that can be studied. The coda wave approach was published by Mayeda et al. (2007). We have applied the coda wave methods to several aftershock sequences in Italy

(Malagnini and Mayeda 2008, Malganini et al., 2008), and have begun to apply it in eastern North America. In the direct wave study, we have investigated the effects of the various analysis choices commonly made, and also developed criteria for assessing the quality of a particular EGF event. We have performed a very detailed direct wave EGF analysis of aftershocks of the Au Sable Forks earthquake (eastern North America), and obtained some of the best constrained source parameters for earthquakes in this tectonic setting. The direct wave analysis method and results are described by Viegas et al. (2009). In addition to applying both methods to these relatively small data sets, we are all performing a test by analyzing the large (M4-5) aftershocks of the 1994 Northridge, CA, earthquake. Mori et al. (2003) performed a detailed study calculating earthquake source parameters for these earthquakes. They used time domain methods and EGF analysis to calculate stress drop and radiated seismic energy for 47 earthquakes. We are now applying our two frequency domain methods to the same earthquakes, thus enabling us to investigate the differences between three different methods. The principal aims of this comparison work are to search for any systematic differences, and also determine which analysis choices lead to the largest uncertainties.

In addition to the possibility of differences between earthquake source spectra obtained from direct and coda waves, in our research we have also uncovered a number of other possible sources of bias in the methods traditionally used by the coda-wave and direct-wave communities in their modeling of the spectra. For example, most direct wave studies fit the spectra individually, whereas the coda-wave studies typically invert a group of events fixing the corner frequency of each earthquake to be the same in all ratios. Also, direct wave studies typically focus on obtaining the parameters for the larger event in an EGF pair, whereas most coda studies ratio all smaller earthquakes to one mainshock in order to obtain parameters for the smaller events in the pairs. We will include analysis of these different approaches in our comparisons. Although they sound small, they can be significant. For example, observations of non-similar scaling in coda wave studies often involve a difference between one or two larger earthquakes and a group of smaller ones (e.g., Malagnini and Mayeda 2008, Malganini et al., 2008). It is possible that this is an artifact from the large earthquakes always being the larger ones in the pairs, and the others the smaller.

The Au Sable Forks Earthquake Sequence, Eastern North America: Direct Waves

Analysis of earthquakes in stable, intraplate, low seismicity regions is important to characterize these regions, but it is hard because of the sparcity of earthquakes and stations, and hence useful data. Relatively little is known about earthquake sources in intraplate regions, and often relationships based on minimal data, or simply extrapolated from interplate regions are assumed due to lack of local information. For example, Somerville et al. (2002) use the recordings of only 3 moderate-sized earthquakes to propose source scaling relationships for earthquakes in the Northeastern USA and other stable continental regions. Their results imply that earthquakes in the Northeastern USA have relatively high stress drops. This result was confirmed by Shi et al. (1998) who analyzed almost 50 small earthquakes from the region. Their study included 8 empirical Green's function pairs (Shi et al., 1996), but mostly individual earthquakes. They also found a decrease in stress drop with seismic moment, at small magnitudes ($<$ M~3). This may indicate that earthquake source scaling is different in this intraplate region, or else may represent a limit to the resolution as was found earlier in the San Andreas Fault plate boundary region (e.g., Abercrombie and Leary, 1993). Shi et al. (1998) were mostly limited by data availability to using regional recordings at single stations, and so to frequencies less than about 25 Hz.

On April 20, 2002 an earthquake of magnitude M_L 5.3 occurred in the northeastern Adirondack Mountains – the first earthquake of such size to be recorded by modern regional broadband networks. Following the mainshock, the Lamont-Doherty Earth Observatory deployed a small portable network to monitor aftershocks (Seeber et al., 2002). Between April 22 and November, 2002, 74 small aftershocks detected and located in the epicentral area of the mainshock. These data (200 samples/s) represent the best recorded earthquakes in the region to date, and so provide an unprecedented opportunity to investigate source parameters in this intraplate setting.

We calculate the source parameters using two methods commonly applied to direct waves recorded at local stations: spectral modeling of the individual three-component P and S waves (e.g., Abercrombie, 1995), and the Empirical Green's Function (EGF) method (e.g., Mori and Frankel, 1990, Abercrombie and Rice, 2005). Both methods require data with a high-frequency content to work well. Many studies consider the EGF method superior as it corrects for all path and site effects by using a smaller, collocated earthquake as an EGF. The EGF method cannot be used to calculate the seismic moment of the earthquakes, but this is the most reliable information that can be obtained from the individual spectral analysis. Using cross-correlation we identify three clusters of earthquakes with very similar waveforms that include the largest aftershocks recorded by the portable network. All clusters include an $M \geq 2$, and a

number of M1-2 earthquakes, and two clusters also each include an M≥3 earthquake. We model the spectra obtained by dividing the spectrum of the large earthquake by the smaller one. We also use regional recordings (100 samples/s) to analyze the M5 mainshock using the largest aftershock (M3.7) as the EGF. These earthquakes are closely located, and the deconvolution produces a source time function, but clearly have a different focal mechanism, and so do not meet the criteria for selecting an EGF that we describe below. Unfortunately, no aftershocks well recorded regionally meet these criteria so we use the largest aftershock, and interpret our results with caution.

It is not clear in many studies how close the EGF events are to a perfect Green's function. They are typically too small to obtain focal mechanisms, and the location uncertainties are larger than the preferred separation between events. We select only events that are located within the uncertainties of the large event, and have a high degree of waveform similarity, determined by cross-correlation. As a further test, we transform all the spectral ratios back to the time domain, and we only use pairs where we are able to resolve a clear source pulse. If a source time function is observable in this way, then it demonstrates that the phase components of the spectra are also very similar. This test is similar to the investigation performed by Mori and Frankel (1990) to determine how closely located earthquakes pairs must be for the EGF method to work well. Multitaper methods have long been preferred to calculate source spectra and spectral ratios as they better represent the frequency content of the waveforms than do cosine and other tapers (e.g., Park et al., 1987). Unfortunately, until recently multitaper codes only worked with amplitude spectra and so could not be used to perform the complex deconvolution. We use the multitaper approach recently developed by Prieto et al. (2008) to perform the full complex deconvolution so that we can use the same frequency analysis to obtain both the best spectra, and retrieve the source time functions.

We first calculate source parameters using the individual spectra, to determine the seismic moments, and also to compare the results of this standard method with that of the preferred EGF method. Before modeling the individual amplitude spectra, we re-sample them on a logarithmic scale, so that the fits were not biased to the high frequencies. We fit the displacement amplitude spectra with the omega-square source model with the sharper corner preferred by Boatwright (1980) and Abercrombie (1995) to obtain the seismic moment, corner frequency and attenuation Quality factor (Q). We perform a grid search around the preferred parameters to investigate the uncertainties within a range of variance of fit of +5%. We take the mean of all available components and stations to calculate the final value. Following Abercrombie (1995) we assume the circular fault model of Madariaga (1976) to calculate source radius (r), and the solution of Eshelby (1957) for a circular crack to calculate stress drop ($\Delta\sigma$). We calculate the radiated seismic energy (E_S) by integrating the velocity-squared spectrum, using the data within the available bandwith and the best fitting model to extend the frequency range (Abercrombie 1995).

We then apply the EGF method to the earthquakes in the clusters we identified. We use the same amplitude spectra to calculate spectral ratios between the different events, and we also use the extension of the multitaper method to the complex spectra to deconvolve the spectral ratios back to the time domain and so obtain estimates of the source time functions. We only continued the analysis if we obtained a clear source pulse, justifying our choice of EGF event. We resample the spectral ratios on a logarithmic scale (in the same way as the individual spectra) and we model the spectra ratios using the same source model as the individual spectra. We use reasonable constraints on the fitting parameters as a further constraint on the use of EGF pairs and ratios. We then calculate source parameters from the spectral fitting as for the individual spectra.

The smallest earthquakes have corner frequencies that are clearly outside the available bandwidth (>80 Hz). The EGF results are preferred because of their better correction for path and site effects. The individual fitting tends to underestimate the corner frequencies (and hence the stress drops) as they get close to the high frequency limit

(Figure 1). The high stress drops we obtain are consistent with the previous studies which find relatively high stress

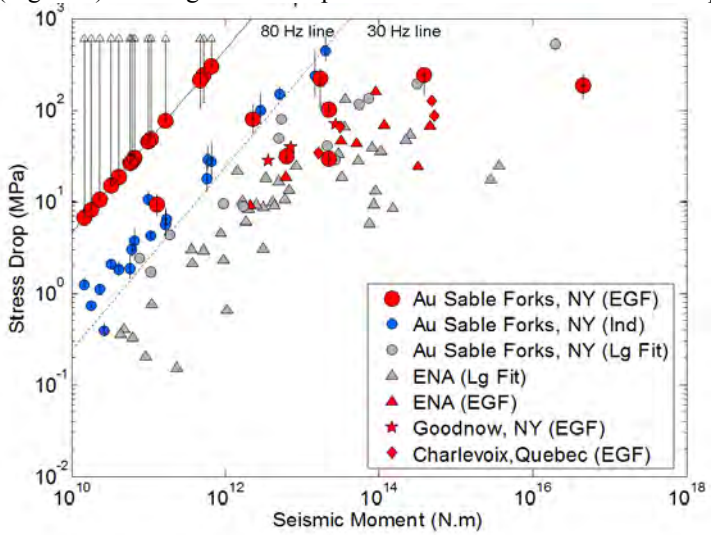

Figure 1: Stress Drop measurements in Eastern North America. Comparison of the Au Sable sequence, with individual fitting and previous studies. The two studies shown in grey are limited to 30 Hz. The individual measurements underestimate stress drop near the bandwidth limit compared to the EGF. Arrows indicate minimum estimates. No evidence for a breakdown in scaling is seen.

drops for intraplate regions such as eastern North America. They are consistent with the results of Shi et al. (1998) for their EGF events, but we do not see a breakdown in constant stress drop scaling at lower magnitudes, suggesting that this was an artifact of the limited bandwidth available to Shi et al.

We obtain relatively high stress drops and apparent stress (proportional to the ratio of E_S/M_0), compared to previous studies, mostly in interplate environments (Figure 2). This is consistent with the hypothesis that faults in intraplate settings with lower strain rates, lower cumulative deformation, and longer healing time between ruptures will be stronger than faster moving faults at plate boundaries. Our results also show some gradual decrease in stress drop and apparent stress with decreasing moment. Unfortunately, this is largely dependent on the uncertainties in the

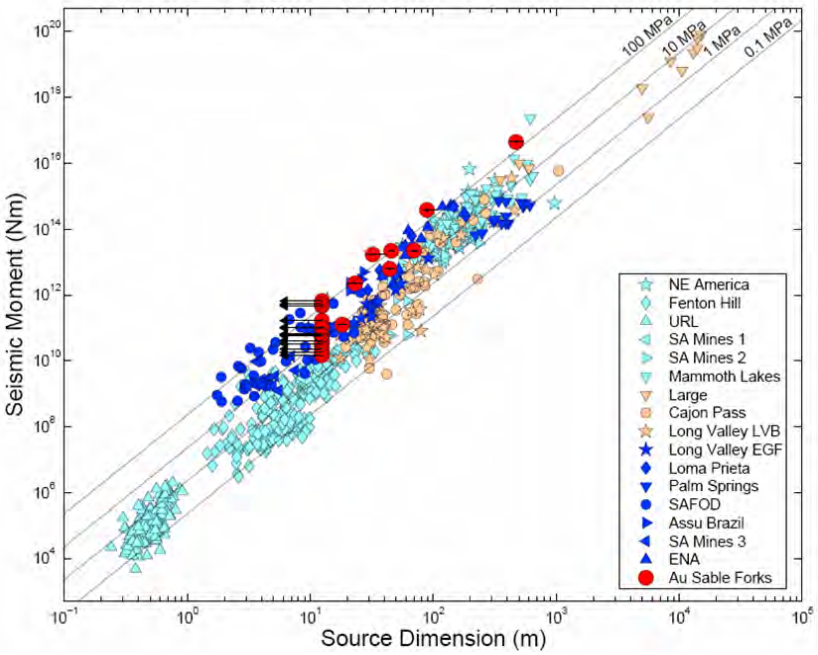

Figure 2a. Comparison of the Au Sable Forks results with previous work mainly from the western USA. Figure updated from Abercrombie and Leary (1993), corrected for different source models. Note that recent EGF studies (dark blue) all have higher stress drop than earlier studies.

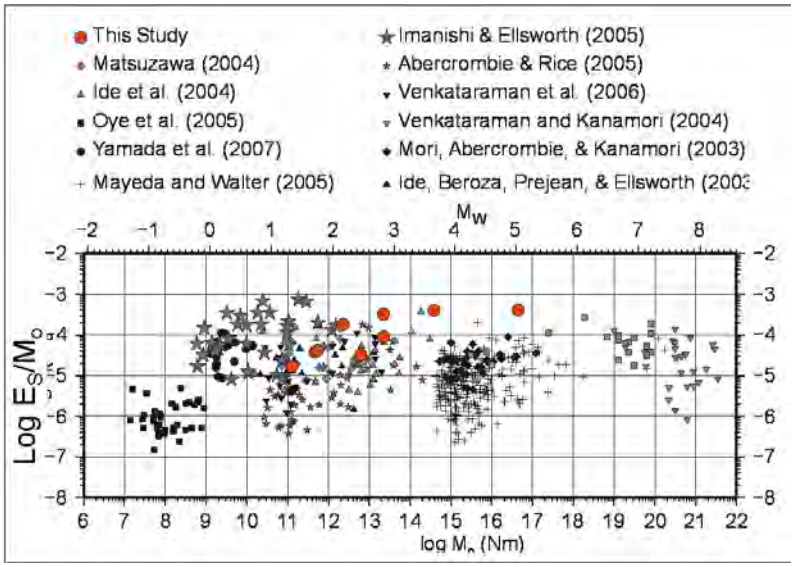

Figure 2b. Comparison of the Au Sable Forks results with previous work mainly from the western USA. Figure updated from Ide and Beroza (2001).

values for the two largest earthquakes. These are less reliable because of the lack of an acceptable EGF event.

The Au Sable Forks Earthquake Sequence, Eastern North America: Coda Waves

After obtaining reliable, high precision direct wave estimates of the source parameters of the earthquakes in the Au Sable Forks sequence, we then applied the coda-wave methods, in order to compare them. We began by performing a calibration study following the procedure of Mayeda and Walter (1996). For this we could only use regional recordings, and so only the 9 largest earthquakes that were recorded at regional distances. This analysis is therefore limited to the 40 samples/s and 100 samples/s of the regional stations. To obtain the calibration spectra, it was necessary to use an apparent stress of at least 10 MPa, significantly higher than the values typically used in previous studies on the west coast. This is consistent with the direct wave estimate of relatively high stress drop. The coda methods essentially follow the source parameterization and model developed by Walter and Taylor (2001). In this approach, the apparent stress and stress drop are not independent parameters, as they are in the methods typically used for direct wave analysis. This difference is more related to tradition than to any requirements of the different data. In the Walter and Taylor (2001), MDAC approach, the apparent stress is simply proportional to the stress drop, and the radiated seismic energy is dependent on the source model chosen. In direct wave studies, radiated seismic energy is calculated relatively independently of the source model, and hence apparent stress is not directly proportional to stress drop. After performing the calibration, we then calculated spectral ratios of all 8 aftershocks to the mainshock, following the methods of Mayeda et al. (2007), and Malagnini and Mayeda (2008), Figure 3. We compare the corner frequencies obtained from the direct wave and coda wave studies (Figure 4). They agree relatively well for the larger events, but the coda method significantly underestimates the corner frequency and stress drop for the smaller events. This is most likely a bandwidth limitation since the direct wave measurements were made on the local recordings which have larger signal and frequency bandwidth than the regional records. This result serves as a reminder that the coda-wave analyses are subject to similar problems and biases as a result of limited bandwidth as have long been recognized in direct-wave studies.

The next step is clearly to use the local records to calculate coda spectral ratios. However, this requires investigation into the use of higher frequency records, resulting from smaller volume scattering in shorter time windows than have previously been used for coda analysis. The window length is limited by the triggered recordings of portable deployments, and the more rapid decay of higher frequency signals.

Does it Matter how the Spectral Ratios are Modeled?

Mayeda and Malagnini (2009) analyzed the source parameters of the Wells, Nevada, M6 earthquake and 6 of its largest aftershocks using the coda spectral ratio method. They found non self-similar scaling when fitting following the MDAC procedures, and a joint inversion as described by Malagnini and Mayeda (2008) and Malganini et al., (2008). In order to investigate the effects of using different fitting approaches, we fit the same spectra using the fitting methods, and two different source models that we are using for the direct-wave analyses, the Brune (1970)

model used in MDAC, and the sharper-cornered version of the same (Boatwright 1980). The results are shown in Figure 5. The three different fitting methods all give broadly similar, overlapping results, but do show significant variation, of the order of 40% in seismic moment, 50% in corner frequency, and 100% in stress drop. The variation in seismic moment is perhaps the least expected. In all ratios, an amplitude ratio between the large earthquake (of known, fixed moment) and the smaller earthquake is calculated. In the sharper-corner model, this long-period amplitude level is smaller, and so the moments of the aftershocks are larger.

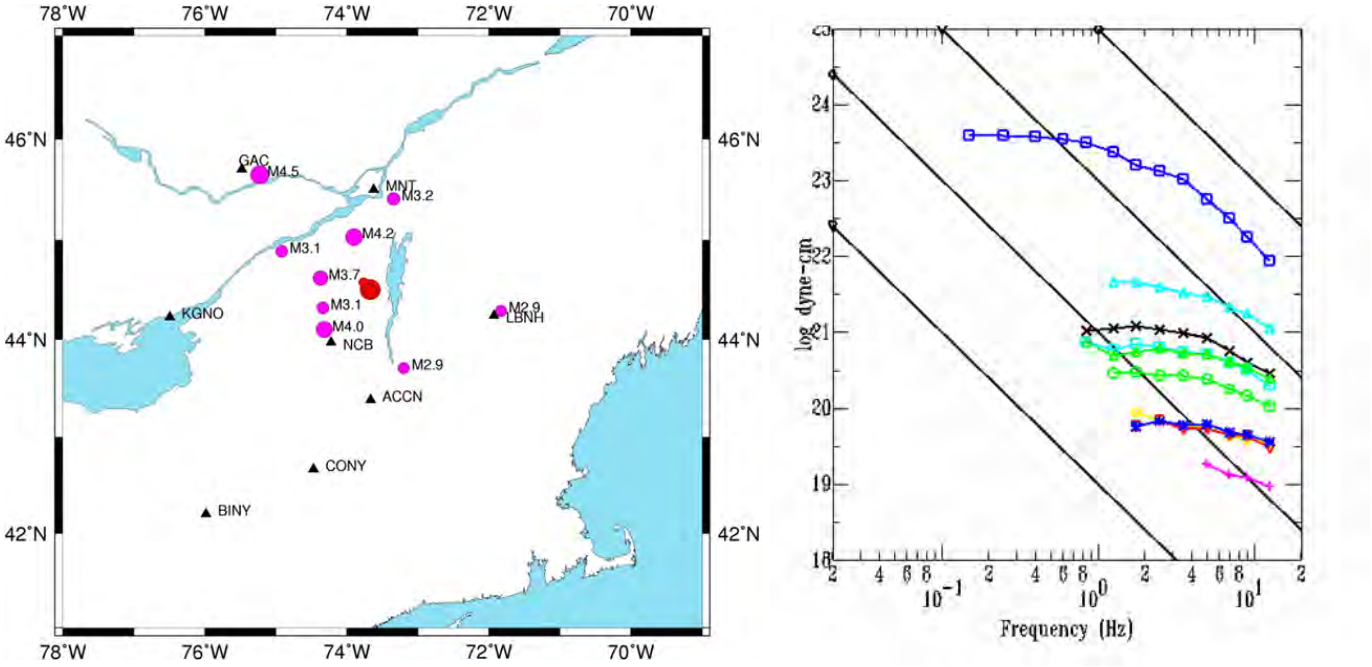

Figure 3. Coda wave analysis of the Au Sable Forks earthquake sequence. (a) map of the earthquakes and stations used. (b) calibrated source spectra of the M5 earthquake (blue) and the 8 larger aftershocks.

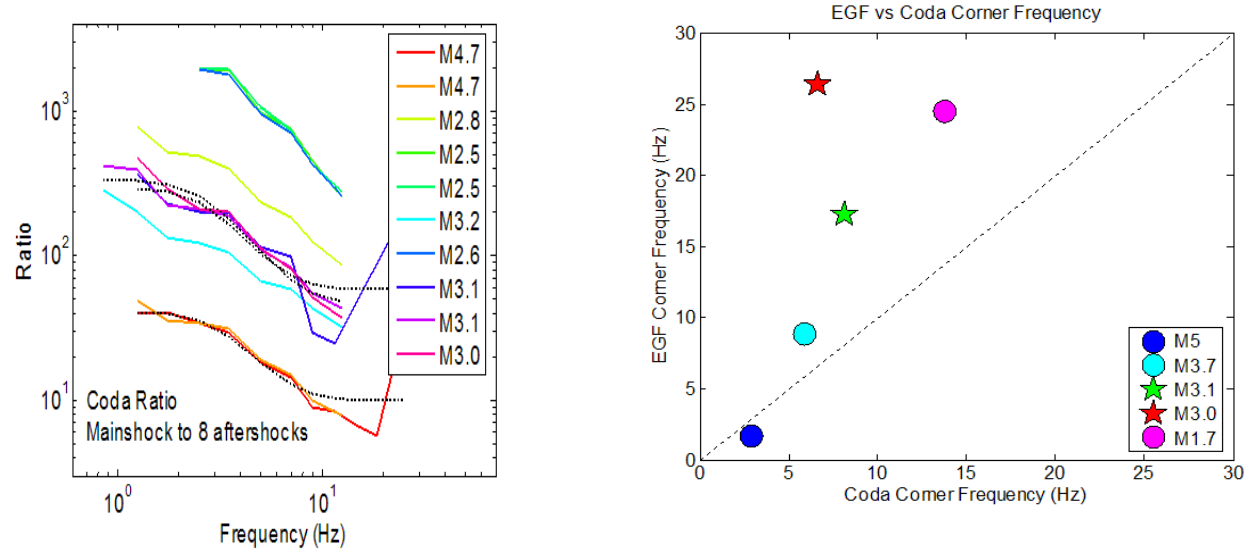

Figure 4. Coda spectral ratios of the Au Sable Forks earthquake with the larger aftershocks (left) and comparison of the direct wave and coda wave estimates of the corner frequencies for 5 earthquakes in the Au Sable Forks sequence. The coda data do not have sufficient high frequency bandwidth to resolve the corner frequencies of the smaller earthquakes well.

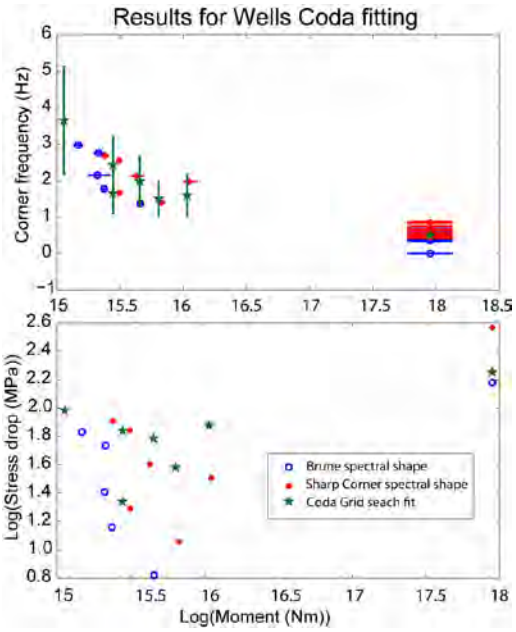

Figure 5. Fitting the spectral ratios of the Wells earthquakes using three different methods: combined inversion following MDAC (green), and individually fitting ratios using Brune (1970) model (blue) and the sharper corner version (red).

The 1994 Northridge, CA, Aftershock Sequence – A Comparison of Multiple Methods.

Mori et al. (2003) used EGFs for 47 large (M4) aftershocks of the M6.7 Northridge, CA, earthquake to obtain well-resolved source time functions. They then calculated the stress drop, radiated energy and apparent stress using time-domain measurements. They found constant stress drop but a possible increase in apparent stress with increasing moment. Mori et al. systematically searched hundreds of possible small earthquakes to find the best EGFs and so this data set provides an excellent opportunity to compare multiple methods. We apply our direct-wave

methods and coda-wave methods to the same earthquakes and can compare them to one another, and the time-domain measurements, without the need to hunt for EGFs. As is usual, the large aftershocks are the large earthquakes in the ratios in the direct wave study, whereas in the coda-wave study these earthquakes are the smaller in ratios to the mainshock. So far we have calculated very preliminary results for a subset of earthquakes, which show some systematic differences. We are waiting to complete the study before we draw any real conclusions as to where the most significant uncertainties occur.

CONCLUSIONS AND RECOMMENDATIONS

Work is proceeding on a number of fronts simultaneously, and we look forward to completing the various studies and drawing the results together soon. So far we have performed the following analyses:

- Northeastern USA (M1-5): Direct waves and preliminary coda waves
- Northridge, CA (M4-6): Preliminary direct and coda waves (existing time domain results for comparison)
- Wells, CA (M4-6): Coda waves, and effect of spectral modeling approach
- Various sequences in Italy (M4-6): Coda waves

In eastern North America the direct and coda wave measurements find High $\Delta\sigma$ and High E_S, consistent with intraplate setting. We also find no evidence for a breakdown in scaling. The Coda and direct wave measurements agree well for large magnitudes, but we need to use local data for the smaller earthquakes. To date, coda wave methods have not been applied to high frequency, locally recorded, triggered waveforms.

In Italy and California, studies of mainshock-aftershock sequences using coda waves continue to find that earthquake scaling is not self-similar with decreasing apparent stress with decreasing moment.

The next steps are to complete these ongoing studies and then compare the results, to determine any biases and uncertainties arising from the choices of data and analysis used. We will:

- Complete application of coda spectral ratio method to northeastern USA earthquakes – including local recordings of smaller earthquakes
- Complete application of both methods to Northridge Sequence (and Wells?) over range *M* to improve comparison
- Include fitting coda spectral ratios with direct approach and vice versa.
- Investigate bandwidth limitations on fitting more carefully
- Quantify comparisons
- include results in MDAC.

ACKNOWLEDGEMENTS

We thank Luca Malagnini for his contribution to the work on coda spectral ratios, German Prieto for developing the multi-taper code to obtain time-domain source time functions, and Won-Young Kim for providing the portable aftershock recordings of earthquakes in eastern North America, and information about his regional wave analysis.

REFERENCES

Abercrombie, R. E. (1995). Earthquake source scaling relationships from -1 to 5 M_L using seismograms recorded at 2.5 km depth, *J. Geophys. Res.* 100: 24,015–24,036.

Abercrombie, R. E. and Leary, P. C., (1993). Source parameters of small earthquakes recorded at 2.5 km depth, Cajon Pass, southern California: implications for earthquake scaling, *Geophys. Res. Lett.* 20: 1511–1514.

Abercrombie, R. E. and J. R. Rice (2005). Can observations of earthquake scaling constrain slip weakening?, *Geophys. J. Int.* 162: 406–424.

Boatwright, J. (1980). A spectral theory for circular seismic sources: simple estimates of source duration, dynamic stress drop, and radiated energy, *Bull. Seismol. Soc. Am.* 70: 1–28.

Brune, J. N. (1970). Tectonic stress and spectra of seismic shear waves from earthquakes, *J. Geophys. Res.* 75: 4997–5009.

Eshelby, J. D. (1957). The determination of the elastic field of an ellipsoidal inclusion and related problems, in *Proceedings Roy. Soc. Lond., A,* 241: 376–396.

Ide, S. & Beroza, G. C. (2001). Does apparent stress vary with earthquake size, *Geophys. Res. Lett.* 28: 3349–3352.

Imanishi, K., W. L. Ellsworth, and S. G. Prejean (2004). Earthquake source parameters determined by the SAFOD Pilot Hole seismic array, *Geophys. Res. Lett.* 31: L12S09, doi:10.1029/2004GL019420.

Izutani Y. and H. Kanamori (2001). Scale-dependence of seismic energy-to-moment ratio for strike-slip earthquakes in Japan, *Geophys. Res. Lett.* 28: 20, 4007–4010.

Kanamori, H., J. Mori, E. Hauksson, T. H. Heaton, L. K. Hutton, and L. M. Jones (1993). Determination of of earthquake energy release and M_L using TERRAscope, *Bull. Seismol. Soc. Am.* 83: 330–346.

McGarr, A., 1999. On relating apparent stress to the stress causing earthquake slip, *J. Geophys. Res.* 104: 3003–3011.

Madariaga, R., 1976. Dynamics of an expanding circular fault, *Bull. Seismol. Soc. Am.* 66: 639–666.

Malagnini, L. and K. Mayeda (2008). High-stress strike-slip faults in the Apennines: An example from the 2002 San Giuliano earthquakes (southern Italy), *Geophys. Res. Lett.* 35: L12302, doi:10.1029/2008GL034024.

Malagnini, L., L. Scognamiglio, A. Mercuri, A. Akinci, and K. Mayeda (2008). Strong evidence for non-similar earthquake source scaling in central Italy, *Geophys. Res. Lett.* 35: L17303, doi:10.1029/2008GL034310.

Mayeda, K. and L. Malagnini (2009). Apparent stress from coda-derived source ratios: regional variations, similarities, and differences, *Seismol. Res. Lett.* 80: 2, pp. 336.

Mayeda, K., L. Malagnini, and W. R. Walter (2007). A new spectral ratio method using narrow band coda envelopes: Evidence for non-self-similarity in the Hector Mine sequence, *Geophys. Res. Lett.* 34: L11303, doi:10.1029/2007GL030041.

Mayeda, K. M. and W. R. Walter, (1996). Moment, energy, stress drop and source spectra of Western U.S. earthquakes from regional coda envelopes, *J. Geophys. Res*. 101: 11,195–11,208.

Mori, J. and A. Frankel (1990). Source parameters for small events associated with the 1986 North Palm Springs, California, earthquake determined using empirical Green functions, *Bull. Seismol. Soc. Am.*80: 278–295.

Mori, J., R.E. Abercrombie, and H. Kanamori (2003). Stress drops and radiated energies of aftershocks of the 1994 Northridge, California, earthquake, *J. Geophys. Res.* 108, No. B11, 2545, doi:10.1029/2001JB000474.

Park, J., C. R. Lindberg, and F. L. Vernon (1987). Multitaper spectral analysis of high frequency seismograms, *J. Geophys. Res.* 92: 12,675–12,648.

Prieto, G. A., R. L. Parker, and F. L. Vernon (2008). A Fortran 90 library for multitaper spectrum analysis, *Accepted in Computers and Geosciences*, June 2008.

Prieto, G. A., P. M. Shearer, F. L. Vernon, D. and Kilb (2004). Earthquake source scaling and self-similarity estimation from stacking P and S spectra, *J. Geophys. Res.* 109: B08310, doi 10.1029/2004JB003084.

Seeber, L., W-Y. Kim, J. G. Armbruster, W-X. Du, A. Lerner-Lam, and P. Friberg (2002). The 20 April 2002 M_w5.0 earthquake near Au Sable Forks, Adirondacks, New York: A first glance at a new sequence, *Seism. Res. Lett.* 73: 480–489.

Shi, J., W. Y. Kim, and P. G. Richards (1996). Variability of crustal attenuation in the northeastern United States from Lg waves, *J. Geophys. Res*. 101: 25231–25242.

Shi, J., W. Y. Kim and P. G. Richards (1998). The corner frequencies and stress drops of intraplate earthquakes in the northeastern United States, *Bull. Seismol. Soc. Am.* 88**:** 531–542.

Somerville, P., N. Collins, N. Abrahamson, R. Graves, and C. Saikia (2002). Ground motion attenuation relation for the central and eastern Unites States. Final Report to NEHRP, U.S. Geological Survey.

Sonley, E., and R. E. Abercrombie (2006). Effects of methods of attenuation correction on source parameter determination, *American Geophysical Union Monograph, EARTHQUAKES Radiated energy and the physics of faulting*, eds. Abercrombie, McGarr, Di Toro and Kanamori.

Stork, A. L. and H. Ito (2004). Source Parameter Scaling for Small Earthquakes Observed at the Western Nagano 800-m-Deep Borehole, Central Japan , *Bull. Seismol. Soc. Am.* 94: 1781–1794, doi: 10.1785/012002214

Venkataraman, A., L. Rivera, and H. Kanamori (2002). Radiated energy from the 16 October 1999 Hector Mine earthquake: regional and teleseismic estimates, *Bull. Seismol. Soc. Am* 92: 1256–1265.

Viegas, G. M., R. E. Abercrombie and W-Y. Kim (2009), Earthquake Source Scaling in the Northeastern United States, *J. Geophys. Res.,* in prep.

Walter, W. R. and S. R. Taylor (2001). A revised magnitude and distance amplitude correction (MDAC2) procedure for regional seismic discriminants: theory and testing at NTS, Lawrence Livermore National Laboratory Report, UCRL-ID-146882, http://www.llnl.gov/tid/lof/documents/pdf/240563.pdf

SOURCES OF ERROR: REGIONAL AMPLITUDE AND TELESEISMIC MAGNITUDE DISCRIMINANTS

Dale N. Anderson

Los Alamos National Laboratory

Sponsored by the National Nuclear Security Administration

Award No. DE-AC52-06NA25396/LA09-ECM-NDD02

ABSTRACT

For both regional amplitude and teleseismic magnitude discriminants there are physical effects that diminish identification accuracy and cannot easily be determined and applied as corrections (e.g., focal mechanism and local material properties). We develop a mathematical model to capture these effects as random, giving an error partition of three sources: correction model inadequacy, station noise, and amplitude correlation. This mathematical model is the basis for a new standard error for multi-station discriminants that includes the variances of model inadequacy and station noise, along with amplitude correlation in its formulation. The developed methods are demonstrated for a collection of Nevada Test Site (NTS) events observed at regional stations and teleseismic data acquired from the International Seismological Centre (ISC).

OBJECTIVES

Source type identification (discrimination) in seismology is unique in that it focuses on the construction of seismic identification features from seismic waveforms and other multi-technology measurements. Most, if not all, statistical classification research begins with the assumption "suppose we have classification features in hand." In contrast, in seismic identification research, significant effort is directed toward the intelligent construction of the identification features, and how to couple to the features most of the associated and relevant sources of error.

Seismic identification features are dynamically adaptable to the number of stations observing an event, the configuration (e.g., geometry) of the observing stations, and the strength of signal at each station. Conceptually, the features are scientifically and statistically constructed to be evidence quality before they are ever combined with a statistical classification method. This paper presents an enhanced construction of the teleseismic m_b versus M_s discriminant and in particular the standard error. Coupled with researched sources-of-error models for a discriminant, a general strategy for the construction of diverse multi-technology discriminants has been developed in Anderson et al. (2007) and Anderson et al. (2009). The revised m_b versus M_s discriminant is illustrated with seismic event data acquired from the ISC and the AWE Blacknest Seismological Centre (BSC), see Figure 1 and description in the following section. These data are available upon request from the author.

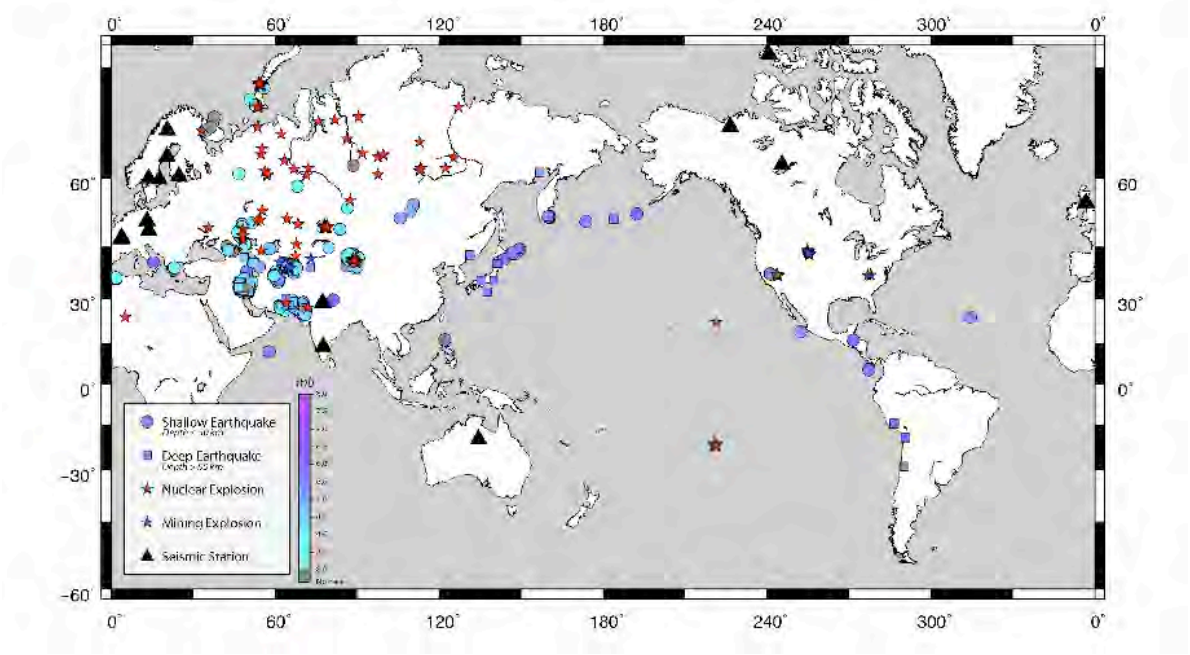

Figure 1. Teleseismic event and station locations.

RESEARCH ACCOMPLISHED

In Anderson et al. (2007), for each teleseismic discriminant a probability model is formulated under a general null hypothesis of H_0: Explosion Characteristics. The veracity of the hypothesized model for each discriminant is measured with a calculation that is exactly, or analogous, to a *p*-value. The hypothesis test formulation ensures that seismic phenomenology is tied to the interpretation of the p-value. Most importantly, the hypothesis test formulation ensures that the physical basis of a discriminant is properly integrated into a probability model that describes the most relevant source of error corrupting the physical measurement. Discriminant *p*-values can also be viewed as standardized discriminants, and can be combined into a unified source type identification with a number of statistical classification methods. Making the null hypothesis H_0: Explosion Characteristics is also important in the context of treaty verification because seismic events are assumed to be single-point explosions and then inferential evidence is used to reject this hypothesis, if possible. The teleseismic events acquired from the ISC and BSC include nuclear explosions from NTS and the former Soviet Union, global earthquakes, and mining explosions from 1964 to 2000. Necessary signal processing was completed by Rocky Mountain Geophysics (RMG), LLC. Seismic measurements from combinations of stations given in Table 1 are used in the demonstration analysis. Arrays EKA, GBA, WRA

and YKA comprise the United Kingdom seismic system. Source type definitions for these data are deep earthquake (DEQ) for a reported depth greater than 50 kilometers, shallow earthquake (SEQ) for a reported depth less than or equal to 50 kilometers and single-point fully contained explosions (EX). The EX population included underground nuclear weapons tests and some single-point fully contained chemical explosions. Acquired data counts are summarized by source type in Table 2. Figure 1 shows the event and station locations.

Teleseismic discrimination between underground nuclear explosions and naturally occurring earthquakes has been summarized in a number of publications (Blandford [1977]; Douglas [1981]; Blandford [1982]; Douglas [2007]). A seismic event couples energy into the earth and this energy is partitioned into waveform phases. The path and distance between event and stations are different and if the phase energy measurements from each station could be reasonably corrected for these effects, the measurements would be quite similar, with differences fundamentally due to near-source and near-station effects. Significant research on correction models includes Mueller and Murphy (1971), Murphy and Mueller (1971) and Patton and Taylor (2008). Current methods model station magnitudes as Gaussian and average to construct an event network magnitude.

Table 1. Array locations used in m_b versus M_s demonstration analysis.

Station	Latitude	Longitude	Description
CLL	51.31	13.00	Collm, Germany
EKA	55.33	-3.16	Eskdalemuir Array, Scotland
GBA	13.60	77.44	Gauribidanur Array, India
HFS	60.13	13.70	Hagfors Array, Sweden
INK	68.31	-133.52	Inuvik, Northwest Territories, Canada
KHC	49.13	13.58	Kasperske, Hory, Czech Republic
KIR	67.84	20.42	Kiruna, Sweden
LOR	47.27	3.86	Lormes, France
MBC	76.24	-119.36	Mould Bay, Northwest Territories, Canada
NDI	28.68	77.22	New Delhi, India
NUR	60.51	24.65	Nurmijarvi, Finland
SSF	47.06	3.51	Saint Saulge, France
UME	63.82	20.24	Umea, Sweden
UPP	59.86	17.63	Uppsala, Sweden
WRA	-19.94	134.34	Warramunga Array, Australia
YKA	62.49	-114.61	Yellowknife Array, Canada

Table 2. Source type summary for teleseismic events.

EX	SEQ	DEQ
395	452	144

Enhanced standard error for the teleseismic m_b versus M_s discriminant.

Research on the m_b versus M_s discriminant is significant (see Marshall and Basham [1972]; Evernden [1975]; Blandford [1982]; and Stevens and Day [1985]). The null hypothesis is $H_0 = \mu_{m_b} - \mu_{M_S} \geq \Delta_0$. A common test discriminant is formed from the difference of network averaged surface-wave and body-wave magnitudes. Subtracting the historical average of this difference, when the seismic source is an explosion, gives Δ_0. The equal variance for m_b and M_s in the standard error is calculated from historical data and is assumed known. Specifically, a common formulation of the test discriminant is

$$Z = \frac{(\tilde{m}_b - \tilde{M}_S) - \Delta_0}{\sigma\sqrt{1/n_{\tilde{m}_b} + 1/n_{\tilde{M}_S}}} \quad (1)$$

where the "~" denotes network averaged magnitudes. The standard error in Equation (1) is inconsistent with the physical basis in that an event observed by a large number of stations will have an unrealistically small standard error. Conceptually this implies that the path and distance corrections for m_b and M_s are accurately known and applied, and these magnitudes are corrupted only by incoherent (uncorrelated) station noise. However, physical path and distance corrections are specific to an event and realistically can only be approximately modeled. If correction model inadequacy (e.g., variations in attenuation) is treated as random, then with historical event data the variance components for correction model error and station noise can be estimated. The conceptual formulation of the random effects model for a magnitude is

$$Y = Magnitude = \mu(source - type) + Event + Noise \quad (2)$$

where *Event* is a random effect that varies from event to event and represents model inadequacy in physical path and distance corrections. *Noise* represents measurement and station noise. The value Δ_0 in Equation (2) is calculated from calibrated values of $\mu(source - type)$ for the magnitudes m_b and M_s. The linear model representation of Equation (2) is

$$Y_{ijk} = \mu_i + E_j + \varepsilon_{(ij)k} \quad j = 1,2,...m_i \; k = 1,2,...n_{ij} \quad (3)$$

Equation (3) reads Y_{ijk} equals a constant source-type mean (μ_i) plus a random event adjustment E_j (model inadequacy) plus a station noise adjustment $\varepsilon_{(ij)k}$. The E_j are iid normal random variables with zero mean and variance σ^2. The $\varepsilon_{(ij)k}$ are iid normal random variables with zero mean and variance τ^2. E_j and $\varepsilon_{(ij)k}$ are independent across all subscripts. This assumption is consistent with near-source and path effects being uncorrelated with station noise. The intra-class correlation $\tau^2/(\tau^2+\sigma^2))$ has an important interpretation. It implies that large adjustment E_j increases correlation between stations because a significant part of this random effect comes from near-source effects applied to all stations observing an event. Small adjustment E_j implies the correction model is good and is conceptually equivalent to error structure from stations with incoherent noise. Small adjustment E_j implies τ^2 is small and the standard error of a network magnitude is reduced further through the station averaging. From the model Equation (3), the new standard error of the m_b versus M_s discriminant is

$$SE_{\tilde{m}_b - \tilde{M}_S} = \sqrt{\tau^2_{m_b} + \frac{\sigma^2_{m_b}}{n_{m_b}} + \tau^2_{M_S} + \frac{\sigma^2_{M_S}}{n_{M_S}}} \quad (4)$$

for both earthquakes and explosions and the test statistic is

$$Z = \frac{(\tilde{m}_b - \tilde{M}_S) - \Delta_0}{\sqrt{\tau^2_{m_b} + \frac{\sigma^2_{m_b}}{n_{m_b}} + \tau^2_{M_S} + \frac{\sigma^2_{M_S}}{n_{M_S}}}} \quad (5)$$

providing a *p*-value for the hypothesis test $H_0 = \mu_{m_b} - \mu_{M_S} \geq \Delta_0$. Note that this extended formulation of the m_b versus M_s discriminant is analogous to the formulation of regional amplitude discriminants in Anderson et al. (2009).

In addition to observed discrimination properties, both m_b and M_s are biased proxy measurements for the size of an event – seismic moment([=] Newton/meter) for earthquakes and yield ([=] kilotons TNT) for explosions. The network magnitudes for m_b and M_s are biased measurements for event size with increased precision over single-station magnitudes. For earthquakes, this bias is significantly due to inadequate correction for event depth, the radiation pattern of the earthquake (fault orientation) and near-source earth structure, which in the aggregate, is modeled as the random correction model error E_j. For explosions, this bias is significantly due to inadequate correction for event depth, the radiation pattern from tectonic release caused by the explosion, and near-source earth structure, also modeled in the aggregate as random correction model error E_j. Applying (apparent performance) the discriminant formulation in Equation (5) to the ISC/BSC teleseismic data gave the *p*-values are shown in Figure 2 for the null hypothesis $H_0 = \mu_{m_b} - \mu_{M_S} \geq 1.35$. Deep earthquakes (DEQ) can attenuate the waves that generate the magnitude M_s and so DEQ events can appear to be single-point explosions. In this case, resolution requires a depth discriminant to eliminate the deeper earthquakes. Note that an interpretation of the m_b and M_s p-value as evidence in support of $H_0 = \mu_{m_b} - \mu_{M_S} \geq 1.35$ leads to no missed explosions. Treating the *p*-value as a standardized discriminant, and choosing a decision line of approximately 0.2 also leads to no missed explosions with a significant reduction in false-alarms.

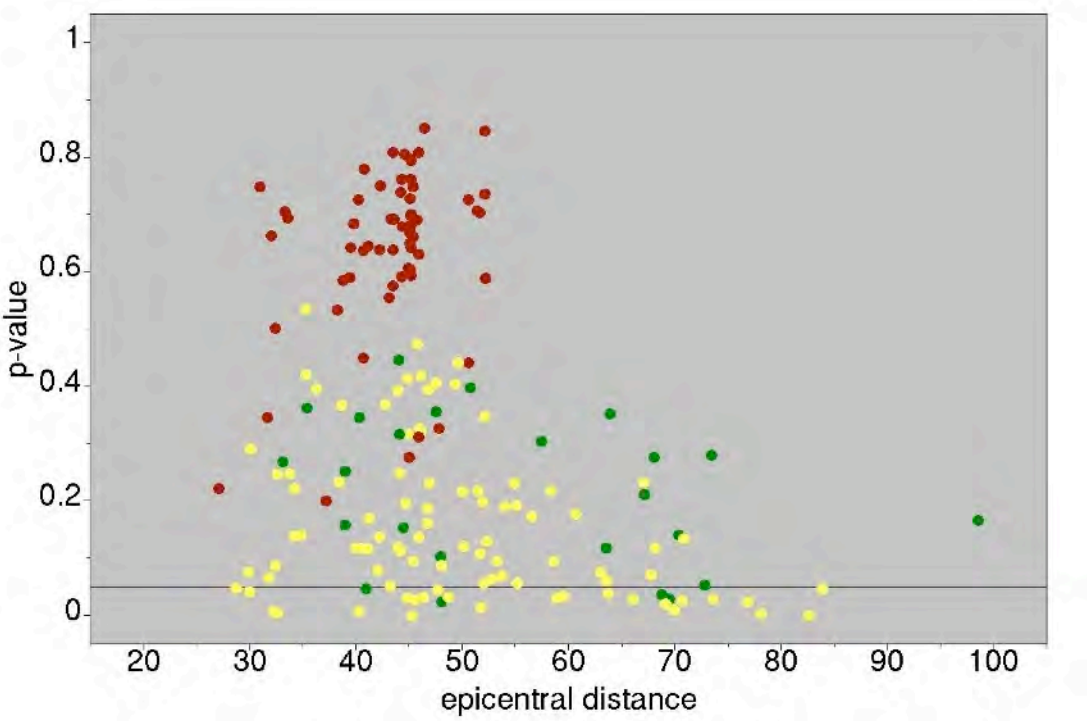

Figure 2. *p* -values for $H_0 = \mu_{m_b} - \mu_{M_S} \geq 1.35$. The abscissa is the average epicentral distance (degrees) between event and seismic stations observing the event. Single-point fully contained explosions are red, shallow earthquakes are yellow, and deep earthquakes are green.

CONCLUSIONS AND RECOMMENDATIONS

A significant aspect of discrimination research should focus on the construction of the discriminants rather than technologies to combine discriminants, as there are many mature technologies for multivariate discrimination (see Hand [2006]). For discriminant research, the fundamental challenge is the mathematical combination of physical basis with probability models to describe sources of error. The criteria for selection of a multivariate discrimination technology are operational utility and relevance. Most seismic discriminants are model-based and as demonstrated in this paper, error partition and characterizing model error should be integral to seismic discriminant construction.

ACKNOWLEDGEMENTS

The authors acknowledge the support of Leslie A. Casey and the National Nuclear Security Administration Office of Nonproliferation Research and Development for funding this work. Dmitry Storchak, director of the ISC, kindly assisted in the acquisition of the ISC data. Marvin Wetovsky, Los Alamos National Laboratory, provided thorough and objective technical editing support.

REFERENCES

Anderson, D. N., D. K. Fagan, M. A. Tinker, G. D. Kraft, and K. D. Hutchenson (2007). A mathematical statistics formulation of the teleseismic explosion identification problem with multiple discriminants, *Bull. Seism. Soc. Am.* 97: 1730–1741.

Anderson, D.N., W. R. Walter, D. K. Fagan, T. M. Mercier and S. R. Taylor (2009). Regional multi-station discriminants: Magnitude, distance and amplitude corrections and sources of error, *Bull. Seism. Soc. Am.* 99: 794–808.

Blandford, R. R. (1977). Discrimination between earthquakes and underground explosions, *Ann. Rev. Earth Plan. Sci.* 5: 111–122.

Blandford, R. R. (1982). Seismic event discrimination, *Bull. Seism. Soc. Am.* 72: 69–87.

Douglas, A. (1981). Seismic source identification: a review of past and present research efforts. In Husebye, E. and Mykkeltveit, S., Eds., *Identification of Seismic Sources–Earthquake or Underground Explosion* , pp. 1–48. D. Reidel Publishing Co., Dordrecht, The Netherlands.

Douglas, A. (2007). Forensic seismology revisited, *Surveys of Geophysics* 28: 1–31.

Evernden, J. F. (1975). Further studies on seismic discrimination, *Bull. Seism. Soc. Am*. 65: 359–391.

Hand, D. J. (2006). Classifier technology and the illusion of progress, *Statistical Science* 21: 1–34.

Marshall, P. D. and P. W. Basham (1972). Discrimination between earthquakes and underground explosions employing an improved Ms scale, *Geophys. J. R. Astr. Soc.* 29: 431–458.

Mueller, R. A. and J. R. Murphy (1971). Seismic characteristics of underground nuclear detonations: Part I. Seismic spectrum scaling, *Bull. Seism. Soc. Am.* 61: 1675–1692.

Murphy, J. R. and R. A. Mueller (1971). Seismic characteristics of underground nuclear detonations: Part II. Elastic energy and magnitude determinations, *Bull. Seism. Soc. Am.* 61: 1693–1704.

Patton, H. J. and S. R. Taylor (2008). Effects of shock-induced tensile failure on mb-Ms discrimination: Contrasts between historic nuclear explosions and the North Korean test of 9 October 2006, *Geophys. Res. Lett.* 35: L14301.

Stevens, J. L. and S. M. Day (1985). The physical basis of the mb:Ms and variable frequency magnitude methods for earthquake/explosion discrimination, *J. Geophys. Res*. 90: 3009–3020.

MINING EXPLOSION IDENTIFICATION AND DISCRIMINANT ASSESSMENT IN TWO UNIQUE REGIONS

Marie D. Arrowsmith[1,2], Brian W. Stump[2], Stephen J. Arrowsmith[1], and Michael A. H. Hedlin[3]

Los Alamos National Laboratory[1], Southern Methodist University[2], and University of California—San Diego[3]

Sponsored by the National Nuclear Security Administration

Award No. DE-FC52-03NA99510
Proposal No. BAA03-38

ABSTRACT

With the contribution of data from high-quality seismic stations throughout the globe, the event detection threshold is reduced to smaller magnitudes. At magnitude 4 and below, delay-fired explosions are often commonly observed along with natural seismicity. The addition of this class within an event catalog leads to several questions which must be addressed: (1) can delay-fired mining explosions be discriminated from earthquakes; (2) can the understanding of mining discriminants illuminate the explosion discrimination process in regions where there are no known nuclear explosions; and (3) are mining discriminants regionally dependent, and are there corrections to account for this dependence? A broader question is in understanding the ability to separate source and propagation path effects from regional data. Addressing this question utilizing regional datasets has direct application to the problems noted above but more generally to our ability to interpret regional seismic records from all types of events including earthquakes. To address these types of questions, we have assembled a database focused on two regions, the Western United States (WUS) and the Altai-Sayan (AS) region of Russia, which are both areas of prolific mining activity. As part of an extensive collaboration with the largest coal mine in the WUS, we have detailed shot information for ~1000 mining events, classified into six distinct blast types; we have limited information for events in the AS.

We have applied three discriminants to data from 11 stations and one array in the WUS. The first discriminant (amplitude ratios) yields station centric results, although the largest mining events separate from earthquakes that are <250 km from the mine; as the earthquake dataset expands spatially, discrimination performance degrades. 1D path corrections provide improvement, but additional calibrations are necessary to optimize this discriminant. The second discriminant (time-frequency) separates the larger types of blasts with the longest source duration at all stations. Smaller blasts do not discriminate because of the shorter shot durations. The third discriminant (time-of-day) may have a secondary role in the discrimination of an individual event but may be quite useful in assessing man-made seismic activity in a regional context. We have utilized waveform correlation techniques to better understand how factors such as mining blast type and location within the mine are manifested in the waveforms. Initial results show good correlation between blast types within two main pits; as the correlation threshold is increased, we are able to resolve spatial location within individual pits for the simplest types of mining blasts. In the AS, we calculated these same discriminants for ~260 earthquakes and ~850 mining events. The amplitude ratio discriminant shows significant overlap of the earthquake and mining populations. Certain events do separate, but the lack of ground-truth makes these events difficult to identify. Similar results are seen for the time-frequency discriminant. We do not know if the discriminant itself fails, or if the majority of our data points are from smaller shots that have shorter time durations. Time-of-day results are similar to the WUS in that presumed mining events fall within working hours and indicate the assessment utility of this tool. These unanswered questions illustrate the need for detailed ground-truth information. Future studies of mining discrimination, particularly where large datasets are to be acquired, should involve cooperation with mine operators in order to address ambiguities such as those identified in the AS study. Although we see mixed results with the amplitude ratio discriminant, there is more success with the time-frequency and time-of-day discriminants.

No discriminant individually is able to successfully act as a surrogate for a single-fired explosion. However, the three discriminants, when used in combination, can provide a means of defining a delay-fired population region that could be integrated into a model such as the Event Classification Matrix (ECM) to aid in identifying events that do not fall within traditional nuclear explosion or earthquake population bounds (Anderson et al., 2007). We have begun testing this methodology by using classification trees and Regularized Discrimination Analysis (RDA) to combine the three discriminants discussed above, which yield a statistical measure of the probability of correctly categorizing mining events.

OBJECTIVES

The two objectives for the final component of this study build on previous work (e.g., Arrowsmith et al., 2008) completed on developing both a comprehensive mining explosion dataset and a suite of mining explosion discriminants. These objectives are the following:

- **Assessment of four mining explosion discriminants using ground-truth data in the WUS and AS.** We assess four independent discriminants including amplitude ratios, time frequency, time-of-day, and waveform correlation.
- **Assessment of techniques for discriminant combination.** We examine two strategies for combining discriminants including classification trees and RDA.

RESEARCH ACCOMPLISHED

Mining Explosion and Regional Earthquake Database

In order to assess discriminant performance, we assembled a database of waveforms for mining events in the US and Russia, discussed in detail in Arrowsmith et al. (2008). In-depth analysis has focused on ground-truth (GT) data in the WUS (Figure 1) and data collected as part of a joint collaboration with the AS Seismological Expedition (ASSE) (Figure 2).

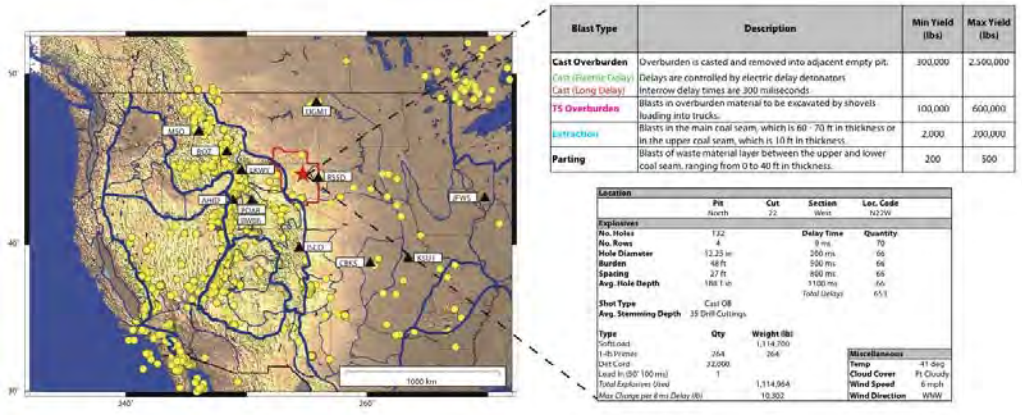

Figure 1. WUS dataset used in the mining discrimination analysis. Left panel shows earthquakes (yellow circles) distributed across major geologic provinces (thick blue lines) and sub-provinces (thin blue lines). Stations are denoted by black triangles. The Black Thunder coal mine (red star) is in the Powder River Basin (red outline). The right panel illustrates GT data collected from Black Thunder; the top figure denotes the main types of shots performed at the mine, while the bottom figure shows specific shot information.

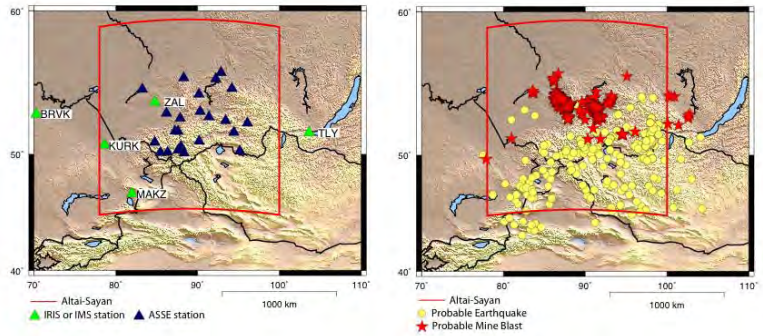

Figure 2. Data from the AS portion of the database (red outline). (Left) Seismic stations in the AS region. Green stations are IRIS (BRVK, KURK, MAKZ, TLY) or International Monitoring System (IMS) (ZAL). Blue stations are operated by the ASSE. We did not have access to ASSE seismic data. (Right) Events provided to the authors by the ASSE; we were given no information on how events were identified as either mining explosions (red circles) or earthquakes (yellow circles).

Magnitude and Distance Amplitude Corrected (MDAC) Spectral Ratios

Regional phase amplitudes are highly influenced by both propagation path and source size. In order to correct for these effects prior to forming ratios, we utilized the MDAC methodology described in Walter and Taylor (2002). The MDAC software will accept simple 1D attenuation (Q_0) models or 2D tomographic imagery; we used 1D averages based upon the geologic features and regions noted in Figure 1 to constrain reasonable attenuation boundaries. Full results obtained for Q_0 and the frequency scaling factor η can be found in Arrowsmith (2009). To correct for source size, we solved for stress drop, varying the values from 0.1 to 30 MPa for the earthquakes featured in Figure 1; we obtained an overall value of 0.1 MPa to best fit the data.

In order to test whether or not the MDAC methodology was adequately removing trends related to distance and source size, we used an F-test to compare two scenarios: the null hypothesis assumes a de-trended population and the alternative hypothesis assumes a trend to the data. The F-test considers the variance around each trend-line; if the tabulated F-statistic (F_{tab}; from a standard table) is greater than the calculated F-statistic (F_{obs}; from the data) at the 0.95 confidence level, we accept the null hypothesis that MDAC has successfully removed the trends. Figure 3 illustrates one result for station PD31 in the 6.0- to 8.0-Hz band. In this case, the trend related to the source has been removed, but the trend related to distance has not (associated Q_0 values are: Pn = 445, Pg = 345, Lg = 315), suggesting that the complicated paths seen in Figure 1 are not being well fit by a 1D attenuation model. Because the stress drop is very low, we forced the stress drop to be 3 MPa (Figure 4) and solved for attenuation (associated Q_0 values are: Pn = 240, Pg = 140, Lg = 140). While the attenuation model fits the data better, the values are below average for the region (see Arrowsmith [2009] for a comprehensive description of WUS attenuation, including references to other studies). The stress drop value of 3 MPa does not fit the data for Lg, but results in a de-trended population for both Pn and Pg. Both sets of results in Figure 3 and 4 illustrate the tradeoffs between source and path seen in the MDAC inversion, and the sensitivity of the population trend with the choice of parameters used in the correction process.

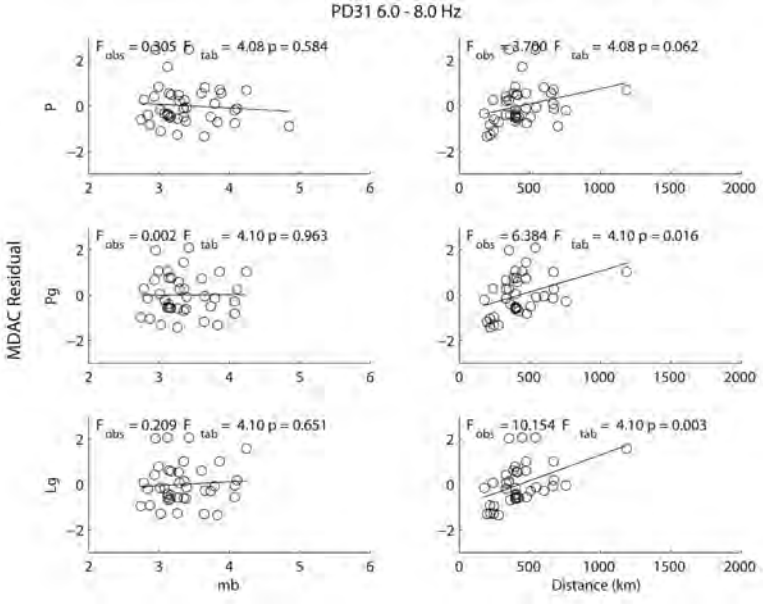

Figure 3. Corrected earthquake log(amplitudes) for *Pn* (denoted as *P*), *Pg*, and *Lg* at station PD31 in the 6.0–8.0 Hz frequency band for an MDAC stress drop of 0.1 MPa. The lefthand column is a function of m_b; the righthand column is a function of distance (km). A regression line has been plotted for each population and the result of the F-statistic analyses are shown for each scenario, including F_{obs}, F_{tab}, and the associated *p*-value.

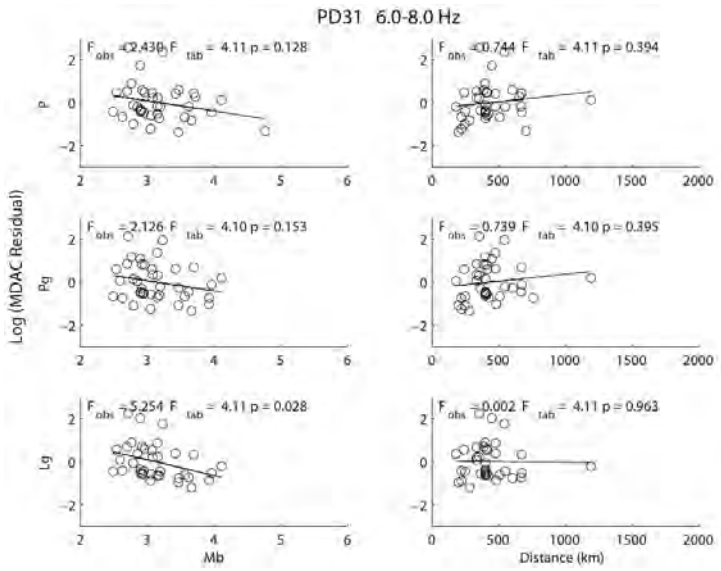

Figure 4. Corrected earthquake log(amplitudes) for *Pn* (denoted as *P*), *Pg*, and *Lg* at station PD31 in the 6.0–8.0 Hz frequency band for an MDAC stress drop of 3 MPa. The lefthand column is a function of m_b; the righthand column is a function of distance (km). A regression line has been plotted for each population and the result of the F-statistic analyses are shown for each scenario, including F_{obs}, F_{tab}, and the associated *p*-value.

We have used the corrected data (using 0.1 MPa stress drop and associated attenuation) to form phase, spectral, and cross-spectral ratios for the eight stations featured in Figure 1. In order to find the optimal ratio at each station, we have used the Mahalanobis distance, a multivariate statistical approach. The Mahalanobis distance weights the distance between two populations based upon the population variability. We pre-selected 12 discriminants, and determined the best amplitude ratio by maximizing the Mahalanobis distance between the earthquake and mining explosion populations. This analysis was performed for four cases: all earthquakes and all mining explosions, all earthquakes and only cast blasts, earthquakes within 250 km of Black Thunder and all mining explosions, and earthquakes within 250 km from Black Thunder and only cast blasts. Results for all stations are summarized in Table 1. The results are very station-centric, and there is high dependence on path when considering earthquakes in the entire region. However, when earthquakes within 250 km of the mine are considered, discrimination performance is greatly enhanced at most stations, making the amplitude ratio discriminant a promising one for mining explosions.

Table 1. The best-performing discriminants for WUS stations for the four scenarios described in the text. The top line in each cell indicates the discriminant used and the bottom line indicates the corresponding Mahalanobis distance value. Results are color-coded by general geologic regime, as defined by the authors based upon geologic provinces featured in Figure 1.

Station	Quakes All Mining	Quakes Cast Blasts	Quakes (250 km) All Mining	Quakes (250 km) Cast Blasts
AHID	Pn(6-8)/Lg(6-8) 0.4572	Pn(6-8)/Lg(6-8) 0.0338	Pg(6-8)/Lg(6-8) 18.2054	Pg(6-8)/Lg(6-8) 18.2054
BOZ	Pn(4-6)/Pn(1-2) 1.5995	Pn(4-6)/Pn(1-2) 1.7336	Pn(6-8)/Lg(6-8) 67.0649	Pn(6-8)/Lg(6-8) 63.4165
BW06	Pg(6-8)/Lg(1-2) 0.6104	Pg(6-8)/Lg(1-2) 0.9644	Pg(6-8)/Pg(1-2) 53.2512	Pg(6-8)/Lg(6-8) 30.3084
CBKS	Pn(4-6)/Lg(4-6) 1.1324	Pn(4-6)/Lg(4-6) 1.0315	Pn(4-6)/Lg(4-6) 11.0146	Pn(4-6)/Lg(4-6) 9.3419
ISCO	Pg(4-6)/Pg(1-2) 1.2961	Pg(4-6)/Pg(1-2) 1.3241	Lg(6-8)/Lg(1-2) 88.7212	Lg(6-8)/Lg(1-2) 90.1181
MSO	Pg(6-8)/Pg(1-2) 1.6058	Pg(6-8)/Pg(1-2) 1.6058	Pg(4-6)/Pg(1-2) 6.7304	Pg(4-6)/Pg(1-2) 6.7304
PD31	Pn(4-6)/Pn(1-2) 0.3745	Pn(4-6)/Lg(4-6) 0.1433	Pn(1-2)/Lg(1-2) 9.1353	Pn(1-2)/Lg(1-2) 4.6621
RSSD	Pg(6-8)/Lg(6-8) 7.9723	Pg(6-8)/Lg(6-8) 15.5696	Pg(6-8)/Lg(6-8) 99.0786	Pg(6-8)/Lg(6-8) 90.261

Time Frequency

The time frequency discriminant utilizes the unique spectral signature of ripple-fired mining events as a function of time and has been described in detail in previous publications (e.g., Arrowsmith et al., 2006; 2007; 2008). Larger blasts (cast blasts) discriminate very well from the earthquake population, and station location seems to play no role in the success of the discriminant, consistent with the fact that this discriminant is strongly related to the distinctive spectral shape resulting from the long source duration. Smaller blasts merge with the earthquake population, and as there are many small blasts in the dataset, it would be easy to assume the discriminant was not working if we did not have the additional explosion features summarized in Figure 1 (right panel). Being able to constrain the type of shot, as well as other types of information on the blasting configuration is invaluable in assessing discriminant success (Figure 5).

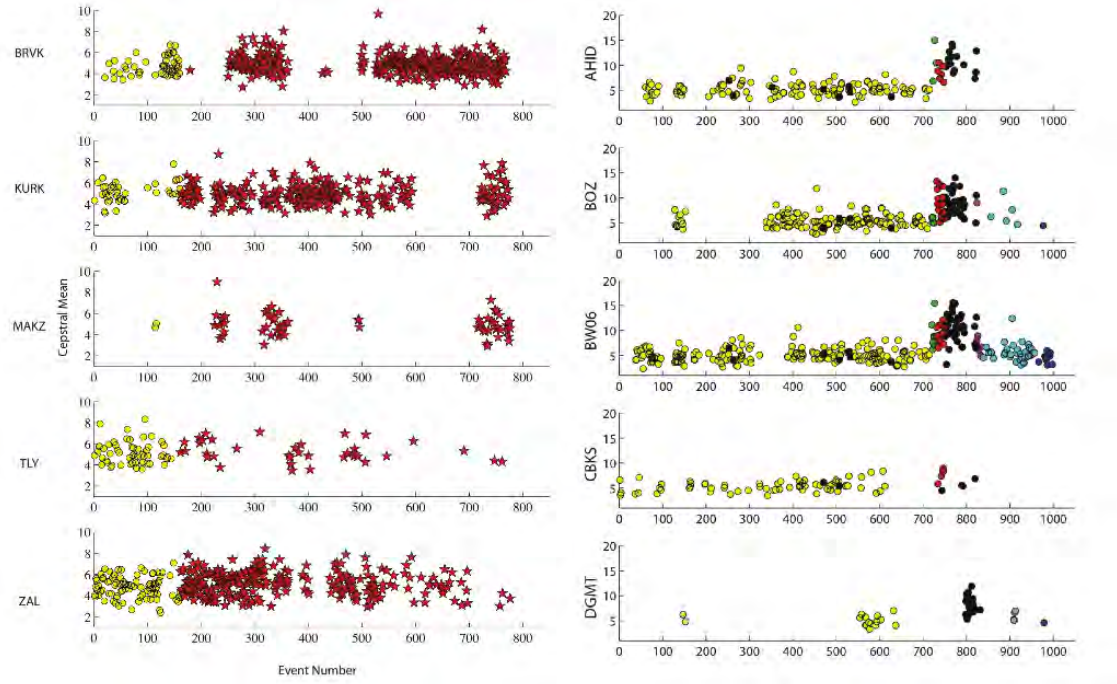

Figure 5. Comparison between AS time frequency results (left) and WUS time frequency results for five stations (right). In the AS, we have no ground-truth information to constrain event type, while in the WUS, we have information such as that shown in the right panel of Figure 1 (events are color-coded as in that panel). In the WUS, we have determined that the larger blast types, such as cast blasts, are essentially the only types of mining explosions that can effectively be discriminated using this technique. Because we do not have detailed GT information in the AS region, we do not know if the discriminant itself fails, or if the shots simply are too small in size (and have a short time duration) to effectively discriminate from the earthquake population.

The Time-of-Day Discriminant

The time-of-day discriminant is extremely useful as a means of verifying catalog consistency (Figure 6) and evaluating the general trends of an active seismic region (Figure 7). While this discriminant alone cannot be used to identify a specific event, it has the potential to help characterize new regions where man-made events are prevalent. When combined with a geographic context, such as in our study, and that of MacCarthy et al. (2008), we gain the ability to focus on areas of specific interest that have an abundance of daytime activity.

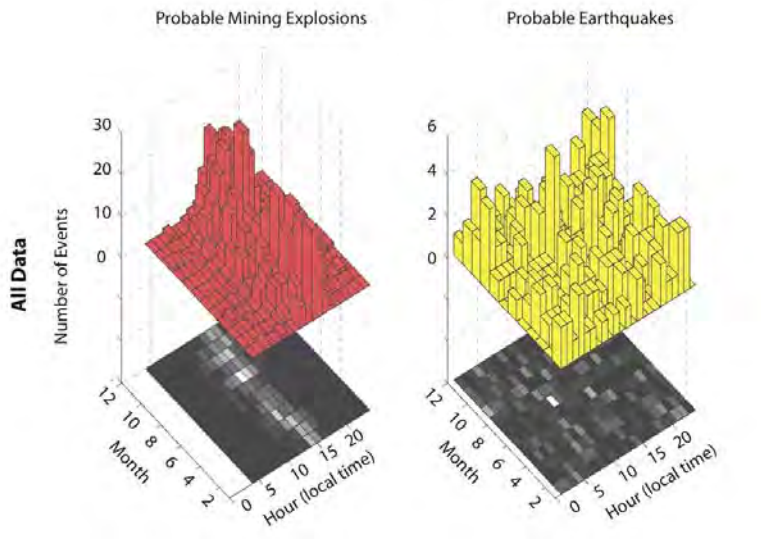

Figure 6. Time-of-day distributions with respect to month and hour of day for the AS dataset for both probable mining explosions (left) and earthquakes (right). Surface reflections of the histograms show trends, where lighter colors indicate larger numbers of events. The concentration of mining events between 10:00 and 17:00 local time as opposed to the random distribution of earthquakes give us confidence in the catalog data provided to us by the ASSE.

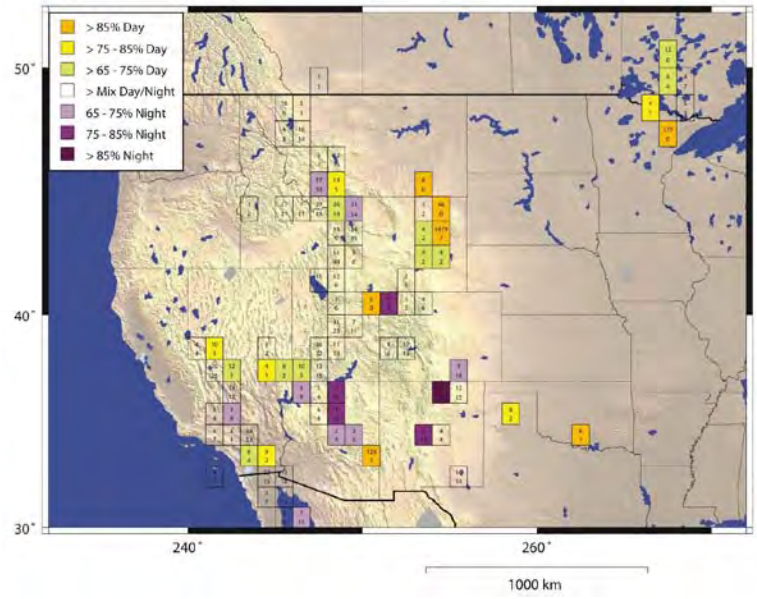

Figure 7. Time-of-day map for events between 8 am and 6 pm local time in the WUS. Event locations are mapped into 1º bins. The daytime count is listed above the nighttime count, and bins are color coded by the percentage of daytime to nighttime events. Areas of high daytime activity, which do not correspond to known mining regions, are discussed in Arrowsmith (2009).

Waveform Correlation for the Black Thunder Mine

A clustering method based on regional waveforms has been developed and applied to a set of ground-truth data from Black Thunder; this mine has spatial dimensions exceeding 5 km (Figure 7) and a variety of source blasting practices provide a basis for investigating the strength of these tools in separating source timing and location effects. Preliminary results at a number of stations suggest that a hybrid technique utilizing multiple correlation cutoffs and a clustering algorithm might be useful in separately identifying location and source timing effects. At modest levels of

correlation, source locations are empirically shown to dominate. Using these results, increasingly larger correlation cutoffs identify nearby events with similar source timing effects. Figures 8 and 9 illustrate the result of changing the correlation coefficient threshold from 0.7 to 0.6.

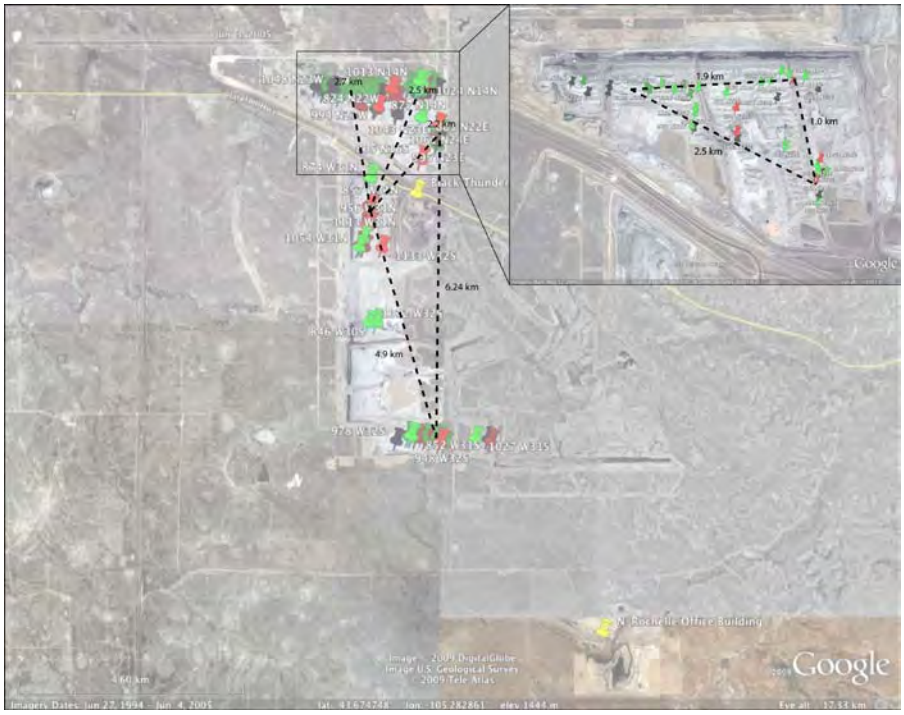

Figure 7. Google Earth satellite image of the mining region, showing close-up of North pits and distances between mining clusters.

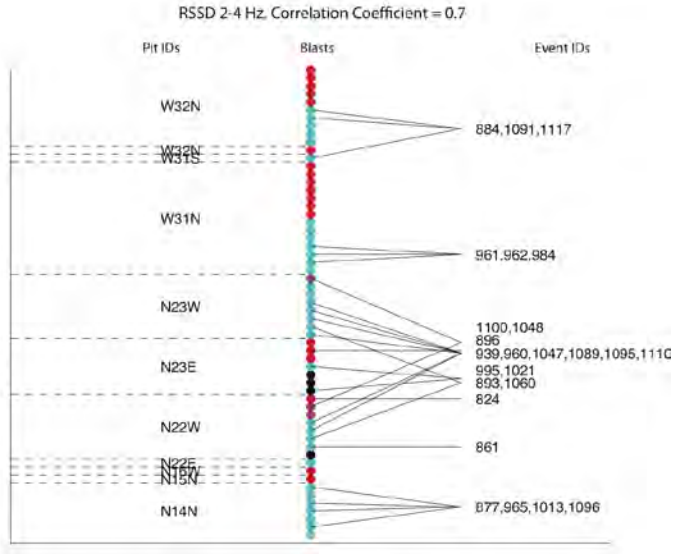

Figure 7. Clustering results for 60 seconds of waveform at RSSD, filtered at 2–4 Hz, with a correlation coefficient of 0.7. Events are colored according to the scheme in Figure 1. The various pit identifiers are listed in the left column.

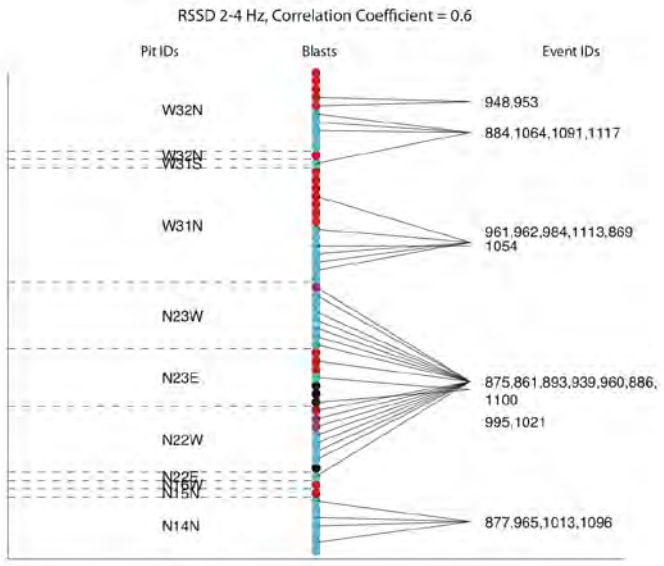

Figure 8. Clustering results for 60 seconds of waveform at RSSD, filtered at 2–4 Hz, with a correlation coefficient of 0.6. Events are colored according to the scheme in Figure 1. The various pit identifiers are listed in the left column.

Discriminant Combination

Combining discriminant measures has been shown to increase overall classification power; however, difficulty lies in combining multiple measures in a statistically sound way while accounting for problems such as missing data. In a comprehensive report, Anderson et al. (1996) investigated eight classification methods for combining discriminants. Current discussions with Dr. Dale Anderson about our dataset have affirmed two methods, classification trees and RDA (Anderson and Taylor, 2002) to be the most suitable for merging discriminant measures. The classification tree considers each discriminant value, partitioning event types into homogenous regions. The process is iterative, and can be branched or pruned based upon the number of discriminants, events, and probability levels achieved at each step in the iteration.

We follow the procedure outlined in Anderson and Taylor (2002) to establish RDA decision rules for identifying events. RDA is a method developed by Friedman (1989) to deal with highly correlated discriminants, and potentially small training samples. RDA encompasses two standard discrimination techniques, linear and quadratic discrimination, and builds a weighted-average covariance matrix. This covariance matrix is dependent on two smoothing parameters, γ and λ. Figure 3 of Anderson and Taylor (2002) illustrates the effect of adjusting γ and λ in order to best define decision regions that fit the true probability of the event classes. An unknown event can then be identified using these decision regions in combination with the Mahalanobis distance metric.

To begin defining decision regions for mining explosions, we have integrated data at all the WUS stations into one single database of measurements consisting of event ID, time-frequency discriminant value, time-of-day, Pg/Lg (6–8 Hz) measurement, geologic region, source type (SEQ, OEX, MEX), where SEQ is a shallow earthquake, OEX is a mining explosion other than cast blast, and MEX is a cast blast. We use a classification tree to characterize probable earthquakes based on time-of-day. Events that fall within the range of hour GMT 18 through 24 (the time when most mining events occur at Black Thunder) are considered unknown events and are set aside for further analysis using RDA.

We searched over γ and λ space using 80% of the dataset to select optimal values, where optimization is achieved by minimizing the false discovery rate (i.e., the false positive rate, given H_0 = explosion). For each matrix of values, we select the minimum γ and λ pair. If there is more than pair that fits the condition, we choose the value that is closest to the origin. We then used 20% of the dataset to test values and make predictions on our ability to categorize events, repeating 100 times for the best γ and λ. The initial results indicate the mean probability of correctly categorizing a mining explosion given a mining explosion is approximately 0.75.

Although further work is needed, the three discriminants, when used in combination, show the potential for defining a delay-fired population region that could be integrated into a model such as the ECM to aid in identifying events that do not fall within traditional nuclear explosion or earthquake population bounds (Anderson et al., 2007).

CONCLUSIONS AND RECOMMENDATIONS

The optimum discriminant for mining explosions would uniquely categorize all mining events, and clearly separate them from earthquakes and, more importantly, underground nuclear explosions. Such a discriminant does not appear to exist; the complex and variable nature of mining explosions, and complexity of path effects at regional distances ensure that this is a difficult problem. Despite this, we have outlined a suite of independent discriminants—each of which provides a different constraint on source physics—that, in combination, can correctly categorize events as mining explosions with a probability of approximately 0.75. Although further work is required to improve upon this result, this study shows that there is considerable promise in developing, if not the optimum discriminant, at least a practical approach that can bring strategic value to operational monitoring needs.

ACKNOWLEDGEMENTS

Data was provided by the IRIS Data Management Center and supplemented by Los Alamos National Laboratory (LANL) and Lawrence Livermore National Laboratory. Additionally, LANL provided computing and advising support throughout the project. Arch Coal gave us access to invaluable data from Black Thunder and Dale Anderson assisted with discriminant combination efforts. The National Science Foundation's Graduate Research Fellowship program provided supplemental assistance for the completion of the companion PhD dissertation (Arrowsmith, 2009) that resulted from this work.

REFERENCES

Anderson, D. N., D. Fagan, M. Tinker, G. Kraft, and K. Hutchenson (2007). A mathematical statistics formulation of the teleseismic explosion identification problem with multiple discriminants, in *Proceedings of the 29th Monitoring Research Review: Ground-Based Nuclear Explosion Monitoring Technologies*, LA-UR-07-5613, Vol. 1, pp. 526–530.

Anderson, D. N. and Taylor, S. R. (2002). Application of regularized discrimination analysis to regional seismic event identification, *Bull. Seismol. Soc. Am.* 92: 2391–2399.

Anderson, D. N, K. K. Anderson, D. N. Hagedorn, K. T. Higbee, N. E. Miller, T. Redgate, and A. C. Rohay (1996). Statistical Classification Methods Applied to Seismic Discrimination, *Pacific Northwest National Laboratory Report,* PNNL-11192US, i–27.

Arrowsmith, M. D. (2009). Mining Explosion Identification as an Application to Treaty Verification, PhD dissertation, Southern Methodist University, 519 p.

Arrowsmith, M. D., S. J. Arrowsmith, B. W. Stump, and M. Hedlin (2008). A suite of discriminants for ground-truth mining events in the Western U.S. and its implications for discrimination capability in Russia, in *Proceedings of the 2008 Monitoring Research Review: Ground-Based Nuclear Explosion Monitoring Technologies*, LA-UR-08-05261, Vol. 1, pp. 544–553.

Arrowsmith, S. J., M. A. H. Hedlin, M. D. Arrowsmith, and B. W. Stump (2007). Identification of delay-fired mining events using seismic arrays: Application to the PDAR array in Wyoming, USA, *Bull. Seismol. Soc. Am.* 97: 989–1001.

Arrowsmith, S. J., M. D. Arrowsmith, M. A. H. Hedlin, and B. Stump (2006). Discrimination of delay-fired mine blasts in Wyoming using an automatic time-frequency discriminant, *Bull. Seismol. Soc. Am.* 96: 2368–2382.

Friedman, J. (1989). Regularized discrimination analysis, *J. Am. Stat. Assoc.* 84: 165–175.

MacCarthy, J. K., H. E. Hartse, M. Greene, and C. Rowe (2008). Using waveform cross-correlation and satellite to identify repeating mine blasts in Eastern Kazakhstan, *Seismol. Res. Lett.* 79: 393–399.

Walter, W. R. and S. R. Taylor (2002). A Revised Magnitude and Distance Amplitude Correction (MDAC2) Procedure for Regional Seismic Discriminants: Theory and Testing at NTS, *Lawrence Livermore National Laboratory,* UCRL-ID-146882, 1–13.

INCORPORATING LOVE- AND RAYLEIGH-WAVE MAGNITUDES, UNEQUAL EARTHQUAKE AND EXPLOSION VARIANCE ASSUMPTIONS, AND INTRASTATION COMPLEXITY FOR IMPROVED EVENT SCREENING

Jessie L. Bonner[1], Anastasia Stroujkova[1], Robert H. Shumway[2],
Robert B. Herrmann[3], and Dale N. Anderson[4]

Weston Geophysical Corporation[1], University of California Davis[2],
St. Louis University[3], Los Alamos National Laboratory[4]

Sponsored by the Air Force Research Laboratory

Contract No. FA8718-09-C-0012
Proposal No. BAA09-75

ABSTRACT

Our objective is to improve seismic event screening using the properties of surface waves. We are accomplishing this through (1) the development of a Love-wave magnitude formula that is complementary to the Russell (2006) formula for Rayleigh waves and (2) quantifying differences in complexities and magnitude variances for earthquake and explosion-generated surface waves.

We have applied the M_s (VMAX) analysis (Bonner et al., 2006) using both Love and Rayleigh waves to events in the Middle East and Korean Peninsula. For the Middle East dataset, consisting of approximately 100 events, the Love M_s (VMAX) is greater than the Rayleigh M_s (VMAX) estimated for individual stations for the majority of the events and azimuths, with the exception of the measurements for the smaller events from European stations to the northeast. It is unclear whether these smaller events suffer from magnitude bias for the Love waves or whether the paths, which include the Caspian and Mediterranean, have variable attenuation for Love and Rayleigh waves.

For the Korean Peninsula, we have estimated Rayleigh- and Love-wave magnitudes for 31 earthquakes and two nuclear explosions, including the 25 May 2009 event. For 25 of the earthquakes, the network-averaged Love-wave magnitude is larger than the Rayleigh-wave estimate. For the 2009 nuclear explosion, the Love-wave M_s (VMAX) was 3.1 while the Rayleigh-wave magnitude was 3.6.

We are also utilizing the potential of observed variances in M_s estimates that differ significantly in earthquake and explosion populations. We have considered two possible methods for incorporating unequal variances into the discrimination problem and compared the performance of various approaches on a population of 73 Western United States (WUS) earthquakes and 131 Nevada Test Site (NTS) explosions. The approach proposes replacing the M_s component by M_s + a*σ, where σ denotes the interstation standard deviation obtained from the stations in the sample that produced the M_s value. We replace the usual linear discriminant a*M_s +b*m_b with a*M_s +b*m_b +c*σ. In the second approach, we estimate the optimum hybrid linear-quadratic discriminant function resulting from the unequal variance assumption. We observed slight improvement for the discriminant functions resulting from the theoretical interpretations of the unequal variance function.

We have also studied the complexity of the "magnitude spectra" at each station. Our hypothesis is that explosion spectra should have fewer focal mechanism-produced complexities in the magnitude spectra than earthquakes. We have developed an intrastation "complexity" metric, Δ_{Ms}, where $\Delta_{Ms} = M_s(i)$-$M_s(i+1)$ at periods i, which are between 9 and 25 seconds. The complexity by itself has discrimination power but does not add substantially to the conditional hybrid discriminant that incorporates the differing spreads of the earthquake and explosion standard deviations.

OBJECTIVES

The Russell (2006) M_s formula has opened up new avenues of scientific research, such as the development of improved regional surface wave Q models (Stevens et al., 2006; Levshin et al., 2006; Cong and Mitchell, 2006) that may further reduce interstation variance of the magnitudes. We believe that application of the M_s(VMAX) technique to Love waves is the next logical step in the scientific process that could lead to improved discrimination. Our objective is to improve seismic event screening using the properties of Rayleigh and Love waves. We are accomplishing this through (1) the development of a Love-wave magnitude formula that is complementary to the Russell (2006) formula for Rayleigh waves and (2) quantifying differences in complexities and magnitude variances for earthquake and explosion-generated surface waves.

RESEARCH ACCOMPLISHED

Love and Rayleigh Wave M_s(VMAX) in the Middle East

We have applied the M_s (VMAX) analysis (Bonner et al., 2006) using both Love and Rayleigh waves to ~100 events located in the Middle East. M_s(VMAX) is for estimated both Rayleigh and Love waves using the Russell (2006) formula:

$$M_s = \log(a_b) + \frac{1}{2}\log[\sin(\Delta)] + 0.0031\left(\frac{T_0}{T}\right)^{1.8}\Delta - \log(f_c) - 0.43 - 0.66\log\left(\frac{20}{T}\right) \quad (1)$$

Our initial hope is to be able to use the same formula for both phases. The details of the processing used to estimate M_s(VMAX) are described in Bonner et al. (2006).

The study area (Figure 1) is located in the zone of continental collision between the Eurasian, African and Arabian plates. The region of study is very complex and spans a variety of different tectonic regimes. The seismicity in South and Central Iran and Turkey is in the upper crust, shallower than ~20 km (e.g., Engdahl et al., 2006). It deepens toward the north in the Alborz region in Northern Iran, where it becomes distributed through the crust. Further to the north in the Central Caspian Sea, the seismicity follows the Apsheron-Balkhan Sill and reaches depths of 30–100 km, deepening toward the north. Turkey seismicity is dominated by strike-slip focal mechanisms and concentrated between depths of 10 and 20 km. In the Zagros fold-and-thrust region, most of the earthquakes are shallower than 30 km, with median depths of 15±7 km.

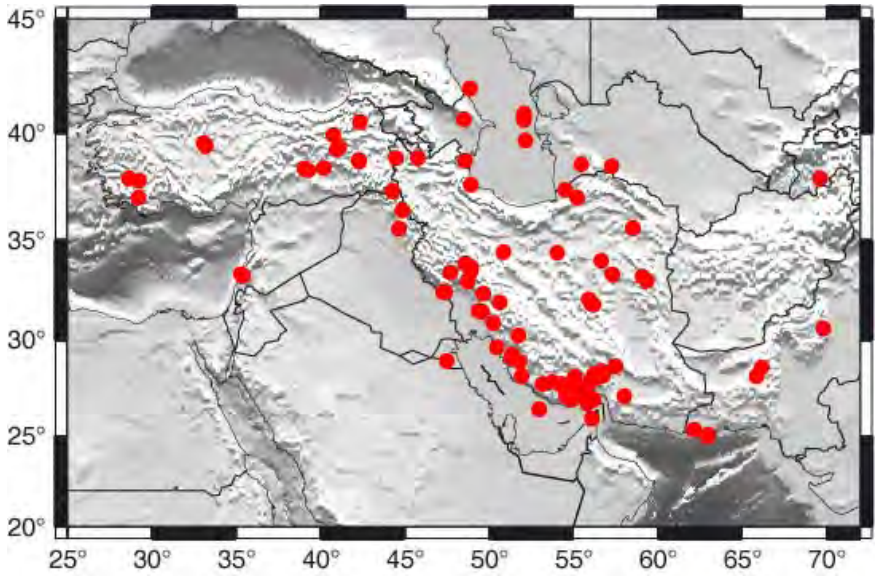

Figure 1. Map of the Middle Eastern events for which M_s(VMAX) for Love and Rayleigh was estimated.

We computed M_s(VMAX) for over 100 seismic events located in this region with reported body wave magnitudes (m_b) between 3.8 and 5.6. The majority of the location and magnitude information (with a few exceptions) was obtained from the NEIC bulletin. The comparison between M_s(VMAX) for Love and Rayleigh waves is shown in Figure 2. The M_s(VMAX) computed using Love waves is greater than the magnitude for Rayleigh waves for the majority of the events of larger magnitudes (above m_b~4). For smaller events, however, we observe a large number of events with the Rayleigh M_s(VMAX) exceeding the Love M_s(VMAX). This peculiarity could be caused by either reduced SNR for smaller magnitude events, or by some unknown source processes, such as a dominant normal fault mechanism. In addition, regional differences in the wave attenuation and/or anisotropy could cause changes in the amplitudes for the rays traveling in different directions. Since the station coverage is not homogeneous, these propagation effects could potentially result in biases in M_s(VMAX) estimate for smaller events with limited sampling.

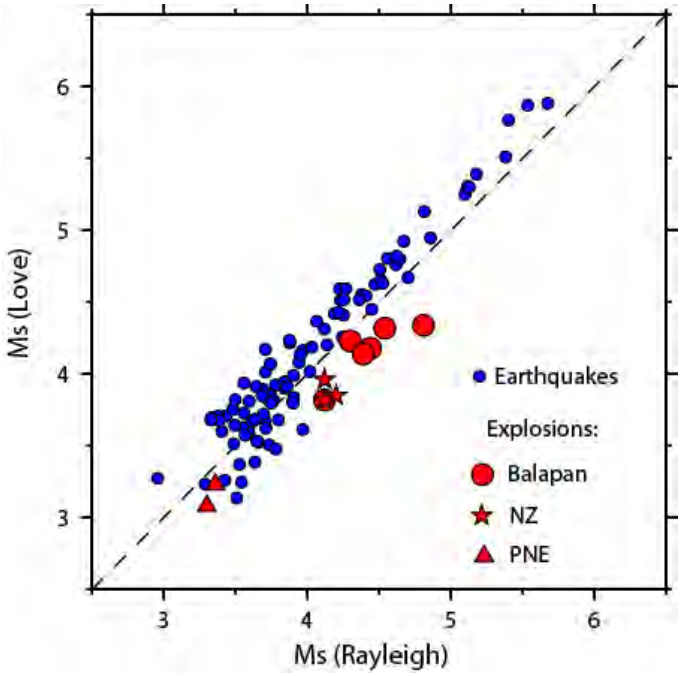

Figure 2. Comparison of M_s(VMAX) computed using Rayleigh and Love waves. Small blue circles show earthquakes, the red symbols show M_s estimate using one station (BRVK) for some Soviet nuclear explosions.

Azimuthal dependency of the estimated M_s(VMAX) for several larger events of known magnitudes (m_b) is shown in Figure 3. The azimuthal differences are most likely caused by source effects (e.g., non-isotropic source radiation), however the propagation effects (e.g., anomalies in regional attenuation, anisotropy) can play a certain role. The stations located between the azimuths 0˚ and 60˚ often have higher magnitude measurements than the stations located in other directions. Notice that for larger events the Love M_s(VMAX) is greater than the Rayleigh M_s(VMAX) for most azimuths. This difference is more pronounced for strike-slip type events, and becomes smaller for the thrust events, common for the Zagros region.

To test whether the azimuthal differences in the magnitudes are caused solely by the focal mechanisms, or if there are propagation effects, we plotted M_s(VMAX) for the individual stations grouped by the direction of propagation. Figure 4a shows the cross-plot between Rayleigh and Love M_s(VMAX) for the stations located to the NE from the corresponding events (back azimuth range between 20º and 70º). There is a significant number of measurements with Rayleigh M_s(VMAX) exceeding Love M_s(VMAX) for smaller events. The measurements for the stations located to the NW of the events (azimuth range between 270º and 360º) show smeared distribution for broader range of magnitudes (Figure 4b). No significant anomaly for smaller events is observed. Therefore it is likely that the reverse in Love and Rayleigh M_s(VMAX) for smaller magnitudes is caused by the regional propagation effects, rather than by the source characteristics.

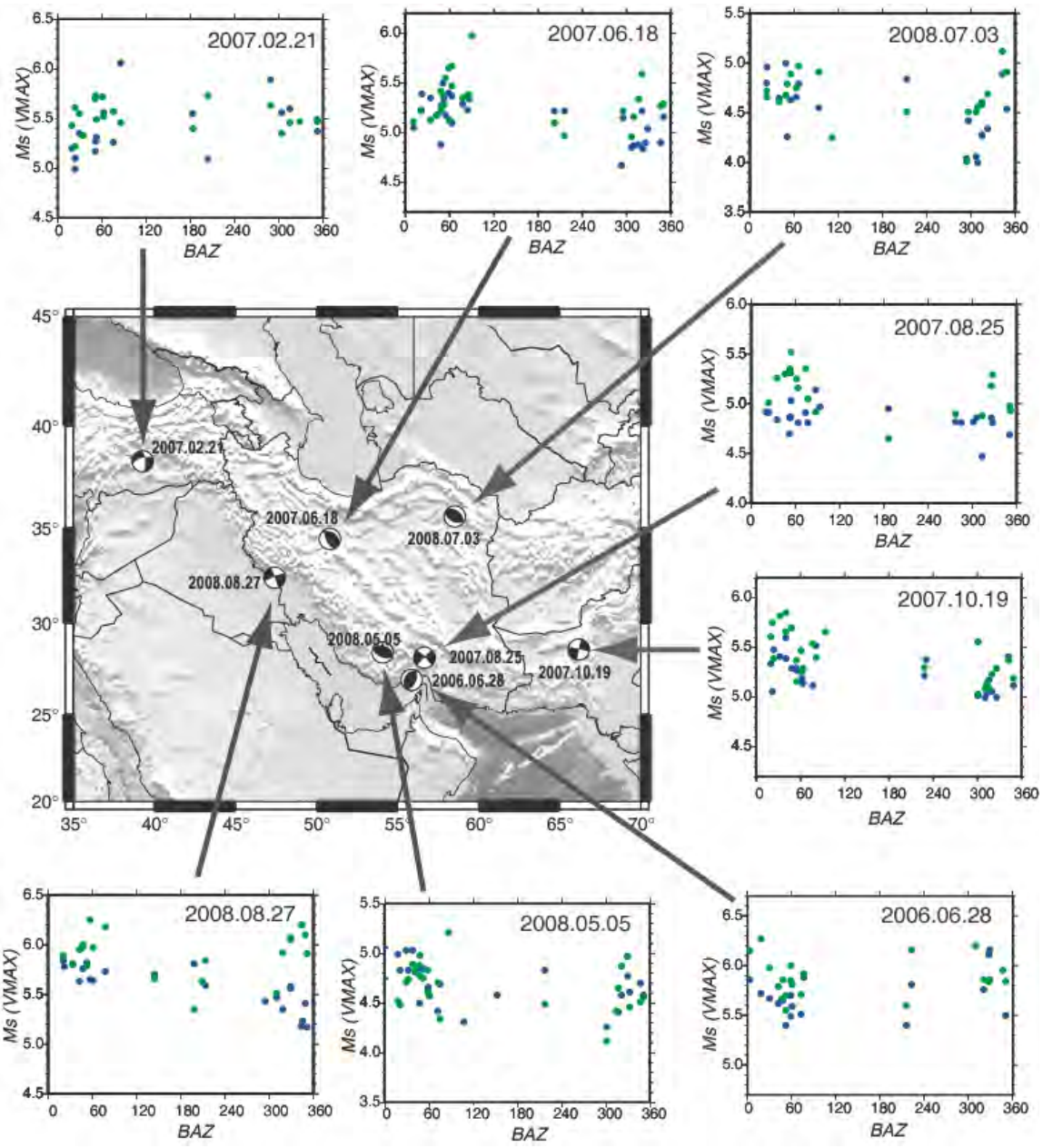

Figure 3. Azimuthal dependence of M_s(VMAX) for some events with known focal mechanisms. Blue and green circles show Rayleigh and Love M_s(VMAX) estimates, respectively.

Love and Rayleigh Wave M_s(VMAX) in the Korean Peninsula

We applied the M_s(VMAX) technique to 31 earthquakes (Figure 5) occurring between 1996–2008 located in the Korean Peninsula and surrounding regions. The events ranged in size between $3.2 < M_w < 5.1$. The distances to the 3C stations (red circles in Figure 5) recording the events ranged from 55 km to 1900 km. For the estimation of Love-wave magnitudes data were converted to transverse motion, while the Rayleigh-wave magnitudes were estimated using vertical component data. The analysis resulted in 298 single-station estimates of M_s(Love) and 266 estimates of M_s(Rayleigh).

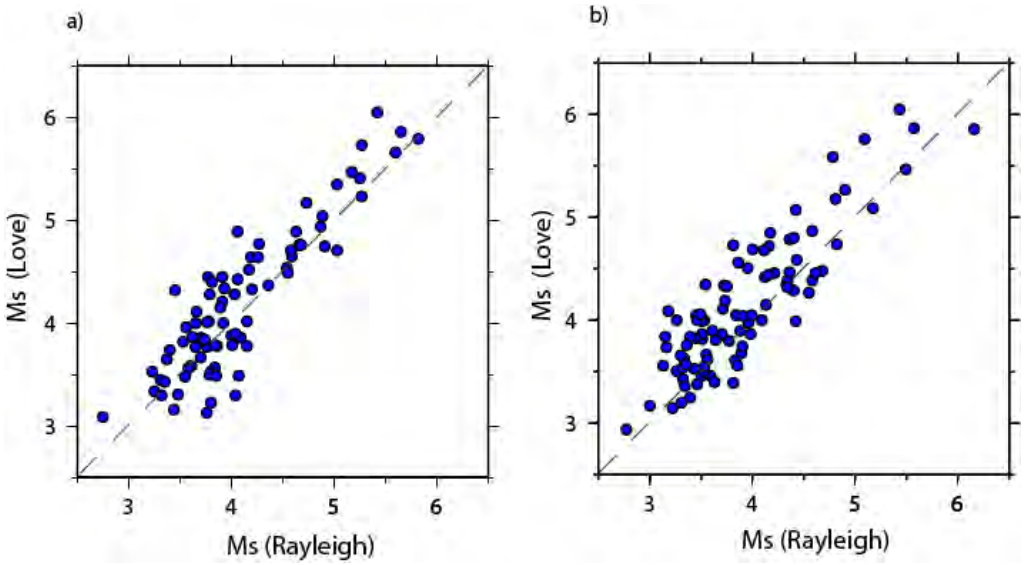

Figure 4. Comparison of M_s(VMAX) computed using Rayleigh and Love waves for individual stations: a) stations located to the NE from the events (back azimuth ranges between 20º and 70º); b) stations located to the NW (back-azimuth ranges between 270º and 360º).

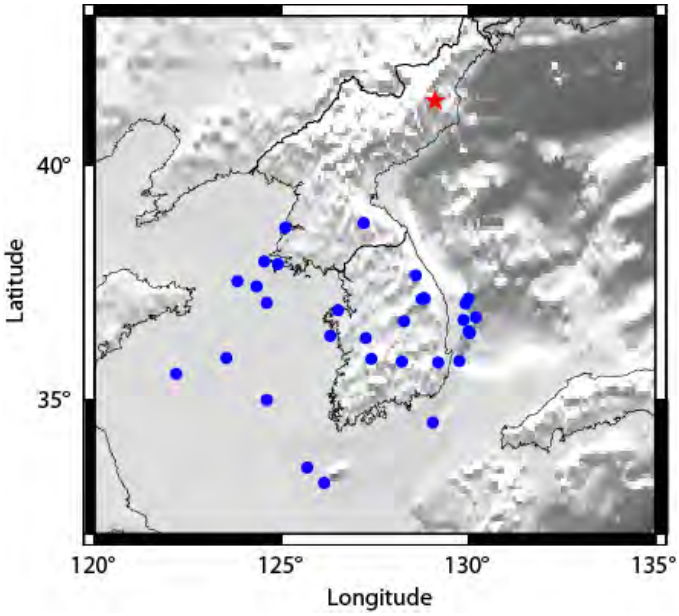

Figure 5. Map of the Korean Peninsula region events (blue circles) for which M_s(VMAX) using Love and Rayleigh waves was estimated. The red star is the approximate location of the North Korean nuclear test.

Figure 6 provides a comparison of Love vs. Rayleigh wave M_s(VMAX) estimates. Applying Equation 1 calibrated for Rayleigh-waves results in a positive bias for the Love-wave magnitudes. This result is consistent with the results for events with M_s(VMAX) > 4 in the Middle East study. Only 6 of the 31 network magnitudes had a larger Rayleigh-wave magnitude than Love-wave magnitude, although when the standard deviation was considered, these events could fall below the line representing equivalent Love- and Rayleigh-wave magnitudes.

In addition to the earthquake dataset we analyzed the two North Korean underground nuclear explosions (UNE). Bonner et al. (2008) found M_s(VMAX)=2.93 for the Rayleigh waves from the 9 October 2006 North Korean UNE. There were no Love waves registered on any of the analyzed stations. The 25 May 2009 announced UNE in North Korean had a larger magnitude [M_s(VMAX)=3.6] and had Love waves large enough for analysis. The M_s(VMAX) estimated for the Love waves was 3.1, which placed it below the earthquake population in Figure 6. The 25 May

2009 event's standard surface wave magnitude, based on Rayleigh waves, plots above the Murphy et al. (1997) screening line for M_s:m_b and is perhaps even more anomalous than its predecessor (Bonner et al., 2006). It appears that the reason the first event did not separate from the earthquake population well was not due to convergence of the populations near m_b ~4.

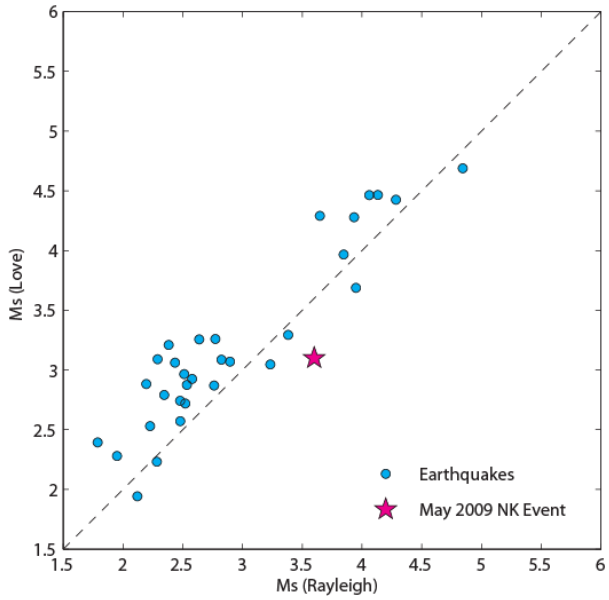

Figure 6. Comparison of M_s(VMAX) computed using Rayleigh and Love waves for the Korean Peninsula region. Small circles show earthquakes while the star shows the M_s estimate for the 25 May 2009 announced nuclear test.

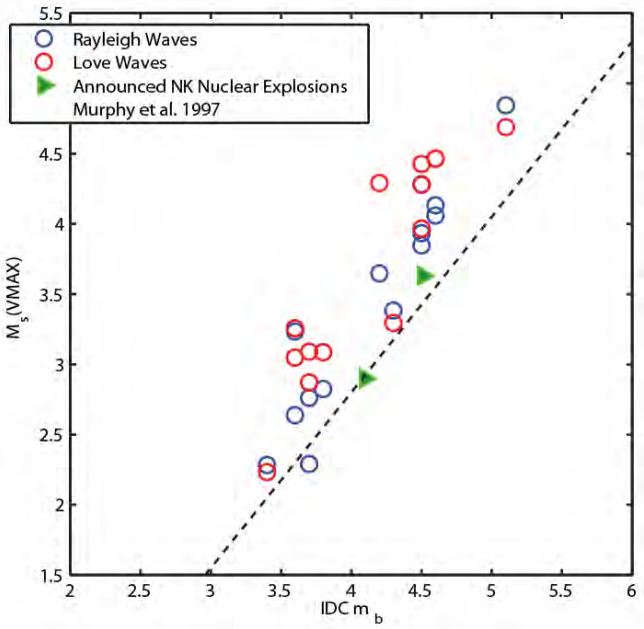

Figure 7. Comparison of network M_s(VMAX) estimates for Rayleigh- and Love-waves versus International Data Centre (IDC) body wave magnitude m_b for Korean Peninsula earthquakes and the two announced North Korean nuclear explosions. The dashed line represents the event screening line proposed by Murphy et al. (1997).

Unequal Variance Assumptions and Improved Discrimination

We have attempted to use the potential of observed variances that differ significantly in earthquake and explosion M_s(VMAX) populations (Figure 7) for improved event screening. We have considered two possible methods for incorporating unequal variances into the discrimination problem and compare the performance of various approaches on a population of 73 WUS earthquakes and 131 WUS explosions.

The conventional statistical approach to separating the distributions with unequal variances would be to derive the likelihood ratio criterion for that case which yields a hybrid discriminant composed of a linear term and a quadratic term with weights dependent on the unequal covariance matrices for the two populations. Taking the solution involving the likelihood ratio guarantees that the probability of correctly ruling out an event as an explosion subject to a fixed probability of failing will be maximized under the multivariate normal assumption for the input variables, usually taken to be M_s and m_b. Sometimes, additional tuning parameters are added to covariance matrices that may improve performance in particular samples or when the joint Gaussian assumptions are not satisfied (see Friedman, 1989; Anderson et al., 2007). The common assumption that the covariance matrices of the two populations are approximately equal reduces the classification function to a linear function of the input variables. For example, the simple difference M_s–m_b is often used as a further approximation. This approach, however, is not recommended because of poor performance in sample populations such as the one considered here.

An alternate method proposes replacing the M_s component by M_s + a*σ, where σ denotes the interstation standard deviation obtained from the stations in the sample that produced the M_s value. In this context, we interpret this as replacing the usual linear discriminant a*M_s +b*m_b by a*M_s +b*m_b+c*σ (Figure 9). We also estimate the optimum hybrid linear-quadratic discriminant function resulting from the unequal variance assumption. While the input standard deviations will not be normally distributed (they follow the chi distribution), the linear approximation may be reasonable for the same reasons that the linear discriminant function works in the usual case. While the two discriminant functions resulting from the two theoretical interpretations of the unequal variance function did slightly better in the test samples used here, all methods except M_s –m_b did extremely well using the WUS dataset. We plan on evaluating this method further using our entire dataset of earthquakes and explosions.

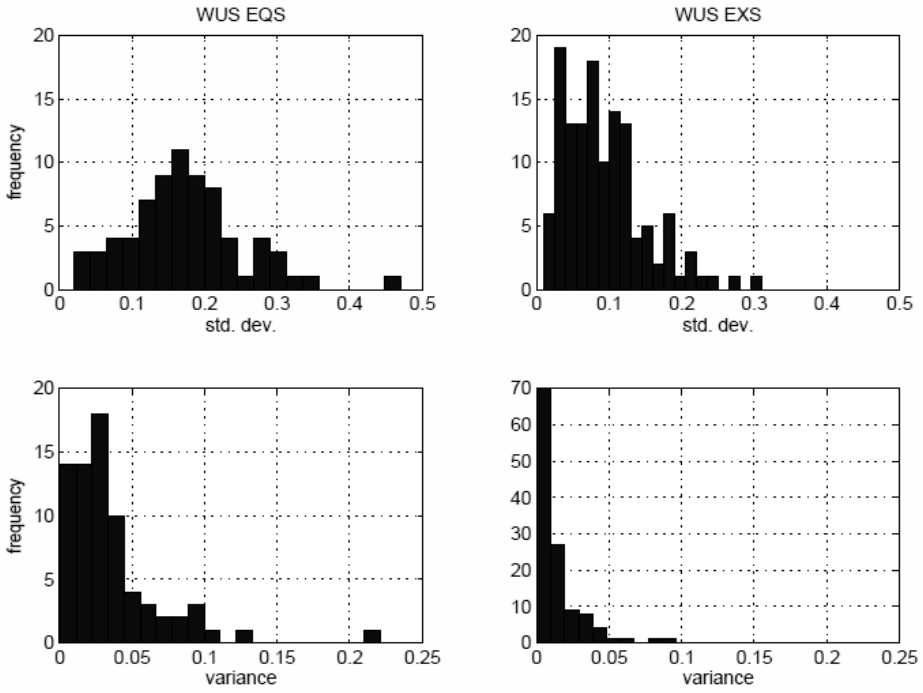

Figure 8. Frequency histograms for the station standard deviations (top) and variances (bottom) for 73 WUS earthquakes and 131 explosions.

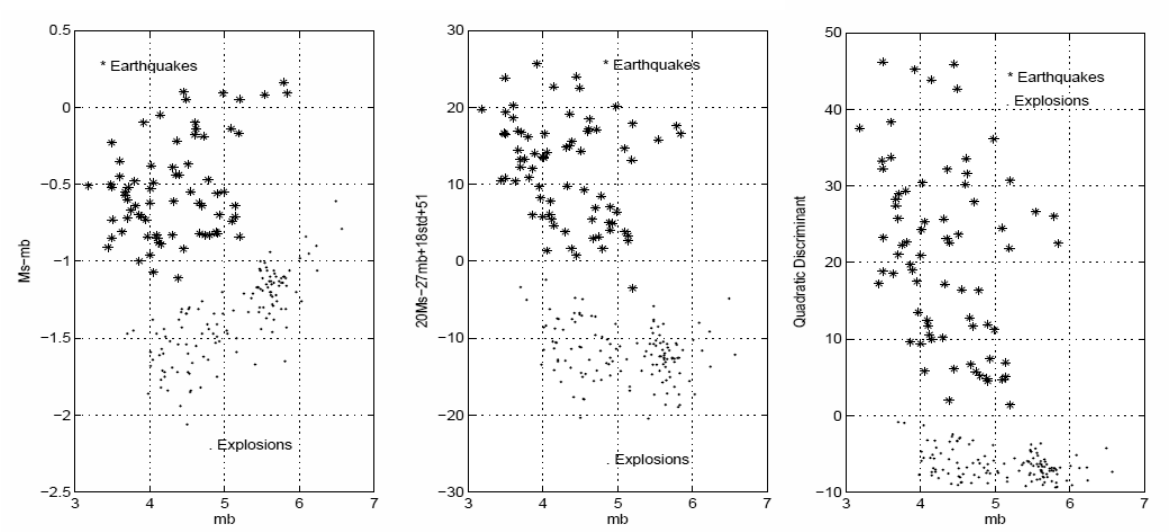

Figure 9. Conventional multivariate discriminant analysis combining M_s(VMAX)-m_b (left), M_s(VMAX), m_b and standard deviation (std) (middle), and multivariate linear-quadratic discriminant analysis (right) for 73 WUS earthquakes and 131 explosions.

A New Metric for Intrastation Complexity

We have also studied the complexity of the "magnitude spectra" at each station. Our hypothesis is that explosion spectra should have fewer focal mechanism-produced complexities in the magnitude spectra than earthquakes (Figure 10). We have tried several different methods, including the intrastation std as a function of period shown in Figure 10 and a "differencing" approach. For periods *i* between 9 and 25 seconds, we estimate:

$$\Delta_{Ms} = M_s(i) - M_s(i+1)\,. \qquad (2)$$

We start at i=9 seconds to minimize edge effects. This results in n=17 new magnitude differences, Δ_{Ms}, for each station. It may be fewer if estimates at some periods fail a signal-to-noise ratio test.

We then estimated several different metrics, M, from Δ_{Ms} for comparison of the differenced magnitudes. Thus far, we have settled on:

$$M = \frac{\Sigma\left|\Delta_{Ms-\overline{\Delta Ms}}\right|}{n} \qquad (3)$$

Figure 11 shows the histograms for the earthquake and explosion populations M while Figure 12 shows the cumulative distribution functions of M. The metric M works well for the application of trying to separate complexity of source spectra. At 90% explosion confidence, around .02 M, there is about a 30% earthquake confidence.

CONCLUSIONS AND RECOMMENDATIONS

Preliminary research shows that Love-wave magnitudes for earthquakes are often equal to or larger than Rayleigh-wave magnitudes. Conversely, for explosions, Love-wave magnitudes are typically smaller than Rayleigh wave estimates, or below background noise levels. However, we observe a number of smaller events with reversed pattern. Interestingly enough, this peculiarity is observed for the Middle East dataset, but not for Korean dataset. We will continue to examine this phenomenon, possibly incorporating M_s maximum likelihood estimates, with hopes of porting the results, theory, and statistical *p*-values into the Event Classification Matrix (ECM; Anderson et al., 2007). Additional aspects of surface wave propagation, including a new intrastation complexity metric and differences in explosion and earthquake magnitude variances, also show promise for improved event screening.

We will also develop an improved formula for estimation of *Ms*(VMAX) using Love waves. Equation 1 was developed using empirical relationships using the Rayleigh waves, which may or may not be calibrated for Love waves.

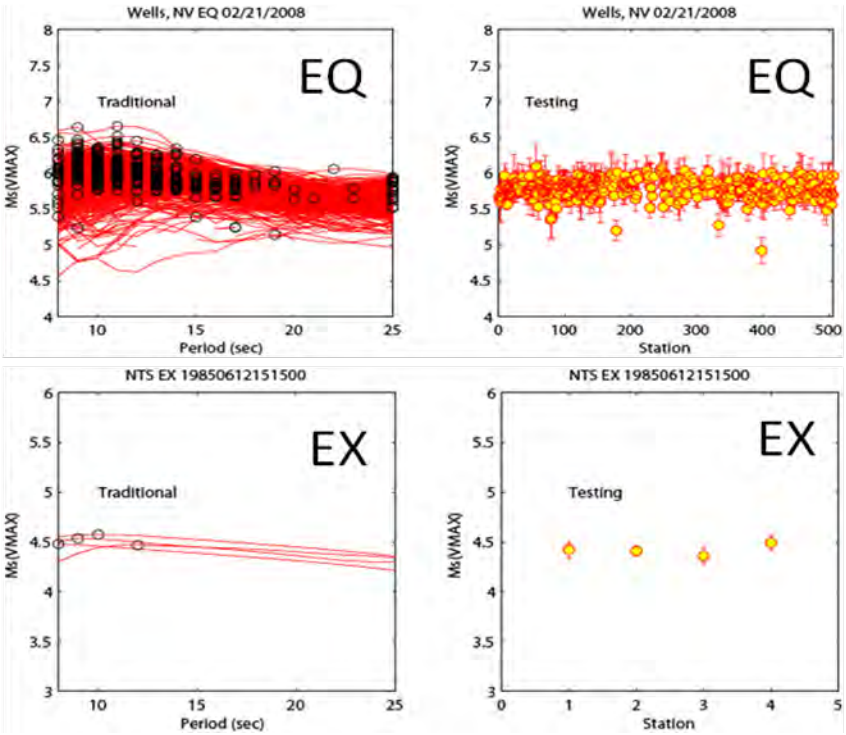

Figure 10. A proposed new approach for improved discrimination. (Left Column) Traditional M_s(VMAX) where the circle is the period of maximum amplitude. (Right Column) The mean of a station's estimate and its standard deviation are formed. Our results suggest that the intrastation standard deviation is typically less for explosions than earthquakes for our WUS database.

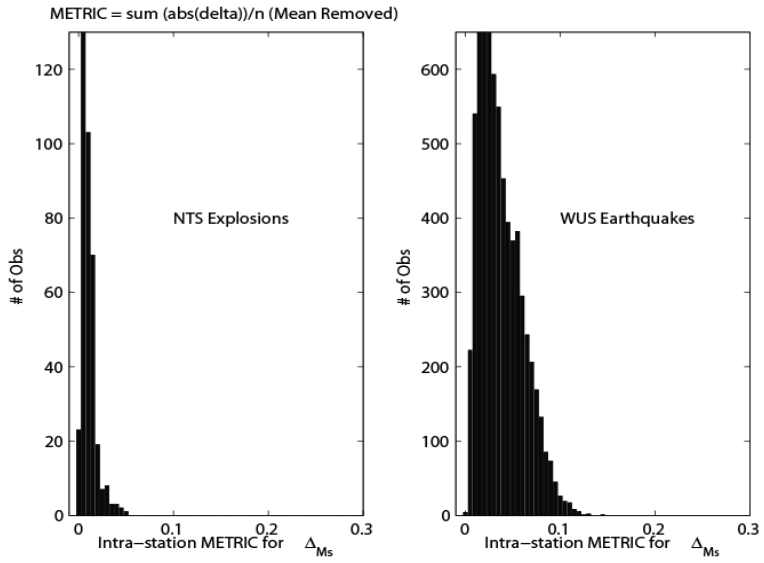

Figure 11. Comparison of the new intrastation metric Δ_{Ms} for NTS explosions (left) and WUS earthquakes (right).

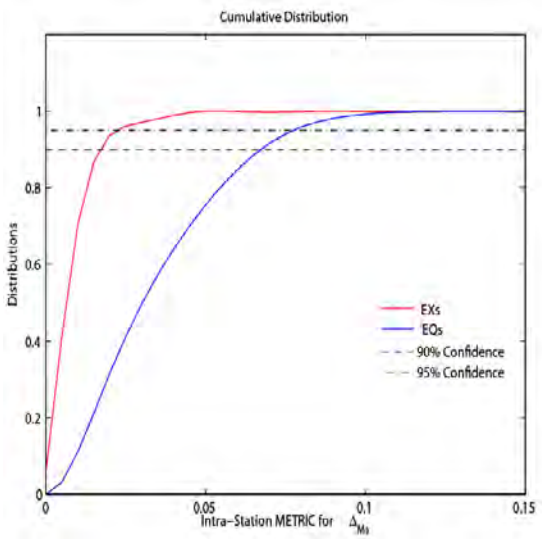

Figure 12. Cumulative distribution functions for metric *M* (Equation 3; Figure 11) for WUS earthquakes and NTS explosions.

REFERENCES

Anderson, D.N., D.K. Fagan, M.A. Tinker, G.D. Kraft and K.D. Hutcheson (2007). A mathematical statistics formulation of the teleseismic explosion identification problem with multiple discriminants, *Bull. Seism. Soc. Am*. 97: 1730–1741.

Bonner, J.L., D. Russell, D. Harkrider, D. Reiter, and R. Herrmann (2006). Development of a Time-Domain, Variable-Period Surface Wave Magnitude Measurement Procedure for Application at Regional and Teleseismic Distances, Part II: Application and M_s –m_b Performance. *Bull. Seism. Soc. Am.* 96: 678–696

Bonner, J. L., R. B. Herrmann, D. Harkrider, and M. Pasyanos (2008). The surface wave magnitude for the 9 October 2006 North Korean nuclear explosion. *Bull. Seism. Soc. Am*. 98: 2598–2506.

Cong, L. and B. Mitchell (2006). Continent-wide maps of 5-50 S Rayleigh-wave attenuation for Eurasia inferred from maps of 1-Hz *Lg* Coda Q and its frequency dependence, in *Proceedings of the 28th Seismic Research Review: Ground-Based Nuclear Explosion Monitoring Technologies*, LA-UR-06-5471, Vol. 1, pp. 3–7.

Engdahl, E.R., J. Jackson, S. Myers, E. Bergman, and K. Priestley (2006). Relocation and assessment of seismicity in Iran region, *Geophys. J. Int.* 167: 761–778.

Friedman, J.H. (1989). Regularized discriminant analysis. *J. Amer. Statist. Assoc.* 84: 165–175.

Levshin, A., X. Yang, M. Ritzwoller, M. Barmin, and A. Lowry (2006). Toward a Rayleigh wave attenuation model for Central Asia, in *Proceedings of the 28th Seismic Research Review: Ground-Based Nuclear Explosion Monitoring Technologies*, LA-UR-06-5471, Vol. 1, pp. 82–92.

Murphy, J. R., B. W. Barker, and M. E. Marshall (1997). Event screening at the IDC using the M_s/*mb* discriminant. Maxwell Technologies Final Report. 23 p.

Russell, D.R. (2006). Development of a time-domain, variable-period surface wave magnitude measurement procedure for application at regional and teleseismic distances. Part I—Theory. *Bull. Seism. Soc. Am*. 96: 665–677.

Stevens, J., J. Given, G. Baker, and H. Xu. (2006). Development of surface wave dispersion and attenuation maps and improved methods for measuring surface waves, in *Proceedings of the 28th Seismic Research Review: Ground-Based Nuclear Explosion Monitoring Technologies*, LA-UR-06-5471, Vol. 1, pp. 273–281.

IDENTIFYING ISOTROPIC EVENTS USING A REGIONAL MOMENT TENSOR INVERSION

Douglas S. Dreger[1], Sean R. Ford[2], and William R. Walter[2]

Berkeley Seismological Laboratory[1] and Lawrence Livermore National Laboratory[2]

Sponsored by the National Nuclear Security Administration

Award No. DE-FC52-06NA27324[1] and DE-AC52-07NA27344[2]
Proposal No. BAA06-42

ABSTRACT

In our previous work the deviatoric and isotropic source components for 17 explosions at the Nevada Test Site (NTS), as well as 12 earthquakes and 4 collapses in the surrounding region of the western U.S., were calculated using a regional time-domain full waveform inversion for the complete moment tensor (Dreger et al., 2008; Ford et al., 2008; Ford et al., 2009a). The events separate into specific populations according to their deviation from a pure double-couple and ratio of isotropic to deviatoric energy. The separation allows for anomalous event identification and discrimination between explosions, earthquakes, and collapses. Confidence regions of the model parameters are estimated from the data misfit by assuming normally distributed parameter values. We developed a new Network Sensitivity Solution (NSS) in which the fit of sources distributed over a source-type plot (Hudson et al., 1989) show the resolution of the source parameters. The NSS takes into account the unique station distribution, frequency band, and signal-to-noise ratio of a given event scenario. The NSS compares both a hypothetical pure source (for example an explosion or an earthquake) and the actual data with several thousand sets of synthetic data from a uniform distribution of all possible sources. The comparison with a hypothetical pure source provides the theoretically best-constrained source-type region for a given set of stations, and with it one can determine whether further analysis with the data is warranted. We apply the NSS to a NTS nuclear explosion, and earthquake, as well as the 2006 North Korean nuclear test, and a nearby earthquake. The results show that explosions and earthquakes are distinguishable; however the solution space depends strongly on the station coverage. Finally, on May 25, 2009, a second North Korean test took place. Our preliminary results show that the explosive nature of the event may be determined using the regional distance moment tensor method. Results indicate that the 2009 event is approximately 5–6 times larger than the earlier test, with an isotropic moment of about 1.8e+22 dyne cm. We perform a series of inversions for pure double-couple, pure explosion, combined double-couple and explosion, full moment tensor, and damped moment tensor inversions to assess the resolution of the isotropic moment of the event.

OBJECTIVES

We build on our previous work to implement the time-domain full-waveform inversion of regional data for the complete moment tensor for source-type identification and discrimination (Dreger et al., 2008; Ford et al., 2008) to develop a method of assessing uncertainty in solutions due to the recording geometry. By means of forward calculations the fit of thousands of possible moment tensor solutions, distributed over a Hudson et al. (1989) source-type plot, the classification of a given seismic event in terms of double-couple, non-double-couple, and isotropic components can be more thoroughly examined. Direct comparisons between the fit of such mechanisms can greatly aide in the classification of event type, and importantly present it in a manner that allows for the assessment of solution resolution and uncertainty in terms of station geometry.

RESEARCH ACCOMPLISHED

Introduction

Ford et al. (2009a) calculated seismic moment tensors for 17 nuclear test explosions, 12 earthquakes, and 3 collapses in the vicinity of the NTS in the Western U.S. They found that the relative amount of isotropic and deviatoric moment provided a good discriminant between the explosions and earthquakes. The observational work to describe the discriminant was accompanied by a theoretical study into the sensitivities of the method and it was found that the ability to resolve a well-constrained solution is dependent on station configuration, data bandwidth, and signal-to-noise ratio (SNR). It is difficult to state steadfast rules for what source-types can be resolved for all conditions, when different conditions lead to different levels of confidence in the solution. Therefore, in this study we develop a confidence analysis specific to the source type, station configuration and data SNR, which we call the network sensitivity solution (NSS).

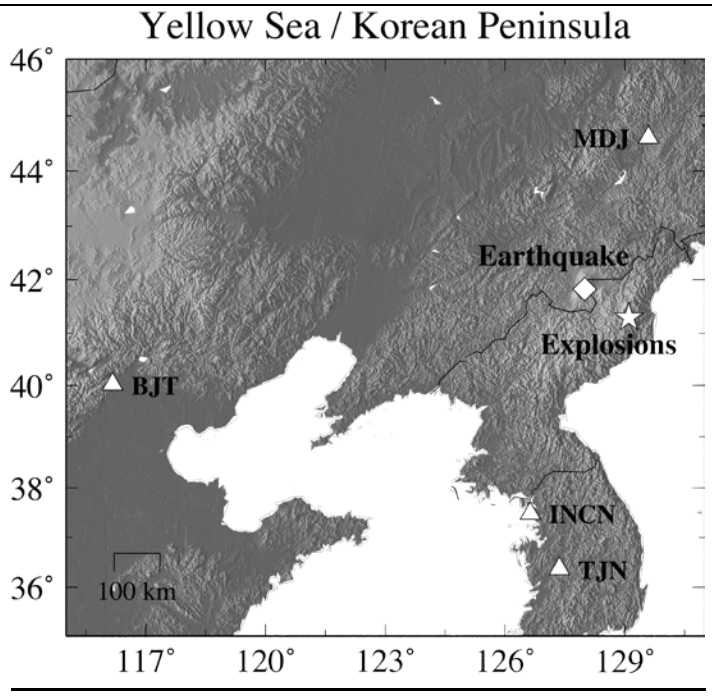

Figure 1. Map of the Yellow Sea / Korean Peninsula with the North Korea tests (5-point star) and nearby earthquake (diamond) as well as the stations used in their analysis (triangles).

There have been many attempts to understand error in seismic moment tensor inversions. Sileny and coathors have done extensive sensitivity testing of the methods they use to calculate the moment tensor. Sileny et al. (1992; 1996), Sileny (1998), Jechumtalova and Sileny (2001), and Sileny (2004) have

collectively investigated the effects of incorrect event depth, poor knowledge of the structural model including anisotropy, noise, and station configuration on the retrieved solution. They found that for only a few stations with data of SNR>5 the moments of various components were sensitive to improper source depth and velocity model, but that the mechanism remained robust, and that spurious isotropic components may manifest in the solution if an isotropic medium assumption is made incorrectly. Roessler et al. (2007) confirm this last result. The probabilistic inversion method by Weber (2006) using near-field full-waveform data helped to inspire the approach taken in this study. Weber (2006) inverts for hundreds of sources using a distribution of hypocentral location based on *a priori* information. Perturbations to the velocity model and noise are also added in the synthetic portion of the study. Empirical parameter distributions are then produced to assess the resolution. Mechanism distribution is plotted with a Riedesel and Jordan (1989) plot, which is also the preference of many of the previously mentioned studies. In the following study we will employ the source-type plot from Hudson et al. (1989), which is described in Ford et al. (2009a). Further details of the inversion method and its practical implementation are also given in Ford et al. (2009a).

Network Sensitivity Solutions

The theoretical NSS tries to answer the question of how well a pure earthquake or explosion can be resolved with very high SNR data for the given event scenario (i.e., data bandwidth and station distribution). To do this we use the GFs to first produce data for a model event (earthquake or explosion) as well as a uniform distribution of synthetic sources representing all possible sources, where the moment of these sources is chosen so as to best fit the model event data. The source-type parameters (Hudson et al., 1989) are calculated for each of the thousands of synthetic sources (Figure 2a). Since the source-type plot does not account for total seismic moment (only relative moment) or source orientation, a single set of source-type parameters (one point on the source-type plot) can represent several sources. For example, a DC source with any strike, rake, or dip, will plot in the center of the source-type plot (Figure 2b). However, as one moves away from the center of the source-type plot (location of a DC mechanism), source orientation becomes less important to the seismic radiation so that the top and bottom of the plot are uniquely represented by an explosion or implosion, respectively.

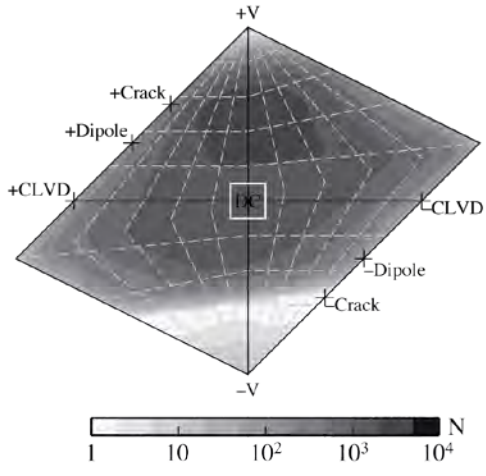

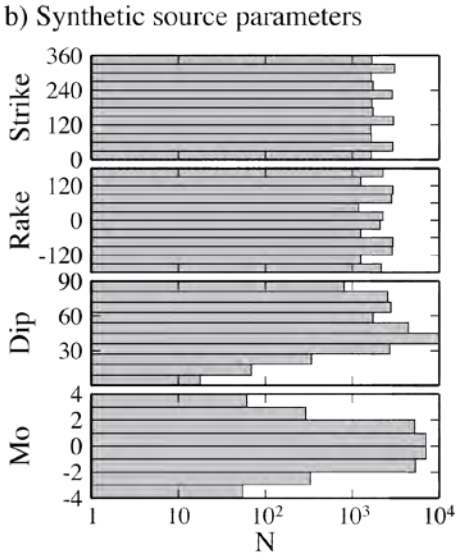

Figure 2. Synthetic sources. a) Source-type plot of synthetic source distribution. Gray scale gives the 0.1-unit smoothed number of events, and the white box outlines the sources described in b). b) Parameters of the synthetic sources contained in the white box in b).

The model event data d is then compared with the synthetic source data s and the fit for each comparison is quantified by the variance reduction (VR)

$$\mathrm{VR} = \left[1 - \frac{\sum_i (d_i - s_i)^2}{\sum_i d_i^2}\right] \times 100 \,. \tag{1}$$

where i are the displacements at all times for all components at all stations.

The VR for each synthetic source is calculated and plotted as a function of source-type parameter on the source-type plot. Since a single set of source-type parameters can represent many sources that could have varying levels of fit to the model event data (and therefore, VR), a moving-maximum window is used to smooth the VR distribution. The source-type plot empirical VR distributions are shown in Figure 2 for a small earthquake located in southeast China.

NSS for a Southeast China Earthquake

Figure 3 gives the theoretical and actual NSSs for the earthquake in China, as well as the waveforms for the data, Best-fit, Example, and Explosion models for comparison. The actual NSS for the earthquake (Figure 3b) shows a well-constrained region similar to the theoretical NSS (Figure 3a). The waveforms of the best-fit model (VR = 67%), shown in Figure 3c, fit the data just as well as a pure DC. This result gives us confidence that the MDJ2 model is a good 1-D approximation of the velocity structure in this region, as the expectation is that the small earthquake should be well represented by a double-couple point-source. Importantly, the analysis also shows that a pure explosion fails to fit the data yielding a best fit variance reduction of only 13%.

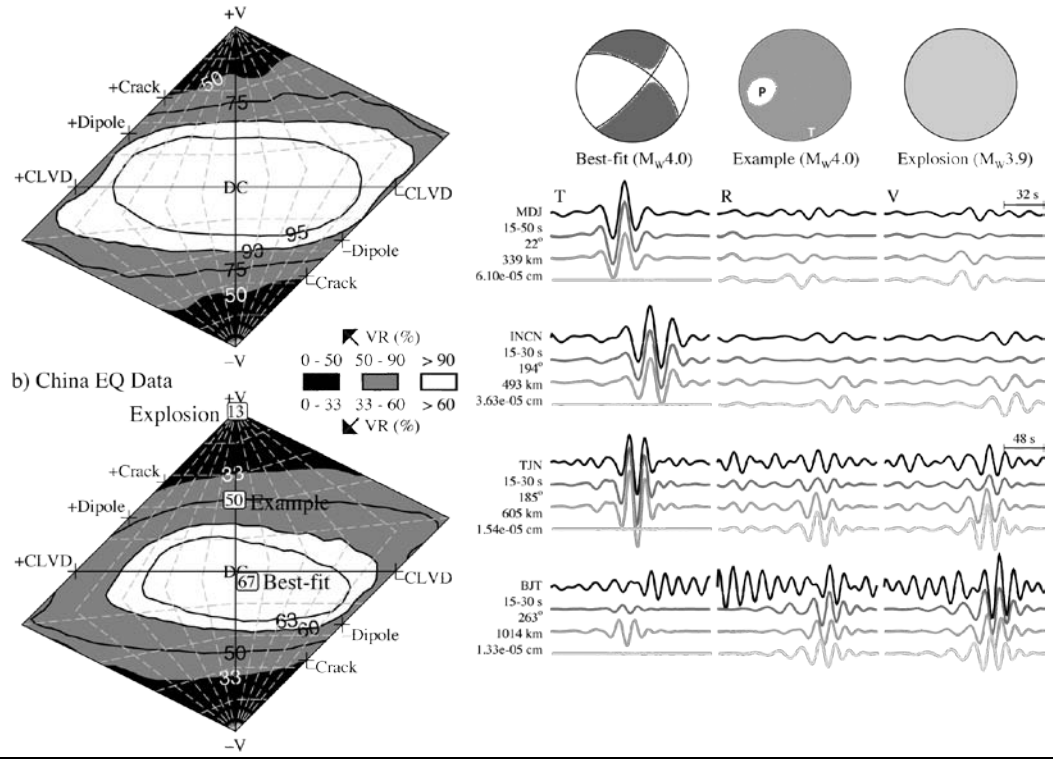

Figure 3. Network sensitivity solution (NSS) for an earthquake (16 Dec 04) near the 2006 North Korea test location. a) Theoretical NSS using one hundred earthquakes with a uniform distribution of fault parameters where the Green's functions are derived from the actual network setup and the data is noiseless. The best-fit model is a pure double-couple (DC) with a VR of 100%. Empirical distributions of other models and the corresponding VR are also given via contours on the source-type plot. b) Actual NSS using data from the China earthquake. The best-fit model with a VR of 67% along with other models and the corresponding VR distributions are shown. For comparison, an Example model (VR = 50%) and a pure Explosion model (VR = 13%) are also plotted and correspond with the models and waveforms given in c). c) Models corresponding to those plotted in b) and their respective forward-predicted waveforms as a function of color compared with the actual waveforms (black line). The left, middle, and right columns are the tangential (T), radial (R), and vertical (V) displacement waveforms, respectively. The text block to the left of the waveforms gives the station name, passband period (s), azimuth, epicentral distance (km), and maximum displacement (cm). The moment magnitudes of the models are also given below the mechanism.

2006 North Korean Nuclear Test

The solution for the October 2006 explosion in North Korea (ODNI, 2006) is much less constrained than the Chinese earthquake due to the simpler radiation pattern. Normally, we would run the inversion without station BJT because the epicentral distance is more than 1000 km and performance of the simpler 1-D velocity model employed here degrades at such great distances. However, preliminary inspection of the theoretical NSS without BJT showed that the solution could not satisfactorily exclude DC sources. Although this understanding could be gained from simple inspection of the station configuration shown in Figure 1b, where without BJT all stations fall along one azimuth with π periodicity (a condition that can always fit the two-lobed Rayleigh radiation pattern of a 45-degree dip-slip mechanism), the example is still instructive for cases that are not so easily visually inspected. With station BJT, the high VR region has the

shape typical of NTS events, illustrating the tradeoff between isotropic and vertical, compressive CLVD sources (e.g. Ford et al., 2009b).

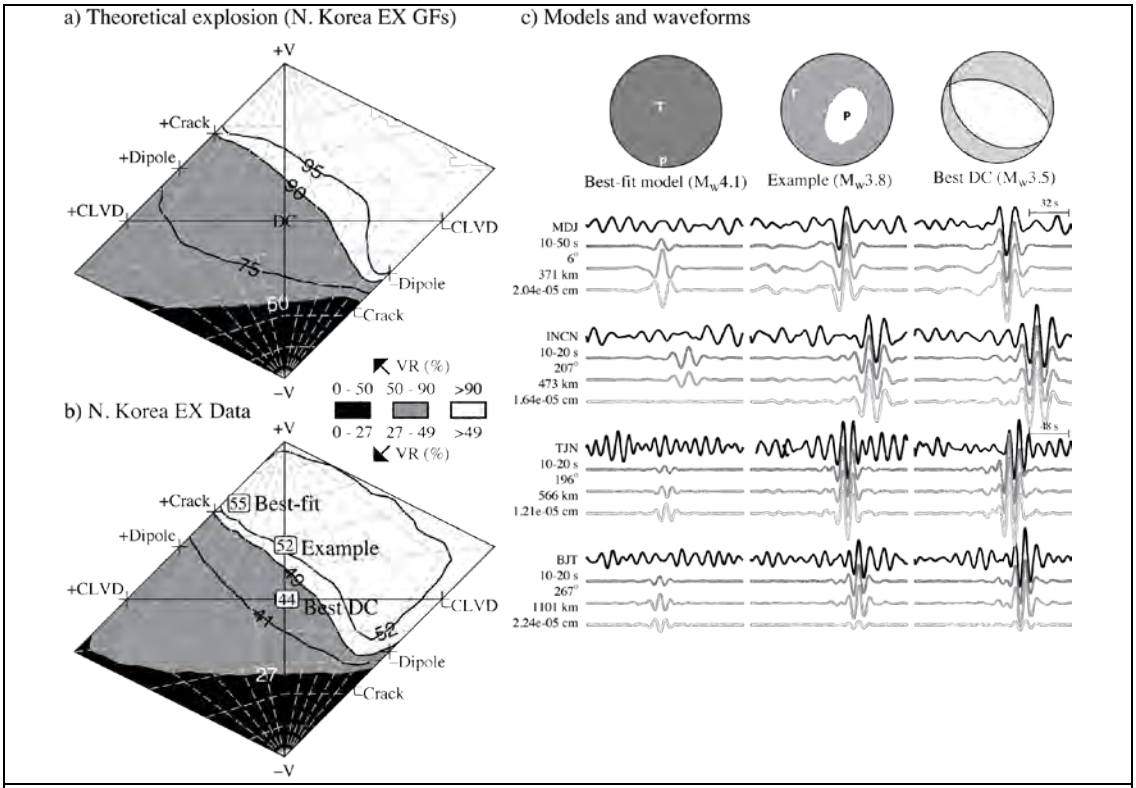

Figure 4. Network sensitivity solution (NSS) for the first North Korea test (9 Oct 06, m_b4.2). a) Theoretical NSS for an explosion where the Green's functions are derived from the actual network setup and the data is noiseless. The best-fit model is an explosion with a VR of 100%. Empirical distributions of models and their corresponding VR are also given via contours on the source-type plot. b) Actual NSS using data from the North Korea test. The best-fit model with a VR of 55% along with other models and the corresponding VR distributions is shown similar to a). For comparison, an Example (VR = 52%) and a Best DC model (VR = 44%) are also plotted and correspond with the models and waveforms in c). c) Models corresponding to those plotted in b) and their respective forward-predicted waveforms as a function of color compared with the actual waveforms (black line). The left, middle, and right columns are the tangential (T), radial (R), and vertical (V) displacement waveforms, respectively. The text block to the left of the waveforms gives the station name, passband period (s), azimuth, epicentral distance (km), and maximum displacement (cm). The moment magnitudes of the models are also given below the mechanism.

The addition of station BJT presents some additional problems for the actual NSS (Figure 4b). BJT is more than 1100 km away from the source, yet the displacement (2.24e-05 cm) is larger than that of station MDJ (2.04e-05 cm), which is only 371 km from the source. The usual method of weighting the data as a function of inverse distance caused the data from BJT to dominate the inversion, since there is only one station at this very great distance. As a corrective measure, we decreased the weight of data from BJT and produced the actual NSS in Figure 4b. As was stated in the discussion of the theoretical NSS, BJT is instrumental in constraining the source to be non-DC. Figure 4c shows that the Best DC model does not produce the observed Rayleigh amplitudes at BJT. Further, there is added confidence that the source is dominantly explosive because the Example mechanism, which fits the waveforms at a VR that is 3% less than the Best-fit model, produces a Love wave that is not observed at MDJ (Figure 4c).

2009 North Korean Test

The pure explosion model for the 2009 test is able to fit the waveforms with a variance reduction of 75% and yields an isotropic moment of 1.8e22 dyne-cm (M_W4.1; all seismic moment values are calculated with the method of Bowers and Hudson, 1999). In contrast, the pure DC solution fits the data much worse at 52% with M_0 = 3.8e22 dyne-cm (M_W4.4). The fact that the single degree of freedom explosion model fits so much better than the four degree of freedom DC model is highly significant and indicates that such a comparison can be a useful discriminant. The strike, rake, and dip of the best-fit DC is 50˚, -85˚, and 10˚. Such a steep dip-slip mechanism is very rare and of all sources calculated by the Global CMT Project (globalcmt.org) less than 1.6% have dips less than 10˚. This type of information can be used as an additional flag for anomalous sources. The differences in the fits between explosion (Best-iso) and DC (Best-DC) sources can be viewed in Figure 5b, where the DC overpredicts the Love wave amplitude at almost all stations and underpredicts the Rayleigh wave amplitudes, especially at station INCN.

Comparisons of waveforms and spectra for the 9 October 2006 nuclear test and 2009 event indicates that the 2009 event is approximately 5.7 times larger than the 2006 event. The isotropic moment for the 2006 event was found to be 0.3e22 dyne-cm (Walter et al., 2007), which agrees with the Koper et al. (2008) value. Therefore, from the waveform comparison the 2009 event should be approximately 1.5e22 to 2.1e22 dyne-cm (scale factor of 5 to 7), which is close to the pure explosion result (1.8e22 dyne-cm) obtained from waveform modeling. Figure 5 shows the raw waveforms at station MDJ for both the 2006 and 2009 North Korea events filtered between 10 and 50 sec. Note that the azimuth to MDJ is 6˚, so the east-west and north-south components are effectively naturally rotated to the tangential and radial directions, respectively. When the waveforms of the 2006 test are magnified by a factor of six, the north-south and vertical components are very similar to the 2009 event. However, the tangential energy that is clear in the 2009 event due to the high SNR is still too small to peak above the noise in the 2006 event.

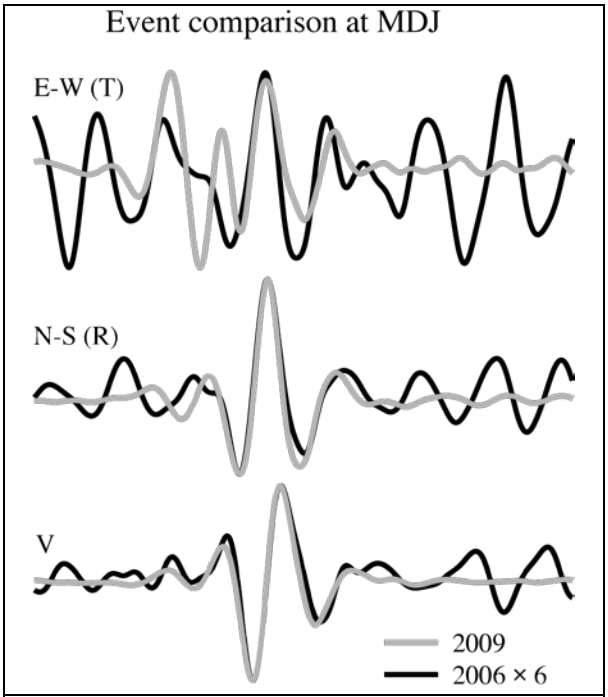

Figure 5. Raw waveforms at station MDJ for both the 2006 and 2009 North Korea events filtered between 10 and 50 sec, where the waveforms for the 2006 event are magnified by a factor of 6. Note that the azimuth to MDJ is 6˚, so the east-west and north-south components are effectively naturally rotated to the tangential and radial directions, respectively. Each trace is 100 sec long and begins 80 s after their respective origin time.

The full moment tensor inversion fits the data at 81% and yields an isotropic moment of 3.6e22 dyne-cm, and a total moment of 6.3e22 dyne-cm (M_W4.5). The deviatoric moment tensor inversion fits the data at 80% and a total moment of 3.2e22 dyne-cm (M_W4.3). If the deviatoric source is decomposed to a compensated linear vector dipole (CLVD; Knopoff and Randall, 1970) and DC sharing the same principal axes, then the source is 70% CLVD. The similarity in fits between the dominantly CLVD deviatoric source and dominantly isotropic full moment tensor shows that at shallow depths, a vertical CLVD mechanism can effectively mimic an explosion at the distances and periods analyzed here. This can be seen in the waveform comparison in Figure 6b. The full moment tensor isotropic moment is two times larger than the pure explosion indicating that the compound source of the full moment tensor solution (DC+CLVD+Isotropic) required to fit the Love waves also modifies the Rayleigh waves causing the isotropic component to increase to compensate.

As mentioned previously, some non-isotropic radiation is required to fit the source due to the observed Love waves as can be seen on the tangential component waveforms in Figure 6b. The same amount of non-isotropic energy could have been present in the recordings of the 9 October 2006 nuclear test, but were obscured due to noise.

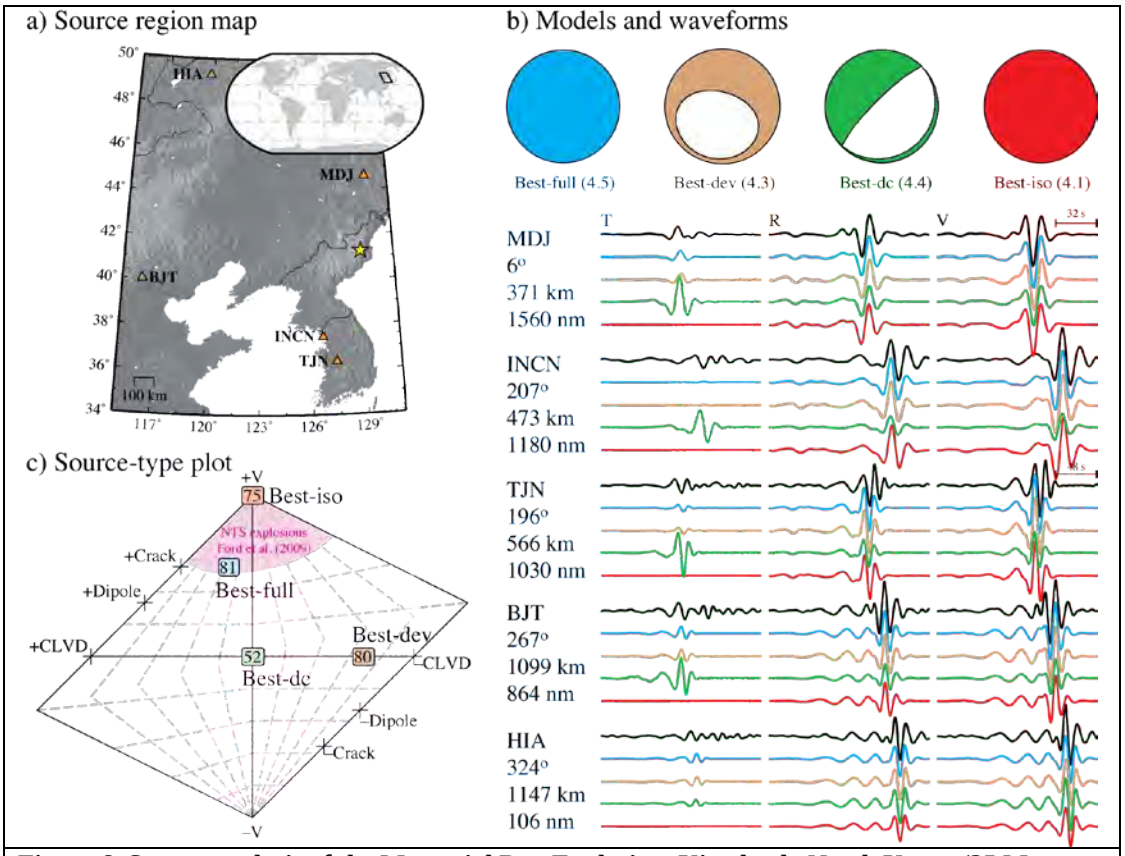

Figure 6. Source analysis of the Memorial Day Explosion, Kimchaek, North Korea (25 May 2009). a) Map of the Yellow Sea / Korean Peninsula with the North Korea explosion (star) as well as the stations used in their analysis (triangles). The region is outlined in the global inset map. b) Models (corresponding to those plotted in c) and their respective forward-predicted waveforms as a function of color compared with the actual waveforms (black line). The left, middle, and right columns are the tangential (T), radial (R), and vertical (V) displacement waveforms, respectively. The text block to the left of the waveforms gives the station name, passband period (s), azimuth, epicentral distance (km), and maximum displacement (nm). The moment magnitudes of the models are also given in parentheses. c) Source-type plot with various solutions corresponding to the models given in b) and their associated fit percent. Standard sources are also noted as well as the region of explosions at the NTS from Ford et al. (2009).

CONCLUSIONS AND RECOMMENDATIONS

Confidence in best-fit solutions for regional full-waveform moment tensor inversions is dependent on station configuration, data bandwidth, and SNR. The best way to characterize that dependence is on a case-by-case basis, where each individual event scenario is analyzed. The NSS attempts to do this characterization and is introduced and implemented in this report for the Oct 06 North Korea test, a nearby earthquake in China, and the May 09 North Korea test. A more complete description of the method is presented in Ford et al. 2009b. The theoretical network sensitivity solution provides solution confidence regions for ideal models (explosion or earthquake) with high SNR data. With this type of network

sensitivity solution, one can learn if the station configuration and bandwidth is sufficient to resolve a given model. The actual network sensitivity solution assesses confidence using the actual data from the event. Goodness-of-fit for each model is parameterized with a percent variance reduction (VR), where the complete VR space can be mapped out on a source-type plot and the well-fit region of solutions is defined by a chosen threshold VR.

The theoretical network sensitivity solutions for the North Korea tests show a trade-off between CLVD and explosion, but the well-fit solution space is separated from a double-couple, indicating that an anomalous event can be resolved. In the case of the North Korea tests, a specific configuration using the very distant station BJT is required to rule out a DC solution. With some additional data weighting, the actual network sensitivity solution of the North Korea test also shows a tight region of well-fit solutions clustered between an opening crack and an explosion, though with the addition of just one more imaginary station, this region is made much smaller (Ford et al., 2009b). The network sensitivity solutions for the earthquake in China provide high confidence in the best-fit solution, which is indistinguishable for a double-couple.

Modeling of low-frequency, regional distance waveforms identifies the 2009 event as primarily an explosion source. Comparison of pure explosion and pure double-couple models indicate that the simpler explosion model fits the waveform data substantially better than the higher degree of freedom double-couple model. While the source type is well determined, the isotropic moment of the full moment tensor inversion has some uncertainty and the M_W is between 4.4 and 4.6. The preferred scalar moment for the event is the isotropic moment of 1.8e+22 dyne-cm (M_W 4.1) of the pure explosion case. However, there are Love waves observed at several stations indicating that the source must have some non-isotropic component. This component could have been present in the previous 2006 test, but was masked by the noise.

ACKNOWLEDGEMENTS

We thank Bruce Julian for scripts to make the source-type plots.

REFERENCES

Bowers, D. and J. A. Hudson (1999). Defining the scalar moment of a seismic source with a general moment tensor, *Bull. Seismol. Soc. Am*. 89: (5), 1390–1394.

Dreger, D. S. , S. R. Ford, and W. R. Walter (2008). Source analysis of the Crandall Canyon, Utah, mine collapse, *Science,* 321: 217.

Ford, S., D. Dreger, and W. Walter (2008). Source Characterization of the August 6, 2007 Crandall Canyon Mine Seismic Event in Central Utah, *Seismol. Res. Lett*. 79: 637–644.

Ford, S. R., D. S. Dreger, and W. R. Walter (2009a). Identifying isotropic events using a regional moment tensor inversion, *J. Geophys. Res*. 114: B01306, doi:10.1029/2008JB005743.

Ford, S. R., D. S. Dreger, and W. R. Walter (2009b). Network sensitivity solutions for regional moment tensor inversions, *Bull. Seismol. Soc. Am.,* Submitted.

Hudson, J. A., R. G. Pearce, and R. M. Rogers (1989). Source type plot for inversion of the moment tensor, *J. Geophys. Res*. 9: (B1), 765–774.

Jechumtalova, Z. and J. Sileny (2001). Point-source parameters from noisy waveforms: Error estimate by Monte-Carlo simulation, *Pure Appl. Geophys*. 158: 1639–1654.

Koper, K. D., R. B. Herrmann, and H. M. Benz (2008). Overview of open seismic data from the North Korean Event of 9 October 2006, *Seism. Res. Lett*. 79: (2), 178–185; doi:10.1785/gssrl.79.2.178.

Knopoff, L. and M. J. Randall (1970). The compensated linear-vector dipole; a possible mechanism for deep earthquakes, *J. Geophys*. *Res*. 75: (26), 4957–4963.

ODNI, Office of the Director of National Intelligence (2006). News Release No. 19-06, www.dni.gov/announcements/20061016_release.pdf

Riedesel, M. and T. H. Jordan (1989). Display and assessment of seismic moment tensors, *Bull. Seismol. Soc. Am*. 79: 85–100.

Roessler D, F. Krueger, and G. Ruempker (2007). Inversion for seismic moment tensors in anisotropic media using standard techniques for isotropic media. *Geophys. J. Int.* 169:136–148.

Sileny, J. (1998). Earthquake source parameters and their confidence regions by a genetic algorithm with a 'memory', *Geophys. J. Int*. 134: 228–242.

Sileny, J. (2004). Regional moment tensor uncertainty due to mismodeling of the crust, *Tectonophysics* 383: 133–147.

Sileny, J., P. Campus, and G. F. Panza (1996). Seismic moment tensor resolution by waveform inversion of a few local noisy records; I, Synthetic tests, *Geophys. J. Int*. 126: 605–619.

Sileny, J., G. F. Panza, and P. Campus (1992). Waveform inversion for point source moment tensor retrieval with variable hypocentral depth and structural model, *Geophys. J. Int*. 109: 259–274.

Walter, W., E. Matzel, M. Pasyanos, D. Harris, R. Gok, and S. Ford (2007). Empirical Observations of Earthquake-Explosion Discrimination Using P/S Ratios and Implications for the Sources of Explosion S-Waves, in *Proceedings of the 29th Monitoring Research Review: Ground-Based Nuclear Explosion Monitoring Technologies*, LA-UR-07-5613, Vol. 1, pp. 684–693,

Weber, Z. (2006). Probabilistic local waveform inversion for moment tensor and hypocentral location, *Geophy. J. Int*. 165: 607–621.

SEISMIC EVENT DISCRIMINATION USING TWO-DIMENSIONAL GRIDS OF REGIONAL P/S SPECTRAL RATIOS: APPLICATIONS TO NOVAYA ZEMLYA AND THE KOREAN PENINSULA

Mark D. Fisk[1], Steven R. Taylor[2], William R. Walter[3], and George E. Randall[4]
Alliant Techsystems[1], Rocky Mountain Geophysics, LLC[2], Lawrence Livermore National Laboratory[3], and Los Alamos National Laboratory[4]

Sponsored by the National Nuclear Security Administration

Award Nos. DE-AC52-07NA28116[1,2], LL07-BAA07-46-NDD03[3], LA07-BAA07-46-NDD03[4]
Proposal No. BAA07-46

ABSTRACT

Building upon previous developments for the Semipalatinsk, Lop Nor, and Nevada test sites (Fisk, 2008; Fisk et al., 2008), two-dimensional (2D) grids of P/S (Pn/Sn, Pn/Lg, Pg/Lg) ratios, for all combinations of frequencies of P- and S-wave spectra, are used to enhance seismic event discrimination for the Arctic region, including the Novaya Zemlya test site (NZTS), and for the Yellow Sea and Korean Peninsula (YSKP). The spectra of regional phases are corrected for source size (under the earthquake hypothesis), geometrical spreading, attenuation, and site effects. For the Arctic, data from station KEV are the main focus of the analysis, which is applied to underground nuclear tests (UNTs) at NZTS, peaceful nuclear explosions (PNEs) in the former Soviet Union, underwater explosions, and earthquakes. The relative spectra from AMD (Amderma, Russia) recordings of a pair of events in the Kara Sea on 16 August 1997 are modeled to estimate stress drop. The corrected Pn/Sn grids exhibit prominent evidence of source differences and modulations in both Pn and Sn spectra for various types of explosions. Grid measurements include narrowband (e.g., 6–8 Hz) Pn/Sn and broader-spectral Pn(2.5–9 Hz)/Sn(4-9 Hz) ratio. Due to spectral variations for explosions, the broader-spectral Pn/Sn reduces the variance and increases the mean separation of explosions and earthquakes, improving discrimination over narrowband Pn/Sn. Robustness is examined with respect to the site and source corrections. Kriged path corrections are also computed and applied. Misfits to the correction model are quantified using the root-mean-squared (RMS) of corrected 2D Pn/Sn grids and a ratio of off-diagonal grid elements. ARCES data illustrate the potential utility of broad spectral features to investigate events. P/S grids and discrimination results are also computed using NORSAR data for 17 UNTs and 9 other nearby events. For the YSKP region, openly available data from stations MDJ in China and TJN in South Korea are used, *á la* Kim and Richards (2007), Koper et al. (2008), and Walter et al. (2007, 2008). The spectral processing and discriminant analyses are applied to earthquakes, mining blasts, and the UNTs in North Korea on 9 October 2006 and 25 May 2009. Grid measurements tested as discriminants include traditional Pg/Lg and Pn/Lg ratios in the 6-8 Hz band, and means, quartiles, RMS values, fractional pixel counts, and others over broader frequencies, e.g., Pn(1–9 Hz)/Lg(0.3–9 Hz). Because there are only two UNTs, mining blasts are included as surrogates for contained explosions; the former generally provide a conservative bound on discrimination performance. The effectiveness of Pg/Lg and Pn/Lg is discussed. Performance is compared using vertical- and three-component (3C) seismic data, and correcting for source size using reported magnitudes or from simultaneous model fits of single-station Pn, Pg, and Lg spectra to estimate M_W. Using 3C data and the model fits both improve discrimination performance. Multivariate discrimination tests are applied to assess the benefit of combining multiple features of the grids. Source model predictions are compared to spectra of regional seismic phases from the UNTs in North Korea. As a separate study (Taylor, 2009), rock damage is investigated as a possible mechanism to explain differences in apparent corner frequencies of explosion P and S waves.

OBJECTIVES

The main objective is to develop and test enhanced discrimination procedures and comparisons to source models, using characteristics of multi-dimensional spectral ratios for regional seismic phases. Fisk (2008) and Fisk et al. (2008) presented two-dimensional (2D) grids of P/S spectral ratios for all combinations of frequencies of P and S wave spectra, that exhibit greater differences in relative spectral amplitudes and shapes between explosions and earthquakes than considered before. Fisk (2008) describes the processing and discrimination methods, and applications to earthquakes and explosions at the Semipalatinsk Test Site (STS), the Lop Nor Test Site (LNTS), and the Nevada Test Site (NTS). Measurements on the 2D grids included traditional narrowband P/S discriminants, cross-spectral P/S ratios, and a root-mean-squared (RMS) misfit to the correction model, under the hypothesis of a Brune (1970) earthquake source. For granite test sites, cross-spectral P/S ratios, using higher frequencies (>2 Hz) of Pn and lower frequencies (<1 Hz) of Sn or Lg, significantly improve discrimination performance over using traditional narrowband P/S measurements. The performance for explosions in porous rock (e.g., at NTS) is much more variable. Fisk (2008) compared the grids and P/S discriminants to model predictions for events at STS, LNTS, and NTS. He also compared model predictions to Pg and Lg spectra and their ratio for the UNT in North Korea on 9 October 2006. He further used model calculations to predict P/S discriminant values for STS, to help substantiate the results and extrapolate how certain discriminants are expected to perform under a broader range of conditions. Here we assess the utility of 2D P/S grids and various spectral measurements for (1) the Arctic region, including NZTS and (2) the Korean Peninsula.

RESEARCH ACCOMPLISHED

Arctic Region

Enhancing discrimination for NZ is especially difficult due to (1) the relative aseismicity of the area; (2) limited ground truth; (3) different times at which seismic stations were installed; (4) limited recordings at regional distances for events at or near NZTS, particularly small events since the moratorium on nuclear weapons testing; and (5) bandwidth limitations due to Nyquist frequencies and noise effects. We focus largely on KEV (Kevo, Finland) data for seismic events over a broad Arctic region. We correct the Pn and Sn spectra for source, geometrical spreading, attenuation, and site effects, and apply the analysis to UNTs at NZTS, peaceful nuclear explosions (PNEs) in the former Soviet Union, several underwater explosions, and regional earthquakes. The grids for the explosions – particularly those underwater, but also many UNTs and PNEs – exhibit clear spectral scalloping. We consider a preliminary set of measurements on the grids that include traditional Pn/Sn discriminants in the 4–6 Hz and 6–8 Hz bands and a broader-spectral Pn/Sn ratio. We also examine path variations for the greater Arctic region and show that their treatment improves discrimination. We further quantify misfits to the correction model, under the hypothesis of a Brune earthquake source, and examine robustness to potential errors in the source and site terms, and to alternate frequency-dependent weighting schemes. We apply the discrimination criteria to several small events near NZ since 2003. Additional analyses performed by Fisk (2009), but not shown here, include (1) modeling relative spectra from AMD (Amderma, Russia) recordings of a pair of events in the Kara Sea on 16 August 1997 to estimate stress drop; (2) investigation of ARCES data; and (3) assessment of P/S grids and discrimination results using NORSAR data for 17 UNTs and 9 nearby events. Although these latter seismic recordings are at distances greater than 20 degrees, their broad spectral characteristics provide compelling evidence of source type.

Figure 1 shows locations of events recorded by ARCES, NORES, NORSAR arrays, station KEV, and/or AMD. Ground-truth source types of many of the events have been published. These events include 12 underground nuclear explosions (peaceful and weapons tests), 56 mining blasts, 5 in-water explosions (including the Kursk accident), 62 earthquakes, and 2 mining-induced tremors on the Kola Peninsula. For purposes of developing discrimination criteria that may be applied to any of the events near NZ since 1992, data from KEV and/or ARCES must be utilized. Most NZTS UNTs were conducted prior to installation ARCES and KEV; they recorded only 3 and 6 UNTs (mb 5.5 to 5.8) from 1982 to 1990. Recordings are also available for 11 other events near NZ from 1992 to 2007, all of which were mb 3.5 or smaller. Ocean-induced seismic noise is high at frequencies below 2–3 Hz at these stations.

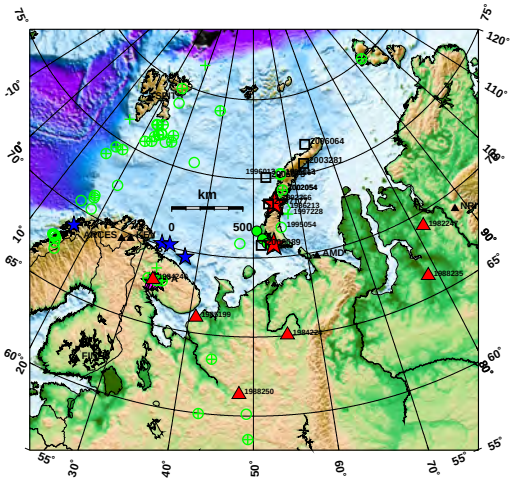

Figure 1. Locations of UNTs (red stars), PNEs (red triangles), mining blasts (magenta stars), in-water explosions (blue stars), and other events. The squares depict events near NZ since 2003.

Figure 2 shows corrected Pn/Sn grids from KEV data for four events (mb ð 3.5) near NZ. Figure 3 shows the grids for four explosions (three underground and one in the Barents Sea. Grids for the underground explosions exhibit similar features as for UNTs at other hardrock test sites, including high cross-spectral Pn/Sn ratios for lower frequencies (e.g., less than 0.5-1.0 Hz) of Sn. Note that the grids for the smaller NZ events (Figure 2) have less usable bandwidth due to low-frequency noise in this region. Although cross-spectral P/S ratios may, in principle, provide better discrimination for NZTS, as for STS and LNTS, SNR limits their utility for small events near NZTS. Note, however, that the grids in Figure 3 illustrate that there are better discriminants to use than traditional narrowband (4–6 Hz or 6–8 Hz) Pn/Sn. The grids for in-water explosions (e.g., bottom right plot of Figure 3) have high Pn/Sn ratios and spectral scalloping at similar frequencies for both Pn and Sn, indicative of water column reverberations and bubble-pulse effects near the source that are imparted to all seismic phases. The grids for many of the PNEs and UNTs (most were salvos) also exhibit spectral scalloping.

Fisk (2008) and Fisk et al. (2008) define criteria using two hypothesis tests, based on the t-distribution, to assess whether an event is rejected as belonging to the explosion and/or earthquake populations. Two p-values are computed, i.e., with respect to each population, giving statistically well-defined criteria to reject or not reject each hypothesis, clear definition of *undetermined*, and flexibility to choose different criteria with respect to different event types, if desired. In the following applications, the significance level is $\alpha = 0.01$. Events rejected by one test and accepted by the other are categorized as the latter event type. Events rejected or accepted by both tests are categorized as *undetermined*. (This category can be split, if desired.) Results based on KEV data for 22 explosions and 37 earthquakes are shown here.

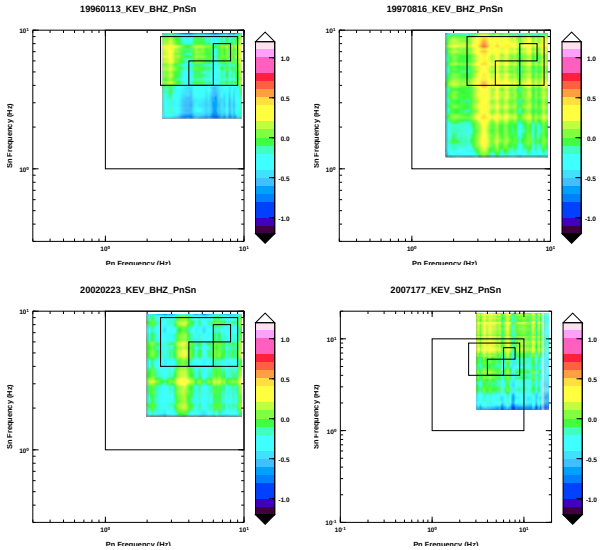

Figure 2. Corrected Pn/Sn 2D spectral ratios from KEV data for four events near NZTS since 1996.

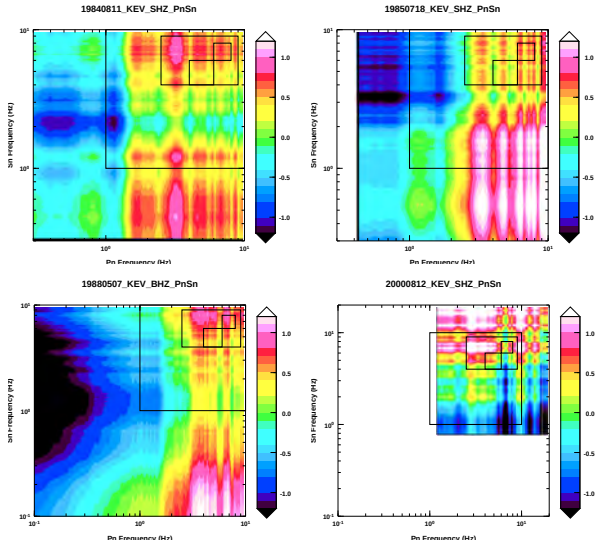

Figure 3. Corrected Pn/Sn 2D spectral ratios, based on KEV recordings of two PNEs (top), an NZTS UNT (bottom left), and the Kursk accident.

Using log Pn/Sn(4-6 Hz), 68% of explosions and 51% of earthquakes are categorized properly. The others are *undetermined*. Using log Pn/Sn(6-8 Hz), 82% and 84% are categorized properly. Figure 4 shows results using a broad-spectral mean of log Pn(2.5-9 Hz)/Sn(4-9 Hz). In this case, 96% and 97% are categorized properly. One PNE and an earthquake are *undetermined*. Progressive improvements for these three Pn/Sn discriminants are due largely to progressive reductions in the variance of the explosion population. Of four events near NZ since 2003 that have KEV data (triangles in Figure 4), three are categorized as *earthquake-like*. The event on jdate 2006073 is *undetermined* using Pn/Sn in the 4-6 Hz or 6-8 Hz bands and also, marginally, using Pn(2.5-9 Hz)/Sn(4-9 Hz), mainly because SNR is low for this event.

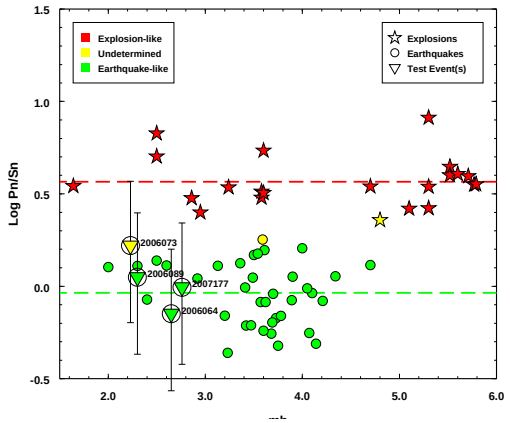

Figure 4. Discrimination results using log Pn(2.5-9 Hz)/Sn(4-9 Hz) measurements from KEV data. The triangles represent four events near NZ since 2006.

Figure 5 shows RMS-misfit versus broad-spectral Pn/Sn values, indicating that all events near NZ since 1995 (large circles) are inconsistent with explosions and consistent with earthquakes, either just near NZ (larger circles and stars) or for the broad Arctic region. The cyan triangles correspond to the various assumed magnitudes used to correct the spectra for an earthquake. The magenta triangles show hypothetical values for the UNT. The RMS-misfit becomes much higher as magnitude is underestimated, particularly for the earthquake. The mean broad-spectral ratio is much less sensitive. The RMS-misfit is a useful indicator of spectra that are inconsistent with the correction model, due to source type or various correction parameters. Figure 5 illustrates that if the corrections are sufficiently inaccurate, an earthquake could be miscategorized as an explosion. The test case shown here indicates that the source parameters would have to be very inaccurate for this to occur. Another grid measurement that particularly highlights errors in source parameters (magnitude or stress drop) is a ratio of the grid values along off-diagonal portions (i.e., a ratio of P/S grid values in the northwest to southeast quadrants).

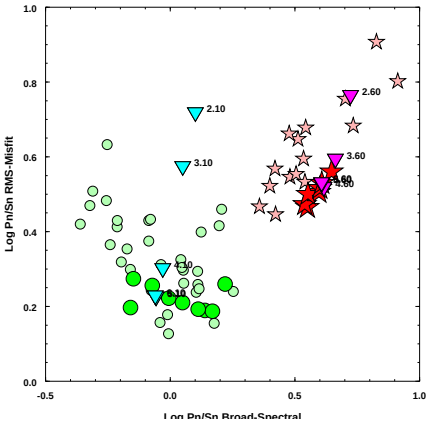

Figure 5. RMS-misfit versus broad-spectral log Pn/Sn values for explosions (stars) and earthquakes (circles). The cyan and magenta triangles are values corresponding to various assumed magnitudes used to correct the spectra for an earthquake and a UNT.

Fisk (2009) also found that the discrimination results are robust to site corrections. It is interesting to assess the impact of path effects, including overall improvements in performance and whether worse performance of Pn/Sn(6-8 Hz), compared to the broad-spectral Pn/Sn, is ameliorated by treating path effects. We use a kriging method (e.g., Fisk and McCartor, 2008) to estimate path corrections as the local Bayesian mean of earthquake data, along with associated uncertainties. For example, Figure 6 shows the spatially-varying mean for the broad-spectral Pn/Sn, showing that there are indeed systematic path variations that can be treated by kriging or another spatial interpolation method. Because the earthquake variance is reduced by kriging path corrections, the significance level can be reduced from 0.01 to 0.005 (99.5% confidence), while achieving comparable discrimination results as without kriging. Using Pn/Sn (6-8 Hz), 77% of the explosions and 88% of the earthquakes are categorized properly. Using Pn(2.5-9 Hz)/Sn(4-9 Hz), 100% of the explosions and 95% of the earthquakes are categorized properly. Considering the increase in assigned confidence level, the performance of both Pn/Sn discriminants improve

by applying path corrections. The broad-spectral Pn/Sn discriminant still outperforms Pn/Sn(6-8 Hz).

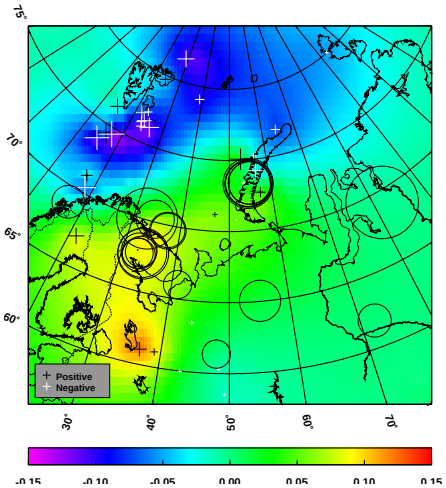

Figure 6. Kriged mean of log[Pn(2.5-9 Hz)/Sn(4-9 Hz)] for KEV, using earthquakes as reference events. Crosses and circles represent earthquakes and explosions. Marker size and color indicate residuals.

Korean Peninsula

We also applied spectral processing and discrimination methods, based on 2D P/S grids, to events in the YSKP region. Figure 7 shows locations of 515 events compiled from various bulletins and publications. Following Kim and Richards (2007), Koper et al. (2008), and Walter et al. (2007, 2008), we used seismic recordings by MDJ in China and TJN in South Korea that are openly available via the IRIS DMC and the Ocean Hemisphere Project Data Management Center (OHPDMC). The stars depict the two UNTs. Bold crosses and circles represent events with recordings from MDJ and TJN, respectively. TJN data are available after 1997. Many TJN and MDJ recordings do not have usable signals for smaller events.The MDJ dataset includes 66 earthquakes, two UNTs, and four small (1-2 ton) chemical explosions conducted in single holes during 1998, part of a refraction survey in China, near the border with North Korea. The TJN dataset includes 38 earthquakes, two UNTs, 25 blasts, and 4 unknown events. (Results for TJN are highlighted here; results for MDJ are comparable.) Figure 8 shows TJN recordings of the UNTs and the nearest earthquake on 2004/12/16, minimizing path differences. Pn/Lg has greater differences between earthquakes and explosions than Pg/Lg. I processed spectra for all three components for MDJ and TJN. I considered cases using 3C data and only the vertical component. As shown by Kim et al. (1997), high-frequency P/S ratios based on 3C data improve discrimination. I corrected the spectra using Q and spreading parameters provided by Walter (2008, pers. comm.). The corrections for source size are based on a Brune model, under the earthquake hypothesis. The form of the corrections is presented by Taylor et al. (2002) and Fisk (2006, 2007), among others. I computed site corrections for Pn, Pg, and Lg at MDJ and TJN by a linear fit of the log spectrum residuals (subtracting the log geometrical spreading, Q, and source terms) versus log frequency for the earthquakes. Figure 9 shows 2D grids of Pn/Lg and Pg/Lg spectral ratios, for all frequencies of P and S wave spectra with adequate SNR, at TJN for the same three events and a mining blast. The top grids have low values, as expected for earthquake spectra that are properly corrected. The grids for the UNTs are quite different, exhibiting similar features as for UNTs at other hard-rock nuclear test sites (cf. Fisk, 2008, 2009). The Pn/Lg grids for the UNTs have higher values than the Pg/Lg grids. The Pg/Lg grid for the mining blast does not deviate as much from zero as the Pn/Lg grid. Modulations are clearly seen in Pn, Pg, and Lg spectra, likely indicative of ripple firing. Modulations observed for multiple phases and/or stations help to confirm that they are due to a (near) source effect.

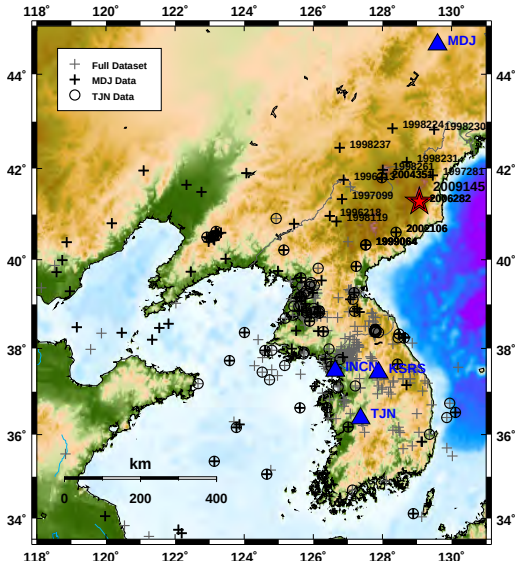

Figure 7. Locations of events and stations. Some events are labeled by Julian date. Black crosses and circles indicate events with data from MDJ and/or TJN, respectively. The stars represent the UNTs.

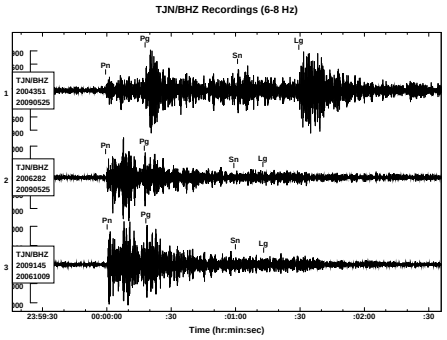

Figure 8. TJN seismograms, filtered in the 6-8 Hz passband, of the 2006 and 2009 UNTs in North Korea and a nearby earthquake on 2004/12/16.

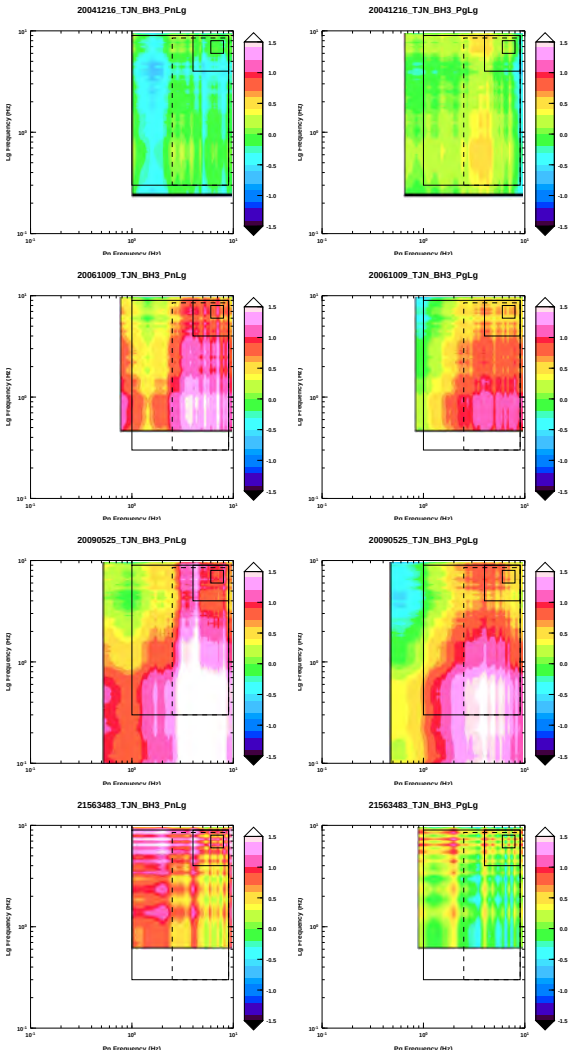

Figure 9. Grids of corrected Pn/Lg (left) and Pg/Lg (right) spectral ratios at TJN for an earthquake, the two UNTs, and a mining blast. The rectangles show spectral bands used to measure various P/S ratios.

Figure 10 shows log Pg/Lg ratios at TJN versus distance in four sets of frequency bands. The top plots show Pg/Lg values in the 4-9 Hz (left) and 6-8 Hz (right) bands. The lower left plot shows mean values using 1.5-9 Hz for Pg and 0.3-9 Hz for Lg. The lower right plot shows RMS values using 1-9 Hz for Pg and 0.3-9 Hz for Lg, intended to quantify the misfit of the correction model to the spectral ratio grid. Pg/Lg values for mining blasts overlap with the earthquakes. Figure 11 shows similar plots of Pn/Lg. There is no significant residual distance dependence for explosions or earthquakes, indicating appropriate corrections. The population variances are larger for Pn/Lg than Pg/Lg discriminants. However, there is also much better separation of the explosion and earthquake populations for Pn/Lg.

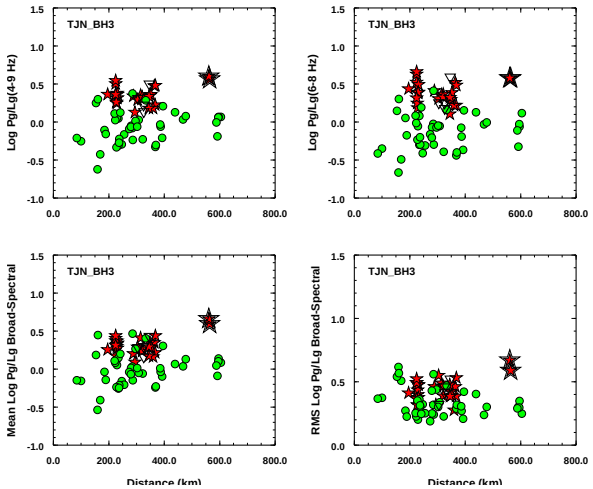

Figure 10. Log Pg/Lg ratios at TJN versus distance for explosions (stars) and earthquakes (circles) in four sets of frequency bands. The two UNTs have the highest values (highlighted stars) in each plot.

The discriminant types and frequency bands shown are a fraction of those tested, including medians, quartiles, minima, maxima, L1 deviations, and variances of the grids in various bands. A new type that discriminates very effectively is a fractional count of pixels above or below high and low thresholds, quantified as the sum of +1 for every pixel with a log Pn/Lg value greater than 0.8 (orange and higher) and –1 for those less than 0.3 (light green and lower), divided by the total number of pixels with adequate signal-to-noise ratio. Conceptually, this quantifies the visual impact of the grids, where ones with mostly high values appear distinct from those with mostly low values. Figure 12 shows these fractional counts of log Pn(1.5-9 Hz)/Lg(0.3-9 Hz) versus distance

for TJN and MDJ. They provides the best (complete) separation of all discriminants examined and also lower variance. Further work is needed to formulate the statistics of these measurements for use in hypothesis testing.

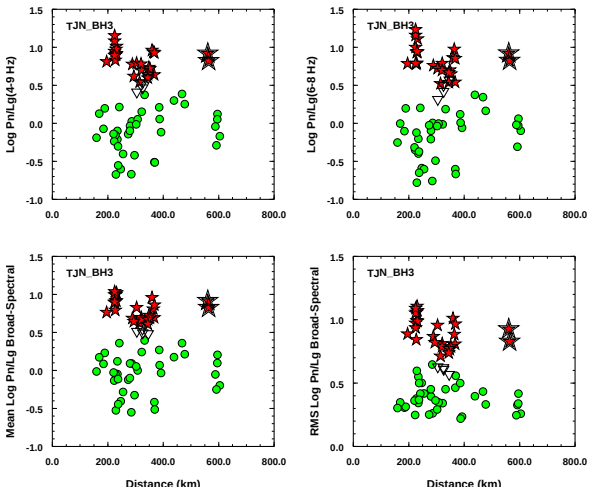

Figure 11. Similar to Figure 10, but for Pn/Lg.

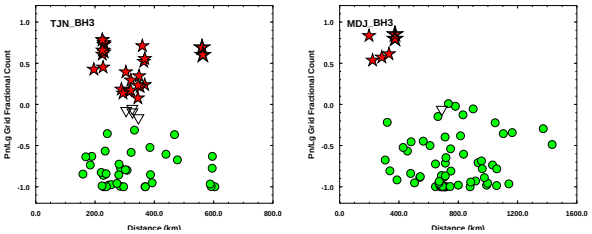

Figure 12. Broad-spectral Pn/Lg fractional grid counts versus distance for TJN and MDJ. It captures visual differences of the grids for earthquakes and explosions, and provides the best discrimination of measurements examined so far.

Figure 13 (top) shows discrimination results for log Pg/Lg(6-8 Hz) using TJN and MDJ 3C data. Only 35% of explosions, including the two UNTs, and 70% of earthquakes are categorized properly. Several types of Pg/Lg measurements and various options were tested, but none performed as well as the Pn/Lg discriminants. Figure 13 (bottom) shows the results for log Pn(1.5-9 Hz)/Lg(1-9 Hz) using from TJN and MDJ 3C data. In this case, 90% of explosions and 96% of earthquakes are categorized properly. Both UNTs are categorized as *explosion-like*. They have p-values with respect to the earthquake population of 0.00032 and 0.000098, i.e., very low probabilities that an earthquake would generate such observations. As found by Fisk (2008, 2009) for other nuclear test sites, there are features of 2D Pn/Lg and Pn/Sn grids that provide better discrimination performance than traditional P/S in the 6-8 Hz band.

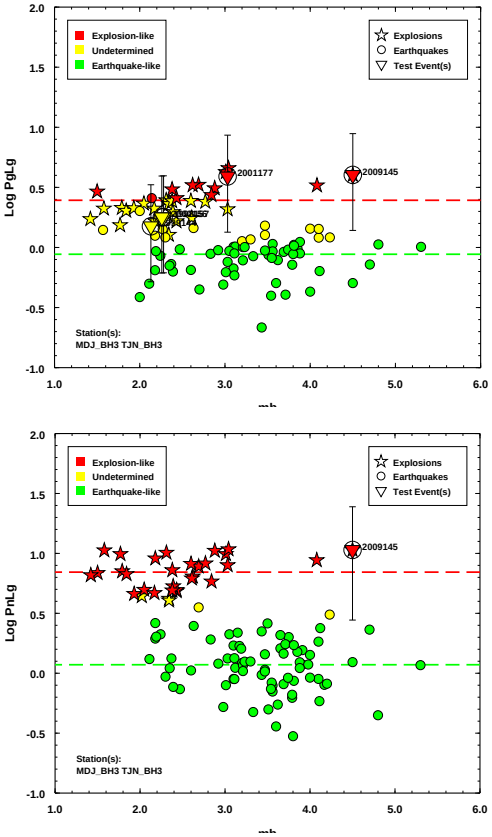

Figure 13. Discrimination results versus magnitude using log Pg/Lg(6-8 Hz) (top) and log Pn(1.5-9 Hz)/ Lg(1-9 Hz) (bottom) from TJN and MDJ 3C data. A 99% confidence interval is shown for the 2009/05/25 UNT and selected other events.

I also applied multivariate outlier and discrimination methods, based on generalized likelihood ratios (GLR) and the bootstrap (Fisk et al., 1993), to assess the benefit of combining multiple grid features. I tested the different techniques and various sets of discriminants. Figure 14 shows the result of using three features of the grids: mean Pn/Lg(4-9 Hz), mean Pn(1.5-9 Hz)/Lg(0.3-9 Hz), and RMS Pn(1-9 Hz)/Lg(0.3-9 Hz). Plotted are p-values with respect to the earthquake and explosion populations. All events are categorized properly at 0.01 significance level. As for the univariate cases, the two UNTs are categorized as *explosion-like*. Their p-values with respect to earthquakes indicate very low

probabilities that an earthquake would have generated the observations.

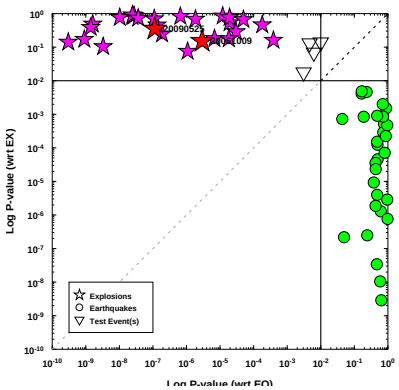

Figure 14. Multivariate results, computed as p-values with respect to earthquake and explosion populations, using 3 Pn/Lg measurements at TJN.

Using kriging (Fisk and McCartor, 2008), Figure 15 shows spatial variations of corrected broadband Pn/Lg at TJN and MDJ. This discriminant, and the others, exhibit systematic path variations for both stations. For TJN, all types of mean Pn/Lg discriminants are systematically lower, on average, for offshore earthquakes. For MDJ, the highest Pn/Lg values are for earthquakes with partial paths to MDJ beneath the Sea of Japan, where water depth is greater than the Yellow Sea (e.g., Figure 15), perhaps indicating stronger attenuation and/or blockage of Lg for such paths. Kriging is not necessary to obtain good discrimination performance, but it is beneficial.

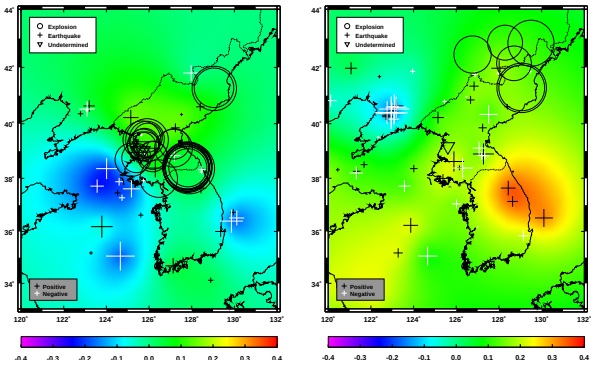

Figure 15. Kriged local mean of broad-spectral Pn/Lg from earthquake data for TJN and MDJ. Circles and crosses represent explosions and earthquakes. Marker size and color indicate the residuals.

Figure 16 shows observed (cf. Walter et al., 2007) and model Pg and Lg spectra (left) and spectral ratios (right) for the 2006/10/09 UNT in North Korea. The model results, using Mueller and Murphy (1971) [MM71] for P waves and with shifted corner frequency for S waves (cf. Fisk, 2006, 2007), compares even better for Lg than Pg, similar to findings by Fisk (2007) for NTS.

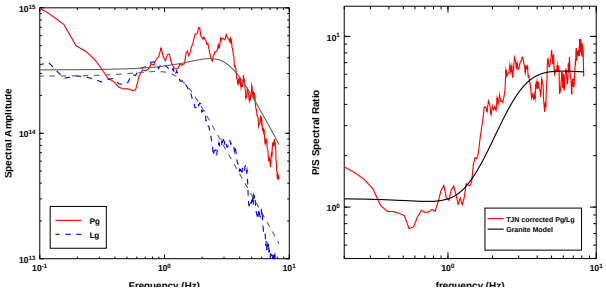

Figure 16. Corrected Pg and Lg spectra (left) and Pg/Lg spectral ratio (right) from the TJN recording of the 2006/10/09 UNT. Also shown are model results.

Rock Damage Mechanics

Taylor (2009) investigated rock damage as a possible mechanism to explain differences in apparent corner frequencies of explosion P and S waves (Xie and Patton, 1999; Fisk, 2006, 2007; Murphy et al., 2009). The main conclusion is that rock damage is a plausible source of explosion S waves and a possible explanation of reduced corner frequencies for S waves, relative to P.

CONCLUSIONS AND RECOMMENDATIONS

Key results for the Arctic region indicate that (1) very good discrimination is obtained; (2) using Pn and Sn measurements over broader spectral ranges is much more stable and informative, improving performance over narrowband P/S discriminants; (3) treatment of systematic path variations improves discrimination; (4) noise effects at frequencies of about 3 Hz and below are very significant for all NZ events since 1992; (5) cross-spectral P/S ratios may provide the best discrimination for NZTS, as for other hardrock test sites, but they have limited utility for available stations and events near NZTS since 1992. To distill the specific discrimination results of Fisk (2009), (1) there does not seem to be any problem identifying NZTS explosions, at least above mb 3.8; (2) the Kara Sea events on 1986/08/01 and 1997/08/16 have spectral features at NORSAR

that are consistent with aftershocks during 1973-1974 and inconsistent with known UNTs; (3) all other small events in the vicinity of NZ since 1992 with KEV data have spectral features consistent with the Kara Sea events; (4) the 1992/12/31 event is the most ambiguous event near NZTS; and (5) the 1995/06/13 event, which also does not have KEV data, has very similar Pn/Sn spectral ratios at ARCES over 6–15 Hz, as the 1992/12/31 event. In addition, their spectra are the least consistent with a Brune earthquake source model. With the exception of these latter two events that need further evaluation, the results of Fisk (2009) provide a comprehensive assessment of source types for all events of relevance to monitoring NZTS.

Key results for the YSKP region are as follows. Features of Pn/Lg grids provide very effective discrimination for events with adequate SNR. Overall performance needs to be quantified, including application rates, for stations available for monitoring. Pg/Lg and Pn/Lg from 3C data improves performance over using vertical-component data. Discrimination criteria using multiple Pn/Lg measurements accurately categorize all events in the explosion and earthquake sets. The best discriminant tested is log Pn(1.5–9 Hz)/Lg(0.3–9 Hz), which quantifies the mean deviation of Pn/Lg to the Brune model over broad frequency ranges. The results are not very sensitive to corrections for source size. The Pn/Lg discriminants exhibit path variations with apparent correlation to geophysical features for TJN and MDJ. Discrimination performance is further improved by applying path corrections. The spatial dependence for MDJ suggests that paths beneath the Sea of Japan may extinguish high-frequency Lg. The 2009/05/25 and 2006/10/09 UNTs in North Korea have very similar spectral features and discrimination results. Using broad-spectral log Pn(1.5–9 Hz)/Lg(1–9 Hz) measurements from TJN and MDJ 3C data, the 2009/05/25 UNT is discriminated from earthquakes at a 99.99% confidence level. Smaller variances of Pg/Lg for earthquakes compensate for less separation from earthquakes than Pn/Lg for the two UNTs. However, none of the Pg/Lg discriminants separate small blasts from earthquakes at TJN or MDJ. Thus, many earthquakes and blasts are *undetermined* using Pg/Lg.

Using MM71 for P waves and with a shifted corner frequency for S waves (cf. Fisk, 2006), agrees very well with the spectra at TJN for the 2006/10/09 UNT. The apparent corner frequency for Lg is lower than that of Pg, which explains the same frequency dependence of P/S spectral ratios for UNTs at all test sites examined (STS, LNTS, NZTS, and test sites in India and North Korea). Walter et al. (2007) showed a model calculation, using a P-to-S transfer function, that also represents the Lg spectrum very well for the 2006 UNT. P-to-S conversion, as well as near source effects are plausible mechanisms to generate S waves from explosions. Many important physical effects need further study.

In summary, the results of the studies for STS, LNTS, NTS, NZTS, and the North Korean test site indicate (1) there are features of the P/S spectral ratio grids over broader spectral ranges that significantly improve performance relative to traditional P/S discriminants; (2) the results are robust to spectral variability for many types of explosions and to the corrections for source and site terms; (3) path-specific corrections (e.g., using kriging) are very beneficial for extended regions, but they are not required to obtain good discrimination performance; and (4) source model comparisons are quite favorable at all of these test sites. Further understanding and source modeling work is needed.

ACKNOWLEDGMENTS

Seismic data from the IRIS DMC and the OHPDMC were used in this study.

REFERENCES

Brune, J. N. (1970). Tectonic stress and the spectra of seismic shear waves from earthquakes, *J. Geophys. Res.* 75: 4997–5009.

Fisk, M. D. (2006). Source spectral modeling of regional P/S discriminants at nuclear test sites in China and the Former Soviet Union, *Bull. Seism. Soc. Am*. 96: 2348–2367.

Fisk, M. D. (2007). Corner frequency scaling of regional seismic phases for underground nuclear explosions at the Nevada Test Site, *Bull. Seism. Soc. Am*. 97: 977–988.

Fisk, M. D. (2008). Enhancement and Modeling of Seismic Event Discrimination Based on Two-Dimensional Grids of Regional P/S Spectral Ratios, ATK-R-1741, ATK Technical Report.

Fisk, M. D. (2009). Seismic Event Discrimination for the Arctic Region using Two-Dimensional Grids of Regional P/S Spectral Ratios, ATK-R-1742, ATK Technical Report.

Fisk, M. D., H. L. Gray, and G. D. McCartor (1993). Applications of Generalized Likelihood Ratio Tests to Seismic Event Identification, PL-TR-93-2221, Phillips Lab., Hanscom AFB, MA.

Fisk, M. D. and G. D. McCartor (2008). Treatment of correlation for clustered reference data in kriging regional seismic discriminants, *Bull. Seism. Soc. Am*. 98: 1768–1780.

Fisk, M. D., S. R. Taylor, H. J. Patton, and W. R. Walter (2008). Applications of a next-generation MDAC discrimination procedure using two-dimensional grids of regional P/S spectral ratios, in *Proceedings of the 30th Monitoring Research Review: Ground-Based Nuclear Explosion Monitoring Technologies*, LA-UR-08-05261, Vol. 1, pp. 583–592.

Kim, W. Y., V. Aharonian, A. L. Lerner-Lam and P. G. Richards (1997). Discrimination of earthquakes and explosions in southern Russia using regional high-frequency three-component data from IRIS/JSP Caucasus Network, *Bull. Seism. Soc. Am.* 87: 569–588.

Kim, W. Y., and P. G. Richards (2007). North Korean nuclear test: seismic discrimination at low yield, *Eos* 88: 158–161.

Koper, K. D., R. B. Herrmann, and H. M. Benz (2008). Overview of open seismic data from the North Korea event of 9 October 2006, *Seism. Res. Lett.* 79: 178–185.

Mueller, C. S. and J. R. Murphy (1971). Seismic characteristics of underground nuclear detonations Part I: seismic spectrum scaling, *Bull. Seism. Soc. Am.* 61: 1675–1692.

Murphy, J. R., B. W. Barker, D. D. Sultanov, and O. P. Kuznetsov (2009). S-wave generation by underground explosions: implications from observed frequency-dependent source scaling, *Bull. Seism. Soc. Am.* 99: 809–829.

Taylor, S. R. (2009). Can the Fisk Conjecture be Explained by Rock Damage Around Explosions?, *Bull. Seism. Soc. Am.*, in press.

Taylor, S. R., A. A. Velasco, H. E. Hartse, W. S. Phillips, W. R. Walter, and A. J. Rodgers (2002). Amplitude corrections for regional seismic discriminants, *Pure Appl. Geophys.* 159: 623–650.

Walter, W. R., E. Matzel, M. E. Pasyanos, D. B. Harris, R. Gok, and S. R. Ford (2007). Empirical observations of earthquake-explosion discrimination using P/S ratios and implications for the sources of explosion S-waves, in *Proceedings of the 29th Monitoring Research Review: Ground-Based Nuclear Explosion Monitoring Technologies*, LA-UR-07-5613, Vol. 1, pp. 684–693.

Walter, W. M. E. Pasyanos, R., E. Matzel, R. Gok, J. J. Sweeney, S. R. Ford, and A. J. Rodgers (2008). Regional seismic amplitude modeling and tomography for earthquake-explosion discrimination, in *Proceedings of the 30th Monitoring Research Review: Ground-Based Nuclear Explosion Monitoring Technologies*, LA-UR-08-05261, Vol. 1, pp. 702– 711.

Xie, J. and H. J. Patton (1999). Regional phase excitation and propagation in the Lop Nor region of central Asia and implications for P/Lg discriminants, *J. Geophys. Res.* 104: 941–954.

TOWARDS AN EMPIRICALLY BASED PARAMETRIC EXPLOSION SPECTRAL MODEL

Sean R. Ford, William R. Walter, Stan D. Ruppert, Eric Matzel, Terri F. Hauk, and Rengin Gok

Lawrence Livermore National Laboratory

Sponsored by National Nuclear Security Administration

Award No. DE-AC52-06NA25396/LL08-Parametrics-NDD02

ABSTRACT

Small underground nuclear explosions need to be confidently detected, identified, and characterized in regions of the world where they have never before been tested. The focus of our work is on the local and regional distances (< 2000 km) and phases (*Pn*, *Pg*, *Sn*, *Lg*) necessary to see small explosions. We are developing a parametric model of the nuclear explosion seismic source spectrum that is compatible with the earthquake-based geometrical spreading and attenuation models developed using the Magnitude Distance Amplitude Correction (MDAC) techniques (Walter and Taylor, 2002). The explosion parametric model will be particularly important in regions without any prior explosion data for calibration. The model is being developed using the available body of seismic data at local and regional distances for past nuclear explosions at foreign and domestic test sites. Parametric modeling is a simple and practical approach for widespread monitoring applications, prior to the capability to carry out fully deterministic modeling. The achievable goal of our parametric model development is to be able to predict observed local and regional distance seismic amplitudes for event identification and yield determination in regions with incomplete or no prior history of underground nuclear testing. The relationship between the parametric equations and the geologic and containment conditions will assist in our physical understanding of the nuclear explosion source.

OBJECTIVES

We aim to develop a practical explosion source parametric spectral model, based on all available data, that describes nuclear explosion *P*- and *S*-wave source spectra for a variety of geologic and containment conditions. This approach follows the simple earthquake parametric spectral model based on Brune (1970), which is used for the MDAC approach (Walter and Taylor, 2002) to improve earthquake/explosion discrimination. In regions without prior explosions, the parametric model could be combined with earthquake-derived path corrections to predict explosion regional phase amplitudes, improve discriminants such as *P*/*S* ratios, and support identification procedures (e.g., Event Classification Matrix, [ECM]) that explicitly need to use explosion discriminant probability density functions.

It is well known that depth and near-source material properties can affect seismic estimates of explosion yield, and prior work at the Nevada Test Site (NTS) (e.g., Walter et al., 1995) has found that explosions in weak materials have lower corner frequencies and steeper spectral fall-offs for *P*-waves than is predicted by the standard Mueller and Murphy (1971) model. As part of this research, we hope to quantify these effects as a function of frequency and wave type. Additionally, many of the most effective regional discriminants (high-frequency *P*/*S* ratios) make use of *S*-waves, as do *S*-wave coda yield estimation techniques, yet there remain many questions about how to predict explosion *S*-wave amplitudes. The development of a combined *P*- and *S*-wave spectral model consistent with observed regional *P*-and *S*-wave data is a goal of this work.

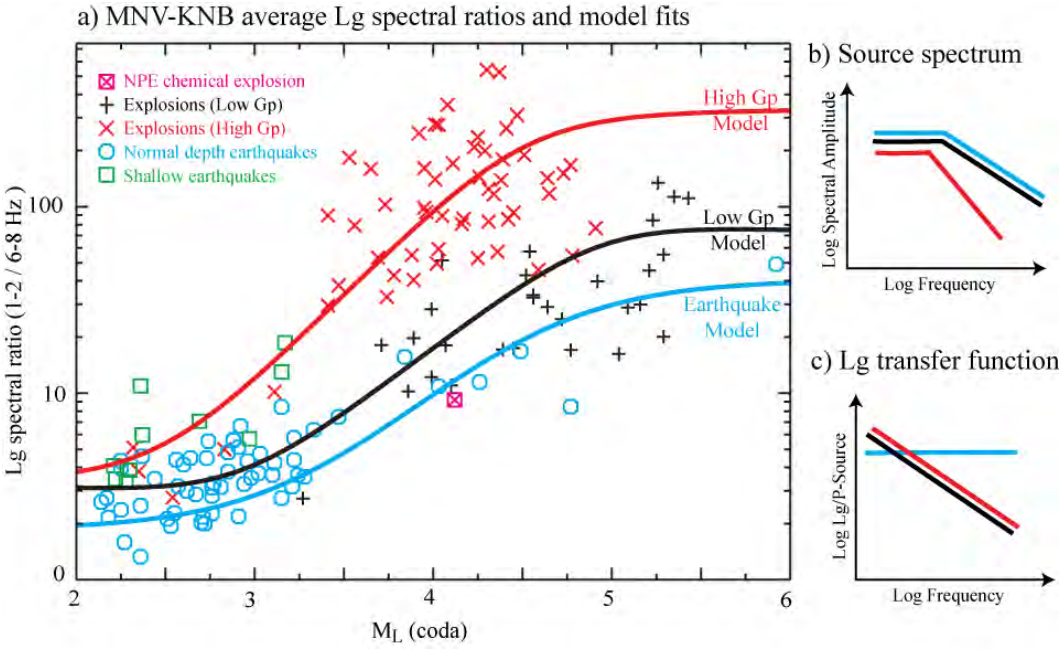

Figure 1. Simple first-order source model fits to low to high frequency spectral ratios of *Lg* amplitudes from Walter et al. (1995, Figure 8). Earthquake displacement spectra are fit with the Brune (1970) model (blue line), which is constant at low frequencies and falls off above a corner frequency as f^{-2}. Explosions are fit with two extremes of the Denny and Goodman (1990) model in order to investigate explosion dependence on emplacement material (namely, gas porosity [*Gp*]). The 'Low *Gp*' model (black line) has an effective fall-off similar to the earthquake model. The 'High *Gp*' model (red line) has a greater fall-off of f^{-3}.

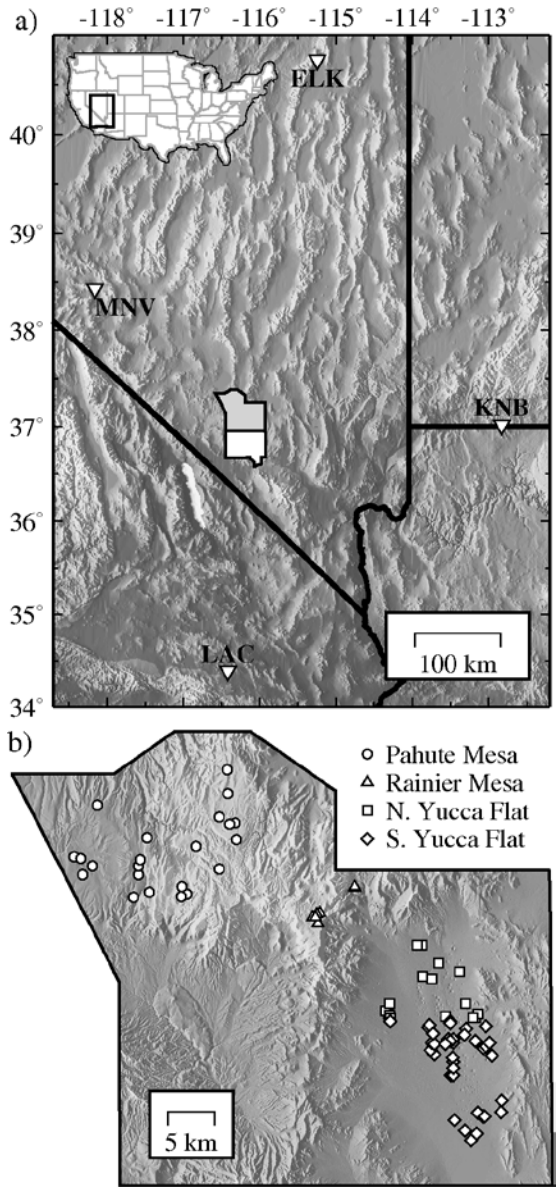

Figure 2. a) Regional map of stations used in the analysis. The location of the map within the continental US is given by the inset map. The NTS is outlined and the shaded section is shown in (b). b) Map of the northern NTS with explosion locations and Vergino and Mensing (1990) area designations.

RESEARCH ACCOMPLISHED

Introduction

In previous work that looked at low to high frequency ratios of regional phase (e.g., *Pn*, *Pg*, *Lg*) amplitudes to separate explosions from earthquakes at NTS, Walter et al. (1995) noted that the results showed a strong dependence on the source media properties. Nuclear tests in weak and/or high gas porosity media tended to have higher values and discriminate better from earthquakes than explosions in stronger and/or lower gas porosity media. For example, in Figure 1 the ratio of the *Lg* amplitude at 1–2 Hz compared with the amplitude at 6–8 Hz is shown as a function of magnitude. The earthquakes (blue circles and green squares) show the expected trend with magnitude going from a low value for small events when the corner frequency is above 8 Hz and both measurements are on the constant part of the source spectra that is proportional to moment. For large magnitudes, the source corner frequency drops below 1 Hz and then both measures are on the part of the source spectra that decays with frequency as f^{-2}, resulting in high spectral ratio values. As magnitude increases, the earthquakes follow a sigmoid curve as shown by the blue line, which is based on the Brune (1970) model. The explosions are split into two categories based on the source media, a high gas porosity (*Gp*) and low strength group (red x) and low *Gp* high strength group (black crosses), and a clear difference between the two can be seen. In fact, the low *Gp* explosions reach spectral ratio values that imply much steeper falloff than f^{-2}.

To fit the explosion data we used two extremes of the Denny and Goodman explosion model (1990), which has two corner frequencies. In the low *Gp* case we allowed the second corner to be at a higher frequency than the range of interest, giving an effective f^{-2} falloff. In the high *Gp* case we forced the corners to be the same, giving an f^{-3} falloff. In both cases we used the observed 3 Hz corner frequency of the 1993 Non-Proliferation Experiment (NPE), a kiloton chemical explosion and assumed the corner frequency scales with the cube root of M_L(coda). Given that a pure explosion should not generate *S*-waves, one way to think about the *Lg* spectral ratio is as the product of the *P*-wave source ratio and a transfer function ratio, where the transfer function is a representation of how efficiently the source generated *P*-waves are converted (by whatever means) into *S*-waves. We estimated the transfer function ratio as a function of frequency as shown in Figure 1, and then multiplied the *P*-wave based Denny-Goodman model curves by these factors and then compared them to the *Lg* spectral ratio in Figure 1. The result is a fairly reasonable first order fit to the data. Interestingly since the explosion *Lg* transfer functions are larger than those for the earthquakes, it shifts the explosion *Lg* spectral ratios to relatively higher values than for the earthquakes, improving the discrimination performance of *Lg* spectral ratios over those of *Pn* alone (see Walter et al. 1995, Figure 7).

While in this case, the Denny and Goodman (1990) model provides a reasonable fit to these NTS data, it is not clear how we would make use of it in other regions. Furthermore the limitation of only two choices of high frequency falloff does not capture the full range of the observations. To develop a practical parametric source spectral model we want to be able to tie parameters like low frequency level, corner frequency and falloff rate to measureable properties like yield, depth, and media properties like gas porosity and strength. In the next section we take a more general approach to fitting the NTS explosion data. We focus first on *Pn* displacement spectra where previous work has shown that after correcting for path effects, the *Pn* spectra are a good representation of the source spectra (e.g., Goldstein et al., 1994). The initial goal is to develop a simplified *P*-wave explosion source model that matches the observed material property effects.

Data and Methods

We employ the NTS explosion dataset of Walter et al. (2004), specifically the raw spectra of that dataset. Waveforms are de-meaned, de-trended and instrument corrected to acceleration. The signal is windowed with a 5% cosine taper that starts before the pick, where the time before the pick is 5% of the total time window. The Fourier transform is calculated and displacement spectra are obtained via double integration in the frequency domain. Finally, the resultant amplitude spectra are interpolated and smoothed to obtain a sampling period of 0.05 $\log_{10}$ Hz.

Spectra for the *Pn* seismic phase for each explosion are calculated from the recordings of stations of the Livermore NTS Network, ELK (Elko, NV), KNB (Kanab, UT), LAC (Landers, CA), and MNV (Mina, NV). The locations of these stations relative to the NTS are given in Figure 2. These spectra are then corrected for geometrical spreading and regional, frequency-dependent attenuation of the form $Q = Q_0 f^{\gamma}$, where Q_0 is Q at 1 Hz and γ is the power-law dependence on frequency, f. We employ the Street et al. (1975) parametric form of geometrical spreading,

$$G(r) = \begin{cases} r^{-1}, & r < r_0 \\ 1/r_0 (r_0/r)^{\eta}, & r \geq r_0 \end{cases} \qquad (1)$$

where r_0 is the distance at which the spreading transitions from spherical- to a cylindrical-type spreading and η is the distance dependence. The attenuation and spreading model parameters for each seismic phase are given in Table 1.

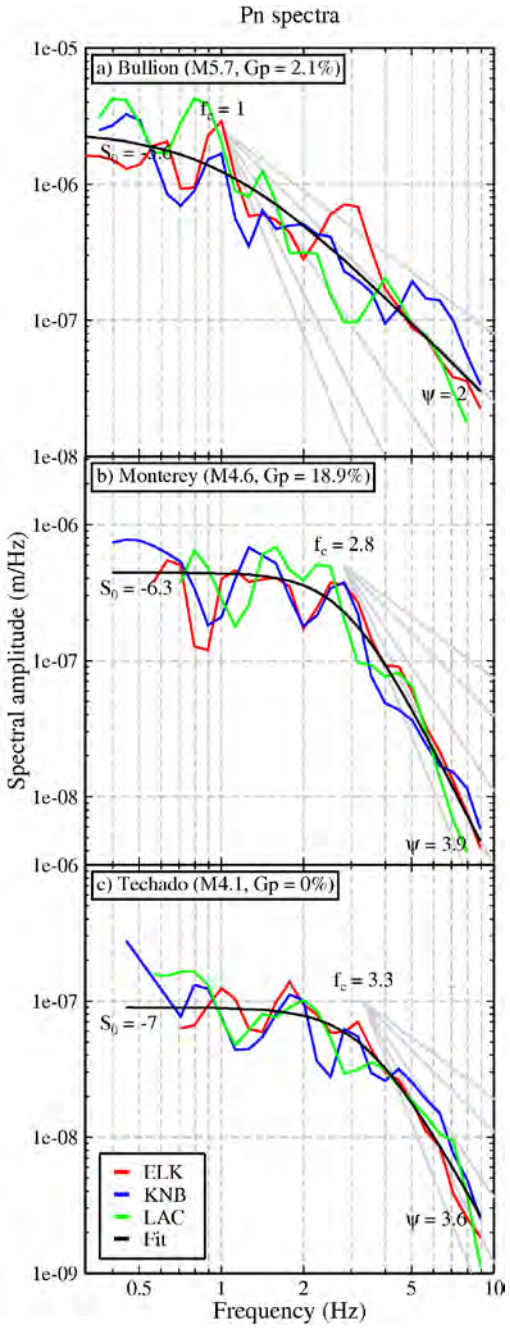

Figure 3. ***Pn*** **spectra examples with the name, magnitude (where** $M = m_b$**[*Pn*]), depth (*Z*), and gas porosity (*Gp*) given in the subtitles. The long-period level (**S_0**), corner-frequency (**f_c**), and fall-off (**ψ**) are given in each plot, and the spectra are colored by station and the fit is shown in the legend in the lowermost plot. a) Spectra for an event with low *Gp* and** ω^{-2} **fall-off. b) Spectra for an event with high *Gp* and high fall-off. c) Spectra for an event with low *Gp* and high fall-off.**

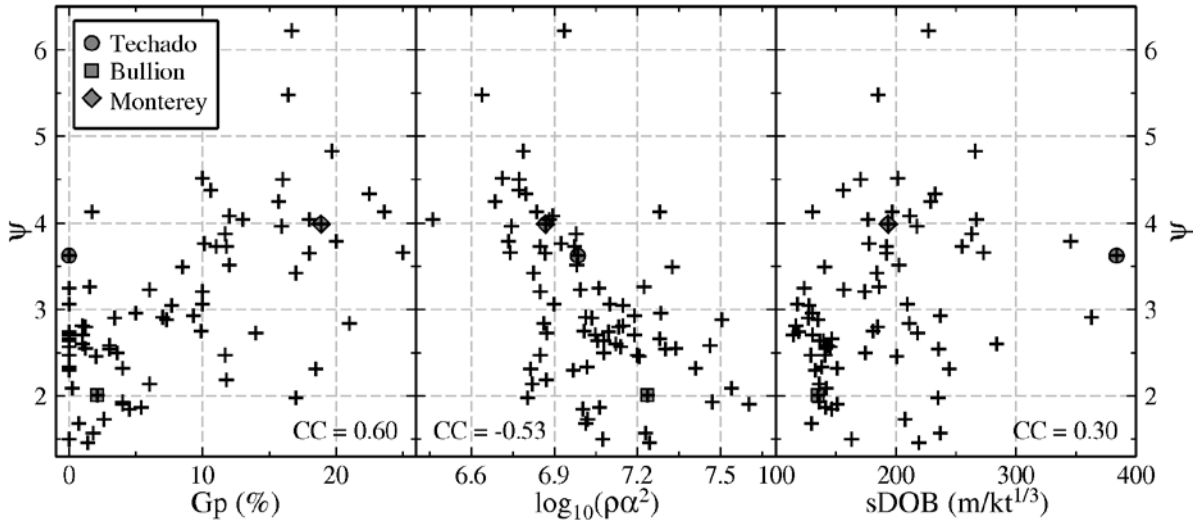

Figure 4. ψ (spectral fall-off) comparison with geophysical parameters, a) gas porosity (*Gp*), b) the log-transform of strength ($\rho\alpha^2$), and c) sDOB = depth/W$^{1/3}$ (W = yield estimated from mb(Pn)). Correlation coefficients (CC) for each comparison are given at the bottom of the plot. Special symbols are given for events with spectra shown in Figure 3.

Table 1. Regional attenuation and geometric spreading parameters.

Phase	η	r_0 (km)	Q_0	γ
Pn	1.1	0.001	210	0.65
Pg	0.5	100	190	0.45
Lg	0.5	100	200	0.54

In the future we will test path-specific attenuation parameters. In order for an event to enter the dataset, we require three of the four stations listed above to have recorded it with a signal-to-noise ratio greater than two. The maximum frequency considered is 9 Hz, since signal recorded above this frequency is often contaminated with non-stationary noise due to multi-band recording problems. In the future we will more systematically identify records with this problem and may be able to use higher frequencies for selected events. The spectra are jointly fit with a simple parametric form given by

$$S(f) = \frac{S_0}{1 + \left(f / f_c\right)^{\psi}} \qquad (2)$$

in a least-squares inversion that also provides standard error for each parameter estimate. Equation (2) describes the simplest behavior expected for seismic spectra. It has a constant level at low frequencies (S_0), which is proportional to static displacement, and falls off at high frequencies with a slope of $f^{-\psi}$ beyond a corner frequency f_c. Examples of the spectra and model fits are proportional to static displacement, and fall off at high frequencies with a slope of $f^{-\psi}$ beyond a corner frequency f_c. Examples of the spectra and model fits are

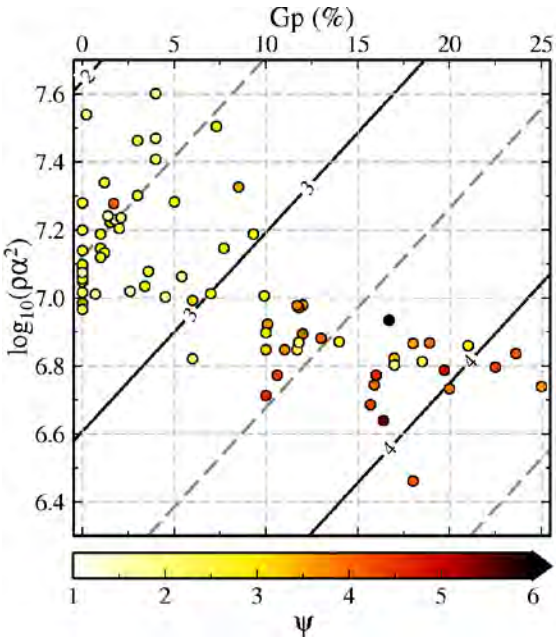

Figure 5. *Pn* spectral fall-off (ψ) as a function of the log-transform of strength ($\rho\alpha^2$) and gas porosity (*Gp*). Small circles are colored according to ψ from the fit to Equation (2) . Contours are for ψ as a planar fit to $\log_{10}(\rho\alpha^2)$ and *Gp* as described by Equation (3).

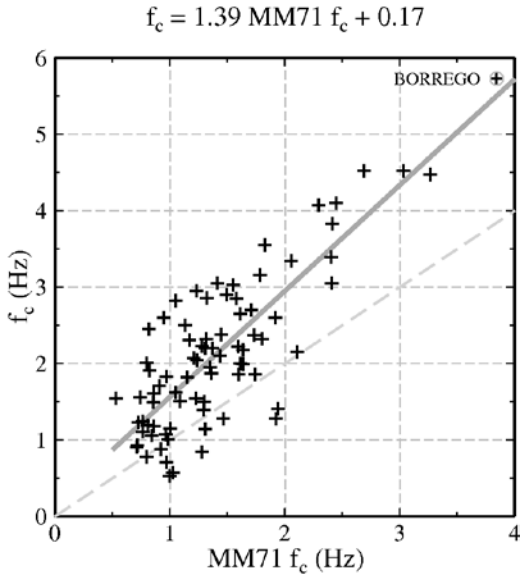

Figure 6. Corner-frequency (f_c) from the fits to Equation (2) compared with those predicted by Mueller and Murphy (1971), MM71 f_c. The linear relationship is given by the equation at the top of the plot and the slope is close to one.

given in Figure 3. BULLION (Figure 3a) is fit well with a standard f^{-2} (ψ=2) spectral fall-off, but MONTEREY (Figure 3b), detonated in weak material, requires a steeper fall-off where the best fit $\psi \approx 4$. In the future, we will compare the model described by Equation (2) with other parametric models.

Preliminary results

We present the results of fitting the *Pn* spectra for NTS explosions in Figure 4. The spectral fall-off (ψ) correlates well with material properties such as gas porosity (*Gp*) and strength ($\rho\alpha^2$), where ρ is the density and α is the compressional velocity near the shot-point. There is less of a correlation with scaled depth-of-burial (sDOB = depth/yield$^{1/3}$). Yield was inferred from m_b(*Pn*) based on the Vergino and Mensing (1990) relationship at NTS. sDOB can give insight to outliers in the ψ comparison with *Gp* and strength. For example, TECHADO (circle in Figure 4) has a very large sDOB and was detonated in a saturated (*Gp* = 0%) medium, but has a relatively high fall-off (ψ = 3.6, Figure 3c), a relationship that is different from the overall trend in the *Gp* data. Interestingly, TECHADO appears as less of an outlier in the fall-off versus strength plot (Figure 3b).

To quantitatively examine the relationship between spectral fall-off and material properties, we plot ψ versus $\log_{10}(\rho\alpha^2)$ and *Gp* and fit a plane to the data in Figure 5. The planar fit is weighted by the inverse variance of ψ. The spectral fall-off generally increases as strength decreases and *Gp* increases. The planar fit of the relationship between these material properties and fall-off is given by

$$\psi = 0.057Gp - 0.97\log_{10}(\rho\alpha^2) + 9.42 \quad (3)$$

As mentioned previously, sDOB has an effect on this relationship and will be investigated further in the future.

We present the best-fit f_c as a function of the corner frequency predicted by Mueller and Murphy (1971) as parameterized by Stevens and Day (1985) for tuff/rhyolite in Figure 6. The corner frequency in this study, f_c, is well-correlated with the Mueller and Murphy (1971) predicted corner-frequency and the slope is close to one. It can be made even closer by decreasing the reference elastic radius used to calculate the proportionality constant used in the Mueller and Murphy (1971) relationship. In the future, we will compare these results with those from *Lg* spectra to examine *S/P* corner frequency scaling in the context of variable spectral fall-off.

CONCLUSIONS AND RECOMMENDATIONS

Our preliminary analysis of *Pn* spectra of NTS explosions shows that a simple spectral model with variable fall-off is appropriate, and the fall-off correlates well with material properties. Corner-frequencies obtained with the variable fall-off model correlate with Mueller and Murphy (1971) corner-frequencies. If we use a smaller elastic radius than the one given for tuff, we believe we could match the trend of the Mueller-Murphy corner frequencies with a slope close to one.

Future work

This initial *P*-wave spectral fitting focused on correlating material properties with the model parameters. We will perform similar analyses for NTS seismic phases, *Pg* and *Lg*, and compare the results with those presented above for *Pn*. The comparison will allow for an examination of *P/S* scaling relationships, which can be compared with results from the Fisk (2007) study at NTS. The results of this study with a variable fall-off spectral model will be compared with other spectral models (e.g., Denny and Johnson [1991] and references therein). In addition, we will formally analyze the error and trade-offs in the estimated parameters of Equation (2). Finally, we will extend the analysis to other test sites to examine regional effects on the model parameters.

REFERENCES

Brune, J. N. (1970). Tectonic stress and the spectra of seismic shear waves from earthquakes, *J. Geophys. Res.* 75: 4997–5009.

Denny, M. D. and D. M. Goodman (1990). A case study of the seismic source function; SALMON and STERLING reevaluated, *J. Geophys. Res.* 95: 19705–19723.

Denny, M. D. and L. R. Johnson (1991). The explosion seismic source function: Models and scaling laws reviewed, in *Explosion Source Phenomenology*, eds. Taylor S. R. et al., AGU Monograph 65: 1–24.

Fisk, M. D. (2007). Corner frequency scaling of regional seismic phases for underground nuclear explosions at the Nevada Test Site, *Bull. Seis. Soc. Amer.* 97: 977–988.

Goldstein, P., S. P. Jarpe, K. M. Mayeda, and W. R. Walter (1994). Separation of source and propagation effects and regional distances, in *Proceedings of the Symposium on the Non-Proliferation Experiment: Results and Implications for Test Ban Treaties,* DOE-CONF-9404100*,* 6-272–6-276.

Mueller, C. S. and J. R. Murphy (1971). Seismic characteristics of underground nuclear detonations, Part I: Seismic spectrum scaling, *Bull. Seis. Soc. Amer.* 61: 1675–1692.

Stevens, J. L. and S. M. Day (1985). The physical basis of m_b:M_S and variable frequency magnitude methods for earthquake/explosion discrimination, *J. Geophys. Res.* 90: 3009–3020.

Street, R. L., R. B. Herrmann, and O. W. Nuttli (1975). Spectral characteristics of the Lg wave generated by central United States earthquakes, *Geophys. J. R. Astro.* 41: 51–63.

Vergino, E. S. and R. W. Mensing (1990). Yield estimation using regional mb(Pn), *Bull. Seis. Soc. Amer.* 80: 656–674.

Walter, W. R, K. D. Smith, J. L. O'Boyle, T. F. Hauk, F. Ryall, S. D. Ruppert, S. C. Myers, R. Abbot, and D. A. Dodge (2004). An assembled western United States dataset for regional seismic analysis, *Lawrence Livermore National Laboratory* , UCRL-TR-206630.

Walter, W. R. and S. R. Taylor (2002). A revised magnitude and distance amplitude correction (MDAC2) procedure for regional seismic discriminants, *Lawrence Livermore National Laboratory*, UCRL-ID-146882.

Walter, W. R., K. M. Mayeda, and H. J. Patton (1995). Phase and spectral ratio discrimination between NTS earthquakes and explosions, Part 1: Empirical observations, *Bull. Seis. Soc. Amer.* 85: 1050–1067.

DEVELOPING AND EXPLOITING A UNIQUE DATASET FROM SOUTH AFRICAN GOLD MINES FOR SOURCE CHARACTERIZATION AND WAVE PROPAGATION

Jordi Julià[1], Andrew A. Nyblade[1], Rengin Gök[2], William R. Walter[2], Lindsay Linzer[3], and Ray Durrheim[3]

Penn State University[1], Lawrence Livermore National Laboratory[2], and
Council for Scientific and Industrial Research[3]

Sponsored by the National Nuclear Security Administration

Award Nos. DE-FC52-06NA27320[1] and DE-AC52-07NA27344[2,3]
Proposal No. BAA06-06

ABSTRACT

In this project, we are developing and exploiting a unique seismic dataset to address the characteristics of small seismic events and the associated seismic signals observed at local (<200 km) and regional (<2000 km) distances. The dataset is being developed using mining-induced events from three deep gold mines in South Africa recorded on in-mine networks (<1 km) composed of tens of high-frequency sensors, a network of four broadband stations installed as part of this project at the surface around the mines (1–10 km), and a network of existing broadband seismic stations at local/regional distances (50–1000 km) from the mines. Data acquisition has now been completed and includes: (i) ~2 years (2007 and 2008) of continuous recording by the surface broadband array, and (ii) tens of thousands of mine tremors in the -3.4 < ML < 4.4 local magnitude range. Events with positive magnitudes are generally well recorded by the surface-mine stations, while magnitudes of 3.0 and larger are seen at regional distances (up to ~600 km) in high-pass filtered recordings.

We have now completed the quality control of the in-mine data gathered at the three gold mines included in this project. The quality control consisted of: (i) identification and analysis of outliers among the *P*- and *S*-wave travel-time picks reported by the in-mine network operator and (ii) verification of sensor orientations. The outliers have been identified through a 'Wadati filter' that searches for the largest subset of *P*- and *S*-wave travel-time picks consistent with a medium of uniform wave-speed. We have observed that outliers are generally picked at a few select stations. We have also detected that trigger times were mistakenly reported as origin times by the in-mine network operator, and corrections have been obtained from the intercept times in the Wadati diagrams. Sensor orientations have been verified through rotations into the local ray-coordinate system and, when possible, corrected by correlating waveforms obtained from theoretical and empirical rotation angles.

Full moment tensor solutions have been obtained for selected events within the Savuka network volume, with moment magnitudes in the 0.5 < Mw < 2.6 range. The solutions were obtained by inverting *P*-, *SV*-, and *SH*-spectral amplitudes measured on the theoretically rotated waveforms with visually assigned polarities. Most of the solutions have a non-zero implosive contribution (47 out of 76), while a small percentage is purely deviatoric (10 out of 76). The deviatoric moment tensors range from pure double couple to pure non-double couple mechanisms.

We have also calibrated the regional stations for seismic coda-derived source spectra and moment magnitude using the envelope methodology of Mayeda (2003). We tie the coda Mw to independent values from waveform modeling. The resulting coda-based source spectra of shallow mining-related events show significant spectral peaking that is not seen in deeper tectonic earthquakes. This coda peaking may be an independent method of identifying shallow events and is similar to coda peaking previously observed for Nevada explosions, where the frequency of the observed spectral peak correlates with the depth of burial (Murphy et al., 2009).

We are now investigating large magnitude events (ML > 3.0) in between the mines that were simultaneously recorded by the three in-mine networks and the surface-mine array. The purpose of this work is to determine joint hypocentral locations and full moment tensor solutions. One difficulty that we have encountered is that the timing systems are not synchronized among the mines. This difficulty can be circumvented when obtaining moment tensor solutions by inverting spectral amplitudes; however, relocating the seismic sources with the combined data set will require the introduction of network corrections in the equations. We expect the joint event locations and moment tensor solutions to be more robust than those obtained from individual in-mine or surface networks, and will allow the calibration of existing discrimination techniques at regional distances.

OBJECTIVES

The main objective of this project is to develop and exploit a unique seismic dataset from mine-related events recorded at in-mine (<3 km), local (3–10 km), and regional (>100 km) distances (Figure 1). The in-mine recordings are being obtained through three in-mine seismic networks consisting of a few tens of high-frequency geophones, which are routinely used to monitor seismic activity in the mines. The local recordings are being acquired through four broadband seismic stations (three Guralp CMG-3T and one Guralp CMG-40T feeding 24-bit RefTek data loggers) deployed under this project and located on the surface of the mining area. Additionally, the regional recordings are being acquired mostly through the AfricaArray stations in South Africa and surrounding countries. The dataset that we are assembling is unique in that it contains (1) events spanning several orders of magnitude, (2) events from a range of source depths, and (3) events from a variety of source types (e.g., pillar collapses, tensile fractures, normal and strike-slip faulting, and sources with a significant volumetric component).

We plan to exploit this dataset by using the mining events in 10 related areas of research aimed at improving U.S. operational capabilities to monitor for low-yield nuclear tests: (1) create an event catalog with accurate origin times and locations; (2) determine seismic moment, radiated energy, corner frequency, and stress drop; (3) obtain focal mechanisms from moment tensor inversion; (4) define several categories of event types (shear slip, tensile failure with volumetric component, explosions, pillar collapse) using focal mechanisms and in-mine observations; (5) define and calibrate a coda Mw scale for southern Africa; (6) using calibrated coda techniques, determine Mw for all cataloged events; (7) investigate the effects of depth and source mechanism on the coda-derived source spectra and evaluate the potential of using coda spectral peaking as a depth discriminant; (8) define and calibrate local-to-regional phase (direct *P* and *S*, *Pn*, *Pg*, *Sn* and *Lg*) propagation characteristics, including the use of the magnitude and distance amplitude corrections technique to determine appropriate geometrical spreading and frequency dependent Q values for the region; (9) characterize relative *P* and *S* excitation and source apparent stress resulting from variations in source parameters, including magnitude, mechanism, depth, rock characteristics, and source type; and (10) define regional phase ratios that can discriminate between the different source categories, and compare these discriminants and their performance with ongoing work done for other types of mining events, such as in Scandinavia and the western U.S.

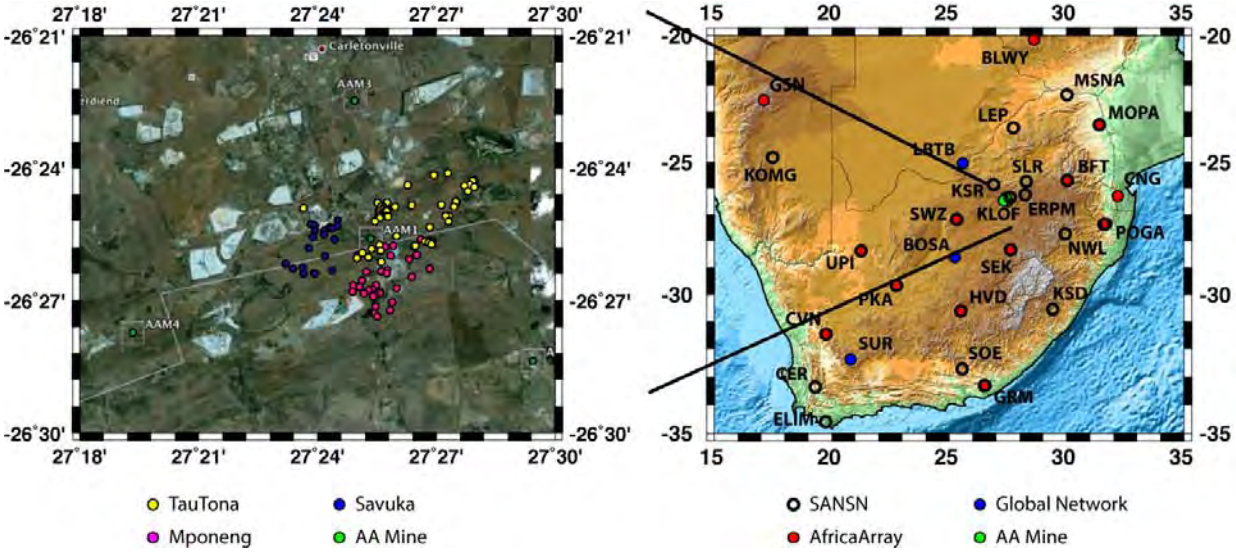

Figure 1. (left) Satellite image from Google Earth showing the Carletonville mining area where the three mines contributing to this project are located. The blue, magenta, and yellow dots are the surface projection of the Savuka, Mponeng, and TauTona in-mine networks, respectively, while the green dots are the surface broad-band stations deployed under this effort. (right) Map of broad-band stations in South Africa. The red dots are the AfricaArray stations, which are shared with the South Africa National Seismic Network (SANSN) shown as hollow circles, and the blue dots are the three permanent GSN stations.

RESEARCH ACCOMPLISHED

Data Gathering

The dataset acquired during this project includes proprietary waveforms for mine tremors recorded by three in-mine seismic networks in the Carletonville district of South Africa (Savuka, Mponeng, and TauTona) and continuous recordings of ground motion at four broadband seismic stations deployed at the surface around the mines (Figure 1).

The in-mine dataset is now complete and consists of high-frequency recordings for tens of thousands of mine tremors occuring during years 2007 and 2008. More specifically, the assembled data set consists of 22,317 events at Savuka with local magnitudes in the $-3.4 < ML < 4.5$ range, 38,915 events at Mponeng with magnitudes in the $-3.8 < ML < 4.7$ range, and 70,861 events at TauTona with magnitudes in the $-4.4 < ML < 4.9$ range, as catalogued by the in-mine network operator Integrated Seismic Systems International (ISSI). The in-mine networks are capable of recording tremors generated at nearby mines, so some overlap exists among the three catalogs.

The data have been provided to us in ASCII format and they have been converted to SAC in order to build the assembled data set. One difficulty when building the database has been identifying the number of stations in each network. The in-mine network operator (ISSI) does not use station names and simply attaches the location and instrument response information to the header of each data file. After counting and sorting all header information, we have identified 24 three-component, high-frequency geophones, with natural frequencies of 4.5, 14, and 28 Hz for Savuka; 80 three-component, high-frequency geophones, with natural frequencies of 4.5, 10, 14, 28, and 30 Hz for Mponeng; and 82 three-component, high-frequency geophones, with natural frequencies at 4.5, 10, 14, 28, and 30 Hz for TauTona. Station names have been given according to SAVXX, MPOXX, and TAUXX, where XX is a 2-digit code arbitrarily assigned to the site, for Savuka, Mponeng, and TauTona stations, respectively. In some instances, we observed up to three different instrument responses for the same location and, in such a situation, we have used three different station names for the same location (one per instrument response).

The first surface-mine broadband station (AAM1) was deployed in January 2007, and three more stations were deployed during the remainder of 2007, which have been operating continuously after installation. The stations are serviced periodically by our South African colleagues and also archived at Penn State. The data holdings at Penn State extend to February 24th, 2009, for AAM1, AAM2, and AAM3, and to August 15th, 2008, for AAM4.

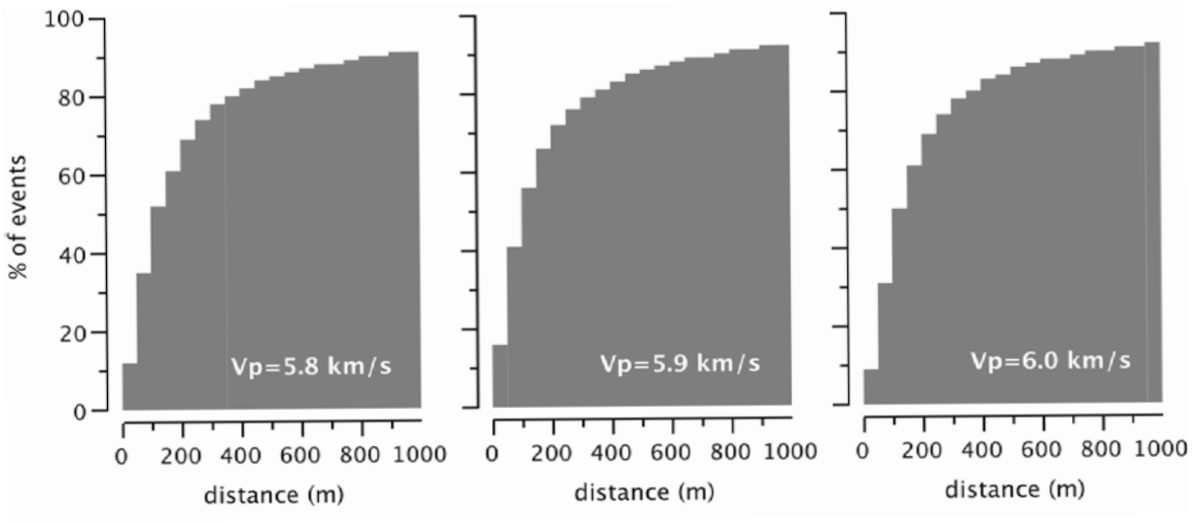

Figure 2. Cumulative histograms of hypocentral migration with respect to the original ISSI locations. The solutions closest to ISSI's are attained for a *P*-wave velocity of 5.9 km/s.

Event Catalogs

Event catalogs for 2007 and 2008 for each mine have been extracted from the header information stored in the original ASCII files. The catalog includes the origin time (South African local time), hypocentral location (in mine coordinates), and local magnitude as reported by ISSI. We have also built event catalogs reporting origin times in universal time (U.T.), locations in geodetic coordinates (lat and lon) and depths with respect to average mean sea level (AMSL).

During one of our visits to the ISSI branch in TauTona mine, we discovered that the origin times reported by ISSI are not actual origin times but trigger times used to label the events (more precisely, the trigger time corresponding to the first station recording a given event). Fortunately, ISSI included travel-time picks for *P* and *S* waves in the header information, and we have verified that accurate origin times can be recovered from the intercept time in Wadati diagrams (i.e., diagrams of *S-P vs P* travel time).

We have attempted a relocation of the seismic sources reported within the in-mine volume at Savuka in order to assess the robustness of the reported event locations. Travel-time picks for both *P* and *S* waves were included in the in-mine dataset, but not all the travel-time picks were utilized by ISSI to locate the seismic sources. To identify outliers we constructed Wadati diagrams from the reported travel-time picks and then utilized only travel-time picks falling along the corresponding Wadati lines in a simple Geiger inversion to relocate the events (see Julià et al., 2009a). Figure 2 displays the cumulative distribution of hypocentral migrations with respect to ISSI's original locations for assumed *P*-wave velocities of 5.8, 5.9, and 6.0 km/s. In all cases, more than 50% of the events migrate less than 150 m. Event locations are provided with an accuracy of ~50 m, according to ISSI.

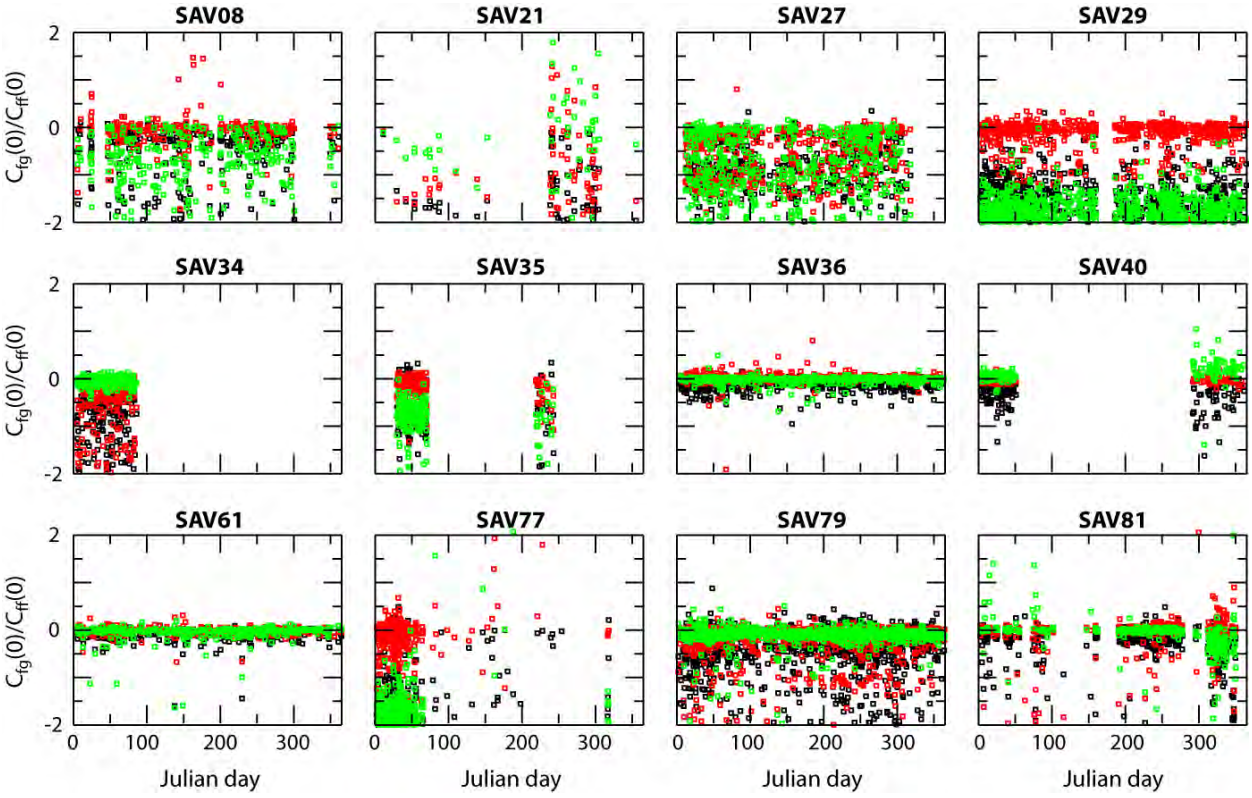

Figure 3. Correlation coefficients between theoretically and empirically rotated waveforms (green, SH; red, SV; black, P). Note that only stations SAV36, SAV40, SAV61, SAV79 and SAV81 show coefficients close to 1 in all three components.

Sensor Orientations

Sensor orientations have been verified for all three in-mine networks by comparing waveforms rotated into the local ray-coordinate system (P,SV,SH) through theoretical and empirical rotation angles. The theoretical angles were obtained from the station and event locations according to

$$\mathrm{tg}\ \varphi = (x_s - x_0)/(z_s - z_0) \quad (1)$$

$$\cos\phi = (z_s - z_0)/[(x_s - x_0)^2 + (z_s - z_0)^2]^{1/2}, \quad (2)$$

where x is North, y is East, and z is Up, and ϕ and φ are the take-off angle and azimuth, respectively, while the empirical rotation angles were obtained from the eigenvectors of the covariance matrix for the *P*-wavetrain as described in Montalbetti and Kanasewich (1970). By inspecting the correlation coefficients between the empirically and theoretically rotated waveforms we have been able to identify stations where both rotations disagree. Figure 3 illustrates the process for some stations operating during 2007 as part of the Savuka network. Note how stations SAV36, SAV40, SAV61, SAV79, and SAV81 have correlation coefficients close to one for all three components, demonstrating that the empirical and theoretical rotations agree. The remaining stations, on the other hand, show different patterns and suggest they have not been accurately oriented.

The procedure outlined above requires that the events be recorded in all three components. Unfortunately, some stations in the in-mine networks had at least one component failing during 2007 and 2008 and could not have the orientation verified. Overall, we found that empirical and theoretical rotations agree for 10 stations at Savuka (out of 19), 7 stations at Mponeng (out of 27), and 16 stations at TauTona (out of 32). Fortunately, we were able to work out corrections for some sensors by simply rotating the waveforms around the vertical axis, but uncertainties of 180^o might still exist due to the symmetry of the covariance matrix utilized for the empirical rotation.

Wadati Filter

We have devised a procedure based on Wadati diagrams to assess and improve the consistency of *P*- and *S*-wave travel-time picks with the assumption of propagation at constant wave-speed. The 'Wadati filter' is a simple search in the (*S*-*P*, *P*) travel-time space that finds the largest subset of (*S*-*P*, *P*) travel-time pairs that follow a straight line. Adjustable parameters include the minimum regression coefficient of the Wadati line, the minimum number of data points, and a range of slopes (which are closely related to the v_p/v_s ratio of the medium). The filter has been tested with travel-time picks reported by ISSI for events recorded by the Savuka in-mine network and we have found it quite effective in identifying defective travel-time picks, as well as travel-times associated to inhomogeneous ray-paths. An example is provided in Figure 4.

Moreover, by comparing histograms of *S*-*P* travel times with and without outliers for each station, we have observed that the majority of the outliers are picked at a reduced number of stations. Our interpretation is that most of the outliers are indeed travel-times associated to non-homogeneous ray-paths joining the event sources with a few select stations. These results are presently under review for publication in the South African Journal of Geology (Julià et al., 2009a).

Moment Tensor Solutions

We have obtained full moment tensor solutions for 76 events with moment magnitudes between 0.5 and 2.5 by inverting *P*, *SV*, and *SH* spectral amplitudes with polarity attached, as measured on mine tremors recorded by the Savuka in-mine network. We assumed a medium of uniform velocity and density (V_P=6.0 km/s, V_S=3.70 km/s, ρ=2.69 g/cm^3), so that the displacements could be expressed as (e.g., Udías, 2000):

$$u_i = G_{ij,k} m_{jk} \qquad i,j,k = 1,2,3 \quad (3)$$

where

$$G_{ij,k} = (1/4\pi\rho v^3 R)\ \gamma_i\gamma_j\gamma_k\ \delta'(t - R/v) \qquad \gamma_i = x_i/R \quad (4)$$

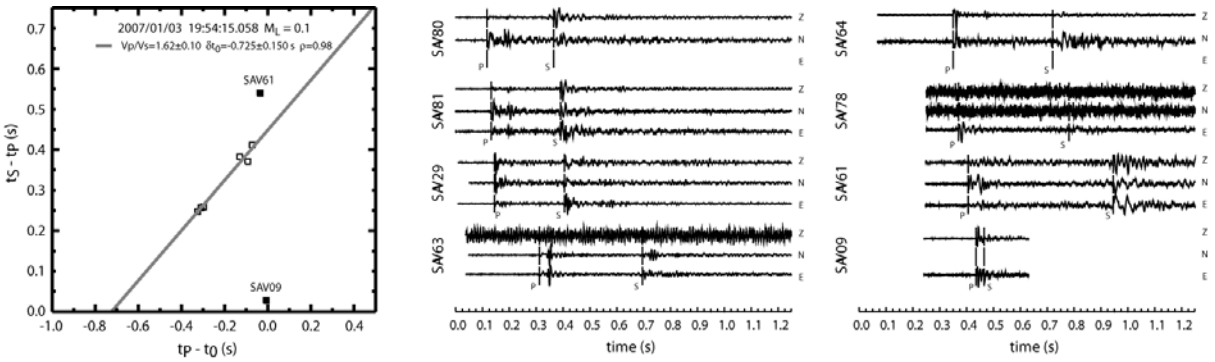

Figure 4. (left) Wadati diagram for a M_L = 0.4 event recorded at Savuka mine, South Africa. The solid squares are measurements rejected by the 'Wadati filter'. The time at the top is a trigger time randomly selected by ISSI to label the event, and used as a reference time in the diagram. (right) Recordings for the same events, sorted by *P*-wave travel-time. Note that the waveforms have been normalized to their maximum amplitude. Stations SAV80, SAV63, SAV64, SAV78, and SAV09 have failing channels.

and where ρ is density, v is the *P*- or *S*-wave velocity, and R is the hypocentral distance. The forward problem was then written by rotating the displacements into the ray-coordinate system and Fourier transforming the resulting equation to obtain spectral amplitudes. This defines a linear problem that was inverted by calculating the natural inverse through a singular value decomposition of the forward problem's matrix (e.g., Menke, 1989).

Spectral amplitudes from the in-mine recordings were obtained through the time-domain procedure of Urbancic et al. (1996). This procedure evaluates the spectral plateau of the *P*- or *S*-wave spectrum by computing the ratio

$$\Omega_o = 4(S_{D2})^{3/2}(S_{V2})^{-1/2} \quad (5)$$

where

$$S_{D2} = 2\int D^2(t)\,dt \quad S_{V2} = 2\int V^2(t)\,dt \quad (6)$$

and D(t) and V(t) are the displacement and velocity, respectively. Following Trifu et al. (2000), the integrals extend between the *P*- and *S*-wave travel times, for the *P*-wave amplitude, and twice the *S*-*P* time after the *S*-wave travel time for the SV and SH amplitudes. The polarity of the spectral amplitudes is assigned visually for each measurement by correlating low-pass filtered waveforms with synthetics.

Figure 5 displays the moment tensor inversion results for a Mw=1.6 event recorded by the Savuka in-mine network, along with the coverage of the focal sphere. The coverage of the focal sphere is limited, but characteristic of mining environments and reflecting the lack of station coverage ahead of the advancing mine stopes. However, the measured *P*- and *S*-wave amplitudes had both positive and negative polarities, which suggests that more than one energy lobe in the radiation pattern was sampled. The moment tensor solution obtained for this event is m_{xx}=-1.25x10^{11} Nm, m_{xy}=0.74x10^{11} Nm , m_{yy}=0.09x10^{11}Nm, m_{xz}=1.20x10^{11} Nm, m_{yz}=0.55x10^{11} Nm, and m_{zz}=-2.66x10^{11} Nm, and has a condition number around 0.16. The eigenvalues for this moment tensor solutions are σ_1=-3.35x10^{11} Nm, σ_2=-1.22x10^{11} Nm, and σ_3=0.74x10^{11} Nm, and $\mathbf{e}_1$ = (0.49,0.04,-0.87), $\mathbf{e}_2$ = (-0.72,0.57,-0.38), and $\mathbf{e}_3$ = (-0.49,-0.82,-0.31). The largest principal stress is thus compressive and oriented near-vertically (deflection from the vertical is ~29^o), consistent with gravity-driven stress conditions in a deep mine.

The trace for this particular moment tensor solution is tr(σ_i)= –3.83x10^{11} Nm, representative of an implosive volumetric source, and the deviatoric eigenvalues are σ^*_1 = -2.07x10^{11} Nm, σ^*_2 = 0.06x10^{11} Nm, and σ^*_3 = 2.01x10^{11} Nm, which are well approximated by a double-couple force equivalent. The eigenvectors of the deviatoric moment tensor are the same as those for the general moment tensor, so the double-couple solution thus has a sub-vertical pressure axis and a sub-horizontal tension axis characteristic of normal faulting. The decomposition of the moment tensor solution for this event thus indicates that stresses have been relaxed through normal faulting and co-seismic closure, consistent with previous findings in South African deep mines (McGarr, 1992a; 1992b).

The moment tensors for the 76 events recorded by the Savuka in-mine network are reported in Julià et al. (2009b) and can be found online at http://www.geosc.psu.edu/~jjulia/julia-esupp.html. The majority of the solutions reveal that the largest principal stress is vertical and compressive and that there is a significant implosive contribution, as illustrated in the example (Figure 5). The deviatoric components, on the other hand, can always be decomposed into two normal faults but other decompositions, such as combinations of DC and CLVD, are also possible.

Regional Coda Magnitudes and Spectra

We have also been looking at the seismic coda from regional events, both natural earthquakes and mine-related, that are recorded at regional stations across South Africa. Regional coda envelopes are useful to establish a calibrated moment magnitude scale for the area and to study source spectra of events.

We used the coda wave method of Mayeda (2003) to calculate source spectra of earthquakes recorded at GSN broad-band stations and the Kaapval seismic array. In order to generate a list of seismic events in the South Africa

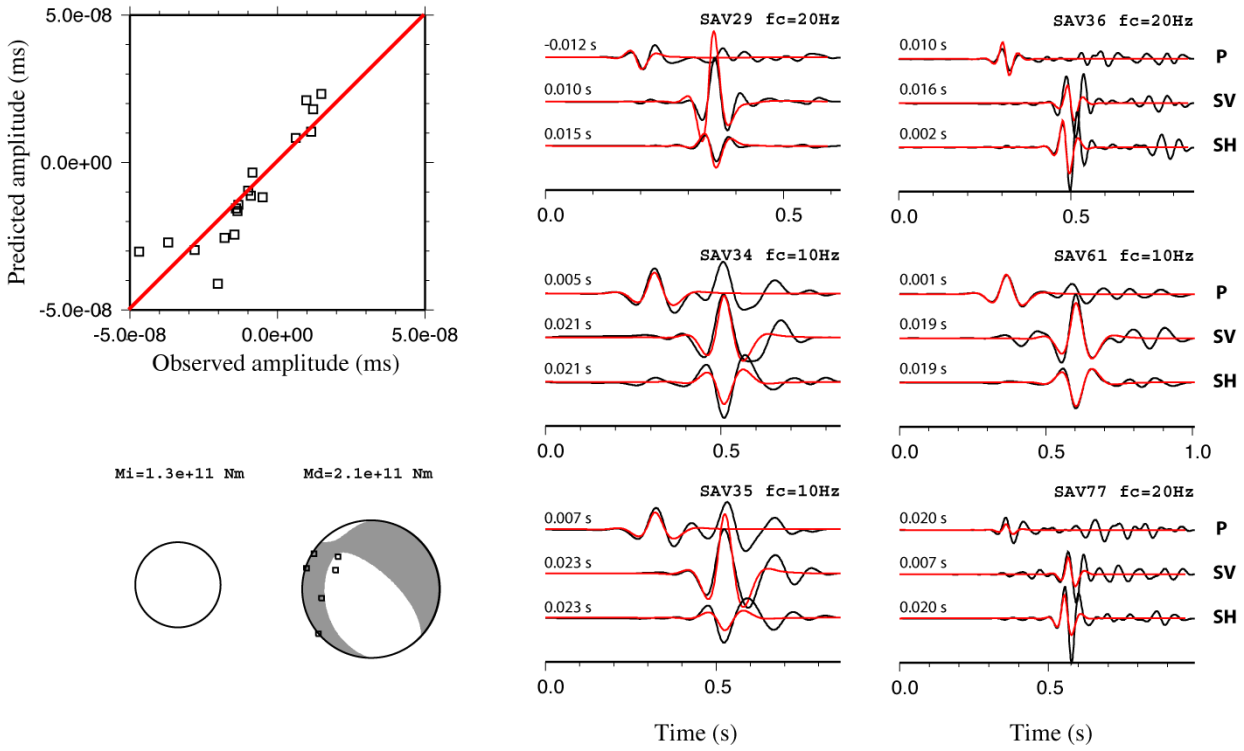

Figure 5. Moment tensor inversion results and coverage of the focal sphere for a ML=1.6 event recorded at Savuka mine. The upper left diagram compares predicted and observed spectral amplitudes for *P*, *SV*, and *SH* components. The lower left diagram shows the P-wave radiation pattern for the isotropic and deviatoric moment tensors, along with the coverage of the focal sphere (overlying the deviatoric "beach-ball"). The waveforms on the right are shown to compare the corresponding observed (black) and predicted (red) *P*, *SV* and *SH* amplitudes in the time domain. The event origin time is at t = 0 s and the synthetic waveforms have been shifted by the amount noted above each trace, to facilitate the comparison with the observations. The time shifts between observed and synthetic waveforms are due to inaccuracies in the event location, assumed wave-speed, and/or anisotropic effects. Note that only spectral amplitudes were inverted, so the observed time shifts did not influence our moment tensor solutions. The waveforms are shown in velocity.

mining districts, we used the seismic bulletins provided by the Council of Geoscience, Pretorai and the Preliminary Determination of Epicenters (PDE) catalogs. The mining-induced events were found to be concentrated around Welkom, Klerkdorp, (Far West, Central, and East) Rand regions. Tectonic events found in the bulletins primarily consisted of a large Mozambique (Mw=7.2) event and its aftershocks. The early and late coda parameters were obtained for a set of earthquakes in the region. Those parameters are distance dependent at each narrow frequency bands (0.05-6 Hz). The raw amplitudes were path corrected using the Street and Herrmann (ESH) method which corrects for geometrical spreading and Q. The path corrected amplitudes at 1.0-1.5 Hz are shown in Figure 1. To scale those non-dimensional amplitudes to absolute moment we use independently waveform modeled Mw's. A constant correction factor at each frequency band can then be used to correct for each event to obtain the moment rate function. We performed a grid-search procedure to obtain the body and surface wave fit at long-period levels. The best fitting is obtained at around 1-4 km and the mechanism is normal-type like. The shallow hypocentral location causes peaking of coda source spectra at 0.4-1.5 Hz. It is probably caused by strong excitation of Rayleigh waves at shallower depth that is then scattered into the coda (Figure 2). The spectral peaking causes overestimated Mw (coda)'s for smaller events where the long period coda levels cannot be measured. Larger magnitude mining induced events has the coda amplitude value up to 0.2-0.3 Hz narrow frequency band where we match the independently waveform modeled magnitudes. Whereas smaller magnitude events does not have an amplitude measurement at that frequency (Events 2 and 3, Figure 2). In other words, coda is abruptly eliminated below 0.2-0.3 Hz for smaller magnitude events. When we extrapolate that Mw value to the level we supposed measure from Table 2, we found that an average constant correction factor is 0.4-0.5.

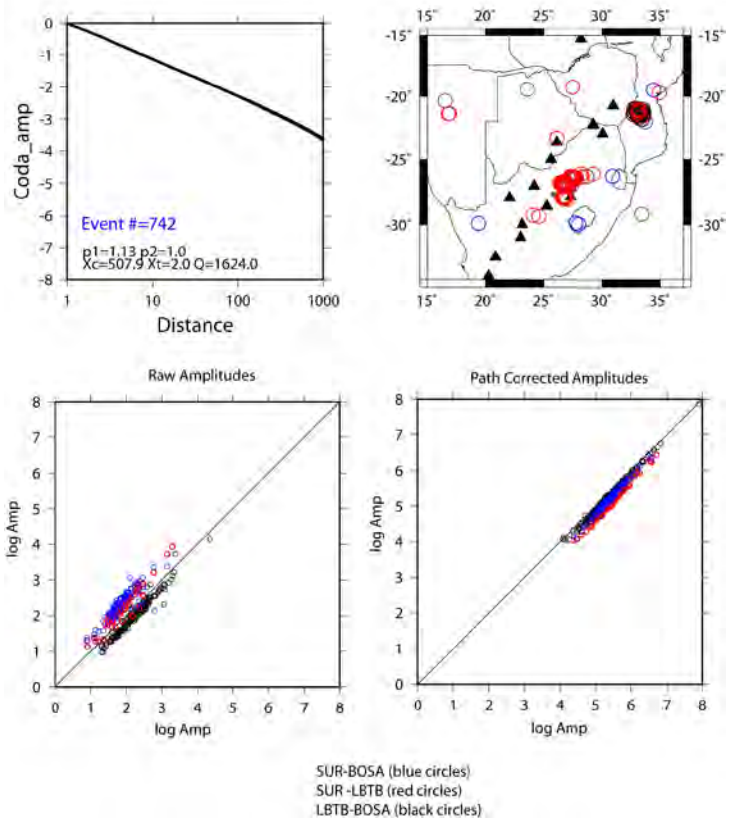

Figure 6. Path calibration at 1.0-1.5 Hz. Upper left panel is the ESH function.

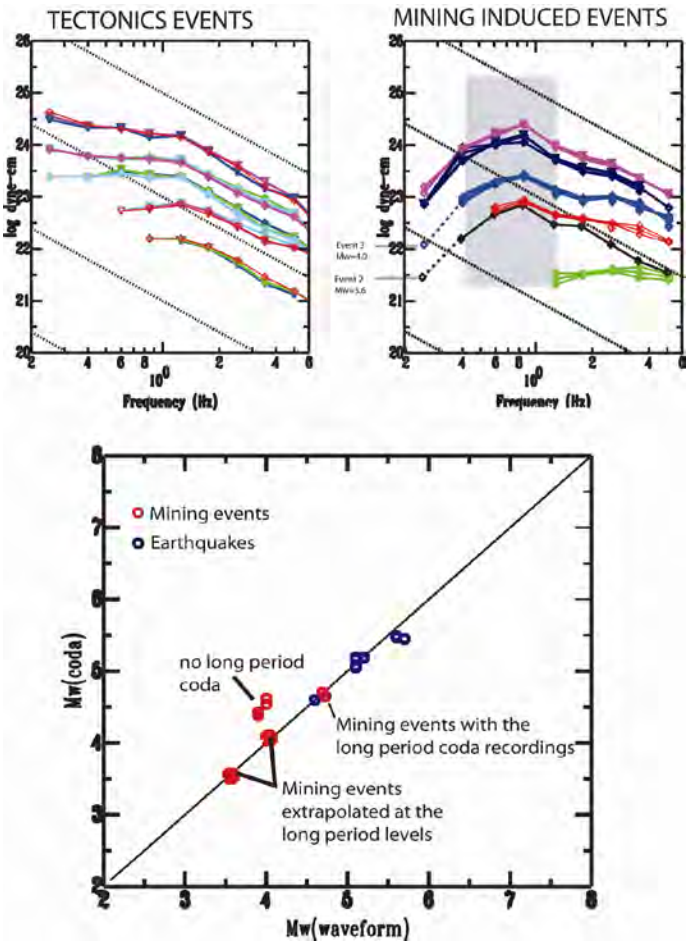

Figure 7. Coda derived source spectra from earthquakes (left) and mining induced events (right). The earthquakes have the usual shape: a near constant proportional to the moment at long periods and falling of as frequency^{-2} at the high frequencies. Coda based Mw's for any event can be determined from the long period level. In contrast the mine events show an unusual peaked shape, which may be an indicator of shallow depth due to Rg excitation and scattering into the coda. The lowest frequency points shown with dashed lines come from long period waveform modeling.

CONCLUSIONS AND RECOMMENDATIONS

So far, we have completed the quality control for all three in-mine networks and we have analyzed data recorded by the Savuka in-mine network only. For the moment tensor study (Julià et al., 2009b), we have used a subset of events with hypocenters located within the in-mine network volume and selected about 100 for which *P*, *SV*, and *SH* spectral amplitudes could be measured at 6 to 7 stations. The largest event included in this high-quality subset had a moment magnitude of 2.5, which was not large enough to be well recorded at regional distances.

We are now comparing the catalogs from the three in-mine networks to determine a subset of large (ML > 3.0) events with epicenters located within the combined networks, including the surface broadband array. Figure 8 shows a preliminary selection for the 2007 catalogs, which shows some large events are within the combined in-mine network. These events have an excellent azimuthal coverage, which will allow the determination of accurate event locations and moment tensor solutions. Discrepancies observed among the timing systems among the in-mine networks will be handled through network corrections and may introduce uncertainty in the event locations. Timing discrepancies, however, will seldom affect moment tensor solutions obtained from spectral amplitudes.

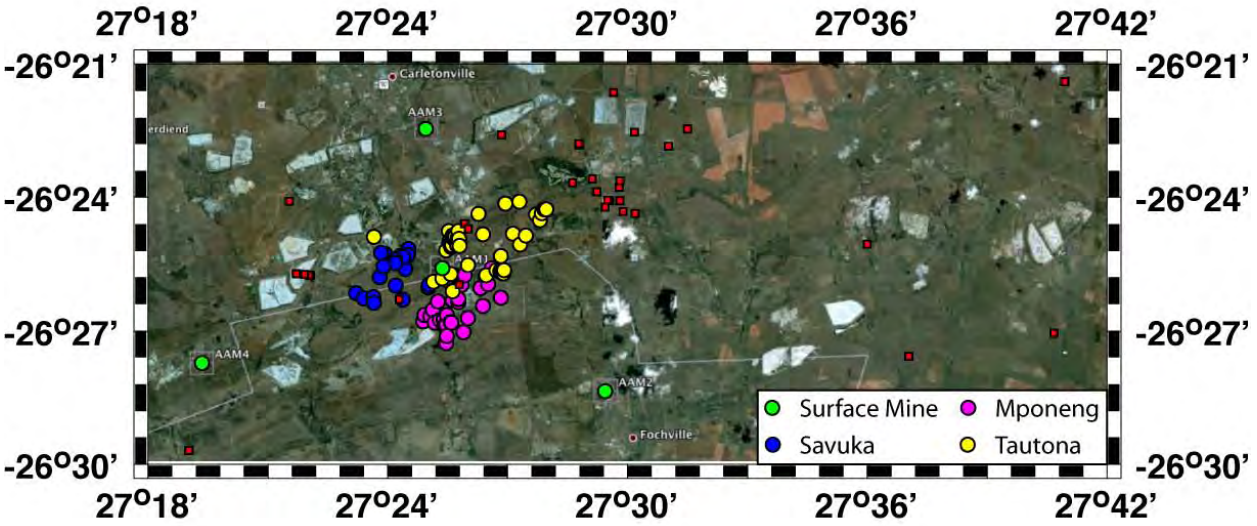

Figure 8. Events with magnitudes (ML) above 3.0 (red squares) recorded during 2007 at all three in-mine networks (color circles). A fair number of events are located within the combined network area. We expect to obtain robust locations and moment tensor solutions from the combined dataset.

ACKNOWLEDGEMENTS

We thank ISSI and Anglo Gold Ashanti for providing the seismic data and mine plans from the Savuka, Mponeng and TauTona mines. We also thank ISSI and the Council for Scientific and Industrial Research for assisting with event locations and solving other technical issues concerning the in-mine data, and we thank the Council for Geoscience for installing and operating the four broadband stations of the surface mine network. The IRIS data management center has provided assistance with archiving and distributing data from the permanent AfricaArray seismic stations, including data used in this study.

REFERENCES

Julià, J., A. A. Nyblade, R. J. Durrheim, L. Linzer, R. Gök, W. Walter, S. M. Spottiswoode, and P. Dirks (2009a). A Wadati filter for mine-induced seismicity, *S. Afr. J. Geol.*: in review.

Julià, J., A. A. Nyblade, R. J. Durrheim, L. Linzer, R. Gök, P. Dirks, and W. Walter (2009b). Source mechanisms of mine-related seismicity, Savuka mine, South Africa, *Bull. Seism. Soc. Am.*: in press.

Mayeda, K. (2003). Stable and transportable regional magnitudes based on coda-derived moment-rate spectra, *Bul. Seism. Soc. Am.* 93: 224–239.

Menke, W. (1989). *Geophysical Data Analysis: Discrete Inverse Theory*, Academic Press, 289 pp.

McGarr, A. (1992a). An implosive component in the seismic moment tensor of a mining-induced tremor, *Bull. Seism. Soc. Am.* 19: 1579–1582.

McGarr, A. (1992b). Moment tensors of ten Witwatersrand mine tremors, *Pure Appl. Geophys.*

Montalbetti, J. M., and E. R. Kanasewich (1970). Enhancement of teleseismic body waves with a polarization filter, *Geophys. J. R. Astr. Soc.* 21: 119–129.

Murphy, K. R., K. Mayeda, and W. R. Walter (2009). Lg-coda methods applied to Nevada Test Site events: Spectral peaking and yield estimation, *Bull. Seism. Soc. Am.* 99: 441–448.

Trifu, C. I., D. Angus, and V. Shumila (2000). A fast evaluation of the seismic moment tensor for induced seismicity, *Bull. Seism. Soc. Am* 90: 1521–1527.

Udías, A. (2000). *Principles of Seismology*, Cambridge University Press, 475 pp.

Urbancic, T.I., C.I. Trifu, R.A. Mercer, A.J. Feustel, and J.A.G. Alexander (1996). Automatic time-domain calculation of source parameters for the analysis of induced seismicity, *Bull. Seism. Soc. Am* 5: 1627–1633.

QUANTIFICATION OF ROCK DAMAGE FROM SMALL EXPLOSIONS AND ITS EFFECT ON SHEAR-WAVE GENERATION: PHASE I—HOMOGENEOUS CRYSTALLINE ROCK

Mark Leidig[1], Randolph J. Martin[2], Peter Boyd[2], Jessie L. Bonner[1], and Anastasia Stroujkova[1]

Weston Geophysical Corporation[1] and New England Research, Inc.[2]

Sponsored by the Air Force Research Laboratory

Contract No. FA8718-08-C-0044
Proposal No. BAA08-99

ABSTRACT

Weston Geophysical Corp., New England Research, Inc., and several geotechnical consultants conducted the New England Damage Experiment (NEDE) in central Vermont during July 2008. A series of five explosions using charges having yields of 135 and 270 lbs and three types of explosives were detonated in homogeneous low-fracture density granite. The goal of the experiment was to generate different amounts of rock damage around the source by using explosives with dramatically different velocities of detonation (VOD), ranging from 0.5 to 8.1 km/sec, and then relate the shear wave generation to the amount of damage. Increased VOD causes increased borehole pressures, which exceed the rock's compressive breaking strength, and results in more extensive fracturing of the source rock. This zone of highly fractured rock prevents the explosive gases from being able to drive long fractures. In contrast, slower VOD explosives generate fewer fractures around the borehole, but the explosive gases are able to enter the cracks and drive long fractures. Surface observation of the test site confirmed this as no fractures were found for the fast VOD explosive, multiple small cracks were seen for the middle VOD explosive, and large fractures with surface displacement were found for the slowest VOD explosive.

We have also used pre- and post-shot core analysis to quantify significant differences in the damage induced by the explosions. The extent of damage can be characterized by determining rock properties. Laboratory measurements of ultrasonic velocities, permeability, resistivity and porosity are sensitive to the microcrack density in the granite. Velocities are slower, permeabilities are higher, resistivities are lower and porosities are higher in the damaged intervals. These results are consistent with a microcrack scale fracture population that is enhanced by the blasts. This damage has been determined to extend vertically to as much as 6–7 meters from the explosive charge emplacement. Larger scale fractures are not apparent below the blasts, but are developed above the blast interval and they extend beyond the interval identified by the laboratory measurements.

Over 140 seismic sensors were installed to record the blast, ranging in distance from 5 m to 30 km. Peak particle velocity (PPV) studies found that the fastest VOD explosive, Composition B, expended much of its energy at the source pulverizing the surrounding rock. The middle VOD explosive, heavy ANFO, produced the largest PPV, while the slowest VOD explosive, black powder, produced PPV one-third the size of the ANFO PPV.

Source scaling studies found the black powder shot produced seismic amplitudes up to an order of magnitude less than the ANFO and Comp B amplitudes above 5 Hz, but created Rayleigh waves similar in amplitude to those from the ANFO shot. The black powder shot produced larger Rayleigh and Love waves than the Comp B shot. The ANFO and Comp B shots generated similar amplitudes above 8 Hz, but the ANFO source Rayleigh waves were up to twice as large and the Love waves were up to three times as large as those from the Comp B shot. The seismic waves followed an almost identical travel path indicating that differences in the source region (e.g., possibly damage) are responsible for the variations in surface and shear wave energy. We continue to analyze the data to determine if the longer fractures from the black powder and ANFO shots appear to be responsible for the increased surface and shear wave energy.

OBJECTIVES

Weston Geophysical Corporation and New England Research, Inc. and several geotechnical consultants collected a unique dataset of damage characteristics from explosions in hard, crystalline rock during July 2008. The NEDE project involved the detonation of five small (135 to 270 lbs) chemical explosions in relatively unfractured, homogeneous Barre granite in Vermont, USA. The objective of the project was to relate differences in rock damage from the explosions to variations in shear waves observed on local to regional distance seismic stations.

RESEARCH ACCOMPLISHED

The New England Damage Experiment

Site Selection. The NEDE was conducted at a granite quarry in Barre, Vermont, USA. The granite in this quarry has a low fracture density and typically forms large blocks. Barre granite has been a worldwide standard for homogeneous granite in commercial, monument, and industrial settings. We conducted pre-shot coring, crosshole velocity imaging, and acoustic televiewer imaging of the boreholes in order to characterize the emplacement media. Some of the results of these studies will be discussed later in this paper when compared to the post-shot damaged measurements.

Explosions. The NEDE included five single-blasthole explosions with total explosive weights ranging from 60 to 122 kg. (Table 1; Figure 1). The explosions were small in order to be contained in a single borehole, to reduce drilling costs, and to limit ground vibrations at nearby structures. Since an objective of this project was to relate rock damage to seismic phase generation, we attempted to design the experiments in order to fracture rock differently. Rock fracturing has been related to velocity of detonation. A slow explosive will often generate a large amount of gas that will drive crack formation; while a faster explosive will tend to rubbleize or powderize the material immediately adjacent to the borehole, and the powdered rock may impede the effects of gas-driven crackage. For more on these effects, the reader is referred to http://www.johnex.com.au/index.php?section=105 (last accessed in June 2009).

Table 1. NEDE origin parameters

Shot	Date	Origin Time	Latitude	Longitude	Elevation (m)	Depth (m)	Yield (kg)	Explosive	VOD (km/sec)
1	12-Jul-08	14:37:42.16	44.1577	-72.47848	509	8.3	60.8	Black Powder	0.53
2	12-Jul-08	16:02:05.02	44.158	-72.47813	509	10.7	61.5	ANFO/EMUL 50:50	4.76
3	12-Jul-08	17:30:40.73	44.1578	-72.4777	503	10.7	61.7	COMP B	
4	12-Jul-08	19:16:15.01	44.1575	-72.47797	508	12.8	122.2	ANFO/EMUL 50:50	4.89
5	12-Jul-08	20:50:12.77	44.1575	-72.47757	503	12.8	122.5	COMP B	8.10

Black Powder. With the assistance of Mr. Tim Rath of Maxam-North America, we designed the NEDE to have a wide range of VODs (Figure 2). For Shot 1, we detonated 60.8 kg of black powder (Figure 3) at a centroid depth of 8.3 meters in a 22.86 cm diameter borehole. The explosives column extended approximately 1 meter above and below the centroid. Schist gravel, with a diameter of 1¼ cm, was used to stem the boreholes. Black powder was used exclusively for hundreds of years in mining and military applications. Today, the use of black powder as an explosive has diminished considerably, but it is often used to detach rock along pre-existing fractures such as in the Vermont slate district. The VOD was measured at 0.53 km/sec for Shot 1 (Figure 2); however, we note that the black powder typically “deflagrates” rather than “detonates” unless under highly confined conditions.

Heavy ANFO. Shots 2 and 4 consisted of a 50:50 blend of Ammonium Nitrate Fuel Oil (ANFO) and Emulsion explosives. The mining industry typically refers to this blend as “Heavy” ANFO, because the mixture increases the density allowing more explosives to be loaded into a borehole. It also helps to waterproof the explosive as compared to pure ANFO. Heavy ANFO is often used in today’s commercial blasting industry because of low cost (e.g., $2/kg) and abundant gas formation that helps fracture the rocks efficiently. Shot 2 consisted of 61.5 kg of Heavy ANFO detonated at a centroid depth of 10.7 m while Shot 4 had almost double the explosives at a centroid depth of 12.8 m. The thicknesses of the explosive columns were approximately 1 and 2 meters for Shots 2 and 4, respectively. Both Heavy ANFO shots were detonated in 22.86 cm diameter boreholes with schist stemming. The measured VOD was 4.76 km/sec and 4.89 km/sec for Shots 2 and 4, respectively.

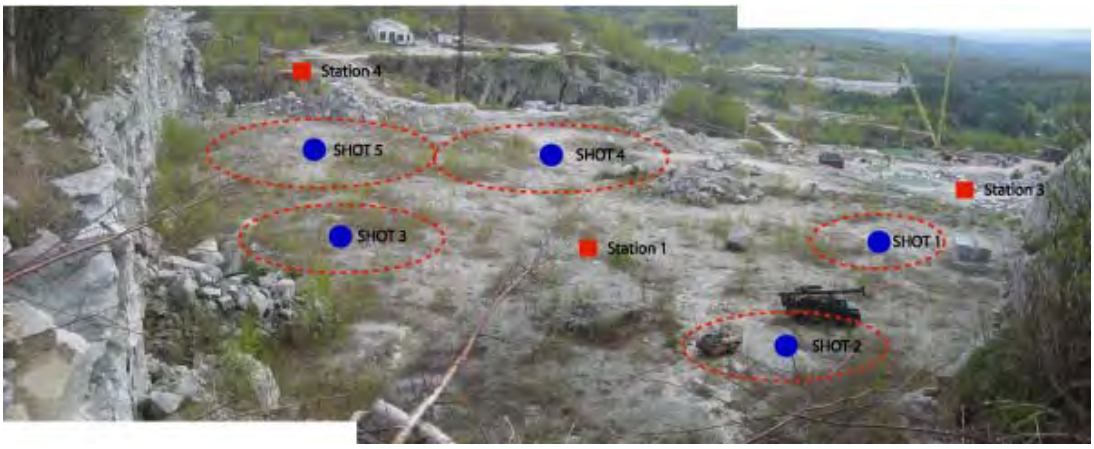

Figure 1. Photos of the test bed where the NEDE explosions (blue circles) were detonated. Also shown are three near-source station locations (red squares) and the estimated elastic radii (red dashed circles).

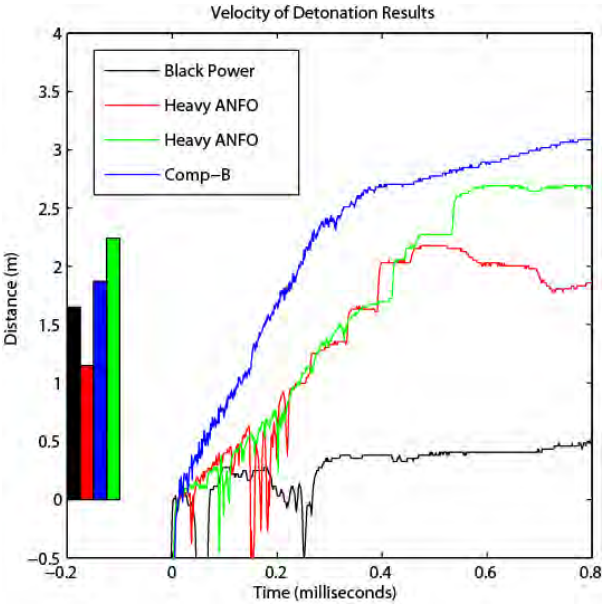

Figure 2. Velocity of detonation recordings for four NEDE shots. A fifth shot was not recorded using VOD equipment. The raw VOD data were aligned so that the approximate start of the resistance wire burn was at distance=0. Also shown are the lengths of the explosives column (bars at left) which correlate well with the VOD data.

Composition B. Shots 3 and 5 consisted of Composition B, a military grade explosive. According to GlobalSecurity.org, "COMP B explosives are made from TNT, RDX, and wax, such as 59.5 percent RDX, 39.5 percent TNT and 1 percent wax. Desensitizing agents are added. Composition B is used by the military in land mines, rockets and projectiles. Cast Composition B has a specific gravity of 1.65 and a detonation velocity of about 25,000 fps and is used as a primer and booster for blasting agents."[1] We had the COMP B charges cast as 45 kg cylinders of 19.1 cm diameter and 94 cm length (Figure 3). One cast charge was used for Shot 3 and two for Shot 5. Because of the space between the 19.1 cm charge and 22.86 cm diameter borehole wall, the casts were lowered into bulk emulsion to ensure adequate coupling, thus resulting in final explosive yields of 61.7 kg and 122.5 kg for Shots 3 and 5, respectively. The charges were placed at the same centroid depths as the Heavy ANFO shots 2 and 4. The VOD for Shot 3 was not measured; however, for Shot 5, the VOD was 8.1 km/sec.

[1] http://www.globalsecurity.org/military/systems/munitions/explosives-compositions.htm

Figure 3. Photo of the explosives used in the NEDE. (Left) Packages of "Polvara Negra" or black powder. (Middle) Containers of pre-mixed Heavy ANFO (50:50 ANFO:Emulsion). (Right) A cast charge of Composition B.

Instrumentation. Instrumentation deployed to record the NEDE explosions consisted of two primary groups: (1) near-source (<1.5 km) acceleration and velocity instruments and (2) near-regional distance (1.5-30 km) vertical component geophones and three-component (3C) high-frequency seismometers deployed along northeast and southeast profiles (Figure 4). Numerous additional regional (> 30 km) seismic stations that comprise seismographic networks in New England (e.g., New England Seismic Network) also recorded the explosions (Figure 5). The design of this instrumentation plan was intended to document the generation and propagation from near-source to near-regional distances of both the compressional and shear energy from the single blasthole explosions.

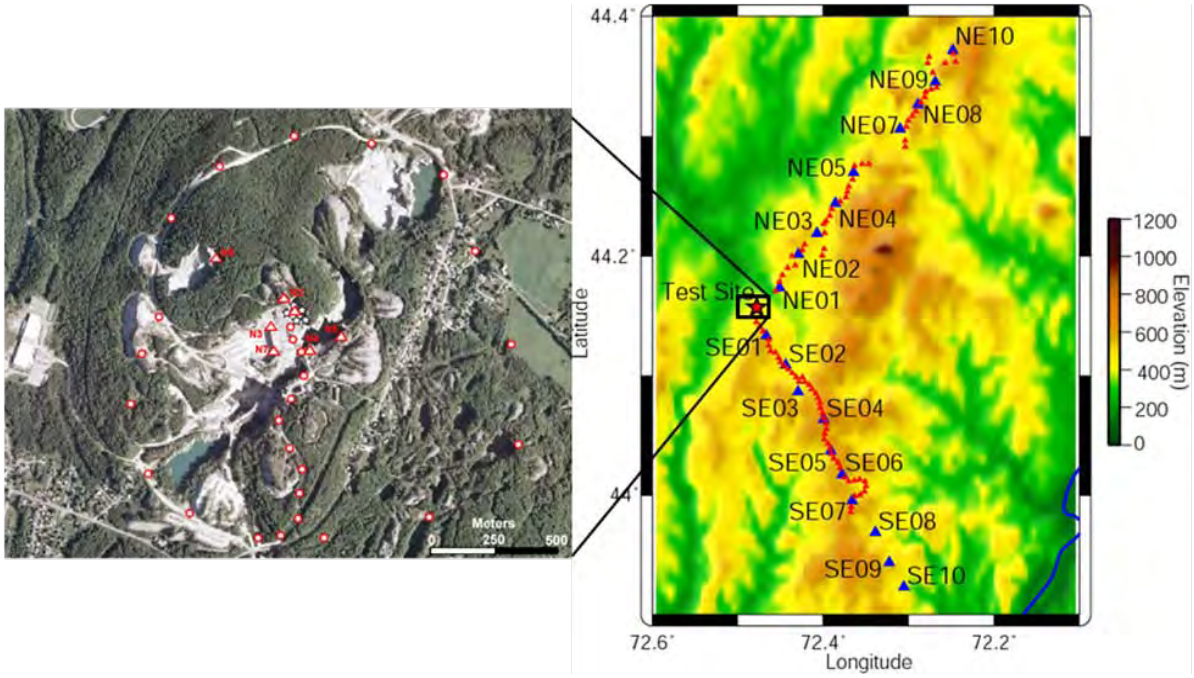

Figure 4. Location of the NEDE explosions and seismometers. (Left) Satellite imagery of the test site and near-source instrumentation. Circles are RT125 or "Texan" single-component (1C) geophones. Triangles are three-component (3C) accelerometer/velocity sensor sites within 600 meters of the test site. (Right) Local distance instrumentation. Blue triangles represent either L22 (southeast profile) or L4 (northeast profile) 3C short-period velocity sensors, while the small red triangles are 1C Texans.

Preliminary Observations: Seismic

Regional Observations. Figure 5 shows the data from Shots 4 and 5 (see Table 1 for info) at station PKME in Maine, which was located 270 km from these two 125 kg explosions. While the signal-to-noise ratio is small, the data show that the *Lg* amplitudes were larger for the Heavy ANFO Shot 4 than the COMP B Shot 5. Also of interest is the impulsive arrival at a group velocity of 4 km/sec (possibly *Sn*?) on the Shot 4 records that is not observed for Shot 5. It is interesting to note that while there were visible cracks on the surface after the Heavy ANFO Shot 4, there were none for the COMP B shot.

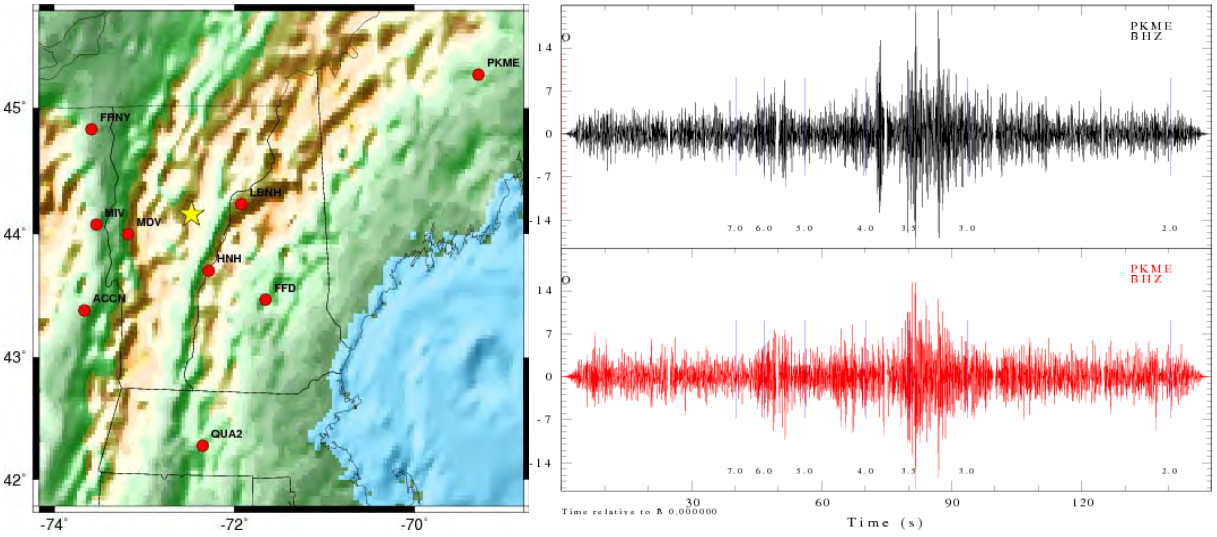

Figure 5. Regional stations (left) that recorded at least one of the NEDE explosions. The signals were recorded as far away as 270 km at station PKME (right).

Spectral Ratios. Empirical source scaling relations using the near-source and local data were compared for the three different explosive types in five different explosions (Table 1). In most cases, spectral ratio data from each distance range document similar scaling. The source scaling studies show that the 61 kg black powder explosion was deficient in high-frequency energy when compared to the 62 kg Heavy ANFO and COMP B charges (Figure 6). At frequencies above 5 Hz, the black powder explosion amplitudes were up to an order of magnitude smaller than the faster VOD explosives. The black powder explosion generated surface waves that were equivalent to the ANFO explosion at frequencies below 5 Hz. The Rayleigh-waves generated from the 61 kg black powder shot were larger than the equivalent COMP B explosion. The black powder charge generated larger-amplitude short-period Love-waves than the COMP B explosion for all azimuths studied, which may provide important data in addressing the continuing problem of determining the source of *S*-wave generation from explosions. The Mueller-Murphy (1971) explosion source model cannot explain the black powder effects using standard empirical relationships between explosion yield and source elastic and cavity radii and static pressures, and will require more detailed study after the damage zones from the explosions have been quantified and the nominal explosion pressures have been estimated.

Comparisons of the Heavy ANFO and COMP B explosions show small differences at body-wave frequencies (> 8 Hz) and larger effects at surface-wave frequencies. The slower VOD Heavy ANFO explosions generated larger-amplitude Rayleigh waves (up to a factor of 2x larger) and Love waves (as large as 3x) than the equivalent COMP B charges (Figure 6). These differences are not modeled adequately using the Mueller-Murphy (1971) source. We propose to use the results from this source scaling study to relate seismic phase generation, particularly for *S*-waves (e.g., *Lg*, Love waves), to damage effects from the explosions.

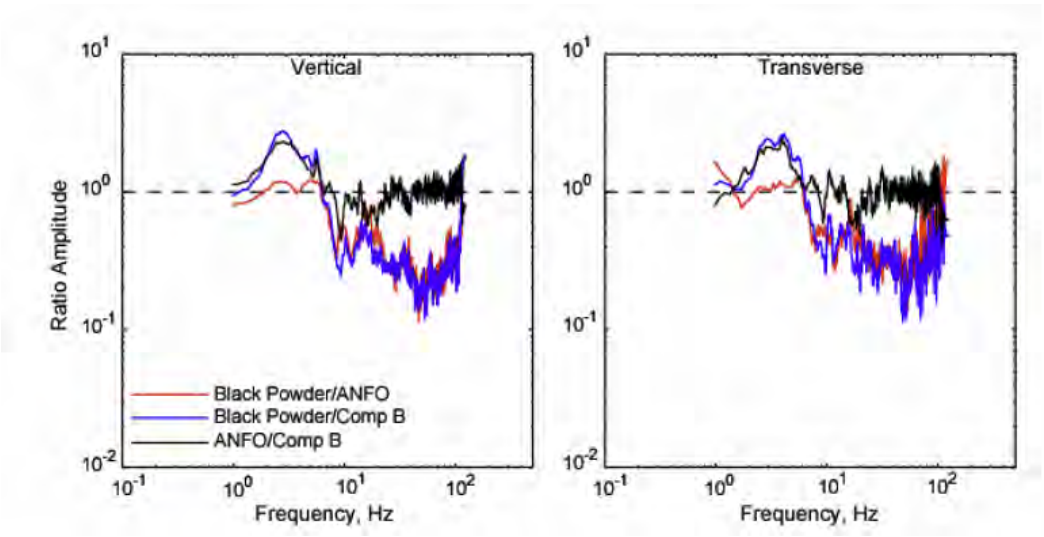

Figure 6. Summary of the mean spectral ratios for vertical (left) and transverse components (right) for different shot combinations (e.g., Black power/ANFO, Black Powder/COMP B, ANFO/COMP B).

Preliminary Observations: Damage

The Rock of Ages granite quarry was selected for the explosion study because the Barre Granite is homogeneous with a low fracture density. Although the granite at the site is massive, it is anisotropic. The anisotropy is a direct result of the rift plane common in most granites. The rift plane is due to the preferred orientation of microcracks. Mineral alignment may also play a small role in the anisotropy. The orientation of the rift at the quarry is well documented and varies between 30° and 60° (Engelder et al., 1977). At the test site, the range of variability in the rift was much smaller, consistently at or near 30°. An examination of the quarry faces in the nearby open pits southeast of the test site show well developed quarry working faces at 30°.

Visible fractures were observed on all quarry faces, and at the site of this study, the outcrop fracture spacing was on the order of 4 to 5 m. The fractures are typically clean and planar with very little brecciation. In a few cases, the fractures appear healed with indications of small scale slip along some of them.

The Barre Granite is a gray fine to medium grained granodiorite. A photomicrograph of the Barre is shown in Figure 7. The composition of the granite is microcline (21%), orthoclase (35%), quartz (27%), biotite (9%), and muscovite (6%) with various accessory minerals (VT Geological Society, web 2008). The composition of the granite is uniform throughout the test site (Richter, 1987).

Visual examinations of the surface after the blasts showed radial fractures from the Black Powder and Heavy ANFO Shots 1, 2, and 4, while COMP B Shots 3 and 5 produced no surface cracks. To further quantify the change in rock properties resulting from the explosions, coreholes were drilled before and after the detonation of the explosives. Two control holes were cored adjacent to the emplacement holes for Shots 2 and 5, (see Table 1). Subsequent to the detonations, three additional holes were cored. One post-shot corehole was adjacent to the 61.5 kg Heavy ANFO shot and two were cored adjacent to the 122 kg shots. Core were collected, documented, and analyzed at NER. There was complete core recovery from the two pre-shot coreholes, and few native fractures were observed. Post-blast core recovery was good overall, but the cores were fragmented and partially incomplete near the blasts. The intervals above the emplacement depth had less fragmentation. There were no large scale induced fractures observed below the shot points. The fracturing is illustrated in Figure 8, which shows the pre-shot core from CH-1 and the post-shot core from the adjacent CH-3 corehole. It is noteworthy that the most intense fragmentation in this section of core occurs below the emplacement interval.

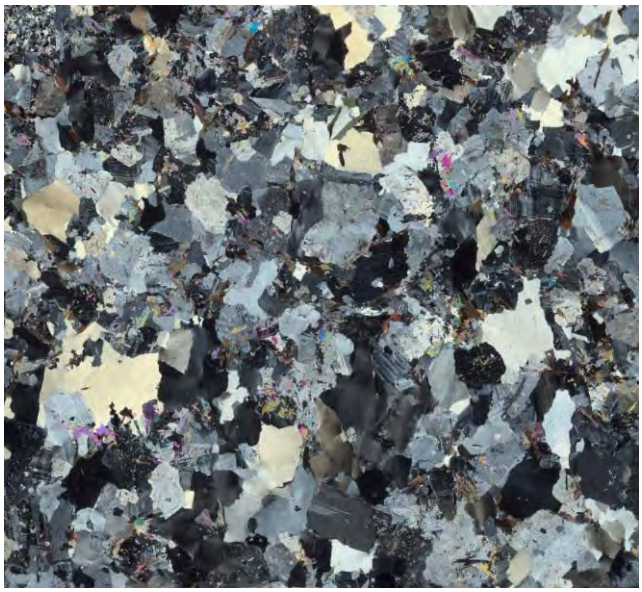

Figure 7. Photomicrograph of Barre Granite thin section taken at a depth of 14.2 m in the CH-1 core. View taken with polarized light. The plane of the section is perpendicular to the rift plane.

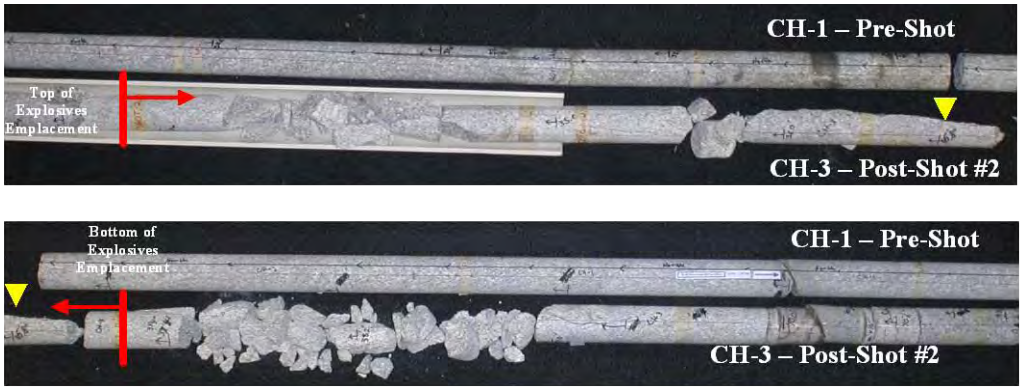

Figure 8. Comparison between cores recovered from the pre-shot and post-shot coreholes adjacent to Shot 2. The cores span the emplacement depth from 10.1 to 11.3 m.

Figure 9 shows an interesting feature observed in the post-shot cores, blast induced disking. It developed over a 1.8 m interval in CH-4. In addition, visual observation of the post-shot cores showed gross changes in the appearance of the core near the working point. The native rock is bluish gray, while the rock recovered near the blasts is lighter colored. The change in appearance is likely due to shattering or crushing of the grains. Further characterization of this observation requires thin section, SEM, and pore structure modeling analysis.

As part of the pre-shot site characterization, a borehole geophysical logging program was undertaken by Hager-Richter Geoscience, Inc. to provide details of the granite *in situ*. Oriented acoustic televiewer logs, optical televiewer logs, and caliper logs were run. The logs verify that there are few fractures. An example of a fracture identifiable in the logs recorded in CH-1 is shown in Figure 10. As the logs were oriented with respect to magnetic North, they were a valuable aid in orientating of the rift plane (using ultrasonic velocity measurements) with respect to fractures. That orientation coincides with the surface observations and reference publications.

The suite of measurements included velocity to identify the orientation of the rift plane, continuous linear velocity scans where possible, permeability and electrical resistivity measurements as a function of pressure, grain and bulk density, porosity calculations, and thin section image analysis. All measurements were performed on oriented

specimens relative to the rift plane. The most detailed data are available for the pre-shot CH-1 and post-shot CH-3 coreholes.

Figure 9. Core disking at 12.5 m depth in CH-4. This corehole is adjacent to Shot 5, which had an explosives emplacement interval between 11.9 m to 13.7 m.

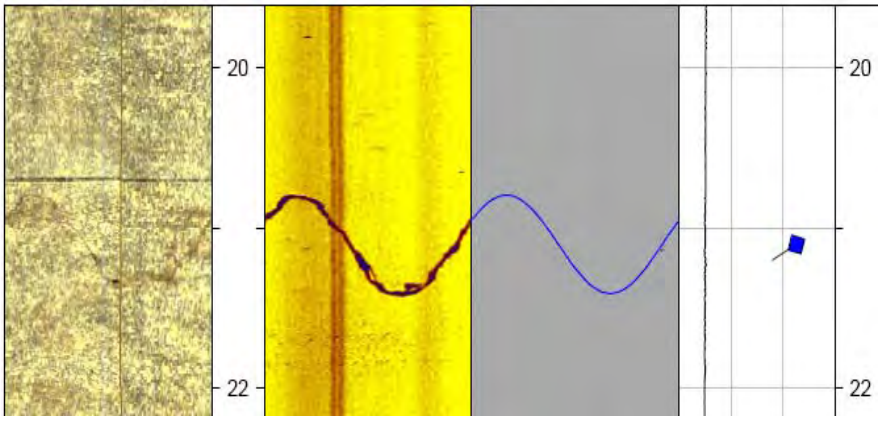

Figure 10. Example of fracture identified by Hager-Richter borehole log run in CH-1. Left to right: Optical Televiewer, Acoustic Televiewer, Fracture outline on borehole wall and tadpole plot showing orientation and dip of fracture. Depths are shown in feet.

Bulk Properties. The Barre Granite is mineralogically homogeneous over a wide area. Little variability in bulk density and grain density were noted, so limited measurements were carried out on the pre-shot specimens. Representative data are presented in Table 2. The data show small variability in the undisturbed cores, but a reduction in density and increase in porosity over the blast interval in CH-3. These changes are most likely due to an increase in the size and density of microcracks.

Table 2. Bulk properties of Barre Granite

	Pre-Shot	Post-Shot
Grain Density, g/cm^3	2.66-2.76	2.66-2.76
Dry Bulk Density, g/cm^3	2.63-2.65	2.60-2.63
Porosity, %	0.7-1.3	1.4-2.5

Velocity Data. Velocity measurements were performed by transmitting ultrasonic compressional and shear waves through diametral chords in the recovered core using a bench top apparatus. The cores were rotated between the velocity transducers, and data were collected, until the acoustically fastest chord was identified. The “Fast” chord is parallel to the rift plane and the chord oriented at 90 degrees to it is the “Slow” direction. Since all measurements on sub cores are oriented with respect to the rift plane, identifying the orientation of the rift in all of the cores facilitates proper sample preparation.

Velocity measurements were also carried out on sections of core recovered from post-shot coreholes CH-3, 4, and 5. The coreholes were adjacent to the 61.5 kg Heavy ANFO, the 122 kg Comp B, and the 122 kg Heavy ANFO shots, respectively. Figure 11 shows comparisons of pre- and post-shot compressional wave velocities as a function of depth in the corehole near the 61.5 kg heavy ANFO shot. Open red diamonds show the pre-shot data, while solid green diamonds show the post-shot velocities. For reference, the centroid depth of the charge was at 10.7 m. The post-blast velocities are significantly lower near the working point; for example, "Fast" velocities of 3,300 m/sec were observed near the working point compared with the pre-shot velocities of 4,300 m/sec, a decrease of 23%. Anomalous behavior was observed below the working point as the post-shot velocities exceed the pre-shot velocities. There is no obvious explanation for this observation, and additional measurements of composition and density need to be carried out to address this effect.

The *P*-wave anisotropy, the difference between the "Fast" and "Slow" *P*-wave velocities, divided by the "Fast" *P*-wave velocities, is presented as a function of depth in Figure 12. The anisotropy remains relatively constant, near 17%, at all depths. There is little indication that the anisotropy was affected by the explosion.

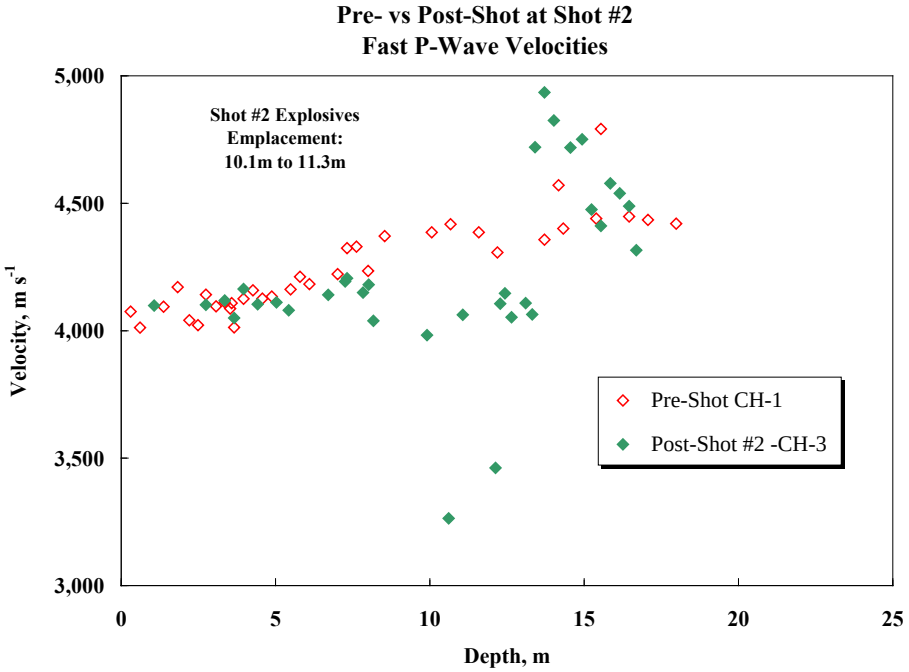

Figure 11. "Fast" compressional wave velocity vs. depth at Shot 2 location. Data from pre- and post-shot coreholes are plotted.

CONCLUSIONS AND RECOMMENDATIONS

The NEDE provided a unique test of explosions with variable VOD (0.5 to 8.1 km/sec) in order to generate variable damage. The slow VOD Black Powder and medium VOD ANFO shots produced radial cracks on the surface; the fast VOD COMP B shots did not. NER has observed intriguing characteristics of the microscopic damage from the cores near the shot points including changes to density and porosity, color changes, and velocity decreases. The seismic data from near-source, local, and regional distances suggest more Rayleigh and SH energy were generated by the Black Powder and ANFO shots than the COMP B. Our preliminary assessment of the experimental data suggests that there could be a direct correlation between damage and *S*-wave generation. For future studies, we will continue to quantify the bulk properties, density, and porosity of the rocks before and after the explosions.

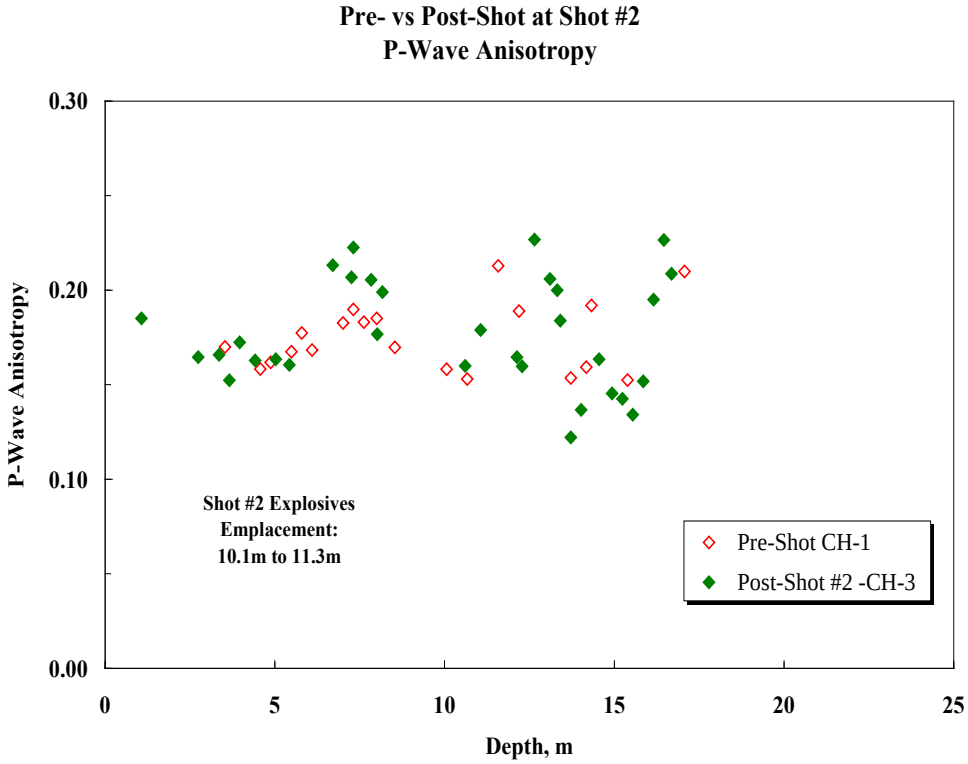

Figure 12. Compressional wave velocity anisotropy vs. depth at Shot 2 location.

ACKNOWLEDGEMENTS

We wish to thank the following people for their help on this project. James Lewkowicz, Delaine Reiter, James Britton, Katherine Murphy, Willie Zamora and IRIS PASSCAL, Hager-Richter Geosciences, Sam Huffstetler, Tim Rath and Maxam-NA, Don Murray and Rock of Ages, Charlie Sammis, Mike's Coring and Boring , Johnson Artesian, Lynne Murray, The Hollow Inn (Barre, VT), and Diane Baker.

REFERENCES

Engelder, T., M. Sbar, and R. Kranz (1977). A mechanism for strain relaxation of Barre Granite: opening of microfractures, *Pure Appl. Geophys*. 115: 27–40.

Mueller, R. A. and J. R. Murphy (1971). Seismic characteristics of underground nulear detonations: Part I, Seismic scaling law of underground detonations, *Bull Seism. Soc. Am*. 61: 1675.

Richter, D. A. (1987). Barre granite quarries, Barre, Vermont, in *Geological Society of America Field Guide – Northeastern Section*, 239–242.

SMALL EVENT YIELD AND SOURCE CHARACTERIZATION USING LOCAL *P* AND *S*-WAVE CODA SOURCE SPECTRA

Kevin M. Mayeda

Weston Geophysical Corporation

Sponsored by the Air Force Research Laboratory

Award No. FA8718-07-C-0010

ABSTRACT

The monitoring mission requires accurate yield estimation for nuclear explosions. Historically, the focus has been on larger yield events (m_b > ~4.5) using teleseismic body wave magnitudes and applying test-site-specific corrections for yield estimates. The regional coda methodology provides unprecedented stability and avoids test site bias because it is based upon absolute source spectra. Increasingly however, there is interest in monitoring smaller events both for yield and source characterization. Unfortunately, these events may only be recorded with adequate signal-to-noise ratio at local distances from one statio. The project goals were to extend the well-established regional coda methodology to local distances using *S* and *P*-wave codas in regions of little to no calibration data and/or regions of high attenuation and lateral complexity. Previous studies show that local coda has a unique property of homogenizing its energy over a volume of the Earth's crust such that path corrections for distances less than ~200 km are not necessary or minimal at worst. The recent 2008 M_w 5.8 Wells, Nevada earthquake was well recorded by the U.S. Array and we show that the local-to-near-regional coda is virtually insensitive to the source radiation pattern and directivity effecxts. Furthermore, we demonstrate the coda wavefield becomes homogenized a few tens of seconds past the expanding direct-wave front. This past year, we have also calibrated a number of paths in Japan and compare those to our previous years' work. We have compared *S*-wave coda path attenuation curves, envelopes shapes, and peak velocity from a variety of regions to look for similarities and differences that could be correlated to the degree of tectonic activity.

This special feature may make it easier to define an *a priori* set of coda calibration parameters that can be transported to new, but geophysically similar regions. For example, it appears that tectonically similar regions have similar coda path, envelope shape, and peak envelope velocity which will allow us to derive average 'local background' models then apply them to other regions for testing and evaluation, including cases to mimic an un-calibrated, single-station deployment.

RESEARCH ACCOMPLISHED

For this year, we have studied the near-regional Lg-coda from the M_w 6.0 Wells, Nevada earthquake of February 21, 2008, as well as a local M_w 4.2 event from the San Francisco Bay area that exhibited a clear case of source directivtiy. The Wells event sequence was unique because the U.S. Array broadband seismic deployment had recorded this event along with its aftershocks, thus providing excellent station coverage and redundancy. Figure 1 below shows that the local to near-regional coda is very stable in comparison to the direct Lg. We have formed amplitude ratios, in this case 3.5 Hz, between the mainshock and a selected aftershock. The coda velocity and envelope shape functions were found to be virtually identical from station to station, in spite of significant geologic variation for paths traveling east versus those to the north and north-west. Though this event did not exhibit strong directivity, we still see a radiation pattern in the direct Lg ratios, or perhaps random variation between the two sources. However for the coda, we see significantly less variation, confirming that the coda is not sensitive to the source mechanism.

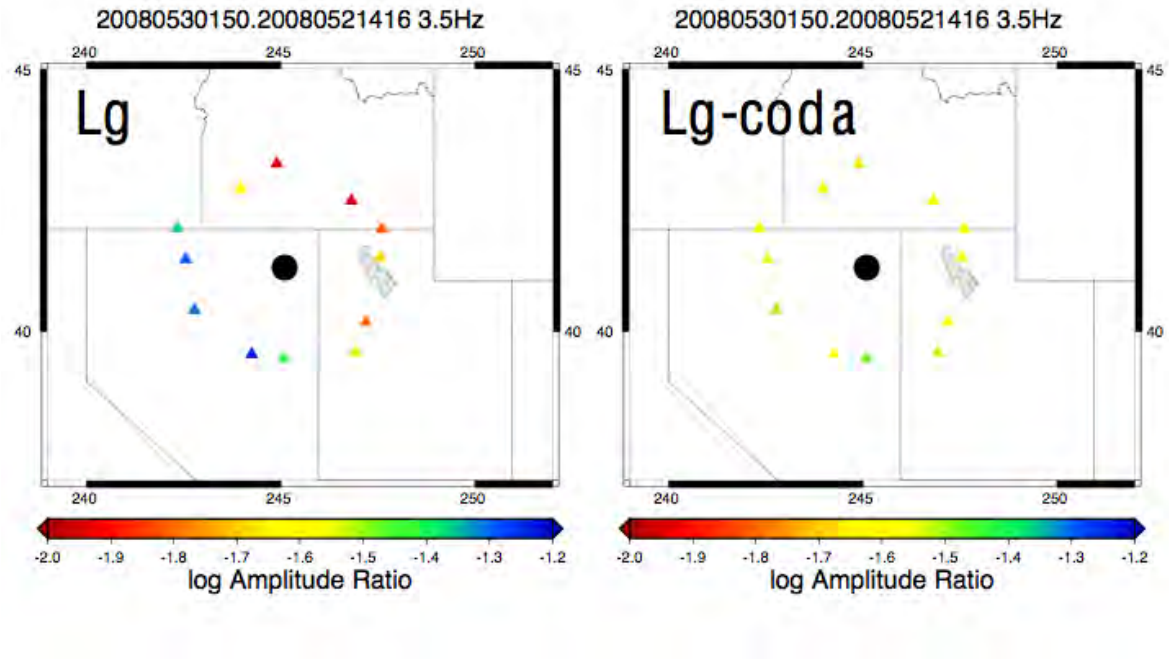

Figure 1. Left figure above shows source ratios for Lg at 3.5 Hz for 12 stations surrounding the Wells mainshock region, roughly 200 km in epicentral distance. We observe large variations even though path and site response are removed by forming the source amplitude ratio. In sharp contrast, the right figure shows the coda-derived source ratios for the same event pair and frequency. As found in other studies, the coda is significantly less variable.

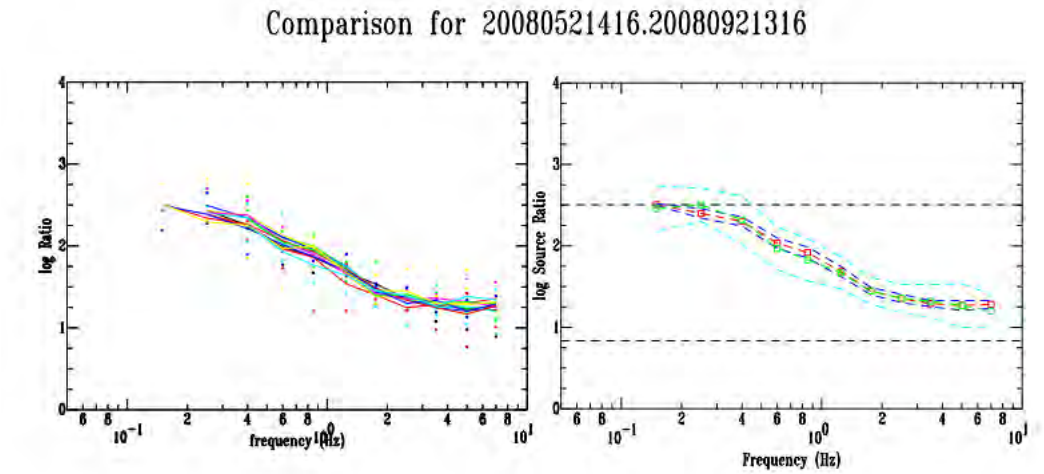

Figure 2. Left figure above shows spectral ratios taken between the Wells mainshock and a co-located aftershock. Solid lines represent coda ratios at the 12 stations and colored dots are the direct Lg source ratios. All stations are roughly 200 km in distance. The figure on the right shows the average and standard deviation for both coda and Lg. For the coda, red is the man and blue is the +/- 1 standard deviation and for Lg, green is the mean and light blue is the +/- 1 standard deviation.

For our second example, we studied an M_w 4.2 event that occurred along the Hayward fault in the San Francisco Bay area. This event was very interesting because there were seismic stations equi-distance from the mainshock along the strike of the Hayward fault. The mainshock exhibited over a factor of 10 larger amplitude in the north-westerly direction (along strike) relative to the south-east direction. The figure below shows that station CVS to the northwest has much larger direct wave amplitudes than station MHC to the southeast, however the coda envelopes are exactly the same after a few tens of seconds. In addition, an aftershock for the same stations and frequency bands does not show any directivity.

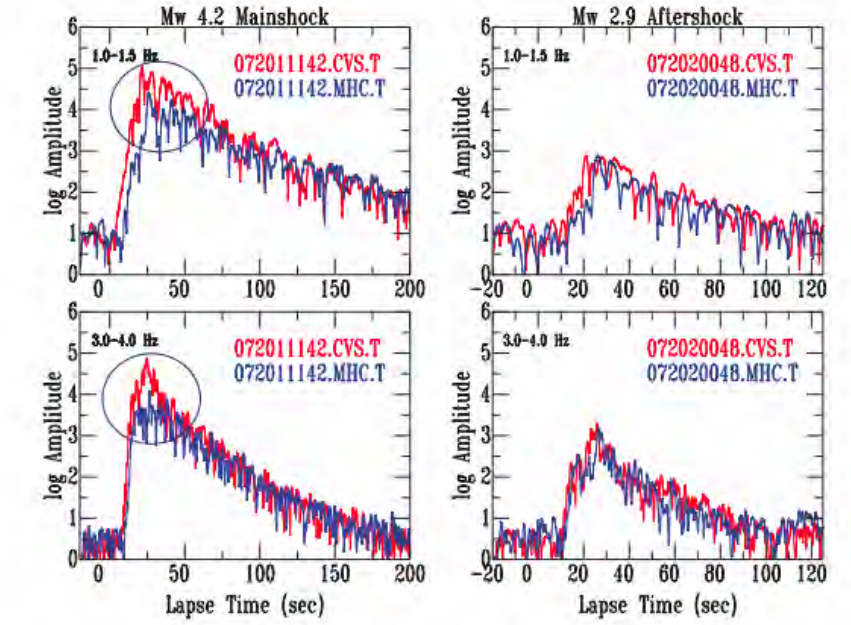

Figure 3. We show a clear case of source directivity (left column) that results in roughly a factor of 10 larger amplitude for the direct waves at station CVS, located to the north of the event and along strike relative to station MHC located to the south. However, the coda levels at both stations are identical. An aftershock shows no evidence of directivity (right column).

We have continued calibrating local and near-regional coda envelopes for a variety of different regions (Figure 4). We have used the same procedure outlined in prior applications of the coda methodology from Mayeda et al. (2003).

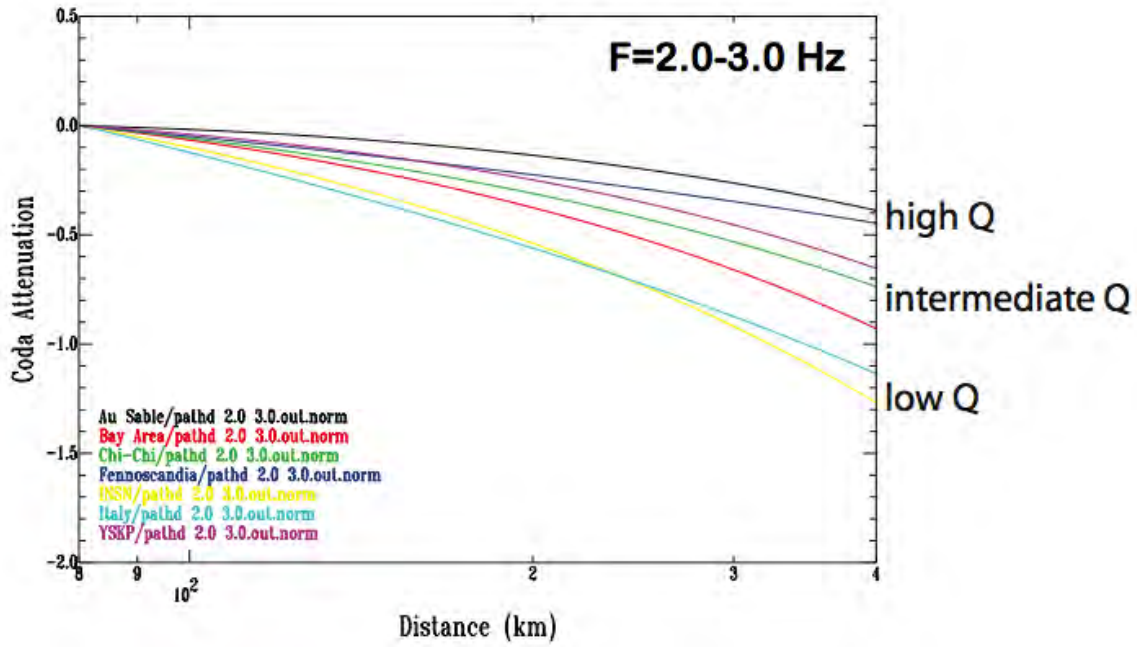

Figure 4. Coda path attenuation for the 2.0-3.0Hz band for seven different regions. In general, we find that tectonically stable regions (e.g., Korea and New York) exhibit the highest Q whereas active regions have much steeper decay (e.g., Iran and Italy).

In general, we can make some preliminary statements on similarities and differences between all the regions studied so far. First, we find that central Italy exhibits the strongest attenuation, followed by Taiwan and western Iran for distances ranging between ~20 and 300 km. On the other hand, Upstate New York and the Korean Peninsula appear to have the lowest attenuation, which is reassuring since both regions are the most tectonically stable. The San Francisco Bay Area is somewhere between the two. We are now looking into datasets in Japan and those results will be forthcoming.

CONCLUSIONS AND RECOMMENDATIONS

In addition to our research of gathering coda envelope shape, path attenuation, and peak envelope velocity information from a variety of tectonic regions (see previous reports), we have also begun to document the coda's property of insensitivity to both the source radiation pattern and directivity. The examples shown in Figures 1, 2, and 3 are strong evidence that the coda's averaging properties also applies to the source heterogeneity, not just path heterogeneity. We still need to look at coda shape parameters that should also be very region dependent, as evidenced by many local coda Q studies in the literature. At this point, we are on track with our proposed statement of work and are forging ahead. This still leaves our local *P*-coda calibration study that will happen in the mid-part of 2009. In our preliminary research, we have also compared coda attenuation parameters for seven different regions for frequencies ranging between 0.5 and 8.0 Hz and are working on a number of sequences in Japan. We will continue to document other regions from which to compare and draw final conclusions. We still need to look at coda shape parameters that should also be very region dependent, as evidenced by many local coda Q studies in the literature. At this point, we are on track with our proposed statement of work and are forging ahead.

ACKNOWLEDGEMENTS

Many thanks to D. Dreger for invaluable information gleaned from personal communications.

REFERENCES

Mayeda, K., A. Hofstetter, J. L. O'Boyle, and W. R. Walter (2003). Stable and transportable regional magnitudes based on coda-derived moment-rate spectra, *Bull. Seismol. Soc. Am*. 93: 224–239.

AN ANALYSIS OF THE SEISMIC SOURCE CHARACTERISTICS OF EXPLOSIONS IN LOW-COUPLING DRY POROUS MEDIA

John R. Murphy and Brian W. Barker

Science Applications International Corporation

Sponsored by the Air Force Research Laboratory

Contract No. FA8718-09-C-0009
Proposal No. BAA09-38

ABSTRACT

The dependence of seismic source coupling of underground nuclear explosions on the characteristics of the explosion source medium is an important consideration in any assessment of nuclear test monitoring capability. In particular, while experience has indicated that normal depth explosions in almost all hardrock and water saturated emplacement media (i.e., "good-coupling" media) are roughly consistent with a single m_b/yield relation for any fixed tectonic source region, explosions in dry, porous media such as the dry tuffs and alluvium found above the water table at the Nevada Test Site (NTS), are typically observed to have m_b values at a given yield that are lower than those in hardrock by about 0.50 ± 0.25 magnitude units. With the exception of the complex cavity decoupling evasion scenario, which is not always feasible, explosions in such low-coupling media define the lower bound on the detection capability required to successfully monitor small, clandestine underground nuclear tests. However, at the present time, no fully reliable seismic source model is available to support quantitative analyses of broadband data recorded from such explosions. The technical objectives of this program are to develop a "Mueller/Murphy" frequency dependent seismic source model for underground nuclear explosions in dry, porous media and to then apply this model to a quantitative assessment of seismic yield estimation capability for such explosions as functions of explosion yield and depth of burial, as well as detailed physical properties of the source medium such as compressional wave velocity and percent by volume of air-filled porosity. This is being accomplished by conducting quantitative source scaling analyses of broadband regional seismic data recorded from explosions in such media at NTS to define their frequency dependent source coupling characteristics relative to the already well-documented seismic source coupling of corresponding explosions in "good-coupling" media at that same test site. The ultimate objective of the project is to improve U. S. operational nuclear test monitoring capability by providing a reliable seismic source model which can be used to quantitatively address seismic detection, identification and yield estimation capability with respect to small underground nuclear tests which might be conducted in such low-coupling media.

OBJECTIVES

The technical objectives of this research program are to develop an analytic approximation for a frequency dependent seismic source model for underground nuclear explosions in dry, porous media analogous to the Mueller/Murphy model for explosions in hardrock and water-saturated media, and to then apply this model to a quantitative assessment of seismic monitoring capability relative to explosions in such media. This is being accomplished by conducting source scaling analyses of broadband seismic data recorded from explosions in such media at NTS to define their frequency dependent source coupling characteristics relative to the already well-documented seismic source coupling of corresponding explosions in "good-coupling" media at that same test site. The ultimate objective is to improve U.S. operational nuclear test monitoring capability by providing a reliable seismic source model that can be used to quantitatively address seismic detection, identification and yield estimation capability as functions of yield, depth of burial and the physical characteristics of the source medium for small underground nuclear tests which might be conducted in such low-coupling media.

RESEARCH ACCOMPLISHED

This project is just beginning, so the following discussion focuses primarily on background and plans as opposed to accomplishments to date. It has long been recognized that normal depth explosions in almost all hardrock and water-saturated emplacement media (i.e., "good-coupling" media) are roughly consistent with a single mb/yield relation for any fixed tectonic source region. In fact, the only media which are known to give consistently different results for fully tamped explosions are saturated clay or water and dry, porous media, such as the dry tuff and alluvium found above the water table at NTS. These observations are summarized in Figure 1, where it can be seen that the average mb value for explosions of fixed low yield in saturated clay or water is expected to be higher by about 0.50 ± 0.25 magnitude units, while the value for explosions in dry, porous media is expected to be lower by about 0.50 ± 0.25 magnitude units relative to that for explosions of the same yield in good-coupling media. It follows that, with the exception of cavity decoupled explosions, which are not always technically feasible, small explosions in dry, porous media pose the greatest challenge to effective seismic monitoring.

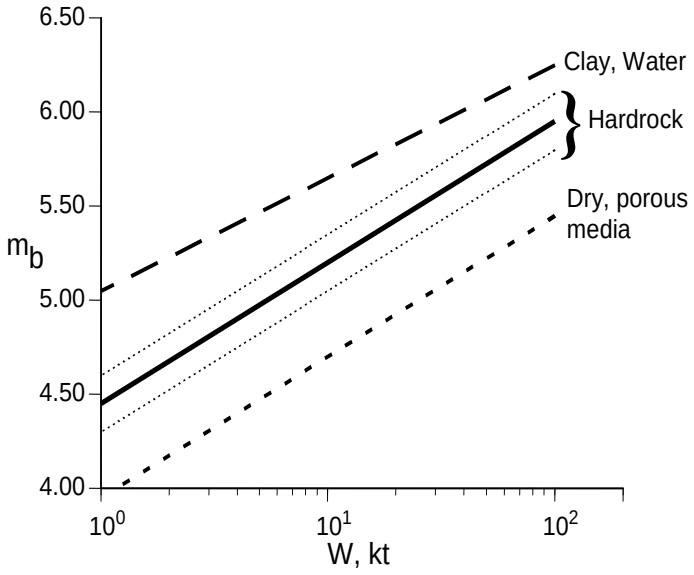

Figure 1. Comparison of mb/yield relations for fully tamped underground nuclear explosions in a fixed tectonic source environment, illustrating the effects of source medium on seismic coupling. It can be seen that the average mb value for explosions of fixed low yield in dry, porous media is expected to be lower by about 0.50 ± 0.25 magnitude units relative to that for explosions of the same yield in hardrock media.

There have been several previous studies of the effects of source medium gas porosity on seismic source coupling of explosions. Vergino and Mensing (1990) examined the effects of gas porosity on mb by filtering the broadband Lawrence Livermore National Laboratory (LLNL) network regional data observed from a large sample of NTS explosions through a synthetic WWSSN response and then estimating mb(Pn) values by applying the standard time-domain estimation procedures to the resulting narrowband data. They postulated a simple linear dependence of mb on the measured gas-filled porosity at the working point of the explosion, and estimated that the average mb value at a fixed yield decreases by about 0.8 magnitude units over the sampled range of air-filled porosity, which extended from about 0 to 30% in this study. Taylor and Dowla (1991) looked at Pn, Pg and Lg spectra from NTS explosions in dry, porous media and also found evidence of reduced low-frequency coupling, as well as possible reduced high-frequency content relative to comparable explosions in saturated media. Their analysis focused on yield estimation through "template matching" - i.e., by comparing observed spectra from new NTS explosions with those observed from previous explosions of known yield. Jones and Taylor (1996) looked at the effects of dry porosity on observed Lg spectra from NTS explosions. Once again, they found reduced seismic coupling and they formulated a source scaling model in terms of observed cavity radius, a variable that is not generally known for explosions of potential monitoring interest. Thus, the results of these different previous studies have been generally consistent in that they all indicated reductions of low frequency seismic coupling efficiency of as much as one full order of magnitude in such media relative to the coupling efficiency of explosions of the same yield conducted in water saturated media below the water table at NTS. However, at the present time, there is no simple P wave seismic source model for explosions in dry, porous media comparable to the Mueller/Murphy (1971) source model for explosions in hardrock or water-saturated sediments. Such a model is needed to support nuclear test monitoring applications related to the frequency dependent seismic detection, identification and yield estimation of small underground nuclear tests in low-coupling media.

As in the previous studies referenced above, the primary source of data for this study are the broadband data recorded from NTS explosions at the four near-regional stations of the LLNL seismic network. We currently have digital data recorded at those stations from some 150 NTS explosions, approximately 100 of which were underground nuclear tests conducted above the water table in dry, porous media. These data are generally of excellent quality, as is illustrated in Figure 2, which shows a record section of data recorded from selected Yucca Flat explosions at LLNL station MNV. In this figure, the top ten traces correspond to recordings of low yield (W < 20 kt) explosions in dry, porous media above the water table (above W.T.) at Yucca, while the bottom three traces represent recordings of larger (~140 kt) explosions conducted in saturated tuffs below the water table (below W.T.) at Yucca. It can be seen that the broadband signal to noise ratios are generally quite high, even for the smaller explosions in low coupling media.

In addition to yields and depths of burial, a number of physical properties of the source emplacement media have been tabulated for these NTS explosions and published in a recent, comprehensive seismic source summary by Springer et al (2002). These include average working point P-wave velocities and densities, as well as measurements of gas-filled porosity and water content. Each of these properties is known to affect the seismic source characteristics of the explosions to some extent, so it is important that their variability be incorporated into any systematic analysis of seismic source coupling.

The distribution of measured gas-filled porosity (percent by volume) values at the working points of the 94 NTS explosions in the station MNV dataset which were detonated in dry, porous media above the water table is shown in Figure 3, where it can be seen that the values range from near zero to almost 30%. Here, the distribution of measured values is observed to be nearly uniform in the range of 0 to 20%, and then decreases somewhat between 20% and 30%. However, even at these higher porosity values, there are still 14 explosions in this database with gas-filled porosity values greater than 20%, so it appears that the available data should be adequate to define the quantitative dependence of frequency dependent seismic source coupling on the percentage of gas-filled porosity of the test medium.

In order to illustrate our proposed analysis procedures, we selected a sample of data recorded at LLNL station MNV from low-yield explosions conducted in highly porous, dry media above the water table at Yucca Flat. Since nuclear tests at NTS were generally conducted at scaled depths of greater than about 125m/kt$^{1/3}$ to ensure containment of the radioactive byproducts of the explosions, we confined our attention to tests conducted at depths of less than 270 m to ensure that the yields were less than 10 kt without needing to reference specific classified yield values. From this

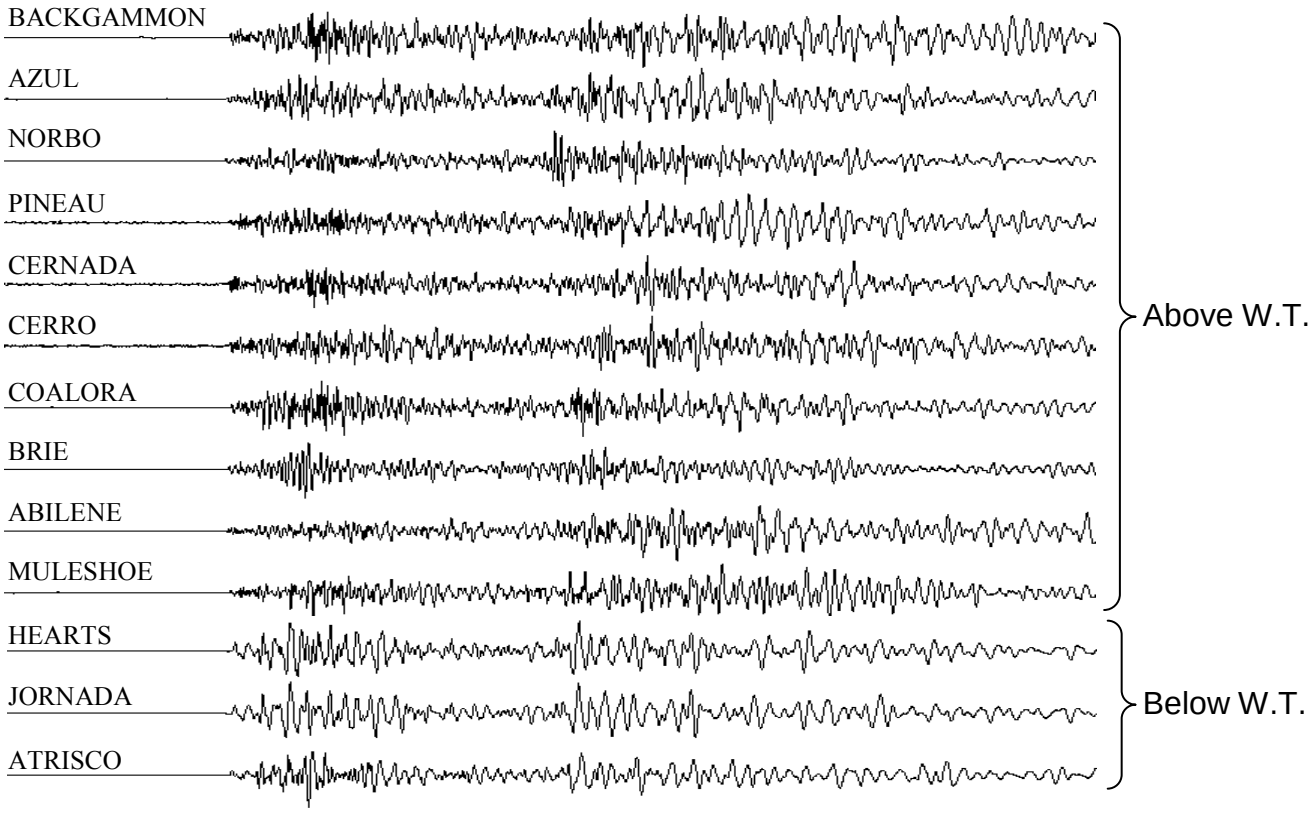

Figure 2. Data recorded from selected Yucca Flat explosions at LLNL station MNV. The top ten traces correspond to recordings of low yield (W < 20 kt) explosions in dry porous media above the water table (above W.T.) at Yucca, while the bottom three traces are recordings of larger explosions conducted in saturated tuff below the water table (below W.T.) at Yucca.

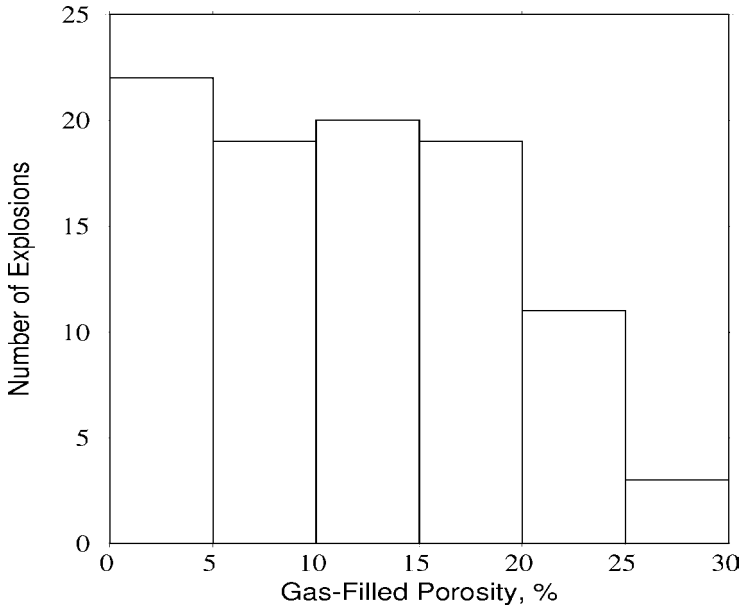

Figure 3. Distribution of reported emplacement medium gas-filled porosity percentages for the selected sample of explosions detonated above the water table at NTS.

subset of the available MNV data, we selected those explosions conducted in dry media having gas-filled porosity values in the highest 20–30% range. This yielded a sample of 9 Yucca Flat explosions for which the data recorded at station MNV were processed and analyzed. As a first step in this analysis, the spectral compositions of the initial P-wave arrivals were estimated for each of these explosions. Smoothed P-wave spectra computed from the first 10 seconds of the signal following P onset are compared for the 9 selected explosions in Figure 4.

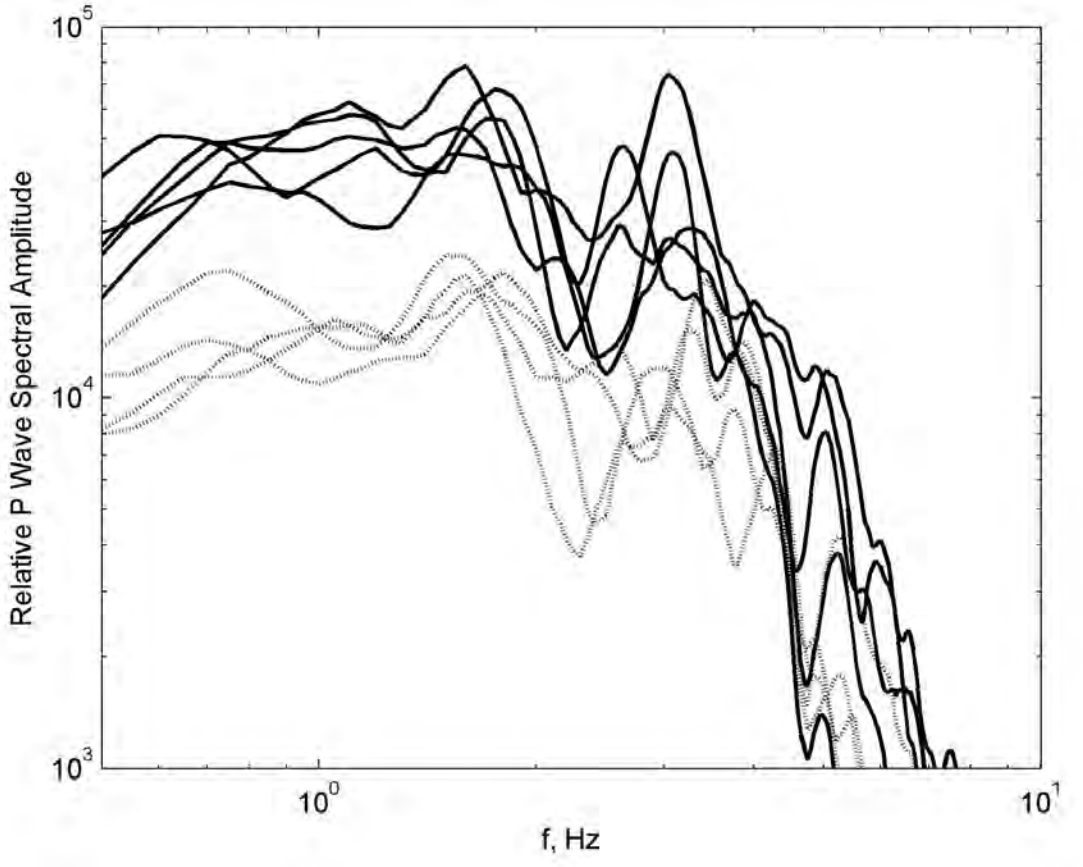

Figure 4. Comparison of P-wave spectra at station MNV for a selected sample of 9 low-yield (W < 10 kt) explosions conducted in high gas-filled porosity (20-30%) media above the water table at Yucca Flat. Two subgroups of explosions having different apparent average yields are differentiated by solid versus dashed lines.

It can be seen that these spectra all have fairly similar shapes and that they appear to separate into two subgroups having average low-frequency amplitude levels which differ by about a factor of three. Consequently, these two subgroups of individual spectra were averaged separately to obtain the two P-wave spectral estimates shown in Figure 5. It can be seen from this figure that the differences in both low frequency amplitude level and corner frequency between these two average spectra are consistent with what would be expected from a significant difference in average yield between these two subgroups of explosions.

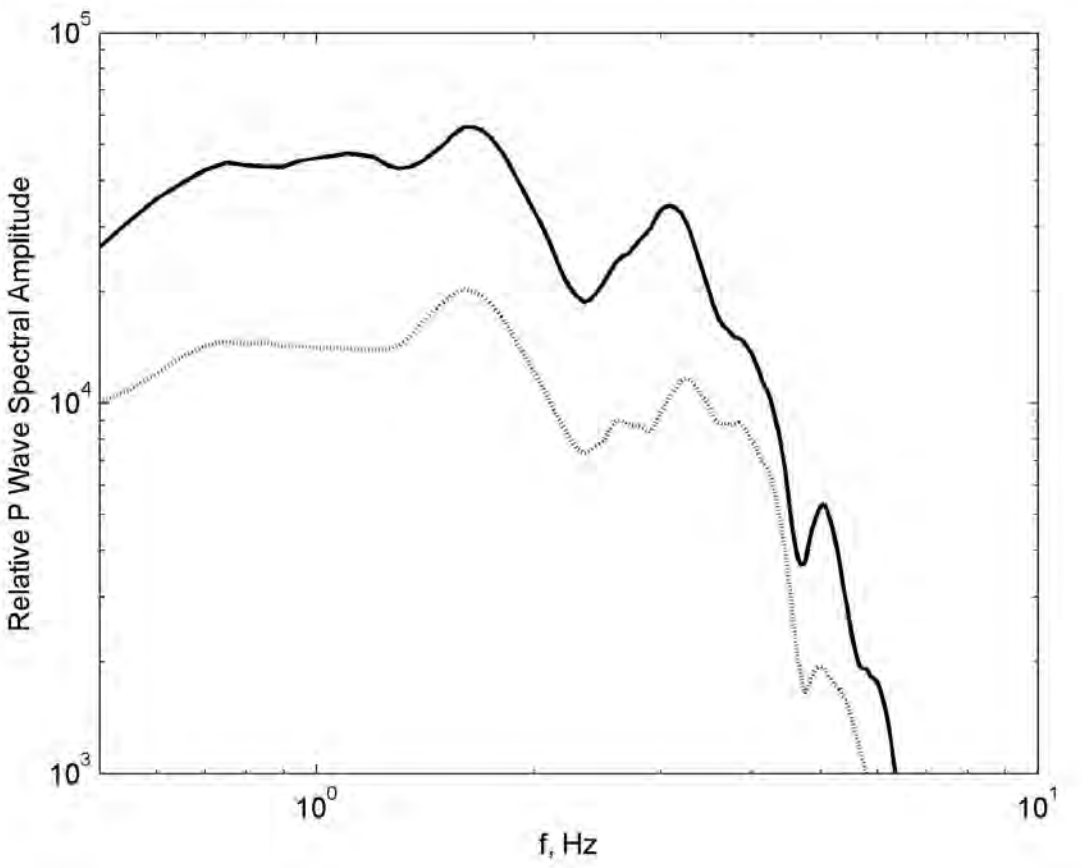

Figure 5. Average station MNV P-wave spectra corresponding to the two subgroups of explosions in dry, porous media shown in the previous figure. These average spectra are taken to be characteristic of P-wave seismic source coupling for two groups of low-yield (W < 10 kt) explosions in such media having average yields which differ by about a factor of 3.

In order to assess the effects of the high gas-filled porosity of the source media in which these explosions were detonated on the frequency dependent source coupling efficiency, it is necessary to make comparisons with corresponding P-wave spectra from explosions of the same yields and depths of burial in good-coupling, saturated media below the water table at Yucca. Unfortunately, there are no low-yield explosions that were conducted in this depth range at Yucca which were detonated in saturated media below the water table, so some scaling is required to make a valid comparison. Three explosions that were conducted in saturated tuff below the water table at Yucca Flat for which yields and depths of burial have been published in the open literature (Springer et al, 2002) are HEARTS, JORNADA and ATRISCO. Each of these had announced yields very close to 140 kt and depths of burial of about 640 m. The P-wave spectra computed from the station MNV recordings of these three explosions were logarithmically averaged to obtain the station MNV P-wave spectral estimate representative of a 140 kt explosion at a depth of 640 m in saturated tuff below the water table shown as a solid line in Figure 6. The Mueller/Murphy source model has been used to scale this average observed spectrum to obtain estimates of the saturated tuff spectra corresponding to the yields and depths of burial of the two average P-wave spectra for explosions in dry, porous media, as shown in Figure 5. We plan to eventually use actual yield values, but for present, unclassified purposes, the observed depths of burial constrain the yields to be less than 10 kt, while the observed Pn signal to noise ratios are characteristic of yields greater than about 1 kt. Therefore, given the differences in the low-frequency amplitude levels for the average spectra of Figure 5, we assigned nominal yields of 2.5 kt and 7.5 kt to the smaller and larger subgroup averages, respectively, in order to illustrate the methodology. The results of scaling the

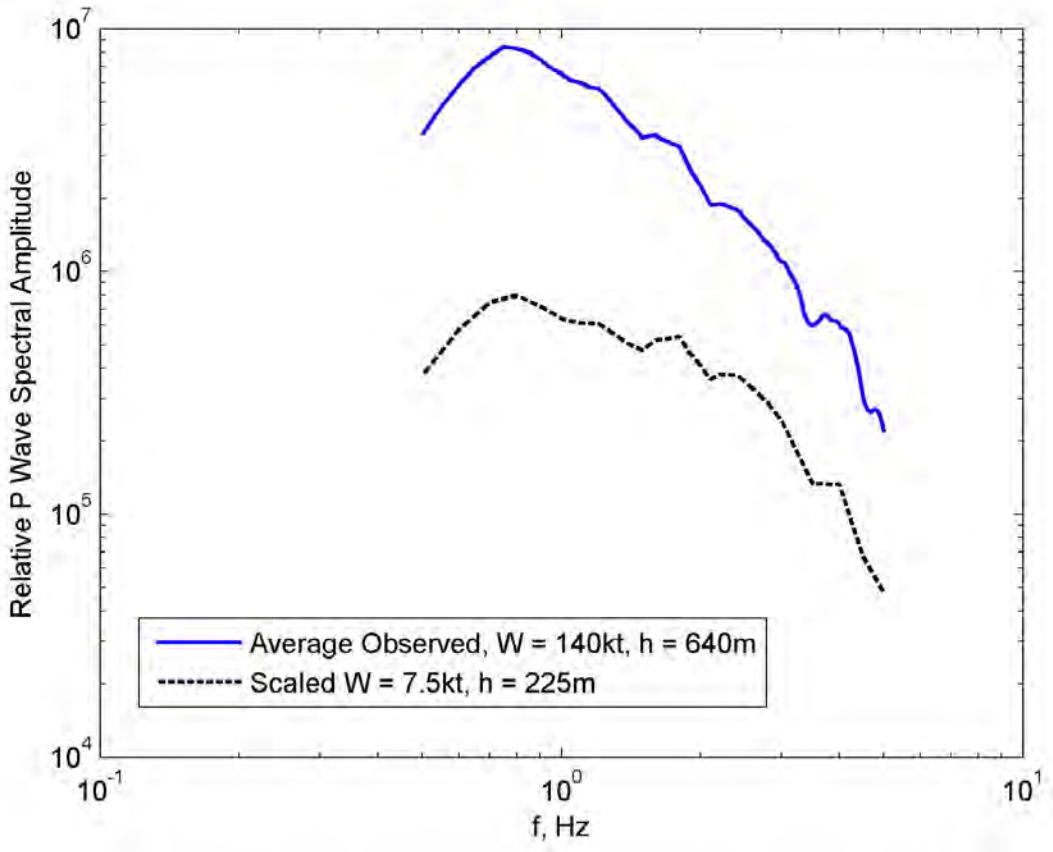

Figure 6. Comparison of the average observed station MNV P wave spectrum corresponding to a 140 kt explosion at a depth of 640 m in saturated tuff at Yucca Flat (solid) with the corresponding P-wave spectrum obtained by scaling to W = 7.5 kt, h = 225 m in that same source medium using the Mueller/Murphy seismic source scaling model (dashed).

average observed spectrum corresponding to W = 140 kt , h = 640 m in saturated tuff to W = 7.5 kt, h = 225 m using the Mueller/Murphy source scaling model are shown as a dashed line in Figure 6, where the frequency dependent nature of the combined yield and depth scaling is clearly evident. This scaled spectrum, together with a corresponding one for a W = 2.5 kt, h = 225 m explosion in the saturated tuff medium were divided by the average spectra for the two subgroups of explosions in dry, porous media to quantify the frequency dependent effects of gas-filled porosity on seismic source scaling efficiency. The resulting spectral ratios are shown in Figure 7, where it can be seen that the two ratios are very consistent and roughly independent of frequency over the range extending from 0.5 to 10 Hz, although there is some very weak suggestion of a possible increase in the spectral ratios with increasing frequency above the respective source corner frequencies which might correlate with an increase in the high-frequency rolloff rate for explosions in dry, porous media as was inferred by Taylor and Dowla (1991). This issue will need to be carefully evaluated in our analysis of the complete data set. In any case, the consistency of the two relative coupling estimates shown in Figure 7 seems to confirm the inferred factor of three difference in the average yields of the two subgroups of selected explosions in dry, porous media, and suggests a reduction in the low-frequency coupling by an average factor of 10–20 due to the effects of gas-filled porosity, at least for these explosions in media with estimated gas-filled porosities in the range of 20–30%.

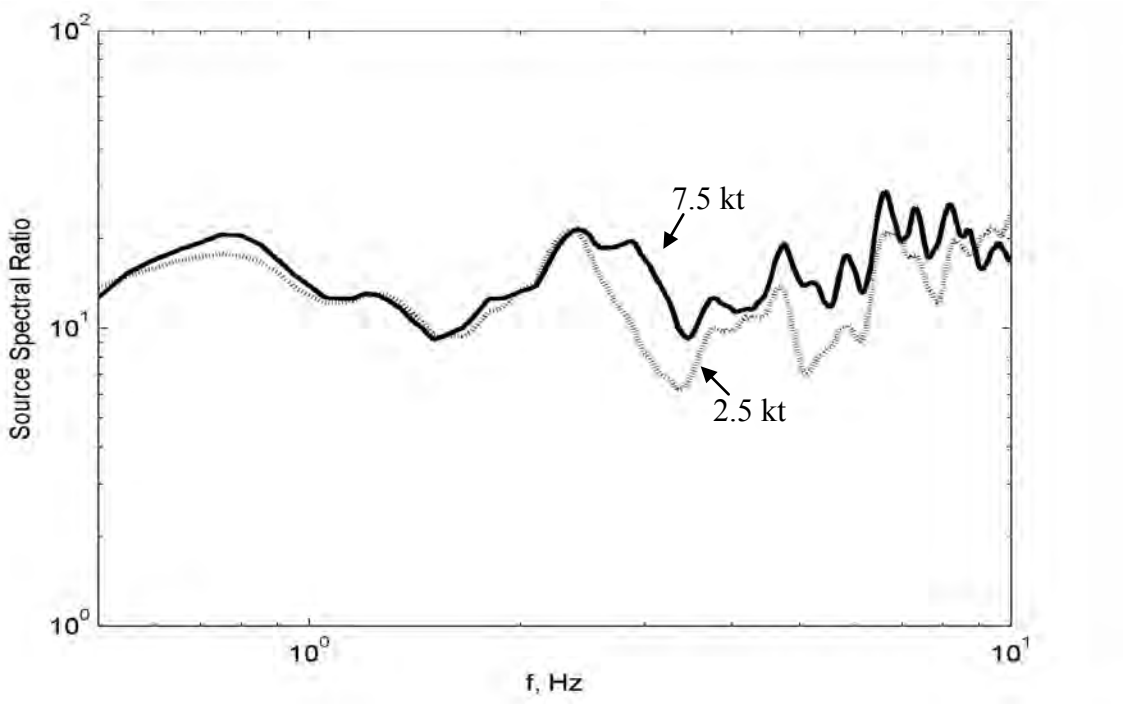

Figure 7. P-wave source spectral ratios for Yucca Flat explosions in saturated tuff relative to explosions of the same yields and depths of burial in dry, porous tuff and alluvium. It can be seen that the two ratios are essentially identical, consistent with the Mueller/Murphy source scaling for the inferred factor of 3 difference in the average yields of the two subgroups of selected explosions in dry, porous media.

The implications of these P-wave spectral ratios with respect to the seismic source function for explosions in high gas-filled porosity media are indicated in Figure 8, which shows a comparison of the Mueller/Murphy seismic source predicted for a 7.5 kt explosion at a depth of 225 m in saturated tuff with the corresponding approximation to the seismic source for that same explosion in dry tuff/alluvium media obtained by dividing the saturated tuff source by a frequency independent factor of 15, consistent with the average spectral ratio results from Figure 7. Also shown on this figure is the Mueller/Murphy source corresponding to the explosion at that depth in saturated tuff that would be expected to produce the same low frequency amplitude level as that of the inferred dry tuff/alluvium seismic source. Note that the yield of this matching saturated tuff explosion (i.e., 0.35 kt) is significantly smaller than the 7.5 kt yield of the corresponding inferred dry tuff/alluvium source and, consequently, its source corner frequency is significantly higher. This has important implications with regard to seismic yield estimation for clandestine underground nuclear tests in unknown source media. That is, for a given observed low frequency amplitude level, the high -requency spectral amplitude levels could be used to determine whether the explosion was conducted in a low- or high-coupling source medium, resulting in a more confident seismic estimate of the yield of the explosion. This diagnostic difference would be even further enhanced if, in fact, the seismic source for explosions in dry, porous media is characterized by an increase in the high-frequency rolloff rate relative to that for explosions in saturated tuff/rhyolite emplacement media.

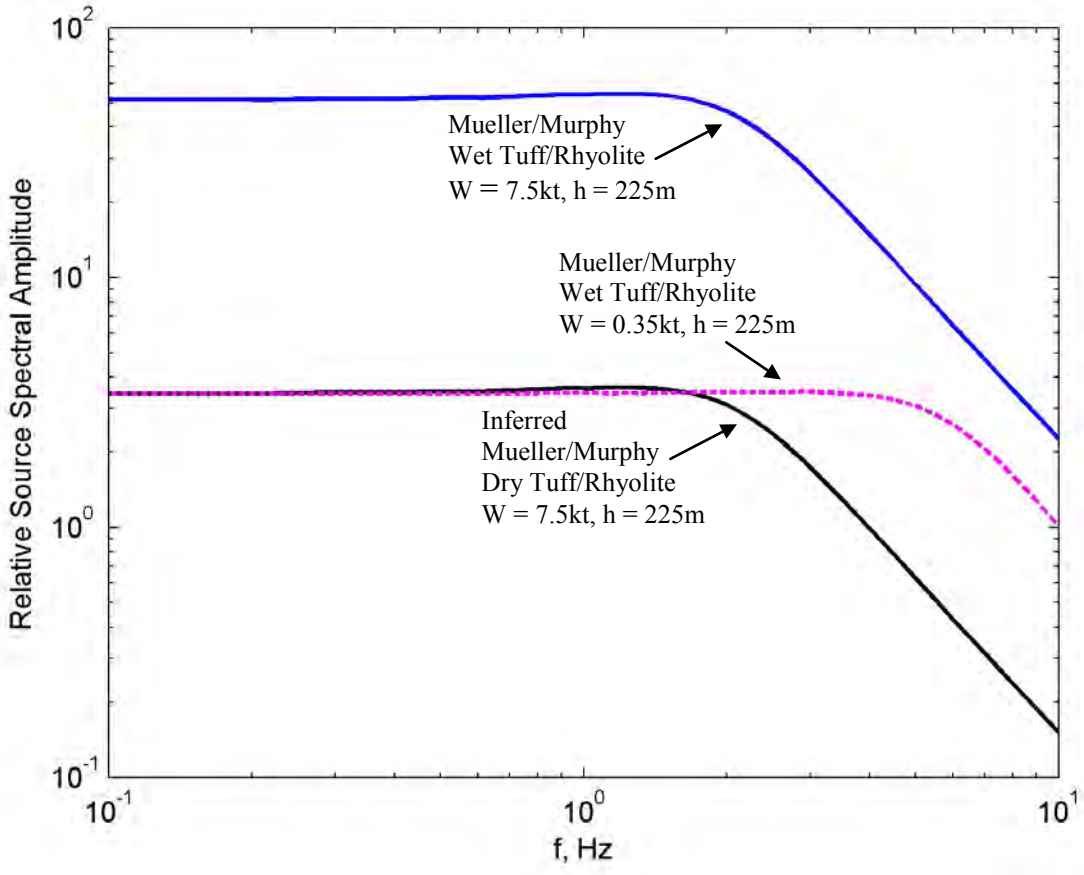

Figure 8. Comparison of the inferred seismic source for a 7.5 kt explosion at a depth of 225 m in dry tuff/alluvium source media with the corresponding Mueller/Murphy seismic sources predicted for 7.5 kt and 0.35 kt explosions at that same depth in a saturated tuff emplacement medium. It can be seen that interpreting the observed spectrum from an explosion in dry tuff as if it were conducted in saturated tuff could lead to a seismic yield estimate which is low by more than a factor of 20 in this case.

CONCLUSIONS AND RECOMMENDATIONS

The dependence of seismic source coupling of underground nuclear explosions on the characteristics of the explosion source medium is an important consideration in any assessment of nuclear test monitoring capability. While experience has indicated that explosions in almost all hardrock and water-saturated emplacement media are roughly consistent with a single mb/yield relation in any fixed tectonic source region, explosions in dry, porous media are observed to have low-frequency seismic source coupling at a given yield that is as much as an order of magnitude lower than that in hardrock. The objectives of this research study are to develop a "Mueller/Murphy" frequency-dependent seismic source model for underground nuclear explosions in such media and to then quantitatively assess the implications of this model with respect to seismic monitoring capability. While this project is just beginning and it is too early for any definitive conclusions, preliminary analysis of selected broadband near-regional data recorded from NTS explosions in dry, porous media have confirmed the previously reported large reduction in low-frequency seismic coupling efficiency relative to that expected from explosions in good coupling media. Moreover, these preliminary results suggest that, while the source corner frequencies for explosions in such media may be diagnostically lower than those expected from explosions of the same yields and depths of burial in good coupling media, the spectral roll-off rates above the corner frequency appear to be roughly comparable in both media. More careful analyses of larger datasets will of course be required to further test the validity of these tentative conclusions.

REFERENCES

Jones, E. M. and S. R. Taylor (1996). Are Lg spectra from NTS explosions self-similar, *Bull. Seism. Soc. Am*. 86: 445–456.

Mueller, R. A. and J. R. Murphy (1971). Seismic Characteristics of Underground Nuclear Detonations, I: Seismic Spectrum Scaling, *Bull. Seism. Soc. Am*. 61: 1675–1692.

Springer, D. L., G. A. Pawloski, J. L. Ricca, R. F. Rohrer, and D. K. Smith (2002). Seismic source summary for all U.S. below-surface nuclear explosions, *Bull. Seism. Soc. Am*. 92: 1806–1840.

Taylor, S. R. and F. U. Dowla (1991), "Spectral Yield Estimation of NTS Explosions," *Bull. Seism. Soc. Am*. 81: 1292–1308.

Vergino, E. S. and R. W. Mensing (1990)."Yield estimation using regional m_b(Pn), *Bull. Seism. Soc. Am*. 80: 656–674.

IMPROVING EARTHQUAKE-EXPLOSION DISCRIMINATION USING ATTENUATION MODELS OF THE CRUST AND UPPER MANTLE

Michael E. Pasyanos, William R. Walter, Eric M. Matzel, Arthur J. Rodgers, Sean R. Ford, Rengin Gök, and Jerry J. Sweeney

Lawrence Livermore National Laboratory

Sponsored by the National Nuclear Security Administration

Award No. DE-AC52-07NA27344/LL09-IRP-NDD02

ABSTRACT

In the past year, we have made significant progress on developing and calibrating methodologies to improve earthquake-explosion discrimination using high-frequency regional *P/S* amplitude ratios. Closely spaced earthquakes and explosions are generally discriminated easily using this method, as demonstrated by recordings of explosions from test sites around the world. In relatively simple geophysical regions such as the continental parts of the Yellow Sea and Korean Peninsula (YSKP), we have successfully used a 1-D magnitude and distance amplitude correction methodology (1-D MDAC) to extend the regional P/S technique over large areas. However, in tectonically complex regions such as the Middle East or the mixed oceanic-continental paths for the YSKP, the lateral variations in amplitudes are not well predicted by 1-D corrections, and 1-D MDAC *P/S* discrimination over broad areas can perform poorly.

We have developed a new technique to map 2-D attenuation structure in the crust and upper mantle. We retain the MDAC source model and geometrical spreading formulation and use the amplitudes of the four primary regional phases (*Pn*, *Pg*, *Sn*, *Lg*) to develop a simultaneous multi-phase approach to determine the *P*-wave and *S*-wave attenuation of the lithosphere. The methodology allows solving for attenuation structure in different depth layers. Here we show results for the *P*- and *S*-wave attenuation in crust and upper mantle layers.

When applied to the Middle East, we find variations in the attenuation quality factor Q that are consistent with the complex tectonics of the region. For example, provinces along the tectonically active Tethys collision zone (e.g., Turkish Plateau, Zagros) have high attenuation in both the crust and upper mantle, while the stable outlying regions like the Indian Shield generally have low attenuation. In the Arabian Shield, however, we find that the low attenuation in this Precambrian crust is underlain by a high-attenuation upper mantle similar to the nearby Red Sea Rift. Applying this 2-D MDAC methodology with the new attenuation models can significantly improve earthquake-explosion discrimination using regional *P/S* amplitude ratios. We demonstrate applications of this technique, including a study at station NIL (Nilore, Pakistan), using broad-area earthquakes and the 1998 Indian nuclear explosion, using a number of regional amplitude ratio discriminants. We are currently applying the technique in the YSKP region as well.

OBJECTIVE

Our objective is to develop and calibrate methodologies to improve earthquake-explosion discrimination using high-frequency regional *P/S* amplitude ratios. It has been demonstrated that closely spaced earthquakes and explosions are generally discriminated easily using this method. For example, the green and red waveforms shown in Figure 1 are a closely located earthquake and explosion pair recorded at the same station and using the same filtering. The explosion (shown in red) has a much larger ratio of *P*-wave energy to *S*-wave energy than the nearby earthquake (shown in green). Lateral variations in attenuation, however, can produce large changes in the amplitudes of regional phases, which can degrade the performance of these discriminants over the broad region. In Figure 1, for instance, the cyan waveform shows an explosion-like earthquake (high *P*-to-*S* ratio) located far from the explosion shown. In the past, we have shown that the MDAC methodology (Walter and Taylor, 2001) can account for simple 1-D attenuation and geometrical spreading corrections, as well as site effects. In complex regions like the Middle East, however, 1-D path corrections are a poor approximation, and we need to develop 2-D path corrections that can account for the structure. Our approach is to calibrate the attenuation structure and use this model to better separate the populations of earthquakes and explosions.

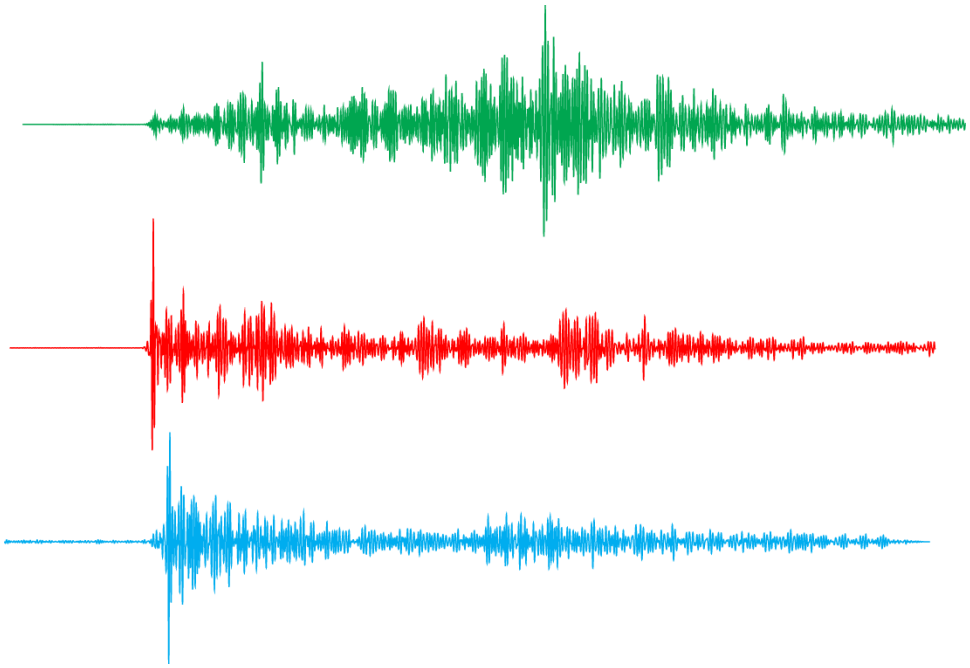

Figure 1. Waveforms of two earthquakes (shown in green and cyan) and the 1998 Indian nuclear explosion (shown in red), recorded at station NIL and filtered between 1 and 2 Hz. (Figure from Pasyanos and Walter, 2009).

RESEARCH ACCOMPLISHED

We have made significant progress on calibrations since the last seismic review (Walter et al., 2008). First, we have developed a four-phase amplitude tomography that allows us to determine a consistent set of attenuation, site, and source corrections for the primary regional phases of *Pn*, *Pg*, *Sn*, and *Lg*. Second, we have demonstrated that we can use the attenuation model to correct phase amplitudes and improve high-frequency *P/S* discriminants. While we primarily discuss results from the Middle East region, we are currently applying the technique in the YSKP region as well.

Amplitude Tomography

Recent work has focused on the attenuation of regional phases in the Middle East and vicinity and has been the subject of several recent publications (Pasyanos et al., 2009a, 2009b). As with most amplitude tomography, we assume that the observed amplitudes are a product of four terms: the source term S, the geometrical-spreading term G, the attenuation term B, and the site term P,

$$A_{ij} = S_i \, G_{ij} \, B_{ij} \, P_j \qquad (1)$$

where i is an event index and j is a station index.

Our methodology, employed in Pasyanos et al. (2009a) for *Lg*, uses an MDAC source model (Walter and Taylor, 2001), which more explicitly defines the source expression in terms of an earthquake source model formulated in terms of the seismic moment. One of the advantages of this approach is so that one can easily estimate the predicted *Lg* amplitudes for an event of any given location and size. We assume a geometrical spreading and provide parameters that relate the initial source term to the moment. Using amplitudes for about 6000 Lg paths, we then initialize the attenuation, site and source terms and solve for all three sets of parameters in several different frequency bands from 0.5 to 10 Hz.

In a subsequent paper (Pasyanos et al., 2009b), we applied the technique to simultaneously invert 1–2 Hz amplitudes of *Pn*, *Pg*, *Sn*, and *Lg* to produce *P*-wave and *S*-wave attenuation models of the crust and upper mantle. The attenuation is modeled as *P*-wave and *S*-wave attenuation surfaces for the crust and as a similar set for the upper mantle. We can use all of the phase amplitudes together by using the appropriate (source, geometrical-spreading, site, and attenuation) terms for each phase. For example, the source terms of the *P*-waves and *S*-waves are different, and path attenuation is calculated by ray paths appropriate for the particular phase. Inverting all of the phases simultaneously (in this case, amplitudes for about 12,000 paths; see Figure 2), allows us to determine consistent attenuation, site, and source terms for all phases, and eliminates non-physical inconsistencies among them.

The terms shown in Equation (1) are specified as follows. The source term S is based on the MDAC source model and for *P*-waves and *S*-waves is specified as

$$S^P = F^P \, M_o / [1+(\tilde{\omega}/\omega^P_c)^2] \qquad (2)$$
$$S^S = F^S \, M_o / [1+(\tilde{\omega}/\omega^S_c)^2] \qquad (3)$$

where M_o is the seismic moment, the F M_o term is the long-period radiated energy, ω is angular frequency, ω_c is the corner frequency and P and S superscripts indicate *P*-waves and *S*-waves. We use the geometrical spreading form of Street et al. (1975):

$$G(R) = \begin{cases} 1/R & \text{if } R < R_o \\ (1/R_o)(R_o/R)^n & \text{if } R >= R_o \end{cases} \qquad (4)$$

where R is distance, R_o is the critical distance, and n is the spreading variable. The values of R_o and n depend on the phase. The attenuation term B is specified as

$$B_{ij} = \exp\left[-\frac{\omega}{2} \sum_{k=1}^{nlayers} \frac{r_k}{Q_k v_k}\right] \qquad (5)$$

where r is distance, Q is the attenuation quality factor, and v is the velocity. The layers sampled depend on the model and phase. We simplify the problem by specifying the velocity structure as a layer over a half-space. This parameterization has the crustal phases *Pg* and *Lg* sampling the crustal layer only, while the mantle phases *Pn* and *Sn* sample both the upper mantle layer and the crustal layer under the source and station. It is possible to expand the number of layers further in the future as regional phase coverage improves. The last term, the site term *P,* is simply a multiplicative factor applied for the station and phase.

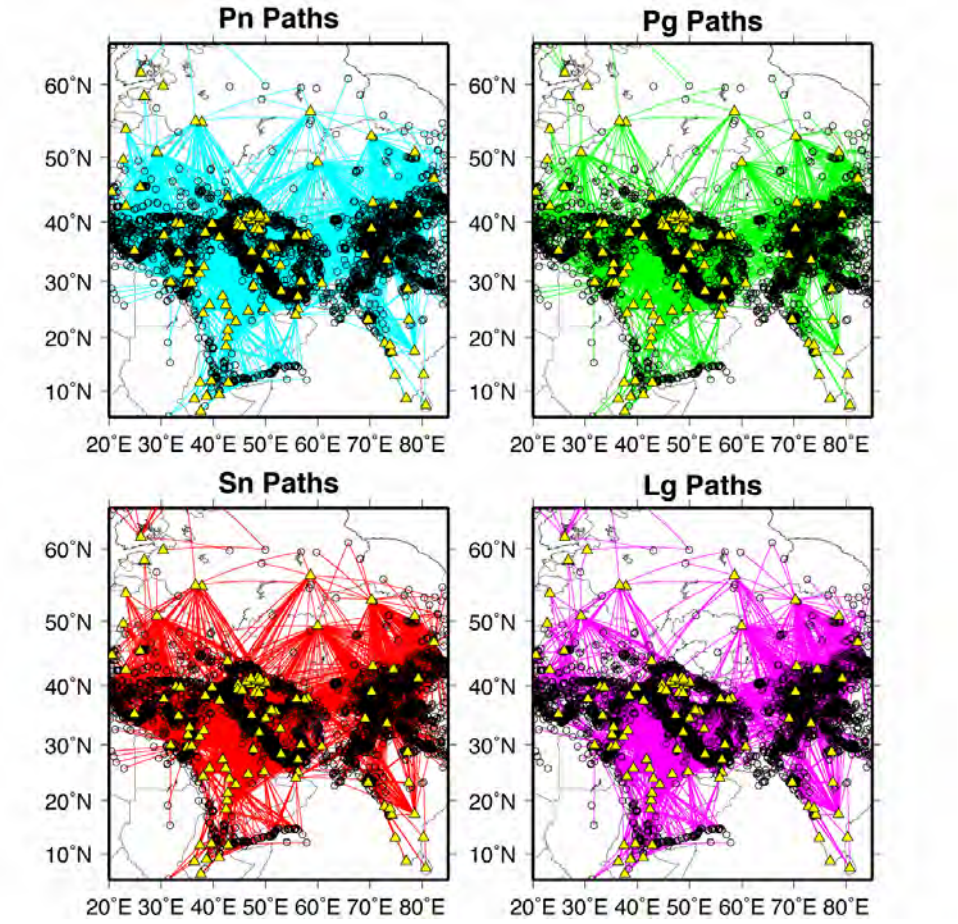

Figure 2. Path map of *Pn*, *Pg*, *Sn*, and *Lg* attenuation measurements in our study area. Stations are shown as yellow triangles, events as black circles, and paths as cyan lines (*Pn*), green lines (*Pg*), red lines (*Sn*), and magenta lines (*Lg*). Figure from Pasyanos et al. (2009b).

We use tomography to determine the *P*-wave and *S*-wave attenuation of the crust and upper mantle, along with corresponding site and event terms. We find variations in the attenuation quality factor Q across the Middle East that are consistent with the complex tectonics of the region. For example, in Figure 3 we find that provinces along the tectonically active Tethys collision zone (e.g., Turkish Plateau, Zagros) have high attenuation in both the crust and upper mantle, while the stable outlying regions like the Indian Shield generally have low attenuation. While variations in crust and upper mantle attenuation are often similar, they are decoupled. In the Arabian Shield, for instance, we find that the low attenuation in this Precambrian crust is underlain by a high-attenuation upper mantle similar to the nearby Red Sea Rift. This is appropriate, given the tectonics of the region, indicated by the volcanics and velocity studies. These studies find slow, hot material in the crust along the rift that spreads out under the Arabian Shield in the mantle (e.g., Camp and Roobol, 1992).

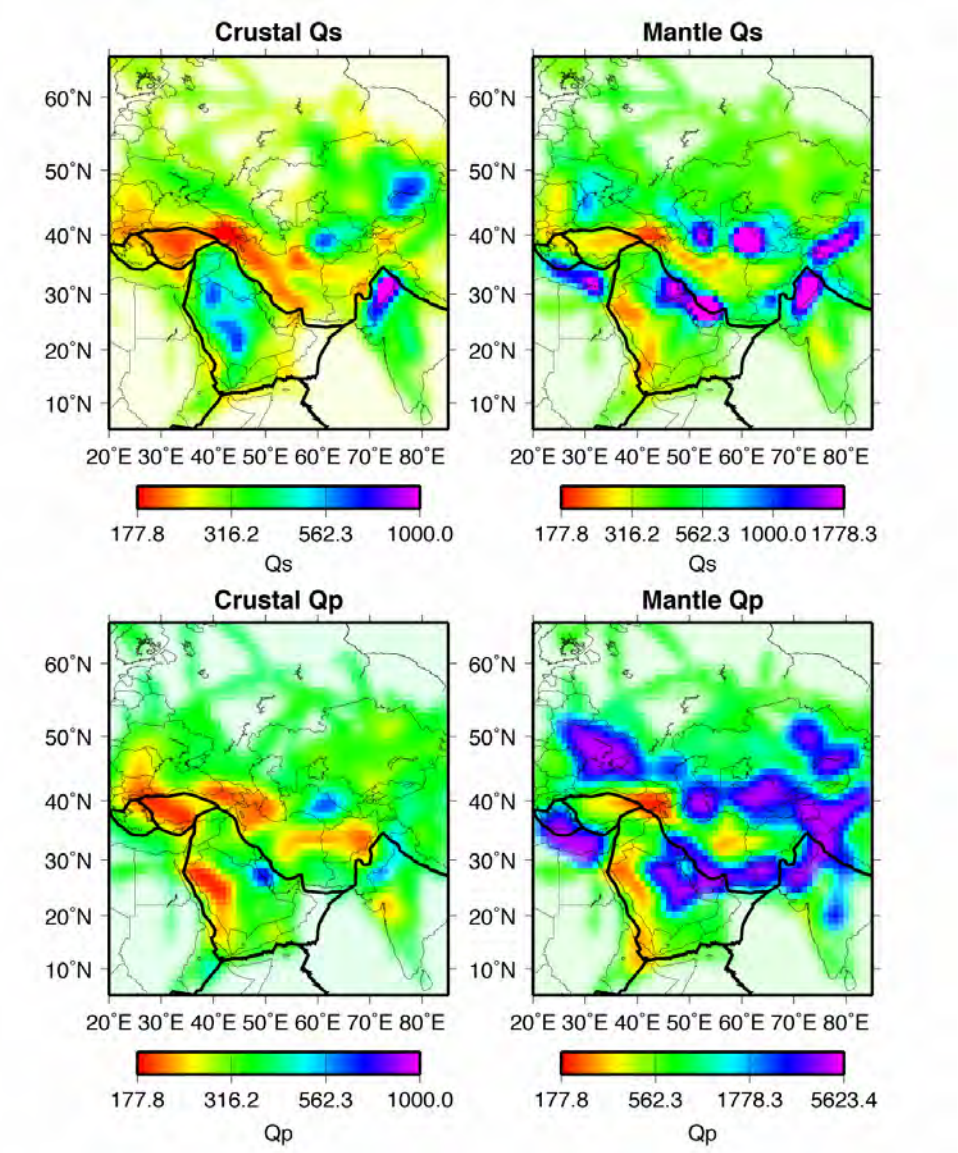

Figure 3. Maps of attenuation quality factor Q for shear-wave attenuation in the crust (crustal Qs), shear-wave attenuation in the mantle (mantle Qs), compressional-wave attenuation in the crust (crustal Qp), and compressional-wave attenuation in the mantle (mantle Qp). Dark lines indicate plate boundaries from Bird (2003). Figure from Pasyanos et al. (2009b).

Discrimination

Applying corrections with the new attenuation models can significantly improve earthquake-explosion discrimination using regional *P/S* amplitude ratios. We demonstrate applications of this technique, including a study at station NIL (Nilore, Pakistan), using broad-area earthquakes and the 1998 Indian nuclear explosion, using a number of regional amplitude ratio discriminants, as presented in Pasyanos and Walter (2009).

P/S discriminants are expressed as the ratio between the *P*-wave amplitude (A^P) and the *S*-wave amplitude (A^S) and, because of the large variations, are usually plotted on a log scale. We examine the ratio of *Pn* amplitudes to *Lg* amplitudes in the 1–2 Hz passband recorded at station NIL in Nilore, Pakistan. Figure 4 shows the ratio of the raw amplitudes as a function of distance and in map view. Besides the clear trend with distance (a result of the differing

geometrical spreading and attenuation of the two phases), there is very large scatter in the earthquake population, which is due to a combination of factors, among them variations in path attenuation. Notice as well that the Indian nuclear explosion of 11 May 1998 (plotted as a red star) falls within the scatter of the earthquakes, and the explosion cannot be reliably discriminated. Notice as well the large colored circles on the left-hand plot that correspond to the waveforms shown in Figure 1. In terms of the raw amplitude ratio, we see that the cyan circle is actually more explosion-like than the actual explosion.

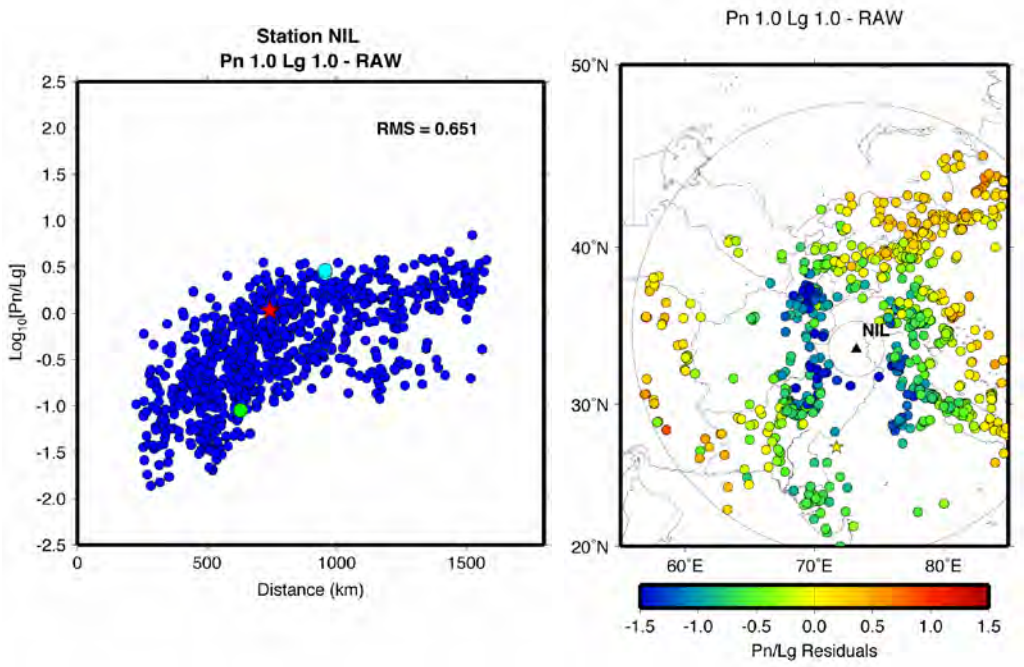

Figure 4. Pn/Lg discriminant at 1–2 Hz frequency recorded at station NIL showing raw data. The left panel shows the discriminant as a function of distance. The three waveforms shown in Figure 1 are indicated here by their corresponding colors. The right panel shows a map view with symbols colored by the *P/S* ratio. Left panel from Pasyanos and Walter (2009).

In order to correct the phase ratio for path and source effects, we adjust the individual amplitudes assuming an earthquake source. We then form our discriminant using the ratio of the corrected amplitudes. This is a division of the amplitudes or a subtraction in log-space:

$$\text{discriminant} = \log\left[\frac{(A^P / A_0^P)}{(A^S / A_0^S)}\right] = \log\left[\frac{A^P}{A^S}\right] - \log\left[\frac{A_0^P}{A_0^S}\right] \qquad (6)$$

where A_0 is the amplitude prediction for an earthquake of that phase and size. As a result, the corrected discriminant should now have a value around 0 (*P/S* ratio of 1) for earthquakes. We input a best estimate of the earthquake size by using a moment magnitude, if available, or otherwise estimating Mw using other magnitude estimates.

The discriminant using corrected amplitudes is shown in Figure 5. The attenuation and geometrical spreading have minimized the trend with distance, the scattering of the earthquake population is reduced, and most important, the explosion separates cleanly from the earthquakes. *Lg* paths traversing regions of high crustal Q (e.g., to the south of NIL) will be normalized by high Lg amplitudes and hence have a higher *P/S* ratio. Those traversing regions of low crustal Q (e.g., to the north) will be normalized by low *Lg* amplitudes and have a lower *P/S* ratio.

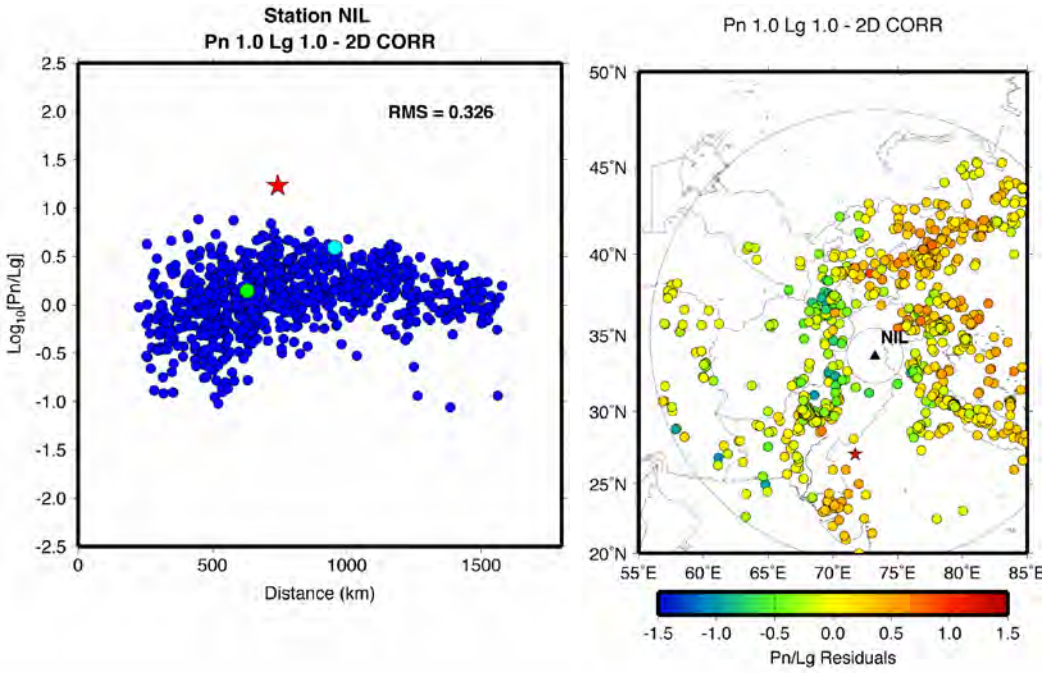

Figure 5. Pn/Lg discriminant at 1–2 Hz frequency recorded at station NIL, showing data with attenuation corrections. The left panel shows discriminant as a function of distance. The three waveforms shown in Figure 1 are indicated here by their corresponding colors. The right panel shows a map view with symbols colored by the P/S ratio. Figure from Pasyanos and Walter (2009).

It is important to note that in many areas where the lateral attenuation variations are low, we could correct the trends in distance and magnitude with a 1D correction. In this region, however, simply removing the trend would reduce the RMS of the earthquake population from 0.65 to 0.62 log-units, but the explosion would not separate from the earthquakes because the corrections would be the same for a given distance. Where lateral variations in attenuation are high, only 2D corrections can start to account for the large observed amplitude variations. After the attenuation corrections are applied, the RMS of the earthquake amplitude residuals reduces further to 0.326.

We also look at the discrimination using a number of other combinations of regional P/S amplitudes, including *Pn/Sn* and *Pg/Lg*. The results are shown in Figure 6. Like the *Pn/Lg* discriminant, in the raw data these discriminants did not cleanly separate the explosion from the earthquake population until the attenuation correction was applied. We can see that the attenuation model of the crust and upper mantle seems to be predictive for all major regional phases (*Pn, Pg, Sn, Lg*), which are all represented in various combinations in the three discriminants (*Pn/Lg, Pn/Sn, Pg/Lg*).

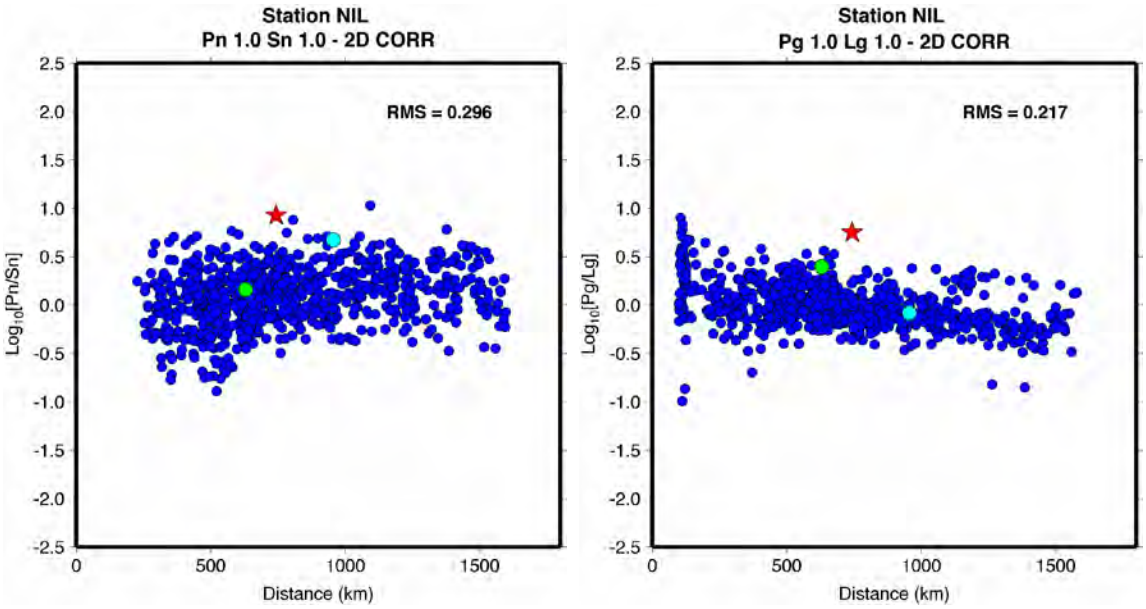

Figure 6. Pn/Sn and Pg/Lg discriminant at 1–2 Hz frequency, recorded at station NIL showing data with attenuation corrections. In both panels, the three waveforms shown in Figure 1 are indicated here by their corresponding colors. Figure from Pasyanos and Walter (2009).

Since regional P/S discriminants generally work better at higher frequencies, we have also applied the attenuation model to higher-frequency discriminants. The path coverage for the upper mantle phases *Pn* and *Sn* is much better than crustal phases at high frequencies, so we have used the *Pn/Sn* discriminant for the 4–6 Hz passband at station HASS in Saudi Arabia (Figure 7). Here, we see a similar reduction in the spread of the earthquake population, as well as an improvement in the discrimination of the 1998 Pakistani nuclear test.

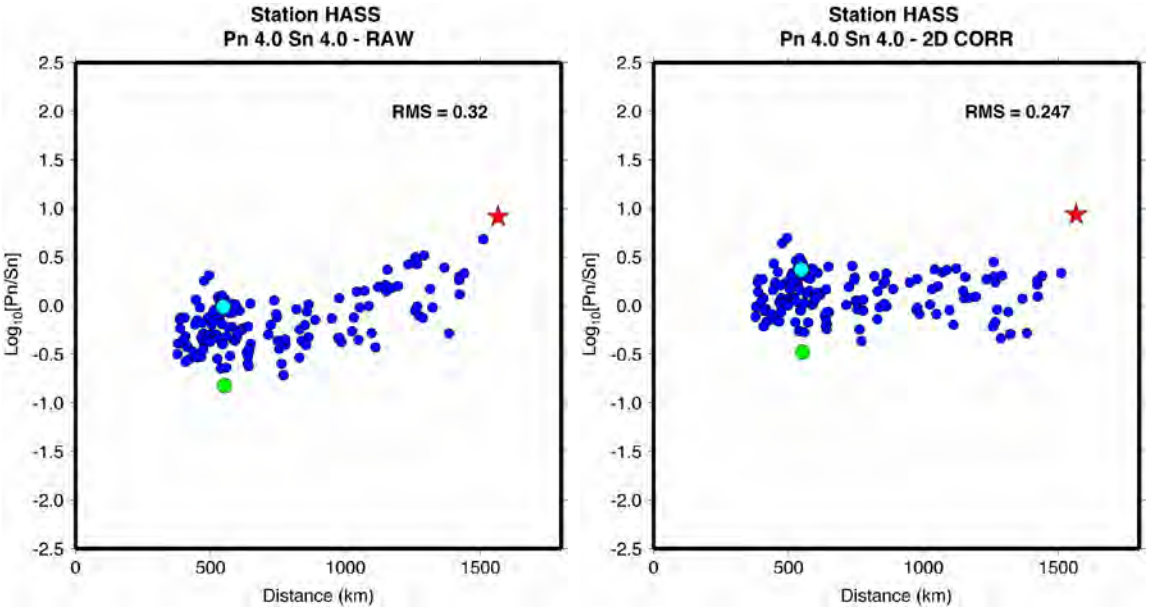

Figure 7. Pn/Lg discriminant at 4–6 Hz frequency, recorded at station HASS, showing raw data and data with attenuation corrections. In both panels, the red star corresponds to the 1998 Pakistani nuclear test, and the green and blue circles are two earthquakes from the Zagros Mts.

Even with attenuation-based path corrections, there is still some variation in the *P/S* ratios, as shown by the green and cyan circles in Figure 7—two Zagros earthquakes that have very different *P/S* ratios. These unmodelled

amplitude variations can come from a number of possible sources, including small-scale Q variations, variations in the source term (from seismic moment, apparent stress, depth, etc.), differences in geometrical spreading, earthquake mislocations, and multipathing, to name a few. We would like to explore the dataset to determine the major causes of the remaining variation.

CONCLUSIONS AND RECOMMENDATIONS

Attenuation tomography can capture the observed variability of regional phase amplitudes. The new attenuation tomography method that we have developed allows us to simultaneously invert for the amplitudes of regional phases Pn, Pg, Sn, and Lg. We have demonstrated that it is possible to use information about attenuation of the lithosphere to improve regional P/S discriminants. The new attenuation model has the potential to greatly improve earthquake-explosion discrimination in the Middle East and other tectonically complex regions. The challenge will come in calibrating attenuation structure at higher frequencies, where the P/S discriminant appears to work better but where data coverage for the tomographic model is sparser. Other challenges will be calibrating broad areas that include aseismic regions.

ACKNOWLEDGEMENTS

We thank Stan Ruppert and Terri Hauk for maintaining the LLNL Seismic Research Database. We thank Doug Dodge and Mike Ganzberger for developing the RBAP code, which is used to make the regional amplitude measurements.

REFERENCES

Bird, P. (2003). An updated digital model of plate boundaries, *Geochem. Geophys. Geosyst*. 4: doi:10.1029/2001GC000252.

Camp, V. and M. Roobol (1992). Upwelling asthenosphere beneath western Arabia and its regional implications, *J. Geophys. Res.* 97: 15,255–15,271.

Pasyanos, M. E. and W .R. Walter (2009). Improvements to regional explosion identification using attenuation models of the lithosphere, *Geophys. Res. Lett.* in press, doi:10.1029/2009GL038505.

Pasyanos, M. E., E. M. Matzel, W. R. Walter, and A. J. Rodgers (2009a). Broad-band Lg attenuation modeling of the Middle East, *Geophys. J. Int.* 177: 1166–1176, doi:10.1111/j.1365-246X.2009.04128.x.

Pasyanos, M. E., W. R. Walter, and E. M. Matzel (2009b). A simultaneous multi-phase approach to determine P-wave and S-wave attenuation of the crust and upper mantle, *Bull. Seism. Soc. Amer.*, in press,

Street, R. L., R. Herrmann, and O. Nuttli (1975). Spectral characteristics of the Lg wave generated by central United States earthquakes, *Geophys. J. R. Astron. Soc*. 41: 51–63.

Walter, W. R. and S. R. Taylor (2001). A revised magnitude and distance amplitude correction (MDAC2) procedure for regional seismic discriminants: Theory and testing at NTS, Lawrence Livermore National Laboratory report UCRL-ID-146882, http://www.llnl.gov/tid/lof/documents/pdf/240563.pdf

Walter, W. R., M. E. Pasyanos, E. Matzel, R. Gok, J. J. Sweeney, S. R. Ford, and A.J. Rodgers (2008). Regional seismic amplitude modeling and tomography for earthquake-explosion discrimination, in *Proceedings of the 30th Monitoring Research Review: Ground-Based Nuclear Explosion Monitoring Technologies,* LA-UR-08-05261, Vol. 2, pp. 702–711.

EXPLOSION SOURCE MODEL DEVELOPMENT IN SUPPORT OF SEISMIC MONITORING TECHNOLOGIES: APPLICATIONS OF NEW MODELS FOR SHOCK-INDUCED TENSILE FAILURE

Howard J. Patton

Los Alamos National Laboratory

Sponsored by the National Nuclear Security Administration

Award No. DE-AC52-06NA25396/LA08-FY08-029-NDD02

ABSTRACT

This paper reports on research activities for the second year of this project developing new explosion source models that include the effects of deep-seated, shock-induced tensile failure. Free surface interactions and the dynamics of shock-wave rebound are responsible for modes of tensile and shear failures leading to permanent deformations in a conical volume over the shot point. A vast majority of nuclear explosions worldwide were conducted under containment conditions that facilitated shock-induced tensile failure. The new model is a superposition of monopole + tectonic release + shock-induced tensile failure sources, the latter represented by a compensated-linear-vector dipole (CLVD) with vertical axis of symmetry. This model was used to explain why M_s for the North Korean test of 9 October 2006 is anomalously large for its m_b. The model also applies to the recent test of 25 May 2009.

Research this past year has been directed at three outstanding observations/problems that challenge our understanding of seismic wave generation by the explosion source. (1) *Anomalous surface waves for Balapan nuclear tests*. In the 70's and 80's, long-period surface waves from these tests were noted for large Love waves and Rayleigh waves with polarity reversals and significant time delays. Repeated attempts to model these observations with just tectonic release were not completely successful. New observations based on deglitched waveforms of the Borovoye archive (Baker et al., these Proceedings) bridge the frequency gap between long-period fundamental modes and higher modes making up the low frequency *Lg* spectrum. This additional bandwidth is needed to resolve source parameters of new models that include tensile failure as well as tectonic release. (2) *Source-related spectral modulations*. Modulations were first observed in the mid-90's for *Lg* spectral ratios of Yucca Flats explosions. Since then they have been observed in *Pg* and *Lg* coda-wave spectra for Pahute and Yucca Flats explosions. The nearfield *Rg*→*S* scattering hypothesis explains spectral modulations as the result of interference between *Rg* waves excited by explosion and CLVD sources, causing modulation in the composite *Rg* wavefield which imprints its spectrum onto the scattered *P* and *S* waves making up regional phases. The strength of the CLVD relative to the monopole decreases with yield due to the increasing force of slapdown, which compacts weak materials and reduces static deformations associated with the CLVD. As such, the *Rg*→*S* scattering hypothesis predicts the existence of modulations in spectral ratios taken between shallow and deep explosions on Pahute Mesa. This prediction was validated by observations, which are being modelled for time histories of the CLVD source. (3) *Direct versus indirect generation of S waves.* A recent publication used plane-layered theory to argue against the importance of near-field scattering (indirect mechanisms) relative to direct generation by the CLVD source. Our studies show that the published results are in error due to (a) deficiencies of Earth models lacking low velocities near the free surface where *Rg* is excited and propagates, and (b) inadequacies of plane-layered theory for scattering estimates.

OBJECTIVE

The objective is to develop new analytical explosion source models based on seismic moment tensor theory for further improvement and advancement of regional seismic discrimination and yield estimation technologies. Such technologies rely heavily upon the source information contained in high-frequency shear (*S*) waves. The use of coda waves following regional *S* phases to estimate explosion yield is one example of an emerging technology offering great promise for improved nuclear monitoring. Unfortunately, an understanding of how explosions excite *S* waves is quite limited, and a widening gulf between theory and practice undermines our confidence to monitor broad areas at small yields. The new models will provide a physical basis for explosion-generated *S* waves and theoretical insights for advancing yield estimation and discrimination capabilities, thereby closing the gulf between theory and practice.

RESEARCH ACCOMPLISHED

This project builds upon spherical (monopole) explosion source models developed in the 1970's. An important aspect of those models is the theory relating seismic amplitudes of *P* waves directly to yield, depth of burial, and material properties of the source medium. Analytical relationships predicted by the theory draw upon empirical yield scaling behaviors of key model constructs, such as the elastic radius. Furthermore, the analytical nature of these models facilitated their use since they were easy to implement by researchers, and as such, they were widely applied to study the explosion source. Their application continues to this day, but with the recognition that a spherical point source is inadequate to explain *S*-wave generation.

Tensile failure is a source of asymmetry known to exist on most underground explosions, even those overburied for their yield. A kinematic description of shock-induced, deep-seated tensile failure is a compensated linear vector dipole CLVD with vertical axis of symmetry in extension. A CLVD can generate *S* waves directly and indirectly through efficient excitation of short-period surface waves (*Rg*) and subsequent scattering into *P* and *S* waves close to the source. My research introduces this source of asymmetry into spherical source models. The new model will require the development of scaling relationships like those for the elastic radius in the case of the spherical model, but for parameters of the tensile failure source, including centroid depth, source process time, and strength of the CLVD force system. A simple analytical form couched in seismic moment tensor theory will be adopted so that the model can be easily incorporated into researchers' preferred wave propagation codes for calculating synthetic seismograms.

This year's research is directed at three outstanding observations/problems that challenge our understanding of seismic wave generation by the explosion source: (1) anomalous observations of long-period surface waves excited by nuclear tests conducted at the Semipalatinsk Test Site (STS) in the 70's and 80's, including the generation of large Love waves and Rayleigh waves with polarity reversals and time delays; (2) spectral modulations starting with the coda of *Pg* waves and persisting down regional waveforms through arrival times for *Sn*, *Lg*, and *Lg* coda, as documented for Nevada Test Site (NTS) explosions in *Lg* spectral ratios and difference spectrograms (Gupta and Patton, 2008), and (3) the problem of regional *S* wave generation by two classes of mechanisms: (a) "direct" excitation involving trapped *pS* conversions in the crust and/or non-spherical sources of tensile and shear failure versus (b) "indirect" generation by near-source scattering of short-period Rayleigh waves (e.g., *Rg*→*S* scattering). Presented first herein is research concerning upper bound estimates of *Rg*→*S* scattering. This research has uncovered a possible physical explanation for *Pn*/*Lg* spectral ratios of STS explosions to turn upward at low frequencies (see Fisk, 2006). The discovery motivated the second research topic discussed where new source models are tested against fundamental- and higher-mode surface waves generated by STS explosions and recorded at Borovoye. I conclude with research investigating spectral modulations that were predicted on the basis of the *Rg*→*S* scattering hypothesis and confirmed by spectral ratio observations between shallow and deep explosions on Pahute Mesa.

Upper Bound Estimates on Rg→S scattering.

A recent paper by Stevens et al. (2009; hereafter referred to as SXB09) presents upper bound estimates of *Rg→Lg* scattering amplitudes using an energy conservation approach for plane-layered Earth models. Their results are based on calculations for two velocity models, one for low-velocity structures at NTS and the other for high-velocity structures at STS. For low-velocity structures, they conclude (1) *Rg→Lg* scattering is a viable mechanism only for *Rg* waves excited by the spherical source (e.g., monopole) below 0.3 Hz, (2) above 0.3 Hz, direct *Lg* from the spherical source will dominate, and (3) scattering of *Rg* excited by the CLVD source never dominates *Lg*. For high-velocity structures, direct *Lg* from the CLVD will dominate above 1 to 3 Hz, while at lower frequencies, *Rg→Lg* scattering amplitudes from the monopole exceed amplitudes of direct *Lg* and dominate over scattered *Rg* amplitudes from the CLVD.

A comments paper by Patton and Gupta (2009; hereafter referred to as PG09) points out (a) deficiencies in scattering estimates based on plane-layered velocity models and (b) bias in the results of SXB09 since their single-source spectra calculations do not account for wavefield interactions between monopole and CLVD sources and their velocity models are not representative of test site structures in the upper 2 km where *Rg* excitation and propagation take place. Contrary to conclusions (1) and (2) of SXB09, PG09 shows that upper bound estimates of *Rg* scattering exceed amplitudes of direct *Lg* for NTS velocity models with low-velocity surface layers (see Figure 1). Compared to *Rg* excitation by a spherical explosion source, CLVD excitation can be rich in high frequencies for shallow source depths (h) in low-velocity surface layers and an important factor in upper bound estimates of *Rg→Lg* scattering, in contradiction to conclusion (3). $M(\omega) \cdot A^0(\omega, h)$ in Figures 1 and 2 is the *Rg* excitation spectrum, where $M(\omega)$ is the Mueller-Murphy spectrum (Mueller and Murphy, 1971; MM71) and $A^0(\omega,h)$ is the reduced excitation spectrum (see Patton and Taylor, 2008) for the axisymmetric portion of the source involving only M_{zz} and $M_{xx} + M_{yy}$ elements of the moment tensor. The caluculation in Figure 1 is for a CLVD seismic moment M_{CLVD} equal to one half the monopole moment M_I (e.g., $K = 2$, see below).

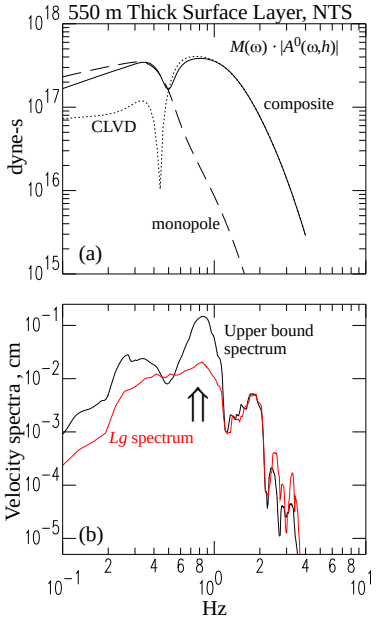

Figure 1. (a) *Rg* source excitation spectra for monopole, CLVD, and composite sources. (b) Composite upper bound *Rg* scattering spectrum and direct *Lg* spectrum for the SXB09 NTS structure with a 550 m thick low velocity surface layer. Both are multi-taper spectra. Arrow indicates the 0.6 to ~1.0+ Hz band where upper bound estimates of *Rg* scattering exceed the direct spectrum.

For high-velocity structures, SXB09 over-state their conclusion about the dominance of scattered waves excited by spherical sources since their calculations do not consider the effects of interactions between *Rg* wavefields radiated by the two sources. On the other hand, calculations in PG09 do so by taking the vector sum of wavefields excited by the monopole and CLVD sources (see Figures 1 and 2). Upper bound estimates based on vector-composite *Rg* spectra are better behaved than separate-source (monopole or CLVD) estimates of SXB09, and comparisons with direct *Lg* spectra are more meaningful since energy conservation should be based on composite *Rg* wavefields, not the wavefields excited by the separate sources. Furthermore, studies of the wavefield interactions at low-frequencies have led to a discovery that might explain interesting departures of *Pn*/*Lg* spectral ratio observations from model predictions (Fisk, 2006; 2007).

The *Rg* composite spectrum in Figure 2 is more peaked than either constituent spectrum and shows a pronounced roll-off in amplitude to low frequencies. This is a consequence of frequency-dependent cancellation between the monopole and CLVD wavefields. The roll-off is present in both upper bound and direct *Lg* spectra and increases as *K* increases (see next section). The source parameter *K* is proportional to the moment ratio, M_{CLVD} / M_I (see Patton and Taylor, 2008; also see equation in Figure 7 below). This roll-off feature is stable for a wide range of *K* values owing to two basic facts: (1) monopole and CLVD sources generate Rayleigh waves with opposite polarities for frequencies less than the CLVD excitation null and (2) the CLVD origin is delayed with respect to the monopole.

Below 1 Hz, *Rg* composite spectra in Figures 1a and 2a show that a low-frequency roll-off is expected to be more noticeable for explosions in hard rock media compared to NTS explosions, where the most obvious result of wavefield interactions is spectral modulation. Under the *Rg*→*S* scattering hypothesis and on the basis these predicted *Rg* composite spectra, spectral characteristics of farfield *S* waves below 1 Hz are expected to be different for STS and NTS explosions. Assuming the MM71 model for *Pn* waves and a flat spectrum at low frequencies, a roll-off in *Lg* spectra qualitatively agrees with the up-turn in STS *Pn/Lg* spectral ratio observations below 1 Hz documented in Fisk (2006). Likewise, modulation seen in the *Lg* spectra is consistent with *Pn/Lg* observations for NTS explosions in Fisk (2007).

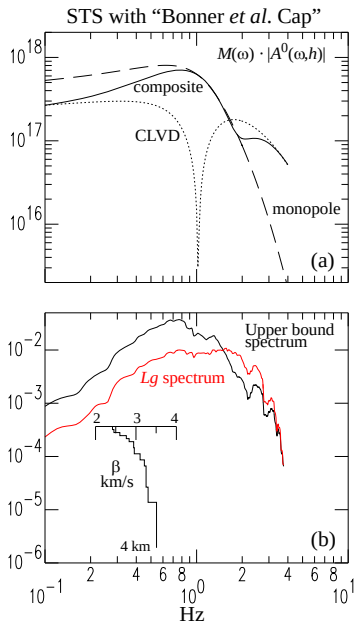

Figure 2. (a) *Rg* source excitation spectra for monopole, CLVD, and composite sources. Monopole and CLVD depths are 600 and 300 m, respectively. *K* = 2. (b) Composite upper bound *Rg* scattering spectrum and direct *Lg* spectrum for modified SXB09 Degelen structure with velocity gradient in the upper 1.5 km. Inset shows *S* profile for the top 4 km.

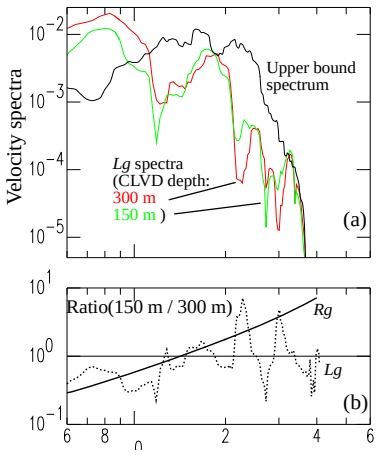

Figure 3. (a) Composite upper bound *Rg* scattering spectrum for a hybrid calculation where CLVD depth is 150 m. *Lg* spectra for 300 (red) and 150 m (green) CLVD source depths are shown for comparison. (b) Ratios of *Rg* source excitation spectra (solid line) and direct *Lg* spectra (dotted line) for composite sources, one with CLVD depth of 150 m and the other with CLVD of 300 m.

The importance of *Rg* scattering at high frequencies (> 3 Hz) ultimately depends on the relative excitation of *Rg* and *Lg* for very shallow sources. Explosions are far from being point sources of dilatation since significant deformations extend from below the shot point to the free surface. Depending on how the deformations are distributed in the column of material over the shot, a point-source CLVD model may have to be replaced by a finite source distributed over depth. We find that depth dependences of *Rg* and *Lg* excitation increase the relative importance of upper bound scattering estimates for very shallow sources. A "hybrid" calculation was run for the SXB09 NTS structure with a 550 m thick low velocity surface layer where the CLVD centroid depth is 150 m instead of 300 m as in Figure 1. In a hybrid calculation, scattering takes place in a different plane-layered structure than the structure in which excitation takes place (see PG09). The results for upper bound *Rg* scattering and direct *Lg* spectra are shown in Figure 3a. It can be seen that the upper bound spectrum is more robust for frequencies above 2 Hz compared to the 300 m case in Figure 1, while the average *Lg* spectral amplitudes remain unchanged. Further detail is provided in Figure 3b showing *Rg* and *Lg* ratios for composite sources where the only change is the CLVD source depth. Compared to the 300 m CLVD depth, the 150-m upper bound spectrum is richer in high frequencies simply because the *Rg* excitation is greater there. Meanwhile, the excitation of *Lg* waves has not changed significantly with respect to the 300 m case.

Tests of New Source Models Against Fundamental- and Higher-Mode Surface Wave Observations.
In the 70's and 80's, long-period excitation of surface waves by nuclear tests conducted at STS in central Asia were noted for anomalous behavior, including the generation of large Love waves and Rayleigh waves with polarity reversals and significant time delays (Rygg, 1979; Helle and Rygg, 1984). Repeated attempts to model the observations with tectonic release (Given and Mellman, 1986; Ekström and Richards, 1994) were not completely successful, although tectonic release models with reverse faulting explained observations the best (Harkrider, 1981; Day and Stevens, 1986; Day et al., 1987). New explosion source models for tensile failure represented by a CLVD have yet to be tested to see if they can explain the full suit of observations, including m_b-M_s scaling with respect to predictions of the Mueller-Murphy model. Due to broader frequency content and a fairly complete recording history of STS explosions, waveform data from the Borovoye archive (Baker et al., these Proceedings) offer an opportunity to re-evaluate old explosion source models and test new ones.

Some 50 Balapan explosions located in Northeast NE, Transition Zone TZ, and Southwest SW test areas (see Ringdal et al., 1992) are currently under study where epicenters and origin times are taken from Kim et al. (2001). For a map of these epicenters, see Figure 2 of Baker et al. (these Proceedings). Filtered vertical-component displacement traces of the TSG DS instrument system are plotted in Figure 4 along with epicentral distances to Borovoye (BRV), teleseismic m_b calculated by Blacknest seismologists (Ringdal et al., 1992), and a reference to the study of Ekström and Richards (1994; E&R94) for those events whose surface waves were analyzed for moment tensor descriptions. The traces are arranged in order of increasing distance from 679.7 to 696.1 km, a span of 16.4 km. Red and blue boxes demarcate the arrivals of fundamental- and higher-mode Rayleigh waves.

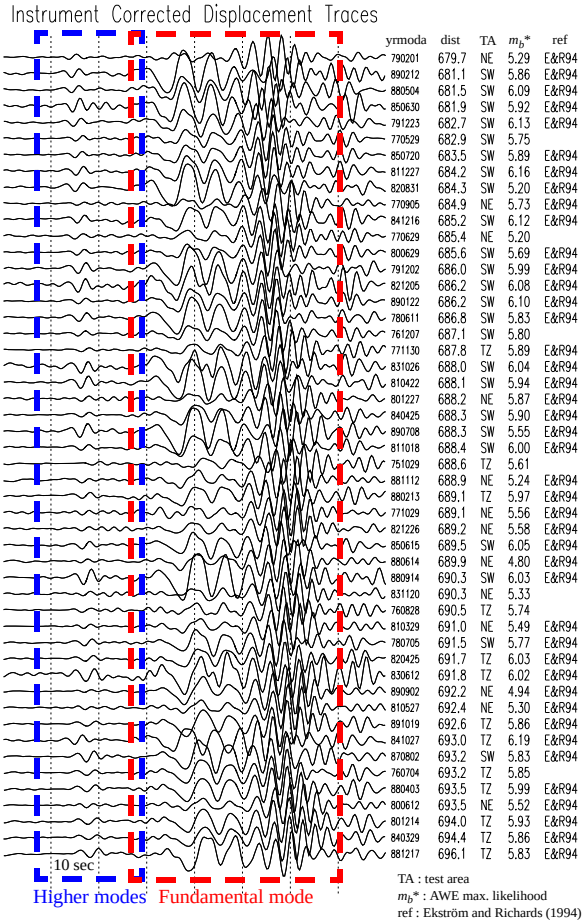

Figure 4. Profile of instrument-corrected, vertical-component displacement traces for the TSG DS instrument system ordered by increasing epicentral distance from the BRV. The frequency pass-band is 0.03 to 0.5 Hz.

For large explosions in the study of Fisk (2006), signal-to-noise ratio (SNR) for *Pn* and *Lg* waves recorded at WMQ and MAK appears adequate for frequencies as low as ~0.2 Hz (see his Figure 11). *Pn/Lg* spectral ratios at low frequencies may be reliable for his large explosion groupings in Figures 14 - 17. The up-turn in Fisk's spectral ratio observations at low frequencies is qualitatively consistent with a roll-off in the spectrum of *Lg* waves if the low-frequency spectrum of *Pn* waves is flat as predicted by the MM71 model. A spectral analysis of higher modes making up *Lg* was conducted to examine the behavior of spectra at low frequencies.

Path-corrected *Lg* displacement spectra in Figure 5 were obtained by Fourier transforming BRV signals recorded on the DS instrument system for a time window corresponding to average apparent velocities of 3.77 and 3.21 km/s. For an average distance of 688 km, the corresponding window length is 32 s. A multi-taper algorithm was applied involving 512-point transforms and 7 tapers. Further details about SNR checks and corrections for attenuation may be found in Baker et al. (these Proceedings). Shown with the spectra are linear fits to the low frequency portion starting at 0.8 Hz. Low-frequency cut-offs of the fits were determined by SNR, but never went below 0.1 Hz. The legend on each spectrum provides test area, estimates of slope and one standard deviation, and the Blacknest m_b. An *R* in parentheses next to the test area indicates that Rayleigh waves are polarity reversed at BRV. This is the case for both NE shots. The shots are ordered by increasing slope moving left to right and top to bottom, and their magnitudes have been restricted to a range of just 0.3 magnitude units (mu) between 5.56 and 5.86. Because of this restricted range, I do not expect yield variations to have a significant impact on the shape of these spectra.

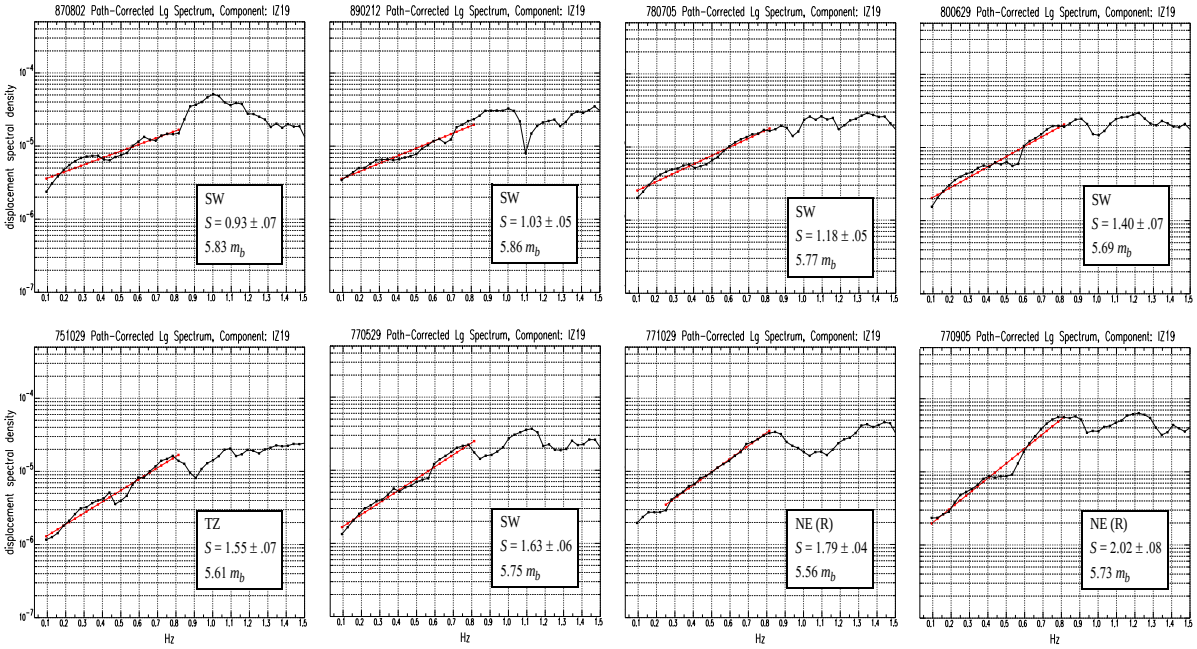

Figure 5. Path-corrected *Lg* displacement spectral densities for 8 Balapan shots recorded on the DS instrument system at BRV. The 6-digit code for year, month, day of the shot is printed in the title above each plot. Red lines are linear fits to the spectra for frequencies below 0.8 Hz. Slope estimates (*S*) and standard deviations are provided along with test area and m_b. The shots are restricted to a narrow range of source strengths based on m_b spanning only 0.3 mu.

Lg displacement spectra are not flat for frequencies below the corner frequency as expected based on the Mueller and Murphy model (Mueller and Murphy, 1971). Rather, the spectral amplitudes roll-off toward low frequency, consistent with the *Pn*/*Lg* observations of Fisk. Furthermore, shots with the highest slopes also show reversed polarity Rayleigh waves at BRV and negative U_1 values from the study of E&R94. These observation suggest a correlation between the low-frequency slope of *Lg* spectra and effects on longer-period fundamental-mode Rayleigh waves. Baker et al. (these Proceedings) explore this possibility in detail with their Figure 5 where the slope of the *Lg* spectrum is plotted against m_b–M_s; m_b is the Blacknest maximum-likelihood estimate and M_s is determined from BRV DS recordings using the Marshall and Basham method (Marshall and Basham, 1972). All M_s determinations but one are based on Rayleigh wave amplitudes in the 17 - 23 s period pass-band. As seen in Figure 5 of Baker et al., a correlation does exist between low-frequency *Lg* spectral slope and M_s corrected for source size using m_b. This finding is very interesting in the context of spectral ratio observations of Fisk (2006). While dismissed by Fisk as a result of noise contamination, the correlation suggests that upturn in *Pn*/*Lg* ratios is real, and is related to roll-off in *Lg* spectra at low frequencies.

Predictions from CLVD source models and the Rg→S scattering hypothesis. Here I will show that a low-frequency roll-off in *Lg* spectra for Balapan explosions can be modeled to first degree using a monopole + CLVD source model and invoking the *Rg*→*S* scattering hypothesis. According to this hypothesis, *Rg* waves radiated by the source are scattered into P and S waves in the nearfield, and the amplitude-frequency dependence of the incident wave is imprinted onto scattered waves. This basic tenet of seismic scattering traces it roots to early studies using coda waves to extract source spectra (e.g., Aki, 1969), and has been repeatedly proven true in many subsequent studies. Some scattered S waves are trapped in the crust and go on to become part of the far-field energy carried by *Lg* waves and its coda. SXB09 show that scattered *Rg* amplitudes far exceed the *Lg* amplitudes excited directly by explosion and CLVD sources in high velocity media for frequencies less than 1 Hz. GP09 concurs with their result, but point out

that SXB09 overlooked *Rg* wavefield interactions between the two sources, which can significantly alter the amplitude-frequency dependence of radiated *Lg* waves as well as *Rg* before scattering occurs.

This fact is illustrated in Figure 6. Synthetic *Rg* and *Lg* excitation spectra (infinite Q) are plotted between 0.1 and 0.8 Hz for monopole + CLVD source models, where centroid depths are 600 and 300 m, respectively. A MM71 source function is assumed for both sources, and the origin of the CLVD is delayed by the time it takes a *P* wave to travel up to the free surface from the monopole and back down to the CLVD centroid depth. The only source parameter varied is *K*, the relative source strength of the CLVD. For each case, the spectrum has been offset by a factor of 2 from the previous one for plotting purposes. (Note the amplitude-frequency dependence is of interest, not the absolute amplitude; also relative amplitude between *Rg* and *Lg* is not preserved on these plots.) As with the observations in Figure 5, a linear fit of $\log_{10}$ amplitude versus frequency is applied to each spectrum, and the fits are shown in Figures 6a and b. Residuals from the fits to synthetic *Rg*, *Lg*, and observed *Lg* spectra have average 1-σ values of 0.094, 0.171, and 0.079, respectively, synthetic *Lg* spectra showing the highest departures from a straight-line approximation, while observed *Lg* spectra for 50 shots show the smallest, and synthetic *Rg* spectra slightly more. Indeed, the synthetic *Lg* spectrum for a pure monopole source (*K* = 1) is relatively flat out to 0.4 Hz and falls off rapidly at lower frequencies, and as do *Lg* spectra for other *K* values. Curvature in *Rg* spectra increases as *K* value increases.

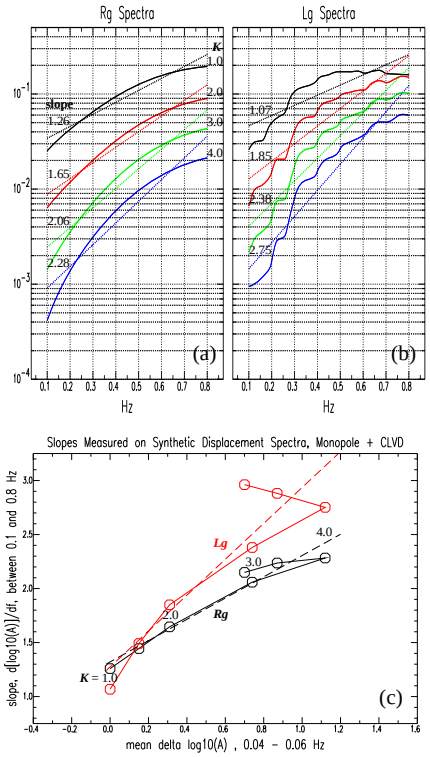

Figure 6. Excitation of *Rg* (a) and *Lg* waves (b) in the Degelen model of SXB09 modified for velocity gradient in the upper 1.5 km (see Fig. 2). Color coding is by *K* value, and linear fits for 0.1-0.8 Hz are shown with annotated slope values. (c) Slope values are plotted against $-M_S$ with respect to a pure monopole (*K* = 1) for synthetic Rayleigh wave spectral amplitudes averaged between 0.04-0.06 Hz. Dash lines are linear fits to 7 sample points; *K* values are annotated for several cases. *K* = 5 is the strongest CLVD source considered (M_{CLVD}/M_I = 1.14).

Cancellation of long-period Rayleigh waves radiated by an explosive monopole and a CLVD with vertical axis of symmetry in extension has been studied by Patton and Taylor (2008) for the effects on M_S, which make explosions discriminate better on m_b-M_S plots. For Rayleigh wave amplitudes measured near 20-s period, M_S decreases with increasing *K* until a value near 4 (M_{CLVD}/M_I = 1) in hard rock media, where Rayleigh waves reverse polarity and grow in amplitude for larger *K* values. Figure 6c shows the expected correlation between the predicted change in M_S (reduction then increase) and the slope measured on synthetic *Rg* and *Lg* spectra keeping yield fixed and varying *K*. *K* ranges from 1 to a maximum of 5 (1.0, 1.5, 2.0, 3.0, 4.0, 4.5, 5.0). As M_S decreases (e.g., $-M_S$ increases) with *K*, *Rg* and *Lg* slopes increase for 1<K<4. Above 4, *Lg* slopes continue to increase, while *Rg* slopes remain constant or decrease slowly. These results show that the scaling of slope values is faster for *Lg* waves than it is for *Rg* waves, as shown by the linear fits in Figure 6c to the results for 7 different *K* values. The scaling goes as 1.7 for *Lg* waves, while it is only 1.0 for *Rg*. A least squares estimate of scaling for observations in Figure 5b of Baker et al. is 0.7 ± 0.3 at the 2-σ level. This estimate is consistent with the preliminary results in Figure 6c for *Rg* waves. Future work will use more realistic source simulations including the effect of source depth and the inclusion of tectonic release. It should be noted however that BRV lies close to nodal plane for most tectonic solutions reported in E&R94, and thus we expect that this station is nearly optimal for studying axisymmetric effects predicted by just a monopole + CLVD model.

Spectral modulations predicted by the *Rg*→*S* scattering hypothesis and confirmation from NTS observations. Under the *Rg*→*S* scattering hypothesis, spectral characteristics of farfield *S* waves below ~1 Hz are expected to be different for STS and NTS explosions: in hard rock, *Lg* displays a pronounce low-frequency spectral roll-off, while for NTS media, the most noticeable feature is spectral modulation. Both features can be explained as the result of *Rg* wavefield interactions between monopole and CLVD sources (see Figures 1a and 2a above). Should the monopole dominate over the CLVD, effects of wavefield interactions are minimal, and the amplitude-frequency dependence of *Rg* waves will be controlled by the explosion source. Therefore, a prediction of the *Rg*→*S* scattering hypothesis is that low-frequency roll-off should lessen as *K*→1, as seen in Figure 6c, and spectral modulation should become muted to the point of vanishing.

An interesting result from Patton and Taylor (2008) was the inference that *K* decreases with yield for Pahute Mesa explosions ranging in size over 2 orders of magnitude. Measurements of *K* values based on moment tensor inversions support this finding (Figure 7). The reduction in *K* was interpreted to be a consequence of compaction, closing voids and less static deformation for the CLVD source as the force of slapdown increases with yield. Ignoring the effects of tectonic release, the largest Pahute Mesa shots look virtually isotropic, while *K* values for most explosions with m_b < 5.75 range between 1.4 and 2.5. The *Rg*→*S* scattering hypothesis predicts that modulation should be absent for large shots and yet present on smaller shots. This prediction can be tested by taking *Lg* spectral ratios between smaller and larger shots, similar to the approach of Patton and Taylor (1995), except in that study larger, normal-buried explosions were in the numerator and smaller overburied explosions in the denominator, just opposite to the way ratios are taken here.

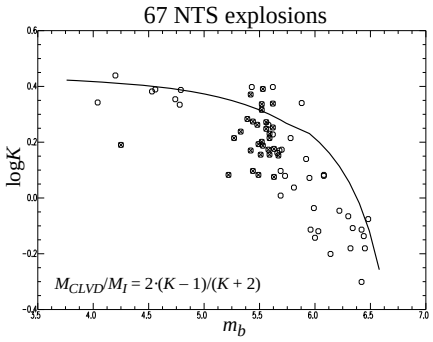

Figure 7. Comparison of inferred *K* (solid line) with measured *K* from moment tensor inversions. Pahute Mesa shots above the water table are plotted with circle-enclosed ×.

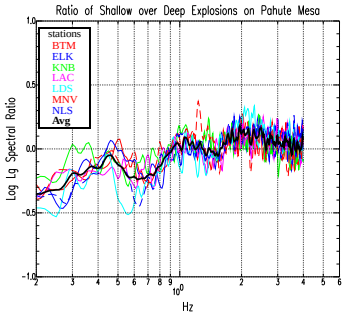

Figure 8. *Lg* spectral ratios by station and network (black line).

The explosion population was split into two groups on the basis of burial depth: 39 smaller events ranging between 540 and 690 m and 14 larger events between 820 and 1450 m. *Lg* displacement spectra were computed for a time window corresponding to apparent velocities of 4.0 and 2.8 km/s. Each $\log_{10}$ spectrum was made zero mean and a log-average was computed on a station by station basis for explosions in each group. Seven stations of the Livermore and Sandia regional NTS networks were used; Sandia stations DRW and TON were excluded because their epicentral distances are too short. Ratios between the average spectra for each group were taken. Figure 8 shows ratios for all 7 stations and the network average.

The conventional spectral ratio method employing an overburied (OB) explosion and nearby normal-depth explosions was applied to ALAMO, BACKBEACH, and NEBBIOLO with GALVESTON serving as the OB explosion. The *Lg* spectral ratios for these three shots are compared with the network results obtained from the shallow/deep explosion groupings in Figure 9. Modulations are observed in both types of spectral ratios, and there is good agreement between the two below 1 Hz, where the modulation shows a distinct null centered near 0.7 Hz. This is in contrast to Yucca Flats explosions, which show modulations and a null centered near 0.55 Hz (Patton and Taylor, 1995). Modulation persists above 1 Hz in the shallow/deep ratio, while the conventional ratios show too much scattered even for network averages using 6 Livermore and Sandia stations. Apparently, averaging many explosions in the shallow/depth ratio calculation has reduced the scatter enough to bring out modulation above 1 Hz. The high frequency trend in the shallow/deep ratio can be explained by averaging Mueller-Murphy source functions for explosions in each group and taking their ratio. This ratio is also plotted in Figure 9, where a MM71 source function for tuff was employed, and yields were computed from source depth using $h = 120 \cdot W^{1/3}$ in meters and W in kilotons. MM71 matches the general frequency trend of the shallow/deep ratio, but it cannot account for the modulations. In summary, a prediction of the $Rg \rightarrow S$ scattering hypothesis based on systematic reduction of K with yield is validated by shallow/deep *Lg* spectral ratio observations for explosions located on Pahute Mesa.

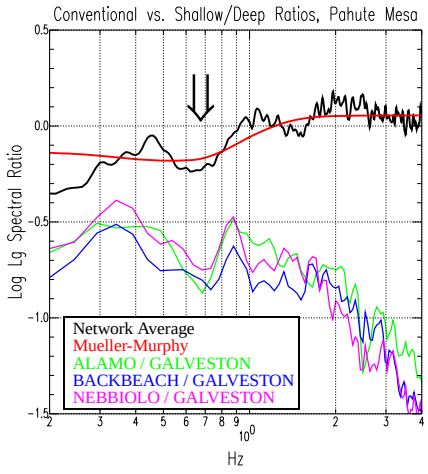

Figure 9. Comparison of *Lg* spectral ratios for conventional (normal-buried / overburied shot) method and network ratio for shallow / deep shots. Red curve is ratio of average MM71 source spectral ratio for shallow/deep groups

CONCLUSIONS AND RECOMMENDATIONS

In year 2 of this project, significant progress has been made developing explosion source models for the generation of *S* waves used heavily by discrimination and yield estimation technologies for regional, broad-area monitoring of nuclear tests at low yields. Three research topics that challenge our understanding of *S* waves generation were studied this year: (1) anomalous long-period surface wave excitation by STS explosions, first noted in the 70's and 80's, but never satisfactorily explained by tectonic release models alone; (2) the cause of spectral modulations observed in regional phases from NTS explosions and a prediction of the $Rg \rightarrow S$ scattering hypothesis; and (3) the relative importance of direct versus indirect (e.g., near-source scattering) mechanisms. These topics are very controversial among explosion seismologists. The role of tensile/shear failure represented by a CLVD source has been recognized and has gained greater acceptance in the community over past 5 years. Nevertheless, characterization of this source is in its infancy, and there is much exciting research ahead. I think there should be a concerted effort to develop an "effective" source time function for the CLVD that accounts for the fact that it is a distributed source and particle displacement time histories may vary significantly as a function of depth. For example, large impulsive particle motions may characterize shallow depths. On the other hand, motions at depth are smaller, yet probably couple better into the Earth and have larger permanent deformations and hence are the main source of CLVD moment.

ACKNOWLEDGEMENTS

The work reported herein has been conducted in part under a sub-contract with Lamont-Doherty Earth Observatory of Columbia University under the auspices of the Air Force Research Laboratory.

REFERENCES

Aki, K. (1969). Analysis of the seismic coda of local earthquakes as scattered waves, *J. Geophys. Res.* 74: 615–631.

Baker, D., W.-Y. Kim, H. J. Patton, G. E. Randall, and P. G. Richards (2009). Improvements to a major digital archive of seismic waveforms from nuclear explosions: The Borovoye seismogram archive, these Proceedings.

Day, S. M. and J. L. Stevens (1986). An explanation for apparent time delays in phase-reversed Rayleigh waves from underground nuclear explosions, *Geophys. Res. Lett.* 13: 1423–1425.

Day, S. M., J. T. Cherry, N. Rimer, and J. L. Stevens (1987). Nonlinear model of tectonic release from underground explosions, *Bull. Seismol. Soc. Am.* **77**: 996–1016.

Ekström, G. and P. G. Richards (1994). Empirical measurements of tectonic moment release in nuclear explosions from teleseismic surface waves and body waves, *Geophys. J. Int.* 117: 120–140.

Fisk, M. D. (2006). Source spectral modeling of regional *P/S* discriminants at nuclear test sites in China and the former Soviet Union, *Bull. Seismol. Soc. Am.* 96: 2348–2367.

Fisk, M. D. (2007). Corner frequency scaling of regional seismic phases for underground nuclear explosions at the Nevada Test Site, *Bull. Seismol. Soc. Am.* 97: 977–988.

Given, J. W. and G. R. Mellman (1986). Estimating explosion and tectonic release source parameters of underground nuclear explosions from Rayleigh and Love wave observations, Final report, Part I, AFGL-TR-86-0171(I), Air Force Geophysics Laboratory, Hanscom Air Force Base, MA, 70 pp.

Gupta, I. N. and H. J. Patton (2008). Difference spectrograms: A new method for studying S-wave generation from explosions, *Bull. Seismol. Soc. Am.* 98: 2460–2468.

Harkrider, D. G. (1981). Coupling near-source phenomena into surface wave generation, in *Identification of Seismic Sources--Earthquake or Underground Explosion, NATO Advanced Study Institute Series,* E. S. Huseby and S. Mykkeltveit, Editors, D. Reidel Publishing Co., Dordrecht, 277–326.

Helle, H. B. and E. Rygg (1986). Determination of tectonic release from surface waves generated by nuclear explosions in Eastern Kazakhstan, *Bull. Seismol. Soc. Am.* 74: 1883–1898.

Kim, W.-Y., P. G. Richards, V. Adushkin, and V. Ovtchinnikov (2001). Borovoye digital archive for underground nuclear tests during 1966-1996, Data report on the web at http://www.ldeo.columbia.edu/res/pi/Monitoring/Data/brv_exp_archive.html, Borovoye Archive for UNT (information product in PDF).

Marshall, P. D. and P. W. Basham (1972). Discrimination between earthquakes and underground explosions employing an improved M_S scale, *Geophys. J. R. Astr. Soc.* 28: 431–458.

Mueller, R. A. and J. R. Murphy (1971). Seismic characteristics of underground nuclear detonations Part I. Seismic spectrum scaling, *Bull. Seismol. Soc. Am.* 61: 1675–1692.

Patton, H. J. and S. R. Taylor (2008). Effects of shock-induced tensile failure on m_b-M_S discrimination: Contrasts between historic nuclear explosions and the North Korean test of 9 October 2006, *Geophys. Res. Lett.* 35: L14301.

Patton, H. J. and I. N. Gupta (2009). Comments on "An upper bound on *Rg* to *Lg* scattering using modal energy conservation" by Stevens, J. L., H. Xu, and G. E. Baker, *Bull. Seismol. Soc. Am.* 99: 906–913, 2009, submitted to *Bull. Seismol. Soc. Am.* April.

Ringdal, F., P. D. Marshall, and R. W. Alewine (1992). Seismic yield determination of Soviet underground nuclear explosions at the Shagan River test site, *Geophys. J. Int.* 109: 65–77.

Rygg, E. (1979). Anomalous surface waves from underground explosions, *Bull. Seismol. Soc. Am.* 69: 1995–2002.

Stevens, J. L., H. Xu, and G. E. Baker (2009). An upper bound on *Rg* to *Lg* scattering using modal energy conservation, *Bull. Seismol. Soc. Am.* 99: 906–913.

REGIONAL PHASE ATTENUATION TOMOGRAPHY FOR CENTRAL AND EASTERN ASIA

W. Scott Phillips, Xiaoning Yang, George E. Randall, Hans E. Hartse, and Richard J. Stead

Los Alamos National Laboratory

Sponsored by the National Nuclear Security Administration

Award No. DE-AC52-06NA25396/LA09-IRP-NDD02

ABSTRACT

Broad area, network based, regional event identification and yield estimation depend on high frequency attenuation maps for direct phases and coda. The development of two-dimensional maps of attenuation has been an active area of research for two decades or more, but much of this effort has focused on *Lg* for bands near 1 Hz. For the past five years, event identification work at Los Alamos National Laboratory has been based on two-dimensional maps of 1-Hz *Pn*, *Pg*, *Sn*, and *Lg*, coupled with best fit, regionally uniform frequency dependence, while coda attenuation has been mapped in two-dimensions for multiple bands between 0.03 and 8 Hz. Recently, we have shown that USArray *Lg* amplitudes can be used effectively in joint inversion for attenuation and source parameters for bands 0.5–8 Hz. This inversion used source parameter constraints from an independent, relative coda study of the Wells, Nevada sequence by K. Mayeda and L. Malagnini to break the tradeoff between attenuation and corner frequency (or apparent stress). U.S.Array studies also showed that two-dimensional 1-Hz attenuation with uniform frequency dependence fits high frequency data relatively poorly. We currently seek to extend these techniques to central and eastern Asia. This area is covered by sparsely situated stations with long deployment histories, and by temporary arrays of high density but limited aperture. Coverage is good for all phases at 1 Hz for areas outside aseismic portions of the Siberian craton. At high frequencies, regional phases decay into noise more rapidly, and can be obscured by the coda of preceding phases. These limitations shrink coverage regions. However, coverage can be improved by extrapolation via the power-law frequency dependence of attenuation, and by joint inversion for multiple phase attenuation and source parameters, as the requirement for two or more observations per event per band can be relaxed. The 2-D attenuation maps improve discrimination power in intermediate bands (2-6 Hz), thus will help to lower discrimination thresholds in Asia.

For the *Pn* phase, standard power-law spreading yields unrealistic attenuation estimates for amplitudes beyond about 600 kilometers. Using data from central Asia stations MAKZ and WMQ, we find that the use of a power-law spreading model results in *Pn* MDAC residuals that exhibit a nonzero mean and a distance trend. To address these issues, we use a synthetic-simulation based frequency-dependent *Pn* geometric spreading model for a spherical Earth in our tomography to develop multi-frequency *Pn* attenuation models. We test a new MDAC formulation using these models, and find that residuals improve, exhibiting zero mean, lower variance, and distance independence.

OBJECTIVES

We are working to produce 2-D attenuation maps for regional phases and bands of interest to event identification, magnitude and yield estimation. Because magnitudes and yields are absolute estimates, proper path correction is critical. However, regional high frequency discriminants are formed by taking amplitude ratios, therefore reduction of variance depends on how weakly the laterally varying attenuation of the different phases is correlated. Our goal is to use 2-D techniques to enhance discrimination power in bands lower than the traditional bands such as 6–8 Hz, thus increasing the numbers of events that pass signal-to-noise criteria, and lowering the discrimination threshold (e.g. Phillips et al., 1998).

RESEARCH ACCOMPLISHED

Pn Geometric Spreading, Attenuation Tomography and MDAC Applications

We are developing two-dimensional (2D), multi-frequency, *Pn* attenuation models for Asia to be used in the Magnitude and Distance Amplitude Correction (MDAC) for improved path corrections. Path correction in MDAC is formulated as a combination of phase geometric spreading and apparent attenuation. For *Pn*, current MDAC implementation uses a power-law geometric-spreading model together with an attenuation term composed of a Q_0 at 1 Hz and its power-law frequency dependence. A uniform frequency dependency is assumed for the attenuation and Q_0 is obtained either as a constant (Taylor, et al., 2002; Walter and Taylor, 2002) or from tracing the ray through a 2D *Pn* Q_0 model (Walter and Taylor, 2002).

Although it is well established that *Pn* has a more complex spreading behavior in a spherical Earth than what a power-law model can describe (e.g., Sereno, 1990), a power-law spreading model is used both in the current MDAC and in developing the 2D *Pn* Q_0 model nevertheless. The use of a power-law *Pn* spreading model is not physically sound. Its use in MDAC also introduces undesirable amplitude-residual behavior such as a distance trend and a nonzero mean. To address this issue, we adopted a frequency-dependent *Pn* geometric-spreading model that is suitable for a spherical Earth (Yang, et al., 2007) in a new formulation of MDAC. The new *Pn* spreading model is expressed as

$$G(r,f) = \frac{10^{n_3(f)}}{r_0}\left(\frac{r_0}{r}\right)^{n_1(f)\log\left(\frac{r_0}{r}\right)+n_2(f)} \qquad (r_0 = 1 \text{ km}) \tag{1}$$

and

$$n_i(f) = n_{i1}\left[\log\left(\frac{f}{f_0}\right)\right]^2 + n_{i2}\log\left(\frac{f}{f_0}\right) + n_{i3} \qquad (i = 1, 2, 3; f_0 = 1 \text{ Hz}), \tag{2}$$

where r is epicentral distance in kilometers and f is frequency in Hz. Coefficients n_{ij} are listed in Table 1. Figure 1 illustrates the general behavior of the frequency-dependent *Pn* spreading model and that of a power-law model in comparison with observed *Pn* amplitudes. At short epicentral distances, the power-law model has a decay rate that is slower than the decay rate of the observed amplitudes. This does not contradict the physics since observed amplitudes are affected by both geometric spreading and medium attenuation and should decay faster. Toward long distances, however, the power-law model exhibits a decay rate that is either similar to or faster than that of the observed amplitudes. This is physically unreasonable and will result in unrealistically large or even negative attenuation estimates if amplitudes at long distances are used. The frequency-dependent spreading model, on the other hand, behaves much better and has a consistent slower decay rate than the decay rate of observed amplitudes toward long distances. Table 2 lists the average Q estimates at several frequencies obtained from observed amplitudes between 400 and 1750 km in Asia, using different spreading-model corrections. It confirms the observation made from Figure 1 that whereas the frequency-dependent spreading model yields reasonable Q estimates at all frequencies, Q estimates from using the power-law spreading model either is negative or seem to be too large.

Table 1. Coefficients of the frequency-dependent *Pn* geometric-spreading model

n_{11}	n_{12}	n_{13}	n_{21}	n_{22}	n_{23}	n_{31}	n_{32}	n_{33}
-0.217	1.79	3.16	-1.94	8.43	18.6	-3.39	9.94	20.7

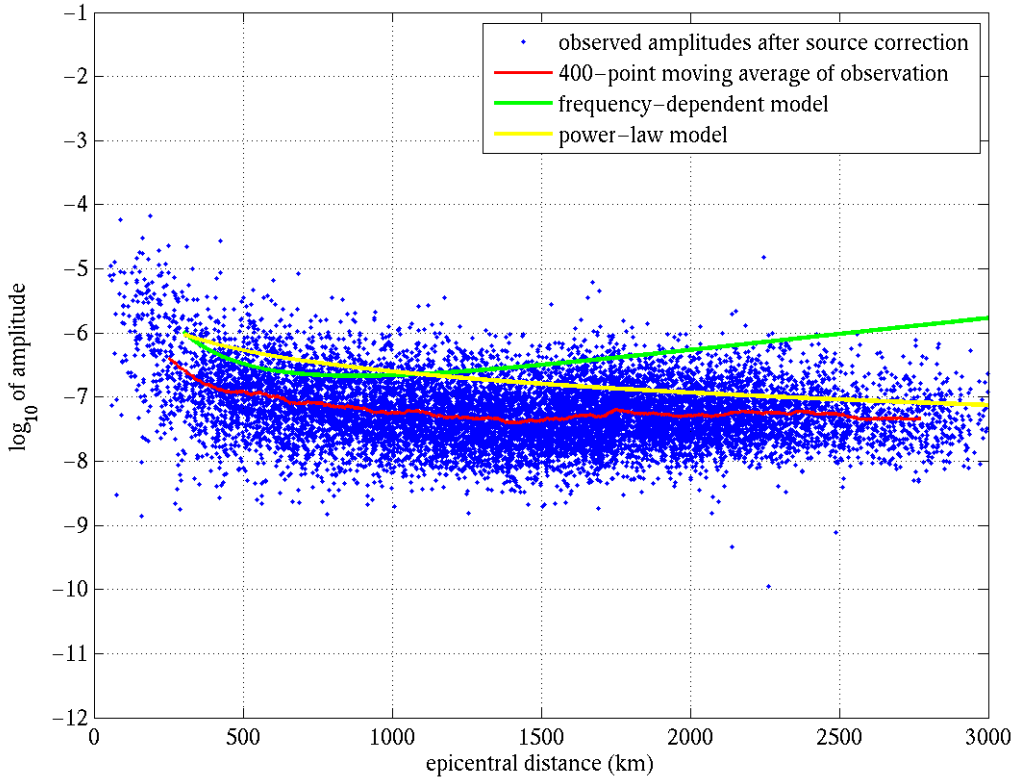

Figure 1. Distance-decay comparison between the frequency-dependent *Pn* spreading model, a power-law spreading model ($G = r^{-1.1}$) and observed 1-Hz *Pn* amplitudes after the source correction. The red line is the 400-point average of the observed amplitudes used to depict the decay of the amplitudes. Amplitudes beyond about 1750 km, where there is a change in the decay rate, are probably from reflections off of the 440-km and/or 610-km discontinuities.

Table 2 Average P_n Q estimated using different geometric-spreading models.

Model Type	1.0 Hz	2.0 Hz	4.0 Hz	6.0 Hz	8.0 Hz
Frequency Dependent	414	365	518	626	770
Power Law	-975	7930	9539	8975	21548

Incorporating the frequency-dependent *Pn* geometric-spreading model as the spreading constraint, we are developing 2D *Pn* attenuation models for Asia at 0.5, 1, 2, 4, 6, and 8 Hz through tomographic inversions. We apply a suite of criteria in selecting the data for the inversion. As an indication that *Pn* phase was well observed, we require that selected events have reported m_b magnitudes. We use a signal-to-noise ratio of 2 for amplitude cutoff. The epicentral distances must be in the range from 400 km to 1750 km. We also decluster events such that there is at most one event in any 1°-by-1° cell. Figure 2 shows our region of interest with event and station distributions for the data collection.

For the tomographic inversion, we discretize the region into 2°-by-2° cells. We use the frequency-dependent *Pn* spreading model to correct the amplitudes for geometric spreading before the inversion. We formulate the problem using Bayes' theorem (Tarantola, 1987), in which model parameters, including attenuation coefficients and source and receiver terms, are solved for with the constraint of *a priori* information. We use the average attenuation coefficients estimated from source- and spreading-corrected amplitudes as the *a priori* attenuation model. We use the scaling relationship of Xie and Patton (1999) between m_b and M_0 to convert m_b to *a priori* source terms. *A priori* receiver terms are set to zero.

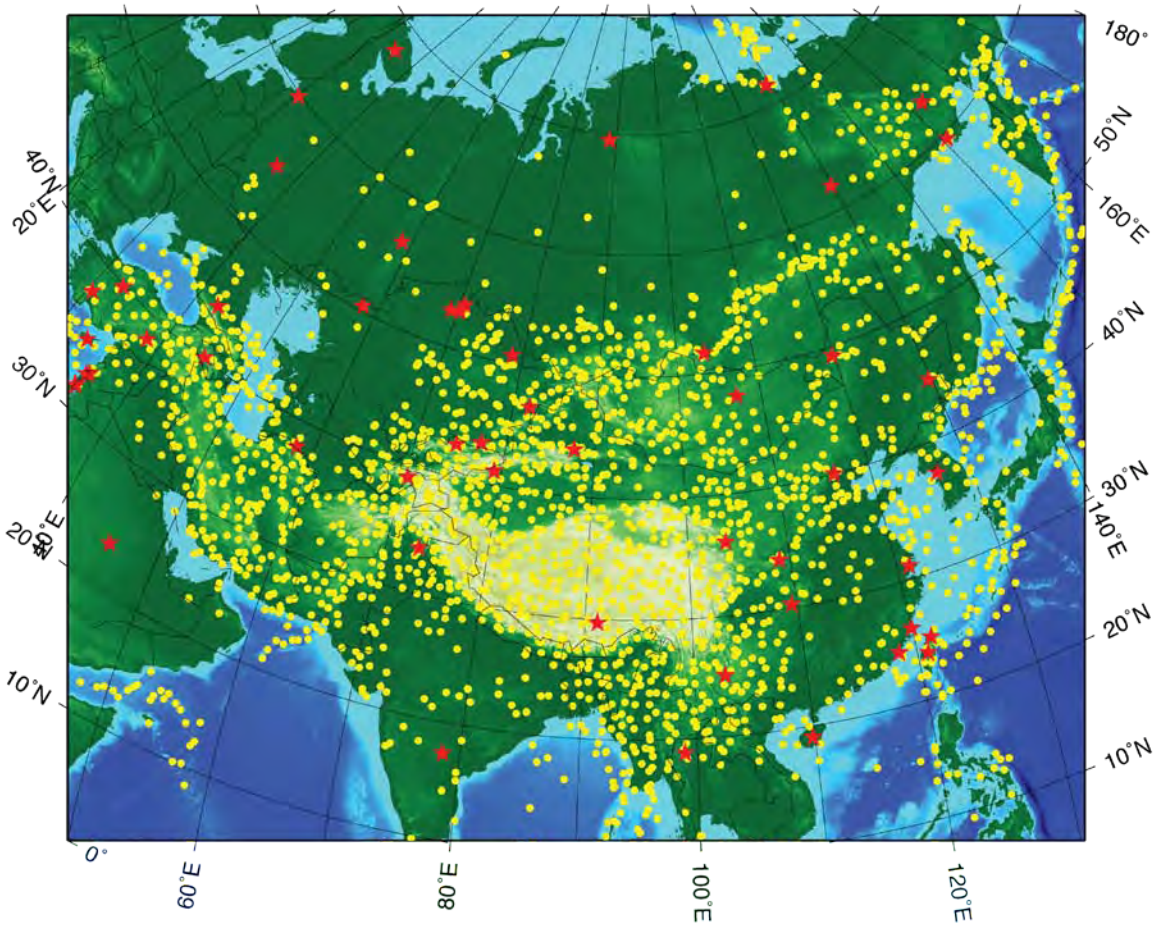

Figure 2. Event (yellow dots) and station (red stars) distributions.

Figure 3 shows the preliminary *Pn* Q maps from the inversion at 0.5, 1, 4 and 8 Hz. *Pn* Qs are obtained from inverted attenuation coefficient γ using the relationship

$$Q = \frac{\pi f}{v\gamma} \qquad (3)$$

where f is frequency and v = 8 km/s is *Pn* velocity. At 0.5 Hz, *Pn* attenuation pattern is relatively smooth with low attenuations seen in the Tarim basin and at the western tip of the Tibetan plateau. Other regions of relatively low attenuation include areas to the west of the Zagros Mountains, south of the eastern Himalayan syntaxis, the Bohai Sea and the Sichuan basin. High attenuation is seen in western Tian Shan and along the western Pacific subduction zones. At 1 Hz, the high attenuation feature in western Tian Shan as well as the low attenuation feature in the Sichuan basin becomes more prominent. The attenuation in the Tibetan plateau and in Zagros Mountains becomes high. Figure 3 shows that attenuation at higher frequencies is more variable for different regions. We see strong contrast of attenuation between high attenuation in western Tian Shan, the Tibetan plateau and the eastern Himalayan syntaxis and low attenuation in the western tip of the Tibetan plateau and the Sichuan basin in the 4-Hz Q map. In the 8-Hz map, the largest contrast is between low attenuation in the Tibetan plateau and high attenuation to the north. The 8-Hz map also illustrates the much-reduced coverage of high-frequency amplitudes.

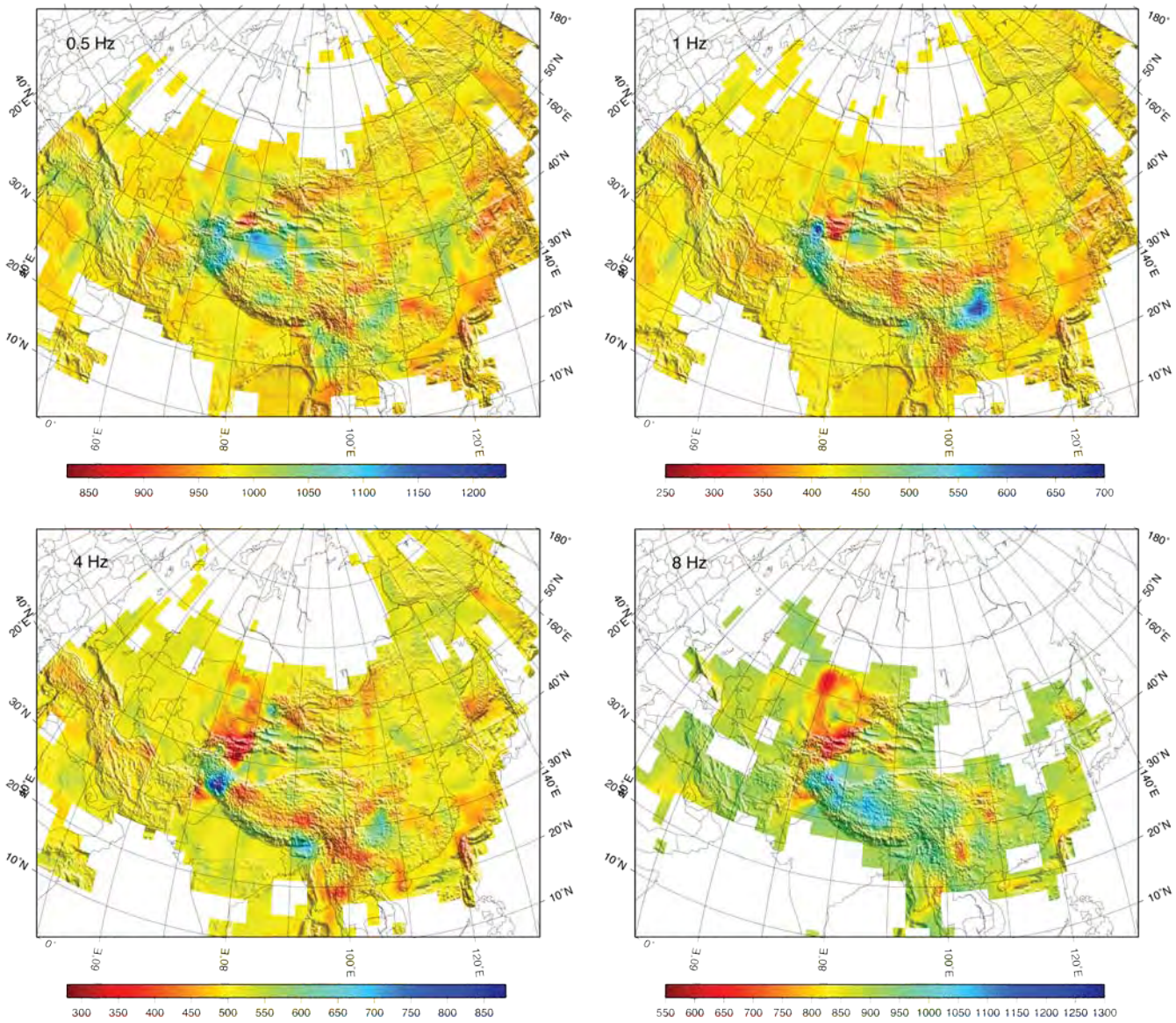

Figure 3. *Pn* tomographic Q maps at 0.5, 1, 4 and 8 Hz.

The frequency-dependent *Pn* spreading model, together with the 2D multi-frequency *Pn* attenuation models that we are developing, provide much improved path corrections to MDAC. Figure 4 gives an example of MDAC amplitude residuals for station WMQ in central Asia after different path corrections. Even though the *Pn* tomographic attenuation models used are preliminary, we already see promising results in their MDAC application to reduce residual variance, nonzero offset and distance trend.

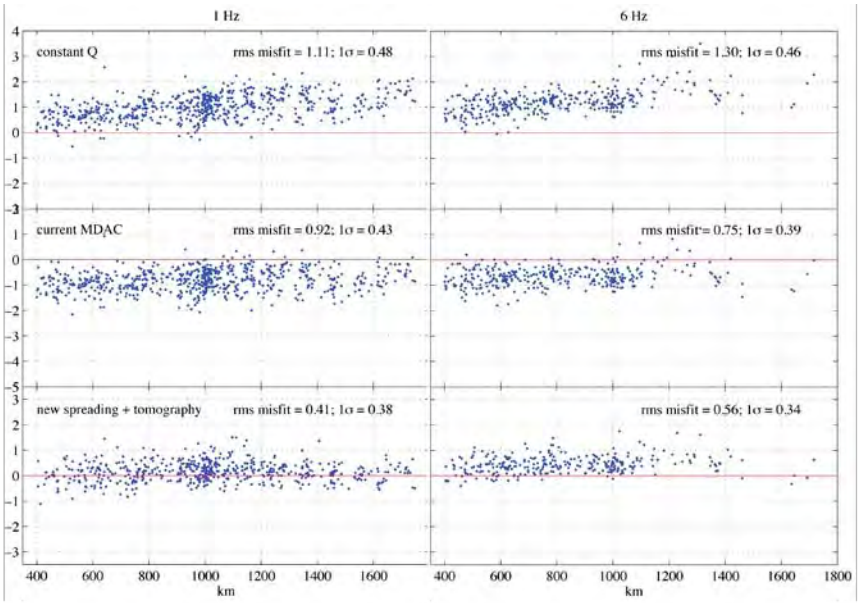

Figure 4. 1- and 6-Hz MDAC residuals for station WMQ in central Asia after different path corrections. The two top panels plot the MDAC residuals after the path correction with a constant Q. The middle panels are current MDAC residuals in which a 2D *Pn* Q_0 map and its uniform frequency dependency is employed for the path correction. In both cases, a power-law spreading model is used. The frequency-dependent *Pn* spreading model and the preliminary 2D *Pn* tomographic attenuation models are used to calculate MDAC residuals plotted in the two bottom panels. The 1σ, or 1 standard deviation, represents the variation of the residuals about the mean. The rms misfit includes both the effect of residual variance and the effect of deviation of residuals from zero such as nonzero offset and distance trend.

Lg, *Sn* and *Pg* amplitude tomography, and *Pg/Lg* discrimination enhancement

We apply standard amplitude tomography techniques (e.g., Phillips and Stead, 2008) to *Lg*, *Sn*, and *Pg* data to create 2-D attenuation maps for bands 0.5–10 Hz across Asia (Figures 5-7). Amplitudes were required to pass a pre-*Pn* signal-to-noise cut of 2.0 and a pre-phase cut of 1.0. In addition, we set critical distances for each station, fit a 1-D Q model to source (*mb*) corrected amplitudes below that distance, and discarded amplitudes beyond that distance that exceeded the model fit by more than 0.5 log10 units. This step eliminated coda measurements that passed our signal-to-noise tests. We also estimated and removed relative channel site effects, as many stations include borehole and surface recordings. We assumed Street et al. (1975) type spreading with 0.5 and 0.7 distance decay starting at 100 km for *Lg* and *Pg*, respectively; and a 1.1 distance decay for *Sn*, starting at 1 km.

The resulting attenuation maps show correlation with regional geology, as has been seen by previous studies in this area (e.g. Jin and Aki, 1988; Mitchell et al., 1997; Taylor et al., 2003; Phillips et al., 2000ab, 2005; Xie et al., 2006; Pei et al., 2006). *Lg* Q is high in stable regions and low in tectonic regions. The maps resolve smaller, high Q, stable blocks such as the Sichuan, Tarim, Tsaidam, Turfan, Amu-Darya and Ordos basins, the Hinggan and Dabie ranges, and the Taishan-Shandong highlands, as well as the larger Siberian cratons, Indian shield, and Kazakh and Guangxi platforms. Further, the maps resolve small low Q regions such as the western Tian Shan, Qilian Shan, southern and eastern boundaries of the Ordos and Sichuan basins, respectively, the Bohai and nearby basins, including the Dongting and Songliao basins, the Baikal Rift, and the Zyrvanka and Lena-Vilyuy basins in Siberia, as well as the broad low Q areas of Tethys convergence including the Tibet-Qinghai region. *Sn* results show smoother patterns that roughly correlate with *Lg*, but with pronounced low Q anomalies in areas such as the Baikal Rift and the Shanxi graben, and across Mongolia for the higher bands. In addition, the Sichuan basin anomaly is shifted slightly to the south, and we see higher Q in southern Tibet, presumably where mantle raypaths sample shield materials. *Pg* also shows rough correlation, but with areas such as southern Tibet again higher Q than for *Lg*. RMS residuals for 1-D

plus variable site, versus full 2-D inversions are shown in Figure 8. We see that *Lg* amplitudes are best fit by the inversion, followed by *Sn*, *Pg*, and *Pn* (power law spreading 1.1) in that order.

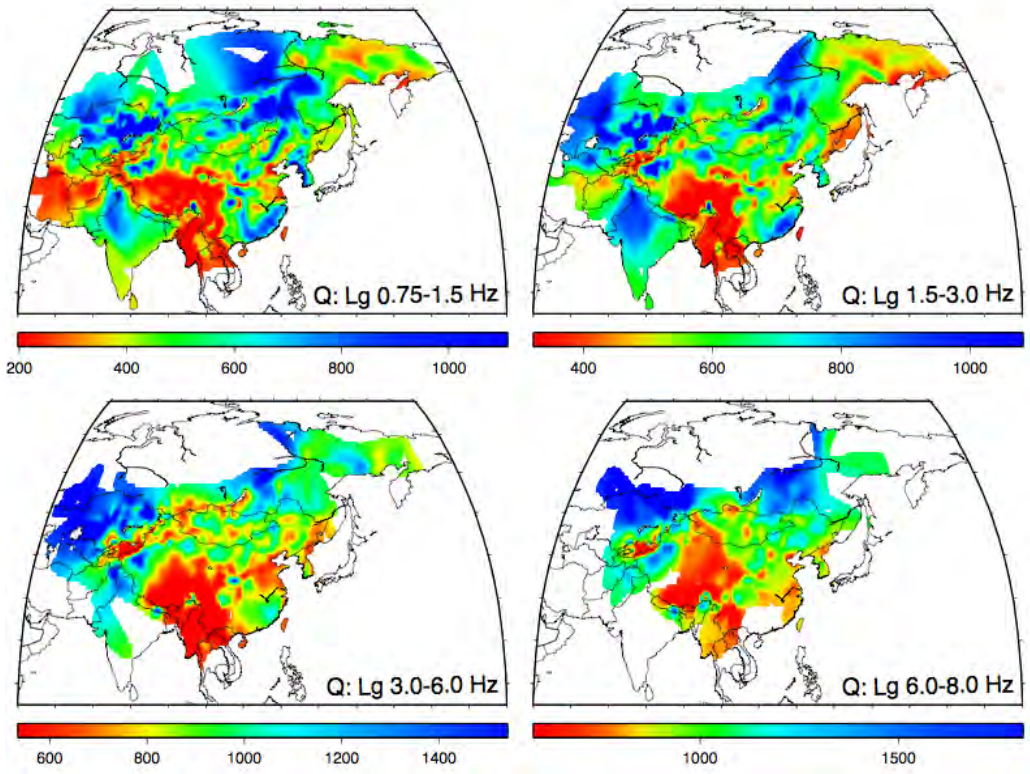

Figure 5. *Lg* attenuation for four bands, as annotated.

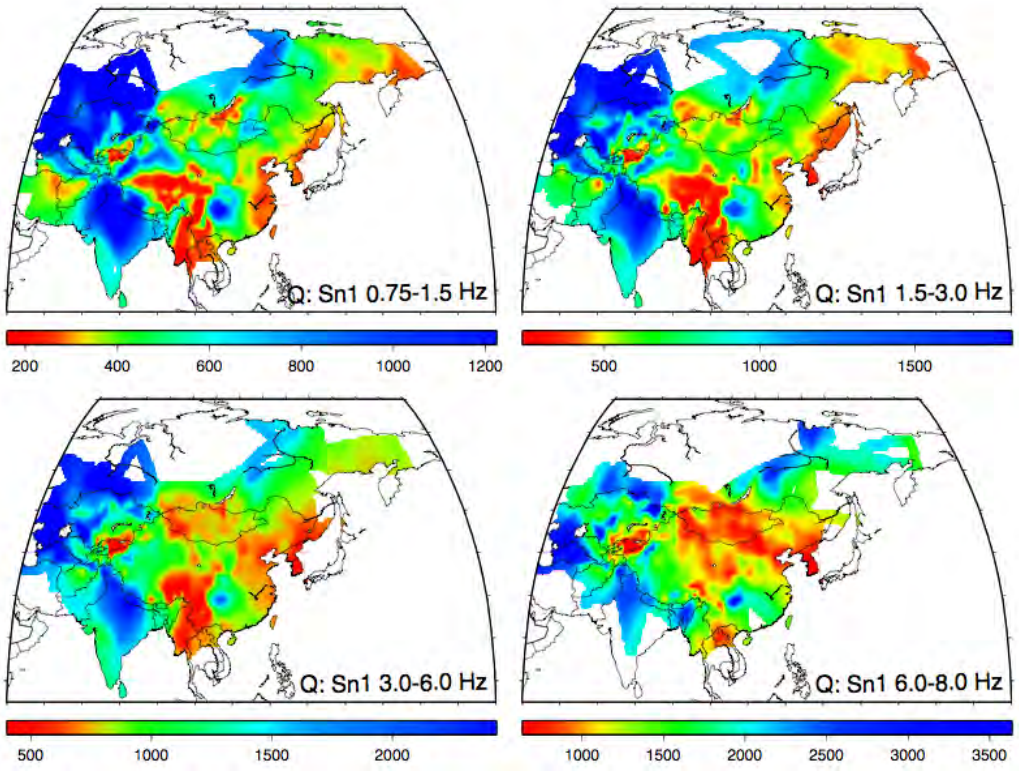

Figure 6. *Sn* attenuation for four bands.

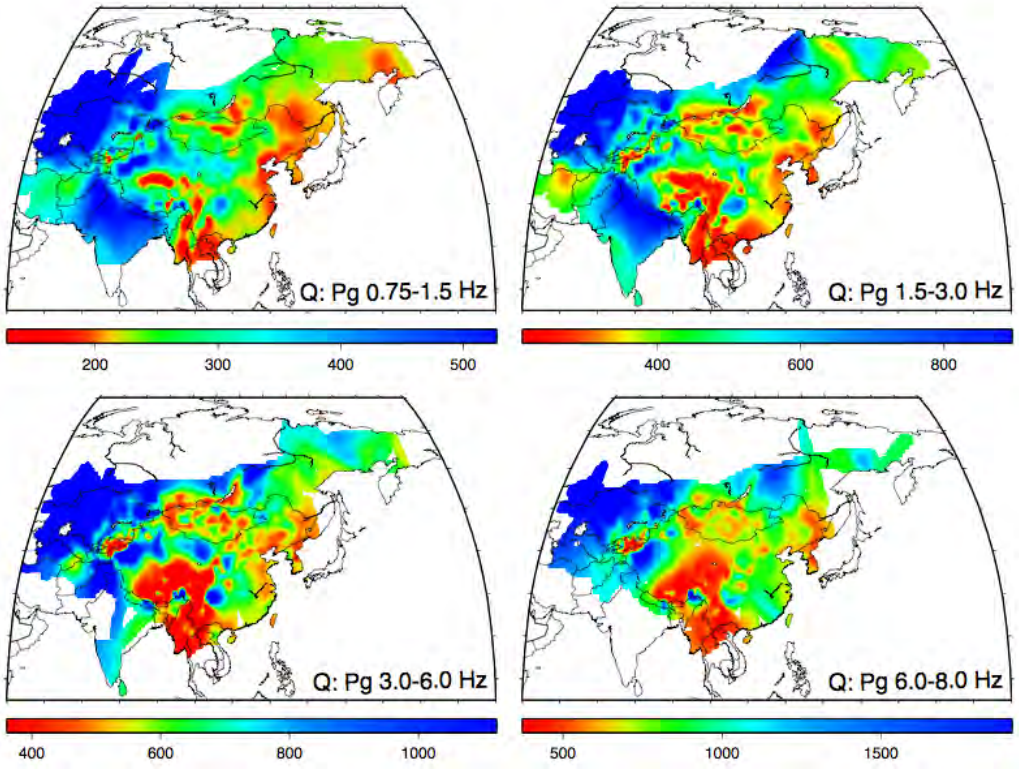

Figure 7. *Pg* attenuation for four bands.

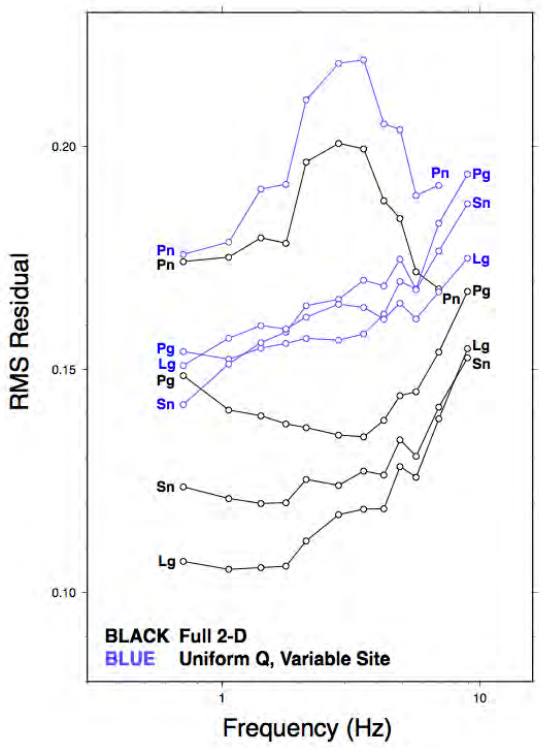

Figure 8. RMS residuals (log10 amplitude ratio) versus frequency for four phase types, including *Pn* based on a power law 1.1 spreading model (2-D not shown).

In spite of the rough correlation between maps, we expect some variance reduction in discriminant ratios because inversions for relative attenuation, based on *Pg*/*Lg* ratios, show significant lateral variation in this region (Phillips et al., 2000b). Indeed, forming *Pg*/*Lg* ratios for all bands gives us discrimination plots that include a number of nuclear and chemical explosions, as well as 10,000 reviewed earthquakes across the study area. The discriminants were combined across the network by averaging corrected phase amplitudes prior to taking ratios, thus, phase amplitudes could be contributed by different station groups for a given event. The 2-D maps have little effect on discrimination at 6–8 Hz, where discrimination is known to perform well with 1-D corrections, and little effect in lower bands (1 Hz), where discrimination is known to perform poorly, even though scatter is reduced substantially; however, the improvement in intermediate bands is very encouraging, as equiprobable estimates decrease from 15% and 12% to 4% for the 3–6-Hz band, and from 23% and 17% to 9% for the 2–4-Hz band (Figure 9), where the first value is for pure 1-D correction (based on a best fit uniform model), the second is for 1-D with variable site terms, and the third is for full 2-D with variable site terms.

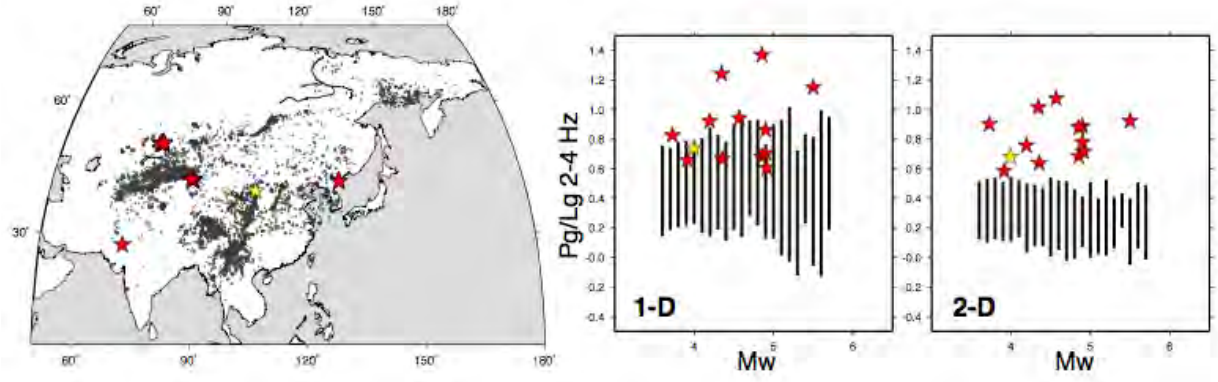

Figure 9. Network *Pg*/*Lg* discriminant ratios vs. Mw (explosions fit with an earthquake model) for the 2-4 Hz band. Red stars represent Asia nuclear explosions (7 Lop Nor, 2 Semipalatinsk, 2 DPRK, 1 India), the yellow star represents the 12/20/07 Chinese mountaintop HE blast, and vertical bars represent 1-sigma scatter of the earthquake population (shown in map as dark gray dots). The two right-hand panels are for pure 1-D, and full 2-D with site terms, as noted. Although descriminants are formed from a mix of data used in, and left out of the inversions, this is not a strict cross-validated comparison.

CONCLUSIONS AND RECOMMENDATION

We are currently perfecting our *Pn* tomographic inversions by testing different hypotheses and techniques, such as the uniqueness of the inversion results, the optimal construction of the a priori model, and the selection of best damping and smoothing and regularization parameters. We have seen that tomographic models enhance discrimination power for *Pg*/*Lg* in intermediate range bands, and expect to extend these results to ratios involving *Pn*, once those issues are resolved. The enhancement of intermediate band discriminants will help to lower the discrimination threshold.

REFERENCES

Jin, A. and K. Aki (1988), Spatial and temporal correlation between coda-Q and seismicity in China, *Bull. Seismol. Soc. Am*. 78: 741–769.

Mitchell, B. J., Y. Pan, J. Xu, and L. Cong (1997). *Lg* coda Q variation across Eurasia and its relation to crustal evolution, *J. Geophys. Res*. 102: 11767–22779.

Pei, S., J. Zhao, C. A. Rowe, S. Wang, T. M. Hearn, Z. Xu, H. Liu, and Y. Sun (2006). M_L amplitude tomography in North China, *Bull. Seism. Soc. Am.* 96: 1560–1566, doi: 10.1785/0120060021.

Phillips, W. S., G. E. Randall, and S. R. Taylor (1998). Path correction using interpolated amplitude residuals: An example from central China, *Geophys. Res. Lett*. 25: 2729–2732.

Phillips, W. S., H. E. Hartse, S. R. Taylor and G. E. Randall (2000a). 1 Hz *Lg* Q Tomography in central Asia, *Geophys. Res. Let*t. 27: 3425–3428.

Phillips, W. S., H. E. Hartse, S. R. Taylor, A. A. Velasco, and G. E. Randall (2000b). Application of regional phase amplitude tomography to seismic verification, *PAGEOPH* 158: 1189–1206.

Phillips, W. S., H. E. Hartse, and J. T. Rutledge (2005). Amplitude ratio tomography for regional phase Q, *Geophys. Res. Lett*. 32: doi:10.1029/2005GL023870.

Phillips, W. S. and R. J. Stead (2008). Attenuation of *Lg* in the western US using the USArray, *Geophys. Res. Lett*. 35: L07307, doi:10.1029/2007GL032926.

Sereno, T. J. and J. W. Given (1990). *Pn* attenuation for a spherically symmetric Earth model, *Geophys. Res. Lett.* 17: 8, 1141–1144.

Street, R. L., R. Herrmann, and O. Nuttli (1975). Spectral characteristics of the *Lg* wave generated by central United States earthquakes, *Geophys. J. R. Astr. Soc.* 41: 51–63.

Tarantola, A. (1987). *Inverse Problem Theory*, Elsevier Science B. V., Amsterdam.

Taylor, S. R., A. A. Velasco, H. E. Hartse, W. S. Phillips, W. R. Walter, and A. J. Rodgers (2002). Amplitude corrections for regional seismic discriminants, *Pure Appl. Geophys.* 159: 623–650.

Taylor, S.R., X. Yang and W.S. Phillips (2003). Bayesian *Lg* attenuation tomography applied to eastern Asia, *Bull. Seism. Soc. Am*. 93: 795–803.

Walter, W. R. and S. R. Taylor (2002). A revised magnitude and distance amplitude correction (MDAC2) procedure for regional seismic discriminantes: theory and testing at NTS, Lawrence Livermore National Laboratory, UCRL-ID-146882, pp. 13.

Yang, X., T. Lay, X.-B. Xie, and M. S. Thorne (2007). Geometric spreading of *Pn* and *Sn* in a spherical Earth model, *Bull. Seism. Soc. Am.* 97: 6, 2053–2065.

Xie, J. and H. J. Patton (1999). Regional phase excitation and propagation in the Lop Nor region of central Asia and implications for P/*Lg* discriminants, *J. Geophys. Res.* 104: B1, 941–954.

Xie, J. K., Z. Wu, R. Liu, D. Schaff, Y. Liu, and J. Liang (2006). Tomographic regionalization of crustal *Lg* Q in eastern Eurasia, *Geophys. Res. Lett*. 33: L03315, doi:10.1029/2005GL024410.

TOWARD END-TO-END SEISMIC SIMULATIONS FOR NUCLEAR EXPLOSION MONITORING

Arthur J. Rodgers[1], Oleg Y. Vorobiev[2], N. Anders Petersson[3], Bjorn A. Sjogreen[3], and Megan Avants[1]

Lawrence Livermore National Laboratory[1], Computational Geosciences Group[2], and
the Center for Advanced Scientific Computing[3]

Sponsored by the National Nuclear Security Administration

Award No. DE-AC52-07NA27344/LL09-Simulation-NDD02

ABSTRACT

This paper describes new research being performed to improve understanding of seismic waves generated by underground nuclear explosions (UNE) by using full waveform simulation, high-performance computing and three-dimensional (3D) earth models. The goal of this effort is to develop an end-to-end modeling capability to cover the range of wave propagation required for nuclear explosion monitoring (NEM) from the buried nuclear device to the seismic sensor. The goal of this work is to improve understanding of the physical basis and prediction capabilities of seismic observables for NEM including source and path-propagation effects. We are pursuing research along three main thrusts. Firstly, we are modeling the non-linear hydrodynamic response of geologic materials to underground explosions in order to better understand how source emplacement conditions impact the seismic waves that emerge from the source region and are ultimately observed hundreds or thousands of kilometers away. Empirical evidence shows that the amplitudes and frequency content of seismic waves at all distances are strongly impacted by the physical properties of the source region (e.g., density, strength, porosity). To model the near-source shock-wave motions of an UNE, we use GEODYN, an Eulerian Godunov (finite volume) code incorporating thermodynamically consistent non-linear constitutive relations, including cavity formation, yielding, porous compaction, tensile failure, bulking and damage. In order to propagate motions to seismic distances we are developing a one-way coupling method to pass motions to WPP (a Cartesian anelastic finite difference code). Preliminary investigations of UNE's in canonical materials (granite, tuff and alluvium) confirm that emplacement conditions have a strong effect on seismic amplitudes and the generation of shear waves.

Specifically, we find that motions from an explosion in high-strength, low-porosity granite have high compressional wave amplitudes and weak shear waves, while an explosion in low strength, high-porosity alluvium results in much weaker compressional waves and low-frequency compressional and shear waves of nearly equal amplitude. Further work will attempt to model available near-field seismic data from explosions conducted at the Nevada Test Site (NTS), where we have accurate characterization of the sub-surface from the wealth of geological and geophysical data from the former nuclear test program. Secondly, we are modeling seismic wave propagation with free-surface topography in WPP. We have modeled the October 9, 2006, and May 25, 2009, North Korean nuclear tests to investigate the impact of rugged topography on seismic waves. Preliminary results indicate that the topographic relief causes complexity in the direct *P* -waves that leads to azimuthally dependent behavior and the topographic gradient to the northeast, east and southeast of the presumed test locations generate stronger shear-waves, although each test gives a different pattern. Thirdly, we are modeling intermediate period motions (10–50 seconds) from earthquakes and explosions at regional distances. For these simulations we run SPECFEM3D_GLOBE (a spherical geometry spectral element code). We modeled broadband waveforms from well-characterized and well-observed events in the Middle East and central Asia, as well as the North Korean nuclear tests. For the recent North Korean test we found that the one-dimensional iasp91 model predicts the observed waveforms quite well in the band 20–50 seconds, while waveform fits for available 3D earth models are generally poor, with some exceptions. Interestingly 3D models can predict energy on the transverse component for an isotropic source presumably due to surface wave mode conversion and/or multipathing.

OBJECTIVES

Advances in numerical methods, improvements in the power and availability of high-performance computing and improved data and methods to estimate three-dimensional (3D) earth models for wave propagation makes it possible to simulate seismic waves with resolution relevant to NEM. This effort seeks to realize the goal of end-to-end simulation of seismic waves from UNE's. Specifically we are working to apply numerical methods for wave propagation to enable simulation of seismic waves from the near-source (shock wave) regime, through the heterogeneous earth to the seismic sensor. The ultimate goal of this research is to improve estimates of explosion size and confidence in source type discrimination by using simulations of seismic waveforms and observables and their uncertainties including both source and path propagation effects. Applications include post-event analysis and predictions for possible future nuclear tests in regions where little or no empirical data are available.

The three thrusts of this study are aimed to address one or more challenges of NEM. Shock wave modeling aims to improve understanding of the effects of emplacement conditions on yield and source-type estimates. Elastic modeling in the presence of surface topography aims improve understanding of how rough topography distorts *P*- and excites *S*-waves (body and surface waves) emerging from shallow explosions to improve prediction of amplitude and *P*-to-*S* partitioning. Finally, intermediate-period regional-complete waveform modeling aims to improve prediction of waveforms and understanding of the biases in source estimates due to path propagation effects.

RESEARCH ACCOMPLISHED

This paper describes several ongoing efforts that are unified in their goal of developing an end-to-end (device-to-detector) capability for modeling seismic waves from UNE's. Simulation of seismic waves from UNE's requires modeling the behavior of earth materials in different regimes. Hydrodynamic methods must be employed to model the shock wave emerging from the device and propagating to distances beyond which the motions are elastic. These methods are computational expensive and require very fine spatial and temporal discretization. This is contrasted by the fact that weakly anelastic propagation methods are computationally more efficient than (non-linear) hydrodynamic methods and are appropriate for most of the path-length. A common theme is that the numerical methods used for modeling wave propagation must rely on high-performance computing to realize simulations to the distances (computational domain size) and desired resolution (i.e., target frequencies and wavelengths of NEM). Furthermore, methods must be general enough to simulate wave propagation in realistic 3D earth models, where material properties vary in each spatial dimension possibly across a broad spectrum of wavelengths. In this paper we report progress along three thrusts: 1) modeling the near-source region of a UNE with emphasis on the hydrodynamic response of geologic media and propagation to seismic distances; 2) modeling of anelastic wave propagation in the presence of free-surface topography; and 3) modeling of intermediate period (10–50 seconds) complete waveforms at regional distances.

Modeling Shock Waves Generated by UNE's and Coupling GEODYN to WPP

We are modeling shock wave propagation in the near-source region with GEODYN, an Eulerian Godunov (finite volume) code incorporating thermodynamically consistent non-linear constitutive relations, including cavity formation, yielding, porous compaction, tensile failure, bulking and damage (Antoun et al., 2001; Antoun and Lomov, 2003; Lomov et al., 2003). This code models the high energy density region near the source and the propagation of the shock wave into the weakly anelastic regime. We validated the code and our material models by comparing the simulation results against available experimental data. In order to propagate motions to seismic distances we are developing a one-way coupling method to pass motions to WPP, a Cartesian anelastic finite difference code developed at LLNL (Nilsson et al., 2007).

Preliminary investigations of UNE's in canonical materials confirm that emplacement conditions have a strong effect on seismic amplitudes and on the generation of shear waves. Figure 1a shows peak velocities (data points) as a function of scaled distance for UNE's for granite, tuff and alluvium as reported by Perret and Bass (1974). Also shown are peak velocities from GEODYN simulations (solid lines). The scaled range is taken as the slant distance divided by the explosive yield to the 1/3 power. Note that the peak velocities are largest for granite, then tuff, then alluvium and the scaled range extends beyond the nominal elastic radius. The differences between peak motions for different materials at a given scaled distance are quite significant, up a factor of ten. While there is scatter in the observational data and the granite data do not span a large range, the simulations provide a reasonably good fit to the

experimental data. This gives us confidence that GEODYN simulations and our material models can accurately model near-source motions in the regions of both non-linear and linear behavior.

In another more specific validation exercise we compared peak displacements from a series of chemical high-explosive (HE) experiments in limestone performed in Kirghizia in 1960 (Murphy et al., 1997). The generic strength model described in Vorobiev (2008) was used in GEODYN to model limestone with 0.5% porosity. In situ experimental measurements of ground motion at different distances from the shot point were reported by Murphy et al. (1997). The explosions and motion recordings reported in this study were conducted in the subsurface in essentially rock whole-space conditions, making them ideal for our simulation validation experiments.

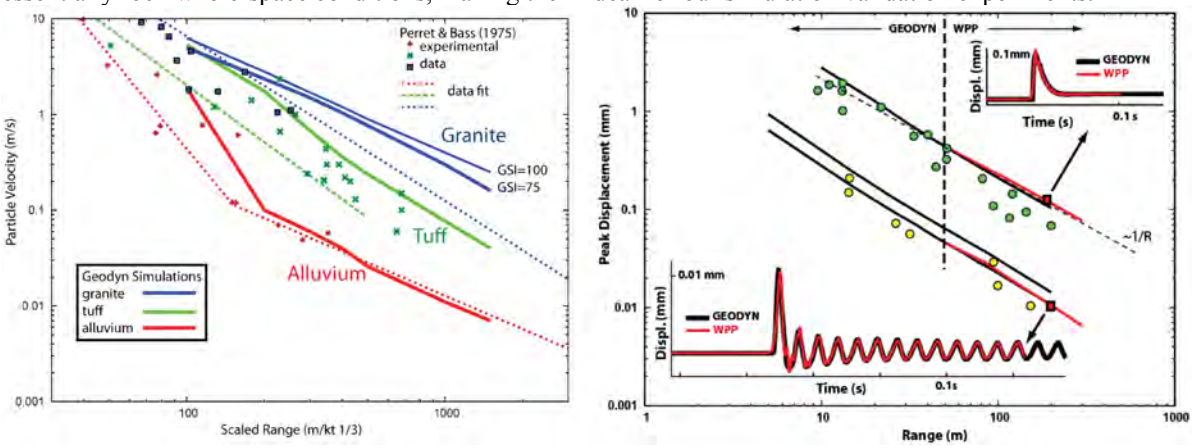

Figure 1. (a, left) Peak velocities as a function of scaled distance for UNE's in granite (blue), tuff (green) and alluvium (red). The symbols indicate observed values from Perret and Bass (1974) and the solid lines are from GEODYN simulations. (b, right) Peak displacements as a function of range for experimental data (circles) from Murphy et al., (1997) and GEODYN calculations (black line). Also shown are the displacement time-histories (inset plots) from GEODYN (black lines) and from the one-way code coupling approach where motions were passed from GEODYN to WPP (red lines), propagated with both codes and compared at 200 m range (red square).

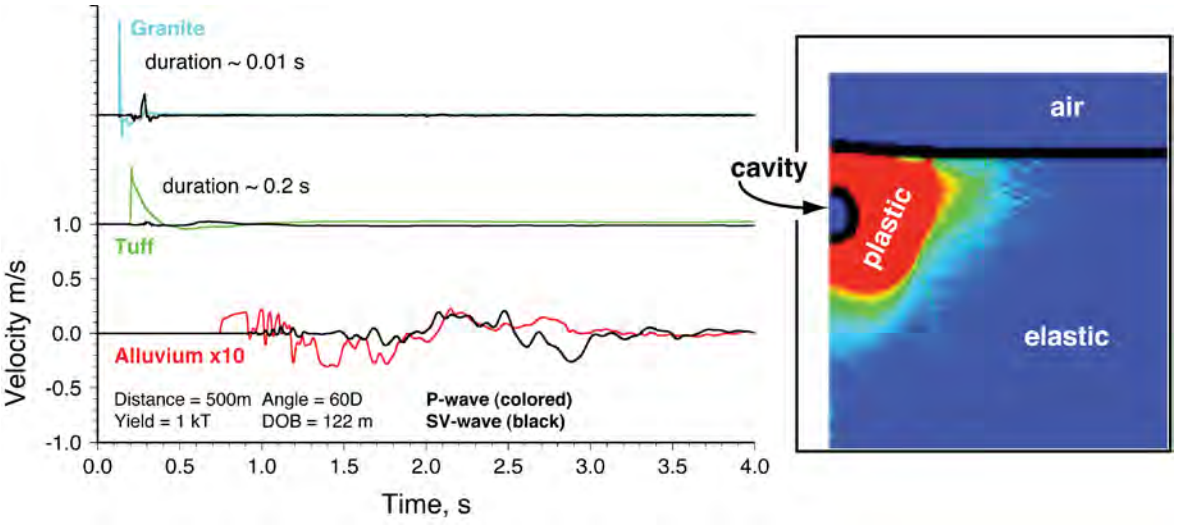

Figure 2. (a, left) *P* -wave velocity time-histories for 1 kT chemical explosions in granite (cyan), tuff (green) and alluvium (red). The corresponding SV-wave time-histories (black) on the same scale as the *P* -wave motions. Note that motions in alluvium are amplified by a factor of ten. (b, right) Post-event strain field for a 1 kT chemical explosion in granite at a normal scaled depth-of-burial (122 m): the inner circle indicates the cavity; red values indicate strains greater then 10^{-6}; and darkest blue outside the cavity corresponds to elastic motions.

We performed a series of GEODYN simulations to investigate the effects of explosion emplacement conditions on ground motions. The simulations were performed in two-dimensions using a uniform solid material (granite, tuff or alluvium) overlain by air. We sampled the wavefield time-histories at a number of points and decomposed the motions into radial (*P*-wave) and vertically polarized transverse (SV-wave) motions. Figure 2a shows the decomposed velocity time-histories at a range of 500 m from the shot point (in the elastic region) at an angle of 60° from the vertical, corresponding to a teleseismic take-off angle. *P*- and SV-wave motions are shown together as colored and black seismograms, respectively. Notice the great difference in the arrival time, pulse duration and *P*-to-SV energy partitioning for the different materials. The shot in granite results in a fast arriving wave with very sort duration (~0.01 s) while the shot in tuff arrives later with a longer duration (~0.2 s). The shot in alluvium results in much weaker motions (shown amplified by a factor of ten in Figure 2a) with more complexity and longer duration than the other materials. The differences in *P* -wave pulse width are also reflected in corner frequencies of amplitude spectra (not shown). Also note the differences in the relative *P* - and SV-wave amplitudes. The shot in alluvium generates 1 Hz *P* - and SV-wave energy of roughly equal amplitude. These differences in *P* - and SV-wave spectral amplitudes result in very different high-frequency *P* /*S* amplitude ratios used for event identification. Preliminary results (not shown) indicate simulated cross-spectral ratios (high-frequency *P* / low-frequency *S*) are consistent with observations from the NTS reported by Walter et al. (1995).

Similar to many other numerical methods for wave propagation, GEODYN allows us to sample the strains and record the peak strain at all points in the computational domain. Figure 2b shows the peak strain around the shot point for a 1 kT chemical shot in granite at the normal scaled depth-of-burial (122 m). The cavity is formed around the shot point and indicated by the inner semi-circle. Colors show the strain with red colors corresponding to plastic strains of 10^{-6} or greater and the darkest blue outside the cavity corresponding to elastic strains. Self-affine properties of the material strength causes the asymmetric pattern of strains (yellow to cyan colors) due to fracture.

In order to simulate seismic ground motions to distances where observations are typically made (> 1 km), we are coupling motions from GEODYN to our anelastic wave propagation code, WPP. This is a one-way coupling where we compute the response of the material in the non-linear regime through to the elastic regime. Motions are saved on a dense grid of points on the faces of a cube and passed to WPP as forcing on an internal surface. Figure 1b shows the results of modeling the experimental data in Murphy et al. (1997) for small chemical explosions in a limestone whole-space. Here we have passed the motions from GEODYN to WPP at a distance of 40 m and propagated motions in both codes to 200-300 m. The GEODYN calculation is extended into the linear elastic regime and results indicate that the peak displacements from both codes match the amplitudes versus range perfectly. Furthermore, the time-histories agree nearly perfectly indicating that numerical artifacts due to interpolation or grid dispersion are minimal. We are currently operationalizing this process to enable routine modeling of seismic motions to seismic distances.

Modeling the Effect of Topography on Seismic Waves from the 2006 and 2009 North Korean Nuclear Tests

We have developed and implemented a method to model free-surface topography with WPP. The rough surface is handled with a conforming grid that follows the topography above some depth, below which the usual Cartesian grid with mesh refinement is used. We have validated our implementation of topography in WPP with canonical solutions as well as compared motions from different implementations (e.g., finite element, hybrid finite element/finite difference) for earthquake scenarios in the San Francisco Bay Area (Aagaard et al., 2009). Note that WPP is open source and available at https://computation.llnl.gov/casc/serpentine/index.html.

The recent nuclear tests in North Korea provide a ready application for the investigation of the effects of topography on ground motions. We performed simulations of explosions on a 40-km domain around the test site. Figure 3a shows the topographic relief, estimated shot locations and computational domain (white outline). The depth of the shots was taken to be 600 m below the local topography of each event and an isotropic source was used. Note that the relief varies greatly near the shot points. The calculations used a purely elastic homogenous material model (v_P = 5810 m/s, v_S = 3350 m/s and ρ = 2660 kg-m/s). We show results from calculations with a grid spacing of 50 meters resolving motions above 4 Hz.

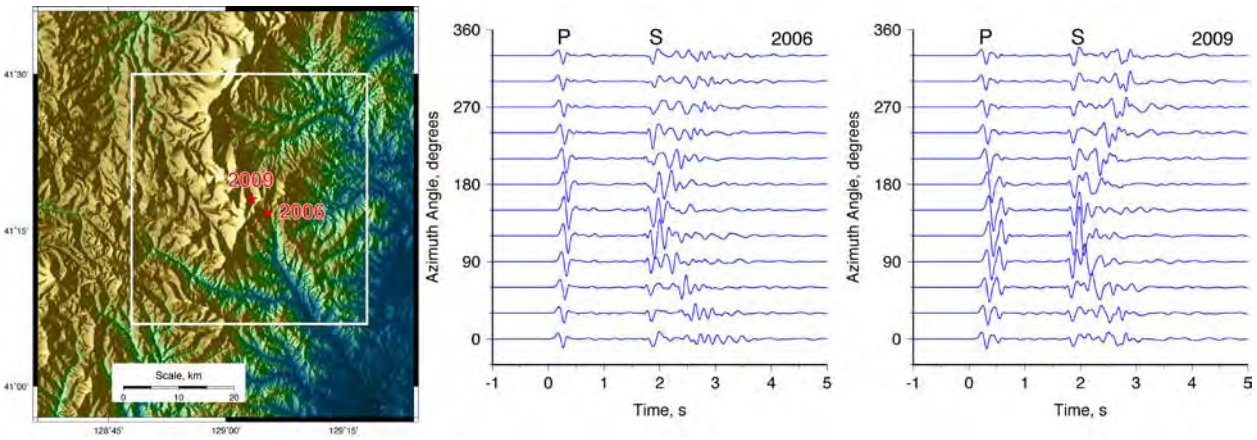

Figure 3. (a, left) Topographic relief in and around the North Korean nuclear test site along with locations of the 2006 and 2009 explosions. Also shown is the computation grid for WPP simulations with topography (white box). (b, center) Vertical displacement motions (down positive) aligned on the *P* -wave for locations below the 2006 explosion (60° from the vertical). (c, right) Same as (b) but for the 2009 explosion.

Figures 3b and 3c show the vertical displacement motions (down positive) below the 2006 and 2009 explosions at locations distributed azimuthally around the shot point at a take-off angle of 60° from the vertical corresponding to teleseismic *P* - and *S*-waves. The timing and particle motions of the time-histories clearly indicate the *P* - and *S*-wave packets marked in the figure. Note that the initial *P* -wave is different in character for the 2006 and 2009 events, with the 2006 event showing a simple compression and dilatation, while the *P* -waves from the 2009 event show a large amplitude compression following the initial compression-dilatation whose amplitudes are particularly strong at azimuths of 30°-150°. Both shots show strong azimuthal variations with the largest *P* - and *S*-wave amplitudes at azimuths of 90°-180°. Because the material model was homogeneous and the sources were identical, the differences in wave propagation behavior can only be attributed to interaction of the wavefield with the free surface and its variation for the different shot points. The variation in response is not surprising however given that the topography varies significantly on scales of the wavelengths of *P* - and *S*-waves in the band 1-4 Hz (1.4-5.6 km for *P* -waves and 0.8-3.4 km for *S*-waves) and on the order of the event separation (less than 5 km). These simulations suggest wave propagation in the presence of topographic relief can rapidly degrade waveform correlation for nearby explosions.

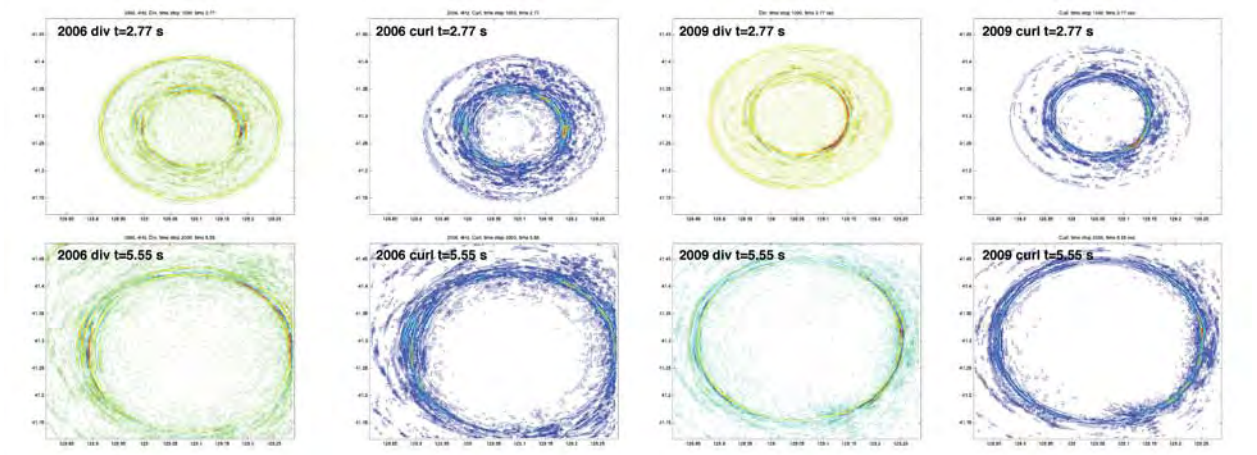

Figure 4. Motions at the surface at two different times (2.77 s and 5.55 s) for the 2006 (left) and 2009 (right) simulations. For each simulation we show the divergence and curl of the velocity field corresponding to the *P* - and *S*-wave motions. Note these are plotted in map view with some compression of the north-south directions.

Additional insight into the complexites of the wavefields emerging from these explosions can be seen in the images of the divergence and curl of the velocity fields at the surface, corresponding to *P* - and *S*-wave motions, respectively. Figure 4 shows the divergence and curl of the velocity field at the surface for the 2006 and 2009 explosions at two different times (2.77 s and 5.55 s). Similar to the seismograms shown above, the wavefields show strong azimuthal dependence. Especially interesting is the variation of the *P* - and *S*-wave amplitudes. The largest amplitudes for both *P* - and *S*-waves at early times for the 2006 event is to the east-to-northeast and west of the shot point, while the 2009 event shows strong amplitudes to the southeast-to-northeast. These azimuths also correspond to locally high topography and large variations in relief (measured by the topographic gradient or slope) relative to the shot point suggesting amplification by topographic highs and enhanced conversion of *P* -to-*S* propagation modes at topographic relief.

Theoretical studies based on incident plane-waves (Bouchon, 1973; Campillo and Bouchon, 1985; Sanchez-Sesma, 1983;) and elastic finite difference (FD) modeling (Boore; 1972) showed that topography impacts seismic motions when the seismic wavelength is comparable to the size of topographic features. These studies indicated that motions are amplified at topographic peaks and de-amplified in valleys. Chaljub (2006) showed that amplification occurs at topographic highs around the Grenoble alpine valley using the spectral element method (SEM) up to 2 Hz. Recently, Myers et al. (2007) clearly showed that *S*-waves are generated by shallow explosions at steep topographic relief using a combination of forward and time-reversed simulations. Further simulations and analyses will be performed to investigate these effects for the North Korean tests.

Modeling Intermediate Period (10-50 seconds) Complete Waveforms in 3D Earth Models

Improvements in topographic imaging methods and the availability of high-quality seismic data (travel times and broadband waveforms) have led to improvements in estimates in 3D seismic structure on continental and regional scales. Examples of recent 3D models include the following models: CUB2.0 (Shapiro and Ritzwoller, 2002); WENA1.0 (Pasyanos et al, 2004); Tethys (van der Lee et al., 2007); s2.9EA (Kustowski et al., 2008); JWM (Reiter and Rodi, 2008) and TX2009 (Simmons et al., 2009). These models resolve structure near the surface on 100-300 km scales and cover global (CUB2.0, S29EA, TX2009) and Eurasia (WENA1.0, Tethys, JVM). Importantly, these models are generated with different methods and data types, in many cases models are estimated from multiple data types. We seek to evaluate these models' ability to predict complete waveforms as a function of frequency. The goal being that if waveform predictions are accurate we may be able to use 3D models and simulations of complete waveforms for event analysis, such as depth determination, moment tensor estimation and yield determination. For this effort we are using the spectral element method (SEM) code SPECFEM3D (Komatitsch and Vilotte, 1998; Komatitsch and Tromp, 1999; Komatitsch et al., 2000). This code computes the response of the earth to moment tensor forcing in spherical geometry with fully 3D seismic velocity (including anisotropy) and density variations.

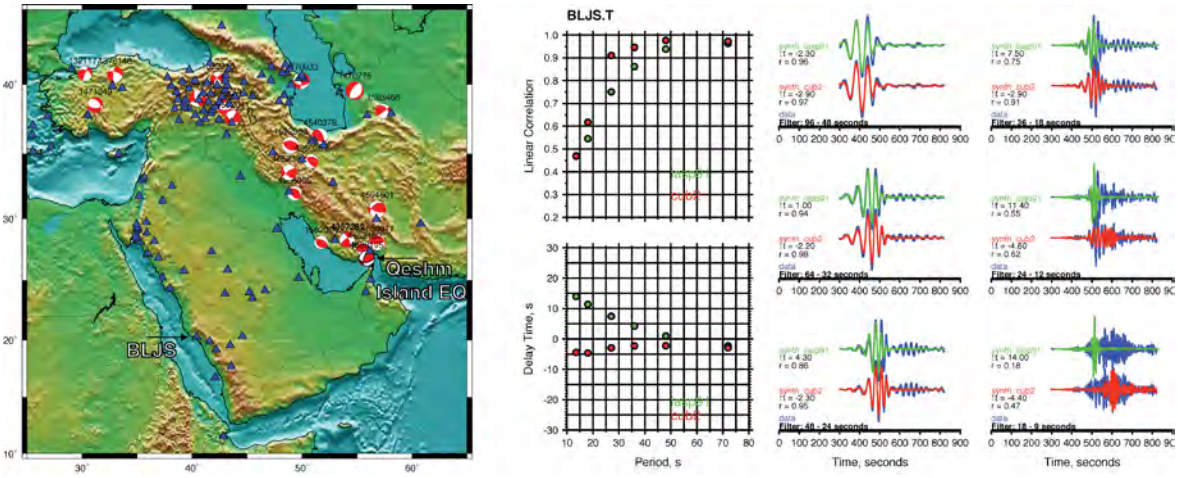

Figure 5 (a, left) Map of events (focal mechanisms) and stations for which we evaluating 3D models of the Middle East. The locations of the 11/27/2005 Qeshm Island earthquake and station BLJS (Saudi Arabia) are indicated. (b, right) Comparison of observed (blue) and synthetic waveforms for the 1D iasp91 (green) and 3D CUB2.0 (red) waveforms for the Qeshm Island events on the transverse component at station BLJS for a suite of frequency bands. Also shown are the linear correlation, r, and delay time, δt, as a function of frequency.

In order to investigate the ability of current 3D models to predict complete waveforms we developed a simple method to systematically compare observed and synthetic waveforms for well-characterized events. The windowed waveform segments for a data-synthetic pair for a given event-station-channel are compared for a suite of overlapping frequency bands (9-96 seconds). At each frequency, we compute the cross-correlation and report the delay time for optimal waveform alignment and the linear correlation at the delay to reduce waveform mismatch into simple measures of timing and waveform shape, respectively.

Figure 5a shows the events and stations for which we have well-determined source parameters from Cut-and-Paste (Helmberger et al., 2008). We show only the comparison of data and synthetics for one path: the 11/27/2005 Qeshm Island, Iran (M_W 5.8) earthquake to station BLJS in southwestern Saudi Arabia. The transverse component waveforms are compared in overlapping frequency bands between 0.1-0.01 Hz (periods 9–96 seconds). Synthetics were computed for the 1D iasp91 (Kennett and Engdahl, 1991) and CUB2.0 (Shapiro and Ritzwoller, 2002) models. This particular path clearly shows how the 3D CUB2.0 model predicts the observed waveform better than the 1D iasp91 model—note that the delay time is closer to 0 (measuring phase error) and the linear correlation (measuring waveform mismatch) is larger across the period band. Note however, that there appears to be scattered surface-wave energy at late times (600-700 seconds) in the band 18–48 seconds that is not predicted by the synthetics and the waveforms are very complex in the band 9–18 seconds where neither model predicts the observed long duration.

Figure 6 shows the waveform misfit performance of the 1D iasp91 and 3D CUB2.0 models for Love waves between 18–36 seconds. The waveform misfit measurements are plotted for each event at the station location with the size proportional to the linear correlation (bigger means better waveform match) and the color according to the color scale. Note that the 3D CUB2.0 model shows markedly better predictions of the observed waveforms with the delay times on average closer to zero and the linear correlations higher than for the 1D iasp91 model (see histograms of waveform misfit). Note that the delay times for the 3D CUB2.0 model show a systematic spatial pattern that suggests how the model could be improved.

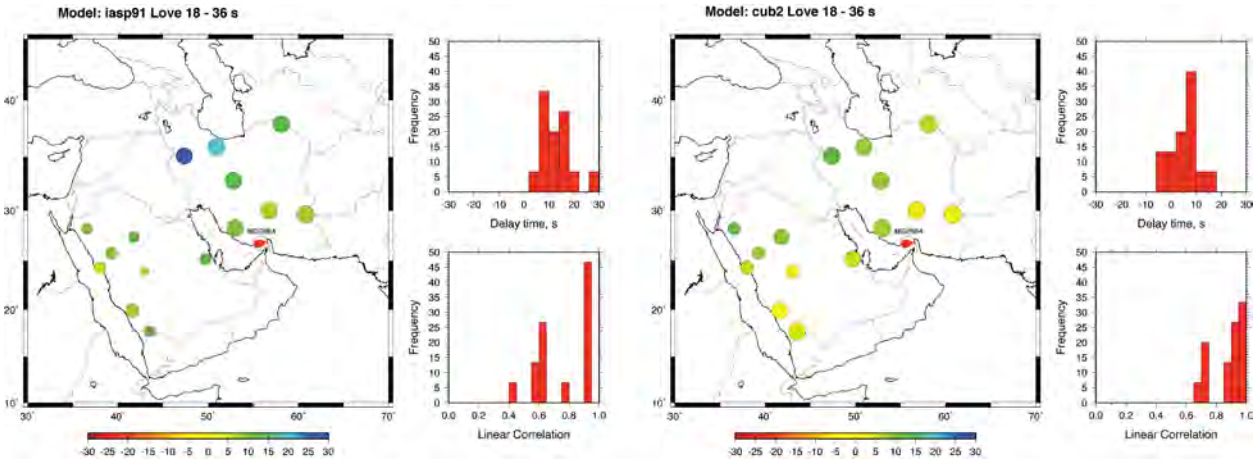

Figure 6. Maps of delay time and linear correlation for observations of the Qeshm Island earthquake Love waves in the period band 18-36 s for the 1D iasp91 (a, left) and 3D CUB2.0 (b, right) models. The waveform misfit measurements are plotted at the station location with the size proportional to the linear correlation (bigger means better waveform match) and the color according to the color-scale. Also shown are histograms of the delay times and linear correlations for each event.

Again the 2006 and 2009 North Korean nuclear tests offer important tests of 3D waveform modeling for NEM. In the previous Monitoring Research Review (Rodgers et al., 2008) we showed that the 3D wave propagation effects likely cause complexity in the BJT (Beijing, China) recordings of the 2006 North Korean nuclear test. However, this event was relatively small ($M_0 = 3x10^{21}$ dyne-cm) and signal-to-noise ratios (SNR) were low. The recent May 25, 2009, nuclear test was about 6 fives larger ($M_0 = 1.8x10^{22}$ dyne-cm) based on complete regional waveform modeling (Dreger et al., 2009). This provides improved SNR over the 2006 event, allowing us to investigate path effects with clearer signals.

We computed SEM synthetics for the 2009 nuclear test using the isotropic source model of Dreger et al. (2009) and three seismic models: iasp91 (Kennett and Engdahl, 1991; s2.9ea (Kustowski et al., 2008) and CUB2.0 (Shapiro and Ritzwoller (2002). Figure 7 shows the three-component waveform comparisons in the frequency band 0.02-0.05 Hz (20-50 seconds) at stations MDJ (Mudanjiang, China), INCN (Inchon, South Korea), TJN (Taejon, South Korea), BJT (Baijiatuan, China), HIA (Hailar, China) and MAJO (Matsushiro, Japan). In this period band, the iasp91 model predicts the observed response quite well with the exception of the oceanic path to MAJO. For the path to MAJO the s2.9ea model predicts the observed waveforms (distance 1144 km) very well. Note that the observed waveforms show weak but clear energy on the transverse components. Dreger et al. (2009) report that these data can be fit with a deviatoric moment tensor with significant CLVD component. Our simulations show that propagation from an isotropic source in the CUB2.0 model results in energy on the transverse component, however the amplitudes are generally weaker and the timing is inconsistent with the observations. Further investigations are needed to determine if current and future 3D models can consistently predict propagation effects and allow for unbiased source estimates.

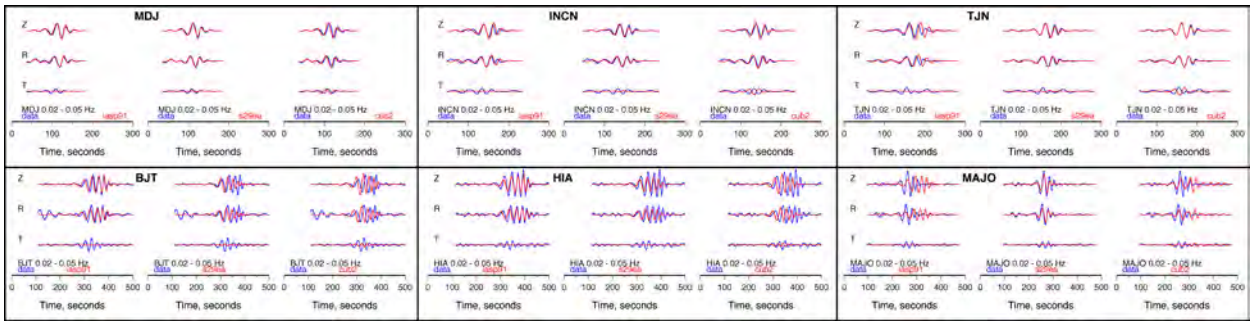

Figure 7. Comparison of observed (blue) and synthetic (red) seismograms for the May 25, 2009 North Korean nuclear test at six regional stations in the band 0.02-0.05 Hz for three models: iasp91, s2.9ea and CUB2.0 (see text). Note the upper row has a different time scale (300 seconds) than for the more distant stations shown in the lower row (500 seconds).

CONCLUSIONS AND RECOMMENDATIONS

This study shows how simulations of wave propagation in 3D earth models on high-performance computers can improve understanding and prediction of seismic observables relevant to nuclear explosion monitoring. The current efforts are focused on: 1) modeling shockwaves emerging from UNE's in different emplacement conditions (geologies) with GEODYN and coupling GEODYN-to-WPP to propagate motions to seismic distances; 2) modeling the effect of surface topography on seismic ground motions with emphasis on the recent North Korean nuclear tests; and 3) modeling intermediate period complete waveforms at regional distances.

Specific conclusions from our shockwave modeling investigations show that the emplacement material has a strong effect on the amplitude and frequency content of seismic motions. We performed a series of fully contained 1-kiloton explosions in three canonical materials (granite, tuff and alluvium). Strong materials (granite) result in very short duration, high-amplitude and high-corner frequency motions, while weaker materials are lower amplitude and have lower corner frequency. We are currently analyzing the effect of depth-of-burial and cavity size on the character of motions. Coupling of GEODYN motions to WPP will allow us to propagate motions to local distances (< 10 km) where we will be able to model ground motion data from historical nuclear tests. This will help understand the impact of emplacement conditions and 3D structure on observed ground motions for actual nuclear tests.

We have enhanced WPP to include free-surface topography and run preliminary simulations of the 2006 and 2009 North Korean nuclear tests. The two shots were located relatively close together (< 5 km) but the simulations show significant differences in the elastic response. Notably the *P* - and *S*-waves that would ultimately propagate to teleseismic distances show azimuthal differences in the amplitudes and waveform shapes. The *P* -waves at a given azimuth show surprising differences in waveform shape for the two events that suggests that in such a region of rough topography the waveforms would decorrelate rapidly with source separation. The topography clearly causes differences in the azimuthal dependence of *S*-wave generation that would likely be revealed in differences in *Sn*, *Lg*

and possibly short-period surface wave generation. More remains to be investigated to improve understanding of how topography impacts observed waveforms in general and for these specific nuclear tests.

We are investigating the ability of 3D seismic models to predict observed regional complete waveforms at intermediate periods (10–50 seconds). The comparison of observed and simulated waveforms should be done in several frequency bands because not surprisingly the propagation is strongly frequency dependent. In the Middle East we have done preliminary comparisons of 3D model performance, but have not analyzed the performance of different models for the available events and waveforms. This type of analysis will help evaluate 3D models for waveform predictions of scenario events, moment tensor estimation using 3D synthetics and starting models for adjoint waveform tomography (Tromp et al., 2005; Savage et al., these Proceedings).

These efforts are preliminary, however results are promising and we believe they should be continued. Currently we are spending a substantial part of the effort on developing methods to accurately and efficiently run simulations. As methods evolve we will focus on comparing simulation results with data.

ACKNOWLEDGEMENTS

We thank Steve Myers for providing his joint relocations of the 2006 and 2009 North Korean nuclear tests. WPP was developed with funding from LLNL Laboratory Directed Research and Development and the Department of Energy Office of Science. We are grateful to the staff of Livermore Computing at LLNL for operating the parallel computers on which we performed many of the simulations used in this study. We also thank the LLNL Geophysical Monitoring Program Information Technology team, led by Stan Ruppert, for providing a productive computing environment that supports these efforts. SEM calculations were performed with the SPECFEM3D package developed by Jeroen Tromp, Dmitri Komatitsch and colleagues and distributed by the Computational Infrastructure for Geodynamics supported by the National Science Foundation (www.geodynamics.org).

REFERENCES

Aagaard, B., R. W. Graves, S. Ma, S. C. Larsen, A. Rodgers, N. Anders Petersson, R. Jachens,T. M. Brocher, R. W. Simpson and D. Dreger (2009). Ground motion modeling of Hayward fault scenario earthquakes II: Simulation of long-period and broadband ground motions, manuscript in preparation, *Bull. Seism. Soc. Am.*

Antoun, T. H., I. N. Lomov and L. A. Glenn (2001). Development and application of a strength and damage model for rock under dynamic loading, proceedings of the 38th U.S. Rock Mechanics Symposium, Rock Mechanics in the National Interest, D. Elsworth, J. Tinucci and K. Heasley (eds.), A. A. Balkema Publishers, Lisse, The Netherlands, 369–374.

Antoun, T. H. and I. N. Lomov (2003). Simulation of a spherical wave experiment in marble using multidirectional damage model, 13th American Physical Society Topical Conference on Shock Compression of Condensed Matter, Portland, OR July 20–25, 2003.

Boore, D. (1972). A note on the effect of simple topography on seismic SH waves, *Bull. Seismol. Soc. Am*. 62: 275–284.

Bouchon, M. (1973). Effect of topography on surface motion, *Bull. Seismol. Soc. Am*. 63: 615–632.

Campillo, M. and M. Bouchon (1985). Synthetic SH-seimograms in a laterally varying medium by the discrete wavenumber method. *Geophys. J. Royal Astro. Soc*. 83: 307–317.

Chaljub, E. (2006). Spectral element modeling of 3D wave propagation in the Alpine Valey of Grenoble, France, *3rd International Symposium on the effects of Surface Geology on Seismic Motion, Grenoble France.*

Dreger, D., S. Ford and W. Walter (2009). Source analysis of the Memorial Day explosion, Kimchaek, North Korea, manuscript in preparation.

Helmberger, D., A. Rodgers, S. Ni, S. Wei, and J. Tromp (2008). Advanced Waveform Simulation for Seismic Monitoring Events, in *Proceedings of the 30th Monitoring Research Review: Ground-Based Nuclear Explosion Monitoring Technologies*, LA-UR-08-05261, Vol. 1, pp. 408–418.

Kennett, B.L.N., and E.R. Engdahl (1991). Traveltimes for global earthquake location and phase identification, *Geophys. J. Int.* 122*:* 429–465.

Komatitsch, D. and J.-P. Vilotte (1998). The Spectral Element Method: An efficient tool to simulate the seismic response of 2D and 3D geologic structures, *Bull. Seismol. Soc. Am*. 88: 368–392.

Komatitsch, D. and J. Tromp (1999). Introduction to the spectral element method for three-dimensional seismic wave propagation, *Geophys. J. Int*. 139: 806–822.

Komatitsch, D., J. Ritsema and J. Tromp (2000). The Spectral-Element Method, Beowolf computing and global seismology, *Science* 298: 1737–1742.

Kustowski B., Ekström G., and A. M. Dziewonski (2008). The shear-wave velocity structure in the upper mantle beneath Eurasia, *Geophys. J. Int.* 174: 978–992.

Lomov. I. N., T. H. Antoun, J. Wagoner and J. Rambo (2003). Three-dimensional simulation of the Baneberry nuclear event, in Proceedings of the 13th American Physical Society Topical Conference on Shock Compression of Condensed Matter, Portland, OR July 20-25, 2003.

Nilsson, S., N.A. Petersson, B. Sjogreen, H.-O. Kreiss (2007). Stable difference approximations for the elastic wave equation in second order formulation, *SIAM J. Numer. Anal*. 45: 1902–1936.

Murphy, J.R., Kitov, I.O., Rimer, N., Adushkin, V.V., Barker, B.W. (1997) Seismic characteristics of cavitydecoupled explosion in limestone: An analysis of Soviet high explosive test data. *J. Geophys.Res.* 102: (12), 27393–27405.

Myers, S., J. Wagoner, and S. Larsen (2007). Numerical experiments investigating the source of explosion *S* waves, in *Proceedings of the 29th Monitoring Research Review: Ground-Based Nuclear Explosion Monitoring Technologies*, LA-UR-07-5613, Vol. 1, pp. 175–184.

Pasyanos, M. E., W. R. Walter, M. P. Flanagan, R. Gok, S. C. Myers, and K. M. Dyer (2007). Enhancements of geophysical models for monitoring, in *Proceedings of the 29th Monitoring Research Review: Ground-Based Nuclear Explosion Monitoring Technologies,* LA-UR-07-5613, Vol. 1, pp. 195–204.

Perret W. R. Bass R. C. (1974). Free-field ground motion induced by underground explosions, Sandia National LaboratoryReport No. SAND74-0252.

Reiter, D. and W. Rodi (2008). A new regional 3-D velocity model for Asia from the joint inversion of *P*-wave travel times and surface-wave dispersion data, in *Proceedings of the 30th Monitoring Research Review: Ground-Based Nuclear Explosion Monitoring Technologies*, LA-UR-08-05261, Vol. 1, pp. 213–221.

Rodgers, A., E. Matzel, M. Pasyanos, A. Petersson, B. Sjogreen, C. Bono, O. Vorobiev, T. Antoun, I. Lomov, W.Walter, and S. Myers (2008). Seismic simulations using parallel computing and three-dimensional Earthmodels to improve nuclear explosion phenomenology and monitoring, in *Proceedings of the 30thMonitoring Research Review: Ground-Based Nuclear Explosion Monitoring Technologies*, LA-UR-08-05261, Vol. 1, pp. 231–240.

Sanchez-Sesma, F. (1983). Diffraction of elastic waves by three-dimensional surface irregularities, *Bull. Seismol. Soc. Am*. 73: 1621–1636.

Savage, B., D. Peter, B. Covellone, A. Rodgers, and J. Tromp (2009). Progress towards next generation, waveform based three-dimensional models and metrics to improve nuclear explosion monitoring in the Middle East, these Proceedings.

Shapiro, N.M. and M.H. Ritzwoller (2002). Monte-Carlo inversion for a global shear velocity model of the crust and upper mantle, *Geophys. J. Int.* 151: 88–105.

Simmons, N., A. Forte and S. Grand. (2009). Joint seismic, geodynamic and mineral physical constraints on three-dimensional mantle heterogeneity: Implications for the relative importance of thermal versus compositional heterogeneity, *Geophys. J. Int*. 177: 1284–1304.

Tromp, J., C. Tape and Q. Liu (2005). Seismic tomography, adjoint methods, time reversal and banana-doughnut kernels, *Geophys. J. Int*. 160: 195–216.

van der Lee, S., S. Chang, M. Flanagan, H. Bedle, F. Marone, E. Matzel, M. Pasyanos, A. Rodgers, B. Romanowicz,and C. Schmid (2007). Joint inversion for 3-dimensional S-velocity mantle structure along the Tethyan Margin, in *Proceedings of the 29th Monitoring Research Review: Ground-Based Nuclear Explosion Monitoring Technologies*, LA-UR-07-5613, Vol. 1, pp. 312–321.

Vorobiev. O. Y. (2008) Generic strength model for dry jointed rock masses, in press, *International Journal of Plasticity,* 10.1016/j.ijplas.2008.06.009.

NUMERICAL MODELING OF S-WAVE GENERATION BY FRACTURE DAMAGE IN UNDERGROUND NUCLEAR EXPLOSIONS

Charles G. Sammis[1], Harsha S. Bhat[1,2], and Ares J. Rosakis[2]

University of Southern California[1] and California Institute of Technology[2]

Sponsored by the Air Force Research Laboratory

Award No: FA8718-08-C-0026
Proposal No. BAA08-82

ABSTRACT

The quasi-static micromechanical damage mechanics originally formulated by Ashby and Sammis (PAGEOPH, 1990) has been expanded in three important ways: 1) An energy density function has been derived that allows a self-consistent inclusion of the effects of dynamic damage evolution on the elastic and anelastic response, 2) whereas the Ashby/Sammis model was only applicable to the case where the initial cracks are all parallel and the same size, we can now include a specified distribution of initial crack sizes with random azimuthal orientation about the loading axis, and 3) we allow for yielding of the weaker minerals in granite at relatively low stress levels which produce strong nonlinearity in the failure envelope and stress-strain curve. This new damage mechanics is validated using published experimental data for Westerly granite. In collaboration with the mechanics group at U.C. Santa Barbara, we have built our new damage mechanics into the commercial finite element program ABAQUS and used it to simulate an explosion in damaged rock. We find that an explosion in a pre-stressed medium or one that contains anisotropic initial damage generates strong *S*-wave radiation in agreement with previous simpler calculations by Johnson and Sammis (PAGEOPH, 2001) and experimental observations in damaged photoelastic plates.

OBJECTIVES

The overall objective of this research program has been to understand and quantify the extent of fracture damage in the non-linear source region of an underground nuclear explosion and to assess its effect on the radiation of seismic energy to the far field. Of particular interest is the generation of high-frequency shear waves that may affect regional discrimination and yield estimation. The specific objective of this year's research has been to build on the work of Deshpande and Evans (2008), to extend the micromechanical damage mechanics originally formulated by Ashby and Sammis (1990), and to incorporate it in numerical models that simulate underground explosions.

RESEARCH ACCOMPLISHED

Our major accomplishment this year has been to make three important improvements in the micromechanical damage mechanics developed by Ashby and Sammis (1990) and expanded by Deshpande and Evans (2008). First, we dropped the assumption, implicit in both formulations, that the growing wing cracks are all parallel and all the same size, which strongly affects the interaction between the growing wing cracks that leads to failure. Second, we calculated the change in elastic energy density associated with the growing wing cracks in a less approximate way than that used by Deshpande and Evans (2008), which has led to a more accurate stress-strain simulation. Third, we account for the fact that granite is multimineralic and that yielding in the weaker minerals begins at relatively low stress levels.

We have built this new mechanics into the dynamic finite element code ABAQUS and produced some initial simulations of damage evolution during an underground explosion. Finally, we have begun experiments in which a hyper-velocity impact is used to simulate an explosion. A hyper-velocity impact creates a much higher energy density at the source than does an exploding wire, which allows us to better scale the damage process from the field to the lab.

Improvments to the Ashby Sammis (1900) Micromechanical Damage Mechanics

Ashby and Sammis (1990) (hereafter referred to as A&S) formulated a micromechanical damage mechanics based on the nucleation, growth and interaction of tensile "wing cracks" nucleated at the tips of an initial distribution of penny-shaped microcracks. The basic elements of their model are illustrated in Figure 1.

A&S demonstrated that their model gives an adequate description of the failure envelope (σ_1 vs σ_3 at failure) at low confining pressures, σ_3, for a wide range of rocks loaded in triaxial compression ($\sigma_1 < \sigma_2 = \sigma_3$, where compression is taken as negative).

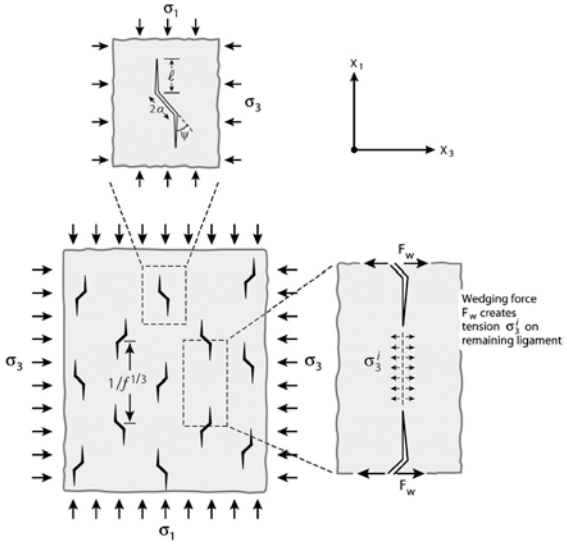

Figure 1. Geometry of damage mechanics model (from Deshpande and Evans, 2008). And initial distribution of flaws of radius *a* are loaded in compression. Sliding on the initial flaws nucleates tensile "wing cracks" at their tips of length *l*. The wedging force produced by the angle cracks creates tension on the remaining ligament creating a positive feedback that leads to instability and failure. The initial damage is defined as $D_o = \frac{4}{3}\pi(\alpha a)^3 N_V$ **where N_V is the volume density of initial flaws. Damage increases as the wing cracks grow according to** $D = \frac{4}{3}\pi(l + \alpha a)^3 N_V$.

However, the failure envelope predicted by this model is nearly linear while the observed failure envelope for Westerly granite is very non-linear, especially at high confining pressures (see Figures 2 and 3). A&S hypothesized that this nonlinearity is caused by a transition to plastic deformation at very high confining pressures. We shall show in a subsequent section that the broad transition zone in Fig. 3 is due to the multimineralic composition of Westerly granite where the weaker minerals yield at relatively low stress levels.

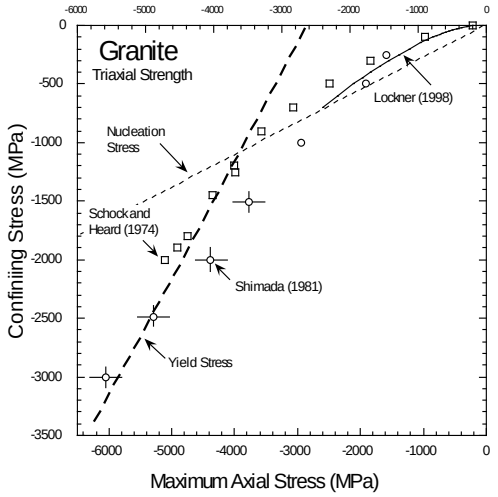

Figure 2. Failure envelope for Westerly granite under triaxial loading $\sigma_1 < \sigma_2 = \sigma_3$. Sources of data are labeled. The heavy dashed line shows the yield stress for quartz. The light dashed line shows the stress state at which the initial flaws nucleate wing cracks. Note that no additional damage can occur for confining stress greater than about 1000 MPa (confining pressure is taken as negative).

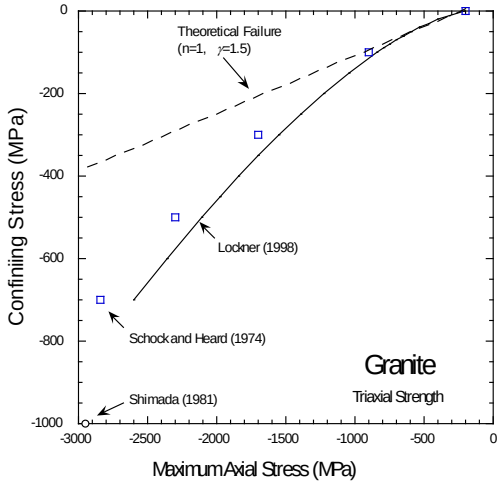

Figure 3. Enlarged view of failure envelope in Fig. 2 near $\sigma_3 = 0$. The dashed curve is the theoretical failure envelope when all flaws are the same size. The variable γ is a correction for a distribution or crack orientations defined in the text. Note that the departure from linearity begins at $\sigma_3 \approx 100$ MPa. The key question is whether this deviation from linearity is due to a distribution of sizes of starter flaws or the mineralic heterogeneity of Westerly granite where the weaker grains begin to yield at significantly

Johnson and Sammis (2001) used the A&S damage mechanics to model the 1 kt chemical explosion detonated in September 1993 as part of the Non-Proliferation Experiment (NPE). They found that the explosion induced fracture damage to a distance up to ten times the cavity radius. More importantly, they found that the damage itself generated significant "secondary radiation" of *P* and *S* waves in the seismic band. However, the A&S formulation they used is incomplete. Although it allows an estimate of the evolving damage and predicts failure, it does not provide an estimate of the stress-strain behavior associated with the increasing damage. For their numerical simulations, Johnson and Sammis (2001) used an empirical stress-strain relation borrowed from soil mechanics, which was not connected to the damage model.

Deshpande and Evans (2006) (hereafter referred to as D&E) extended the A&S damage mechanics to include stress-strain behavior by deriving the internal energy density as a function of stress, which they then differentiated to find the strain. They wrote the energy density W as

$$W = W_o + N_V \Delta W_1 + N_V \Delta W_2 \qquad (1)$$

where W_o is the elastic energy density, ΔW_1 is the change in energy density per crack due to sliding on the preexisting cracks, and ΔW_2 is the change in energy density per crack due to the growth of wing cracks. The axial strain for any stress state (σ_1, σ_3) may be calculated from the energy density as

$$\varepsilon_1 = \frac{\partial W(\sigma_1, \sigma_3)}{\partial \sigma_1} \tag{2}$$

The first two terms in the energy density are quadratic in σ_1 and thus give a linear stress-strain curve on differentiation. The second term reduces the effective Young's modulus, as in O'Connell and Budiansky (1974). The third term is not quadratic and produces curvature in the stress-strain curve, in the sense of the observations in Figures 2 and 3. The question is, how much curvature?

The perturbation in internal energy due to the growth of wing cracks can be written

$$\Delta W_2 = \frac{2\pi}{E_o} \int_{\alpha a}^{l+\alpha a} K_I^2 r dr \tag{3}$$

where K_I is the mode I stress intensity factor at the tips of the wing cracks and *l*, α, and *a* are defined in Figure 1. A&S derive an analytical expression for K_I that can be integrated to find ΔW_2.

In their formulation, D&E simplify the integration in eqn. (3) by assuming the wing cracks grow at a fixed value of *l/a* and write

$$\Delta W_2 = \frac{2\pi}{E_o} \int_0^a K_I^2 r dr \tag{4}$$

Since K_I^2 is a constant for fixed *l/a,* they can remove it from the integral giving a very simple result. However, we have shown (Sammis et al., 2009) that this simplification is too extreme in that ΔW_2 becomes independent of the evolving damage. Hence in the D&E approximation, wing-crack growth produces zero additional strain when the strain is calculated as $\varepsilon_1 = \partial W / \partial \sigma_1$ according to equation (2).

However, Sammis et al. (2009) point out that $K_I = K_{Ic}$ (its critical value) during quasi-static crack growth so it can be removed from the integral in eqn. (3) giving an equally simple result

$$\Delta W_2 = \frac{3}{4} \frac{K_{Ic}^2 D_o}{E_o \alpha a} \left[\left(\frac{D}{D_o} \right)^{2/3} - 1 \right], \tag{5}$$

where $D_o = \frac{4}{3}\pi(\alpha a)^3 N_V$ is the initial damage associated with the angled cracks, $D_o = \frac{4}{3}\pi(l + \alpha a)^3 N_V$ is the current damage, and N_V is the volume density of initial flaws. Since *D* increase with σ_1 up to failure, the nonlinear strain contributed by the growing wing cracks is non-zero.

Even with this correction, we found that the damage model fails to predict the observed curvature in the failure envelope. Figure 3 compares the theoretical and observed failure envelopes which diverge at confining pressures above about 100 MPa. Figure 4 shows the nonlinear portion of the stress strain curve for Westerly granite at a confining pressure of 200 MPa from Lockner (1998). The extra strain associated with the growth of wing cracks (the only nonlinear contribution in the model) is more than an order of magnitude smaller than the measured nonlinearity.

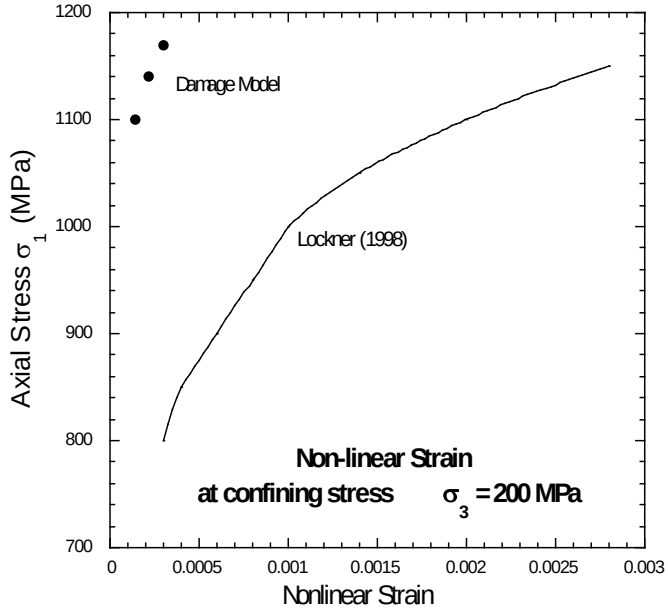

Figure 4. **Non-linear strain in Westerly granite at a confining pressure of 200 MPa (redrawn from Lockner, 1998). Note that significant non-linear strain begins at an axial stress equal to about half of the failure stress and that the non-linear portion of the strain at failure is about 0.003. The non-linear strain associated with the growth of wing cracks (solid circles) is about one order of magnitude smaller.**

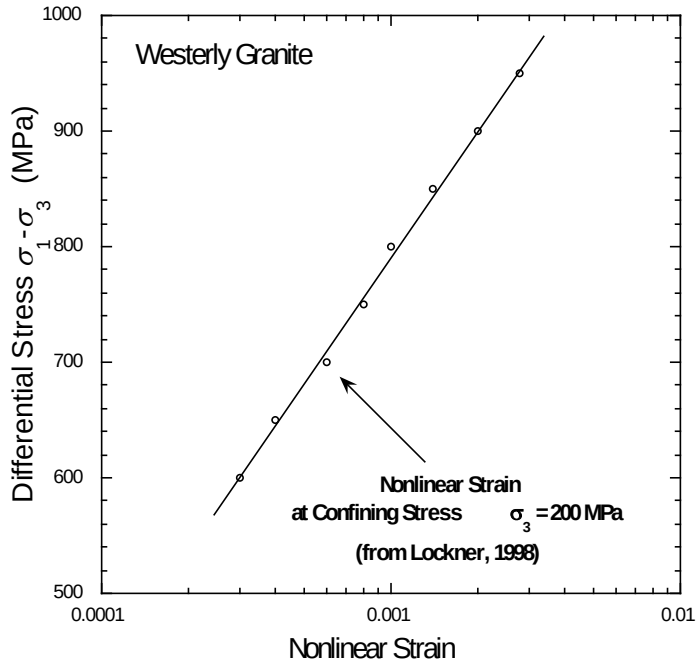

Figure 5. Same as Fig.4 but with logarithmic nonlinear strain and differential stress. The straight line implies that the stress-strain curve is of the form

$$\sigma_1 - \sigma_3 = A \log \varepsilon_{nonlinear} + B$$

By dropping two simplifying assumptions made by both A&S and D&E the damage mechanics can produce more nonlinearity in the failure envelope: 1) we no longer assume that all the initial flaws are parallel and 2) we no longer assume that all flaws are the same size. We can drop the assumption that all flaws are parallel by modifying the interaction term. We still assume that all flaws are all at an angle α to the x_1 loading axis but allow the x_2 and x_3 components of their normal vectors to be randomly distributed. The effect is to reduce both the wedging force and average cross-section area supporting the interaction. We drop the second assumption that all flaws are the same size by simply keeping track of the growth and interaction of a distribution of initial flaw sizes. We chose the distribution measured in Westerly granite by Hadley (1976) shown in Figure 6. This is a bimodal distribution having a population of flaws at the grain boundary scale (about 1 mm) and a second power-law (fractal) distribution of microcracks at the 10–100 micron scale.

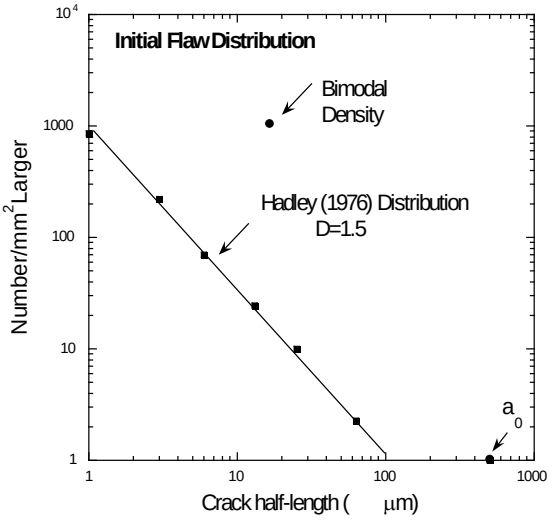

Figure 6. Initial flaw distribution in Westerly granite measured by Hadley (1976). This is a bimodal distribution with flaws of radius a near the size of the grain boundaries (about 0.5 mm) and a second fractal population of microcracks with radii less than 100 microns. The point labeled "Bimodal Density" is the density of smaller flaws required to produce the observed curvature in the failure envelope. However, even with this larger density, the stress-strain curve does not have enough nonlinearity.

Although both corrections produced more damage prior to failure, the total strain at failure (as shown by the closed circles in Fig. 4) was still only about 5×10^{-4}, a full order of magnitude smaller than the measured value. These corrections also failed to produce the observed curvature in the failure envelope in Figures 2 and 3. Even with the extra damage, the failure envelope was nearly linear. We could simulate the observed curvature in the failure envelope by increasing the density of microfractures relative to the grain boundaries (closed circle labeled "bimodal density" in Fig. 6), but this required micro-fracture densities two orders of magnitude larger than those measured by Hadley (1976).

One way that we can generate the observed nonlinearity in both the failure envelope and stress-strain curves is to account for the multimineralic composition of Westerly granite. If the yield stress in the Feldspars and micas is significantly less than the yield stress of quartz, then nonlinear flow of the weak minerals will transfer stress to the quartz, which will carry a stress well above the average macroscopic loading stress. The quartz grains fail at the higher stress levels predicted by brittle damage mechanics, but the apparent macroscopic failure stress, being an average of the flow-stress of the weaker minerals and the brittle strength of quartz, is much smaller, as observed.

A simple model that can produce the required curvature in both the failure envelope and stress-strain curve is shown in Figure 7. Although we have not yet fully explored this model the preliminary results are encouraging. As illustrated in Figure 8, the observed failure stress lies between the flow stress of the weaker minerals and the elastic failure of quartz. Moreover, the extra elastic strain in the stronger mineral as it is loaded by the flow of the weaker ones is close to the observed nonlinear stain at failure in Figure 4.

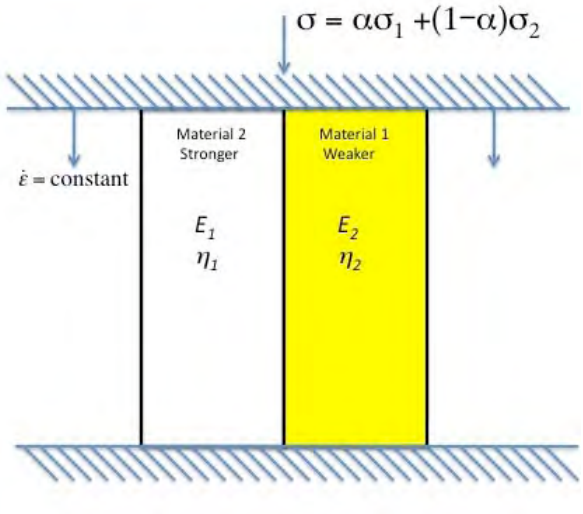

Figure 7. Simple model of a two-mineral rock loaded in compression at a constant loading rate $\dot{\varepsilon} = \text{constant}$. The loading stress σ is the average of the stresses carried by each mineral weighted according to its cross-sectional area. For the stronger mineral 1,

$$\varepsilon = \varepsilon_{1elastic} + \varepsilon_{1plastic}$$

$$\varepsilon_{1elastic} = \sigma_1 / E_1$$

$$\dot{\varepsilon}_{1plastic} = \sigma_1 / \eta_1$$

with the same expressions for the elastic and plastic strains in the weaker mineral 2.

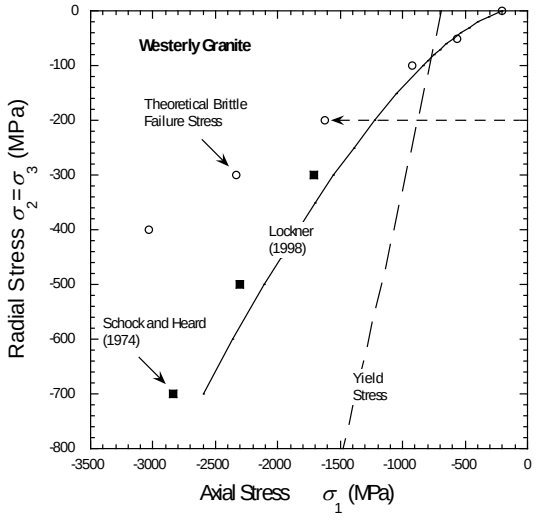

Figure 8. **Failure envelope for Westerly granite. The open circles are the strength predicted by the brittle damage mechanics. Note that brittle failure is an adequate description to a confining stress of about -100 MPa. The solid curve is the failure envelope measured by Lockner (1998). The dashed arrow shows a confining stress of -200 MPa. Note that the measued failure stress is an average of the brittle failure stress predicted by damage mechanics and the flow stress of the weaker minerals.**

The incorporation of damage mechanics into the ABAQUS dynamic finite element code: the numerical simulation of an underground explosion and the generation of *S* waves from the damage

Numerical calculation of this problem was done using a commercial Finite Element Package, ABAQUS. A user-defined subroutine, VUMAT, was written that incorporates the micro-mechanics based damage constitutive law described above. The model dimensions are scaled by the radius of the explosion hole, *a*. The size of the domain of computation is *120a* x *120a* (see Figure 9). This domain was finely meshed with about 120000 triangular elements. The boundary conditions applied were a constant uniaxial or biaxial loading. The initial condition for the problem was a sudden release of pressure along the inner periphery of the hole simulating an explosion. The entire calculation was done under the assumption of plane-stress conditions.

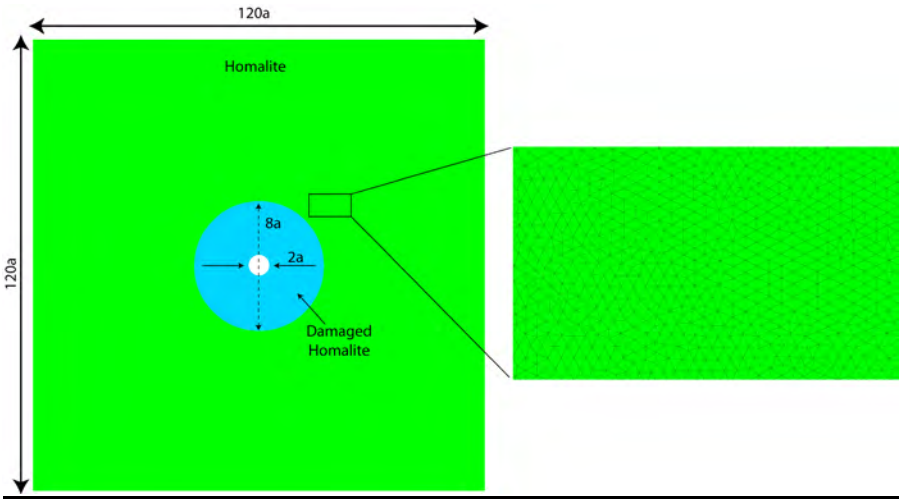

Figure 9. **Geometry and mesh design for the 2D ABAQUS simulation of and explosion shown in Figure 10.**

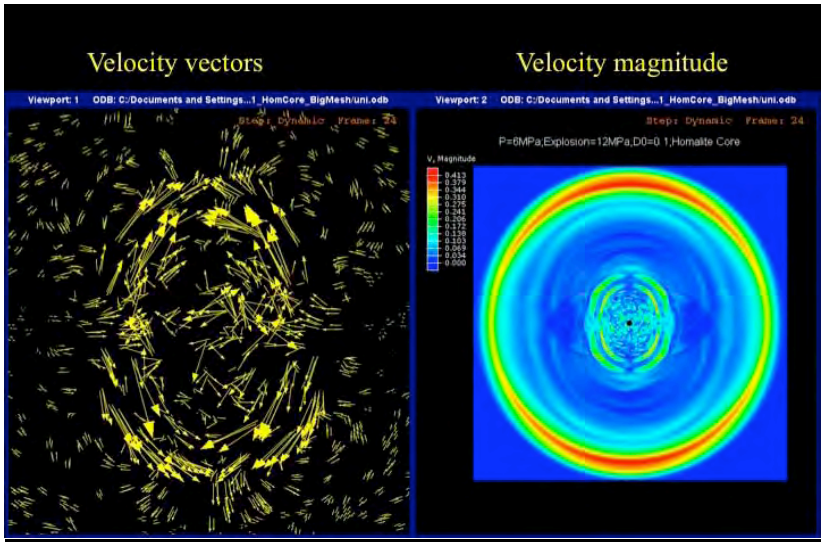

Figure 10. Velocity vectors and magnitude showing the development of S waves in the damaged area, which then propagate to the far field. These calculations used the previous D&E formulation where all initial flaws are the same size and are parallel.

The experimental simulation of an undergroud explosion using hypervelocity impact

Our experiments reported last year used a wire that was exploded by a high-voltage pulse. When this explosion occurred in the center of a damaged region under non-hydrostatic load, strong *S* waves were observed to emerge. However, the explosion was not sufficiently strong to nucleate new damage from the existing cracks. One was to produce a more intense source (in 2D experiments) is by using a high-velocity impactor.

Figure 11 shows the pattern of radial and circumferential fractures generated in a Homalite plate by a high-velocity impactor. Note the similarity to fracture patterns produced by underground explosions. We are currently developing the experimental capability to perform this experiment on loaded plates and to measure the resultant *S*-wave radiation.

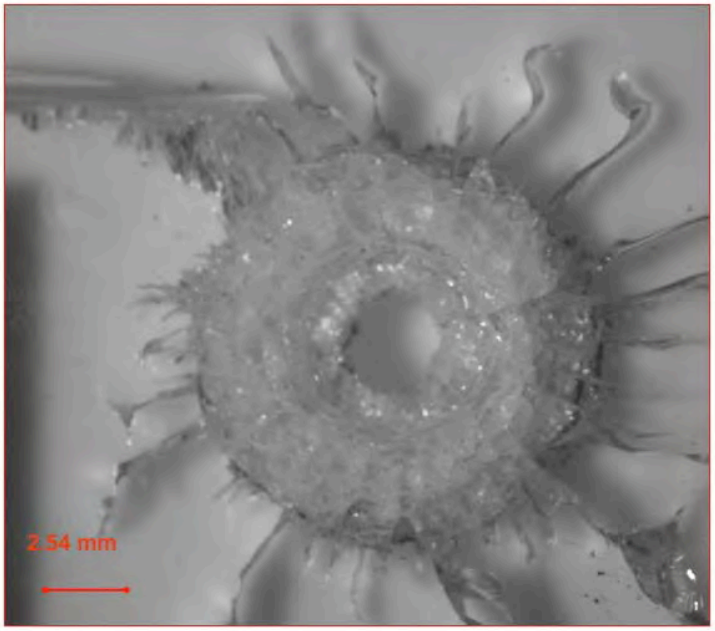

Figure 11. Fracture pattern generated by a high-velocity impact on an undamaged Homalite plate. Note that the pattern of radial and circumferential fractures is the same as that observed in underground explosions. The impactor was an equidimensional nylon slug, (L/D ~ 1, D=0.070") with an impact velocity of 6.48 km/s

CONCLUSIONS AND RECOMMENDATIONS

Our primary achievement this year has been the following significant improvements in the Ashby and Sammis (1990) damage mechanics:

1) We have derived an expression for changes in the internal energy density associated with the growth of damage. Although we followed the method developed by Deshpande and Evans (2008), we corrected fundamental errors in their formulation.

2) We extended the previous formulations to allow non-parallel initial fractures.

3) We extended the previous formulations to allow a range of initial flaw sizes.

Even with these improvements, we were unable to reproduce the observed failure envelope and stress strain curves for Westerly granite for confining pressures above about 100 MPa. We conclude that a simulation of the deformation of granite at high confining stress requires that we allow for plastic flow of the weaker constituent minerals.

We have built our damage mechanics into the ABAQUS finite element code and simulated a 2D explosion in damaged Homalite that generated significant *S* wave energy in the damage material. We are currently including the above improvements in the code, after which we will continue with the simulations of explosions.

Finally, we have begun 2-D experiments that use a high-velocity impact to simulate an explosion. The higher energy density in the impact does far more damage than does the exploding wire used in our prior experiments, which should allow us to better explore the seismic radiation generated by the growth of new damage.

ACKNOWLEDGEMENTS

We wish to thank Vikram Deshpande for his assistance in building our damage mechanics into the ABAQUS numerical code.

REFERENCES

Ashby, M. F. and C. G. Sammis (1990). The damage mechanics of brittle solids in compression, *PAGEOPH* 133: 489–521.

Brace, W. F. (1965). Some new measurements on linear compressibility of rocks, *J. Geophys. Res.* 70: 391–398.

Deshpande, V. S. and A. G. Evans (2008). Inelastic deformation and energy dissipation in ceramics: A mechanism-based constitutive model, *J. Mechanics and Physics of Solids* 56: 3077–3100.

Hadley, K. (1976). Comparison of calculated and observed crack densities and seismic velocities in Westerly granite *J. Geophys. Res* 81: 3484–3494.

Johnson, L. R. and C. G. Sammis (2001). Effects of rock damage on seismic waves generated by explosions, *PAGEOPH*, 158, 1869-1908.

Lockner, D.A. (1998). A generalized law for brittle deformation of Westerly granite, *J. Geophys. Res.* 103: 5107-5123.

O'Connell, R. J. and B. Budiansky (1974). Seismic velocities in dry and saturated cracked solids*, J. Geophys. Res.* 79: 5412–5426.

Sammis, C. G., H. S. Bhat, and A .J. Rosakis (2009). The micromechanics of brittle solids in triaxial compression*, J. Geophysical Res.*, submitted.

SOURCE PARAMETERS OF SEISMIC EVENTS IN THE MINES OF KOLAR GOLD FIELDS

C. Srinivasan, Y. A. Willy, and P. C. Nawani

National Institute of Rock Mechanics, Champion Reefs, KGF-563 117

Sponsored by the Ministry of Earth Science, Government of India.

Award No. WOS092143

ABSTRACT

Rockbursts are a common phenomenon in mines during mining operations. A network of geophones was used to locate and assess the stability of mine workings. An important parameter needed to assess the damage potential and severity of a rockburst is the Richter local magnitude (M_L). It was not possible to obtain M_L measurements from the records of the geophone network due to saturation effects. A strong-motion accelerograph was installed after the closure of the mines and recorded many rockbursts. The strong-motion accelerograms, recordings of rockbursts, were used to obtain Wood-Anderson synthetic seismograms for getting accurate and reliable values of M_L. Using 100 typical strong-motion accelerograms of rockbursts in the mines, magnitudes were computed. The maximum magnitude obtained from several rockbursts during has been found to be 2.8. The strong-motion seismic data have also been used to compute the source parameters of seismic events. Analysis of the seismic events revealed that the local magnitudes of these events were between -2.78 and 2.8. Seismic moment varied between 7.94×10^{19} and 2.00×10^{22} dyne-cm, seismic stress drop varied between 7.5 and 118 bars, source radius between 35 and 136 m, and average corner frequency between 3 and 10 Hz. The results of the source parameters of the mining tremors completely agree with corresponding results for natural earthquakes. The regression trend-line obtained from the plot of dynamic shear stress difference as a function of magnitude for rockburst $M_L < 2.8$ and earthquake $M_L > 3$ has been found to be $\log(\underline{R}a) = 0.31 + 0.89\ M_L$. The details are discussed in this paper.

OBJECTIVES

The objective of this study is to use strong-motion data in the mines of the Kolar Gold Fields to compute source parameters.

RESEARCH ACCOMPLISHED

Rockbursts have been a common phenomenon since the beginning of the 20th century in the mines of the Kolar Gold Fields (KGF), which is situated in Karnataka. Rockbursts have caused severe damage to buildings on the surface and underground mine workings in several instances. An important parameter needed to assess the damage potential and severity of a rockburst is M_L. However, it has not been possible to obtain M_L from the records of conventional seismographs due to saturation effects. The rockbursts had been monitored using a seismic monitoring system since 1979. Rockbursts were the usual phenomenon in the KGF mines during mining activity (Krishnamurthy and Srinivasan, 1980). However, rockbursts continued to occur even after the closure of the mines. Rising water levels in the structure of the mines may be one possible cause of frequent rockbursts as was reported elsewhere in the world. Normally, the frequency and severity of rockbursts increase during the rainy season (Srinivasan et al., 2000). Figure 1 shows the surface mining region of the KGF and the location of the strong motion accelerograph.

The strong motion accelerograph has been able to record several rockbursts, as it is in close vicinity to the mines of the KGF, which has formed the basis for the estimation of their local magnitudes. The accelerograms of rockbursts have been used to compute local magnitudes and the source parameters.

DATABASE USED

A noticeable major rockburst occurred on 02/11/2005 at 18:14:56 in the old and abandoned mines of the KGF. The rockburst was very severe and the effect was felt by residents of adjoining areas and surrounding townships. The rockburst caused panic among the residents and it is reported that the people came out of their houses. The peak ground acceleration recorded due to this rockburst was 0.22g. This level of acceleration falls in the category of caution zone for houses and buildings, many being very old and in depilated condition. Following the major rockburst, many seismic events were recorded by the strong motion accelerograph. The data were used to compute the source parameters using the software *Seisan*.

METHODOLOGY

A single triaxial seismogram of accelerometer traces, recorded at the KGF has been used to estimate location and source parameters. While the data is not sufficient for calculating a moment tensor or focal mechanism, estimates of location (based on polarization of the *P*-wave) and *S*-*P* separation are possible by fitting a Brune acceleration spectrum to the spectra of these waves. Figure 2 shows the seismogram for the event's *P*-arrival at 18:14:51.04. All three components are superimposed in the seismogram. Figure 3 shows the acceleration spectra of the *S*-wave for the event, with a Brune acceleration model.

From the *S*-*P* separation of the relatively clear *P*- and *S*-arrivals seen in Figure 2 and assuming respective *P*- and *S*-wave velocities of 5.5 km/s and 3.5 km/s, the hypocentral distance appears to be around 3,100 m. From the polarization of the *P* wave, the source is deduced to be approximately 1,994 m south and 831 m east of the KGF, and between 1,100 m and 2,200 m deep (assuming surface effects in the observed Z-component with a scaling factor of between 1.0 and 2.0). The quality of the polarisation is not very high, so some error in this estimate is to be expected.

From the acceleration spectra in Figure 3, we derive that the event has a corner frequency of between 4 Hz and 5 Hz, and by fitting a Brune acceleration spectrum, the seismic moment is estimated as being approximately 6.4×10^{12} Nm using the single station at KGF. Again, as this is a single station, the actual scalar seismic moment at source could be different, due to a possibly non-isotropic focal mechanism.

The typical seismic signal picked up by the strong motion accelerograph is shown in Figure 4. The strong motion data have been converted to *Seisan* format and source parameters of seismic events were computed. The *Seisan* output file is shown in Figure 5. The results obtained for several events are shown in Table 1.

Table 1. Source parameters of seismic events recorded by the strong motion accelerograph.

Event	Date	Time	M_L	Source Radius (m)	Stress Drop (bars)	Seismic Moment (Dyne-cm)	Average Corner Frequency
1	2005.11.02	04:35:33.3	1.70	136.2	13.1	7.94×10^{19}	9.25
2	2005.11.02	04:35:36.5	0.45	0.13	10.1	2.00×10^{22}	9.45
3	2005.11.02	05:30:05.3	1.87	0.54	56.0	5.01×10^{19}	2.32
4	2005.11.03	01:50:47.1	1.68	0.42	76.7	1.26×10^{22}	3.12
5	2005.11.04	15:40:03.2	2.50	0.42	40.8	6.31×10^{21}	3.05
6	2005.11.05	07:15:50.5	-1.17	0.32	7.5	5.01×10^{20}	3.91
7	2005.11.06	08:35:31.2	1.82	0.48	35.4	1.00×10^{22}	2.59
8	2005.11.18	15:01:08.0	2.46	0.127	118.0	3.98×10^{20}	10.66
9	2005.11.20	04:48:39.7	1.97	0.35	58.0	5.01×10^{21}	3.61
10	2005.11.20	05:19:38.2	-2.6	0.42	118.20	2.00×10^{22}	3.05
11	2008.05.20	03:58:15.07	2.0	0.50	9.5	2.80×10^{21}	2.59
12	2008.04.02	01:21:27.0	1.9	0.6	11.6	6.02×10^{20}	2.18
13	2008.03.08	12:50:54.0	2.7	0.1	3.5	2.34×10^{21}	9.24

The source parameters computed for a deep gold mine in South Africa and deep mines of the KGF are shown for comparison in Table 2.

Table 2. Comparison of source parameters

Source Parameters	KGF Mine	South African Mine
Seismic Parameters	1.7	0.8
Seismic Moment(D-cm)	2.94×10^{22}	6.4×10^{19}
Stress Drop (MPa)	1.01	0.5338.3
Source Radius (m)	130	38.3
Corner Frequency	9.45	5.0

The rockburst picked up by the strong motion accelerograph in the mines of the KGF as well as the earthquakes recorded in Koyna dam were compared and similarities found. The mines of the KGF filled with water after their closure during 2001.

The acceleration of rockbursts and earthquakes along with their hypocentral distances are plotted in Figures 6 and 7. Hypocentral distances were estimated from the interval between *P*- and *S*-waves, assuming velocities of 5.5 and 3.5 km/sec for the *P* and *S* velocities respectively (McGarr, 1974).

Figure 6 shows the dependence of dynamic shear stress differences defined by $\tilde{\sigma} = \rho R a_{\max}$ (with ρ as density taken as 2.8 gm/cm^3, R as distance in kilometer and a_{max} as the peak ground acceleration in cm/sec^2) on the estimated strong-motion magnitude values. The events with magnitudes below zero have been deleted as they might also occur due to a different source mechanism than that for the rockbursts. The magnitude dependence of $\tilde{\sigma}$ is defined by the following least-squares equation.

$$\text{Log } \tilde{\sigma} = 0.31 + 0.89\, M_L \qquad (1)$$

The equation is similar to the equation obtained by McGarr et al. (1981) for different mining conditions. The data for several significant earthquakes in the Koyna dam area are plotted in Figure 7. The trend line for tremors from the

mine fits quite well to the larger magnitude earthquakes in the Koyna area. Thus, the KGF rockbursts are generated by a similar mechanism to the Koyna dam earthquakes. Both may be of triggered nature due to pore-pressure diffusion. The similarity between the rockbursts in the KGF and the earthquakes in the Koyna area is further established by the dependence of the peak velocity v on the magnitude as shown in Figure 7, which can be defined by the following least-squares equation,

$$\text{Log } Rv = 3.74 + 1.12 \ M_L, \quad (2)$$

where Rv is in cm^2/sec. The magnitude dependence for defines the dependence for the Koyna earthquakes equally well.

CONCLUSIONS AND RECOMMENDATIONS

The seismic signals recorded using geophones in the near field are generally saturated and are not suitable for estimating the true magnitudes. The strong-motion accelerograms recorded due to rockbursts are therefore used to obtain the Wood-Anderson synthetic seismograms in the present study. The methodology adopted to compute the local magnitudes from strong-motion data has used an improved correction factor for distance attenuation and has applied the correction for the site soil condition to get very realistic estimates of the magnitude. The magnitudes are found to be quite consistent for some events for which independent estimates based on broadband records could be made. The dynamic shear-stress difference as a function of magnitude for tremors from mine (M_L <2.8) and the earthquakes in Koyna area (M_L >3) is seen to have strikingly similar nature. The identical scaling of dynamic shear-stress of tremors from mine and earthquake lends support to the mechanical similarity of mine tremors and earthquakes in the Koyna area. This is also supported by the dependence of the velocity on magnitude for the two types of events.

ACKNOWLEDGEMENTS

The authors are thankful to the Ministry of Mines for permitting the presentation of this paper at the Monitoring Research Review in the USA. The Department of Science and Technology is thanked for providing the strong motion accelerograph. Dr. I. D. Gupta, Additional Director, CWPRS, Pune assisted in the local magnitude computation.

REFERENCES

Krishnamurthy, R. and C. Srinivasan, (1980) Current seismic studies for the detection of rockbursts in Kolar Gold Fields, Indo-German Workshop on Rock Mechanics, NGRI, Hyderabad.

McGarr, A. (1974). Earthquake prediction:absence of a precursive change in seismic velocities before a tremor of magnitude 3.75, *Science* 185: 1047–1049.

McGarr, A., R. W. E. Green and S. M. Spottiswoode (1981). Strong ground motion of mine tremors: some implications for near-source ground motion parameters, *Bull. Seismol. Soc. Am*. 71: 1, 295–319.

Spottiswoode, S. M. and A. McGarr (1975). Source parameters of tremors in a deep-level gold mine, *Bull. Seismol. Soc. Am*. 65: 1, 93–112.

Srinivasan, C., Sagaya Benady, and Sivakumar, C. (2000). Fluid Induced Seismicity in Kolar Mining Region, Proceeding Workshop on Dam Safety Including Instrumentation of Dams,15–17, November,2000, Trivandrum.

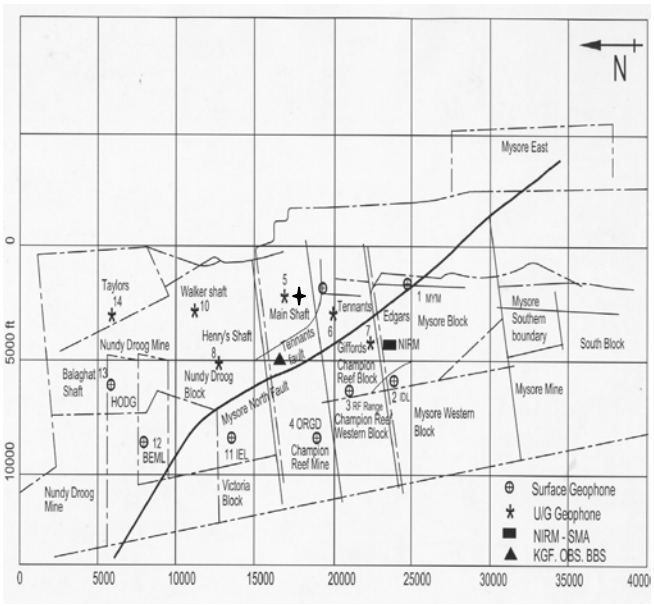

Figure 1. Surface plan showing mining region of the KGF. The strong-motion accelerograph was installed at the National Institute of Rock Mechanics. The epicenter of major rockburst recorded on 2.11.2005 was 500 ft south of main shaft (5). Line traces are the Mysore North Fault, the Tennant Fault, and the Gifford Fault.

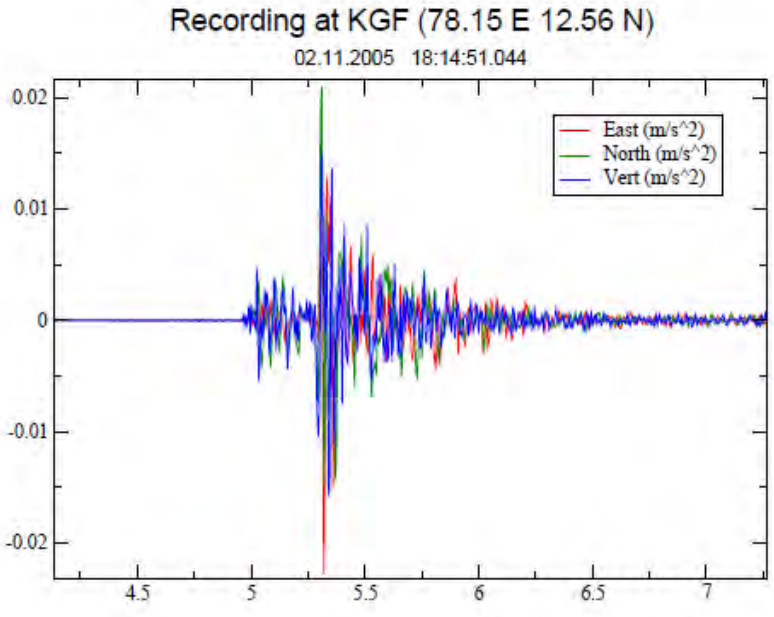

Figure 2. Seismogram for the event with *P*-arrival at 18:14:51.044 + 4.95.00.

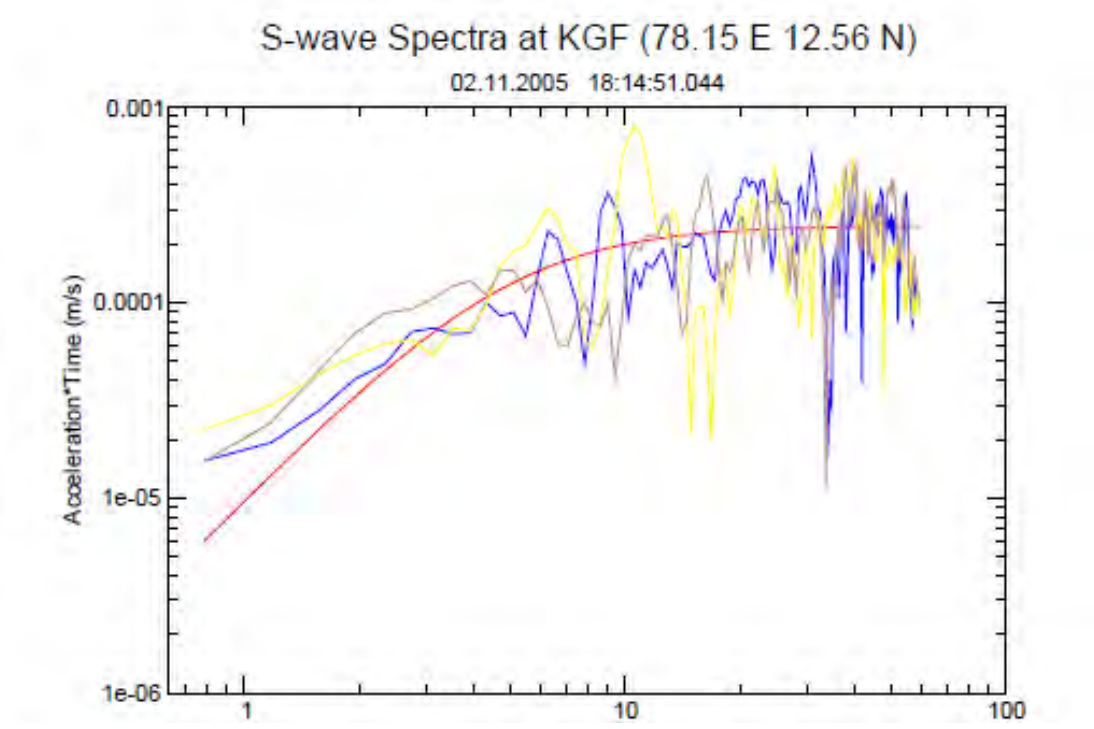

Figure 3. Acceleration spectra of the *S* wave for the event, with a Brune acceleration model (red line). The spectra have been truncated to not include the low sensor response above 50 Hz.

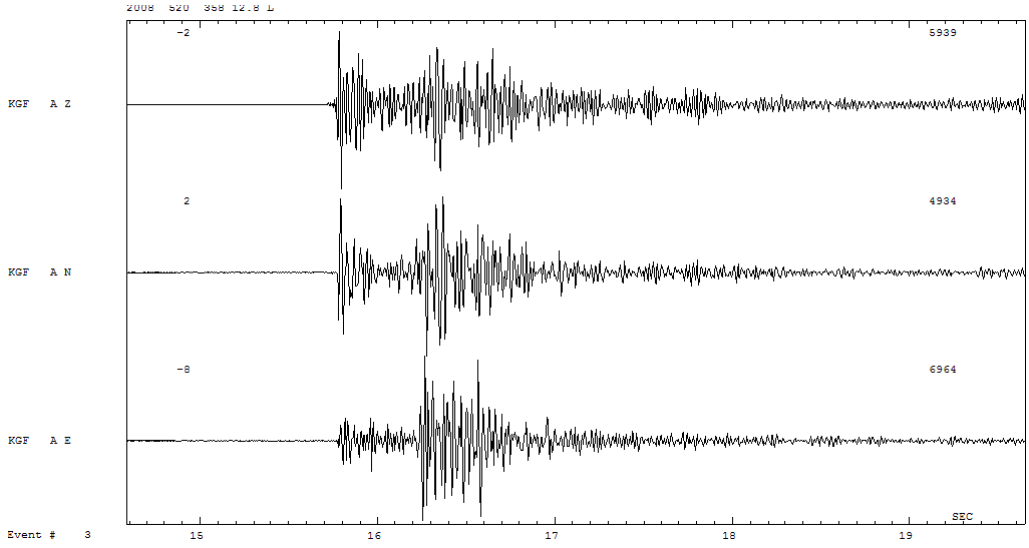

Figure 4. Typical seismic signal picked up by the strong motion accelerograph.

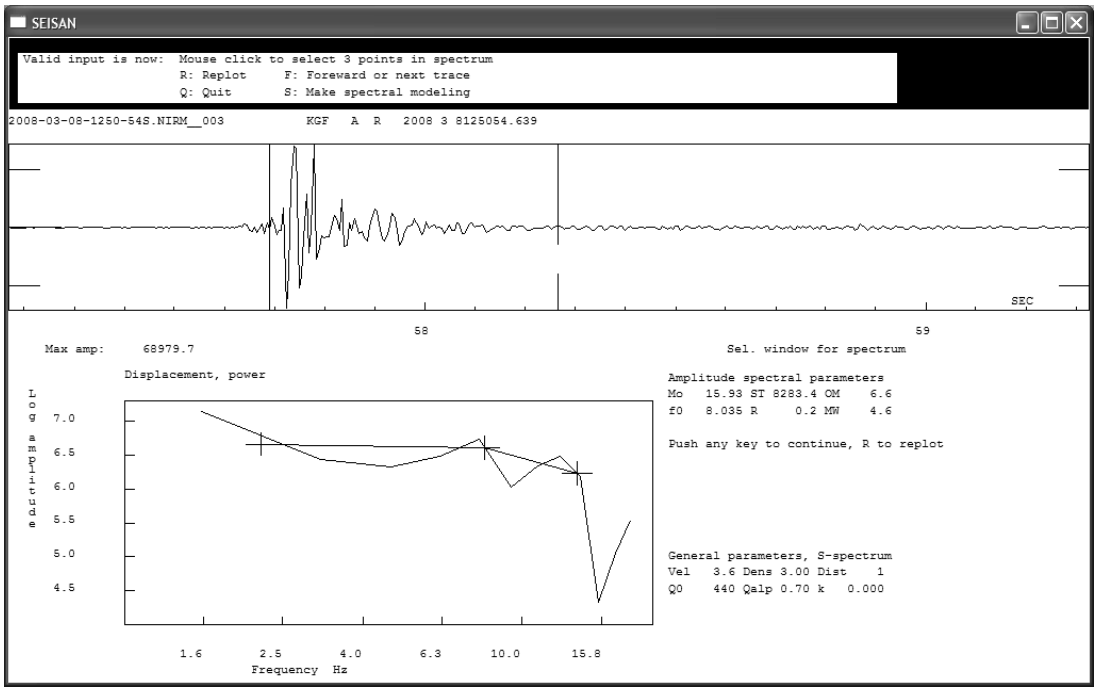

Figure 5. Typical output of source parameters computed using the *Seisan* software.

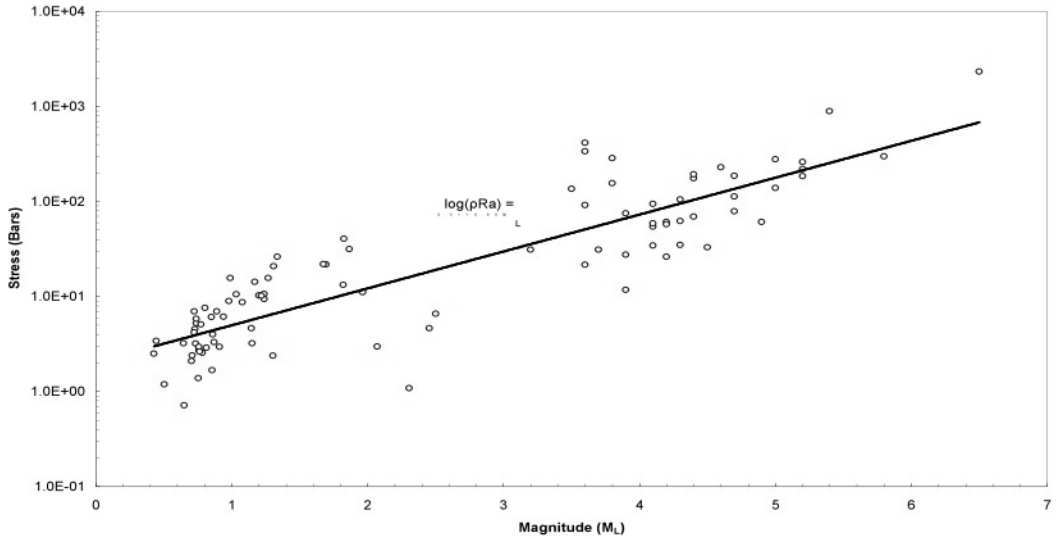

Figure 6. Dynamic shear stress difference as a function of magnitude for tremors of $M_L < 2.8$ and earthquakes of $M_L > 3$.

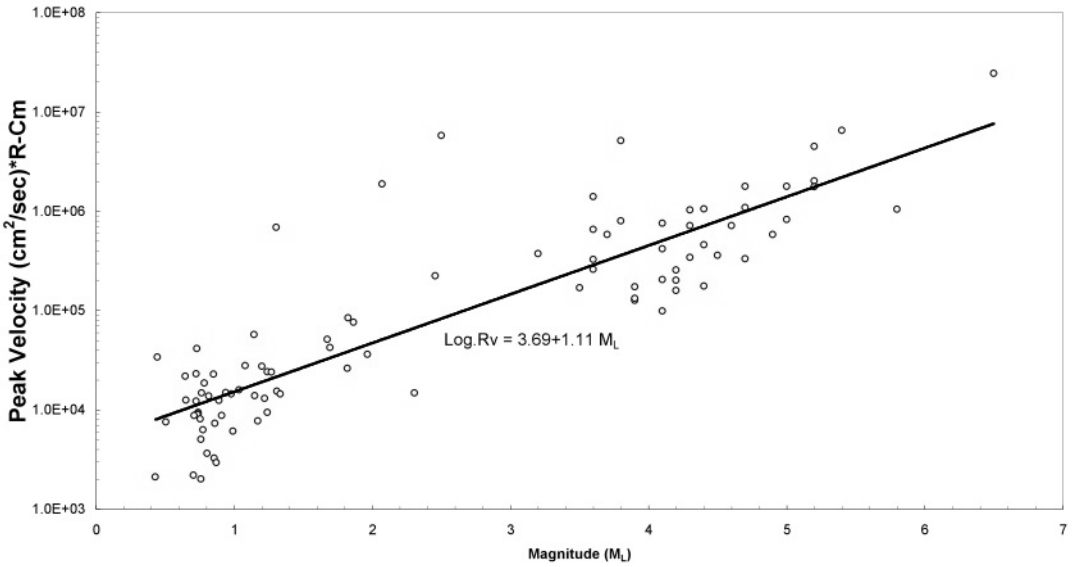

Figure 7. Peak ground velocity as a function of magnitude for tremors of $M_L < 2.8$ and earthquakes of $M_L > 3$.

WAVE PROPAGATION FROM COMPLEX 3D SOURCES USING THE REPRESENTATION THEOREM

Jeffry L. Stevens and Heming Xu

Science Applications International Corporation

Sponsored by the Air Force Research Laboratory

Contract No. FA8718-08-C-0010
Proposal No. BAA08-57

ABSTRACT

In spite of extensive prior research on generation of seismic waves by underground nuclear explosions, it is still not possible to provide a complete explanation for the observed wavefields, particularly at regional distances. Spherically symmetric explosion models embedded in layered elastic media effectively model the *P* phases generated by explosions, and the major characteristics of some reflected and transmitted phases. Nonlinear axisymmetric finite difference calculations of explosions including gravity and the effect of the free surface can model a more realistic explosion source that directly generates shear waves. These models explain more characteristics of explosion-generated seismic waves, including some aspects of regional shear phases. However, it is clear that linear and nonlinear near-source 3D effects are important in many cases. *SH* waves are commonly observed within a few km of explosions, too close to have been generated by (simple) conversion of vertical and radial components, and often larger than those components. Furthermore, it has not been established what impact 3D effects have on discriminants and on explosion yield estimates. It is important, therefore, to be able to model and understand how 3D source and source region heterogeneity affect the seismic wavefield, and what impact this has on parameters used for nuclear monitoring.

We are in the second year of a project to develop and test a three-dimensional nonlinear finite element code CRAM3D, which will be used to calculate nonlinear explosion sources that have both 3D source geometry and may occur in a 3D heterogeneous medium. The code includes the same well-tested material models that have been used in earlier axisymmetric calculations. In addition, we are developing algorithms based on the representation theorem to propagate the motion from these source region calculations to any desired distance. We have implemented a technique that allows us to propagate the results of near source 3D finite element calculations to regional and teleseismic distances. The Green's function and its derivatives are used in conjunction with the numerical solutions on a monitoring surface enclosing the complex source region. Full-waveform solutions at distance, due to complex explosion sources, are computed with the full-waveform Green's function using wavenumber integration; surface wave solutions are computed with the surface wave Green's functions using mode summation; and far field body wave solutions are computed with the outgoing waves from the source region. The excellent agreement in the surface wave portion between the full-wave solutions and surface-wave solutions demonstrates the accuracy of the implementation of the representation theorem and the respective Green's functions and their derivatives.

To test the code, we have performed calculations using cavities of three shapes: spherical, rectangular and elliptical, each with the same volume. An explosion with the same yield was detonated inside each cavity. We compare the solutions from these three cavity explosions in the near field and at distance. Gravity is included in the calculations, and we start with an equilibrium solution obtained by running the finite-element CRAM3D with overburden pressure only, prior to the start of the explosion calculation. Nonlinear deformation is seen around the cavity. The results show very good agreement between 2D and 3D solutions at distance for the spherical cavity explosion. Nonspherical wave components from nonspherical rectangular and elliptical cavities are clearly seen in the near field. The rectangular cavity shows more pronounced tangential motion than the elliptical cavity away from axes of symmetry.

OBJECTIVES

The objective of this project is to investigate the generation of complex seismic waves by explosions in media with 3D heterogeneity using a method based on the exact representation theorem for propagating complex 3D source calculations to local, regional and teleseismic distances.

RESEARCH ACCOMPLISHED

Introduction

Source physics, near source scattering, and propagation effects are all important to understanding seismic phases used in nuclear monitoring. Significant bodies of literature exist that address each subject individually. In addition to extending our understanding of source physics and near source scattering to include the effects of realistic 3D heterogeneity, this project links the progression of energy from its generation by the source, through the near source region, and into its partitioning among local, regional, and teleseismic phases. Distinguishing the far-field *P*- and *S*-waves enables us to quantify the effects of 3D structure on both *P*- and *S*-wave generation. Complete regional waveforms show how this energy is partitioned among the distinct phases, which are important to event detection, identification, and magnitude estimation. How energy is distributed among surface wave modes determines *Lg* amplitudes and *Rg* amplitudes, including near source conversions between these phases. Modal excitation of *Lg* as well as *Rg* has a significant depth dependence that is often neglected in nuclear monitoring studies (Baker et al., 2004), and these amplitudes can be disrupted further by near source effects and source region structure. This can either degrade or improve discrimination capability depending on how well it is understood.

While it is not surprising to observe *SH* waves from any single event, it is surprising to note it is always present; at regional distances, *SH* scales with yield about as well as *P*-waves. While there are many mechanisms, such as near-source scattering, tectonic release, etc. that can generate *SH* waves, all of these effects should be highly variable from one event to the next. To address this question, we need to look at the types of 3D source effects that can exist, the range of variability that would be expected from them, and whether the predictions are consistent with observations.

Source Region Calculations and Propagation Using the Representation Theorem

Our approach is to perform 3D explosion source region calculations, and then to propagate the wavefield to local, regional and teleseismic distances using layered earth Green's functions. We are interested in near-source heterogeneities in both the nonlinear and linear regimes, and therefore require both nonlinear and linear 3D codes to model the source region. In previous projects, we have used two nonlinear codes, STELLAR and CRAM, which are described briefly in Table 1 (we have also used the 1D nonlinear code SKIPPER, which is a spherically symmetric version of CRAM), and the 2D and 3D linear elastic code TRES3D.

Table 1. Numerical simulation tools used in this project

Numerical Simulation Tools	
STELLAR	Eulerian finite difference code. Used to simulate the early time history of the explosion shock. It handles material strength correctly, which is difficult for a Eulerian code. Uses second order accurate Riemann solver scheme. 1D, 2D planar and axisymmetric, and 3D.
CRAM	Lagrangian nonlinear finite difference code. Has been used extensively for axisymmetric explosion calculations. A 3D version of the code is being developed in this project.
TRES3D	Elastic finite difference code. 2D planar and axisymmetric, and 3D.
Elastodynamic Representation Theorem	The time dependent displacements and stresses from 3D source region calculations are saved on a monitoring surface located outside of the region of nonlinear response and/or 3D heterogeneity. A numerical implementation of the representation integral is then used to compute the corresponding far-field seismic radiation.

In past projects, we have used these codes in the following ways:

1. Axisymmetric CRAM was used together with the representation theorem to propagate the results of nonlinear axisymmetric finite difference calculations to regional and teleseismic distances (Day et al., 1987; Stevens et al., 1991; Stevens et al., 2004).
2. Axisymmetric STELLAR was used to calculate the early stages of an explosion. The solution at an appropriate time was overlain onto CRAM to be propagated out to the linear, elastic region. The representation theorem was used to propagate the waveform to regional and teleseismic distances (Rimer et al., 1994). A similar technique was used to overlay results from the Los Alamos National Laboratory code SOIL onto CRAM and propagate the results (Davis et al., 1992).
3. 3D STELLAR was used to calculate near-field waveforms from explosions in rectangular cavities (Stevens et al, 2006).
4. TRES3D was used to calculate the scattering from explosions in a region with 3D heterogeneity and topography (Stevens et al., 2004).

In the current project, we are doing the following: 1) using STELLAR to perform very near source nonlinear 3D calculations and TRES3D to perform linear elastic near source and source region 3D calculations; 2) developing a 3D version of CRAM to model explosions from the source out through the very important nonlinear to linear transition region; and 3) completing the implementation of the elastodynamic representation theorem for full waveforms, modes and body waves.

The technique for propagating numerical calculations using the representation theorem is to save displacements and stresses on a monitoring surface surrounding the nonlinear and/or heterogeneous region of the calculation, and then to convolve these with a Green's function appropriate for the external region (Stevens et al, 1991). In the cases that we have done previously, two-dimensional axisymmetric nonlinear finite difference calculations were performed to model the nuclear explosion, and the stresses and displacements from the calculation were saved on a cylindrical surface in the elastic region outside the region of complex nonlinear behavior. We then invoked the representation theorem and integrated the stresses and displacements with an axisymmetric Green's function to calculate the displacement at any point outside of the calculation. We performed such calculations in 2D, using Green's functions for far-field body waves, for modes and for full regional waveforms using wavenumber integration. The equations for the Green's functions for surface waves are given by Bache et al. (1982). The Green's functions for the complete seismograms are computed using a ring load source, from an algorithm based on the work of Luco and Apsel (1983) and Apsel and Luco (1983). The Green's functions for body waves are generated by a procedure similar to that described by Bache and Harkrider (1976) using a saddle point approximation to calculate a far-field plane wave for a given takeoff angle from a source in a plane-layered medium. Our objective in using multiple types of Green's functions is to gain as much insight as possible into the nature of the seismic wavefield generated by the source. An important part of the current project is to adapt these techniques to propagate seismic waves from 3D source calculations. Although any closed surface can be used for representation theorem integration, we use a cylindrical surface for axisymmetric problems, and a rectangular surface for 3D problems.

3D implementation of the representation theorem

The key to extending the axisymmetric representation theorem discussed above to 3D is to recognize that while the deformation in the source region may be arbitrarily complex, if the structure can be approximated as a plane-layered medium outside of the source region, then the known Green's function for a plane-layered medium applies (this also assumes that we can neglect the interaction of any backscattered waves returning to the source region after leaving it). Note that the representation theorem is exact. That is, no matter how complex the 3D motion is on the source region boundary, it will be correctly propagated by the representation theorem. The following benchmark test demonstrates the performance of the method by comparing the results with equivalent finite difference calculations and wavenumber integration seismograms.

The representation theorem states that displacement at an observation point is made up of contributions due to body forces throughout the source volume, plus contributions due to the traction and displacement on the source volume surface (Aki and Richards, 1980). In the three-dimensional numerical finite difference calculations, we save displacements and stresses due to the seismic source on a monitoring surface on the boundary of a rectangle (five planar surfaces, excluding the upper surface), and calculate Green's functions from each point on the monitoring surface to the receiver and thus, the synthetic seismogram at the receiver point *X* outside of the monitoring surface is obtained by integrating over the monitoring surface S_M :

$$u_i = \iint_{S_M} \{G_j^i(\xi;X) * T_j^M(\xi) - u_j^i(\xi) * S_{jk}^i(\xi;X) n_k\} dA \quad (1)$$

in the frequency domain, where $G_j^i(\xi;X)$ and $S_{jk}^i(\xi;X)$ are the Green's function and the stress tensor on the monitoring surface due to a unit impulsive force at X in direction *i*, T_j^M is the traction on the monitoring surface due to the seismic source, *u* is the displacement on the monitoring surface, and *n* is the normal to the monitoring surface. The operator * denotes convolution and the summation convention is assumed.

Equation 1 is applicable to any Green's function for the exterior model, and so we can use a full waveform Green's function, far-field body wave Green's function, and/or modal Green's function as we have discussed earlier for axisymmetric problems. We have implemented this technique for full waveform seismograms calculating the Green's functions using wavenumber integration. We have also implemented the technique for body waves and for modes using corresponding Green's functions.

The synthetic seismograms are computed using the following steps:

1. Displacements and stresses are saved on the monitoring surface during the finite difference calculations.
2. If necessary, the monitoring solutions are resampled onto a coarse grid, as permitted by the required resolution. If there is a symmetry boundary, the entire monitoring surface is constructed first.
3. The finite difference solutions at each point on the monitoring surface are transformed into the frequency domain.
4. The displacement and stress Green's functions due to the three orthogonal forces at the receiver location are calculated for each location on the monitoring surface in the frequency domain (using reciprocity).
5. Equation (1) is used to obtain the solution at the receiver in the frequency domain.
6. The solution is transformed back to the time domain.

Step 5 is implemented with a generalized interface code, which takes as inputs the monitoring wavefields and the Green's functions and stress fields for any of the full-waveforms, surface waves or body waves. Specifically, full-waveform solutions at distance, due to complex explosion sources, are computed with the full-waveform Green's function using wavenumber integration. Surface wave solutions are computed with only with the surface wave Green's functions using mode summation. Far field body wave solutions are computed with the outgoing waves from the source region. The principal advantage of this approach is that it allows us to perform detailed calculations of the source region and then propagate the results to distances that would be impractical or impossible to include in the same numerical calculation. In addition to reducing cost and time, the hybrid method is also more accurate, as numerical dispersion increases with the size and duration of numerical calculations.

Benchmark Tests with Gravity

We have implemented an explicit three-dimensional Lagrangian finite element algorithm that is capable of using multiple processors (Stevens and Xu, 2008). All of the nonlinear material models from 2D CRAM have been implemented and gravity is included. The cavity is placed near the center of the grid and is enclosed by a spider grid which facilitates applying the pressure boundary condition and rezoning elements, as implemented in the two-dimensional axisymmetric code, CRAM.

To test the code, we have performed calculations using three kinds of cavities: spherical (radius 5m), rectangular (each side 8.06m) and elliptical (three axis lengths are 6m, 5m and 4.1667m), each with the same volume. The same yield (0.2kt) explosion is detonated in each cavity. The material external to the cavity is a model for Degelen granite (Stevens et al., 2003). The model consists of two layers: the top layer is 30m thick elastic and the bottom layer is nonlinear. Gravity is included in the calculations, and we start with an equilibrium solution obtained by running the finite-element CRAM3D with overburden pressure only, prior to the start of the explosion calculation. We compare the solutions from these three cavity explosions in the near field and at distance. The shapes of the cavities are shown in Figure 1 and the seismograms in the near field are shown in Figure 2. Each seismogram plot corresponds to a receiver in the same pattern in Figure 1. The radial, tangential and vertical components are represented by red, green and blue lines. The top right plots correspond to the spherical cavity and show no visible tangential motion (green lines) at these receivers. The bottom left plots correspond to the rectangular cavity and show clear tangential motion off the symmetry axes (vertical, horizontal and diagonal). The bottom right plots correspond to the elliptical

cavity and show some visible tangential motion off the symmetry axes (vertical and horizontal). The main waveform characteristics in the elliptical case are quite similar to those in the spherical case.

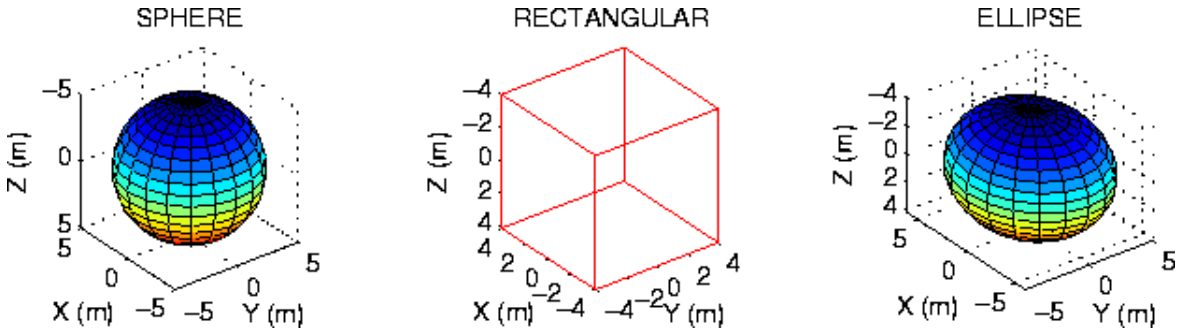

Figure 1. Three cavity shapes with the same volume used for 3D nonlinear explosion calculations.

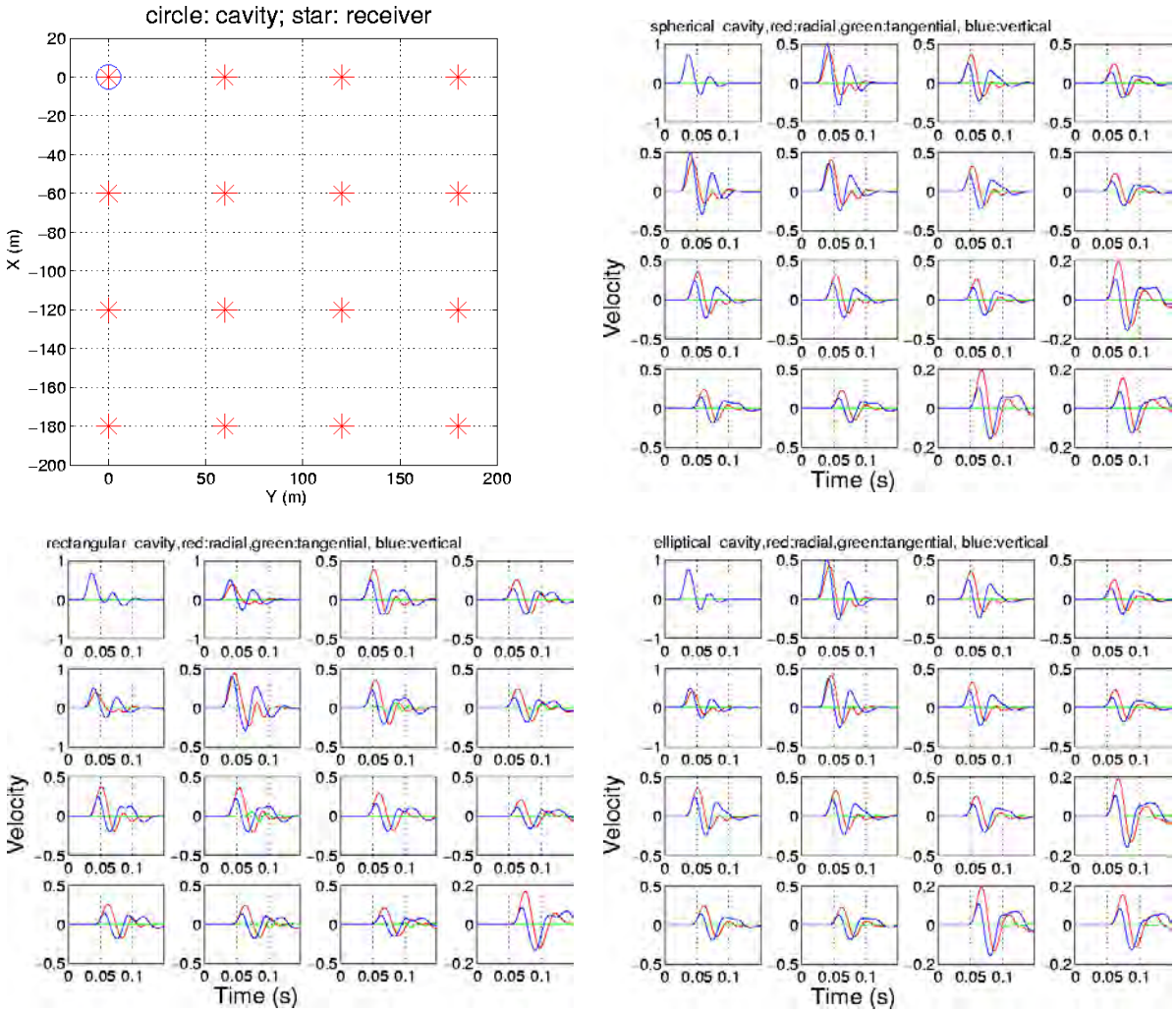

Figure 2. Near field receiver locations (top left): blue circle indicates the cavity location. The near field waveforms due to different cavities are shown at top right and bottom. Red, green and blue lines correspond to radial, tangential and vertical components. Note the tangential components from the non-spherical cavities (bottom two figures).

All the three explosions yield nonlinear deformation around the cavity in Figure 3. The horizontal (top) and vertical (bottom) slices across the cavity center are shown for comparison. Again, both spherical and elliptical cavities show similar patterns but the nonlinear deformation region is enlarged for the rectangular cavity relative to the other two cavities, most likely caused by the effects of the corners.

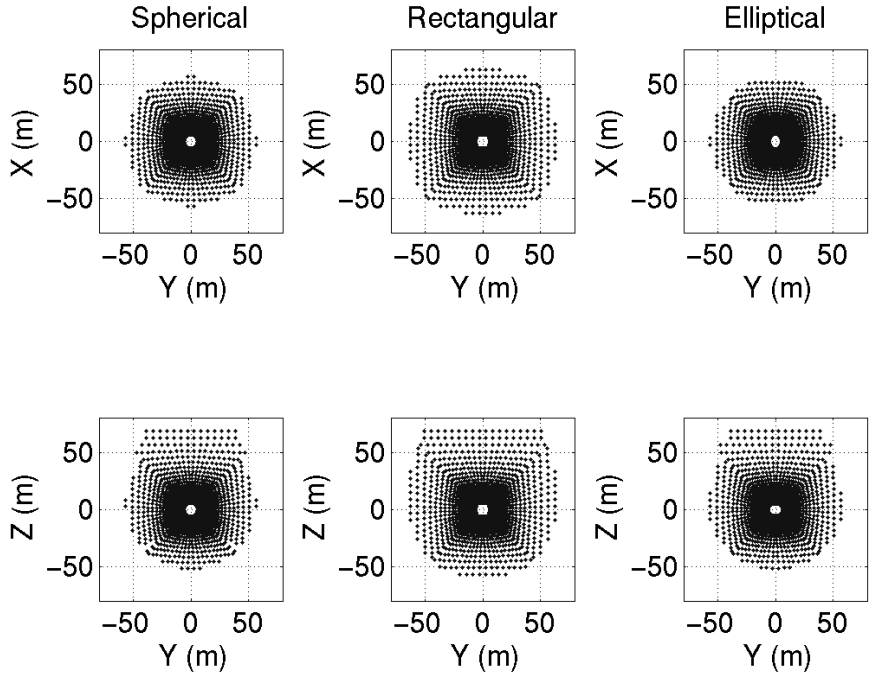

Figure 3. Nonlinear deformation extent around the cavities. The top plots are the horizontal slices across the cavity center and the bottom illustrate vertical slices. The asymmetry in the Z direction is caused by the variation of overburden pressure with depth. More nonlinear deformation occurs above the cavity than below.

Far field solutions are obtained with the representation theorem (Equation 1) by using the displacements and stresses recorded on the monitoring surfaces in the finite-element calculations. An interface code was developed to correctly match the numerical solutions with the Green's functions and the corresponding stresses. We compare the full waveforms and surface waves at two different locations with the same distance. One is at x=2000m,y=1500m (location 1, no symmetry) on the surface and the other at x=2500m and y=0m (location 2 at the symmetry axis). The full waveforms are computed by the wavenumber integration method and the surface waves are computed using mode summation. The results at the two locations for the three cavities are shown in Figure 4. The left corresponds to the location 1 and the right location 2. Each panel has three components. The red and green lines indicate the full waveform solutions and surface wave solutions, respectively, and the blue dashed lines, the 2D full waveform solutions in the spherical cavity case. All the waveforms are low pass filtered below 5Hz. It is clearly seen that the mode summation solutions (green lines, Figure 4) match the surface wave portions of the full waveform solutions (red lines, Figure 4) for all the cavity types at two locations very well. For the spherical cavity full-waveform solutions, there is also very good agreement between 2D (blue dashed lines, Figure 4) and 3D, validating the proper implementation of the Lagrangian finite-element algorithms and the representation theorem in 3D. It is also noted that the spherical and elliptical cavities have the similar waveforms at distance, as in the near field. The wave amplitudes are slightly larger for the rectangular cavity (center row, Figure 4) and consistent with nonlinear deformation extent. The tangential motions are very small for the three cavities and indicate that the source asymmetry due to a small yield, as seen in the horizontal nonlinear deformation distribution (top row, Figure 4), is quite weak at low frequencies, which is also verified by comparing the waveform solutions at the two locations.

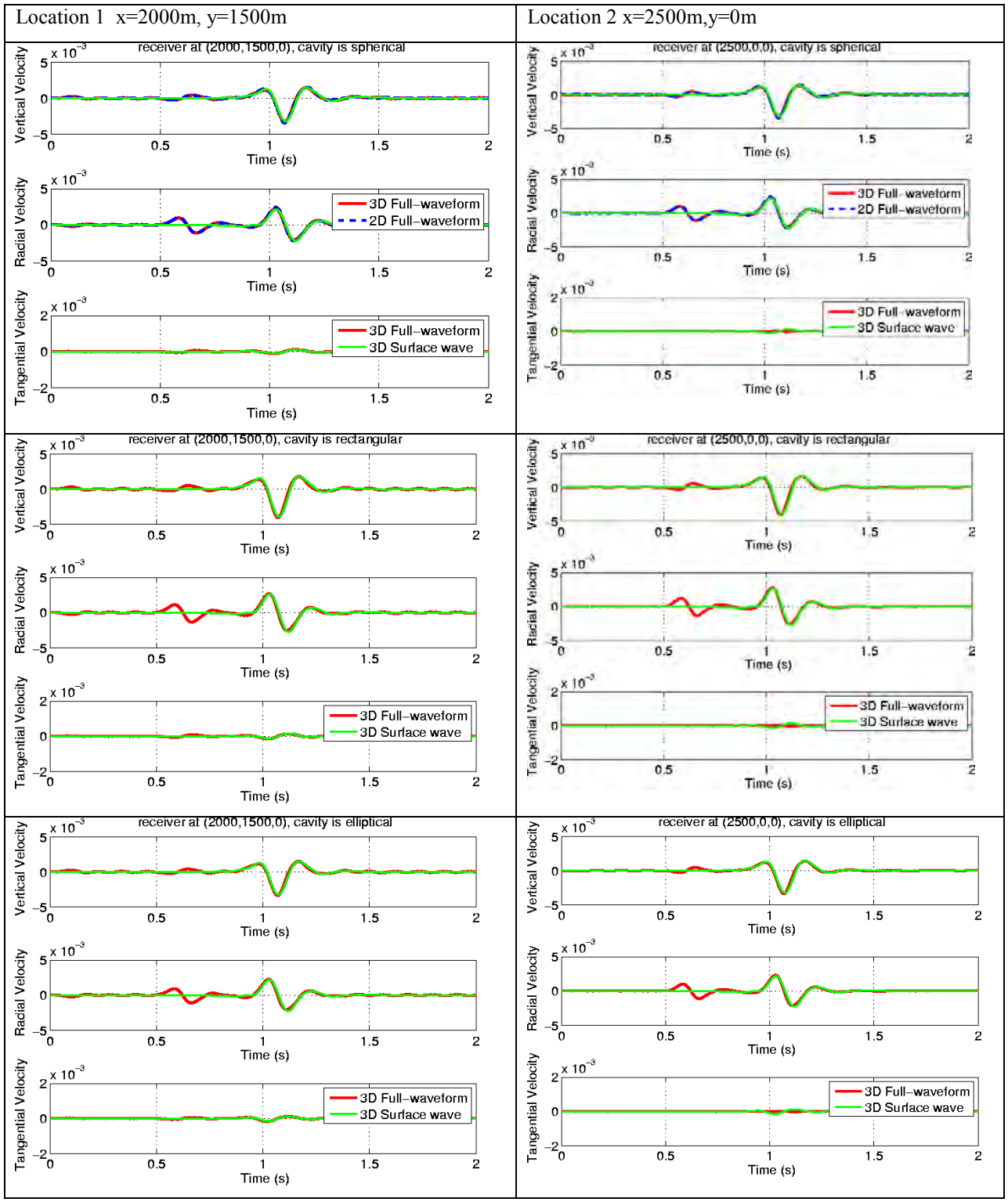

Figure 4. Far field waveforms using the wavenumber integration method and mode summation. Waveforms at location 1 are shown on the left, location 2 on the right. There is excellent agreement between the full-waveform solutions and surface wave solutions for the surface wave part of the waveform. Excellent agreement is also demonstrated for the full waveform solutions in 2D (blue dashed lines) and 3D (top).

CONCLUSIONS AND RECOMMENDATIONS

We are in the second year of a project to understand 3D effects on seismic radiation from underground nuclear explosions. We have nearly completed development of a 3D version of CRAM, the Lagrangian code we have used previously for performing axisymmetric calculations of underground explosions. We have also implemented an interface code, which utilizes any Green's functions in order to propagate the results of the near field 3D calculations to regional and teleseismic distances using the representation theorem. The objectives are to complete implementation of the numerical methods and then perform 3D calculations to understand and model the effects of 3D source region heterogeneity and the seismic response to it in a realistic source scenario.

REFERENCES

Aki, K. and P. G. Richards (1980). *Quantitative Seismology -- Theory and Methods*, W. H. Freeman and Company, San Francisco, CA.

Apsel, R. J. and J. E. Luco (1983). On the Green's Functions for a Layered Half-Space, Part II, *Bull. Seism. Soc. Am*. 73: 931–951.

Bache, T. C. and D. G. Harkrider (1976). The Body Waves Due to a General Seismic source in a Layered Earth Model, *Bull. Seism. Soc. Am*. 66: 1805–1819.

Bache, T. C., S. M. Day and H. J. Swanger (1982). Rayleigh Wave Synthetic Seismograms from Multi-Dimensional Simulations of Underground Explosions, *Bull. Seism. Soc. Am*. 72: 15–28.

Baker, G. E., J. L. Stevens and H. Xu (2004), *Lg* Group Velocity: A Depth Discriminant Revisited, *Bull. Seism. Soc. Am.* 94: 722–739.

Davis, C. G., W. E. Johnson, J. L. Stevens, N. Rimer, T. G. Barker, E. J. Halda, E. Bailey, and W. Proffer (1992). Seismic signals from asymmetric radiation-hydrodynamic calculations, Los Alamos National Laboratory report LA-12506-MS.

Day, S. M., J. T. Cherry, N. Rimer and J. L. Stevens (1987). Nonlinear model of tectonic release from underground explosions, *Bull. Seism. Soc. Am*. 77: 996–1016.

Luco, J. E. and R. J. Apsel (1983). On the Green's Functions for a Layered Half-Space, Part I, *Bull. Seism. Soc. Am*. 73: 909–929.

Rimer, N., T. Barker, S. Rogers, J. Stevens, and D. Wilkins (1994). Simulation of seismic signals from partially coupled nuclear explosions in cylindrical tunnels, Rep. DNA-TR-94-136, Defense Nuclear Agency, Alexandria, VA.

Stevens, J. L., T. G. Barker, S. M. Day, K. L. McLaughlin, N. Rimer, and B. Shkoller (1991). Simulation of teleseismic body waves, regional seismograms, and Rayleigh wave phase shifts using two-dimensional nonlinear models of explosion sources, AGU Geophysical Monograph 65: Explosion Source Phenomenology, S. Taylor, H. Patton, P. Richards, Eds., ISBN 0-87590-031-3, 239–252.

Stevens, J. L., N. Rimer, H. Xu, G. E. Baker and S. M. Day (2003). Near field and regional modeling of explosions at the Degelen Test Site, SAIC final report to DTRA, SAIC-02/2050.

Stevens, J. L., G. E. Baker, H. Xu, T. J. Bennett, N. Rimer and S. M. Day (2004). The Physical Basis of *Lg* Generation by Explosion Sources, SAIC Final Report submitted to the National Nuclear Security Administration under contract DE-FC03-02SF22676, December.

Stevens, J. L., S. Gibbons, N. Rimer, H. Xu, C. Lindholm, F. Ringdal, T. Kvaerna, and J. R. Murphy (2006). Analysis and simulation of chemical explosions in nonspherical cavities in granite, *J. Geophys. Res*. 111: doi:10.1029/2005JB003768.

Stevens, J.L and H. Xu (2008). Wave propagation from complex 3D sources using the representation theorem, in *Proceedings of the 30th Monitoring Research Review: Ground-Based Nuclear Explosion Monitoring Technologies*, LA-UR-08-05261, Vol. 1, pp 682–691.

IMPROVING M_s:m_b DISCRIMINATION USING MAXIMUM LIKELIHOOD ESTIMATION: APPLICATION TO MIDDLE EAST EARTHQUAKE DATA

Anastasia Stroujkova and Jessie L. Bonner

Weston Geophysical Corporation

Sponsored by the National Nuclear Security Administration

Contract No. DE-AC52-04NA25547
Proposal No. BAA04-63

ABSTRACT

During this project, we have combined the Russell (2006) surface wave magnitude (M_s) formula and the M_s(VMAX) measurement technique (Bonner et al., 2006) for improved event discrimination at regional and teleseismic distances. The MATLAB-based processing program is called EVALSURF and includes Rayleigh-wave detection algorithms and phase match filtering using the Pasyanos (2005) group-velocity models. The program has been applied to earthquakes and explosions in Eurasia and offered improved earthquake screening performance compared to other well known formulas. We used EVALSURF to evaluate the anomalous M_s from the 2006 North Korean nuclear explosion (Bonner et al., 2008) and have applied it to the larger 2009 event. For the final year of our project, we are researching new methods for improving M_s-m_b discrimination for earthquakes and explosions.

The Maximum Likelihood Estimate (MLE) was proposed by Ringdal (1976) to reduce the network bias due to non-detection. We estimated the M_s *(VMAX)* magnitudes for approximately 100 seismic events located in the Middle East using MLE approach and compared the results with conventional-averaged estimates. To evaluate the performance of the method, we tested it using a set of simulated events recorded by the network with an assigned magnitude close to a threshold value. In our simulation experiments, we chose the same number of the events and the same station distribution as in our Middle East dataset. We found that the bias introduced by the averaging depends on the standard deviation of the inter-station M_s*(VMAX)* measurements. The bias is increasing as M_s *(VMAX)* decreases below 4 m.u., which represents the upper bound for the station magnitude thresholds.

An important part of the MLE application is evaluation of the detection thresholds for the stations used for the magnitude estimation. The threshold values for each station could be estimated using a "noise magnitude" for each event-station pair using the broadband ambient noise estimates for the Global Seismographic Network (GSN) e.g., Berger et al., (2004). A different way to assign the threshold values is to find the smallest magnitude actually detected by each station. In this article we estimated the detection threshold using both techniques and obtained similar results with both methods.

Finally, we applied the MLE estimate to the Middle East event dataset. We found significant differences between the conventional averaging and the MLE estimates for the magnitudes near the detection threshold for most of the stations (< 4 m.u.). The MLE estimates above M_s *(VMAX)* > 4 m.u. are identical to the results of the averaging.

OBJECTIVES

Developing a methodology for calculating surface wave magnitudes that is valid at both regional and teleseismic distances, applicable to events of variable sizes and signal-to-noise ratios, calibrated for variable structure and propagation, and easy to automate in an operational setting, is an important monitoring goal. Our objectives are to create such a methodology, and to use it to lower M_s estimates and detection thresholds. We hope that the method will provide a seamless tie between M_s estimates at regional and teleseismic distances.

To accomplish our objectives, we developed the Matlab program EVALSURF (Bonner et al., 2006) , which estimates variable-period (8 < T < 25 sec; recently updated to 40 sec) Rayleigh-wave magnitudes using the Russell (2006) and M_s(VMAX) measurement technique (Bonner et al., 2006) for comparison to the historical formulas of Marshall and Basham (1972) and Rezapour and Pearce (1998). The program uses the updated Lawrence Livermore National Laboratory group velocity models for Eurasia (Pasyanos, 2005) to identify, phase match filter, and extract the fundamental-mode Rayleigh waves for analysis. During the past year, we have determined a methodology to estimate the M_s detection thresholds for European and Asian GSN stations as well as estimating Maximum Likelihood Estimates of magnitudes.

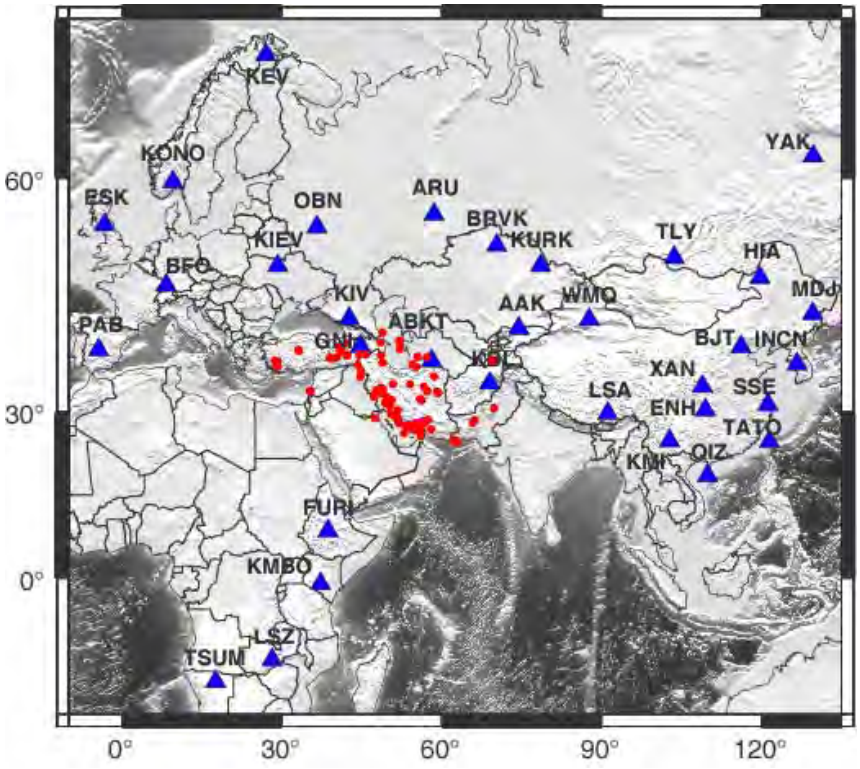

Figure 1. Map of the seismic events (red circles) and stations (blue triangles) used for M_s *(VMAX)* study.

RESEARCH ACCOMPLISHED

M_s (VMAX) or Variable-period, MAXimum amplitude magnitude estimates is a time-domain technique for determining surface wave magnitudes at variable periods between 8 and 25 s using both regional and teleseismic waves (e.g., Russell, 2006; Bonner et al., 2006):

$$M_s = \log(a_b) + \frac{1}{2}\log(\sin(\Delta)) + .0031\left(\frac{T_0}{T}\right)^{1.8}\Delta - \log(f_c) - 0.43 - 0.66\log\left(\frac{20}{T}\right) \qquad (1)$$

where a_b is the amplitude of the Butterworth-filtered surface waves (zero-to-peak in nanometers), f_c is the filter frequency of a zero-phase Butterworth band-pass filter with corner frequencies ($1/T$- f_c, $1/T$+ f_c), T=20 sec is the reference period. For variable periods 8 sec < T < 25 sec, the equation is corrected to T=20 sec, accounting for source effects, attenuation, and dispersion.

Previously we computed M_s (VMAX) for over 100 seismic events located in the Middle East region (Figure 1) with reported body wave magnitudes (m_b) between 3.8 and 5.6 (NEIC). We extended the period range to 40 s to improve magnitude estimation for larger or deeper events. During this reporting period we compared the magnitude estimation using conventional averaging between the individual station magnitude measurements and the Maximum Likelihood Estimation (e.g. Ringdal, 1976).

Maximum Likelihood Magnitude Estimate

Using the Maximum Likelihood Estimate (MLE) to reduce the network bias due to non-detection was proposed by Ringdal (1976). Generalization of this procedure to include data clipping was proposed by von Seggern and Rivers (1978). The network magnitude bias is caused by the loss of information from non-reporting stations. For small and intermediate size events this means that the stations with the magnitude measurements below a certain threshold may not report the signal and therefore get ignored. This effect is called "censoring". A number of studies have shown that the magnitude bias could be significant, particularly for the events close to the detection threshold (Ringdal, 1976; Evernden and Kohler, 1976).

The MLE method is based on the assumption that for a given event the magnitude estimates follow a Gaussian distribution with unknown mean and variance $M_s \sim N(\mu, \sigma)$. We assume that an event is detected by a station if the station magnitude exceeds a certain threshold magnitude a_i ($i = 1, \ldots, n$), where n is a number of the stations in the network. Ringdal (1976) provided an expression for the maximum likelihood estimate of an event magnitude with a true magnitude μ:

$$L(m_1 \ldots m_n / \mu, \sigma) = \prod_{i, m_i > a_i} \frac{1}{\sigma} \phi\left(\frac{m_i - \mu}{\sigma}\right) \prod_{j, m_j < a_j} \Phi\left(\frac{a_j - \mu}{\sigma}\right), \qquad (2)$$

where ϕ and Φ are the Gaussian PDF and CDF respectively. This expression is maximized numerically in order to obtain a maximum likelihood estimate of the magnitude μ.

The threshold values for each station a_i could be estimated using "noise magnitude" for each event-station pair. We converted the broadband ambient noise estimates for the Global Seismographic Network (GSN, e.g., Berger et al., 2004) from decibels to nanometers (nm) and input them into the M_s (VMAX) formula (1) for variable-period surface waves. We propagated these noise estimates at periods (T) between 8 and 40 s to distances Δ corresponding to each earthquake-station pair. Table 1 (columns 3-6) shows the estimates of the magnitude threshold for a representative event in the region (2006.06.03).

A different way to assign the threshold values is to find the smallest magnitude actually detected by each station. In this article, we follow the work of Ringdal (1976), who found the thresholds by averaging over the three smallest detected magnitudes. The second column in Table 1 (in Appendix A) shows the values estimated using this approach. Figure 2 shows the correspondence between the estimates made with different methods for different periods for the stations with both estimates available. The magnitude thresholds show the best agreement for the period T=20 sec (blue circles). Notice that a different set of stations was used for the thresholding application. The threshold values using the minimum M_s (VMAX) approach are missing for the stations with not enough M_s (VMAX) measurements to obtain a reliable threshold. Some of the noise floors were not reported, which resulted in missing values in columns 3-6 of Table 1.

An important issue to consider is which stations should be added to MLE estimates as censored values. In practice selection of the stations for threshold Ringdal (1986) divided all stations into: a) detecting stations, b) non-detecting

stations due to noise; and c) non-detecting stations due to maintenance issues. For the third group of stations, Ringdal suggests computing the probabilities of each station of being off-line and adding them randomly. We, however, only used the reporting stations to use as either measured or a censored (threshold) value.

Another issue, mentioned in Ringdal (1986) is the increase of noise due to special circumstances, such as time intervals coinciding with large events and their aftershocks overlapping with the event in question. In this case we did not estimate the magnitudes even though they were significantly above the detection threshold. These events require special attention, for instance using the information about the noise amplitude just before the event to establish the detection threshold.

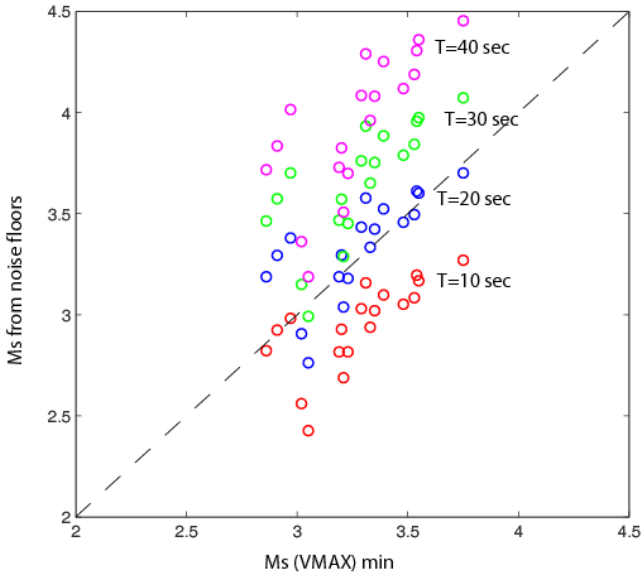

Figure 2. Comparison of the magnitude thresholds computed with different methods with each circle corresponding to one station having both threshold values defined in Table 1. Horizontal axis: detection threshold computed by averaging 3 lowest magnitudes actually detected by the station (Ringdal, 1976); vertical axis: detection threshold computed using the noise floors for different periods for a representative event (2006.06.03). The best agreement (dashed line) is for T=20 sec.

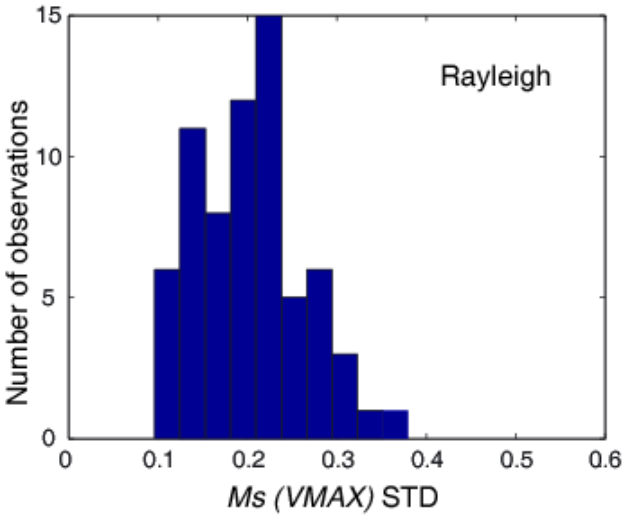

Figure 3. Histogram of M_s (VMAX) RMS residuals for nearly 100 events located in the Middle East.

It was noted by Ringdal (1976) that the estimate of the true magnitude μ depends on the inter-station magnitude variance σ. Figure 2 shows the histogram of M_s (VMAX) RMS residuals for the Middle East dataset with the mean values of approximately 0.2. To evaluate the performance of the method for our dataset, we created a set of simulated events recorded by the network with an assigned magnitude close to a threshold value. In our simulation experiments, we chose the same number of the events and the same station distribution as in our Middle East dataset. The individual station magnitudes for each event were normally distributed with the variance of $\sigma = 0.2$. We used the threshold magnitudes estimated using both methods shown in Table 1.

The synthetic testing of the MLE algorithm was implemented as follows. For a fixed magnitude value μ we generated a set of station measurements with normal distribution of the measurement errors $N(\mu, \sigma)$. For the measurement standard deviation we used the value $\sigma = 0.2$ obtained for our dataset. In addition we performed the simulations with $\sigma = 0.4$, which was used in the earlier simulations by Ringdal (1976) based on the work by Veith and Clawson (1972). For each of the n stations of each hypothetical event we determined detection/no detection, by comparing m_i and a_i. All the stations with $m_i < a_i$ were designated as non-detections and removed from the averaging magnitude estimate. Then we estimated network event magnitude using the conventional averaging over all stations detected the event, and by maximizing the likelihood function using both detecting and non-detecting stations.

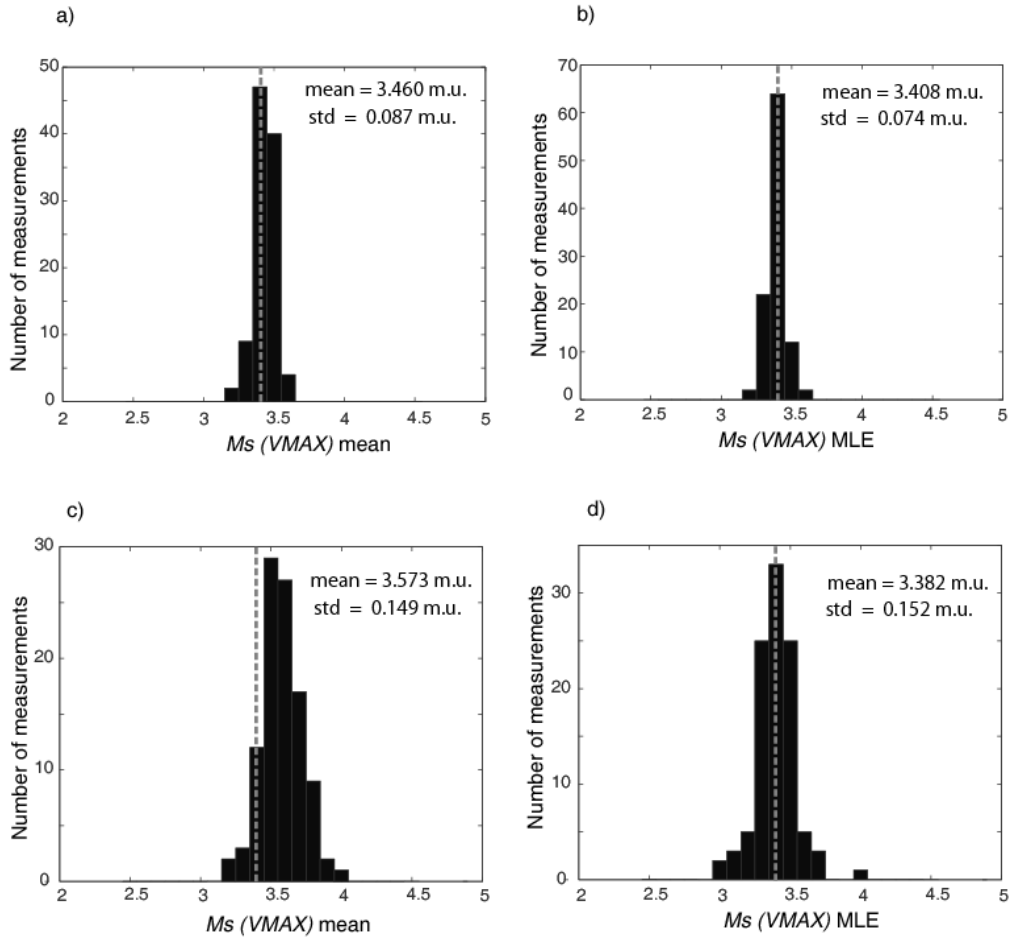

Figure 4. Histograms of M_s (VMAX) estimates for 100 synthetic events with M_s *(VMAX)* =3.4 and the same reporting station distribution as in the Middle East dataset. a) M_s *(VMAX)* estimated as a mean value of the station measurements with σ=0.2; b) M_s *(VMAX)* estimated using MLE approach with station measurement σ=0.2; c) M_s *(VMAX)* estimated as a mean value of the station measurements with σ=0.4; b) M_s *(VMAX)* estimated using MLE approach with station measurement σ=0.4.

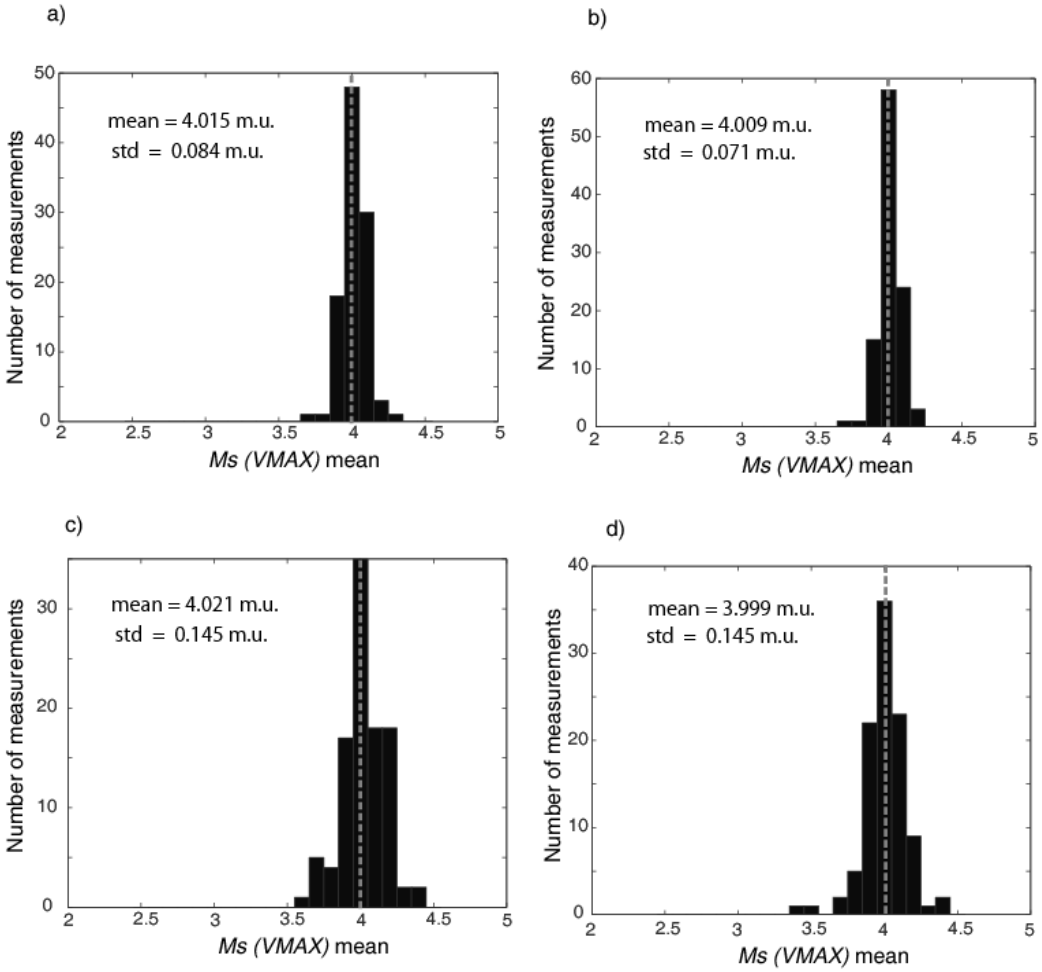

Figure 5. Histograms of M_s (VMAX) estimates for 100 synthetic events with M_s *(VMAX)* =4.0 and the same reporting station distribution as in the Middle East dataset. a) M_s *(VMAX)* estimated as a mean value of the station measurements with σ=0.2; b) M_s *(VMAX)* estimated using MLE approach with station measurement σ=0.2; c) M_s *(VMAX)* estimated as a mean value of the station measurements with σ=0.4; b) M_s *(VMAX)* estimated using MLE approach with station measurement σ=0.4.

The results of both estimates are shown in Figures 4 and 5. Figure 4 shows the histogram of the estimates for the true magnitude $\mu = 3.4$. This value is below or close to the detection threshold for several stations (Table 1); therefore we expect the conventional averaging estimates to have relatively large network bias. For example, Figures 4a and 4c show the histograms of the M_s (VMAX) estimates using the conventional average (Figure 4a) and the MLE technique (Figure 4b) for the measurement $\sigma = 0.2$. The mean value of the recovered magnitude values is 3.460 (compare with $\mu = 3.4$) using the averaging, and 3.408 using the MLE approach. Thus the bias is 0.06 in the former case and 0.008 in the latter case. The bias is more pronounced if the larger value of the measurement error is used (e.g. $\sigma = 0.4$, Figure 4c and 4d). In this case the magnitude estimate bias is 0.173 for the conventional averaging and -0.018 for the MLE approach. However the bias is not as significant as obtained by Ringdal (1976), probably because in this study we used larger station network. Only 13 stations were used in the Ringdal (1976) study.

Figure 5 shows the distribution of the estimated magnitudes for $\mu = 4.0$. This value is higher than the detection threshold for all stations, so there is not a significant difference between the average and the MLE estimation. Even

in case of larger inter-station variance the bias of the conventional averaging estimate is relatively small (0.015-0.021 m.u.).

Application of MLE Technique to the Middle East Dataset

We estimated M_s (VMAX) using a standard approach (station average) and an MLE approach for the Middle East dataset discussed earlier. For the earthquake dataset we used a slightly different thresholding approach than was used for the synthetic dataset. For the synthetic data, all the measured values below the threshold values a_i were replaced with the threshold values and marked as "censored". For the real dataset, some of the measured values were below threshold, in which cases we used the measured values. For the events with the magnitudes significantly larger than the threshold magnitude with missing stations due to unusually high noise, we didn't use the threshold values if the average magnitude exceeded the threshold value by more than 0.6 m.u., which corresponds to a standard error multiplied by 3.

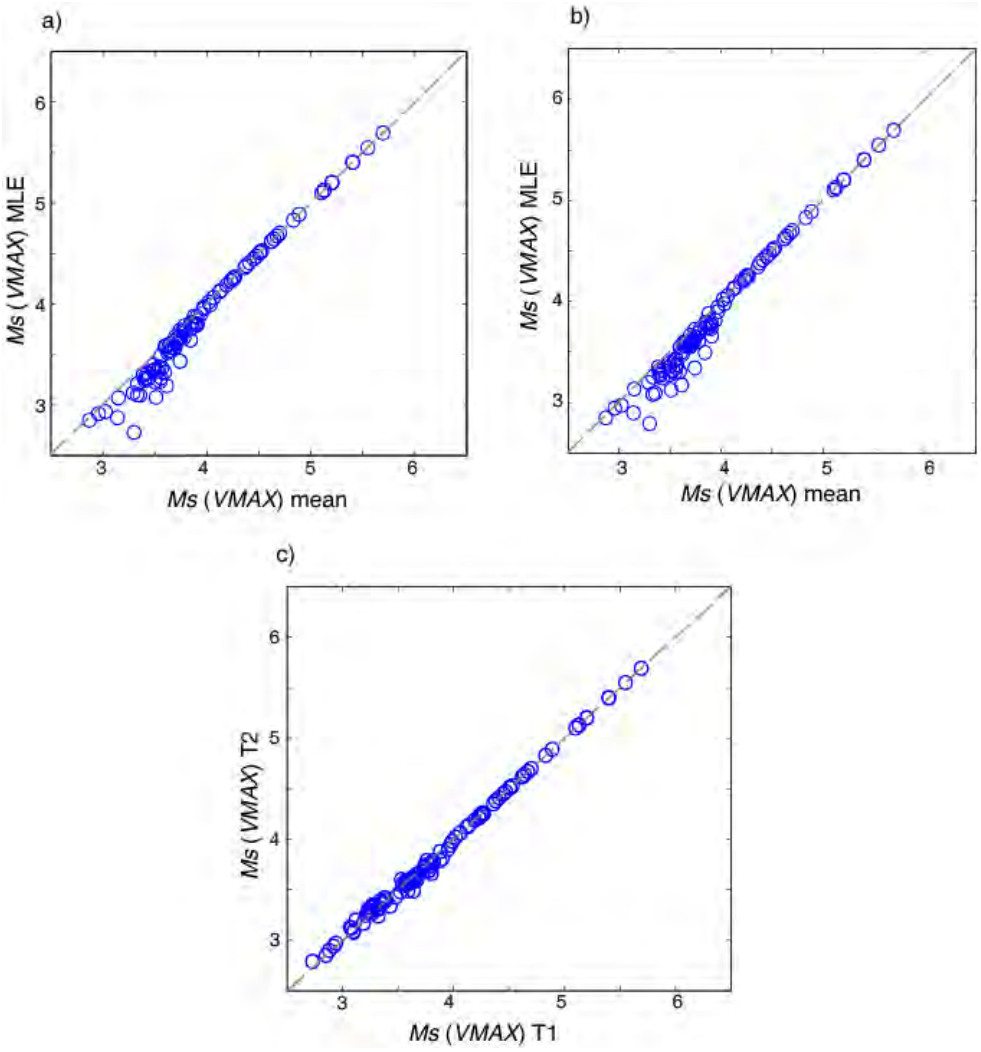

Figure 6. Comparison between the mean and the MLE estimates of the M_s *(VMAX)* applied to the Middle East event dataset: a) using minimum detected magnitude threshold; b) using noise magnitude approach; c) cross-plot between the two MLE estimates with different threshold definitions (T1 as in (a) and T2 as in (b)).

Figure 6 shows the cross-plot between the mean and the MLE estimate of M_s *(VMAX)*. We repeated both estimates using the two types of the station threshold estimates, shown in Table 1. Figure 6a shows the results using the minimum magnitude approach, while Figure 6b shows the MLE estimate using the station noise floor approach. Both thresholding approaches produce similar results as shown in Figure 6c; however, there are some differences between the individual events. As mentioned earlier, different sets of stations were used to generate the censored values due to data availability. Above the magnitude of approximately 4.1 both MLE and conventional estimates are essentially equal. Below this point there is a significant positive bias for the conventional network average estimate. In addition, the events occurring during high-noise time intervals, such as large earthquakes and their aftershock sequences require special consideration and should be processed with caution.

CONCLUSIONS AND RECOMMENDATIONS

MLE technique was developed to reduce the network magnitude estimation bias for magnitudes near the detection threshold. We evaluated the detection thresholds for the series of stations used for the magnitude estimation in the Middle East. Most of the stations used in this study are located in the Eurasia, and several stations are located in Africa. We evaluated performance of the MLE estimate using a simulated dataset with magnitudes close to a network detection threshold magnitude. The bias due to non-detections is somewhat smaller than the bias estimated in Ringdal (1976). We attribute it to a larger number of stations used in this study.

We estimated the M_s *(VMAX)* magnitudes using MLE approach and compared it with conventional averaged estimates for the dataset consisting of approximately 100 events located in the Middle East. The major differences between the two estimates are observed for the magnitudes smaller than 4.

Future work will include application of the MLE approach to Love waves. We are also going to continue research on the different ways to find and apply station magnitude thresholds, and to evaluate network detection capabilities.

ACKNOWLEDGEMENTS

We wish to thank Drs. Robert Shumway and David Russell for insightful discussions concerning this project. We also thank Peter Davis for providing us with the GSN noise curves used in this study. We are grateful to Jim Lewkowicz for his continued support.

REFERENCES

Berger, J., P. Davis, and G. Ekstrom (2004). Ambient earth noise: a survey of the Global Seismographic Network, *J. Geophys. Res.* 109: B11307.

Bonner, J. L., D. Russell, D. Harkrider, D. Reiter, and R. Herrmann, (2006). Development of a Time-Domain, Variable-Period Surface Wave Magnitude Measurement Procedure for Application at Regional and Teleseismic Distances, Part II: Application and M_s—m_b Performance. *Bull. Seism. Soc. Am.* 96*:* 678–696.

Bonner, J., R. B. Herrmann, and H. Benz (2008). Rapid estimates of seismic moment using variable-period surface-wave magnitudes. *Seism. Res. Letts.* 79: 349.

Engdahl, E. R., J. Jackson, S. Myers, E. Bergman, and K. Priestley (2006). Relocation and assessment of seismicity in Iran region, *Geophys. J. Int.* 167: 761–778.

Evernden, J. F., and W. M. Kohler (1976). Bias in Estimates of mb at small magnitudes, *Bull. Seism. Soc. Am.* 66: 3*,* 1887–1904.

Marshall, P. D. and P. W. Basham, (1972). Discrimination between earthquakes and underground explosions employing an improved M_S scale. *Geophys. J. R. Astr. Soc*. 29: 431–458.

Pasyanos, M. E. (2005). A variable-resolution surface wave dispersion study of Eurasia, North Africa, and surrounding regions, *J. Geophys. Res*. 110: No. B12, B12301 10.1029/2005JB003749.

Rezapour, M., and R.G. Pearce, (1998). Bias in surface-wave magnitude M_s due to inadequate distance correction. *Bull. Seism. Soc. Am.* 88: 43–61.

Ringdal, F. (1976). Maximum-Likelihood Estimation of Seismic Magnitude, *Bull. Seism. Soc. Am.* 66: 3*,* 789–802.

Ringdal, F. (1986). Study of magnitudes, seismicity, and earthquake detectability using a global network, *Bull. Seism. Soc. Am.* 76*:* 6*,* 1641–1659.

Russell, D. R. (2006). Development of a time-domain, variable-period surface wave magnitude measurement procedure for application at regional and teleseismic distances, part I: theory, *Bull. Seism. Soc. Am*. 96: 2, 665–677.

Veith, K. F. and G. E. Clawson (1972). Magnitude from short-period *P*-wave data, *Bull. Seism. Soc. Am.* 62: 435–452.

von Seggern, D. and D. W. Rivers (1978). Comments on the use of truncated distribution theory for improved magnitude estimation, *Bull. Seism. Soc. Am.* 6: 1543–1546.

Table 1. Comparison of the magnitude threshold values computed using the two approaches described in the article. The omitted threshold values in the column 2 mean that there was not enough M_s (VMAX) measurements to obtain a reliable threshold. The values in the columns 3-6 were skipped for the stations for which the noise floors were not reported.

Station	Minimum M_s (VMAX)	Magnitude thresholds computed for the event 2006.06.03			
		T=10 sec	T=20 sec	T=30 sec	T=40 sec
AAK	3.21	2.69	3.04	3.29	3.51
ABKT	-	2.40	2.73	2.94	3.12
ANTO	2.94	-	-	-	-
ARU	3.20	2.93	3.30	3.57	3.83
BFO	3.33	2.94	3.33	3.65	3.96
BJT	3.54	3.20	3.61	3.96	4.31
BRVK	3.23	2.82	3.18	3.45	3.70
ENH	3.48	3.05	3.46	3.79	4.12
ERM	-	3.24	3.70	4.11	4.55
ESK	3.53	3.08	3.50	3.84	4.19
FURI	-	2.78	3.14	3.39	3.62
GNI	3.05	2.43	2.76	2.99	3.19
GRFO	3.19	-	-	-	-
GUMO	-	3.07	3.55	4.01	4.50
HIA	3.31	3.16	3.58	3.93	4.29
INCN	3.55	3.17	3.60	3.97	4.36
KBL	2.78				
KBS	3.39	3.10	3.52	3.88	4.25
KEV	3.35	3.02	3.42	3.75	4.08
KIEV	3.19	2.82	3.19	3.47	3.73
KIV	3.02	2.56	2.91	3.15	3.36
KMBO	3.51	-	-	-	-
KMI	-	3.03	3.42	3.74	4.05
KONO	3.29	3.03	3.43	3.76	4.08
KURK	2.86	2.82	3.19	3.46	3.72
LSA	2.91	2.92	3.29	3.57	3.83
LSZ	-	3.26	3.67	4.01	4.35
MDJ	-	3.13	3.57	3.95	4.33
OBN	-	2.83	3.21	3.49	3.75
PAB	-	3.07	3.48	3.83	4.18
PMG	-	3.48	3.99	4.49	5.03
QIZ	-	3.14	3.56	3.90	4.24
SSE	-	3.09	3.51	3.88	4.25
SUR	-	3.33	3.78	4.19	4.61
TATO	-	3.20	3.63	4.00	4.38
TLY	2.97	2.98	3.38	3.70	4.02
TSUM	3.75	3.27	3.70	4.07	4.45
WMQ	-	2.85	3.22	3.49	3.75
XAN	-	3.07	3.48	3.81	4.13

SOURCE MECHANISMS FOR EXPLOSIONS IN BARRE GRANITE

Anastasia Stroujkova[1], Jessie L. Bonner[1], Xiaoning Yang[2], Brian W. Stump[3], and William R. Walter[4]

Weston Geophysical Corporation[1], Los Alamos National Laboratory[2], Southern Methodist University[3], and Lawrence Livermore National Laboratory[4]

Sponsored by the National Nuclear Security Administration

Contract Nos. DE-AC52-08NA28655[1,3], LA08-BAA08-97-NDD03[2], and LL08-BAA08-97-NDD03[4]
Proposal No. BAA08-97

ABSTRACT

The previously conducted Arizona Source Phenomenology Experiments (SPE) and the Non-Proliferation Experiment (NPE) represent two unique datasets that could provide critical information about the partitioning of important regional phases, such as *P*, *S*, and *Lg*, from explosions. A new explosion experiment named the New England Damage Experiment (NEDE) was conducted in July 2008 in a granite quarry near Barre, VT. Five explosions with various types of explosives with different Velocities Of Detonation (VOD) have been detonated: low VOD (black powder, Shot 1); medium VOD (ANFO+emulsion, Shots 2 and 4); and fast VOD (COMP B, Shots 3 and 5). The yields for these five single-fired blasts ranged from 134 to 270 lbs of explosives. The main objective of the experiment was an *in situ* study of the influence of VOD on resulting amount of damage and failure modes.

An important part of this project is to compare the moment tensors from these explosions with other data from different media and confining conditions. The moment tensor inversion was performed using the methodology developed in Stump and Johnson (1977). The inversion code was written by David Yang (Yang, 1997). To compute the Green's functions required for the inversion we developed a 1D velocity model of the testing area using the laboratory measurements and the seismic refraction data. The Green's functions were computed using the wavenumber integration technique (Herrmann, 2002). We used five near-source stations to reconstruct moment tensors for each explosion, as well as their time histories. The solutions have the dominant diagonal elements; however some explosions have significant off-diagonal components. The horizontal diagonal components (M_{xx} and M_{yy}) are similar in size, while the vertical M_{zz} is approximately twice as large as each of the horizontals. The size of the isotropic component varies between 72% and 79% for different shots and doesn't appear to correlate with the type of the explosives used in our experiments. The moment tensors from the previous experiments conducted in granites (Morenci copper mine) are consistent with the results obtained in Barre granites.

OBJECTIVES

Recent advances in explosion source theory indicate that the damage that occurs near an explosion is a prominent source of *S*-wave energy. The Ashby and Sammis (1990) model for crack nucleation and growth predicts *S*-wave generation in the far field (Sammis, 2002). The moment tensor information is important for understanding issues related to shear wave generation mechanism(s) and other aspects of the source phenomenology. Modeling by Patton et al. (2005) and Stevens et al. (2003a) have shown the importance of the cone of damage above a source, modeled by a compensated linear vector dipole (CLVD), in generating *Rg* in the near field and *S (Lg)* in the far field, respectively. The phenomenology in the CLVD regime includes block motions, crack damage, and spallation.

The Arizona SPE and the NPE represent two unique datasets that could provide important information about the generation from *S*-waves from explosions. A new explosion experiment (NEDE) was conducted in July 2008. An objective of this project is to compare the moment tensors from these explosions with other data from different media and confining conditions.

RESEARCH ACCOMPLISHED

Experiment Summary

Weston Geophysical Corporation, New England Research, Inc., and a variety of blasting consultants conducted the field phase of the New England Damage Experiment (NEDE) in a granite quarry near Barre, VT. The experiment was conducted in July 2008, and further experiment details are given in Leidig et al. (2008). The purposes of this experiment were to investigate: (1) generation of fractures from small explosions in homogenous, relatively un-fractured granite, (2) quantify the near-source, local, and regional distance phase generation from the explosions, and (3) compare and contrast the seismic phase generation to the rock damage. We studied moment tensors of the five explosions that were carried out during this experiment.

The test site is situated in the Siluro-Devonian alkaline pluton injected into sedimentary rocks (Figure 1a), later subjected to a regional metamorphism during Acadian orogeny (e.g., Richter, 1987). The emplacement metasediments belong to Gile Mountain and Waits river formations represented by schists and quartzites. Figure 1b shows the map of the experiment with the test site and the near-source stations shown.

The fine-grained grey Barre granite has been quarried for over 200 years as a monument stone due to its low fracture density and homogeneous composition. While coring the granite for our test applications, the driller often had to snap the core from the bottom of the hole due to a lack of naturally occurring fractures. The upper 50 feet of fractured and weathered granite had been stripped off at this site, which allowed us to be closer in depth to the relatively unfractured, monument-quality Barre granite (see Leidig et al. [2009, these Proceedings] for further information).

Five explosions were detonated at the test site on 12 July 2008 (Table 1). The yields for these five single-fired blasts ranged from 134 to 270 lbs of explosives. Three explosive types with dramatically different VOD were used: black powder (low VOD, Shot 1); ANFO+emulsion (medium VOD, Shots 2 and 4); and COMP B (fast VOD, Shots 3 and 5). The NEDE explosions were recorded on over 140 seismic instruments, including short-period seismometers, high-g accelerometers, and a high-resolution video camera, deployed at distances of less than 5 m to 30 km from the explosions. To compute moment tensors we used only the data from the 3C instruments located closer than 500 m from the stations (e.g., Table 2).

Velocity Model Development

In order to calculate Green's functions at the near-source stations (less than 500 m from the sources) we first needed to develop a velocity model valid for the upper 100 m. To develop the velocity model, we used data from both seismic field and laboratory rock core measurements. The velocities in the upper part of the subsurface down to 60 ft (about 20 m) were measured using cores from several boreholes (Peter Boyd, see acknowledgements) by New England Research (NER). The measurements show a gradual velocity increase from approximately 4.0 km/s at the surface to 4.4 km/s at a depth of approximately 30 meters, where it reaches a plateau (Figure 2a, red triangles).

The velocity below 20 m was found by examining the travel times of the first arrivals. Figure 2b shows the travel times picked manually for the near-source 3C and Texan stations. The picks show considerable scatter due to a heterogeneous near-surface structure, elevation differences, and possibly timing errors for different shots. The apparent velocity estimated by fitting a straight line is V_p = 4.9 km/s. The shear-wave velocity (V_s = 2.72 km/s) was found using a V_p/V_s ratio of 1.8. These velocities, however, describe the average velocity in the first 300–400 m below the surface and it is impossible to pinpoint where the velocity changes from 4.4 km/s to 4.9 km/s. Therefore, for the purpose of constructing the Green's functions, we set the lower layer V_p to 4.5 km/s, which corresponds to the highest velocity measured in the rock samples. The final velocity profile is shown in Figure 3a.

Strong velocity anisotropy has been reported at the site from both rock sample measurements made by NER and seismic travel time studies (e.g., Leidig et al., 2008). The differences between laboratory measured fast and slow velocities are on the order of 10–20 %. Engelder et al. (1977) attributed the anisotropy in Barre granite to the opening of microfractures due to residual stresses. Most of the microfractures' strike azimuths are close to 30º, which is approximately parallel to the rift orientation.

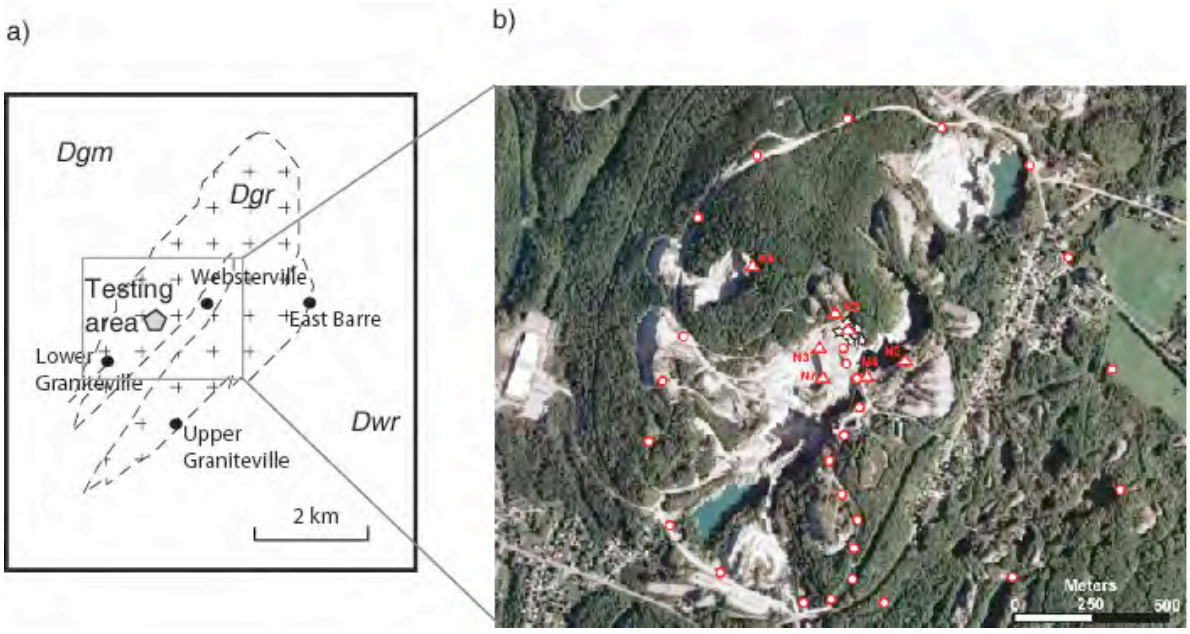

Figure 1. a) The geological map of Barre pluton (from Richter, 1987). The geological formations are: *Dgr* – Devonian granites, *Dgm* – Gile Mountain formation, *Dwr* – Waits river formation. b) The Google Earth picture of the area marked in a bounding box in a). The shots (white stars with black outline) are seen in the middle of the image (the test site). Also shown the near-source 3C stations N1-N7 and Texans NT01-NT27.

Table 1. Origin Characteristics for NEDE Shots.

Shot	Latitude (ºN)	Longitude (ºW)	Elevation (m)	Borehole/ Centroid Depth (m)	Stemming (m)	Yield (lbs)	Explosive
1	44.15774	-72.47848	509	9.1/8.5	7.3	134	Black Powder
2	44.15800	-72.47813	509	11.3/10.7	10.1	135.5	ANFO/Emul 50:50
3	44.15780	-72.47770	503	11.3/10.7	10.4	136	COMP B
4	44.15751	-72.47797	508	13.7/12.8	11.6	269.5	ANFO/Emul 50:50
5	44.15754	-72.47757	503	13.7/12.8	11.9	270	COMP B

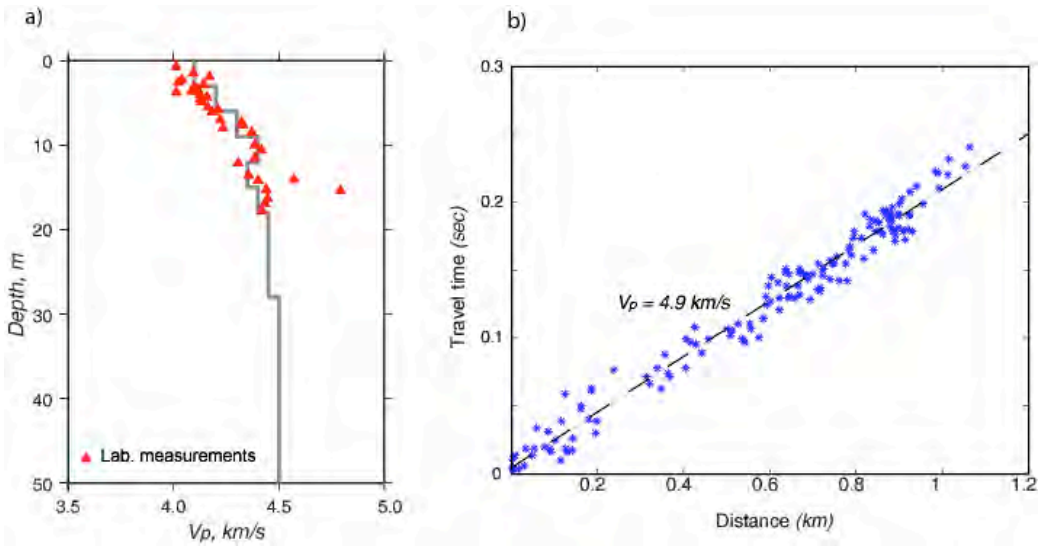

Figure 2. a) Final velocity (V_p) model. Triangles show the velocity measurements made by NER at CH1 site prior to the explosions. b) Travel time picks for the near-source 3C stations and Texans. Dashed line shows the linear least square fit with the slope corresponding to V_p=4.9 km/s.

Table 2. Distances and elevation differences between the shots and the stations.

Shot #	Distance/Elevation difference, *m*				
	N2	N3	N5	N6	N7
1	58.8/24	86.2/-17	238.4/-3	356.7/-20	161.4/-7
2	49.0/24	126.3/-17	227.5/-3	364.0/-20	198.5/-7
3	89.9/30	142.3/-11	186.6/3	404.8/-14	196.0/-1
4	98.6/25	110.8/-16	190.6/-2	404.9/-19	157.4/-6
5	116.2/30	142.4/-11	163.1/3	429.0/-14	180.5/-1

To perform the moment tensor inversion we used five 3C stations (N2, N3, N5, N6 and N7) located at distances between 58 m and 429 m from the explosions (Table 2). Figure 3 shows comparison between the vertical components of the data and the explosion Green's functions (*ZEX*). There are significant discrepancies between the data and the Green's function amplitudes, especially for the stations located further away from the test site (Stations N5-N7). The synthetic *Rg* amplitudes are significantly larger than the measured amplitudes. Since the large signal in the synthetics is produced by the free-surface interaction, it depends on the shot depth, source excitation, roughness of the free surface (surface wave scattering) and the attenuation of the upper layer. This discrepancy was noted in Yang and Bonner (2009), where the authors proposed to adjust the shot depths in order to reduce *Rg* amplitudes. In this experiment, the stations with large discrepancies are located at about the same depth or lower then the datum for the explosion boreholes (Table 2, Leidig et al., 2008). Therefore the depth adjustments would not be helpful in this case.

Figure 4a shows peak amplitudes of *Rg* measured using the data from the Texans located between 0.6 and 1.2 km. To correct for the geometric spreading, the amplitudes were multiplied by a square root of distance. The amplitudes show systematic decrease for azimuths from about 60º through 210º. One explanation is a scattering of *Rg* by topographic features: there is a deep trough from previous excavations extending from NE toward SW. The depth of the water-filled pit near stations N4 and N5 could reach 90 m (Leidig et al., 2008). The amplitude decrease could also be caused by a lithological change from the granites to the emplacement rocks of Gile Mtn. formation (schists). The lithology change could be inferred from the geological map (Figure 1a) from Richter (1987).

Figure 4b shows the waveform data from the Texan stations located between 600m and 1000m from the explosions. The waveforms are corrected for the geometric spreading and plotted as a function of the station azimuths. The

decrease in *P*-wave amplitudes in the azimuth range between 60º and 210º (Figure 4b) also supports the idea that the amplitude decay is due to a lithology change, since *P*-wave amplitudes are less sensitive to the topographic scattering. This figure demonstrates that there is a strong propagation-induced azimuthal pattern, which can potentially influence the moment tensors. In order to minimize the propagation effects, we only used the stations located within 500 m from the explosions.

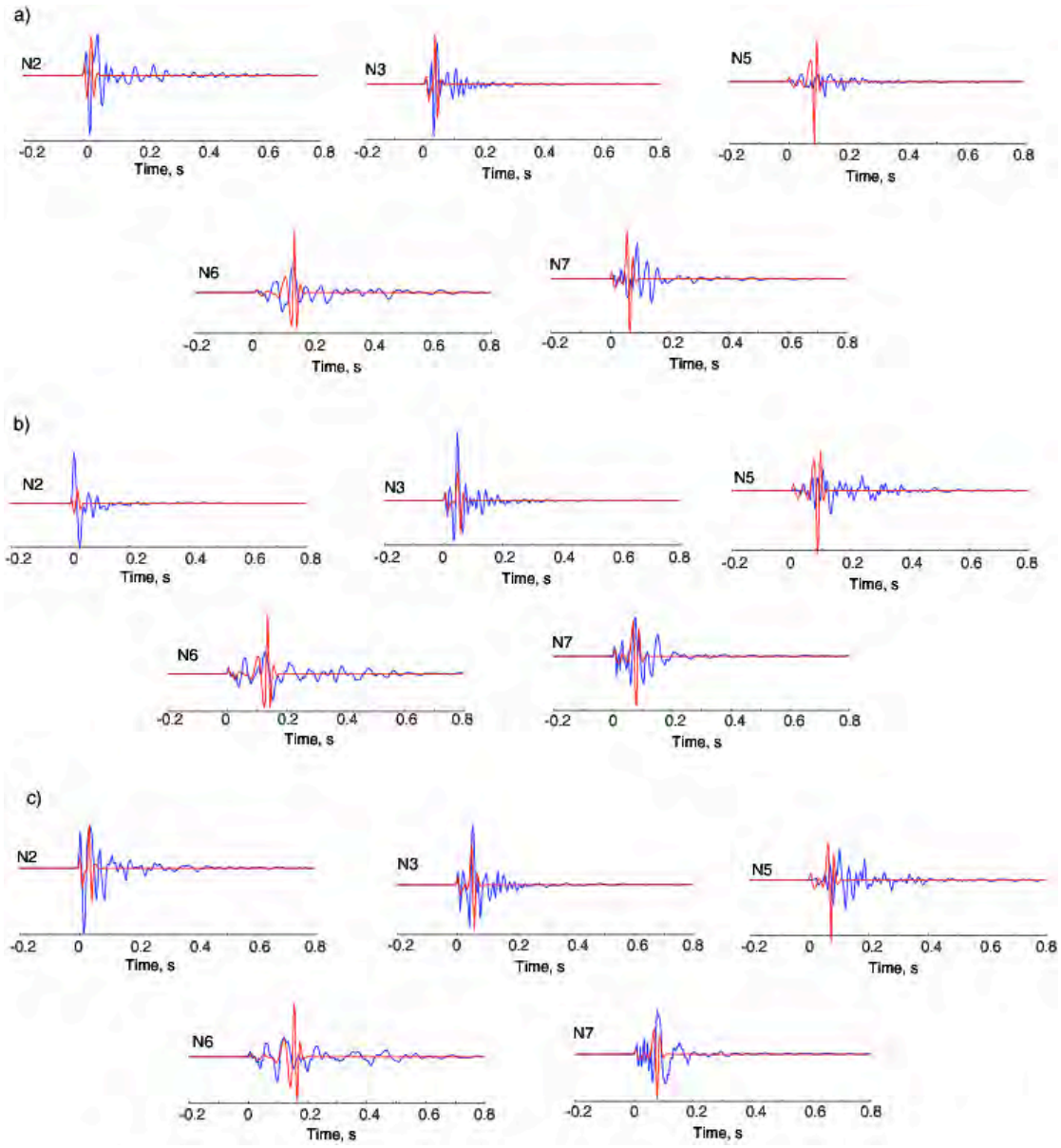

Figure 3. Comparison between the data (blue) and the Green's functions (red). Traces are scaled to maintain the same ratio between the data and the Green's function amplitudes. a) Shot 1; b) Shot 2; c) Shot 3; d) Shot 4; e) Shot 5.

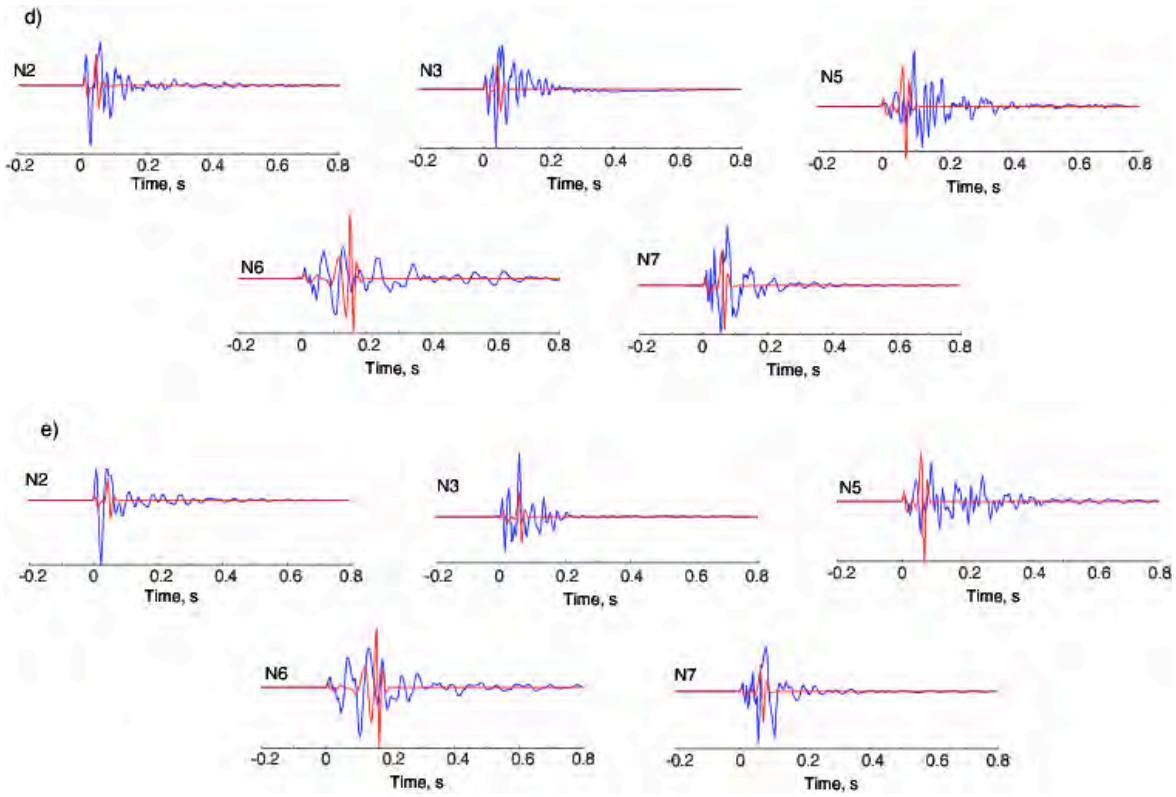

Figure 3. ***Continued.***

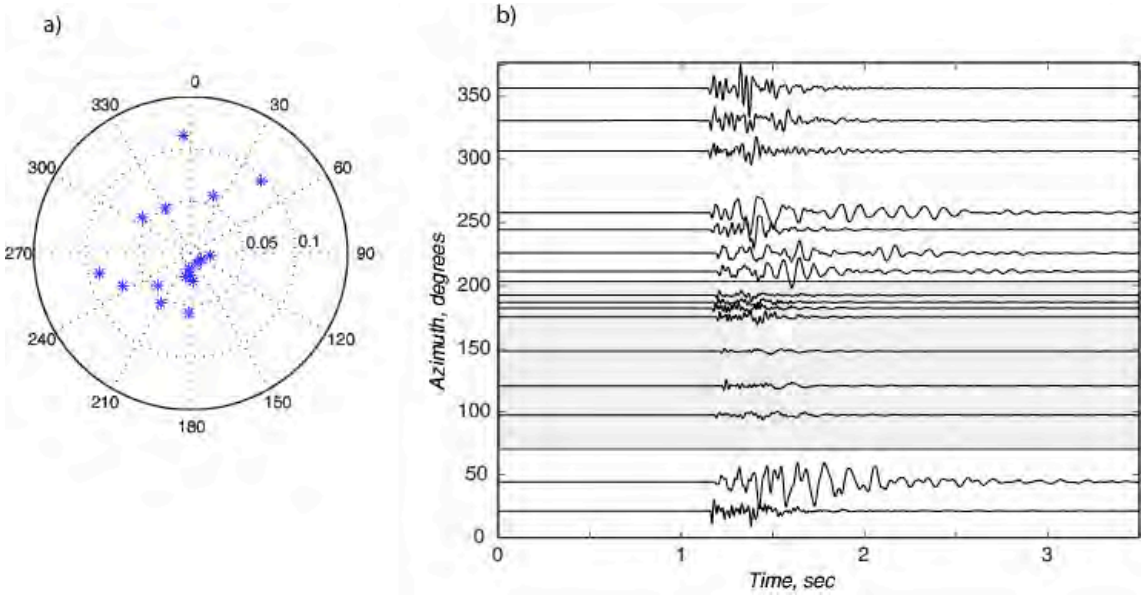

Figure 4. a) A polar plot of *Rg* peak amplitudes multiplied by a square root of distance for Shot 5. The amplitudes are from the near-source Texans. b) The waveforms from Shot 5 recorded at the near-source Texans. The amplitudes are corrected for the geometrical spreading. The shaded area shows the azimuth range where the significant amplitude decrease is observed.

Inversion Results

The moment tensor inversion was performed using the methodology developed in Stump and Johnson (1977) using the inversion code written by David Yang (1997). The inversion is performed in the frequency domain by solving a system of linear equations (Stump and Johnson, 1977):

$$d_i = G_{ij,k} m_{jk} \quad (1)$$

where d_i are the measured ground velocities, $G_{ij,k}$ are the Green's functions for ground velocities, and m_{jk} are the components of the moment tensor to be determined. The inversion is repeated for each frequency, and then transformed back into the time domain to produce moment tensor time histories. The solution of the linear system (1) is performed using singular value decomposition (SVD). The Green's functions $G_{ij,k}$ are calculated using *CPIS3.30* software package (e.g., Herrmann, 2002).

The first step in data preprocessing included the application of the instrument corrections and re-sampling to 250 samples per second. Then, the observed traces were manually aligned with the Green's functions. The inversion produced both high-frequency and low-frequency artifacts in the time-dependent moment-rate tensor components. According to Yang (1997) the high-frequency noise is due to imperfect (manual) alignment of the data and the Green's functions. The low-frequency artifacts are due to differences between the model and actual medium (Green's function discrepancies). To minimize the effect of the artifacts the time-domain moment tensors were bandpass-filtered between 8 Hz and 50 Hz.

To analyze the moment tensor solutions we calculated the percentages of the isotropic component using the relationship (Feignier and Young, 1992):

$$R = \frac{tr(M) \times 100\%}{|tr(M)| + \sum |m_i|} \quad (2)$$

where M is the moment tensor, and m_i are the deviatoric eigenvalues. For a purely isotropic source $R = 100\%$. The percentages can be calculated for each time slice of the moment tensor. To assign the percentage of an isotropic component for each explosion we found R for the time slice where the value $|tr(M)|$ reaches its maximum.

The resulting time-dependent moment tensors are shown in Figure 5. The diagonal elements dominate for most explosions. The amplitudes of M_{xx} and M_{yy} components of the moment tensors are similar, while the amplitudes of M_{zz} components exceed the horizontals by almost a factor of 2. This could correspond, for instance, to a combination of a volumetric source and a single force or a CLVD. The percentages of the isotropic component vary between 72% and 79% for different shots. There is no apparent correlation between the explosive type and the moment tensor. For example, Shot 2 (ANFO+emulsion) has the largest isotropic components (79%, Table 3). On the other hand, Shot 4 (also ANFO+emulsion) has the largest off-diagonal and the smallest isotropic components (72%, Table 3). We note that Leidig et al. (2009, these Proceedings) do see differences in the shear waves generated by the different shot types. The relatively high percentage of non-isotropic component could be an artifact of an inadequate velocity model.

Table 3. Moment tensor inversion results

Shot #	M_{xx} $\times 10^{12}$ N×m	M_{xy} $\times 10^{12}$ N×m	M_{xz} $\times 10^{12}$ N×m	M_{yy} $\times 10^{12}$ N×m	M_{yz} $\times 10^{12}$ N×m	M_{zz} $\times 10^{12}$ N×m	% *iso*
1	2.0327	0.0665	-0.0933	2.0270	-0.2380	3.6346	78
2	2.8945	0.0055	-0.7483	2.8456	-0.2131	4.4661	79
3	3.0699	-0.1931	0.1275	3.3284	0.4748	6.1910	75
4	5.3061	-0.2564	1.2209	5.1246	1.4592	10.1972	72
5	4.4442	-0.0915	0.0273	4.7618	0.1109	8.7154	77

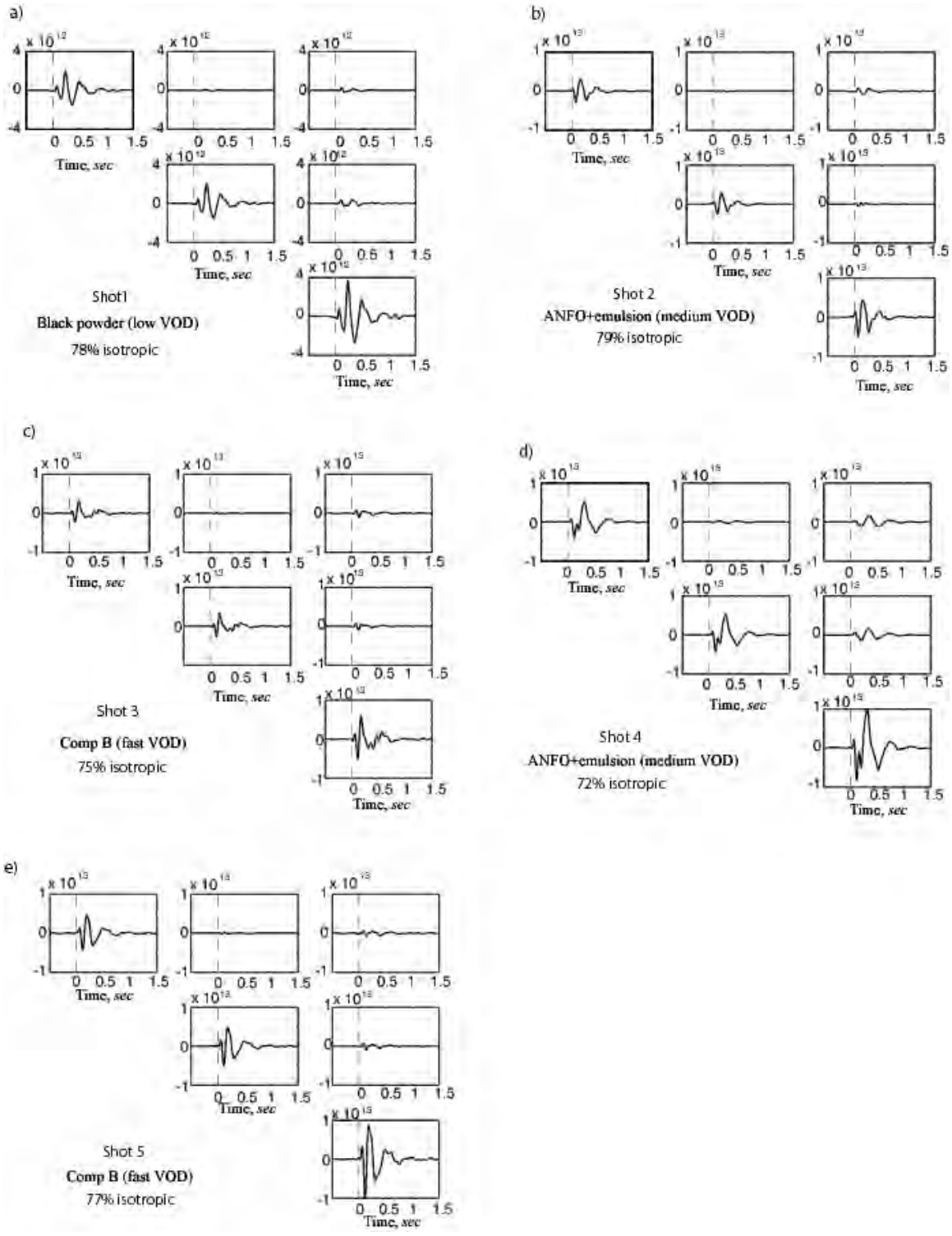

Figure 5. Moment tensor inversion results for: a) Shot 1; b) Shot 2; c) Shot 3; d) Shot 4; and e) Shot 5. Each shot panel shows 6 traces corresponding to 6 moment tensor components (M_{xx}, M_{xy}, M_{xz}, M_{yy}, M_{yz} and M_{zz}).

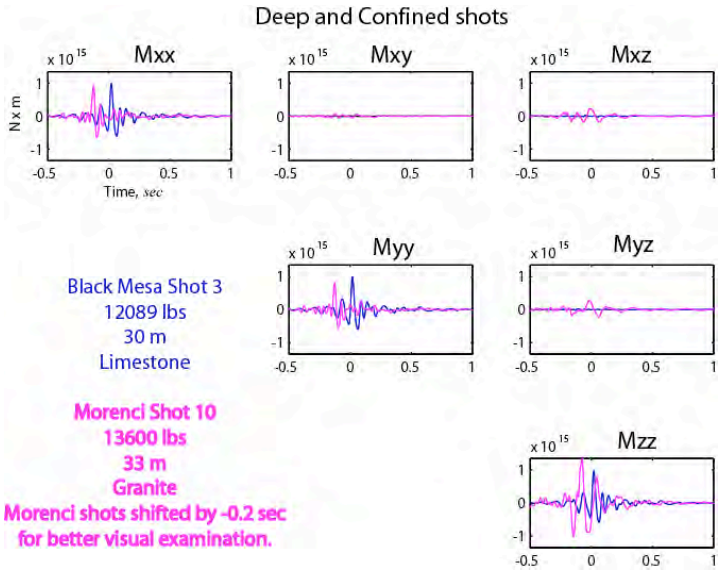

Figure 6. A comparison between the moment tensors for explosions in limestone at a coal mine (Black Mesa, shown in blue) and granite at a copper mine (Morenci, shown in magenta). From Zhou et al. (2005).

Figure 6 shows the moment tensor inversion results from previous explosion experiments. Both shots shown in Figure 6 are confined. One of the shots was carried out in a coal mine in limestone (Black Mesa), the other one was conducted in a copper mine in granites (Morenci). The diagonal elements of the moment tensor dominate. However, the relative size of the diagonal elements for the Black Mesa shot are almost the same, while for the Morenci shot the amplitude of M_{zz} components exceed the amplitudes of M_{xx} and M_{yy} components.

The inferred CLVD component could be either an artifact of an inadequate velocity model, or it could be explained by a non-point source from the cone of damage above a source. Unfortunately we had a very limited number of stations usable for the inversion. More research is needed on the influence of the noise on the moment tensor resolution.

CONCLUSIONS AND RECOMMENDATIONS

We continue to examine the differences in the moment tensors for chemical explosions in different media with variable confining conditions. In this article we used a frequency-domain linear inversion to find the time-dependent source moment tensors of five chemical explosions detonated during the New England Damage Experiment, conducted in Barre, VT in the summer of 2008. The goal of this experiment is to characterize the rock damage from an explosive source and to identify the source(s) of shear wave generation.

The Green's functions required for the moment tensor inversion were computed using *CPIS3.30* software (Herrmann, 2002). We developed a 1D Earth model for the test site based on the laboratory velocity measurements as well as seismic refraction travel time data. The moment tensor inversions have the dominant diagonal elements; however some explosions have significant off-diagonal components. The horizontal diagonal component (M_{xx} and M_{yy}) are similar in size, while the vertical M_{zz} is about twice as large as each of the horizontals. This may be a combination of either an isotropic and a CLVD sources, or an isotropic and a vertical force. The size of the isotropic component varies between 72 % and 79 % for different shots. The ratio of the isotropic component doesn't appear to correlate with the type of the explosives in our experiments, despite the differences in the shear waves generated by the different shot types (Leidig et al., [2009, these Proceedings]). The moment tensors from the previous experiments conducted in granites (Morenci copper mine, Zhou et al., 2005) are consistent with the results obtained in Barre granites. For future work, we will examine the moment tensors for the NPE for comparison to these results.

ACKNOWLEDGEMENTS

We wish to thank David Yang for his assistance on this project and for loaning us his code. We also wish to thank Peter Boyd for providing velocity information for the cores from NEDE.

REFERENCES

Ashby, M.F. and C. G. Sammis (1990). The damage mechanics of brittle solids in compressions, *Pure Appl. Geophys*. 133: 489–521.

Engelder, T., M. Sbar, and R. Kranz, (1977). A mechanism for strain relaxation of Barre Granite: opening of microfractures, *Pure Appl. Geoph*ys. 115: 27–40.

Feignier, B. and R. P. Young (1992). Moment tensor inversion of induced microseismic events: evidence of non-shear failures in the -4<M<-2 moment magnitude range, *Geophys. Res. Lett.* 19: 1503–1506.

Herrmann, R., H. (2002). An overview of synthetic seismogram computation. In *Computer Programs in Seismology, Version 3.30*.

Leidig, M., R. Martin, P. Boyd, J. Bonner, and A. Stroujkova (2009). Quantification of Rock Damage from Small Explosions and its Effect on Shear-Wave Generation: Phase I—Homogenous Crystalline Rock, these Proceedings.

Leidig, M., J. Bonner, J. Britton, K. Murphy, D. T. Reiter, J. Lewkowicz, S. Huffstetler, P. Boyd, R. Martin, D. Murray, A. Garceau, T. Rath, P. West, J. Trippiedi, M. McGinley, A. McGinley, W. Zamora, L. Foley, D. Richter, R. Garfield, A. Martinez, J. Reid., and R. Haas, (2008). Quicklook: Quantification of Rock Damage from Small Explosions and its Effect on Shear-Wave Generation, Weston Geophysical Corp. Report WG-QL0801, 77 p.

Patton, H., J. Bonner, and I. Gupta, (2005). *Rg* Excitation by Underground Explosions: Insights from Source Modeling the 1997 Kazahkstan Depth of Burial Experiments. *Geophys. J. Int.* doi:10.1111/j.1365-246X.2005.02752.x

Richter, D. A. (1987). Barre granite quarries, Barre, Vermont, in *Geological Society of America Field Guide – Northeastern Section*, 239–242.

Sammis, C. G. (2002). Generation of High-Frequency *P* and *S* Wave Energy by Rock Fracture During a Buried Explosion: Its Effect on *P/S* Discriminants at Low Magnitude, in *Proceedings of the 24th Seismic Research Review - Nuclear Explosion Monitoring: Innovation and Integration*, LA-UR-02-5048, Vol 1, pp. 542–551.

Stevens, J.L., G. E. Baker, H. Xu, T.J. Bennett, N. Rimer, and S.M. Day (2003a). The physical basis of *Lg* generation by explosion sources. in *Proceedings of the 25th Seismic Research Review - Nuclear Explosion Monitoring: Building the Knowledge Base*, LA-UR-03-6029, Vol. 1, pp. 456–465.

Stevens, J.L., N. Rimer, H. Xu, G.E. Baker, S.M. Day, (2003b). Near-field and regional modeling of explosions at the Degelen test site. SAIC Final Report SAIC-02/2050.

Stump, B., and L. Johnson (1977). The determination of source properties by the linear inversion of seismograms, *Bull. Seis. Soc. Am*. 67: 1489–1502.

Yang, X. (1997). Mining explosion and collapse source characterization and modeling with near-source seismic data. Ph.D. Thesis, Southern Methodist University, Dallas, Texas.

Yang, X. and J.L. Bonner (2009). Characteristics of chemical explosive sources from time-dependent moment tensors. *Bull. Seism. Soc. Am.* 99: 36–51.

Zhou, R., B. W. Stump and X. Yang (2005). Moment tensor inversions of single-fired mining explosions at a copper mine in Arizona, *Eos Trans. AGU*, 86(52), Fall Meet. Suppl., Abstract S11B-0166.

Proceedings of the 2009 Monitoring Research Review: Ground-Based Nuclear Explosion Monitoring Technologies

September 21–23, 2009

Tucson, Arizona

Volume II

Hydroacoustic Monitoring
Radionuclide Monitoring
Infrasound Monitoring
Data Processing and Analysis

Approved for Public Release; further dissemination unlimited.

National Nuclear Security Administration

AIR FORCE RESEARCH LABORATORY

LA-UR-09-05276

2009

Proceedings of the 2009 Monitoring Research Review: Ground-Based Nuclear Explosion Monitoring Technologies

To view these Proceedings online, visit
https://na22.nnsa.doe.gov/mrr/2009

Vol. II

ACKNOWLEDGEMENTS

The National Nuclear Security Administration (NNSA) and the Air Force Research Laboratory (AFRL) gratefully acknowledge the important contributions of the following people for their work to produce the ***Proceedings of the 2009 Monitoring Research Review: Ground-Based Nuclear Explosion Monitoring Technologies.***

Authors of papers for excellent research, technical documentation, and cooperation with electronic submission processes.

Dr. Anton M. Dainty, Mr. Robert J. Raistrick, Dr. Frederick R. Schult, AFRL/VSBYE, and ***Ms. Doris Richards***, ESC/PAM, for review and clearance of abstracts and papers related to AFRL contracts.

Dr. Stanley D. Ruppert, Lawrence Livermore National Laboratory (LLNL), for assistance in ensuring that the CDs could be read on a variety of platforms and for burning the CDs.

Mr. Marvin A. Wetovsky, Los Alamos National Laboratory (LANL), Managing Editor of the Proceedings.

Ms. Eileen F. Patterson, LANL, for technical editing of papers.

Dr. Marie D. Arrowsmith, LANL, for technical editing of papers, design of the CD label, composition of the hardcopy covers, and numerous technical consultations.

Ms. Leslie A. Casey, NNSA, for review and clearance of abstracts and papers related to NNSA contracts and for NNSA overall support of the Proceedings.

Ms. Mary L. Girven, Sandia National Laboratories (SNL), for making everyone's job easier with web-based technology for abstract and paper submission, on-line review and approval tools, and creation of the master files for the hardcopy, CD, and website versions of the Proceedings.

Ms. Guadalupe (Lupe) Massoth, SNL, for providing assistance to Mary Girven on website development and help in creating the master files.

Dr. William R. Wallter, LLNL; ***Dr. Stephen C. Myers***, LLNL; ***Dr. Dale N. Anderson***, LANL, ***Mr. Ward L. Hawkins***, LANL; ***Dr. Martin E. Keillor,*** Pacific Northwest National Laboratory (PNNL); ***Dr. Theodore W. Bowyer***, PNNL; ***Dr. Timothy S. McDonald***, SNL; and ***Dr. Christopher J. Young***, SNL, for a myriad of internal management and technical reviews of NNSA abstracts and papers.

PREVIOUS PROCEEDINGS

Year	Title of the Proceedings
2008	Proceedings of the 30th Monitoring Research Review: Ground-Based Nuclear Explosion Monitoring Technologies
2007	Proceedings of the 29th Monitoring Research Review: Ground-Based Nuclear Explosion Monitoring Technologies
2006	Proceedings of the 28th Seismic Research Review: Ground-Based Nuclear Explosion Monitoring Technologies
2005	Proceedings of the 27th Seismic Research Review: Ground-Based Nuclear Explosion Monitoring Technologies
2004	Proceedings of the 26th Seismic Research Review: Trends in Nuclear Explosion Monitoring
2003	Proceedings of the 25th Seismic Research Review: Nuclear Explosion Monitoring: Building the Knowledge Base
2002	Proceedings of the 24th Seismic Research Review: Nuclear Explosion Monitoring: Innovation and Integration
2001	Proceedings of the 23rd Seismic Research Review: Worldwide Monitoring of Nuclear Explosions
2000	Proceedings of the 22nd Annual DoD/DoE Seismic Research Symposium: Planning for Verification of and Compliance with the Comprehensive Nuclear-Test-Ban Treaty (CTBT)
1999	Proceedings of the 21st Seismic Research Symposium: Technologies for Monitoring the Comprehensive Nuclear-Test-Ban Treaty

Table of Contents - Volume II

4. Hydroacoustic Monitoring 603

4-01 **Matsumoto, H., D. Bohnenstiehl, R. Dziak, M. Park, and M. Fowler**
Hydroacoustic Monitoring of the Scotia Sea: Autonomous Hydrophone Experiment 605

5. Radionuclide Monitoring 613

5-01 **Biegalski, S., M. Deinert, T. Saller, and B. Wooten**
Modeling of Radioxenon Production and Release Pathways 615

5-02 **Cooper, M., J. Ely, D. Haas, J. Hayes, M. Keillor, and J. McIntyre**
Radiation Detection Challenges 624

5-03 **Farsoni, A. and D. Hamby**
Characterization of Triple-Layer Phoswich Detector for Radioxenon Measurements 631

5-04 **Hennig, W., W. Warburton, A. Fallu-Labruyere, K. Sabourov, M. Cooper, J. McIntyre, A. Gleyzer, M. Bean, E. Korpach, K. Ungar, W. Zhang, P. Mekarski, R. Ward, S. Biegalski, and D. Haas**
Radioxenon Measurements with the PhosWatch Detector System 641

5-05 **Hull, E., R. Pehl, J. Lathrop, P. Mann, R. Mashburn, B. Suttle, H. Miley, C. Aalseth, T. Bowyer, and T. Hossbach**
Mechanically Cooled Large-Volume Germanium Detector Systems for Nuclear Explosion Monitoring 653

5-06 **Humble, P., R. Williams, and J. Hayes**
Finite Element Modeling of Adsorption Processes for Gas Separation and Purification 659

5-07 **Keillor, M., C. Aalseth, A. Day, J. Fast, E. Hoppe, B. Hyronimus, T. Hossbach, H. Miley, and A. Seifert**
Assembly and Initial Results: an Ultra-Low-Background Germanium Crystal Array for High Efficiency and Coincidence Measurements 667

5-08 **Martin, G., C. Xie, K. Yocum, J. Colaresi, and H. Miley**
Improving Germanium Detector Resolution And Reliability 677

5-09 **Yocum, K., J. Colaresi, and H. Miley**
Improvement in Ge Detector Cooling 686

6. Infrasound Monitoring 695

6-01 **Arrowsmith, S., H. Hartse, G. Randall, and S. Taylor**
Infrasound as a Depth Discriminant: Construction of a Unique Dataset and Preliminary Analyses 697

6-02 **Arrowsmith, S., I. Che, C. Hayward, J. Park, and B. Stump**
Multiple-Array Detection, Association and Location of Infrasound and Seismo-Acoustic Events - Utilization of Ground Truth Information 706

6-03 **Gibson, R., D. Drob, and D. Broutman**
Advancement of Techniques for Modeling the Effects of Fine-Scale Atmospheric Inhomogeneities on Infrasound Propagation 714

6-04 **Gitterman, Y., M. Garces, J. Bowman, D. Fee, H. Israelsson, A. Hofstetter, and V. Pinsky**
Near-Source and Far-Regional Infrasound Observations For Sayarim Test Explosions 724

6-05 **Hart, D. and T. McDonald**
Infrasound Sensor and Porous-Hose Filter Evaluation Results 735

6-06 **Stump, B., C. Hayward, S. Arrowsmith, G. Randall, K. Pankow, R. Burlacu, and S. Taylor**
Infrasound from Earthquakes: Signal Characterization 742

6-07 **Whitaker, R.**
Infrasound Signals from Ground Motion Sources 750

7. Data Processing and Analysis 759

7-01 **Arai, N., T. Murayama, M. Iwakuni, and M. Nogami**
An Approach for Denoising Waveform Data by Auto-Regressive Algorithm 761

7-02 **Bonner, J., R. Herrmann, M. Leidig, K. Mayeda, and A. Ferris**
Development of a Software Toolbox for Systematic Evaluation of Seismometer-Digitizer System Responses 771

7-03 **McIntyre, J., B. Schrom, M. Cooper, D. Haas, and J. Hayes**
Beowulf : A Beta-Gamma Detector Calibration Graphical User Interface 779

7-04 **Procopio, M., C. Young, and J. Lewis**
Using Machine Learning to Improve the Efficiency and Effectiveness of Automatic Nuclear Explosion Monitoring Systems 788

7-05 **Ringdal, F., T. Kvaerna, S. Gibbons, S. Mykkeltveit, and J. Schweitzer**
Basic Research on Seismic and Infrasonic Monitoring of the European Arctic 798

7-06 **Ruppert, S., D. Dodge, T. Hauk, M. Ganzberger, D. Harris, and E. Matzel**
Enhancing Seismic Calibration Research Through Software Automation and Scientific Information Management 808

819

Appendices

Acronyms, etc. 821

Guide to Seismic Phases 825

Hydroacoustic Monitoring

HYDROACOUSTIC MONITORING OF THE SCOTIA SEA: AUTONOMOUS HYDROPHONE EXPERIMENT

Haruyoshi Matsumoto[1], DelWayne R. Bohnenstiehl[2], Robert P. Dziak[1], Minkyu Park[3], and Matthew J. Fowler[1]

National Oceanic and Atmospheric Administration[1], North Carolina State University[2], and the Korea Polar Research Institute[3]

Sponsored by the National Nuclear Security Administration

Award No. DE-AI52-08NA28654
Proposal No. BAA08-36

ABSTRACT

Collaborating with the Korea Polar Research Institute, the National Oceanic and Atmospheric Administration and North Carolina State University began operating autonomous hydrophones (AUH) in the Scotia Sea waters near South Georgia Island in December 2007. An array consisting of six AUHs was successfully installed in an area of 86,000 km^2 to monitor the low-frequency acoustic events and ambient noise conditions for a period of about 13 months. Five of the AUHs were successfully recovered in January 2009; however, one instrument on the north side of the island was lost. All five of the recovered hydrophones recorded undisrupted 16-bit acoustic signals throughout the deployment, with four instruments sampled at 250 Hz and one instrument sampled at 1000 Hz. Our preliminary analysis reveals a bell-shaped seasonal ambient noise pattern of high in the fall and low in mid-winter, which is common to the partially ice-covered Southern Ocean. The seasonality of noise agrees with the formation of sea ice and ice break-up processes during the fall and the maximum sea ice extent during the winter in the region. During the first six months from December 2007 through June 2008, the five-AUH array located 200 seismic and 232 ice tremor events, while the National Earthquake Information Center (NEIC) registered 89 seismic events in the southwestern Atlantic Ocean region, indicative of the high sensitivity of the hydroacoustic method even at high latitudes. For shallow earthquakes along the Scotia subduction system, the AUH stations record a double peaked T-wave arrival packet. The first peak in T-wave energy is interpreted to be a secondary P-to-T conversion from the parabolic-shaped Scotia Volcanic Arc, which lies to the west of the epicenteral zone and to the east of the array. The second arrival corresponds to energy sourced in the vicinity of the seismically determined epicenter and is of larger amplitude and enriched in high frequencies relative to the first peak. The unique ambient noise and acoustic propagation environment of the Southern Ocean are discussed, and comparisons of seismic- and AUH-derived source locations are presented.

OBJECTIVES

Monitoring underwater low-frequency sound is one of the critical components of the global nuclear explosions monitoring effort. The objective is to ensure that no nuclear weapon tests conducted in the ocean or near the surface above the ocean go undetected. One area where such a signal can be hidden from the eyes of the international community is the Scotia Sea. In the Scotia Sea propagation across the Antarctic Convergence Zone (ACZ) is poorly understood and the sound path to the International Monitoring system (IMS) hydrophones is partially or completely blocked by either the continents or islands and their associated seafloor ridge and arc systems.

The Scotia Sea is a small area of the southwest corner of the Atlantic Ocean surrounded by Tierra del Fuego and the Falkland, South Georgia, South Sandwich, and South Orkney islands and the Antarctic Peninsula. It is a tectonically complex area of marginal basins bordered by the Antarctic and South American plates, as well as the South Shetland, and Sandwich microplates. Due to the poor distribution of seismic stations and larger than 20 degree of separations between the stations (HOPE-South Georgia Island, EFI-East Falkland Islands and PMSA-Palmer Station), the minimum seismic detection threshold in the area has been close to m_b 5.0. The hypocenter map from the International Seismic Center catalog (1964–1991) and the moment tensors of shallow centroids from Harvard's Centroid Moment Tensor (CMT) catalog (1977–1998) indicate the area is seismically active but is missing smaller events due to this sparse seismic distribution of monitoring stations in the area.

In contrast to global seismicity records, which suggest sparse seismicity, a regional seismic study of the South Shetland Island area based on both land-based and ocean-bottom seismometers (OBSs) shows a high level of local seismicity (Robertson Maurice et al., 2003). Our initial assessment of the hydrophone records from the 2005–2006 Bransfield deployment indicates a similar high rate of activity, with the detection of thousands of T-waves from seafloor earthquakes that cannot be associated with events in the global seismic catalog. These observations suggest a high occurrence rate of seismic events ($m_b > 3.0$) that can be utilized as natural sound sources for the propagation studies across the ACZ, with energy extending into the 30–45 Hz range.

Large icebergs are also known to produce hydroacoustic signals with distinct resonant characteristics similar to the harmonic tremor that often accompanies volcanic activity (e.g., Talandier et al., 2006; Chapp et al., 2005; Okal and MacAyeal, 2006). Ice tremors off Antarctica have been identified by the IMS hydrophone arrays as far away as the Northern Hemisphere and have been used to track the motion of the source icebergs. One ice-tremor signal in particular is estimated to have a source level of ~245 dB re $1\mu Pa|_{1m}$, equivalent to $m_b > 6$ earthquake. Icebergs breaking off in the Weddell Sea and drifting into the Scotia area should provide a significant number of these ice signal sources with known coordinates identified by QuickScat satellite imagery, which is provided by courtesy of the Center for Remote Sensing (CERS) at Brigham Young University (BYU).

By taking advantage of the high sensitivity of the hydroacoustic method (e.g., Fox et al., 2001; Bohnenstiehl et al., 2002; Dziak et al., 2004; Helffrich et al., 2006), our strategy was to install an acoustic array consisting of six AUHs for one year starting in December 2007 in the Scotia region and to analyze hydroacoustic activities in those areas after the recovery of the AUHs in early 2009. We expected that the arrays' low regional detection threshold of m_b 2.0–3.0, due to the low attenuation properties of ocean-sound propagation and the 16-bit data resolution of the AUH data would afford a wide dynamic range of source levels, from the T-waves originating at the seafloor to the ice tremors from the surface.

Our goal is to provide a catalog of estimated hydroacoustic source locations with source levels and origin times, as well as associated arrival times and received levels. Located sound sources will be used to construct empirical blockage maps that can be compared with traditional line-of-sight blockage criteria or ray invariant approaches (e.g., Upton et al., 2006; Harben et al., 2003; Eggen and Dushaw, 2002).

RESEARCH ACCOMPLISHED

Collaborating with the Korea Polar Research Institute, National Oceanic Atmospheric Administration, and North Carolina State University began with the operation of AUHs in the Scotia Sea region in December 2007. Five AUHs (M1–M5, white circles in Figure 1) were deployed from the R/V Yuzhmorgeologiya on the south side of the South Georgia Island during the first cruise. In April of 2008, the last AUH (M6) was deployed by a British Antarctic Survey ship, RRS JC Ross, at 280 nm NNE of the South Georgia Island. The array was optimally configured to

investigate sound propagation and interferences affected by the ACZ and land mass in the area, using the earthquakes and ice-related hydroacoustic events in the Scotia Sea as sound sources.

The recovery of hydrophones began in January of 2009 by the M/V Pharos SG. The operation went well, and five southern hydrophones (M1–M5) were successfully recovered. All five continuously recorded low-frequency acoustic signals (2–110 Hz) at a 250-Hz sampling rate for 13 months. However, recovery of the northern hydrophone, M6, became difficult due to weather conditions and ship schedules. A logistic decision was made to defer the M6 recovery to a later cruise. In April 2009, M/V Pharos SG sailed out again to recover the M6 mooring. Unfortunately, we found that at some point during the 1-year deployment, the top section (float and hydrophone) had been separated, leaving the rest of the mooring on the seafloor. The top 2000 m of mooring was made of a high-tension anti-strumming cable, and all the components were new. We were puzzled and disappointed at the loss of our instrument and data. Although there is a small chance that the instrument may wash ashore someday, our experience tells us that the chance is slim to none, so the instrument is deemed lost.

The lack of M6 data will limit our ability to assess the long-range effect interference by the ACZ and land mass to propagation of the sound northward. We will utilize data from all five recovered AUHs and from the IMS hydrophone from Ascension Island to compare the sound levels within the ACZ and outside of the ACZ. The five-hydrophone array encompasses a large area of approximately 80,000 km^2, with average element spacing of 280 km between 56^{o}S and 59^{o}S parallels. We are comparing the sound levels among the hydrophones and will assess the sound propagation within the ACZ and make comparisons with the model. We have completed locating the hydroacoustic events in the Scotia Sea area using the five hydrophones, and thus far we have detected 40% more earthquakes than the National Earthquake Information Center (NEIC) catalogs within the same period. Here we discuss the preliminary result our study of the 13 months of data.

Preliminary Data Analysis

All five Scotia Sea hydrophone spectrograms exhibit a bell-shaped seasonal ambient noise pattern, high in the fall and low in mid-winter. Figures 2a and 2b show 13-month-long spectrograms at the M3 and M5 sites, respectively. Throughout the deployment, the calls of fin whales (~18 Hz) were observed, the most frequent occurring during the spring and late fall. The calls of blue whales were also observed during from austral fall to early winter (April to June). These calls appeared as lines near ~30 Hz and ~90 Hz. A bell-shaped spectrogram (in light blue) was the result of wide-band noise generated by ice breaking up and forming during the fall. Such noise became quieter in late winter when the sea ice in the region reached its maximum extent. A minimum of three hydrophones are required to locate events. Although ice-related events are ubiquitous, source levels of the most ice events (e.g., sea ice breakups) are low and not all events are locatable. In comparisons of the M3 (Figure 2a) and M5 (Figure 2b) spectrograms, attenuation of sea ice noise is evident as a result of transmission loss from the ice edge to the hydrophone mooring.

The average clock shift at the end of the 13-month deployment was 1.9 seconds. The internal temperature sensors indicate that at the hydrophone mooring depth (~500 m), temperature was between –1.5 ^{o}C and +2^{o}C, exhibiting small seasonal changes as a result of the strong influence of the Antarctic Circumpolar Current. Small temperature variations of the sea water would allow us a correction of timing by linear interpolatation and allow us to locate events within several a kilometer of resolution. Measurements taken with expendable bathythermographs during the cruise indicated that even during the austral summer, the propagation mode is surface limited in this region.

Figure 3 shows the epicenters of earthquakes derived from the AUH data during the first six months of deployment from December 29, 2007, through June 30, 2008. The green dots are the epicenters from National Earthquake Information Center (NEIC), which registered 89 earthquakes in its catalog. Our AUH array detected 200 earthquakes (yellow) during the same period. Approximately twice as many earthquakes were detected through the hydroacoustic method as a result of efficient sound propagation through the ocean, even in the area where the SOFAR sound channel is lacking. In addition, 232 ice tremor events (blue) were detected. Interestingly, almost no hydroacoustic events were located in the Weddell Sea. We think this is due not to the absence of events in this area but rather to the dissipation of sound energy by the dense sea ice coverage in the latitudes higher than 60^{o}S; the sound repeats reflections at the rugged sea ice surface and refractions, making the area seem to be an acoustically quieter spot. The southern-most edge of the locatable ice tremors (blue) approximately coincides with the sea ice edge during the winter of 2008–2009 (CERS database, BYU).

Another interesting finding so far is evidence of the Scotia Arc acting as an acoustic radiator for the hydroacoustic events occurring east of the volcanic chain (Figure 4). There is an early-arriving peak in the T-wave signals that appears to radiate from the shallow bathymetry of the arc after traveling as a P-wave over a considerable distance (~50–250 km). The larger-amplitude peak in the T-wave signal, which can arrive up to a couple minutes later, follows this and is sourced from near the NEIC epicenter (M 6.6 earthquake indicated by a yellow star, Figure 4). The early arrival can be more "diffuse," which may reflect the fact that the arc is a parabola. Figure 5 shows a plot of the time difference between T-wave peaks, which can be seen to scale with the distance to the crest of the arc, as measured along a great circle path between the NEIC epicenter and hydrophone.

Early studies of T-waves generated near arcs and islands described similar multi-peaked T-wave arrivals, which were assumed to also be related to local bathymetry near the epicenter (Johnson and Norris, 1968; Johnson et al., 1963). Using a bathymetric scattering model, de Groot-Hedlin and Orcutt (2001) later simulated the arrival patterns associated with a number of fore-arc events near Fox Island in the Aleutians. For such events, hydrophone stations in the Pacific typically record a symmetric first-arriving T-wave sourced in deep water near the epicenter and a later-arriving, slope-generated T-wave typically characterized by lower amplitudes and longer durations. There also have been reports of T- to P-wave conversions (Okal, 2001) and T-waves reflected by the continental mass (Hansen and Bowman, 2005); however, this is the first indication that P-waves may propagate through an island arc and be converted to T-waves on the opposite side, coupling into the water column by a down-slope conversion process. Moreover, we find that the second peak within the coda is still usable to locate the earthquake epicenter. For the Scotia Arc T-waves, the high-frequency component of the P-T conversed phase appears lost during propagation through the solid earth, leaving low-frequency energy (< 20 Hz) dominant (Figure 4). Similar effects have been documented in other trench environments for P-to-T converted phases that undergo long solid-earth propagation paths (e.g., de Groot-Hedlin and Orcutt, 2001; Obara, 2009).

CONCLUSIONS AND RECOMMENDATIONS

After one year of deployment, five AUHs were recovered and one was lost during this experiment. The data quality of the five hydrophones is excellent, with negligible clock errors. The analysis of AUH data has begun, and so far the hydroacoustic events during the first three months have been located. As compared with the land-based teleseismic network, the hydroacoustic method has detected twice as many events. Ice-related hydroacoustic events are ubiquitous in this area and, as compared with the T-phase of earthquake origins, twice as many ice events were located. Ice being on the surface, using the ice sound rather than bottom-generated T-waves may be more practical for modeling the propagation of sound from a near-surface explosion. We have also found evidence of P-waves being converted to T-waves through the Scotia Island arc and, as the T-wave exits, the arc acting as an effective parabolic radiator, making the sound field more complex.

ACKNOWLEDGEMENTS

We would like to express our gratitude to Drs. Chris Hindley and Anthony Martin of the British Antarctic Survey for carrying out the deployment of M6 in the international waters on the north side of the South Georgia Island. We also thank the officers and crew of the R/V Yuzhmorgeologiya and MV Pharos SG for deploying and recovering the hydrophones under unfavorable weather conditions. We are also indebted to the base commander Mr. Richard McKee on the Falkland Islands for help coordinating the hydrophone recovery operation. Data on iceberg position and sea ice extent were provided by the courtesy of CRS at BYU. Finally we express our deep gratitude to the Korea Polar Research Institute for providing the ship time and logistic support at the King Sejong Antarctic base.

REFERENCES

Bohnenstiehl, D. R., M. Tolstoy, D. K. Smith, C. G. Fox, and R. P. Dziak (2002). Aftershocks sequences in the mid-ocean ridge environment: An analysis using hydroacoustic data, *Techtonophysics*, 354: 49–70.

Chapp, E., D. R. Bohnenstiehl, and M. Tolstoy (2005). Sound-channel observation of ice-generated tremor in the Indian Ocean," *Geochem. Geophys. Geosyst.*, 6: Q06003, doi:10.1029/2004GC000889.

de Groot-Hedlin, C. D. and J. A. Orcutt (2001). Excitation of T-phases by seafloor scattering, *J. Acoust. Soc. Am.*, 1944–1954.

Dziak, R. P., D. K. Smith, D. R. Bohnenstiehl, C. G. Fox, D. Desbruyeres, H. Matsumoto, M. Tolstoy, and D .J. Fornari (2004). Evidence of a recent magma dike intrusion at the slow spreading Lucky Strike segment, Mi-Atlantic Ridge, *J. Geophys. Res.* 109: B12102.

Eggen, C. and B. D. Dushaw (2002). A MATLAB driven GUI supporting computation of a two-dimensional field of view and simulation of propagation between points," MTS/IEEE Conference, October 29–31, 2002, Biloxi, MS, Abstract #612.

Fox, C. G., H. Matsumoto, and T-K. A. Lau (2001). Monitoring Pacific Ocean seismicity from an autonomous hydrophone array, *J. Geophys. Res.* 106: 4183–4206.

Hanson, J. A. and J. R. Bowman (2005). Methods for monitoring hydroacoustic events using direct and reflected T-waves in the Indian Ocean, *J. Geophys. Res.* 111: B02305.

Harben, O. E., E. Matzel, Z. Upton, and J. Pulli (2003). Hydroacoustic blockage calibration for discrimination, in *Proceedings of the 25th Seismic Research Review – Nuclear Explosion Monioring: Building the Knowledge Base*, LA-UR-03-6029, Vol. 1, pp. 524–529.

Helffrich G. et al. (2006). Hydroacoustic detection of volcanic ocean-island earthquakes, *Geophys. J. Int.* 167: 1529–1536.

Johnson, R. H. and R. A. Norris (1968). T-wave radiators in the western Aleutians, *Bull. Seismol. Soc. Am.* 58:1–10.

Johnson, R.H. and J. Northrup and R. Eppley (1963), Sources of Pacific T-phases, J. Geophys. Res. 68: 4251–4260.

Obara, K. and T. Maeda (2009). Reverse propagation of T waves from the Emperor seamount chain, *Geophy. Res. Let.* 36: L08304.

Okal, E. A., and D. R. MacAyeal (2006). Seismic recording on drifting icebergs: catching seismic waves, tsunamis and storms from Sumatra and elsewhere, S*eismol. Res. Let.* 77: 6, 659–671.

Okal, E. A., (2001). Converted T phases recorded on Hawaii from Polynesican nuclear test: A preliminary report, *Pure Appl. Geophys.* 158: 457–474.

Robertson Maurice, S. D., D. A.Wiens, P. J. Shore, E. Vera, and L. M. Dorman (2003). Seismicity and tectonics of the South Shetland Islands and Bransfield Strait from a regional broadband seismograph deployment, *J. Geophys. Res.* 108: B10, 2461.

Talandier, J. et al. (2006). Hydroacoustic signals generated by parked and drifting icebergs in the Southern Indian and Pacific Oceans, *Geophys. J. Inst.* 165: 817–834.

Upton, Z. et al. (2006). A reflected energy prediction model for long-range hydroacoustic reflection in the oceans, *J. Acoust. Soc. Am.* 119: 153–160.

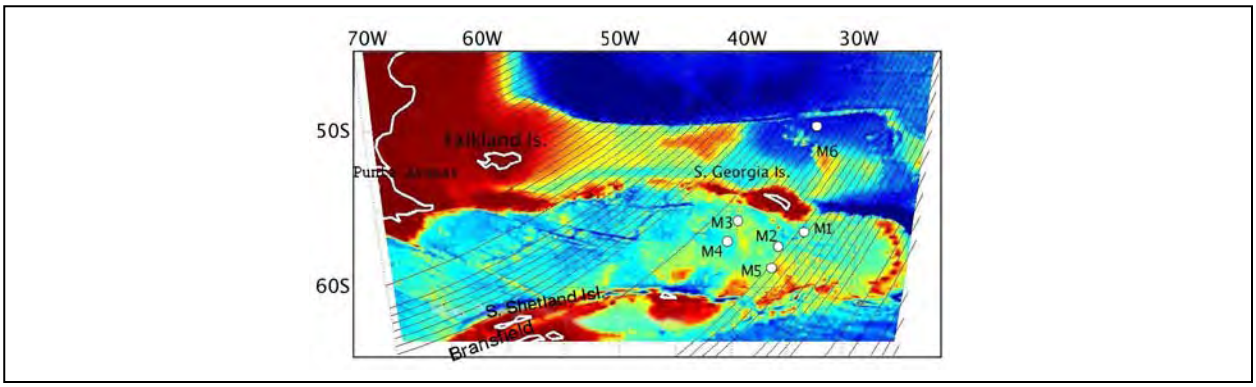

Figure 1. Hydrophone mooring locations.

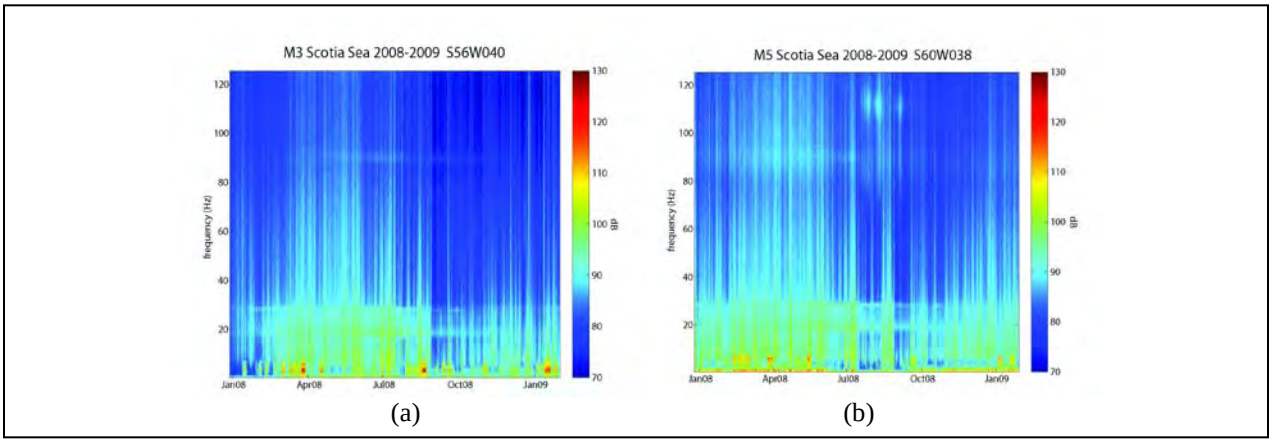

(a) (b)

Figure 2. Seasonal noise spectrograms from December 2007 through January 2009. Spectrum levels are in dB relative to µPa^2/Hz. Spectrogram (a) is at the mooring M3, and (b) is at M5. The influence of ice noise, particularly in high frequencies, is much more pronounced at the southern hydrophone (M5), which was near the edge of sea ice during the 2008 austral winter.

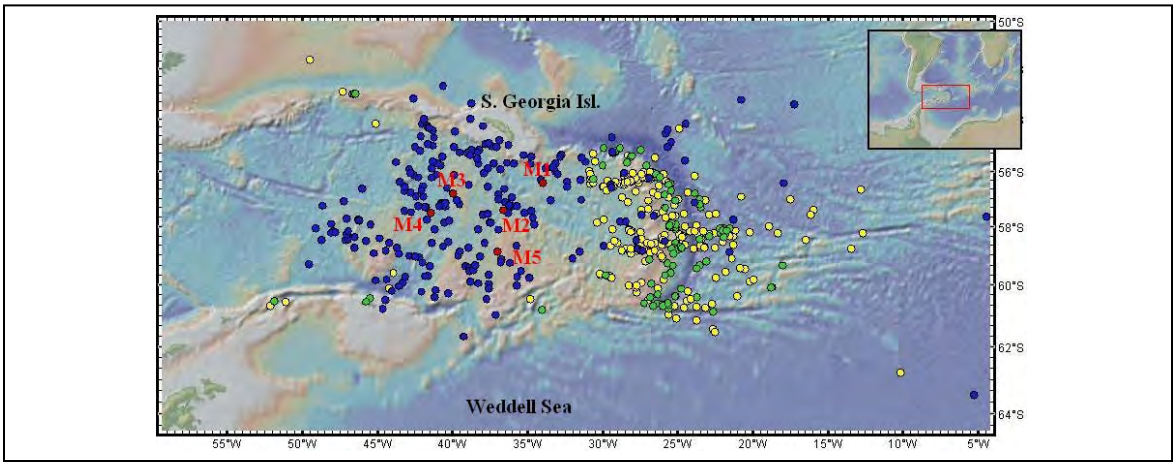

Figure 3. Epicenters map derived from NEIC data (green) vs. AUH data (blue: ice, yellow: earthquake) from December 29, 2007, through June 30, 2008. Red circles indicate the mooring locations.

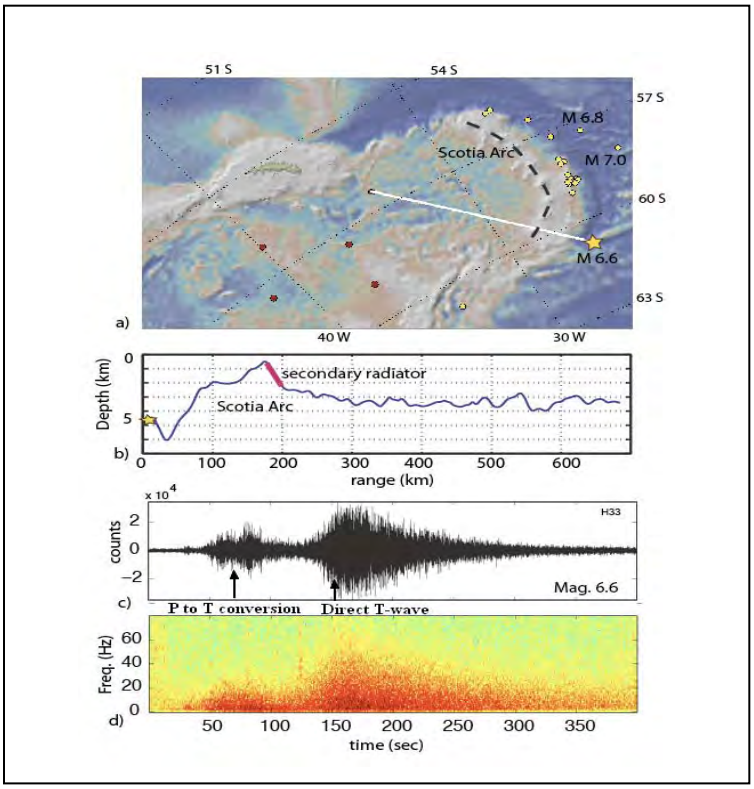

Figure 4. (a) Map showing NEIC locations of the 28 earthquakes (yellow dots) identified as having double-peaked T-wave arrivals. These events lie to the east of the Scotia Arc, with the exception of one event behind a prominent ridge to the south. Shallow subduction interface events, which are closest to the volcanic arc, are the most common to exhibit this behavior. For events on the outer rise (more distant from the arc) the earlier-arriving phase is seen only for the events of greatest magnitude. (b) The bathymetric profile from source to receiver for the example arrival shown in (c) and (d). The first peak is typically a lower amplitude and deficient in high-frequency components, relative to the second. In this example, the time separation between the peaks is ~100 sec, consistent with its propagation as a P-wave along a 180-km-long path prior to conversion. Note that the larger, later-arriving phase is sourced from the deep-water epicenter and can still be used for location purposes.

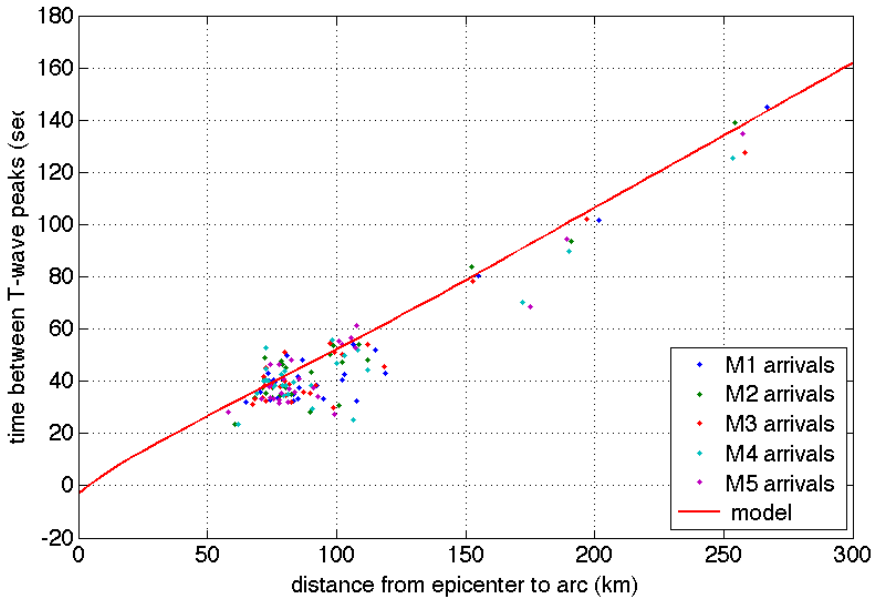

Figure 5. Time difference between T-wave peaks within each arrival package plotted against the distance to the arc. Red line shows the predicted time difference, assuming P-wave propagation through an iasp91 model from a fixed 10-km-deep source and a T-wave velocity of 1.465 km/sec through the water column.

Radionuclide Monitoring

MODELING OF RADIOXENON PRODUCTION AND RELEASE PATHWAYS

Steven R. F. Biegalski, Mark Deinert, Thomas G. Saller, and Brian B. Wooten

The University of Texas at Austin

Sponsored by the National Nuclear Security Administration

Award No. DE-AC52-09NA28608
Proposal No. BAA09-57

ABSTRACT

Since the Limited or Partial Test Ban Treaty in 1963, nuclear explosion tests have largely been conducted in underground facilities. One of the main motivations for underground testing is to contain the fission product releases from the nuclear explosion. To monitor the emissions from underground nuclear tests, the world community relies upon atmospheric monitoring for radioxenon among other technologies.

When an atmospheric radioxenon signal is observed, the isotopic ratios are examined to see if they match the expected values for nuclear explosions. These isotopic ratios are utilized to distinguish between nuclear explosion sources of radioxenon and other anthropogenic sources such as the commercial nuclear industry and the radiopharmaceutical industry. Current methods to predict the various isotopic ratio signatures have largely focused on modeling the production source. While this is a good first order approximation, it does not account for the chemical and isotopic fractionation that occurs during environmental transport of radioxenon and its parent radionuclides. This fractionation causes a significant change in the isotopic ratios from their point of creation to the point where they are collected in the atmosphere.

The goal of this work is to develop transport models for xenon and its parent radionuclides for underground nuclear explosions, commercial light water reactors, and radiopharmaceutical production facilities.

OBJECTIVES

Radioxenon may be produced through one of two methods. The first method is through the fission process and the second method is through an activation reaction. All xenon isotopes with mass greater than or equal to 129 are fission products (except ^{130}Xe). Very high mass radioxenons like ^{143}Xe and ^{144}Xe are produced in fission, but they have half-lives on the order of one second so they are not very relevant to this work. Stable xenon isotopes including ^{131}Xe, ^{132}Xe, ^{134}Xe, and ^{136}Xe are also fission products but they are not relevant to this work since they do not decay. The main fission products of interest include ^{131m}Xe, ^{133m}Xe, ^{133}Xe, and ^{135}Xe. The ^{235}U fission yields and half-lives for these radionuclides are listed in Table 1. The combination of high fission yields and relatively short half-lives make these radionuclides prime candidates for detection of underground nuclear explosions.

Table 1. Half-lives and fission yields of the four radioxenon isotopes of interest (Chadwick et al., 2006).

	^{131m}Xe	**^{133m}Xe**	**^{133}Xe**	**^{135}Xe**
Half-Life	11.9 days	2.19 days	5.24 days	9.09 hours
^{235}U Fission Yield Per 100 Fissions				
Direct (%) – Thermal	3.48×10^{-7}	1.89×10^{-3}	6.66×10^{-4}	7.85×10^{-2}
Direct (%) – Fast	2.41×10^{-7}	4.23×10^{-3}	1.45×10^{-3}	1.20×10^{-1}
Cumulative (%) – Thermal	4.05×10^{-2}	1.95×10^{-1}	6.70	6.54
Cumulative (%) – Fast	4.51×10^{-2}	6.72	1.98×10^{-1}	6.60

Figure 1 shows a diagram of the ^{135}Xe production process through nuclear fission. Similar production paths exist for each radioxenon fission product. The two sources for fission product atoms are direct production from fission and the decay of parent radionuclides along the same mass chain. The probability of direct production from fission is known as the direct yield. This value is listed in Table 2 for ^{235}U. The direct yield is a function of both the atom that fissioned as well as the energy of the neutron initiating the fission. Fission yields from spontaneous fission are purely a function of the atom undergoing fission since there are no incident particles. The cumulative yield is the probability of production both from direct production and from the decay of parent fission products. The two loss mechanisms for atoms shown in Figure 1 are decay and neutron absorption. For the majority of these nuclides, decay is the primary loss mechanism. However, neutron absorption has a high probability of occurrence in atoms such as ^{135}Xe due to its exceptionally large 2,943,100 b cross-section.

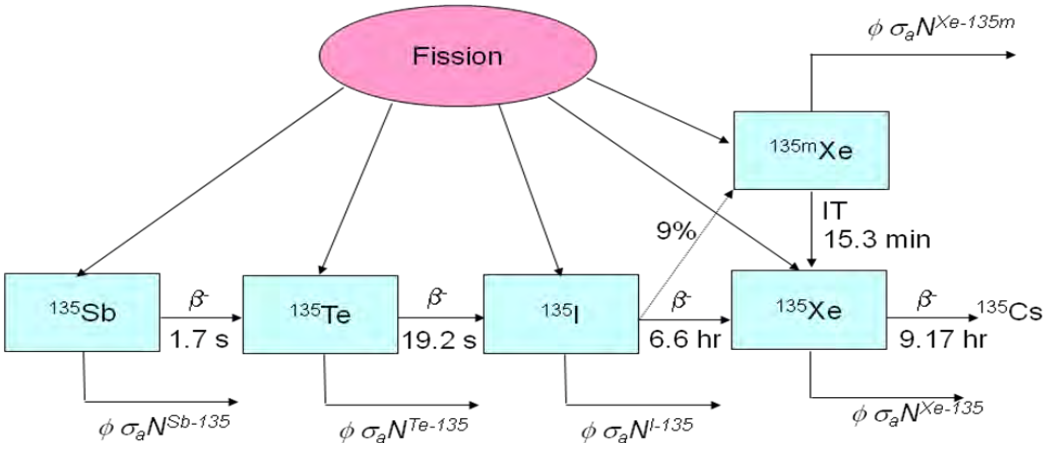

Figure 1. Production process for ^{135}Xe through nuclear fission.

The radioxenon isotopic ratios provide signatures that may be utilized to distinguish between the production source. The goal of the work detailed in this proposal is to develop computational models that calculate the Xe fission product signatures from underground nuclear explosions, commercial nuclear reactors, and medical isotope production environments. These models will include proper treatment of the chemical fraction of Xe from its parent nuclides. This work will reduce the uncertainty associated in utilizing radioxenon ratios to differentiate between nuclear explosions and other anthropogenic sources.

RESEARCH ACCOMPLISHED

Underground Nuclear Explosions

Underground nuclear tests result in the release of xenon isotopes from direct fission yield as well as the release of isotopes that decay to xenon. In addition to isotope production, the rapid fission process releases a substantial amount of energy into the local environment that results in thermal and moisture gradients that will affect multiphase transport below ground. Modeling the movement of xenon in the subsurface is further complicated by the fact that it is mildly soluble in water (von Antropoff, 1910; Dresel and Waichler, 2004) and sorbs to the surfaces of many porous media (Maghusin et al, 1997; Filimonova et al., 2004). As a result, gaseous diffusion as well as transport of dissolved xenon, and its precursors, would need to be considered for a full treatment of xenon mobility after an underground nuclear test. In addition, the binary diffusion coefficients for xenon gas will be slightly different for each of the individual isotopes, owning to the differences in their masses. For the purpose of tracking isotope ratios, as would be important for monitoring under the Comprehensive Nuclear-Test-Ban Treaty, the decay of radioxenon would also need to be taken into consideration.

If gas phase diffusion were the only factor in the transport of xenon in the subsurface the movement of xenon could be modeled using Equation 1.

$$\frac{\partial C_i}{\partial t} = \nabla \cdot (D_i \nabla C_i + S_i - g C_i) \quad (1)$$

Here C_i is the concentration of the i'th xenon isotope, D_i is its diffusion coefficient, S_i is the rate of xenon production from β^- decay of the respective iodine isotope and g is a function that takes into consideration the rate at which xenon isotopes are lost through sorption, dissolution in fixed subsurface moisture, or through decay. The concentration of iodine is itself time dependent and subject to transport.

Some data exists on the binary diffusivity of xenon and a value of 0.10 $cm^2\ s^{-1}$ has been reported (Dresel and Waichler, 2004). However, the diffusivity is a function of the temperature and pressure within a system and is generally given by Equation 2.

$$D_{T_j P_j} = D_{T_j P_j} \frac{p_i}{p_j} \left(\frac{T_j}{T_i} \right)^{3/2} \frac{\Omega_i}{\Omega_j} \quad (2)$$

Here T is temperature, p is pressure, Ω is the molecular collision integral and i, j are the respective states at which the diffusivity is desired [Bird *et al.*, 1960]. The diffusivity of two isotopes of mass $M_A > M_B$ is also predicted by classical theory to be proportional to:

$$(D_B/D_A) \sim (M_B/M_A)^{1/2} \quad (3)$$

The solubility of xenon in water is small but potentially significant if the yield of a subsurface test is small and the device was deeply buried. A value of 0.10 at 293 K is reported in von Antropoff (1910) which is in keeping with the values available in the literature. This same paper also shows that the solubility of xenon is mildly temperature dependent, ranging from a low of 0.90 at 323 K to 0.23 at 273 K. The sorbtivity of xenon on subsurface media is less well established and additional experimental is required to establish saturation values.

If Equations 1, 2, and 3 where the only ones required to model xenon transport in the subsurface, the problem would already be complicated. Unfortunately, this is not the case. Because xenon and its precursors can dissolve in water, they can also be transported with it as it redistributes itself after a nuclear test, or as it moves through evaporative processes in the vadose zone. It is well established that the movement of a liquid phase in a porous medium that is itself subject to thermal gradients is given by Equation 4.

$$q_{liq}/\rho = -D_{\theta liq}\nabla\theta - D_{T liq}\nabla T - Ki \quad (4)$$

Here q_{liq} is the liquid phase fluid flux, ρ is its density, $D_{\theta liq}$ is the Darcy diffusion coefficent, θ is the moisture content of the media, T is temperature, K is the hydraulic conductivity of the media and i is a unit vector. The parameter $D_{T liq}$ is the thermal liquid diffusivity which is equal to $K\sigma P_c$ where, σ is the surface tension of the water, and P_c is the capillary pressure (Philip, 1957).

Because thermal gradients are important in Equations 2 and 4 it is important to be able to model the subsurface temperature response to both the weapons test and other relevant heat sources (e.g., surface solar flux which can drive evaporation from the vadose zone). Energy transport within the subsurface can be well modeled using Equation 5.

$$C\frac{\partial T}{\partial t} = \nabla\cdot\lambda\nabla T + \rho L\nabla\cdot D_{\theta vap}\nabla\theta \quad (5).$$

Here C is the volumetric heat capacity of the soil, λ is the thermal conductivity of the soil, and L is the latent heat of evaporation, and $D_{\theta vap}$ is the water vapor diffusivity (Bird et al., 1960). Importantly, $D_{\theta liq}$, $D_{T liq}$, λ, and K are all strong functions of θ which makes Eqs (3–4) highly nonlinear and, in most cases, analytically untractable.

Models are being developed utilizing the above equations for the calculation of radioxenon transport resulting from an underground nuclear weapon test.

Commercial Nuclear Reactors

A collaboration has been established with Crystal River nuclear power station in Florida. Data mining has been initiated to obtain radioxenon release data from the nuclear power plant. Initial comparisons have been made between the reported release data and fuel cycle models run in ORIGEN. Figure 2 shows a comparison between the Crystal River 3 (CR3) radioxenon release data and the data resulting from ORIGEN runs. The ORIGEN runs represent a fuel burnups ranging from 0.1 MWd/MTU to 70,500 MWd/MTU. The CR3 release data is largely to the left of the radioxenon values modeled in ORIGEN due to the use of holding tanks at CR3. Noble gasses are accumulated and held for release. During this period, the radioxenon decays causing a decrease in both the $^{133m}Xe/^{131m}Xe$ and $^{135}Xe/^{133}Xe$ ratios.

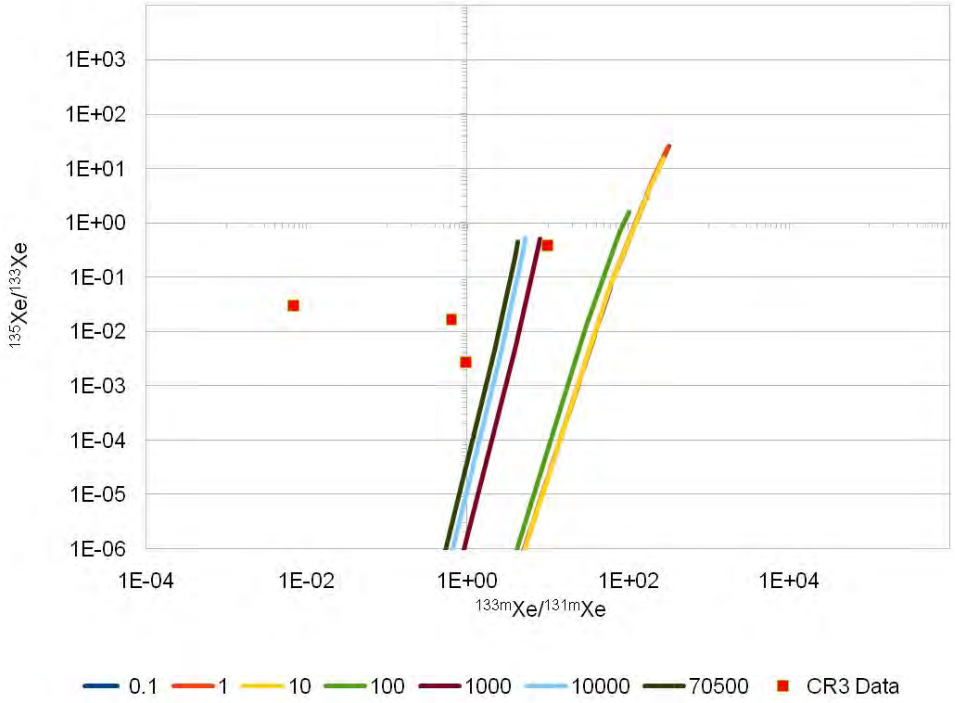

Figure 2. Comparison of ^{131m}Xe, ^{133m}Xe, ^{133}Xe, and ^{135}Xe release data (CR3 Data) and results from ORIGEN-ARP calculations for plant operations . ORIGEN burnup values are in units of MWd/MTU.

Medical Isotope Production

An extensive modeling effort was initiated to calculate the source signatures resulting from medical isotope production. ORIGEN-ARP, ORIGEN 2.2, and Excel have been utilized. ORIGEN-ARP was utilized for commercial reactor modeling. ORIGEN 2.2 was utilized for cases where fast neutron fission is required to model. ORIGEN 2.2 also the capability to model the separation of daughter isotopes from their parents. Excel calculations were conducted from derived activation and decay equations. These equation are quite complex and are utilized for quality control checks on the ORIGEN calculations.

As a starting point the source signature of a nuclear weapon was modeled. Figure 3 illustrates this signature for both a ^{235}U and a ^{239}Pu device. There are two lines for each weapon signature. The line to the left represents the radioxenon signature resulting from complete separation of radioxenon from its parents immediately after the explosion. The line to the right represents the signature of radioxenon with the complete cumulative production from parent fission products. Since partial fractionation is a likely scenario for underground nuclear explosions, these two lines set the normal bounds for radioxenon source signatures from nuclear weapons tests. The results shown in Figure 3 are commensurate with those shown in Kalinowski and Tuma (2009).

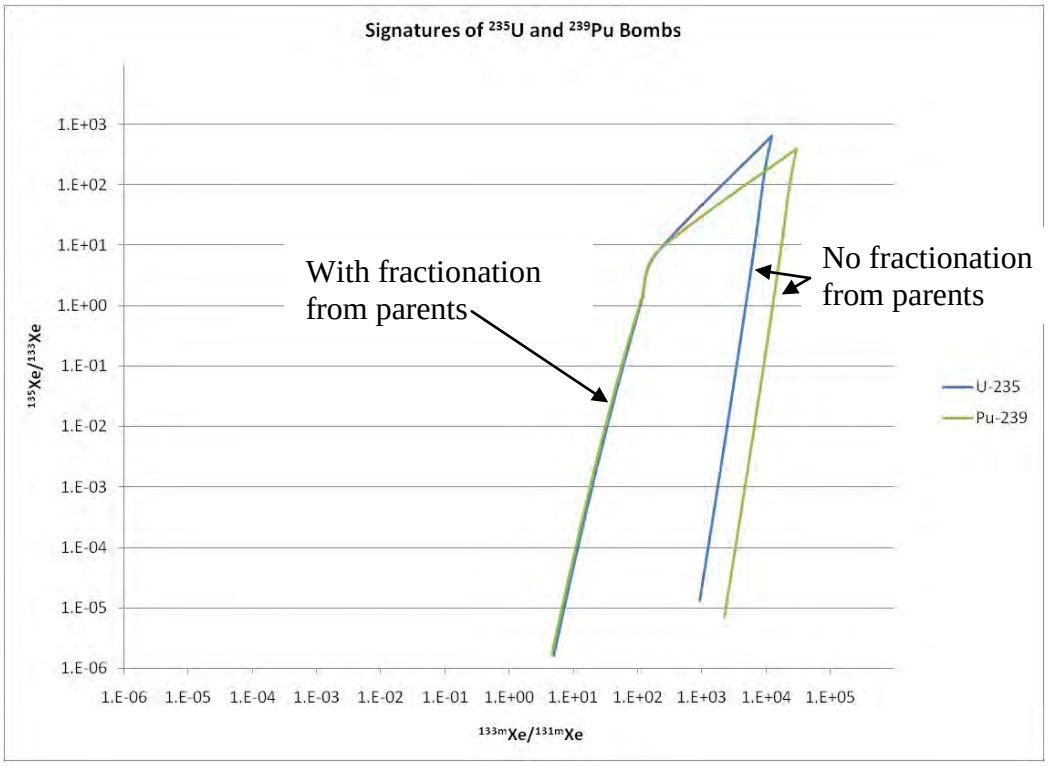

Figure 3. **Source signature of ^{235}U and ^{239}Pu weapons.**

The next step was to model a default medical isotope production radioxenon signature. Production of medical isotopes through highly enriched uranium target activation was the method modeled since this is one of the most common production methods. An irradiation time of five days, a decay time of 12 hours, and subsequent separation and decay are modeled. The irradiation and decay values are reported to be standard times for such production (Nuclear and Radiation Studies Board, 2009). The radioxenon signature for the standard medical isotope irradiation is shown in Figure 4. The data show that the two source signatures are very close and likely not discernable in an environmental monitoring scenario.

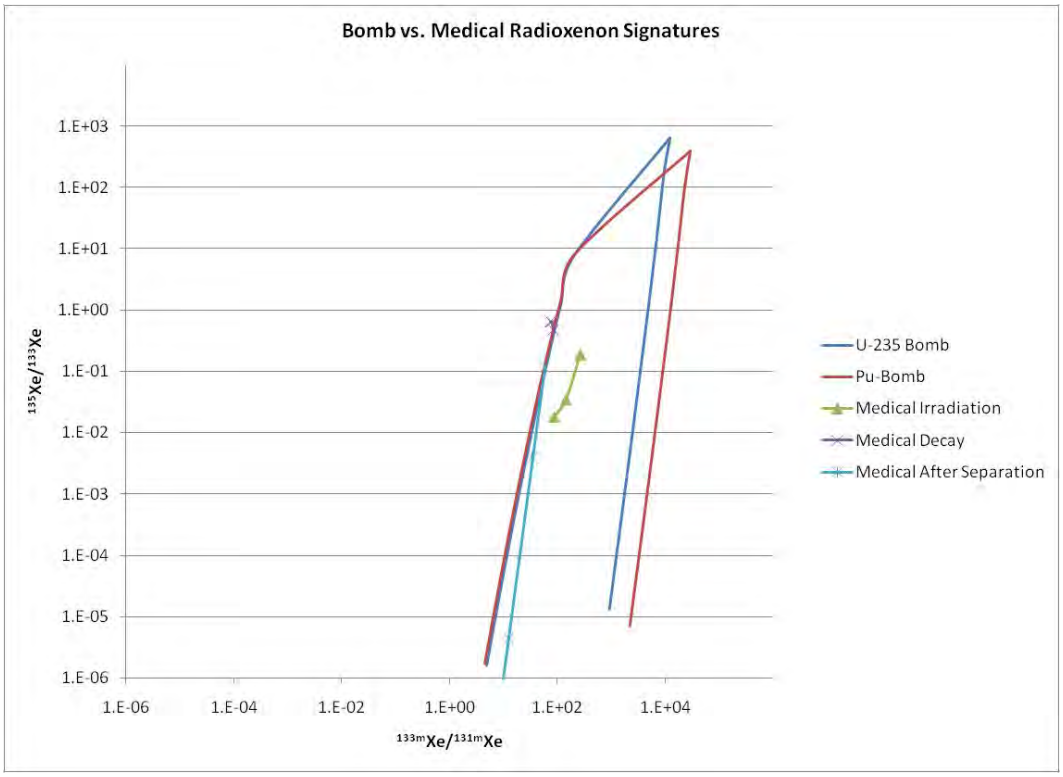

Figure 4. Radioxenon source signature comparison between nuclear weapon and medical production.

A sensitivity study was conducted to determine the magnitude of the effect due to changes in the radioxenon ratios. Table 2 summarizes the results of the study. Of the six variables studied, only two showed a moderate impact on the radioxenon ratios: irradiation time and use of a holding tank. Figures 5 and 6 show the magnitude of changes in radioxenon signatures due to irradiation time and use of a holding tank, respectively. Note that the values do not change much due to the use of a holding tank for 30, 60, and 90 days due to the respective half-lives of the radioisotopes being examined.

Table 2. Sensitivity study for radioxenon signature from medical isotope production facility.

Parameter	**Range of Values**	**Effect on Radioxenon Ratios**
Neutron Flux	10^{11} to 10^{15} n cm^{-2} s^{-1}	Minimal
Cross Sections	BWR, PWR, and Pure Thermal	Minimal
Fuel Enrichment	19.9% to 95% ^{235}U	Minimal
Irradiation Time	5 to 21 days	Moderate
Decay Time	6 hours to 7 days	Minimal
Use of Holding Tank	0 to 90 days	Moderate

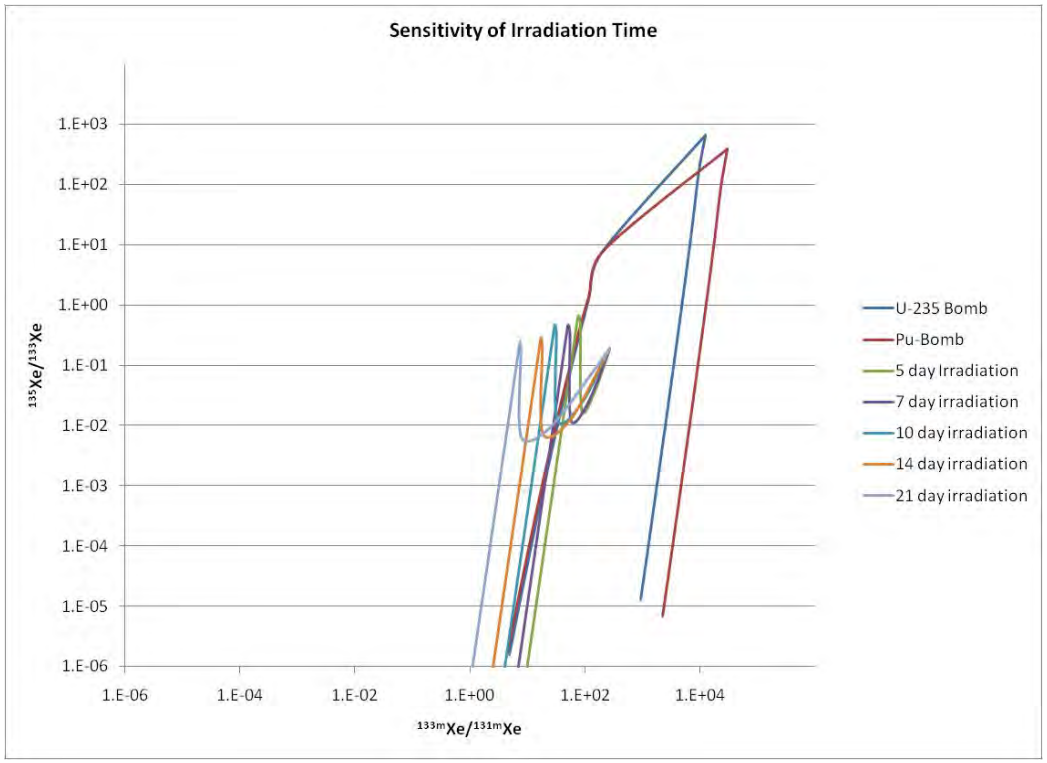

Figure 5. Radioxenon ratios resulting from changes in irradiation time.

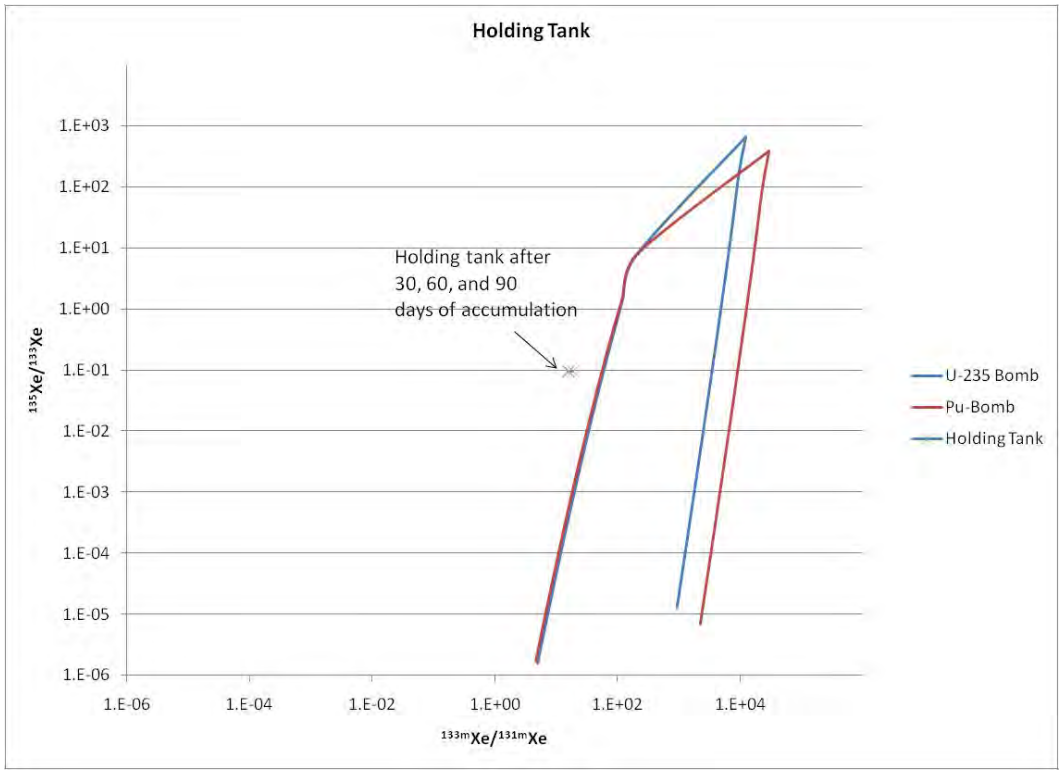

Figure 6. Radioxenon signature resulting from use of holding tank.

CONCLUSIONS AND RECOMMENDATIONS

Initial studies have been conducted to examine the radioxenon signatures resulting from underground nuclear weapons tests, commercial nuclear reactor facilities, and medical isotope production facilities. Further modeling efforts will ensue to increase the fidelity of our understanding of these source signatures. Experiments will also be conducted to provide data that may improve the models.

REFERENCES

Bird R. B., W. E. Stewart, and E. N. Lightfoot (1960). *Transport Phenomena*, John Wiley & Sons, New York.

Maghusin, P. C. M., A. Bolz, K. Sperling, and W. S. Veeman (1997). The use of ^{129}Xe NMR spectroscopy for studying soils. A pilot study, *Geoderma* 80: 449–462.

Chadwick, M. B., P. Oblozinsky, M. Herman, et al (2006). Next generation evaluated nuclear data library for nuclear science and technology, *Nuclear Data Sheets* 107: 2931–3060.

Dresel P,E. and S. R. Waichler (2004). Evaluation of Xenon gas detection as a means for identifying buried Transuranic Waste at the Radioactive Waste Management Complex, Idaho National Environmental and Engineering Laboratory, PNNL-14617.

Filimonova S. V., H. Knicker, W. Häusler, I. Kögel-Knabne (2004). ^{129}Xe NMR spectroscopy of adsorbed xenon as an approach for the characterisation of soil meso- and microporosity, *Geoderma* 122: 25.

Kalinowski M. B. and M. P. Tuma (2009). Global radioxenon emission inventory based on nuclear power reactor reports," *J. Environ. Radioactivity* 100: 58–70.

Nuclear and Radiation Studies Board (2009). Medical Isotope Production without Highly Enriched Uranium, National Academies Press (2009).

Philip J. R. (1957). Evaporation and moisture and heal fields in the soil, *J. Meteorol.* 14: 354.

von Antropoff A. (1910). The solubility of Xenon, Krypton, Argon, Neon, and Helium in water, in *Proceedings of the Royal Society of London, Series A, Containing Papers of a Mathematical and Physical Character,* 83: 565 474–482.

RADIATION DETECTION CHALLENGES

Matthew W. Cooper, James H. Ely, Derek A. Haas, Jim C. Hayes, Martin E. Keillor, and Justin I. McIntyre

Pacific Northwest National Laboratory

Sponsored by the National Nuclear Security Administration

Award No. DE-AC05-RLO1830/PL08-MRVL-NDD05

ABSTRACT

Most ground-based radioxenon nuclear detonation detection systems rely on a combination of detectors to measure beta-gamma signatures for treaty monitoring (Hayes et al., 1999; Bowyer et al., 1999). The detection packages often use a plastic scintillator to detect the beta or conversion electron particle and a crystal scintillator such as NaI or CsI to detect the gamma- or x-ray. While these detection systems work well, there was a need to simplify the setup, calibration and improve robustness. The redesign, which led to using CsI(Na) well detectors, sought to achieve higher detection efficiency, better shock resistance, and less temperature dependence (Cooper et al., 2007), as shown in Figure 1. Preliminary testing showed excellent characteristics. After further study two issues were discovered that need to be overcome. First, there is potential for a dead layer, due to the manufacturer handling of the crystal, to be present on both the CsI and NaI crystals. The second issue is an energy drift caused by incorrect mating of PMT and PMT base to the crystal. These two issues cause adverse effects on the measurement of radioxenon or any other radiological measurement. It is clear that additional handling and inspection procedures are necessary during the manufacturing process. This paper will discuss the matter in more detail and give evidence of the presence of these issues in PNNL purchased crystals. The paper will also propose procedures for handling and testing of high-quality CsI and NaI crystals that get delivered on future purchases.

OBJECTIVES

The objective of this paper is to discuss apparent causes of low detection efficiency and detector gain drifts. These two issues have recently been identified with purchased components which points out the need for performance confirmation testing prior to incorporation of parts into a system.

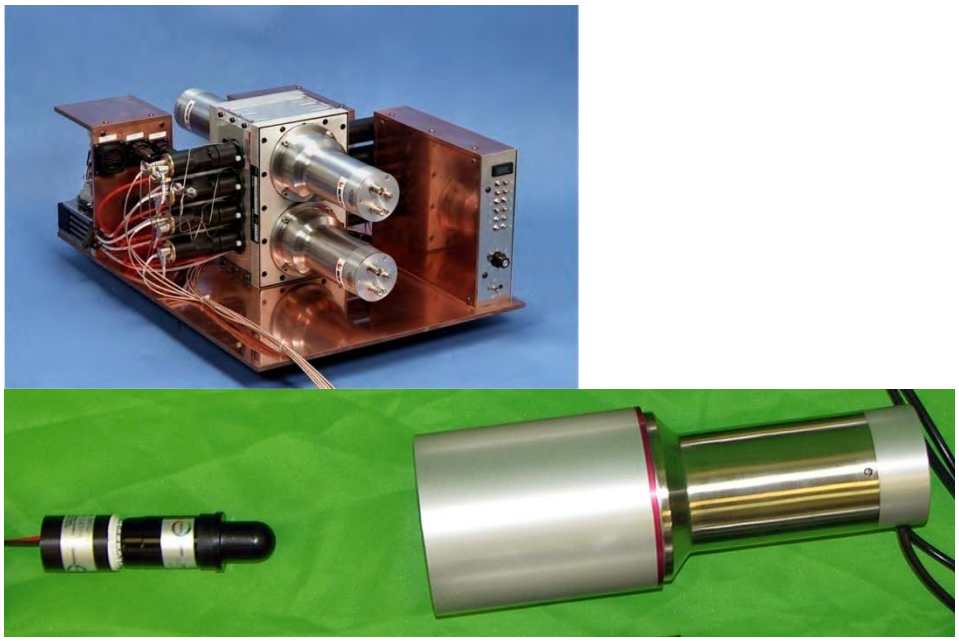

Figure 1. The top figure shows an older beta-gamma detector style that relies on multiple PMTs to determine both the beta and gamma energies. The bottom figure shows a portion of the replacement detector in a semi-complete stage.

The first issue is a low detection efficiency for the 31 keV x-ray from ^{133}Xe. Low detection efficiency is caused by additional material present between the sample and the active crystal. The additional material causes some of the

x-rays to partially (sometimes completely) deposit their energy before reaching the active detector. This effect causes a broadening of the peak (poor energy resolution) and in the worst case it can cause a drop in detection efficiency. This is the most likely cause of the low detection efficiency in the CsI.

The second issue is detector gain drifts. Gain drifts are continuous shifts in the energy calibration of a detector. Gain shifts and drifts are often be caused by instability in photo-multiplier tube (PMT) high voltage (HV), incorrect selection of PMT, instability in data acquisition electronics or potentially software bugs in the data analysis code. Figure 2 has a many 10 minute spectra taken over approximately 16 hours. These spectra used a ^{137}Cs source inserted into the detector and left there over the entire 16 hours. A color scale is used to represent the counts in each spectrum with the highest counts being in red. Figure 2 shows the observed drift is still occurring even after 16 hours, although it has slowed significantly. Gain drifts and shifts can cause misinterpretation of data and can be very difficult to discern.

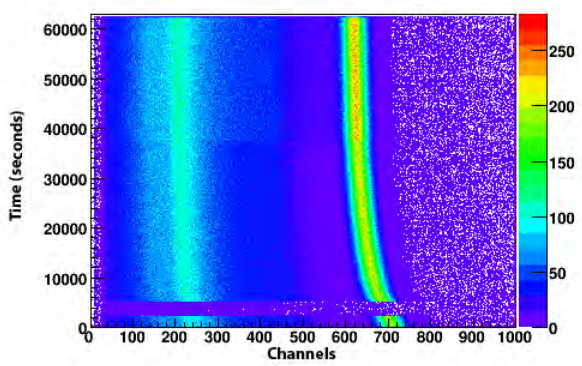

Figure 2. A contour plot showing a 13% gain drift over a ~16 hour period. The ^{137}Cs spectra were accumulated in 10 minute increments. The line originating at channel 700 represents the shifting 661.7 keV Cs-137 gamma-ray.

RESEARCH ACCOMPLISHED

Low Detection Efficiency

Low x-ray detection efficiency was observed during initial characterization of the detector system, however it came as a surprise since the prototype detectors did not have a similar low efficiency. The most probable cause for the drop in x-ray efficiency is a dead layer on the crystal surface. This effect would increase the number of interactions outside the active crystal (undetected events). A. Gleyzer (see Acknowledgements) also noted that CsI(Na) crystals are likely to have a dead layer caused by hydration and may be due to poor handling during fabrication. This affect has been long known (Reeder 2004), but was unexpected. To understand the efficiency of the detector a Monte Carlo simulation was performed (Keillor 2009) in addition to extensive testing of the detectors.

The Monte Carlo simulation was performed using PStudy (Brown et al., 2004) to generate a series of Monte Carlo Neutral Particle (MCNP5) simulations (Booth et al., 2003). An unexpected finding from this study is a correlation between the dead layer thickness and the intensity of the 31 keV x-ray. When simulating the presence of ^{133}Xe in the well detector, there is an 80 keV gamma-ray and a 31 keV x-ray. As the dead layer increases, the intensity of the full energy peak (FEP) at 80 keV decreases in intensity while the 31 keV peak increases in intensity. Under normal circumstances, additional material between the source and the detector will decrease the intensity of the lower energy peak more than the higher energy peak. Figure 3 shows simulated spectra corresponding to dead layers of 0 mm and 0.21 mm thick.

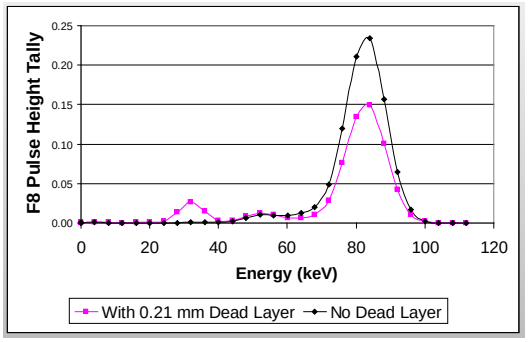

Figure 3. MCNP5 simulation of ^{133}Xe within a CsI well detector.

To confirm the presence of a dead layer in the purchased CsI detector, several sample detectors were selected. The selected detectors include a NaI(Tl), CsI(Na) (proto-type) and CsI(Na) which exhibited the low efficiency. Two experiments were run against all three detectors. Initially a ^{241}Am source with a 59.5 keV gamma-ray was used, however it also has two lower energy gamma-rays at 26.34 and 21.00 keV as well as several x-rays that are near the ~31 keV energy of interest. Because the ^{241}Am has these low energy gamma- and x-rays it turns out to be more complicated than originally hoped for (see Figure 4).

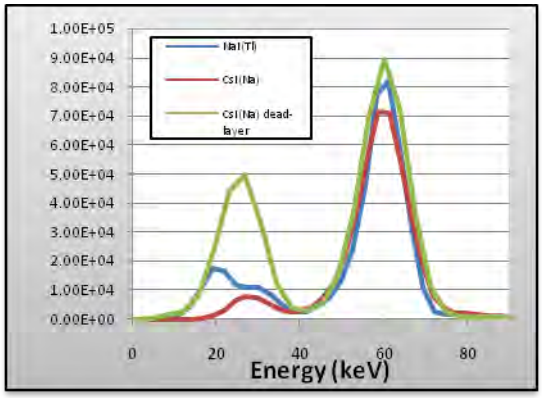

Figure 4. Spectra from three detectors: NaI, CsI and CsI (dead-layer) using a ^{241}Am source.

After analyzing the ^{241}Am spectra and noting the increase in the 30 keV peak as well as the complex features seen in the NaI spectrum, a simpler analysis was sought. Using a ^{57}Co source avoids most of the problems inherent in the ^{214}Am spectra. A comparison of the ^{57}Co spectra (Figure 5) from the same three detector set (NaI, CsI and CsI with dead layer), demonstrates that the dead layer of the newer CsI(Na) introduces a ~31 keV peak in the spectrum, while the other two detectors did not display this feature. All 3 spectra display the 122 and 136 keV unresolved peak, as well as an x-ray escape peak on the low energy side of the main peak.

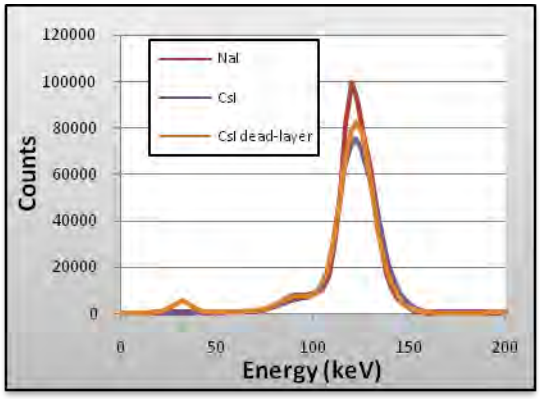

Figure 5. Co-57 spectra for three different well detectors showing the various levels of dead layer present.

Gain Drifts

Gain shifts and drifts are often observed in detection systems. The first step for eliminating a gain drift is, obviously, to recognize it is occurring. The second step is to discover what component is causing the behavior and fixing it. However, if it is not possible to fix the gain drift it is important to actively correct for the drifting.

In this particular case there are two factors playing a role. First there is a brief drift observed during system startup, which is due to the high voltage powering on and settling into a particular voltage setting. This is observed over several minutes time and has two components. The first component is due to a voltage monitoring loop that is built into the high voltage circuit. This voltage monitor can take several minutes to settle into the appropriate voltage setting upon which it no longer causes drifting. The second component is due to thermal loads on the circuit. As the circuit warms up there are slight changes to the characteristics of the circuit which translates into small gain drifts while the circuit reaches an equilibrium temperature. These two effects amount to approximately a 5% shift, the majority of which is during the first hour (Figure 6).

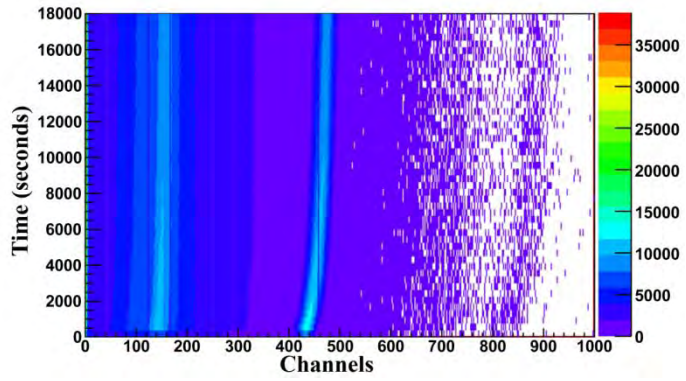

Figure 6. A contour plot showing a ~5% gain drift over a ~5 hour period. The ^{137}Cs spectra were accumulated in 10 minute increments. The line originating at channel 410 represents the shifting 661.7 keV ^{137}Cs gamma-ray.

The second factor leading to gain drifts in this detection system is dependent upon detection rate. This long-term drift can be seen in Figure 2 and was far more difficult to determine. It is observed by inserting a 5 mCi ^{137}Cs source into the detector. The drift occurs when going from background detection rates to high count rates, but the effect can be moderated by gradually increasing the count rate rather than have large jumps in the count rate. Attempts to see the gain drift on an oscilloscope proved to be too challenging, even with some averaging tools to check pulse heights.

A duplicate detector system was established to investigate the drifts on an independent system. Identical hardware and software were used in the test system, although, the test detectors used were of similar geometry but from a different manufacturer. Attempts to re-create the drifts in the electronics using a pulser and detector proved unsuccessful. This suggested that the effect is either within the detector or there may have been internal components in the electronics that were not identical. A change of some of the internal electronics components (DACQ cards and HV cards) did not fix the drift problem, which left the detector as the most likely cause. Since the drift was only observed on the gamma detectors, these were targeted. After swapping each of the well detectors in the system, testing commenced. Repeat test were performed using the 5 mCi ^{137}Cs source. Figure 7 shows no gain drift is observed with rate changes after the detector change was made. This can be seen by the straight vertical red line (661.7 keV ^{137}Cs) gamma-ray line that is centered at channel 250 in the figure.

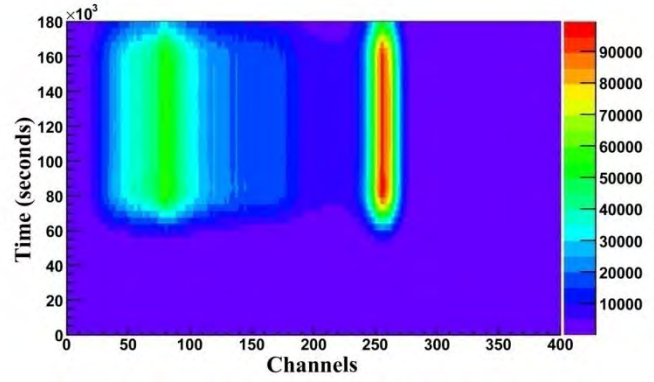

Figure 7. A contour plot showing no gain drift over a 24 hour period. The ^{137}Cs spectra were accumulated in 10 minute increments. The line at channel 255 represents the shifting 661.7 keV Cs-137 gamma-ray.

CONCLUSIONS AND RECOMMENDATIONS

This paper draws attention to the need for rigorous testing of nuclear detectors prior to use in detection systems, even when previous generations of the detectors have not shown any adverse characteristics. The potential for a detector dead-layer to complicate the analysis of xenon measurement data when CsI(Na) scintillators are used has been observed and will become a standard characteristic to check in initial testing. The presence of cesium in the detector crystal allows x-rays to be generated which interfere with xenon x-rays when there is partial energy capture. The Iodine x-rays cause a similar problem in resolving the xenon x-rays. Further, the presence of an inactive dead layer on the crystal increases the chance of detecting only partial energy from the event (seeing only the 30 keV from Cs or I). CsI(Na) crystals can be produced without this dead layer effect, so they are not necessarily unsuitable for xenon measurement applications. Detector buyers interested in low energy events should consider specifying the acceptable dead layer thickness, perhaps by specifying the acceptable ratio of counts in the 122 keV and 30 keV peaks from measurement of a ^{57}Co check source.

Another issue that should be checked during initial detector testing is gain drifts. The testing should use equipment that is known to be stable and not have gain shifting or drifting present. Currently it is believed that poor matching between the PMT and base is the cause of the drift. This hypothesis will be tested once manufacturer specified PMT bases arrive. It should be noted that the drifting (5%) due to system start up in no way effects data quality for system results, but does affect the quality assurance/quality control method (Cooper et al., 2007). However, the gain drift associated with the PMT bases mismatch does impact data quality. This drives home the necessity of detector component matching.

The challenges illustrated in this work show why considerable care is critical when designing and building a high-performance detection system. Steps both early and late in the process can have dramatics impact in the final system.

ACKNOWLEDGEMENTS

We would like to thank A. Gleyzer for valuable information gleaned through personal communication.

REFERENCES

Booth, T. E., F. B. Brown, J. S. Bull, R. A. Forster, J. T. Goorley, H. G. Hughes, R. D. Mosteller, R. E. Prael, A. Sood, J. E. Sweezy, A. Zukaitis, M. Boggs, and R. Martz (2003). A transport process approach to understanding Monte Carlo transport methods, Los Alamos National Laboratory document LA-UR-03-1987 (Revised 10/3/05).

Bowyer, T. W., J. I. McIntyre, and P. Reeder (1999). High sensitivity detection of Xe isotopes via beta-gamma coincidence counting, in *Proceedings of the 21st Seismic Research Symposium: Technologies for Monitoring the Comprehensive Nuclear-Test-Ban Treaty*, LA-UR-99-4700, Vol. 2, pp. 231–241.

Brown, F.B., J. E. Sweezy, and R. Hayes (2004). Monte Carlo parameter studies and uncertainty analyses with MCNP5, LA-UR-04-0499, http://mcnp-green.lanl.gov/pdf/LA-UR-04-04991.pdf

Cooper, M. W., J. I. McIntyre, T. W. Bowyer, A. J. Carman, J. C. Hayes, T. R. Heimbigner, C. W. Hubbard, L. Lidey, K. E. Litke, S. J. Morris, M. D. Ripplinger, R. Suarez and R. Thompson (2007). Redesigned Beta-Gamma Radio-Xenon Detector, *Nucl. Instr. & Meth. A* 579: 426–430.

Cooper M. W., J. C. Hayes, T. R. Heimbigner, C. W. Hubbard, J. I. McIntyre, MD Ripplinger, and B.T. Schrom (2007). Automated QA/QC checks for β-γ coincidence detector, in *Proceedings of the 29th Monitoring Research Review: Ground-Based Nuclear Explosion Monitoring Technologies,* LA-UR-07-5613, Vol. 2, pp. 739–746.

Hayes J. C, K. H. Abel, T. W Bowyer, T. R Heimbigner, M. E. Panisko, P. L. Reeder, J. I. McIntyre, R. C. Thompson, L. C. Todd, and R. A Warner (1999). Operations of the automated radioxenon sampler/analyzer—ARSA, Chapter 6. Radionuclide Monitoring in *Proceedings of the 21st Seismic Research Symposium: Technologies for Monitoring the Comprehensive Nuclear-Test-Ban Treaty,* LA-UR-99-4700 Vol. 1, pp. 249–260.

Keillor, M. E., M. W. Cooper, J. C. Hayes, and J. I. McIntyre (2008). Degradation of 81 keV ^{133}Xe Gamma-Rays into the 31 keV X-Ray Peak in CsI Scintillators. *J. Radioanal. Nucl. Chem*., doi 10.1007/s10967-009-0244-y.

Reeder, P.L., T.W. Bowyer, J.I. McIntyre, W.K. Pitts, A. Ringborn and C. Johansson (2004). Gain Calibration of a Beta/Gamma Coincidence Spectrometer for Automated Radioxenon Analysis, *Nucl. Instr. & Meth A*, 521: 586–599.

CHARACTERIZATION OF TRIPLE-LAYER PHOSWICH DETECTOR FOR RADIOXENON MEASUREMENTS

Abi T. Farsoni and David M. Hamby

Oregon State University

Sponsored by the National Nuclear Security Administration

Contract No. DE-FC52-06NA27322
Proposal No. BAA06-36

ABSTRACT

Monitoring the atmosphere for xenon radioisotopes is one of the routines used to confirm a nuclear weapons test. The International Monitoring System (IMS) has been established to install and employ radioxenon detectors in various locations to verify nuclear weapons tests around the world. A beta/gamma coincidence spectroscopy technique has been shown to be the best measurement solution for monitoring ultra-low concentrations of radioxenons. The majority of radioxenon detection systems, such as the Automated Radioxenon Sampler and Analyzer (ARSA), use separate detectors to capture beta/gamma coincident events. In the ARSA detector, to detect one beta/gamma coincidence event, anode signals from six photomultiplier tubes must be collected and analyzed. Additionally, to reduce the memory effect, four identical gas cells are employed on a rotational basis to provide continuous monitoring. This therefore involves 12 photomultiplier tubes (PMTs) in one detection unit, making it a complex system that is difficult to calibrate. To simplify the coincidence detection setup, a phoswich detector can be used in which beta/gamma coincidence events are detected using one single photomultiplier tube.

We have developed a phoswich detector with three scintillation layers. The first layer is a thin plastic scintillator to detect beta and conversion electrons. The second layer is a CaF_2 scintillator which is intended for x-ray (30 keV) detection. And, a NaI(Tl) scintillator is used as the third layer for gamma ray detection. Coincident events are discriminated from single events, including background radiations, using digital pulse shape analysis. In this paper we discuss several characteristics of our system, including: (1) background measurements, (2) energy resolution, (3) the ability of our innovative digital pulse shape processing technique in discriminating beta-only, gamma-only and gamma-beta coincidence events, (4) energy calibration procedure and (5) results from our recent measurements with commercially available ^{133}Xe.

OBJECTIVE

A major element of the IMS network is monitoring xenon radioisotope releases from nuclear explosions. To detect ultra-low radioxenon, several detection systems, such as ARSA and SAUNA, have been developed and are currently under test. These systems detect radioactive xenon by employing separate detectors to measure beta-gamma coincidence events in their gas cell, facilitating background rejection. The beta-gamma coincidence technique makes these systems very sensitive to the four xenon radioisotopes ^{131m}Xe, ^{133m}Xe, ^{133}Xe and ^{135}Xe (McIntyre et al., 2001 and 2006). Using this technique, a 2D beta-gamma spectrum is updated only when the beta and gamma detectors are triggered within a predetermined time. Because of employing 12 PMTs in the ARSA system, such a complex system can easily become out-of-calibration after a long counting run.

Phoswich detectors have recently been considered as an alternative to simplify radioxenon detection (Ely et al., 2003; Hennig et al., 2005; Farsoni et al., 2008). In a phoswich detector, two or more scintillation layers are coupled to a single PMT. The energy deposition in each layer from incident beta and/or gamma, in coincidence or singles, is then determined via digital pulse shape analysis of the PMT's anode pulses.

A two-channel phoswich detector has been designed specifically for radioxenon detection (Farsoni et al., 2007). The detector consists of a thin hollow disk (2 mm thickness and 76.2 mm diameter) as the xenon gas cell, surrounded by two identical planar triple-layer phoswich detectors. In designing the detector, several priorities have been considered, including improving the 30-keV x-ray/(CE + beta) coincidence region, increasing the system sensitivity by employing both dual and triple coincidence counting, improving light collecting uniformity, and decreasing the overall cost by simplifying the detector design. To digitally capture the PMT's anode pulses from the two phoswich detectors, a two-channel high-performance digital pulse processor (250 MSPS, 12 bits per channel) was designed and constructed. We also developed a graphical user interface (GUI) for controlling the digital processor, detecting coincidence events and reconstructing 2D coincidence beta/gamma spectra (Farsoni et al., 2008).

A prototype and full-scale triple-layer phoswich detector has been constructed to characterize one half of the final detection system. In this paper we discuss several characteristics of our system, including (1) background measurements, (2) energy resolution, (3) the ability of our innovative, digital, pulse-shape-processing technique to discriminate between beta-only, gamma-only and gamma-beta coincidence events, (4) energy calibration procedure, and (5) results from our recent measurements with commercially available ^{133}Xe.

RESEARCH ACCOMPLISHED

Prototype Phoswich Detector

A prototype phoswich detector with three scintillation layers has been constructed (Figure 1). The first layer is a thin plastic scintillator (1.5 mm) to detect beta and conversion electrons. The thickness of BC-400 is sufficient to absorb the vast majority of beta/CE particles emitted from radioxenons. The second layer is a CaF_2 scintillator (2.0 mm), which is intended for x-ray (30 keV) detection. The third layer is a NaI(Tl) scintillator (25.4 mm) to detect high-energy gamma-rays. Since the NaI(Tl) is highly hygroscopic, this layer is isolated from other scintillators using a 6.35-mm quartz optical window.

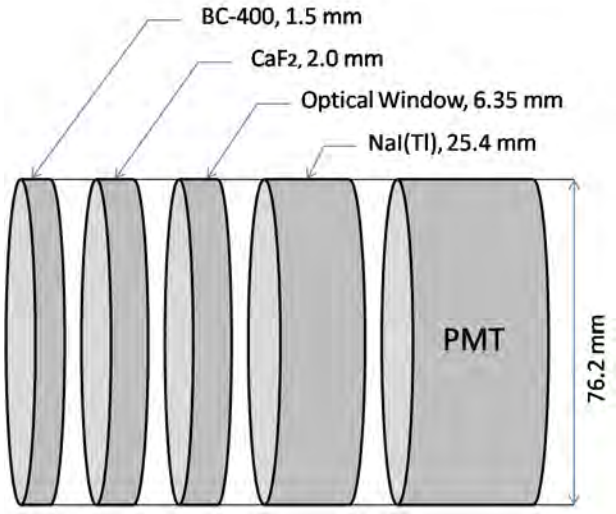

Figure 1. Schematic diagram of the prototype triple-layer phoswich detector.

Event Discrimination and Energy Measurement

Coincident events are discriminated from single events, including background radiations, using digital pulse shape analysis. Depending on how the incident radiation releases its energy within each layer of the phoswich detector, seven possible pulse shapes or types could be generated at the PMT's anode output. Using three digital triangular filters (Farsoni at al., 2008), the integration or sum of three areas (A, B, and C in Figure 2) of the anode pulse is calculated. These sums are used for pulse shape discrimination and energy measurement purposes.

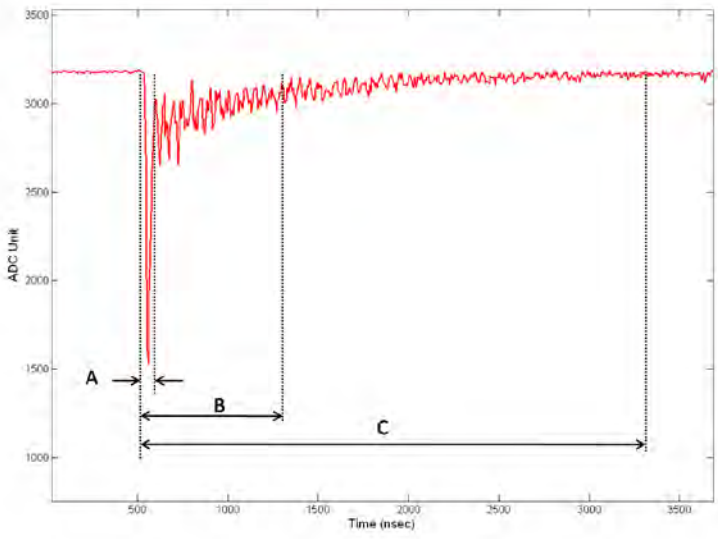

Figure 2. A typical phoswich pulse when a coincidence event has occurred in the detector. Three filter sums (A, B, and C) are used to discriminate different events and measure the energy released in each phoswich layer.

Using these sums, two ratios—fast component ratio (FCR) and slow component ratio (SCR)—are calculated from each captured pulse to discriminate different pulse shapes. The FCR and SCR range from zero to unity.

Figure 3 shows a 2D scatter plot of the FCR and SCR when the phoswich detector is exposed to a ^{137}Cs source. During this experiment, the ^{137}Cs source was shielded against beta and conversion electrons. Regions 1, 2 and 4 represent single events in plastic (BC-400), CaF_2 and NaI layers, respectively. Regions 3 and 5 show coincidence events of CaF_2-plastic and NaI-plastic, respectively. Regions 6 and 7 accommodate either Compton scattering events between NaI and CaF_2 or unknown events. Events in these regions have no useful information for our application and thus are rejected.

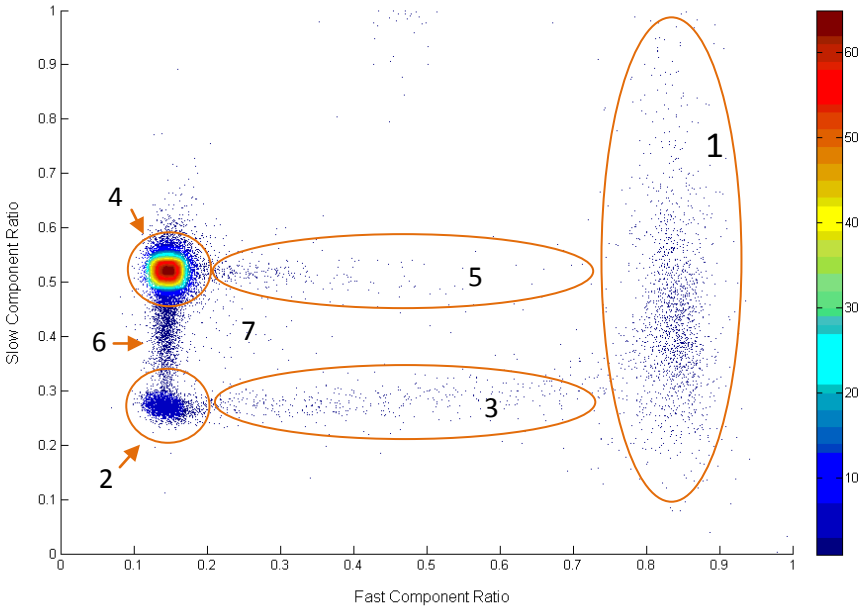

Figure 3. Scatter of fast and slow component ratios from ^{137}Cs. Seven marked regions correspond to seven pulse shapes, indicating how gamma rays interact with the three layers of phoswich detector.

Ideally, beta-only events from the plastic scintillator (Region 1) should be populated in a vertical distribution with an average FCR close to unity. Region 1 in Figure 3 has an average FCR of 0.84. To investigate possible reasons, beta-only events in Region 1 were carefully examined. Events in this region, as depicted in Figure 4, show a significant "ringing effect" following the fast decaying component of the plastic scintillator. The same results were observed from a pure beta emitter. We believe that this effect is responsible for underestimating the FCR of beta-only events in Region 1. This effect is also observed with coincidence events when a fast decaying component is followed by a slow component (Figure 2). A moving average filter was used to check the net response of this effect (blue waveform in magnified portion of Figure 4). The response of this filter shows a nonzero area under the baseline. Obviously, this introduces errors in both pulse-shape analysis and energy measurement. We found a linear relationship between the sum A and the net area due to a ringing effect under sums B and C when a fast pulse from the plastic scintillator appears at the anode output. From this analysis, two correction factors were obtained and applied to all pulse processing and energy calculations in this paper. The detector manufacturer confirmed that the detector's PMT (9305KFLB) has a low-quality voltage divider and that it is responsible for this effect. Two other phoswich detectors with high-quality PMTs have been ordered and will be characterized in the near future.

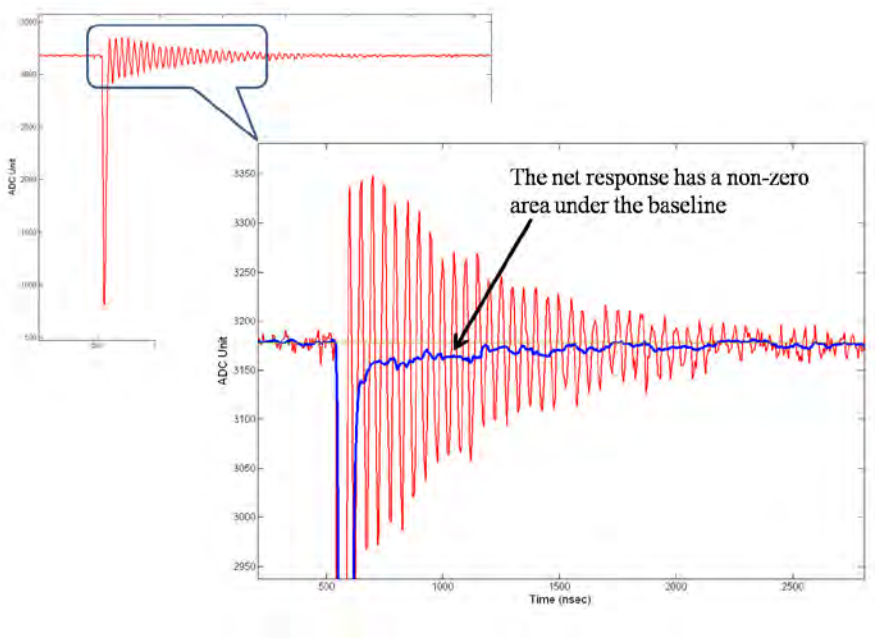

Figure 4. A fast pulse (after radiation absorption in plastic scintillator) is followed by a ringing effect. In the magnified portion, a moving average filter was used (blue waveform) to examine the average baseline level after the fast scintillation pulse.

Phoswich Detector Characterization

Background measurement

To measure the background count rate and investigate the system capability to discriminate different events, the phoswich detector was placed in a lead enclosure with a wall thickness of 2 in. The total background count rate from all events is 4.91 cps, of which 0.02 cps and 0.08 cps are coincidence events in NaI-plastic (Region 5) and CaF_2-plastic (Region 3), respectively. The total background count rate of the ARSA detector is ~30 cps, of which 0.1 cps is coincidence. The fraction of coincidence events in NaI-plastic is low (0.44%) but it is relatively high (1.72%) in CaF_2-plastic. We suspect that the ringing effect, mentioned before, mischaracterizes some events in the coincidence regions of 3 and 5, shown in Figure 3.

Energy calibration and resolution measurements

A ^{137}Cs source was used to calibrate three layers of the phoswich detector. Figure 5 depicts the 2D energy histogram from ^{137}Cs. Figure 5, left, shows the 2D energy histogram for the plastic (Ep) and CaF_2 (Ec) scintillators, whereas Figure 5, right, shows that of the plastic (Ep) and NaI (En) scintillators. Again, Regions 3 and 5 were used to reconstruct these histograms, respectively. In this measurement, the ^{137}Cs source was shielded against beta and conversion electrons to capture only gamma interactions with the phoswich layers. Since there is no beta coincidence with gamma rays, the 2D coincidence histograms shows only Compton scattering between layers. When a 662-keV gamma ray is scattered from one scintillator and is absorbed in the other scintillator, the total energy deposition should be equal to the original energy (662 keV). This forms a line of constant energy in the 2D histogram. Therefore, the intersections of black dashed lines with the corresponding energy axis in Figure 5, left, and Figure 5, right, were used to calibrate each layer.

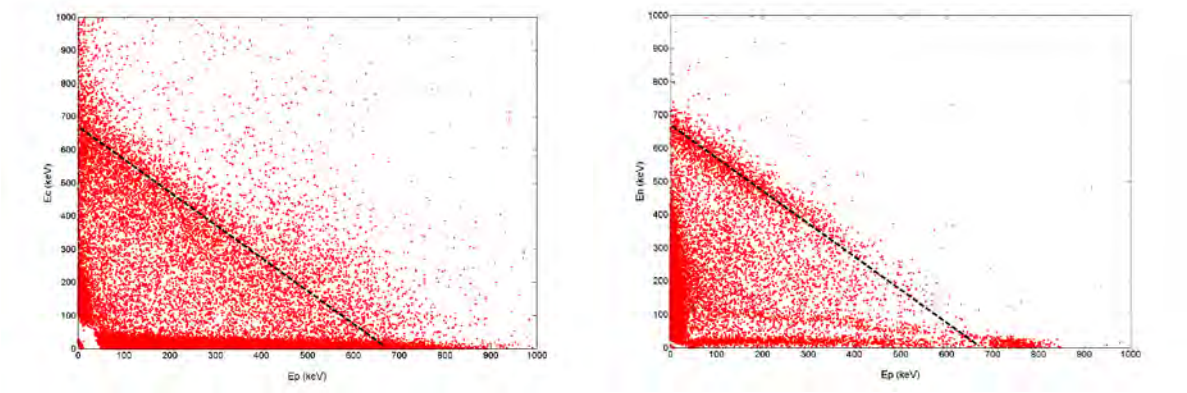

Figure 5. Two-dimensional energy histograms from a ^{137}Cs source. The one on the left is the 2D energy histogram for the plastic (Ep) and CaF_2 (Ec) scintillators, whereas the one on the right is that of the plastic (Ep) and NaI (En) scintillators.

Single events in Regions 2 and 4 of Figure 3 were used to reconstruct the NaI (blue) and CaF_2 (red) energy spectra (Figure 6). The NaI histogram shows all features of a healthy and typical spectrum from ^{137}Cs. Characteristic x-rays from ^{137m}Ba (30 keV) and lead shield (75 keV), backscatter peak, Compton edge and 662-keV photopeak are pronounced in the NaI spectrum. Because of a high-threshold setup for this experiment, only Compton scattering events can be seen in the CaF_2 spectrum. The measured resolution—full width by half maximum (FWHM)—for 662 keV of ^{137}Cs was 7.9%. The ARSA system has a resolution of 12% for 662-keV gamma rays (Reeder et al., 2004). NaI-only and CaF_2-only events have a fraction of 87.1% and 5.2% from all events, respectively. The fraction of coincidence events between these layers and plastic scintillator were 0.3% and 0.83%, respectively.

Two lab sources (^{109}Cd and ^{57}Co) were used to measure the energy resolution (FWHM) of 22-keV, 88-keV, and 122-keV x-rays and gamma rays. The energy resolution of 22 keV is 36%, which was measured from events in Region 2. Using the Region 4 in Figure 3, the energy resolution of 88 keV and 122 keV was 17% and 13.9%, respectively. The ARSA system has a resolution of 22% for 122-keV gamma rays (Reeder et al., 2004).

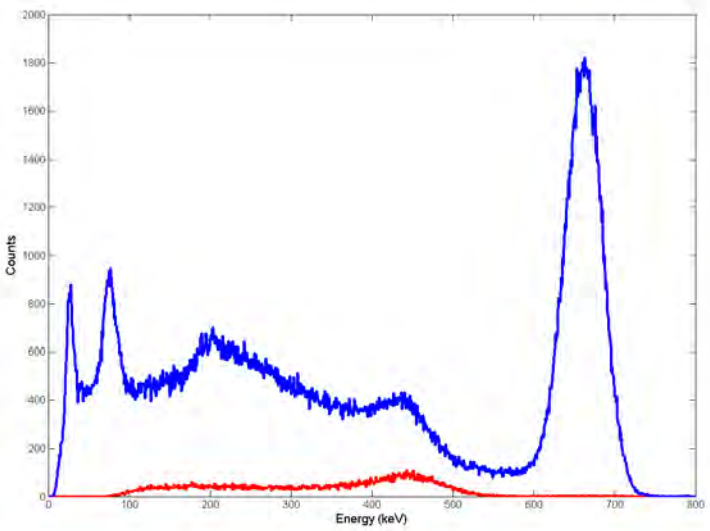

Figure 6. The ^{137}Cs spectra in NaI (blue) and CaF_2 (red), which were collected from events in Figure 3's Regions 4 and 2, respectively.

Radioxenon measurements

Commercially available ^{133}Xe gas was used to evaluate the capabilities of the phoswich detector and our digital pulse shape discrimination technique in radioxenon monitoring. Figure 7 shows 2D energy spectra from ^{133}Xe processed from Regions 3 and 5 of Figure 3, respectively. In both Figures, beta-gamma coincidence lines of 30-keV x-rays and 80-keV gamma rays from ^{133}Xe can be identified. As expected, the 30-keV x-rays are more pronounced in the CaF_2 coincidence spectrum, whereas the NaI coincidence spectrum shows higher efficiency for detection of the 80-keV gamma rays.

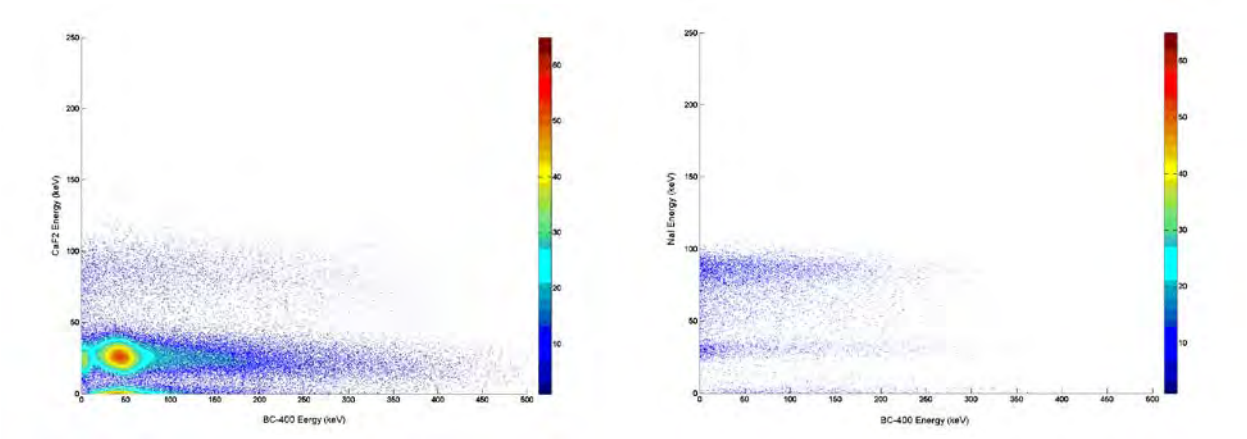

(a) (b)

Figure 7. Two-dimensional beta-gamma coincidence energy histograms from ^{133}Xe. As expected, the 30 keV x-rays are more pronounced in the CaF_2 coincidence energy spectrum (left), whereas the NaI coincidence spectrum (right) shows higher efficiency for detection of the 80 keV gamma rays.

Figure 8 shows energy histograms from the CaF_2 scintillator when the phoswich detector was exposed to ^{133}Xe. The red spectrum is reconstructed from events in Figure 3's Region 2 (CaF_2-only events). The blue spectrum is also from the CaF_2 layer, but when it is in coincidence with an event in the plastic scintillator (Region 3). The 30 keV and 80 keV peaks from ^{133}Xe can be seen in this figure. The energy resolution of 30 keV from the plastic-CaF_2 coincidence histogram was measured to be 43%. This value for ARSA detector (in NaI) is 32%. If we define the beta-gamma coincidence efficiency as the number of net coincidence counts in a region of interest (peak), divided by the number of all counts in that region (Hennig et al., 2007), the histograms in Figure 8 show a coincidence efficiency of 98.8% for detecting beta-gamma coincidence events in the 30-keV x-ray region of ^{133}Xe.

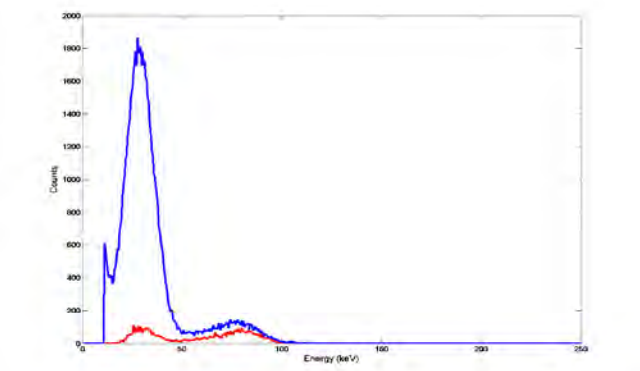

Figure 8. CaF_2 energy spectra from ^{133}Xe. Red and blue spectra were processed from events in Figure 3's Region 2 (CaF_2-only events) and Region 3 (BC400-CaF_2 coincidence events), respectively.

In Figure 9, energy histograms of the ^{133}Xe from the NaI(Tl) scintillator are shown. The red spectrum is reconstructed from events in Region 4 (NaI-only events) of Figure 3. The blue spectrum is also from NaI layer, but when it is in coincidence with events in the plastic scintillator (Region 5). Both 30-keV and 80-keV peaks from ^{133}Xe can be seen here with a higher efficiency for 80-keV gamma rays. The energy resolution of 80 keV from the plastic-NaI coincidence spectrum was measured to be 18%. The coincidence efficiency, as defined before, is 48.5% for detecting beta-gamma coincidence events in 80-keV gamma ray region of ^{133}Xe.

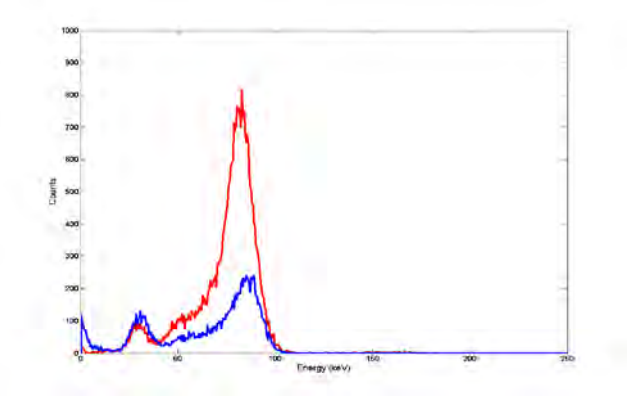

Figure 9. NaI(Tl) energy histograms from ^{133}Xe. Red and blue spectra were processed from events in Figrue 3's Region 4 (NaI-only events) and Region 5 (BC400-NaI coincidence events), respectively.

Beta energy histograms gated with two regions of interest in the gamma energy spectrum of ^{133}Xe, 30 keV and 80 keV, are shown in Figure 10. The blue histogram is processed from events in Region 3 (plastic-CaF_2 coincidence events) when a beta event from the plastic in coincidence with 30-keV x-ray from the CaF2 is detected. The 30-keV gated beta histogram shows a peak at 45 keV. This peak represents conversion electrons emitted in coincidence with 30-keV x-rays from ^{133}Xe. The energy resolution of this peak was measured to be 46%. This value was 50% in the ARSA system (Reeder et al., 2004). The red energy histogram in Figure 10 is reconstructed from events in Region 5 of Figure 3 (plastic-NaI coincidence events) when a beta event from the plastic is in coincidence with an 80-keV gamma ray from the NaI. The 80-keV gated beta energy histogram shows a beta continuum with no peak, as expected. Because of the possibility for triple-coincidence events in the 30-keV x-ray line from ^{133}Xe, where a beta particle and a 45-keV conversion electron can be coincidently deposited in the plastic scintillator, the endpoint of the 30-keV gated beta histogram (blue) is extended into higher energies (~400 keV).

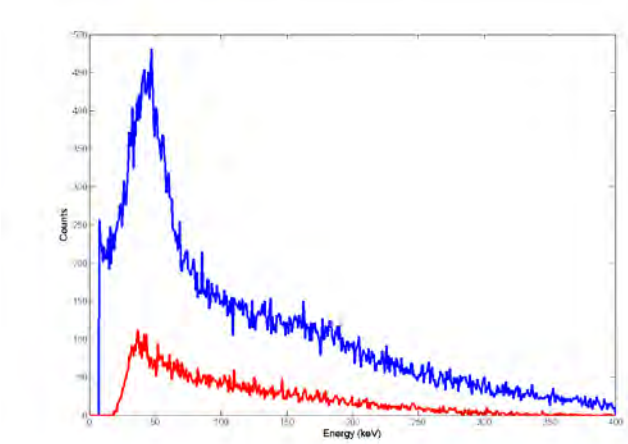

Figure 10. Beta energy histograms in plastic scintillator gated with (blue) 30-keV x-rays in CaF_2 and (red) 80-keV gamma ray in NaI. The 30-keV gated beta histogram shows a peak at 45 keV. This peak represents conversion electrons emitted in coincidence with 30-keV x-rays from ^{133}Xe.

As discussed earlier, the key characteristics of the current prototype phoswich detector and its digital pulse shape discrimination technique suffers from a ringing effect due to its low-quality PMT. Two new phoswich detectors with high performance PMTs are presently being constructed and will be characterized for radioxenon measurement in the near future.

CONCLUSION

We have characterized a triple-layer phoswich detector using radioactive lab sources and ^{133}Xe. The results provided in this paper demonstrate the ability of our innovative digital pulse shape processing technique to discriminate between beta-only, gamma-only, and gamma-beta coincidence events from a triple-layer phoswich detector. The phoswich detector shows a much lower background count rate than the ARSA detection system (4.91 cps vs. 30 cps). Compared with the ARSA system, in most gamma energy lines, we measured a better energy resolution. The energy resolution of the conversion electron peak at 45 keV from ^{133}Xe was measured to be 46%. This energy resolution is 50% in the ARSA system. Our measurements with this prototype phoswich detector show a coincidence efficiency of 98.8% and 48.5% for detecting beta-gamma coincidence events at 30-keV and 80-keV gamma lines of ^{133}Xe, respectively. Due to a low-quality PMT, a ringing effect appears following fast pulses from the plastic scintillator. This introduces errors in both pulse shape analysis and energy measurement. Although correction factors were applied to eliminate or reduce this effect, we believe that the overall performance of the phoswich detector and our digital pulse shape discrimination technique will be improved with a better PMT. Two new phoswich detectors with high-quality PMTs have been ordered and will be characterized for radioxenon measurement in the near future. These two detectors will form a two-channel phoswich detection system to detect and measure dual- and triple-coincidence events from xenon radioisotopes.

REFERENCES

Ely, J. H., C. E. Aalseth, J. C. Hayes, T. R. Heimbigner, J. I. McIntyre, H. S. Miley, M. E. Panisko, and M. Ripplinger (2003). Novel Beta-gamma coincidence measurements using phoswich detectors, in *Proceedings of the 25th Seismic Research Review – Nuclear Explosion Monitoring: Building the Knowledge Base*, LA-UR-03-6029, Vol. 2, pp. 533–541.

Farsoni, A. T., D. M. Hamby, K. D. Ropon, and S. E. Jones (2007). A two-channel phoswich detector for dual and triple coincidence measurements of radioxenon isotopes, in *Proceedings of the 29th Seismic Research Review: Ground-Based Nuclear Explosion Monitoring Technologies*, LA-UR-07-5613, Vol. 2, pp. 747–756.

Farsoni, A. T., D. M. Hamby, C. S. Lee, and A. J. Elliott (2008). Preliminary experiments with a triple-layer phoswich detector for radioxenon detection, in *Proceedings of the 30th Monitoring Research Review: Ground-Based Nuclear Explosion Monitoring Technologies*, LA-UR-08-05261, Vol. 2, pp. 739–748.

Hennig, W., H. Tan, W. K. Warburton, and J. I. McIntyre (2005). Digital pulse shape analysis with phoswich detectors to simplify coincidence measurements of radioactive xenon, in *Proceedings of the 27th Seismic Research Review: Ground-Based Nuclear Explosion Monitoring Technologies,* LA-UR-05-6407, Vol. 2, pp. 787–794.

Hennig, W., H. Tan, W. K. Warburton, A. Fallu-Labruyere, K. Sabourov, J. I. McIntyre, M. W. Cooper, and A. Gleyzer (2007). Characterization of phoswich well detectors for radioxenon monitoring, in *Proceedings of the 29th Monitoring Research Review: Nuclear Explosion Monitoring Technologies,* LA-UR-07-5613, Vol. 2, pp. 757–763.

McIntyre, J. I., K. H. Able, T. W. Bowyer, J. C. Hayes, T. R. Heimbigner, M. E. Panisko, P. L. Reeder, and R. C. Thompson (2001). Measurements of ambient radioxenon levels using the automated radioxenon sampler/analyzer (ARSA), *J. Radioanal. Nucl. Chem*. 248: 629–635.

McIntyre, J. I., T. W. Bowyer, and P. L. Reeder (March 2006). Calculation of minimum detectable concentration levels of radioxenon isotopes using the PNLL ARSA system, technical report, PNNL-13102.

Reeder, P. L., T. W. Bowyer, J. I. McIntyre, W. K. Pitts, A. Ringbom, and C. Johansson (2004). Gain calibration of coincidence spectrometer for automated radioxenon analysis, *Nucl. Instru. Methods Phys. Res., Sect. A* 521: 586–599.

RADIOXENON MEASUREMENTS WITH THE PHOSWATCH DETECTOR SYSTEM

Wolfgang Hennig[1], William K. Warburton[1], Anthony Fallu-Labruyere[1], Konstantin Sabourov[1], Matthew W. Cooper[2], Justin I. McIntyre[2], Anshel Gleyzer[3], Marc Bean[4], Ed P. Korpach[4], Kurt Ungar[4], Weihua Zhang[4], Pawel Mekarski[4], Rebecca M.Ward[5], Steven R. F. Biegalski[5], Derek A. Haas[2,5]

XIA LLC[1], Pacific Northwest National Laboratory[2], PhotoPeak, Inc[3], Radiation Protection Bureau, Health Canada[4], the University of Texas at Austin[5]

Sponsored by the National Nuclear Security Administration

Award No. DE-FG02-04ER84121

ABSTRACT

Many of the radioxenon detector systems used in the International Monitoring System (IMS)and in other applications employ beta/gamma coincidence detection to achieve high sensitivity. In these systems, the coincidence detection is implemented by requiring simultaneous signals from separate beta and gamma detectors. While very sensitive to small amounts of radioxenon, this approach requires careful calibration and gain matching of several detectors and photomultiplier tubes. An alternative approach is the use of a phoswich detector in which beta-gamma coincidences are detected by pulse shape analysis. The phoswich requires only a single photomultiplier tube and thus is easier to set up and calibrate, and can be assembled into a more compact and robust system.

In the past, we developed a COTS detector system, named PhosWatch, which consists of a CsI(Tl)/BC-404 phoswich detector, digital readout electronics, and on-board software to perform the pulse shape analysis. Several units of this system have now been manufactured and are currently being evaluated at several radioxenon research laboratories. In this paper, we will report results from production tests and some of the evaluations, including a side-by-side comparison of a SAUNA detector and a PhosWatch system using atmospheric radioxenon samples and a comparison of an ARSA-type detector and a PhosWatch system with samples made by irradiating stable xenon isotopes. In addition, we will show initial results obtained with a higher speed version of the readout electronics, digitizing at 500 MHz and thus able to better resolve the BC-404's fast pulses.

OBJECTIVES

The amount of radioactive xenon in the atmosphere is measured in several stations of the IMS established by the Comprehensive Nuclear-Test-Ban Treaty. Roughly half of these stations use a radioxenon detection system that employs beta/gamma detection, the Swedish Automatic Unit for Noble gas Acquisition (SAUNA; Ringbom et al., 2003); most of the other half use a high resolution gamma detection system with a germanium detector, the French SPALAX unit (Fontaine et al.,2004). In addition, several radioxenon research laboratories use the Automated Radioxenon Sampler and Analyzer (ARSA) or a beta/gamma well detector (BGW), both developed at Pacific Northwest National Laboratory (PNNL) (Reeder et al., 1998; Cooper, 2007a). The ARSA, SAUNA, and BGW all make use of beta/gamma coincidence to suppress background and achieve high sensitivity to the characteristic events from the radioxenon isotopes of interest, which emit beta particles or conversion electrons (CEs) in coincidence with gamma rays or X-rays.

While these systems are very sensitive to small amounts of radioxenon, their complex arrangement of separate beta and gamma detectors also requires careful calibration and gain matching, which can make them cumbersome to operate. An alternative approach is the use of a single phoswich detector (Ely, 2003; Hennig et al., 2006b; Farsoni et al., 2007) in which beta/gamma coincidences are detected by pulse shape analysis (PSA). We previously reported the development of a commercial off-the-shelf (COTS) radioxenon detector system consisting of a phoswich detector, readout electronics, and PSA software, named the PhosWatch (Hennig et al., 2008). The phoswich detector consists of a fast plastic scintillator cell containing the Xe gas and mainly absorbing beta particles and CEs, optically coupled to, and surrounded by, a slower CsI(Tl) scintillator mainly absorbing X-rays and gamma rays. It thus requires only a single photomultiplier tube (PMT) and electronics readout channel. Beta/gamma coincidences create characteristic “fast/slow” signals that can easily be distinguished from “slow only” or “fast only” non-coincident interactions by PSA algorithms implemented in the digital signal processor of the readout electronics, a DGF Pixie-4 module (Hennig et al., 2007b).

Having built a number of PhosWatch systems to commercial production standards, the objective of the work presented in this paper was to test and evaluate their performance in radioxenon monitoring applications, including comparisons to existing systems. All detectors were first tested and characterized at XIA for energy resolution and background. Then three PhosWatch systems were transferred to Health Canada, The University of Austin, and PNNL for evaluation. At Health Canada, the PhosWatch system is operated side by side with a SAUNA system using atmospheric radioxenon samples acquired with a SPALAX system. At The University of Austin, the PhosWatch system is operated in comparison to an ARSA-type system using radioxenon created by irradiating stable xenon isotopes in a local reactor. At PNNL, the PhosWatch system was tested with Xe and Rn samples. Further evaluation is still in progress at all three sites. Below we describe the results of these evaluations and in addition will show initial results obtained with a higher speed version of the readout electronics, digitizing at 500 MHz and thus able to better resolve the fast pulses from the BC-404.

RESEARCH ACCOMPLISHED

Production Tests at XIA

A total of 7 phoswich well detectors were built in a small-scale commercial production run and named PW3a-PW9. They all consist of a 1"-diameter BC-404 plastic cell with 2 mm wall thickness enclosed in, and optically coupled to, a 3" diameter, 3” tall CsI(Tl) cylinder in the geometry of the second prototype PW3 (Hennig et al., 2007a). (PW3a is the prototype PW3 rebuilt with a new PMT and crystal.) The PSA algorithms to separate beta/gamma coincidences from non-coincident interactions and to measure the energy deposited in the CsI (Ec) and in the BC-404 (Ep) have been described previously (Hennig et al, 2006a). Detectors were tested for vacuum tightness and typically leaked less than 1 Torr/h when evacuated to 1 Torr and disconnected from the pump.

Detectors were characterized by measuring resolutions at various energies with a number of test sources. As shown in Figure 2, the photon energy resolutions of PW3a-PW9 at medium to high photon energies are significantly better than resolutions reported for the ARSA detector (Reeder et al., 2004), and the later detectors (PW6-PW9), with improvements in detector assembly and careful selection of PMTs for low noise, reach an average ~7.3% FWHM at 662 keV. These later detectors thus match or exceed the resolutions reported for the BGW detector (Cooper, 2007a) in the preferred CsI(Na) variant and the SAUNA II detector. As summarized in Table 1, for low energy photons (Ec = 30 keV) and for CE from ^{131m}Xe (Ep = 129 keV), the phoswich detectors reach energy resolutions similar to

the other detector systems. Note that count rates and other experimental conditions can not be assumed to be the same for measurements performed at different times and institutions.

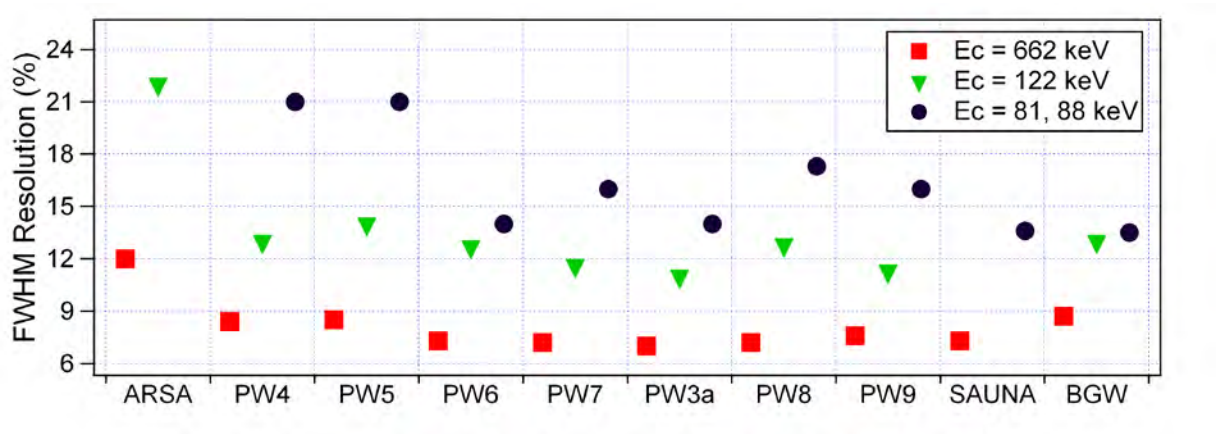

Figure 1. Resolution of photon energies for radioxenon detectors. Phoswich detectors are listed in order of production. The 81 and 88 keV data sets used internal ^{109}Cd and ^{133}Xe sources, respectively; other data sets used ^{137}Cs and ^{57}Co sources outside the detector. Non-phoswich data are from (Reeder, 2004; Cooper, 2007; Ringbom 2007), or measurements at Health Canada.

Table 1. Energy resolutions and background rates for radioxenon detection systems.

Detector system	PhosWatch (typical values)	ARSA (Reeder, 2004; PNNL data)	SAUNA (A. Ringbom, 2007)	BGW (Cooper, 2007a; PNNL data)
Resolution for 662 keV γ-rays	7.3%	12%	7.3%	8.7%
Resolution for 30 keV X-rays	28-35%	32%	23-30%	18%
Resolution for 129 keV CE	26-33%	25-30%	19%	25%
Background in lead enclosure (total)	3-8 counts/s	~30 counts/s (larger crystal)	7.5-12 counts/s	~5.5 counts/s
Background in lead enclosure (coincident)	0.02-0.08 counts/s	~0.1 counts/s	0.03-0.03 counts/s	~0.025 counts/s

In monitoring applications, the samples of radioxenon collected are very small, so the background count rate of the detector has to be as low as possible. In a lead enclosure (2" lead with 0.5" copper lining) we measure an overall rate of 3–8 counts/s for PW4–5 and PW8-9, of which ~0.02–0.08 counts/s are coincidences, and only ~0.002-0.004 counts/s fall in the ^{133}Xe regions of interest (ROIs) at 30 keV and 80 keV. PW6, PW7, and PW3a showed higher background rates (~10 counts/s total, ~0.5 counts/s coincident) due to small amounts of ^{40}K in the PMT and the CsI. This contamination has been eliminated for PW8 and PW9 by careful screening of crystals and PMTs before assembly. All detectors reject over 99% of radiation from an external ^{137}Cs source as non-coincident. Typical background rates for the larger ARSA detector and the similar sized SAUNA and BGW detectors are also listed in Table 1.

Evaluation at Health Canada and PNNL

As part of the evaluation of the PhosWatch system in monitoring application, Xe samples acquired with a SPALAX system were re-measured in parallel with PW5 and a SAUNA system at Health Canada. Figure 2 shows the number of coincidence events detected by PW5 in ROIs at Ec = 80 keV and Ec = 250 keV as a function of ^{133}Xe and ^{135}Xe

activity measured by the SPALAX system. While error bars must be assumed to be 10% or more due to uncertainties in the sample transfer, disregard of other isotopes, and simplifications in the correction for decay between measurements, the data shows a good linear correlation, indicating that PW5 results are consistent with the SPALAX results.

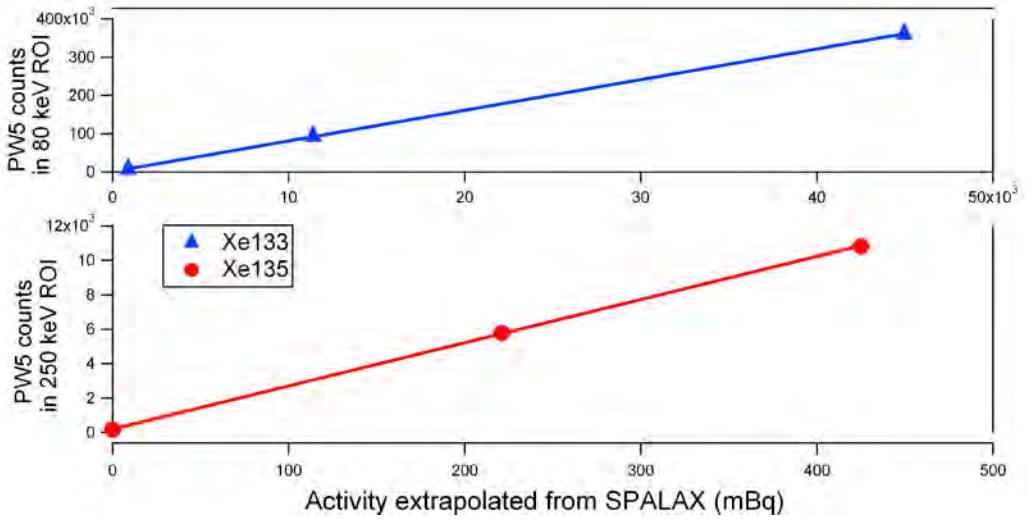

Figure 2. Counts in PW5 regions of interest vs. nominal activity from SPALAX measurement for several samples from a Canadian monitoring station.

Figures 3 and 4 show 2D and 1D energy spectra for a SPALAX sample divided between PW5 and a SAUNA detector. At the low photon energies of this sample, peak resolution is better for this SAUNA than for PW5 (the latter being one of our earlier phoswich detectors) but since the quantitative analysis only uses the number of counts in a ROI and peaks are well separated, the difference is not critical. In this and other measurements, we also observe that the background in PW5 is lower, and that the "memory effect" from Xe retained in the plastic from previous samples is about equal in this SAUNA and in PW5.

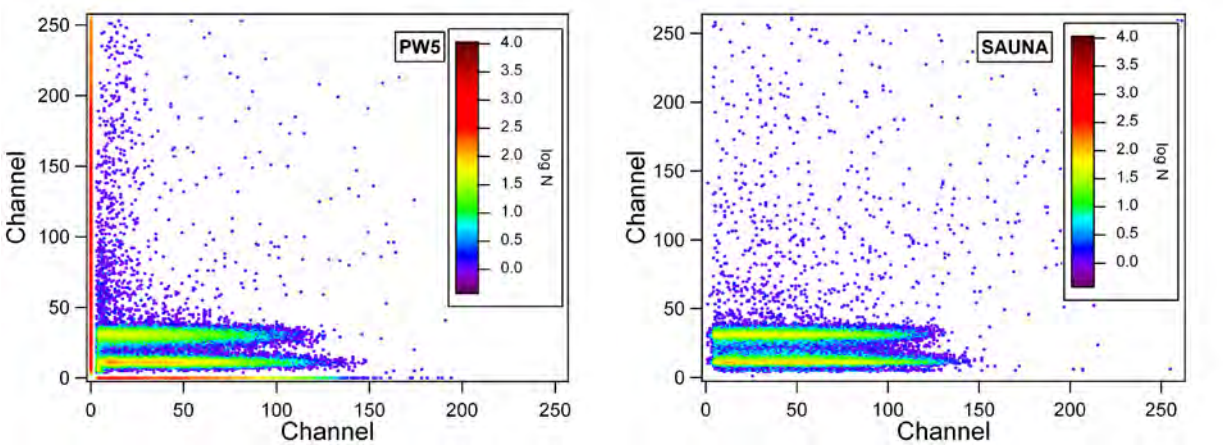

Figure 3. 2D histograms from a SPALAX sample split between PW5 (left) and SAUNA (right).

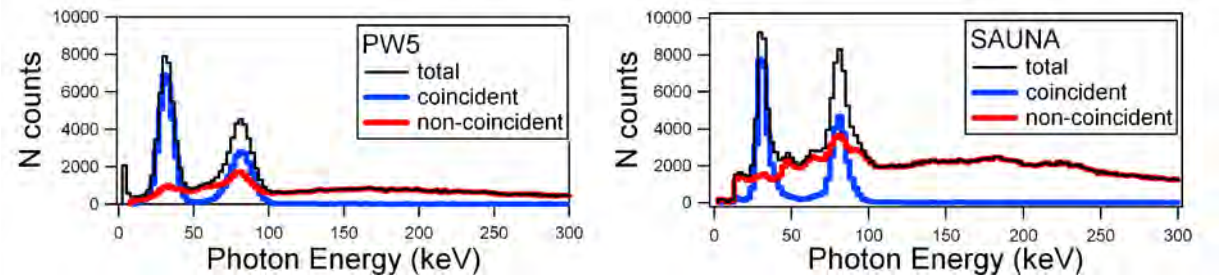

Figure 4. 1D spectra of photon energy for PW5 and SAUNA (data from Figure 3 projected to vertical axis).

To obtain a basis for quantitative analysis of PhosWatch spectra, the detector geometry was modeled with a Geant4 simulation, both for radiation processes and optical processes. We assumed the BC-404 cell to be filled with 15% xenon and 85% nitrogen, and used the following input parameters (besides literature constants): an outer reflectivity of 0.95, PMT quantum efficiency 30%, photocathode reflectivity 17%, signal risetimes (after a low pass Nyquist filter in the electronics) 100 ns for CsI, 13 ns for BC 404, and a coincidence time window for the PSA of 100 ns. We then compute the coincidence detection efficiency for each ROI as

$$\varepsilon_{\beta\gamma_ROI} = \frac{C_{ROI}}{C_A \times BR_{ROI}} \qquad (1)$$

where C_{ROI} and C_A are the number of counts in the ROI and in total, respectively, and BR_{ROI} is the beta-gamma branching ratio for the ROI. To verify the simulation, we used the data in Figure 3 and a preceding background measurement to compute $\varepsilon_{\beta\gamma_133Xe_30}$ and $\varepsilon_{\beta\gamma_133Xe_80}$ from the product of gamma and beta efficiency, which are obtained from the ratios of coincident counts (in the ROI) and singles counts (projection of coincident and non-coincident events to beta or gamma axis). As shown in Figure 5, the simulated $\varepsilon_{\beta\gamma_ROI}$ (x marks) agree well with the $\varepsilon_{\beta\gamma_ROI}$ estimated from the data (solid circles). Also shown are $\varepsilon_{\beta\gamma_ROI}$ given by the manufacturer for the SAUNA system at Health Canada (solid triangles) and phoswich $\varepsilon_{\beta\gamma_ROI}$ derived from Xe and Rn measurements at PNNL (open symbols), using 98% detection efficiency for conversion electrons from ^{131m}Xe as the starting point for the method described in (Cooper, 2007b). Note that again experimental conditions and especially ROI boundaries may vary. In particular, in PNNL measurements, the Rn count rate was very low and backgrounds were high, leading to large uncertainties in the computed efficiency, which may explain the difference from the simulation. The most directly comparable efficiency between the different systems and methods may thus be $\varepsilon_{\beta\gamma_131mXe}$, because with the clearly defined peak well away from the axes, the effects of ROI boundaries are minimal. This value is 79.8% from simulations, 81% from the PNNL measurements, and 57% for this SAUNA. Overall, we see that $\varepsilon_{\beta\gamma_ROI}$ is significantly higher for PW5 than for this SAUNA, especially at low energy. One reason for the higher efficiency in the phoswich is that detection of low-energy X-rays is enhanced if they are in coincidence with a beta particle since the latter creates a large pulse in the PMT that is easy to trigger on.

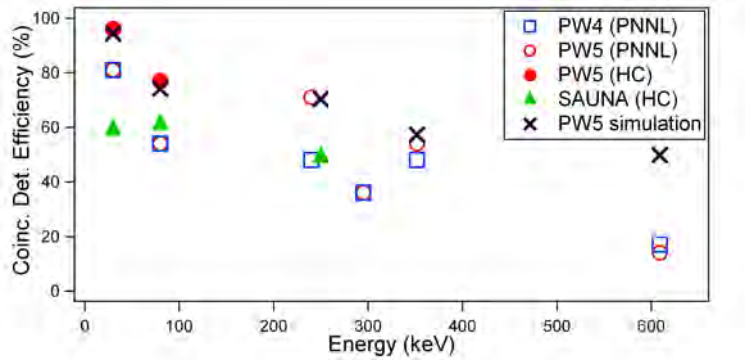

Figure 5. Coincidence detection efficiency of PW4, PW5 and a SAUNA detector installed at Health Canada. Values at 30 and 80 keV are from ^{133}Xe, not ^{131m}Xe or ^{222}Rn.

Using the simulated $\varepsilon_{\beta\gamma_ROI}$ and a preceding background measurement for quantitative analysis of the PW5 data shown in Figure 5, we compute the concentrations of radioxenon isotopes shown in Table 2 (sample 1). We found 127 mBq/m^3 of ^{133}Xe in the sample at the time of the SPALAX measurement; concentrations for other isotopes were below 20 mBq/m^3. Computing the PW5 ^{133}Xe concentration separately for 6 ROIs that contain ^{133}Xe contributions showed variations from 122-129 mBq/m^3, indicating very good consistency within the PW5 measurement itself. The minimum detectable concentration (MDC) for this data is 0.5 mBq/m^3. Analysis of the SAUNA data taken in parallel to the PW5 measurement computed a ^{133}Xe concentration of 155 mBq/m^3 with an MDC of 0.2 mBq/m^3, and ROI variations from 145-168 mBq/m^3. The original SPALAX analysis measured a concentration of 194 mBq/m^3. (It has no comparable ROIs since it is not a beta/gamma coincidence system). In a second data set (sample 2), PW5 measured a ^{133}Xe concentration of 1274 mBq/m^3, the SAUNA measured 1486 mBq/m^3, and the SPALAX system measured 1873 mBq/m^3. We note that in both data sets, PW5 and SAUNA consistently measure ~65% and ~80% of the SPALAX values, respectively, and attribute this to the loss of sample volume during transfer and/or in the dead volume of the gas connections.

The MDC is derived from the standard deviation of background counts and interference between the ROIs in a particular measurement (Axelson, 2003) as the smallest activity detectable above background (at a 95% confidence level). By definition, it also depends on non-statistical factors such as the volume of air collected and the time since collection. The IMS requirement for ^{133}Xe is 1 mBq/m^3. Both systems, in both measurements, are well below this limit. In practice, the non-statistical factors are at least as important as the background factors; in particular, in the present case the volume is given by the SPALAX air collection and the split between SAUNA and PW5 (nominally 50% each). Since MDC and statistical uncertainties for the computed concentrations are small compared to the variations seen between ^{133}Xe ROIs as well as non-physical negative numbers presumed due to calibration issues, we consider the observed variations the most suitable measure of the precision of the measurements.

Table 2. Measured radioxenon concentrations in two samples acquired with SPALAX and re-measured with a SAUNA detector and with PW5. SAUNA and PW5 results include adjustments for decay since the SPALAX measurement. (The ^{135}Xe ROI was not fully contained in the spectrum in PW5 data.)

mBq/m^3		**SPALAX original sample**	**SAUNA re-measure ½ sample**			**PW5 re-measure ½ sample**		
Sample		**conc.**	**conc.**	**MDC**	**variation**	**conc.**	**MDC**	**variation**
1	**^{133}Xe**	194	156	0.2	145 -168	128	0.5	122 -129
	^{131m}Xe	5.8	1.3	1.6		4.4	1.4	
	^{133m}Xe	7.1	3.1	1.9		2.9	2.0	
	^{135}Xe	0	1.0	2.9		(1.0)	(3.3)	
	+/- error (all isotopes)	5-11%	<1			<1		
2	**^{133}Xe**	1873	1486	0.4	1380 -1691	1274	0.6	1208 -1288
	^{131m}Xe	14.1	-21.4	5.2		14	4.2	
	^{133m}Xe	108	55	6.0		50	6.3	
	^{135}Xe	806	788	3.8		(419)	(3.6)	
	+/- error (all isotopes)	--	1.5-8.3			1.3-5.3		

Evaluation at The University of Austin

In experiments at The University of Texas' Nuclear Engineering Teaching Laboratory, radioxenon gas was produced at by activating stable enriched xenon gas in the 1.0-MW TRIGA reactor. Samples were measured in PW6 and results were compared to equivalent measurements with an ARSA-type detector. Measurements were performed with all 4 isotopes; below we focus on the results from ^{135}Xe. Analysis and further measurements with other isotopes are in progress. To produce ^{135}Xe, ^{134}Xe was irradiated in the reactor and underwent a neutron capture

reaction. The stable gas is enriched to 99.61% ^{134}Xe. The sample used in the ARSA-type detector was irradiated in beam port 2 (BP2), which is tangential to the core. The gas samples used for PW6 were produced using in-core irradiation, irradiated in the lead-lined 3L facility, which lies within the 7L facility. Irradiation time and powers were adjusted to account for differences in fluxes and produce similar activities. The fluxes, irradiation times, and irradiation powers are listed for both irradiations in Table 3.

Table 3. Irradiation time, power and fluxes for measurements at The University of Texas.

Detector	Isotope	Power (kW)	Time	Flux (n/cm^2/s)
ARSA-type	Xe-134	950	8 h	1x10^8
PW6	Xe-134	100	15 min	1x10^{11}

The ARSA-type detector system used in this experiment contains two NaI crystals and four beta cells, like the ARSA system. The beta cells are inserted into holes in the NaI assembly. Each beta cell is connected to two PMTs, as is each gamma cell, for a total of 12 PMTs. The entire apparatus is cased in lead housing to reduce background from cosmic radiation. The data processing was done by NIM and CAMAC electronics. Gain matching was performed for the beta and gamma cells and the energy was calibrated using standard sources (Haas, 2008).

While the stable xenon gas that underwent irradiation was highly enriched in ^{134}Xe (99.61%), it still contains small quantities of the other xenon isotopes, most notably ^{132}Xe, which is present in 0.29% abundance. Thus these other isotopes are irradiated along with the ^{134}Xe, making the sample slightly impure. This impurity is augmented by the short-lived nature of ^{135}Xe, as it is the shortest lived of the radioisotopes with a half life of 9.14 hours. Consequently, the activity of ^{135}Xe only dominates the sample for approximately 4.5 days, at which point ^{133}Xe decay begins to dominate the sample activity. The computed activity of various isotopes of xenon over time is shown in Figure 6. Due to the transient nature of ^{135}Xe, data used in this experiment to characterize the detectors was taken from the first day of data collection to ensure that adequate ^{135}Xe was present.

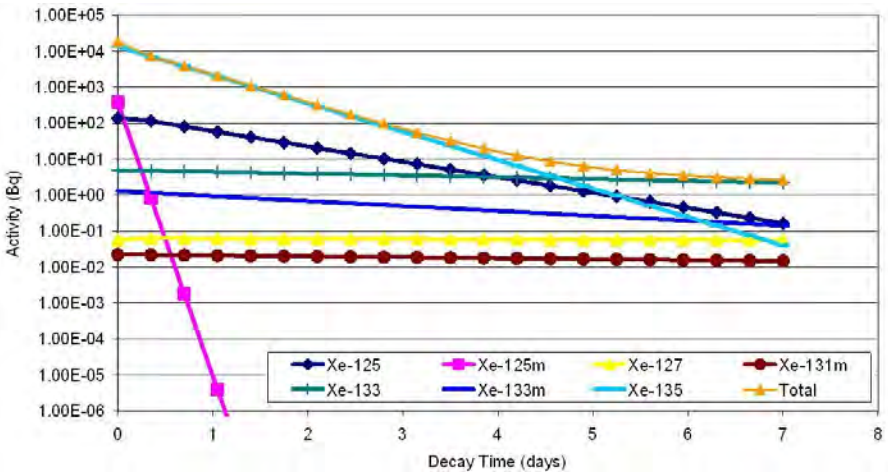

Figure 6. Activity contributions from radioxenon isotopes after irradiation of ^{134}Xe for 15 min at 100 kW.

To verify that the dominant isotope produced and detected in measurements with PW6 was, in fact, ^{135}Xe, a half-life measurement was made using the raw data. The count rate in the peak region was calculated at five points over the course of a day and plotted versus time. The resulting graph is presented in Figure 7. An exponential curve fit yields the equation shown on the graph, with a decay constant λ = 7.45x10-2 h^{-1}. This equates to a 9.31 h half-life, which is within 2% of the known half-life of ^{135}Xe, 9.14 h. Thus the count rate data collected by the phoswich detector confirms the dominant presence of ^{135}Xe with a high degree of accuracy.

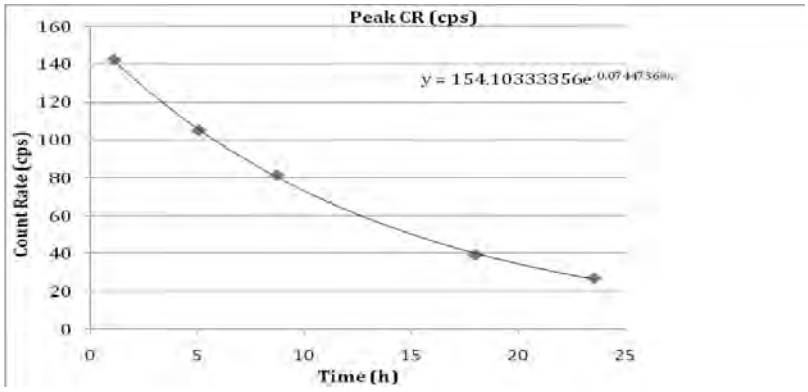

Figure 7. Count rate in PW6 measurement versus time, consistent with theoretical ^{135}Xe half-life.

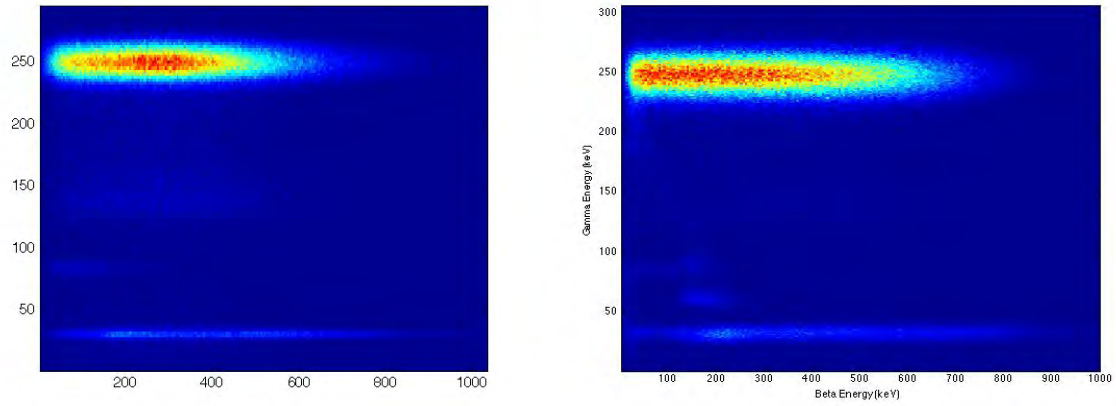

Figure 8. ^{135}Xe spectra from the ARSA-type detector (left) and PW6 (right). Axes are scaled in keV.

The ^{135}Xe spectra from both the ARSA-type detector and PW6 are shown in Figure 8. Both spectra feature the characteristic ^{135}Xe peak at Ec = 250 keV, and also show peaks at Ec = 81 and Ec = 30 keV. The 81 keV peak is a gamma peak from ^{133}Xe, while the 30 keV peak is an X-ray. The two spectra are comparable; however, notable differences do exist:

1) The 250 keV peak in the PW6 spectrum appears wider than the comparable peak in the ARSA spectrum. For PW6, the FWHM resolution is 12 % (30 keV), for the ARSA-type detector, the resolution is 9.6% (about 24 keV). The 81 keV gamma peak is also far narrower and clearer for the ARSA-type detector than for PW6.

2) The beta counts in the PW6 spectrum appear to be clustered at lower energies, and the tailing off of the beta distribution as the energy reaches a maximum (910 keV) is less dramatic, as well.

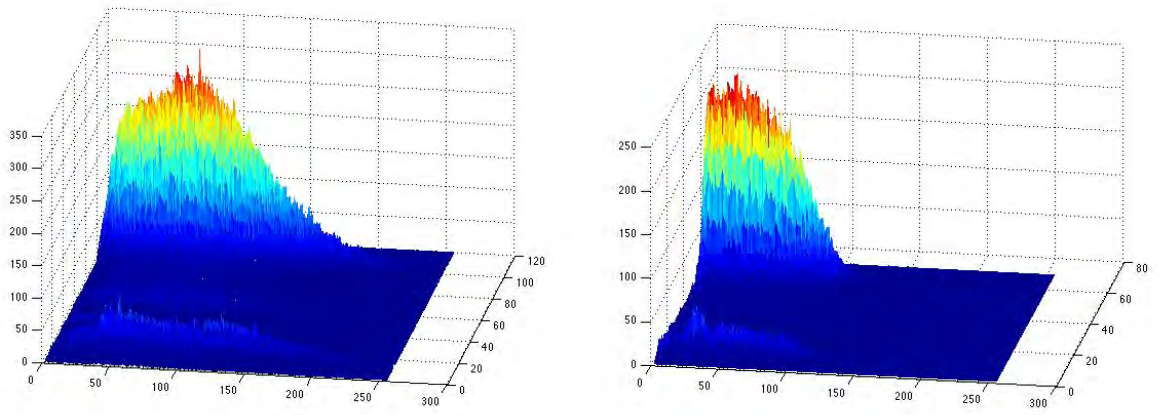

Figure 9. 3D surface plots of ^{135}Xe from ARSA-type detector (left) and PW6 (right). Axes are in channels.

The differing beta distributions between the two plots is even more evident in the surface plots, shown in Figure 9.The vertical axis is a measure of counts, while the x and y axis show beta and gamma channel, respectively. From these graphs it is clear that beta distribution is wider and tails off more slowly for the ARSA-type detector for both the 250 keV and 30 keV peaks, while the distribution for the phoswich detection rises and falls more sharply. The beta distributions for the 250 keV ROI (counts projected to the beta axis) and the theoretical distribution ("actual") are shown in Figure 10. The shape of the phoswich curve is very close to the theoretical distribution. The peak for the ARSA spectrum is at around 300 keV, which is higher than for the theoretical distribution and the PW6 spectrum. This difference in peak energy is due to the thinner wall of the plastic cell in the ARSA-type detector, which allows a portion of the high energy beta to deposit only a fraction of their energy in the plastic (effectively moving counts from high beta energy to lower beta energy).

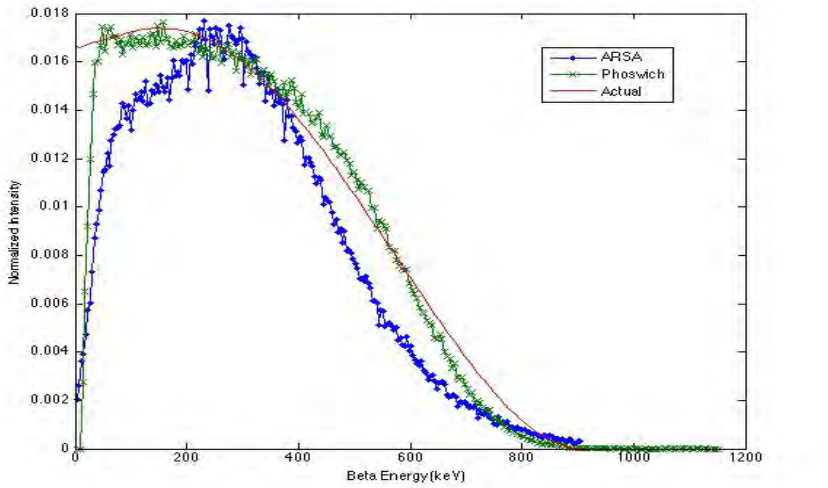

Figure 10. Theoretical, ARSA-type and PW6 beta distributions

Initial Results from 500 MHz Electronics

The DGF Pixie-4 used in the phoswich measurement digitizes the incoming detector signal at a rate of 75 MHz (13.3ns sampling) and this is sufficient to deliver good results in the PhosWatch system, as described above. Given the very fast pulses from the BC-404 (~2 ns decay time), it may however be beneficial to digitize the detector signal at a higher rate. As XIA is in the process of developing a Pixie-4 type module digitizing at 500 MHz, we used a prototype of this module, named P500, to explore possible improvements of the PhosWatch system with the higher speed electronics. In a preliminary test, a planar 1" CsI/BC-404 phoswich detector (PW1 from Hennig et al., 2006a)

was connected to a fast PMT (XP2020), irradiated with ^{137}Cs, and read out with a P500 and a Pixie-4. Detector waveforms were processed offline with the same PSA algorithms used in the standard measurements.

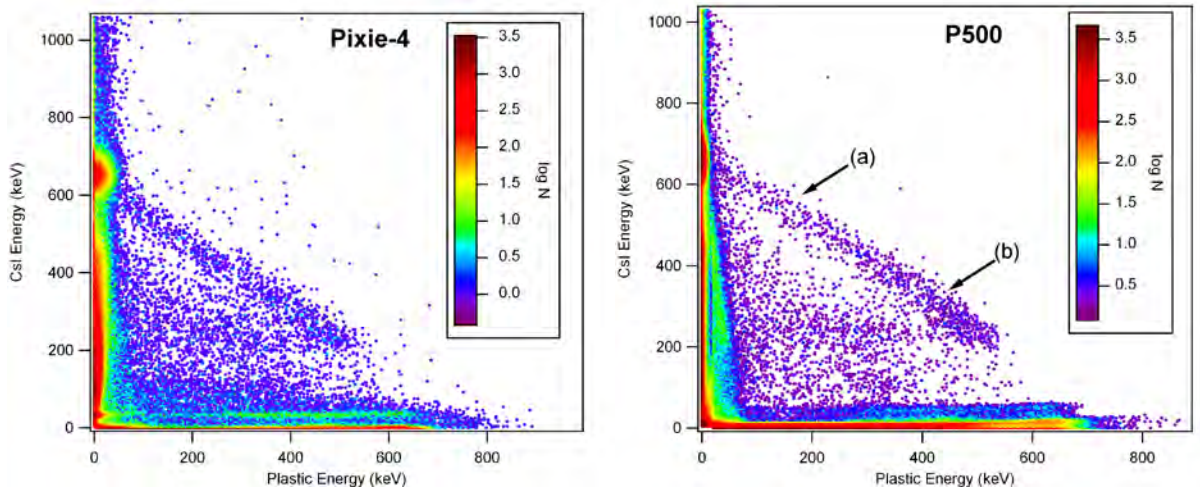

Figure 11. 2D energy histogram from PW1 computed offline from Pixie-4 and P500 waveforms. In contrast to Figure 3, non-coincident events are *not* contracted to the axes.

2D energy histograms of these measurements are shown in Figure 11. Both histograms show the typical features for ^{137}Cs measurements. Since in the planar geometry the source can be brought close to the BC-404, we can also detect the 624 keV CE from the second decay branch of ^{137}Cs, which is in coincidence with a ~30 keV X-ray. The main difference between the two systems is illustrated by looking at two events from the line of constant energy in detail: In each set of waveforms (a) and (b), as marked in Figure 11, the total energy deposited is ~662 keV, but in (a) only ~180 keV is deposited in the plastic while in (b) ~450 keV is deposited in the plastic. While in waveforms (a) there is almost no plastic contribution visible to the eye for the Pixie-4 waveform, the P500 waveform shows a distinct fast plastic spike.

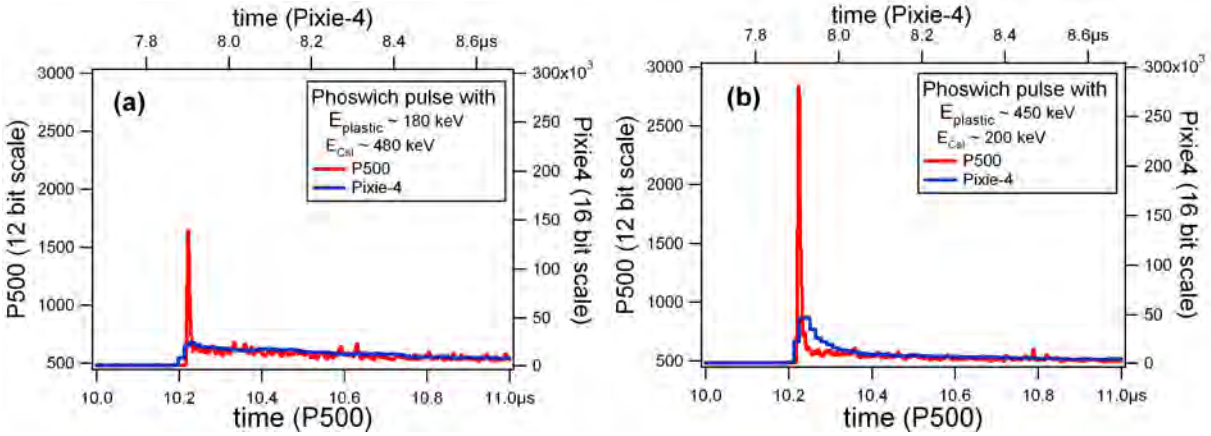

Figure 12. Phoswich waveforms captured by Pixie-4 and P500. The waveforms (a) and (b) are examples of events with energies falling into the Compton scatter line of constant energy at positions marked in Figure 11.

This better detection of the fast component translates directly in a better separation of event types. For example, part of the PSA calibration process includes measuring the slope formed by plotting the sum over the initial portion of the pulse (P) against the sum over the later portion of the pulse (C) for both plastic only and CsI only events. As shown in Figure 13, the slopes of the P vs. C distributions are much more "orthogonal" for the P500 than for the Pixie-4. Since the plastic contribution extends over so much less time in the P500, the length of P can be reduced from ~100ns to ~20ns, i.e. there is hardly any CsI contribution in P.

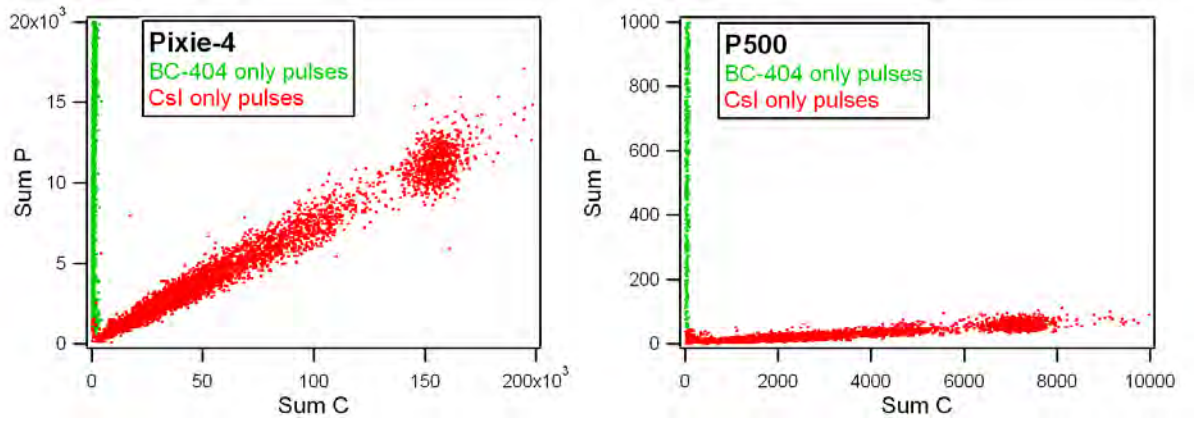

Figure 13. Scatter plots of P vs. C computed from phoswich waveforms. Axes are scaled to the same *ratio* for Pixie-4 and P500 plots.

In further characterization of the P500 system, we find that the energy resolution for the 624 keV CE is essentially equal (~14% FWHM), but resolutions are somewhat worse for 662 keV gamma rays (~10% for P500 vs. ~9.2% for Pixie-4 for this detector). In part, this can be attributed to the offline processing method, which omits the continuous baseline averaging implemented in online measurements that usually leads to improvements in resolution. Other factors may be the electronic noise in the system, which seems to particularly affect slow pulses and/or the precision of the Analog-to-Digital Converter (ADC) (12 bit for the P500 vs. 14 bit for the Pixie-4). We also find that the line of constant energy is slightly curved, similar to the behavior in some spectra reported from the SAUNA and BGW systems, and attribute that to the higher non-linearity associated with the fast ADC.

Future investigations in will include a closer look at reasons for increased noise, poorer linearity and degraded energy resolution. Also, for best results in this particular application, it may be beneficial to limit the P500 bandwidth, trading "orthogonality" of the scintillator contributions for more sampling points on the fast plastic spike and/or using the (pin compatible) 14bit, 400 MSPS ADC for better dynamic range and better linearity.

CONCLUSIONS AND RECOMMENDATIONS

In summary, we tested the PhosWatch radioxenon detector unit with standard test sources and with radioxenon samples from the atmosphere and from isotope irradiation. Overall, PhosWatch energy resolutions are comparable to existing systems, matching or exceeding resolutions at mid-high energies (~7.3% FWHM for 662 keV gamma rays for the later production batches) and reaching approximately 30% for both 30 keV energy X-rays and 129 keV CE. Background rates, memory effect, MDC, and coincidence detection efficiencies for the phoswich detectors are comparable to, and sometimes better than, values for existing systems. The phoswich detectors showed good consistency and precision in measurements with atmospheric samples, and produced comparable spectra in measurements with irradiated samples. The PhosWatch system also offers a significant advantage in ease of use and transportability. Since the design features only one PMT and does not depend on time coincidence, it eliminates the need for gain matching and – together with the compact electronics – greatly reduces the physical size of the detector, making it easier to deploy in the field. In future work, we will continue the side-by-side evaluations, and further explore performance improvements with the electronics digitizing at 500 MHz, which should allow even better detection of coincidences since fast plastic pulses are resolved better.

ACKNOWLEDGEMENTS

We thank A. Ringbom for helpful information about the SAUNA system gleaned through private communications.

REFERENCES

Axelson, A. and A. Ringbom (2003) Xenon air activity concentration analysis from coincidence data, FOI report FOI-R-0913-SE

Cooper, M. W., J. I. McIntyre, T. W. Bowyer, A. J. Carman, J. C. Hayes, T. R. Heimbigner, C. W. Hubbard, L. Lidey, K. E. Litke, S. J. Morris, M.D. Ripplinger, R. Suarez, and R. Thompson (2007a). Redesigned β-γ radioxenon detector, *Nuclear Instruments and Methods in Physics Research* A 579: 426–430.

Cooper, M.W., J. C. Hayes, T. R. Heimbigner, C. W. Hubbard, J. I. McIntyre, M. D. Ripplinger, and B. T. Schrom (2007b). Automated QA/QC check for β-γ coincidence detector, in *Proceedings of the 29th Monitoring Research Review: Ground Based Nuclear Explosion Monitoring Technologies*, LA-UR-07-5613, Vol. 2, pp. 739–746.

Ely, J. H., C. E. Aalseth, J. C. Hayes, T. R. Heimbigner, J. I. McIntyre, H. S. Miley, M. E. Panisko, and M. Ripplinger (2003). Novel Beta-Gamma coincidence measurements using phoswich detectors, in *Proceedings of the 25th Seismic Research Review—Nuclear Explosion Monitoring: Building the Knowledge Base*, LA-UR-06-6029, Vol. 1, pp. 533–541.

Farsoni, A.T., D.M. Hamby, K.D. Ropon, and S.E. Jones (2007). A two-channel phoswich detector for dual and triple coincidence measurements of radioxenon isotopes, in *Proceedings of the 29th Monitoring Research Review: Ground-Based Nuclear Explosion Monitoring Technologies*, LA-UR-07-5613, Vol. 2, pp. 747–756.

Fontaine, J.-P., F. Pointurier, X. Blanchard and T. Taffary (2004). Atmospheric xenon radioactive isotope monitoring, *Journal of Environmental Radioactivity* 72: 129–135

Haas, D.A., (2008). Producing beta-gamma Coincidence Spectra of Individual Radioxenon Isotopes for Improved Analysis of Nuclear Explosion Monitoring Data, Ph.D. dissertation, The University of Texas at Austin.

Hennig, W., H.Tan, W. K. Warburton, and J. I. McIntyre (2006a). Single channel beta-gamma coincidence detection of radioactive Xenon using digital pulse shape analysis of phoswich detector signals, *IEEE Transactions on Nuclear Science* 53: (2) 620.

Hennig, W., H.Tan, A. Fallu-Labruyere, W. K. Warburton, J. I. McIntyre and A. Gleyzer (2006b). Design of a phoswich well detector for radioxenon monitoring, in *Proceedings of the 28th Seismic Research Review: Ground Based Nuclear Explosion Monitoring Technologies*, LA-UR-06-5471, Vol. 2, pp. 801–810.

Hennig, W., H.Tan, A. Fallu-Labruyere, W. K. Warburton, J. I. McIntyre, and A. Gleyzer (2007a). Characterization of phoswich well detectors for radioxenon monitoring, in *Proceedings of the 29th Monitoring Research Review: Ground Based Nuclear Explosion Monitoring Technologies*, LA-UR-07-5613, Vol. 2, pp. 757–763.

Hennig, W., Y.X. Chu, H.Tan, A. Fallu-Labruyere, W. K. Warburton, and R. Grzywacz (2007b). The DGF Pixie-4 spectrometer – Compact Digital Readout Electronics for HPGe Clover Detectors, *Nuclear Instruments and Methods in Physics Research* B 263, 175–178.

Hennig, W., H. Tan, W. Warburton, A. Fallu-Labruyere, K. Sabourov, M. Cooper, J. McIntyre, and A. Gleyzer (2008). Development of a COTS Radioxenon Detector System Using Phoswich Detectors and Pulse Shape Analysis, in *Proceedings of the 30th Monitoring Research Review: Ground Based Nuclear Explosion Monitoring Technologies*, LA-UR-08-05261, Vol. 2, pp. 758–767

Reeder, P. L., T. W. Bowyer, and R. W. Perkins, (1998). Beta-gamma counting system for Xe fission products, *Journal of Radioanalytical and Nuclear Chemistry* 235: (1–2), 89–94.

Reeder, P. L., T. W. Bowyer, J. I. McIntyre, W. K. Pitts, A. Ringbom, and C. Johansson (2004). Gain calibration of coincidence spectrometer for automated radioxenon analysis, *Nuclear Instruments and Methods in Physics Research* A 521: 586–599.

Ringbom, A., T. Larson, A. Axelson, K. Elmgren, and C. Johansson (2003). SAUNA—a system for automatic sampling, processing and analysis of radioactive xenon, *Nuclear Instruments and Methods in Physics Research* A 508: 542–553.

MECHANICALLY COOLED LARGE-VOLUME GERMANIUM DETECTOR SYSTEMS FOR NUCLEAR EXPLOSION MONITORING

Ethan L. Hull[1], Richard H. Pehl[1], James R. Lathrop[1], Peggy L. Mann[1], Ronnie B. Mashburn[1], Bruce E. Suttle[1], Harry S. Miley[2], Craig E. Aalseth[2], Theodore W. Bowyer[2], and Todd W. Hossbach[2]

PHDs Co.[1] and Pacific Northwest National Laboratory[2]

Sponsored by the National Nuclear Security Administration

Award No. DE-FC52-06NA27323
Proposal No. BAA06-37

ABSTRACT

Compact, maintenance-free, long-lived, mechanically cooled germanium-detector systems are being developed to operate large-volume germanium detectors for field applications. These detector systems are necessary for remote long-duration liquid-nitrogen free deployment of large-volume germanium gamma-ray detectors. The Radionuclide Aerosol Sampler/Analyzer (RASA) nuclear explosion monitoring system will benefit from the availability of these new detector systems. Three prototype detector systems (RASA 1, RASA 2, and RASA 3) have been developed, fabricated, and tested. The cryostats have been demonstrated to cool very large detectors to temperatures as low as 50 K. The vacuum design has demonstrated no measurable degradation for at least two years. These detector systems have been demonstrated to successfully instrument high-purity germanium detectors. Microphonic noise from the vibrating cooler can obscure the gamma-ray spectroscopy. The single most-significant technical issue encountered during this program has been microphonic noise. Recent advances have led to a better understanding of the source and the sensitivity to microphonic noise. The third-generation system, RASA 3, has recently demonstrated good spectroscopic performance with the cooler operating at full power. The performance appears to be repeatable. The microphonic noise issues have been greatly reduced by mechanical changes afforded by the new RASA 3 design, making the detector system design viable for nuclear explosion monitoring.

OBJECTIVES

PHDs Co. is developing mechanically cooled detector systems for large-volume germanium detectors. Maintenance-free Stirling-cycle mechanical coolers are being used. These coolers have operating lifetimes exceeding five years. The relatively large heat lift of these coolers quickly cools a detector to very low operating temperatures for gamma-ray spectroscopy measurements. Lower operating temperature improves the reliability of germanium detectors by lowering surface leakage currents (Pehl et al., 1973). These features will make liquid-nitrogen free operation of the largest germanium gamma-ray detectors viable and convenient for nuclear explosion monitoring. The RASA detector system will benefit from the availability of such detectors (Bowyer et al., 1997; Miley et al., 1998).

Mechanical cooling of germanium detectors has historically been a difficult endeavor. The viability of mechanically cooled germanium detector systems depends upon three major technical issues: temperature, vacuum, and vibration. Previous years have seen analysis of these factors and their impact on detector performance (Hull et al., 2006). The first two prototype detector systems, RASA 1 and RASA 2, were then brought to working order with a coaxial germanium detector (Hull et al., 2007; Hull et al., 2008). During the evolution of these first two prototypes, extremely low operating temperatures were achieved in an extremely stable vacuum system showing no degradation. However, there were problems with microphonic noise that could not be controlled or even duplicated from one thermal cycle to the next. Most recently, a third prototype germanium detector system (RASA 3) has been designed and fabricated. The system employed a right-angle design in the body of the cryostat that places the axis of the cooler orthogonal to the axis of the detector. With this new modification, reasonably good gamma-ray spectroscopy has been consistently achievable with the cooler operating at full power. This encouraging result should lead to a viable PHDs Co. design for cooling RASA coaxial germanium detectors in a cryogenic system that has great longevity, reliability, and performance.

RESEARCH ACCOMPLISHED

The older prototypes, RASA 1 and RASA 2, were used in an attempt to continue troubleshooting the insidious microphonic noise issue. A photograph of RASA 2 is shown in Figure 1. On separate trials, the following steps were made in an attempt to identify the source of the microphonic noise in the detector. Each change required cycling the detector from cryogenic temperatures up to room temperature, making the change, and then again cooling the detector. The detector and the infrared shield were both floated to bias voltage. The position and mounting of the junction field-effect transistor (JFET) were changed. The circuit board holding the JFET was changed to make it nearly 100% ground plane relative to the gate lead of the JFET. A grounded copper faraday cage was built around the JFET. A grounded copper faraday cage was also built around the detector contact pin connected to the gate of the JFET. An external JFET was installed on the system. Large (~0.2 μF) high-voltage filter capacitors were added on the bias line. The bias line was internally shielded. The aluminum parts were sanded and cleaned. Extra lateral supports were added to limit the sideways motion of the detector and infrared shield. The copper cooling braids were changed in width and length (this helped on one occasion). The copper braids were replaced with folded copper and aluminum foils. The Sunpower Cryotel CT cooler was replaced with the much smaller Cryotel MT cooler having somewhat less vibration. Despite all of these changes on the RASA 1 and RASA 2 detector systems, the microphonic noise was not greatly improved. Changes to the copper braid did result in slightly better microphonic noise on one occasion, but the result could not be repeated. The change finally making the difference was the switch to the new RASA 3 cryostat. Apparently the right-angle design of the system provided the necessary isolation to allow the detector to function with consistently less microphonic noise.

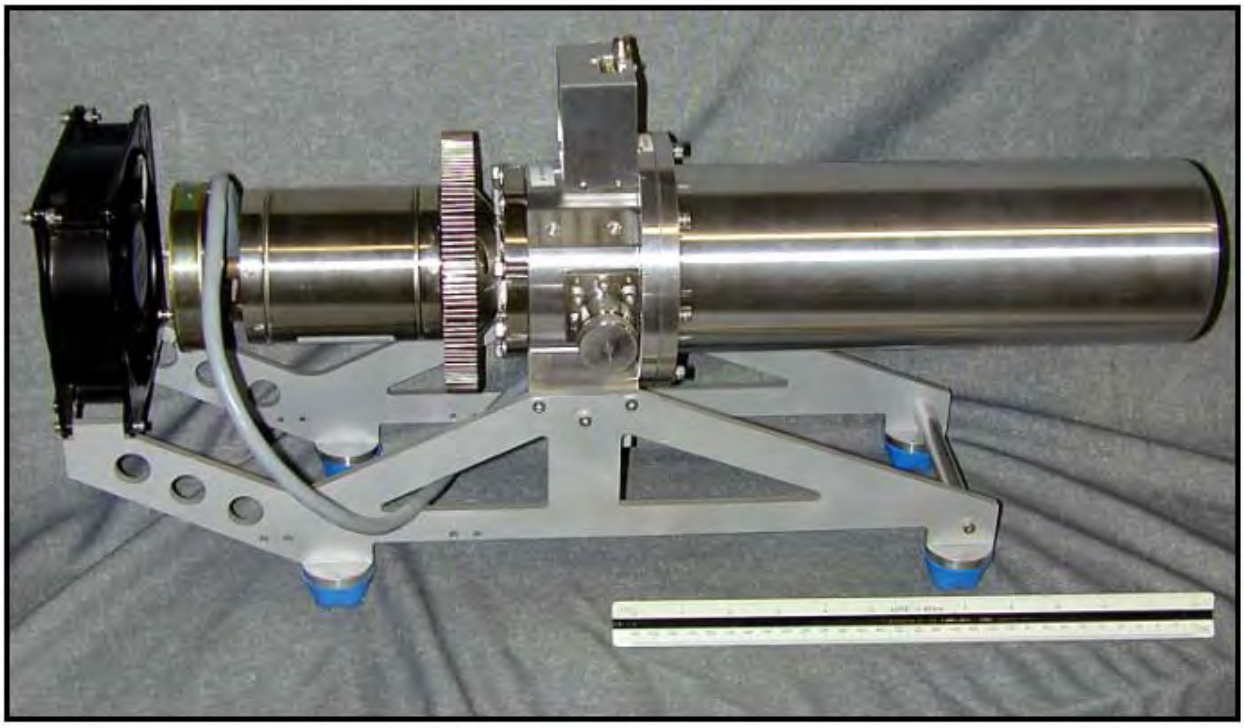

Figure 1. The RASA 2 prototype is a relatively compact overall design. This prototype system places the detector directly in line with the axis of the vibrating mechanical cooler. The coaxial germanium detector is held inside the rightmost end of the aluminum cap. The cooler is shown on the left next to the fan.

The later part of the third year of this project has seen a single extremely significant accomplishment—the microphonic noise problems associated with the vibrating cooler were finally diminished. After attempting numerous fruitless modifications (described above), the RASA 3 cryostat has proven to stabilize the microphonic noise problems from the vibrating cooler. Taken from our planar imaging detector designs, the RASA 3 employs a right-angle cryostat. The coaxial germanium detector is held at a right angle with respect to the axis of the linear Stirling-cycle cooler. For the past few years, PHDs Co. has had the capability of fabricating planar germanium detectors in similar cryostats having no significant microphonic noise issues. Planar orthogonal strip detectors have been fabricated having 16 × 16 orthogonal strips displaying no significant microphonic noise issues from the vibrating cooler. In many ways orthogonal-strip germanium detectors are far more complex than single-channel coaxial germanium detectors. Because it has 32 external JFETs, one might conclude that the orthogonal strip detectors would be far more vulnerable to microphonic noise than a single-channel coaxial detector, since the single-channel coaxial detector has an internal JFET. Surprisingly, the orthogonal-strip detectors are virtually free of microphonic noise. The only significant difference between these planar-detector systems and the RASA systems is the right-angle cryostat design of the strip detector systems. In our first two RASA detector systems (RASA 1 and RASA 2), the detector shared a common centerline with the cooler axis, as shown in Figure 1. It was hypothesized that this mechanical configuration allowed a problematic resonance to cause the detector itself to vibrate excessively in its mounting, despite holding the detector with ~ 100 lb of force in compression.

The RASA-3 mechanically cooled detector system was assembled and debugged. The fully assembled system is shown in Figure 2. A PHDs Co.-fabricated p-type coaxial germanium detector was removed from the RASA 1 cryostat and loaded into the RASA 3 system. After several minor modifications the system successfully cooled the detector into the 50–60 K region. With the detector at these temperatures, the operation of the detector should be much more stable long term. The long-lived cooler and the metal-sealed cryostat should provide operation of the detector for more than 5 years.

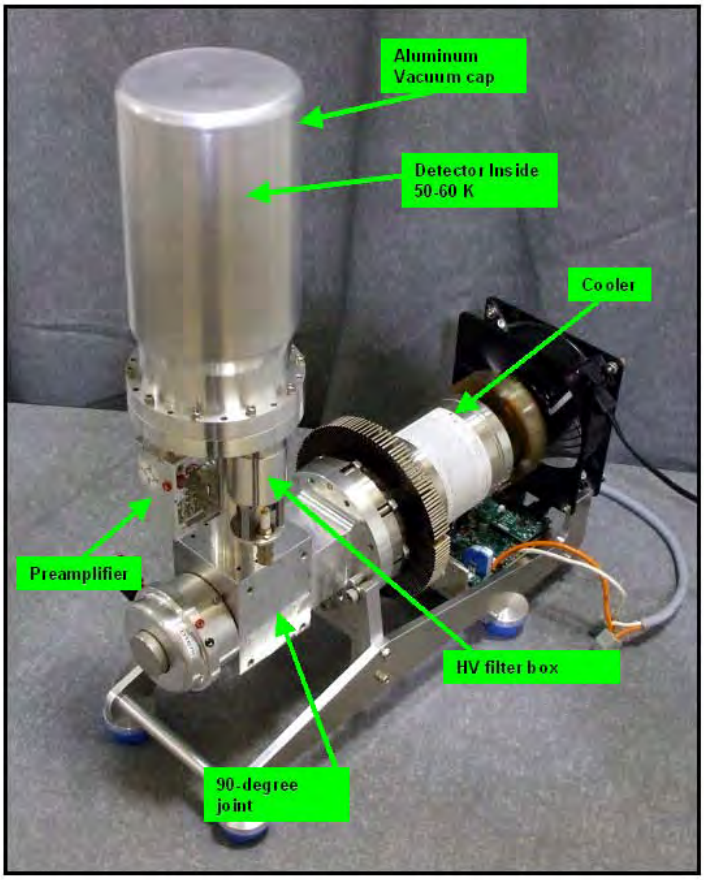

Figure 2. The RASA 3 prototype shown here holds and cools a 70-mm-diameter, 70-mm-long coaxial germanium detector. The 90-degree joint separates the cooler axis from the detector, keeping the vibrating cooler from directly affecting the detector. This detector system successfully cools the detector to the 50-60 K region while adding very little microphonic noise from the mechanical cooler. Some additional size was added to accommodate the right-angle design. The RASA 3 detector system still allows the detector to be placed in the proper location near the filter paper in the RASA station.

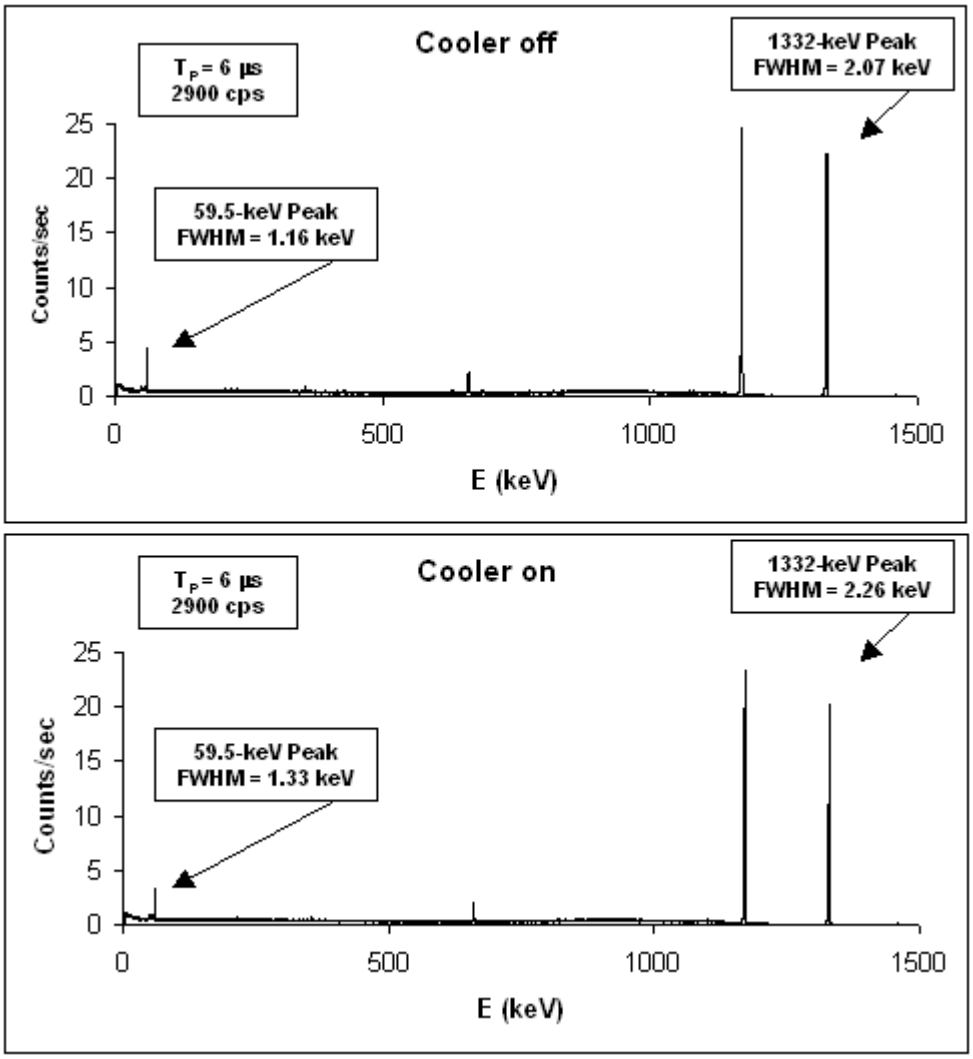

Figure 3. These energy spectra were accumulated from the detector in RASA 3 using a unipolar peaking time of 6 µs. The top view shows the spectroscopy with the cooler switched off briefly, while the bottom view shows a spectrum accumulated with the cooler operating at full power. There is still a small component of degradation from microphonic noise when the cooler is operating. No special electronic filtering was used to eliminate microphonic noise for this measurement.

Aside from the spectroscopy shown in Figure 3, the microphonic noise was analyzed on the oscilloscope. The signals from the detector preamplifier were shaped in a TC244 shaping amplifier using a peaking time of 6 µs. Very little microphonic noise was visible on the baseline. This was established with the 122-keV gamma-ray peak set to 6 V on the oscilloscope. This allows the baseline JFET channel noise to be easily observed on the 100- and 200-mV voltage scales. Channel noise from the JFET dominates when the cooler was not operating. When the cooler is switched on, there is a brief burst of noise when it starts, and then the noise almost immediately returns to the cooler-off level. The microphonic noise has not been eliminated through the use of any special electronic filtering—it has simply been eliminated from the system altogether. This result, along with the spectroscopy, was heralded as a great success. More important, the good performance appears to be stable with the new RASA 3 design. The system has been operated for weeklong periods with no degradation. In addition, the detector and all internal parts have been completely disassembled and reassembled multiple times with no significant degradation in detector performance. During the past few years, this had been the most significant problem. The performance was not repeatable. Sometimes disassembling the system would improve or degrade the performance dramatically.

There was never any certainty with respect to the origin or sensitivity to the microphonic noise issues. The new right-angle design in the RASA 3 cryostat appears to make the significant difference necessary to provide stable and repeatable detector performance.

CONCLUSIONS AND RECOMMENDATIONS

The RASA 1 and RASA 2 prototype detector systems have been designed, fabricated, and tested as demonstrations of a new integrated mechanical cooling detector system suitable for use with RASA stations. These two systems cool large coaxial detectors to extremely low temperatures in a 100% metal sealed cryostat providing long-lived detector operation. However, the usefulness of RASA 1 and RASA 2 were constantly hindered by a microphonic-noise problem degrading the spectroscopy of the detector. Fortunately, the third generation prototype, RASA 3, has demonstrated good spectroscopy that is nearly free of microphonic noise issues. Moreover, this encouraging result appears to be repeatable. Along with the low operating temperature and excellent quality vacuum, the improvement in the microphonic noise makes the PHDs Co. RASA 3 cryogenic system viable for use in RASA stations.

REFERENCES

Bowyer, S. M., H. S. Miley, R. C. Thompson, and C. W. Hubbard (1997). Automated particulate sampler for Comprehensive Test Ban Treaty verification (the DOE radionuclide aerosol sampler/analyzer), *IEEE Transactions on Nuclear Science* 44: 551–556.

Hull, E. L., R. Pehl, J. Lathrop, P. Mann, R. Mashburn, B. Suttle, H. Miley, C. Aalseth, T. Bowyer, T. Hossbach. G. Rybicki, and J. Buchholtz (2008). Mechanically cooled large volume germanium detector systems for nuclear explosion monitoring, in *Proceedings of the 30th Monitoring Research Review: Ground-based Nuclear Explosion Monitoring Technologies*, LA-UR-08-05261. Vol. 2, pp 772–777.

Hull E. L., R. Pehl, J. Lathrop, P. Mann, R. Mashburn, B. Suttle, H. Miley, C. Aalseth, T. Bowyer, and T. Hossbach (2007). Mechanically cooled large volume germanium detector systems for nuclear explosion monitoring, in *Proceedings of the 29th Monitoring Research Review: Ground-based Nuclear Explosion Monitoring Technologies*, LA-UR-07-5613. Vol. 2, pp. 770–779.

Hull, E. L., R. Pehl, J. Lathrop, R. Mashburn, H. Miley, C. Aalseth, and T. Hossbach (2006). Mechanically cooled large volume germanium detector system for nuclear explosion monitoring, in *Proceedings of the 28th Seismic Research Review: Ground-Based Nuclear Explosion Monitoring Technologies,* LA-UR-06-5471, Vol 2, pp. 821–830.

Miley, H. S., S. M. Bowyer, C. W. Hubbard, A. D. McKinnon, R. W. Perkins, R. C. Thompson, and R. A. Warner (1998). A description of the DOE radionuclide aerosol sampler/analyzer for the Comprehensive Test Ban Treaty. *J. Radioanal. Nucl. Chem.* 235: 83–87.

Pehl, R. H., E. E. Haller, and R. C. Cordi (1973). Operational characteristics of germanium detectors at higher temperatures, *IEEE Trans. Nucl. Sci*. 20: 494.

FINITE ELEMENT MODELING OF ADSORPTION PROCESSES FOR GAS SEPARATION AND PURIFICATION

Paul H. Humble, Richard M. Williams, and Jim C. Hayes

Pacific Northwest National Laboratory

Sponsored by the National Nuclear Security Administration

Award No. DE-AC05-RLO1830/PL07-ZINC-NDD02

ABSTRACT

In the design and fabrication of improvements to automated radioxenon collection systems for nuclear explosion monitoring, there is an ever present need to reduce size, power consumption, and complexity. Most automated systems have used adsorption based techniques for gas collection and/or concentration and purification. These processes include pressure swing adsorption, vacuum swing adsorption, temperature swing adsorption, gas chromatography and hybrid processes that combine elements of these techniques. To better understand these processes, and help with the development of improved hardware, a finite element software package (COMSOL Multiphysics) has been used to develop complex models of these adsorption based operations. The partial differential equations used include a mass balance for each gas species and adsorbed species along with a convection conduction energy balance equation. These equations in conjunction with multicomponent temperature dependent isotherm models are capable of simulating separation processes ranging from complex multibed pressure swing adsorption processes, and multicomponent temperature programmed gas chromatography, to simple two-component temperature swing adsorption. These numerical simulations have been a valuable tool for assessing the capability of proposed processes and optimizing hardware and process parameters.

OBJECTIVES

The objective of this work was the development of mathematical models of adsorption and chromatographic processes used for processing radioxenon from atmospheric air. These models enable a better understanding of adsorption processes and serve as useful tools in the development of improved processes and hardware. The purpose of this work is the development of improved collection and separation techniques for the next international radioxenon systems.

Measuring radioactive xenon in the atmosphere is an important technique in nuclear explosion monitoring, and has been included as one of the techniques used for verification under the Comprehensive Nuclear-Test-Ban Treaty (CTBT). Bowyer et al. (1999) described an automated radioxenon sampler-analyzer (ARSA) system developed for CTBT monitoring that collected and analyzed four xenon radionuclides: ^{131}mXe, ^{133}mXe, ^{133}Xe, and ^{135}Xe. The activity ratios of these radionuclides are unique for a nuclear detonation and the ability to measure these ratios is important in differentiating a nuclear detonation from a nuclear reactor release. Dilution in the atmosphere and radioactive decay require collecting and concentrating xenon from a large volume of air. The ARSA system trapped xenon by passing a stream of compressed, dry, and CO_2 depleted atmospheric air through a cooled charcoal bed. Ringbom et al. (2003) describe the Swedish Automatic Unit for Noble gas Acquisition (SAUNA) that collects xenon using larger charcoal beds at ambient temperatures. Both of these systems use chromatographic techniques for sample purification. There is a need to reduce the cost, size and power requirements of such systems. Since a large portion of the size and energy requirement is dictated by gas processing, better collection and separation techniques are required to develop smaller, cheaper, and lower power systems with greater flexibility.

The separation and purification of trace gasses from atmospheric samples is most often accomplished using processes including cryogenic adsorption, membrane permeation, pressure swing adsorption, temperature swing adsorption, and chromatography. These techniques use differences in adsorption affinity and/or transport properties of gas species in a porous material to accomplish component separation. Chromatographic and adsorption process are especially similar and can be described using the same mass and energy balance equations. Mathematical models of adsorption and chromatographic separations can be used to develop improved processes and hardware for the capture and concentration of xenon from atmospheric air. This paper describes time dependent models of such processes developed and implemented using COMSOL Multiphysics. These models have helped in comparing proposed processes and developing new techniques and hardware to separate and concentrate xenon.

The mathematical equations presented have been used to model both adsorption and chromatographic processes ranging from 1D multi-component chromatography to 3D temperature dependent pressure swing adsorption. These equations are similar to those others have used to model adsorbing systems (Yang 1997, Farooq 1991, Farooq 1993) The models are general enough to simulate separation processes based on kinetic or equilibrium properties. This makes it possible to use the same set of equations to model materials ranging from activated carbon to molecular sieves.

RESEARCH ACCOMPLISHED

Model Description

The following four assumptions and simplifications have been used in developing the mathematical model: 1) The flow of gasses through the porous media is described by Darcy's law. This implies flow through the bed where the gas velocity is proportional to the pressure gradient. 2) The ideal gas law is used to describe the relationship between gas density (concentration), pressure, and temperature. 3) Adsorption equilibrium is described using temperature dependent competitive Langmuir isotherms, and in implementation it is assumed that each species has the same saturation capacity. However, it is possible to use other equations describing multicomponent adsorption. 4) Mass transfer between the gas and adsorbed phase is described using a linear driving force model. This implies that the rate of adsorption or desorption is proportional to the difference between the actual amount adsorbed and the amount that would be adsorbed if the bed where at equilibrium. To model equilibrium driven processes, the rate constant of the linear driving force model is made large enough such that equilibrium is closely approximated. Kinetically driven processes can be modeled by substituting suitable rate constants.

The system of partial differential equations used to model these processes is derived starting with Darcy's Law (equation 1) and the ideal gas law (equation 2) to define gas velocity and pressure. The variable c_i represents the concentration of species *i* in the gas phase based on the gas phase volume as opposed to the total system volume. A description of the constants and variables appearing in the mathematical model is shown in Table 1.

$$v = \frac{-\kappa}{\varepsilon \cdot \mu} \cdot \nabla P \tag{1}$$

$$P = R \cdot T \cdot \sum_i c_i \tag{2}$$

Equations 1 and 2 can be combined to provide the convective flux term of an overall time dependent mass balance equation for each gas phase species (equation 3).

$$\varepsilon \frac{\partial c_i}{\partial t} + \nabla \cdot (-\varepsilon \cdot D_{i,gas} \nabla c_i - c_i \frac{\kappa}{\mu} \nabla (R \cdot T \sum_{j=1}^{n} c_j)) = F_i \tag{3}$$

The dispersive term describes gas phase diffusion, but can also be adjusted to account for Taylor dispersion arising from laminar flow mixing in the inter particle flow paths.

There is no convection term for adsorbed species and the overall mass balance equation for adsorbed species simplifies to equation 4. The surface diffusion (dispersion) term can also be neglected in most cases. However, including a dispersive term may improve model stability by decreasing the sharpness of moving fronts in the time dependent model.

$$\frac{\partial c_{iad}}{\partial t} + \nabla \cdot \left(D_{i,sur} \nabla c_{iad} \right) = -F_i \tag{4}$$

The rate of species transfer from the adsorbed phase to the gas phase (F_i) is defined in equation 5. This equation is the linear driving force model with the equilibrium condition modeled using a multi-component Langmuir isotherm where the ideal gas law has been used to convert from partial pressure to gas phase concentrations.

$$F_i = K_i \cdot \left[c_{iad} - \frac{\rho_{bed} R \cdot T \cdot N_{io} b_i c_i}{1 + R \cdot T \cdot \sum_i (b_i c_i)} \right] \tag{5}$$

Equation 6 defines the temperature dependent term b_i (related to the Henry constant) in the temperature dependent Langmuir isotherm.

$$b_i = \frac{b_{o,i}}{N_{io}} \cdot \exp\left(-\frac{q_{st,i}}{R \cdot T} \right) \tag{6}$$

Additionally, an energy balance equation that includes convection and conduction is used to model heat transfer in the adsorption bed (equation 7). In the derivation of this equation it is assumed heat transfer between the solid and gas phase is fast enough such that temperature equilibrium is achieved and a single temperature at each point in the bed can be used for both the gas and solid phase.

$$\left((1-\varepsilon) \rho_s C_{p,s} + \varepsilon \rho_g C_{p,g} \right) \frac{\partial T}{\partial t} + \nabla \cdot \left(-k \nabla T \right) + \rho_g C_{p,g} \left(-\frac{k}{\mu} \nabla \left(R \cdot T \cdot \sum_i c_i \right) \right) = -\sum q_{st,i} F_i \tag{7}$$

Table 1. Description and units for constants and variables appearing in mathematical model

v	Gas superficial velocity (m/s)
κ	Permeability (m^2)
ε	Bed void fraction
μ	Viscosity (Pa·s)
P	Pressure (Pa)
R	Gas constant (J/mol·K)
T	Temperature (K)
c_i	Concentration of species i in the gas phase (mol/m^3)
c_{iad}	Concentration of species i in the adsorbed phase based on bed volume (mol/m^3)
$D_{i,gas}$	Species i diffusion (or dispersion) constant in the gas phase (m^2/s)
$D_{i,sur}$	Species i diffusion (or dispersion) constant in adsorbed phase (m^2/s)
F_i	Rate of species i transfer from adsorbed to gas phase ($mol/s \cdot m^3$)
ρ_{bed}	Mass of adsorbent per bed volume (g/m^3)
N_{io}	Maximum number moles of species i on adsorbed phase (mol/g)
K_i	Linear driving force rate constant for species i (1/s)
$b_{,i}$	Henery's law constant for species i divided by N_{io} (1/Pa)
$b_{o,i}$	Temperature independent constant for species i (mol/g·Pa)
ρ_s	Density of solid (g/m^3)
ρ_g	Density of gas (g/m^3)
$q_{st,i}$	Infinite dilution isoteric heat of adsorption (J/mol)
k	Thermal conductivity of the bed (W/m·K)
$C_{p,s}$	Solid phase heat capacity (J/g·K)
$C_{p,g}$	Gas phase heat capacity (J/g·K)

The basic mathematical model consists of mass balance equations (3 and 4) for each gas phase and adsorbed species, and the energy balance equation (7) to describe the transport of heat in the bed and define the temperature. These partial differential equations will describe both adsorption and chromatographic processes. However, the boundary conditions used in implementing the model will be different for these separation processes.

Model Results

One of the first processes modeled using the described equations was gas chromatography in an adsorbing carrier gas. Of interest was how the adsorbing carrier impacts peak shape and separation efficiency. Figure 1 shows the modeling results for a separation of three components in an adsorbing carrier gas. In this simulation two of the components are more strongly adsorbed than the carrier and one component is more weakly adsorbed. Such separations may occur in gas processing after the initial collection. For instance, separating xenon in a gas mixture containing oxygen, nitrogen, and CO_2 using a nitrogen carrier gas. In Figure 1 the first peak on the right corresponds to the gas species with the smallest adsorption affinity, this species has lower affinity compared to the carrier gas. The other two peaks correspond to species with a higher adsorption affinity.

Another basic process that was modeled is the pressure swing enrichment of xenon from a gas consisting of a dilute mixture of xenon in nitrogen. Such an enrichment process is similar to those used in both the ARSA and SAUNA systems. Figure 2 shows how the gas phase concentration changes during depressurization. The finite element model is able to show how the pressure drop through the bed influences the gas phase concentration during the depressurization.

An important feature of these models is the ability to simulate a series of processes such as a pressure swing followed by an increase in temperature or flow of a purge gas. Such processes occur in gas processing when concentrating and isolating a desired product from a multi-component mixture. For instance, a pressure swing step can be used to initially concentrate xenon in air, increasing the temperature can be used to desorb xenon and further increase the gas phase concentration, and then gas chromatography can be used to separate xenon from other species by flowing a carrier gas through the bed.

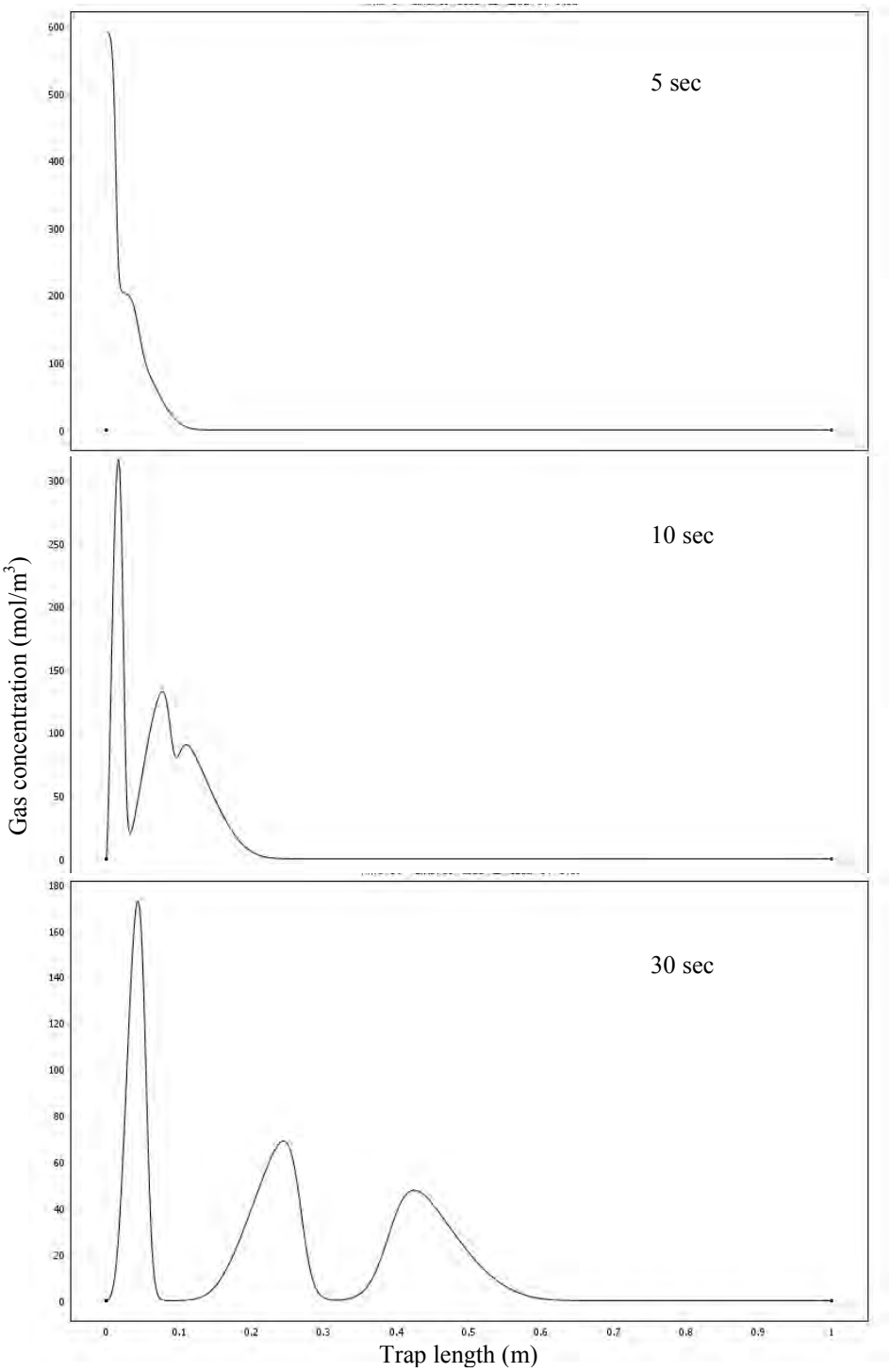

Figure 1. Simulation of a gas chromatographic separation of 3 components in an adsorbing carrier gas.

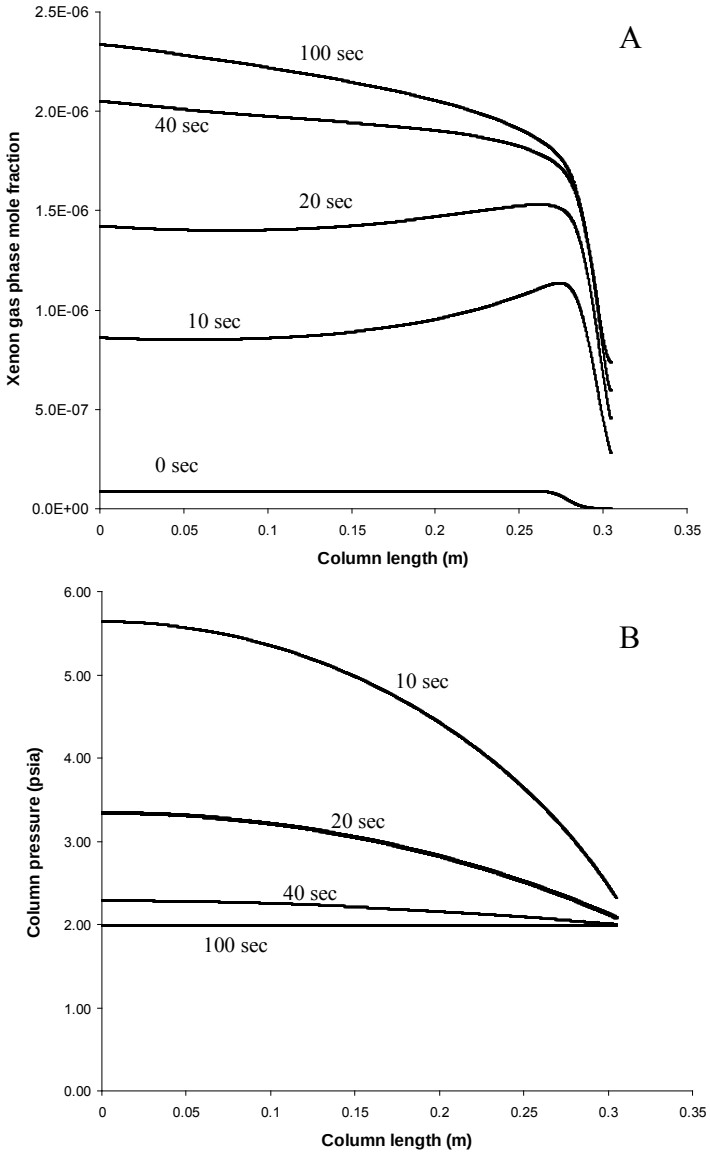

Figure 2. Mole fraction of xenon (A) during column depressurization (B). The column was depressurized by setting the outlet pressure to 2 psia. Xe was adsorbed on the column at 80 psia inlet pressure.

The equations presented can also be used to simulate heat and mass transfer in more complex geometries. This makes it possible to model the performance of hardware, and see how factors such as bed diameter and length impact performance. This ability helps in the optimization of hardware and processing. An example of this capability is shown in Figure 3. This figure shows the temperature profile inside an adsorbing cylindrical bed at 10 seconds, where the outside of the bed is held at room temperature (298 K). The bed temperature increases due to the heat of adsorption and heat is dissipated out through the walls of the bed, as well as convection of gas through the bed. Simulations such as these show how the thermal conductivity of the adsorbent, bed geometry, permeability (related to packing size and shape), and pressurization rate influence performance. Many of these parameters are difficult to experimentally measure. For instance, it is possible to measure a few temperatures inside and outside an adsorbing bed, but a simulation can show the temperature at all points inside a bed, and how the temperature profile develops over time. The model allows one to adjust parameters to optimize performance, before a design or process is committed to hardware. Of course, the model results need to be experimentally verified.

In our experience there is a synergy in combining mathematical simulation and experiment. One such example is a pressure swing process for enriching xenon developed using input from a simulation. An experimental device was constructed and tested, but did not perform as expected. It was hypothesized that the discrepancy may be due to higher dispersion in the experimental device compared to the simulation. The simulation was run with increased gas phase dispersion, confirming a negative impact on process performance. The simulation was then used along with permeability and dispersion correlations for packed beds to optimize the bed packing size for the process. Experimental results with the new packed beds were in line with the simulation results. The mathematical model helped identify what design parameters could be involved in the poorer than expected performance, and identify needed improvements. Further experiments verified the simulation results.

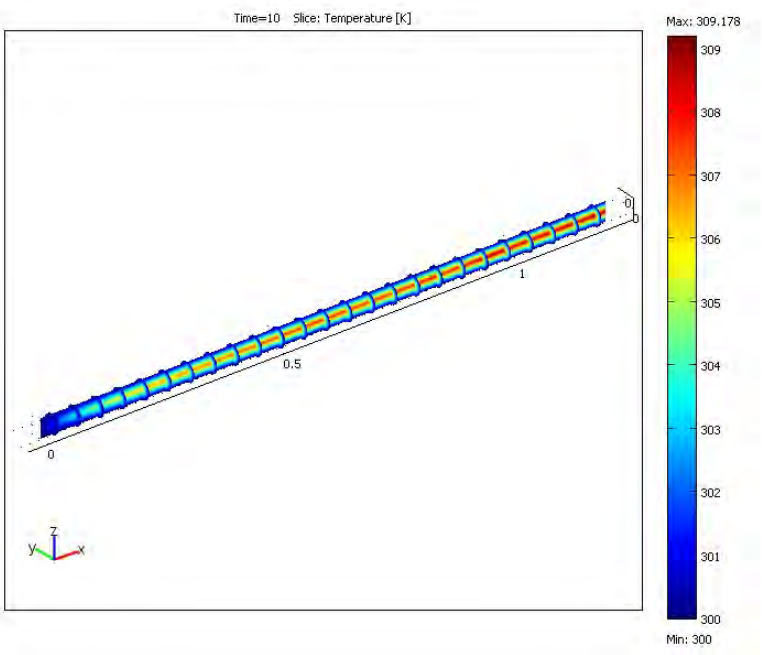

Figure 3. This simulation of a pressurizing activated carbon bed shows the temperature profile inside the bed at 10 seconds after pressurization begins.

CONCLUSIONS AND RECOMMENDATIONS

Mathematical models of gas phase adsorption processes have been developed and used to simulate operations used to capture and purify xenon from atmospheric air. The equations derived are general enough to model pressure swing, vacuum swing, temperature swing, and chromatographic processes. Simulation results have been used to verify experimental results, and develop improved hardware and operating procedures. The synergy between simulation and experiment has been an important factor in optimizing processes. Simulation allows better understanding of a process by allowing the visualization of variables not easy accessed experimentally such as the temperature profile, adsorbed phase concentration and gas phase concentration inside the bed. Experimental verification is essential to insure the physics in the model adequately describe reality. This comparison has increased our understanding of adsorption based processes and has been helpful in troubleshooting and improving separation techniques.

The model results are only as good as the parameters going into them. Good isotherm data for adsorbents is especially important. Some of this data can be found in the literature, but data for other adsorbents is desired. Mathematical models are important tools for assessing how a new adsorbent may improve a process. To use these tools adsorption isotherms and other physical adsorbent properties need to be measured. At present, the models have used activated charcoal and molecular sieve properties obtained from the literature. Our future work will include

extending the number of adsorbents that can be modeled. This will require obtaining samples of promising adsorbents and experimentally measuring the adsorption and physical properties of these materials. Numerical simulation with an increased library of materials will be used to identify improved techniques and optimize hardware for processing radioxenon from atmospheric air. The goal of this work is to develop improved collection processes for the next generation international radioxenon systems.

ACKNOWLEDGEMENTS

We would like to acknowledge Dr. Carlos Fraga for his isotherm measurements, Dr. Randy Kirkham for his help setting up and operating experimental pressure swing systems, and the rest of Jim Hayes' gas processing group for their support and insight into adsorption based gas processing.

REFERENCES

Bowyer. T. W., K. H. Abel, C. W. Hubbard, M. E. Panisko, P. L. Reeder, R. C. Thompson, and R. A. Warner (1999). Field testing of collection and measurement of radioxenon for the Comprehensive Test-Ban-Treaty, *J. Radioanal. Nucl. Chem.* 204: 109–122.

Ringbom, A., T. Larson, A. Axson, K. Elmgren, and C. Johansson (2003). SAUNA-a system for automatic sampling, processing, and analysis of radioactive xenon, *Nuclear Instruments and Methods in Physics Research A.* 508: 542–553

Yang, R. T. (1997) Gas Separation by Adsorption Processes. London: Imperial College Press.

Farooq, S and D.M. Ruthven (1991). Numerical simulation of a kinetically controlled pressure swing adsorption bulk separation process based on a diffusion model, *Chemical Engineering Science* 46: 2213–2224.

Farooq. S., M.N. Rathor, and K. Hidajat (1993). A predictive model for a kinetically controlled pressure swing adsorption separation process, *Chemical Engineering Science* 48: 4129–4141.

ASSEMBLY AND INITIAL RESULTS: AN ULTRA-LOW-BACKGROUND GERMANIUM CRYSTAL ARRAY FOR HIGH EFFICIENCY AND COINCIDENCE MEASUREMENTS

Martin E. Keillor, Craig E. Aalseth, Anthony R. Day, James E. Fast, Eric W. Hoppe, Brian J. Hyronimus, Todd W. Hossbach, Harry S. Miley, and Allen Seifert

Pacific Northwest National Laboratory

Sponsored by the National Nuclear Security Administration

Award No. DE-AC05-RLO1830/Pl07-RNLABS-NDD02

ABSTRACT

Treaty verification, environmental surveillance, and physics experiments continue to require increased sensitivity for detecting and quantifying radionuclides of interest using gamma-ray spectrometry. This can be accomplished by establishing high detection efficiency and reducing instrument backgrounds. A current effort for increased sensitivity in high resolution gamma spectroscopy will produce an intrinsic germanium (HPGe) array designed for high detection efficiency, ultra-low-background performance, and useful coincidence efficiencies. The system design is optimized to accommodate filter paper samples, e.g., samples collected by the Radionuclide Aerosol Sampler/Analyzer (RASA). The system will provide high sensitivity for weak collections on atmospheric filter samples, as well as offering the potential to gather additional information from more active filters using gamma cascade coincidence detection. The instrument will also be capable of making advances in low-dose neutron activation analysis. The first of two ultra-low-background vacuum cryostats has been assembled, with a second in progress. Traditional methods for constructing ultra-low-background detectors were followed, including use of materials known to be low in radioactive contaminants, use of ultra pure reagents, clean room assembly, etc. The cryostat is constructed mainly from copper electroformed into near-final geometry at Pacific Northwest National Laboratory (PNNL). Details of the detector assembly, vacuum tests, and test measurement results are presented.

OBJECTIVES

Two ultra-low-background cryostats are currently under construction for the NA-22 funded "Radionuclide Laboratories" (RN Labs) project. The design and performance expectations for this instrument have been discussed previously (Keillor et al, 2008 and 2009). Each cryostat will house seven high-purity germanium crystals (HPGe). We are building these cryostats from a limited set of materials that are known to have very low levels of radioactive impurities. The vast majority of each cryostat is made from pure copper (< 1μBq/kg, see Aalseth et al., 2009) electroformed into near-final geometry at PNNL under class 1000 clean room conditions.

The RN Labs instrument is designed to take advantage of low background performance, high detection efficiency, and γ-γ coincidence signatures to provide unprecedented gamma spectroscopy sensitivity. The project is focused on improving gamma analysis capabilities for Nuclear Detonation Detection (NDD) applications, e.g., nuclear treaty monitoring. The instrument also has the potential for basic nuclear physics research. For example, the potential for this detector to measure the half-life of predicted rare decay modes of ^{130}Te is being investigated. In addition, we have also built and tested a large area multi-wire proportional counter (MWPC) active anti-cosmic detector (Soplata et al, 2009). An active anti-cosmic system is a crucial component to allow the instrument to achieve high sensitivities for NDD measurements.

RESEARCH ACCOMPLISHED

This paper details the acceptance testing of HPGe crystals refurbished by Princeton Gamma Tech (PGT) and crystals purchased new from Canberra Semiconductor. It also provides an update on the current status of copper electroforming for the project. The results of initial tests with plastic scintillator anti-cosmic detectors are briefly discussed, as are the design and testing of analog signal processing electronics. Finally, results of vacuum testing for the first cryostat are covered.

Initial Germanium Crystal Testing

HPGe crystals were obtained from both PGT and Canberra Semiconductor for use in the RN Labs instrument. The crystals are nominally 63-mm-diameter and 70-mm-height semi-coaxial P-type detectors with a guard "ditch" surrounding the central bore hole. The fragile contact is protected by gold plating at the entrance of the bore hole. Eight HPGe crystals available from a previous project (Kazkaz et al., 2003) were available for use on the RN Labs research. A contract was arranged with PGT to refurbish these eight crystals. All eight of these crystals were received, tested, and removed from the shipping cryostats. The agreement with PGT did not include an energy-resolution specification for these refurbished crystals, so acceptance was based on the results of an I-V curve measurement. Figure 1 is an example of a typical I-V curve for these PGT crystals. The crystals were stored in a nitrogen dry box for various periods of time (up to ~1 year) after initial testing and then moved to vacuum storage. The crystals are currently in vacuum storage awaiting installation in one of the RN Labs cryostats.

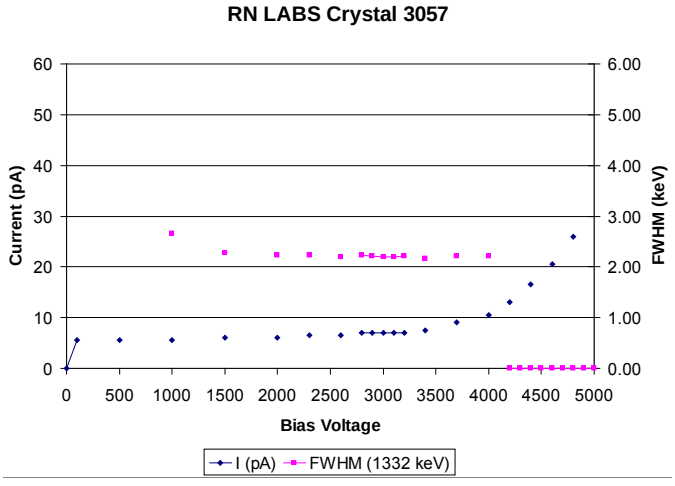

Figure 1. I-V Curve for One of the HPGe Crystals Refurbished by PGT. Energy resolution at 1332 keV is also plotted.

An initial shipment of four new crystals from Canberra Semiconductor was tested against factory specifications. After testing, the first of these crystals was removed from its shipping cryostat. Upon removal, we noted that (1) excessive amounts of indium were used on the crystal surface (inconsistent with a low background detector (Figure 2) and (2) the "pogo pin" style of signal contact was used. This latter point made the crystals unsuitable for use in RN Labs, both due to indium at the bottom of the central bore hole and the lack of protective gold plating at the entrance to the bore hole (required for the wire-loop style contact). These features were not consistent with the order specifications, so all four detectors were returned to Canberra for repair. This issue delayed the receipt of the final eight crystals, however Canberra recognized the discrepancy and has returned the original 4 crystals, along with two additional crystals. These detectors have all performed very well in acceptance testing (Figure 3). The eight PGT and six Canberra crystals give us a full complement of 14; the two final crystals due in from Canberra will give us spares in the event that trouble arises with any of the crystals during or after installation in the array.

Figure 2. HPGe Crystal Received from Canberra. The large indium patch is the silver colored material at the top of the image. The end of the "pogo pin" contact rod is visible inside the bore hole, and the visible end of the bore hole is not plated with gold.

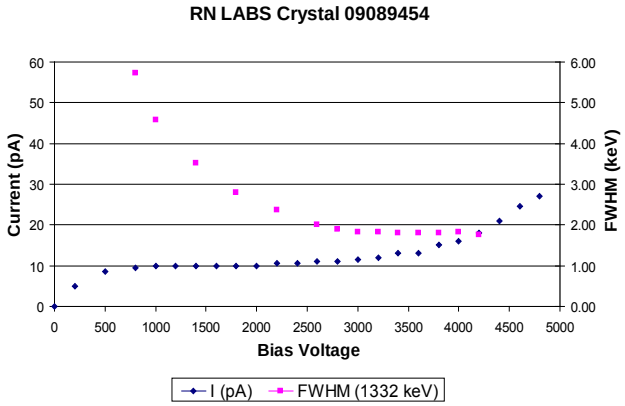

Figure 3. I-V curve typical of the Canberra crystals. The energy resolution at 1332 keV is also plotted.

Electroforming Update

In general, electroforming parts for RN Labs has proceeded smoothly, and the vast majority of parts have been successfully completed. Figure 4 shows nearly all of the copper parts required for the first cryostat, along with the electroformed cross arm and cold finger for the second cryostat (still on mandrels in this image).

Unfortunately, we have experienced difficulty in electroforming three specific large copper parts necessary for the project. The affected parts are the infrared radiation (IR) shields and the domed entrance window. The IR shields are very thin parts that take a matter of a few days to electroform, so we anticipate that there is sufficient time to resolve the issues discussed below and complete these parts. The entrance window is a much more challenging part, both due to its geometry and its thickness. This part will take ~ two to three months to electroform so that completing the thin entrance window within FY09 depends upon rapid resolution of poor copper nucleation and adhesion issues, or upon developing an alternative solution.

Obtaining proper copper nucleation and adhesion to the stainless steel mandrels is essential to proper growth of the part. Figure 5 displays two separate attempts to electroform an entrance window and an attempt at one of the IR shields. These parts all suffered from poor nucleation so that the resulting copper had significant holes. Holes are not acceptable for either the entrance window (which must hold vacuum) or the IR shields (which must prevent infrared radiation from striking the HPGe crystals). We are in the process of determining the source of these issues.

Additives employed in typical electrochemical manufacturing processes aid in the development of nucleation. However, to obtain the greatest purity copper possible, we do not use additives since it has been established that these materials and even inert particles such as alumina (from abrasives used for surface preparation) can be incorporated in the growing copper matrix during electrodeposition.

To determine the nucleation and growth mechanisms at play under the electrodeposition conditions used, various copper samples were analyzed via scanning electron microscopy (SEM) with electron backscatter diffraction (EBSD) to determine their microstructure, including grain size and orientation. Secondary ionization mass spectrometry (SIMS) and laser ablation inductively coupled plasma mass spectrometry (LA-ICP-MS) were also performed to determine relative surface concentrations of impurities and to map impurity localization on the copper surface.

Figure 4. Completed parts for the first cryostat of the RN Labs HPGe array.

Figure 5. Copper Nucleation Problems. Large electroformed parts that have suffered nucleation issues, resulting in numerous holes in the copper.

For SEM and SIMS analysis, samples were mounted in epoxy for metallographic polishing and given a series of successively finer-grit mechanical polishing steps using diamond grits with a final polish of colloidal silica. For LA-ICP-MS, electroplated copper samples were etched in 3% H_2O_2/1% H_2SO_4.

All of the samples showed a very fine grain size at the interior surface directly in contact with the mandrel (Figure 6). After a few hundred microns, this tended to transition to a larger elongated grain structure that often had a strong texture. For some samples, the texture continued to refine itself out to the edge of the sample, producing very large, highly oriented grains (Figure 7).

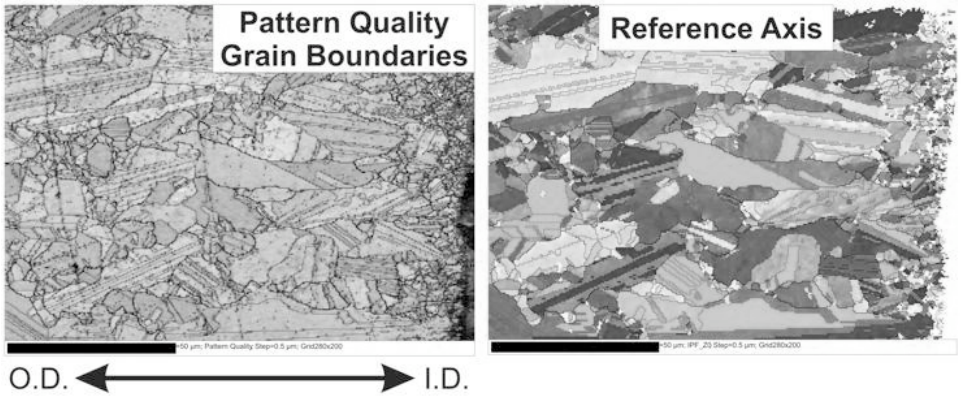

Figure 6. SEM image showing transition of the copper grain structure.

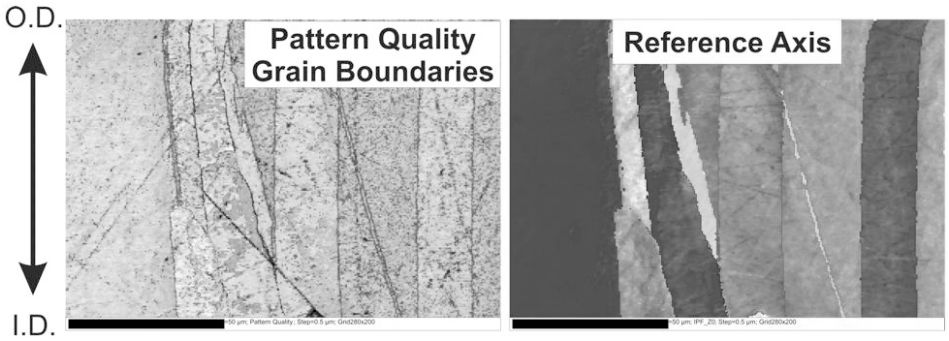

Figure 7. SEM image showing large, oriented grain structure.

These data provide evidence for instantaneous nucleation and highly selective grain growth during the electrodeposition process. Further work is needed to distinguish between nucleation and growth patterns and the effects of self-annealing or recrystallization.

The solution to the difficulties encountered in electroplating these large parts is to provide more controlled surface conditions that favor uniform nucleation on the stainless steel mandrels. Electropolishing, an electrochemical cleaning process, is being aggressively investigated to resolve the problem. Chemical etching is another possible solution that is also being tested.

We are also investigating alternative plating geometries that would be quicker to produce. Figure 8 shows an alternative entrance window geometry that would allow plating of the entrance window separate from the thicker plate surrounding the window. In this geometry, the window will be electroformed as a 6” diameter part, then e-beam welded into the heavier plate. We are pursuing this alternative in parallel with plating the part as a single unit.

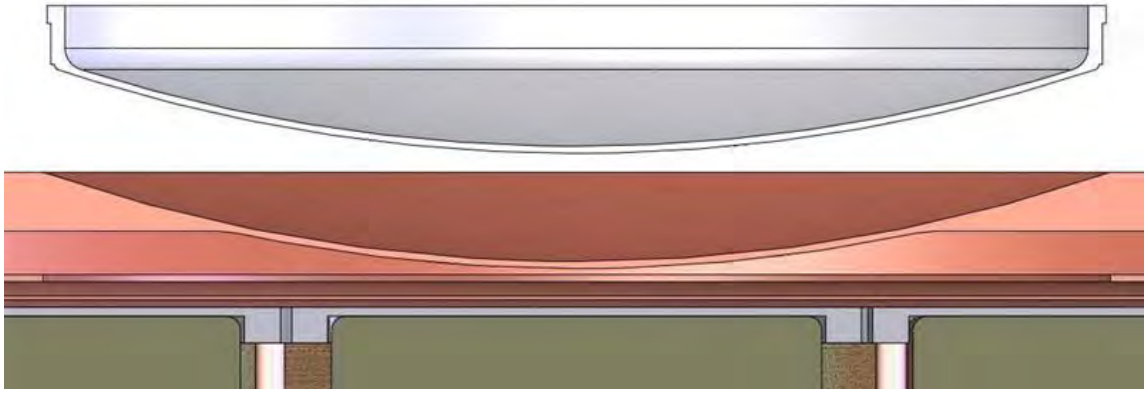

Figure 8. Alternative plating geometry for entrance window. The upper part of the figure shows an entrance window plated on a 6 inch mandrel. This window will then be e-beam welded into the annular plate. This geometry is less likely to suffer from the nucleation issues we have experienced with the larger 11 inch mandrel.

Anti-cosmic Scintillator Testing

An important part of the overall background performance of the RN Labs instrument is suppression of cosmic-ray backgrounds. Tests have been performed with plastic scintillator cosmic-ray detectors, and a design for an effective active cosmic-ray veto system for RN Labs has been prepared. The results of these initial laboratory tests indicate that two inch thick scintillating plastic panels will provide acceptable cosmic-ray identification while remaining relatively insensitive to external gamma-ray backgrounds (Figure 9). Based on the results of these tests, scintillator paddles for active anti-cosmic shielding have been designed and ordered.

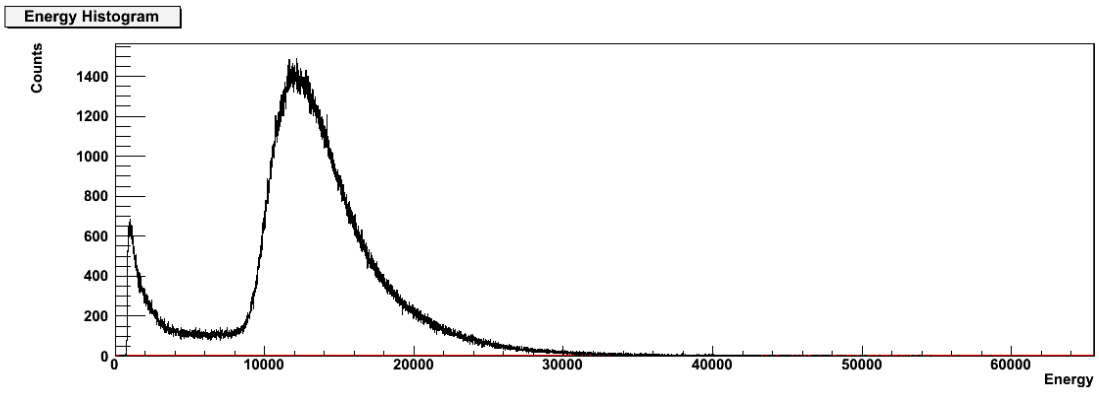

Figure 9. Muon peak in plastic anti-cosmic detector. This figure shows the muon through-peak in a two inch thick plastic scintillator. This spectrum is from "tagged" muons, in other words events observed in two independent scintillators at the same time. Energy is in ADC channel units. The rising continuum at the low energy end is caused by coincident detection of scattered gamma-rays; we anticipate good separation between gamma-rays and muons, as displayed in this spectrum.

Electronics Testing

Another critical part of the RN Labs array is the amplification and analog signal path for the very small electrical signals that are produced in the HPGe crystals as a result of radiation interactions. A sensitive front-end amplifier made with radiopure materials has been designed and tested, along with a low-background signal cable design.

Final production of the front-end amplifiers for RN Labs has not been completed, but 16 research prototypes have been prepared to support initial instrument testing. These custom PNNL components will be combined with a semi-custom commercial preamplifier (BridgePort Instruments) for the final signal conditioning before output signals are digitized for further analysis. Tests with the first revision of the semi-custom preamplifiers are now complete, and several small design revisions were identified to provide better (lower) noise performance. Revised prototypes are expected to be available on time for integration into the RN Labs instrument. A parallel research path using commercial off-the-shelf preamplifiers has also been pursued to reduce project risk and has proven to provide the necessary performance for RN Labs should the revised semi-custom solution not meet expectations.

Vacuum Testing of Cryostat #1

The vacuum boundary of cryostat #1 has been assembled for vacuum testing. This assembly includes the main body of the cryostat, the cross arm, and the service body (Figure 10). The main body of the cryostat, in this test configuration, requires three seals around the circumference of the chamber. Each seal is ~ 36 inches long. In the final configuration of the cryostat, the plate containing the entrance window will be e-beam welded to the corresponding cylinder, eliminating one of these three seals. Several smaller seals are located on the service body, including the cross arm-to-service body connection, the pump-out port plate, a blank plate, and the service body-to-Dewar connection. The vacuum integrity of welds was tested: e-beam welds on each end of the cross arm, welds on the service body, and a laser weld test for the 50-pin feed-through on the service body. Thunderline Z high-voltage feedthroughs were cemented into the service body with Torr Seal, and these seals were also checked for vacuum leaks.

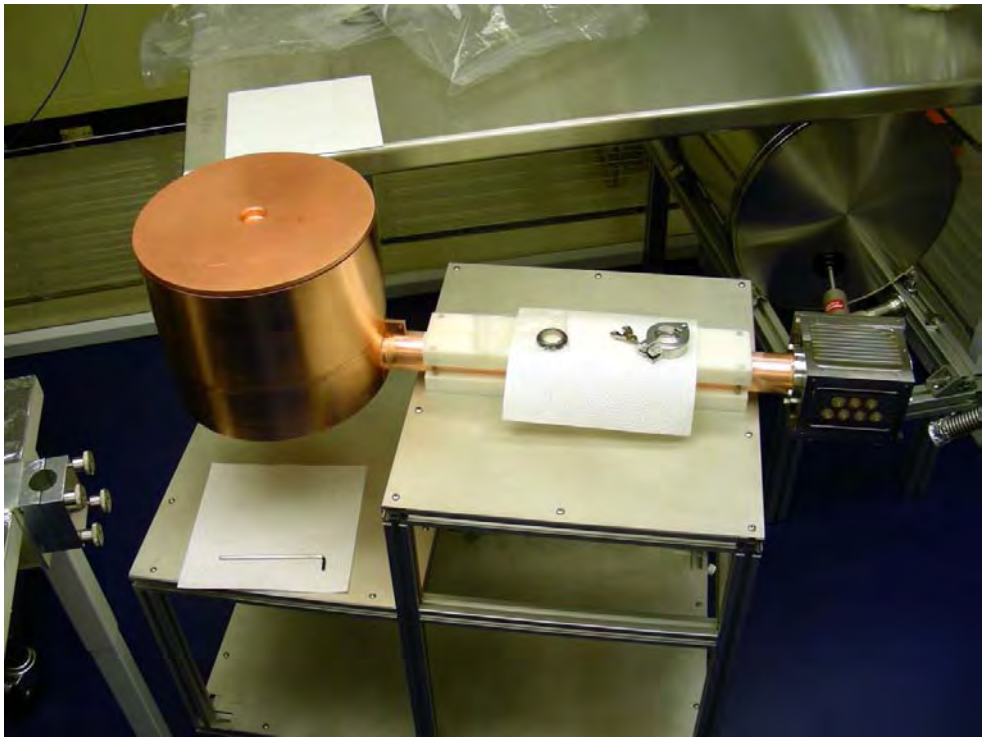

Figure 10. Vacuum testing of the first RN Labs cryostat. The top plate in this image is a test piece; production of a large, thin entrance window for the cryostat is one of the more challenging aspects of the cryostat production.

The large-diameter seals are created by pressing indium wire into step features on the mating surfaces. Due to the ~11.5” diameter of the cryostat, we have found it necessary to use 0.060” diameter wire. Use of small diameter wire is highly desirable due to the natural radioactivity of indium; the 0.060” diameter is larger than we had hoped for, however is consistent with typical manufacturer recommendations for this size vessel. The 0.49 MeV beta endpoint of ^{115}In is high enough that some bremsstrahlung contribution from the seals is likely; this will be modeled in a

Monte Carlo simulation in the near future. If it is found that the indium will contribute a significant contribution to the low energy continuum, an alternative metal seal will be investigated.

During leak testing of the cryostat and electrical service body, we were initially unable to achieve the seal for the bottom plate. It appears that the "hoop" warped slightly during e-beam welds of the cross arm and cross arm gussets. A steel form of the correct diameter was machined and pressed into the hoop, correcting the out-of-round condition and allowing the seal to be achieved. Subsequently, the cryostat seals have been leak tested and found to perform at better than 1.0E-10 mb-liter/sec.

The leak testing process also revealed one pin-hole through the electroformed copper material. This hole was found in the large, open ended cylinder forming the side walls of the cryostat. This copper material is 0.125" thick, thus it was somewhat surprising to find a pin-hole (although not unprecedented!). This vacuum leak was successfully repaired with the application of a very small amount of Vacseal to the exterior of the part. The entire copper cryostat was then enclosed in a plastic bag; helium was added to the bag and the leak check response was below 1.0E-10 mb-liter/sec.

Leak testing of the cross arm and service body revealed no response to helium at any of the welds, nor at any of the o-ring seals on the service body. Leaks were observed at three of the high voltage (HV) feedthroughs. These three feedthroughs were accidentally bent when the service body was assembled (see Figure 11); the service body was turned onto the side containing the HV feedthroughs, bending three pins. These three pins were subsequently straightened; however, it is now apparent that the seals between the pins and ceramic insulators were compromised. These feedthroughs will be replaced. We have also fabricated a temporary cover to prevent recurrence of damaged HV feedthroughs.

Figure 11. HV feedthrough pins. Three pins were bent when the service body was accidentally placed with this side down. Leak testing has shown that the vacuum integrity of these feedthroughs was compromised, and they will be replaced. A temporary cover was fabricated to prevent recurrence.

CONCLUSIONS AND RECOMMENDATIONS

We are progressing rapidly toward construction of the first RN Labs seven crystal array. The vacuum jacket of the first cryostat has been assembled and successfully passed stringent leak testing. Preparations for thermal tests of the Dewar/cold-finger/cold-plate combination are in progress. After successful thermal performance is confirmed, the first half of the array will be populated with HPGe crystals. Preparation of the second cryostat is following shortly behind the first.

Unanticipated challenges with electroforming have delayed the schedule for production of three of the electroformed parts. We expect to resolve these problems with plenty of time to complete the IR shields for the system during FY09. The delays are more problematic for the entrance window because of the long period of time required for it to be electroformed. We have completed a new design for this part, and it is currently being electroformed. In the interim, the existing oxygen-free high-conductivity copper test piece will allow us to proceed with assembly and testing of the first array.

REFERENCES

Aalseth, C. E., O. T. Farmer, J. E. Fast, E. W. Hoppe, T. W. Hossbach, J. D. Kephart, K. E. Litke, M. Liezers, H. S. Miley, E. E. Mintzer, and J. S. Reeves, *Nucl. Inst. & Meth A*, 2009 (submitted).

Kazkaz, K., C. E. Aalseth, T. W. Hossbach, V. M. Gehman, J. D. Kephart, and H. S. Miley (2003). 2003 IEEE Nuclear Science Symposium Conference Record, 2003, V. 1, 87–91.

Keillor, M. E., C.E. Aalseth, A. R. Day, J. E. Fast, E. W. Hoppe, B. J. Hyronimus, T. W. Hossbach, H. S. Miley, A. Seifert, and G. A. Warren (2008). Design and construction of an ultra-low-background 14 Germanium crystal array for high efficiency and coincidence measurements, in *Proceedings of the 30th Monitoring Research Review: Ground-Based Nuclear Explosion Monitoring Technologies*, LA-UR-08-05261, Vol. 2, pp. 778–786.

Keillor, M. E., C.E. Aalseth, A. R. Day, J. E. Fast, E. W. Hoppe, B. J. Hyronimus, T. W. Hossbach, H. S. Miley, and A. Seifert (2009). *J. Radioan. Nuc. Chem*. (in press), 10.1007/s10967-009-0248-7. http://www.springerlink.com/openurl.asp?genre=article&id=doi:10.1007/s10967-009-0248-7

Soplata, A. and M. E. Keillor (2009). In preparation for submission to the DOE Journal of Undergraduate Research.

IMPROVING GERMANIUM DETECTOR RESOLUTION AND RELIABILITY

Gregory N. Martin[1], Changkun Xie[1], K. Michael Yocum[1], James F. Colaresi[1], and Harry S. Miley[2]

CANBERRA Industries, Inc.[1] and Pacific Northwest National Laboratory[2]

Sponsored by the National Nuclear Security Administration

Award No. DE-AC52-08NA28650
Proposal No. BAA08-10

ABSTRACT

High purity germanium (HPGe) detectors used in radionuclide assay systems such as Radionuclide Aerosol Sampler/Analyzer (RASA) systems must be in operation for long periods of time without maintenance. To meet this critical need, HPGe detector reliability and resolution performance should be improved through the development of new surface passivation techniques to passivate and protect the surface area between electrical contacts. The goal of this research is to develop two surface film techniques for passivating detector intercontact surfaces: wet chemically grown oxide (WCO) films and sputtered films. Each film will be characterized to determine its surface chemistry and coating quality. Qualification will be carried out by examining the detector performance under various experimental conditions.

To evaluate these new passivation techniques, a set of baseline data was established for HPGe detectors using the current standard silicon oxide passivation technique at CANBERRA. Two 100% relative efficiency Standard Electrode Germanium (SEGe) detectors were fabricated using silicon oxide as the passivant. The performance evaluation of the standard SEGe detectors has been completed. This evaluation included CANBERRA standard product test procedures, as well as the temperature dependence test, rapid thermal cycle test, and pump/bake test. These data will be referenced to evaluate the performance for detectors fabricated using new passivation techniques.

A unique WCO technique has been developed to grow native germanium oxides directly on HPGe detector surfaces. The oxides are expected to be good passivants for detector interelectrode surfaces because they natively saturate the dangling bonds and result in a low density of surface charge states. These states lead to surface channels which can be a direct cause of leakage current. A HPGe detector was successfully fabricated using the WCO technique. Test results demonstrate the effectiveness of the new WCO technique in producing SEGe detectors with the following important characteristics: very low leakage current, excellent noise properties, ability to withstand thermal stress and maintain physical integrity, and stability over a long period of operation. Further evaluation of the natively grown oxides using the new WCO technique is underway on larger SEGe detectors to analyze the inherent noise contribution from the surface and compare it with that of silicon oxide surfaces. A sputtered film technique will be developed later in this project.

OBJECTIVES

HPGe detectors used in radionuclide assay systems such as RASA systems must operate unattended for long periods of time. Current commercially available germanium detectors using the SiOx (x~2) passivation technique have shown excellent performance and reliability which fulfill the needs of most laboratory applications in radiation detection and measurement. However, for remote systems such as RASA designed for nuclear detonation detection and analysis, this critical need for long term operation requires research to further improve detector performance and reliability.

One of the key factors affecting germanium detector performance and reliability is the passivation of the intercontact area between the electrical contacts. The contacts create the diode structure and, under reverse bias, collect charge produced by photon interactions with the germanium material. The intercontact surface has to be passivated to electrically separate the detector contacts. A successful intercontact surface must allow very little reverse leakage current under the stress of as much as 5000 volts of reverse bias. In addition, the intercontact surface must create little electrical noise. Both surface leakage noise and passivant dielectric noise must remain low to achieve excellent signal-to-noise ratio. For germanium detectors, a SiOx coating created by a well-controlled evaporation of silicon monoxide is traditionally used to passivate germanium surfaces (Holland, 1970). Although SiOx passivations have been an acceptable solution for many commercial detector products, some variability in reverse leakage currents as well as field-line distortion effects associated with intercontact surfaces have been observed. Some deleterious surface effects resulting from the evaporated silicon monoxide on germanium have been previously investigated (Dinger, 1976). The existence of weak-field regions and surface channels responsible for leakage current results from both fast electronic states (germanium surface) and slow electronic states (SiOx film, adsorbed gases) (Bardeen et al., 1956). On the other hand, uncontrolled growth of native oxide layers, which contain empty states with energy levels in the germanium band gap, can cause accretion of electrons on the germanium surface region, creating an inversion layer in P-type material or an accumulation layer in N-type material. Such effects in P-type germanium have been described by Brown (1953). Therefore, in order to further improve detector resolution and reliability, development of passivation techniques by improving or replacing the present SiOx passivation has become necessary to achieve a more consistently neutral intercontact surface (Martin et al., 2008).

The objective of this research is to investigate new passivation techniques that provide better resolution and reliability of performance than the current standard SiOx technique used in the detector industry. First, a set of baseline data for HPGe detectors will be established using the standard CANBERRA SiOx passivation technique. Two 100% SEGe detectors are to be manufactured following CANBERRA detector fabrication procedures. The performance of the SEGe detectors is to be evaluated, using CANBERRA product test procedures, as well as the temperature dependence test, rapid thermal cycle test, and pump/bake test. Then, two surface film techniques for passivating HPGe detector surfaces will be developed: WCO films and sputtered films. Future studies will focus on characterizing each coating to determine its surface chemistry and physical integrity. Passivation qualities and their inherent noise contribution to the overall system noise will be evaluated and analyzed under various experimental conditions. The goals in developing novel surface passivation techniques are the reduction of both surface leakage noise and passivant dielectric noise resulting in improved detector performance and reliability.

RESEARCH ACCOMPLISHED

Standard detector fabrication and characterization

Two 100% SEGe detectors were fabricated following the standard CANBERRA detector fabrication procedures to evaluate the detector resolution and reliability using the SiOx coating for passivating the intercontact surface. Two P-type HPGe coaxial detectors with a net active impurity level below 1.7×10^{10} cm^{-3} and a mass of ~2200 grams as the starting raw material were used as evaluation devices.

The detectors were manufactured by first mechanically polishing the surfaces to remove gross damage left from the machining process. Microscopic damage was removed by a concentrated nitric acid based etch followed by water and methanol rinses. Then the devices were immersed into a bath of lithium salt for lithium diffusion at an elevated temperature. A Li-doped layer with thickness approximately 1 mm was formed to achieve an n^+ electrical contact for each device. Following the diffusion, a drilled core hole was implanted with high energy boron to form a p^+

electrical contact. The intercontact surface was limited to a small annular region near the core by a unique wrap-around lithium contact. After the intercontact area was etched to ensure the surface was microscopically free of mechanical damage or scratches, the detectors were transferred into a vacuum chamber. A SiOx passivation film of 100–200 nm thickness was then deposited by physical vapor deposition (PVD).

Figure 1. CANBERRA CP-5® cryocooler, integrated electronics and cryostat. The two fabricated SEGe detectors were individually installed in the cryostat for evaluation of the detector performance.

Preliminary tests to check the detectors' leakage current showed that both detectors had very low leakage current under high voltage bias up to 5000 volts. This demonstrated the electrical contacts were non-injecting, and the passivated intercontact area did not exhibit high leakage current due to surface channel formation. As shown in Figure 1, the two fabricated detectors were mounted individually into a CANBERRA Cryo-Pulse® 5 (CP-5) cryocooler to cool the detector and preamplifier first stage field effect transistor. The CP-5 is an electrically powered cryocooler designed for use with germanium and silicon radiation detectors. It utilizes a pulse-tube cooler, which is a relatively new concept in cryogenic coolers as compared to Stirling coolers. The cooler not only keeps the detector at low temperatures down to 80 K without the need of liquid nitrogen, which requires daily maintenance, but also allows control of the detector temperature to study detector performance at different temperatures.

Resolution results of both detectors (serial numbers P3488B and P3489B) are shown in Table 1. Depletion voltage was determined by monitoring the peak shift of ^{57}Co energies when the detector is under increasing reverse biases. Above the depletion voltage of 4000 volts, the resolution represented by full width at half maximum (FWHM) and full width at tenth maximum (FWTM) for ^{60}Co (1.33 MeV) and ^{57}Co (122 keV) sources was measured. The electronic noise was also measured using a precision pulser. It was observed that increasing the reverse bias deteriorates the detector resolution, which is largely due to the increase of leakage current. The relative efficiencies of both detectors are around 100% which is in agreement with their dimensions and mass.

Table 1. Detector resolution for the two SEGe detectors fabricated with the standard SiOx passivation technique.

Detector number	Bias (kV)	RESOLUTION FWHM/FWTM (keV) ^{60}Co		^{57}Co		Pulser	P/C	Eff.
P3488B	4.0	2.05	3.93	1.29	2.33	1.18	72.9	110%
P3489B	4.0	2.12	4.08	1.27	2.35	1.18	73.1	99%

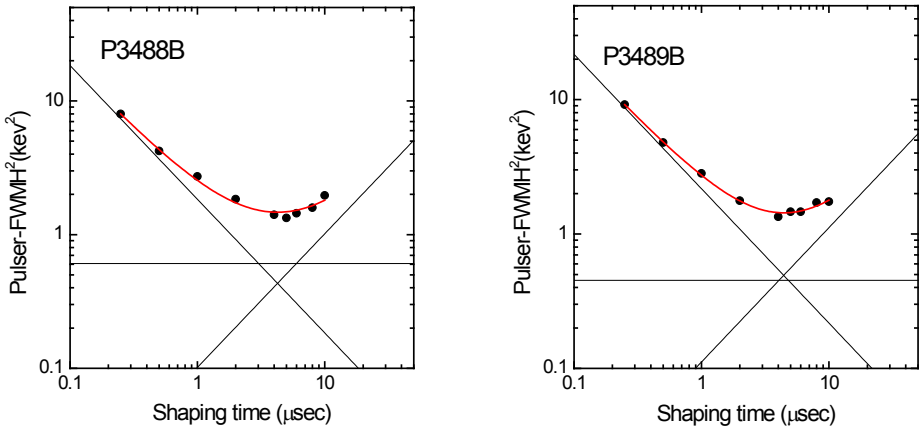

Figure 2. Noise analysis of the detectors (P3988B and P3989B) fabricated with the standard SiOx passivation technique. Detector noise (i.e., pulser FWHM) as a function of shaping time was measured at 93 K.

In radiation measurement it is a major challenge to reduce noise and amplify signal strength, thus improving the signal-to-noise ratio. The sources of electronic noise in spectroscopic measurements fall into three main categories: series noise, parallel noise, and *1/f* noise. The contribution of series noise as a fraction of the signal related to detector capacitance is inversely proportional to the square root of shaping time as defined by a semi-Gaussian shaper. Parallel noise associated with detector leakage current is proportional to the square root of shaping time. The *1/f* noise component is independent of shaping time (Knoll, 1999). The term *1/f* noise is a category of noise believed to be caused by many factors including electrical contacts and the intercontact surfaces. Although the physical mechanism of *1/f* noise is still an open question, an inversion layer across the intercontact surface can introduce a profound contribution to the *1/f* noise, which may affect detector resolution and introduce surface leakage current as well.

The above analysis gives us the three components of contribution to the noise FWHM. Squaring the measured pulser FWHM gives:

$$FWHM^2 = \frac{k_1}{\tau} + k_2\tau + k_3 \qquad (1)$$

Where k_1 k_2 and k_3 are fitting parameters, and τ is shaping time. The pulser FWHM was measured as a function of shaping time from 0.25 to 10 μsec for both detectors at several temperatures. The data (pulser-FWHM^2) were fitted with the above equation from a nonlinear least squares method. Typical results are shown in Figure 2 for both detectors at 93 K. The three components of the noise are also individually shown in the figure as direct lines. It was found that both detectors had similar noise characteristics at 93 K. The fitted parameters k_1, k_2 and k_3 were 1.83, 0.10, and 0.61, respectively, for the detector P3488B; the fitted k_1, k_2 and k_3 are 2.17, 0.11, and 0.45, respectively, for the detector P3489B. Therefore, the k_3 parameters representing the *1/f* noise contribution were between 0.4 and 0.6 for the detectors fabricated with the standard SiOx passivation technique. Further increase of detector temperature above 98 K would increase the detector leakage current, which would significantly increase the contribution of parallel noise, while the series noise and *1/f* noise would remain nearly unchanged.

To test the SiOx passivation method for ruggedness, three tests were performed on the detectors: rapid thermal cycles, atmospheric aging, and pump and bake. Plots of leakage current as a function of reverse bias at each stage of

tests for one of the devices P3489B are shown in Figure 3. The other device (P3488B) showed similar results but to a different degree. For the experiments, the device P3489B was removed from its CP-5 vacuum cryostat and five rapid thermal cycles from 87 K to approximately 300 K were performed. The leakage current worsened moderately after the five thermal cycles increased from 0.07 nA to 0.15 nA at 4000 volts reverse bias, suggesting that the passivant may be damaged to some extent by the fast thermal expansion and contraction processes. Then, the device was placed in a nitrogen-purged cabinet at room temperature for four weeks of aging. The subsequent measurement showed that the leakage current increased to a large degree, which made the device reinstallation for further resolution tests meaningless. Therefore, the intercontact surface was etched with nitric acid-based solution to remove the old passivant, and then repassivated using the standard technique to form a new SiOx film. The subsequent leakage measurement showed that the leakage current improved significantly. The device was then mounted into a CANBERRA 7500SL Slimline vacuum cryostat for a pump and bake test. After an overnight pump and bake at 100°C, the leakage current remained unchanged. These results led us to the conclusion that the standard SiOx passivant is susceptible to atmospheric treatments or contamination, which may cause an increase of leakage current through a surface channel, while the thermal variation for the device kept in a vacuum cryostat does not affect the performance of the device.

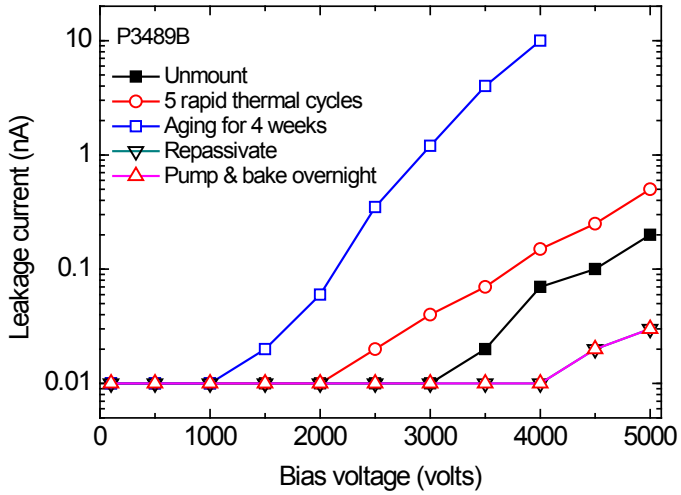

Figure 3. Leakage current as a function of reverse bias under various conditions investigating the passivation stability of the standard SiOx film.

Development of WCO passivation technique

In the next major phase of the research, the goal was to grow a native oxide passivation film directly on HPGe detector surfaces. By definition a native oxide is directly grown on the germanium surface with a resulting decrease in the density of unconsumed germanium bonds (dangling bonds) which act as charge generation sites. However, the literature suggests that the GeO_2 compound can have two phases, one is solvable in water/HF and the other is not (Valyocsik, 1967). It is imperative that only water-insolvable GeO_2 film is grown on detector surfaces so that it may withstand the environmental conditions in surrounding air. The newly developed WCO technique uses a hydrofluoric acid/oxidizer mixed solution. A miniscule amount of oxidizer is added into a large amount of HF acid solution, so that only a water/HF insoluble GeO_2 phase is grown on Ge surfaces, and the water soluble phase is prevented. Several experimental efforts were made to optimize the growth conditions for the native GeO_2 passivation. Different oxidizers with different concentrations mixed with HF acid at room temperature were considered and tested as the reaction solution. By optimizing the growth conditions, a technique was developed to produce natively grown passivation films on HPGe.

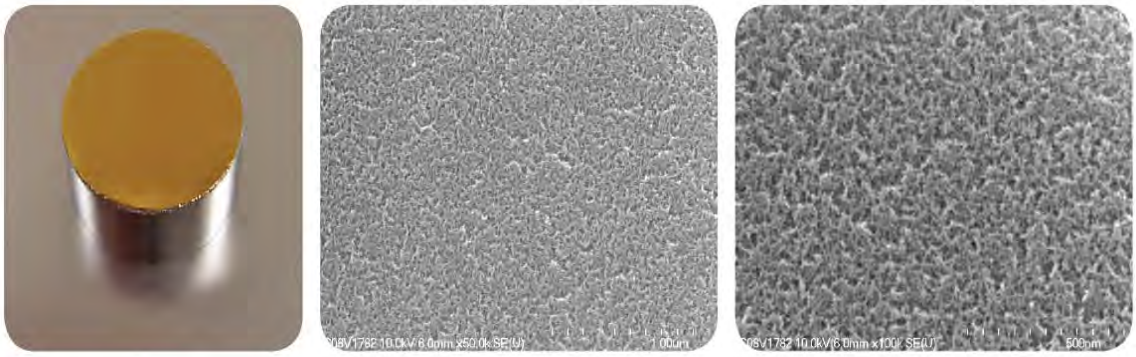

Figure 4. Passivation film grown on HPGe and its scanning electron micrographs. The film was created by a mixture of hydrofluoric acid and a specially formulated oxidizer using the WCO technique.

Figure 4 shows pictures of a germanium oxide film with gold-like color, which was natively grown on a HPGe surface by the WCO technique. The SEM (scanning electron microscope) topography of the film surface in high resolution demonstrates that the oxide films produced by this WCO technique are very dense, homogenous, and for the most part, defect-free. No porous or fissure structures are found on the passivated surface, which greatly helps to make detector surfaces impervious to ambient atmospheric conditions. Note that the naturally occurring native germanium oxide which results from exposure to atmospheric moisture and oxygen is an inferior compound, which is not only highly non-stoichiometric, but also contains the soluble form of oxides. Therefore, it is very important to form a stoichiometric and defect-free oxide film on HPGe surfaces for passivation. To determine the composition and chemistry of the oxide film, an X-ray Photoemission Spectroscopy (XPS) analysis was performed on the oxide samples. Figure 5 shows the spectrum of XPS analysis of the film. The deconvolution of the peak profile indicates two compositions in the data including metallic germanium and its oxides. The chemical shift of the oxide peak in binding energy with respect to the metallic germanium peak suggests that the oxide film is in the stoichiometric form of GeO_2. As the growth solution used contains a large amount of HF, the grown oxides are the stable HF-insoluable GeO_2 phase. The growth of the stable GeO_2 film suggests that the oxide film is of high quality and the expectation is that a successful detector passivation can be fabricated by the new WCO technique.

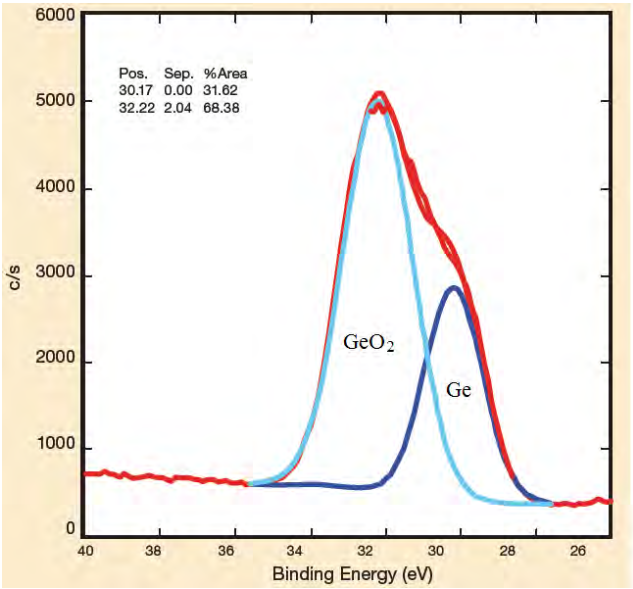

Figure 5. XPS analysis of the film indicating that the germanium oxide is of the form GeO_2 which is the desired stoichiometry.

Figure 6. Fabricated detector with the WCO passivant (left), and assembled cryostat and electronics (right).

To investigate the performance of the GeO_2 passivant, a small SEGe detector was fabricated utilizing the WCO technique. A P-type HPGe crystal (detector No. P84648A) with a net impurity level below 2.00×10^{10} cm^{-3} and a mass of 547 grams was used as the starting raw material for the detector fabrication. After fabricating the inner boron implanted contact and outer lithium diffused contact, the intercontact surface in the groove region was exposed to the pre-mixed WCO growth solution. The groove presented a gold-colored GeO_2 film, which is insoluble in water and hydrofluoric acid as previously discussed. The completed detector along with the assembled electronics and a CANBERRA 7500SL dipstick cryostat where the detector is installed is shown in Figure 6. Figure 7 shows its leakage current and capacitance as a function of applied reverse bias for the detector at 87 K. The leakage current is below 0.01 nA and remains flat to the range of 5000 volts. The depletion voltage is about 2300 volts, and the capacitance after full depletion is about 23 pF. This result suggests that the new WCO passivation technique provides very low leakage current. The WCO passivant not only successfully blocks the current flow between electrical contacts, but also generates few or no surface states in the band gap which may otherwise facilitate thermal excitation of electrons and induce leakage current.

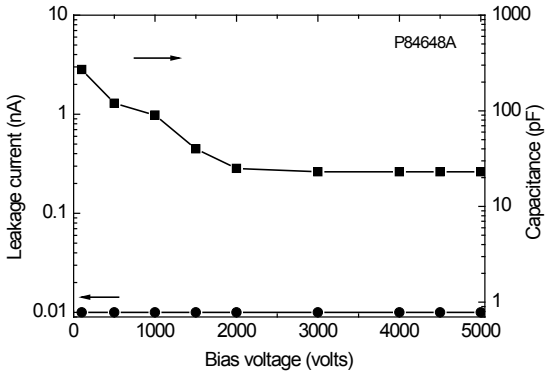

Figure 7. Leakage current and capacitance as a function of applied reverse bias from 0 to 5000 volts. The detector was fabricated with the developed WCO technique.

Table 2 shows test results of the detector (P84648A). Increasing the reverse bias appears to slightly improve the detector resolution. At 3 kV bias, the FWHM of ^{60}Co at 1.33 MeV and ^{57}Co at 122 keV are 1.72 keV and 0.88 keV, respectively. At 3 kV bias, the detector efficiency is 21%, which is a little less than what expected based on the dimensional size of the detector. This is possibly due to the thick Li layer (0.62 mm) for this detector, which decreases its active volume and thus slightly reduces its efficiency. Following the above tests, the detector was warmed up to room temperature for a thermal cycle test. This was done to determine the performance stability in case of a power failure or long term storage at room temperature. As shown in Table 3, the detector maintained its good resolution after the thermal cycle. To check stability under prolonged operation, a 4.5 kV bias was applied overnight. Subsequent measurements with ^{57}Co and ^{60}Co sources indicated that the detector resolution did not deteriorate, suggesting that the detector performance can remain stable for extended periods of operation. Finally,

the detector was kept in the cryostat at room temperature for three months; the next measurement at 3 kV reverse bias showed that the detector's resolution and efficiency was maintained.

Table 2. Detector evaluation for detector P84648A passivated with the developed WCO technique.

Bias (kV)	RESOLUTION (keV) ^{60}Co	^{57}Co	Pulser	P/C	Eff.
2.5	1.76 3.23	0.88 1.64	0.73	52.9	20.9
3.0	1.72 3.19	0.88 1.64	0.73	53.9	21.0
3.5	1.73 3.14	0.85 1.56	0.73	54.0	22.2
4.0	1.74 3.18				22.4
4.5	1.71 3.16				22.5
5.0	1.71 3.14				22.4
Thermal cycle					
4.5	1.70 3.13	0.88 1.62	0.76	55.3	23.9
Overnight bias					
4.5	1.71 3.16	0.90 1.68			
After 3 months for the cryostat at room temperature,					
3.0	1.74 3.24	0.89 1.72	0.77		21.6

With a collimated ^{241}Am source, measurements were made of the FWHM of the 59.5 keV peak at different locations along the side of the detector from the grooved end to its front window. The measured resolution at the back edge of the detector where the intercontact surface with the WCO passivant is located was comparable to those at other positions of the body and its front window. This result further confirms that there were no significant surface charge states or a surface inversion layer around the back end which would otherwise affect the device's charge collection process deteriorating the resolution.

In Figure 8, the results of a noise analysis of the detector are plotted. The FWHM of the pulser was measured for the detector as a function of shaping time from 0.5 to 10 μsec. The data were fitted with Equation (1) via a nonlinear least-squares method. The fitted parameters k_1, k_2 and k_3 were 0.65, 0.02, and 0.37, respectively. As discussed previously, these values of k_1, k_2 and k_3 are associated with detector's capacitance noise, leakage noise, and *1/f* noise, respectively. Although this detector has a relatively low capacitance because of its size as compared to the above two large (100% relative efficiency) detectors fabricated with the standard SiOx passivation technique, it showed a very low leakage current noise and *1/f* noise as well.

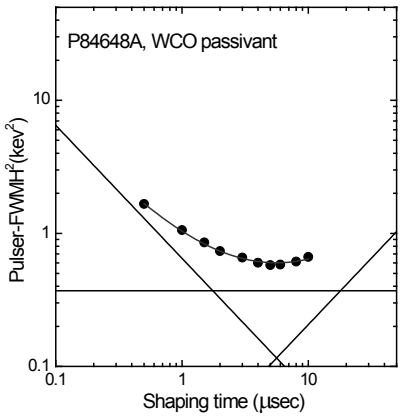

Figure 8. Noise analysis of the detector passivated with the WCO technique.

CONCLUSIONS AND RECOMMENDATIONS

Two large-volume (~100% relative efficiency) SEGe detectors have been manufactured using the standard SiOx passivation technique. Baseline data were established by characterizing each detector using CANBERRA standard test procedures which include the measurement of relative efficiency, electronic noise analysis, and resolution measurements. Testing the current SiOx method for ruggedness with thermal cycles, atmospheric aging, and pump/bake, suggest that SiOx film is subject to atmospheric treatments and contamination which may introduce a surface channel that results in increased leakage current. Since the surface characteristics of high-purity germanium can be influenced both by the net impurity concentration at the intercontact surface and by local crystallography, the same detector elements will be used throughout our development efforts to ensure a solid comparison between passivation techniques.

For a preliminary investigation, a small germanium detector (~25% relative efficiency) was successfully fabricated with the newly developed WCO passivation technique. The detector showed very low leakage current and excellent noise properties. The advantage of the WCO technique is that it involves only a wet-chemical process which is convenient for large-scale production. Immediately after etching the intercontact surface, an in-situ growth of the passivation film is easily accomplished with the surface exposed to a pre-mixed growth solution. Since the device is not transferred from wet to dry chemistry, this greatly minimizes the surface exposure to most contaminants including water vapor, oxygen, and organics that are present in the surrounding environment, Natively-grown oxides produce fewer electrical surface states by taking advantage of the natural tendency of native oxides to passivate the dangling bonds of surfaces better than other materials. The test results demonstrated the effectiveness of the new WCO technique in producing SEGe detectors with the following important characteristics: very low leakage current, excellent noise properties, ability to withstand thermal expansion and contraction while maintaining physical and chemical properties, maintenance of good measurement resolution after thermal cycling, stability over a long period of operation, and stability over long time storage in cryostat.

Current ongoing efforts in the research include studying the device performance for the WCO passivation technique being applied to large volume (~100 % relative efficiency) SEGe detectors. The compatibility of the WCO passivation with the geometry and configuration of electrical contacts will also be investigated to achieve the best detector performance and reliability. Further evaluation of the natively grown oxides using the WCO technique will be to analyze the inherent noise contribution from the surface and compare it with that of SiOx passivated surfaces. The sputtered film techniques will be developed later in this project.

ACKNOWLEDGEMENTS

Our thanks to Audrey Carmichael for proofreading project reports and James Bradbury for program management during this research.

REFERENCES

Bardeen, J., R. E. Coovert, S. R. Morrison, J. R. Schrieffer, and R. Sun (1956). Surface conductance and the field effect on germanium, *Phys. Rev.* 104: 47–51.

Brown, W. L. (1953). N-type surface conductivity on p-type germanium, *Phys. Rev.* 91: 518–527.

Dinger, R. J. (1976). Effect of evaporated dielectric materials on the surface of high purity germanium, *J. Electrochem. Soc.: Solid-State Science and Technology* 123: 1398–1404.

Holland, L. (1970). Vacuum Deposition of Thin Films, Chapman & Hall Ltd.

Martin, G. N., K. M. Yocum, J. F. Colaresi, and H. S. Miley (2008). Improving germanium detector resolution and reliability, in *Proceedings of the 30th Monitoring Research Review: Ground-Based Nuclear Explosion Monitoring Technologies*, LA-UR-0805261, Vol. 2, pp. 787–792.

Valyocsik, E. W. (1967). Germanium oxidation in nitric acid, *J. Electrochem. Soc.: Solid-State Science,* 114: 176–181.

IMPROVEMENT IN GE DETECTOR COOLING

K. Michael Yocum[1], James F. Colaresi[1], and Harry S. Miley[2]

CANBERRA Industries, Inc.[1] and Pacific Northwest National Laboratory[2]

Sponsored by the National Nuclear Security Administration

Award No. DE-AC52-08NA28656
Proposal No. BAA08-09

ABSTRACT

High Purity Germanium (HPGe) detectors used by the International Monitoring System (IMS) radionuclide monitoring stations rely on Joule-Thomson (J-T) mechanical coolers to provide the low temperature necessary for operation. Cryocooler advances in recent years have resulted in commercial availability of Stirling and Pulse Tube mechanically cooled detector systems with improved reliability and enhanced HPGe detector performance. The Cryo-Cycle™ and Cryo-Pulse® 5 are two such commercial products being modified and evaluated for application in IMS Radionuclide Aerosol Sampler/Analyzer (RASA) systems.

An ultra-high vacuum (UHV) remote detector chamber and service body assembly has been designed and modeled for use on the Cryo-Pulse® 5. The cryostat assembly incorporates a low cross section metal end cap seal, UHV compatible hardware and joining techniques, permanent vacuum getter pumps, and low thermal loss UHV vibration isolation mounts between the enclosure and the internal cryogenic components. Most of the components have been fabricated. Assembly and testing are underway. Characterization of a UHV pumping station has been performed using residual gas analysis in preparation for evaluating the long-term vacuum reliability of cryostat components and assemblies. Nitrogen gas extractors have been researched for integration with the Cryo-Cycle™ hybrid cooler. Cryostat vacuum improvements on the Cryo-Cycle™ will be derived from the same sealing technologies used on the Cryo-Pulse® 5. Details of the investigations and progress are presented.

OBJECTIVES

The RASA Mark 4 and implementation of the Cryo-Pulse® 5 and Cryo-Cycle™ have been described previously by Yocum et al., (2008). The RASA was developed at the Pacific Northwest National Laboratory (PNNL) in the 1990s to meet Comprehensive Nuclear-Test-Ban Treaty (CTBT) requirements for aerosol radionuclide measurements, as described by Bowyer et al. (1997) and Miley et al. (1998). All of the aerosol samplers currently operating in the field rely on Joule-Thomson direct coolers. Performance of Joule-Thomson (J-T) coolers for this application has been problematic. The standard Cryo-Pulse®5 has been under evaluation and operating successfully in a prototype RASA system for over one year at Patrick AFB, Florida.

The goal of this project is to investigate improvements in HPGe detector cooling technology for use in the RASA Mark 4. Explorations in both direct pulse tube cooling and hybrid Stirling cooling are being conducted. CANBERRA Cryo-Pulse® 5 and the Cryo-Cycle™ standard products provide the starting point for this effort. UHV technology is being incorporated in the Cryo-Pulse®5 to improve long-term vacuum integrity and to eliminate the possibility of partial thermal cycles. This includes the use of metal vacuum seals, onboard vacuum pumps such as non-evaporable getter (NEG) pumps and ion pumps, and use of UHV compatible internal components.

A nitrogen gas generator is being integrated with the Cryo-Cycle™ cooler to maintain a seven-day cooling buffer in the event of a power outage. An uninterruptible power supply (UPS) will be used with both direct and hybrid coolers to provide redundant protection against partial thermal cycles and to keep the Cryo-Pulse® 5 at operating temperature in the event of short power outages.

Task 1

Task I is the design and testing of improvements to direct cooling with the Cryo-Pulse® 5. These comprise improvements in cryostat end cap sealing, incorporation of UHV technology in the detector cryostat construction, and investigation of vibration isolation/mitigation techniques.

Task 2

Task II is the integration of a nitrogen gas generator with the hybrid Cryo-Cycle™ cooler and evaluation for use in a RASA Mark 4 system. Operation with an uninterruptible power supply (UPS) will also be investigated.

RESEARCH ACCOMPLISHED

Both of the tasks have in common a detector chamber that must interface with the RASA assembly. The detector chamber designed is 4.0” in diameter and capable of containing an HPGe detector element of greater than 120% relative efficiency. The RASA incorporates a background radiation shield with a fixed 4.3” diameter penetration into which the detector chamber is inserted. To maximize the effectiveness of the shield, the design employs a remote detector chamber (RDC). This allows the shield penetration to be effectively closed by addition of a lead back-shield directly behind the RDC after the detector chamber is inserted (i.e. no-stream-path design). The RDC back-shield in close proximity to the detector element attenuates the ambient radiation background and increases the sensitivity of the detector as compared to designs incorporating long end caps to reach inside the RASA shield. The detector chamber, vacuum cryostat, ion pump, NEG pump, pinch-off tube and mechanical cooler for the UHV Cryo-Pulse® 5 are assembled using demountable metal seals. These in combination with welded UHV electrical feedthroughs and a metal pinch-seal comprise the UHV vacuum envelope. An outline drawing for the UHV Cryo-Pulse® 5 is shown in Figure 1.

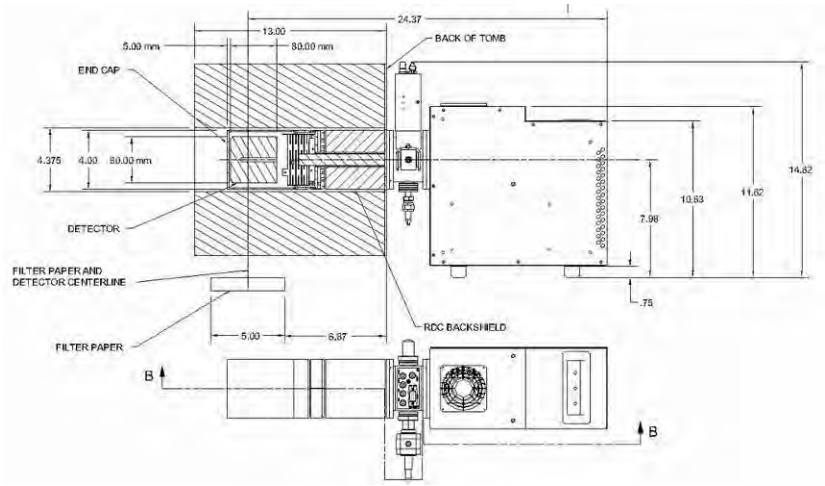

Figure 1. Outline drawing of the UHV Cryo-Pulse®5 inserted into the RASA cave.

End Cap Seal

The newly designed end cap incorporates a metal seal, is compatible with UHV, and has a slim profile to allow the maximum detector element diameter within the diameter of the end cap. The design was modeled using SolidWorks simulation software, COSMOS. It was optimized for parameters including deflection, preload, yield, flow, fatigue, and thermal response. The resultant seal assembly cross section (i.e., Detector Chamber Inner Radius minus Detector Chamber Outer radius) is 3.5 mm. This is accomplished using an indium seal flange design with a clamp fastener as shown conceptually in Figure 2. Extensive stress analyses were carried out on the end clamp fastener and indium seal to ensure the design would satisfy the vacuum integrity requirements.

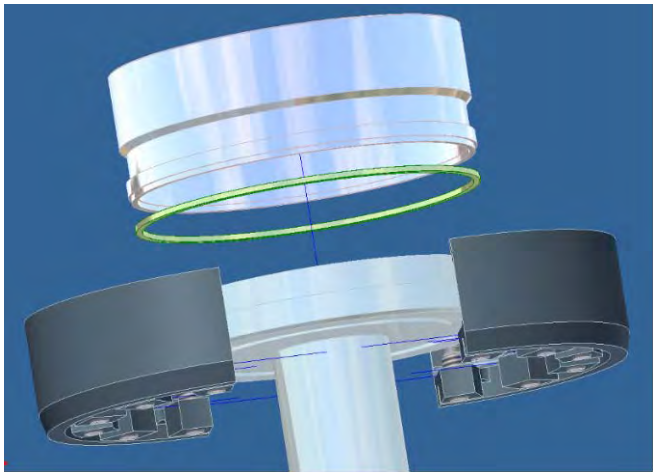

Figure 2. Concept drawing and fabricated RDC assembly, both with test end cap.

The assembly shown in Figure 2 was fabricated and tested for functionality. The test results were in good agreement with the modeling. The indium seal was assembled and tested multiple times for vacuum integrity and ease of assembly. The assembly was heated to 100°C and helium leak tested to $<10^{-9}$ atm. cc/sec. Seal leakage and permeability were tested using the helium bag test. While attached to the helium leak detector a plastic bag filled with helium was placed around the assembly. Helium was undetectable to a leak rate of $<10^{-9}$ atm. cc/sec. after 12 hours, which indicates there are no small leaks or areas with high permeability.

UHV Service Body

A flanged service body was designed and fabricated as shown conceptually in Figure 3. The service body connects the RDC assembly to the Cryo-Pulse® 5 vacuum housing and provides electrical feedthroughs to connect the preamplifier to the detector front-end. The service body flanges were designed to use Garlock's Helicoflex® delta seals. These seals are expensive and not reusable. Indium gasket material is used in the delta seal grooves during the prototype testing. UHV compatible feedthroughs from Solid Sealing Technology (SST) were welded to the side of the assembly. Mini-conflat flanges were welded on as shown to accommodate the ion pump, NEG pump, and pinch-off tube. The service body assembly was fabricated and tested for leak tightness in combination with the RDC assembly. In similar fashion to the RDC leak tests, the combined assembly was determined to be helium leak tight to $<10^{-9}$ atm. cc/sec. with low permeability.

Figure 3. Concept drawing and fabricated UHV service body.

A mock-up of the complete UHV Cryo-Pulse® 5 assembly is shown in Figure 4. The remaining parts of the vacuum enclosure to be fabricated are the vacuum housing inside the cabinet and the full-length aluminum end cap. The vacuum housing has been machined and is to be sent out for welding of the electrical feedthrough. The end cap is to be fabricated and welded.

Figure 4. Mock-up of the complete UHV Cryo-Pulse® 5 with test end cap.

Internal Supports

Materials and techniques to mechanically support the components inside the cryostat to provide an adequate cold path to the detector element were investigated. Axial and radial flexures were constructed from stainless steel for the mechanical supports. These components were modeled for thermal load and heat flux. The assembly was modeled to simulate stress and deflection under a 3G load as shown in Figure 5.

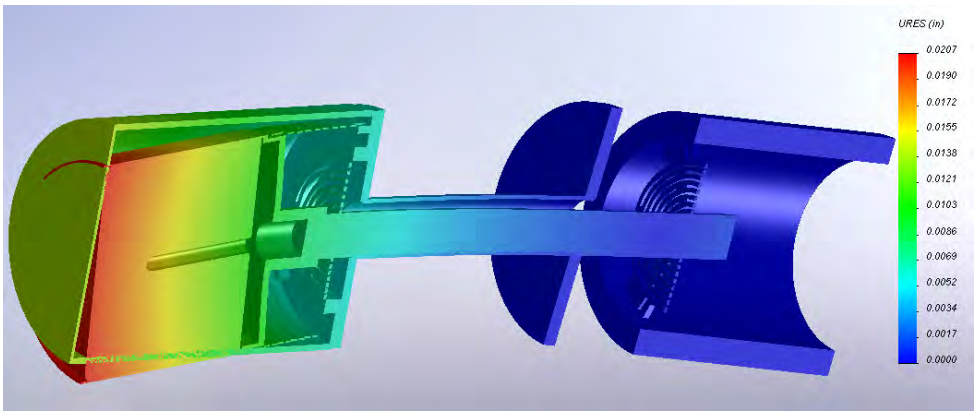

Figure 5. Deflection with a 2 kg detector mass under 3G load.

Modeling predicted a combined conductive heat load of < 0.75 watts for the three flexures required to support the detector and cold path components. Two of the flexures were tested and the heat loads predicted by modeling were confirmed. The third support will be tested after final assembly.

The vibration characteristics of the assembly in Figure 5 were simulated and the natural frequency and harmonics are listed in Table 1. The first harmonic is primarily axial direction.

TABLE 1. Vibration Characteristics of the Flexure System

Mode No.	Frequency (Rad/sec)	Frequency (Hz)	Period (Sec)
1	189.59	30.175	0.03314
2	305.34	48.596	0.020578
3	305.48	48.618	0.020568
4	865.78	137.79	0.007257
5	1019.7	162.29	0.006162

Residual Gas Analysis

The service body, RDC weldment, dummy end cap, ion pump, and pinch tube were assembled with all metal seals and tested for helium leak tightness on a UHV pumping station. The UHV pumping station is an all-metal seal, turbo-pumped system backed by an oil-free roughing pump. Base pressure of the system is in the low 10^{-10} torr range. Residual gas analysis (RGA) of the system after several days of mild baking before and after adding the cryostat assembly reveals that the major residual gas constituent is hydrogen as shown in Figure 6. Hydrogen is to be expected since it dissolves in stainless steel during manufacture and diffuses out slowly at low temperatures. Heating for hours or days at temperatures in excess of 400°C can accelerate the diffusion as discussed by O'Hanlon (1989). The assembly is limited to a maximum temperature below 150°C because of the low melting point of the end cap indium seal. The apparent preponderance of hydrogen is exacerbated by the fact that lighter gases are pumped less efficiently by the turbo-pump. Fortunately, the NEG pump has an extremely high capacity of up to 20-30 torr-liters/g for hydrogen as discussed by Ferris (2002). Residual hydrogen in the UHV Cryo-Pulse® 5 vacuum enclosure is not expected to present a problem.

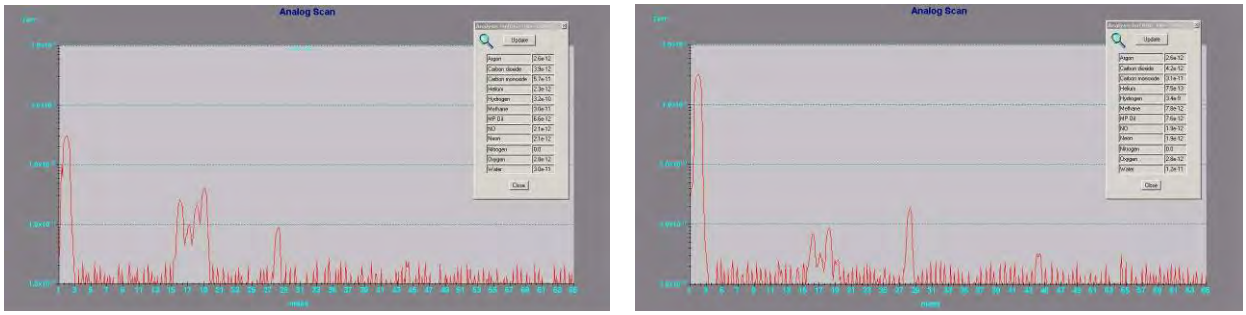

Before **After**

Figure 6. RGA of the UHV system before and after adding the UHV cryostat assembly.

Other reactive gases such as O_2, CO, CO_2, N, and H_2O will be adequately pumped by the NEG pump in the final cryostat assembly. Methane and light hydrocarbons, as well as inert gases, are not pumped by the NEG pump. An ion pump is included on the cryostat to pump noble gases, CH_4, and light hydrocarbons.

Vibration Mitigation

Vibration decreases the signal-to-noise ratio and degrades the performance of HPGe detectors. Noise induced by mechanical vibration is referred to as a microphonic response (MR). When a surface at potential V vibrates with respect to another surface at ground potential the capacitance between the 2 surfaces is modulated by a $\Delta C(t)$, inducing a charge ΔQ in the circuit. If this ΔQ is coupled to the input of the preamplifier, either through the detector capacitance or directly onto the detector signal path, it is integrated in the preamplifier along with the signal charge and is amplified in proportion. The effect of MR on the signal can be mitigated electronically by the band pass of the amplifier, baseline restoration, and by many other signal conditioning techniques both digital and analog. Mechanical techniques for reducing MR are vibration damping, vibration isolation, structural design to shift frequencies and reduce resonance, stiffening, etc. All of these elements must be balanced in the design of the UHV Cryo-Pulse® 5 system.

The compressor is a source of vibration that frequently gives rise to MR on Stirling and J-T electrical coolers. In the case of the Cryo-Pulse® 5, the compressor is driven by dual piston linear motors. Techniques have been developed by the cooler manufacturer, Thales Cryogenics, to control the pistons independently in order to actively reduce the overall system vibration. The cooler system typically consists of a pulse tube cooler, DSP micro-controller based drive electronics, and an accelerometer. Normally the accelerometer is mounted directly on the compressor. The control loop is shown schematically in Figure 7.

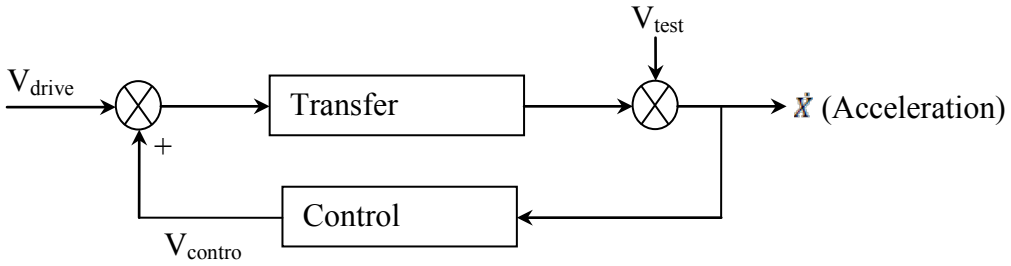

Figure 7. Schematic representation of the active noise cancellation control loop.

The linear compressor is driven by a sinusoidal drive voltage V_{drive}. The vibration control system uses a control algorithm that attempts to reduce the measured acceleration to zero by adjusting the drive parameters of one of the linear motors of the compressor. The transfer function G and the algorithm parameters are determined by measuring the initial uncontrolled acceleration and the acceleration after adding a known test voltage V_{test} to the drive voltage. This test voltage causes an imbalance and will change the vibration levels of the system. With the correct transfer

function and algorithm parameters in place, the drive voltage of one of the linear motors is continuously corrected with a control voltage, V_{contro}. This control voltage consists of not only the drive frequency with the required amplitude, but also of several of the harmonics of this drive frequency. In this way the drive frequency and its first harmonics (up to the first 15–20 harmonics) of this drive frequency can be reduced quite effectively. The control algorithm uses the transfer function G of the entire dynamic system. This means not only the dynamics of the cooler will be included in the transfer function determination, but also in the dynamics of the entire mounting structure. Application of this technique to a standard Cryo-Pulse® 5, similar in configuration to the UHV unit being developed, reduced the amplitude of the primary vibration at 50 Hz by a factor of 10 on the external surface of the detector chamber. Further refinement and testing is required to optimize and determine the benefit of this type of active vibration cancellation to overall detector performance.

Investigate Commercial Solutions to Nitrogen Gas Extraction from Air

An advantage of the Cryo-Cycle™ system over conventional cryocoolers is its hybrid operation; that is, the actual cooling of the detector is accomplished with liquid nitrogen (LN), rather than direct electrical cooling. The Cryo-Cycle™ system stores up to 22 liters of LN in a Dewar. Maintaining the Dewar as a closed system and continually reliquifying the boil-off gas with a Stirling a cooler eliminate losses due to boil-off. Nitrogen can be lost to the system during a power outage or through small leaks. In a remote application such as the RASA, LN is not available to replace any losses. Pairing the Cryo-Cycle™ with a nitrogen gas extractor to automatically re-charge the nitrogen solves this problem. A CANBERRA 7186 LN level monitor can be used to control the operation of the nitrogen gas extractor.

The research team met with two vendors of nitrogen gas extraction systems. OnSite Gas Systems manufactures pressure swing adsorption (PSA) systems while Parker Hannifin makes both PSA and membrane separation systems. OnSite did not offer systems small enough for this application. Several other vendors were researched. A summary of the findings is shown in Tables 2 and 3 below.

Table 2. PSA systems.

	Bora	**Bora**	**LNS gas**	**Parker**	**Dionex**
Model	750	1250	N2-SIROCCO-3A	LCMS 12-1	MSQ10la
Type	PSA	PSA	PSA	PSA	PSA
Price	$9,542.00	$11,132.00	$18,125.00		
Size (WxHxD)	9"x14"x17"	9"x14"x17"	19"x 25" x 32.8"	14"x35"x26"	17"x25"x16”
Weight	45 lbs	50 lbs	253 lbs	198 lbs	104 lbs
Noise	<48dB	<48dB	<60dB		
Purity	99.999%	99.995%	99.999%	99.50%	
Output	0.750 LPM	1.25 LPM	3 LPM	12 LPM	10 LPM
Service interval	4000 hrs -filters 8000 hrs compressor	4000 hrs -filters 8000hrs compressor	4000 hrs filter 24000hrs trained service		
Power Requirements	110/230V 50/60 Hz 820 W	110/230V 50/60 Hz 820 W	110/230V 50/60 Hz	110/230V 50/60 Hz	220V 50/60Hz 1 kW

Table 3. Membrane systems.

	Dionex	Chrysalis-LC-MS-Nitrogen	Parker
Model	msq18la-068126	M4 with pure gas option	NitroFlow Lab
Price		$18,093.00	$14,000.00
Size (WxHxD)	17" x 35" x 16"	12" x 27" x 35"	36” x 28” x 12”
Weight	90 lbs	204 lbs	204 lbs
Noise	59 dB	58 dB	<58 dB
Purity	99.5%	96 - 99.9%	99.5%
Output	18 LPM	8 LPM	17 LPM
Type	Membrane	Membrane	Membrane
Power requirements	230V 50/60Hz	110/230V 50/60Hz	230V 50Hz 1400 W

Both PSA and membrane nitrogen generator systems were explored. PSA systems use charcoal and sometimes zeolite molecular sieves to adsorb and exhaust oxygen during the pressure swing cycle. In membrane systems the incoming air passes through tubes where oxygen and water vapor permeate through the walls of the tubes leaving the nitrogen in the flow stream. Membrane systems offer advantages such as simplicity, low maintenance, and small footprint when compared to PSA systems. However, membrane filters generally do not reach the nitrogen purity levels of PSA systems without additional filters that increase complexity and maintenance requirements. Purity is a critical issue because the boiling point of liquid oxygen (LOX) is higher than that of LN. Under certain circumstance (e.g., a large gas leak) oxygen in the gas stream can lead to preferential collection of LOX in the Cryo-Cycle™ Dewar. Inclusion of oxygen monitors on the output of nitrogen gas generators is a common feature.

Both PSA and membrane systems require compressed air to operate so an air compressor is required for the RASA application. Size, reliability, power consumption, noise, and mechanical maintenance are important considerations. These requirements and other maintenance requirements for the nitrogen generator filters and mechanical systems are mitigated by the expectation that the normal duty cycle of the system will be short. Except in the event of unexpected gas leaks in the Cryo-Cycle™, degradation of the cryostat vacuum, power outages, or initial filling of the Dewar the services of the nitrogen generator may not be required for months or years at a time. Based on the investigation, a BORA 1250 will be purchased. The time required to initially fill the Dewar is expected to be 20–25 days. The detector should be usable 3–5 days after the filling process is begun. These times will be more accurately determined when the unit is tested.

CONCLUSIONS AND RECOMMENDATIONS

A small cross section indium end cap seal has been designed and tested. This seal can be used to improve the long-term vacuum integrity of both Cryo-Pulse® 5 and Cryo-Cycle™ based products. Other components of the UHV Cryo-Pulse® 5 vacuum enclosure including the RDC assembly, service body, and support flexures have been fabricated, assembled, and tested. RGA tests indicate there are no leaks in the vacuum enclosure parts fabricated and the outgassing rates and permeability are low. The Cryo-Pulse® 5 vacuum housing and end cap are in process. The next step is to completely assemble the vacuum enclosure and analyze the vacuum by RGA as the internal components are added. Investigation of the long-term integrity, cooling performance, and detector performance will be carried out after the assembly is complete.

The Cryo-Cycle™ investigation will continue with the purchase of a nitrogen generator followed by system integration and testing. Tests will be performed to characterize the overall performance. An improved cryostat will

be designed that makes use of the vacuum techniques developed for the UHV Cryo-Pulse® 5. These improvements include RDC with metal seal end cap, welded feedthroughs, and metal pinch seal.

ACKNOWLEDGEMENTS

Thanks go to the CANBERRA Detector R&D staff for their tireless effort and insightful investigations. It is with appreciation that we acknowledge the contributions of our vendors; Willem van de Groep, Thales Cryogenics, and Reuven Unger, SunPower. Thanks to George Rybicki, Patrick AFB for his hospitality and help with the mechanical details of the RASA Mark 4 and the application. And finally, thanks go to our sponsor the NNSA for providing us with the opportunity and means to pursue this work.

REFERENCES

Bowyer, S. M., H. S. Miley, R. C. Thompson, and C. W. Hubbard (1997). Automated particulate sampler for comprehensive-test-ban treaty verification (the DOE radionuclide sampler/analyzer), *IEEE Trans. Nuc. Sci.*, NS-44, 3: 551–556.

Ferris, M., (2002). NEG pumps magic in the vacuum chamber, *Vacuum Technology and Coating, August,* 52–59.

Miley, H. S., S. M. Bowyer, C. W. Hubbard, A. D. McKinnon, R. W. Perkins, R. C. Thompson, and R. A. Warner (1998). Automated aerosol sampling and analysis for the comprehensive-test-ban treaty, *IEEE Trans. Nuc. Sci.*, NS-45: 3, 1034–1039.

O'Hanlon, J. F. (1989). *A User's Guide to Vacuum Technology*, Hoboken: John Wiley and Sons.

Yocum, K. M., G. N. Martin, J. F. Colaresi, and H. S. Miley (2008). Improvements in Ge Detector Cooling, in *Proceedings of the 30th Monitoring Research Review: Ground-Based Nuclear Explosion Monitoring Technologies*, LA-UR-08-05261, Vol. 2, pp. 824–833.

Infrasound Monitoring

INFRASOUND AS A DEPTH DISCRIMINANT: CONSTRUCTION OF A UNIQUE DATASET AND PRELIMINARY ANALYSES

Stephen J. Arrowsmith[1], Hans E. Hartse[1], George E. Randall[1], and Steven R. Taylor[2]

Los Alamos National Laboratory[1] and Rocky Mountain Geophysics, LLC[2]

Sponsored by the National Nuclear Security Administration

Contract No. DE-AC52-06NA25396/LA09-Depth-NDD02

ABSTRACT

In ground-based nuclear explosion monitoring, the depth of an event is an important consideration for event identification. However, without a station near the epicenter, seismic depth determination of small, shallow events is difficult. A current capability for the identification of shallow sources is the presence of the seismic phase, Rg. However, Rg is often not observed seismically, as it is very sensitive to the details of the structure of the upper crust and is disrupted by horizontal changes in structure and topography. Infrasound signals can be generated by near-source pumping of the atmosphere from shallow sources. Therefore, an infrasound detection is generally an indicator of a shallow (or surface) source, and has the potential to be used as a surrogate for Rg. As a first step towards constructing an infrasonic depth discriminant, we are constructing a large dataset of shallow earthquakes and explosions with well-constrained depths and associated infrasound signals at multiple arrays. By correcting for the effects of stratospheric and thermospheric winds on infrasonic amplitudes, we are exploring a multiple linear regression approach for separating effects of depth, source mechanism, magnitude and distance (predictor variables) on observed infrasonic amplitudes (dependent variable). This empirical approach will be complemented by the development of physical models that tie with the observations. To highlight our approach, we focus on infrasonic and seismic observations from the Wells, Nevada earthquake sequence. We demonstrate the importance of separating epicentral and secondary infrasonic arrivals, and report on our preliminary findings.

OBJECTIVES

Our goal in this effort is to develop an infrasonic discriminant for event depth. The aim is to develop infrasonic amplitude corrections for various source, path, and receiver effects so that – if location, mechanism, and magnitude are known seismically – we can estimate the event depth for shallow events based on infrasonic constraints.

The two objectives for Year 1 of this project are as follows:

- **Compilation of a dataset of events.** As outlined below, we are compiling a unique dataset for tackling this problem.

- **Preliminary analysis of factors affecting infrasound detection.** We have begun assessing source effects (using earthquake sequences) and path effects (using ground-truth surface explosions). This component lays the foundation for our research objectives in Years 2 and 3.

RESEARCH ACCOMPLISHED

Compilation of a Dataset of Events

(a) Dataset Specifications

A major focus of the first year of this effort is the construction of an extensive dataset of infrasonic observations of surface explosions and earthquakes with well-constrained focal depths. In contrast with previous studies, we require a rigorous set of conditions to be met:

- **Each event must be recorded at >1 infrasound array.** The infrasound association problem is inherently non-unique for a single array due to the long window of possible arrival times and current limitations in predicting observed phases. In addition, as outlined below, a single array observation cannot reliably distinguish between *epicentral* and *secondary* infrasound. In order to robustly associate an infrasound signal with a particular physical mechanism, we require that the event be observed at multiple arrays.

- **Each event must have an accurate focal depth, magnitude, and mechanism.** It is important that we have accurate independently determined source parameters with associated uncertainties. Relying purely upon conventional seismic catalogs is insufficient due to the trade-off between origin-time and depth (unless a seismic station is located directly above the epicenter). Thus, we require either ground truth on surface explosions or detailed seismic modeling/relocation of event depths for earthquakes.

- **Each event must be associated with high-resolution atmospheric specifications.** As shown by Mutschlecner et al. (1999), winds can have a significant effect on infrasonic amplitudes. Thus, we require 3D atmospheric wind specifications for each event in order to correct for this effect. As part of this effort, we propose to extend the Mutschlecner et al. (1999) relationship, which utilized only winds between 45 and 55 km altitude.

Given these tight constraints, we are focusing on regional-scale infrasound networks in Korea and the Western U.S., where we are able to obtain high-quality ground truth and the array density is sufficient to obtain multiple observations of seismo-acoustic events (Figures 1 and 2). Figure 1 shows the locations of events in the Western U.S. from which we are currently searching for infrasound signals at >1 array. We are also measuring infrasonic amplitudes of ground-truth events in the Korean peninsula (Figure 2).

(b) Semi-automatic amplitude measurement

For each event, we compute the amplitudes of the associated infrasound arrivals using a semi-automated procedure. Infrasonic amplitudes have conventionally been measured as a simple peak-to-peak amplitude of the maximum phase in the signal (e.g., Mutschlecner and Whitaker, 2005). However, this measurement has two limitations: (1) it cannot be reliably measured automatically, and (2) it is less representative of the average strength of a signal than the root mean square (RMS) power (e.g., Brown et al., 2008). For the dataset we are acquiring in this project, it is impractical to pick amplitudes for every arrival, and it is therefore essential that we can reliably measure amplitudes in a semi-automated way. We utilize an algorithm (illustrated in Figure 3) that is similar to a multiple frequency band, automatic amplitude measurement algorithm developed for seismic data (Hartse et al., 1997), with two modifications:

- Since we cannot reliably predict the arrival time of the signal, we compute the time of the maximum waveform envelope within the possible arrival window (computed using a group velocity range from 0.34 km/s to 0.22

km/s), and apply an additional check that the backazimuth of the beam at that time must be consistent with the known great-circle backazimuth for the event.

- A subset of automated amplitude measurements are checked manually in order to validate that the algorithm is working effectively.

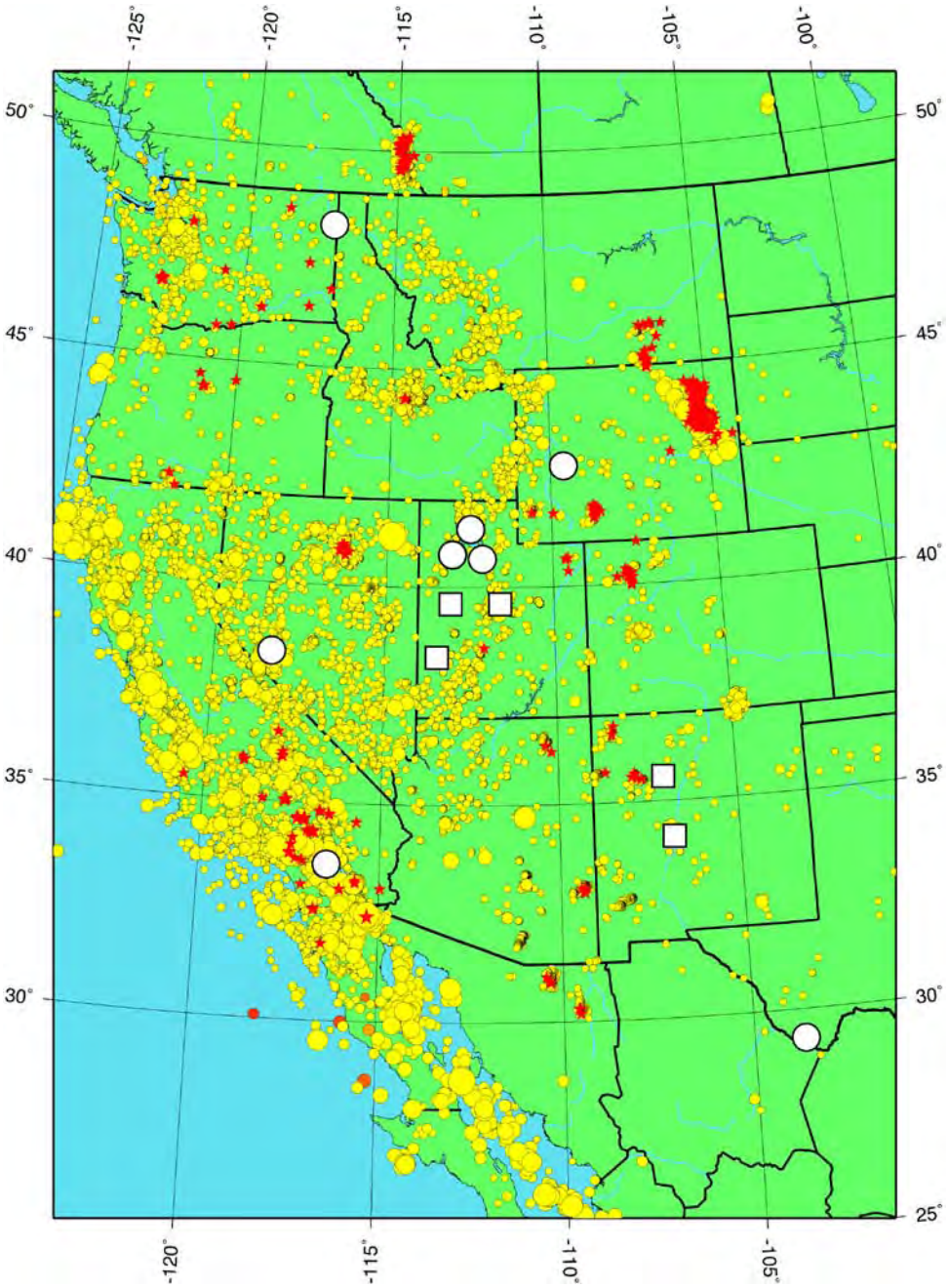

Figure 1. Summary of earthquakes (yellow circles) and mining explosions (red stars) in the Western U.S. between 2004 and 2009. Mining explosions are obtained from the USGS mining event list (however, some reported earthquakes may actually be mining explosions). Operational infrasound arrays are shown as white circles, while approximate locations of planned arrays are shown as white squares (we will leverage data from these arrays for Years 2 and 3 of this project).

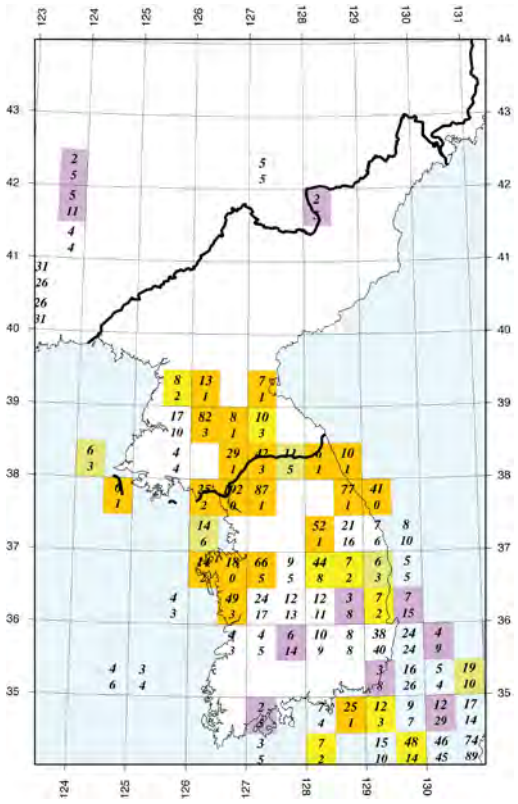

Figure 2. Summary of Korean dataset (largely consisting of ground-truth seismo-acoustic events from surface explosions, courtesy of Il-Young Che at KIGAM). Each 0.5°×0.5° bin lists the number of daytime events (top number) and nighttime events (bottom number) and is color-coded by the percentage of daytime versus nighttime events. Regions with large percentages of manmade events are shaded orange and yellow.

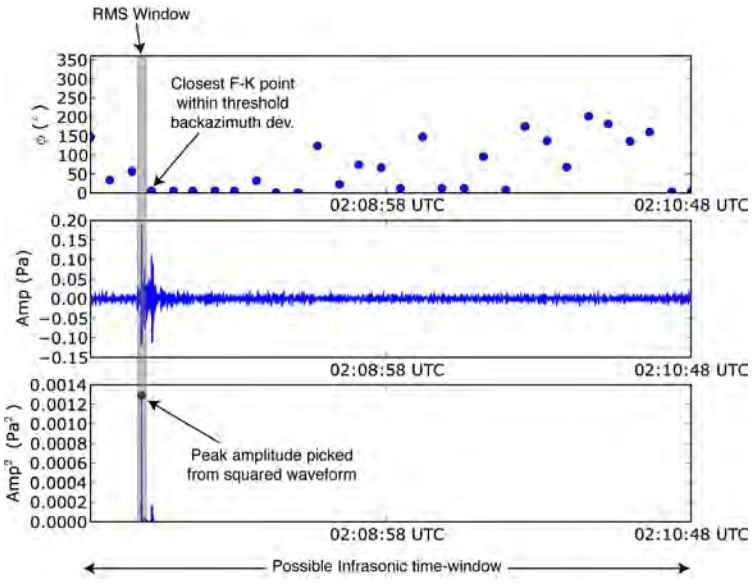

Figure 3. Illustration of the automatic amplitude measurement algorithm developed for this study. The time corresponding to the peak amplitude is measured from the squared waveform (bottom panel). The RMS amplitude is then measured within a time window of duration equal to 5 cycles (for the lowest frequency) (middle panel). Finally, an additional check is applied that the time corresponding to the amplitude must be within a threshold deviation from the ground-truth backazimuth (top panel).

Preliminary Analysis

(a) Separation of different physical mechanisms for infrasound generation

Since our ultimate goal is to relate infrasound amplitudes – corrected for magnitude, slip angle, distance, and atmospheric winds – to source depth, it is essential that we can separate infrasound signals that are generated by different physical mechanisms. Here, we define the following terms:

- **Epicentral infrasound.** This is infrasound that is generated at the epicenter by direct pumping of the atmosphere.
- **Secondary infrasound.** This is infrasound that is generated by the interaction of seismic surface waves and crustal structure (e.g., topography) away from the epicenter.

In a recent paper on this project work, published in *Geophysical Research Letters* (Arrowsmith et al., 2009), we show that secondary infrasound from the Wells, Nevada earthquake sequence is generated by the mainshock and numerous aftershocks, and that it manifests as high amplitude signals (greater in amplitude than epicentral infrasound). For this event sequence, secondary infrasound appears to be unique at each array, whereas epicentral infrasound can be distinguished as being common to multiple arrays. At station BGU, secondary infrasound can be uniquely identified as being generated by the interaction of surface waves with an isolated peak called Floating Island (Figures 4 and 5).

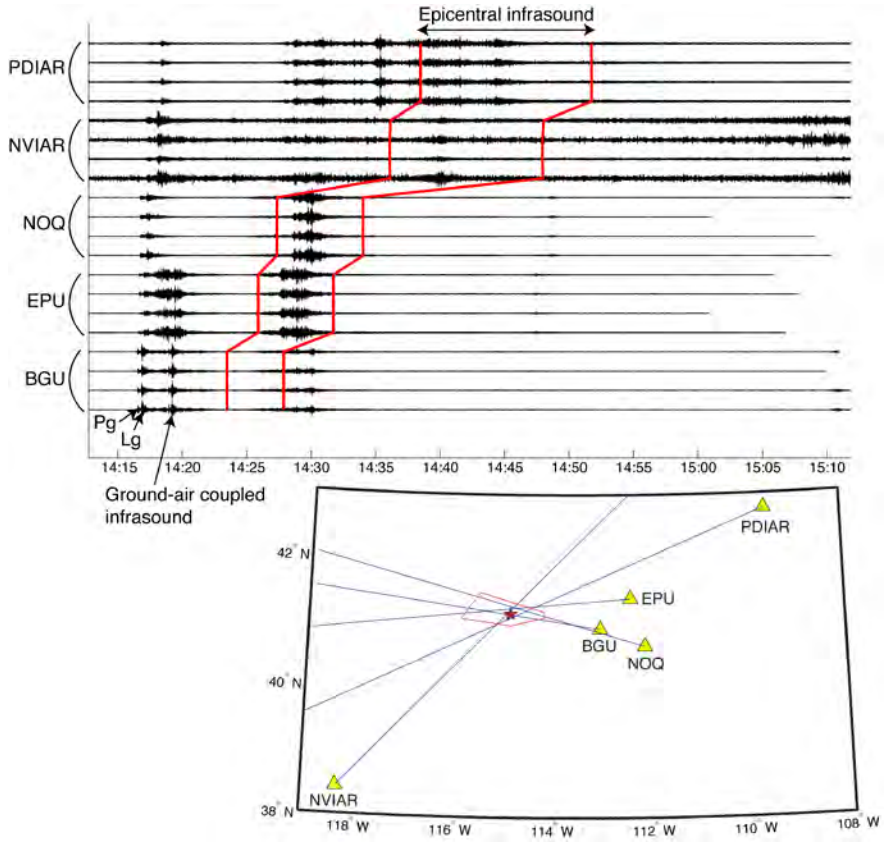

Figure 4. Infrasonic observations of the Wells, Nevada mainshock at five infrasound arrays in the Western U.S. Epicentral infrasound is common to all arrays, whereas secondary infrasound is unique to each array.

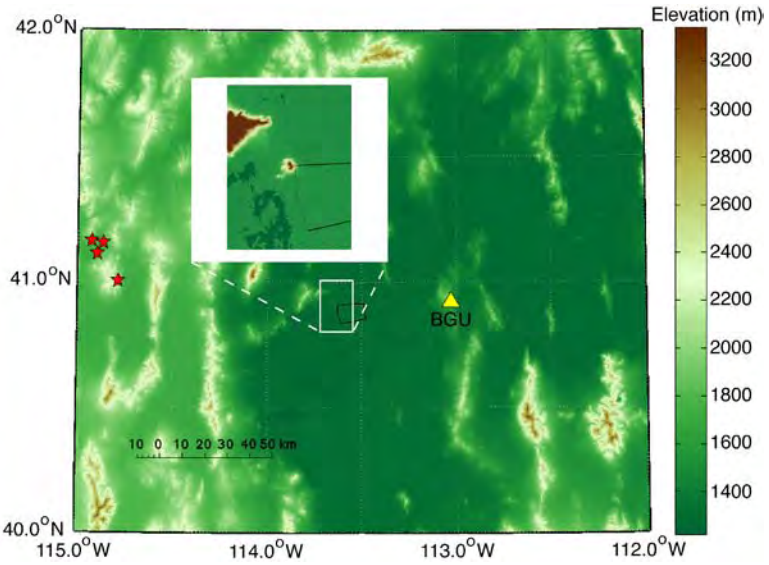

Figure 5. Map showing the locations of the Wells, Nevada mainshock and three major aftershocks (red stars), each of which generated signals from a point source associated with an isolated peak called Floating Island (inset map).

(b) The Wells earthquake sequence

Earthquake sequences provide a unique opportunity to study the effects of source parameters on relative differences in infrasonic amplitudes, because path effects can be assumed to be essentially fixed. Also, relative earthquake location algorithms can be used to determine accurate relative depths from seismic data. The Wells, Nevada earthquake sequence is highlighted in this paper as an invaluable research opportunity because a number of aftershocks were detected infrasonically at multiple arrays (Table 1).

Table 1. Infrasonic observations of the Wells, Nevada earthquake sequence.

Origin Time	Magnitude (ms)	Abs(Slip Angle)	Depth (relocated)	Amplitude at NOQ (Pa)
02/21/2008 14:16:02	5.8	90	9.824	1.9318
02/21/2008 14:20:51	4.4	-	8.923	0.2513
02/21/2008 14:34:43	3.67	-	10.728	0.3189
02/21/2008 22:47:28	2.86	-	3.885	0.4549
02/21/2008 23:57:51	4.35	51	-	0.1000
02/22/2008 23:27:45	3.78	85	14.507	0.1935
03/15/2008 16:22:33	3.33	85	8.974	0.4605

From a total of 37 events with Ml>3.5 (Smith et al., 2009), 7 were detected infrasonically. Figure 6 represents a summary of the observations. The source parameters (magnitude, depth, and slip angle) are represented on this plot as well as a simple summary of which events were detected. Larger magnitude events (Ms>3.5) that were not detected were all oblique-slip events. To our knowledge, these findings are the first documented evidence for

infrasound signals from earthquakes with Ms<4.0 (Le Pichon et al., 2006). Although this dataset is relatively sparse, it highlights the interplay between magnitude, depth, and slip angle on infrasonic amplitudes. For example, events "a" and "b" in Figure 5 are essentially the same in all respects apart from magnitude (which is reflected by much larger amplitudes from the larger event, "b"). Events a and c are similar except for depth (which is reflected by lower amplitudes at the deeper event, "c"). Our goal in Years 2 and 3 of this project is to quantify these effects by incorporating 100's to 1000's of observations from the dataset described above.

We are attempting to make direct measurements of Rg (short-period Rayleigh waves) from Wells aftershocks using nearby stations. The idea is to examine the minimum observed period of Rayleigh waves as a crude estimate of event depth. This technique was used in the Bayesian Single Event Technique (BSEL; Fagan et al., 2009) to set Bayesian priors on event depth. Figure 7 shows examples of four Wells, NV aftershocks that illustrate our strategy. Figures 7a and 7c show dispersion and group velocity grams for events detected by infrasound and Figures 7b and 7d for events not detected. The station from the USArray site N12A, that is located approximately 34 km to the southwest of the Wells, NV sequence along a predominantly basin path. The top two events were of similar size and occurred within approximately 1 hour of one another and reported to be of similar depth (~4 km). However, event 7a was recorded by infrasound and 7b was not. The main difference in the dispersion between the two events is that clear dispersion is observed for 7a for a period between approximately 1 and 3.5 seconds while the minimum observed period for event 7b is approximately 2.5 to 3 seconds. This could indicate that Event 7a occurred at a shallower depth than 7b and therefore generated infrasound signals. Event 7c was magnitude 4.8, had a reported depth of 10.5 km, and was clearly detected by infrasound. However, there is a suggestion of Rg dispersion between about 2 and 4.5 seconds that could indicate a shallower depth than that reported. Event 7d was of magnitude 3.2 and a reported depth of 14.5 km and was not recorded infrasonically. As expected for a deeper event, there is no evidence of short-period Rayleigh wave dispersion. We will be attempting to develop phase-matched filters and polarization filters to better enhance the Rg waves from the Wells, NV aftershocks in order to better constrain event depth.

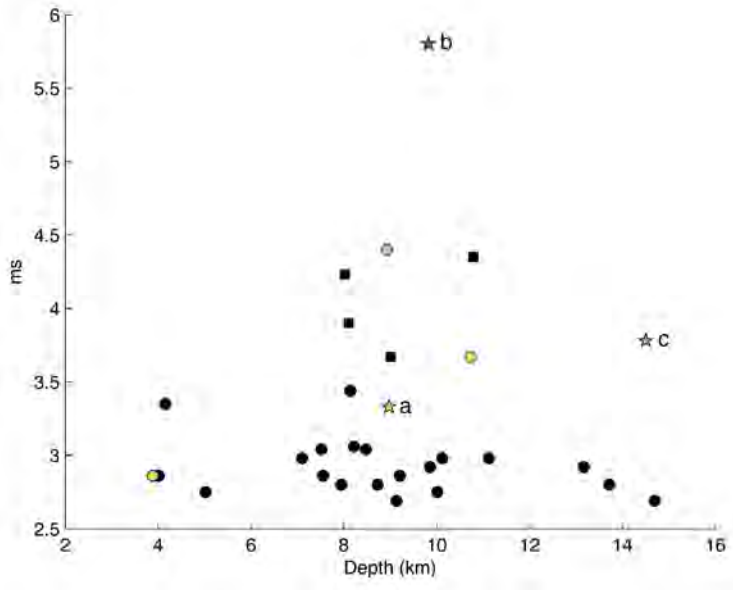

Figure 6. Graph summarizing detected (colored) and undetected (black) events in the Wells earthquake sequence. Colors represent the amplitudes recorded at NOQ (hot colors representing high amplitudes fade to cool colors for lower amplitudes). Symbols are representative of the slip angle as follows: pentagrams represent dip-slip events (80<s<=90), squares represent oblique-slip events (s<65) and circles represent events with unknown slips. Depths were computed using the HypoDD method by Ken Smith at UNR. Slip angles were obtained from moment tensor inversions by Bob Hermann at Saint Louis University.

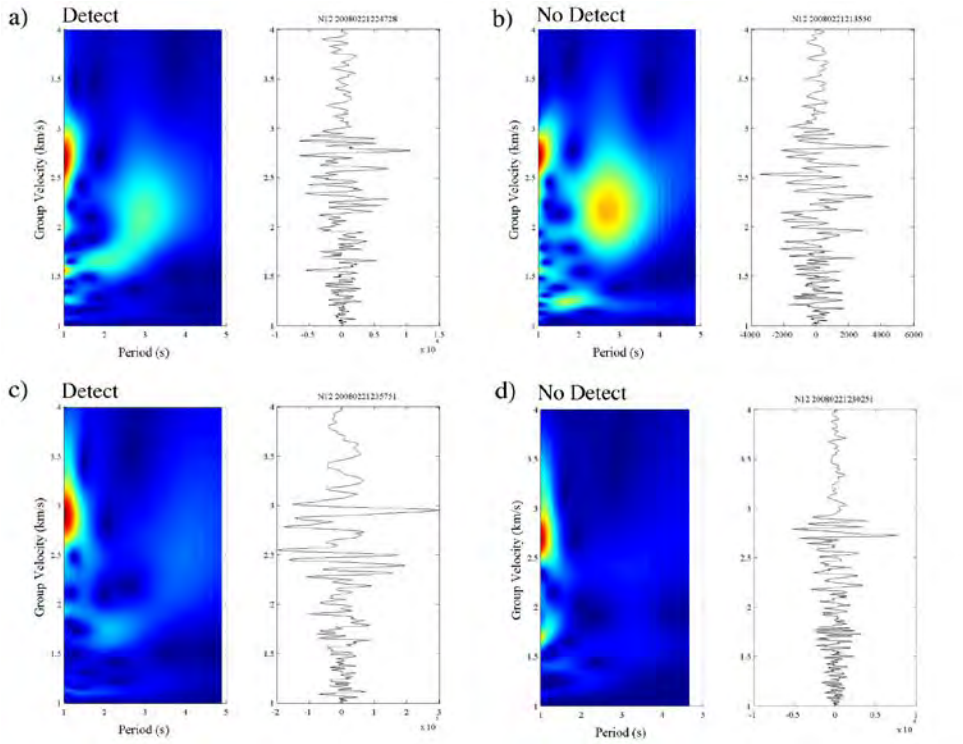

Figure 7. Dispersion plots and group-velocity grams for four Wells, NV aftershocks recorded at USArray station N12A (see text for details).

(c) Earthquakes and Explosions: Source vs. path effects

The dataset we are acquiring comprises both earthquakes and surface explosions in order to exploit the advantages of each. While surface explosions do not have a depth component, or a slip component, we are able to obtain many more robust observations of surface explosions than earthquakes (in part, due to the fact that they are more efficient generators of infrasound). A preliminary analysis of amplitudes from this extensive dataset of surface explosions is underway. We propose to exploit this dataset to develop reliable infrasonic path corrections that extend the earlier relationship of Mutschlecner et al. (1999). The relationship of Mutschlecner et al. (1999) reduces the effect of stratospheric winds on infrasonic amplitudes, and has proven effective in allowing for the regression of corrected amplitudes with source magnitude (Mutschlecner and Whitaker, 2005; Le Pichon et al., 2006). However, there is still scatter in corrected amplitudes that may be due to either source or path effects. With the recent availability of state-of-the-art 4D atmospheric models (3D+time), we have an opportunity to extend this relationship, which previously relied upon the only wind specifications readily available at the time (winds between 45 and 55 km).

CONCLUSIONS AND RECOMMENDATIONS

An unprecedented dataset is needed to address the fundamental research question of this effort: How can we estimate event depth using infrasound? The major focus of Year 1 of this effort has been on acquiring a dataset that is sufficiently robust to address this issue. A parallel focus has been to begin to explore the factors influencing the amplitudes of infrasound signals that we observe at regional scales. The goal for Years 2 and 3 of this effort is to develop these preliminary qualitative observations into quantitative relationships that can provide the framework for an infrasound depth discriminant.

ACKNOWLEDGEMENTS

We thank Il-Young Che of KIGAM for providing seismo-acoustic events in Korea, Ken Smith of UNR for providing his relocations of Wells earthquakes, and Rod Whitaker of LANL for providing helpful comments and feedback.

REFERENCES

Arrowsmith, S.J., R. Burlacu, R. Whitaker, and G. Randall (2009). A repeating secondary source of infrasound from the Wells, Nevada, earthquake sequence, *Geophys. Res. Lett.* 36: L11817, doi:10.1029/2009GL038363.

Brown, D. J., N. Brachet, and R. Le Bras (2008). Enhancements to the CTBTO Operational Automatic Infrasound Processing System, in *Proceedings of the 2008 Monitoring Research Review: Ground-Based Nuclear Explosion Monitoring Technologies,* LA-UR-08-05261, Vol. 2, pp. 853–861.

Fagan, D. K., S. R. Taylor, F. R. Schult, and D. N. Anderson (2009). Using ancillary information to improve hypocenter estimation: Bayesian Single Event Location (BSEL), *Pure Appl. Geophys.* 166: 521–545.

Hartse, H.E., S.R. Taylor, W.S. Phillips, and G. Randall (1997). A Preliminary Study of Regional Seismic Discrimination in Central Asia with Emphasis on Western China, *Bull. Seism. Soc. Am.* 87: 551–568.

Le Pichon, A., P. Mialle, J. Guilbert, and J. Vergoz (2006). Multistation infrasonic observations of the Chilean earthquake of 2005 June 13, *Geophys. J. Int.* 167: 838–844.

Mutschlecner, J. P., R. W. Whitaker, and L. H. Auer (1999). An empirical study of infrasound propagation, *Tech. Rep. LA-13620*, *UC-706*, Los Alamos Natl. Lab., Los Alamos, N.M.

Mutschlecner, J.P. and R.W. Whitaker (2005). Infrasound from earthquakes, *J. Geophys. Res.* 110: doi:10.1029/2004JD005067.

Smith, K., J. Pechmann, M. Meremonte, and K. Pankow (2009). Preliminary Analysis of the Mw 6.0 Wells, Nevada, Earthquake Sequence, *in preparation*.

MULTIPLE-ARRAY DETECTION, ASSOCIATION AND LOCATION OF INFRASOUND AND SEISMO-ACOUSTIC EVENTS – UTILIZATION OF GROUND-TRUTH INFORMATION

Stephen J. Arrowsmith[1], Il-Young Che[2], Christopher T. Hayward[3], Junghyun Park[3], and Brian W. Stump[3]

Los Alamos National Laboratory[1], Korea Institute of Geoscience and Mineral Resources[2]
and Southern Methodist University[3]

Sponsored by the Air Force Research Laboratory and the National Nuclear Security Administration

Award Nos. DE-AC52-06NA25396[1] and FA8718-08-C-008[2,3]
Proposal No. BAA08-65

ABSTRACT

This work is intended to provide automated methodology for processing seismic and infrasound data from seismo-acoustic arrays and to apply the methodology to regional networks for validation with ground truth information. As reported last year, the project has developed automated techniques for detecting, associating and locating infrasound signals. Work reported this year focuses on refinement of both the detection and location component of the program. Ground truth information developed on the Korean Peninsula is further used to refine the methodology.

New location developments are underway. We are incorporating an infrasonic grid-search location method into a Bayesian framework that provides conditional probabilities on the location given the observed data (inter-array time delays and backazimuths) and a prior distribution. The prior provides ancillary information on the event location, which can be as simple as empirical bounds on backazimuth deviations and group velocities. However, we are investigating extending this simple approach through the use of a 3D ray-tracing algorithm to impose more specific constraints based on available atmospheric specifications.

Finally a set of ground truth seismo-acoustic events have been developed for the Korean Peninsula and include a large number of events from a limestone quarry in the Republic of Korea. In-mine seismic and acoustic observations provide the basis of the detailed ground truth. These events occur daily with multiple events on active days and span nearly two years, providing the basis of assessing spatial and temporal variations in propagation path, including variations in backazimuth as well as phase and group velocity. The reported analyses of these data provide empirical bounding constraints for the location algorithm that is under development.

OBJECTIVES

There are two primary objectives to our effort on the second year of this contract. Each objective builds on the automatic algorithms for detection, association, and location of infrasound events developed in the first year of this project.

- **Development of an infrasound location algorithm with a firm statistical basis**. This objective is a natural extension to the bounding-constraint algorithm developed in Year 1. We formulate a scheme for calculating likelihood values at each node in the grid search method based on the agreement between observed and predicted values for backazimuth and arrival time. This scheme provides the opportunity to compute robust confidence bounds on infrasound locations.
- **Preliminary analysis of infrasound propagation effects using ground-truth data from Korea.** The groundt ruth dataset being acquired for this project provides an opportunity to test and validate new automated algorithms. We report on the preliminary analysis of this dataset, highlighting the effect of seasonal variations in atmospheric winds on travel-times in the Korean peninsula. Propagation path variations such as those documented in this study can be incorporated into the location algorithm.

RESEARCH ACCOMPLISHED

Infrasound Location Algorithm

We are currently extending the grid-search based infrasound location methodology of Arrowsmith et al. (2008a), discussed in last years proceedings (Arrowsmith et al., 2008b), by incorporating it into a Bayesian framework. This development enables us to compute non-ellipsoidal confidence bounds on the event location using two constraints: arrival times $\mathbf{t} = [t_1,...,t_n]$ and backazimuths $\theta = [\theta_1,...,\theta_n]$.

Bayes' theorem is given by:

$$P(t_0,x_0,y_0,v|\mathbf{t},\theta) = \frac{P(\mathbf{t},\theta|t_0,x_0,y_0,v)}{P(\mathbf{t},\theta)} P(t_0,x_0,y_0,v). \quad (1)$$

First, we formulate the value of the *likelihood function*, $P(\mathbf{t},\theta|t_0,x_0,y_0,v)$ at each point in our parameter space. We define our likelihood function as:

$$P(\mathbf{t},\theta|t_0,x_0,y_0,v) = \prod_i \Theta(\mathbf{t},\theta|t_0,x_0,y_0,v) \prod_i \Phi(\mathbf{t},\theta|t_0,x_0,y_0,v) \quad (2)$$

where

$$\Theta_i(t,\theta|t_0,x_0,y_0,v) = \frac{1}{\sqrt{2\pi(\sigma_\theta^2+\sigma_\kappa^2)}} \exp\left[-\frac{1}{2}\left(\frac{\gamma_i^2}{\sigma_\theta^2+\sigma_\kappa^2}\right)\right] \quad (3)$$

and

$$\Phi_i(t,\theta|t_0,x_0,y_0,v) = \frac{1}{\sqrt{2\pi(\sigma_\phi^2)}} \exp\left[-\frac{1}{2}\left(\frac{\varepsilon_i}{\sigma_\phi}\right)^2\right] \quad (4)$$

are the individual likelihoods for the i^{th} array, based on backazimuth and arrival time constraints respectively .The residual terms, γ_i and ε_i, are given by:

$$\gamma_i = \theta_i - \arctan\left(\frac{y_i - y_0}{x_i - x_0}\right) \quad (5)$$

and

$$\varepsilon_i = t_i - \left(t_0 + \frac{\sqrt{(x_i - x_0)^2 + (y_i - y_0)^2}}{v} \right) \quad (6)$$

where the i^{th} array is located at (x_i, y_i), (x_0, y_0, t_0) represents a point and time in our parameter space, and v represents the group velocity that is assumed to be constant at all arrays in the likelihood term.

The uncertainties in backazimuth, σ_θ and σ_κ, represent the standard deviation in the measurement error (a function of array geometry and F-K approach) and the standard deviation in the error produced by the wind respectively. Similarly, the uncertainty in arrival time estimation is denoted by σ_ϕ.

We impose physical constraints on the model parameters in the Bayesian prior term, $P(t_0, x_0, y_0, v)$, as follows:

$$P = \begin{cases} \text{positive constant} & 0.22 \le v \le 0.34 \\ 0 & \text{otherwise} \end{cases}. \quad (7)$$

This constraint assures that the group velocity associated with our solution (x_0, y_0, t_0) lies within the infrasonic range (for direct waves through to thermospheric returns).

The final solution (or posterior), $P(t_0, x_0, y_0, v | \mathbf{t}, \theta)$, is the likelihood of the event location and origin time given our observed data (arrival times and backazimuths). This likelihood is a function that spans some pre-defined geographic region and time window. We apply a grid-search method in order to find the location and origin time associated with the maximum likelihood, with confidence regions defined by the likelihood distribution.

Example

We apply our Infrasonic Bayesian Locator (IBL) to a ground-truth rocket motor explosion recorded at three arrays in Utah (Stump et al., 2007). This event is discussed in Arrowsmith et al. (2008a) and is summarized in Table 1. The known station and event geometry is shown in Figure 1, in addition to the calculated likelihood function Θ – based on backazimuth constraints only – as a function of x and y with t_0 and v fixed at their optimum values. Figure 2 is similar to Figure 1 except that the arrival-time based likelihood function, Φ, is plotted for comparison.

Table 1. Summary of the Utah Test and Training Range explosion ground truth and observations used in this article to illustrate the IBL algorithm.

Ground truth data	**Location**	41.13152°N, 112.89577°W	
	Origin Time	2007/08/27 20:43:12.0	
Observations	**BGU**	Arrival-time	2007/08/27 20:44:27
		Backazimuth	30.96°
	EPU	Arrival-time	2007/08/27 20:45:35
		Backazimuth	237.80°
	NOQ	Arrival-time	2007/08/27 20:47:17
		Backazimuth	304.22°

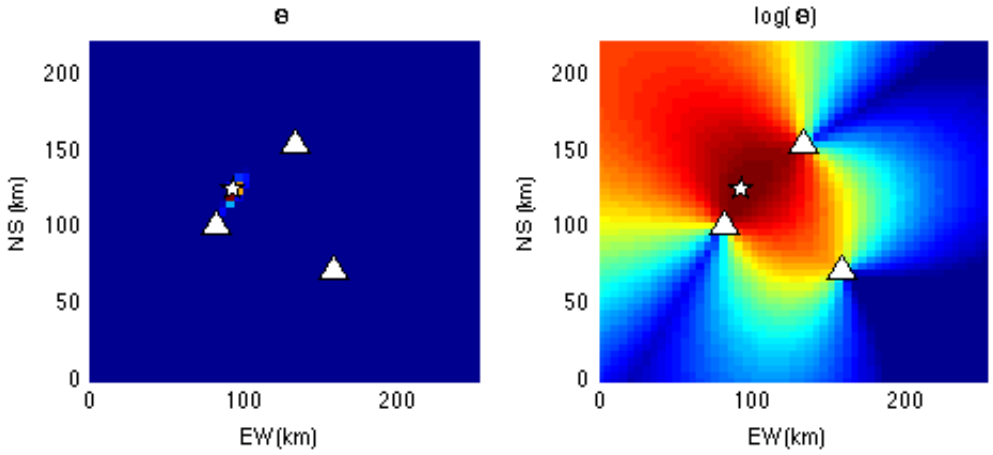

Figure 1. Solutions obtained for the Utah Test and Training Range explosion summarized in Table 1. Left: Plot of the backazimuth function Θ over x and y with t_0 and v fixed at their optimum values. Right: Plot of the natural logarithm of Θ, again with t_0 and v fixed at their optimum values.

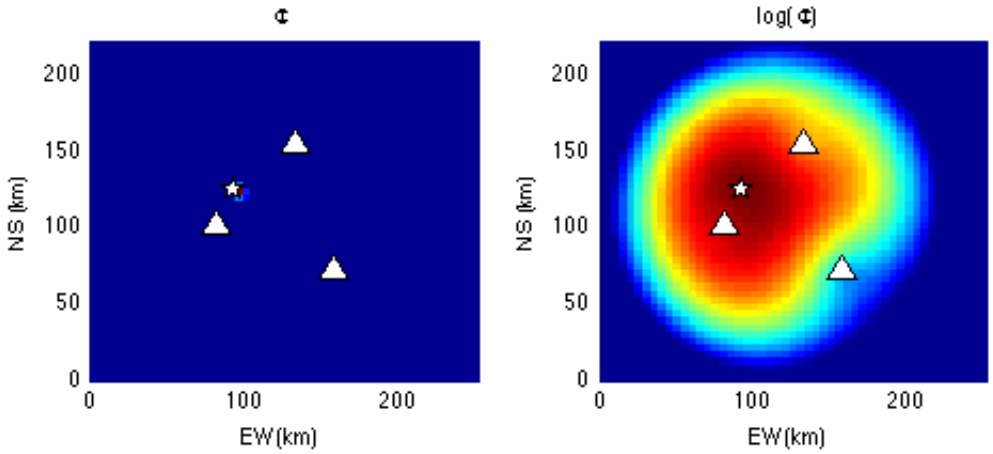

Figure 2. Left: Plot of the arrival time function Φ over x and y with t_0 and v fixed at their correct values. Right: Plot of the natural logarithm of Φ, again with t_0 and v fixed at their optimum values.

The posterior likelihood function (obtained using Bayes' theorem, outlined above) is shown in Figure 3. It is interesting to note that, whereas in Figures 1 and 2 (for backazimuth and travel-time constraints individually) we obtain ellipses, in Figure 3 (once these separate constraints have been effectively combined) we observe a circular region that is better constrained. This result highlights the value of incorporating both backazimuth and arrival time constraints into the solution.

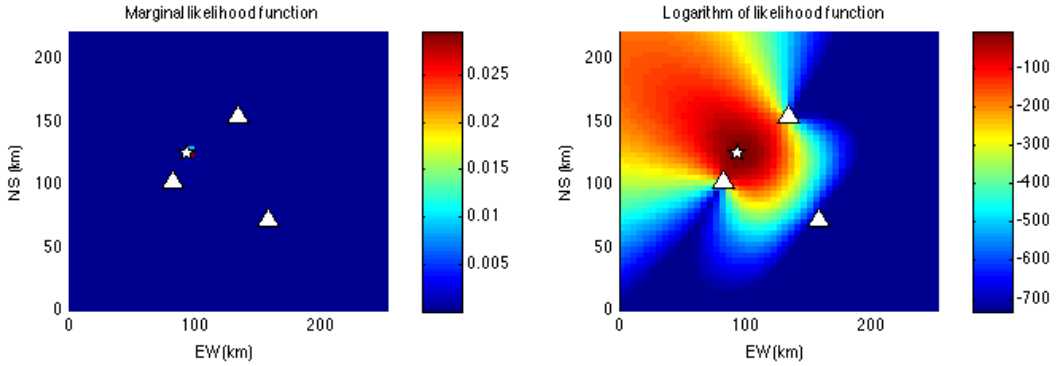

Figure 3. Left: The posterior likelihood function of the variables x_0 and y_0. For this array geometry, the likelihood contours produced by the backazimuths run perpendicular to those produced by the arrival times. The result, seen in this figure, is a well-constrained, circular source region. Right: The natural logarithm of the same posterior likelihood function.

Collection of Long-Term Ground-Truth Events from a Limestone Mine in Korea

Surface blasting activities at industrial mines are good examples of point sources that produce impulsive infrasonic signals. Well-defined blasting information can be utilized to study the characteristics of infrasound propagation in the atmosphere and to verify infrasonic source location methods. In particular, long-term collection of ground-truth events from a mine, conducting daily blasting, provides the basis for assessing spatial and temporal variations of infrasound propagation depending on seasons.

Figure 4(a) shows the locations of several seismic stations (black triangles) and two seismo-acoustic arrays (CHNAR and ULDAR) in South Korea. The inner box illustrates the distribution of seismic events near the east coast of South Korea from 2005 to 2006. The Korea Earthquake Monitoring System (KEMS) reviewed more than 900 events most with seismic magnitudes of less that M_L 2.0. Of these events, those followed by distinct infrasonic signals detected by infrasound arrays were discriminated as surface explosions, not earthquakes, and are marked by yellow circles in the figure. A field survey identified a large open-pit limestone mine (red dot in the figure) in the scattered distribution of these seismic events. This mine blasts several tons of explosives nearly every working day and can be considered as an infrasonic bell since many infrasonic signals from the mine have been recorded at the seismo-acoustic arrays in Korea.

Two temporary seismo-acoustic stations were deployed approximately ~300 m apart from the blasting point during two years starting from April 2007 in order to collect detailed ground-truth information at the mine. Three-component seismometers and acoustic sensors were used to document the sources. The acoustic sensor was connected to a wind-noise reducer. Seismic and acoustic data were digitized at 100 samples per second.

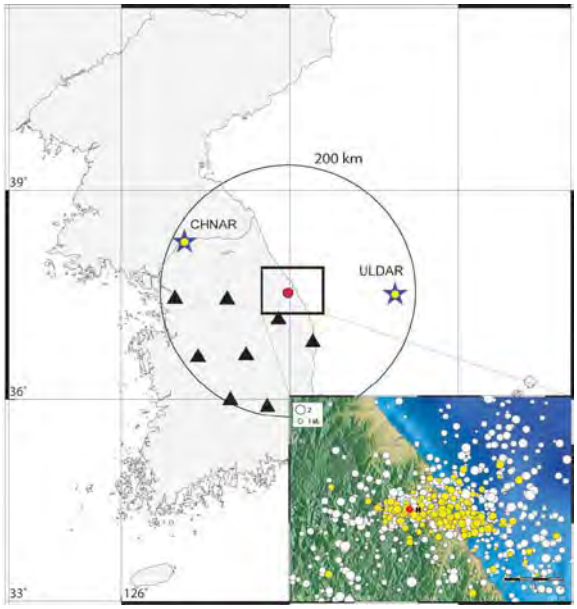

Figure 4. (a) Locations of the mine (red dot), seismic stations (black triangles), and infrasound arrays (CHNAR, ULDAR). Inner box shows distribution of seismic events around the mine in 2005-2006.

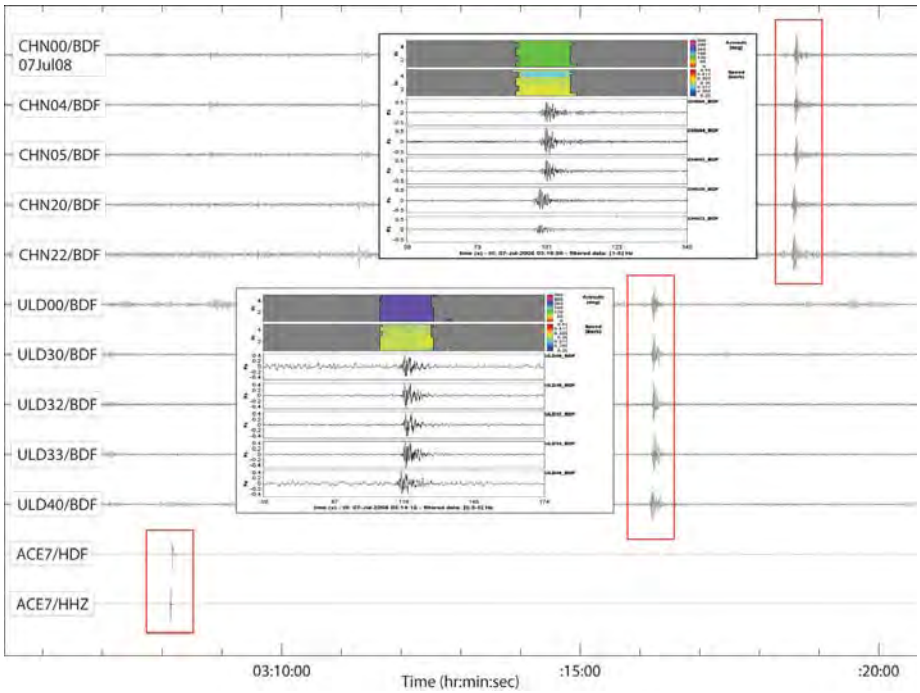

Figure 4. (b) Infrasonic signals and PMCC results for a delay-fired shot at the mine, recorded at CHNAR, ULDAR, and near-field seismo-acoustic station.

Preliminary Analysis of Infrasound Propagation Using the Ground Truth Information

During the two years of sensor operation, the mine conducted 1066 blasts, averaging more than one blast per a day. All blasts were delay-fired shots and the total explosives used were up to 11.2 tons per blast. The temporary stations recorded the near-field seismic and acoustic pressure changes from these blasts, thereby providing data to constrain the exact origin time, location and blast information.

To quantify the seasonal variation in infrasound propagation we used infrasound array observations at two different observation locations, CHNAR and ULDAR. Each array is located at a similar distance from the mine, 181 km and 169 km, respectively. However, the propagation path environments are quite different. CHNAR is located to the NW from the mine, producing a continental path over land. The propagation direction for ULDAR is nearly opposite in direction to CHNAR, eastward from the mine, and across open ocean. Figure 4(b) displays recordings of a delay-fired shot, recorded at the seismo-acoustic arrays (CHNAR and ULDAR), and the temporary station.

Using the complete dataset, we estimated the origin time of each blast from near-field seismic recording, bottom waveform in the figure. We applied the PMCC method to the distant array data to detect the blast-associated infrasonic signals. Wave parameters were estimated and included arrival time, azimuth, apparent velocity, and amplitude of detected signals at each array. Horizontal propagation velocity of infrasound signals, also called celerity, is used not only in infrasonic location, but also infrasonic phase identification. In general, this velocity can be estimated by ray-tracing through a realistic atmospheric velocity model. In the absence of a realistic atmospheric model, the velocity can be estimated using ground truth events with known origin times such as in this study. The horizontal velocities for all the blasts in the ground truth dataset were estimated based on ground-truth source time and infrasound arrival times at both arrays. Figure 5 displays the variation of infrasound travel times from the mine to two arrays over a period of two years.

Based on this analysis we conclude:

- Although propagation distances are similar, travel times of the first arrival (main phase) are significantly different along the paths to the two arrays. For CHNAR, horizontal velocities range from 0.26 to 0.29 km/s corresponding to stratospheric returns. On the other hand, infrasound signals arrive at ULDAR with fast horizontal velocities, ~0.34 km/s corresponding to tropospheric phases.
- For CHNAR, travel times vary systematically with the seasons, arriving up to 68 seconds faster in summertime. Thus, the horizontal velocity showed cyclic variations with velocities near ~0.26 km/s in the winter-spring time, and increasing to ~0.29 km/s in the summertime, and decreasing to ~0.27 km/s in the autumn. This variation in velocity indicates that travel times of infrasound signals can be strongly dependent on seasonal ambient sound velocity structure in the atmosphere.
- The travel times to ULDAR show little seasonal variation. There is some diurnal variation of horizontal velocity. These observations may be a result of the dominant effect of the ocean on temperatures at the ocean-atmosphere boundary.
- These path variations contribute to signal detectability as well. Signals at CHNAR have the highest detectability in the summertime, but many signals were not detected during autumn-winter-spring seasons, even though strong source signals were generated at those times. Compared with CHNAR, detectibility of ULDAR was low only in summer, but stable during the other seasons. Thus the seasonal detectability of the two arrays was opposite to each other, as shown in the figure.

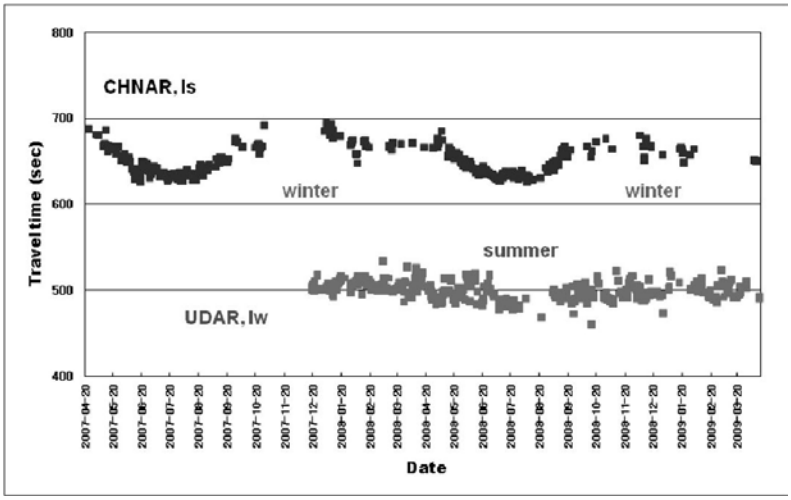

Figure 5. The variation of travel time of infrasound arrivals from the mine to CHNAR and ULDAR during the two years of the ground-truth dataset. Note that ULDAR was installed in December 2007.

CONCLUSIONS AND RECOMMENDATIONS

We have developed the framework for implementing a statistical infrasound event locator. At present, the algorithm is implemented in a Cartesian coordinate system, suitable for local to regional distances, awaiting straightforward conversion to a spherical coordinate system. The algorithm provides a thorough characterization of the source region defined by likelihood contours around the estimated source location. We are in the process of assigning probability values to these contours by numerically integrating the posterior likelihood function (which has a total integral equal to 1). In an example case, we show that the combination of both arrival time and backazimuth constraints results in an improved solution over using either constraint separately.

The preliminary analysis of the ground truth data set indicates that travel times of infrasound strongly depend on seasons as well as path environments. In particular, infrasonic waves to CHNAR propagated as guided waves between the ground and stratosphere. Infrasonic waves to ULDAR also propagated as guided waves, but observed horizontal velocities indicate that wave ducts were formed at relatively lower heights in the troposphere, even though propagation distances to these arrays are similar. The data also show that detectability is dependent on season. Detectability in summer is higher than spring-winter-autumn seasons in the direction to CHNAR with ULDAR showing reverse detectibility. These results indicate that infrasound propagation is related to path environment and seasonal wind in and around the Korean Peninsula. We interpret the time variation in detectability as partially controlled by prevailing periodic winds, northwesterly in the winter and southeasterly in the summer. To investigate these characteristics in detail, further research is required to compare the measured horizontal velocities with predicted ones from atmospheric modeling. These results also illustrate that seasonal and path dependent celerities may improve infrasound location procedures.

ACKNOWLEDGEMENTS

We thank Ryan Modrak for his help in developing and coding the IBL algorithm, and Dale Anderson for patiently explaining Bayesian statistics and for fruitful discussions on how to incorporate infrasound location into a Bayesian framework.

REFERENCES

Arrowsmith, S. J., R. Whitaker, S. Taylor, R. Burlacu, B. Stump, M. Hedlin, G. Randall, C. Hayward, and D. ReVelle (2008a). Regional monitoring of infrasound events using multiple arrays: application to Utah and Washington State, *Geophys. J. Int.* 175: 291–300.

Arrowsmith, S. J., C. Hayward, B. Stump, R. Burlacu, I.-Y. Che, and G. Singh (2008b). Multi-array detection, association and location of infrasound and seismo-acoustic events in Utah in *Proceedings of the 30th Monitoring Research Review: Ground-Based Nuclear Explosion Monitoring Technologies*, LA-UR-08-05261, Vol. 1, pp. 844–852.

Stump, B., R. Burlacu, C. Hayward, K. Pankow, S. Nava, J. Bonner, S. Hock, D. Whiteman, A. Fisher, T. S. Kim, R. Kubacki, M. Leidig, J. Britton, D. Drobeck, P. O'Neill, K. Jensen, K. Whipp, G. Johnson, P. Roberson, R. Read, R. Brogan and S. Masters (2007). Seismic and infrasonic energy generation and propagation at local and regional distances: Phase I – Divine Strake Experiment, *Air Force Research Laboratory*, AFRL-RV-HA-TR-2007-1188.

ADVANCEMENT OF TECHNIQUES FOR MODELING THE EFFECTS OF FINE-SCALE ATMOSPHERIC INHOMOGENEITIES ON INFRASOUND PROPAGATION

Robert G. Gibson[1], Douglas P. Drob[2], and David Broutman[2]

BBN Technologies[1] and the Naval Research Laboratory[2]

Sponsored by the National Nuclear Security Administration

Award Nos. DE-AC52-08NA28652[1] and DE-AI52-08NA28653[2].
Proposal No. BAA08-05

ABSTRACT

Propagation studies of a growing number of infrasound observations indicate that fine-scale atmospheric inhomogeneities contribute to infrasonic arrivals that are not predicted by standard modeling techniques. In particular, gravity waves, or buoyancy waves, are believed to contribute to the multipath nature of infrasound propagation and to cause penetration of infrasound into the classical shadow zones that are predicted by conventional modeling techniques. Propagation modeling studies using simplified parameterizations of gravity wave spectra suggest that gravity waves represent the primary component of fine-scale atmospheric inhomogeneity that affects infrasonic arrivals at regional ranges.

The influence of atmospheric gravity waves on the upper atmosphere provides a significant source of geophysical uncertainty in atmospheric specifications. A large fraction of the gravity wave spectrum in operational numerical weather prediction models is either filtered out during the data assimilation process or else not resolved by the models. Existing approaches to modeling infrasound through gravity waves have relied on one-dimensional vertical wavenumber spectral models of gravity waves. This simplified model approach captures the vertical spatial scales in gravity waves as a function of height. Improved resolution of these wave fields through more sophisticated computational techniques to achieve more complete spectral parameterization is an important research challenge.

Atmospheric specification techniques are being developed that incorporate realistic models of gravity waves that are self-consistent with the background flow field and that include effects of altitude, range-dependence, and time-dependence over relevant scales. One shortcoming of existing gravity wave field models currently used with infrasound propagation models is that they ignore the typically strong refraction of the background gravity waves by variations in the mean winds and mean stratification above 15 km. These limitations are addressed by including the refraction effects of the gravity wave field by the background atmosphere as defined by the NRL-G2S semi-empirical specification. A local atmospheric gravity wave field is represented using the summation of vertical eigenfunctions approximated by a computationally efficient Fourier-space ray-tracing technique. Using this methodology, wave perturbation fields (horizontal wind components, pressure, density, and temperature) are calculated that are self-consistent with the background atmospheric flow.

Broadband, full-wave infrasound predictions computed using the parabolic equation (PE) method are used to model atmospheric infrasound from explosions at ranges of 100s to 1000s of km. Model predictions using the PE method are conducted using range-dependent specifications of the atmosphere from NRL-G2S that are modified by the addition of perturbation terms to the mean atmospheric wind profiles to represent gravity wave effects, in order to characterize the fine-scale atmospheric structure not resolved by numerical weather prediction models. Synthesized infrasound waveforms, obtained using the Fourier-synthesis time-domain PE method, are compared with observed infrasound signals from ground-truth events in order to evaluate the modeling capabilities.

OBJECTIVES

The objective of this research effort is to improve understanding of the effects of gravity waves and other fine-scale atmospheric inhomogeneities on infrasound propagation. The improved understanding of the relevant atmospheric and infrasonic physics will result in enhanced capabilities for modeling infrasound features and waveforms.

It is evident that existing propagation modeling, coupled with state-of-the-art atmospheric characterizations, fails to adequately predict infrasonic arrivals in all circumstances. In particular, there have been numerous events for which infrasound arrivals are observed by sensors in regions that are predicted by standard modeling techniques to be in shadow zones (e.g., Bhattacharyya et al., 2003; Kulichkov, 2004; Mutschlecner and Whitaker, 2006). This issue is relevant over both local and regional ranges. Recent scientific work in gravity waves, long-range acoustic propagation, and infrasound has indicated that fine-scale atmospheric inhomogeneities contribute to unexpected infrasonic arrivals. We endeavor to address this issue through systematic evaluation of the relevant atmospheric phenomena, advancement of the state of the art of modeling the interactions between fine-scale atmospheric inhomogeneities and infrasound, improved atmospheric specification, and model validation.

Specifically, the objectives are as follows:

- Review recent scientific progress in the understanding of gravity waves, their temporal and spatial variability, and their statistics, in order to develop an improved model of the characteristics of gravity waves that are relevant to infrasound propagation.
- Develop atmospheric specification techniques that incorporate realistic models of gravity waves in a manner that maintains self-consistency with the background flow field and that includes effects of latitude, longitude, and time-evolution over relevant scales.
- Exercise the improved gravity wave models with infrasound propagation models. Examine variability of infrasound predictions over a statistical ensemble of gravity wave realizations. Perform sensitivity studies to establish the effects of key atmospheric model variables on infrasound prediction.
- Perform model validation studies using ground truth datasets, focusing on local and regional ranges.

The effort is anticipated to increase understanding of the regional and local propagation of infrasound through the dynamic atmosphere and also to improve the capability to predict infrasound arrivals and features relevant to phase classification. Research results are anticipated to include spectral-based atmospheric variability specifications; numerical modeling subroutines that enable improved propagation modeling via incorporation of effects of gravity waves and related fine-scale atmospheric structure phenomena; and a summary of model/data comparison results.

RESEARCH ACCOMPLISHED

Atmospheric Specification

The atmospheric structure responsible for the propagation of infrasound can change rapidly. Global climatological models have largely been replaced in current infrasound modeling practice by the NRL Ground to Space (G2S) model of Drob et al. (2003) and Drob (2004), which was developed to provide background atmospheric information for the Nuclear Explosion Monitoring Research and Development program. The G2S data processing system combines operational numerical weather prediction (NWP) specifications with the upper atmospheric empirical models, NRLMSISE-00 and HWM-93 (Picone et al., 2002; Hedin et al., 1996). The near-real-time system incorporates 1ºx1º and 1ºx1.25º resolution global NWP input fields to the nearest 6-hour interval in the lower atmosphere. The HWM-93 model was recently upgraded to HWM-07 by Drob et al. (2008) via the assimilation of recent upper atmospheric research satellite-based measurements and ground-based measurements.

However, these specifications are unable to resolve all fine-scale stochastic phenomena, e.g., atmospheric irregularities smaller than the model resolution, fine-scale structures above 35 km, and gravity wave fluctuations that cannot be deterministically measured or internally generated by the model. Fine-scale atmospheric structure not characterized by near-real-time atmospheric models such as G2S has been identified as a likely source of refraction, advection and scattering effects that may play a significant role in infrasound propagation. In particular, gravity waves are of interest because their spatial scales are of the same order as infrasonic wavelengths. Gravity waves result from oscillations of air parcels displaced by buoyancy and restored by gravity. The oscillations have time scales ranging from minutes to tens of hours. Vertical length scales of gravity waves are in the range of 0.1 to 15 km, and horizontal scales can span from 10 to 1,000 km. The multi-scale nature of gravity waves presents a

challenge to quantification of their properties. Owing to the important influences of gravity waves on the atmosphere's general circulation, vertical structure, and spatiotemporal variability, gravity wave dynamics is a significant atmospheric science research topic area. Recent research progress includes a better understanding of gravity wave source characteristics and evolution with altitude due to changes in wind conditions and atmospheric stability (e.g., Fritts and Alexander, 2003). The development of high-fidelity physically-based gravity wave parameterizations is an active research area.

BBN has previously developed a baseline wind variability model (Norris and Gibson, 2002; Gibson, et al., 2008) for predicting infrasound deviations due to atmospheric effects that are not resolved by the existing atmospheric specifications. The basic variability model uses a power-law wind perturbation spectrum based on the spectral gravity wave model of Gardner (1995, 1993), and generates realizations of horizontal wind perturbation profiles due to gravity waves. A source spectrum is defined near the ground, and as the wave spectrum is propagated up in height, attenuation is modeled by introduction of diffusive damping. Therefore, height-dependent gravity wave dependencies are modeled. Range-dependent effects can be approximated by selecting a dominant horizontal correlation length and combining wind perturbation profiles using Gaussian weighting functions.

Approaches to Improved Gravity Wave Modeling

As discussed above, baseline approaches to modeling infrasound through gravity waves have relied primarily on one-dimensional vertical wavenumber spectral models. This simplified model approach captures the vertical spatial scales in gravity waves as a function of height. We are currently extending this capability by accounting for additional dimensional variability, including horizontal wavenumber.

Furthermore, given a spectral model, numerous parameters must be defined in order to apply it. In the baseline work, a single representative set of parameters was defined for use in all propagation scenarios. In the current effort, spatial and temporal dependencies are considered. For example, parameters may be quantified based on latitude and Julian day. The baseline implementation of the Gardner model does not account for the fact that gravity wave fields can vary dramatically with altitude, latitude, and season (e.g., Eckermann, 1995).

Another shortcoming of the baseline gravity wave model is that it ignores the typically strong refraction of gravity waves by variations in the mean winds and the mean stratification above 15 km. These limitations are being addressed by including the refraction effects of the gravity wave field by the background atmosphere as defined by the G2S specification. There are several existing models that include the effects of refraction on a spectrum of gravity waves (e.g., Fritts and Lu, 1993; Eckermann, 1995; Warner and McIntyre, 2001). These models involve ray-tracing directly in the Fourier domain. They are purely spectral and have not been used to generate a spatial realization of the gravity wave field. For this current application, we have considered a different Fourier formulation that predicts refraction effects locally in the spatial domain and is computationally very fast. The formulation involves ray tracing in Fourier space, in a way that efficiently approximates the vertical eigenfunctions for a given background. The ray solutions are then Fourier synthesized to give the spatial solution. Since wave phases are also computed, a wide range of problems can be considered, from deterministic mountain waves, to semi-deterministic gravity waves generated by convection, to fully random wave fields.

For this application, it is possible to represent a local atmospheric gravity wave field using the summation of vertical eigenfunctions. The associated mathematical expression is

$$w(x,y,z,t) = \sum_{\omega} e^{-i\omega t} \int_{-\infty}^{\infty} \int W(k,l,z) e^{i(kx+ly)} dk dl \qquad (1)$$

where the gravity waves have vertical velocity w, frequency ω, and horizontal wavenumber components k, l in the horizontal directions x, y, respectively. The vertical coordinate is z and the time is t. A very efficient way to solve for w is via ray tracing, and in particular by ray tracing in the Fourier domain (i.e., in k, l space) with z as the parametric variable. In this manner critical layers are handled in a natural way, plus the solution permits no resonant singularities. Trapped waves are represented by a uniform approximation involving the Airy function. Furthermore, if it is assumed that the winds are horizontally homogeneous and stratified over a limited sub-domain then k and l are constant along each ray. Thus the ray tracing integration is one-dimensional. Another advantage to this approach is that the horizontal variability in the wave field (and the associated horizontal correlation scales) also follows directly from the specified horizontal wavenumber dependence of the wave source spectrum. Self-consistent wave

field calculations where the background profiles vary over distances greater than 500 km can also be synthesized via the superposition of several overlapping range independent realizations. Additional theoretical details of the Fourier gravity wave ray tracing method are presented in Broutman et al. (2003, 2006, and 2009). Comparisons with mountain-wave observations are given in Eckermann et al. (2006) and Alexander et al. (2009).

An example of results for the gravity wave field computed from (1) using the Fourier-space ray tracing technique is shown in Figure 1. The left panel shows a random realization of w in a uniform background. The right panel shows how the same spectrum of gravity waves is refracted by an idealized wind jet centered at 25 km altitude, with a peak speed of 5 m/s. In this example the gravity wave source height is z = 0. Most of the gravity waves encounter either turning points or critical layers before reaching the center of the wind jet, so the gravity wave field is weak above the wind jet. As expected from linear theory, the largest gravity wave amplitudes occur where the turning points are concentrated, just below the peak of the wind jet. Note that Figure 1 is derived from a two-dimensional calculation. In three dimensions, there is in reality more gravity wave propagation through the wind jet because the refraction weakens as the horizontal propagation direction moves away from the wind direction.

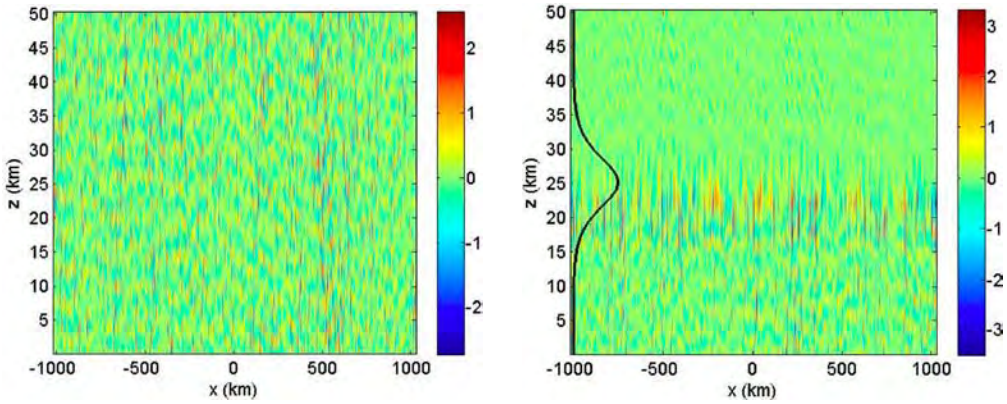

Figure 1. Vertical velocity *w* for a random realization of a spectrum of gravity waves. Left panel: for a uniform background wind; Right panel: for a mean wind jet centered at 25 km altitude, with peak speed 5 m/s (denoted by the bold curve). The solution is calculated with 1024 horizontal wavenumbers on a spatial grid with 2 km grid spacing. Ten frequencies were used for the sum in Eq. (1). The solution has been scaled by exp(-*z*/2*H*), where *H* = 7.5 km is the density scale height.

All of the prerequisites for calculating the vertical and horizontal amplitudes of the random gravity wave perturbations are provided by the available G2S specifications. Stochastic gravity wave perturbation fields (U', V', T', P' and ρ'), i.e., horizontal wind components, temperature, pressure and density, as a function of z, x, y and t can be calculated given the corresponding G2S background atmospheric fields (U, V, T, P, and ρ) over the same spatial domain z, x, y. This approach accounts for the important seasonal, latitude and longitude dependence of the various auxiliary model parameters, such as the gravity wave spectrum lower cut off wave number (m*), which, together with the background atmospheric state, govern the nature and amplitude of the gravity wave spectrum. Using this methodology, wave perturbation fields are calculated that are self-consistent with the background atmospheric flow.

An example calculation of a self-consistent gravity wave field is presented in the following figures for a regional scenario. Figure 2 shows background atmospheric profiles at two locations separated by 375 km, for an arbitrarily chosen date and time (05:00 UT on 01/11/2002). Altitude-dependent and range-dependent gravity wave perturbations of U, V, W, and T are computed for a 3D data cube (512 km x 512 km x 151 km, with 4 km x 4 km x 1 km resolution). We use a random realization of a realistic gravity wave spectrum (Warner and McIntyre, 2001) launched from an altitude of 15 km. Five frequencies ω are used in this preliminary test case, although the refraction of the gravity waves produces a full range of intrinsic frequencies. Each Fourier component is ray-traced to give an approximation of the vertical eigenfunctions W. The ray solutions are then Fourier synthesized via (1) to give the spatial wavefield. Figures 3 and 4 show perturbation fields, over slices of altitude versus range, in an East-West and a North-South plane, respectively. Figure 5 shows the atmospheric profiles including gravity wave perturbations.

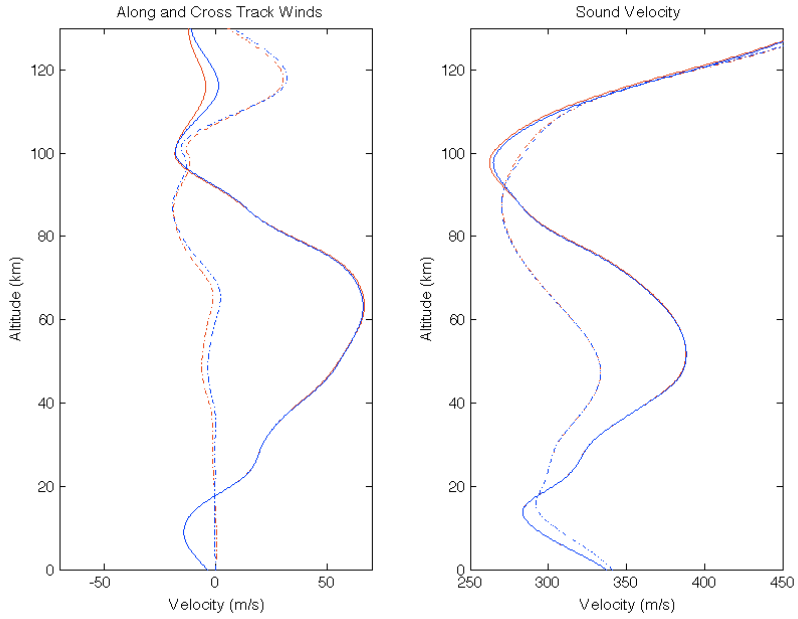

Figure 2. Atmospheric profiles (from HWM-93 and NRLMSISE-00) for a propagation scenario consisting of a source location (red) 375 km east of station I01AR (blue). Along-track winds (+ westward) and effective sound velocities are shown as solid lines. Cross-track (+ northward) winds and effective sound velocities are shown as dashed lines.

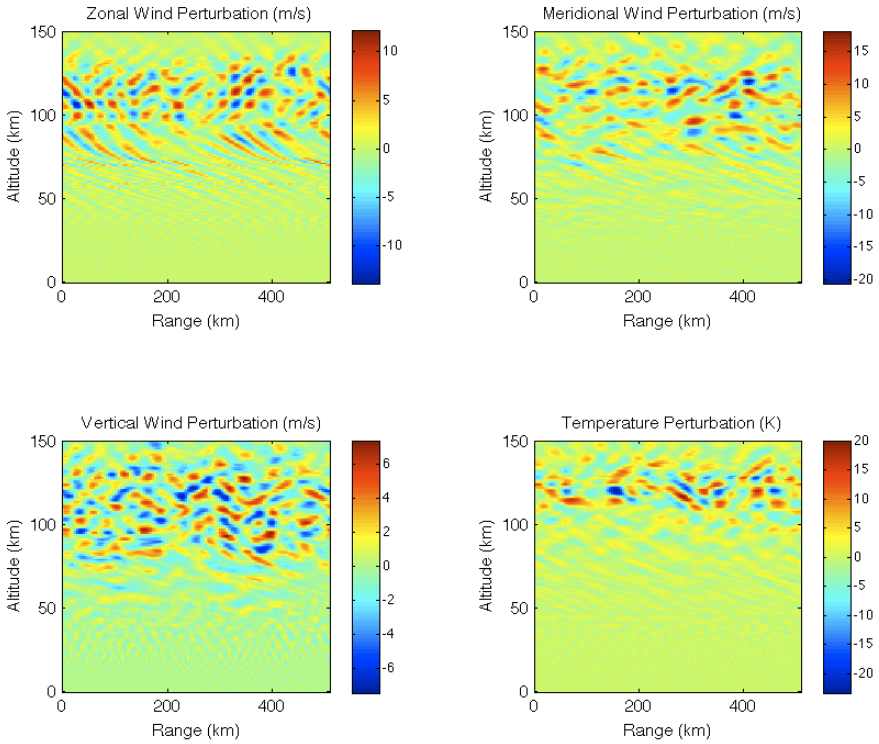

Figure 3. Perturbation fields, altitude vs. range, East-West plane, corresponding to scenario in Figure 2.

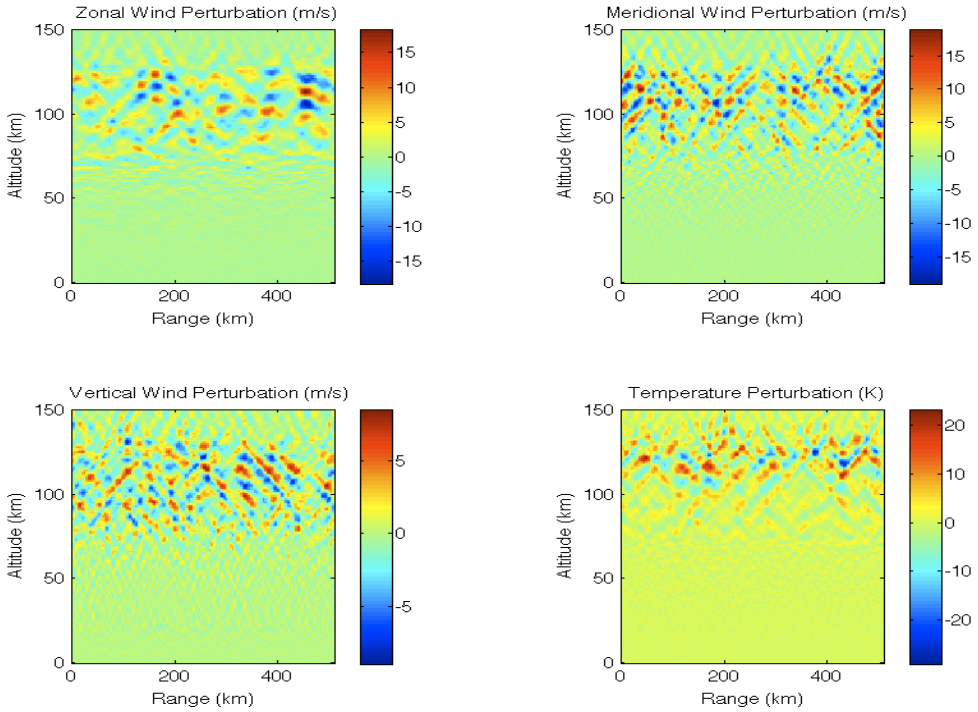

Figure 4. Perturbation fields, altitude vs. range, North-South plane, corresponding to scenario in Figure 2.

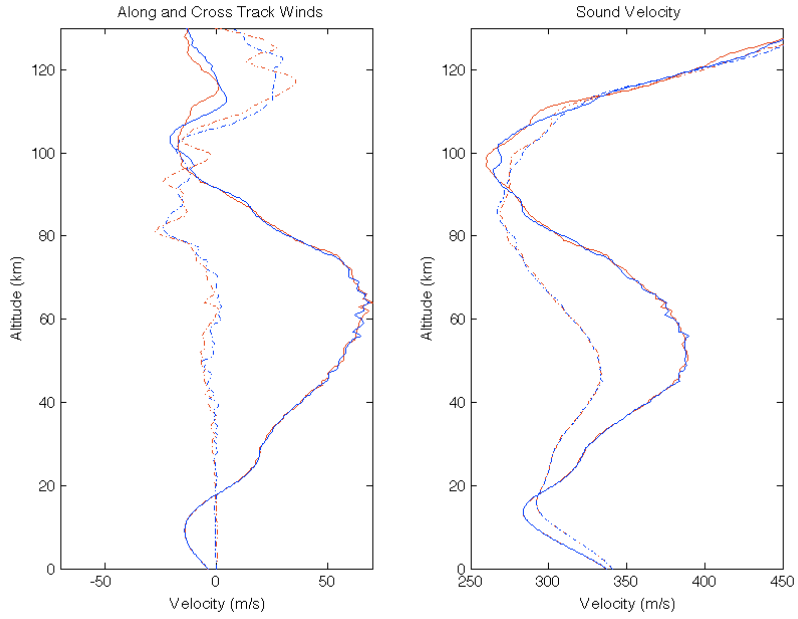

Figure 5. Atmospheric profiles including gravity wave perturbations for the propagation scenario discussed above. Color and line styles are the same as in Figure 2.

It can be observed in the figures that wave amplitudes generally grow with altitude, limited by wave-breaking and ultimately by viscosity above an altitude of about 100 km. In this example, vertical wind perturbations of 7 m/s,

temperature perturbations of 20 K, and horizontal wind perturbations of >15 m/s are predicted in the 80 to 130 km altitude region. There is a significant amount of wave-trapping below about 40 km, most clearly indicated by the more vertically oriented wave phases in the vertical velocity plots (lower left panels of Figures 3 and 4). The trapped waves have shorter horizontal scales, leaving longer scales at higher altitudes.

Applications to Infrasound Propagation Modeling for Ground-Truth Events

The G2S atmospheric specifications described above, the baseline gravity wave models due to Gardner, and a suite of infrasound propagation models (including 3D ray-tracing, parabolic equation (PE), time-domain parabolic equation (TDPE), and normal modes) are currently integrated into the tool kit InfraMAP (Gibson and Norris, 2002; Norris and Gibson, 2004). InfraMAP (*Infrasonic Modeling of Atmospheric Propagation*) has been developed by BBN for use in the study of infrasound propagation and monitoring. InfraMAP can be applied to predict attenuation, travel times, bearings, amplitudes, and waveforms for infrasonic events. The most recent version of InfraMAP includes TDPE waveform prediction capabilities (Tappert et al., 1995) based on either a canonical blast wave or any user-defined source waveform. PE and TDPE calculations incorporate effects of horizontal wind components (both mean and perturbations) by utilizing the effective sound speed approximation.

Using the baseline gravity wave model, propagation studies have been conducted for various scenarios and ground truth events. An example to quantify gravity wave effects on infrasound propagation is the Ghislenghien, Belgium, gas pipe explosion of 30 July 2004. (Evers and Haak, 2006) This event was a surface explosion of approximately 40 tons yield. It was detected at arrays throughout Europe. Here we consider the 379 km path to the Flers, France, infrasound station. Figure 6 shows the PE amplitude field predictions at 1.0 Hz for the cases in which fine-scale gravity wave perturbations are excluded and included. The mean atmospheric profiles were defined using range-dependent G2S specifications. The propagation modeling includes effects of atmospheric absorption in the thermosphere (Sutherland and Bass, 2004), which can be seen to strongly reduce predicted amplitudes of thermospheric arrivals. Stratospheric ducting can be observed in the model predictions. Without gravity wave perturbations, little energy penetrates the stratospheric shadow zone and reaches the receiver location. With gravity wave perturbations, additional scattered energy is predicted to penetrate the shadow zone and reach the receiver.

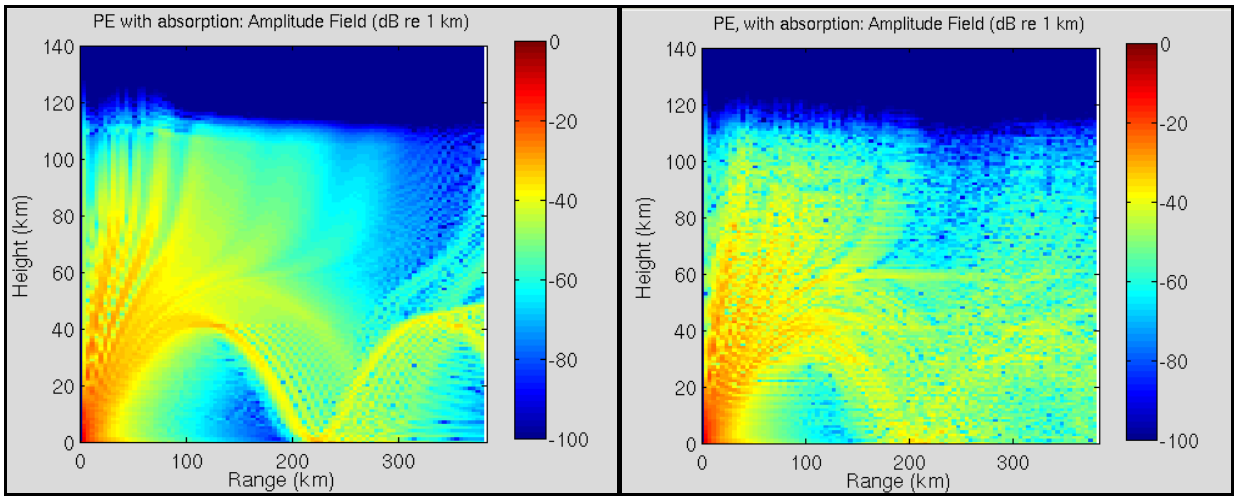

Figure 6. PE amplitude predictions at 1.0 Hz without gravity waves (left panel) and with gravity waves (right panel), for infrasound propagation from the Ghislenghien, Belgium, explosion to Flers, France.

A TDPE waveform prediction along the same propagation path is shown in Figure 7. The TDPE simulation presented here is computed over a bandwidth of 0-4 Hz and includes effects of gravity wave perturbation. With gravity waves, waveform predictions show substantial received energy. Three phases are predicted in the synthetic waveform and the arrival times of these three phases are consistent with those in the observation at Flers as reported by Evers and Haak (2006).

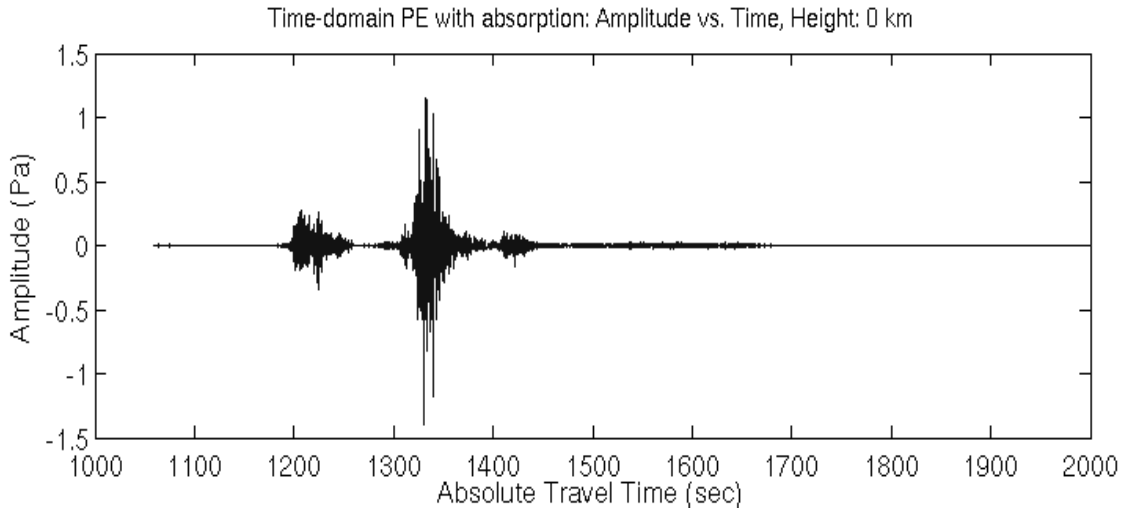

Figure 7. TDPE synthetic waveform, computed over 0 - 4.0 Hz bandwidth, including gravity wave perturbation, for infrasound propagation from the Ghislenghien, Belgium, explosion to Flers, France.

An additional example is presented for the Buncefield, England, fuel tank explosion of 11-Dec-2005. (Ceranna et al., 2007) This event was a surface explosion of approximately 30 tons yield. It was detected at arrays throughout Europe. Here we consider the 334 km path to the Flers, France, infrasound station. Figure 8 shows the TDPE simulation computed over a bandwidth of 0-4 Hz, including the effects of gravity wave perturbation.

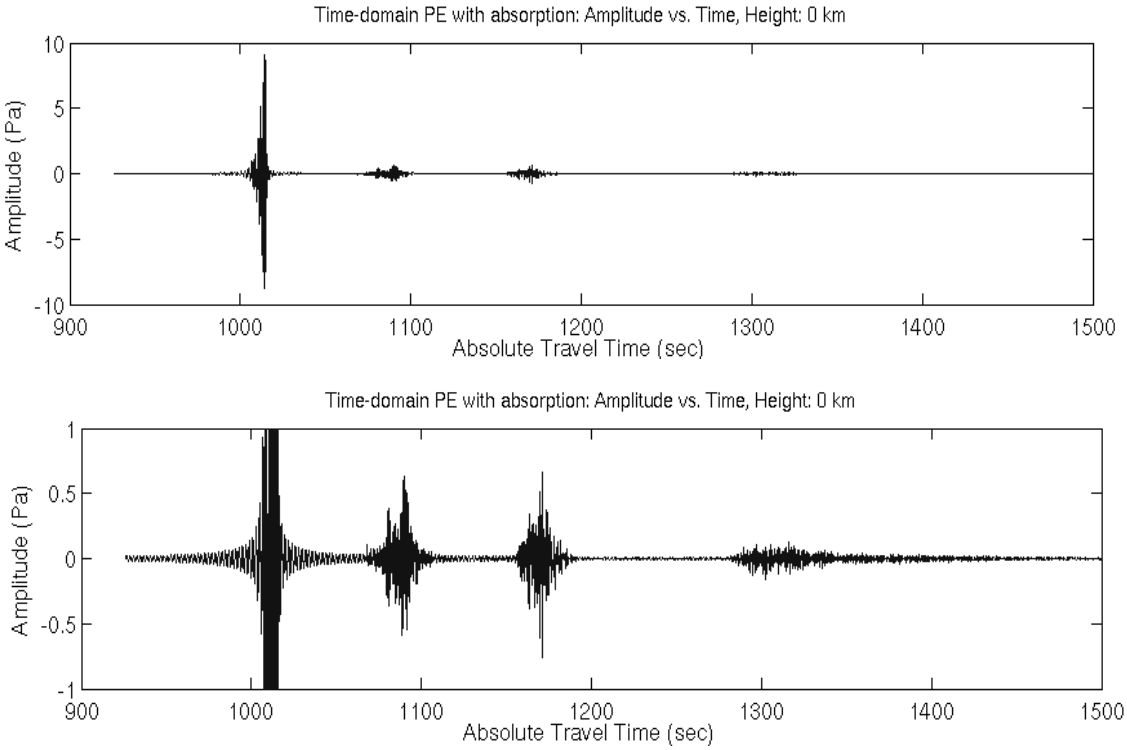

Figure 7. TDPE synthetic waveform, computed over 0 - 4.0 Hz bandwidth, including gravity wave perturbation, for infrasound propagation from the Buncefield, England, explosion to Flers, France. The synthetic waveform is shown using two different amplitude scales in the upper and lower panels.

The mean atmospheric profiles were defined using range-dependent G2S specifications, and effects of thermospheric absorption are included. Four phases are predicted in the synthetic waveform and the arrival times of these four phases are consistent with those in the observation at Flers as reported by Ceranna et al. (2007).

CONCLUSIONS AND RECOMMENDATIONS

Substantial evidence for the importance of atmospheric variability due to fine-scale inhomogeneity has been indicated by TDPE waveform predictions for events observed at regional ranges. In several instances, conventional propagation modeling has failed to predict observed arrivals due to the lack of a stratospheric duct in the baseline atmospheric characterization; these observations exist in so-called "shadow zones." However, modeled infrasound arrivals that consider energy refracted or scattered from gravity waves agree well in waveform shape, extent and arrival time with observations. These results indicate the considerable benefit to regional monitoring that is to be gained by understanding gravity wave effects on infrasound. While implementation of our existing baseline gravity wave model enables prediction of certain infrasound features, there is significant additional understanding of the fundamental physics yet to be gained and additional model fidelity that is needed.

We will continue extension of the new gravity wave calculation technique to the full 3D domain, integrating calculations with G2S mean atmospheric profiles for scenarios of interest, and considering horizontally varying mean fields of wind and density. We will also explore the numerical parameter space for source spectrum shape constants, empirical wave amplitude normalization scale factors, wave-breaking, viscosity characterization, and the optimal source spectrum seeding altitude. The formulation allows a range of frequencies ω in (1), but work so far has concentrated on source spectra with one or a few frequencies, for computational simplicity. We will investigate optimal frequency discretizations for source spectra, using a fuller range of frequencies. The new gravity wave perturbation fields will be incorporated with existing infrasound propagation models. The new formulations will be tested, compared against baseline models, and used to study additional infrasound ground truth events of interest.

REFERENCES

Alexander, M. J., S. D. Eckermann, D. Broutman, and J. Ma (2009). Momentum flux estimates for South Georgia Island mountain waves in the stratosphere observed via satellite, *Geophys. Res. Lett*., 36, L12816, doi:10.1029/2009GL038587.

Bhattacharyya, J., H. Bass, D. Drob, R. Whitaker, D. ReVelle, and T. Sandoval (2003). Description and Analysis of Infrasound and Seismic Signals Recorded from the Watusi Explosive Experiment, in *Proceedings of the 25th Seismic Research Review—Nuclear Explosion Monitoring: Building the Knowledge Base,* LA-UR-03-6029, Vol. 2, pp. 587–596.

Broutman, D., J. W. Rottman, and S. D. Eckermann (2003). A simplified Fourier method for nonhydrostatic mountain waves. *J. Atmos. Sci*., 60, 2686-2696.

Broutman, D., J. Ma, S.D. Eckermann, and J. Lindeman (2006). Fourier-ray modeling of transient trapped lee waves. *Mon. Wea. Rev*., 134, 2849-2856.

Broutman, D., S. D. Eckermann, and J. W. Rottman (2009). Practical application of two turning-point theory to mountain-wave transmission through a wind jet, *J. Atmos. Sci*., 66, 481-494.

Ceranna, L., D. Green, A. Le Pichon and P. Mialle (2007). The Buncefield Explosion: A benchmark for infrasound analysis in Europe, *Proceedings of the Infrasound Technology Workshop*, Tokyo.

Drob, D. P., J.M. Picone, and M.A. Garcés (2003). The Global Morphology of Infrasound Propagation, *J. Geophys. Res.* 108: doi:10.1029/2002JD003307.

Drob, D. P. (2004). Atmospheric Specifications for Infrasound Calculations, *Inframatics*, No. 5.

Drob, D.P., *et al*. (2008). An empirical model of the Earth's horizontal wind fields: HWM07, *J. Geophys. Res.*, 113, A12304, doi:10.1029/2008JA013668.

Eckermann, S. D. (1995). Effect of background winds on vertical wavenumber spectra of atmospheric gravity waves, *J. Geophys. Res.* 100: 14,097–14,112.

Eckermann, S.D., D. Broutman, J. Ma and J. Lindeman (2006). Fourier-ray modeling of short wavelength trapped lee waves observed in satellite imagery near Jan Mayen. *Mon. Wea. Rev*., 134, 2830-2848.

Evers, L. and H. Haak (2006). Seismo-acoustic analysis of explosions and evidence for infrasonic forerunners, *Proceedings of the Infrasound Technology Workshop*, Fairbanks.

Fritts, D. C., and W. Lu (1993). Spectral estimates of gravity wave energy and momentum fluxes, II: Parameterization of wave forcing and variability, *J. Atmos. Sci.* 50: 3695–3713.

Fritts, D. C., and J. M. Alexander (2003). Gravity Wave Dynamics and Effects in the Middle Atmosphere, *Rev. of Geophys.* 41: 1, 1003.

Gardner, C. (1993). Gravity Wave Models for the Horizontal Wave Number Spectra of Atmospheric Velocity and Density Fluctuations, *JGR* 98; D1, 1035–1049.

Gardner, C. (1995). Scale-Independent Diffusive Filtering Theory of Gravity Wave Spectra in the Atmosphere, *The Upper Mesosphere and Lower Thermosphere: A Review of Experiment and Theory*, Geophysical Monograph 87, AGU.

Gibson, R., and D. Norris (2002). Development of an Infrasound Propagation Modeling Tool Kit, *Defense Threat Reduction Agency Technical Report DTRA-TR-99-47*, Alexandria, VA.

Gibson, R. G., D. E. Norris and D. P. Drob (2008). Investigation of the effects of fine-scale atmospheric inhomogeneities on infrasound propagation, in *Proceedings of the 30th Seismic Research Review—Ground-Based Nuclear Explosion Monitoring Technologies*, LA-UR-08-05261, Vol. 2, pp. 872–881.

Hedin, A.E., E.L. Fleming, A.H. Manson, F.J. Scmidlin, S.K. Avery, R.R. Clark, S.J. Franke, G.J. Fraser, T. Tsunda, F. Vial, and R.A. Vincent (1996). Empirical Wind Model for the Upper, Middle, and Lower Atmosphere, *J. Atmos. Terr. Phys.* 58: 1421–1447.

Kulichkov, S.N. (2004). Long-range propagation and scattering of low-frequency sound pulses in the middle atmosphere, *Met. Atmos. Phys*. 85: No. 1–3, pp. 47–60.

Mutschlecner, J., and R. Whitaker (2006). *Infrasonic Signals from the Henderson, Nevada, Chemical Explosion*, LA-UR-06-6458.

Norris, D., and R. Gibson (2002). InfraMAP Enhancements: Environmental/Propagation Variability and Localization Accuracy of Infrasonic Networks, in *Proceedings of the 24th Seismic Research Review—Nuclear Explosion Monitoring: Innovation and Integration*, LA-UR-02-5048, Vol. 2, pp. 809–813.

Norris, D., and R. Gibson (2004). Advanced Tools for Infrasonic Modeling, *Inframatics*, No. 5.

Picone, J., A. Hedin, D. Drob, and A. Aiken (2002). NRLMSISE-00 empirical model of the atmosphere: statistical comparisons and scientific issues, *J. Geophys. Res.* 107: 1468.

Sutherland, L. and H. Bass (2004). Atmospheric absorption in the atmosphere up to 160 km. *J. Acoust. Soc. Am.*, 115, 1012-1032.

Tappert, F., J.L. Spiesberger, and L. Boden (1995). New full-wave approximation for ocean acoustic travel time predictions, *J. Acoust. Soc. Am*., 97, 2771-2782.

Warner, C.D., and M.E. McIntyre (2001). An ultrasimple spectral parameterization for nonorographic gravity waves, *J. Atmos. Sci.* 58: (14), 1837–1857.

NEAR-SOURCE AND FAR-REGIONAL INFRASOUND OBSERVATIONS FOR SAYARIM TEST EXPLOSIONS

Yefim Gitterman[1], Milton A. Garces[2], J. Roger Bowman[3], David Fee[2],
Hans G. Israelsson[3], Rami Hofstetter[1], and Vladimir I. Pinsky[1]

Geophysical Institute of Israel[1], Infrasound Laboratory of University of Hawaii[2], and
Science Applications International Corporation[3]

Sponsored by the Army Space and Missile Defense Command

Award No. W9113M-07-C-0189

ABSTRACT

During the second year of this project we continued preparations for a large surface calibration explosion of 80 tons TNT at Sayarim Military Range (SMR), Israel, planned for August 2009. The Geophysical Institute of Israel (GII) calibrated low-frequency electret condenser sample microphones at the Infrasound Laboratory, University of Hawaii (ISLA), using a specialized infrasonic source – a subwoofer rotary speaker. Signals were also referenced to Chaparral 2.2 and 5.0 sensors. The microphone sensitivity was found roughly flat to acoustic pressure over the range 3–17 Hz.

We also completed processing and analysis of observations for a series of ammunition detonations and experimental explosions conducted in summer 2008. An extensive dataset of near-source acoustic observations, for the broad charge range of 0.2–10 tons, allowed for the determination of a yield scaling relationship based on signal amplitude and energy. Some of the relatively small Sayarim explosions were detected at International Monitoring System (IMS) infrasound station I48TN (Tunisia, 2500 km), and I26DE (Germany, 2800 km), using array-processing techniques. These observations confirmed favorable westward infrasonic propagation conditions in the Mediterranean region during summer.

Additionally, two test explosions of 1 ton and 5 tons (mix of TNT, Composition B and RDX) were conducted at SMR in December 2008. The test explosions provided a means to train field and scientific staff in test preparation, coordination, logistics, charge design, and assembly in anticipation of the main explosion in August 2009. We measured high-pressures from the air-blast waves at close distances. High-speed video recordings provided validation of these explosives in anticipation of the main explosion, as well as estimation of TNT equivalent yields. Data obtained from the test series were used for the design and logistics of the main calibration explosion.

We analyzed signals from the December test explosions, recorded on seismic and acoustic channels of portable and permanent stations deployed at near-source and local distances. We compared energy generation for different explosives, including cratering conditions, and investigated the influence of wind direction on infrasound arrivals.

Modeling of the long-range atmospheric propagation of infrasound was conducted using global G2S atmospheric profiles and local atmospheric data. The optimal date and time window of the experiment (August 2009) as well as the locations of portable infrasound systems in Mediterranean region were selected based on experimental and infrasound modeling results.

OBJECTIVES

- Calibration of GII microphones;
- Analysis of observations of Sayarim explosions at IMS stations;
- Testing of explosives feasibility, charge design and assembling procedures for the main explosion;
- Analysis of seismo-acoustic signals from test explosions at near-source and local distances; and
- Modeling of long range atmospheric propagation of infrasound in the Mediterranean region.

RESEARCH ACCOMPLISHED

The activities and research during the project's second year included preparations for conducting the main surface calibration explosion at Sayarim, and observations of infrasound waves in a broad distance range.

Calibration of GII Microphones

We calibrated three low-frequency electret condenser sample microphones at ISLA, using a specialized infrasonic source – a subwoofer rotary speaker. Signals were also referenced to co-located Chaparral 2.2 and 5.0 sensors, which were recently calibrated (Figure 1). The testing setup consisted of a laptop and a wave file to generate a time dependant signal that increased in frequency (i.e., a sweep). This method allowed a well-controlled signal to be run through the rotary speaker to provide a relatively flat and broadband infrasonic output signal. A 12-minute frequency sweep test between 0.1–25 Hz was performed for all microphones, with the gain set to 14 dB (Figure 2). The microphone sensitivity was found to be roughly flat to acoustic pressure over the range 3–17 Hz, with values about 1.3 V/Pa.

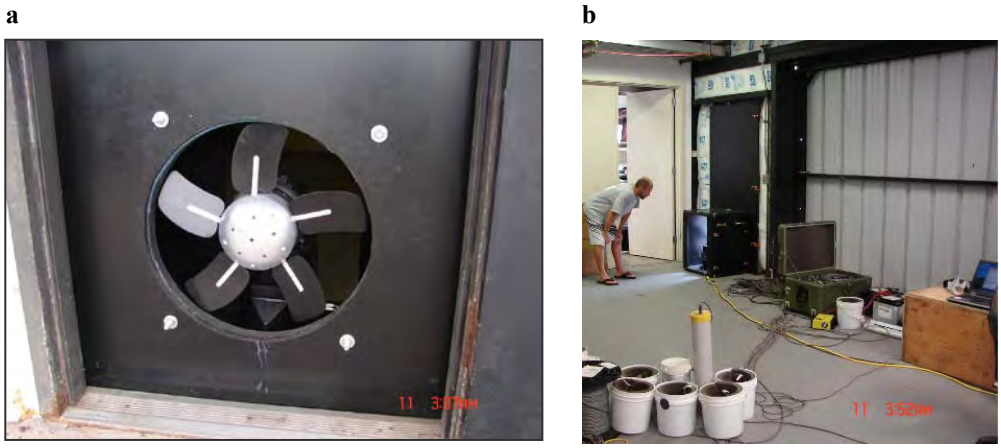

Figure 1. Calibration of GII microphones at ISLA by subwoofer rotary speaker (a), when a microphone (in a tube) was co-located with reference calibrated Chaparral sensors (b).

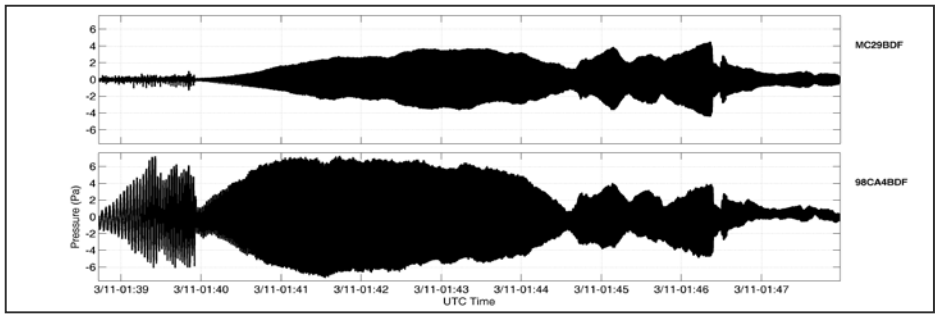

Figure 2. Waveforms for a frequency sweep test, with Mic29 on top and the reference sensor below (the scale is the same). The test started at low frequencies, where microphones have a diminished response. For higher frequencies, after ~01:44 UTC, similar amplitudes are observed for both sensors.

Observations of Sayarim Explosions at IMS Stations

GII collaborated with Science Applications International Corporation (SAIC) in the analysis of infrasound signals from Sayarim explosions observed at IMS stations. GII supplied SAIC with Ground Truth Information (GTI) for 148 old ammunition detonations conducted at SMR during 2005–2008. The explosions were recorded by the Israel Seismic Network (ISN), which provided estimations of location (accuracy ~1–2 km) and detonation time (accuracy ~0.3–0.5 sec). GTI0 for 12 experimental and ammunition explosions conducted within the project duration was also provided (exact yield, coordinates and detonation time, measured by GII team). Based on this GTI, the SAIC team analyzed records of four IMS infrasound stations close to SMR (Figure 3) and found clear infrasound signals for many SMR explosions. Special array-processing procedures, including the automated generation of plots and manual review of signal-processing plots to confirm signals were used to analyze data.

Two samples of this analysis are presented below.

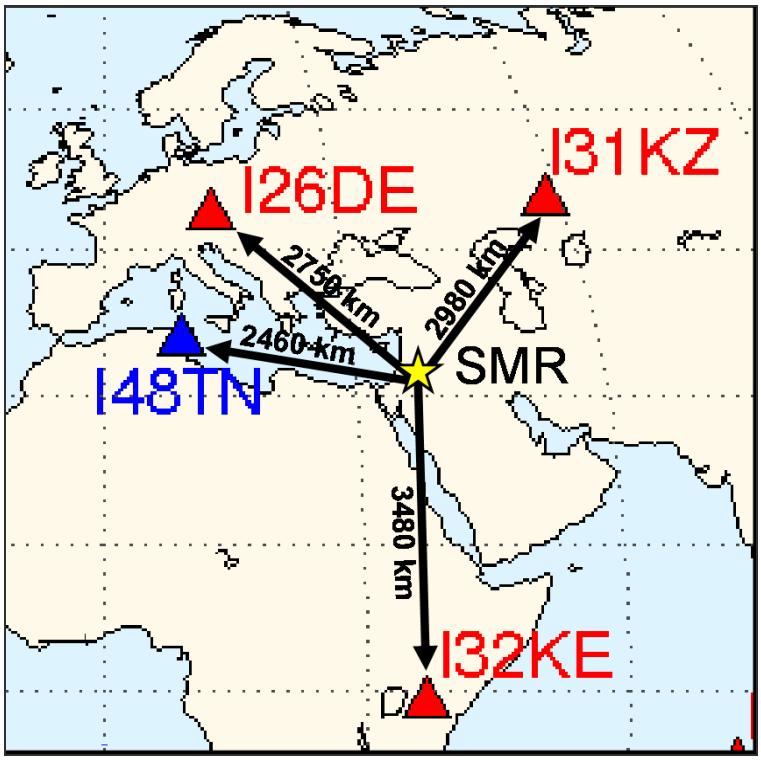

Figure 3. SMR shots were analyzed at the four closest IMS stations.

July 23, 2007 event. Two explosions were conducted at SMR with coordinates corresponding to the known place for demolition of old ammunitions (GTI0: 29.994N/34.805E), with a delay of 1 min 27 sec (Table 1). Clear acoustic phases were found at seismic channels of the ISN, confirming ammunition detonations (Figure 4).

Table 1. GTI parameters of two explosions at SMR on July 23, 2007.

No.	Origin Time, GMT	Latitude N	Longitude E	Local Magnitude	Charge**, tons
1	12:31:29.6*	29.9932*	34.7899*	2.3*	5-7
2	12:32:56.7*	29.9819*	34.7947*	2.3*	5-7

* estimation by ISN location procedure; ** estimation by the magnitude

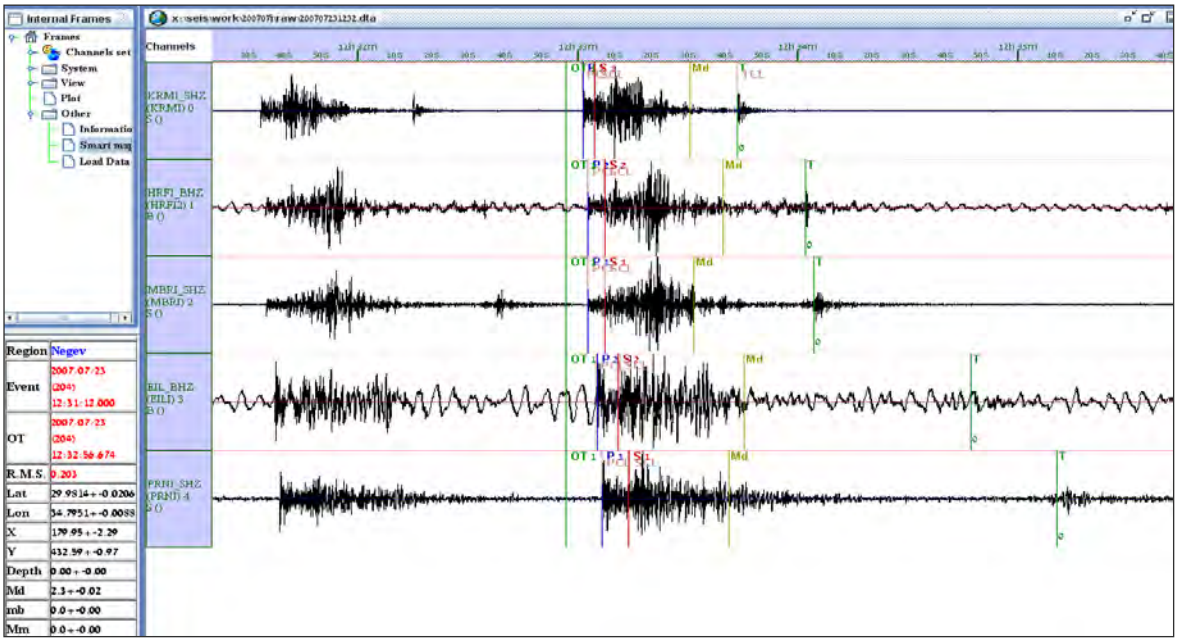

Figure 4. Seismogram of two explosions at SMR, showing clear acoustic phases at ISN seismic channels. Phase picking, estimation of the origin time, coordinates and local magnitude, provided by jSTAR software (Pinsky et al., 2007), are shown for the second explosion.

A wave group of about six to eight arrivals was found at two IMS stations (Table 2, Figure 5), corresponding to different infrasound phases that propagate through different atmospheric layers, from the two explosions on July 23, 2007. Due to the small time delay between the explosions, the infrasound phases from the two explosions are not separated, but merged into one group.

Table 2. Observations from two SMR explosions on July 23, 2007 at two IMS stations.

Station	Lat., N	Lon., E	Azimuth °		Distance, km	First arrival	Propagation time, sec	Group velocity, m/s
			Actual	Measured				
I48TN	35.8052	9.323	98	~100	2461.4	14:40:00	7710	320
I26DE	48.8516	13.7131	132	~130	2753.0	~14:57:00	~8730	~315

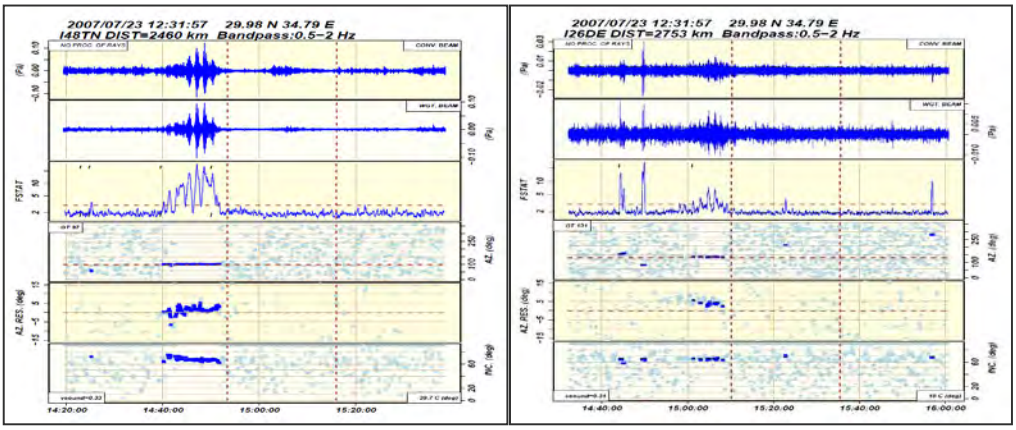

Figure 5. Observations of Sayarim explosions at two IMS stations on July 23, 2007: I48TN (a) and I26DE (b).

June 25, 2008 event. Two test explosions were jointly conducted by GII and the Israel Defense Force (IDF) at SMR, with an approximate ten minute delay: an ammunition detonation and an experimental project shot (Gitterman and Hofstetter, 2008). Accurate GTI was collected and measured (Table 3). Signals from the two shots, recorded at two close ISN stations with opposite backazimuths, showed a drastic difference in the amplitude ratio of seismic and acoustic phases (Figure 6).

Table 3. GTI parameters of two explosions at SMR on June 25, 2008.

No.	Charge, tons	TNT equiv., tons	Origin Time, GMT	Latitude, N	Longitude, E	Local Magnitude
7	8.63	10.36	10:27:48.1	29.99156	34.80462	2.5
8	1.02	1.224	10:37:05.4	29.99446	34.80417	2.0

Stronger signals are observed in the northwest direction and shown in Figure 6, caused by atmospheric conditions (wind velocity and direction). Favorable infrasound propagation conditions were also present towards IMS station I48TN, providing a clear signal observation from a rather small shot of ~1 ton, as shown in Figure 6 (Explosion 8).

Two separate groups of arrivals are observed at IMS station I48TN at 2460 km: six to seven arrivals from the ~10 ton explosion (Explosion 7) of old ammunition, and after about ten minutes, another three to four arrivals, evidently from the experimental ~1 ton explosion (Explosion 8) (Figure 7). Besides the suitable propagation times, the signal-event association is also confirmed by consistent array-estimated azimuths corresponding to the actual value (Table 4).

Table 4. Observations of two SMR shots on June 25, 2008 at IMS station I48TN.

No.	Distance, km	Azimuth, deg.		Arrivals	Propagation time, sec	Group velocity, m/s
		actual	measured			
7	2461.4	98	~100	First ~12:37:00	~7752	~317
				Max ~12:45:30	~8262	~298
8	2461.3	98	~100	First ~12:50:00	~7975	~307
				Max ~12:54:30	~8245	~299

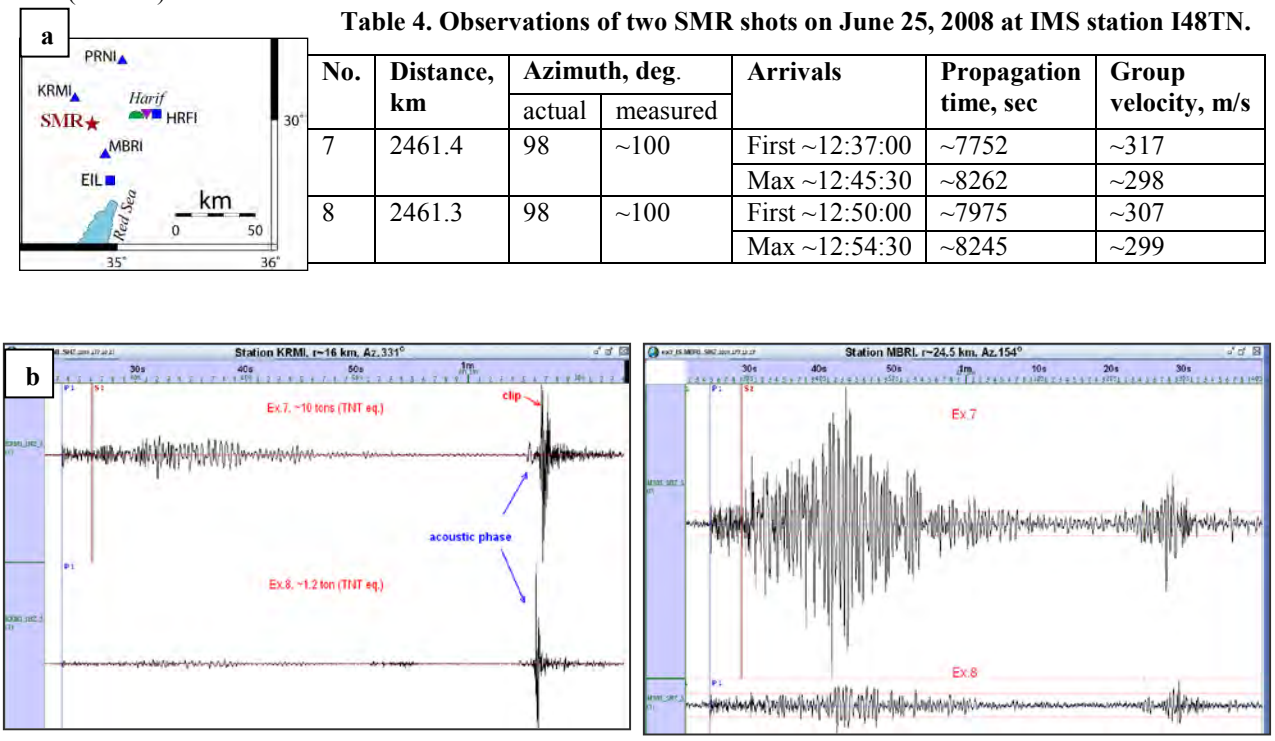

Figure 6. Map of local stations and recorded explosions at SMR (a) and seismograms of two shots at two ISN stations, with the absolute scale applied (b).

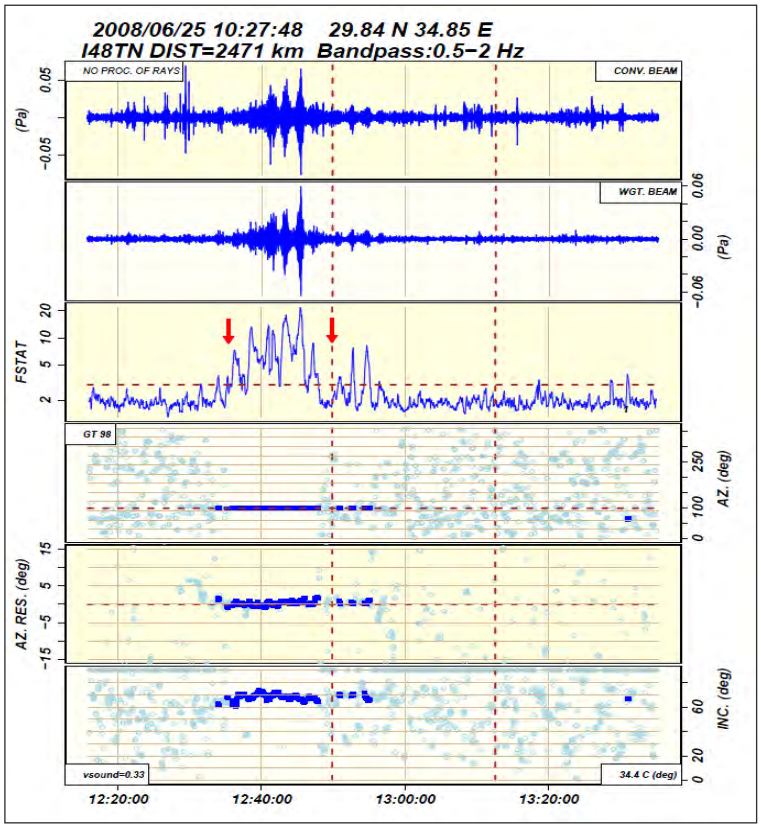

Figure 7. Observations of Sayarim shots at IMS infrasound station I48TN on June 25, 2008. Red arrows show two groups of arrivals.

Testing of Explosives Feasibility and Charge Design.

Two experimental surface shots of 1 ton and 5 tons (Series 3) were conducted in December 2008, with the goals of 1) training project staff in logistics operations, assembling of charge units, and charge building; 2) measuring high pressures and high-speed video, for the estimation of TNT equivalency for a variety of used explosives (recuperated TNT, Composite B and RDX); and (3) determining the efficiency of upward detonation with respect to charge design for maximizing the coupling of acoustic energy to the atmosphere.

Parameters of the explosions are presented in Table 5, and Figure 8 shows the charge view and successive snapshots from recording by high-speed video camera (Phantom-3, at 4000 frames/sec), installed at 600 m.

Table 5. Parameters of Sayarim explosions, December 2008 (coordinates 30.09007 N, 34.79499 E, h=523 m).

No.	Date	Origin Time, GMT	Local Coordinates		Design	Charge weight, ton
			X, km	Y, km		
1	12/2	13:12:35.9	179.978	444.642	Tower, 3 big bags	1.04
2	12/3	10:22:16.2	179.978	444.630	Cubic-like, 16 big bags	5.08

Figure 8. Recuperated explosives used in Series 3: cast TNT pieces and RDX powder to fill voids (a); view of the 5 ton charge, assembled of big bags containing pieces of explosives and red detonation cord, attached to the booster under a wooden platform (b); snapshots of high-speed video of the 1 ton shot during the first second after the initiation (c).

Some specific effects of the surface explosion were observed on the high-speed video: propagation of detonation in the detonation cord with a velocity of ~6500 m/s, the air-blast wavefront in the air, and spreading of the fireball. The observed fireball radius was roughly estimated as ~20–25 m for the 1 ton shot, and 35–40 m for the 5 ton shot; the predicted radius for the main 80 ton explosion is ~100-120 m; this estimate is important for planning near-source sensor deployment. Some optical effects of unclear origin were observed at 0.25 ms and 1 ms (Figure 8c).

Boosters were placed on the ground (Figure 8a), and upward detonation was applied in this experiment, unlike the downward detonation in the two 1-ton test shots in Series 2 in June 2008 (Gitterman and Hofstetter, 2008), in order to increase the explosive energy released to the atmosphere.

High-pressure measurements were made to validate the effectiveness of the charge design and the variety of recuperated explosives as well as to estimate the charge equivalency to homogenous pure TNT. Four XTL-190-5G pressure gauges (Figure 9a) were installed in the distance range 140–250 m. Both explosions were recorded well at all sensors (sampling rate 2 MHz). A sample record for 1 ton at the closest sensor is shown in Figure 9b; measured parameters are presented in Table 6. Predicted peak pressures were also calculated using DDESB Blast Effects

Computer Version 4.0 (BECV4) (Swisdak, 2000), for TNT explosives at open storage and actual altitude 523 m and temperature 20°C.

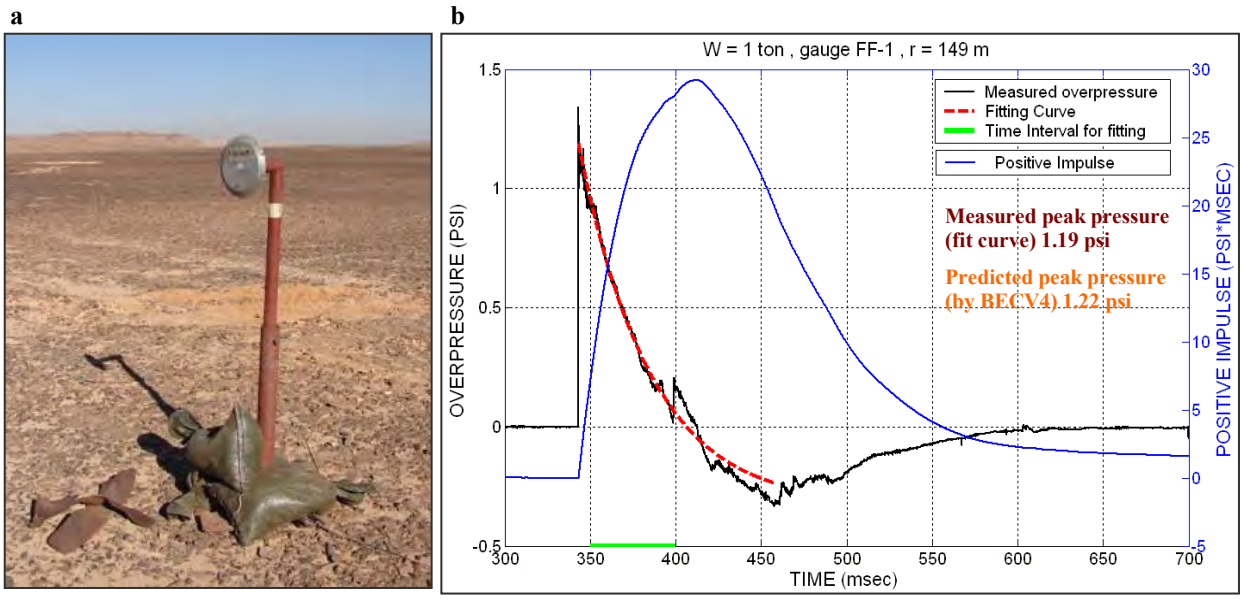

Figure 9. The closest high-pressure gauge FF-1 at 149 m from the 1 ton explosion (a), and the appropriate record (b). Predicted peak pressure is obtained by BECV4 for 1.04 ton TNT.

Table 6. High pressure measurements for the 1 ton explosion and predictions by BECV4 for the 1.04 ton TNT charge, altitude 523 m, temperature ~20°C.

Gauge	Distance m	Peak overpressure, psi			Positive Phase Duration, msec			Positive Phase Impulse, psi*msec		
		predicted	measured		predicted	measured		predicted	measured	
			Abs. Max	Fit curve		Actual	Fit curve		Actual	Fit curve
FF-1	149.4	1.22	1.34	1.19	55.7	68.8	64.5	29.9	29.2	28.5
FF-2	202.0	0.83	1.45	0.85	61.0	67.4	69.3	22.3	23.0	22.7
FF-3	199.4	0.85	1.35	0.90	60.7	82.8	71.8	22.6	21.9	21.8
FF-4	244.4	0.66	0.69	0.62	64.2	72.8	74.1	18.5	17.7	17.7

Due to some irregularities in the high-pressure time history (especially in the beginning of the signal), we estimated the time history using an exponential function. This yielded a more reliable estimation of the peak overpressure and positive phase duration values (see Figure 9b).

All measured peak pressure and impulse values correspond approximately to estimations of equivalent TNT (Table 6). Negative factors, such as inhomogeneity of the charges, variety of explosive types, and numerous air voids in the charge body, were compensated by a higher-than-TNT explosive energy for Composite B and RDX, and by the upward detonation.

Cratering effects observed for surface explosions can be considered an indicator for explosive energy partitioning between seismic waves in the ground and acoustic waves in the atmosphere. A striking distinction was found for the experimental project explosions at SMR with charges equivalent to 1 ton of TNT and Composite B with different detonation directions. For two explosions in Series 2 (TNT and Composite B), conducted in June 2008 (Gitterman and Hofstetter, 2008), the boosters were placed on the top of the charge (Figure 10a), providing the downward detonation. Both explosions produced large, deep (~0.5 m) craters (a little deeper for the explosion with

more powerful Composite B) (Figure 10b). As presented above, the downward detonation was applied to the 1 ton explosion in December 2008, resulting in a very small shallow crater (Figure 10c, d). In the explosion area, the subsurface layer of ~0.5-1 m consists of powder, loose sediments, with consolidated sediments below.

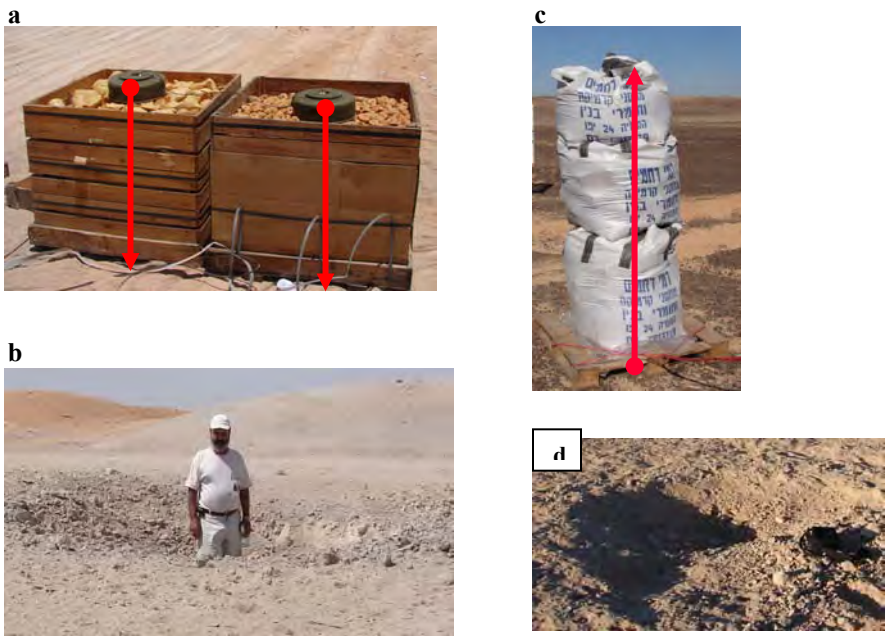

Figure 10. Cratering effects for two explosions in June 2008 at SMR of 1 ton TNT and Composite B, where downward detonation (a) created a large deep crater (b), and upward detonation, in December 2008 (c), produced a very small shallow crater (d).

A smaller crater for the upward detonation shows that more explosive energy was released to the atmosphere, and less energy was focused into the ground, compared to the downward detonation. Based on high-speed video and high-pressure observations, the TNT equivalency for the variety of charges (e.g., recuperated explosives) was proven, and the efficiency of the upward detonation and the charge design were also confirmed by cratering features.

Modeling of Long-Range Atmospheric Propagation of Infrasound in Mediterranean Region.

Preliminary modeling of the long-range atmospheric propagation of infrasound was conducted by the ISLA team using global G2S atmospheric profiles and local data collected for this experiment (Figure 11). These calculations demonstrated favorable conditions for infrasonic propagation in the Mediterranean in the western direction in the summer months (Figure 12). This was confirmed for the Sayarim explosions of ~10 tons and 1 ton in June 2008, which were well observed at IMS station I48TN (Figure 7). In the opposite direction, for similar explosions of 1 ton and 5 tons in December 2008 (Table 5), no signals were found at this station, indicating the effect of the change in stratospheric winds on regional propagation.

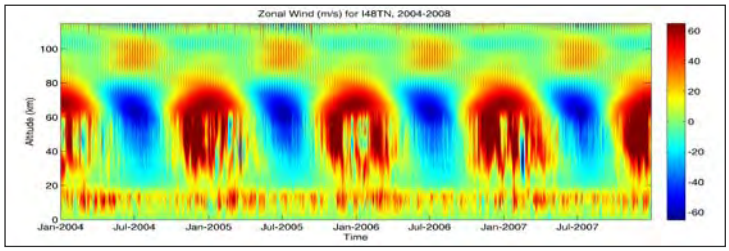

Figure 11. Atmospheric profile data (altitudes 0-140 km at 6 hr increments) for the direction to I48TN, for four recent years.

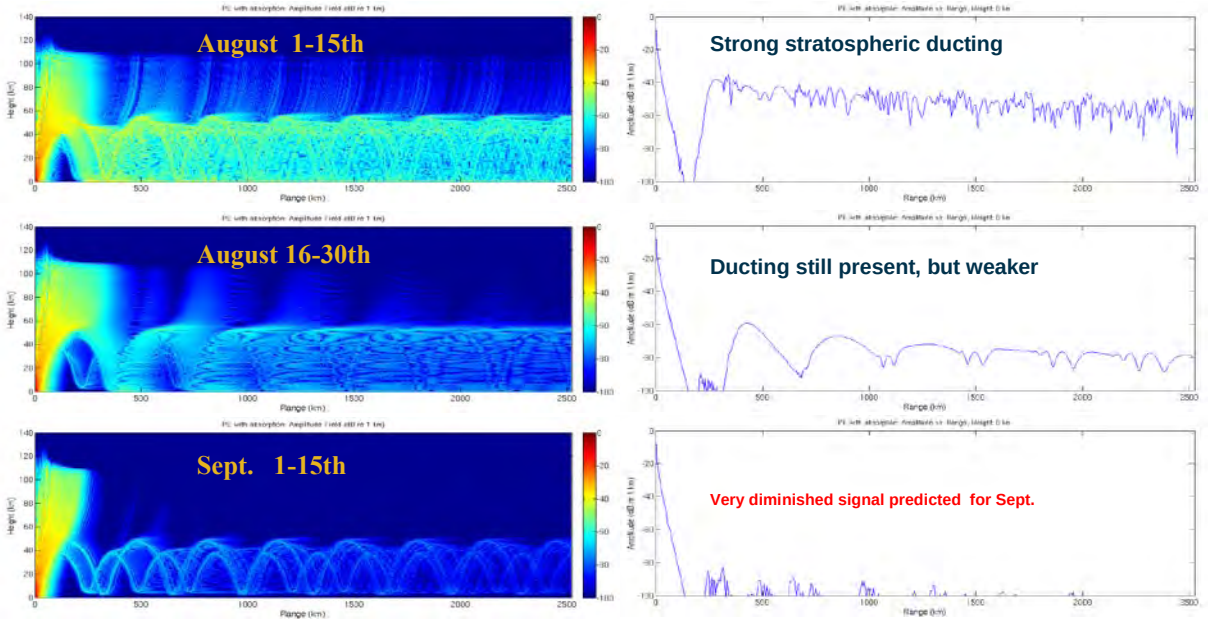

Figure 12. Average profile for infrasound propagation modeling for I48TN (Tunisia) at different periods.

Optimal date and time windows of the experiment and locations of portable infrasound systems in the Mediterranean region were selected (Figure 13) based on the following experimental and infrasound modeling results:

- Stratospheric easterly winds die out by early September:
  - Decreasing probability of detection for long-range westward stations past July;
- Cyprus station not as affected by prevailing stratospheric winds (due north location):
  - Stations from Crete to the west have likely stratospheric arrivals in July/August;
- Minor contribution from meridional (N-S) winds for all locations;
- Two week averages produce more reliable atmospheric models;
- Late night/early morning shot times give highest probability for detection:
  - Lowest ambient noise conditions,
  - Tropospheric Nocturnal Duct, and
  - Lowest effective sound speed at surface.

Based on atmospheric (wind) conditions and modeling of infrasound propagation to large distances, and also on the logistics of conducting the explosion and station deployment, the main explosion date was determined to be on August 26, 2009, the detonation time window: 6AM-9AM (local time), and possible locations of portable infrasound systems in the Mediterranean region were selected and surveyed (Figure 13).

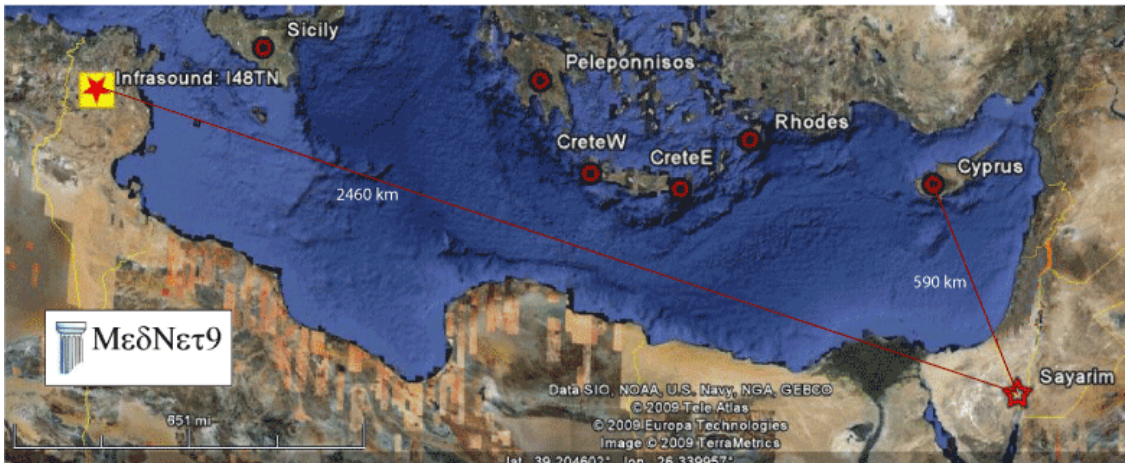

Figure 13. Planned portable deployment of infrasound arrays in the Mediterranean region during the Sayarim Calibration Explosion. Sites are also being considered in Turkey.

CONCLUSIONS AND RECOMMENDATIONS

- GII microphone sensor systems were calibrated at ISLA; frequency response and sensitivity were defined;
- Observations of rather small Sayarim explosions at the two closest IMS stations indicate the likely recording of the main calibration explosion at four and more IMS stations, placed at distances more than 3500 km;
- The conducted experimental explosions helped determine explosive feasibility, charge design, and assembly procedures for the main explosion; the TNT equivalency for the charges consists of a variety of recuperated explosives, and efficiency of upward detonation;
- Modeling of long-range atmospheric propagation of infrasound in the Mediterranean region provided a basis for the selection of the detonation time window of the main calibration explosion, and locations of long-range portable stations.

ACKNOWLEDGEMENTS

Thanks to blast manager Kobi Shimon of Elita Security Ltd. and his team for conducting the experimental explosions. E. Stampler and the team of IDF Experiment Division provided high quality video-recording and high-pressure measurements. We appreciate the valuable support and help of Dr. D. Havatzelet of the Israel Ministry of Defense in providing the experiment measurements. Thanks to GII personnel U. Peled for preparation and installation of portable stations and N. Perelman for processing and analysis of high-pressure records.

REFERENCES

Gitterman Y. and R. Hofstetter (2008). Infrasound Calibration Experiment in Israel: Preparations and Test Shots, in *Proceedings of the 30th Monitoring Research Review: Ground-based Nuclear Explosion Monitoring Technologies*, LA-UR-08-05261, Vol. 2, pp. 882–893.

Pinsky V., A. Polozov, D. Kadosh, A. Avirav, and R. Hofstetter (2007). New seismic system for acquisition and analysis in Israel. Abstracts of XXIV General Assembly of IUGG, July 2–13, 2007, Perugia, Italy.

Swisdak M. (2000). DDESB Blast Effects Computer, Version 4.0.

INFRASOUND SENSOR AND POROUS-HOSE FILTER EVALUATION RESULTS

Darren Hart and Timothy S. McDonald

Sandia National Laboratories

Sponsored by the National Nuclear Security Administration

Award No. DE-AC04-94AL85000/SL07-CE-NDD02

ABSTRACT

The Ground-Based Nuclear Explosion Monitoring Research and Development (GNEMRD) program at Sandia National Laboratories (SNL) is regarded as the primary center for unbiased expertise in testing and evaluation of geophysical sensors and instrumentation for nuclear explosion monitoring. Over the past three years Sandia has evaluated over 60 Chaparral Physics 2.5 low-gain infrasound sensors. Results delivered to the customer are the sensitivity and an estimated pole-zero instrument response for the individual sensors. Once these sensors are installed in the field, the sensors inlets are typically attached to a wind-noise reduction system (e.g., porous-hose array). The addition of the wind-reduction system to the calibrated sensor brings into question the reported results, until the new system (sensor + wind-reduction technique) is evaluated for its response, of amplitude and phase, to both coherent and incoherent signals. One area of focus has been to understand the effects of porous-hose filters used at some monitoring sites for reducing acoustic background signals. A set of experiments was designed to estimate the relative gain of the porous-hose filter system in various configurations: Fiskers and Garden Rite brands at lengths of 25, 50, and 75 feet; a group of 10 "aged" F brand hoses; a set of three "new" Garden Rite hoses; a comparison between the field performance of a single coiled hose and one stretched out in a straight line; and a controlled indoor experiment with coherent signals. The basic plan is to first characterize three Chaparral Physics 2.5 low gain infrasound sensors at a single frequency and verify their instrument responses versus a reference Microbarometer 2000. The initial test configuration was to place and coil the hoses within an acoustic isolation chamber. Acoustic "white noise" is fed into the chamber and data is collected for a half-hour. The relative gain of the porous-hose filters is estimated by computing the ratio of the power spectra. With the chamber experiment complete a single 50-ft porous-hose was fielded in both a coiled and straight configuration, and acoustic background was used to show the hose response to a random acoustic source. The final experiment was set up to determine the response of the porous-hose to a coherent acoustic signal generated within a controlled indoor environment. Results show differences in the high-frequency filtering amplitude response between the different porous-hose configurations and the acoustic input signals.

OBJECTIVES

Over the past year the Component Evaluation project of the Ground-Based Nuclear Explosion Monitoring Research and Development program at Sandia has taken initial steps to better understand the complexities of the porous-hose wind-filter reduction systems used at some infrasound stations. The complexities arise when only the sensors are evaluated for their instrument response (both amplitude and phase) to dynamic input signals and the porous-hoses portion of the field system is left uncharacterized, or ignored. Here we show results of the variability in filtering characteristics observed between different brands and different lengths of porous-hose and within a single brand to a random "white" acoustic signal. We then move into the field with a set of experiments to show the differences between the coiled-hose chamber experiment and a typical deployment of the porous-hose. The acoustic input was limited to using acoustic background signals for analysis. The final experiment was to deploy a single 50-ft porous-hose in a controlled indoor environment to observe the response of the porous-hose to coherent acoustic signals. Through these experiments we show the variability of the porous-hose wind reduction system to a variety of acoustic sources.

Introduction

Over the past two years, Sandia has evaluated over 60 Chaparral Physics model 2.5 low-gain infrasound sensors. Once the sensors are evaluated they are returned to the customer for deployment. The sensors are evaluated for sensitivity, noise, dynamic range and instrument response. When the sensors are deployed in the field, they are typically attached to a wind-noise reduction system (WNRS). These WNRSs can take several forms, e.g., rosette pipe or porous-hose array. In this paper we will take a look into the filter characteristics of the porous-hose WNRS and its effect on both incoherent and coherent signals. Our goal is to better understand the implications of not correcting infrasound time series data for the amplitude and phase response of the WNRS.

The research for this paper was separated into four main areas:

1. Evaluation of reference sensors and acoustic input signal
2. Chamber evaluation of porous-hose filters
3. Field exercise using acoustic background signals (single hose and random acoustic input)
4. Controlled exercise with coherent signals (single hose and random acoustic input)

RESEARCH ACCOMPLISHED

Evaluation of Reference Sensors

For this experiment, three Chaparral Physics model 2.5 infrasound sensors were used. Their calibration was done using a technique referred to as "Comparison Calibration" (CompCal), which allowed us to transfer a calibration of a known reference sensor to the unknown sensors. The CompCal technique requires a reference sensor with well-known characteristics (e.g., self-noise, amplitude and phase response). We used the Microbarometer 2000, SN1380 as our reference sensor. Figure 1 shows our infrasound test bed with isolation chamber, acoustic source and reference sensor. A Smart24 digitizer was used to record the output of the four sensors, as well as generate the calibration sinusoid used as input to the acoustic source. A 5-V peak-to-peak 1-Hz sine wave was generated and the output of the acoustic source was recorded by the four sensors. Table 1 shows the results of using a sine-fit algorithm to determine the characteristics of the recorded signals.

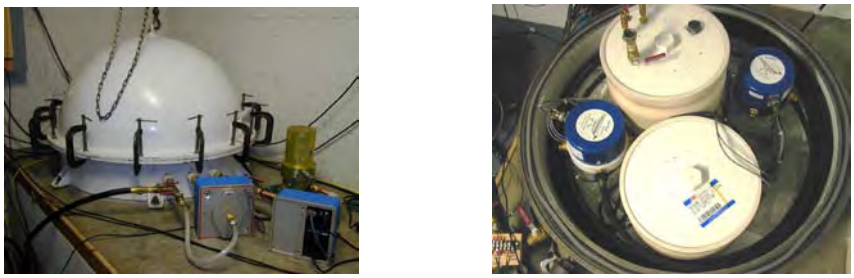

Figure 1. Sandia's acoustic test chamber (white dome) and acoustic source and MB2000 (left). The picture at right shows the inside of the acoustic test chamber, with two CP 2.5 sensors, porous-hose, and volume-reducing fixtures .

Table 1. Compiled results from a comparison calibration of the Chaparral 2.5 sensors relative to the MB2000.

Sensor	Output Voltage (V)	Sensitivity @ 1 Hz (V/Pa)	Acoustic output (Pa)	DWR LSB (V/Count)	Calibration @ 1 Hz (Pa/Count)
1380(MB)	0.576	0.1000	5.7638	3.27E-06	3.270E-05
071911	2.558	0.4439	5.7638	3.27E-06	7.367E-06
071912	2.334	0.4049	5.7638	3.27E-06	8.075E-06
071959	2.312	0.4012	5.7638	3.27E-06	8.151E-06

The next step is to perform the Response Verification test on the three CP 2.5 sensors. This test requires a "white" noise acoustic signal. A WaveTek model 132S signal generator was used to produce the input to our acoustic source (APS Dynamics Model 330 piston-phone). This produced a consistent signal that will be used in subsequent testing to characterize the filtering effects of the porous hoses. We observe the sensors to have a common response to the acoustic signal between 0.1 and 30 Hz. We applied the single frequency calibration (1 Hz) calculated previously to the raw waveforms. Deviations in the power spectrum represent variations in the instrument responses not accounted for in our procedure. The final step is to ratio the spectra relative to the MB 2000 to give the "relative gain" between the two acoustic systems. In this case they are identical over the pass band and result in the expected unity gain.

Chamber Evaluation of Porous-Hose Filters

With the calibration factors calculated and sensors characterized, we can focus on characterizing the filtering characteristics of the hoses attached to the sensors to reduce undesired signal content. In the past, the Fiskers® brand (F) has been accepted as the preferred brand to use. Recently, the F brand has become unavailable due to the manufacturer ending production. The Garden Rite® brand (GR) is being considered as a replacement. We are looking to determine if the two brands have a consistent response to our control acoustic signal. We also looked at the effect of the hose length at 25, 50, and 75 ft. These tests were performed with the hoses coiled within the acoustic test chamber.

Fiskers

Comparing the spectra of the three lengths of F brand hose relative to the open reference sensor, we obtain the gain response plot shown in Figure 2.

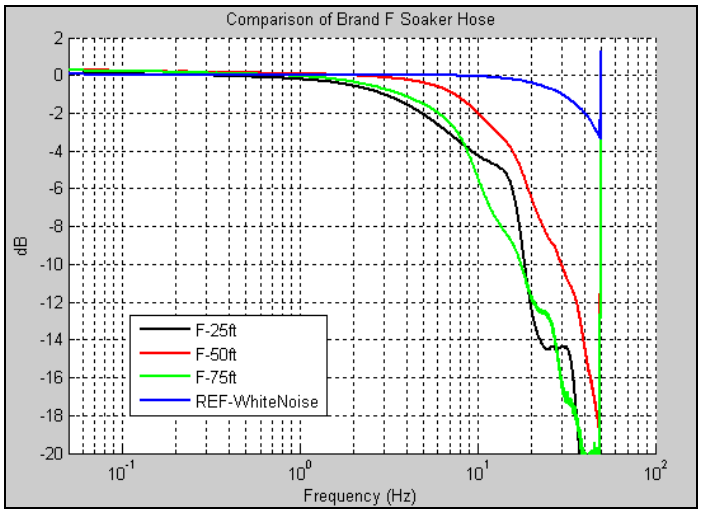

Figure 2. Comparison of relative gain for F brand porous-hose filters to the control "white noise" spectrum.

We observe different low-pass characteristics of the F brand. The -3dB corner varies from 16.4 Hz for the 50-ft length to 6.6 Hz for the 25-ft length. Unity gain is observed between 0.05 and 0.4 Hz. No clear change in response is observed with the change in hose length.

Garden Rite

Comparing the spectra of the three lengths of GR hose relative to the open reference sensor, we obtain the gain response plot shown in Figure 3.

We observe unique filter characteristics of the GR brand. The -3dB corner is much higher at 40Hz, and varies little between the different lengths. Unity gain is observed between 0.05 and 2.0 Hz. Above 2 Hz, the gain increases above unity before continuing to roll off. The GR brand appears to be more consistent in response independent of hose length.

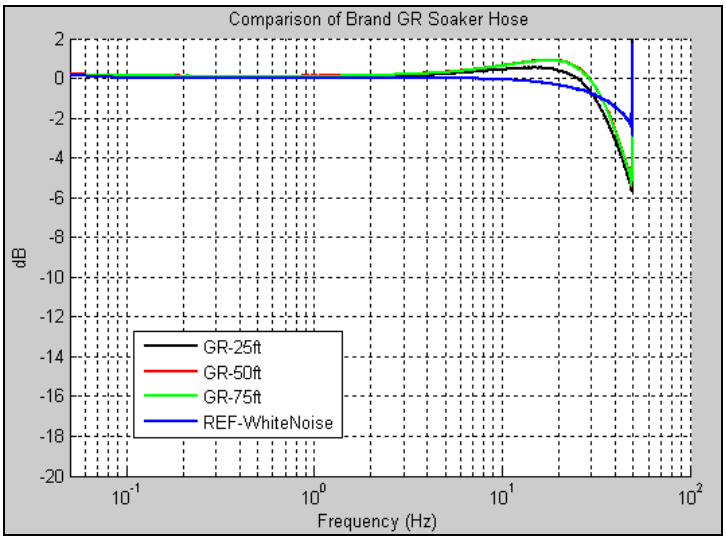

Figure 3. Comparison of relative gain for GR porous-hose filters to the control "white noise" spectrum.

Field Exercise with Acoustic Background Signals

Since July 2008, Sandia has had three element infrasound arrays operational with the intent of better understanding the wind-noise reduction of the porous-hose filter. Each site has two co-located Chaparral Physics 2.5 sensors. One

test consisted of configuring the two sensors as follows: one sensor is exposed to open acoustic input, while the second is attached to a single straight 50-ft hose. A second test (during a different time period) had the hose in a coil of the same approximate dimensions as tests done in the acoustic chamber.

A 3-hour segment of acoustic background was analyzed. Power spectra and relative gain were computed. The power spectra for the open port (no wind-reduction system attached to sensor) show strong harmonics at 16 and 32 Hz. But most important, the low frequencies of 0.03–10 Hz are unaffected.

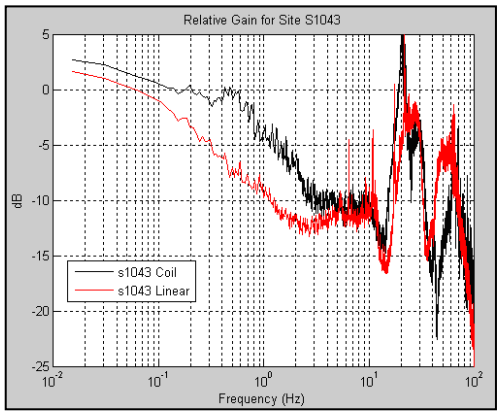

Figure 4. Relative gain for site s1043, illustrating differences between the linear and coiled porous-hose configurations to background acoustic input.

We observe a difference between the linear and coil porous-hose configurations (Figure 4), which may be due to the differing times of data acquisition between the two configurations. A slight gain reduction was observed (1.7 dB) at 0.1 Hz, with a change in corner frequency: 0.2 Hz for the linear hose and 0.8 Hz for the coil. This field test should be repeated with the co-location of three sensors configured to record the same acoustic input, with one sensor open to acoustic input, the second attached to the linear hose, and the third in the coiled configuration.

Controlled Exercise with Coherent Signals

In June 2009 an experiment was set up to determine the filtering characteristics of a single 50-ft porous-hose to a coherent acoustic source. The experiment was conducted in a sealed building with a hallway long enough to deploy the 50-ft porous-hose. The sensors and digitizer used in this stage were different from the ones used in previous experiments and therefore were first characterized for sensitivity at 1 Hz. The sensor and digitizer characterization results are given in Table 2 with the applied calibration factor for at 1 Hz.

Table 2. Compiled results from the comparison calibration of the Chaparral 2.5 sensors relative to the reference MB2000 serial number 1380 and DC-accuracy test of the digitizer for LSB determination.

Sensor	Sensitivity @ 1 Hz (V/Pa)	DWR LSB (V/Count)	Calibration @ 1 Hz (Pa/Count)
071943	0.418	3.28122E-06	7.8479E-06
061809	0.381	3.27698E-06	8.6078E-06

Prior to attaching the porous hose to either sensor, two sets of data were collected to document the baseline differences between the sensors. The main differences between the sensors are their sensitivities: 0.418 versus 0.381 V/Pa, equating to approximately –0.8 dB for sensor 061809 to sensor 071943. The first dataset was collected with both sensors co-located and all four inlets uncapped. The second dataset was collected with both sensors co-located and three of the four inlets capped. The second dataset was seen as a closer approximation to the final comparison, where one sensor would have the hose attached to the fourth uncapped inlet. Figure 5 shows the results of determining the relative gain between the two sensors. The gamma squared coherence was above 0.98 for the pass band of 0.01–10 Hz, allowing for broad-band interpretation of the results. Results show that the expected

relative gain at 1 Hz is approximately –0.8 dB, and the relative phase differences are low, less than +/–4 degrees between 0.01 and 10 Hz.

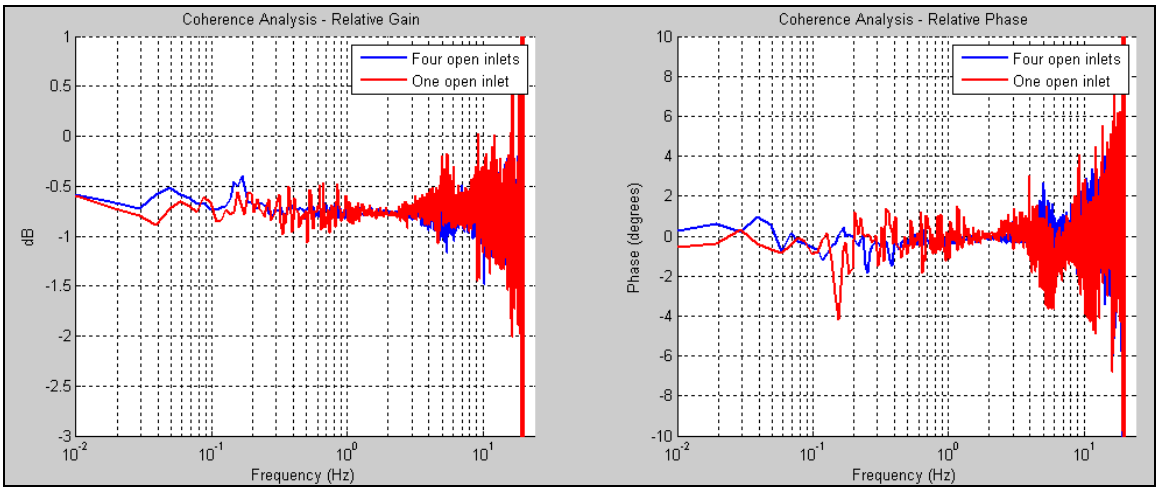

Figure 5. Relative gain and phase for co-located sensors to determine the baseline characteristics of sensors prior to attaching porous hose for coherent acoustic signals.

In the next two sets of data collected the porous-hose was first connected to the open inlet on sensor 071943, while sensor 061809 was open to acoustic input. The second dataset was then collected with the porous-hose moved to sensor 061809 and sensor 071943 open to acoustic input. This was done to verify that any changes from the baseline datasets could be traced to the sensor with the porous-hose attached. Figure 6 shows the results of determining the relative gain between the two sensors. The gamma squared coherence was above 0.95 for the pass band of 0.01–2 Hz, allowing for a slightly smaller amount of pass band for interpretation of the results. Results show the porous-hose has a flat filter response from 0.01 to 0.1 Hz, with no gain or attenuation. Above 0.1 Hz, we see an unexpected amplification, gaining of the input signal as seen by the sensor with the hose attached relative to the open-port sensor. The amplification peaks at 1 Hz, by almost 2.8 dB, and is characterized by a non-uniform gain relationship for the 0.1–2-Hz band. We also observed a considerable change in the phase relationship between the two sensors. Above 0.1 Hz the sensors varied by as much as 8 degrees near 1 Hz.

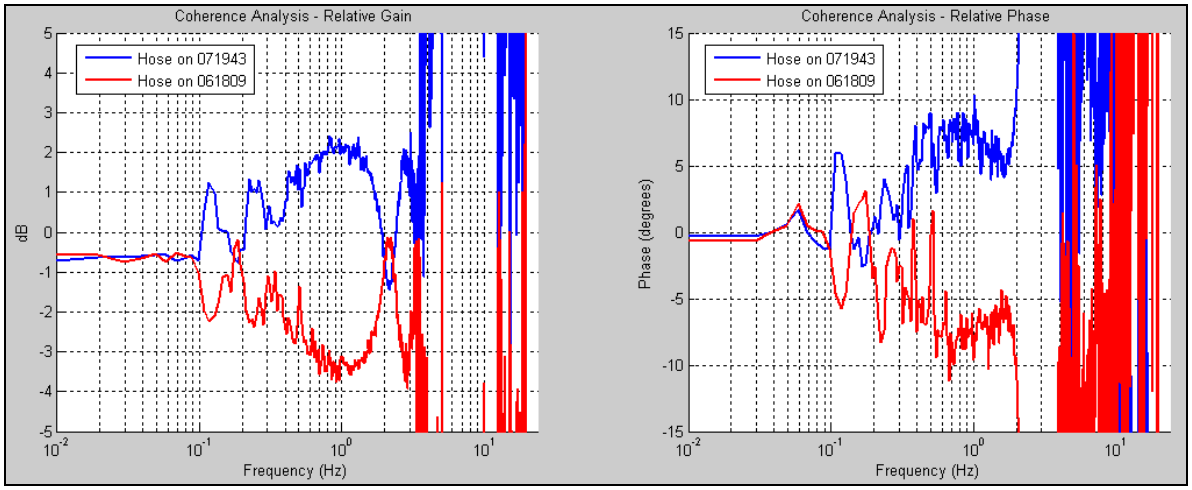

Figure 6. Relative gain and phase for co-located sensors with attached porous-hose for coherent acoustic signals.

In the final dataset the porous-hose was switched to the sensor that was previously considered to be the open-port sensor. In using the coherence analysis technique, we consistently selected the same channel as the reference (channel 2 for sensor 071943) and channel 3 (for sensor 061809) as the one for comparison. This allowed for the

same relative gain at low frequencies, as shown by the overlying relative gain plots for the 0.01–0.1 pass band for the two different configurations of the porous-hose between the two sensors used in the experiment. We observed that by moving the porous-hose to the sensor that previously was open, the relative gain is inverted compared with the previous configuration. This indicated that when the porous-hose is moved to the other sensor, the same gain and phase effects follow the hose.

CONCLUSIONS AND RECOMMENDATIONS

- There exists a large variation in the filter characteristics among different brands of porous-hose.
- The foremost influence on a hose's acoustic filtering characteristics is related to the manufacturing process used to produce the porous material. Factors influencing the final product are variations ratios of raw materials, cooling rate and time, extrusion rate, etc. along the length of the produced hose.
- A large amount of corner frequency variation was observed within the F brand (5–18.6 Hz).
- The GR brand passed 2–4 dB more acoustic signal at 10 Hz.
- These tests show the GR brand has insufficient filter characteristics for monitoring activities.
- Field testing the coil versus the linear hose configuration showed that coiling the hose increased the pass band corner frequency.
- We observe a high variability in the characteristics exhibited by the hose filters. Hoses are typically not part of the calibrated system response. This could result in a great deal of misunderstanding of the amplitude response.
- For coherent signals, as one might expect from an explosive source, we observed no gain or attenuation effects for the 0.01 to 0.1 Hz pass band.
- Above 0.1 Hz, we observed an unexpected gain, amplification of the coherent signal, as picked up by the sensors with the porous hose attached, by as much as 2.8 dB relative to the collocated open port sensors. Not only was the amplitude affected by the porous hose, we also observed that the relative phase increased and varied in a non-uniform manner (across frequency).

The experiments shown in this report were designed to address the undocumented filtering characteristics of the porous-hose wind-noise reduction system used at some nuclear monitoring stations. When considering the filtering effects to incoherent acoustic input, the porous-hose performs as one would hope by reducing the amplitude of the random acoustic signals at primarily the higher frequencies. The GR brand appears to have a broader pass band (0.1–40 Hz) than the Fisker brand (0.1–10 Hz). More work should be done to determine if a larger sample set of GR hoses has the same filter response to incoherent acoustic input. When the filtering characteristics of the F brand to coherent signals was addressed, an unexpected result was observed. The acoustic signals observed by the sensor with the hose attached were of larger amplitude than that of the open port sensor. We are unsure of the mechanism that would cause such an amplification, but are working to explain this effect. As time permits, Sandia will continue to conduct experiments to better understand the filtering effects related to amplitude and phase that a wind-reducing filter has on both coherent and incoherent acoustic signals.

INFRASOUND FROM EARTHQUAKES: SIGNAL CHARACTERIZATION

Brian W. Stump[1], Chris T. Hayward[1], Stephen J. Arrowsmith[2], George E. Randall[2], Kristine Pankow[3], Relu Burlacu[3], and Steven R. Taylor[4]

Southern Methodist University[1], Los Alamos National Laboratory[2], University of Utah Seismograph Stations[3], and Rocky Mountain Geophysics, LLC[4]

Sponsored by the National Nuclear Security Administration

Award Nos. DE-AC52-09NA29325[1,3,4] and DE-AC52-06NA25396[2]
Proposal No. BAA09-49

ABSTRACT

There is a need to improve the understanding of the scaling and physics involved in regional recordings of epicentral infrasound from small earthquakes. This need stems from a wish to use infrasound presence and characteristics to improve depth discriminants. Current regional depth discriminants rely on recording the *Rg* seismic phase or intermediate period surface waves. These phases are sensitive to upper crustal structural details, but are often disrupted by horizontal changes in structure and topography. A number of studies have used single infrasound array data to argue that small earthquakes (M<4) generate infrasound signals. Wide spatial separation of infrasound arrays coupled with the time variation of atmospheric models make the association of infrasound signals from small earthquakes with seismic observations non-unique. This is because event association is often dependent on a single backazimuth estimate within a relatively wide range of arrival times. We propose to address this non-uniqueness, as well as assess smaller magnitude events, by deploying a total of six infrasound arrays in and around the Intermountain seismic belt in Utah. The University of Utah (UU) is the regional seismic network operator responsible for the location and characterization of earthquakes in the region and will integrate the six proposed infrasound arrays into the daily network operations. These arrays will provide the data needed to independently locate the infrasound sources using crossing backazimuth estimates for unique association with the seismic sources. Models of infrasound generation by earthquakes will be developed using a collection of earthquake scaling relations dependent on depth, magnitude and mechanism that are currently used for strong-ground motion assessment for earthquake hazards. Special attention to earthquake depth estimation, including synthetic modeling of seismograms and analysis of the *Rg* phase, will provide an assessment of both the depth estimate and its variance. The infrasound and ground motion observations made during the course of this study will be used to refine the source excitation model for infrasound using two different approaches, including the application of the Rayleigh integral. The application of this physical based approach to infrasound generation is intended to lead to a possible infrasound based depth discriminant that could be integrated into the Event Classification Matrix (ECM) (Anderson, 2007). In a related effort, preliminary analysis of infrasound from the Wells earthquake sequence is reported in Stump et al. (2009, these Proceedings), which describes the first deployment of infrasound gauges in Utah.

OBJECTIVES

Objective 1: Improved understanding of earthquake generated infrasound.

An understanding of earthquake-generated infrasound is critical to the development of seismo-acoustic discriminants that distinguish between surface explosions and earthquakes. Numerous studies have identified infrasound from surface explosions (Arrowsmith et al., 2008; McKenna et al., 2007; Che et al., 2002), but have also recognized that varying atmospheric conditions and propagation characteristics may suppress recording at a particular station on a particular day. Previous studies of earthquake generated infrasound signals (epicentral infrasound) recorded at distances beyond 220 km have shown that medium to large earthquakes can generate infrasound (e.g., Mutshlecner and Whitaker, 2005; Le Pichon et al., 2006). The observations suggest a linear relationship between earthquake magnitude and infrasound duration and a linear relationship between earthquake magnitude and the log of infrasonic amplitude (Figure 1).

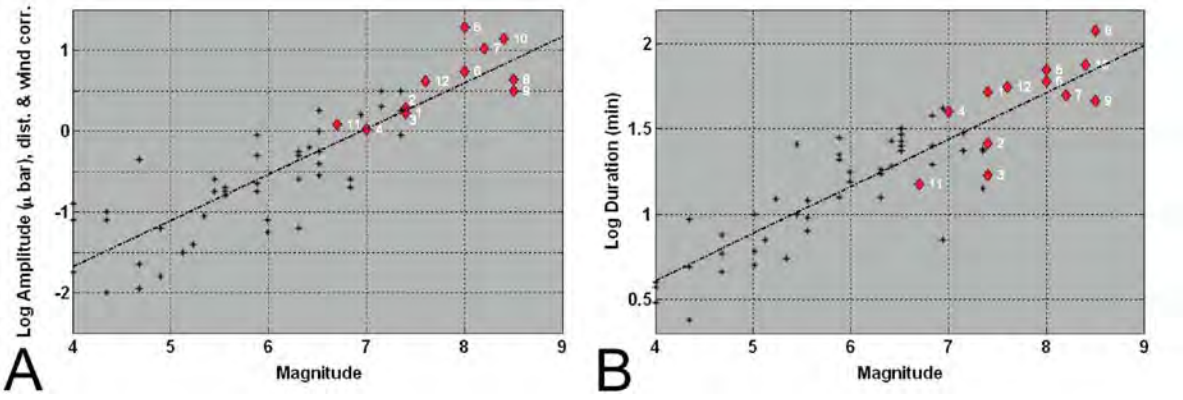

Figure 1. Previous observations of earthquake-generated infrasound showing the relationship between wind-corrected amplitudes (A) and signal durations (B) with earthquake magnitude. Black dots are from the analysis of infrasound signals for the set of earthquakes in Mutschlecner and Whitaker (2005). The red points are from an independent study by Le Pichon et al. (2006) for a different set of generally larger events. The combined datasets cover a magnitude range of four to nearly nine. Earthquakes less than magnitude four were not analyzed (from Le Pichon et al. [2006]).

Previous studies of earthquake generated infrasound suffer from the following four primary limitations: (1) most observations for smaller magnitude events are single-array only; (2) effects of earthquake depth, focal mechanism, and local geology were not studied nor modeled in detail; (3) there have been no detailed studies of infrasound from small earthquakes, M < 4; and (4) observational studies have focused on long-range infrasound (i.e., stratospheric and thermospheric returns) and not on local or near-regional infrasound (i.e., distances < 220 km).

This work will address the limitations as follows:

- **Previous studies only consider single-array observations.** When observations are limited to a single-array, signal association of a particular earthquake with an infrasound arrival is based on a single backazimuth estimate within a relatively wide range of arrival times. The complex temporal atmospheric variability, the large number of extraneous coherent infrasound signals, and highly variable site noise conditions make conclusive seismic-to-infrasound association or non-association difficult. At the International Data Centre (IDC), 90% of infrasound detections are from coherent noise sources (Brachet and Coyne, 2006). To robustly associate infrasound signals with seismic events requires multiple observations on a network of infrasound arrays (Arrowsmith et al., 2008). This research will include extending the operation of three existing Utah seismo-acoustic stations (Stump et al., 2007) and collocating three additional infrasound arrays at existing UU seismic stations. Robust detection and association algorithms, recently developed in collaboration between Los Alamos National Laboratory (LANL), Southern Methodist University (SMU), UU and Rocky Mountain Geophysics (RMG) (Arrowsmith et al., 2008), will be employed to address the non-uniqueness limitation of previous studies.
- **Previous studies only consider earthquake magnitude scaling relations.** Other than magnitude, there has been no detailed study of the relationship between earthquake source characteristics and infrasound generation. This study will address the problem in two steps. First, observational earthquake infrasound scaling relations

will be developed using seismically constrained depth and peak ground motion estimates. Second, epicentral infrasound will be modeled based upon predicted or observed ground accelerations and used to calculate the resultant recorded infrasound signal (Whitaker, 2007). Modeled results will be compared with observational records to refine the infrasound source excitation model.

- **Previous studies only consider infrasound from large earthquakes.** There has been no study of infrasound generation or its absence from small earthquakes (M < 4). This study includes a large dataset of small magnitude earthquakes (Figure 2).
- **Previous studies only investigate infrasound at long ranges.** Previous studies have focused only on long-range observations. This study will utilize six acoustic arrays in an active seismic region (Figure 2). At distances less than 220 km, waveform characteristics, especially amplitude, vary significantly with source-to-receiver range. This is an effect of the highly variable lower atmosphere that dominates the propagation characteristics. The dataset acquired as part of this proposal will provide the basis for a detailed exploration of such waveform characteristics.

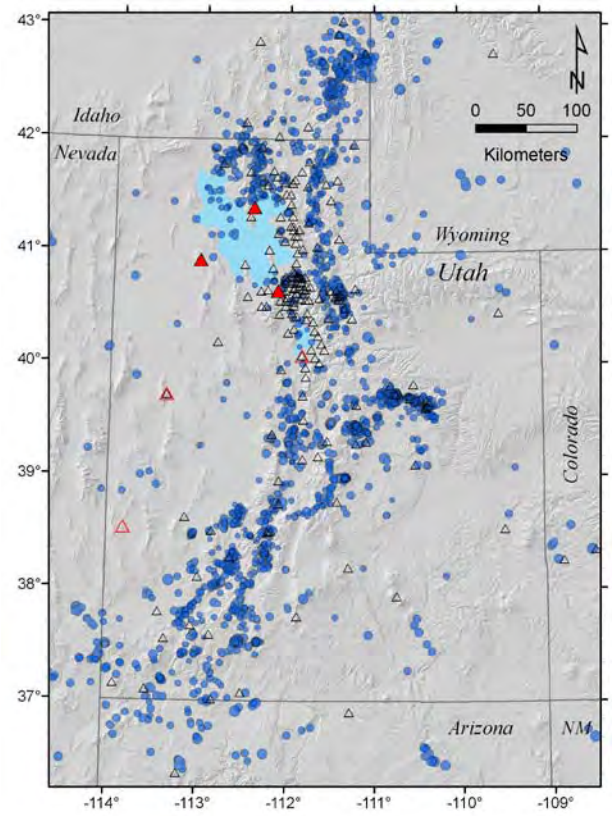

Figure 2. Map of existing Utah seismo-acoustic stations (red filled triangles), proposed seismo-acoustic stations (red open triangles), seismic stations (black open triangles) and three years of crustal earthquakes from the UUSS catalog, approximately the same duration as the proposed project (light blue circles).

Objective 2: Development of an infrasonic depth discriminant.

The dataset created in Objective 1 will be used for research and development of an infrasound depth discriminant to be incorporated into the ECM framework currently being developed at the National Laboratories. This implementation will address a significant limitation with existing depth discrimination capabilities, which rely on the presence of the seismic phase *Rg*, commonly not observed. A key prerequisite for developing and testing an infrasound depth discriminant is an independent robust depth determination. As part of this proposal, we will have access to a large number of well-constrained earthquake depths (see the section entitled *Seismic network description and known sources*). In addition, we will utilize *Rg* and intermediate period surface wave seismic arrivals with a forward modeling approach to better constrain earthquake depths for additional events.

RESEARCH PLANNED

Seismic network description and known sources

The University of Utah Seismograph Stations (UUSS) operates a regional and urban seismic network of more than 200 seismic stations. Data and metadata from UUSS seismic stations are archived at the Incorporated Research Institutions for Seismology (IRIS) Data Management Center (DMC). An overview of data processing and analysis procedures can be found on the UUSS website at http://www.quake.utah.edu/EQCENTER/LISTINGS/overview.htm. In addition, beginning May 2007, UUSS began integrating EarthScope Transportable Array (TA) stations into routine analysis, processing, and data product generation. Many of the TA stations have been moved, but while deployed, the TA stations in Utah contributed to improved event azimuthal coverage, and provided important additions to observations of the Crandall Canyon mine event (August 2007) and the Wells, Nevada earthquake sequence (February 2008).

To characterize the instrumental seismicity of the Utah region, we categorized events from the UUSS earthquake catalog with minimum magnitude M 0.0 for the period January 1, 1981 to December 31, 2007. For this period, more than 36,000 events were identified; 49% of these events occurred in the mining area of Wasatch Plateau and Book Cliffs (Arabasz et al., 2007) and 15% have well-constrained focal depths (for the definition of well-constrained focal depth, we use the criteria from Arabasz et al. [1992], where the distance to the nearest station is less than the focal depth or 5.0 km, and the depth error is less than or equal to 2.0 km). The depth for the subset of events with well-constrained focal depths varies from 0 to 29 km (one event recorded in 1992 has a depth of 55 km) and the magnitudes (duration or local) vary between 0.0 and 4.6. Figure 2 shows the location of seismic stations, existing and proposed acoustic arrays, and epicenters for 2005–2007.

In addition to the cataloged seismicity, UUSS also records energy generated by man-made sources such as mining blasts, highway construction, and rocket motor detonations. Each quarter, blasts are identified and eliminated from the UUSS earthquake catalog using information from the mine operators or waveform cross-correlation with known blasting areas.

Routine UUSS data processing includes generation of peak ground-motion amplitudes (acceleration and velocity) and 5% damped spectral response values for three different periods (0.3, 1 and 3 seconds) from all strong-motion and broadband stations in the network (including TA stations). For Utah earthquakes greater than magnitude 3.0, UUSS uses the computed amplitudes and spectral response values to produce a regional ShakeMap, a graphical representation of ground shaking from earthquakes (Wald et al., 1999). UUSS also generates scenario ShakeMaps, using regionally appropriate predictive ground motion relations. ShakeMaps for observed events and scenarios describe spatial variance of ground-motion amplitudes as a function of source distance, local geology, depth, and earthquake mechanism. These ground motion estimates can be used to drive models of earthquake-generated infrasound.

Existing and planned acoustic arrays

Six seismo-acoustic arrays are planned for this project. Three arrays are already installed and are integrated into the UUSS network (the acoustic arrays are collocated with existing seismic stations at BGU, EPU, and NOQ; Figure 2). Table 1 describes the characteristics of the three existing seismo-acoustic arrays operated by UUSS.

Table 1. Existing seismo-acoustic arrays operated by UUSS.

	NOQ array	BGU array	EPU array
Number of elements	4	4	4
Sensor type	Chaparral 2	Chaparral 2	Chaparral 2.5
Digitizer	REF TEK 130	REF TEK 130	REF TEK 130
Real-time telemetry	Yes	Yes	Yes
Aperture (m)	161 x 122	136 x 139	159 x 121
Average distance between sensors (m)	118	115	119
Installation date	May 4, 2006	April 17, 2007	July 13, 2007
Collocated seismic station	BB	BB	SP
Archived data start at IRIS DMC	May 4, 2006	N/A	N/A

Figure 2 also shows the provisional locations for the three additional acoustic arrays collocated with existing UUSS seismic stations FSU, WMUT, and a broadband seismic station to be installed in southwestern Utah as part of a state funded project. SMU will supply Chaparral microphones for the acoustic arrays at no cost to the project. An equipment request has been submitted to the Program for the Array Seismic Studies of the Continental Lithosphere (PASSCAL) for the data recorders, solar panels, and telemetry systems needed to support the six acoustic arrays. Data will be telemetered to UUSS, saved in Seismic Analysis Code (SAC) format on DVDs and in SEED format at the IRIS DMC.

Data analysis

Data analysis will utilize the LANL developed InfraMonitor software package to detect, associate and locate events (Arrowsmith et al., 2008). This algorithm has been implemented for automatic pipeline processing of large quantities of data at LANL and UU. Events detected and associated at >1 seismo-acoustic array will be reviewed by an analyst.

The first component of InfraMonitor, the robust detection algorithm (Arrowsmith et al., 2008b), uses an adaptive noise hypothesis to account for variations in ambient noise, rather than using an idealized model. InfraMonitor includes a coherent detector for processing array data and an incoherent detector for processing single element data (Arrowsmith et al., 2008b). For this study, infrasound array data will be processed with a coherent detector and seismic data will be processed with an incoherent detector.

The incoherent detector developed and implemented in InfraMonitor first transforms the background noise into a near-normal distribution and then applies a robust outlier detection algorithm to identify signals (Arrowsmith et al., 2008b). In tests with seismic data, we have shown that the incoherent detector performs similarly well.

The second component of InfraMonitor searches for groups of signals at separate arrays that have a common source (associations) by scanning detection bulletins at each seismo-acoustic array and hypothesizing an approximate location. This process uses a grid-search algorithm where arrivals are associated based on backazimuth consistency and inter-array delay times. A region of interest is parameterized with a grid mesh and associated arrivals are searched for at each grid node.

The automatic detection and association algorithms described above will be used to search for infrasound signals from regional earthquakes. We will populate a database with infrasound observations (and non-observations), in order to develop relationships between infrasound waveform characteristics and earthquake magnitude, depth, source mechanism and local geology.

ANTICIPATED RESULTS AND IMPLICATIONS

Earthquake source development and validation

We plan to extend the relationships shown in Figure 1 (Mutshlecner and Whitaker, 2005; Le Pichon et al., 2006) to include other scaling relations between the earthquake source (such as depth and peak ground motion) and infrasound generation. Then ground motion estimates from the earthquake sources and propagation characteristics will be used to model coupling to the infrasound wavefield.

Earthquake scaling relations

Two parameters of particular interest in developing scaling relations are the source depth and peak ground-motion. Well-constrained depth estimates for earthquakes for correlation with infrasound detections will be obtained from results of temporary source region aftershock deployments and waveform modeling for events with moment tensor estimates. Since most of the Wells aftershock sequences and ~15% of the Utah seismic catalog events have good depth estimates, this study includes a substantial test dataset in contrast to less well instrumented regions of the world. Additionally, for events with moment tensor estimates, we have had success modeling event depth with long to intermediate period surface and body waves using simple earth models. A simple example is shown in Figure 3 using the vertical displacement data at Dugway, UT (DUG) for the Wells, NV event, the Harvard centroid moment tensor (CMT) mechanism, and reflectivity synthetics for a range of depths.

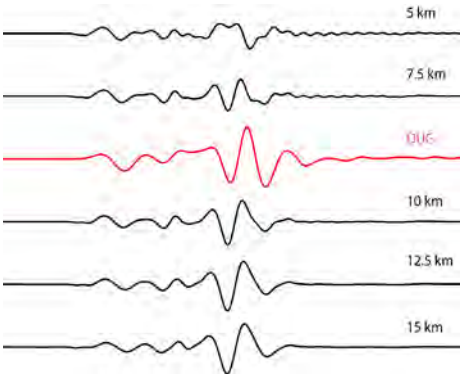

Figure 3. Comparison of synthetic seismograms for depths of 5, 7.5, 10, 12.5 and 15 km in black with the DUG displacement in red. Although the waveform fit is preliminary, the general arrival time of body and surface wave energy is good and the relative surface wave to body wave amplitudes indicate the depth is likely deeper than 7.5 km. All waveforms are on the same scale.

The second parameter of interest, the peak ground motion, is related to magnitude for which there is a scaling relation developed for stratospheric-ducted infrasound of medium to large earthquakes (Figure 1). However, peak ground motion is also a function of local geology – softer soils typically have higher ground motions than rock. In this analysis, we are interested in both near-source peak motions for the generation of 'epicentral infrasound' and in the spatial distribution of peak ground motions for the generation of secondary infrasound sources. ShakeMaps combining the measured ground-motion with predictive relations, such as Pankow and Pechmann (2004) or Boore et al. (1997), produce spatially coherent maps of ground-motion and intensity (for example see http://www.seis.utah.edu/ shake/1000012101 /pga.html). The ShakeMap methodology (Wald et al., 2003) produces: (1) estimates of the peak ground-motion in the near source region and (2) spatial maps of peak ground motions. For the above ShakeMap example (event ID 1000012101, an M 3.5 earthquake in northern Utah), the near-source had peak ground accelerations greater than 1.2% g. ShakeMaps can easily be generated for all earthquakes of interest and scenario events.

For the purposes of developing scaling relations, we will build a database of earthquake parameters including: location, magnitude, depth, depth quality factor, predicted peak ground acceleration and peak ground velocity in the source region, distance to the closest seismic station and type of station, average shear velocity in the upper 30 m (Vs30) in the source region, and faulting mechanism (when available). The estimated Vs30 in the source region will be obtained from locally produced Vs30 maps for the Utah region (Christenson et al., 2004) and topographically derived Vs30 maps (Wald and Allen, 2007) outside of the Utah region. The earthquake database will be combined with the infrasound data processing to generate scaling relations. In addition to the database, we will also construct a catalog of ground motion grid files. Combining the grid files with the scaling relations for peak ground motion will show potential sources of non-epicentral infrasound generation.

Infrasound modeling

Given an acceleration time and spatial history at the ground surface, the near source infrasound signal may be computed at an observation point above by application of the Rayleigh integral. The Rayleigh integral can be expressed (Pierce, 1989) as:

$$p(R_0,t) = \frac{\rho}{2\pi}\int \frac{a(r,(t-R/c))}{R} dA_s$$

where a is the acceleration of the ground, r is a location on the ground (referenced to a center position), dA_S is an element of area on the ground, R is the distance from the ground element to the observing point, t is time, ρ is the air density, c is the speed of sound in air, p is the air pressure, and R_0 is the observation location. The acceleration values may be derived from actual surface measurements and mapped to the desired radial/angular grid for the numerical integration. Alternatively measured surface ground motions could be the basis of parametric acceleration models that could be used in the integration. Then near-field infrasound signals may be computed and relations explored as a function of earthquake characteristics such as magnitude and depth.

Alternatively, a time-domain finite-difference numerical hydrodynamics program may be used to calculate the pressure field in a two-dimensional, cylindrically symmetric domain, (r,z) geometry where r is the radius and z is the height. LANL has used a version of the program Caveat (Addessio et al., 1992) for nearly 20 years. In this application, the ground motion provides a time dependent velocity boundary condition at the bottom (z=0) of the Caveat grid. The evolution of the resulting pressure wave field is easily followed.

Two sources of ground motion will be used as input for infrasound modeling. First, when actual recorded waveforms in the near-source region are available, such as the Wells aftershock sequence, the data will be interpolated and scaled to build the input grid for modeling. Second, for events where no near-source recordings exist, we will use data archived at the National Strong Motion Data Center. Waveforms will be selected to represent the appropriate tectonic regime, depth and magnitude. We can also select different waveforms based on frequency content and waveform characteristics to assess the variation in infrasound generation to the specifics of the waveform. The amplitudes of the selected waveforms will be scaled to match the peak ground acceleration grid generated in developing the scaling relations.

Implementation of results into ECM depth discrimination

The focus of this part of the proposal is to develop a method to identify a shallow seismic source based on a seismo-acoustic detection. We emphasize seismo-acoustic detection in this work because we are attempting to utilize infrasound signals to place constraints on the source type and depth of accompanying seismic signals. The method will be formulated so that it can be incorporated into the ECM of Anderson et al. (2007). It must therefore have a sound physical basis as well as a foundation in mathematical statistics. A common seismic indicator for the identification of a shallow source is the presence of the short-period surface wave, *Rg*. However, *Rg* is often not observed, because it is sensitive to the details of upper crustal structure. In contrast, infrasound signals can be generated by near-source pumping of the atmosphere from shallow sources or strong ground motion from large earthquakes. In other words, an infrasound signal associated with a corresponding seismic signal for a small event may act as a surrogate for an *Rg* detection. In this proposal, we will statistically quantify a seismo-acoustic detection as an indicator of a depth event in a form that can be included in the ECM.

REFERENCES

Addessio, F. L., J. R. Baumgardner, J. K. Dukowicz, N. L. Johnson, B. A. Kashiwa, R. M. Rauenzahn, and C. Zemach (1992). CAVEAT: A Computer Code for Fluid Dynamics Problems with Large Distortion and Internal Slip, *Los Alamos National Laboratory*, Technical Report LA-10613, Rev. 1.

Anderson, D. N., D. K. Fagan, M. A. Tinker, G. D. Kraft, and K. D. Hutchenson (2007). A Mathematical Statistics Formulation of the Teleseismic Explosion Identification Problem with Multiple Discriminants, *Bull. Seism. Soc. Am.* 97: 1730–1741.

Arabasz, W. J., R. Burlacu, and K. L. Pankow (2007). An overview of historical and contemporary seismicity in central Utah, in Willis, G. C., Hylland, M. D., Clark, D. L., and Chidsey, T. C., Jr., Eds., Central Utah—Diverse geology of a dynamic landscape: Utah Geological Association Publication 36.

Arabasz, W. J., J. C. Pechmann, and E. D. Brown (1992). Observational seismology and the evaluation of earthquake hazards and risk in the Wasatch Front area, Utah, in Gori, P. L. and W. W. Hays, Eds., Assessment of regional earthquake hazards and risk along the Wasatch Front, Utah: U.S. Geological Survey Professional Paper 1500-A-J, D1–D36.

Arrowsmith, S. J., R. Whitaker, S. R. Taylor, R. Burlacu, B. Stump, M. Hedlin, G. Randall, C. Hayward, and D. ReVelle (2008). Regional Monitoring of Infrasound Events Using Multiple Arrays: Application to Utah and Washington State, submitted to *Geophys. J. Int*.

Arrowsmith, S. J., R. Whitaker, G. Randall, S. R. Taylor, and D. Anderson (2008b). The F-Detector Revisited: Improved Strategies for Detecting Signals at Single Stations and Arrays, paper presented at the Seismological Society of America Annual Meeting, Santa Fe, NM, 16-18 April.

Boore, D. M., W. B. Joyner, and T.E. Fumal (1997). Equations for Estimating Horizontal Response Spectra and Peak Accelerations from Western North American Earthquakes: A Summary of Recent Work, *Seism. Res. Lett.* 68: 128–153.

Brachet, N. and J. Coyne (2006). The Current Status of Infrasound Data Processing at the International Data Centre, in *Proceedings of the 28th Monitoring Research Review: Ground-Based Nuclear Explosion Monitoring Technologies*, LA-UR-06-5471, Vol. 2, pp. 873–881.

Che, I.-Y., M.-S. Jun, J.-S. Jeon and K. Min (2002). Analysis of Seismo-Acoustic Events I: the Korean Peninsula, *Geophys. Res. Lett.* 29: 12

Christenson, G.E., F. X. Ashland, M. D. Hylland, G. N. McDonald, B. Case (2004) Database compilation, coordination of earthquake-hazards mapping, and study of the Wasatch fault and earthquake-induced landslides, Wasatch Front, Utah: U.S. Geological Survey, National Earthquake Hazards Reduction Program Final Technical Report, award no.03HQAG0008, CD-ROM.

Le Pichon, A., P. Mialle, J. Guilbert and J. Vergoz (2006). Multistation infrasonic observations of the Chilean earthquake of 2005 June 13, *Geophys. J. Int*. 167: doi:10.1111/j.1365-246X.2006.03190.x

McKenna, M. H., B. W. Stump, S. Hayek, J. R. McKenna and T. R. Stanton (2007). Tele-infrasonic studies of hard-rock mining explosions, *J. Acoust. Soc. Am.* 122: 97–106.

Mutschlecner, J.-P. and R.W. Whitaker (2005). Infrasound from earthquakes, *J. Geophys. Res.* 110: doi:10.1029/2004JF005067.

Pankow, K. L. and J. C. Pechmann (2004). The SEA99 Ground-motion predictive relations for extensional tectonic regimes: Revisions and a new peak ground velocity relation, *Bull. Seism. Soc. Am.* 94: 341–348.

Pierce, A. D. (1989). Acoustics an introduction to its physical principles and applications, Acoustical Society of America, NY.

Stump, B., R. Burlacu, C. Hayward, T. Kim, S. Arrowsmith, R. Zhou, and K. Pankow (2009). Seismo-acoustic generation by earthquakes and explosions and near-regional propagation, these Proceedings.

Stump, B., R. Burlacu, C. Hayward, K. Pankow, S. Nava, J. Bonner, S. Hock, D. Whiteman, A. Fisher, T.S. Kim, R. Kubacki, M. Leidig, J. Britton, D. Drobeck, P. O'Neill, K. Jensen, K. Whipp, G. Johnson, P. Roberson, R. Read, R. Brogan and S. Masters, Seismic and Infrasonic Energy Generation and Propagation at Local and Regional Distances: Phase I – Divine Strake Experiment, Air Force Research Laboratory, AFRL-RV-HA-TR-2007-1188, 11 October 2007.

Wald, D. J., V. Quitoriano, T. H. Heaton, H. Kanamori, C. W. Scrivner, and C. B. Worden (1999). TriNet "ShakeMaps": Rapid Generation of Instrumental Ground Motion and Intensity Maps for Earthquakes, *Southern California Earthquake Spectra* 15: 537–556

Wald, D. J., C.B. Worden, V. Quitoriano, and K. L. Pankow (2003). ShakeMap Manual: Technical manual, user's guide and software guide: U.S. Geological Survey Techniques and Methods, Book 12, Section A, Chap. 1, 132 p.

Wald, D. J. and T. I. Allen (2007). Topographic slope as a proxy for seismic site conditions and amplification, *Bull. Seism. Soc. Am.* 97: 1379–1395.

Whitaker, R. (2007). Infrasound Signals as Basis for Event Discriminants, in *Proceedings of the 29th Monitoring Research Review: Ground-Based Nuclear Explosion Monitoring Technologies*, LA-UR-07-5613, Vol. 2, pp. 905–913.

INFRASOUND SIGNALS FROM GROUND MOTION SOURCES

Rodney W. Whitaker

Los Alamos National Laboratory

Sponsored by the National Nuclear Security Administration

Award No. DE-AC52-06NA25396/LA-07-Infrasound-NDD02

ABSTRACT

We present progress on an ongoing research project looking at near-field infrasound signals as a basis for discriminants between underground nuclear tests (UGT) and earthquakes (EQ). We have completed a series of finer zoned time-domain, finite-difference calculations for the set of 30 underground tests included in earlier reports. An update on the modeling approach for earthquake ground motion will be presented. For the earthquakes discussed in our 2005 paper (Mutschlecner and Whitaker, 2005), we have begun looking at source mechanisms that may correlate with the infrasound observations. A new development was pursued during the last year that provided infrasound data, on the duration and amplitude for underground tests and earthquakes, to the Event Classification Matrix (ECM) framework. The analysis followed the standard ECM approach for deriving p-values and forming a bi-variate discriminate that showed very good separation of the two data sets. Three UGTs, Houston, Misty Echo and Texarkana, are closest to the EQ group and will be studied to find what contributes to this behavior. Nevertheless, the inclusion of infrasound in the ECM framework is an exciting development.

OBJECTIVES

The objective of this research is to find differences in the near-field infrasound signals of UGTs and earthquakes that can be the basis for establishing discriminants between the two sources. Such differences in the near-field signal would likely survive to longer range. Here we will present results relating earthquake source mechanisms to infrasound signal as well as new, un-planned, results that add infrasound to the ECM.

RESEARCH ACCOMPLISHED

Background

We will discuss recent analysis on earthquake infrasound signals and new work on UGT and EQ amplitude and duration discriminants. Before presenting those topics, we will review some results on infrasound signals from earthquakes for the benefit of the reader.

Mutschlecner and Whitaker (2005) presented data on infrasound signals from earthquakes with magnitudes from 4.0 to 7.0. Their work concentrated on stratospheric returns and provided data from 31 earthquakes. (See Whitaker and Mutschlecner (2008) for some discussion of thermospheric returns.) LePichon et al. (2006) discussed infrasound signals from a set of generally larger magnitude earthquakes. Figure 1 below is based on LePichon et al (2006) and shows two sets of infrasound data for log(wind corrected amplitude) vs magnitude, (A), and log(signal duration) vs magnitude, (B). For these plots the magnitude M_S was used. The black dots are from the analysis of infrasound signals for the set of earthquakes in Mutschlecner and Whitaker (2005), while the red points are from the LePichon paper.

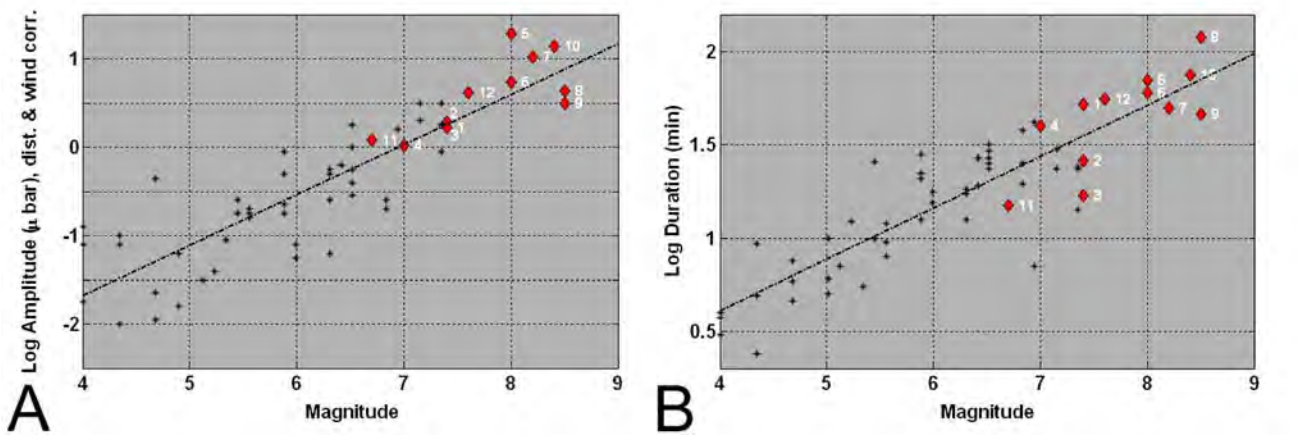

Figure 1. The two sets of EQ events as reported in Mutschlecner and Whitaker (2005) and LePichon et al. (2006). This version of the figure was provided directly by Dr. LePichon.

This comparison of two independent sets of earthquake infrasound signals shows good agreement and continuity. An obvious area of research would be to extend this analysis to lower magnitude events.

Earthquake Source Parameters

The Mutschlecner and Whitaker (2005) paper presented characteristics of infrasound signals from earthquakes as a starting point for future researchers, but earthquake source mechanisms were not considered in that paper. Here we will begin to look at aspects of source mechanisms. It is easy to see that some component of vertical ground motion would be required in order to couple the ground motion into the atmosphere. In this contribution we are discussing ground motions in and around the epicenter. We will suppose that larger EQs that are not too deep and have predominantly vertical epicenter ground motion are good sources for infrasound generation. Earthquakes may have additional ground motions away from the epicenter due to secondary excitations from surface waves for example. Such examples would have more complicated infrasound signals due to the added regions of excitation. LePichon et al. (2002, 2003, and 2006) discuss examples of the more complicated sources.

As a starting point for examining source mechanisms, we will show central moment tensor solutions for the P axis plunge and the T axis plunge from the Global Central Moment Tensor database, http://www.globalcmt.org for the events in the Table A2.1. We use the P axis plunge and the T axis plunge as these directly indicate the maximum pure compression and tension orientations for the solution. Data were found for 29 of the 39 events. In the simplest case, one might suppose that the source data would show large epicenter vertical ground motions, realizing that such simplicity is hardly ever borne out. We looked at the minimum deviation from vertical for either the P or T axis in this examination such that lower values imply a greater contribution to vertical epicenter motion from the direct ground motion. In the plots, this variable is Minplgdev, and the results are shown in Table A2.2.

In Figure 2 we plot values of Minplgdev as a function of M_S. For these data, there is not a clear dependence on magnitude.

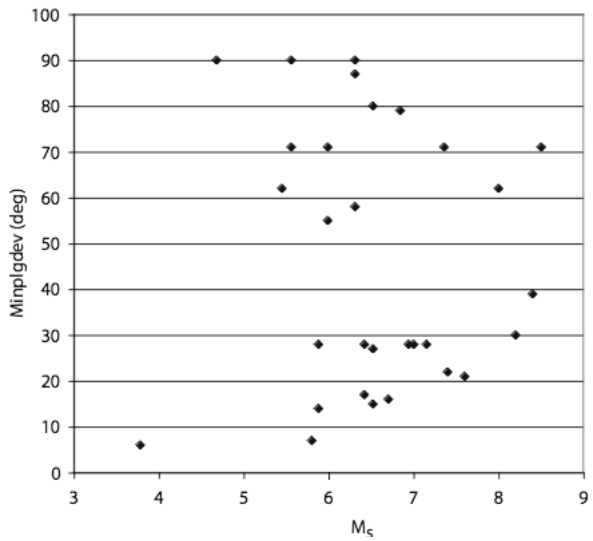

Figure 2. The Minplgdev vs magnitude for the events in Table A2.2.

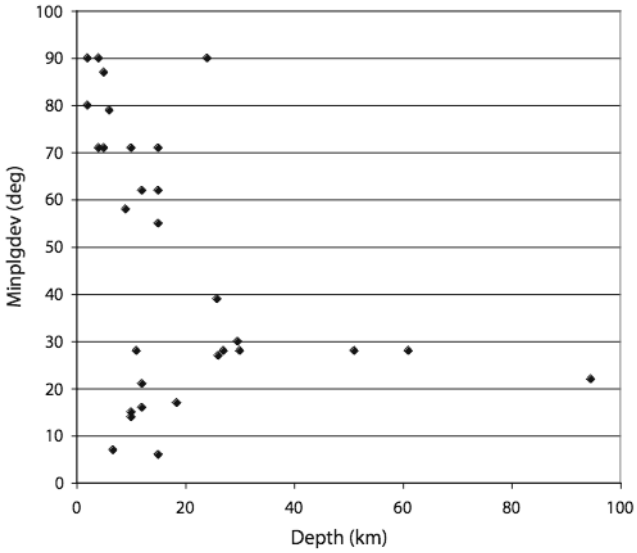

Figure 3. Minplgdev vs EQ depth

In Figure 3, we show Minplgdev vs depth. Here we see a group of shallow EQs with larger values of Minplgdev (motion not along the vertical). These are numbers 1, 2, 4, 7, 9, 11, 12, 15, 21, 22, 25, 29, 34, and 36. An obvious question is how do these events plot in the amplitude vs magnitude relation? In Figure 4, we show the ones from the Mutschlecner and Whitaker (2005) paper.

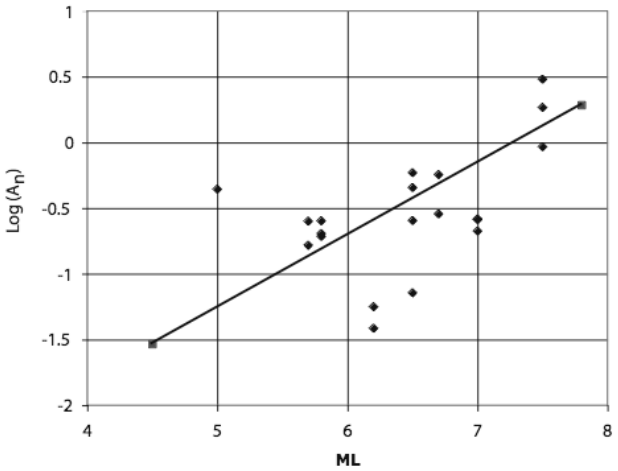

In Figure 4 some of the events were observed by more than one infrasound station, giving more than 12 points from the list above. The line represents the regression fit from Mutschlecner and Whitaker (2005).

Figure 4. The normalized amplitude vs magnitude events for low vertical ground motion events in the Mutschlecner and Whitaker (2005) dataset.

For comparison Figure 5 shows all of the events in the Mutschlecner and Whitaker paper.

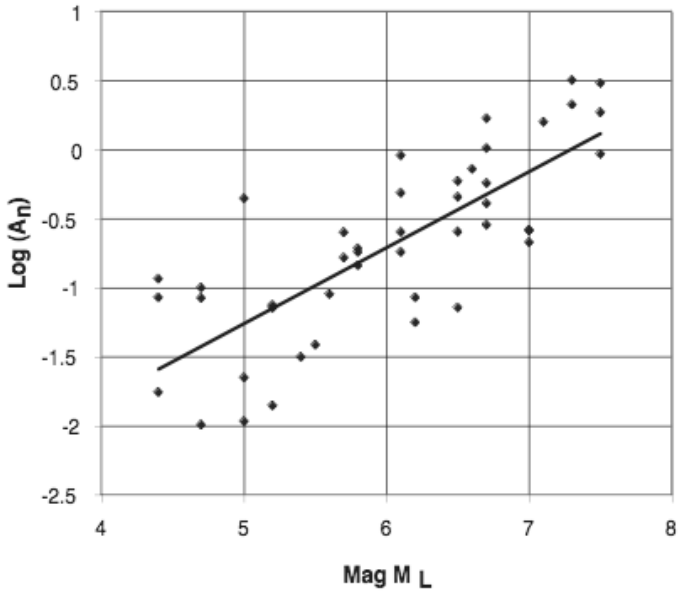

Figure 5. The full set of normalized amplitude vs magnitude.

One can see that not all the data in Figure 4 fall below the fit relation. And there are some points in Figure 5 (between magnitudes 4.5 and 5.5) that fall below the regression line and have larger potential for better vertical ground motion, at least as we examine in this contribution. Our simple approach, which represents a first look at infrasound EQ signals and EQ source parameters, is clearly not capturing all the generation processes. This points to the need for more data on infrasound signals from earthquakes as well as the associated earthquake source parameters for understanding the important ground motion drivers as well as to extend the relation shown in Figure 1 to smaller magnitude events.

Adding an Infrasound Discriminant to the ECM

During the year an opportunity arose that was not part of the original plan of work but was considered relevant to the project. This was to try to quantify the preliminary discriminants between UGTs and EQs that had been found during the earlier infrasound program (1982 – 1992) at Los Alamos National Laboratory (See Appendix 1). This program was a Department of Energy funded project to measure the atmospheric infrasound signal generated by the vertical ground motion from UGTs. At least two arrays were operated continuously in the 1982 – 1992 period (St. George, UT, and Los Alamos, NM). Because of continuous operation, in addition to the UGT sources, other sources could be measured as well, such as EQs. The two measures were wind corrected amplitude (WCA) and signal duration, from stratospheric returns, with UGTs showing larger WCA and EQs showing longer durations. Actually the amplitudes are normalized for winds and distance as given in Mutschlecner and Whitaker (2005). The wind effects are those from stratospheric heights that are seasonally dependent and have a large effect on observed amplitudes. Distance normalization is needed because of the span of ranges of the earthquakes from the infrasound stations.

We have taken the first step toward incorporating infrasound data, on the amplitude and duration of UGT and EQ signals, into the ECM framework, Anderson et al. (2007). This is the first non-seismic technology to be incorporated into the ECM. With this work, we can really determine whether the early indication of a discriminant between UGTs and EQs could be quantified including sources of error.

First, from the analysis of covariance, we show the results for the individual p values for normalized amplitude and duration in Figure 6, where p-values were based on log (amplitude) and log (duration).

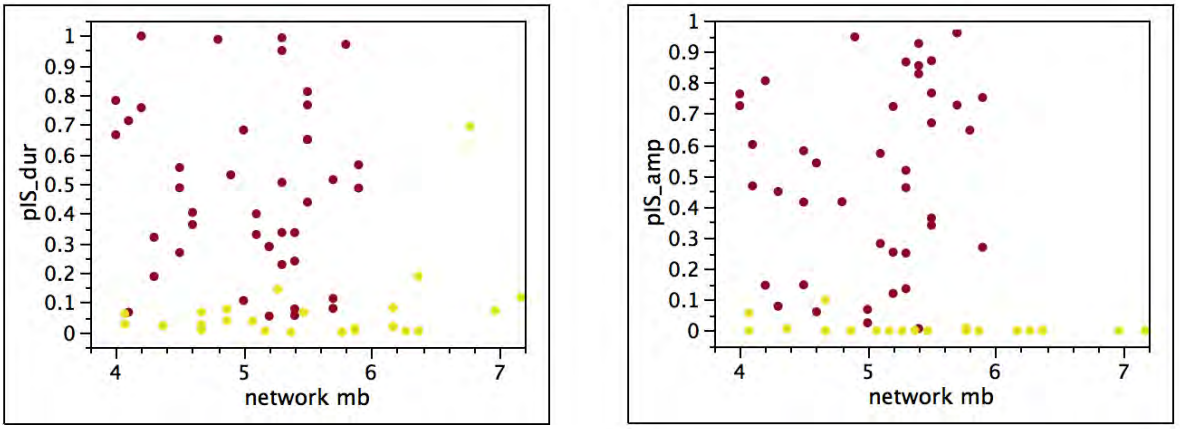

Figure 6. Individual p-values vs network mb for duration, left, and normalized amplitude, right. Here UGT events are red and EQ events are yellow.

These can be combined into a bi-variate discriminate as shown in Figure 7, with the same color-coding as in Figure 6.

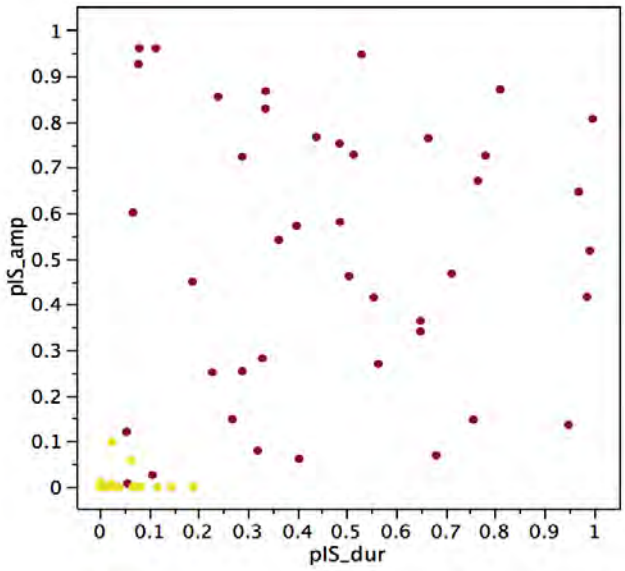

Figure 7. The combined result for amplitude and duration for the UGT and EQ data.

The three UGT events in the lower left of Figure 7 are: Houston, U19AZ; Misty Echo, U12N; and Texarkanna, U7CA. Examination of the ground motion records for these three events do not show any unusual features. Because there was a special infrasound experiment for Texarkana, we know that the jet stream was directed along the line from the Nevada Test Site to the infrasound array at St. George, UT. At 12 km altitude there was a zonally directed wind of 40 m/s that ducted energy along rays with elevation angles of 12^0 or less at 12 km altitude. This insonified

the region traditionally known as the zone of silence. Because we had a number of stations from 110 km (from the event) to St George, we measured the pressures in this strong tropospheric duct. The station at 110 km had the largest measured amplitude. Because of this, the stratospheric return was probably reduced from what would have been oberserved without the tropospheric duct. Thus of the three events, at least one had significant propagation effects.

This is a first step that shows a promising discriminant. In future work we need to establish how this discriminant would transport to other tests site, how additional stations can be incorporated into a network estimate, and what data quality issues need to be considered in the analysis.

CONCLUSIONS

We have presented an examination, for a limited set of EQ events with measured infrasound, of the relation between indicators of epicentral vertical ground motion. The results are mixed as would be expected for complex ground motion sources such as EQs. There was not a simple "rule of thumb" found for the events of this study. Vertical epicenter ground motion may not be the only source of good infrasound generation. Clearly for secondary regions away from the epicenter, surface waves play an important role. Other mechanisms may play an important role.

ACKNOWLEDGMENTS

The author is grateful to Drs. Dale Anderson, Stephen Arrowsmith, George Randall and Richard Stead for useful discussions. Stephen Arrowsmith and Richard Stead also helped with getting some of the earthquake source parameters used in this report. Dr. Marie Arrowsmith and Mr. Marv Wetovsky provided critical editorial comments. Ms Christy Flaming provided illustration expertise.

REFERENCES

Anderson, D. N., Fagan, D. K., Tinker, M. A., Kraft, G. D., and Hutchenson, K. D. (2007). A mathematical statistics formulation of the teleseismic explosion identification problem with multiple discriminants, *Bull. Seism. Soc. Am.* 97:1730–1741.

Le Pichon, A., P. Mialle, J. Guilbert and J. Vergoz, (2006). Multistation infrasonic observations of the Chilean earthquake of 2005 June 13, *Geophys. J. Int.* 167: 838–844

Le Pichon, A., J. Guilbert, A. Vega, M. Garces, and N. Brachet (2002). Ground-coupled air waves and diffracted infrasound from the Arequipa earthquake of June 23, 2001, *Geophys. Res Lett.* 10.

Le Pichon, A., J. Guilbert, M. Vallée, J. X. Dessa, and M. Ulziibat (2003). Infrasound imaging of the Kunlun Mountains for the great 2001 China earthquake, *Geophys. Res. Lett*. 30: 15, pp. 1814, doi:10.1029/2003GLO17581,2003.

Mutschlecner, J. Paul and Rodney W. Whitaker (2005). Infrasound from earthquakes, *J. Geophys. Res., 110,* D01108, doi:10.1029/2004JD0050067.

Whitaker, R. W. and J. P. Mutschlecner (2008). A comparison of infrasound signals refracted from stratospheric and thermospheric altitudes*, J. Geophys. Res*. 113: D08117, doi:10.1029/2007JD008852

APPENDIX 1

Here we will show the earlier findings comparing UGT and EQ signal amplitudes and signal durations that indicated the discrimination potential. The set of Eqs in these two plots is not quite the same as reported in Mutschlecner and Whitaker (2005). Figure A1 presents the results for signal duration, and Figure A2 presents results for wind corrected amplitude.

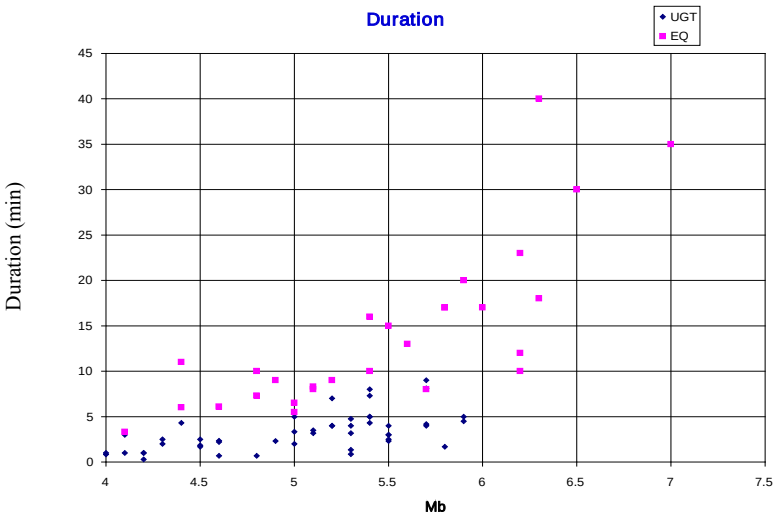

Figure A1. Comparison of infrasound signal durations for UGTs (blue) and EQs (pink) vs seismic magnitude. Durations are in minutes.

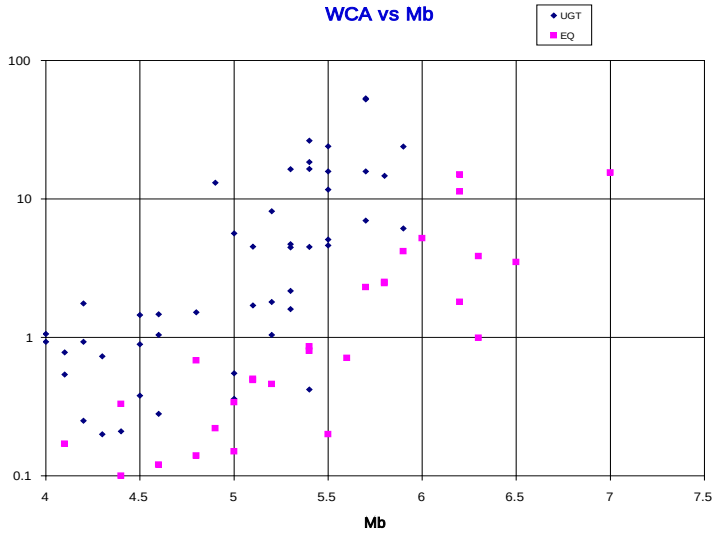

Figure A2. Comparison of infrasound signal amplitudes (microbars) for UGTs (blue) and EQs (pink) vs seismic magnitude.

APPENDIX 2: Table A2.1

Earthquakes for which Global CMT solutions were sought. The table includes the events in Figure 1 with mumbers 1 through 31 are from Mutschlecner and Whitaker (2005) and numbers 32 through 39 from LePichon et al. (2006).

EQ number	date	Time (UT)	Lat (deg)	Long (deg)	Depth (KM)	ms
1	11/3/02	22:12:41	63.52	-147.44	4	7.36
2	2/22/02	19:32:41	32.38	-115.35	10	5.56
3	2/28/01	18:54:32	47.15	-122.73	51	6.42
4	10/16/99	9:46:44	34.59	-116.27	6	6.84
5	1/17/94	12:30:55	34.21	-118.54	18.4	6.42
6	10/2/92	7:19:57	34.6	-116.64	3	4.01
7	6/28/92	15:05:31	34.2	-116.83	5	6.31
8	6/28/91	14:43:55	34.26	-118.01	11	5.88
9	10/24/90	6:15:21	38.05	-119.16	12	5.45
10	4/18/90	13:53:51	36.92	-121.68	5	5.34
11	2/28/90	23:43:36	34.14	-117.7	5	5.99
12	1/16/90	20:08:22	40.23	-124.14	2	5.56
13	1/15/90	5:29:03	37.99	-118.21	5	4.68
14	11/29/89	6:54:38	34.46	-106.89	13	4.35
15	1/30/89	4:06:23	38.82	-111.61	24	4.68
16	1/19/89	6:53:29	33.92	-118.63	12	5.12
17	12/16/88	5:53:05	33.98	-116.68	8	4.9
18	12/3/88	11:38:26	34.15	-118.13	13	4.68
19	1/28/88	2:54:02	32.91	-115.68	6	4.35
20	1/25/88	13:17:51	31.74	-115.84	5	4.9
21	11/24/87	1:54:14	33.08	-115.78	4	6.31
22	11/24/87	13:15:56	33.01	-115.84	2	6.52
23	11/24/87	2:15:26	33.25	-115.62	5	4.01
24	10/1/87	14:42:20	34.08	-118.08	10	5.88
25	7/21/86	14:42:26	37.5	-118.4	9	6.31
26	4/30/86	7:07:18	18.4	-102.47	26	6.52
27	9/21/85	1:37:14	17.8	-101.65	30	6.94
28	9/19/85	13:17:47	18.19	-102.53	27	7.15
29	11/23/84	18:08:25	37.48	-118.65	15	5.99
30	11/23/84	19:12:34	37.44	-118.64	0	5.23
31	5/2/83	23:42:38	36.22	-120.32	10	6.52
32	6/13/05	22:44:40	-20.02	-69.23	94.5	7.4
33	5/26/03	9:24:39	38.94	141.57	61	7
34	11/14/01	9:27:16	35.8	92.91	15	8
35	6/23/01	20:34:23	-17.28	-72.71	29.6	8.2
36	11/3/02	22:13:28	63.23	-144.89	15	8.5
37	4/10/05	10:29:17	-1.68	99.54	12	6.7
38	3/28/05	16:10:31	1.67	97.07	25.8	8.4
39	10/8/05	3:50:51	34.38	73.47	12	7.6

Table A2.2

Events from Table A2.1 for which Global CMT data were found.

EQ Number	PAXPLG deg)	TAXPLG (DEG)	MINPLGDEV (DEG)	DEPTH (km)
1	7	19	71	4
2	19	14	71	10
3	62	28	28	51
4	3	11	79	6
5	6	73	17	18.4
7	0	3	87	5
8	8	62	28	11
9	28	15	62	12
11	5	19	71	5
12	0	0	90	2
15	0	0	90	24
21	0	0	90	4
22	7	10	80	2
24	14	76	14	10
25	32	10	58	9
26	27	63	27	26
27	28	62	28	30
28	28	62	28	27
29	35	22	55	15
31	15	75	15	10
32	68	22	22	94.5
33	27	62	28	61
34	28	13	62	15
35	29	60	30	29.6
36	7	19	71	15
37	16	74	16	12
38	38	51	39	25.8
39	10	69	21	12

Data Processing and Analysis

AN APPROACH FOR DENOISING WAVEFORM DATA BY AUTO-REGRESSIVE ALGORITHM

Nobuo Arai, Takahiko Murayama, Makiko Iwakuni, and Mami Nogami

National Data Center-1 of Japan (Japan Weather Association)

Sponsored by the CTBT National Operations, Ministry of Foreign Affairs, Japan

ABSTRACT

The waveform data from the Comprehensive Nuclear-Test-Ban Treaty (CTBT) International Monitoring System (IMS) are mainly used for making the epicenter and characteristics of an observed event clear. Waveform data usually consist of signals from natural or man-made phenomena and site-specific noise from the ambient surroundings.

Unfortunately, if the dominant frequency of a signal is within the frequency band of the site-specific noise and the amplitude of the signal is close to the detection limit, the signal may be buried within the noise.

Bandpass filtering of data is often used to reduce the influence of the background noise (such as the site-specific noise) and enhance signal-to-noise ratios (SNRs). However, this approach is not adequate for extracting signals from raw data because such an approach does not distinguish the nature of different waveforms.

In order to remove site-specific noise components from observed raw data, an auto-regressive (AR) algorithm can be applied to extract a pure signal. The time series of the background noise is simulated by an AR model, and then a pure signal would be extracted by removing the simulated noise component from the raw data.

Effectiveness in utilizing such a concept has been tested on infrasound data observed at the IMS with affirmative results.

In this research, we demonstrate both the possibility and the capability of denoising waveform data utilizing the AR algorithm technique.

OBJECTIVES

Sources of infrasonic noise predominantly consist of eddies generated by local atmospheric disturbances (e.g., "local winds"). Reducing the influence of local winds or extracting a signal from noisy data is a significant issue at many CTBT IMS infrasound monitoring stations.

We present data from the CTBT infrasound monitoring station, IS30. Although each array element is designed to minimize the effects of wind-generated noise, it is difficult to extract signals from observed data when strong winds occur near the station.

Bandpass filtering of data is often used to remove this wind-generated noise. However, this approach is not adequate for extracting signals from raw data because such an approach does not distinguish the nature of different waveforms. Moreover, if the dominant frequency of the signal is within the frequency band of the site-specific noise and the amplitude of the signal is close to the detection limit, the signal may be buried within the noise.

Therefore, the objective of this research is to reduce the influence of background noise (such as wind-generated noise) and enhance the SNR by using a new technique that is frequency-band independent.

RESEARCH CONDUCTED

Infrasonic noise is predominantly wind-generated. Generation of wind noise is described as a stochastic process, and the state of wind can be stationary within a short period.

Thus, to remove site-specific noise components from observed raw data, an AR algorithm is applied for the extraction of a pure signal. The time series of the background noise is simulated by an AR model, and the pure signal is extracted by removing the simulated noise from the observed raw data.

The AR algorithm is a new technique for denoising waveform data and consists of three components: the simulation method of the background noise, the reduction procedure of the background noise, and the extraction of pure signal, and is described as follows.

Fundamental conceptual model of the waveform data

The concepts of denoising and the subsequent extraction of pure signal are shown in Figure 1.

As shown schematically in the outline below, the approach we used in this research consisted of eliminating background noise from the observed data so as to obtain pure signal.

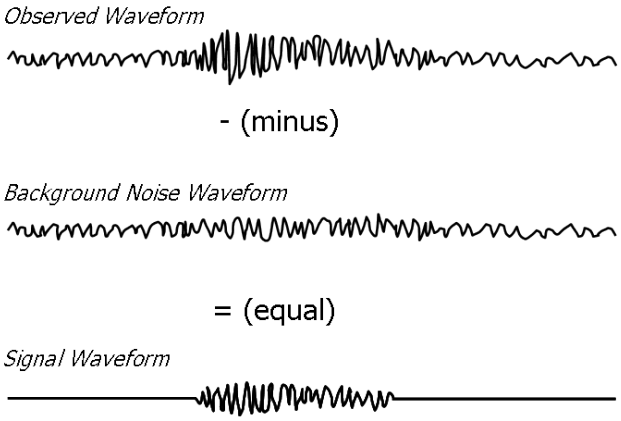

Figure 1. Conceptual image of denoising procedure on waveform data.

The actual observed infrasound data (y_n) also contains a trend component in addition to the background noise illustrated in Figure 1.

Hence, we assumed the following equation based on the time series analysis method (e.g., Vaseghi, 1996; Kitagawa, 1993):

$$y_n = t_n + r_n + s_n + w_n \quad (1)$$

where t_n is the trend component, r_n is background noise, s_n is signal, and w_n is observation noise, at time n.

State space model

In order to estimate the time series of each component, we utilize the state space model. With the assumption that y_n is the time series of l variate, the state space model is represented by the following equation:

$$x_n = Fx_{n-1} + Gw_n \quad \text{(System Model)} \quad (2)$$

$$y_n = Hx_n + \varepsilon_n \quad \text{(Observation Model)} \quad (3)$$

where x_n is the state vector, which is directly unobservable; k is the dimensional vector; w_n is the system noise (or the state noise); and m is the order dimensional white noise in accordance with zero mean and the variance-covariance matrix (Q_n).

On the other hand, ε_n is the observation noise, and l is the order dimensional white noise in accordance with zero mean and the variance-covariance matrix (R_n).

F, G, and H are matrixes of $k \times k$, $k \times m$, and $l \times k$, respectively.

The state space model is interpreted in two ways, as follows:

1) The observation model (Equation [3]) is assumed to be the regressive model.

   In this case, the model shows the mechanism in which y_n is observed. The state x_n shows the regression coefficient, and the system model shows the change of the regression coefficient with respect to time.

2) The state vector x_n is the signal to be estimated.

   In this case, the system model shows the mechanism of the signal generation, and the observation model shows the shape when a signal is actually observed, with the noise component added to that signal.

Applied concrete cases are explained in terms of each component model.

The following section describes each component model (r_n, background noise; s_n, signal; and t_n, trend component;).

Background noise component model and signal component model

We have modeled the background noise component r_n and the signal component s_n using an AR model because their time series' are short period in nature.

An AR model is a type of random process that is often used to model and predict various types of natural phenomena. AR models of background noise r_n and signal s_n are given by the following equations:

$$r_n = \sum_{j=1}^{m} a_j r_{n-j} + u_n \quad (4)$$

$$s_n = \sum_{j=1}^{l} b_j s_{n-j} + v_{n1} \quad (5)$$

These are based on parameters a_j and b_j, where $j = 1,...,m$ and $j = 1,...,l$. There is a direct correspondence between these parameters and the covariance function of the process. This correspondence can be inverted to determine the parameters from the autocorrelation function (which is itself obtained from the covariances), where u_n and v_{n1} are white noise processes each with a zero mean and respective variances τ_1^2, τ_2^2.

Using Equation (4) as an example and defining the state vector as $x_n = (r_n, r_{n-1}, \cdots, r_{n-m+1})^t$, the following equations hold between x_n and x_{n-1}:

$$x_n = F_1 x_{n-1} + G_1 u_n \tag{6}$$

$$x_n = \begin{bmatrix} r_n \\ r_{n-1} \\ \vdots \\ r_{n-m+1} \end{bmatrix}, \quad F_1 = \begin{bmatrix} a_1 & a_2 & \cdots & a_m \\ 1 & & & \\ & \ddots & & \\ & & 1 & 0 \end{bmatrix}, \quad G_1 = \begin{bmatrix} 1 \\ 0 \\ \vdots \\ 0 \end{bmatrix} \tag{7}$$

where F_1 and G_1 is a matrix of $m \times m$ and an m-dimensional vector, respectively. And, as the first component of the state (x_n) is r_n, the observation model (r_n) (Equation [8]) below, given $H_1 = \begin{bmatrix} 1 & 0 & \cdots & 0 \end{bmatrix}$ is:

$$r_n = H_1 x_n \tag{8}$$

The variances of the system noise and observation noise are $Q = \tau_1^2$ and $R = 0$; thus, the state space model of the AR model is given by Equation (8).

As in the case of the background noise model, when the matrices of the state space model are assumed, see Equations (9) and (10), the state space model of the signal component is represented by Equation (11).

$$x_n = \begin{bmatrix} s_n \\ s_{n-1} \\ \vdots \\ s_{n-m+1} \end{bmatrix}, \quad F_2 = \begin{bmatrix} b_1 & b_2 & \cdots & b_m \\ 1 & & & \\ & \ddots & & \\ & & 1 & 0 \end{bmatrix}, \quad G_2 = \begin{bmatrix} 1 \\ 0 \\ \vdots \\ 0 \end{bmatrix}, \quad H_2 = \begin{bmatrix} 1 & 0 & \cdots & 0 \end{bmatrix} \tag{9}$$

$$x_n = F_2 x_{n-1} + G_2 v_{n1} \tag{10}$$

$$s_n = H_2 x_n \tag{11}$$

Trend component model

Infrasound observations contain long-period pressure changes (from a few minutes to a dozen or so minutes), such as a gravity wave of the Earth. We estimated the time series of a long-period wave by using the trend component model t_n.

The simplest way to estimate the trend of a time series is to use the polynomial trend model. This model is expressed by the following equation (the time series [y_n] is composed of the polynomial equation [t_n] and residuals [w_n]):

$$y_n = t_n + w_n \tag{12}$$

where w_n is a white noise process with zero mean and variance σ^2. The trend component model t_n is the polynomial equation represented by the following equation:

$$t_n = a_0 + a_1 x_n + \cdots + a_m x_n^m \tag{13}$$

This equation is the specific model. In order to extend this model to a more flexible function, the k^{th}-stochastic difference equation (14) is provided as a useful alternative. In this equation, it is assumed that the k^{th} difference of t_n is close to zero.

$$\Delta^k t_n = v_{n2} \tag{14}$$

where v_{n2} is a white noise process with zero mean and variance τ_3^2.

The trend component model (14) is generally represented by the following equation, given $\Delta \equiv 1 - B$ (the time subtraction operator defined by $\Delta t_n \equiv t_n - t_{n-1}$):

$$\Delta^k = (1 - B)^k = \sum_{i=0}^{k} {}_k c_i (-B)^i \tag{15}$$

When c_k is defined by $c_i = (-1)^{i+1}{}_k c_i$, Equation (15) is represented by the following:

$$t_n = \sum_{j=1}^{k} c_k t_{n-i} + v_{n2} \tag{16}$$

This model can be considered the AR model of the k^{th}-order dimension although not the stationary state. Therefore, when the matrices of the state space model are assumed, as in Equations (17) and (18), the state space model of the trend component model is represented by Equation (19).

$$x_n = \begin{bmatrix} t_n \\ t_{n-1} \\ \vdots \\ t_{n-k+1} \end{bmatrix}, \quad F_3 = \begin{bmatrix} c_1 & c_2 & \cdots & c_k \\ 1 & & & \\ & \ddots & & \\ & & 1 & 0 \end{bmatrix}, \quad G_3 = \begin{bmatrix} 1 \\ 0 \\ \vdots \\ 0 \end{bmatrix}, \quad H_3 = \begin{bmatrix} 1 & 0 & \cdots & 0 \end{bmatrix} \tag{17}$$

$$x_n = F_3 x_{n-1} + G_3 v_n \tag{18}$$

$$t_n = H_3 x_n \tag{19}$$

The parameter setting of the state space model for the resolution of the observed infrasound data

When the equations for each time series component are combined with the state space model explained above, the following parameters of the state space model are provided.

$$F = \begin{bmatrix} F_1 & & \\ & F_2 & \\ & & F_3 \end{bmatrix}, \quad G = \begin{bmatrix} G_1 & & \\ & G_2 & \\ & & G_3 \end{bmatrix}, \quad H = \begin{bmatrix} H_1 & H_2 & H_3 \end{bmatrix}, \quad Q_n = \begin{bmatrix} \tau_1^2 & 0 & 0 \\ 0 & \tau_2^2 & 0 \\ 0 & 0 & \tau_3^2 \end{bmatrix} \tag{20}$$

By using the state space model defined by Equation (20), the observed data are broken down into each waveform (the trend, the background noise, and the signal).

Thus, we can take away the trend and background noise from the observed data to finally get a waveform consisting of pure signal.

Kalman filter

In dealing with the state space model, it is a vital hypothesis that the state (x_n) is estimated based on the observed data of the time series (y_n). In order to estimate this state, we have used the Kalman filter algorithm in this research. The Kalman filter is a recursive estimator and based on linear dynamical systems discretized in the time domain. We could effectively calculate the conditional marginal distribution of the state (x_n). In what follows, the notation $x_{n/m}$ represents the estimate of x at time n, given observations up to and including time m.

The state of the filter is represented by two variables:

$x_{n/m}$: the estimate of the state at time n given observations up to and including time m

$V_{n/m}$: the error covariance matrix (a measure of the estimated accuracy of the state estimate)

The Kalman filter has two distinct phases: <Predict> and <Update>. The predict phase uses the state estimate from the previous time-step to produce an estimate of the state at the current time-step. In the update phase, measurement information at the current time-step is used to refine the prediction to arrive at a new, more accurate state estimate, again for the current time-step.

< Predict >

$$x_{n/m} = F_n x_{m/m} \quad \text{(Predicted state)} \quad (21)$$

$$V_{n/m} = F_n V_{m/m} F_n^{\ t} + G_n Q_n G_n^{\ t} \quad \text{(Predicted estimate covariance)} \quad (22)$$

< Update >

$$K_n = V_{n/m} H_n^{\ t} (H_n V_{n/m} H_n^{\ t} + R_n)^{-1} \quad \text{(Kalman gain)} \quad (23)$$

$$x_{n/n} = x_{n/m} + K_n (y_n - H_n x_{n/m}) \quad \text{(Updated state estimate)} \quad (24)$$

$$V_{n/n} = (I - K_n H_n) V_{n/m} \quad \text{(Updated estimate covariance)} \quad (25)$$

Order dimension of the trend model and AR model

With regards to the order dimension of the trend model and AR model, we have used the Akaike Information Criterion (AIC). AIC is a measure of how well an estimated statistical model fits (e.g., Sakamoto, etc., 1981). It is based on the concept of entropy, which in effect offers a relative measure of the information lost when a given model is used to describe reality and can be said to describe the tradeoff between bias and variance in model construction, or loosely speaking, that of precision and complexity of the model.

AIC is a tool for model selection. Given a dataset, several competing models may be ranked according to their AIC, with the one having the lowest AIC being the best. From the AIC value, one may infer that, for example, the top three models are in a tie and the rest are far worse, but one should not assign a value above which a given model is "rejected."

The AIC is derived by the following equation:

$$AIC = 2k - 2\ell(\hat{\theta}) \quad (26)$$

where k is the number of parameters in the statistical model, and $\hat{\theta}$ is the maximized value of the log-likelihood function for the estimated model.

Examples of the Application of Waveform Denoising

Examples of removing the trend and the noise, resulting in the extraction of pure signal, are shown in Figures 2 through 4.

Below is a case of an aircraft that crashed while attempting to land at the Narita Airport in Japan on March 22, 2009. The infrasound signal was generated by the explosion, and CTBT IMS infrasound monitoring station IS30 detected the signal. The figure below shows that once the trend and the noise components are eliminated, pure signal is clearly detected.

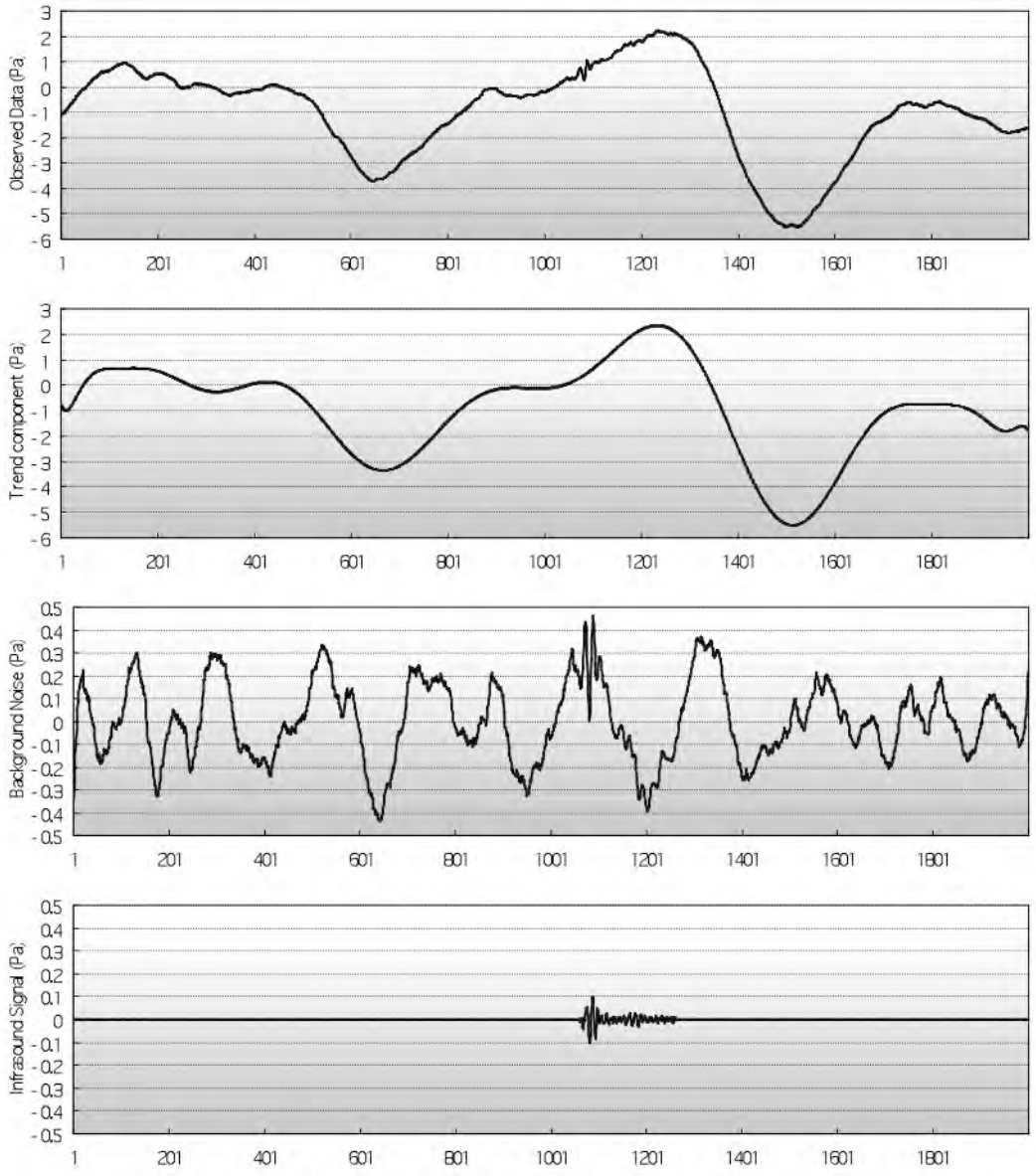

Figure 2. The infrasound waveform (documented during an aircraft accident on 22 March) recorded at the CTBT IMS infrasound station IS30 and the estimated results of each time series, namely (top) the observed raw data, (top middle) the trend component simulated by the trend component model, (bottom middle) the background noise simulated by the AR model, and (bottom) the extracted infrasound signal.

The case of a volcanic eruption is shown in Figure 3.

Mt. Asama, which is located in central Japan, experienced a minor eruption on February 2, 2009, and the CTBT IMS infrasound monitoring station IS30 recorded an infrasound signal. By means of eliminating the trend and the noise components from the observed data, the infrasound signal generated by the eruption is clearly detected.

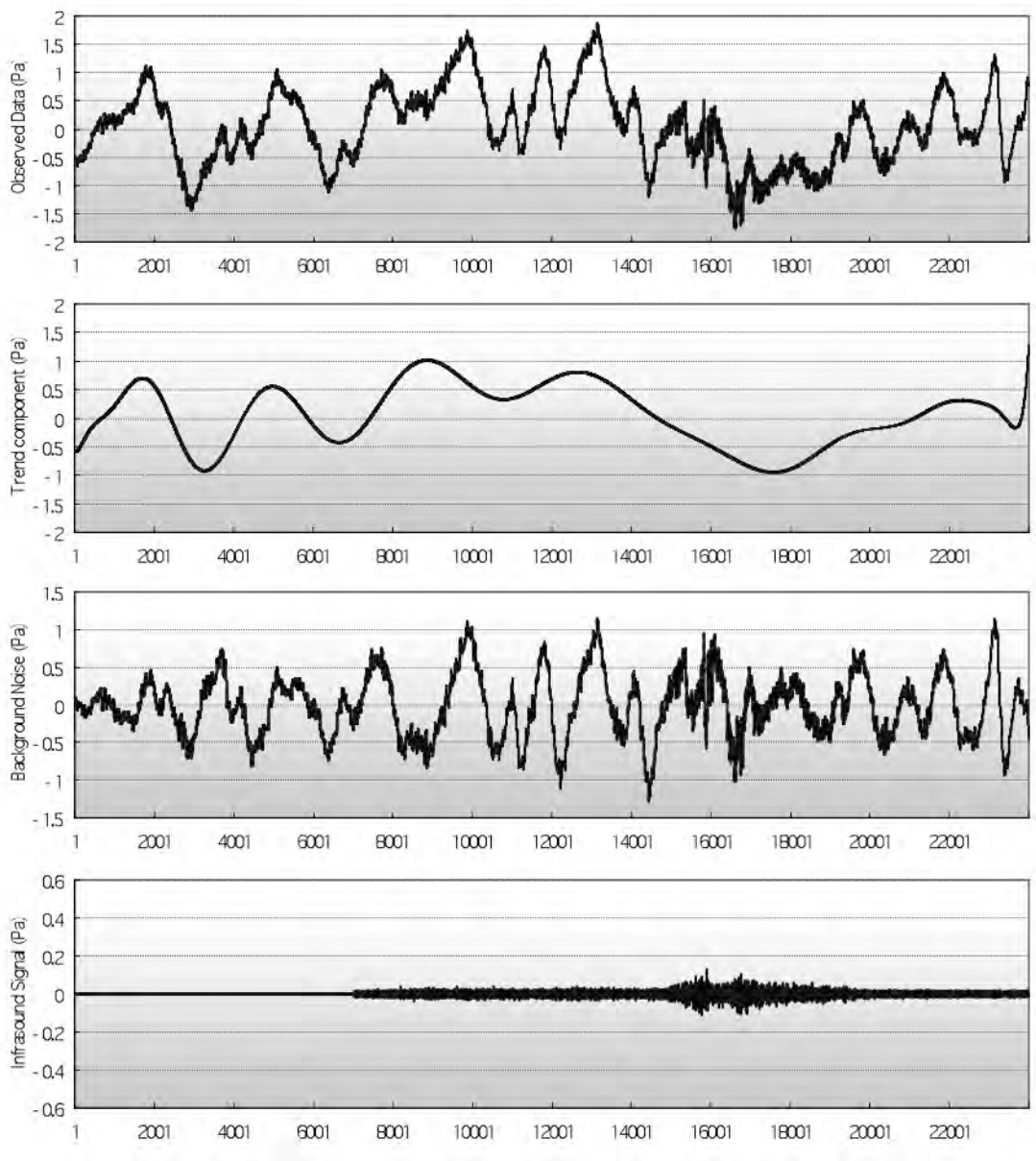

Figure 3. The infrasound waveform (produced as a result of the Mt. Asama eruption on February 2, 2009) recorded at the CTBT IMS infrasound station IS30 and the estimated results of each time series, namely (top) the observed raw data, (top middle) the trend component simulated by the trend component model, (bottom middle) the background noise simulated by the AR model, and (bottom) the extracted infrasound signal.

A lightning occurrence is shown in Figure 4.

IS30 recorded an infrasound signal when lightning struck approximately 60 km away from the array on July 27, 2008. After eliminating the trend and the noise components, the pulsed infrasound signal produced by the lightning is detected.

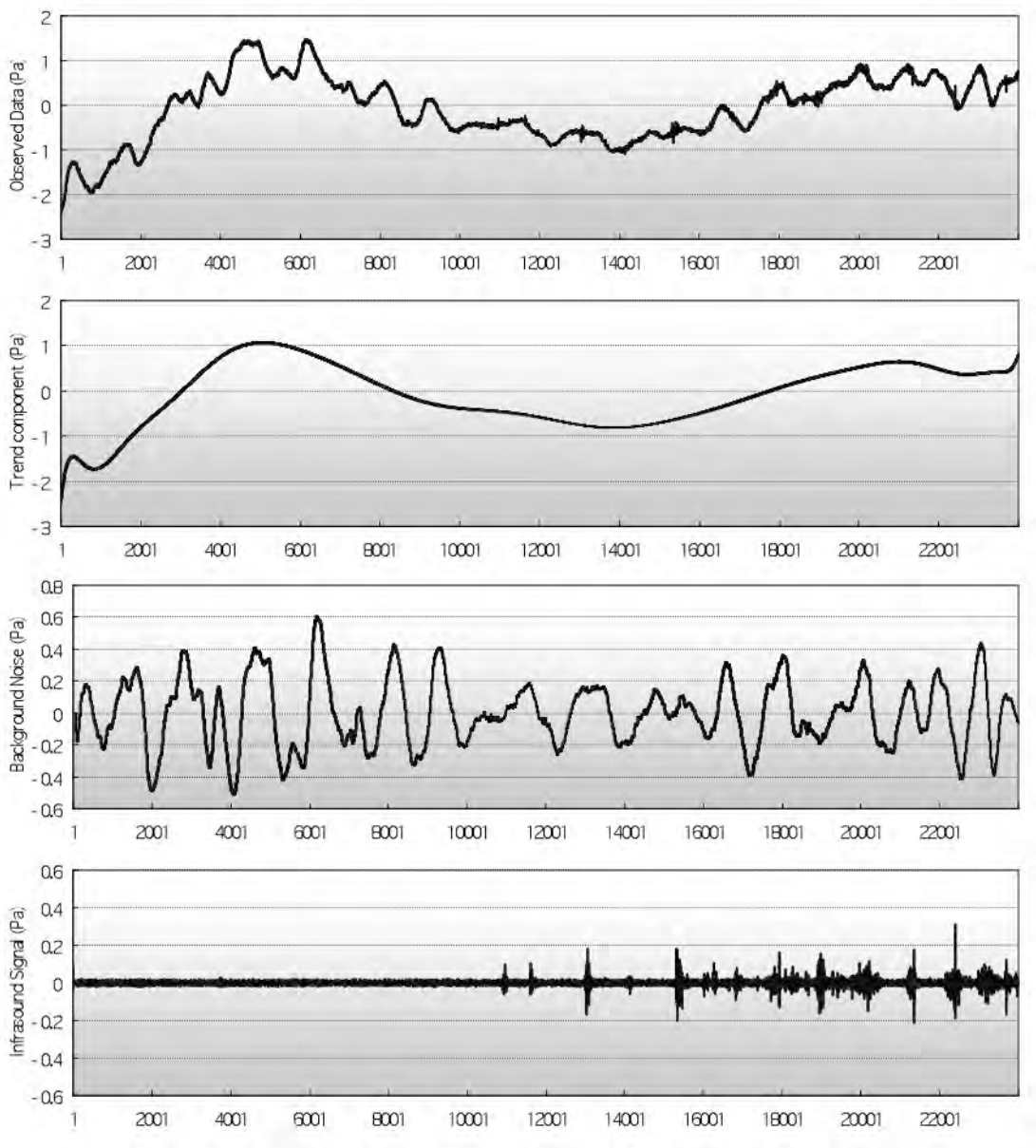

Figure 4. The infrasound waveform (produced by lightning on July 27, 2008) recorded at the CTBT IMS infrasound station IS30 and the estimated results of each time series, namely (top) the observed raw data, (top middle) the trend component simulated by the trend component model, (bottom middle) the background noise simulated by the AR model, and (bottom) the extracted infrasound signal.

CONCLUSIONS AND RECOMMENDATIONS

As has been demonstrated above, in order to remove site-specific noise (such as wind-generated noise) components from observed raw data, an AR algorithm can be applied to extract a pure signal. The time series of the trend and the noise have been simulated by the trend model and AR model respectively, and then a pure signal can be extracted by removing the simulated noise component from the observed raw data.

Effectiveness in utilizing such a concept has been tested by infrasound data observed at the CTBT IMS infrasound monitoring station IS30, with positive results in several cases. However, the effectiveness of the AR model was not substantially discussed and examined and should be continuously evaluated by using other infrasound monitoring data.

REFERENCES

Vaseghi, S. (1996). Advanced digital signal processing and noise reduction, Second edition, John Wiley & Sons Ltd.

Kitagawa, G. (1993). The time series analysis programming, Iwanami Shoten.

Sakamoto, Y., etc. (1981). Akaike Information Criterion, Statistics, D. Reidel Publishing Company.

DEVELOPMENT OF A SOFTWARE TOOLBOX FOR SYSTEMATIC EVALUATION OF SEISMOMETER-DIGITIZER SYSTEM RESPONSES

Jessie L. Bonner[1], Robert B. Herrmann[2], Mark Leidig[1], Kevin M. Mayeda[1], and Aaron Ferris[1]

Weston Geophysical Corp.[1] and St. Louis University[2]

Sponsored by the National Nuclear Security Administration

Contract No. DE-FG02-09ER85548

ABSTRACT

Calibration datasets based on the absolute amplitudes of a seismic signal require accurate knowledge of the seismometer-digitizer response. Body- and surface-wave magnitudes, moment estimation, multi-station source characterization, and attenuation model development all require digital seismic data to be corrected for the two components of a digital seismic system: the seismometer and digitizer. When the seismometer and digitizer characteristics are known, deconvolution of the digital system response is relatively straightforward (e.g., transfer command in Seismic Analysis Code [*SAC*], Goldstein et al., 2003). However, even with a known response, problems in timing and incorrect polarities can often contaminate any calibration parameters derived from these data. When either one or both components of the response for a seismometer system are unknown, the data are often not considered suitable for seismological tasks that require absolute amplitude measurements. Thus, for the nuclear explosion monitoring mission, the seismic response of the seismometer-digitizer system is essential.

Weston Geophysical Corporation proposes to develop a software toolbox that will recover the seismometer response for recorded seismic data. The toolbox will include 1) a database of known seismometer and digitizer responses with all possible gain settings; 2) methods for estimating response "transfer" functions between stations with and without known responses; 3) techniques for using synthetic seismograms for response validation; and 4) advanced methods for timing and polarity quality control. The toolbox will provide nuclear test monitoring scientists with a valuable asset to characterize datasets that can improve their ability to detect, locate, and discriminate underground nuclear explosions.

OBJECTIVES

We are developing a software toolbox to estimate, assess, and chronicle the seismometer and digitizer response from recorded seismic data. The specific technical objectives will include developing a comprehensive database of known seismometer and digitizer responses with all possible gain settings. Next, we will assemble a set of seismic analysis tools (Figure 1) to iteratively recover the instrument response using two approaches. First, we will estimate a station response transfer function by fitting the seismic data at an unknown station to the background noise and recorded signals from nearby stations with known responses. Second, we will perform variable-period body, coda modeling, and surface-wave modeling to fit the observed data at a station with unknown response to predicted synthetics.

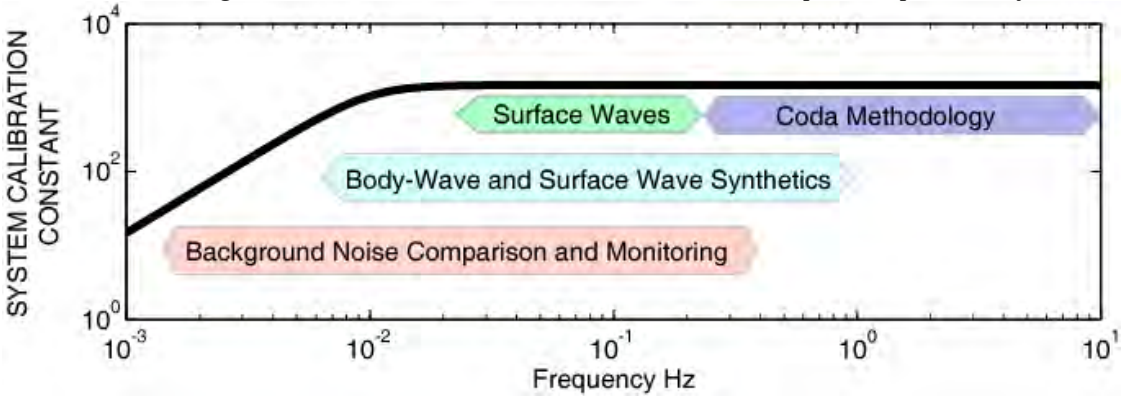

Figure 1. Schematic showing our planned methods for recovering the seismometer-digitizer response for recorded seismic data. The methods include developing transfer functions using surface wave and coda methods, developing synthetics for comparison to the observed data, and monitoring broadband background noise for timing and gain changes.

RESEARCH ACCOMPLISHED

Database Development

We are compiling a comprehensive, current database of seismometers and digitizers currently used (or in development) to monitor global earthquakes and explosions. The objective of this database will be to serve as a starting point when trying to recover a seismometer-digitizer response.

System Response Estimation

We are assembling a set of seismic analysis tools to recover the instrument response by 1) developing a response transfer function that fits the seismic data to the background noise and recorded signals from nearby stations with known responses, and 2) using variable-period body and surface wave modeling to fit the observed data to predicted synthetics. To demonstrate our research plan, we include a recent example of acquiring a test dataset for which both seismometer and digitizer response information were not available. We developed a working seismometer-digitizer response for these data using various seismic methods.

Seismic Data. Hundreds of new seismic stations have been deployed in Eurasia over the past few years, and many of these data are available for download. A problem often encountered with these new data involves compiling the correct seismometer and digitizer responses as well as information concerning the data quality. One such network (designated in this paper the "test network") provides the waveform data from their 10–20 stations that record regional events and also provides the seismometer calibration sheets (Figure 2). The sheets provide information on the type of seismometers that comprise the stations of this network, including CMG-3T instruments with a nominal velocity output of approximately 2 x 750 V/m/sec. The pole-zero table representative of a flat velocity response between 100 seconds and 50 Hz (Figure 3) was also available on the website. While this was important information, it was not complete. The digitizer least significant bit, which is needed in order to convert the data from counts to ground motion velocity in *m/sec*, remained unknown.

CMG-3T CALIBRATION SHEET

WORKS ORDER:	0515	DATE:	16.02.96
SERIAL NUMBER:	T3347	TESTED BY:	SDG

	Velocity Output V/m/s (Differential)	Mass Position Output (Acceleration output) $V/m/s^2$	Feedback Coil Constant $Amp/m/s^2$
VERTICAL	2 x 750.7	1866	0.02828
NORTH/SOUTH	2 x 758.0	1677	0.03106
EAST/WEST	2 x 750.9	1749	0.03239

Power Consumption: 66 mA @ 12 V input
Calibration Resistor: 51K

NOTE: A factor of 2 x must be used when the sensor outputs are used differentially (also known as push-pull or balanced output). Under no conditions should the negative outputs be connected to the signal ground. A separate signal ground pin is provided.

Figure 2. Seismometer calibration sheet downloaded from the seismic network operator's webpage.

POLES AND ZERO TABLE

WORKS ORDER NUMBER: 0515

SENSOR SERIAL NO: T3345

Velocity response output, Vertical Sensor:

POLES (HZ)	ZEROS(HZ)
$-7.07 \times 10^{-3} \pm j\, 7.07 \times 10^{-3}$	0
$-80.5 \pm j\, 30.8$	0
	+150.5

Normalizing factor at 1 Hz: A = - 49.5

Sensor Sensitivity: See Calibration Sheet.

NOTE: The above poles and zeros apply to the vertical and the horizontal sensors and are given in units of Hz. To convert to Radian/sec multiply each pole or zero with 2π. The normalizing factor A should also be recalculated.

Figure 3. Poles and zeroes table for a seismometer in a test seismic network.

Guralp System Investigation. We searched the seismometer manufacturer's webpage and obtained specific information about their equipment. Since this manufacturer often sells their sensors and digitizers in combination, we assumed that the analog data from the CMG-3T were digitized using a DM24 digitizer, which has an input voltage range of ±10 volts. The point of this exercise was to develop an "initial" estimate of the response. For a 24-bit digitizer, this would correspond to a least significant bit of 1.19 μVolts/count assuming unity gain. Combining this assumed bit weight with the velocity output obtained from the seismometer calibration sheets (e.g., 2*750 V/m/sec), we estimated an "initial" digital sensitivity of 7.9E-10 m/sec/count. At this stage in our response recovery, we assumed that the downloaded data were in counts, but ultimately, our technique will not rely on this assumption.

Developing a Response Transfer Function. We now had an "initial" working estimate for the seismometer-digitizer response, based on actual sensor calibration data from the network operator's website together with generic information about the digitizer obtained from the manufacturer's website. We then applied this total system response to convert the velocity data from counts to displacement in nanometers.

The next stage in our response recovery was to compare the noise and signals from one of the unknown stations with the noise and signals from a nearby station with a known system response, $R_2(\omega)$. This method essentially develops a transfer function $T(\omega)$ between the response at a known station and the response at the station of interest $R_1(\omega)$, where

$$R_1(\omega)=R_2(\omega)*T(\omega). \qquad (1)$$

Because our techniques consider certain bands of the response, the recovered response $R_1(\mathrm{w})$ may not be continuous across the entire frequency band.

For example, an m_b=5.7 event occurred and its data from the Global Seismograph Network (GSN) and the test network were available for download. We compared the response-corrected signal and noise at station GNI (a GSN station in Armenia) and a nearby station in the test network (referred to as "Station M1") with unknown response given their similar propagation paths and epicentral distances. We then estimated the period-dependent surface wave magnitudes (Russell, 2006; Bonner et al., 2006) for the GNI and Station M1 data. The results are shown in Figure 4a. The figure shows the surface-wave magnitudes (solid lines) based on amplitudes between periods of 8 and 40 seconds. Also shown are the noise estimates (dashed lines) for the two stations at these same periods. Given the similarity in epicentral distance, propagation paths, and backazimuths to the event, we would not expect a significant difference in the surface-wave magnitudes for these two stations. However, there is a 0.5 magnitude unit (m.u.) difference (amplitude factor > 3x) between the GNI- and Station M1-based estimates, which is far greater than would be expected based on source or station effects. Also discouraging is that the noise estimates for the two stations are also offset by ~0.5 m.u. We decided that our initial estimate at the digitizer LSB was incorrect or that the sensor was operating at a different gain setting.

We note that the shapes of the noise estimates at the two stations are similar except for a static offset. By increasing the noise estimates at Station M1 to match the GNI noise data, we were able to estimate a new potential digitizer LSB for Station M1 of 4.0 μVolts/count (compared to our original estimate of 1.19 μVolts/count). Figure 4b shows that there is essentially no difference between the GNI surface wave magnitude estimate and the Station M1 estimate based on the new "calibrated" response (e.g., 6.72 versus 6.75). The GNI path samples part of the South Caspian Basin, and the surface wave amplitudes at periods < 20 secs have been attenuated while being less affected at longer periods.

At a later date than the analysis shown in Figure 4, we were able to obtain a copy of the digitizer calibration sheets for Station M1 and others in its network. These sheets provided the actual digitizer LSB for the instruments: 3.5 μVolts/count. When this value was used to correct the data for the instrument response, we obtained similar magnitudes (6.75 vs. 6.70) to our "calibrated" estimate (Figure 4b).

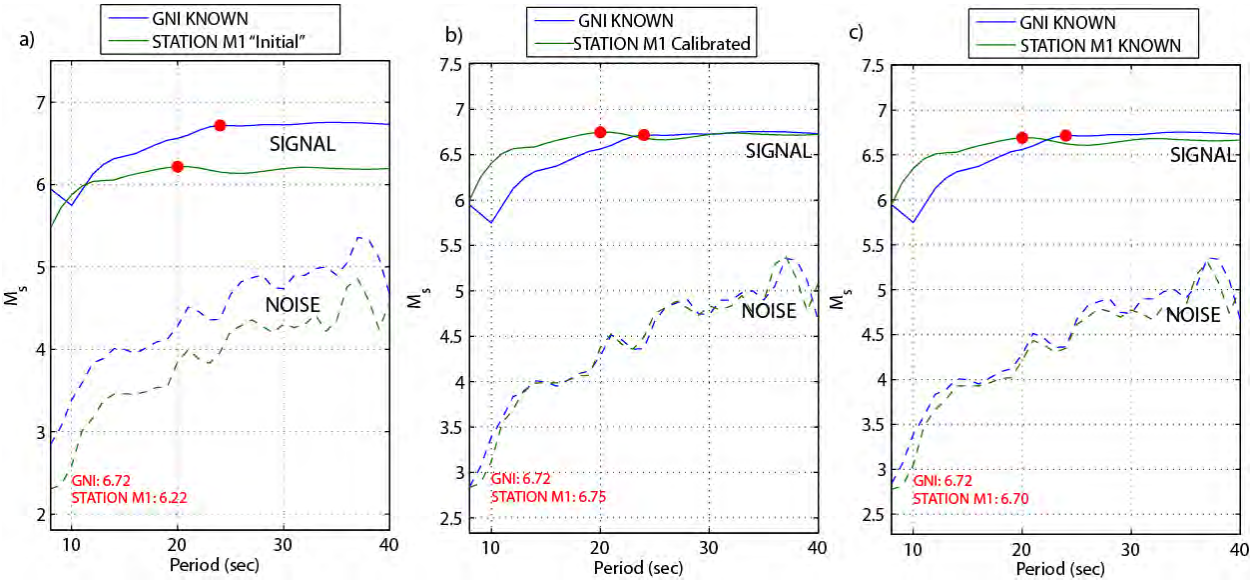

Figure 4. Evaluating different digitizer constants in terms of signal magnitudes and noise levels at GNI and Station M1--a seismic station with unknown response. a). Initial "guess" LSB of 1.19 μVolts/count. b) "Calibrated" LSB estimate of 4.0 μVolts/count based on fitting the long-period noise levels. c) Actual LSB of 3.5 μVolts/count based on digitizer calibration sheet.

Testing with Synthetics. Synthetic seismograms can be used to evaluate response estimates. This exercise requires the waveforms of an event large enough to be modeled, and also large enough to be independently tested and evaluated. We obtained the recordings of an M_w=7.9 earthquake on the same test network discussed in Figures 2–4. Since the epicentral distances ranged from 36 to 49 degrees, waveform modeling is not very sensitive to the upper mantle. In work for the USGS, Herrmann et al. (2008) implemented a detailed procedure for rapid moment tensor inversion using teleseismic *P*, *SV* and *SH* waves (see http://eqinfo.eas.slu.edu/Earthquake_Center/MomentTensor.html). A simple modification of that procedure created a forward modeling procedure for seismic network quality control (QC). Given a moment tensor solution, the teleseismic waveforms are lowpass filtered in such a way that the source time function does not have to be specified in detail. A direct comparison can then be made between observed and predicted signals.

The example shown in Figure 9 is for test network broadband stations with the derived broadband response for the systems (e.g., Figure 4). The *P*-wave comparisons are good, although the Station Z may have a timing problem. The peak amplitudes are generally within 50% of each other for the assumed response. The comparison of the SH components (Figure 5) may be affected by the assumptions of a point source for this large earthquake as much as the assumption that the horizontal components are correctly oriented.

For the network discussed in Figures 5 and 6, the number of posted teleseismic recordings is very small. However, the recordings of M > 4 earthquakes are often available. Forward modeling can be performed if the velocity and attenuation models are known along the source-receiver path and if the moment tensor is known. Such modeling will illustrate component orientation and timing problems. Of course the same data can be inverted for the moment tensor using velocity models for the path that are derived from the knowledge base. An approach here would be to start with larger events, seen by other nearby broadband stations to build confidence in the velocity models and the component orientation, followed by modeling of the smaller earthquakes to track the history of the data channels.

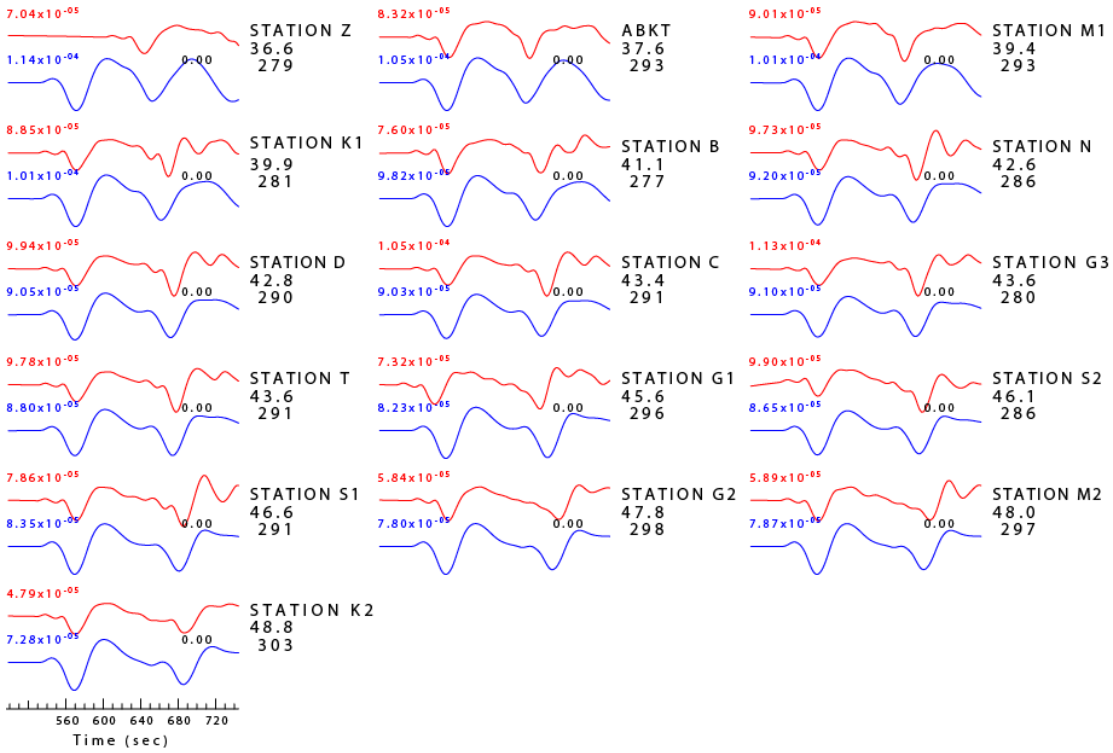

Figure 5. *P*-wave Vertical Component Comparison: Comparison of the observed traces (red) corrected with our calibrated system response and predicted traces (blue) ordered in terms of increasing epicentral distance. Each pair of traces is annotated with a station name, epicentral distance in degrees, source to station azimuth in degrees. Each pair of traces is plotted with the same scale and the peak amplitudes are indicated at the left of each trace. Finally the time shift between the *P*-wave first arrival picked and the theoretical *P*-wave first arrival in the predicted trace is indicated, with a positive sign indicating that the predicted trace has been shifted to the right by the given number of seconds as a function of source to station azimuth in degrees.

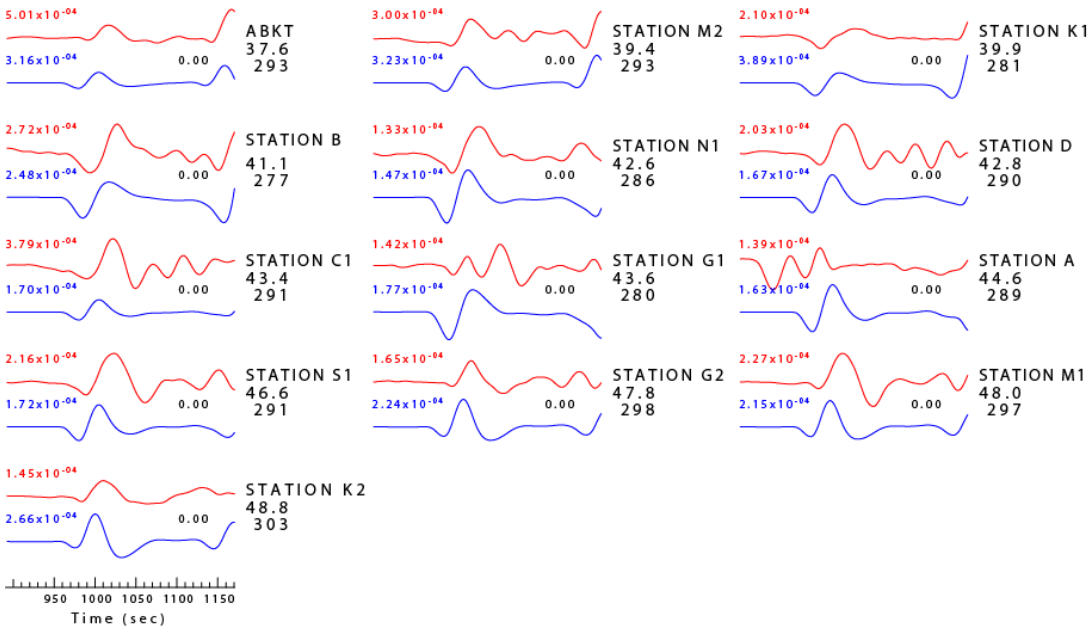

Figure 6. SH-wave T Component Comparison. See Figure 5 caption for details.

Advanced Data Quality Control

In addition to the recovery of the instrument response, the methods in this proposed toolbox could also provide other network QC features such as timing problems and polarity reversals. While examining the test network data using long period synthetic modeling, we determined several components had reversed polarity. Additionally, continuous monitoring of background noise levels will highlight possible network/station operator gain adjustments. Timing problems will also be illuminated by analyzing the noise field through the cross correlation of station pairs (Figure 7). During this project, we will address the possibility of incorporating these additional QC features in the toolbox.

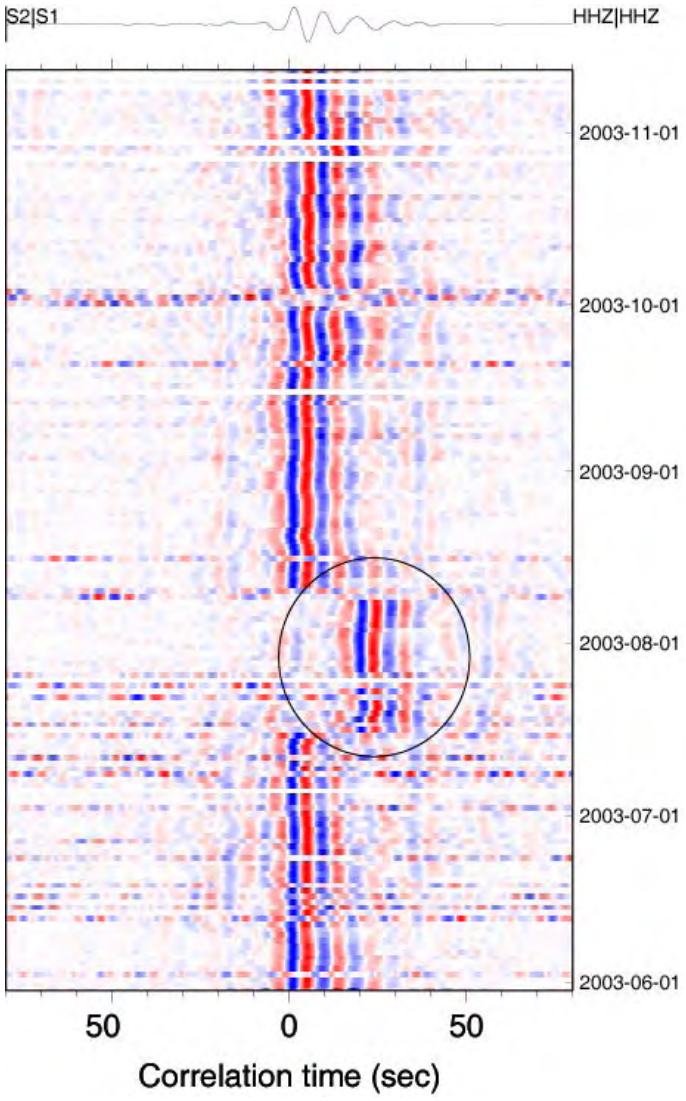

Figure 7. Two-station continuous correlation functions for a 5.5 month period for two nearby stations in the test network. Each row of the image represents a daylong correlation function, although only 100 seconds are displayed. Data processing includes spectral whitening prior to cross correlation followed by filtering to 0.08 - 0.15 Hz. The station pair is separated by 32 km. The anomalous time shift (black circle) in the dominant signal starting in mid-July and lasting approximately 1 month indicates a timing problem with one of the stations.

CONCLUSIONS AND RECOMMENDATIONS

We have just initiated the development of this software toolbox for recovery of seismometer-digitizer responses, and there are many questions that remain before we can determine its effectiveness. We hope the toolbox will be included in future versions of the *Seismic Analysis Code (SAC)*, which is a preferred seismic software analysis tool for many scientists. As a SAC module, the toolbox would provide nuclear test monitoring scientists with a valuable asset to characterize and improve calibration datasets. Products derived from these calibration datasets will improve their ability to detect and locate seismic events. In addition, the toolbox could highlight changes in instrument behavior in seismic networks that are used to monitor earthquakes for global seismic hazard prediction and assessment.

REFERENCES

Bonner, J. L., D. Russell, D. Harkrider, D. Reiter, and R. Herrmann, (2006). Development of a time-domain, Variable-Period Surface Wave Magnitude Measurement Procedure for Application at Regional and Teleseismic Distances, Part II: Application and M_s—m_b Performance. *Bull. Seism. Soc. Am.* 96: 678–696.

Goldstein, P., D. Dodge, M. Firpoand, and Lee Minner, (2003). *SAC2000: Signal processing and analysis tools for seismologists and engineers*, Invited contribution to *The IASPEI International Handbook of Earthquake and Engineering Seismology*, Edited by WHK Lee, H. Kanamori, P.C. Jennings, and C. Kisslinger, Academic Press, London.

Herrmann, R. B., H. Benz, and C. Ammon (2008). Systematic moment tensor estimation for North America earthquakes, *Seism. Res. Letts.* 79: 349.

Russell, D. R., (2006). Development of a time-domain, variable-period surface wave magnitude measurement procedure for application at regional and teleseismic distances. Part I—Theory, *Bull. Seism. Soc. Am*. 96: 665–677.

BEOWULF: A BETA-GAMMA DETECTOR CALIBRATION GRAPHICAL USER INTERFACE

Justin I. McIntyre, Brian Schrom, Matt W. Cooper, Derek A. Haas, and James C. Hayes

Pacific Northwest National Laboratory

Sponsored by the National Nuclear Security Administration

Award No. DE-AC05-RLO1830/PL07-DCS-NEM02

ABSTRACT

Pacific Northwest National Laboratory (PNNL) has demonstrated significant advancement in using beta-gamma coincidence detectors to detect a wide range of radioxenon isotopes. To obtain accurate activities with the detector, it must be properly calibrated by measuring a series of calibration gas samples. The data are analyzed to create the calibration block used in the International Monitoring System (IMS) file format. Doing the calibration manually has proven to be tedious and prone to errors, requiring a high degree of expertise. The Beowulf graphical user interface (GUI) is a software application that encompasses several components of the calibration task and generates a calibration block, as well as, a detailed report describing the specific calibration process used. This additional document can be used as a quality assurance certificate to assist in auditing the calibration. This paper describes the capabilities of Beowulf and lays out a representative report generated by the ^{137}Cs calibration and quality assurance source.

OBJECTIVES

With the fielding of automated radioxenon systems throughout the IMS network, it has become important to have a standardized method for calibrating the sophisticated radioxenon beta-gamma coincidence nuclear detectors. Advanced and robust methods have been developed that allow the detector to be calibrated, however no advanced software has been developed that has proceduralized the process and made it both easier for experts and possible for non experts to quickly and confidently calibrate, verify, and certify a detector (Bowyer et al., 1996, 1998). Currently, much of the calibration of the detector uses typical desktop calculation tools (MS Excel) or other more robust but difficult to use tools such as ROOT (http://root.cern.ch/drupal/). To fill this gap, PNNL has demonstrated significant advancement in using beta-gamma coincidence detectors to detect a wide range of radioxenon isotopes. To obtain accurate activities with the detector it must be properly calibrated by measuring a series of calibration gas samples. The Beowulf GUI is a software application that encompasses several components of the calibration task and generates a calibration block, as well as a detailed report describing the specific calibration process used. This additional document can be used as a quality assurance and quality control (QA/QC) certificate to assist in auditing the calibration of nuclear detectors.

In order to fully calibrate a beta-gamma nuclear detector it is important to first set up the detector components to achieve the desired energy range and energy response. For older detector assemblies this requires gain matching of the photo-multiplier-tubes (PMT's) and the associated lower level discriminators (Reeder and Bowyer, 1998). For newer models of detectors, there is no need for PMT gain matching for a single detector component but gain matching between detectors is important to achieve consistent energy scales across all of the individual detector components (Cooper et al., 2007). Having properly adjusted the HV, which controls the gain of each PMT to the desired range, the detector assembly is then ready take a number of calibration spectra. These spectra are needed to calibrate the detector and generate the configuration parameters needed to convert the counts in a given spectra and region of interest (ROI) into concentrations for the radioxenon isotopes of interest (^{131m}Xe, ^{133m}Xe, ^{133}Xe, and ^{135}Xe).

The spectra needed are as follows: a detector background spectra,; a ^{133}Xe spectra, a ^{135}Xe spectra, a ^{131m}Xe spectra and a ^{222}Rn spectra. Missing from this list is a spectra for ^{133m}Xe, which decays into ^{133}Xe and is an interference. In addition this isotope of xenon is difficult to produce in significant quantities. The ^{131m}Xe is used as a surrogate because it closely matches the radiometric signature of ^{133m}Xe (i.e., a conversion electron (CE) in coincidence with a 31-keV x-ray). The ^{222}Rn spectrum is needed for subtraction of radon daughter interferences that may be present in samples collected. Furthermore, the radon daughter response (^{214}Pb and ^{214}Bi) provides additional gamma-ray energies, resolutions and additional beta energies used to populate the configuration files. Having the five calibration spectra it is then possible to calculate the gamma-ray energies and resolutions for all available x-rays and gamma-rays, the beta and CE energies and CE resolutions, the ROI sizes and locations, the interference terms from ^{214}Pb, and ^{133}Xe, and the detection efficiencies for each ROI.

RESEARCH ACCOMPLISHED

The Beowulf GUI, displays the calibration spectra, allows the user to determine peak locations, the full-width-half-maximums (FWHM) for gamma, x-ray and CE peaks, the total number of counts in each peak, or beta distribution, and does a number of calculations that produce the calibration parameters needed to populate the detector configuration files. The program is laid out with tabs for each isotope needed for calibrating the detector plus a secondary tab for determining the gamma and beta efficiencies for each of the isotopes under consideration.

Xenon-133 Analysis Tab

Figure 1 shows a preliminary screen capture of the Beowulf GUI showing a ^{133}Xe spectra collected for calibration purposes. The top panel is where the actual calculations are performed for each isotope and it is in this panel that user can select which of datasets to analyze. The second panel (top-right) is the two-dimensional beta gamma histogram. This panel is used to determine the ROI's for each isotope and to verify the beta and gamma channel to energy conversions.

The four panels below these two are separated into the gamma-singles, and beta-gated gamma spectrum (middle panels 3 and 4) and the beta-singles and gamma gated beta spectra (the two bottom panels 5 and 6). It is worth pointing out that a singles spectrum has all of the counts that a single detector records without regard to the other detector. So for a gamma singles spectrum (panel 3) all of the gamma events recorded by the NaI(Tl) well detector are shown whether there was a coincident event in the plastic beta-cell detector or not. The spectra shown in this panel is the gamma singles spectrum for the isotope spectra (blue line) and the detector background spectrum (green line) along with the time adjusted background subtracted spectrum (red line). The fourth panel shows the beta-gated gamma spectrum where the line colors are blue is the coincidence ^{133}Xe spectrum, green is the coincidence background spectrum, and red is the background subtracted coincidence spectrum. From the background subtracted gamma singles and background subtracted beta-gated coincidence spectra it is possible to determine the beta efficiency for the 31-keV x-ray line (lower energy peak) and the 80-keV gamma line from ^{133}Xe. It is also possible to determine the locations of these two peaks in channel space and use them as part of the channel to energy conversion block in the final configuration files.

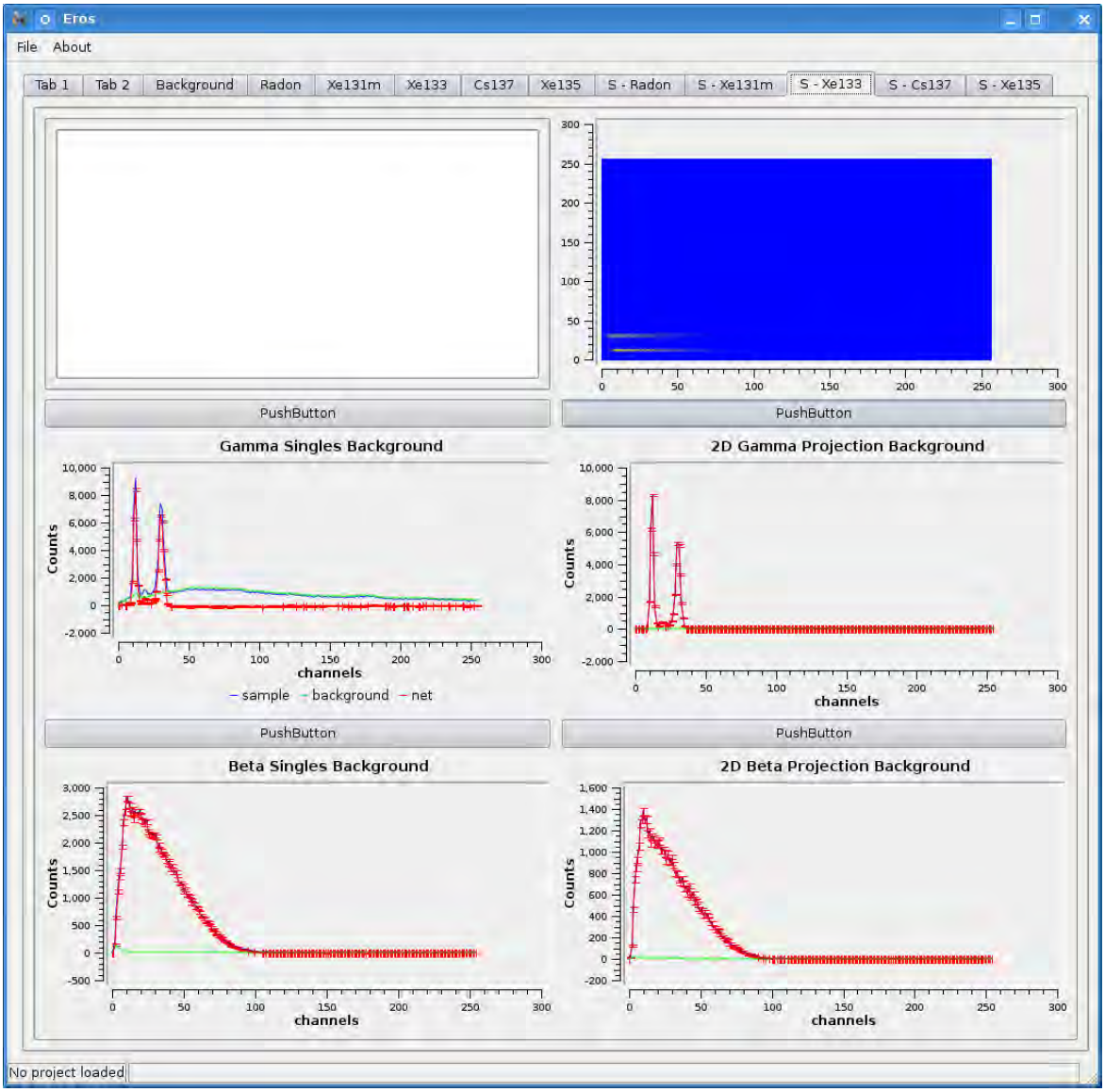

Figure 1. A screen capture of the Beowulf GUI with the ^{133}Xe calibration spectrum shown.

The two bottom panels show the beta-singles and gamma-gated coincidence beta spectra for ^{133}Xe and the detector background. The color coding for the different spectra is the same as mentioned earlier. Like the gamma spectra these spectra along with the decay branching ratios for the different gamma and x-ray lines allow the GUI operator to determine the gamma efficiency for the 31-keV x-ray and 80-keV gamma. While not as easy to see as the x-ray and gamma it is also possible to determine the beta end point energies for the x-ray and gamma distributions.

Radon Analysis Tab

Figure 2 shows the Radon tab with several radon calibration spectra from the same calibration file plus the detector background file. What is actually seen in the panels is not ^{222}Rn but instead the decay products ^{214}Pb and ^{214}Bi, which have strong beta-gamma coincidence signatures that interfere with the xenon isotope signatures. The gamma singles and beta-gated gamma spectra show this interference best and indicate that it causes problems across the entire energy range of the detector. The interference of the radon is determined by determining the ratio of counts associated with radon in each ROI and dividing these counts by the counts in ROI 1 (the fifth peak from the right in

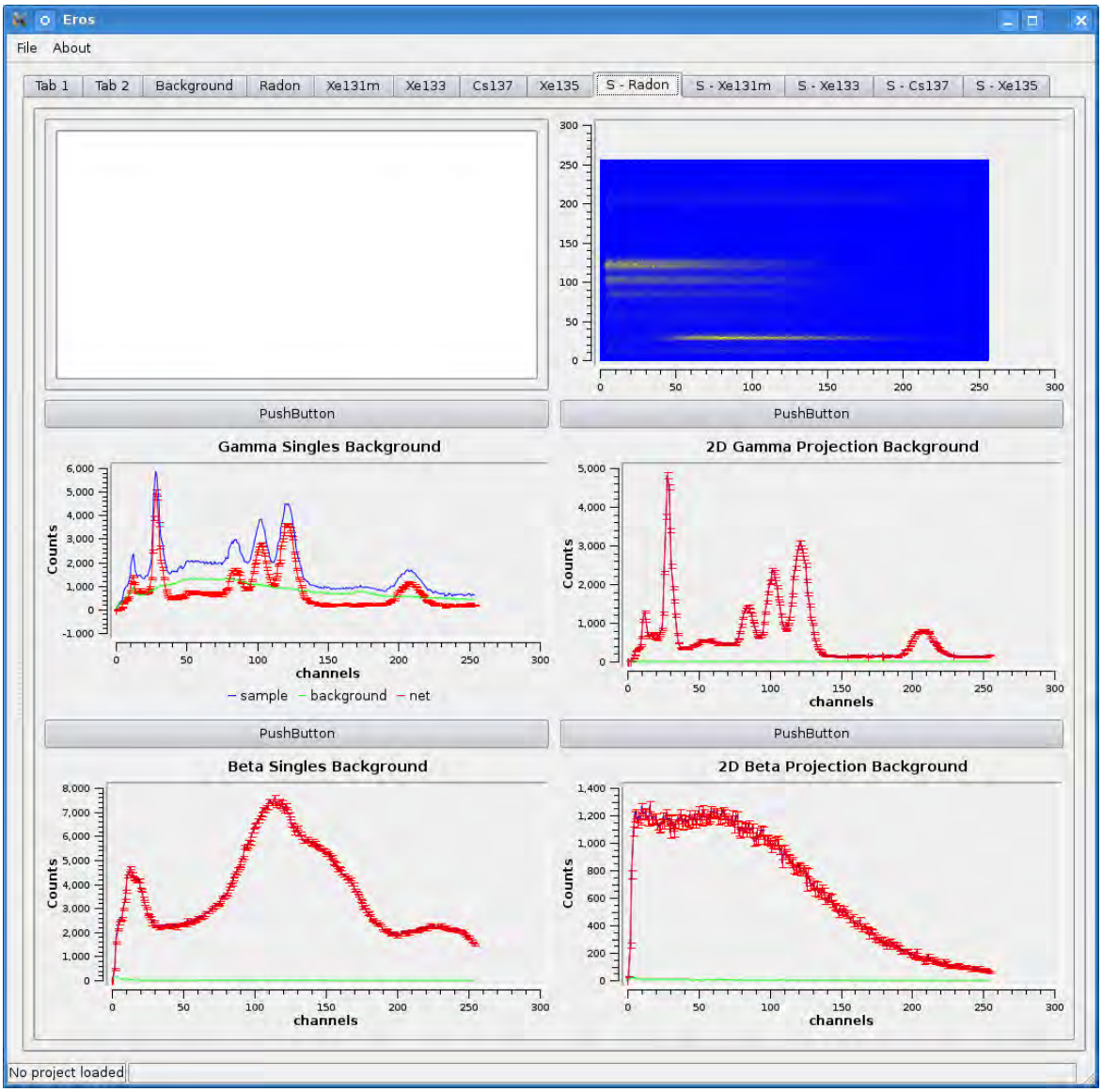

Figure 2. Radon-222 calibration spectra used for gamma and beta energies and radon interference ratio terms used in the radioxenon concentration calculations.

the beta-gated gamma-singles spectrum, panel 4). This ROI is only populated by the radon daughter ^{214}Pb and gives a direct measure of the radon interference throughout the entire two-dimensional spectra.

The spectra shown on the radon tab can also be used to further define the gamma channel to energy conversion and the beta channel to energy conversion, as well as the energy resolution for each of the 5 gamma peaks and one x-ray peak. It is interesting to note that the beta singles spectrum has several alpha decays present as well as the beta spectra for the ^{214}Pb and ^{214}Bi.

Cesium-137 QA/QC Analysis Tab

A tab has been defined to address the QA/QC spectra taken using a ^{137}Cs source that has mono energetic gamma-ray at 661.7-keV. This set of spectra allows the testing on the nuclear detector in the absence of other radiometric

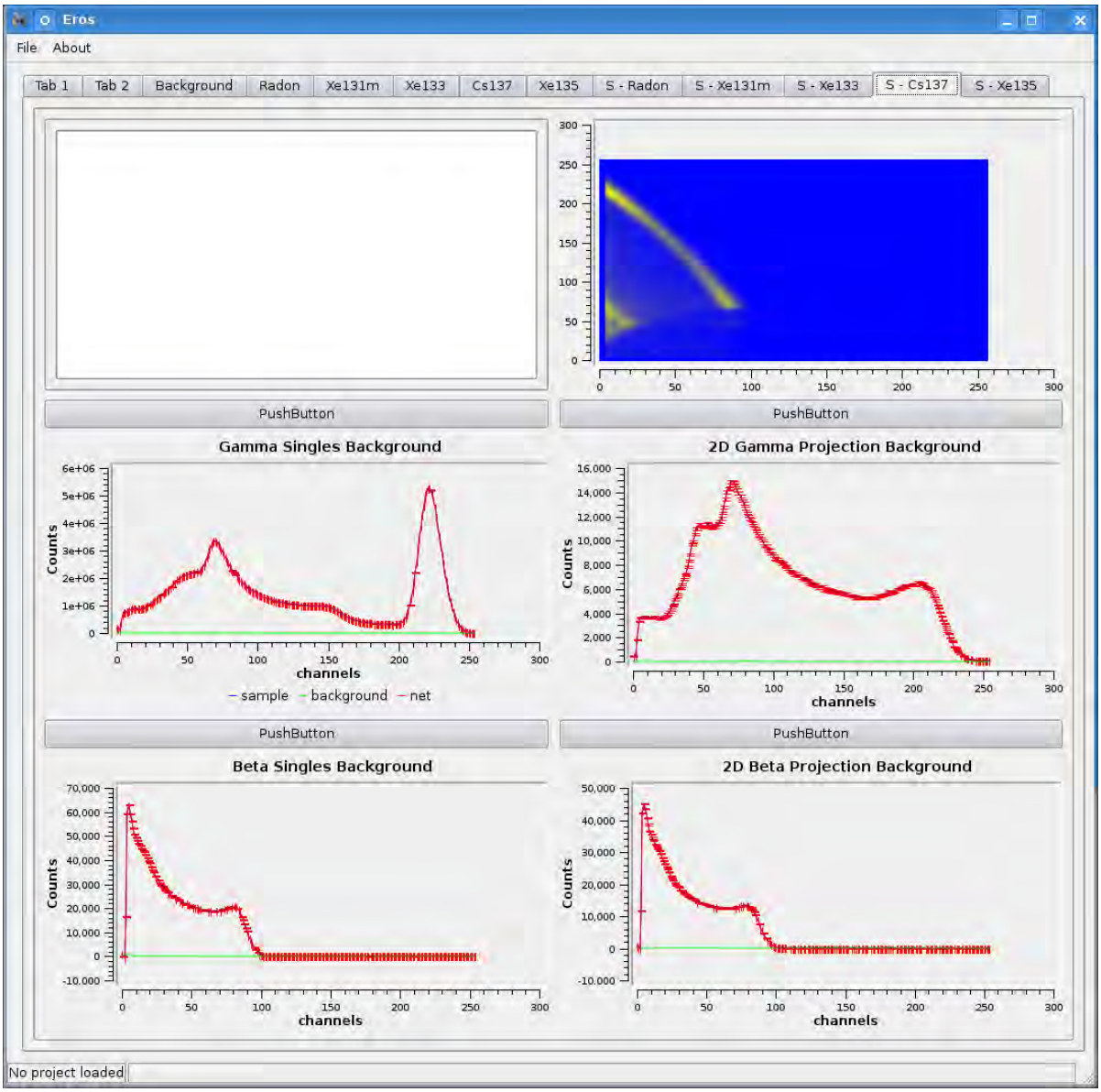

Figure 3. Screen capture of the QA/QC 137Cs Compton scatter spectra used to check the beta energy scale, the beta resolution and the gamma and beta energy calibrations and efficiencies.

signatures from the xenon and radon daughter isotopes and because it is sealed source pellet it can be easily and automatically insert and removed from the detector on a daily basis. One of the key features of the detector response is the Compton scatter energy line (Reeder et al., 2001). Figure 3 is a screen capture of the QA/QC ^{137}Cs tab and it clearly shows the Compton scatter line in the two-dimensional plot (panel 2). This line is a constant energy line where the energy has been shared between the gamma detector (Compton scattered gamma) and the beta detector (Compton scattered electron). Because the gamma and beta energy along this line is constant it is possible to use the calibrated gamma axis to determine the calibration of the beta axis. This is done by taking a slice from left to right across the gamma axis and projecting the subsequent beta response onto the beta axis. This provides an average gamma energy and the location of the beta peak is at 661.7-keV minus the gamma-energy. The beta resolution can also be determined by finding the FWHM of the project beta peak.

These data are also used to determine changes in the gamma and beta energy calibration (panels 3 and 5) and also to track the beta and gamma efficiency. The 661.7-keV gamma is clearly seen in panel 3 with the pure Compton scatter spectrum shown in panel 4. Panels 5 and 6 look very similar because the beta detector responds to the Compton scattered electrons and has very little detection efficiency for the full 661.7-keV gamma peak. The only difference between the two is the gamma gating requirement for the beta-gamma coincidence spectrum (Panel 6).

Auto-Report Feature

An additional capability of the Beowulf GUI is the automatic generation of calibration reports. This feature allows the technician to generate a detailed report for each of the calibration tabs. The ^{137}Cs QA/QC report is shown below and includes both a description of the process and the actual values and parameters obtained. It is envisioned that a report file will be auto-generated for each of the calibration processes used to fully characterize the nuclear detector.

Calibration for
"IFX01-xy1-2008/11/06-00:06:44"

Auto-calibration v0.2 for beta-gamma, Pixie4 Quad-detector setup

Fri Jul 10 14:18:14 2009

Run with parameters:

Commandline parameter	Value
sampleFileName	Cell4-cs137_110608.pbg
betaGain	1
betaOffset	0
numBetaBins	256
betaEnergyLow	0
betaEnergyHigh	1000
gammaGain	1
gammaOffset	0
numGammaBins	256
gammaEnergyLow	0
gammaEnergyHigh	730
gammaCutLowEnergy	200
gammaCutHighEnergy	500
gammaCutN	5
iStart	10

1 Introduction

The process of putting a count into a histogram from a Pixie4 capture card goes through a couple of steps. The steps are:

1. Convert ADC value to energy
2. Convert Energy to bin number

The conversion of ADC to energy is done through the following equation:

1

$$E(ADC) = A * ADC^2 + B * ADC + C \quad (1)$$

where: (2)

ADC Value from Pixie4 (3)

A Nonlinear term (4)

B Linear term (5)

C Offset term (6)

The conversion to bin number depends on the number of bins and the energy span represented by the histogram. Nominally, the bin number can be figured out by:

$$BIN(E) = \frac{E - E_{low}}{E_{high} - E_{low}} * N_{bins} \quad (7)$$

One additional step happens because counts are not allowed to be divided. A weighted probability, based on the portion of the "count" that covers the bin number, is used with a random process to determine what bin number the actual count gets added to. For the remainder of this calibration, this fact will be ignored.

The point of this auto-calibration code is to determine, and possibly adjust, the A, B, and C coefficients in equation 1.

There are three items mentioned above that are confusing, but need to be kept strait:

ADC Native number from Pixie4 with range from $0 - 2^{16} - 1$

Bin Number The bin number in the histogram. Normally 256 bins, but can be set with command option

Energy Real energy in keV. Usually between 0-1000keV

Channel is NOT used anywhere as it is a confusing, ill-defined term.

1.1 Strategy

The first assumption this code makes is that the file being analyzed is a ^{137}Cs spectrum and that γ singles and coincidence $\beta - \gamma$ data are available.

The second assumption is that this code requires the user (or external agent), to pass in the current A, B, and C coefficients.

These assumptions allow the following process to happen:

2

- Find two points in the γ singles spectrum
- Find an energy calibration for this spectra.

From this point forward, we assume that the γ axis is calibrated and that the calibration is identical for singles and coincidence axises.

Using the known calibration of the γ axis, cuts can be made on the $\beta-\gamma$ coincidence data. The γ ray emmitted by ^{137}Cs at 661.67keV is detected in the coincidence counter because some fraction of its energy is deposited in the β cell when it Compton scatters and the remaining energy is deposited in the γ detector. Since the γ energy is known, the β energy can be solved for by subtracting the γ energy from 661.66keV.

1. Find 200.5keV in γ Compton backsatter peak.
2. Find 661.67keV in γ singles.
3. Get γ ADC to energy function
4. Get γ energy to bin number function (needed for finding β energy)
5. Get γ bin number to energy function (needed for finding β energy)
6. Divide $\beta-\gamma$ coincidence spectrum into regions based on γ values.
7. For each cut region, project data onto β axis. This will have a Gaussian appearance.
8. Find the centroid, β bin number, of the Gaussian and the corresponding β energy by subtracting from the corresponding γ energy.
9. Using all of the found energy centroids and corresponding ADC values, do a nonlinear fit to get a β ADC to energy function. The 2^{nd} order fit is for informational purposes only.
10. Using all of the found energy centroids and corresponding ADC values, do a linear fit to get a β ADC to energy function. This is the one that gets used.

2 Gamma (γ)

$$energy(BIN) = A * BIN^2 + B * BIN + C \quad (8)$$

Basing calibration point on ^{137}Cs energy 200.5keV

where:

hv'	energy of scattered gamma ray
hv	total energy
m_0c^2	rest mass energy of electron

$$hv'|_{\theta=\pi} = \frac{661.6\text{keV}}{1+\frac{2\times 661.6\text{keV}}{511\text{keV}}} = 184.32\text{keV} \quad (10)$$

One	Two
found at bin number	75.0366
estimated ADC	213.971

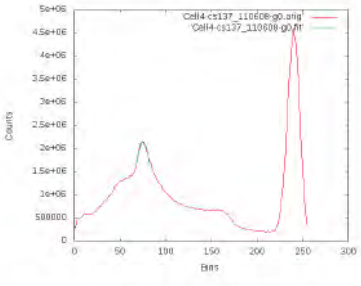

Figure 3: Fitting the 200.5keV ^{137}Cs gamma singles peak

Fit settings:

Parameter	Value
scale	$1.58048e+06 \pm 589.213$
centroid	75.0366 ± 0.00461983
sigma	12.0097 ± 0.0142535
fwhm	28.2808 ± 0.0335645
resolution	0.376893 ± 0.00044791

Basing calibration point on ^{137}Cs energy 661.67keV

One	Two
found at bin number	239.901
estimated ADC	684.093

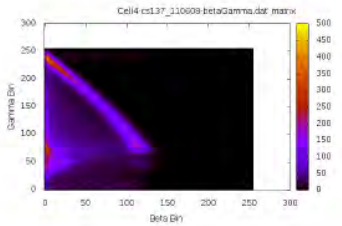

Figure 1: Beta Gamma coincidence

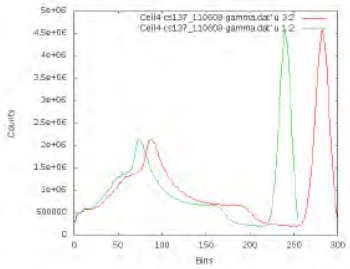

Figure 2: Gamma singles

^{137}CsCompton peak The compton energy peak energy is found with the following equation, taken from Knoll 3^{rd} ed., p310

$$hv'|_{\theta=\pi} = \frac{hv}{1+\frac{2hv}{m_0c^2}} \quad (9)$$

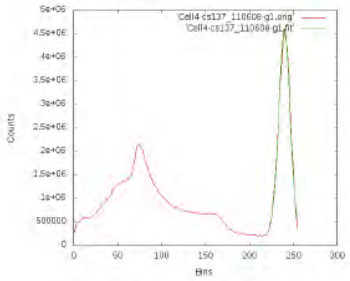

Figure 4: Fitting the 661.67keV ^{137}Cs gamma singles peak

Fit settings:

Parameter	Value
scale	$4.25016e+06 \pm 710.059$
centroid	239.901 ± 0.000920846
sigma	8.6731 ± 0.0109744
fwhm	20.4236 ± 0.00258426
resolution	$0.0851334 \pm 1.07772e-05$

$$Energy(ADC) = 0 * ADC^2 + 0.980959 * ADC + -9.39729 \quad (11)$$

$$Bin(Energy) = 0 * Energy^2 + 0.357492 * Energy + 3.35945 \quad (12)$$

$$Energy(bin) = 0 * bin^2 + 2.79727 * Energy + -9.39729 \quad (13)$$

3 Beta (β)

Beta: energy(BIN) $= A * BIN^2 + B * BIN + C$ Fit settings:
Fitting ^{137}Cs coinc spectrum between gamma 200keV and 500keV
Fitting ^{137}Cs coinc spectrum between gamma bin number 74 and bin number 182

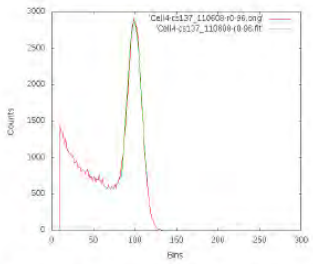

Figure 7: Coincidence β projection based on γ cuts. β centroid 99.2524β energy 371.76

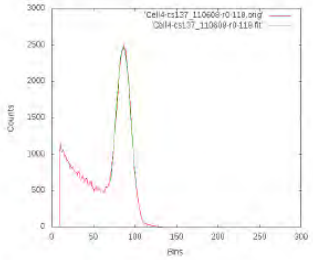

Figure 8: Coincidence β projection based on γ cuts. β centroid 86.1604β energy 310.22

Fit settings (2nd order, information only):

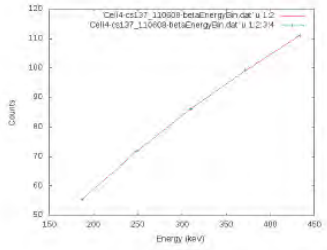

Figure 11: Energy vs. found centroids

$$\chi = 0.292567 \quad (15)$$

Fit settings (1st order):

$$energy(ADC) = 0 * ADC^2 + 1.13033 * ADC + -63.8948 \quad (16)$$

$$\chi = 145.89 \quad (17)$$

4 Results

Brief summary of analysis

Parameter	Value
Date analyzed	Fri Jul 10 14:18:14 2009
Acquired on	Thu Nov 6 00:06:44 2008
Real time	74692 seconds
Live time	36616.3 seconds (49.0231%)
Dead time	38075.7 seconds (50.9769%)

Beta: energy(ADC) $= A * ADC^2 + B * ADC + C$

Settings	Current	New	Relative change
A	0.00000	0	N/A
B	1	1.13033	N/A
C	0	-63.8948	N/A

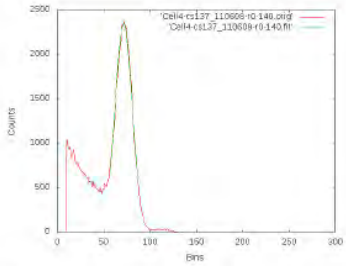

Figure 9: Coincidence β projection based on γ cuts. β centroid 71.6991β energy 248.68

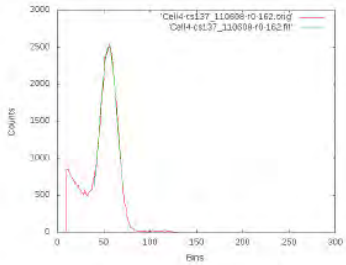

Figure 10: Coincidence β projection based on γ cuts. β centroid 55.4477β energy 187.14

$$energy(ADC) = 0.00109213 * ADC^2 + 0.420484 * ADC + 44.9614 \quad (14)$$

Gamma: energy(ADC) $= A * ADC^2 + B * ADC + C$

Settings	Current	New	Relative change
A	0.00000	0	N/A
B	1	0.980959	N/A
C	0	-9.39729	N/A

CONCLUSIONS AND RECOMMENDATIONS

The calibration of the beta-gamma nuclear detector requires a large set of calibration spectra that are used to generate an extensive calibration configuration file. The configuration file is used by the radioxenon concentration calculations to convert sample files, gas background files, and detector background files into accurate radioxenon concentrations. The development of a sophisticated GUI that can determine these calibration configuration parameters can greatly reduce the time required to calibrate the beta-gamma detectors and makes it possible for a well trained technician to do the work rather than a subject matter expert with several years of experience.

REFERENCES

Bowyer, T. W., K. H. Abel, W. K. Hensley, C. W. Hubbard, M. E. Panisko, R. W. Perkins, P. L. Reeder, R. C. Thompson, and R.A. Warner (1996). *Automatic Radioxenon Analyzer for CTBT Monitoring*, PNNL-11424, Pacific Northwest National Laboratory, Richland, WA, http://www.ctbt.doe.gov.

Bowyer, T.W., K. H. Abel, C. W. Hubbard, M. E. Panisko, P. L. Reeder, R. C. Thompson, and R. A. Warner (1998). *J. Radioanal. Nucl. Chem.* 240: 1, 109.

Cooper M. W., J. I. McIntyre, T. W. Bowyer, A. J. Carman, J. C. Hayes, T. R. Heimbigner, C. W. Hubbard, L. S. Lidey, K. E. Litke, S. J. Morris, M. D. Ripplinger, R. Suarez, and R. C. Thompson (2007). Redesigned Beta-Gamma Radioxenon Detector, *Nuclear Instruments and Methods in Physics Research. Section A, Accelerators, Spectrometers, Detectors and Associated Equipment* 579: 1, 426–430, doi:doi:10.1016/j.nima.2007.04.092

Reeder, P. L. and T. W. Bowyer (1998). Pacific Northwest National Laboratory, Richland, WA. *Nucl. Instr. Meth. Phys. Res. A.* 408: 582–590.

Reeder, P. L., T. W. Bowyer, J. I. McIntyre, and W. K. Pitts (2001). Pacific Northwest National Laboratory, Richland, WA 99352, USA, *J. Radioanal. Nucl. Chem.* 248: 3 617–622.

USING MACHINE LEARNING TO IMPROVE THE EFFICIENCY AND EFFECTIVENESS OF AUTOMATIC NUCLEAR EXPLOSION MONITORING SYSTEMS

Michael J. Procopio, Christopher J. Young, and Jennifer E. Lewis

Sandia National Laboratories

Sponsored by the National Nuclear Security Administration

Award No. DE-AC04-94AL85000/SL08-IRP-NDD02

ABSTRACT

An analysis is performed on the seismic-event data processed from 1999 through 2009 by the International Data Centre (IDC) of the Comprehensive Nuclear-Test-Ban Treaty Organization (CTBTO). The analysis shows that the overall quality of the final IDC bulletin is excellent, but achieving this level of quality requires a significant amount of analyst effort. In particular, automatic processing produced 421,244 origin hypotheses, or about 118 per day over the nearly 11-year period of operation. Of these, 224,643 (53%) do not survive analyst review while the remaining 196,601 (47%) are approved. In addition, analysts build another 30,606 origins (13% of analyst approved total) that the automatic processing missed. Thus analyst-approved origins occurred at a rate of about 64 per day. It is evident that significant improvement of the automatic system, and hence decrease in the analyst workload, is possible both by decreasing the number of false events as well as by decreasing the number of missed real events.

Previous work in analyzing a much smaller portion of the IDC data (Gauthier, 2009) found that some attributes in the data appear well-suited for discriminating among the different families, or categories, of events. That evaluation used principled but ad-hoc methods to show a basic ability of certain attributes, such as number of stations and signal-to-noise ratio, to predict the true category of a particular detected origin, which may or may not be valid. In particular, a method was devised that identified with very high confidence many “false origins” which did not survive analyst review in the final Reviewed Event Bulletin (REB) table.

Building off the premise that there are predictive features in the origin and arrival data, the study herein proposes the use of modern machine learning and data mining methods to train models on previously labeled data found in existing archives. These models are then used to identify events produced by the automatic system which would otherwise be rejected after manual analyst review. In contrast to previous work in this area, the proposed methods are able to consider multiple data attributes simultaneously. Such an improved event detection system would reduce the analyst burden required in reviewing the events, the majority of which do not survive analyst review in current automatic systems.

Our study shows that contemporary supervised machine learning algorithms, including Support Vector Machines and Random Forests, are in the majority of cases able to correctly identify events that an analyst would reject after manual review. However, more work is needed in the areas of data attributes, data mining algorithms, and cost-sensitive learning in order to improve event categorization rates to acceptable levels, without appreciable gain in the false positive rate (FPR) of the categorizer.

OBJECTIVES

The objectives of this work are three-fold. First, we perform an analysis of a ten-year archive of IDC data in order to assess the percentage of the events produced by the automated event detection system that are not confirmed by analysts (hereafter referred to as "false events"). Manual analyst effort must be spent on screening out such events (false alarms). This analysis also characterizes the number of events missed altogether by the automatic system (missed detections).

Second, we propose the application of supervised machine learning (ML) to train predictive models on data from large, tagged event libraries. We show that these models are capable of identifying false events produced by the automatic system, which can be automatically screened out without manual analyst review. We give several examples of machine learning methods applied to this problem, ranging from simple methods yielding highly interpretable models, to more elaborate methods whose models may be more difficult to interpret.

Finally, based on the empirical results, we suggest a roadmap to help guide future research in this area. This work will improve the performance of machine learning methods on the task of screening out false events from the automatic detection system.

RESEARCH ACCOMPLISHED

Introduction

The verification regime of the CTBT includes the International Monitoring System (IMS) and the IDC. One purpose of this paper is to review the quality of the IDC bulletin of waveform-technology (seismic, hydroacoustic, and infrasonic) detected events throughout the history of operations to determine if there are characteristics of the data that could be utilized to understand and improve automatic seismic-event processing.

Previous work analyzing a month of IDC data (Gauthier, 2009) found that some attributes of the data appear well-suited to assist in discriminating among the different families, or categories[1], of events. That evaluation used principled but ad-hoc methods to show a basic ability of certain attributes, or features, to identify the true category of a particular automatically detected origin, which may or may not be valid. In particular, a method was devised that identified with very high confidence many "false events" which did not survive analyst review in the final REB table.

The study presented here uses modern machine learning and data mining methods to train models on labeled data drawn from the full IDC dataset (approximately 10 years), and then uses those models to make predictions on separate data whose categories are not known to the machine learning models. The results of the models' predictions versus the known ground truth are compared and can be measured quantitatively.

IMS Network and IDC Processing

The current IMS network of seismic (primary and auxiliary), hydroacoustic, and infrasonic sensors provides good overall global coverage, given the limited distribution of land area (Figure 1). The IDC pipeline processes waveforms to produce detections, which are then associated with one another to create events. The pipeline is designed to meet requirements for both responsiveness and quality of the event bulletin. Three automatic event lists are produced with increasing quality as more data becomes available; these lists are known as Supplementary Event Lists and are referred to as SEL1, SEL2, and SEL3. The final of these (SEL3) is then reviewed by analysts to produce a high-quality REB. For this study, we focus on differences between SEL3 and REB.

[1] Although the terms "classifier" and "classification" are standard in machine learning, data mining, and related disciplines, we adopt the equivalent terms "categorizer" and "categorization" in this paper to avoid confusion with similar terms used in the nuclear explosion monitoring field.

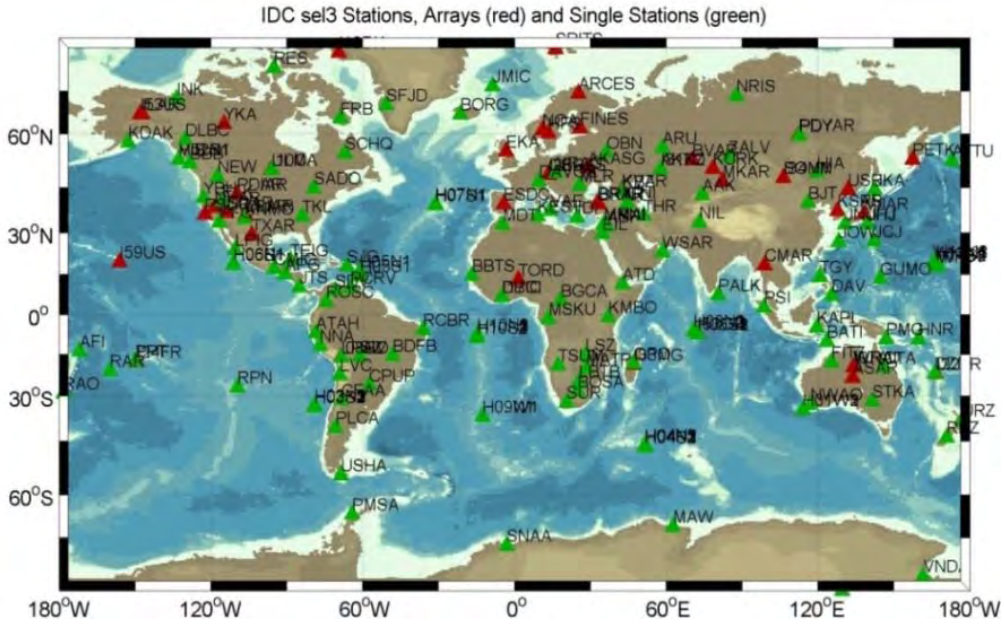

Figure 1. The IMS network, including seismic, hydroacoustic, and infrasonic stations

Analysis of IDC Event Catalogs

On average, only 47% of the automatically built events in SEL3 survive analyst review. This proportion seems to be fairly stable over the operating history of the IDC, despite the addition of new stations. Conversely, those events that are approved by analysts form approximately 87% of the REB. The additional 13% are newly built by the analysts, though they may make use of arrivals that were included in SEL3 events. Figure 2 shows the distribution of events into SEL3 and REB by year. This distribution is generally consistent from year to year (disregarding 1999 and 2009, for which only partial data was available).

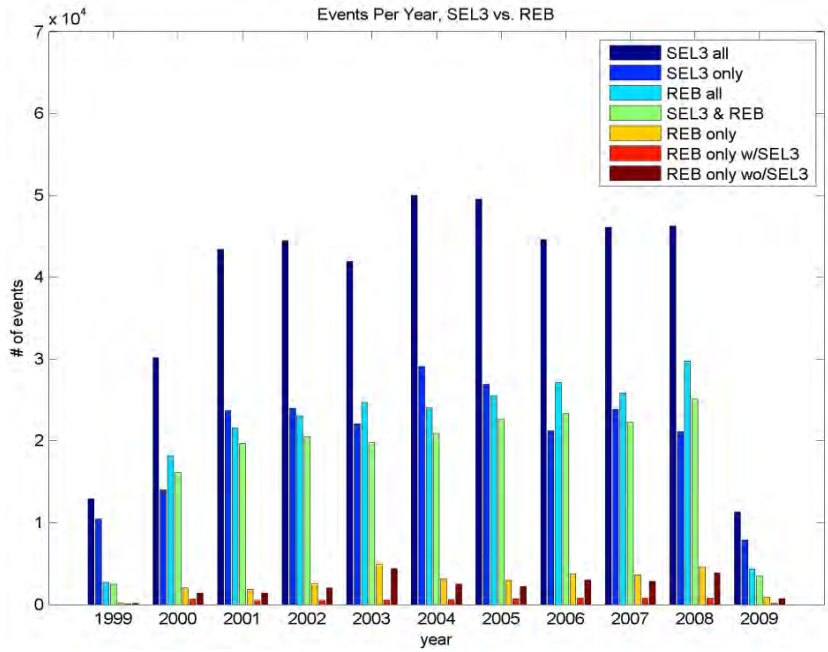

Figure 2. Categorization of automatic and analyst reviewed events for 1999-2009.

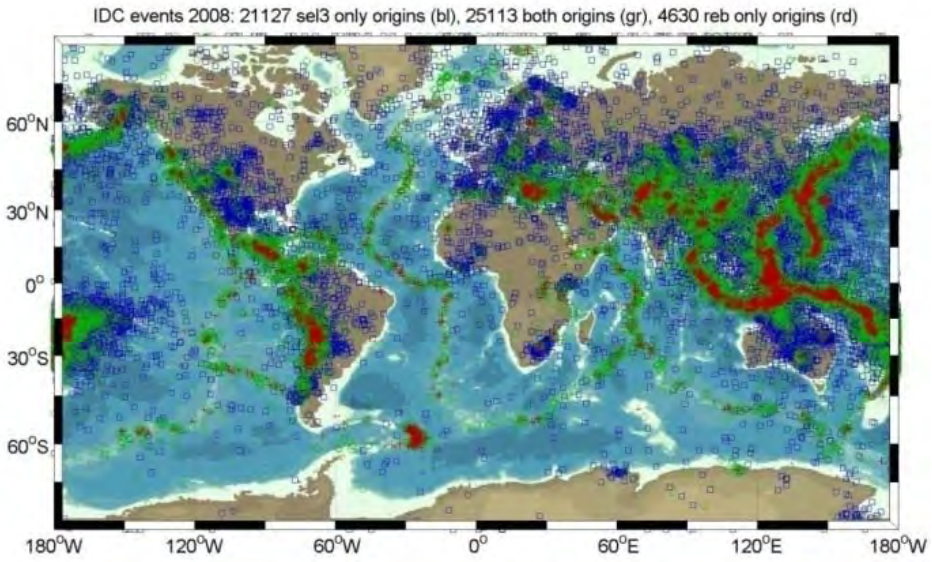

Figure 3. Comparison of automatic and analyst review events, 2008.

REB events occur almost entirely along the plate boundaries, as would be expected for earthquakes (Figure 3). SEL3 events that end up in the REB follow the plate boundaries, but not as reliably. Rejected SEL3 events can be very far from plate boundaries indicating false detections and/or false phase identifications.

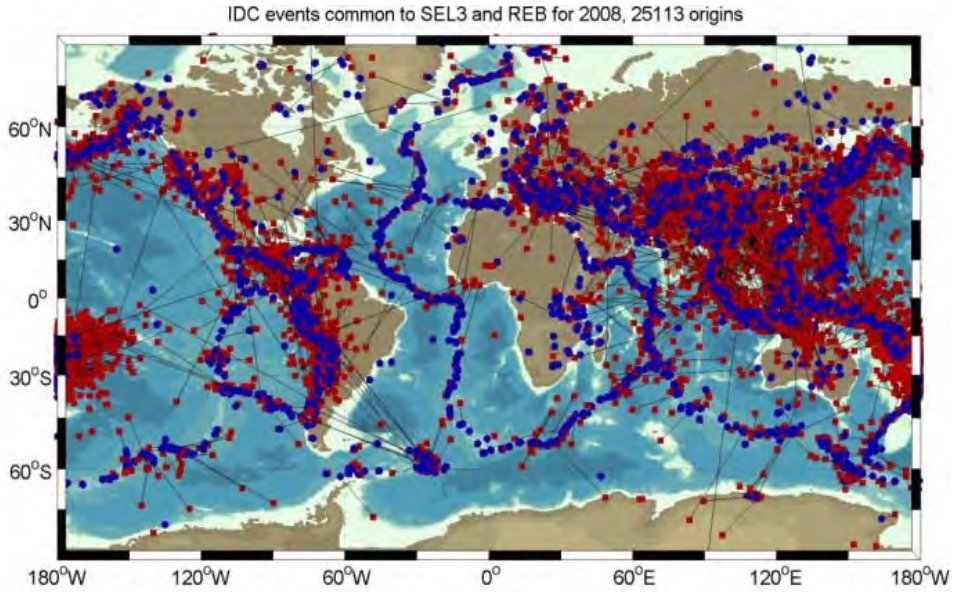

Figure 4. Relocation vectors for SEL3 events in REB, 2008. Red circles indicate SEL3 events, blue circles indicate REB events.

Many SEL3 events that are approved by analysts are shown to have large relocation vectors suggesting problems with probability of detection calculations in the Global Associator (GA) software (Figure 4). Predicted azimuth and slowness should show large variations between SEL3 and REB locations, with the smaller residuals corresponding to the REB-adjusted locations. GA grid points nearby the REB-locations would have been considered during the association step, but further ones were preferred. This problem may indicate the need for better azimuth and slowness calibration.

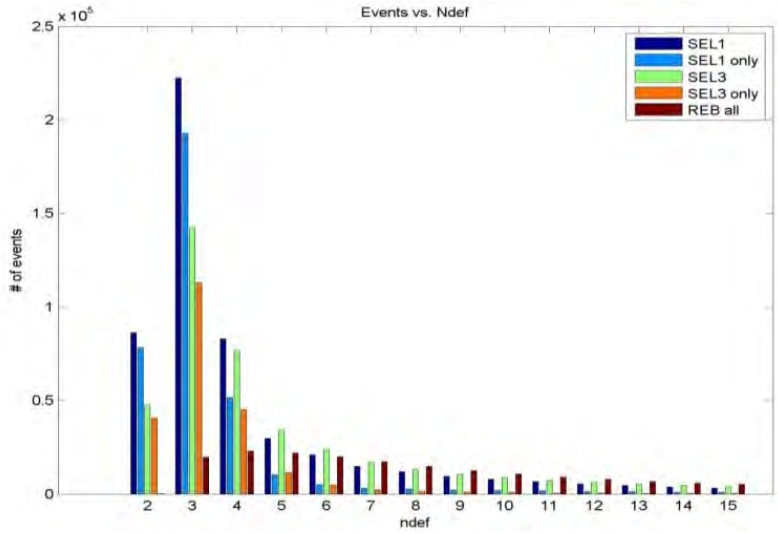

Figure 5. Number of events vs. number of location-defining phases, automatic vs. analyst reviewed, 1999-2009

The event definition criteria for automatic events is a combined weight of 3.55 (seismic travel time at a single station has a weight of 1.0), implying that an event can be built with time-defining phases from as few as two stations if azimuth and slowness are used. By comparison, analyst approved events must have a weight count of 4.6 or more and must have defining phases from 3 or more primary seismic stations (for terrestrial events). SEL1, with no auxiliary or late-arriving seismic data is dominated by 2 and 3 station events (Figure 5). However, 91% of 2 station and 87% of the 3 station SEL1 events do not result in REB events, so the payoff for building these events is small. SEL3 reduces those percentages somewhat to 85% and 79%, presumably due to the additional data that becomes available, but clearly a large amount of analyst effort is being used to screen these marginal events, suggesting that the automatic system may be building too many of them.

Of the 44,993,580 arrivals present in the IDC dataset considered in this study, only 4,049,843 (9%) are associated with SEL3 events. The total number of REB associated arrivals is 3,651,404, but this includes new arrivals added by the analysts. Thus, the vast majority of automatic detections are never used to produce REB catalog events. This disproportion is intentional because the consequences of missing an important detection are far more costly than those of producing a false detection. However, stations with anomalously high proportions of automatic arrivals to REB arrivals may be good candidates for further tuning.

Automatic Detection System Event Categories

The automatic detection system produces an event bulletin that gets filtered several times before finally resulting in the final list, SEL3 (referred to as the set SEL3-ALL in the results). The events in SEL3-ALL undergo analyst review, which divides the events produced by the automatic bulletin into two categories. The first category comprises all incorrectly categorized detections, known as False Automatic Origins (Gauthier, 2009). Because these origins were incorrectly predicted by the automatic system, they are labeled here as False Positives. These events go on to get screened out by the analyst; hence they do not survive analyst review (Figure 6).

The remaining events that do not get screened out are known as Good Automatic Origins (Gauthier, 2009), and are labeled as True Positives. Because these events endure through to the REB, they are labeled as SEL3&REB (i.e., those events in the intersection of the sets SEL3 and REB).

There also exists a set of events that should have been detected by the automatic system, but were not. These events are ones manually identified by an analyst and added to those surviving analyst review from the automatic system. These events, known as Extra Analyst-Built Origins, are labeled as False Negatives (or missed detections), because the automatic system incorrectly failed to identify them as true events.

The events surviving analyst review are combined with the additional events manually identified by an analyst; these are combined together to form the REB, and this set of events is referred to as REB-ALL. We note that both sets SEL3&REB and REB-ONLY can be further divided into subcategories (Gauthier, 2009); this is not represented here, but will be considered in future work.

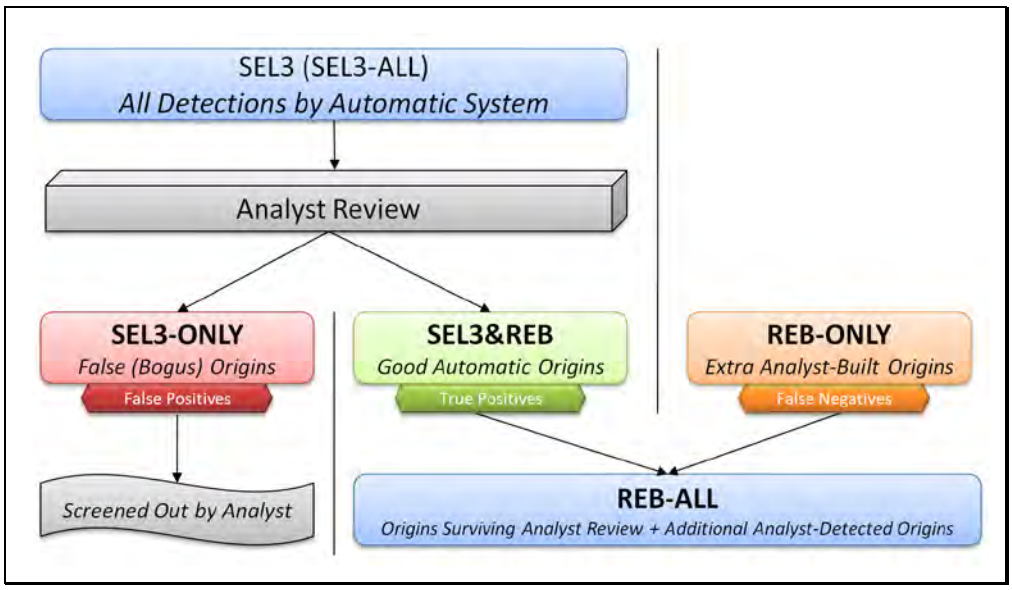

Figure 6. Overview of Automatic Detection System Event Families

Scenarios where valid measures exist for true positives, true negatives, false positives, but not true negatives are common in information retrieval. Traditionally, such scenarios are evaluated in terms of *precision* and *recall*, which measure the effectiveness of such a system. Type 1 and Type 2 error rate can also be used to characterize performance. In future work, the performance of the automatic system can be evaluated in these terms.

Use of ML Methods to Screen out False SEL3 Events

We propose the use of ML algorithms to process event features to try to reduce the number of false automatic events that IDC analysts must screen. Machine Learning methods can accommodate as many features as the researcher wants to evaluate in order to provide the best categorization performance.

For this initial empirical study for determining the feasibility of the machine learning approach on reducing analyst burden in the automatic detection system, we concentrate specifically on the problem of screening out events (False Origins) that an analyst would otherwise have to screen out. Thus, the problem we address is the automatic *discrimination*, or separation, of events which would eventually be assigned to the set SEL3-ONLY from those in SEL3&REB (Figure 6). Thus, the problem as framed is a two-category or *binary* problem, where the categorizer (i.e., the model learned on training data) predicts only one of two possible category labels for a given event in SEL3-ALL. The task of using ML methods to identify missed detections of the automatic system is not considered in the study presented here.

In our approach, we train supervised machine learning models using various algorithms on half of the tagged origins from SEL3-ALL, i.e., origins whose category is known. The model is then evaluated over the remaining test data set, i.e., the set of data disjoint from the training data set used to train the models initially. The goal is for the categorizer to correctly predict the true category (either SEL3-ONLY or SEL3&REB) for as many test origins in SEL3-ALL as possible. Because the ground truth category for each of these test origins is known, the performance of any particular categorization method can be evaluated by comparing the categorizer's predicted output with the known ground-truth labels.

Evaluation Approach: Contingency Table

We evaluate the trained ML models using the well-established contingency table approach, seeking to reduce the overall error rate (combination of false positive and false negative rates [FNRs]). Figure 7 shows the contingency table, also known as a *confusion matrix* in the machine learning and statistical literature, which characterizes all four possible outcomes of a binary prediction in a two-category problem.

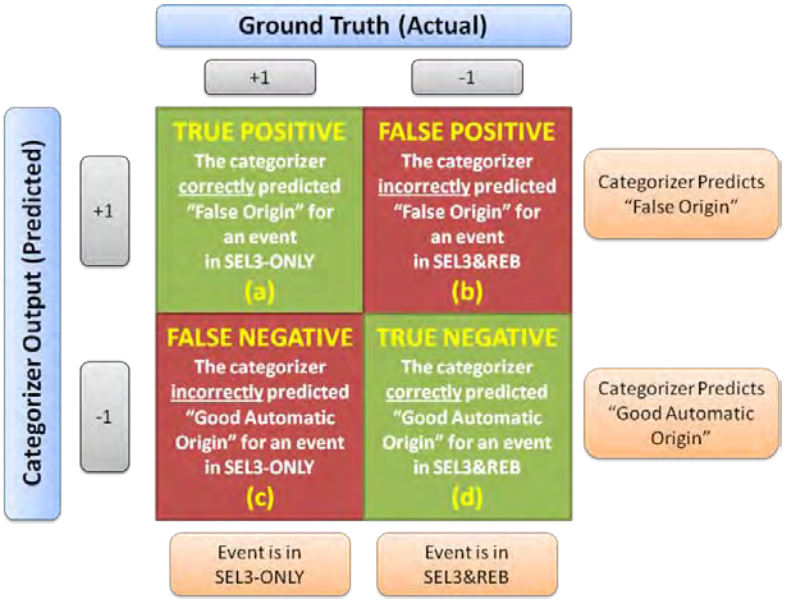

Figure 7. Contingency Table showing the four possible outcomes in a binary (two-category) categorization problem, as applied to the SEL3 false event detection task.

Essentially, the categorizer can predict one of two categories, while the ground truth is also one of two categories, resulting in four possible scenarios. These scenarios form the cells in the matrix in Figure 7 and are referred to as true positives, false positives, false negatives, and true negatives. It is important to differentiate this evaluation approach and terminology from that in Figure 6. This is because *false positive* and *false negative* have different meanings in the context of categorizer prediction in the above SEL3 false event screening task (Figure 7), versus the meaning of *false alarms* and *missed detections* in the automatic event detection task (Figure 6).

Features Used

In general, ML approaches begin with identifying potentially useful data attributes, known as features. In this study, we used 18 features available from the IDC database tables for SEL3 events. These consist of nine origin-based features and nine arrival-based features, the latter which we group by event and then take the average to yield a single numerical value for each origin. Together these features, corresponding to a single observation (origin), form a *feature vector* for that origin. These features are summarized in Table 1. We note that selection of features is crucial for a high-performing machine learning categorization system, and further investigation of useful features is an important area of future work.

Table 1. Features considered in the study.

Origin Features				**Arrival Features, Grouped by and Averaged by Origin**		
#	**Name**	**Description**		**#**	**Name**	**Description**
1	ndef	*number of location defining phases*		**10**	avg(snr)	*signal-to-nose ratio*
2	nass	*number of associated phases*		**11**	avg(amp)	*amplitude, instrument corrected*
3	depth	*estimated depth*		**12**	avg(rect)	*rectilinearity*
4	sdobs	*standard error of observations*		**13**	avg(deltim)	*time uncertainty*
5	smajax	*semi-major axis of error*		**14**	avg(abs(timeres))	*time residual*
6	sminax	*semi-minor axis of error*		**15**	avg(delaz)	*azimuth uncertainty*
7	sdepth	*depth error*		**16**	avg(abs(azres))	*azimuth residual*
8	stime	*origin time error*		**17**	avg(delslo)	*slowness uncertainty*
9	numsta	*number of observing stations*		**18**	avg(abs(slores))	*slowness residual*

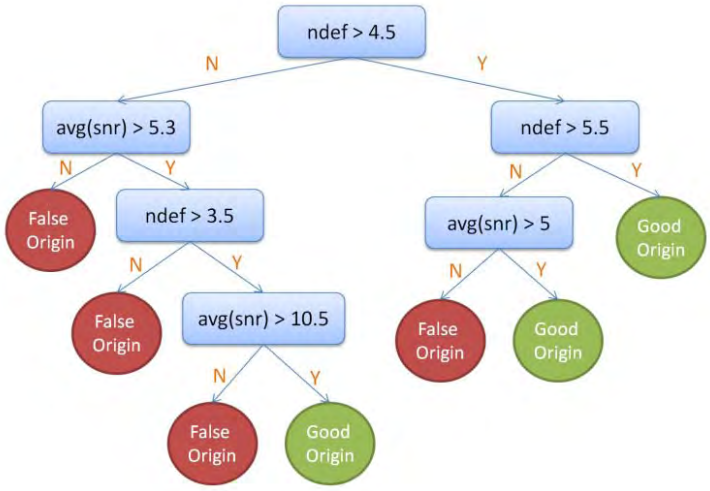

Figure 8. Example of an interpretable decision tree model providing non-linear two-category categorization for two input attributes.

Machine Learning Algorithms

In this study, we consider three machine learning algorithms, comparing the results to a first-order baseline method. Results for both of these models, as well as the more complex models below, are given in the experimental results shown in Table 2.

- **Baseline: Single Split on a Single Attribute**. For comparison, we developed a baseline method that makes categorizations based on splitting on single attributes; ndef and avg signal-to-noise ratio (SNR) are obvious choices for single attributes. The split location for the particular attribute is chosen simply as that which maximizes event categorization accuracy. For ndef, this yields the following model: ndef <= 4 is a false automatic origin, ndef >= 5 is a good automatic origin. For avg(SNR) the split logic is similar, but the threshold value is 5.5.

- **CART (Classification and Regression Trees) Decision Trees**. CART trees, due to Breiman et al. (1984), provide a simple mechanism of learning categorization rules from data. The resulting models, expressed as binary decision trees, can give non-linear categorization yet are generally interpretable (in contrast to the models yielded by other methods, such as Neural Networks). In this study, we learn a decision tree on two attributes, ndef and avg(SNR); the resulting tree is shown in Figure 8. In contrast to the single-split baseline, it allows for a more complex, non-linear separation of the two categories.

- **Random Forests**. The Random Forests technique, due to Breiman (2001), is a state-of-the-art machine learning ensemble method that combines *bagging* with *random trees*. This method is robust to noise, requires minimal parameterization and tuning, and performs well in the presence of possibly irrelevant features. Moreover, this method has a heavy theoretical basis. Here, this method is applied it to all 18 features simultaneously. We specified the number of trees, a parameter of the algorithm, as 30. The resulting model, composed of many simple decision trees, can be readily evaluated quantitatively but not easily visualized or interpreted.

- **Support Vector Machines (SVMs).** Like Random Forests, The SVM algorithm is a relatively recent method (Vapnik, 1995) and considered to be state-of-the-art. As opposed to decision trees, SVMs use kernel methods to achieve linear separation of data in a transformed feature space that may be of higher dimension than the original input data. The resulting decision boundary, when projected in the original space, can yield non-linear categorization, depending on the type of kernel used. In this study, we use the Radial Basis Function kernel, and chose parameters $c = 2$ and $g = 2$ based on 10-fold cross validation.

Experimental Results

A summary of quantitative experimental results from the study is given in Table 2.

Table 2. Experimental results summary.

Algorithm	Feature(s) Used	False Negative Rate	False Positive Rate	Accuracy
Baseline (Single-Split)	avg(SNR)	59.5%	9.0%	65.7%
Baseline (Single-Split)	ndef	11.6%	34.5%	76.9%
Decision Tree	ndef & avg(SNR)	13.8%	29.8%	78.2%
Support Vector Machine	All features	14.4%	27.8%	78.9%
Random Forest	All features	15.8%	18.2%	83.1%

We report the False Negative Rate, False Positive Rate, and Accuracy for each approach. The False Negative Rate and False Positive Rate metrics give a useful characterization of the breakdown of the different types of errors, while accuracy is a single-value summary statistic that weights both types of errors equally. Equations for each metric are given below in Table 3; also given is the formula in terms of the quadrants of the contingency table in Figure 7.

Table 3. Performance metrics used in the study.

Metric	Standard Equation	Equation (Figure 7)
False Negative Rate	$\frac{Number\ of\ False\ Negatives}{Number\ of\ True\ Positives\ +\ Number\ of\ False\ Negatives)}$	$\frac{c}{a+c}$
False Positive Rate	$\frac{Number\ of\ False\ Positives}{Number\ of\ False\ Positives\ +\ Number\ of\ True\ Negatives}$	$\frac{b}{b+d}$
Accuracy	$\frac{Number\ of\ True\ Positives + Number\ of\ True\ Negatives}{Total\ Number\ of\ Observations}$	$\frac{a+d}{a+b+c+d}$

The experimental data given in Table 2 provides a number of insights. The best performance in the study was given by the Random Forests method using all 18 features as listed in Table 1. This performance exceeded that of the Support Vector Machine by a statistically significant amount (5.3% increase in accuracy), notable since many problem domains lend themselves to a particular category of machine learning algorithm.

In comparison to naively splitting on a single attribute, the approaches which consider multiple attributes yield greater categorization performance. However, the best performing method (Random Forests, accuracy of 83.1%) compared to the single-split baseline using ndef (accuracy of 76.9%) represents only an 8% increase. It is clear that ndef alone is a very predictive feature, which follows intuition. Meanwhile, the other features selected enable statistically significantly higher categorization rates, but not drastically so. More predictive features are needed.

For all approaches, the proportion of types of errors (false positives versus false negatives) was not equal. In particular, the False Positive Rate was usually higher than the False Negative Rate. This is an important observation, because for monitoring, different types of errors do not have equal cost. In particular, any miscategorization associated with potentially missing an event has much higher cost than an error which simply results in additional analyst burden (i.e., the time required to review the event manually). Considering the types of errors separately results in a complex interpretation of the performance scores reported in Table 2. Although Random Forests had the highest overall accuracy, splitting on a single attribute—avg(SNR)—resulted in the lowest False Positive Rate. This result must be considered with that of the *trivial categorizer*, that is, the categorizer that simply predicts all "Good Automatic Origins." Such a categorizer would have a zero False Positive Rate, but very poor accuracy, and of course, no real impact in terms of screening out events and reducing analyst burden.

In general, the overall accuracy rates and in particular the false positive rates yielded by the methods in this study need to be improved in order to be seriously considered for inclusion in an automated event detection system. We provide a number of recommendations for future research that could lead to more accurate categorization of events.

CONCLUSIONS AND RECOMMENDATIONS

Applying Machine Learning to utilize a large number of readily available features to screen events that analysts will reject can lead to improved performance, over a simplistic categorizer, but the results are still not good enough to use because of the possibility of screening real events of interest. We believe that significantly better results can be achieved by use of new and enhanced features, and especially by the use of *cost-sensitive learning* to bias the categorizer towards lowering the False Positive Rate (FPR, see Table 3) at the expense of the False Negative Rate (FNR), reflecting actual monitoring system goals.

An important objective from this study was to inform future research directions in order to make the machine learning approach more effective. Future work will fall under three main areas: identification of additional features to help inform categorization; improved categorization algorithms; and the use of cost-sensitive learning to help improve results. These areas are discussed below.

Useful features are the most important part of any machine learning categorization task. Poor categorization performance will occur if features that do not support the discrimination task are used. There are a number of ways to improve the features for this problem. First, the power of existing features can be improved by applying special scalings and transforms. Second, new features can be computed as functions of existing features (e.g., distance between first and second detecting stations). Finally, entirely new features can be extracted from raw waveforms; this is an area of ongoing research (Meyer et al., 2009).

Future work will involve additional experimentation with various approaches and the categories of algorithms in order to improve performance. An important consideration is that once the best general type of categorizer is identified, improvements will often be incremental among best categorizers, for the same feature set. Presently, decision trees and related ensemble methods such as Random Forests perform best. Other categories of algorithms will also be investigated, including probabilistic categorizers (Naïve Bayes), neural networks, and K-nearest-neighbor approaches. We are cautious to not draw strong conclusions in regards to best algorithms for this task, as this will be very heavily feature-dependent.

In this domain, like many domains, the penalty for one type of error (incorrectly predicting a “False Origin”) is much greater than the other type of error (incorrectly predicting a “Good Automatic Origin”). Machine Learning has *cost-sensitive* methods for handling unequal costs. Different error costs can be explicitly accounted for when training models in order to bias the model towards one type of error. Unequal error costs can also be considered when evaluating the performance of a categorizer. For example, if specific costs are known, a weighted average of the errors can be made, where one type of error receives more weight in the final score. A more elaborate evaluation technique is Receiver Operating Characteristic (ROC) analysis, where all possible error costs are considered; the resulting Area Under the ROC Curve (AUC) summary statistic is a robust evaluation metric (Provost et al., 1998).

REFERENCES

Breiman, L.(2001). Random Forests. *Journal of Machine Learning Research*, 45: (1), 5–32.

Breiman, L., J. Friedman, C. J. Stone, and R. A. Olshen (1984). *Classification and Regression Trees*. Chapman and Hall, Boca Raton, FL.

Gauthier, J. H. (2009). Preliminary Analysis of the International Data Centre Pipeline, Sandia National Laboratories Technical Report #2009-4223.

Meyer, F., K. M. Taylor, D. Kaslowsky, M. Procopio, and C. Young (2009). Evaluation of Empirical Mode Decomposition and Chirplet Transform for Regional Seismic Phase Detection and Identification [abstract]. *Seismo.l Res. Lett.* 80: (2), 347–348.

Provost, F., T. Fawcett, and R. Kohavi (1998). The Case against Accuracy Estimation for Comparing Induction Algorithms. In *ICML '98: Proceedings of the Fifteenth International Conference on Machine Learning*.

Vapnik, V. (1995). *The Nature of Statistical Learning Theory*. Springer-Verlag.

BASIC RESEARCH ON SEISMIC AND INFRASONIC MONITORING OF THE EUROPEAN ARCTIC

Frode Ringdal, Tormod Kværna, Steven J. Gibbons, Svein Mykkeltveit, and Johannes Schweitzer

NORSAR

Sponsored by the Army Space and Missile Defense Command

Contract No. W9113M-05-C-0224

ABSTRACT

This project is a research effort aimed at improving seismic and infrasonic monitoring tools at regional distances, with emphasis on the European Arctic region, which includes the former Novaya Zemlya test site. The project has three main components: a) to improve seismic processing in this region using the regional seismic arrays installed in northern Europe, b) to investigate the potential of using combined seismic/infrasonic processing to characterize events in this region and c) to carry out experimental operation, evaluation and tuning of the seismic threshold monitoring technique.

We have continued our studies of a sequence of surface explosions in northern Finland, carried out for the purpose of destroying old ammunition. These explosions are taking place in August and September each year, and provide very useful reference events for infrasound sources since the location is known and the origin times are very tightly constrained by seismic observations. Previously, we have studied recordings mainly at the ARCES seismic array (at a distance of about 175 km) and the Apatity seismic/infrasound array (at a distance of about 280 km). However, in early 2008 an experimental 3-site array of microbarographs was installed within the ARCES seismic array, thus providing additional data for studying the 36 explosions which took place in the fall of 2008. Acoustic signals were detected on the microbarograph sensors following every one of the explosions, and on the seismic sensors following all but one. The non-detection was due to an interfering (unrelated) seismic signal.

While the seismic array has served well as a surrogate infrasound array in the past, our results show that microbarograph sensors are essential to capture very weak infrasound signals. Moreover, the onset of the infrasound phases inferred from microbarograph recordings are often significantly earlier (by up to 60 seconds) than for the seismic sensors. In our previous studies of the Finnish explosions, using ARCES seismic sensors, we have noted acoustic signals arriving 500-700 seconds after the origin time. By studying the experimental microbarograph recordings, we have now detected a number of arrivals occurring between 800 and 950 seconds after origin time. These are associated with considerably higher apparent velocities than the earlier arrivals, consistent with the steeper angles of incidence which would be anticipated from thermospheric returns. Such presumed thermospheric arrivals were observed for 11 of the 36 explosions.

We have continued using the current array network of infrasound stations in northern Europe for studying a variety of infrasonic sources. On 15 January 2009, a meteor was observed over parts of northern Norway. We have used available recordings from the experimental infrasound deployment within the ARCES array, the Apatity infrasound array and the stations of the Swedish Infrasound Network to analyze this event. We have made a location estimate using backazimuths from the stations within the network. We have confirmed the location by making distance estimates from each station using a standard celerity value of 0.29 km/s and traveltimes obtained by calculating the difference between the time of the main signal energy observed at each station and the (reportedly accurate) origin time of the event. This latest meteor observation supplements two previous such observations in Norway during 2006. Establishing a database of such events will be important for future studies of infrasound wave propagation.

As part of our ongoing study of regional monitoring, we are investigating the notorious difficulties in obtaining accurate slowness estimates from the Spitsbergen array. The complex geology of Spitsbergen influences the incoming wavefield in such a way that the apparent phase velocity varies greatly with azimuth. In the future we plan to address this problem by making more extensive use of the three-component seismometers in the array.

OBJECTIVE

The objective of the project is to carry out research to improve the current capabilities for monitoring small seismic events in the European Arctic, which includes the former Russian test site at Novaya Zemlya. The project has three main components: a) to improve seismic processing in this region using the regional seismic arrays installed in northern Europe, b) to investigate the potential of using combined seismic/infrasonic processing to characterize events in this region and c) to carry out experimental operation, evaluation and tuning of the seismic threshold monitoring technique, with application to various regions of monitoring interest.

RESEARCH ACCOMPLISHED

Study of Infrasound Signals Generated by Atmospheric Explosions in Finland

The Finnish military destroys expired ammunition at a site in northern Lapland in a sequence of explosions every year between August and September. Each explosion has a yield of approximately 20000 kg and the seismic signals recorded at the ARCES array in northern Norway indicate a magnitude of approximately 1.5. The events have been of great interest due to the generation of infrasound signals which have been recorded on the seismic traces at ARCES and by both seismic and microbarograph instruments at Apatity (Vinogradov and Ringdal, 2003; Gibbons et al., 2007). These explosions provide very useful reference events for infrasound sources since the location is known (67.934^{o}N, 25.832^{o}E: see Figure 1) and the origin times are very tightly constrained by the seismic observations. It now appears that infrasound from these events can be observed at far greater distances than previously assumed with signals likely to come from these sources being observed at the International Monitoring System (IMS) infrasound arrays I18DK (Qaanaaq, Greenland) and I26DE (Freyung, Germany) making the events useful for studies of long-distance sound propagation (Bahavar et al., 2008).

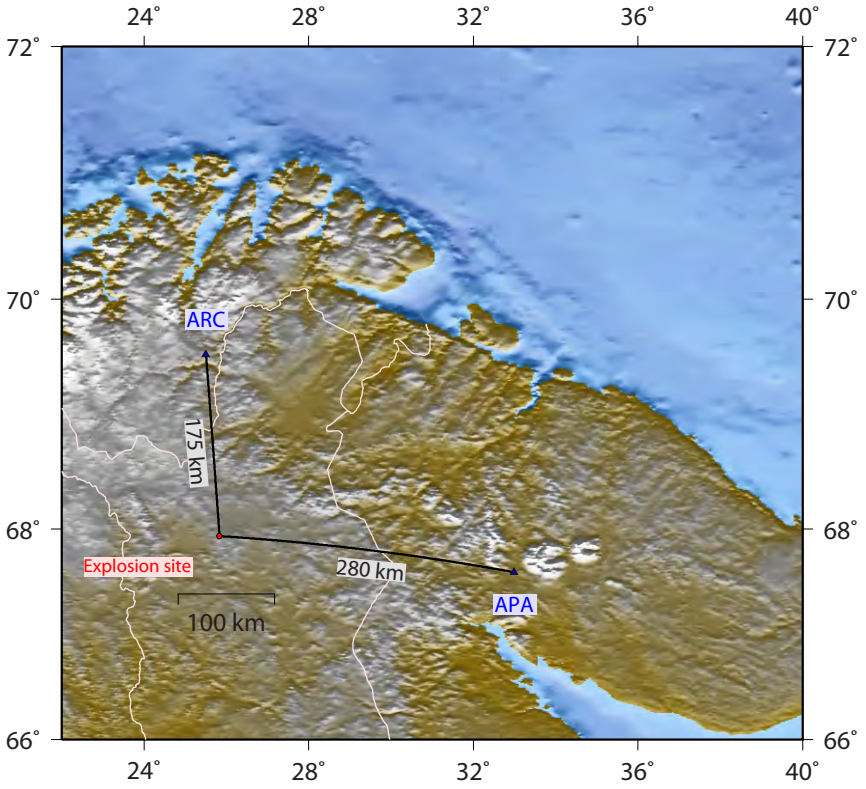

Figure 1. Location of the Finnish explosion site (67.934^{o}N, 25.832^{o}E) in relation to the arrays at ARCES and Apatity.

During 2008 a total of 36 such explosions were conducted between August 13 and September 11. As in previous years, a very high degree of similarity was observed between the seismic signals from the events allowing them all to be detected with an essentially zero false alarm rate using a multichannel correlation detector (Gibbons and Ringdal, 2006).

The 2008 explosion sequence has been of special interest since an experimental 3-site array of microbarographs deployed within the ARCES array (Roth et al., 2008) has allowed for a direct comparison of the infrasound signals recorded on the seismometers and those recorded on co-located microbarographs. Due to local environmental restrictions (which have also delayed indefinitely the deployment of the IMS infrasound array IS37) no wind noise reduction system has been allowed other than the use of porous hoses. A full description of the installation, including instrumentation and data samples, is provided by Roth et al. (2008), and preliminary data analysis is provided by Ringdal et al. (2008).

Figure 2 displays the waveforms observed on co-located seismic and infrasound sensors at the ARA1 site of the ARCES array for each of the 36 events in 2008. The seismic traces in the left panel show the seismic P- and S- phases arriving 29 and 49 seconds respectively after each shot and also acoustic signals between 500 and 700 seconds. Whilst the acoustic phases are generally visible in the filtered data, they are of somewhat smaller amplitude than in some previous years. (Gibbons et al., 2007, display a corresponding plot for 2002 in which the amplitudes of the acoustic phases are frequently greater than those for the seismic phases.) An additional complication which has been particularly problematic for 2008 is the presence of unrelated seismic signals in the interval in which the acoustic phases are anticipated. Signals visible between 500 and 700 seconds after events 14, 15, 16, and 24 are very clearly regional or teleseismic signals unrelated to the explosions in Finland which may make the detection of acoustic phases at these times difficult or impossible.

The right hand panel of Figure 2 shows microbarograph data from the same ARCES site, covering the same time intervals. The seismic arrivals are not visible in these waveforms. More often than not, the acoustic phases recorded on the seismic instruments are also visible on the microbarograph traces, with a significantly higher amplitude than the background noise. On other days, the background noise is very much higher and matches the amplitudes of the observed signals.

The only way to identify which parts of the waveforms truly correspond to acoustic signals from the direction of interest is to perform slowness analysis. We calculate cross-correlation coefficient traces between pairs of signals and then loop around a grid of slowness vectors and calculate the mean values for the corresponding time delays (c.f. Brown et al., 2002). If the slowness vector corresponding to the maximum average cross-correlation coefficient does not fall within limits appropriate for a wavefront propagating with air-sound speed from a plausible backazimuth then we have to assume that the observed signal is probably not an acoustic phase from one of our events. With the seismic sensors, we have traces from 25 sites and so can perform slowness analysis either with the full array or with one of many possible subsets of sensors. There are only three sensors in the infrasound subarray. Whilst it is possible to obtain reasonable slowness estimates if all three sensors record a signal well, there is no redundancy and should a single one of the sensors fail, or be subject to excessive noise, no direction estimate is possible.

One feature which has not previously been observed in recordings from these events is the presence of acoustic phases with higher apparent velocities between around 800 and 950 seconds. They are detected only marginally for three events (6, 15, and 36) on the seismic sensors, but are clearly visible on the microbarograph data for several more. We will illustrate these observations by using event 15 as an example.

Slowness estimates for event 15, both for a typical phase in the 500-700 second interval and for one of the newly observed phases between 800 and 950 seconds, are shown in Figure 3. The two plots at the left side of this figure are based on the seismic recordings (innermost nine sites of ARCES) whereas the two plots to the right are generated from the three microbarographs. The leftmost plots (based on seismic data) show a clear infrasound signal at 625 seconds, whereas an interfering seismic signal obscures the sound wave at 928 seconds. The rightmost plot (based on microbarograph data) show two clear infrasound signals, with the signal at 928 seconds having a significantly higher phase velocity than the signal at 625 seconds.

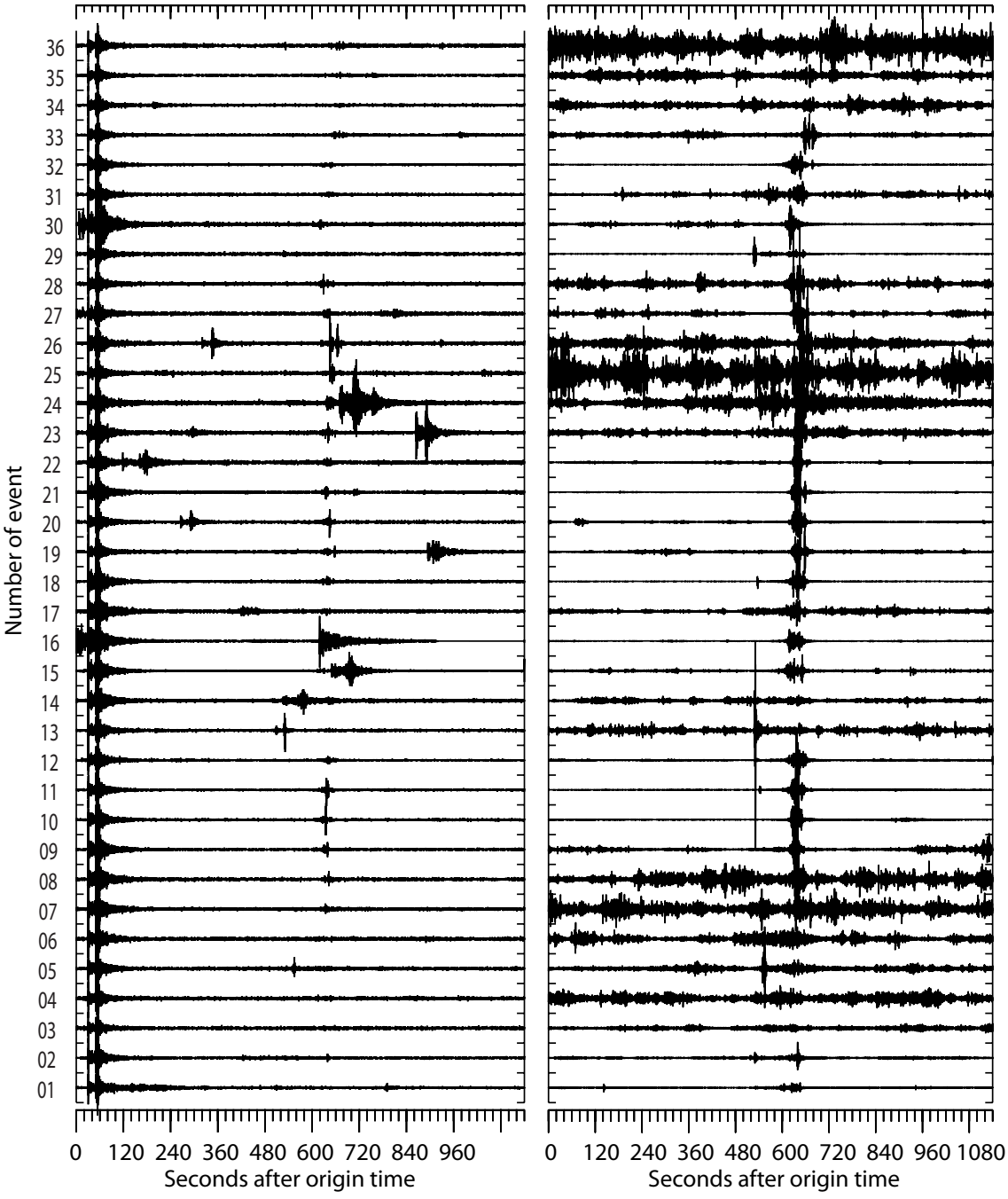

Figure 2. Waveforms from the short-period vertical seismic sensor ARA1_sz (left) and the co-located microbarograph sensor ARA1_BDF (right) for the Finnish explosions during 2008. The same vertical scale is applied to all of the traces within each panel. All waveforms are bandpass filtered between 2 and 7 Hz.

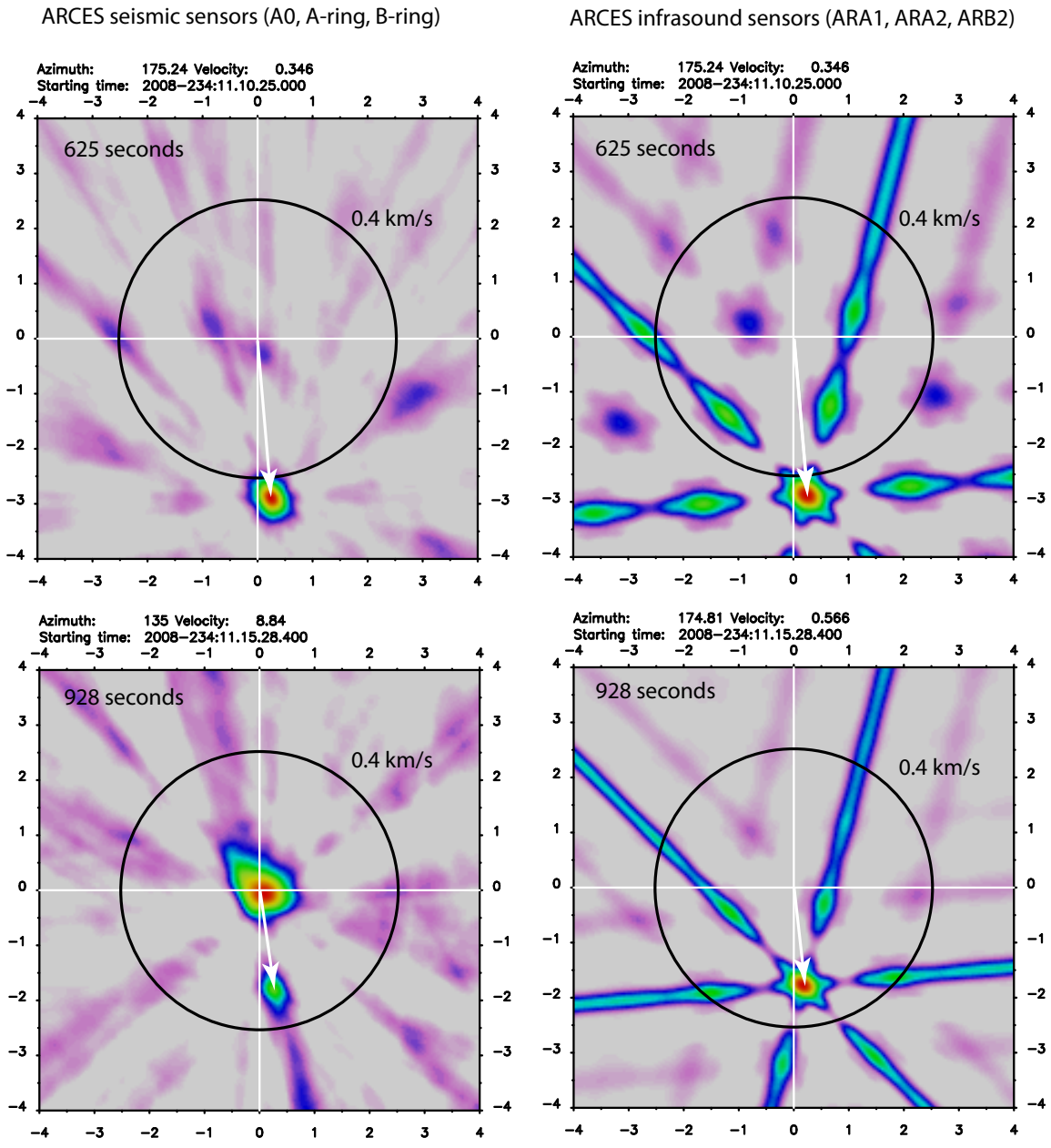

Figure 3. Slowness estimates at 625 seconds (above) and 928 seconds (below) after the explosion at 11.00 UTC on August 21, 2008. For the seismic estimates (the two plots to the left), only the innermost nine sites of the ARCES array are used. The seismic estimate for the later arrival (lower left panel) indicates an apparent velocity consistent with seismic wave speed, although evidence is seen for energy arriving with sound speed. The circles correspond to an apparent velocity of 0.4 km/s.

The significantly higher apparent velocity for the later arrival (lower right panel of Figure 3) is consistent with a steeper angle of incidence as would be anticipated for a thermospheric arrival. At a distance of 178 km, the range of travel times 800 to 950 seconds corresponds to celerities between 0.187 kms^{-1} and 0.223 kms^{-1}, which is comparable

with the values plotted by Mutschlecner and Whitaker (1999) for thermospheric arrivals observed from explosions at the Nevada Test Site, observed at a distance of approximately 210 km.

Infrasound Recordings of the Meteor North of Norway on 15 January 2009

In the evening of 15 January 2009, light flashes and a fireball were observed over parts of northern Norway. The object was reported to propagate in a north-northwesterly direction into the Barents Sea. Based on newspaper reports, the time of the event is estimated to 19:40 GMT.

The signals from the meteor, recorded at the 4 infrasound arrays operated by the Swedish Institute of Space Physics (IRF) were analyzed within a short time after the event. Prof. Liszka of IRF estimated the signals to originate halfway between mainland Norway and Svalbard. For details see *http://www.irf.se/Topical/Other/?newsid=7&group=P2*.

We will here provide results from additional analysis of signals at the IRF stations (Liszka and Kværna, 2008), as well as at the infrasound station in Apatity (Vinogradov and Ringdal, 2003) and at an experimental infrasound deployment within the ARCES array (Roth et. al., 2008).

For each of the stations we have processed the infrasound data using vespagram analysis. Using a fixed apparent velocity around 0.333 km/s, we have calculated the resulting normalized beam power for a range of back-azimuths, where the maximum represents an estimate of the back-azimuth of the arriving signal. In our calculations we have used a window length of 10 seconds and a window step of 1.0 second. Because of the larger array apertures, the ARCES and Apatity infrasound data were processed in the 1 - 4 Hz frequency band, whereas the stations of the Swedish Infrasound network were all processed in the 2 - 5 Hz band. Figure 4 shows the results from the vespagram analysis of ARCES and Apatity data together with the raw and bandpass filtered waveforms.

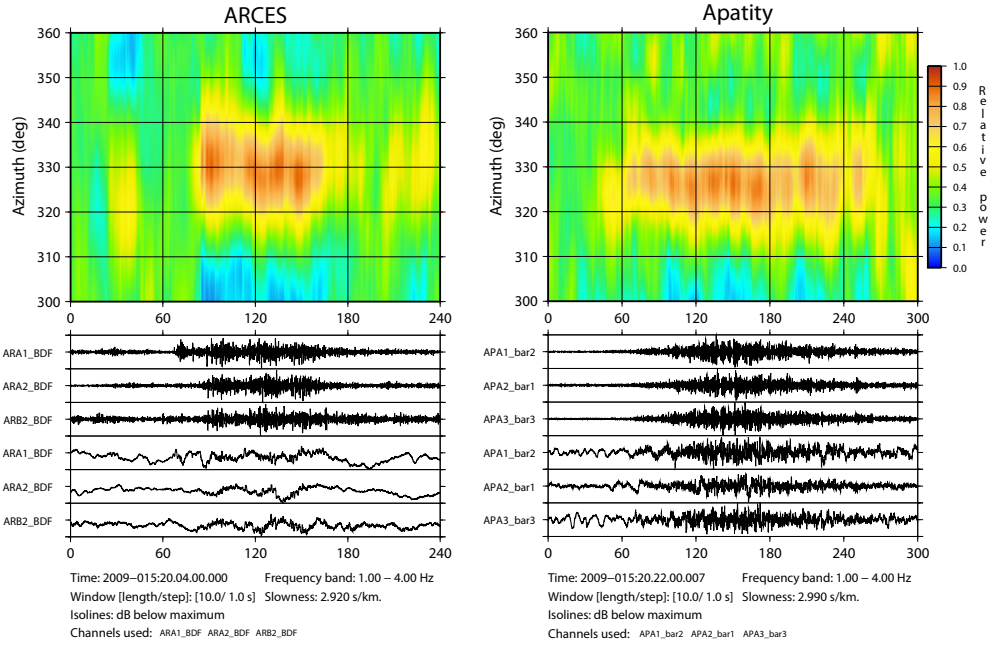

Figure 4. Azimuthal vespagrams from analysis of ARCES and Apatity infrasound data for the time interval around the signals from the meteor on 15 January 2009. The upper three traces of each panel show the bandpass filtered waveforms, whereas the three lower traces show the raw data. Notice that different time scales are used for the two stations. A constant slowness close to 3 s/km has been used when calculating the azimuthal vespagrams.

Compared with analysis of a large number of infrasound signals from the previously described military ammunition destruction site in Finland (Gibbons et. al. 2007), we have found a relatively large variability in back-azimuth estimates. This variability can be caused by several factors, like wind conditions, local noise sources, low SNR or data quality problems. In this study, we have assigned a variability of ± 8 degrees around the average back-azimuth

estimates for each station, and the corresponding back-azimuthal sectors from each station are shown in Figure 5. As indicated in Figure 5, there is a small area of intersection in the Barents Sea, close to the Finnmark coast.This area is an indication of the source region of the infrasound signals, i.e., where the meteorite exploded.

Another approach to source location is to use the reported origin time of the event. According to a newspaper report, the origin time of 19:40 GMT was read from the display of a cellular telephone at the time of the meteor observation. This gives us the possibility to calculate the travel-time to each station, which again can be scaled with a standard celerity for stratospheric arrivals of 0.29 km/s to obtain a distance estimate. The intersection of the distance arcs provide indications of the location of the event, and we thereby obtain an estimate of 72.1^{o} N, 20.3^{o}E, which is consistent with the intersections of the sectors in Figure 5.

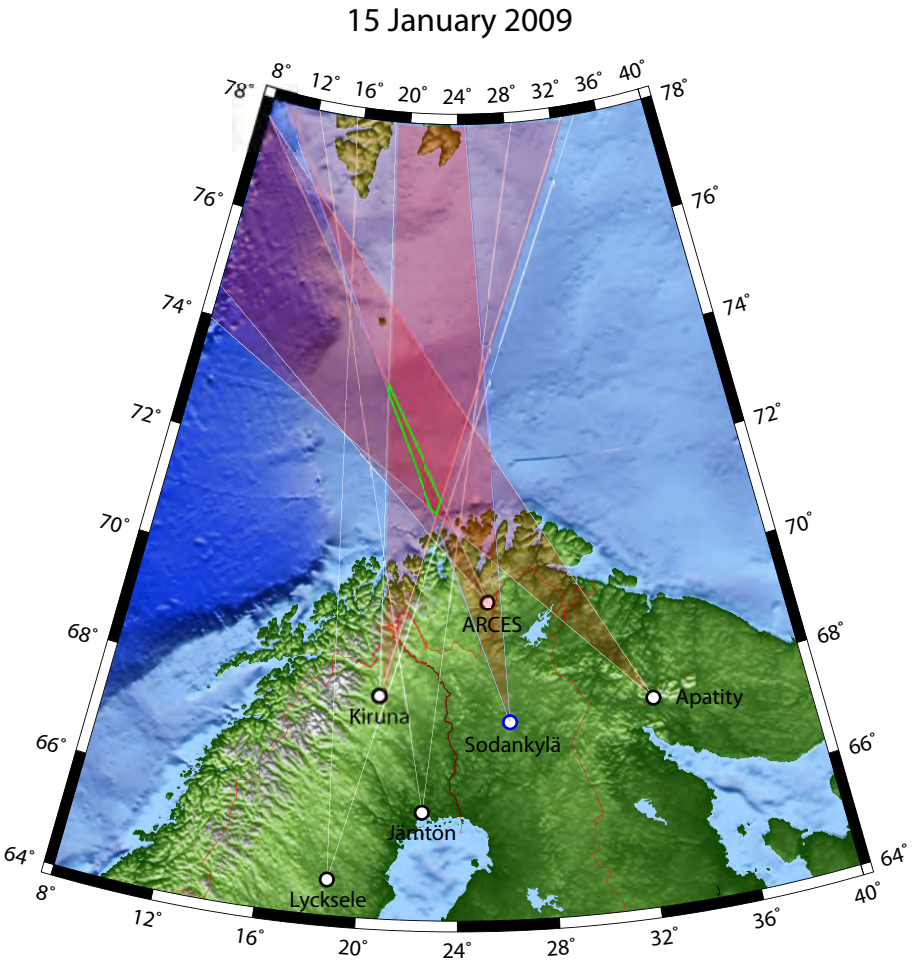

Figure 5. Map showing the sectors of back-azimuths of infrasound signals from the meteor as observed at the infrasound stations in Sweden, Finland, NW Russia and Norway. For each station, a sector of ±8 degrees around the average back-azimuth estimate is plotted. The highlighted green polygon shows the area of common intersection. No corrections for the wind field are introduced to the back-azimuth estimates.

Resolving Ambiguity in Slowness Estimates

The SPITS and ARCES arrays are crucial to the seismic monitoring of small events in the European Arctic. Small events (lower than magnitude 3) on or close to Novaya Zemlya are not usually detected by any additional IMS

stations. With so few observations, good recordings of S-phases are essential for accurate event location - especially given the large azimuthal gap to the North and East. If S-phases are not detected automatically, there is an increased risk that detected P-phases will remain unassociated and that the event will be missed.

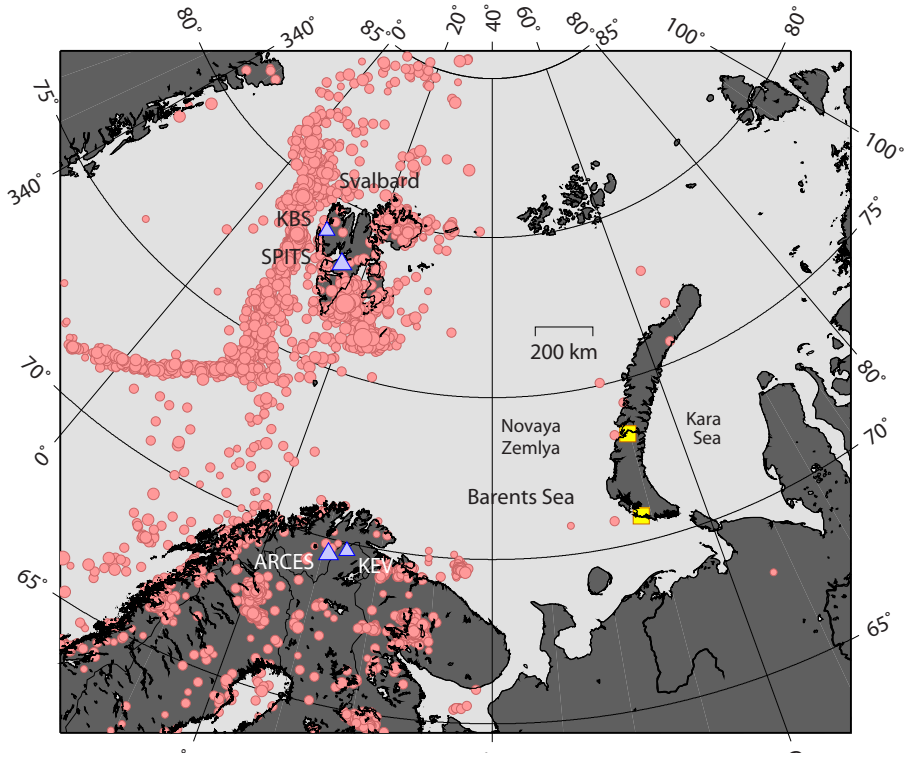

Figure 6. Seismicity of the European Arctic (1998-2009) from the NORSAR reviewed regional seismic bulletin. Yellow squares indicate the sites of former Soviet nuclear test sites on Novaya Zemlya.

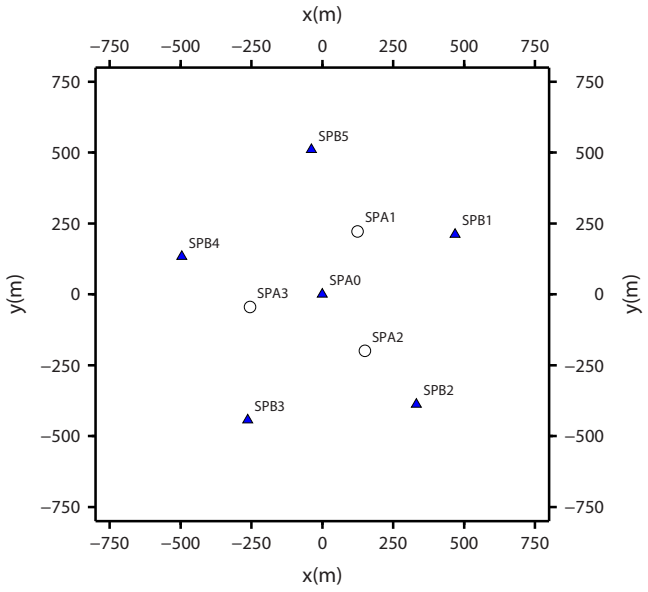

Figure 7. Map showing the configuration of the Spitsbergen array (SPITS). The blue triangles are three-component stations.

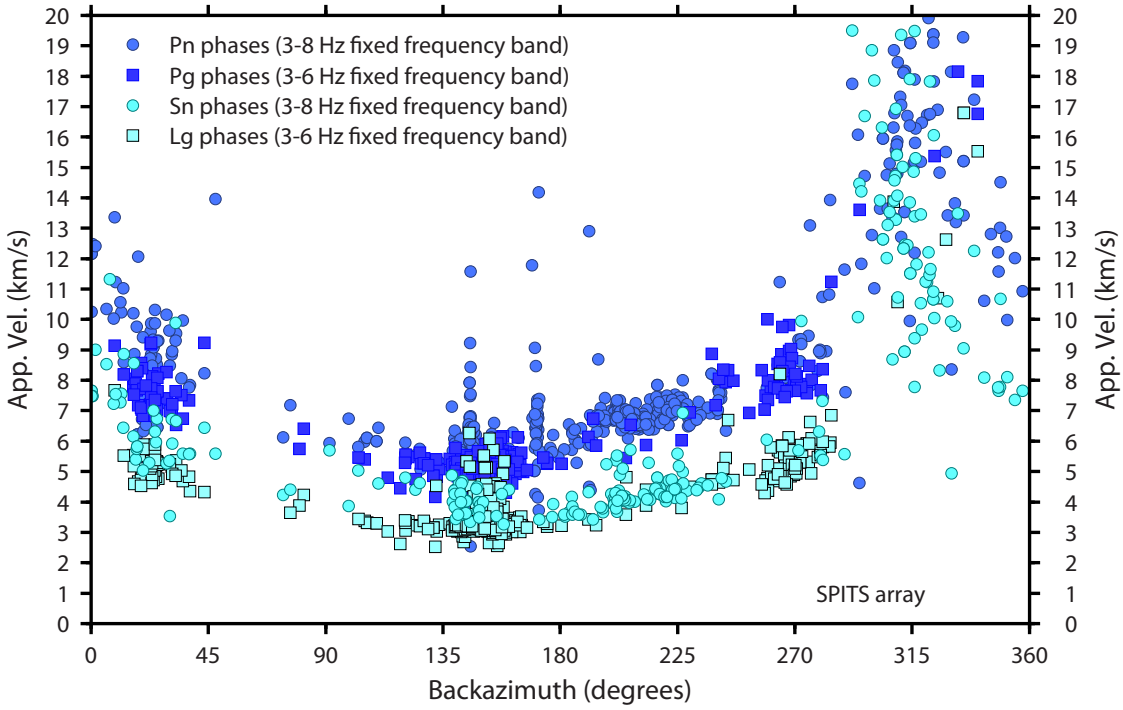

Figure 8. Apparent velocity of regional phases recorded by the SPITS array as a function of geographical backazimuth. The backazimuths are based on the solutions in the NORSAR analyst-reviewed regional bulletin. The slowness estimates have been made by fixed band f-k analysis as indicated, using only the vertical seismometers. The plot does not take into account epicentral distance and does not show SPITS backazimuth deviations relative to the reference backazimuth.

Large amplitude Lg phases are often observed for continental propagation paths which are well-recorded on vertical sensors. Lg propagation is blocked in the Barents Sea and we rely on good recordings of Sn-phases. As demonstrated in many situations, the amplitude of the S-phases on the horizontal components is greater than on the vertical. In previous studies we have documented that only a modest improvement in SNR for the Sn-phase is obtained by beamforming on the vertical components. The achievable improvement using 3-component data is far greater. A more extensive use of the 3-C array for processing secondary phases would significantly improve SNR and at the same time allow more reliable azimuth and slowness estimates to be made.

Geological structure below the SPITS array influences the incoming wavefield such that the apparent velocity measured varies greatly as a function of backazimuth (see Figure 8). This can to some degree be corrected for by applying a sinusoidal correction term. However, there is a significant overlap between regional P and S apparent velocities which is problematic for phase identification. The problem is most acute for the region to the northwest with regional phases (both P and S) often having very high apparent velocities (frequently in the range 15-20 km/s). It is hoped that 3-C processing will help to resolve issues in phase identification.

CONCLUSIONS AND RECOMMENDATIONS

The infrasound database that has been developed based on the explosions in northern Finland provides a unique resource for studies of infrasonic propagation under controlled conditions. One of the main topics to be studied is the surprising observations of various infrasound phases in what is often denoted as a “quiet” zone (less than 200 km distance). The observation of apparently thermospheric phases as indicated in this paper is particularly interesting. We plan to carry out various modelling exercises in order to further investigate the propagation of infrasound phases

at local distances. At the same time, we will continue to accumulate ground truth data of a variety of infrasound sources.

This study has revealed significant ambiguity in regional phase identification and slowness estimation for the Spitsbergen array. In view of the important role of this array in monitoring the European Arctic, it is essential to resolve this problem We recommend that further studies be undertaken, using three-component array processing, to attempt to improve upon this situation.

Previous studies, documented in various NORSAR Semiannual Technical Summaries, have shown a remarkably efficient seismic wave propagation from events near Novaya Zemlya across the Barents Sea to the Spitsbergen array. By analyzing data from a newly installed high-frequency element in the ARCES array in northern Norway, we have found that similar propagation characteristics are observed for this array as well. We consider that there is still much to be gained by making improved use of the high-frequency recordings in the European Arctic, and we recommend that a systematic mapping of the high-frequency propagation characteristics of this region be undertaken.

We note that the available high-frequency data so far does not include events to the east and north-east of the ARCES array, and the high-frequency propagation from the Novaya Zemlya region to ARCES is therefore still unknown. As more data is accumulated, we recommend that a detailed study of the high frequency propagation characteristics for various paths in the region be carried out. We also recommend that data from temporary seismic stations installed as part of the International Polar Year be fully exploited in such a study.

REFERENCES

Bahavar, M., Barker, B. W., Bennett, T. J., Israelsson, H. G., Kohl, B. C., Kung, Y.-L., Murphy, J. R., and Oancea, V. (2008). Nuclear Explosion and Infrasound Event Resources of the SMDC Monitoring Research Program, in *Proceedings of the 2008 Monitoring Research Review: Gound-Based Nuclear Explosion Monitoring Technologies,* LA-UR-08-05261, Vol. 2, pp. 923–931.

Brown, D. J., C. N. Katz, R. Le Bras, M. P. Flanagan, J. Wang, and A. K. Gault (2002). Infrasonic Signal Detection and Source Location at the Prototype International Data Centre, *Pure Appl. Geophys.* 159: 1081–1125.

Gibbons, S. J. and Ringdal, F. (2006). The detection of low magnitude seismic events using array-based waveform correlation, *Geophys. J. Int.* 165: 149–166.

Gibbons, S. J., Ringdal, F., and Kværna, T. (2007). Joint seismic-infrasonic processing of recordings from a repeating source of atmospheric explosions, *J. Acoust. Soc. Am.* 122: EL158-EL164.

Liszka, L. and T. Kværna (2008): Propagation of infrasound from chemical explosions. *Inframatics Newsletter, No. 20, March 2008,* 1–10.

Mutschlecner, J. P., and Whitaker, R. W. (1999). Thermospheric Infrasound Signals, in *Proceedings of the 21st Seismic Research Symposium: Technologies for Monitoring The Comprehensive Nuclear-Test-Ban Treaty,* LA-UR-99-4700, Volume 1, pp. 151–158.

Ringdal, F., Kværna, T., and Gibbons, S. J. (2008). Initial studies of signals recorded by ARCES infrasound sensors. *In NORSAR Scientific Report: Semiannual Technical Summary No. 2-2008, NORSAR, Kjeller, Norway,* 60–85.

Roth, M., Fyen, J., and Larsen, P. W. (2008). Setup of an experimental infrasound deployment within the ARCES array. *In NORSAR Scientific Report: Semiannual Technical Summary No. 2-2008, NORSAR, Kjeller, Norway.* 52–59.

Vinogradov, Y. and Ringdal, F. (2003). Analysis of infrasound data recorded at the Apatity array. *In NORSAR Scientific Report: Semiannual Technical Summary No. 1-2003, NORSAR, Kjeller, Norway,* 68–77.

ENHANCING SEISMIC CALIBRATION RESEARCH THROUGH SOFTWARE AUTOMATION AND SCIENTIFIC INFORMATION MANAGEMENT

Stanley D. Ruppert, Douglas A. Dodge, Teresa F. Hauk, Michael D. Ganzberger, David B. Harris, and Eric Matzel

Lawrence Livermore National Laboratory

Sponsored by the National Nuclear Security Administration

Award No. DE-AC52-07NA27344/LL09-IRP-NDD02

ABSTRACT

The National Nuclear Security Administration (NNSA) Ground-Based Nuclear Explosion Monitoring Research and Development (GNEMRD) Program at Lawrence Livermore National Laboratory (LLNL) continues to make significant progress enhancing the process of deriving seismic calibrations and performing scientific integration, analysis, and information management with software automation tools. Our tool efforts address the problematic issues of very large datasets and varied formats encountered during seismic calibration research. New information management and analysis tools have resulted in demonstrated gains in efficiency of producing scientific data products and improved accuracy of derived seismic calibrations.

The foundation of a robust, efficient data development and processing environment is composed of many components built upon engineered versatile libraries. We incorporate proven industry "best practices" throughout our code and apply sophisticated source code and bug tracking management as well as automatic generation and execution of unit tests for our experimental, development, and production lines. Significant software engineering and development efforts have produced an object-oriented framework that provides database-centric coordination between scientific tools, users, and data. Nearly a billion parameters, signals, measurements, and metadata entries are stored in a relational database accessed by an extensive object-oriented multi-technology software framework that includes elements of stored procedures, real-time transactional database triggers and constraints, as well as coupled Java and C++ software libraries to handle the information interchange and validation requirements. In contrast with previous years, software development work this past year has emphasized development of automation at the data ingestion level. This change reflects a gradually changing emphasis in our program from processing a few large datasets that result in a single integrated delivery to processing many different datasets from a variety of sources. The increase in the number of sources had resulted in a large increase in the amount of metadata relative to the final volume of research products. Software developed this year addresses the following problems:

- Efficient metadata ingestion and conflict resolution
- Automated ingestion of bulletin information
- Automated ingestion of waveform information from global data centers
- Site metadata and response transformation required for certain products

This year, we also made a significant step forward in meeting a long-standing goal of developing and using a waveform correlation framework. Our objective for such a framework is to extract additional calibration data (e.g., mining blasts) and to study the extent to which correlated seismicity can be found in global- and regional-scale environments.

OBJECTIVE

The NNSA GNEMRD Program has made significant progress enhancing the process of deriving seismic calibrations and performing scientific integration with automation tools. We present an overview of our software automation efforts and framework to address the problematic issues of improving the workflow and processing pipeline for seismic calibration products, including the design and use of state-of-the-art interfaces and database centric collaborative infrastructures. These tools must be robust, intuitive, and reduce errors in the research process. This scientific automation engineering and research will provide the robust hardware, software, and data infrastructure foundation for synergistic GNEMRD Program calibration efforts. The current task of constructing many seismic calibration products is labor intensive, complex, expensive and error prone. The volume of data as well as calibration research requirements has increased by several orders of magnitude over the past decade. The increase in quantity of data available for seismic research over the last two years has created new problems in seismic research; data quality issues are hard to track given the vast quantities of data, and this quality information is readily lost if not properly tracked in a manner that supports collaborative research. We have succeeded in automating many of the collection, parsing, reconciliation and extraction tasks individually. Several software automation tools have also been produced and have resulted in demonstrated gains in efficiency of producing derived scientific data products. In order to fully exploit voluminous real-time data sources and support new requirements for time-critical modeling, simulation, and analysis, continued expanded efforts to provide scalable and extensible computational framework will be required.

RESEARCH ACCOMPLISHED

The primary objective of the Scientific Automation Software Framework (SASF) efforts is to facilitate the development of information products for the GNEMRD regionalization program. The SASF provides efficient access to, and organization of, large volumes of raw and derived parameters, while also providing the framework to store, organize, integrate, and disseminate derived information products for delivery into the NNSA Knowledge Base (KB).

These next-generation information management and scientific automation tools are used together within specific seismic calibration processes to support production of tuning parameters for the United States Atomic Energy Detection System (USAEDS) run by the Air Force. The automation tools create synergy and synthesis between complex modeling processes and very large datasets by leveraging a scalable and extensible database-centric framework. The requirements of handling large datasets in diverse formats, and facilitating interaction and data exchange between tools supporting different calibration technologies, has led to an extensive scientific automation software engineering effort to develop an object-oriented database-centric framework using proven research-driven workflows and excellent graphics technologies as a unifying foundation.

The current framework supports integration, synthesis, and validation of the various information types and formats required by each of the seismic calibration technologies. For example, the seismic location technology requires parameter data (site locations, bulletins) and time-series data (waveforms) and produces parameter measurements in the form of arrivals, gridded geospatially registered correction surfaces, and uncertainty surfaces. In past years, our automation efforts have been focused largely on research support tools, RBAP (Regional Body-wave Amplitude Processor) and KBALAP (Knowledge Base Automated Location Assessment and Prioritization) (Ruppert et al., 2005; Elliott et al., 2006; Ruppert et al., 2007; Hauk et al. 2008). However, this year, we have shifted the development effort to address some fundamental changes in the nature and use of the data integrated into our system.

Much of our data ingestion infrastructure was written in the late 1990s when seismological data centers were fewer in number and possessed minimal capabilities. At that time, there was little infrastructure to support automated retrieval of data, so our codes all required that the data to be loaded exist on our intranet. In addition, at the start of the last decade our efforts were devoted solely to the support of the base program objectives, and we had only a single analysis tool (SAC) (Ruppert et al., 1999). Today, we ingest data from many sources for use in creating a variety of research products over and above the calibration products of the base program. The change is shown schematically in Figure 1 below.

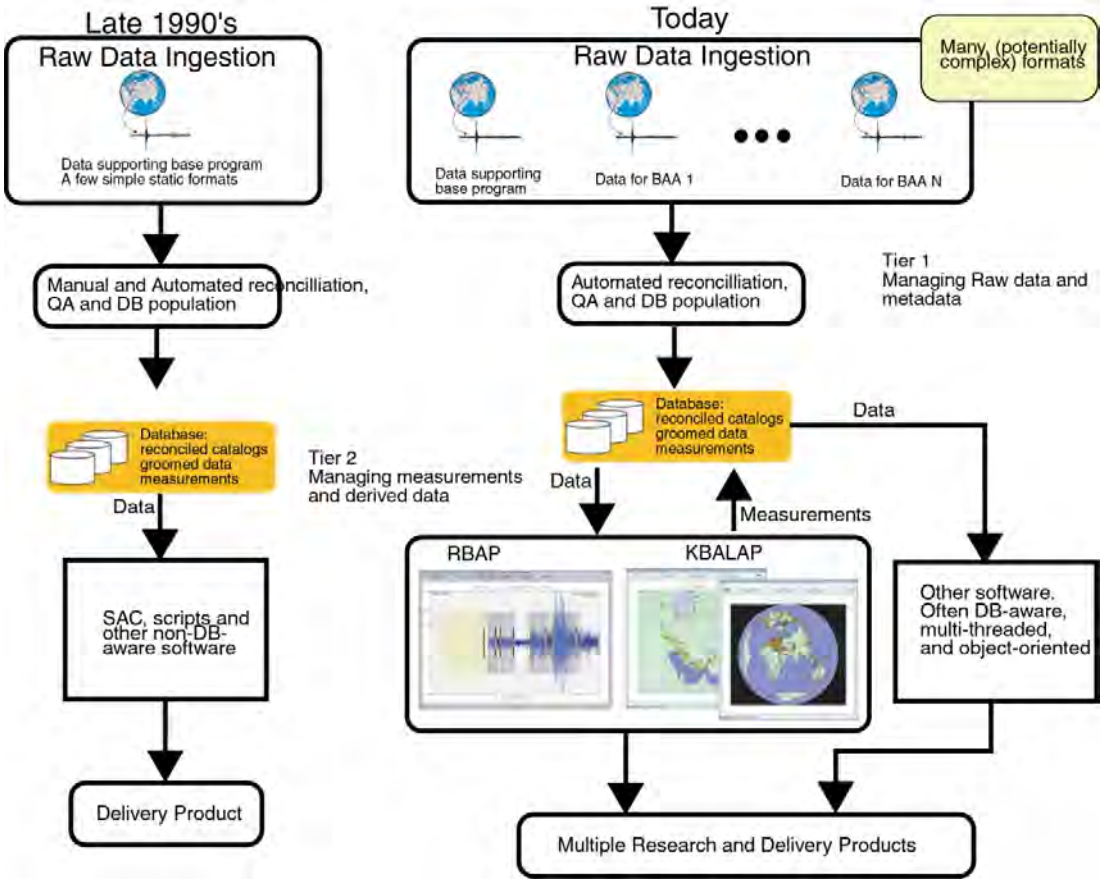

Figure 1. A schematic comparison of differences in dataflow between the late 1990s and today.

Ten years ago, the bulk of our data was from a few global sources, and a common processing was applied to the data to produce a single integrated delivery product. Today, in addition to global data sources, data from scores of local and regional networks flow into our system. Many different types of processing may be applied to the data to produce a number of research products.

Information products created using the LLNL SRDB may be grouped under two major categories or tiers: Tier 1, primary data products and Tier 2, derived products. In order to calibrate seismic monitoring stations, the LLNL SRDB must incorporate and organize the following categories of primary and derived measurements, data, and metadata:

Tier 1: Contextual and Raw Data

Station Parameters and Instrument Responses
Global and Regional Earthquake Catalogs
Selected Calibration Events
Event Waveform Data
Geologic/Geophysical Datasets
Geophysical Background Models

Tier 2: Measurements and Research Results
Phase Picks
Travel-Time and Velocity Models
Rayleigh and Love Surface Wave Group Velocity Measurements
Phase Amplitude Measurements and Magnitude Calibrations
Detection and Discrimination Parameters

Although we have taken advantage of many of the new sources of data as they became available, for the most part our data ingestion has retained a multistep process. The sequence has generally been (1) obtain data via FTP, email, tape, or other physical media; (2) stage data, and (3) use a variety of automated loading tools to add data to database.

At the beginning of our automation efforts in early 2000, we automated each of these individual steps, in the Knowledge Base Integration Tool Suite (KBITS) (Ruppert et al., 1999), in order to quickly and efficiently process large volumes of common/simple formatted data. This allowed us to go from 500K to 200M waveforms (Table 1) (Ruppert et al., 1999; Hauk et al., 2008). Examples include global bulletins and data from a few data centers in known, usually invariant, formats. Subsequent efforts focused on automation of measurement and metadata production of Tier 2 topics. Tier 2 efforts of our software development effort included production and refinement of analysis tools such as RBAP, KBALAP, GT-MERGE (Ruppert et al., 2007; Hauk et al., 2008).

Although KBITS software automation made each individual step of loading Tier 1 data more efficient, further gains in efficiency and capability can be achieved through better integration and consolidation of individual steps. This approach also applies for acquisition and loading of both bulletins and waveforms. Channel data have been mostly obtained from SEED files and from CSS flat files. However, over time there has been a slow shift in the nature of the data that our researchers require, and this is putting increasing strain on our semi-automated data loading efforts. In the late 1990s, we concentrated most of our efforts on a relatively small number of stations for which we could get data in large blocks. For this scenario, a small amount of manual effort could result in a large number of rows in the WFDISC, ORIGIN, and ARRIVAL tables. Today, with the increased importance of BAA (Broad Agency Announcement) research projects in our program, we are processing many more relatively small datasets. So, the proportion of time spent loading metadata per waveform row loaded has increased substantially.

Table 1. The change in complexity of our data processing environment in terms of data volumes and display and output requirements.

1999 Status	2009 Status
• 0.1 TB storage	• 200 TB storage
• 10K Events	• 3M events
• 500K waveforms	• 200M waveforms
• 100K measurements	• 750M measurements
• Single program	• Multiple programs
• Single data domain	• Multiple data domains
• Single tool (SAC)	• Multiple tools (RBAP, KBALAP, GTMERGE, KBITS, delivery schema)
	• Uncertainties/validation/metadata
	• GUI/GIS/mapping/visualization
	• Support calibration efforts such as GTMerge and EventID deliveries
	• Support multiple BAA projects

It is also the case that changing metadata can be much more difficult today than it was several years ago. This is mostly because a large number of rows in many tables can be affected by a change to metadata. It is more difficult to keep track of all the potentially affected data, and it can be time consuming just to update the affected rows.

Meanwhile, seismological data centers have grown in number and matured in sophistication to the point that it appears feasible to get a significant fraction of the data into our system automatically. Based on all these factors, we decided that the time was right to shift some focus back to our data ingestion effort and try to introduce some automations where possible. To that end, we have constructed, in the last year, three pilot applications for automating data ingestion. These are **UsgsEnsClient**, **Station Metadata Tool**, and **Waveform Retriever**.

UsgsEnsClient

This tool takes advantage of the United States Geological Survey (USGS) Earthquake Notification Service (ENS) (USGS ENS Documentation, 2009) to get a first-look origin into our system within an hour or so of the event occurrence. Although we continue to load global bulletins as before, by having the event in our system early on, we are able to analyze events of interest much more rapidly than would be the case if the origin information had to be retrieved manually and run through our old bulletin loading system. We do not currently retrieve events for the entire Earth through this mechanism. Instead we have defined several regions of interest for which we load all ENS solutions. Nevertheless, since its inception, this system has reliably loaded over 63,000 events.

Station Metadata Tool

The Station Metadata Tool software is a Java application that builds on our previous work in merging data from multiple sources into a single SITE table in CSS format. The STATION_METADATA schema and supporting software (Hauk et al., 2008) have proven useful in tracking the provenance of SITE data and making informed choices in the face of conflicting information. However, it is only a partial solution to the problem of maintaining complete up-to-date metadata for our system.

That software was predicated on the idea of periodic (relatively infrequent) manual introduction of new data. When this occurred, the software would analyze the data for inconsistencies, and after they were resolved, the entire SITE table would be rebuilt. As it happens, even the major data sources—National Earthquake Information Center (NEIC) and International Seismological Center (ISC) station books—are revised several times per year. In addition, virtually every week, there is some new set of stations from an unconventional source that is required to be loaded into our database. The SITE rebuilding mechanism is just too cumbersome for this workflow.

Also, getting the SITE information into the database is only part of the problem. Once the SITE data are in place, we are still faced with a largely manual process of building/updating channel and response information. Of course, since there are potentially many channels per SITE, this process can be quite onerous.

Another issue that we face in loading SITE data is the rather frequent occurrence of conflicting station codes. We are frequently asked to load data obtained from a temporary deployment or from a cooperative agreement with a regional network operator. Often in these cases some station codes are already in use by the NEIC, or else a local code has been adopted for a NEIC station. It is possible to research each station code before attempting to load the station, but done manually, this is a somewhat tedious task. Fortunately, it is a process that can be automated.

There is now a wealth of information about seismic stations and instrumentation on the Web. Probably the most advanced access system for seismic metadata is the Data Handling Interface (DHI) framework currently implemented by the Incorporated Research Institutes for Seismology Data Management Center (IRIS DMC), the University of California at Berkeley Data Center and others. This framework allows direct programmatic access to metadata. With this system it is easy for a client to request site data, channel data, and instrument response data.

A client can also easily enumerate all the networks and stations known to the server. The principal limitation of this service (at least at the IRIS DMC) is that metadata is available only for stations for which archived waveform data are available.

In addition to IRIS, the NEIC, ISC, and Observatories and Research Facilities for European Seismology (ORFEUS) data centers have station data available via FTP, and static Web pages. For these sources, it is straightforward (although somewhat fragile) to write methods based on Web parsing and distillation that provide a programmatic query interface. We have written a Java interface for finding station metadata and have produced implementations for the above-mentioned data centers. This is one of the core pieces of the new Metadata Tool.

The Metadata Tool is an interactive station metadata search, entry, and editing tool. It introduces a considerable amount of automation into this process to ease the burden on the user. First, for several major sources of station metadata (NEIC, ISC, IRIS, ORFEUS) the tool automatically retrieves SITE data for new or modified stations with a single button click. For a station that a user is considering to enter manually, the tool will identify all known (within its universe of data centers) information about the station. For retrieved codes that are new to our system, and for which there are no nearby stations (either in our system or in one of the external databases), the software automatically populates both the STATION_METADATA schema entries and the LLNL.SITE entry. In the case of conflicts, the software presents all available information to the user, allowing the user to resolve the conflict. Steps taken to resolve conflicts are automatically recorded in the STATION_METADATA schema, along with user comments. After conflict resolution is complete, the LLNL SITE table is updated with the resulting new information.

For new entries with conflicting codes, the conflict is automatically recognized, and the user is prompted to remap the local code to the NEIC code or to a new non-conflicting code, as required. In these cases, the software also establishes a context remap that our other data loading software will use when loading waveforms or arrivals for the affected stations.

The Metadata Tool has three options for loading channel and sensor data. In the case in which IRIS has a record of the metadata, the user can just select the desired channels from a list and click a button to request the data from IRIS. This causes all necessary SITECHAN, SENSOR, and INSTRUMENT rows to be built and the response file to be installed in the correct location in our file system. For cases in which the user has a set of response files and knows what channels they are to be applied to, the software will build the required tables based on a minimal amount of user input and will copy the user-supplied response files to the correct place in our file system. The last supported case is a generic option. With this option, the user simply identifies the bands for which instrument responses are required. The software then builds generic response information from stored templates.

Instrument Response Conversion and Database Integration

We collect and maintain metadata for many seismic stations around the globe. Currently, we have over 14,000 distinct station/channel combinations for which we have instrument responses. The vast majority of those responses are from IRIS in Standard for the Exchange of Earthquake Date (SEED) format (SEED Reference Manual, 2009). The IRIS RESP format is used for all internal processing and analysis. For certain products we also maintain and produce a PAZFIR format from the original IRIS RESP formatted files (Figure 2). This section describes the conversion framework we developed for accomplishing this task and some of the challenges it addresses.

Because the IRIS RESP format allows for considerable variation in the blockettes that can be present in a response file and because usage of the blockettes has evolved with time, it hasn't always been possible to generate an equivalent PAZFIR for every possible RESP response. Thus, an integral part of our processing framework has been including a mechanism to test all converted responses. The response processing code is written primarily in Matlab, utilizing some of the parsing logic previously developed by George Randall and Richard Stead at Los Alamos National Laboratory. The code iterates over a directory of RESP files, and for each file, it uses the algorithms to convert the response to PAZFIR. Next it calls the Java JEvalResp code (Instrumental Software Technologies, Inc., 2009) to produce a Frequency-Amplitude-Phase (FAP) file from the original RESP file. The code then executes the Matlab version of the NDC unscaled_response code to produce a second FAP file constructed on the same set of

frequencies as the first. Finally, the code reads the two FAP files, converts them to complex vectors, and computes the residual. Depending on the size of the residual, the converted response is either accepted or rejected.

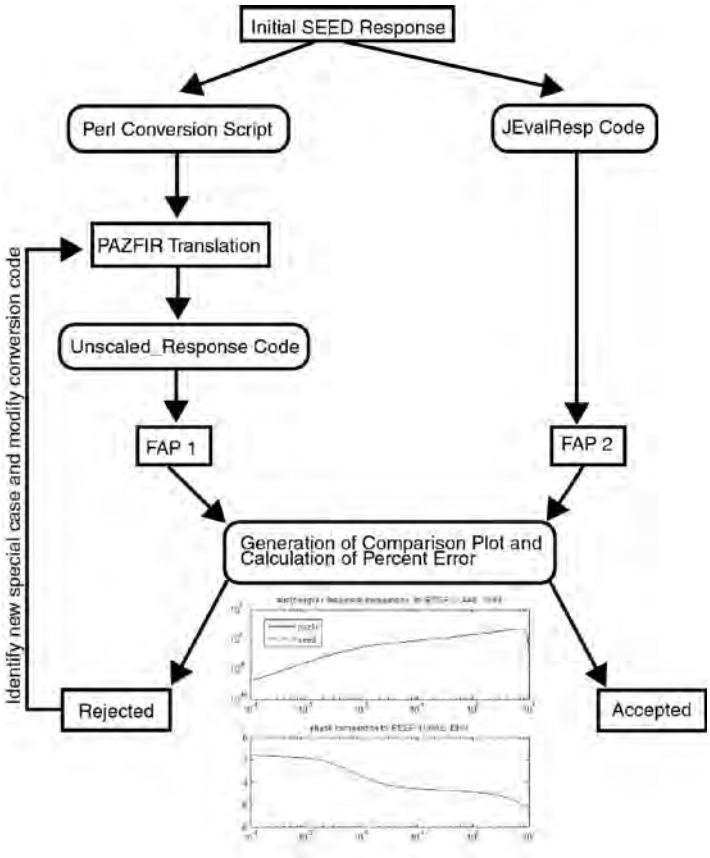

Figure 2. A schematic diagram of the response conversion framework that we have been using to convert IRIS RESP format responses into the PAZFIR format.

Once all the responses have been converted to a target format, the final step is to integrate them into the target database. If the source response is an IRIS SEED file, then it may in fact hold one or more individual response epochs. If that is the case, then special consideration is applied to break those out into individual target responses. As we integrate response epochs in a target database, we must ensure that they agree with existing station and channel epochs as well as ensure that there are no waveforms for which we miss instrument response coverage. Any discrepancy needs to be addressed to ensure we have accurate and consistent metadata across the various target database tables.

Waveform Retriever

The Waveform Retriever is the third piece of automation software that we have developed this year. It is a DHI client whose purpose is to retrieve all available event waveform segments for a defined set of stations and channels. Retrieved data are merged as required into our WFDISC table. The tool also verifies that all required metadata are in place before any new WFDISC rows are written and will make SITECHAN, SENSOR, and INSTRUMENT rows as required using methods developed for the Metadata Tool. The Waveform Retriever can be used with the IRIS BUD

server or with the archive server, so it is suitable for both special event analysis or for routine data loading. Our expectation is that we will develop a framework around this tool that will replace our current semi-automated system with a fully automated system.

Prototype Subspace Detection System

For many years our program has had interest in developing a correlation-based detection system that could operate on our many terabytes (and growing) collection of continuous and segmented waveforms. In addition to facilitating our understanding of the degree to which correlated seismicity exists on a global scale, the resulting database of categorized event segments could prove quite valuable in improving our travel time and seismic discriminant calibrations.

Primarily because of resource limitations, we have never implemented such a system. An additional factor in delaying our implementation of such a system has been the prohibitive amount of labor that would be required in building and maintaining the set of templates that would be required to process our entire holdings. This year, Ringdal et al. (these Proceedings) are investigating the possibility of developing an adaptive correlation detector framework. The goal was to develop a framework capable of creating its own templates with minimal supervision. The system that resulted from this effort was reasonably successful, and we are intending to adapt it to our requirements.

The framework developed for the BAA project can operate on an arbitrary number of channels from one or more stations. The system starts with a single STA/LTA or array power detector. Each detection by that detector results in the creation of a rank-one sub-space detector. For all subsequent segments, the sub-space detectors run in parallel with the STA/LTA detector. This policy of automatically spawning subspace detectors from unique STA/LTA triggers has worked well on the test sets processed so far, in part because the system is very fast. For example, approximately 89,000 seconds of 100-sps, single-channel Mt. St. Helens data were processed in 8.5 seconds. The great speed is due in part to the innovative decimation algorithm used (Harris and Paik, 2006).

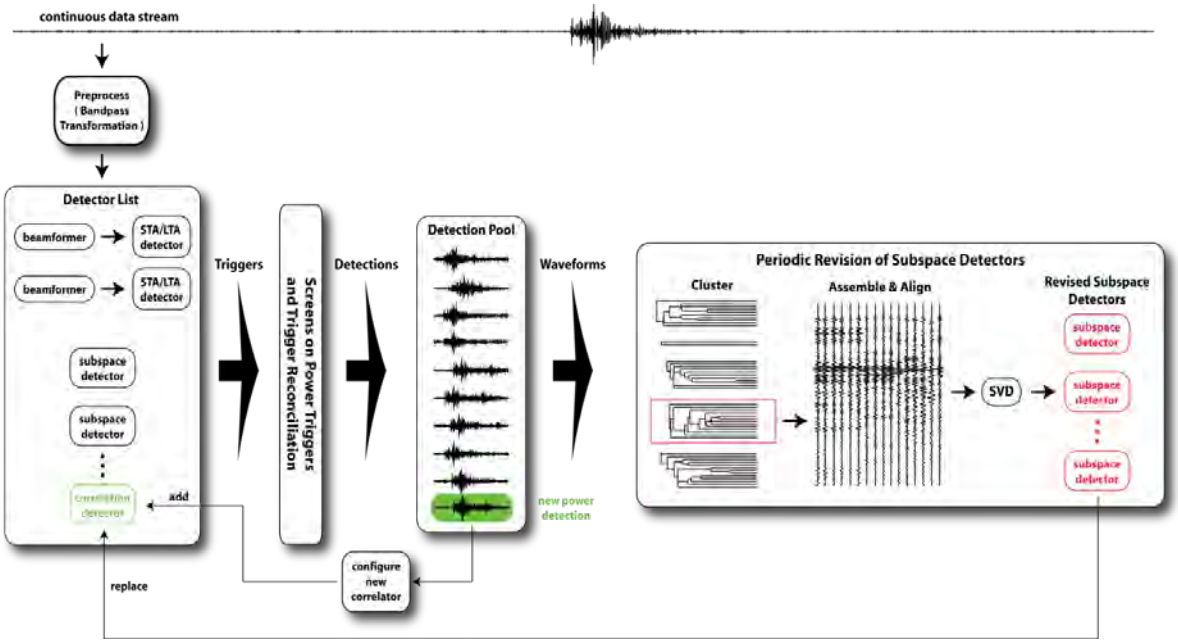

Figure 3. (from Figure 1 of Ringdal et al., these Proceedings) A framework for signal detection consisting of both conventional power detectors and correlation detectors generated automatically from a continuously updated pool of waveform templates. The conventional detectors are permanent members of the list and serve to detect signals for which previous observations do not exist. Periodically the system halts processing of the data stream and replaces the correlation detectors with subspace detectors built from clusters of waveforms in the detection pool. This function tends to check the growth of unlimited numbers of detectors. This research prototype operates without operator intervention, which practical systems would require.

Periodically, a supervisor component halts the detection process in order to coalesce the current set of subspace detectors. The reason for this step is that many signal segments may have waveforms that are similar to the templates for multiple rank-1 subspace detectors. In these cases, multiple detectors will declare detections. This complicates any post-detection association process. We refine the detector collection by extracting the detections for all automatically spawned detectors since the last refinement. All possible pair-wise correlations are computed for the set of signals followed by a complete-link cluster analysis. For each of the resulting clusters, the signals are aligned using their cross-correlation-derived shifts. For each set of aligned signals, a singular value decomposition (SVD) is calculated and a new subspace basis from ranks 1–3 is computed. Each basis is used to create a new subspace detector. At that point, all the input detections are assigned to the new detectors, and the detectors are added to the framework. Any input detectors left with no detections are then retired, after which the detection process is resumed. This process is outlined in Figure 3 above from (Harris, these Proceedings).

The framework built for the BAA research includes a database-hosted persistence layer that stores triggers, detections, and detector information. The detector information includes not only the parameters under which the detector operates, but also the subspace templates stored as BLOBs. This framework is a good start toward what will be required for deployment in a system to meet our program's needs. Additions to the framework will include the following:

- Index tables for both continuous and segmented waveforms. These tables will track both availability of data from scanning by detectors and records of what has already been scanned (required for restartability and work sharing among threads).
- A mechanism to correlate detections with events identified externally. This will support arrival correlation, identification of mine blast clusters, and general studies of correlated seismicity.
- A monitoring and dispatching system that is responsible for controlling detector threads, viewing the status of active detectors, and accessing cluster statistics.

CONCLUSIONS AND RECOMMENDATIONS

We present an overview of our software automation efforts and framework to address the problematic issues of consistent handling of the increasing volume of data, collaborative research efforts and researcher efficiency, and overall reduction of potential errors in the research process. By combining research-driven interfaces and workflows with graphics technologies and a database-centric information management system, coupled with scalable and extensible cluster-based computing, we have begun to leverage a high-performance computational framework to provide increased calibration capability. These new software and scientific automation initiatives will directly support our current mission, including rapid collection of raw and contextual seismic data used in research; provide efficient interfaces for researchers to measure and analyze data; and provide a framework for research dataset integration. The initiatives will improve time-critical data assimilation and coupled modeling and simulation capabilities necessary to efficiently complete seismic calibration tasks. This GNEMRD Program's scientific automation, engineering, and research will provide the robust hardware, software, and data infrastructure foundation for synergistic calibration efforts.

ACKNOWLEDGEMENTS

We acknowledge the assistance of the LLNL computer support unit in implementing and managing our computational infrastructure. We thank Jennifer Aquilino, Laura Long, and John Hernandez for their assistance in configuration and installation of our Linux cluster and HPC, storage, and desktop workstations. We also thank Chris Young for information he provided about the response processing code's execution of the Matlab version of the NDC unscaled_response code.

REFERENCES

Elliott. A., D. Dodge, M. Ganzberger, T. Hauk, E. Matzel, and S. Ruppert (2006). Enhancing seismic calibration research through software automation and scientific information management, in *Proceedings of the 28th Seismic Research Review: Ground-Based Nuclear Explosion Monitoring Technologies*, Vol. 2, pp. 967–975.

Ringdal, F., S. Gibbons, D. Harris, and D. Dodge (2009). Adaptive waveform correlation detectors for arrays: Algorithms for autonomous calibration, these Proceedings.

Harris, D. B. and T. Paik (2006). Subspace detectors: Efficient implementation, Lawrence Livermore National Laboratory report UCRL-TR-223177.

Hauk, T. F., D. A. Dodge, M. D. Ganzberger, E. M. Matzel, and S.D. Ruppert (2008). Enhancing seismic calibration research through software automation and scientific information management, in *Proceedings of the 30th Monitoring Research Review: Ground-Based Nuclear Explosion Monitoring Technologies*, LA-UR-08-05261, Vol. 2, pp. 978–987.

Instrumental Software Technologies, Inc. (2009). Home page, July 2: http://www.isti.com .

Ringdal, F., S. Gibbons, D. Harris, and D. Dodge (2009). Adaptive waveform correlation detectors for arrays: Algorithms for autonomous calibration, these Proceedings.

Ruppert, S., T. Hauk, J. O'Boyle, D. Dodge, and M. Moore (1999). Lawrence Livermore National Laboratory's Middle East and North Africa research database, in *Proceedings of the 21st Seismic Research Symposium: Technologies for Monitoring the Comprehensive Nuclear-Test-Ban Treaty*, LA-UR-99-4700, Vol. 1, pp. 234–242.

Ruppert, S. D., D. A. Dodge, A. B. Elliott, M. D. Ganzberger, T. F. Hauk, E. M. Matzel, and F. Ryall (2004). Enhancing seismic calibration research through software automation, *in Proceedings 26th Seismic Research Review: Trends in Nuclear Explosion Monitoring*, LA-UR-04-5801, Vol. 2, pp. 780–789

Ruppert S. D., D. A. Dodge, A. B. Elliott, M. D. Ganzberger, T. F. Hauk, E. M. Matzel, and F. Ryall (2005). Enhancing seismic calibration research through software automation and scientific information manage ment, in *Proceedings 27th Seismic Research Review: Ground-Based Nuclear Explosion Monitoring Technologies*, LA-UR-05-6407, Vol. 2, pp. 937–945.

Ruppert, S., D. Dodge, M. Ganzberger, T. Hauk, E. Matzel (2007). Enhancing seismic calibration research through software automation and scientific information management, in *Proceedings of the 29th Monitoring Research Review: Ground-Based Nuclear Explosion Monitoring Technologies*, LA-UR-07-5613, Vol. 2, pp. 965–974.

SEED Reference Manual, SEED Format Version 2.4 (2009). January–July 2: http://www.iris.edu/manuals/SEEDManual_V2.4.pfd .

USGS ENS Documentation (2009). Page last modified January 6 18:04:11 UTC, July 2: https://sslearthquake.usgs.gov/ens/?page=help.

Appendices

Acronyms, etc.

Acronym	Definition
ACZ	Antarctic Convergence Zone
ADC	analog-to-digital converter
AFRL	Air Force Research Laboratory
AFTAC	Air Force Technical Applications Center
AK135	seismic travel time model
ANFO	ammonium nitrate fuel oil
ANSS	Advanced National Seismic System
ARSA	Automated Radioxenon Sampler/Analyzer
BAA	Broad Agency Announcement
BEM	boundary element method
CC	correlation coefficient
CDSN	Chinese Digital Seismic Network
CLVD	compensated linear vector dipole
CMT	Harvard centroid moment tensor
CNDSN	Chinese National Digital Seismic Network
COTS	commercial off the shelf
CRUST2.0	crustal model (Bassin et al., 2000)
CSS	Center for Seismic Studies data format
CTBT	Comprehensive Nuclear-Test-Ban Treaty
CTBTO	Comprehensive Nuclear-Test-Ban Treaty Organization
CUB2.0	3D global models (Shapiro et al., 2002)
DC	double couple
DD	double difference
DMC	Data Management Center (IRIS)
DOB	depth of burial
DoD	Department of Defense
DOE	Department of Energy
DOF	degrees of freedom
DOS	Department of State
DSS	deep seismic sounding
ECM	Event Classification Matrix
EDR	Earthquake Data Reports - a USGS publication
EFT	earth-flattening transform
EGF	Empirical Green Function
EHB	Engdahl, E.R., van der Hilst, R. & Buland, R., 1998. Global teleseismic earthquake relocation with improved travel times and procedures for depth determination, *Bull. Seismol. Soc. Am* . 88, 722-743
ENS	Earthquake Notification Service (from USGS)
ETOPO	earth topographic (database)
EventID	tool to implement event discrimination (Hartse et al., 1997; Walter et al., 1999)
FD	finite difference
FE	finite element
FFT	Fast Fourier Transform
F-K	frequency wavenumber
FSU	Former Soviet Union
FWHM	full width at half maximum
G2S	ground-to-space

Acronym	Definition
GB	Gaussian beam
GII	Geophysical Institute of Israel
GIS	geographical information system
GMEL	Grid-search Multiple Event Location
GMT	generic mapping tool
GNEMRD	Ground-Based Nuclear Explosion Monitoring Research and Development Program
GRACE	gravity recovery and climate experiment
GSN	global seismographic network
GT	ground truth
GTx	ground truth information of accuracy x km
HE	high explosive
HPGe	high purity germanium
HPXe	high-pressure xenon
Hz	hertz
IASPEI	International Association of Seismology and Physics of the Earth's Interior
iasp91	standard earth model
IPGG	Institute of Petroleum Geology and Geophysics
IDA	International Deployment of Accelerometers
IDC	International Data Centre
IDG	Russian Institute for the Dynamics of the Geospheres
IIEES	International Institute of Earthquake Engineering and Seismology
IMS	International Monitoring System
InSAR	Interferometric Synthetic Aperture Radar
IRIS	Incorporated Research Institutions for Seismology
ISC	International Seismological Centre
ISTC	International Science and Technology Center
JVE	Soviet Joint Verification Experiment
KB	Knowledge Base
KBCIT	Knowledge Base Calibration Integration Tool
KMA	Korean Meteorological Administration
KNDC	Kazakhstan National Data Center
LANL	Los Alamos National Laboratory
LDEO	Lamont-Doherty Earth Observatory
LLNL	Lawrence Livermore National Laboratory
LNM	low-noise model
LVZ	low velocity zones
MatSeis	seismic analysis package developed by SNL using Matlab
mb	body wave magnitude
MDAC	magnitude and distance amplitude corrections
MEMS	microelectromechanical systems
MIT	Massachusetts Institute of Technology
Ms	surface wave magnitude
MSE	mean squared error
MSU	Michigan State University
Mw	moment magnitude
NA-22	Office of Nonproliferation Research and Development
NEIC	National Earthquake Information Center
NEM R&D	Nuclear Explosion Monitoring Research and Development
NISN	North Iraq Seismographic Network
Nm	newton-meters

Acronym	Definition
NNSA	National Nuclear Security Administration
NORSAR	Norwegian Seismic Array
NPE	Nonproliferation Experiment
NRL	Naval Research Laboratory
NSF	National Science Foundation
NTS	Nevada Test Site
ORFEUS	Observatories and Research Facilities for European Seismology
PASSCAL	Program for the Array Seismic Studies of the Continental Lithosphere
PDE	preliminary determination of epicenters
PE	parabolic equation
PNE	peaceful nuclear explosions
PNNL	Pacific Northwest National Laboratory
PPV	peak particle velocity
PSD	power spectral density
PSU	Penn State University
Q	Seismic Q factor (reciprocal of attenuation)
RASA	Radionuclide Aerosol Sampler Analyzer
REB	Reviewed Event Bulletin - an IDC report
RESP	SEED response files
RF	receiver functions
RMS	root mean square (errors)
ROC	receiver operating characteristic
RSTT	regional seismic travel-time model
SAC	seismic analysis code
SAIC	Science Applications International Corporation
SBIR	Small Business Innovation Research
SCEC	Southern California Earthquake Center
SCSN	Southern California Seismic Network
SEED	Standard for the Exchange of Earthquake Data
SEM	spectral element method
SLBM	Seismic Location Baseline Model
SLU	St. Louis University
SMDC	Space Missile Defense Command (Army)
SMU	Southern Methodist University
SNL	Sandia National Laboratories
SNR	signal-to-noise ratio
SOFAR Channel	SOund Fixing And Ranging - primary sound channel in the ocean
SPE	source phenomenology experiments
STA/LTA	short-term average/long-term average
STS	Semipalatinsk Test Site
SUS	signal underwater sound
t* (t-star)	A measure of the "damping" or attenuation along a path. T* is the ratio of the travel time along a ray path to the average Q (seismic "quality" factor) along it.
TOD	time of day
T-phase	hydroacoustic phase
UCSD	University of California, San Diego
UHV	ultra-high vacuum
UNE	underground nuclear explosions
USAEDS	United States Atomic Energy Detection System
USGS	United States Geological Survey

Acronym	Definition
USNDC	United States National Data Center
VOD	velocity of detonation
WWSSN	World Wide Standardized Seismographic Network
YSKP	Yellow Sea and Korean Peninsula

Guide to Seismic Phases

The change of seismic velocities within Earth, as well as the possibility of conversions between compressional (P) waves and shear (S) waves, results in many possible wave paths. Each path produces a separate seismic phase on seismograms. Seismic phases are described with one or more letters, each of which describes a part of the wave path. Upper case letters denote travel through a part of the earth (e.g. P or S), and lower case letters denote reflections from boundaries. A complete, standardized nomenclature for seismic wave paths is available at the web site: http://www.isc.ac.uk/doc/analysis/2003p13/index.html. This information has also been published [Storchak, D.A., J. Schweitzer, P. Bormann (2003), "The IASPEI Standard Seismic Phase List", Seismol. Res. Lett. 74, 6, 761-772], and a pdf file of this publication is available from the same web site.

In the verification context, wave propagation in Earth is divided into *teleseismic* (distances greater than 2000 kilometers) paths and *regional* (distances less than 2000 kilometers) paths.

Teleseismic Phases

In these plots, the seismic event is at the left, and seismic ray paths are shown to possible stations at several angular distances from the event.

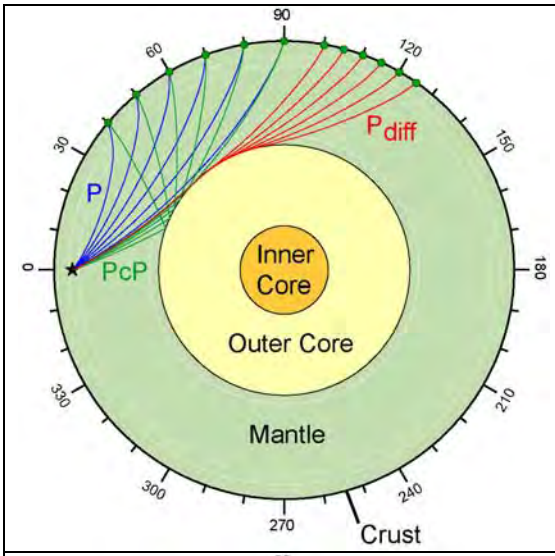

P A primary (compressional) wave that follows a simple path from event source to the station.

PcP A P wave that goes downward through the mantle (the first "P"), is reflected from the top of the outer core ("c") and goes upward through the mantle to the station (second "P").

P_{diff} A P wave that has been bent (diffracted) around the outer core boundary and arrives at a station in the ray "shadow" of the outer core.

S A secondary (shear) wave that follows a path similar to the P wave (not shown).

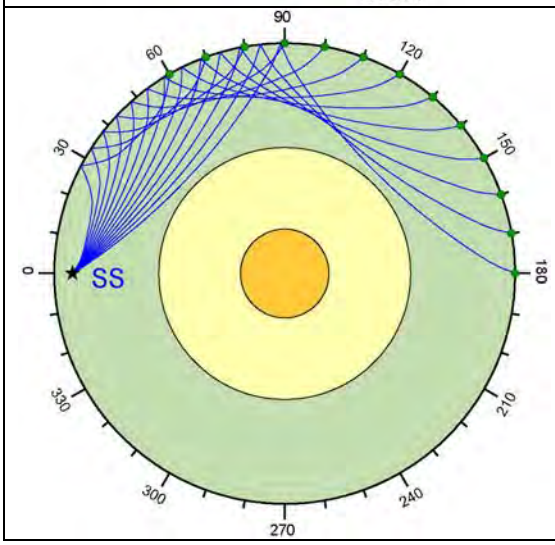

SS A shear wave that has traveled through the mantle ("S"), undergone one reflection from the underside of Earth's surface and traveled again through the mantle (second "S"). Unlike with most other reflected waves, there is no separate letter to denote the reflection at the surface; it is implicit.

PP A compressional wave that follows paths similar to those of SS (not shown).

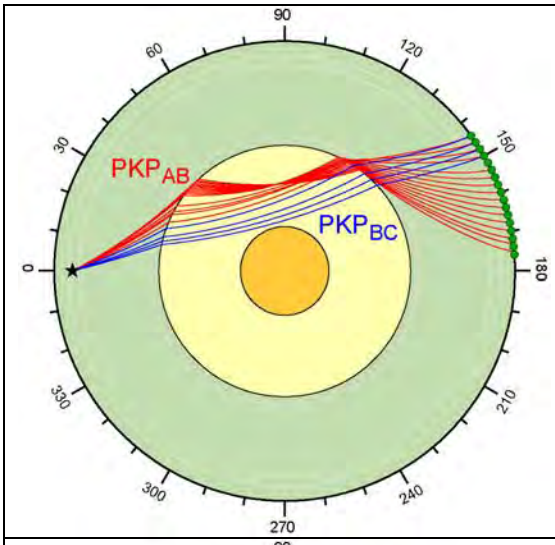	**PKP** A P wave that has traveled through the mantle ("P"), been transmitted across the mantle-outer core boundary and traveled through the outer core ("K"), transmitted back across the outer core-mantle boundary and traveled as a P wave to the station ("P"). Because of the large difference between the P wave velocity in the mantle and the outer core, this wave is bent (refracted) strongly at the boundary. Seismic waves can follow slightly different paths (labeled PKP_{AB}, PKP_{BC}) and still arrive at about the same time.
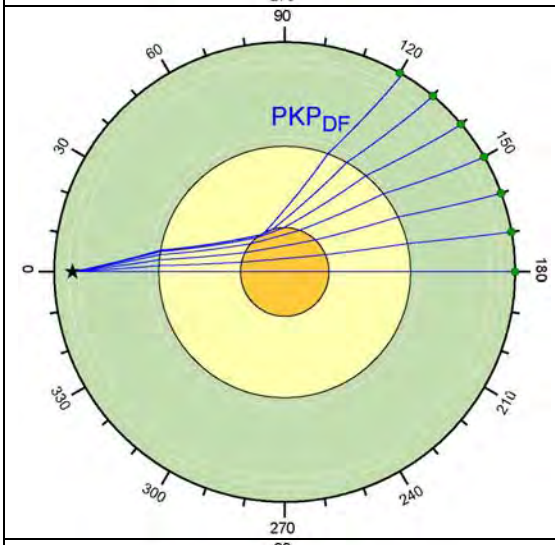	**PKIKP** A P wave that has traveled through the mantle ("P"), been transmitted across the mantle-outer core boundary ("K"), crossed the outer-core inner-core boundary and traveled through the inner core as a P wave ("I"), then followed a similar path in reverse to get from the inner core to the station (the second "KP"). An alternate name for this phase is PKP_{DF} (shown in the path illustration).
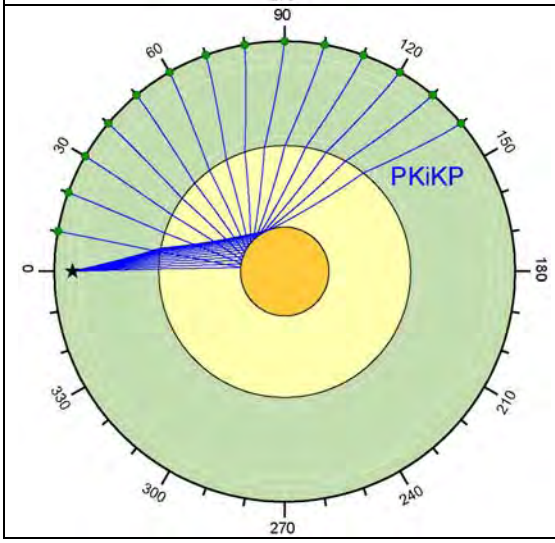	**PKiKP** This phase has followed a series of paths similar to the PKIKP phase, except it was reflected off the top of the inner core-outer core boundary (this is the "i" part of the path), rather than being transmitted through the inner core.

Figures courtesy of Ed Garnero, Arizona State University (http://garnero.asu.edu/research_images/index.html)

Depth Phases

A number of "depth" phases are referred to in the proceedings. The paths of these phases are nearly the same as P waves. The depth phases all result from a reflection from the Earth's surface near the epicenter of the event. The time delay between the P wave and the depth phase is proportional to the depth of the event (hence the term "depth" phase).

pP A P wave that started out upward from the source ("p"), reflected off the Earth's surface, and traveled to the station as a P wave ("P").

sP An S wave that started out upward from the source ("s"), reflected off the earth's surface and also converted to a P wave, which then traveled to the station as a P wave ("P").

pwP Similar to the pP phase. A P wave that started out upward from the source ("p"), reflected off the ocean surface ("w" - water) and traveled to the station as a P wave ("P").

Regional Phases

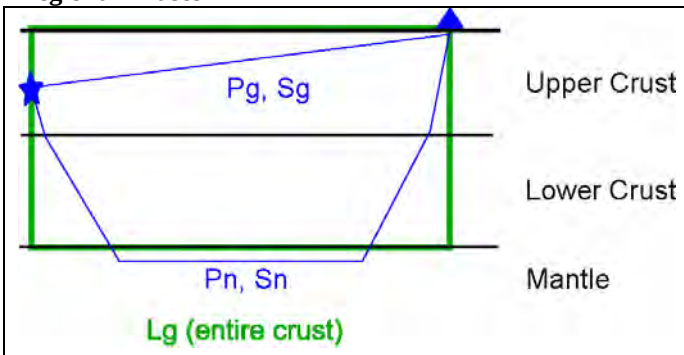

A highly simplified representation of the crust of Earth, which is seldom so simple and flat. Changes of crustal thickness and velocities can disrupt crustal phases, notably Lg.

Pg (Sg) At short event-station distances, an upgoing P (S) wave from a source in the upper crust (depicted here) or a P (S) wave bottoming in the upper crust. At larger distances the Pg phase includes arrivals resulting from multiple P-wave reverberations within the entire crust that propagate at a group velocity around 5.8 km/s.

Pn (Sn) A P (S) wave bottoming in the uppermost mantle or an upgoing P wave from a source in the uppermost mantle

Lg A wave group observed at larger regional distances and caused by superposition of multiple S-wave reverberations and S to P and/or P to S conversions inside the whole crust. The maximum energy travels with a group velocity around 3.5 km/s